Springer Series in Biomaterials Science and Engineering 5

Mei Zhang
Rajesh R. Naik
Liming Dai *Editors*

Carbon Nanomaterials for Biomedical Applications

Springer

Springer Series in Biomaterials Science and Engineering

Volume 5

Series Editor
Min Wang
Department of Mechanical Engineering, The University of Hong Kong, Hong Kong, China

The Springer Series in Biomaterials Science and Engineering addresses the manufacture, structure and properties, and applications of materials that are in contact with biological systems, temporarily or permanently. It deals with many aspects of modern biomaterials, from basic science to clinical applications, as well as host responses. It covers the whole spectrum of biomaterials – polymers, metals, glasses and ceramics, and composites/hybrids – and includes both biological materials (collagen, polysaccharides, biological apatites, etc.) and synthetic materials. The materials can be in different forms: single crystals, polycrystalline materials, particles, fibers/wires, coatings, non-porous materials, porous scaffolds, etc. New and developing areas of biomaterials, such as nano-biomaterials and diagnostic and therapeutic nanodevices, are also focuses in this series. Advanced analytical techniques that are applicable in R & D and theoretical methods and analyses for biomaterials are also important topics. Frontiers in nanomedicine, regenerative medicine and other rapidly advancing areas calling for great explorations are highly relevant. The Springer Series in Biomaterials Science and Engineering aims to provide critical reviews of important subjects in the field, publish new discoveries and significant progresses that have been made in both biomaterials development and the advancement of principles, theories and designs, and report cutting-edge research and relevant technologies. The individual volumes in the series are thematic. The goal of each volume is to give readers a comprehensive overview of an area where new knowledge has been gained and insights made. Significant topics in the area are dealt with in good depth and future directions are predicted on the basis of current developments. As a collection, the series provides authoritative works to a wide audience in academia, the research community, and industry.

More information about this series at http://www.springer.com/series/10955

Mei Zhang • Rajesh R. Naik • Liming Dai
Editors

Carbon Nanomaterials for Biomedical Applications

Springer

Editors
Mei Zhang
Department of Biomedical Engineering
Case Western Reserve University
Cleveland
Ohio
USA

Liming Dai
Department of Macromolecular Science
Case Western Reserve University
Cleveland
Ohio
USA

Rajesh R. Naik
Soft Matter Materials Branch
Air Force Research Laboratory
Dayton
Ohio
USA

ISSN 2195-0644 ISSN 2195-0652 (electronic)
Springer Series in Biomaterials Science and Engineering
ISBN 978-3-319-22860-0 ISBN 978-3-319-22861-7 (eBook)
DOI 10.1007/978-3-319-22861-7

Library of Congress Control Number: 2015952021

Springer Cham Heidelberg New York Dordrecht London

Printed on acid-free paper

Springer International Publishing AG Switzerland is part of Springer Science+Business Media (www.springer.com)

Contents

Contributors

Omar A. Banda Department of Biomedical Engineering, University of Delaware, Newark, DE, USA

Laurel M. Burk Department of Physics and Astronomy, The University of North Carolina at Chapel Hill, Chapel Hill, NC, USA

Dongsook Chang Department of Chemical Engineering, Massachusetts Institute of Technology, Cambridge, MA, USA

Rumei Cheng Institute of Advanced Materials for Nano-Bio Applications, School of Ophthalmology & Optometry, Wenzhou Medical University, Wenzhou, Zhejiang, China

Long Y. Chiang Department of Chemistry, Institute of Nanoscience Engineering Technology, University of Massachusetts Lowell, Lowell, MA, USA

Yuri Choi Department of Energy Engineering, School of Energy and Chemical Engineering, UNIST, Ulsan, Republic of Korea

Petr Cígler Laboratory of Synthetic Nanochemistry, Institute of Organic Chemistry and Biochemistry AS CR, v. v. i., Prague 6, Czech Republic

Liang Cui College of Chemistry, Chemical and Environmental Engineering, Laboratory of Fiber Materials and Modern Textile, the Growing Base for State Key Laboratory, Qingdao University, Qingdao, China

Erika Ellis Department of Biomedical Engineering, College of Engineering, University of Arkansas, Fayetteville, AR, USA

Michael R. Hamblin Wellman Center for Photomedicine, Massachusetts General Hospital, Boston, MA, USA

Department of Dermatology, Harvard Medical School, Boston, MA, USA

Harvard-MIT Division of Health Sciences and Technology, Cambridge, MA, USA

Jan Havlík Laboratory of Synthetic Nanochemistry, Institute of Organic Chemistry and Biochemistry AS CR, v. v. i., Prague 6, Czech Republic

Keely A. Heintz Department of Biomedical Engineering, University of Delaware, Newark, DE, USA

Jie Huang CAS Key Laboratory of Nano-Bio Interface, Suzhou Key Laboratory for Nanotheranostics, Division of Nanobiomedicine, Suzhou Institute of Nano-Tech and Nano-Bionics, Chinese Academy of Sciences, Suzhou, China

Liyi Huang Wellman Center for Photomedicine, Massachusetts General Hospital, Boston, MA, USA

Department of Infectious Diseases, Guangxi Medical University, Nanning, China

Yingying Huang Wellman Center for Photomedicine, Massachusetts General Hospital, Boston, MA, USA

Department of Dermatology, Harvard Medical School, Boston, MA, USA

Jakub Hývl Laboratory of Synthetic Nanochemistry, Institute of Organic Chemistry and Biochemistry AS CR, v. v. i., Prague 6, Czech Republic

Sha Jin Department of Biomedical Engineering, College of Engineering, University of Arkansas, Fayetteville, AR, USA

Yun Kyung Jung Department of Chemistry, School of Natural Science, Ulsan, Republic of Korea

Ramazan Kayacan Department of Mechanical Engineering, Süleyman Demirel University, Isparta, Turkey

Byeong-Su Kim Department of Chemistry, School of Natural Science, Ulsan, Republic of Korea

Department of Energy Engineering, School of Energy and Chemical Engineering, UNIST, Ulsan, Republic of Korea

Hyun-Jun Kim Department of Mechanical Engineering, Korea Advanced Institute of Science and Technology (KAIST), Daejeon, Republic of Korea

Yong Lin Kong Department of Mechanical and Aerospace Engineering, Princeton University, Princeton, NJ, USA

Cenker Küçükeşmen Department of Prosthodontics, Süleyman Demirel University School of Dentistry, Isparta, Turkey

Rajesh Kumar Department of Mechanical Engineering, Korea Advanced Institute of Science and Technology (KAIST), Daejeon, Republic of Korea

Christopher N. Lam Department of Chemical Engineering, Massachusetts Institute of Technology, Cambridge, MA, USA

Bruce P. Lee Department of Biomedical Engineering, Michigan Technological University, Houghton, MI, USA

Yueh Z. Lee Department of Radiology, The University of North Carolina at Chapel Hill, Chapel Hill, NC, USA

Jun Li Department of Chemistry, Kansas State University, Manhattan, KS, USA

Yuting Li Department of Biomedical Engineering, Michigan Technological University, Houghton, MI, USA

Jingquan Liu College of Chemistry, Chemical and Environmental Engineering, Laboratory of Fiber Materials and Modern Textile, the Growing Base for State Key Laboratory, Qingdao University, Qingdao, China

Dusan Losic School of Chemical Engineering, The University of Adelaide, Adelaide, SA, Australia

Jianping Lu Department of Physics and Astronomy, The University of North Carolina at Chapel Hill, Chapel Hill, NC, USA

Yufei Ma CAS Key Laboratory of Nano-Bio Interface, Suzhou Key Laboratory for Nanotheranostics, Division of Nanobiomedicine, Suzhou Institute of Nano-Tech and Nano-Bionics, Chinese Academy of Sciences, Suzhou, China

Foram Ranjeet Madiyar Department of Chemistry, Kansas State University, Manhattan, KS, USA

Embry–Riddle Aeronautical University, Daytona Beach, FL, USA

Noah Malmstadt Mork Family Department of Chemical Engineering and Materials Science, University of Southern California, Los Angeles, USA

Manu S. Mannoor Department of Mechanical and Aerospace Engineering, Princeton University, Princeton, NJ, USA

Michael C. McAlpine Department of Mechanical and Aerospace Engineering, Princeton University, Princeton, NJ, USA

Pawel Mroz Wellman Center for Photomedicine, Massachusetts General Hospital, Boston, MA, USA

Department of Dermatology, Harvard Medical School, Boston, MA, USA

Eva Muchová Laboratory of Synthetic Nanochemistry, Institute of Organic Chemistry and Biochemistry AS CR, v. v. i., Prague 6, Czech Republic

Hetty T. Nie Department of Biomedical Engineering, University of Delaware, Newark, DE, USA

Il-Kwon Oh Department of Mechanical Engineering, Korea Advanced Institute of Science and Technology (KAIST), Daejeon, Republic of Korea

Bradley D. Olsen Department of Chemical Engineering, Massachusetts Institute of Technology, Cambridge, MA, USA

Helena Raabová Laboratory of Synthetic Nanochemistry, Institute of Organic Chemistry and Biochemistry AS CR, v. v. i., Prague 6, Czech Republic

Ivan Řehoř Laboratory of Synthetic Nanochemistry, Institute of Organic Chemistry and Biochemistry AS CR, v. v. i., Prague 6, Czech Republic

Kristina Runas Mork Family Department of Chemical Engineering and Materials Science, University of Southern California, Los Angeles, USA

Amanda M. Schrand Air Force Research Laboratory, Munitions Directorate Eglin AFB, Eglin, FL, USA

Sulbha K. Sharma Wellman Center for Photomedicine, Massachusetts General Hospital, Boston, MA, USA

He Shen CAS Key Laboratory of Nano-Bio Interface, Suzhou Key Laboratory for Nanotheranostics, Division of Nanobiomedicine, Suzhou Institute of Nano-Tech and Nano-Bionics, Chinese Academy of Sciences, Suzhou, China

Donglu Shi The Materials Science and Engineering Program, University of Cincinnati, Cincinnati, OH, USA

John H. Slater Department of Biomedical Engineering, University of Delaware, Newark, DE, USA

Jitka Šlegerová Laboratory of Synthetic Nanochemistry, Institute of Organic Chemistry and Biochemistry AS CR, v. v. i., Prague 6, Czech Republic

Saijie Song CAS Key Laboratory of Nano-Bio Interface, Suzhou Key Laboratory for Nanotheranostics, Division of Nanobiomedicine, Suzhou Institute of Nano-Tech and Nano-Bionics, Chinese Academy of Sciences, Suzhou, China

Felipe F. Sperandio Wellman Center for Photomedicine, Massachusetts General Hospital, Boston, MA, USA

Instituto de Ciencias Biomedicas, Universidade Federal de Alfenas, Alfenas, MG, Brazil

LuxiZhang Swisher Department of Chemistry, Kansas State University, Manhattan, KS, USA

Feng Wang Department of Physics and TcSUH, University of Houston, Houston, TX, USA

Min Wang Department of Chemistry, Institute of Nanoscience Engineering Technology, University of Massachusetts Lowell, Lowell, MA, USA

Russell Wang Department of Comprehensive Care, Case Western Reserve University, School of Dental Medicine, Cleveland, OH, USA

Ye Wang School of Chemical Engineering, The University of Adelaide, Adelaide, SA, Australia

Yilong Wang The Institute for Biomedical Engineering and Nano Science, Tongji University School of Medicine, Shanghai, China

Yuhua Xue Institute of Advanced Materials for Nano-Bio Applications, School of Ophthalmology & Optometry, Wenzhou Medical University, Wenzhou, Zhejiang, China

Huantong Yao Department of Biomedical Engineering, College of Engineering, University of Arkansas, Fayetteville, AR, USA

Mengxin Zhang CAS Key Laboratory of Nano-Bio Interface, Suzhou Key Laboratory for Nanotheranostics, Division of Nanobiomedicine, Suzhou Institute of Nano-Tech and Nano-Bionics, Chinese Academy of Sciences, Suzhou, China

Zhijun Zhang CAS Key Laboratory of Nano-Bio Interface, Suzhou Key Laboratory for Nanotheranostics, Division of Nanobiomedicine, Suzhou Institute of Nano-Tech and Nano-Bionics, Chinese Academy of Sciences, Suzhou, China

Otto Zhou Physics and Astronomy, Lineberger Comprehensive Cancer Center, The University of North Carolina at Chapel Hill, Chapel Hill, NC, USA

Part I
Carbon Nanomaterials for Biomedical Applications

Chapter 1
Perspectives on Carbon Nanomaterials in Medicine Based upon Physicochemical Properties: Nanotubes, Nanodiamonds, and Carbon Nanobombs

Amanda M. Schrand

1.1 Introduction

Carbon nanotubes (CNTs) have been used in a variety of engineering [1] and biomedical applications [2] over the past decade as drug, protein, and nucleic acid delivery tools [3, 4] for the destruction of cancer cells [5, 6], diagnostics [7], and as noninvasive and highly sensitive imaging aids (due to their intrinsic near-infrared fluorescence and Raman and photoacoustic signals) [8]. The rich surface chemistry of nanocarbon materials lends itself to numerous modifications including the attachment of specific drugs such as the antifungal drug amphotericin B and the antitumor agent methotrexate [4], deoxyribonucleic acid (DNA) [9, 10], and polyethylene glycol (PEG) [11]. The term "theranostics" was coined to emphasize both the therapeutic and diagnostic capability of CNTs and has been applied in the context of oncology (the study of cancer) and nanomedicine [12] with CNT-mediated targeted hyperthermia becoming one mechanism of action [13]. Carbon nanostructures also span fields as diverse as medicinal biochips [14], new high-performance platforms for magnetic resonance (MR) molecular imaging [15], tissue engineering [16], and neuroscience [17]. One of the rigorous challenges is to ensure the biocompatibility and potential for biodegradability of carbon nanomaterials [18]. So far, the results are inconclusive to the short- and long-term beneficial and detrimental effects at the single cell and body system levels (Fig. 1.1), although many studies have been performed [20–23]. For the purpose of simplicity, this chapter does not attempt to include the multitude of carbon nanomaterials available for study such as carbon dots, C60 fullerenes, etc., but rather focuses on one of the newest classes of popular carbon nanomaterials: nanodiamonds (NDs).

A. M. Schrand (✉)
Air Force Research Laboratory, Munitions Directorate Eglin AFB, Eglin, FL 32542, USA
e-mail: Amanda.schrand@eglin.af.mil

M. Zhang et al. (eds.), *Carbon Nanomaterials for Biomedical Applications,*
Springer Series in Biomaterials Science and Engineering 5,
DOI 10.1007/978-3-319-22861-7_1

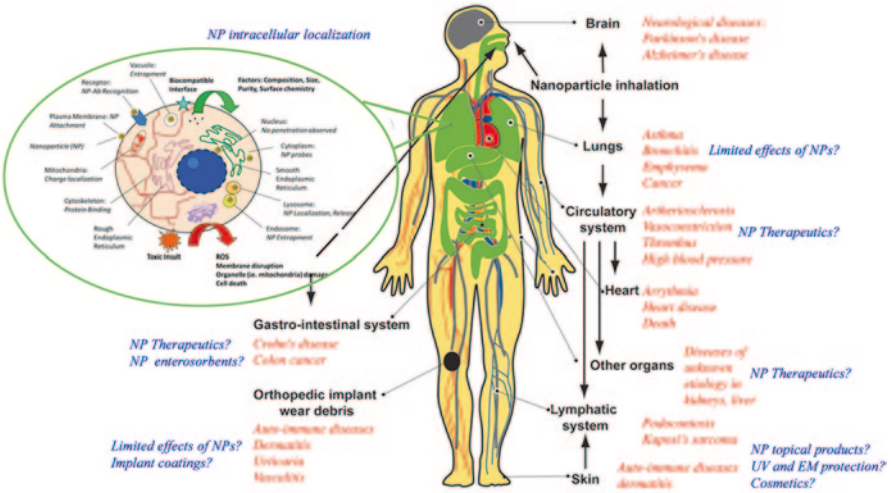

Fig. 1.1 Summary of nanoparticle interactions within a single cell and systems of the body. (Adapted from [19, 70]). *NP-Ab* nanoparticle-antibody, *UV* ultraviolet, *EM* electromagnetic, *ROS* reactive oxygen species

1.2 Differential Toxicity of Carbon Nanomaterials

In contrast to the historical perspective that carbon-based materials present minimal reactivity toward cells of the body [24], nano-sized carbons are characterized by very small sizes, high surface-to-volume ratios, and reactive surface chemistries, which can impact cellular permeability and dynamics [25, 26]. However, not all carbon-based nanoparticles (NPs) display similar biocompatibility profiles. One common assay utilized to assess cytotoxicity in cell cultures is the 3-(4,5-Dimethylthiazol-2-yl)-5-(3-Carboxymethoxyphenyl)-2-(4-Sulfophenyl)-2H-Tetrazolium (MTS) assay [82]. This assay consists of a cell-permeable, soluble tetrazolium salt and electron coupling reagent (phenazine methosulfate) that is added to the cellular environment after the appropriate dosing periods. During incubation with MTS, the dehydrogenase enzymes present within the mitochondria of healthy cells reduce the MTS into a dark purple, water-soluble formazan compound, which can be quantified with a microplate reader at 490 nm. Absorbance values measured at zero incubation time are subtracted from the final readings to account for background absorbance due to the NPs or the solution. The changes are compared to controls (cells not exposed to NPs), and percent reduction is calculated.

Many examples of this assay can be found in the literature with regard to carbon nanomaterial cell culture studies. For example, Schrand et al. demonstrated differential biocompatibility between neuronal and lung cell lines after exposure to aqueous suspensions of carbon NPs (ND; carbon black, CB; multi-walled nanotube, MWNT; single-walled nanotube, SWNT) at concentrations from 25 to 100 μg/mL for 24 h with the 3-(4,5-dimethylthiazol-2-yl)-2,5-diphenyltetrazolium bromide (MTT) assay [27]. The trend for biocompatibility was ND > CB > MWNT > SWNT. The lung cells

(macrophages) were more greatly affected by the presence of carbon NPs generating up to five times the amount of reactive oxygen species (ROS) compared to the neuroblastoma cells after exposure to either MWNTs or SWNTs. However, there was a lack of ROS generation from either cell line after incubation with the NDs as well as intact mitochondrial membranes further supporting the low toxicity of NDs. These studies suggest a complex role for cell-specific responses and purity (i.e., residual catalyst content) in the inflammatory response as well as other factors that may be related to dispersion/aggregation dynamics. By comparison, the incubation of fluorescently labeled NDs (5–100 μg/mL, 24 h) with three different cell types revealed no significant differences in biocompatibility compared to control cells (MTT assay). The different cell lines were representative of both rodent and human cell lines including murine neuroblastoma (N2A), human skin cells (HaCat), and rat alveolar macrophage (CRL-2192). Additionally, morphological examination did not show any alterations in cell shape compared to controls. Another example is the work by Zhu et al. on the cytotoxicity assessment of human lung macrophages after exposure to unpurified or acid-purified multi-walled CNTs [28]. In addition to the MTS assay, the cells were assessed for the generation of ROS, morphological changes, and uptake. The results demonstrate that multi-walled CNTs can accumulate in human lung macrophage cells to different degrees based on their surface chemistry where MWNT–COOH reduce cell viability in a dose-dependent manner under the given experimental conditions (5–50 μg/mL, 2–24 h). However, images of individual cells can demonstrate morphological changes even at the lowest concentrations.

Although there has been no direct link between the primary dimension of carbon NPs and their resultant biocompatibility, Jia et al. [29] found that the toxicity of carbon NPs followed a mass sequence of biocompatibility with C60 > quartz > MWNT > SWNT in alveolar macrophages after exposure for 6 h. By comparison, Grabinski et al. [30] found that larger carbon fibers or carbon nanofibers were more biocompatible than MWNTs or SWNTs in mouse keratinocytes (HEL-30) [30]. Smaller-sized CB (14 nm) compared to larger-sized CB (260 nm) increased the production of ROS and macrophage inflammatory protein-2 messenger ribonucleic acid (MIP2 mRNA) expression [31, 32]. In contrast, other studies have shown that smaller or shorter CNTs were more biocompatible than larger-sized CNTs or carbon fibers [33–36].

The examination of carbon NPs with regard to both size and surface chemistry was studied by Liu et al. [37]. They examined the biocompatibility of carboxylated NDs (cNDs) and uncarboxylated NDs and CNTs in human lung A549 epithelial cells and HFL-1 normal fibroblasts [37]. Treatment with ND or cND (5 and 100 nm) at concentrations ranging from 0.1 to 100 μg/mL for 4 h followed by recovery for 24–48 h did not affect the overall cell morphology including the cytoskeleton or nuclei, did not reduce cell viability per the MTT assay, and did not alter the expression of protein extracts via sodium dodecyl sulfate-polyacrylamide gel electrophoresis (SDS-PAGE) analysis. The smaller 5-nm cNDs slightly reduced viability compared to the larger 100-nm cNDs but with no significance. In contrast, uncarboxylated CNTs (10–50 nm and 100–200 nm) significantly decreased cell viability at concentrations as low as 0.1 μg/mL in A549 cells or 1 μg/mL in

HFL-1 cells, compared to concentrations greater than 10 μg/mL for carboxylated CNTs (cCNTs). There was also a more pronounced cytotoxic effect for the longer 100–200-nm cCNTs compared to the shorter 10–50-nm cCNTs [37].

Therefore, to date, research shows that when compared side by side to other carbon nanomaterials (CNTs, fullerenes), NDs are consistently better tolerated by cells [27, 38, 39]. One major factor in the variability between studies is the purity of the samples. Impurities (or contaminants) such as residual metal catalysts (i.e., Fe, Ni, Co) in CNTs [40–57] and other materials containing Fe and transition metals [58–60] are now routinely screened prior to and during toxicity studies. Although NDs are not synthesized via metal catalysts, metal contaminants are introduced from the containers used for the detonation of ND, which must be removed by post-synthesis purification procedures [61]. For example, some initial ND powders contained ~5.7% Fe, which was reduced to ~1.2% Fe [62]. Additional methods for cell culture analysis of carbon and metal-based NPs for health- and safety-related assessment include a variety of biochemical and microscopic techniques [63–68], for example, modification of existing procedures such as DNA damage with microfluidic electrophoretic separation technology [69]. For an overview of methods for studying biocompatibility at the cellular and system level as well as a historical perspective on diamond particle biocompatibility, please see previous work [66, 70–73].

1.3 Considerations for Nanodiamond in Medicinal Applications

There has been an explosion of potential applications for NDs due to their large-scale production [74] and commercial availability (Diamond Center, PlasmaChem) in designer forms. However, it is the purity, fluorescence, variety of surface modifications, and high biocompatibility that have contributed to their popularity among other carbon NPs. Indeed, NDs can maintain most, if not all, of their inherently desirable properties upon surface functionalization (such as fluorescence, biocompatibility, etc.) in contrast to many other forms of carbon or more traditional NPs such as semiconductor quantum dots (see recent reviews by Mochalin et al., Schrand et al., Ho, Xing, and Dai [66, 71, 75–77]). Furthermore, they can be imaged with multiple modalities including Raman spectroscopy, fluorescent confocal microscopy, electron microscopy, etc. [38, 78–81].

1.4 Nanodiamond Property–Biocompatibility Relationship: In Vitro Studies

Although the majority of the literature, including our previous work [27, 39, 66, 67, 70–72, 80–83], has demonstrated high biocompatibility for different types of NDs, there are some studies that have shown negative effects in blood cells and deeper

at the genomic level [83, 84]. Therefore, smaller, nano-sized diamonds are being scrutinized for biological interactions due to their superior physicochemical properties for incorporation into cutting-edge biomedical innovations (i.e., nano-sized therapeutic carriers, probes, labels; Schrand et al. 2009; [72]).

By definition, well-purified NDs are almost perfect crystalline structures with negligible fractions of non-diamond carbon. They consist of polyhedra with a diamond core built up of sp^3 carbon, which may be partially coated by a graphitic shell or amorphous carbon with dangling bonds terminated by various functional groups. An additional characteristic feature of NDs is nitrogen impurities (up to 2–3 wt%), which can form complexes in the core of ND particles, and the presence of twins and grain boundaries in the crystallites [75]. A summary of ND properties for consideration in biocompatibility or toxicity studies is presented in Table 1.1.

Table 1.1 Properties of nanodiamonds (NDs) for biological consideration. (Adapted with permission from Schrand et al. 2009)

Physicochemical properties of NDs for biomedical applications		
Property	Characteristics	Application
Structural	Small size of primary monocrystalline particles (~4–5 nm)	Unique interactions with bio-compounds on same size scale
	Availability of variable sizes and narrow size fractions	Diverse applications based on size (UV protection, photonic structures)
	Different forms (i.e., particulate, coating/film, substrate)	Tailorability for different bio-environments
	Large specific surface area (300–400 m^2/g)	High affinity/adsorption capacity for binding proteins, enzymes; enterosorbents, purification
	Low porosity/permeability of films	Component of small pore membranes for ultrafiltration or lion-porous membrane for extended time storage
	High specific gravity (3.5 g/cm^2)	Dense structure for solid phase support
Chemical	Chemically resistant to degradation/corrosion, pH stability	Implants, coatings, films, substrates for cell growth
	High chemical purity	Biocompatible interface
	Possible sp^2 carbon shells	Adsorption of hydrophobic biomolecules, EM radiation absorption for thermal therapy
	Numerous oxygen-containing groups on surface	Hydrophilic, water-dispersible suspensions for further coupling to bio-entities/into other matrices
	Ease of surface functionalization (chemical, photochemical, mechanochemical, enzymatic, plasma- and laser-assisted methods)	Attachment of drugs and biomolecules; polymer, metal composite materials
	Radiation/ozone resistance	X-ray, protective coatings and surfaces, detection devices
	Large number of unpaired electrons on the surface	Free radical scavenger/multiple radical donor, electrochemistry

Table 1.1 (continued)

Physicochemical properties of NDs for biomedical applications		
Property	Characteristics	Application
Biological	High biocompatibility, low toxicity	Cell, tissue, organ, and organism studies
	Readily bind bioactive substances (i.e., proteins, DNA, etc.) with retained functionality	Targeted therapeutics/molecules, labels, hormones, inhibitors, antigens, drugs
	Solid phase carrier	Multiple cell delivery methods including ballistic, transfection
Optical	Photoluminescence: non-photobleaching, nonblinking, originates from N-vacancy defects	Fluorescent probe and imaging tool for biolabeling
	High refractive index, optical transparency	Scattering optical label for live cells, possible UV sunscreen
	Unique Raman spectral signal	Nondestructive detection with living cells
Mechanical	High strength and hardness	Composite additive, possible cell lysis, ballistic delivery to tissues and cells, autoclaving
	Fine abrasive	Homogenization of composites/cosmetics, skin polishing
Electrochemical	Electrochemical plating with metals	Improves durability, life of medical instruments/implants
	Redox behavior of DND	Chem/biosensors: potential production of ROS
Thermal	Can withstand very high/low temperatures	Sterilization (i.e., autoclave), composite manufacturing, liquid nitrogen storage
Technical	Inexpensive, mass production (i.e., detonation synthesis)	Commercial availability
	Exist naturally in meteorites and laboratory synthesized by diverse techniques	Availability of various quality/purity samples

NDs nanodiamonds, *UV* ultraviolet, *ROS* reactive oxygen species, *DND* detonation nanodiamond, *EM* electromagnetic, *DNA* deoxyribonucleic acid, *N* nitrogen

1.4.1 Nanodiamond Size Studies

Investigations into size-dependent biological behavior of NDs have not proven any measurable differences. For example, an early study on ND biocompatibility by Yu et al. [85] investigated relatively large synthetic abrasive diamond powders (type 1b, 100 nm, Micron+(Micro Diamond Abrasive) MDA, synthesized by Element Six, acid purified) that were proton beam irradiated to introduce very stable, bright, and internal fluorescent nitrogen vacancy defects [85]. They found very high viability, indicative of in vitro biocompatibility, with human kidney cells (293T) after 3 h of incubation at concentrations up to 400 μg/mL assessed with the MTT assay. Smaller, nonfluorescent, detonation NDs (2–10 nm, supplied from the NanoCarbon Research Institute Inc.) at lower maximum concentrations (≤100 μg/mL) over

longer periods of time (typically 24 h) were studied by Schrand et al. from 2007 to 2009 [27, 39, 83] (Schrand et al. 2009) and [86] in other cell lines. Liu et al. found that there were slight, but not significant, reductions in cell viability after incubation with smaller 5-nm cNDs compared to larger 100-nm cNDs [36].

1.4.2 Influence of Nanodiamond Surface Chemistry and Contaminants

The effects of processing techniques including, but not limited to oxidation procedures, aggregate disintegration, high-temperature heat treatment, etc. on NDs should be evaluated with regard to alterations in the surface chemistry, which may impact on cellular functions [34, 87–89]. For example, the impact of surface chemistry on 2–10-nm detonation-produced NDs, purified with strong acids or bases, on cell viability was examined by Schrand et al. [38]. At concentrations up to 100 μg/mL, all of the NDs, containing surface groups such as –COOH, –COONa and –SO_3Na, were nontoxic to a variety of cell types including neuroblastomas, macrophages, PC-12 cells, and keratinocytes after 24 h with the MTT assay. The most noticeable difference between two cell types (neuroblastoma and macrophage) was in the amount of carbon NPs internalized by the cells, which was likely related to the greater decreased viability and increased ROS for the macrophages. The inherent function of the macrophages to initiate an inflammatory response or programmed cell death may also occur to a greater extent in this immune cell. However, despite these proposed cell-specific differences, there was a lack of ROS generation and a retention of mitochondrial membrane integrity in cell lines incubated with NDs.

Studies on the biocompatibility of acid-purified NDs in RAW 264.7 murine macrophages by Huang et al. monitored the response of genes involved in inflammation including the production of three different cytokines: interleukin-6 (IL-6), tumor necrosis factor α (TNFα), nitric oxide synthase (iNOS), and the Bcl-x gene involved in apoptotic behavior/toxicity [86]. After 24–72 h of incubation with 100-μg/mL NDs, no significant change in the expression of the cytokines was detected with the real-time polymerase chain reaction (RT-PCR) compared to controls. Additional experiments examining morphological changes and DNA fragmentation in macrophages as well as viability with the MTT assay in HT-29 human colorectal adenocarcinoma cells revealed the high innate biocompatibility of the NDs.

In addition to surface chemistry alterations, other contaminants to the underlying elemental composition can include residual ceramic or other abraded material fragments from mechanical (bead milling) or ultrasonic processing for aggregate disruption (i.e., ZrO_2 in ND from stir-media milling for dispersion), fragments of graphitic/amorphous structure at grain boundaries, and approximately 2 wt% fullerene-like conjugated sp^2 carbon [90–92]. More recently, there has been progress in dry milling with water-soluble salts and sugars, which show promise as biocompatible and environmentally friendly alternatives for aggregate disruption [93]. Other considerations for effects on biocompatibility include various levels of nitrogen doping [94] or residual solvents from dispersion processes, which may be inher-

ently toxic such as tetrahydrofurane or dimethyl sulfoxide [95, 96]. Functionalization of NDs with biomolecules for biological applications did not seem to induce cytotoxicity in Chinese hamster ovary (CHO) cells, and these functionalized NDs retained their ability to localize intracellularly [97].

Of concern, however, are some other studies, which have suggested that NDs may possess some deleterious effects toward biological organisms. For example, Silbajoris et al. [98] found that ND particles can induce up to 14-fold increases in IL-8 expression in human airway epithelial cells. IL-8 is a chemokine involved in the inflammatory response; this upregulation implies that the ND particles retain the ability to trigger an inflammatory response when inhaled. Moreover, embryonic stem cells have been shown to yield moderately increased expression of DNA proteins, such as p53 and MOGG-1, when they are incubated with NDs [84]. This response was more pronounced when the cells were exposed to oxidized NDs rather than pure NDs, implying a role of surface chemistry. Still, these levels are much lower than those observed when cells were incubated with MWNTs, suggesting that NDs may still be the most biocompatible and promising relative to other forms of NPs.

Studies with stable and fluorescent rhodamine-labeled NDs incubated with both animal and human cell lines did not induce morphological changes and maintained high viabilities at concentrations up to 100 μg/mL [38, 80, 81]. Studies with fluorescently labeled NDs by Vaijayanthimala et al. [99] also did not implicate any toxicity at exposures for 5 h at concentrations as high as 100–200 μg/mL across multiple cytotoxicity endpoints. The mechanisms of uptake and intracellular localization are examined in greater detail in the following section.

1.4.3 Nanodiamond Intracellular Localization and Kinetics: An Important Consideration for Long-Term Biocompatibility

The kinetics of both nonfluorescent and fluorescent ND (FND) entry and localization inside cells has been examined with microscopic, radiolabeling, and spectroscopic techniques. Internalized ND aggregates are localized within the cytoplasm but not within the nucleus [38, 80, 81, 85, 100, 101]. Recently, the authors of this review and other groups [99, 102] have addressed this issue by using FNDs to track their localization into cells based on time and concentration [80, 81]. Schrand et al. [80] initially elaborated upon the preparation of cells for assessing ultrastructural localization of NPs with transmission electron microscopy (TEM) to show the time-dependent uptake of NDs in neuro-2A (N2A) cells. Follow-on studies with FNDs and both electron and fluorescent microscopy were performed to investigate the time-dependent uptake of ND into cells as well as determine their localization [81]. The TEM studies enabled both verification of uptake and higher-resolution subcellular localization of NDs. Images in Fig. 1.2a, b show the FNDs outside cells (white arrows), internalized into membrane-bound structures resembling early endosomes inside cells (black arrows) as well as free in the cytoplasm after lysosomal processing (Fig. 1.2b).

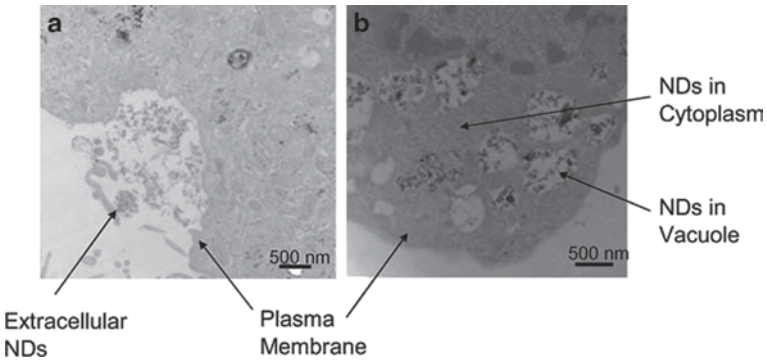

Fig. 1.2 Internalization and localization of nanodiamonds *(NDs)* in neuroblastoma (neuro-2A, N2A) cells. **a**, **b** Transmission electron microscopy (TEM) images of thin sections of N2A showing *NDs* interfacing with the plasma membrane as well as internalized into the cytoplasm and vacuoles. (Adapted with permission from [80])

Because an endocytic mechanism appeared to be at work, the co-localization of ND in distinct subcellular locations was probed with organelle-specific stains for early endosomes and lysosomes in a chronological study [81]. Confirmation of the increased uptake of NDs over time was demonstrated with confocal microscopy after static incubation with 10 µg/mL of NDs over 1–24 h (Fig. 1.3). Early endosomes are observed during the early stages of clathrin-dependent endocytosis as membrane vesicles pinch off containing extracellular transports including NPs. Lysosomes are single-membrane compartments found in most eukaryotic cells that are responsible for the breakdown of materials. In the case of endocytosis, lysosomes develop gradually from late endosomes, which are vesicles that initially carry materials into the cell. The coalescence of the endosome with the low pH environment of the lysosome causes the degradation and release of the contents. Therefore, we expect to observe early localization of ND to endosomes, followed by localization to lysosomes, and finally to the cytosol. In cells fixed and stained for detecting early endosomes, control N2A cells show diffuse green staining with some punctate spots that represent invaginating early endosomes (Fig. 1.3a). After 1 h, green punctate dots can still be observed; however, there is some overlap of red signal from ND with the green dots, suggesting that there is early and rapid localization to early endosomes (Fig. 1.3b). After 3 h, there was some overlapping of the red signal from ND and the green signal representative of lysosomes resulting in yellow spots, suggesting that ND co-localized with the lysosomes (Fig. 1.3c). After 6 h, the density of this overlap greatly increases, suggesting that movement to the lysosomes follows early endosomes localization (Fig. 1.3d). After 24 h, most of the ND appeared to be released from the lysosomes and was found in the cytoplasm as red aggregates while the lysosomes remained stained in green (Fig. 1.3e).

Other studies have confirmed that FNDs rely upon energy-dependent clathrin-mediated endocytosis to enter the cell [99]. Similarly, Liu et al. provided evidence

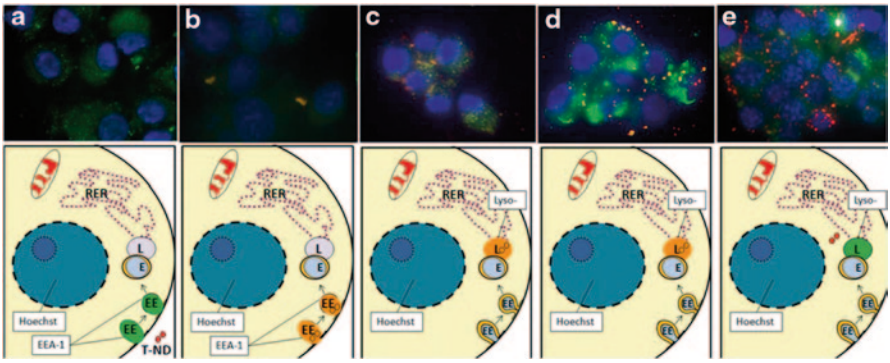

Fig. 1.3 Confocal microscopy of neuro2A (N2A) cells for co-localization of ND-T Nanodiamond Carboxytetramethylrhodamine (TAMRA) (10 mg/mL) and early endosomes or lysosomes after various time points. *Labels:* ND-T *(red),* Hoechst nuclear dye *(blue),* and LysoTracker/early endosome antigen 1 *(EEA1) (green)*. Combined *red* and *green* signals, indicative of co-localization of ND-T in lysosomes or early endosomes, appear in *yellow* or *orange*. **a** Control with *EEA1*. **b** 1 h, stained for *EEA1*. **c** 3 h, stained for LysoTracker. **d** 6 h, stained for LysoTracker. **e** 24 h, stained for LysoTracker. Notice that not all ND-Ts are localized to lysosomes, but some NDs are free in the cytoplasm, and not all lysosomes contain ND-T. Images were taken at 60× magnification. *EEA1* at 3, 6, 24 h and LysoTracker at 0, 1 h were omitted for clarity and ease of presentation. (Adapted with permission from [81]). *EE* early endosome, *L* lysosome, *E* endosome

to suggest that cNDs enter cells via both clathrin-mediated endocytosis and macropinocytosis [103]. Moreover, the surface charge of FNDs has been shown to affect uptake: The uptake of poly-L-lysine-coated FNDs was better than that of oxidative-acid-purified FNDs at the same concentration. In addition, NDs may enter cells through the process of phagocytosis. Karpukhin et al. demonstrated that detonation nanodiamonds (DNDs) may be phagocytosed by neutrophils, leading to ROS production [104]. A more recent study has implicated that FNDs may exit the cellular cytosol through the process of exocytosis. For example, Fang et al. demonstrated through flow cytometry that up to 30% of FNDs exocytosed from 3T3-L1 preadipocytes after 6 days [102]. However, exocytosis was much lower for HeLa and 489-2.1 cells, implicating the crucial effect of cell type. The occurrence of exocytosis suggests that the presence of FNDs within the cell is a dynamic equilibrium process. Ongoing studies by the author and ITC colleagues suggest that carbon dot-decorated NDs also localize inside skin cells [105]. Although carbon dots are not a new class of carbon nanomaterials [106], when a specific acid treatment of detonation soot is performed, forming tiny rounded sp^2 carbon species (carbon dots) result and can be covalently attached to the surface of detonation diamond NPs. The photoluminescence of the carbon dot-decorated NDs can be tailored by changing the oxidation process parameters. Carbon dots-decorated NDs possessing stable luminescence are demonstrated to be excellent probes for bio-imaging applications and inexpensive additives for nanocomposites.

1.5 In Vivo Considerations for Nanodiamond Biocompatibility

The use of animals including mice, rats, and rabbits for in vivo nanotoxicity studies allows a more in-depth understanding of NP kinetics. However, even within the same animal model, there has been a great divergence in toxicity results for pulmonary studies of CNTs in animals [107–113] or C60 in aquatic species and animals [114–120]. It is suspected that differences in the starting materials (i.e., metal impurities, residual solvent) or administration routes/procedures may be responsible for the varied biocompatibility results. In contrast, micro- or nano-sized diamonds show consistently positive results for in vivo applications. For example, micron-sized diamond particles did not contribute to inflammation when introduced to implant traversing canals in rabbits [121], canine knee joints [122], or the complement system [123], and NDs do not affect the weight or reproductive ability of mice or induce inflammation in rats [124–130]. The latter studies will be briefly summarized below.

Unfortunately, the early in vivo studies with detonation NDs were complicated by the low colloidal stability and high polydispersity, which made it difficult to establish dose–response relationships. In one study, ND suspensions in starch gel were orally introduced to animals with a catheter in order to increase the sedimentation stability [131]. Other treatments to remove contaminants and further functionalize the surface of NDs with hydrophilic surface moieties (i.e., oxy, carboxyl, and carbonyl groups) were used to produce medical-quality ND hydrosols. The ability to prepare stable and sterile ND hydrosols that could be cryogenically stored and administered by various methods led to a series of long-term experiments in animals, including mice, rats, and dogs. The species-specific responses to 0.002–1.0 wt% ND administered by different means (i.e., oral, intravenous, intramuscular) were studied and are summarized below [125, 126, 128–131].

In mice, completely replacing water in the diet of animals aged between 3 and 6 months with 0.002–0.05 wt% ND hydrosols neither caused death nor affected the growth or internal organ (liver, lungs, heart, kidneys, and pancreas) weight dynamics compared to control animals. Further, the substitution of water with ND hydrosols did not influence mouse reproductive ability, for at least the first three generations as animals consuming ND hydrosols from birth produced healthy offspring. Within the duration of the experiments, the total amount of ND delivered to the animals was between 16 and 450 mg per mouse depending on the concentration of ND in hydrosols. The effects of NDs on blood cells and blood plasma chemistry were examined after prolonged substitution of water with ND hydrosols with minimal changes. Similar studies in rats showed that intramuscularly injected NDs localized at the injection sites as gelatinous clots that contained considerable amounts of protein components on their surface. However, no pronounced visual or histological manifestations of inflammation were detected. The low toxicity was confirmed with an estimated median lethal dose (LD_{50}) of > 7000 mg/kg compared to an LD_{50} of 3000 mg/kg for sodium chloride orally administered to rats. In another

series of experiments, dogs intravenously injected with 0.3–20 mL of sterile ND hydrosols in glucose (0.001–5 wt%) did not die after the dosage [125, 126, 128–131].

Studies have also exposed NDs to mice via intratracheal instillation [132]. This study reported that the NDs localized largely to the lung, although there is also distribution in the spleen, liver, bone, and heart. The authors implied that there could be dose-dependent toxicity in these organs based on histological and biochemical evaluation. Similarly, Yuan et al. found that NDs mostly accumulated in the liver after intravenous injection with the spleen and lung being other target organs [133]. Approximately 60 % of the initial NDs remained in the liver, and approximately 8 % remained in the lung both 30 min and 28 days after initial exposure, with potentially cytotoxic effects. Finally, Rojas et al. reported similar results with amino-functionalized DNDs, with the majority of particles localized to the lung, spleen, and liver [134]. These particles were excreted through the urinary tract. The addition of surfactant agents did not change the biodistribution, although it did diminish excretion through the urinary tract.

These studies suggest that the significant amount of NDs that make it inside the cell may pose a significant cytotoxic risk at the in vivo level. In support of this concern, Marcon et al. reported that cNDs could induce embryotoxicity and teratogenicity, interfering with neurulation and gastrulation with high mortality in *Xenopus laevis* embryos [135].

Recent studies of fluorescently labeled NDs either fed to or microinjected into *Caenorhabditis elegans* worms [136] demonstrate that bioconjugation can tailor the localization to either the intestinal lumen (bare NDs) or intestinal walls (dextran or bovine serum albumin-coated NDs, BSA-coated NDs). By comparison, microinjected NDs are dispersed in the distal gonad and oocytes at approximately 30 min after injection and effectively delivered to the embryos. The injected NDs are present in the cytoplasm of many cells in the early embryos (Fig. 1.6b) but are predominantly localized to the intestinal cells of the late embryo. A comparison of the worm life spans, brood sizes, and ROS production demonstrate that both the life span and the potential for progeny production are unaffected by the treatments with either dextran- or BSA-coated NDs. Therefore, the longevity of *C. elegans* measured over 25 days, the reproductive potential measured over 4 days, and the stress response after 4 h did not produce any deleterious effects compared to controls.

Yuan et al. [133] investigated the pulmonary effects and localization of NDs in mice intratracheally administered 1 mg/kg NDs and examined at 1–28 days postexposure. There were no long-term signs of biochemical, ultrastructural, or histopathological alterations, but there was a temporary lung index increase at the early time point of 1 day postexposure. Further, the ND burden within alveolar macrophages decreased over time. Representative histopathological and TEM imaging of lung tissue from mice intratracheally instilled with 1 mg/kg NDs-50 at 1 day postexposure. The normal lung architecture indicates that exposures to NDs does not produce detectable pulmonary toxicity. However, the high-resolution TEM images of lung tissue show NDs localized to phagosomes within macrophages.

Cumulatively, these past in vivo studies suggest that NDs possess enormous potential based on their biodistribution throughout animal models. Moreover, their

cytotoxicity does not appear to be a major concern, although there seems to be some disagreement depending upon the animal model utilized and the particular end points that are assessed. However, most importantly, NDs appear to possess valuable biological effects and properties characteristic of an enterosorbent (detoxifying agent), which may be exploited in potential biomedical and bioengineering applications.

1.6 Carbon Nanobombs

The development of nanostructures that can be remotely activated to produce a desired effect is an attractive strategy for a diverse range of applications ranging from electronics, cancer therapeutics, and drug delivery platforms to sophisticated biosensors. Near-infrared (NIR) light, which spans wavelengths from ~700–1100 nm holds particular promise in bionanotechnology-enabled applications because both NIR light and NPs have the potential for remote activation leading to exquisite localization and targeting scenarios. Additionally, control of both spatial and temporal energy input in the form of highly localized heating results in precise destruction with low collateral damage to the surrounding environment, cells, and tissues. The heat delivered to the target depends upon many factors including laser power, NP concentration, efficiency of NPs to convert energy to heat, heat dissipation rates, solvent type, volume, etc.

A recent fundamental study by Schrand et al. examined aqueous solutions of carbon and metal-based NPs (CB, single-walled CNTs, silver NPs, and copper NPs) upon exposure to continuous NIR ($\lambda = 1064$ nm) laser irradiation at powers of 2.2 W and 4.5 W [137]. The differential heating of bulk aqueous suspension of NPs with varying physicochemical properties revealed maximum temperatures of 67°C with visible evidence of condensation and bubble formation (Fig. 1.4a–f). It is unknown whether the bubbles formed due to micro/nanoexplosions of the NPs or simply localized heating around NP aggregates. In either case, the generation of heat/pressure in aqueous environments poses utility in medical as well as marine applications. The doubling of the power from 2.2 to 4.5 W led to doubling of the bulk solution temperature (Fig. 1.4g, h). The basis of the NP heating was hypothesized to be due to the strong intrinsic optical absorbance in the NIR spectral window and the transduction of this NIR photon energy into thermal energy. The highest absorbance and heating was found for the CB spherical NPs followed by carboxylic acid-purified single-walled CNTs, raw single-walled CNTs, then gold nanoparticles (GNPs). The use of ultraviolet-visible (UV-vis) measurements prior to NP heating was also used to accurately predict these trends prior to NIR irradiation.

Follow-on studies with hybrid NPs systems by Schrand et al. in 2012 elucidated NIR laser interactions with bio-conjugates. Specifically, SWNTs bio-conjugated to GNPs of three different sizes (10, 30, 60 nm), then exposed to 1064 nm NIR laser irradiation displayed size-dependent heating kinetics (Fig. 1.5) [138]. For example, the SWNT-GNP hybrids containing the smallest GNPs experience greater heating

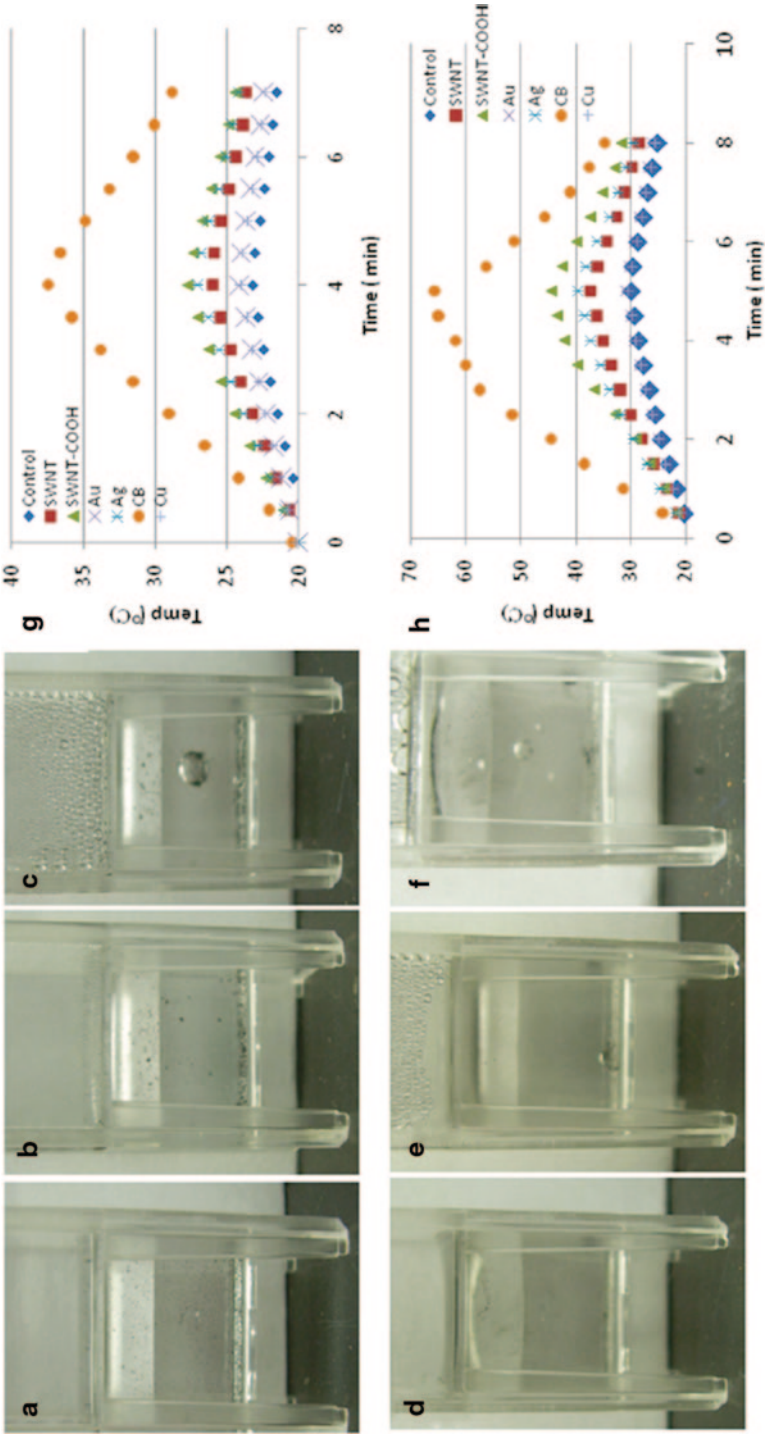

Fig. 1.4 Digital images of representative cuvettes before and after laser exposure. **a–c** Single-walled nanotube *(SWNT)*-COOH and **d–f** Carbon black (CB). **a, d** Before exposure. **b, e** After 2.2 W for 7 min. **c, f** After 4.5 W for 8 min. Notice the bubbles and condensate for both nanoparticle (NP) solutions after 4.5 W. Experimental heating kinetics of NP solutions irradiated with **g** 2.2 W laser power measured at 30 s intervals over 7 min. **h** 4.5 W laser power measured at 30 s intervals over 8 min. (Adapted with permission from [137])

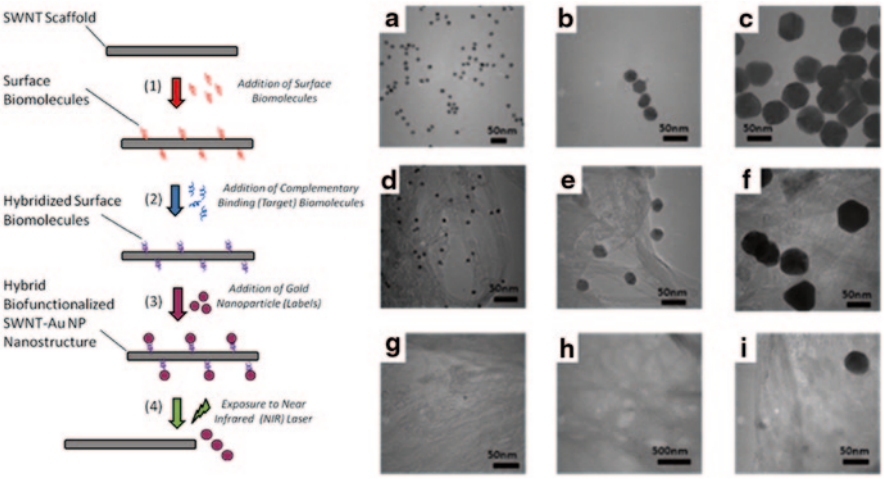

Fig. 1.5 Overview of the biomolecular functionalization and capture process to form hybrid single-walled nanotube—gold nanoparticle (*SWNT*-GNP) nanostructures, which are further modified upon near-infrared (NIR) laser exposure and **a**–**i** representative transmission electron micrographs demonstrating labeling of biofunctionalized SWNTs with GNPs before and after exposure to NIR. *(1)* Binding of biomolecules onto SWNT surface. *(2)* Hybridization of complementary target binding sequences. *(3)* Addition of GNPs. *(4)* Detachment of GNPs via NIR laser exposure. Transmission electron microscopy (TEM) images of **a** 10-nm GNPs, **b** 30-nm GNPs, **c** 60-nm GNPs, **d** SWNT-GNP10 nm, **e** SWNT-GNP30 nm, **f** SWNT-GNP60 nm, **g** SWNT-GNP10 nm post NIR, **h** SWNT-GNP30 nm post NIR, and **i** SWNT-GNP60 nm post NIR. (Adapted from [138])

and subsequent GNP release upon NIR laser irradiation compared to SWNT surfaces modified with larger 60 nm GNPs. The authors hypothesize that the greater attachment efficiency of the smaller GNPs to the biomolecules allowed for increased heat transduction. Therefore, it is possible to physically modify, through heating or potentially pressure/explosive-driven phenomena, the surface of hybrid nanostructures remotely via NIR laser irradiation leading to selective and small area bio-target ablation. It can be envisioned from this work and others that reactive components could be stabilized upon or inside various nanostructures. Indeed, energetic fills of copper azide have been confined inside CNTs [139]. Therefore, nanostructures will likely become much more sophisticated over time to contain multiple components for effective detonation at the nanoscale. Additionally, schemes that rely upon dissociation of one component for the next stage of reaction could be initiated in this manner.

However, a photoacoustic mechanism resulting in localized heating and subsequent pressure buildup has been proposed for the selective bio-effects of bundles of single-walled CNTs in cell cultures as cancer-destroying "nanobombs" (Fig. 1.6 and 1.7) [140, 141]. Single-walled CNTs were reported by Panchapakesan et al. [140] to kill human BT474 breast cancer cells by adsorbing water molecules in SWNT sheets or water loosely adsorbed on top of the cells upon exposure to laser light of 800 nm at light intensities of approximately 50–200 mW/cm^2. Temperature monitoring revealed that the water molecules inside the cells rose to more than

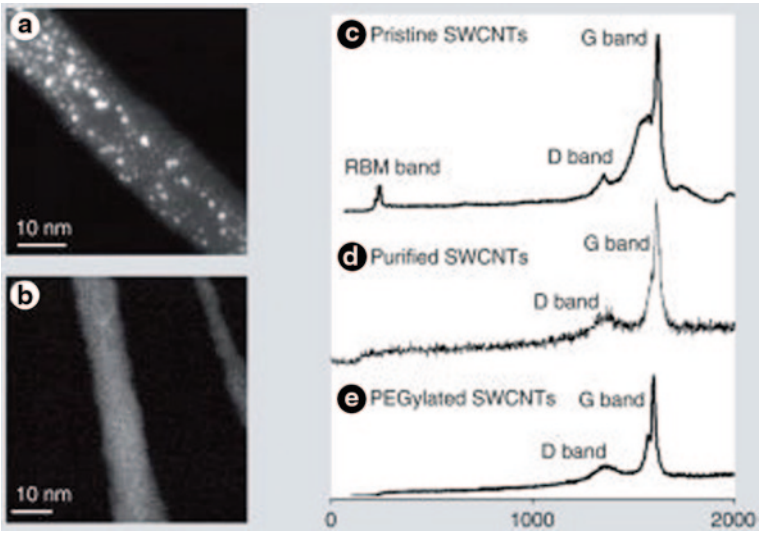

Fig. 1.6 Z-contrast scanning transmission electron microscopy (STEM) images and Raman spectra of polyethylene glycol *(PEG)*ylated single-walled carbon nanotubes *(SWCNTs)*. **a** STEM image of a *PEG-SWCNT* bundle conjugated with anticancer drug cisplatin. *Bright dots* correspond to clusters of Pt atoms (i.e., cisplatin molecules). **b** STEM image of a *PEG-SWCNT* bundle alone shows no bright dots. **c**–**e** Raman spectra showing signature peaks (relative intensities) of **c** pristine *SWCNTs,* **d** purified or acid-treated *SWCNTs,* and **e** *SWCNTs* wrapped with *PEG*. *RBM* radial breathing mode. (Adapted with permission from [142])

100 °C. Conversion of optical energy into thermal energy and the subsequent confinement of thermal energy in SWNT caused the water molecules to evaporate and develop extreme pressures in SWNT causing them to explode in solutions. In another study by Kang et al. [141], cancer cells were selectively targeted for destruction by first functionalizing SWNTs with folate acid, which selectively binds to overexpressed folate cell surface receptors. The SWNT explosion inside the cells is initiated when the cells with internalized SWNTs are irradiated with a 1064-nm Q-switched millisecond pulsed laser. The results are 85% of cancer cells with SWNT uptake die within 20 s compared to 90% retention of normal cell viability. The bulk temperature of the cell cultures does not increase in excess of 3°C. Therefore, SWNT-based nanobomb agents can potentially outperform most nanotechnological approaches in killing cancer cells without toxicity.

It is worth mentioning here that the targeting and tracking of carbon nanomaterials in biological systems has been accomplished with a variety of microscopic and spectroscopic techniques including Raman spectroscopy and various forms of electron microscopy (Fig. 1.6) [80, 142]. Methods to enhance detection and contrast include the attachment of cisplatin on bio-conjugates and were visualized with Z-contrast STEM. For example, PEG-SWNT–cisplatin was attached to the targeting ligand epidermal growth factor (EGF) to successfully inhibit the growth of head and neck tumor xenografts in mice [142]. Representative STEM and Raman spectra

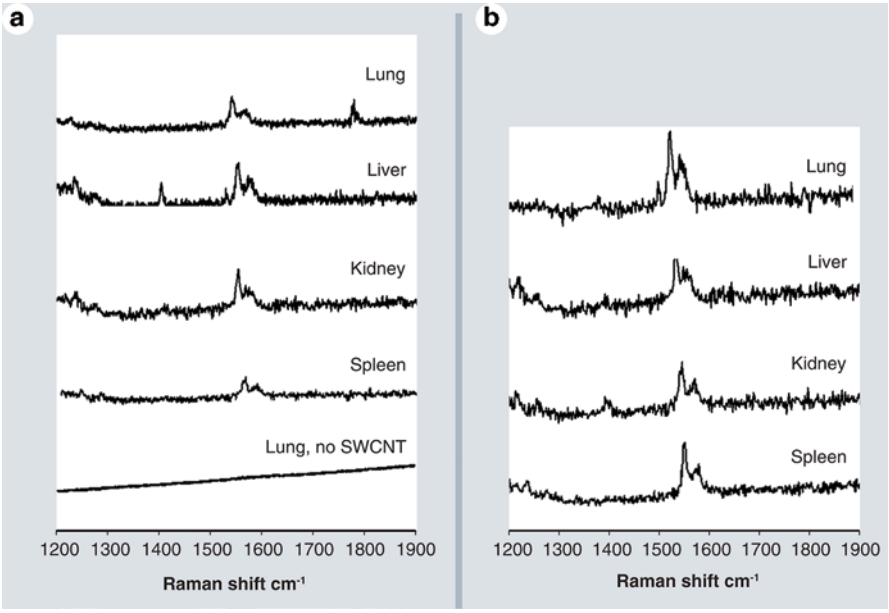

Fig. 1.7 **a** Raman spectra of tissues from vital organs removed from the mice after being treated with polyethylene glycol (PEG)-single-walled carbon nanotubes *(SWNTs)*. Mice treated with PEG-SWNTs 24 h post intravenous injection, tissue removed 24 h post intravenous injection for Raman analysis with control lung tissue. The Raman G band for *SWNTs* in the 1500–1600 cm^{-1} region is clearly observed in mice treated with PEG-SWNTs, while spectral analysis of tissues of mice not treated with *SWNT (bottom trace)* showed no indication of the characteristic G band. **b** Raman spectra of tissues of vital mouse organs after being treated with non-PEG-SWNTs, 24 h post intravenous injection. All spectra are the average of three spots from a given tissue slide. (Adapted with permission from [142])

for pristine and functionalized single-walled CNTs are shown in Fig. 1.6 and 1.7. Notice the prominent G-band between 1500–1600 cm^{-1} indicative of the presence of SWNTs in the tissue samples 24 h post intravenous injection (Fig. 1.7b).

Similar analogies to the above-described biological studies have also been performed to study the ignition characteristics of SWNTs remotely activated by a camera flash for distributed ignition in liquid rocket fuel sprays and homogeneous-charged compression ignition (HCCI) engines [143, 144]. Specifically, the SWNT-mediated flash-ignition was investigated with respect to the effects of O_2 concentration and the presence of solid oxidizers such as ammonium perchlorate (AP) on the minimum ignition energy as well as the duration and temperature of the reaction [143]. Ignition parameters such as ignition delay, burn temperature, and burn duration could be tailored by mixing CNTs with other NPs and powdered material to meet certain ignition requirements with the potential for scalability. Additionally, the photo-ignition approach can lead to light weight, low power, and robust systems with volumetric distributed ignition capability.

1.7 Future Goals for the Nanocarbons in Medicine

The factors that determine long-term toxicity or biocompatibility will probably never be directly extrapolated from cell culture studies to human health. However, through cell culture and animal studies a greater understanding of the detailed mechanisms at work for the interactions, uptake, localization, release, and biochemical effects is underway. With regard to certain classes of carbon NPs, the current body of research overwhelmingly suggests that NDs are biocompatible with many mammalian cell lines [27, 39, 66, 67, 70–72, 80–82, 85, 86, 105]. Regardless of the size of the NDs, both in vivo and in vitro studies of NDs of varying purities with conjugations to fluorophores or other biomolecules retained levels of cell high viability and minimal protein and genomic alterations. However, the role of ND size should be examined in a systematic manner because 5-nm NDs, which have >15% of the carbon atoms on their surface, have shown different properties than 100-nm NDs [145]. An understanding of size effects is further complicated by the dynamic nature of NPs in fluids, including protein corona formation and tight or loose aggregate formation as well as cellular surface interactions. At this time, most NPs, including NDs, cannot be controlled as individual particles in biological environments to target entry into the cell nucleus or across tightly controlled barriers (i.e., blood-brain barrier) without direct microinjection or other invasive methods. It will still be interesting, however, to quantify the uptake amount of NDs into individual cells or systems to partially elucidate size-dependent effects on biocompatibility. With regard to advancing testing methods, the strength of in vitro biocompatibility studies could be improved by providing consistent positive and negative controls and benchmark NPs to assess the validity of the toxicity assays. This includes independent testing of the solvents or surfactants incorporated with the NPs as well as common matrices in the case of polymer nanocomposites. Because micron-sized diamond particles were chosen as negative control particles for other ceramics, nano-sized diamonds could be proposed as control particles for nano-sized carbon biocompatibility studies. However, the properties would need to be uniform, of high purity and the binding of the biochemical assay probes (i.e., MTT or ROS) should continue to be scrutinized for directly interfering with the toxicity assay results [146, 147].

Advances in ND synthesis methods, purification procedures, and functionalization routes necessitates further investigation into the mechanisms responsible for either the positive or negative effects. Unfortunately, the detailed purity and surface chemistry of the NDs used in many experiments have not been detailed alongside the biocompatibility results, making it difficult to ascertain the significance, if any, of the impurities and surface functional groups. Further, these surface groups may be masked by biomolecules such as serum proteins, which effectively “coat” the ND surface. Alternatively, the surface groups or impurities may be unstable or soluble thereby releasing unwanted chemical species into the biological environment. Given the number of chemical species applied to NDs in recent experiments, it is essential to better understanding the evolving properties of NDs in biological environments related to the cellular response and kinetics. A recent review by [148]

discusses the implications of complex ND-based drug-imaging-targeting delivery systems on biocompatibility.

The recent animal studies have shown great progress in examining the biocompatibility of NDs with promising results. However, extensive fundamental studies will be required before clearly understanding the long-term bio-effects of NDs. In particular, questions remain regarding (1) the doses used during the studies, (2) optimal routes of administration (oral, intratracheal, intravenous, etc.), (3) the effects of their very small primary particle size for translocation into unintended areas of the body or cell, (4) proper tracking, and (5) clearance/bio-persistence. The use of radiotracers [132] has aided the tracking of NDs; however, there are conflicting results for localization to the lung, liver, kidney, heart, and blood with or without effects, which need to be clarified. For example, Zhang et al. [132] administered 20× the dose of Yuan et al.[133]. Further, the few studies that demonstrate negative effects at the cellular and genomic level upon exposure to NDs should be clarified in the context of the ND properties, cell lines, and assays. For example, the intratracheal administration of NDs did not produce pulmonary toxicity and allowed clearance by macrophages, but certain cell types may be less robust during the early embryonic stages [84, 135]. Mechanical damage has not been shown, although it should not be ruled out due to different synthesis and processing methods, which could result in sharp edges and bio-persistence similar to studies with micron-sized diamond particles [149, 150]. Side effects of such phenomena could include respiratory ailments, alterations in fluid composition [62, 151, 152], malfunctioning transport [27, 36, 85], or accumulation and resistance to elimination by cells or tissues. For example, although the NDs were routed to lysosomes, they were unable to be degraded within 24 h and accumulated in the cytoplasm [80, 81]. Although many cells of the body undergo cell death through natural cellular renewal processes (i.e., skin, lung macrophages, etc.), the localization and cell-specific differences should also be considered in the mechanism of NP uptake, accumulation, and localization for truly understanding biocompatibility [153].

Before NDs are incorporated into health-care products such as skin creams, shaving gels, or toothpastes, the penetration depth of NDs into the skin or gums would need to be evaluated. The biomedical use of NDs in implantable materials should carefully examine the mechanism and extent of direct ND interaction with cellular membranes, proteins, and fluid electrolyte/osmotic balance should be elucidated in more complex systems. Although much of the literature to date demonstrates the utility of CNTs in nanomedicine as “carbon nanobombs,” other forms of carbon NPs may find utility in this area. Indeed, fullerenes have demonstrated medicinal properties. However, one note regarding some of the fundamental work in photoacoustic effects of CNTs is that the tubes must be in bundles to perform the desired explosive action via shock wave-induced disruption of cell membranes. Examining the latest breakthroughs in the field of nanoenergetics may be a logical path to establish a way forward for powerful, yet nanoscale methods applicable for selective cell and tissue destruction. However, the structure-property–biocompatibility relationship for carbon or hybrid NPs is complex. Most likely real conclusions will only be drawn in a case-by-case scenario based upon the vast degree of NP variation (i.e., differences

in synthesis methods, differences between manufacturers, laboratories, methods, purification procedures, functionalization routes, chemicals, and further alterations to NP properties during their lifecycle, etc.), which further complicate gaining an accurate understanding of the properties responsible for both detrimental and beneficial effects on biological systems.

References

1. A.M. Schrand, T. Benson-Tolle, in *Chapter 18: Carbon Nanotube and Epoxy Composites for Military Applications*, ed. by L. Dai. Carbon Nanotechnology: Recent Developments in Chemistry, Physics, Materials Science, and Device Applications, (Elsevier, Amsterdam, 2006)
2. D.A. Gomez-Gualdrón, J.C. Burgos, J. Yu, P.B. Balbuena, Carbon nanotubes: engineering biomedical applications. Prog. Mol. Biol. Transl. Sci. **104**, 175–245 (2011)
3. S. Prakash, A.G. Kulamarva, Recent advances in drug delivery: potential and limitations of carbon nanotubes. Recent. Pat. Drug. Deliv. Formul. **1**(3), 214–221 (2007)
4. M. Prato, K. Kostarelos, A. Bianco, Functionalized carbon nanotubes in drug design and discovery. Acc. Chem. Res. **41**(1), 60–68 (2008)
5. S.Y. Madani, N. Naderi, O. Dissanayake, A. Tan, A.M. Seifalian, A new era of cancer treatment: carbon nanotubes as drug delivery tools. Int. J. Nanomed. **6**, 2963–2979 (2011)
6. S. Prakash, M. Malhotra, W. Shao, C. Tomaro-Duchesneau, S. Abbasi, Polymeric nanohybrids and functionalized carbon nanotubes as drug delivery carriers for cancer therapy. Adv. Drug. Deliv. Rev. **63**(14–15), 1340–1351 (2011)
7. T. Kurkina, K. Balasubramanian, Towards in vitro molecular diagnostics using nanostructures. Cell. Mol. Life. Sci. **69**(3), 373–388 (2012)
8. F. Liang, B. Chen, A review on biomedical applications of single-walled carbon nanotubes. Curr. Med. Chem. **17**(1), 10–24 (2010)
9. W. Cheung, F. Pontoriero, O. Taratula, A.M. Chen, H. He, DNA and carbon nanotubes as medicine. Adv. Drug. Deliv. Rev. **62**(6), 633–649 (2010)
10. L. Zhu, A.M. Schrand, A.A. Voevodin, D.W. Chang, L. Dai, S.M. Hussain, Assessment of human lung macrophages after exposure to multi-walled carbon nanotubes Part II. DNA Damage Nanosci. Nanotechnol. Lett. **3**, 94–98 (2011b)
11. M. Bottini, N. Rosato, N. Bottini, PEG-modified carbon nanotubes in biomedicine: current status and challenges ahead. Biomacromolecules. **12**(10), 3381–3393 (2011)
12. A. Tan, L. Yildirimer, J. Rajadas, H. De La Peña, G. Pastorin, A. Seifalian, Quantum dots and carbon nanotubes in oncology: a review on emerging theranostic applications in nanomedicine. Nanomedicine (Lond) **6**(6), 1101–1114 (2011)
13. C. Iancu, L. Mocan, Advances in cancer therapy through the use of carbon nanotube-mediated targeted hyperthermia. Int. J. Nanomedicine **6**, 1675–1684 (2011)
14. A.O. Tarakanov, L.B. Goncharova, Y.A. Tarakanov, Carbon nanotubes towards medicinal biochips. Wiley Interdiscip. Rev. Nanomed. Nanobiotechnol. **2**(1), 1–10 (2010)
15. K.B. Hartman, L.J. Wilson, Carbon nanostructures as a new high-performance platform for MR molecular imaging. Adv. Exp. Med. Biol. **620**, 74–84 (2007)
16. B.S. Harrison, A. Atala, Carbon nanotube applications for tissue engineering. Biomater. **28**(2), 344–353 (2007)
17. E.B. Malarkey, V. Parpura, Carbon nanotubes in neuroscience. Acta. Neurochir. Suppl. **106**, 337–341 (2010)
18. A. Bianco, K. Kostarelos, M. Prato, Making carbon nanotubes biocompatible and biodegradable. Chem. Commun. (Camb). 47(37), 10182–8 (2011)
19. C. Buzea, B. Pacheco, I.I., K. Robbie, Nanomaterials and nanoparticles: sources and toxicity. Biointerphases **2**, MR17–MR172 (2007)

20. K. Inoue, H. Takano, R. Yanagisawa, S. Hirano, M. Sakurai, A. Shimada, T. Yoshikawa, Effects of airway exposure to nanoparticles on lung inflammation induced by bacterial endotoxin in mice. Environ. Health. Perspect. **114**(9), 1325–1330 (2006)
21. P. Hoet, A. Nemmar, B. Nemery, M. Hoylaerts, in *Hemostatic and thrombotic effects of particulate exposure: Assessing the mechanisms*, ed. by N. Monteiro-Riviere, C.L. Tran. *Nanotoxicology: Characterization, dosing, and health effects*, (Informa Healthcare, Zug, 2007), pp. 247–266
22. L. Pramatarova, R. Dimitrova, E.P.T. Spassov et al., Peculiarities of hydroxyapatite/nanodiamond composites as novel implants. J. Phys. Conf. Ser. **93**, 012049 (2007)
23. Q. Zhang et al., Fluorescent PLLA–nanodiamond composites for bone tissue engineering. Biomaterials **32**, 87–94 (2011)
24. R.A. Freitas Jr., *Nanomedicine Volume IIA: Biocompatibility*. (Landes Bioscience, Georgetown, 2003)
25. R.H. Hurt, M. Monthioux, A. Kane, Toxicology of carbon nanoparticles: status, trends, and perspectives on the special issue. Carbon **44**, 1028–1033 (2006)
26. L. Dai (ed.), *Carbon Nanotechnology: Recent Developments in Chemistry, Physics, Materials Science and Device Applications*. (Elsevier, Amsterdam, 2006)
27. A.M. Schrand, L. Dai, J.J. Schlager, S.M. Hussain, E. Ōsawa, Differential biocompatibility of carbon nanotubes and nanodiamonds. Diam. Relat. Mater. **16**, 2118 (2007a)
28. L. Zhu, A.M. Schrand, A.A. Voevodin, D.W. Chang, L. Dai, S.M. Hussain, Assessment of human lung macrophages after exposure to multi-walled carbon nanotubes Part I. Cytotoxicity. Nanosci. Nanotechnol. Lett. **3**, 88–93 (2011a)
29. G. Jia, H. Wang, L. Yan, X. Wang, R. Pei, T. Yan, Y. Zhao, X. Guo, Cytotoxicity of carbon nanoparticles: single-wall nanotube, multi-wall nanotube, and fullerene. Environ. Sci. Technol. **39**, 1378 (2005)
30. C. Grabinski, S. Hussain, K. Lafdi, L. Braydich-Stolle, J. Schlager, Effect of particle dimension on biocompatibility of carbon nanoparticles. Carbon **45**, 2828 (2007)
31. M.R. Wilson, J.H. Lightbody, K. Donaldson, J. Sales, V. Stone, Interactions between ultrafine particles and transition metals in vivo and in vitro. Toxicol. Appl. Pharmacol. **184**, 172 (2002)
32. P.S. Gilmour, A. Ziesenis, E.R. Morrison, M.A. Vickers, E.M. Drost, I. Ford et al., Pulmonary and systemic effects of short-term inhalation exposure to ultrafine carbon black particles. Toxicol. Appl. Pharmacol. **195**, 35 (2004)
33. R.L. Price, K.M. Haberstoh, T.J. Webster, Improved osteoblast viability in the presence of smaller nanometer dimensioned carbon fibres. Nanotechnology **15**, 892 (2004)
34. Y. Sato, A. Yokoyama, K. Shibata, Y. Akimoto, S. Ogino, Y. Nodasaka, T. Kohgo, K. Tamura, T. Akasaka, M. Uo, K. Motomiya, B. Jeyadevan, M. Ishiguro, R. Hatakeyama, F. Watari, K. Tohji, Influence of length on cytotoxicity of multi-walled carbon nanotubes against human acute monocytic leukemia cell line THP-1 in vitro and subcutaneous tissue of rats in vivo. Mol. Biosyst. **1**, 176 (2005)
35. A. Magrez, S. Kasas, V. Salicio, N. Pasquier, J.W. Seo, M. Celio, S. Catsicas, B. Schwaller, L. Forro, Cellular toxicity of carbon-based nanoparticles. Nano Lett. **6**, 1121 (2006)
36. C. Liu, H. Huang, P. Song, S. Fan, Machining carbon nanotubes into uniform slices. J. Nanosci. Nanotechnol. **7**, 4473 (2007)
37. K. Liu, C. Cheng, C. Chang et al., Biocompatible and detectable carboxylated nanodiamond on human cell. Nanotechnol. **18**, 325102 (2007)
38. A.M. Schrand, *Characterization and In Vitro Biocompatibility of Engineered Nanomaterials* (The School of Engineering, University of Dayton, Dayton, 2007) pp. 93–123
39. A.M. Schrand, H. Huang, C. Carlson, J.J. Schlager, E. Osawa, S.M. Hussain, L. Dai, Are diamond nanoparticles cytotoxic? J. Phys. Chem. B. **111**, 2 (2007b)
40. G. Oberdorster, J.N. Finkelstein, C. Johnston, R. Gelein, C. Cox, R. Baggs, A.C. Elder, Acute pulmonary effects of ultrafine particles in rats and mice. Res. Rep. Health Eff. Inst. **96**, 5–74 (2000)
41. G. Oberdorster, A. Maynard, K. Donaldson, V. Castranova, J. Fitzpatrick, K. Ausman, J. Carter et al., Principles for characterizing the potential human health effects from exposure to nanomaterials: elements of a screening strategy. Part. Fibre. Toxicol. **2**, 8 (2005)

42. T. Ashikaga, M. Wada, H. Kobayashi, M. Mori, Y. Katsumura, H. Fukui, S. Kato et al., Effect of the photocatalytic activity of TiO(2) on plasmid DNA. Mutat. Res. **466**, 1 (2000)
43. D.M. Brown, V. Stone, P. Findlay, W. Macnee, K. Donaldson, Increased inflammation and intracellular calcium caused by ultrafine carbon black is independent of transition metals or other soluble components. Occup. Environ. Med. **57**, 685 (2000)
44. D.M. Brown, M.R. Wilson, W. Macnee, V. Stone, K. Donaldson, Size-dependent proinflammatory effects of ultrafine polystyrene particles: a role for surface area and oxidative stress in the enhanced activity of ultrafines. Toxicol. Appl. Pharmacol. **175**, 191 (2001)
45. D. Hohr, Y. Steinfartz, R.P. Schins, A.M. Knaapen, G. Martra, B. Fubini, P.J. Borm, The surface area rather than the surface coating determines the acute inflammatory response after instillation of fine and ultrafine TiO2 in the rat. Int. J. Hyg. Environ. Health. **205**, 239 (2002)
46. B. Rehn, F. Seiler, S. Rehn, J. Bruch, M. Maier, Investigations on the inflammatory and genotoxic lung effects of two types of titanium dioxide: untreated and surface treated. Toxicol. Appl. Pharmacol. **189**, 84 (2003)
47. A. Hoshino, F. Kujioka, T. Oku, M. Suga, Y.F. Sasaki, T. Ohta, M. Yasuhara, K. Suzuki, K. Yamamoto, Physicochemical properties and cellular toxicity of nanocrystal quantum dots depend on their surface modification. Nano Lett. **4**, 2163 (2004)
48. M. Muller, S. Mackeben, C.C. Muller-Goymann, Physicochemical characterisation of liposomes with encapsulated local anaesthetics. Int. J. Pharm. **1–2**, 139 (2004)
49. L. Ding, J. Stilwell, T. Zhang, O. Elboudwarej, H. Jiang, J.P. Selegue, P.A. Cooke et al., Molecular characterization of the cytotoxic mechanism of multiwall carbon nanotubes and nano-onions on human skin fibroblast. Nano Lett. **5**, 2448 (2005)
50. C. Kirchner, T. Liedl, S. Kudera, T. Pellegrino, M.A. Javier, H.E. Gaub, S. Stolzle et al., Cytotoxicity of colloidal CdSe and CdSe/ZnS nanoparticles. Nano Lett. **5**, 331 (2005)
51. K. Soto, A. Carrasco, T. Powell, K. Garza, L. Murr, Comparative In vitro cytotoxicity assessment of some manufactured nanoparticulate materials characterized by transmission electron microscopy. J. Nanopart. Res. **7**, 145 (2005)
52. B.D. Chithrani, A.A. Ghazani, W.C. Chan, Determining the size and shape dependence of gold nanoparticle uptake into mammalian cells. Nano Lett. **6**, 662 (2006)
53. C.M. Sayes, F. Liang, J.L. Hudson, J. Mendez, W. Guo, J.M. Beach, V.C. Moore et al., Colvin, functionalization density dependence of single-walled carbon nanotubes cytotoxicity in vitro. Toxicol. Lett. **161**, 135 (2006)
54. H.W. Chen, S.F. Su, C.T. Chien, W.H. Lin, S.L. Yu, C.C. Chou, J.J. Chen, P.C. Yang, Titanium dioxide nanoparticles induceemphysema-like lung injury in mice. FASEB. J. **20**, 2393 (2006)
55. D.B. Warheit, T.R. Webb, C.M. Sayes, V.L. Colvin, K.L. Reed, Pulmonary instillation studies with nanoscale TiO2 rods and dots in rats: toxicity is not dependent upon particle size and surface area. Toxicol. Sci. **91**, 227 (2006)
56. Z.P. Xu, Q.H. Zeng, G.Q.L. Gq, A.B. Ui, Inorganic, nanoparticles as carriers for efficient cellular delivery. Chem. Eng. Sci. **61**, 1027 (2006)
57. S. Pal, Y.K. Tak, J.M. Song, Does the antibacterial activity of silver nanoparticles depend on the shape of the nanoparticle? A study of the gram-negative bacterium Escherichia coli. Appl. Environ. Microbiol. **73**, 1712 (2007)
58. L.N. Daniel, Y. Mao, T.C. Wang, C.J. Markey, S.P. Markey, X. Shi, U. Saffiotti, DNA strand breakage, thymine glycol production, and hydroxyl radical generation induced by different samples of crystalline silica in vitro. Environ. Res. **71**, 60 (1995)
59. J.C. Ball, A.M. Straccia, W.C. Young, A.E. Aust, The formation of reactive oxygen species catalyzed by neutral, aqueous extracts of NIST ambient particulate matter and diesel engine particles. J. Air. Waste. Manag. Assoc. **50**, 2000 (1897)
60. J.F. Long, W.J. Waldman, R. Kristovich, M. Williams, D. Knight, P.K. Dutta, Comparison of ultrastructural cytotoxic effects of carbon and carbon/iron particulates on human monocyte-derived macrophages. Environ. Health. Perspect. **113**, 170 (2005)
61. E. Osawa, Recent progress and perspectives in single-digit nanodiamond. Diam. Relat. Mater. **16**, 2007 (2018)

62. V.S. Bondar, A.P. Puzyr, Nanodiamonds for biological investigations. Phys. Solid. State. **46**, 716, 2004
63. R.C. Murdock, L. Braydich-Stolle, A.M. Schrand, J.J. Schlager, S.M. Hussain, Characterization of nanomaterial dispersion in solution prior to in vitro exposure using dynamic light scattering technique. Toxicol. Sci. **101**(2), 239–253 (2008)
64. J.E. Skebo, C.M. Grabinski, A.M. Schrand, J.J. Schlager, S.M. Hussain, Assessment of metal nanoparticle agglomeration, uptake, and interaction using a high illuminating system. Int. J. Tox. **26**, 135–141 (2007)
65. A.M. Schrand, K. Szczublewski, J.J. Schlager, L. Dai, S.M. Hussain, Interaction and biocompatibility of multi-walled carbon nanotubes in PC-12 cells. Int. J. Neuroprot. Neurogener. **3**(2), 115–121 (2007c)
66. A.M. Schrand, J. Johnson, L. Dai, S.M. Hussain, J.J. Schlager, L. Zhu, Y. Hong, E. Osawa, in *Chapter 8: Cytotoxicity and Genotoxicity of Carbon Nanomaterials*, ed. by Prof. T. Webster. *Safety of Nanoparticles: From Manufacturing to Clinical Applications*, (Brown University, Springer, Berlin, 2009b)
67. A.M. Schrand, L. Dai, J.J. Schlager, S.M. Hussain in *Chapter 5: Toxicity Testing of Nanomaterials*, ed. by N. Bhoghal. *'New Technologies for Toxicity Testing'*, (Landes Bioscience, Austin, 2012c)
68. A.M. Schrand, M.F. Rahman, S.M. Hussain, J. Schlager, D.A. Smith, S.F. Ali, Metallic nanoparticles and their toxicity assessment. Wiley Interdiscip. Rev. (WIREs) Nanomed. Nanobiotechnol. **2**(5), 544–568 (2010c)
69. A.M. Schrand, T. Powell, T. Sollmann, S.M. Husain, Assessment of carbon- and metal-based nanoparticle DNA damage with microfluidic electrophoretic separation technology. J. Nanosci. Nanotechnol. **15**, 1053–1059 (2015)
70. A.M. Schrand, S.A. Ciftan Hens, O.A. Shenderova, in *Chapter 26: Nanodiamond Particles: Properties and Perspectives for Bioapplications*, *Handbook of Nanoscience, Engineering, and Technology*, ed. by W.A. Goddard, III, D.W. Brenner, S.E. Lyshecski, G.J. Lafrate 3rd edn. (Taylor and Francis, LLC, 2012d)
71. A.M. Schrand, S.A.C. Hens, O.A. Shenderova, Nanodiamond particles: properties and perspectives for bioapplications. Crit. Rev. Solid. State. Mater. Sci. **34**, 45–54 (2009a)
72. A.M. Schrand, J.B. Lin, *Chapter 16: Characterization of Detonation Nanodiamonds Biocompatibility*, 2nd edn, ed. by O. Shenderova, D. Gruen Ultrananocrystalline Diamond (2012a)
73. S.M. Hussain, L.K. Braydich-Stolle, A.M. Schrand, R.C. Murdock, K.O. Yu, D.M. Mattie, J.J. Schlager, M. Terrones Toxicity evaluation for safe use of nanomaterials: recent achievements and technical challenges. Adv. Mat. **21**, 1–11 (2009)
74. Y.R. Chang, H.Y. Lee, K. Chen et al., Mass production and dynamic imaging of fluorescent nanodiamonds. Nat. Nanotechnol. **3**, 284–288 (2008)
75. V.N. Mochalin, O. Shenderova, D. Ho, Y. Gogotsi, The properties and applications of nanodiamonds. Nat. Nanotechnol. **7**, 11–23 (2012)
76. D. Ho, Beyond the sparkle: the impact of nanodiamonds as biolabeling and therapeutic agents. ACS. Nano **3**(12), 3825–3829 (2009)
77. Y. Xing, L. Dai, Nanodiamonds for nanomedicine. Nanomedicine **4**, 207–218 (2009)
78. J.I. Chao, E. Perevedentseva, P.H. Chung et al., Nanometer-sized diamond particle as a probe for biolabeling. Biophys. J. **93**, 2199–2208 (2007)
79. I.P. Chang, K.C. Hwang, C.S. Chiang, Preparation of fluorescent magnetic nanodiamonds and cellular imaging. J. Am. Chem. Soc. **130**, 15476–15481 (2008)
80. A.M. Schrand, J.J. Schlager, L. Dai, S.M. Hussain, Preparing cells dosed with nanomaterials for assessment of internalization and localization with transmission electron microscopy. Nat. Protoc. **5**, 744–757 (2010a)
81. A.M. Schrand, J.B. Lin, S. Ciftan Hens, S.M. Hussain, Temporal and mechanistic tracking of cellular uptake dynamics with novel surface fluorophore-bound nanodiamonds. Nanoscale **3**, 435–445 (2010b)
82. A.M. Schrand, L. Dai, J.J. Schlager, S.M. Hussain, in *Chapter 5: Toxicity Testing of Nanomaterials*, ed. by N. Bhoghal. New Technologies for Toxicity Testing (Landes Bioscience, Austin, 2012b)

83. A.M. Schrand, J. Johnson, L. Dai, S.M. Hussain, J.J. Schlager, L. Zhu, Y. Hong, E. Ōsawa, in *Cytotoxicity and genotoxicity of carbon nanoparticles*, ed. by T. Webster. Safety of Nanoparticles: From Manufacturing to Clinical Applications (Springer Publishing, Brown University, New York, 2008)
84. Y. Xing, W. Xiong, L. Zhu et al., DNA damage in embryonic stem cells caused by nanodiamonds. ACS. Nano **5**, 2376–2384 (2011)
85. S.J. Yu, M.W. Kang, H.C. Chang, K.M. Chen, Y.C. Yu, Bright fluorescent nanodiamonds: no photobleaching and low cytotoxicity. J. Am. Chem. Soc. **127**, 17604 (2005)
86. H. Huang, E. Pierstorff, E. Osawa, D. Ho, Active nanodiamond hydrogels for chemotherapeutic delivery. Nano Lett. **7**, 3305–3314 (2007)
87. C.M. Sayes, F. Liang, J.L. Hudson, J. Mendez, W. Guo, J.M. Beach, V.C. Moore, C.D. Doyle, J.L. West, W.E. Billups, K.D. Ausman, V.L. Colvin, Functionalization density dependence of single-walled carbon nanotubes cytotoxicity in vitro. Toxicol. Lett. **161**, 135 (2006)
88. M. Bottini, S. Bruckner, K. Nika, N. Bottini, S. Bellucci, A. Magrini, A. Bergamaschi, T. Mustelin, Multi-walled carbon nanotubes induce T lymphocyte apoptosis. Toxicol. Lett. **160**, 121 (2006)
89. A. Magrez, S. Kasas, V. Salicio, N. Pasquier, J.W. Seo, M. Celio, S. Catsicas, B. Schwaller, L. Forro, Cellular toxicity of carbon-based nanoparticles. Nano Lett. **6**, 1121 (2006)
90. A. Krueger, F. Kataoka, M. Ozawa, T. Fujino, Y. Suzuki, A.E. Aleksenskii, A.Y. Vul, E. Osawa, Unusually tight aggregation in detonation nanodiamond: identification and disintegration. Carbon **43**, 2005 (1722)
91. E. Osawa, Recent progress and perspectives in single-digit nanodiamond. Diam. Relat. Mater. **16**, 2007 (2018)
92. H.J. Huang, L.M. Dai, D.H. Wang, L.S. Tan, E. Osawa, Large-scale self-assembly of dispersed nanodiamonds. J. Mater. Chem. **18**, 1347 (2008)
93. A. Pentecost, S. Gour, V. Mochalin, I. Knoke, Y. Gogotsi, Deaggregation of nanodiamond powders using salt- and sugar-assisted milling. ACS. Appl. Mater. Interfaces **2**, 3289–3294 (2010)
94. J.C. Carrero-Sanchez, A.L. Elias, R. Mancilla, G. Arrellin, H. Terrones, J.P. Laclette, M. Terrones, Biocompatibility and toxicological studies of carbon nanotubes doped with nitrogen. Nano Lett. **6**, 1609 (2006)
95. S.K. Manna, S. Sarkar, J. Barr, K. Wise, E.V. Barrera, O. Jejelowo, A.C. Rice-Ficht, G.T. Ramesh, Single-walled carbon nanotube induces oxidative stress and activates nuclear transcription factor-kappaB in human keratinocytes. Nano Lett. **5**, 1676 (2005)
96. E. Oberdörster, S. Zhu, T. Blickley, P. Mcclellan-Green, M. Haasch, Ecotoxicology of carbon-based engineered nanoparticles: effects of fullerene (C60) on aquatic organisms. Carbon **44**, 1112 (2006)
97. S. Vial, C. Mansuy, S. Sagan, T. Irinopoulou, F. Burlina, J.P. Boudou, G. Chassaing, S. Lavielle, Peptide-grafted nanodiamonds: preparation, cytotoxicity and uptake. Chembiochem. **9**(13), 2113–2119 (2008)
98. R. Silbajoris, J.M. Huang, W.-Y. Cheng, L. Dailey, T.L. Tal, I. Jaspers, A.J. Ghio, P.A. Bromberg, J.M. Samet, Nanodiamond particles induce Il-8 expression through a transcript stabilization mechanism in human airway epithelial cells. Nanotoxicology **3**, 152–160 (2009)
99. V. Vaijayanthimala, Y.-K. Tzeng, H.-C. Chang, C.-L. Li, The biocompatibility of fluorescent nanodiamonds and their mechanism of cellular uptake. Nanotechnology **20**, 425103 (9pp) (2009)
100. C.C. Fu, H.Y. Lee, K. Chen, T.S. Lim, H.Y. Wu, P.K. Lin, P.K. Wei, P.H. Tsao, H.C. Chang, W. Fann, Characterization and application of single fluorescent nanodiamonds as cellular biomarkers. Proc. Natl. Acad. Sci. U S A **104**, 727 (2007)
101. F. Neugart, A. Zappe, F. Jelezko, C. Tietz, J.P. Boudou, A. Krueger, J. Wrachtrup, Dynamics of diamond nanoparticles in solution and cells. Nano Lett. **7**, 2588 (2007)

102. C.-Y. Fang, V. Vaijayanthimala, C.-A. Cheng, S.-H. Yeh, C.-F. Chang, C.-L. Li, H.-C. Chang, The exocytosis of fluorescent nanodiamond and its use as a long-term cell tracker. Small **7**(23), 3363–3370 (2011)
103. K.K. Liu, C.C. Wang, C.L. Cheng et al., Endocytic carboxylated nanodiamond for the labeling and tracking of cell division and differentiation in cancer and stem cells. Biomaterials **30**, 4249–4259 (2009)
104. A.V. Karpukhin, N.V. Avkhacheva, R.Y. Yakovlev, I.I. Kulakova, V.A. Yashin, G.V. Lisichkin, V.G. Safronova, Effect of detonation nanodiamonds on phagocyte activity. Cell. Biol. Int. **35**(7), 727–733 (2011)
105. O.A. Shenderova, S. Suzanne Hens, I.I. Vlasov, S. Turner, Y.-G. Lu, G. Van Tendeloo, A. Schrand, S.A. Burikov, T.A. Dolenko, Carbon Dot–Decorated Nanodiamonds. Part. Part. Syst. Charact. **31**, 580–590 (2014)
106. L. Cao, X. Wang, M.J. Meziani, F. Lu, H. Wang, P.G. Luo, Y. Lin, B.A. Harruff, L.M. Veca, D. Murray, S.Y. Xie, Y.P. Sun, Carbon dots for multiphoton bioimaging. J. Am. Chem. Soc. **129**(37), 11318–11319 (2007)
107. C.W. Lam, J.T. James, R. Mccluskey, R.L. Hunter, Pulmonary toxicity of single-wall carbon nanotubes in mice 7 and 90 days after intratracheal instillation. Toxicol. Sci. **77**, 126 (2004)
108. D.B. Warheit, B.R. Laurence, K.L. Reed, D.H. Roach, G.A. Reynolds, T.R. Webb, Comparative pulmonary toxicity assessment of single-wall carbon nanotubes in rats. Toxicol. Sci. **77**, 117 (2004)
109. A.A. Shvedova, E.R. Kisin, R. Mercer, A.R. Murray, V.J. Johnson, A.I. Potapovich, Y.Y. Tyurina, O. Gorelik, S. Arepalli, D. Schwegler-Berry, A.F. Hubbs, J. Antonini, D.E. Evans, B.K. Ku, D. Ramsey, A. Maynard, V.E. Kagan, V. Castranova, P. Baron, Unusual inflammatory and fibrogenic pulmonary responses to single-walled carbon nanotubes in mice. Am. J. Physiol. Lung. Cell. Mol. Physiol. **289**, L698 (2005)
110. J.C. Carrero-Sanchez, A.L. Elias, R. Mancilla, G. Arrellin, H. Terrones, J.P. Laclette, M. Terrones, Biocompatibility and toxicological studies of carbon nanotubes doped with nitrogen. Nano Lett. **6**, 1609 (2006)
111. J. Muller, F. Huaux, N. Moreau, P. Misson, J.F. Heilier, M. Delos, M. Arras, A. Fonseca, J.B. Nagy, D. Lison, Respiratory toxicity of multi-wall carbon nanotubes. Toxicol. Appl. Pharmacol. **207**, 221 (2005)
112. K. Donaldson, R. Aitken, L. Tran, V. Stone, R. Duffin, G. Forrest, A. Alexander, Carbon nanotubes: a review of their properties in relation to pulmonary toxicology and workplace safety. Toxicol. Sci. **92**, 5 (2006)
113. T.K. Leeuw, R.M. Reith, R.A. Simonette, M.E. Harden, P. Cherukuri, D.A. Tsyboulski, K.M. Beckingham, R.B. Weisman, Single-walled carbon nanotubes in the intact organism: near-IR imaging and biocompatibility studies in Drosophila. Nano Lett. **7**, 2650 (2007)
114. E. Oberdörster, S. Zhu, T. Blickley, P. Mcclellan-Green, M. Haasch, Ecotoxicology of carbon-based engineered nanoparticles: effects of fullerene (C60) on aquatic organisms. Carbon **44**, 1112 (2006)
115. T. Tsuchiya, I. Oguri, Y.N. Yamakoshi, N. Miyata, Novel harmful effects of [60] fullerene on mouse embryos in vitro and in vivo. FEBS. Lett. **393**, 139 (1996)
116. T.H. Ueng, J.J. Kang, H.W. Wang, Y.W. Cheng, L.Y. Chiang, Suppression of microsomal cytochrome P450-dependent monooxygenases and mitochondrial oxidative phosphorylation by fullerenol, a polyhydroxylated fullerene C60. Toxicol. Lett. **93**, 29 (1997)
117. C.Y. Usenko, S.L. Harper, R.L. Tanguay, In vivo evaluation of carbon fullerene toxicity using embryonic zebrafish. Carbon N Y. **45**, 2007 (1891)
118. G.L. Baker, A. Gupta, M.L. Clark, B.R. Valenzuela, L.M. Staska, S.J. Harbo, J.T. Pierce, J.A. Dill, Inhalation toxicity and lung toxicokinetics of C60 fullerene nanoparticles and microparticles. Toxicol. Sci. **101**, 122 (2008)
119. A.A. Tykhomyrov, V.S. Nedzvetsky, V.K. Klochkov, G.V. Andrievsky, Nanostructures of hydrated C60 fullerene (C60HyFn) protect rat brain against alcohol impact and attenuate behavioral impairments of alcoholized animals. Toxicology **246**, 158 (2008)

120. A. Baun, N.B. Hartmann, K. Grieger, K.O. Kusk, Ecotoxicity of engineered nanoparticles to aquatic invertebrates: a brief review and recommendations for future toxicity testing. Ecotoxicology **17**, 387 (2008)
121. P. Aspenberg, A. Anttila, Y.T. Konttinen, R. Lappalainen, S.B. Goodman, L. Nordsletten, S. Santavirta, Benign response to particles of diamond and SiC: bone chamber studies of new joint replacement coating materials in rabbits. Biomaterials **17**, 807 (1996)
122. R.L. Tse, P. Phelps, Polymorphonuclear leukocyte motility in vitro. V. Release of chemotactic activity following phagocytosis of calcium pyrophosphate crystals, diamond dust, and urate crystals. J. Lab. Clin. Med. **76**, 403 (1970)
123. M. Doherty, J.T. Whicher, P.A. Dieppe, Activation of the alternative pathway of complement by monosodium urate monohydrate crystals and other inflammatory particles. Ann. Rheum. Dis. **42**, 285 (1983)
124. V.Y. Dolmatov, in *Application of Detonation Nanodiamond in Ultra Nanocrystalline Diamond: Synthesis, Properties, and Applications,* ed. by O.A. Shenderova, D.M. Gruen (William Andrew Publishing, Norwich, 2006), p. 513
125. A.P. Puzyr, V.S. Bondar, S.E. Al, Dynamics of the selected physiological responses in laboratory mice under the prolonged oral administration of nanodiamonds suspensions Siberian Med Obozrenie. Sib. Med. Rev. (in Russian) **4**, 19, 2004a
126. A.P. Puzyr, V.S. Bondar, Z.Y. Selimhanova, A.G. Tyan, E.V. Bortnikov, E.V. Injevatkin, Results of studies of possible applications of detonation nanodiamonds as enterosorbents Siberian Med Obozrenie. Sib. Med. Rev (in Russian) **2–3**, 25, 2004b
127. V. Bondar, D. Baron, Al. Et, Changes in bio-chemical parameters of blood plasma at administration of nanodiamond to laboratory animals. Bull. Sib. Med. (in Russian) **4**, 182 (2005)
128. A.P. Puzyr, V.S. Bondar, Z.Y. Selimkhanova, A.G. Tyan, E.V. Inzhevatkin, E.V. Bortnikov, Results of in vitro and in vivo studies using detonation nanodiamonds/complex systems under extreme conditions. KSC SB RAS Krasnoyarsk **229**, (2005a), p. 229
129. A.P. Puzyr, V.S. Bondar, A.G. Selimkhanova, E.V. Tyan, Inzhevatkin, V.S. Bondar, D. Baron, Physiological parameters of laboratory animals at oral administration of nanodiamond hydrosols. Bull. Sib. Med. (in Russian) **4**, 185 (2005b)
130. A.P. Puzyr, E.V. Bortnikov, N.N. Skobelev, A.G. Tyan, Z. Yu, G.G. Selimkhanova, G.G. Manashev, V.S. Bondar, A possibility of using of intravenous administration of sterile colloids of modified nanodiamonds. Sib. Med. Obozr./Sib. Med. Rev. (in Russian) **1**, 20 (2005c)
131. V.Y. Dolmatov, L.N. Kostrova, Detonation-synthesized nanodiamonds and the feasibility of developing a new generation of medicinals, Superhard Materials (in Russian), **3**(82) (2000)
132. X. Zhang, J. Yin, C. Kang, J. Li, Y. Zhu, W. Li, Q. Huang, Z. Zhu Biodistribution and toxicity of nanodiamonds in mice after intratracheal instillation. Toxicol. Lett. **198**(2), 237–243 (2010)
133. Y. Yuan, X. Wang, G. Jia et al., Pulmonary toxicity and translocation of nanodiamond in mice. Diam. Relat. Mater. **19**, 291–299 (2010)
134. S. Rojas, J.D. Gispert, R. Martin et al., Biodistribution of amino-functionalized diamond nanoparticles. In vivo studies based on 18F radionuclide emission. ACS. Nano **5**, 5552–5559 (2011)
135. L. Marcon, F. Riquet, D. Vicogne, S. Szunerits, J.-F. Bodart, R. Boukherroub Cellular and in vivo toxicity of functionalized nanodiamond in xenopus embryos. J. Mater. Chem. **20**, 8064–8069 (2010)
136. N. Mohan, C.S. Chen, H.H. Hsieh, Y.C. Wu, H.C. Chang, In vivo imaging and toxicity assessments of fluorescent nanodiamonds in Caenorhabditis elegans. Nano Lett. **10**, 3692–3699 (2010)
137. A.M. Schrand, B.M. Stacy, S. Payne, L. Dosser, S.M. Hussain, Fundamental examination of nanoparticle heating kinetics upon near infrared (NIR) irradiation. ACS. Appl. Mater. Interfaces **3**, 3971–3980 (2011)

138. A.M. Schrand, M. Fan, B.M. Stacy, J. Speltz, S. Payne, L. Dosser, S.M. Hussain, Surface modification of gold-carbon nanotube nanohybrids under the influence of near infrared laser exposure. JVST. B. **30**(3), D119 (2012e)
139. V. Pelletier, S. Bhattacharyya, I. Knoke, F. Forohar, M. Bichay, & Y. Gogotsi, Copper azide confined inside templated carbon nanotubes. Adv. Funct. Mat. **20**, 3168–3174 (2010)
140. B. Panchapakesan, S. Lu, K. Sivakumar, K. Taker, G. Cesarone, E. Wickstrom, Single-wall carbon nanotube nanobomb agents for killing breast cancer cells. Nanobiotechnology **1**(2), 133–139 (2005)
141. B. Kang, D. Yu, Y. Dai, S. Chang, D. Chen, Y. Ding, Cancer-Cell targeting and photoacoustic therapy using carbon nanotubes as "Bomb" agents. Small **5**, 1292–1301 (2009)
142. A.A. Bhirde, S. Patel, A.A. Sousa, V. Patel, A.A. Molinolo, Y. Ji, R.D. Leapman, J.S. Gutkind, J.F. Rusling, Distribution and clearance of PEG-single-walled carbon nanotube cancer drug delivery vehicles in mice. Nanomedicine **5**(10), 1535–1546 (2010)
143. A. Badakhshan, S. Danczyk, Photo-ignition of liquid fuel spray and solid fuel by carbon nanotubes. TMS 2012 functional and structural nanomaterials: fabrication, properties, applications and implications
144. B. Chehroudi, Distributed Ignition Using Single-Walled Carbon Nanotubes (SWCNTs) with applications in aerospace and future automotive engines. Recent. Pat. Space Technol. **210** (67), 67–75 (2010)
145. J.S. Tu, E. Perevedentseva, P.H. Chung, C.L. Cheng, Size-dependent surface CO stretching frequency investigations on nanodiamond particles. J. Chem. Phys. **125**, 174713 (2006)
146. N.A. Monteiro-Riviere, A.O. Inman, B.M. Barlow, R.E. Baynes, Dermatotoxicity of cutting fluid mixtures: in vitro and in vivo studies. Cutan. Ocul. Toxicol. **25**, 235 (2006)
147. J.M. Worle-Knirsch, K. Pulskamp, H.F. Krug, Oops they did it again! Carbon nanotubes hoax scientists in viability assays. Nano Lett. **6**, 1261 (2006)
148. Y. Zhu, J. Li, W. Li, Y. Zhang, X. Yang, N. Chen, Y. Sun, Y. Zhao, C. Fan, Q. Huang, The biocompatibility of nanodiamonds and their application in drug delivery systems. Theranostics. **2**(3), 302–3112 (2012)
149. H. Maxwell, *The Poisoner's Handbook* (Loompanics Unlimited, Port Townsend, 1988)
150. G. Davies, *Diamond* (Adam Hilger Ltd., Bristol, 1984)
151. L.C. Huang, H.C. Chang, Adsorption and immobilization of Cytochrome c on nanodiamonds. Langmuir **20**, 5879 (2004)
152. T.S. Huang, Y. Tzeng, Y.K. Liu, Y.K. Chen, K.R. Walker, R. Guntupalli, C. Liu, Immobilization of antibodies and bacterial binding on nanodiamond and carbon nanotubes for biosensor applications. Diam. Relat. Mater. **13**, 1098 (2004)
153. M. Ricarda-Lorenz, V. Holzapfel, A. Musyanovych, K. Nothelfer, P. Walther, H. Frank, K. Landfester, H. Schrezenmeier, V. Mailander, Uptake of functionalized, fluorescent-labeled polymeric particles in different cell lines and stem cells. Biomaterial **27**, 2820 (2006)

Chapter 2
Carbon Nanomaterials for Drug Delivery

Rumei Cheng and Yuhua Xue

2.1 Introduction

Carbon nanomaterials with unique nanostructure (CMNS) are the most studied materials in nanotechnology, despite some conflicting results about their safety profiles [1, 2]. Although their structures are simple, carbon nanomaterials provide exceptional physical and chemical properties including high electrical and thermal conductivities, unique optical properties, and extreme chemical stability. The field concerning nanostructured carbon materials is the most rapidly developing research field in the past decades due to their potential applications in all fields that might affect our lives [3]. One of the greatest values of carbon nanomaterials will be in the development of new and effective medical treatments, particularly for the therapy of various diseases [4]. The predominately nanostructured carbon materials are graphene (GN, 2-D, sp^2 carbon), carbon nanotubes (CNTs, 1-D, sp^2 carbon), and carbon nanohorns (CNHs, 1-D, sp^2 carbon) and nanodiamonds (NDs, 0-D, sp^3 carbon). GN is a two-dimensional structure, while the CNT is regarded as the GN rolling up into the seamless tubular hollow cylinder in nanoneedle shape. In the case of CNHs, the single GN sheet rolled into a cone. The structures of different materials are shown in Fig. 2.1.

Despite the four types of carbon materials are different in shapes, they are all nanostructured materials with many intriguing features that make them attractive drug delivery carriers [5]. Firstly, the nanostructured carbon materials can disperse in aqueous solutions. Besides from direct translocation through cellular membranes, the CMNS also present the ability to enter cells via energy-dependent endocytic pathways [6]. Secondly, they can enter and accumulate in tumor tissues via the

Y. Xue (✉) · R. Cheng
Institute of Advanced Materials for Nano-Bio Applications, School of Ophthalmology & Optometry, Wenzhou Medical University, 270 Xueyuan Xi Road, 325027 Wenzhou, Zhejiang, China
e-mail: yuhua_xue@hotmail.com

M. Zhang et al. (eds.), *Carbon Nanomaterials for Biomedical Applications,*
Springer Series in Biomaterials Science and Engineering 5,
DOI 10.1007/978-3-319-22861-7_2

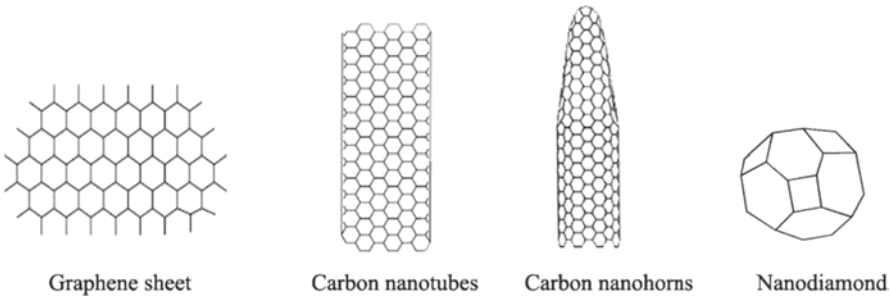

Fig. 2.1 Structures of graphene *(GN),* carbon nanotubes *(CNTs),* carbon nanohorns *(CNHs),* and nanodiamond *(ND)*

enhanced permeability and retention (EPR) effect [7]. The EPR effect enables the carbon nanomaterials to transport therapeutic agents preferentially to tumor sites. It makes the targeted delivery of antitumor drugs more effectively. Thirdly, the carbon nanomaterials exhibit extraordinary ability for drug loading onto the surface via both covalent and non-covalent interactions owing to their high aspect ratios and surface areas. The drugs can also be packed into the interior cores of CNTs and CNHs [8]. To further augment the efficacy of CMNS-based drug delivery system (DDS), various targeting molecules (such as folic acid (FA) and antibodies) can be incorporated into the drug-loaded CMNS. In addition, imaging tags like radioactive nuclides and fluorescence probes linking with CMNS help to observe their intracellular trafficking and biodistribution in vitro and in vivo easily and noninvasively.

Employing the above-mentioned advantages of the three carbon nanomaterials, many progresses have been achieved for the purpose of drug delivery by using GN, CNTs, and CNHs as carriers. This chapter mainly focuses on the different methods of preparation of drug-loaded carbon nanomaterials including their modification, characterization, and applications as drug delivery carriers.

2.2 GN for Drug Delivery

2.2.1 GN-Based Inorganic Nanohybrids for Drug Delivery

The GN is hydrophobic, but it still can be dispersed in aqueous solutions by surfactants or hydrophilic polymers. Although it can adsorb some drugs via π–π stacking, cation–π, and van der Waals interactions, the composites are not easy to disperse in blood. In fact, the application of the GN in drug delivery mainly focused on graphene oxide (GO), which can be prepared by oxidation of graphite and followed by exfoliating in the water via Hummers' method [9]. GO is a layered stack of puckered sheets with AB stacking, which completely exfoliates upon the addition of mechanical energy. The exfoliation of multiple layers of graphite is due to the

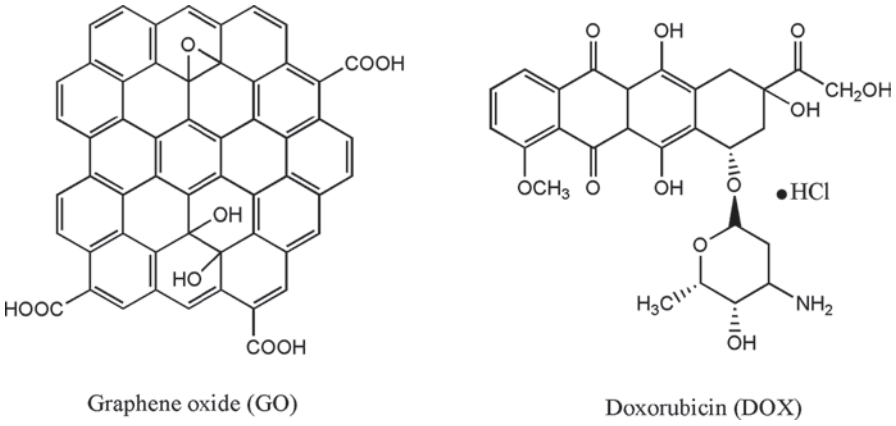

Fig. 2.2 Structures of graphene oxide *(GO)* and doxorubicin *(DOX)*

strength of interactions between water and the oxygen-containing (epoxide, hydroxyl, and carboxyl) groups introduced into the basal plane during oxidation. The hydrophilicity introduces water to intercalate between the sheets and disperse them as individuals. The functionalized GO with hydroxyl and carboxylate groups has the ability to covalently bond with various drugs in mild conditions, and it can also adsorb the drugs via non-covalent interactions such as π–π, hydrogen bonding, and hydrophobic force. Compared with covalent modification, non-covalent ones are considered to have less impact on the conjugated structure, and mechanical and electrical properties of GN. Doxorubicin (DOX) and camptothecin (CPT) are the most studied drugs loaded on GO.

The GO–DOX hydrochloride nanohybrid was easily achieved by simply mixing the two compounds (Fig. 2.2) [10]. The loading of DOX onto GO was based on π–π and hydrophobic interactions. An efficient loading of DOX on GO was 2.35 mg/mg. The release of DOX from GO–DOX was strongly pH dependent. At the solution pH of 5, the DOX release rate gradually declined after 5 h and about only 11 % of the total bound DOX was released in 30 h. The release behaviors at basic and acidic conditions indicated that the total releasing amount of DOX within 30 h for these cases was much higher than that at neutral conditions. About 25 and 71 % of the total bound DOX was released at pH of 10 and 2, respectively. It may be due to the partial dissociation of hydrogen bonding that the DOX gets soluble in acidic solutions.

The GO functionalized with Fe_3O_4 or SiO_2 nanoparticles can also be used as drug carriers. They formed multifuctionalized inorganic nanohybrids. The GO complexes with Fe_3O_4 nanoparticles produced superparamagnetic hybrid nanoparticles (GO–Fe_3O_4). After introducing GO to Fe_3O_4, the sedimentation of Fe_3O_4 magnetic nanoparticles was reduced after they were deposited onto GO [11]. About 18.6 wt% of Fe_3O_4 deposited on GO. The loading capacity of DOX on GO–Fe_3O_4 hybrid was 1.08 mg mg^{-1}, which is higher than liposomes (8.9 wt%) [12], for which the loading capacity is always below 1 mg mg^{-1}. After congregating in acidic solution, both the

GO–Fe_3O_4 hybrids before and after loading with the DOX can be moved regularly by the force of an external magnetic field.

Although the GO–Fe_3O_4 hybrid can target the cells by external magnetic field, it tends to aggregate in acidic solution and serums. Thus, attached small signal molecules would improve its solubility, stability, and target tumor more effectively. They were attached with different target moleculas such as FA. A dual-targeting drug delivery and pH-sensitive drug release GO system was developed by linking Fe_3O_4 with FA (Fig. 2.3) [13]. DOX as an antitumor drug was loaded onto the surface of the multifunctionalized GO via a simple mixture and adsorbed by π–π stacking and hydrophobic interactions. The maximum capacity of this nanocomposite is 0.387 mg mg^{-1} (38.7%). Many targeted tumor cells had overexpress folate receptors. The DOX -loaded multifunctionalized GO can be quickly and effectively delivered into SK3 cells (a human breast cancer cell) and significantly inhibited its growth. The HeLa cell lines is a type of human cervical carcinoma cell, which is

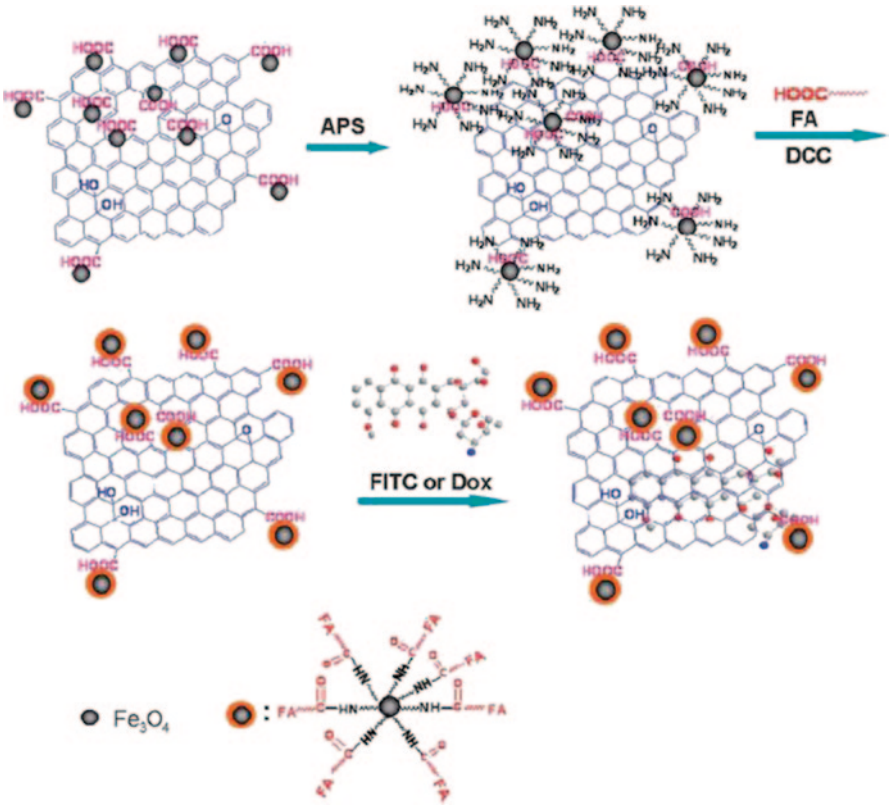

Fig. 2.3 The preparation of the multifunctionalized GO-based anticancer drug carrier with dual-targeting function and pH sensitivity. *APS* 3-aminopropyl triethoxysilane, *DOX* doxorubicin hydrochloride, *DCC N,N'*-dicyclohexylcarbodiimide, *NHS N*-hydroxysuccinimide, *FITC* fluorescein isothiocyanate

widely used as a model for folate receptor-positive cells. The cytotoxicity of DOX-loaded GO–Fe_3O_4 nanohybrid was much higher than the pure GO–Fe_3O_4 nanohybrid without DOX, but lower than that of GO–Fe_3O_4–FA–DOX under the same drug concentration in HeLa cell. The release of DOX from the nanohybrid at neutral and basic conditions was very slow. Only about 7.5 and 11% of the total bound DOX was released for 80 h under neutral conditions (pH 7) and basic conditions (pH 9), respectively. However, in acidic conditions, DOX was released very quickly in the early stage, but the release rate gradually declined after 5 h and about 24% of the total bound DOX was released from the nanohybrid in the first 80 h. It was due to the enhancement of the solubility of DOX and the protonated amine groups to release more loaded drugs.

In order to observe the target ability of GO, it was modified with CdTe–Fe_3O_4/SiO_2 microspheres [14]. The CdTe quantum dots (QDs) made the possibility of visualization of particle distributions in cells. Firstly, the amino functionalized CdTe–Fe_3O_4/SiO_2 nanoparticles were prepared by reverse microemulsion method [15]. As a consequence, the CdTe–Fe_3O_4/SiO_2 particles were surrounded by $-NH_2$ groups, and they can react with the carboxylate groups on GO. The formed GO-based nanocomposite was magnetic fluorescent. Then the DOX was attached to GO nanohybrid by π–π stacking and hydrophobic interaction. The capacity of the nanocomposite increased with the increase of the initial concentration of DOX. The maximum DOX loading capacity was 919 mg g^{-1} (or 91.9% in weight); however, it was lower than that of the original GO. Such a value was still higher than that of some common drug carriers, such as liposomes, for which the loading capacity was usually below 10% [16]. The reasons affecting the maximum capacity were (i) the active surface areas on the GO-based magnetic fluorescent hybrids and (ii) the ratio of GO in the hybrids in weight. The DOX release was pH dependent. Under neutral and basic conditions, the DOX was released slowly, while low pH value was beneficial to more release amount and quicker release rate. At pH 7.4 and 8.5, after 6 days, about 49 and 46% of DOX were released, respectively. In the solution of pH value of 3, 80% of loading DOX was released in 1 day. There was no obvious cytotoxicity (>80% cell viability) observed for the GO-based nanocomposite at a higher concentration of 10 mg L^{-1} for HepG2 cells (liver hepatocellular cells). An obvious decrease in cell viability occurred when the cells were incubated with DOX loading hybrids for 24 h even at a concentration as low as 1 mg L^{-1}. The GO-based composite entered the tumor cells through the endocytosis mechanism, which resulted in the strong fluorescence in HepG2 cells.

The gold nanocluster (GNC) attached GO also presented luminescent property, and the hybrid can be use as a drug delivery carrier [17]. The GNC was firstly modified with dodecanethiol–cetyltrimethylammonium bromide (CTAB). Then the dodecanethiol–CTAB-capped GNC simply mixed with the GO solution to produce the GNC–GO nanohybrid. It displayed two emission peaks at 606 and 705 nm. The loading of DOX did not change the fluorescence. The drug delivery to the HepG2 cells could be imaged by fluorescence. DOX-loaded GNC–GO inhibited HepG2 cell growth more strongly than DOX and GNC–GO alone. It indicated that the DOX–GNC–GO is more effectively transported into the cell cytoplasm.

2.2.2 Polymer-Modified GN for Drug Delivery

The GO was soluble and stable in water but readily aggregated in phosphate-buffered saline (PBS), cell growth medium, and fetal bovine serum (FBS). This might be the electrostatic and salt effect that broke the equilibrium state of GO in solutions [18]. To solve the problem, water soluble and biocompatible polymers were employed to stabilize the GO. Such modification made the GO–drug system dispersing in aqueous solution and blood stability, so the polymer–GO was regarded as a promising drug nanocarrier.

The polyethylene glycol (PEG)ylate–GO composite was studied as a polymer–GO carrier [19]. The ultrasmall nano-GO with lateral dimensions down to <10 nm was preferred for DOX loading to deliver to tumor cells. To enhance its stability in aqueous solutions, PEG was grafted to the small GO. Even when the GO is linked with PEG, the GO sheets still contained some smaller aromatic domains, which favored the DOX adsorbing to GO by π–π interaction. The GO–PEG (>100 mg/L) showed harmless for Raji cells, while the DOX-loaded nanoscale GO (NGO)–PEG exhibited high cytotoxicity to Raji cells as well as the DOX behaviors. If the rituxan (CD20 + antibody) is conjugated to GO–PEG, the nanocomposite would selectively target specific cancer cells for killing. Enhanced DOX delivery and cell killing had increased above 20 % with Raji cells treated with Rituxan–GO–PEG–DOX at lower concentration at 2 μmol L^{-1}. Drug release was dependent on the chemical environment. In acidic solutions, the DOX can be protonated and dissolved slowly. About 40 % of DOX loaded on GO–PEG was released over 1 day in a solution with pH of 5.5. The release rate was reduced when the solution was neutral, only 15 % of loading DOX released after 2 days.

A CPT analogue SN38 can also be stable in aqueous solution after loading on the PEGylate–GO (Fig. 2.4) [20]. Their interaction is based on noncovalent van der Waals force. A total of 1 g of GO–PEG loaded about 0.1 g of SN38. SN38 is a water insoluble aromatic molecule, and the GO–PEG–SN38 complexes were water soluble at concentrations up to 1 mg/mL, which improved the drug delivery. The release of SN38 from the nanocomposite was controllable. The release of SN38 from GO–PEG is about 30 % in serum in 3 days. The drug-loaded nanocomposite exhibited high potency with inhibition concentration (IC_{50}) values of about 6 nM for HCT-116 cells (colon cancer cells). It is about 1000-fold more potent than CPT-11 (CPT-11, a Food and Drug Administration (FDA)-approved SN38 prodrug for colon cancer treatment) and similar to that of free SN38 dissolved in dimethyl sulfoxide (DMSO).

The GO–PEG nanosheets can also load the photosensitizer chlorin e6 (Ce6) and DOX simultaneously [21]. The Ce6- and DOX-loaded GO nanocomposite (Ce6–DOX–GO–PEG) were 148.0–180.0 nm in size. DOX and Ce6 with a molar ratio of 1:2 provided the highest synergism. GO–PEG nanosheets increased the cellular uptake and tumor tissue accumulation of Ce6 compared to treatment with free drugs. Combining DOX and chlorin e6, Ce6–DOX–GO–PEG could accumulate in tumor tissues over 3 days. Moreover, in squamous cell carcinoma tumor-bearing mice, the

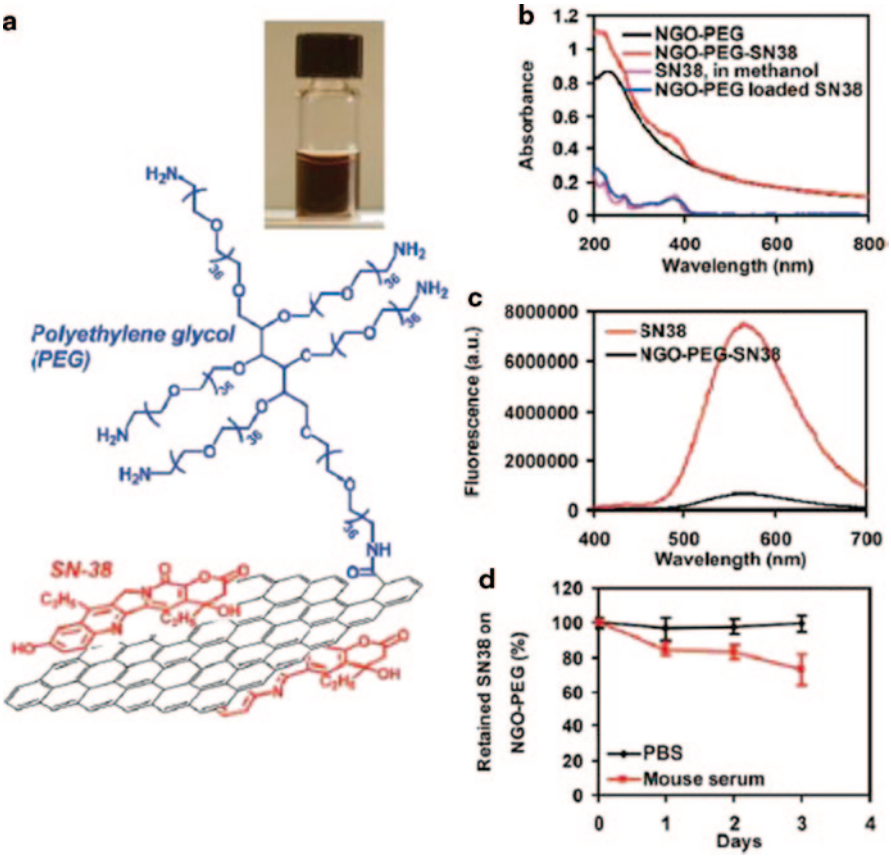

Fig. 2.4 SN38 loading on NGO–PEG: **a** schematic draw of SN38-loaded NGO–PEG; *(inset)* a photo of NGO–PEG–SN38 water solution. **b** UV–visible absorption spectra of NGO–PEG, NGO–PEG–SN38, SN38 in methanol, and difference spectrum of NGO–PEG and NGO-PEG-SN38. The SN38 absorbance at 380 nm was used to determine the loading. **c** Fluorescence spectra of SN38 and NGO–PEG–SN38 at [SN38] = 1 μM. Significant fluorescence quenching was observed for SN38 adsorbed on NGO. **d** Retained SN38 on NGO–PEG over time incubated in PBS and serum, respectively. SN38 loaded on NGO–PEG was stable in PBS and released slowly in serum. Error bars were based on triplet samples. *NGO* nanoscale graphene oxide, *PBS* phosphate-buffered saline

photodynamic anticancer effects of Ce6–DOX–GO–PEG were higher than those of Ce6–GO–PEG or DOX–GO–PEG.

The PEGylate–GO further linked the branched polyethylenimine (BPEI) resulting in PEG–BPEI–GO ternary nanocomposite [22]. The PEG–BPEI was covalently conjugated with the carboxylic acid group of GO using *N*-Ethyl-*N*′-(3-dimethylaminopropyl)-carbodiimide (EDC)/*N*-hydroxysuccinimide (NHS) chemistry, and the resulting PEG–BPEI–GO has been reduced by hydrazine monohydrate. It exhibited good colloidal stability and remained stable as dispersion after loading with DOX via π–π stacking and hydrophobic interactions. Photothermally

controlled drug release via endosomal disruption had finally induced higher cancer cell death. The nanocomposite had a higher near-infrared (NIR) absorbance, and it can trigger the release of loaded DOX after photothermal treatment. Under NIR irradiation (808 nm, 6 W/cm^2, 30 min), cell viability remained above 90% for PEG–BPEI–GO. However, cell viability of PEG–PBEI–GO–DOX-treated cells was about 20% decreased in the NIR irradiation condition as compared with the dark condition. These phenomenons clearly show the enhanced and controllable release of drug molecules from PEG–BPEI–GO by the photothermal effect. This DOX-loaded nanocomposite can effectively inhibit the growth of HeLa and human prostate carcinoma PC-3 cells.

Another PEGylated GO was linked by –NH_2–S–S– disulfide group (Fig. 2.5) [23]. It can response to the tumor relevant molecule, glutathione (GSH). A sheddable methoxy PEG (mPEG) shell with a disulfide linkage attaching to GO made up of the drug carrier. It can respond to GSH changes in the tumor cells for intracellular

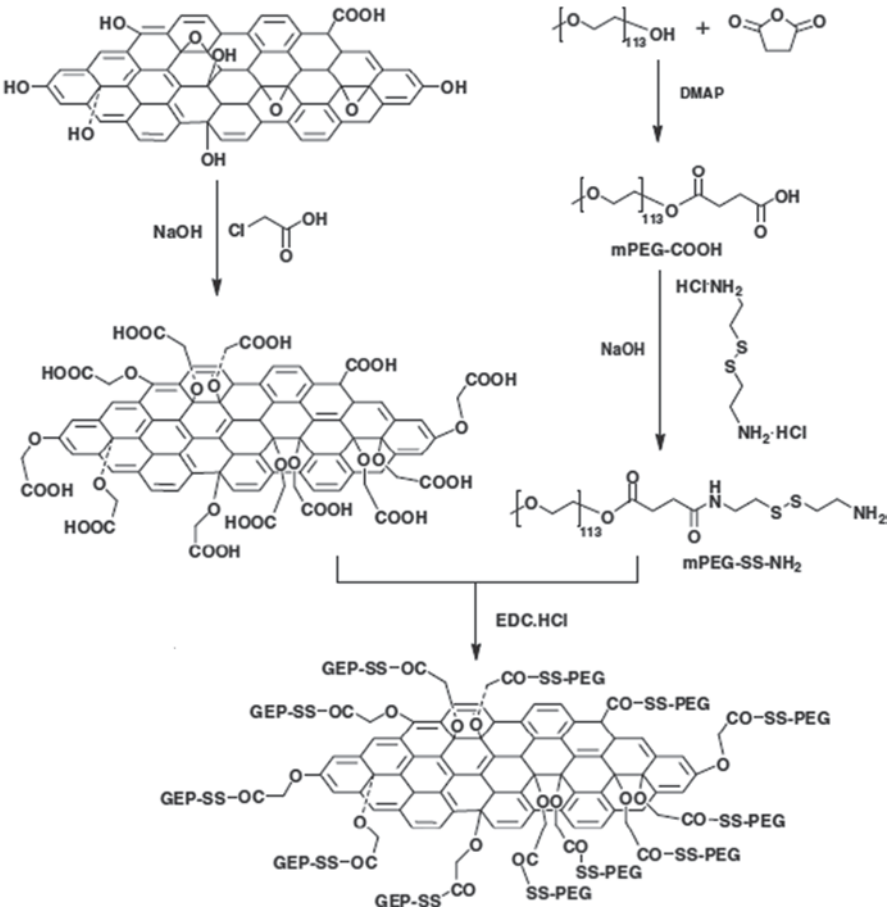

Fig. 2.5 Synthesis pathway of disulfide-linked NGO–SS–mPEG. *PEG* polyethylene glycol

drug delivery. It has been reported that the cytosolic GSH level in some tumor cells has been found to be at least four fold higher compared with normal cells [24]. The GSH can quickly cleave the disulfide linkage by reduction reaction in tumor site, which leads to drug release. The antitumor drug DOX hydrochloride was loaded to the carrier also by π–π stacking and hydrophobic interactions between DOX and GO. The pharmaceutical system was also pH-dependent similar to the above PEG–GO system. The GSH-mediated drug release was carried out in HeLa cells in terms of GSH concentration and tumor cell viability. The carrier itself did not show significantly inhabitation of the growth of Hela cells even up to a concentration of 1 mg mL^{-1}. Either free DOX or DOX -loaded carrier had effectively reduced the viability of HeLa cells in a dose-dependent fashion. The maximum efficacy of about 90% growth inhibition after 24 h was achieved at the concentrations of equivalent DOX dose >20 mg L^{-1}. At higher DOX concentrations, the passive uptake of DOX–carrier nanocomposite was high so that tumor cells were killed with or without the presence of GSH. However, the addition of GSH-reduced ethyl ester to cell culture media potentiates the inhibitory effect of DOX-loaded nanocomposite, particularly at the concentrations of 0.25 and 0.125 mg mL^{-1}. Upon exposure to 10 mm GSH, reductive cleavage of the disulfide-linked PEG shell initiated rapid release of encapsulated DOX.

The transferrin-modified PEGylate–GO (Tf–PEG–GO) became glioma-targeted drug delivery carrier [25]. The PEG used here was the amine terminated six-armed PEG to form amide linkage with GO and transferrin. The DOX and Tf–PEG–GO is also simply mixed and adsorbed by non-covalent force. The DOX loading ratio (the weight ratio of loaded drug to carriers) was estimated to be 115.4% of Tf–PEG–GO, closing to that of PEG–GO (127%). The DOX–PEG–GO and DOX–Tf–PEG–GO were used to evaluate their cytotoxicities to C6 glioma cells. The IC_{50} values (50% glioma inhibition drug concentration) of DOX–PEG–GO, DOX–Tf–PEG–GO, and free DOX were 13.61, 63.01, and 28.43 μg/mL, respectively. It indicated that Tf–PEG–GO–DOX presented a 4.63 intensification of cell inhibition compared to PEG–GO–DOX. Because TfR was overexpressed at the surface of glioblastoma cells, it would compete with Tf–PEG–GO–DOX to bind TfR on the cell surface after adding free Tf into the culture medium. Within 12 h, the cellular uptake index of Tf–PEG–GO–DOX was much higher than that of PEG–GO–DOX. The Tf-PEG-GO-DOX and PEG-GO-DOX were also performed to the brain glioma bearing rats. As a result, the DOX distribution in other tissues displayed that DOX was accumulated mostly in both the spleen and the liver. Interestingly, the concentrations of Tf–PEG–GO–DOX and PEG–GO–DOX in the spleen and the liver were significantly lower than that of the free DOX group. By the log-rank test, the median survival time of Tf–PEG–GO–DOX was significantly prolonged compared with that of the saline control, DOX, or PEG–GO–DOX, which reached nearly 41.7, 31.6, and 19.0% life span extension, respectively. The targeted delivery of DOX to the glioma tissue is achieved.

Chitosan (CHI) can graft to GO via a facile amidation process [26]. The CHI-grafted GO GO-CHI has maximum amount of CHI up to 64%, which guaranteed the nanocomposite good aqueous solubility and biocompatible. The GO-CHI can

load CPT via π–π stacking and hydrophobic interactions. GO-CHI possessed 20% of weight-loading capacity for CPT. In the study on the cytotoxicity to HepG2 and HeLa cells, the GO-CHI-CPT exhibited a potency with a 50% growth inhibition concentration (IC_{50}) of ~29 μM, while free CPT displays a ≈20% growth inhibition near the same concentration. It meaned that the GO-based nanocomposite can improve the drug efficacy without increasing the drug dose. The cell membrane was negatively charged, and the GO-CHI-CPT was easy to be protonated and became the positive charged particles. This course made the GO-CHI-CPT to enter the cells much easier through an efficient endocytic process. Interestingly, the GO-CHI was also able to condense plasmid DNA into stable, nanosized complexes. Such DNA hybrids showed reasonable transfection efficiency in HeLa cells at a nitrogen/phosphate mixture ratio of four. The nanoparticles in the diameter range of 100–200 nm with a narrow polydispersity were preferred.

CHI is viable polymeric material to enhance the biocompatibility of the matrix for controlled release of therapeutic molecules, while FA is a ligand for targeting cell membrane and promoting endocytosis via the folate receptor (Fig. 2.6) [27]. The preparation process of the nanocomposite has three steps. Firstly, the FA conjugated to CHI via the amide groups. Secondly, the DOX loaded to GO by noncovalent forces. Thirdly, the DOX –GO was encapsulated with the folate–CHI to produce the nanocomposite. The release of DOX was similar to the PEG–GO at different pHs. The loading and release of DOX depended upon the hydrogen bonding interaction with GO and was a function of pH.

CHI-modified GO composites as nanocarries for anticancer drugs (e.g., CPT) and genes via π–π stacking and hydrophobic interactions have been realized. However, the covalent between antitumor drug and GO is not well studied. Incorporation of GO with the CHI–xanthone schiff base could provide additional pH sensitivity which is useful for controlled release of the as-designed drugs [28]. As can be seen from the Fig. 2.7, a novel nanostructured antitumor drugs from GO–CHI–xanthone (GCS) base compound was designed, in which CHI–xanthone (CS) schiff base acted as the tumor inhibitor while GO worked as the drug delivery carrier. The pH-triggered simultaneous release of the CS from the GCS was achieved by changing the solution from acidic to base conditions. The as-synthesized GCS showed less cytotoxicity against the normal human retina cells when a concentration of 10 nM was applied. In the same concentration, the GCS induced nearly 50% HeLa cells apoptosis. It exhibited super antitumor activity when compared with xanthone and paclitaxel (PTX) under the same conditions.

Except PEG, other polymers were employed to covalently bond with GO for drug delivery. The GO sheets grafted with a thermo-responsive polymer would produce desirable DDS [29]. The poly(*N*-isopropylacrylamide) (PNIPAM) is a thermal responsive polymer. PNIPAM was incorporated onto GO by applying click chemistry. The PNIPAM-grafted GN sheets (PNIPAM–GS) consisted of about 50% polymer, which formed a long-term stable dispersion. The PNIPAM–GS sheets had good solubility and stability in physiological solutions and PBS solutions. It had a hydrophilic to hydrophobic phase transition at 33 °C, which was relatively lower than that of a PNIPAM homopolymer due to introduced nanoGO as shown

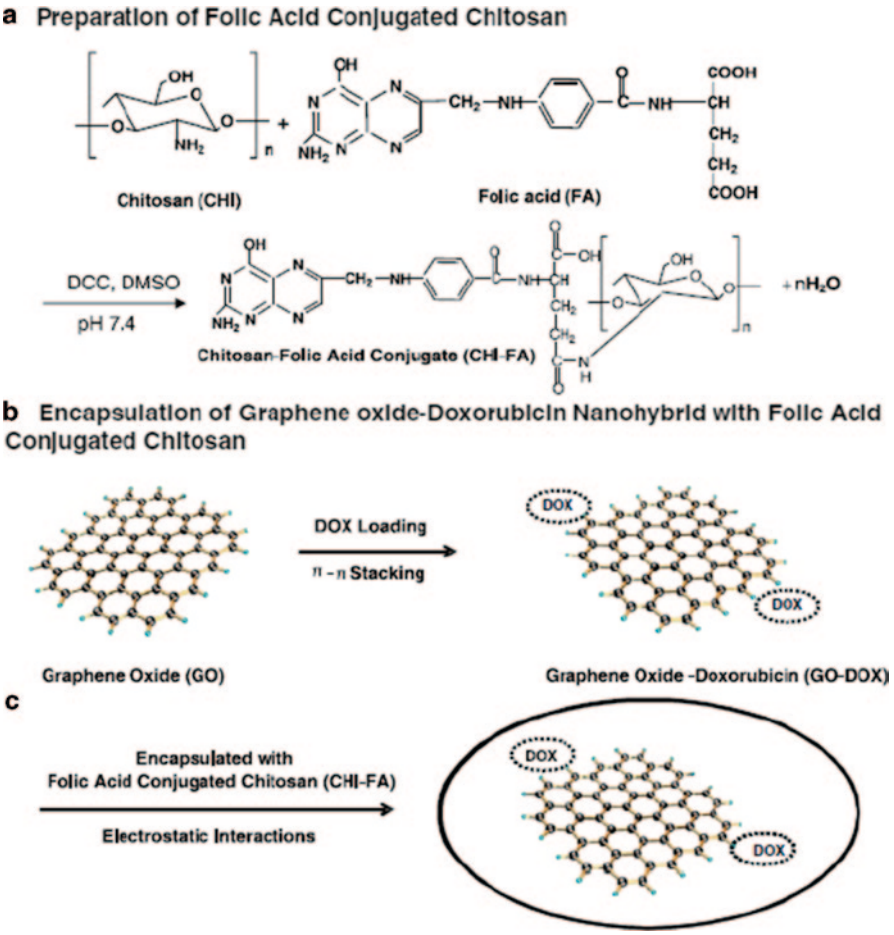

Fig. 2.6 Scheme for the synthesis of nanocarrier **a** conjugation of chitosan with folic acid, **b** loading of graphene oxide with doxorubicin, and **c** encapsulation of graphene oxide-loaded doxorubicin with folic acid conjugated chitosan

in Fig. 2.8. The GO was about 166.5 nm in size with a polydispersity index (PDI) of 0.384 at 25 °C, while the grafted GN sheets increased to 189.6 nm with the PDI decreased to 0.261. This is due to the PNIPAM chains grafted onto the surfaces of GN sheets. Mixing of CPT with PNIPAM–GS in DMSO resulted in a CPT-loaded nanocomposite. The binding of CPT onto the PNIPAM–GS was due to hydrophobic interactions and π–π stacking. The capacity of 1 g PNIPAM–GS for CPT is about 0.185 g, which is two times greater than the loading capacity of the PEG–GO carrier. The drug could sustain release in PBS and reached to a plateau at 19.4% CPT after 72 h. The CPT–PNIPAM–GS strongly inhibited the growth of metastatic skin tumor cells (A-5RT3).

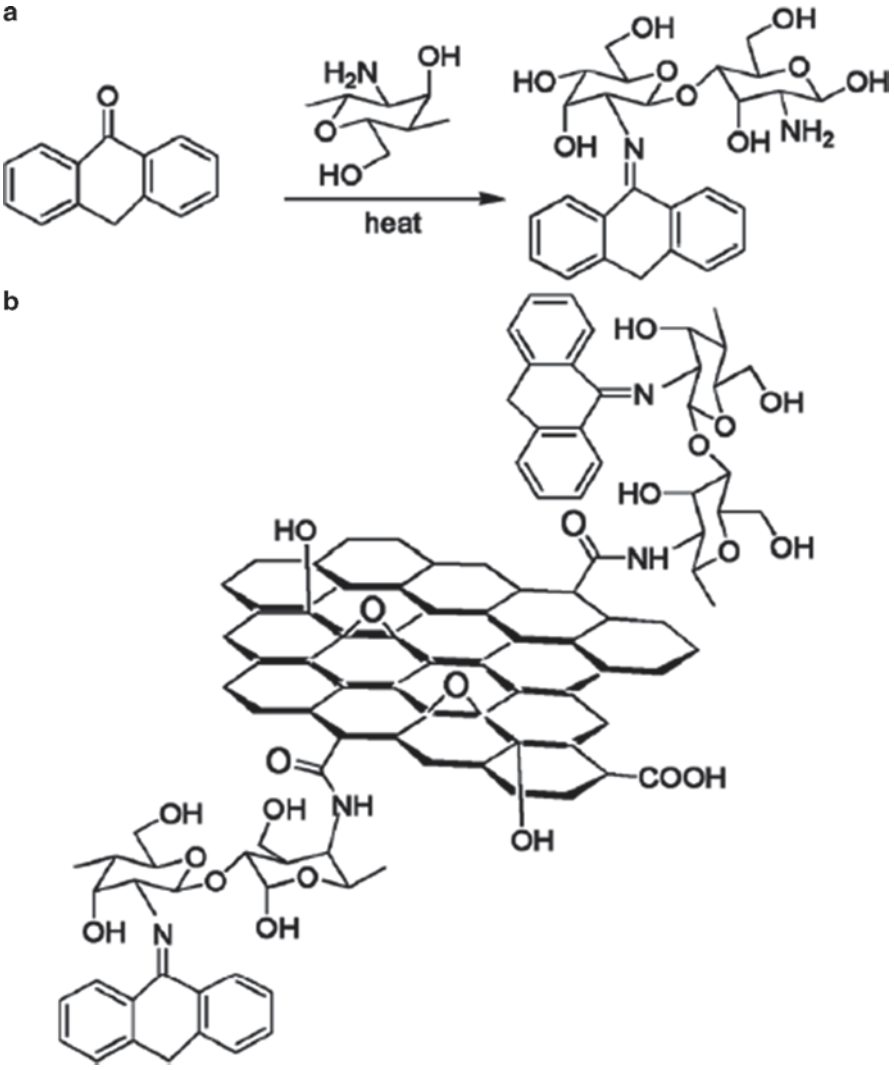

Fig. 2.7 **a** Schematic synthesis of CS and **b** schematic representation of the GCS nanocomposite

The poly(*N*-vinyl caprolactam) (PVCL) was grafted to GO by in situ atom transfer radical polymerization (ATRP) to impart aqueous stability in the buffer and other biological solutions [30]. A carboxyl activating agent (EDC/NHS) was used to initiate the formation of an amide linkage. The ATRP initiators were attached to the GO sheets through the reactions of hydroxyl and amine groups in GO with 2-bromo-2-methyl propionyl bromide to obtain the GO–PVCL, as shown in Fig. 2.9. The CPT simply mixed with GO–PVCL in DMSO solution resulting in CPT-loaded GO–PVCL nanocomposite. The driven force is also π–π interaction between the GO and the CPT. The maximum loaded CPT was about 20 % weight of GO–PVCL.

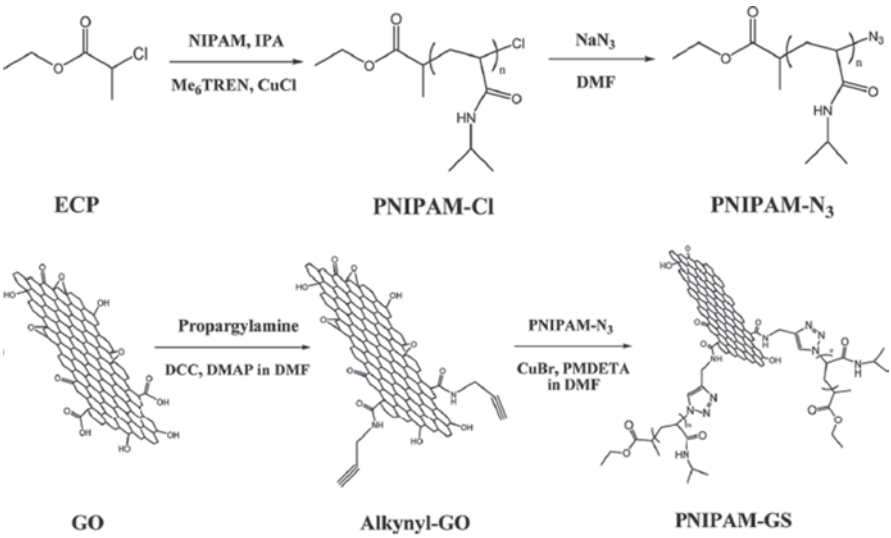

Fig. 2.8 Synthesis route of PNIPAM-GS. *PNIPAM* poly(*N*-isopropylacrylamide, *DMF* dimethyl forma-mide, *DCC N,N′*-dicyclohexylcarbodiimide, *PMDETA N, N,N″,N″,N″*-pentamethyl diethylene-triamine, ethyl 2-chloropropionate (ECP), 4-dimethylaminopyridine (DMAP)

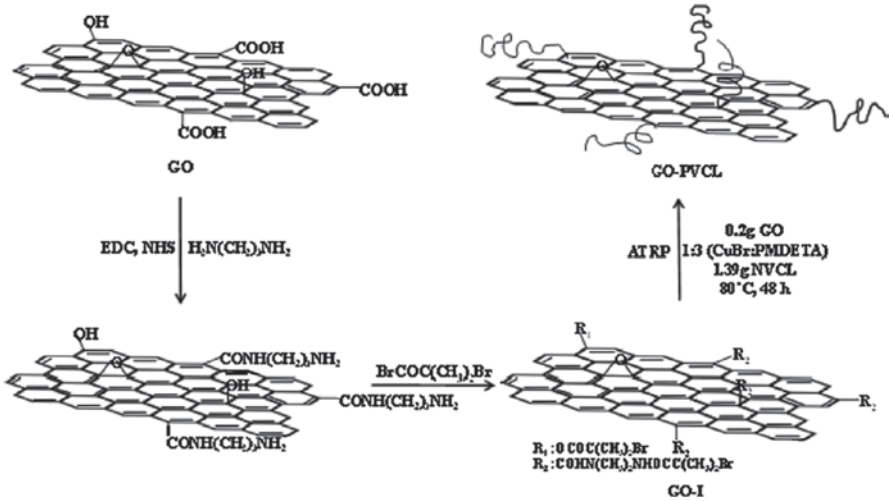

Fig. 2.9 Schematic diagram showing the synthesis of GO–PVCL. *PVCL* poly(*N*-vinyl caprolactam), *EDC N*-Ethyl-*N′*-(3-dimethylaminopropyl)-carbodiimide, *PMDETA N, N,N″,N″,N″*-pentamethyl diethylenetriamine, *NVCL N*-vinyl caprolactam, *ATRP* atom transfer radical polymerization

Small amounts of CPT were released from the GO surface in water and PBS over a 72 h period at 37 °C, highlighting the strong non-covalent interactions between CPT and the GO sheets. The amount of drug released from GO–PVCL–CPT in aqueous solutions was lower than that from polymer micellar systems. The CPT was attached to the surface of the GN sheets by π–π stacking instead of being encapsulated in polymermicelles or nanoparticles. It suggested that different types of small aromatic and hydrophobic molecules with poor water solubility can be loaded onto the surface of the GO–PVCL in aqueous media through non-covalent interactions, which are strong enough to prevent rapid desorption under normal physiological conditions. However, at the pH of 5.5, 60% of CPT was released within 3 days. This was similar to the behavior of DOX, due to the increased hydrophilicity and solubility of CPT in acidic solution. The pure GO–PVCL without CPT loading was nontoxic to the cells. In contrast, GO-PVCL-CPT induced significant cancer cell death. The enhanced efficacy was owing to the drug bound to the GO–PVCL. The GO–PVCL–CPT and free CPT produced 50 and 20% growth inhibition, respectively, at 10 nM CPT after 24 h.

Another controllable release DDS was designed by using β-CD functional GN hydrogel [31]. Then GN hydrogel was obtained by polymerization of *N*, *N*-dimethylacrylamide (DMAA) and it is black cylindrical. The CPT entered the CD rings on the GN hydrogel. The CPT was released from β-CD functional GN hydrogel more slowly than that from GN hydrogel without β-CD. The cumulate CPT release from β-CD functional GN hydrogel reached 50% after 35 h. For the GN hydrogel without β-CD, the CPT was fast released at the beginning 2 h and the cumulate CPT release reached 50%. If the β-CD was linked by FA, the nanohybrid can target the tumor cell more effectively. As is shown in Fig. 2.10, a drug carrier was designed by using the FA as a target unit and an adamantanyl porphyrin acted as a linker unit, while the GO acted as a carrier unit [32]. The β-CD was also incorporated into the hybrid to hold the antitumor drug in the ring of CD. By employing the advantage of the strong hydrophobic interaction between the CD cavity and adamantane moiety, the biocompatibility and target effect of DOX/2/GO system significantly improved. The loading of DOX to the complex was driven by the π–π interaction and hydrogen bonding. DOX and 1/2/DOX/GO displayed similar anticancer activity toward HeLa cell lines. The anticancer activity of DOX/2/GO decreased by 52% as compared with that of 1/2/DOX/GO.

Another gelatin functionalized GN nanosheets (gelatin–GNS) was obtained by simply mixed GO with gelatin solution at 95 °C for 24 h [33, 34]. The gelatin guaranteed good dispersibility and stability of the GO. The gelatin–GNS can load the methotrexate (MTX) via strong π–π stacking interaction. The drug loaded on gelatin–GNS was embedded in and protected by gelatin. The standard curve equation of MTX solutions was $A = 57.369\ C + 0.0112$, $R^2 = 0.9993$, and the saturated adsorption capacity could be calculated to be 21.1 μg MTX to 75 μg gelatin–GNS. The MTX–gelatin–GNS composite could sustain the release of MTX from the nanocarrier during the first 12 h in various pH conditions. There were 40.3, 65.8, and 80.9% MTX released from the MTX–gelatin–GNS composite in the pH 7.4, 5.3, and 2 within 12 h. The observation indicated that the total release amount of MTX after

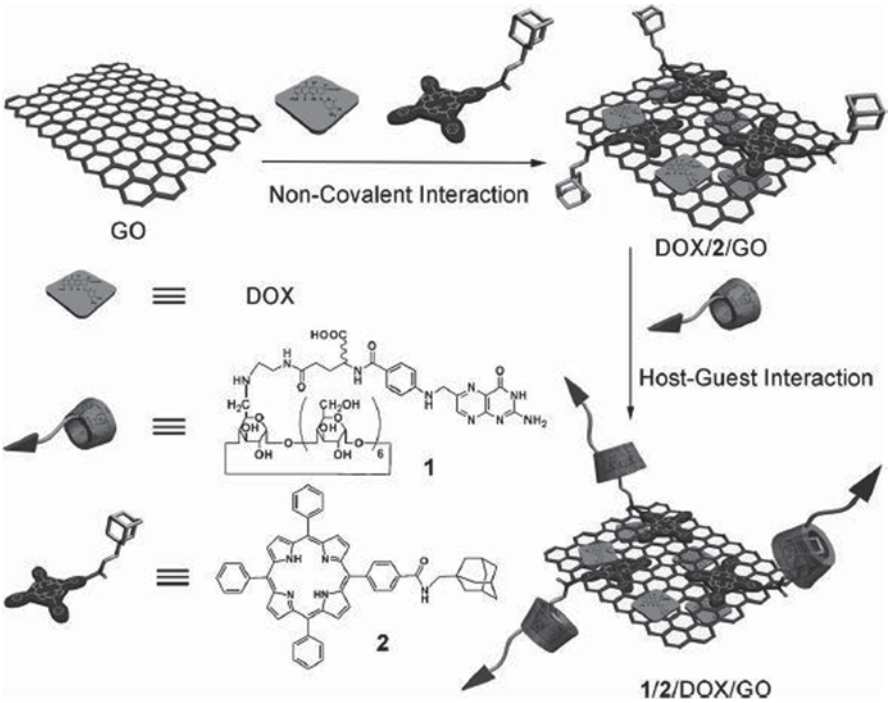

Fig. 2.10 Synthesis of 1/2/DOX/GO from graphene oxide, DOX, adamantane-modified porphyrin, and folic acid-modified cyclodextrin. *DOX* doxorubicin

24 h for these cases of acidic solutions was much higher than at neutral conditions. It is because the much higher solubility of MTX under acid condition than that under neutral condition. The MTX (with NH_2 groups) got protonated resulting in the partial dissociation of hydrogen-bonding interaction, and the decomposition of the gelatin under acid conditions would also lead to the release of MTX. The inhibition rate of free MTX and MTX–gelatin–GNS to human lung cancer A549 cells was 59.4 and 56.7%, respectively, at 24 h. They showed a similar cancer cell inhibition rate, and gelatin-mediated sustained drug release process comes to an end in 24 h at a dose of 20 μg mL^{-1}.

The synthesized polymer pluronic F127 (PF127) were also used to prepare GN-based DDS [35]. The PF127 is triblock copolymers bond by poly(ethylene oxide) (PEO) and poly(propylene oxide) (PPO), composed of PEO_{99}–PPO_{67}–PEO_{99}. The pluronic F127 was dissolved in GO solution, and then the GO was reduced by hydrazine to produce GN. The formed GN was stable by pluronic F127 in aqueous solution. Then the DOX was added to get the DOX–PF127–GN nanohybrid. The DOX can reach a loading capacity of 289% (w/w). It can stable in cell medium due to the hydrophobic PPO segments binding to the hydrophobic surface of GN via hydrophobic effect, whereas the hydrophilic PEO chains extending into water. As can be expected, the DOX interacted with the PF127–GN is hydrophobic interactions

and π–π stacking, and the DOX release is pH dependent as its behaviors in the PEGylate–GO composite. The pharmaceutical system, DOX–PF127–GN significantly inhabits the growth of human breast adenocarcinoma MCF-7 cells.

When using the *p*-aminobenzoic acid (AA) functionalized the GO, another small molecule modified GO was achieved. It can be reduced to GN, but remains the AA groups. To enhance the aqueous stability of reduced aminobenzoic acid–GN, the polyethyleneimine (PEI) was introduced into the nanocomposite to form PEI–AA–GN [36]. The FA–PEI–AA–GN drug carrier could be finally produced by further covalent binding FA molecules to PEI–AA–GN. The as-synthesized carrier can specifically target CBRH7919 cancer cells by overexpress FA receptor. The DOX was loaded to the carrier to inhibit the growth of CBRH7919 cancer cells. The weight of loaded DOX to the FA–PEI–AA–GN was approximately 28.62 %. The release of DOX from the DOX loading FA–PEI–AA–GN was not only pH dependent but also salt dependent. The pH-dependent release of DOX was very similar to the DOX release from PEGylate–GO nanocomposite. In PBS at PH 7.4, the release of drug was also very clear, and it might be due to the salt effect (NaAc in acetate-buffered saline (ABS) and NaCl in PBS). Such salt dependence of drug release from rGO sheets could be exploited for drug-delivery applications. The DOX/FA–PEI–AA–GN can enhance the cancer cell apoptosis effectively and can also push the cancer cells to the vulnerable G2 phase of the cell cycle, which is most sensitive and susceptible to damage by drugs or radiation.

2.3 CNTs for Drug Delivery

2.3.1 Delivery of Anticancer Drugs

CNTs contain single-walled CNTs, double-walled CNTs, triple-walled CNTs, and multiwalled CNTs. The pristine CNTs are insoluble in organic and inorganic solvents, and they have a tendency to agglomerate or bundling, and this behavior restricts use of CNTs in vivo. Functionalization is a good choice to improve solubility and agglomeration of CNTs. The chemical modification of CNTs was achieved by carboxylation, acylation, amidation, esterification, PEGylation, and polymers wrapping. The tail end of CNTs is oxidized better than sidewall due to high curvature. The chemical modification of pristine CNTs with most widely used strong oxidative agents (concentrated H_2SO_4:HNO_3 = 3:1) generates various functional groups such as carboxyl, ketone, and ester. The oxygenated CNTs exhibit better solubility. Surface-modified CNTs are able to carry numerous anticancer drugs, such as DOX, cisplatin (Cis), docetaxel (DTX), gemcitabine (Gem), mitoxantrone, and non-anticancer drugs, such as antimicrobial, anti-inflammatory, antihypertensive, and antioxidant agents.

Cisplatin (cis) is a second-generation platinum anticancer drug widely used for cancer treatment. Cisplatin have conjugated amine functionalized single-wall nanotubes (SWNTs; SWNT–PL–PEG–NH_2) by succinate as one of ligands (Fig. 2.11)

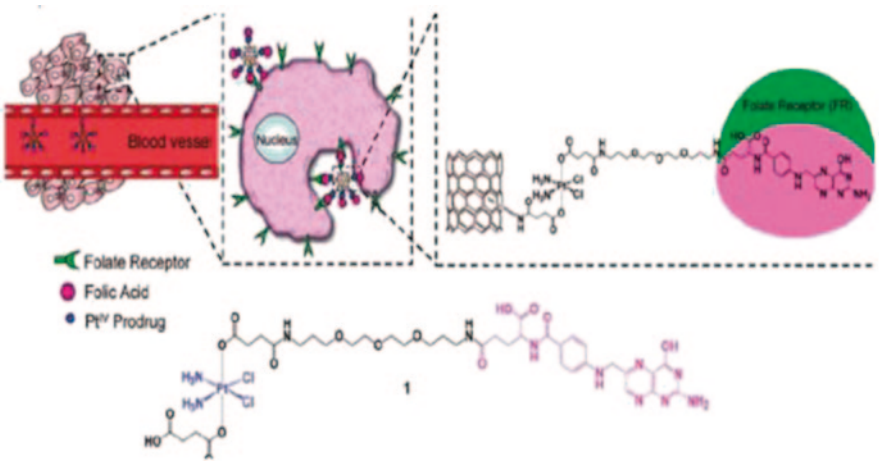

Fig. 2.11 Folate receptor *(FR)*-mediated targeting and SWNT-mediated delivery of SWNT–PL–PEG–NH_2 by endocytosis and structure of SWNT–PL–PEG–NH_2

[37]. Platinum can be released efficiently from SWNTs and receptor in the cancer cell environment. Functionalized SWNTs as warhead carry platinum to the tumor cell and release cisplatin when Pt(IV) were reduced to Pt(II) in intracellular. The SWNTs deliver the folate-bonded Pt(IV) into the folate-receptor overexpress cancer cell by endocytosis. The reductive cisplatin enter nucleus and insert targeted nuclear DNA. Compared to folate receptor-negative testicular carcinoma cells, the experiment results exhibited that cell viability of folate receptor-positive human choriocarcinoma (JAR) and human nasopharyngeal carcinoma (KB) cell lines is significantly lowered using amine-functionalized SWNTs (SWNT–PL–PEG–NH_2) treatment.

The [cis-Pt$(NH_3)_2$] moiety was conjugated with CNTs containing surface-modified carboxylic groups [38]. The cisplatin and epidermal growth factor (EGF) were attached to the SWNTs to specifically target squamous cancer, and SWNT–cisplatin without EGF was as a controlled group, and QD luminescence offered visualization to track the SWNT bioconjugate in cell and mice. It was observed that the SWNT–cisplatin–EGF entered cancer cells by receptor-mediated endocytosis. As a contrast, controlled groups were unable to reach the cell nuclei. The SWNT–cisplatin–EGF biojugates with 1.3 μM cisplatin, which showed more efficiency at cell killing than 10 μM free cisplatin. The experimental results have showed that the regression of tumor growth was rapid in mice treated with targeted SWNT–cisplatin–EGF relative to nontargeted SWNT–cisplatin.

The chemical-modified CNTs offset the potential side effects of DOX·HCl by π–π stacking, hydrophobic and electrostatic interactions mechanism. The SWCNT−HBA−DOX nanocarrier system was designed through hydrazone bonds of SWCNT−HBA and DOX (Fig. 2.12) [39]. The hydrazine-modified SWNTs formed by covalently attached hydrazinobenzoic acid (HBA) on the walls of SWNTs. The anticancer drug DOX was conjugated to the HBA segments of SWNT by hydrazine

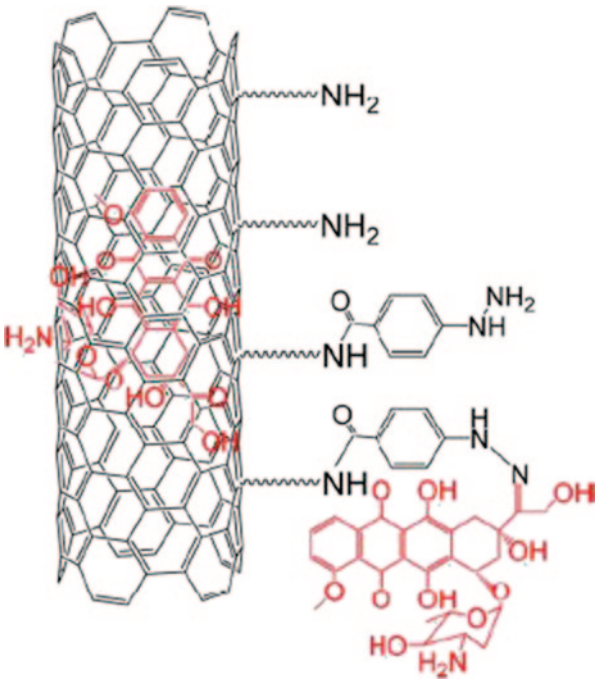

Fig. 2.12 Schematic representation of the SWCNT−HBA−DOX

as bridge. The resulting hydrazone bonds supply a strong pH-responsive drug release and offer efficient DOX release near the acidic tumor microenvironment, suggesting its targeted carrier system. The DOX released from SWNT–HBA–DOX and SWNT–DOX was about 51 and 37% after 12 h, respectively. Compared with SWNT–DOX coated by hydrophobic interaction and π–π stacking, the SWNT–HBA–DOX exhibited the significant advantage of high loading capacity and prolonged release of DOX, and thus improved its cytotoxicity against cancer cells. The hydrazone showed the super sensitivity than π–π stacking interaction at acidic pH. The SWNT–HBA–DOX also showed higher cytotoxicity to HeLa cells than that of SWNT–DOX conjugate under the same concentration.

The SWCNT drug delivery based on polysaccharide sodium alginate ALG and CHI-modified SWCNTs for controlled release of DOX were also reported [40]. As we know, the CHI is cationic and ALG is anionic, they confer the coated SWCNTs with different zeta potential. CHI is stable at pH 7.4 but degrades readily in acidic pH (e.g., lysosomal pH and the pH characteristic of certain tumor environments.), and ALG-coated SWCNTs showed the highest DOX-loading capacity. The developed FA and polysaccharide (CHI and ALG) wrapped SWCNTs selectively accumulated in the cancerous tissues. The CHI/ALG–SWCNTs showed higher loading efficiencies than the CHI–SWCNTs. The release of the DOX loaded is pH triggered and stable in PBS buffer at pH 7.4 at 37 °C. The cells treated with DOX–FA–CHI/ALG-SWCNTs show a brighter red fluorescence than that of DOX–CHI/ALG–SWCNTs and free DOX, indicating that the FA conjugated nanotubes are taken up more

efficiently into the HeLa cells. The internalized drug is selectively released into the acidic environment of the lysosomes and enters the cell nucleus to bind DNA. This interaction inhibited transcription and induced the cell death.

The SWNT drug delivery for breast cancer inhibition in mice by conjugating PTX to the nontoxic lipid molecule docosanol for functionalization with CNT was developed [41]. FA as a target was also conjugated to CNT system. The drug molecule, for example, PTX, was conjugated to a long-chain lipid via a reversible ester bond. The SWNT–lipid–drug was made by exploiting the lipid "tail" in the drug to form lipid–drug/SWNT complex through strong hydrophobic interactions. The formulation was made multifunctional delivery using a tumor-targeting molecule FA that was conjugated to the end of the PL–PEG exploiting an amide bond formed between amine group of PL–PEG and carboxyl group of FA. This formulation could overcome the existing challenges of CNT in drug deliveries and broadened their use for multifunctional deliveries. The use of lipid molecule is unique and advantageous as it allows delivery of a range of drugs in multifunctional delivery applications. The SWNT–lipid–PTX approach afforded high drug-loading capacity; furthermore, the targeted SWNT–lipid–PTX showed much improved drug efficacy and lower nonspecific toxicity in vitro in comparison to free drug Taxol and nontargeted SWNT–lipid–PTX at 48 h (78.5% vs. 31.6 and 59.1% in cytotoxicity, respectively). The in vivo toxicity of SWNT–lipid–drug was evaluated. The mice were injected with a SWNT–lipid–drug carrier, as well as Taxol and the targeted SWNT–lipid–PTX, and saline injection was used as a negative control (Fig. 2.13). The targeted SWNT–lipid–PTX was found nontoxic to normal cell by evaluation using biochemical analysis.

Fig. 2.13 Photos of representative tumor-bearing mice from control and treatment groups at experimental end point. Tumors were indicated within *black squares*. *SWNT* single-wall nanotubes, *PTX* paclitaxel

A DDS was prepared via a CNT vehicle by QD-conjugated CNTs for in vivo imaging [42]. An anticancer drug PTX was efficiently loaded in PLGA-coated CNT against human PC-3MM2 prostate cancer cells. The drug-loading capacity is 112.5 ± 5.8 μg mg^{-1}. The CNT–QD were injected into mice by tail vein and showed good targeting to specific sites by fluorescence visualization in live animals. The QD-conjugated CNT exhibit a strong luminescence suitable for noninvasive optical in vivo imaging. The accumulation of Cd in liver, kidney, stomach, and intestine is 70.36, 2.42, 0.86 and 1.00 μg g^{-1} after 1 day of injection, respectively. Except for kidney, the accumulation associated with liver, stomach, and intestine obviously lowered after 3 days. The Cd amounts showed slightly enhanced in all organs after 6 days. The evaluation of cytotoxicity of this novel DDS exhibited that CNT–QD was predominantly uptaken by liver, kidney, stomach, and intestine.

Frank Alexis et al. [43] introduced biocompatible block-co-polymer poly(lactide)-poly(ethylene glycol) (PLA–PEG) to CNTs loaded with anticancer drug PTX. This novel drug system can effectively control drug reservoir and release and prevent aggregation in aqueous solution. The CNT–PLA–PEG could load 1.65 wt% PTX. Biodistribution studies in mice showed CNT coated with PLA–PEG can pass through the kidneys and bladder as well as liver and spleen, suggesting a lower degree of aggregation in tissues. The further research showed that copolymer-coated CNTs significantly reduced in vitro toxicity and inflammatory response. Compared to non-coated CNTs, in vivo studies show no long-term inflammatory response with CNT coated with PLA–PEG (CLP), and the surface coating significantly decreases acute toxicity. The CNT–PLA–PEG DDS at concentrations of 70 nM PTX was as effective as free PTX incubated for 6 h at 140 nM.

Multiwalled CNT DDS was designed by covalently combining CNTs with the antitumor agent 10-hydroxycamptothecin (HCPT) using hydrophilic diamintriethylene glycol as the spacer between nanotube and drug moieties [44]. The 16% drug-loading capacity was achieved. The release of HCPT was faster in acidic than neutral solution. The cumulative release lowered 15% of total loaded amount at pH 5.0 or 7.4, indicating the good stability of the ester bond. The high release rate was shown in fetal bovine serum. It was observed that multiwalled nanotubes (MWNT)–HCPT conjugates exhibit long blood circulation and high drug accumulation in the tumor site. The MWNT–HCPT and free HCPT, all exhibited dose-dependent antitumor features. The group treated with MWNT–HCPT showed similar tumor suppression effect to the group treated with free HCPT at two times dosage in the initial 9 days, but better effect from 9th to 15th day. The experimental results showed that MWNT–HCPT conjugates are superior in antitumor activity both in vitro and in vivo to clinical HCPT formulation.

Fatemeh Atyabi et al. developed folate conjugation of PEGylated MWCNTs for the delivery of DOX. The low-PEGylated and high-PEGylated MWCNTs exhibited different loading efficiency, with 84.3 ± 3.1% and 49.3 ± 5.4%, respectively [45]. DOX cumulative released from non-PEGylated, low-PEGylated, and high-PEGylated CNTs were 11.25, 21.66, and 30.11% in 24 h, respectively. The release rate of DOX from non-PEGylated, low-PEGylated, high-PEGylated, and folate-targeted MWCNTs reached 15.26, 24.17, 42.50, and 54.4% in 72 h, respectively. The higher

pegylation degrees induced higher release rate of DOX due to the increased hydrophilicity of CNT surface. Folate-targeted CNTs expressed a 3.2-fold decrease in IC_{50} value compared with non-targeted CNTs. The folate-targeted MWCNT showed higher degree of cellular uptake and internationalization than that of non-targeted MWCNT in HeLa cells (derived from human cervical cancer cells) using the confocal microscopy. The vivo study showed that non-PEGylated CNTs can be easily endocytosed by hepatocytes and change the macroscopic appearance of liver from red to black. The liver uptake of CNTs significantly decreased as the amount of the hydrophilic part of carriers CNTs increased. The different amount of PEG in the formulation showed different degree of liver uptake (Fig. 2.14).

Wu et al. [46] synthesized the functionalized MWCNTs through the covalent graft of PEI on shortened MWCNTs and further conjugated fluorescein isothiocyanate (FITC) and prostate stem cell antigen monoclonal antibody (mAbPSCA). The detailed preparation procedure is illustrated in Fig. 2.15.

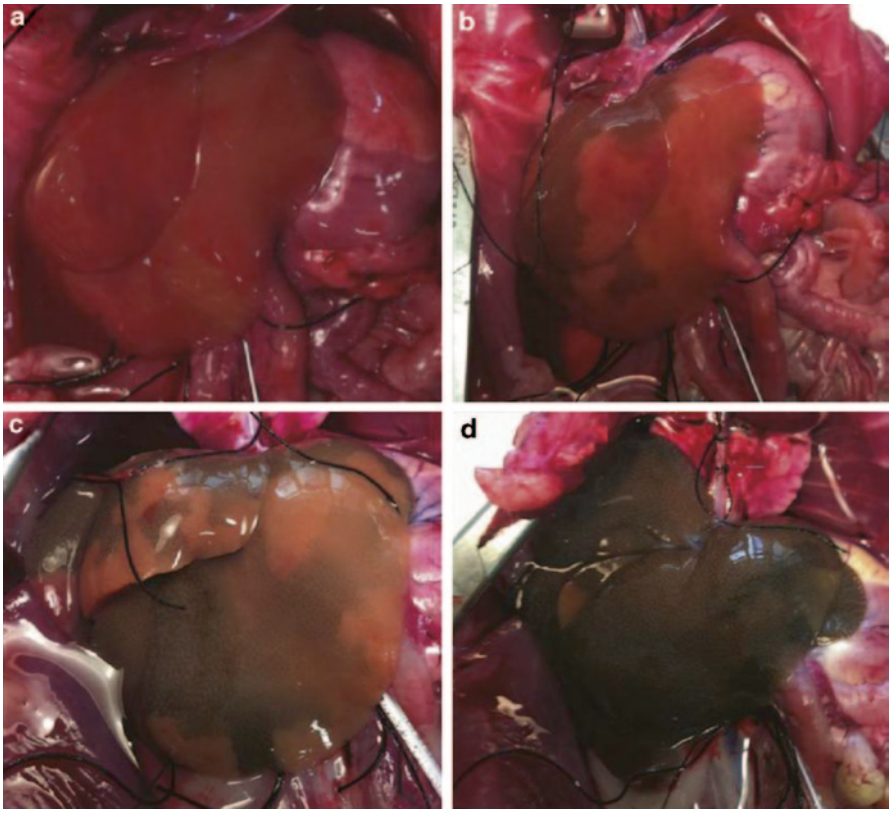

Fig. 2.14 Macroscopic appearance of liver after 3 h of liver perfusion with DOX (**a**), delivered DOX by high-PEGylated CNT (**b**), delivered DOX by low-PEGylated CNT(**c**) and delivered DOX by non-PEGylated CNT (**d**)

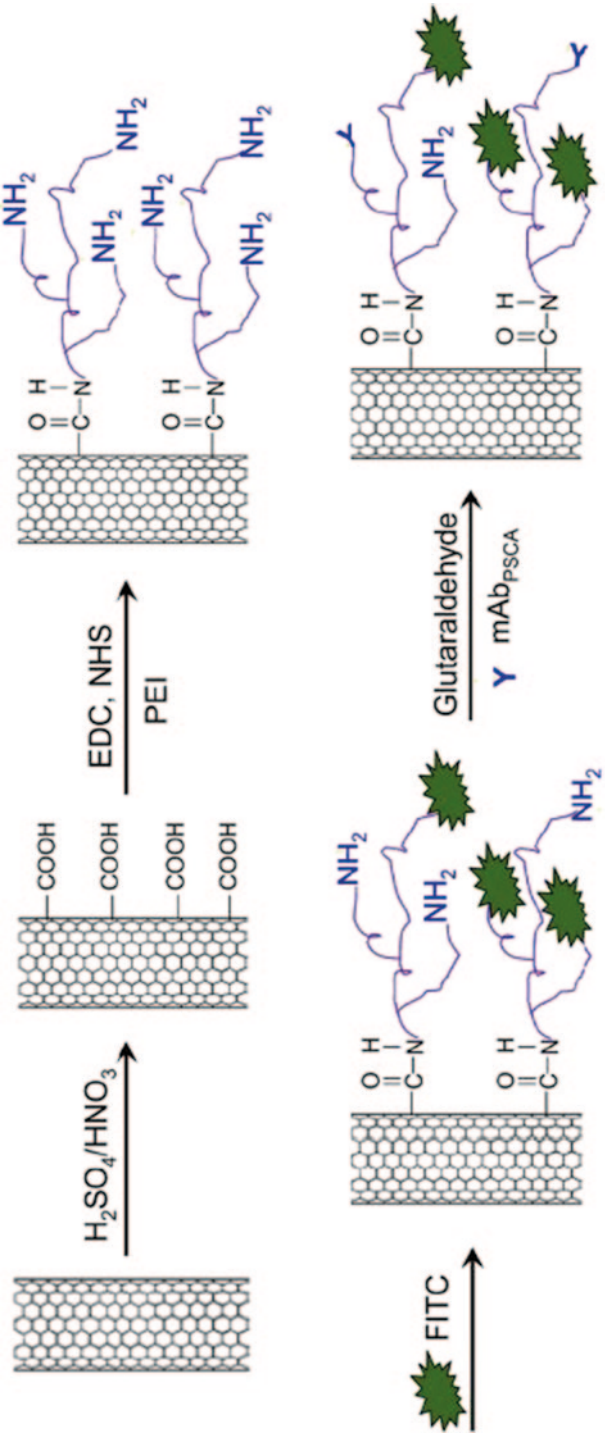

Fig. 2.15 Schematic diagram of the synthesis process for CNT–PEI(FITC)–mAb. *CNT* carbon nanotube, *PEI* polyethylenimine, *mAb* monoclonal antibody, *FITC* fluorescein isothiocyanate, *EDC N*-ethyl-*N′*-(3-dimethylaminopropyl)-carbodiimide, *NHS N*-hydroxysuccinimide

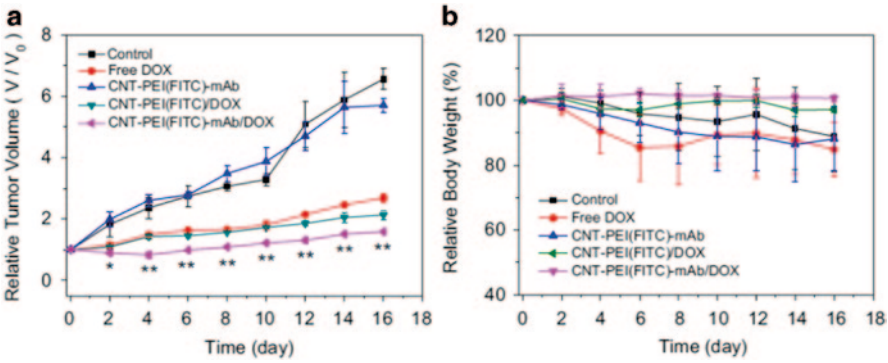

Fig. 2.16 In vivo therapy effects of CNT–PEI(FITC)–mAb/DOX in nude mice bearing PC-3 tumor: **a** Tumor growth curves for mice treated with free DOX, CNT–PEI(FITC)–mAb, CNT-PEI(FITC)/DOX and CNT–PEI(FITC)–mAb/DOX, in comparison with the blank control. **b** Body weight curves normalized to day 0 for different groups during the experiments. *CNT* carbon nanotube, *PEI* polyethylenimine, *mAb* monoclonal antibody, *FITC* fluorescein isothiocyanate, *DOX* doxorubicin

The as-prepared CNT–PEI(FITC)–mAb shows good biocompatibility and negligible hemolytic activity. The conjugation of antibody enhances the cellular uptake capability of the material by PSCA-overexpressed cancer cells. The CNT–PEI(FITC)–mAb/DOX showed high loading capacity, 300 mg g^{-1}. The DOX-release patterns of the CNT–PEI(FITC)–mAb/DOX are sustained and pH sensitive, and acidic microenvironments of cancer cells triggered the drug release. The PC-3 (PSCA-overexpressed) and MCF-7 (PSCA-low-expressed) cells were used in the study. There was a considerable increase in the cytotoxic effect of CNT–PEI(FITC)–mAb/DOX to PC-3 cells in comparison with MCF-7 cells. As can be seen from Fig. 2.16, compared with CNT–PEI(FITC)/DOX-treated group (2.13 ± 0.15-fold tumor growth), mice treated with CNT-PEI(FITC)-mAb/DOX showed considerable slowdown of tumor growth (1.58 ± 0.04-fold tumor growth). The mice weight treated with CNT–PEI(FITC)–mAb/DOX showed no change. However, high loss of weight was observed for the free DOX group.

Zhang's group reported a gastric cancer stem cells (CSCs) specifically targeting DDS (SAL–SWNT–CHI–HA complexes) based on CHI-coated SWNTs loaded with salinomycin (SAL) functionalized with hyaluronic acid (HA) to selectively kill gastric CSCs [47]. The in vitro release of SAL from SAL–SWNTs–CHI–HA is pH triggered, and accumulative release achieved high percentage of 60 % in 12 h at pH of 5.5. The results of cellular uptake indicated that FITC–SWNTs–CHI–HA complexes can selectively target CD44+ cells and internalize into the CD44+ cells by receptor-mediated endocytosis. Compared with CD44+, the SAL–SWNTs–CHI–HA complex showed complete inhibition of self-renewal capacity. The penetration of SWNTs–CHI–HA into CSC mammospheres also was researched, as shown in Fig. 2.17.

The three functional hybrid material composed of methacrylic acid (MAA), quercetin (Q), and CNTs through the free radical reaction was designed for the delivery

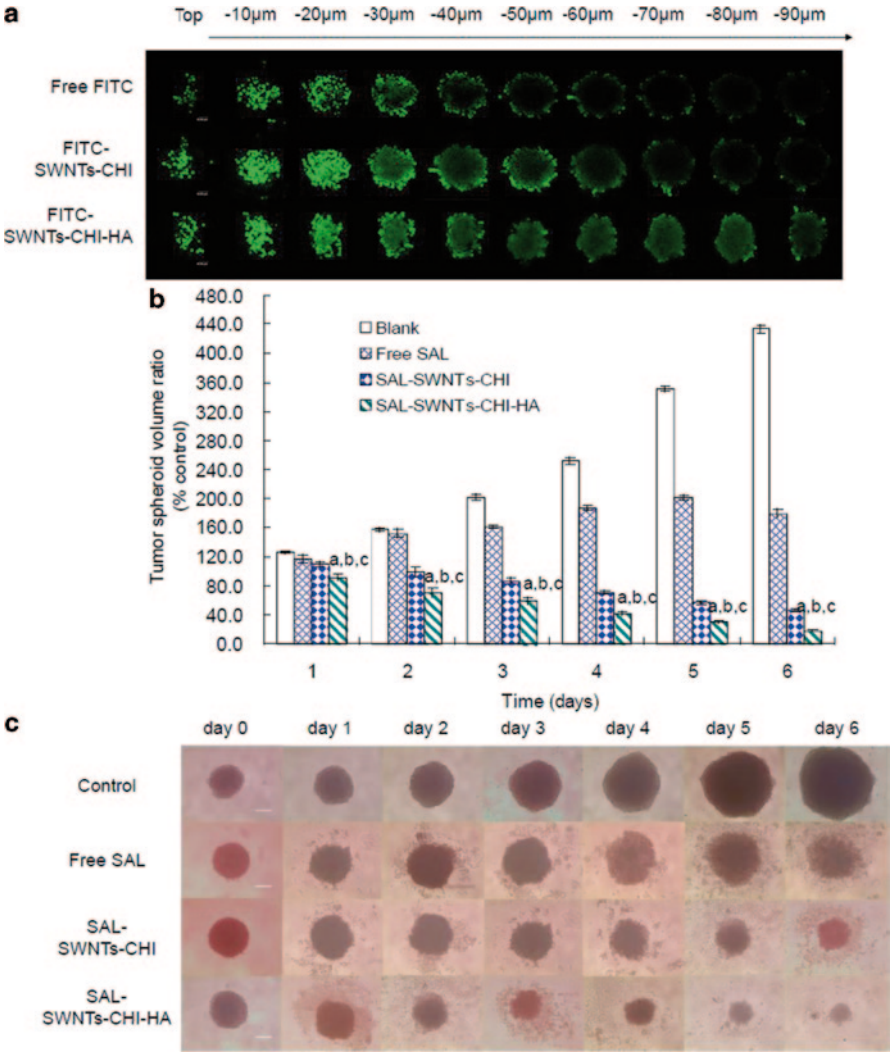

Fig. 2.17 Inhibitory effect on CSCs mammospheres. **a** Confocal images of CSCs mammospheres incubated with various FITC formulations of for 12 h. **b** Inhibitory and effect on the growth of CSCs mammospheres after applying different SAL-containing formulations. **c** The CSCs mammospheres images treated with different SAL-containing formulations under invert microscope. *SAL* salinomycin *SWNT* single-wall nanotubes, *HA* hyaluronic acid, *CHI* chitosan

of cisplatin [48]. The flavonoid quercetin (Q) is a natural anticancer compound. The CNT–PMAA–Q showed high drug-loading capacity (2.33 mg/g) compared with that of PMAA–Q (2.01 mg/g). They revealed that CNT–PMAA–Q showed higher growth inhibition than PMAA–Q and free cisplatin. The CNT–PMAA–Q/cisplatin DDS showed synergistic anticancer activity against human neuroblastoma cells (IMR-32) in vitro.

N. K. Jain et al. synthesized estrone (ES) and FA anchored PEGylated MWCNTs-loaded DOX to inhibit growth of human breast MCF-7 cells [49]. The DOX tended to attach to sidewalls of SWCNTs via π–π and hydrophobic interactions. The release of DOX is pH dependent. The DOX/FA–PEG–MWCNT and DOX/ES–PEG–MWCNT both showed faster initial release and followed sustained and slower periods at pH 7.4 and 5.3 buffer solution. Flow cytometric analysis indicated preferential higher uptake of DOX/ES–PEG–MWCNTs compared to DOX/FA-PEG-MWCNTs, DOX/PEG–MWCNTs, DOX/ox–MWCNTs, DOX/MWCNTs, and free DOX after 3 h incubation in MCF-7 cells owing to receptor-mediated endocytosis. The tumor volume obviously decreased after being incubated with DOX/ES–PEG–MWCNTs and DOX/FA-PEG-MWCNTs for 30 days, showing the longer survival span 43 and 42 days, respectively, compared with survival time of 12 days for control group.

The DDS (SWNT@MS–PEG/DOX) based on a novel PEG modified mesoporous silica (MS)-coated SWNTs was developed by loading DOX for the cancer combination therapy, namely, chemotherapy and photothermal therapy [50]. The cumulative release of DOX from SWNT@MS–PEG/DOX achieved 25 % of total in PBS at ph 7.4 after NIR irradiation for 4 h compared with 12.5 % released quantity of SWNT–PEG/DOX, indicating that NIR light triggered drug release behavior. It was found that SWNT@MS–PEG/DOX showed a higher cumulative and faster releasing rate of DOX than that from SWNT–PEG/DOX at a lower pH, and no obvious cytotoxicity even at the highest concentrations in 4T1 murine breast cancer cells, HeLa human cervical cancer cells, and 293T human embryonic kidney cells for incubation 48 h. The fluorescence reoccurrence of DOX could be an indicator of drug release in the 4T1 cells. As shown in Fig. 2.18, the cells incubated with SWNT@MS–PEG/DOX showed significantly enhanced DOX fluorescence after laser exposure, no dramatic discrepancy was found in free DOX-treated cells after laser irradiation. It found that relative cell viability treated by SWNT@MS–PEG/DOX was laser power intensity dependent, while apoptosis of 4T1 cells induced by free DOX was not significantly affected before and after laser irradiation. The tumor size of mice injected with SWNT@MS–PEG/DOX obviously decreases; even tumors on two mice completely disappeared post treatment compared with the group treated with free DOX, suggesting a remarkable synergistic antitumor effect.

Achraf Al Faraj et al. developed functionalized magnetic SWCNTs for the diffusion-weighted MRI and cancer therapy [51]. They synthesized iron and mouse endoglin/CD105 mAb bifunctionalized PVP-coated SWCNTs nanocarrier to delivery DOX into breast cancer. The SWCNT·+CD105+DOX conjugates exhibited high apoptosis, DNA damage, and oxidative stress in 4T1 cells. The decrease manner of bioluminescence is dose and time dependent. The SWCNT·+CD105+DOX group showed extremely weak bioluminescence at concentration of 2.5 μg/mL after 48 h, and the MRI measurement indicated tumor size obviously decreased (150 mm^3) by intravenous injection after 14 days compared with that of DOX (540 mm^3), SWCNT+CD105(700 mm^3), and SWCNT·+CD105 (750 mm^3) groups.

Prasanta Kumar Das et al. fabricated SWCNTs coating biotinylated amphiphile for the delivery of fluorescently labeled Cy3-oligoneucleotide (Olg) and DOX

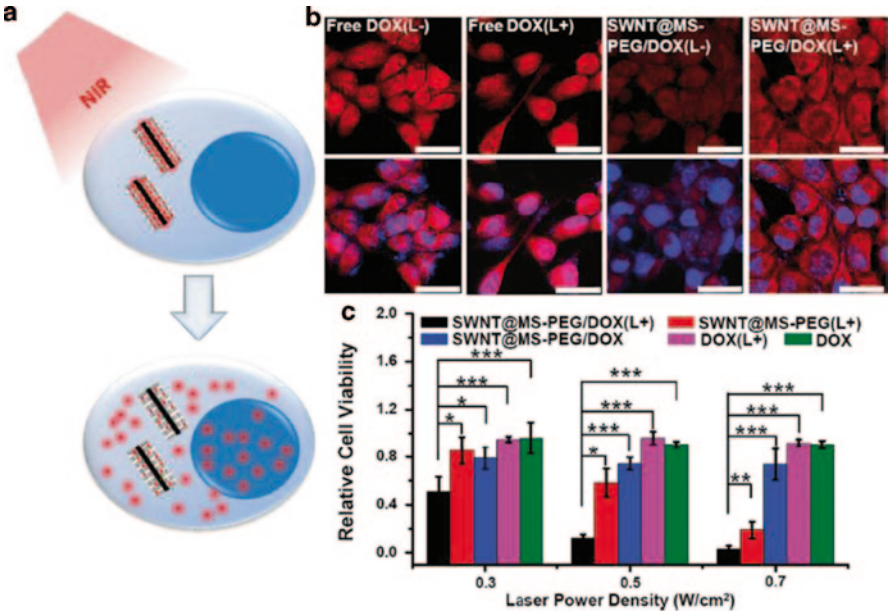

Fig. 2.18 NIR-triggered intracellular drug release. **a** A scheme showing NIR-triggered drug release from SWNT@MS–PEG/DOX in vitro. The uncovered DOX fluorescence from its quenched state inside SWNT@MS–PEG/DOX could be an indicator of drug release. **b** Confocal fluorescence images of 4T1 cells incubated with SWNT@MS-PEG/DOX (or free DOX; [DOX]=25μM) for 1 h, washed with PBS to remove extracellular nanoparticles, and then treated with laser irradiation (808 nm, 0.4 W cm^{-2}, 20 min; L+). Un-irradiated cells were used as the controls (L−). *Red* and *blue* colors represent DOX fluorescence and DAPI-stained cell nuclei, respectively. The scale bar: 25 μm. **c** Relative viabilities of 4T1 cells after various treatments. In this experiment, 4T1 cells were incubated with SWNT@MS–PEG/DOX(L+), SWNT@MS–PEG(L+), SWNT@MS–PEG/DOX, DOX(L+), and free DOX ([DOX]=25 μM), for 1 h, and then wash with fresh cell culture and irradiated with the 808 nm laser at different power densities for 20 min. Afterwards cells were re-incubated for additional 24 h before the MTT assay. *DAPI* 4′,6-diamidino-2-phenylindole, *SWNT* single-wall nanotubes, *MS* mesoporous silica, *PEG* polyethylene glycol, *DOX* doxorubicin

into the cancer cells [52]. The amphiphile functionalized SWCNTs (SWCNTs-1) showed low cytotoxicity and good stability in the media of salt and protein. They investigated target-specific cell uptake of SWCNTs-1-loaded Cy3-Olg into HeLa and HepG2 cells showing successful internalization, as a contrast, free Cy3-Olg exhibited poor self-internalization ability. The HeLa and HepG2 cells showed highly intense red fluorescence microscopic images, confirmed high uptake for Cy3-Olg-loaded SWNT-1 compared with CHO cells and HEK-293 cells of lacking overexpressed biotin receptors. The CHO cells showed 92% of cells surviving, and only 54% of the HeLa cells were found to be alive at concentration of 2.5 μg mL^{-1} of SWNT-1-DOX. As the concentration increasing to 10 μg mL^{-1}, more than 60% of the HeLa cells were killed in contrast to that of only 15% for the CHO cells.

Mohd Zobir Hussein et al. reported anticancer efficiency of oxidized MWCNT (MWCNT-COOH)-loaded betulinic acid (BA) by π–π stacking and hydrophobic

interaction [53]. The loading capacity of BA was 14.5–14.8% (w/w). About 98% of BA loaded on MWCNT–BA was released over 22 h in a solution of pH 7.4. The release rate was reduced when the solution was acid, only 22% of loading BA was released within 24 h at pH 4.8. The MWCNT–BA showed no cytotoxicity effects at concentrations <50 μg/mL in embryo fibroblast cells after 72 h of treatment; however, high concentration of 50 μg/mL produced only 36% cell viability. Compared with HepG2 cells, the MWCNT–BA nanocarrier exhibited significant cell growth inhibitory to A549 cells in a concentration-dependent manner.

Zhong et al. prepared light and pH-sensitive PEG–DOX@SWCNTs DDS by noncovalently functionalizing SWCNTs with PEG–hydrazone–DOX [54]. The DOX-loading capacity was 31.2%. The 30% cumulative release of DOX from the PEG–DOX@SWNT was achieved at pH 5.0 in 48 h under irradiation compared with 17% cumulative release at pH 5.0 and 12% cumulative release at pH 7.4 without irradiation. The laser energy from irradiation weakened the interaction between DOX and CNTs, and resulted in greater release of DOX. As shown in the Fig. 2.19, the DOX fluorescence was obviously observed in the nucleus and some SWCNTs was found in the cytoplasm of the MCF-7 breast cancer after 2 h incubation of PEG–DOX@SWCNTs. As a contrast, the DOX fluorescence was hardly observed at pH 7.4 even after 24 h incubation. The free DOX distribution did not showed significant difference in MCF-7 cells between the pH 6.0 and the pH 7.4 groups. The viability of cells obviously showed difference at concentration of 10 μg mL^{-1} with or without laser irradiation.

2.3.2 Delivery of the Other Drugs

The antimicrobials are substances that either kill or inhibit the growth of microorganisms, like bacteria, fungi, viruses, or even parasites, instead of cancer cells. Azithromycin (AZ-1) is an antibiotic derived from erythromycin A with improved biological and pharmacodynamic properties over the parent compound. The Hossein Reza Darabi et al. fabricated azithromycin–SWCNT conjugates through cleavable ester or thioamide bonds [55]. The resulting azithromycin–SWCNT conjugates showed controlled release behavior in buffer solution of pH 6.8. The AZ-1 functionalized SWCNT (SWCNT-4) had a significant in vitro activity against *Micrococcus luteus* at 18 h of incubation compared with p-SWCNT and AZ-2 functionalized SWCNT.

Miodrag Č olic et al. fabricated dapsone-modified multiwall CNTs (dap-MWCNTs) through introducing O-(7-azabenzotriazol-1-yl) *N,N,N′,N′* tetramethyluronium hexafluorophosphate (N-HATU) and *N, N*-diisopropylethylamine (DIEA) onto the surface of the nanotubes [56]. The biological effect of dap-MWCNTs was surveyed using rat peritoneal macrophages (PMØ). Dap-MWCNTs did not show significant cytotoxicity, much like the unconjugated oxidized MWCNTs. Higher concentration of CNTs could induce apoptosis, with oxidized MWCNTs causing more extensive apoptosis than dap-MWCNTs due to elevated oxidative stress. The

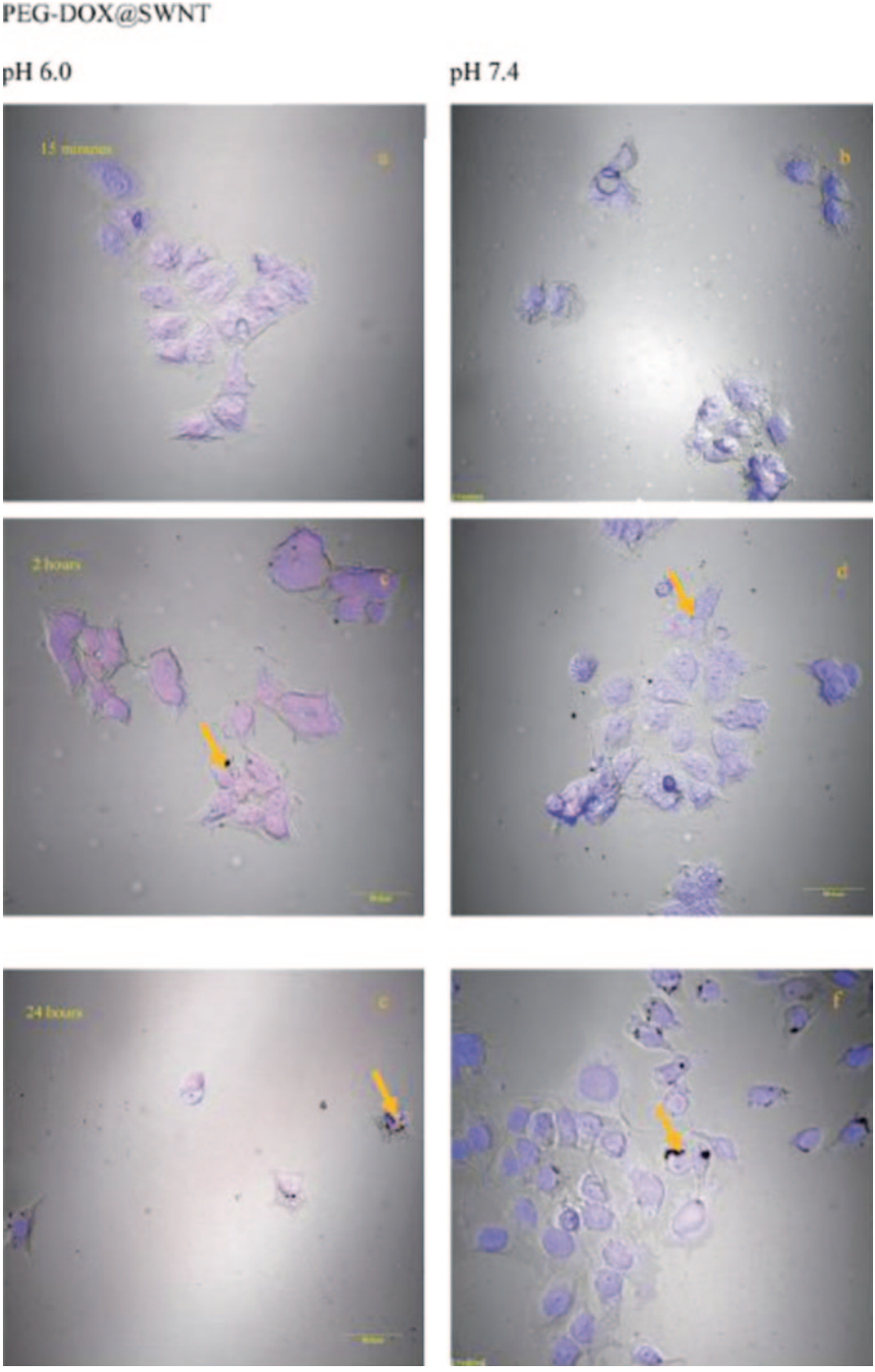

Fig. 2.19 The bright field and confocal images of PEG–DOX@SWNT in MCF-7 cells. The MCF-7 cells were incubated with PEG–DOX@SWNT for different times: 15 min (**a** and **b**), 2 h (**c** and **d**) and 24 h (**e** and **f**). The releasing of DOX at pH 6.0 (**a**, **c**, and **e**) was much more efficient than that at pH 7.4 (**b**, **d**, and **f**). Most DOX are located in the nucleus of MCE-7 cells whereas most SWNTs are located in the cytoplasm of MCE-7 cells (as showed by *yellow arrows*)

dap-MWCNTs did not trigger oxidative stress, however, caused delayed apoptosis of PMØ after 3 days. This result can be confirmed by the inherent antiapoptotic activity of dapsone and the protection of reactive carboxylic functional groups on the CNTs.

The antifungal agent amphotericin B (AmB) was covalently bond to amino-f-CNTs via ether bonds with ethylenediamine as the spacer with 72.4 % drug loading [57]. The antileishmanial efficacy of f-CNT–AmB was significantly higher than that of AmB against intracellular amastigotes in vitro. The compound f-CNT–AmB exhibited stronger inhibition of amastigote replication in hamsters compared with those treated with AmB. The in vivo toxicity assessment of the compounds in BALB/c mice revealed no significantly hepatic or renal toxicity.

In another study performed by Renato Gennaro et al., AmB was conjugated onto surfaces of functionalized multiwalled and single-walled CNTs (f-CNTs), with AmB loading of 25 and 10 % w/w, respectively [58]. These conjugates were tested for their antifungal activities against a collection of reference and clinical fungal strains in comparison to pristine AmB and a conventional colloidal dispersion AmB deoxycholate formulation. The f-MWCNT–AmB and f-SWCNT–AmB conjugates all showed broad-spectrum antifungal activity that was considerably more potent than AmB alone. The f-MWCNT–AmB with minimum inhibition concentration (MIC) values lowered than 10 μg/mL against most of the microorganisms, except for *Candida famata* SA550 strain (MIC 20 μg/mL), and MIC of f-SWCNT–AmB was between 5 and 20 μg/mL exhibiting a good antifungal activity. The f-CNTs did not show any antifungal activity without conjugating with AmB even at concentration MIC > 80 μg/mL. The f-MWCNT–AmB was overall more active than the SWNT conjugate due to high loading capacity and good dispersity. Furthermore, the f-CNT−AMB did not show any significant toxic effect on Jurkat human cells (derived from a human T cell leukemia) at antifungal concentrations.

It is an attractive means to visualize the interaction of AmB with living cells and natural biomembranes through conjugation of AmB to fluorescent markers. Alberto Bianco's group prepared functionalized CNTs with AmB and FITC toward mammalian cells (Human Jurkat lymphoma T cells) to assess toxicity and uptake as well as to evaluate the antifungal activity of CNT–AmB conjugates [59]. The specific synthesized route was depicted in Fig. 2.20. The CNT–AmB conjugates did not show significant cytotoxicity into mammalian cells even at the highest dose compared with 40 % of the cells died in the presence of AmB. The cell uptake of CNT–AmB was achieved within 1 h by fluorescence observation, and internalization of CNT–AmB was dose dependent. It can pass into the cell cytoplasm and mainly localized around the nuclear membrane as revealed with fluorescent microscopy (Fig. 2.20). The mechanism of penetration is spontaneous mechanism, not mediated by endocytosis.

Betulin (BET) with a pentacyclictriterpenoid structure has antileishmanial property and was used as antileishmanial agent. Vikash Kumar Dubey's group has successfully synthesized f-CNT–BET by carbodimide-based esterification reaction with BET-loading efficiency of 78.3 % [60]. The f-CNT–BET showed super released behavior in acidic condition compared with neutral pH condition. The accumulative

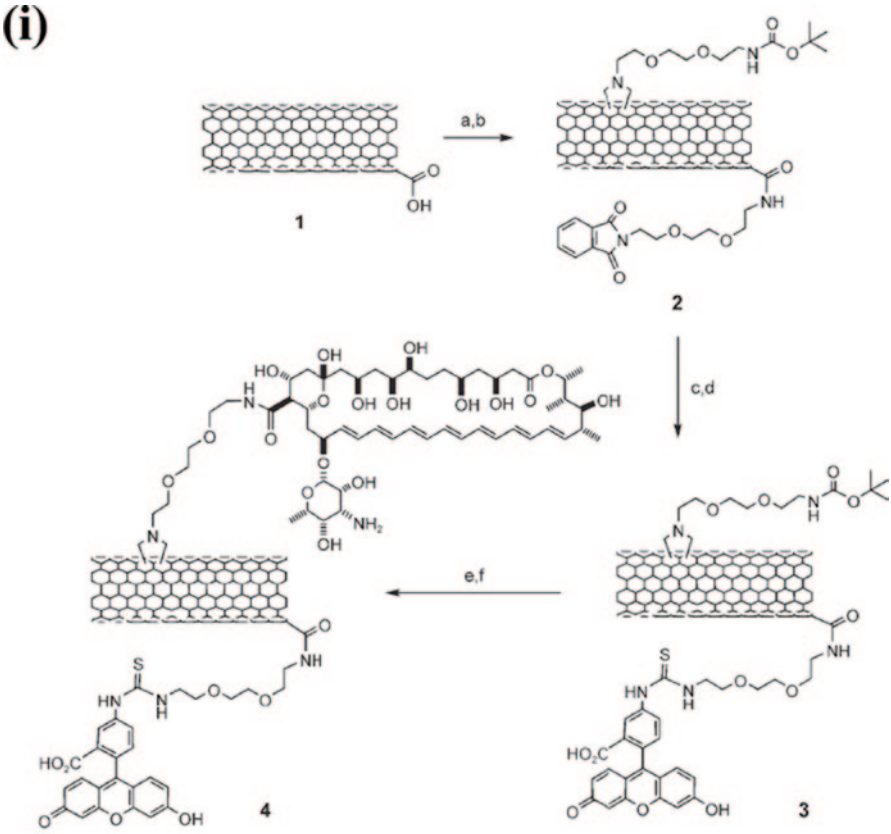

Fig. 2.20 *(i)* **a** Neat$(COCl)_2$; Pht–N$(CH_2CH_2O)_2$–CH_2CH_2–NH_2, dry THF, reflux; **b** Boc–NH–$(CH_2CH_2O)_2$–CH_2CH_2–$NHCH_2COOH$/(CH_2O)n, DMF, 125 °C; **c** Hydrated NH_2–NH_2, EtOH, reflux; **d** FITC, DMF; **e** HCl 4 M in dioxane; **f** Fmoc-AmB, HOBt/EDCxHCl/DIPEA, DMF; 25 %

release of BET reached up to 38.4 ± 1.8 and 12.5 ± 1.1 % at pH 5.8 and 7.4 in 72 h, respectively. The IC_{50} value of BET, f-CNT, and f-CNT–BET was 211.05 ± 7.14, 24.67 ± 3.11, and 72.63 ± 6.14 μg/mL in macrophage cell line J774A.1, respectively. The results indicated that BET, f-CNT, and f-CNT–BET did not have any significant toxicity to the macrophage cells in vitro by 3-(4,5-dimethylthiazol-2-yl)-2, 5-diphenyltetrazolium bromide (MTT) method. The f-CNT–BET showed high antileishmanial activity with increased efficacy compared to BET as confirmed by antileishmanial studies on intracellular amastigote in vitro.

The Anna Piperno et al. reported an approach for fabricating β-cyclodextrin covalently bond to MWCNT (β-CD-MWCNT) by click chemistry as nanocarriers for the delivery acyclovir (Acy) to the three human alpha herpesvirus (HSV-1, HSV-2, and VZV) [61]. They probed the recognition ability of β-CD–MWCNT to toward guanine-based drug. It was found that recognition and entrapment of Acy versus G on β-CD–MWCNT were dependent on the different interactions. The DSC analysis confirmed the interaction between Acy and β-CD–MWCNT. The 6.5 and 12.2 % drug loading of G and Acy were calculated, respectively. The 15 % cumulative release was showed after 8 days in PBS at pH 7.4. As a contrast, free Acy showed a faster dissolved rate. The Acy/β-CD–MWCNT can interfere with HSV-1 replication and exhibit higher antireplicative effect than the free Acy.

Cui et al. designed based on conducting polymer polypyrrole (PPy) and multiwalled CNTs DDS by electropolymerization in an electrically controlled drug release manner [62]. The treated CNTs showed five to six times O/C ratio than the untreated CNTs, offering more hydrophilicity on both the exterior and interior surfaces. The CNTs filled with dexamethasone (Dex) in their inner cavities were coated by PPy film and Dex was sealed inside the CNTs, and the amount of Dex released from PPy/CNTs film was negligible in PBS of pH 7.4. This result proved the effective sealing of the open ends of CNTs. The electrically controlled drug release was performed in PBS with aggressive electrical stimulation for 20 h using repeated stimulation of −2 V for 5 s followed by 0 V for 5 s. The 53.3 μg Dex was released from PPy/CNT film, compared with 38.8 μg release amount of pure PPy. The PPy films with thinner CNTs showed higher drug-loading capacity and release amount.

Giuseppe Cirillo et al. designed functionalized CNTs by gelatin–fluoroquinolones bioconjugates synthesized by using radical grafting fluoroquinolones onto the protein side chains [63]. The CNTs–Gel–FQs were assessed the biocompatibility on human mesenchymal stem cells (hMSCs) and tested antibacterial properties on *Escherichia coli* and *Klebsiella pneumoniae,* respectively. The fluoroquinolones consist of ciprofloxacin (CP), levofloxacin (LV), and lomefloxacin (LM). Compared with free FQs and Gel–FQs conjugates, the CNTs–Gel–FQs showed significant antibacterial activity by CNTs-mediated internalization. Moreover, the CNTs–Gel–FQs was highly biocompatible in whole system.

---

piperidine in DMF. *BOC* tert-butyloxycarbonyl, *DIPEA* diisopropylethylamine, *DMF* dimethyl formamide, *EDC* *N*-Ethyl-*N*′-(3-dimethylaminopropyl)-carbodiimide, *FMOC* fluorenylmethyloxycarbonyl, *FITC* fluorescein isothiocyanate, *HOBt* 1-hydroxybenzotriazole, *Pht* phthalimide group. (*ii*) Epifluorescence *(top)* and confocal *(bottom)* microscopy images of Jurkat cells incubated for 1 h at 37 °C with 10 and 40 μg mL^{-1} of CNT–AmB conjugates, respectively. Jurkat cells have an average diameter of 10 μm

2.4 CNHs for Drug Delivery

SWNHs are another type of nanocarbon material that have the potential to be useful in nano-medicine. SWNH has hydrophobic graphite structure. They consist of single tubes of 2–5 nm in diameter and a length of around 40–50 nm (Fig. 2.21).

The SWNHs were chemically modified with functional groups to increase hydrophilicity and biocompatibility. SWNHs have more defect sites and are more fragile than CNTs. Therefore, they are apt to be treated by softer oxidant, such as hydrogen peroxide, to generate carboxylic groups [64]. These groups could be used for further chemical reactions with other moieties. A new targeted DDS based on oxidized SWCNHs (oxSWCNHs) was developed.

Zhong et al. reported that insulin-like growth factor receptor (IGF-IR) antibody-directed CNHs-based drug delivery targeted to kill cancer cells in vivo and in vitro [65]. OxSWNHs were coated with the anticancer drug vincristine (VCR) by physical adsorption, and then wrapped 1,2- distearoyl-sn-glycero-3-phosphoethanolamine-*N*-[methoxy(polyethylene glycol) (DSPE–PEG)–IGF-IR mAb through an amide linker to obtain the DDS, VCR@oxSWNHs–PEG–mAb. The cytotoxicity study of oxSWNH–PEG–mAb indicated that cell viability remained above 80% even in the highest concentration of 100 μg/mL in MCF-7 cells after 48 h incubation. The DDS of VCR@oxSWNHs–PEG and VCR@oxSWNHs–PEG–mAb showed enhanced cytotoxicity in cultured MCF-7 cells in vitro compared with free VCR. The antibody targeted SWNHs delivery system afforded higher antitumor efficacy without obvious adverse effects to normal organs in tumor mice in vivo. At the same time, in addition, moderate inflammatory cell infiltration was also observed in VCR@oxSWNHs–PEG and VCR@oxSWNHs–PEG–mAb groups compared with VCR group.

A photothermally enhanced chemotherapy DDS, DOX-SWNH/ deoxycholic acid (DCA)–hydroxypropyl chitosans (HPCHS) nanoparticles, with SWNH as the photothermal agent and DOX was used as the chemotherapy agent [66]. The DOX–SWNH/DCA–HPCHS DDS was prepared by coating a DOX prodrug to amphiphilic DCA–HPCHS-modified SWNHs through hydrophobic–hydrophobic interaction. The DOX–SWNH/DCA–HPCHS nanoparticles possessed high stability in physiological solutions including water, PBS, RPMI-1640, and FBS. Photothermal heating could increase the chemotherapy efficacy of DOX due to light-triggered

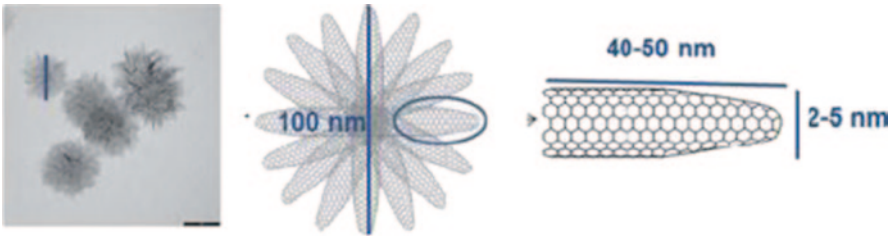

Fig. 2.21 *(Left)* TEM images of the SWCNHs; *(centre)* graphical structure of the SWCNHs; *(right)* single tube of the SWCNHs

DOX release or promotion of cell uptake of DOX carriers. The DOX–SWNH/DCA–HPCHS resulted in *ca*. 73% cell growth inhibition, and SWNH/DCA–HPCHs inhibited cell growth merely by *ca*.13% at a concentration of 5 μg mL^{-1} under 808 nm laser irradiation, whereas as contrast with nonirradiated 4T1 cells, DOX-SWNH/DCA-HPCHS did not show signicant cytotoxicity even at concentrations 10 μg mL^{-1}.

Small-sized SWNHs (S-SWNHs) have highly hydrophilic property and remarkably resistance to cellular uptake by macrophages, tumor cells, and normal cells [67]. As a contrast, large-sized SWNH aggregates (L-SWNHs) L-SWNHs were highly internalized in RAW 264.7, KB, FHs 173We, and HeLa cells. However, the functionalized S-SWNHs can selectively enter cells; for example, S-SWNHs attached phospholipid PEG cannot enter RAW 264.7 macrophages completely; functionalized with FA S-SWNHs, namely FA-S-SWNHs, are taken up by FA receptor-overexpressing KB cells but not by normal human embryonic cells.

Masako Yudasaka et al. reported DDS that cisplatin (CDDP) was incorporated inside SWNHs with opened holes [68]. Cisplatin, a representative water-soluble small-molecule drug, can also be effectively deposited on and inside of SWNHox aggregates (CDDP@SWNHox) (Fig. 2.22). Further, it has been shown that when cisplatin was released from these aggregates, it remarkably reduced the viability of cancer cells. It was observed that CDDP@SWNHox adhered to the cell surfaces in

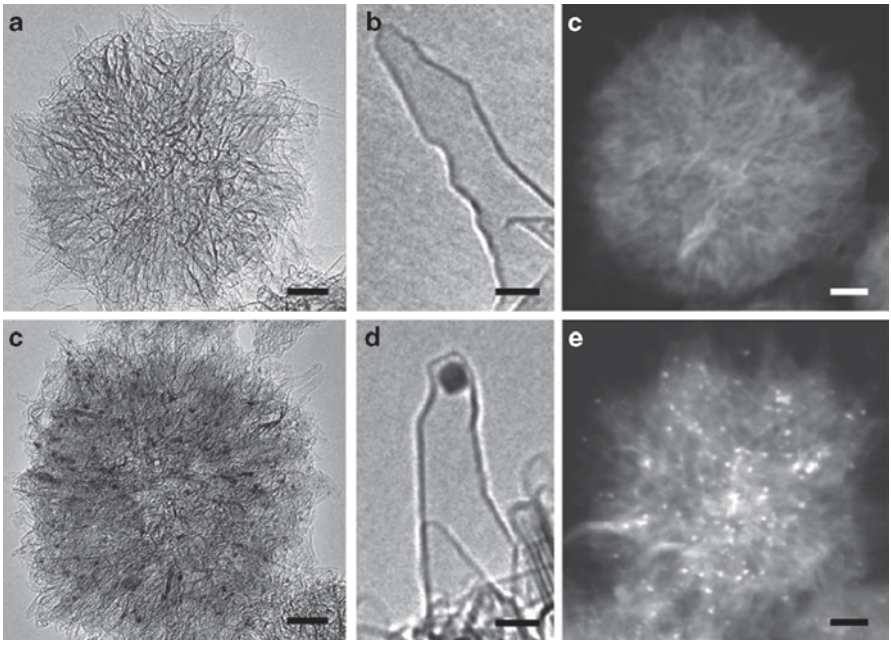

Fig. 2.22 (**a**, **b**) HRTEM images of SWNHox (*scale bars* of 10 and 2 nm, respectively). (**c**) Z-Contrast image of SWNHox aggregate (10 nm). (**d**, **e**) HRTEM images of CDDP@SWNHox (10 and 2 nm) in which *black spots* are cisplatin clusters. (**f**) Z-Contrast image of CDDP@SWNHox in which *bright spots* are cisplatin clusters (10 nm)

vitro and increased the local concentration of CDDP released from CDDP@SWNHox, leading to effective cell killing. In vivo, the specimens (saline, CDDP, SWNHox, and CDDP@SWNHox) were intratumorally injected to transplanted tumors of mice, and that CDDP@SWNHox showed higher anticancer effect than the intact CDDP. Furthermore, SWNHox itself also showed the anticancer effect for the first time in this study.

The anti-inflammatory agent DEX was deposited on as-grown SWNHs and their oxidized form, oxSWNHs [69]. The oxSWNHs showed six times higher drug capacity than that of SWNHs. Adsorption kinetics indicated that oxSWNHs had higher affinity for DEX than as-grown SWNHs. The DEX–oxSWNH conjugates exhibited sustained release of DEX into PBS (pH 7.4) at 37 °C, and the cumulative amount of DEX released got about 50% within 2 weeks. When incubate in cell culture medium, about 50% of the total bound DEX had been released by 24 h. The transfected cells of ST2 (mouse bone marrow stromal cell) incubated with DEX–oxSWNHs for 12 h showed dose-dependently activated luciferase expression; in contrast, empty oxSWNHs did not induce activation. The synthesis of SWNHs was involved of metal catalyst and no cytotoxicity of oxSWNHs was observed. The DEX–oxSWNHs exhibited good biocompatibility on the cell growth.

The PEG–DOX was immobilized on the oxSWNHs via π–π and hydrophobic interactions [70]. The PEG–DOX–oxSWNH complex was purified by dextran-based chromatographic media (Sephadex G25) due to good dispersibility in aqueous solution. By contrast, untreated oxSWNHs and DOX-treated or PEG-treated oxSWNHs were unable to penetrate the column. The PEG–oxSWNHs or oxSWNHs did not affect the cell proliferation. The PEG–DOX–oxSWNH conjugates exhibited DOX-dependent apoptotic activity against NCI-H460 human non-small cell lung cancer cells in vitro. The incidence of apoptosis induced by 0.2 mg/mL 5PEG–DOX–oxSWNHs (correspond to 5.4 μg/mL free DOX) was lower than that of 10 ng/mL free DOX, attributing to the slow release of DOX from the PEG–DOX–oxSWNH conjugates.

Wagner B. De Almeida et al. calculated the stabilization energy of cisplatin@CNHs conjugates to determine if they can form an effective DDS [71]. The theoretical results indicated the cisplatin@CNHs complex had a good stability with the cisplatin placed close to the bottom of the nanohorn cone structure. The cisplatin can be carried out through the biological media without strongly interacting with other reactive species and reach the final molecular to target inside the DNA structure.

The antibiotic vancomycin hydrochloride (VCM) was able to be adsorbed onto and inside functionalized phospholipid–PEG-oxidized SWNH (SWNHox) and released in a controlled manner and avoided severe side effects by too high concentration of VCM in blood [72]. The drug-loading capacity of VCM–SWNHox–PEG was 38% (w/w), and the cumulative release of VCM from the VCM–SWNHox–PEG complex got about 18% (10 μM) after 9 days. As we know, specific targeting and sustained release of steroidal drugs is beneficial to minimize the systemic side effects. The prednisolone (PSL) adsorbed on oxSWNHs by noncovalent interaction

and the adsorption capacity was 0.35–0.54 g/g depending on the sizes and numbers of holes on the oxSWNHs. The PSL–oxSWNH showed a fast release in culture medium in contrast with in PBS. The PSL-attached oxSWNHs were directly injected into the tarsal joints of rats with collagen-induced arthritis and anti-inflammatory effects was found in vivo, such as decreased numbers of osteoclastic cells compared with the control group [73].

Kiyotaka Shiba et al. reported that oxSWNHs-loaded cisplatin (CDDP) through their nanowindows was modified by the PEG–peptide aptamer (nanomaterial-binding peptide, NHBP) conjugate, and it formed well-dispersed CDDP-loaded CNHs (CDDP@oxSWNHs/20PEG–NHBP) DDS [74]. Compared with the CDDP@oxSWNHs quickly forming micrometer-sized agglomerates, the CDDP@oxSWNHs/20PEG–NHBP complexes were well dispersed in both the PBS and cell culture medium even after incubation for 3 days. The oxSWNHs/20PEG–NHBP complexes themselves showed good biocompatibility. The surface modification of CDDP@oxSWNHs using 20PEG–NHBP did not affect the release of CDDP from the conjugates. It was found that the CDDP@oxSWNHs/20PEG–NHBP exerted a dose-dependent cytotoxic effect on the NCI-H460 cell (a human lung cancer cell line).

The functionalized single-walled CNHs (SWNHs) composed of a comb-shaped PEG (cPEG) and peptide (NHBP-1) was synthesized [75]. Compared with 20PEG–NHBP, the bioconjugates composed of linear 20 kDa PEG and a single NHBP-1 peptide, the resultant cPEG–$NHBP_3$ conjugate endowed single-walled CNHs with good dispersibility in vitro. The oxSWNHs coated cPEG–$NHBP_3$ or 20PEG–NHBP was injected into the tail veins of BALB/c mice at a dose of 3 mg/kg, and untreated oxSWNHs as a controlled group. The untreated oxSWNHs significantly form agglomerates in liver, spleen, and minor in lung. The treating oxSWNHs with cPEG–$NHBP_3$ or 20PEG–NHBP formed few larger particles in lung. The smaller aggregates were hardly observed from the mice lung capillaries in vivo experiments (Fig. 2.23).

The novel DDS was designed by modified oxSWCNHs with polysaccharide sodium ALG (SA) immobilized humanized anti-vascular endothelial growth factor (anti-VEGF) mAb for targeting delivery of DOX to human breast adenocarcinoma (MCF-7) cells [76]. The loading capacity of 1 g DOX per gram of ox-SWCNHs was achieved and the complex showed higher anticancer effect than those of the free DOX. Pharmaceutical efficiency showed that the relative tumor volumes (RTV) of normal saline (NS) group, oxSWCNH/SA-mAb group, DOX group, and DOX@oxSWCNHs/SA-mAb group were approximately 61, 56, 14, and 7.2, respectively, with drug dosage 2.5 mg/kg. Histopathological studies in mice showed that free DOX could induce severe liver and heart injury, and DOX@oxSWCNHs/SA-mAb did not demonstrate any detectable hepatotoxicity, cardiotoxicity, and nephrotoxicity.

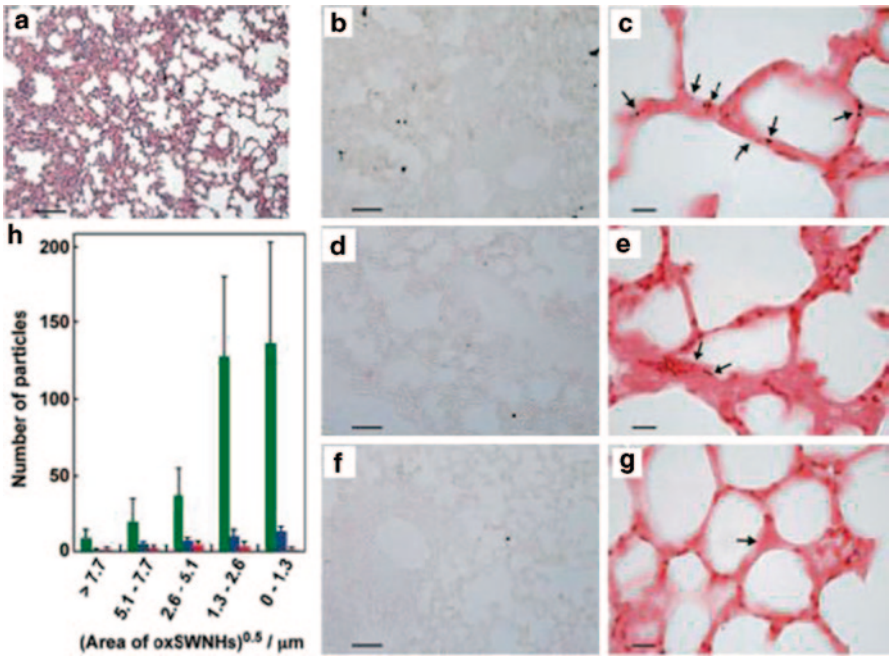

Fig. 2.23 Accumulation of agglomerated oxSWNHs in the lung after intravenous injection into mice. Shown are photomicrographs of lung sections from mice injected with unmodified oxSWNHs (**a**, **b**, **c**), 20PEG-NHBP/oxSWNHs (**d**, **e**) or cPEG–$NHBP_3$/oxSWNHs (**f**, **g**). The sections were stained with hematoxylin and eosin (**a**), unstained (**b**, **d**, **f**), or stained with eosin (**c**, **e**, **g**). *Arrows* indicate aggregated oxSWNHs observed as *black dots* in lung capillaries. In the unstained micrographs, the numbers of oxSWNHs agglomerates having the indicated sizes were counted using Image-J (**h**). The *green, blue,* and *red bars* represent the numbers of unmodified oxSWNHs, 20PEG-NHBP/oxSWNHs, and cPEG-$NHBP_3$/oxSWNHs, respectively. *Scale bars* represent 50 μm (**a**, **b**, **d**, **f**) or 10 μm (**c**, **e**, **g**)

2.5 NDs for Drug Delivery

NDs, as another member of the carbonnanoparticle (CNP) family, have evoked an increasing interest in studies of the biocompatibility and application as drug delivery vehicles. NDs with individual sizes ranging from 2 to 10 nm were usually synthesized by detonation techniques. The NDs is also called detonation ND (DND) due to synthesis by detonation technique. When an oxygen-deficient explosive mixture of trinitrotoluene/hexogen (TNT/RDX) is detonated in a closed chamber, diamond particles with a diameter of ca. 5 nm are formed at the front of detonation wave in the span of several microseconds. It can be well dispersed in aqueous solutions. It is known that NDs are chemically inert, and preliminary studies showed that they were nontoxic toward several cell lines [77]. Moreover, NDs could be surface-functionalized easily with carboxyl groups and their derivatives for specific or nonspecific binding with nucleic acids and proteins, showed possible application

in biomedicine [78]. It can load the all trans retinoic acid (ATRA) in the treatment of acute promyelocytic leukemia (APL) [79]. The DND was firstly treated by oxidation with H_2SO_4 and $KMnO_4$, followed by an esterification modification with ATRA in sulfuric acid–alcohol solutions. The formed nanoparticles have an average size of 5 nm. The DND with different ATRA (10, 20, 30, and 40 μmol/L) were investigated. The functionalized DND is biocompatibility to HL-60 cells with a low inhibition ratio 3%, similar to the datum for DMSO (2%). When the cells treated by both ATRA and DND–ATRA complex, the inhibition ratios increased with the increase of ATRA concentration. The inhibition ratios by the DND–ATRA were all higher than that by pure ATRA allowing an increase of 30–40%. The DND played an important role in the delivery of ATRA to HL-60 cells. The largest inhibition ratio for HL-60 cells was as high as 49% treated by DND–ATRA with ATRA 30 μmol/L. With further increase in the ATRA concentration, the inhibition ratio of DND–ATRA slightly decreased to 46%.

The image of dispersed NDs was shown in Fig. 2.24. The NDs can adsorb the 10-HCPT, a CPT analogue used in the treatment of certain cancers [80]. By simply mixing NDs with HCPT in water, the NDs can adsorb 0.4 wt% of HCPT. The adsorbed amount of HCPT was very low probability due to low solubility of HCPT in neutral aqueous solution. In weak basic solution, the solubility of HCPT in water promoted HCPT adsorption on NDs. The adsorption of HCPT on the NDs slowly increased with incubation time, with no saturation of adsorption observed even at 120 h. The maximum loading of HCPT obtained by a mixture of 4 mg/mL HCPT in NaOH (pH = 8.2) solution with 2 mg/mL NDs achieved 48.3 mg per 100 mg NDs at 120 h. This loading value exceeded the 8–10 wt% loading efficiency for conventional liposomes drug carriers. The release of HCPT from the HCPT–NDs achieved highest amount of 60% in dilute NaOH solution with pH = 8.2. In pure water, the release amount was about 30%, while it was about 38% in the PBS solution. In

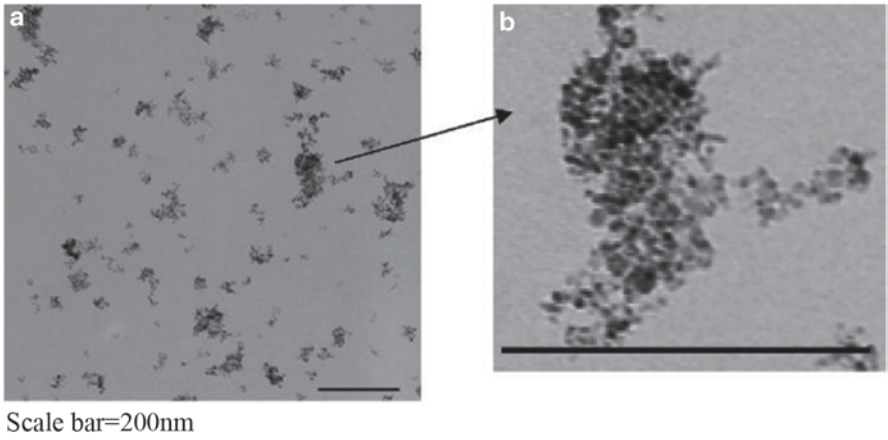

Fig. 2.24 **a** TEM image of NDs; **b** higher-magnification view of NDs shown by *arrow* in a. The scale bar corresponds to 200 nm

cell culture medium, NDs aggregated to form a kind of porous clusters, with many nanoscaled channels or pores as well as vacancies in the interior of the cluster. After adsorbed on the surface of ND clusters, HCPT could slowly diffuse toward the center of the clusters along these nanoscaled pores. When compared with HCPT alone, HCPT–ND complexes exhibited a much higher potency to cause appreciable cell death. Apparently, the enhanced efficacy was due to the delivery of more HCPT with poorer cellular penetration into cells by NDs.

The typical anticancer drug, DOX can also be adsorbed to NDs [81]. Although the NDs can disperse in water well, the DOX loaded NDs aggregated and precipitated very soon. To redisperse the DOX-NDs, they were then coated by DSPE–PEG-2000 (DSPE–PEG 2 K) producing the DNX complex. The DNX can inhibit the lung metastasis of breast cancer (using the 4T1 cells). The therapeutic effect of DOX was dependent on its ability to inhibit the synthesis of nucleic acid through intercalation after entrance into nucleus. DOX, NDs-DOX complex (NDX), and DSPE-PEG 2K coating NDX (DNX) be rapidly internalized by 4T1 cells. However, the speed of entering the cells was different for the three materials. When they were incubated with cells for 10 min, they located in the lysosome, but most of DOX was localized in the lysosome. After incubation for 30 min, free DOX and NDX still resided in lysosome, whereas DNX escaped from lysosome and entered into nucleus. NDs were found to move inside the cells quickly and were capable of ferrying the drug inside living cells efficiently. DNX with small particle size and good dispersibility might also have the similar trans-membrane ability, leading to the high accumulation of DOX in nucleus. The IC_{50} value (the concentration that inhibited cell growth by 50%) of DOX was 9.48×10^{-4} mg/mL in cells treated with free DOX, and decreased to 4.93×10^{-4} mg/mL after absorption to NDs. After coating by DSPE–PEG 2 K, the cytotoxicity of DOX further increased to the IC_{50} value of 1.65×10^{-4} mg/mL, which was 5.75-fold less than that of free DOX. DNX induced most cell apoptosis, leading to 51.13% cell apoptosis, equivalent to 50 and 30% increase compared to that induced by free DOX (34.14%) and NDX (39.31%), respectively.

The polyglycerol (PG) NDs was also prepared as illustrated in Fig. 2.25. The grafted PG not only largely increased the aqueous dispersibility of DND–PG (>80 mg/mL in water, DND was the NDs, and PG was the PG) but also provided numerous amendable hydroxyl groups for further functionalization [82]. Some of the hydroxyl groups of DND–PG were first reacted with tosyl chloride (TsCl) and the resultant tosylates (DND–PG–OTs) were substituted by azido groups (DND–PG–N_3). DND–PG–N_3 was further conjugated with arginylglycylaspartic acid (RGD) peptide through click chemistry of the azido groups with the propiolic amide of RGD peptide, yielding DND–PG–RGD. To immobilize DOX on DND–PG–RGD, hydrazine moiety was introduced through substitution of the *p*-nitrophenyl group in the *p*-nitrobenzoate (DND–PG–N_3–$PhNO_2$) to give DND–PG–N_3–$NHNH_2$ after click conjugation of RGD peptide (DND–PG–RGD–$NHNH_2$), DOX was immobilized as hydrazone (DND–PG–RGD–DOX). The content of DOX in DND–PG–DOX and DND–PG–RGD–DOX was quantified to be 5.6 and 12.2 wt%, respectively. The 24.7% of DOX were released by 12 h when DND–PG–DOX was incubated in PBS solution (pH 7.4). Then, the released DOX increased slightly even

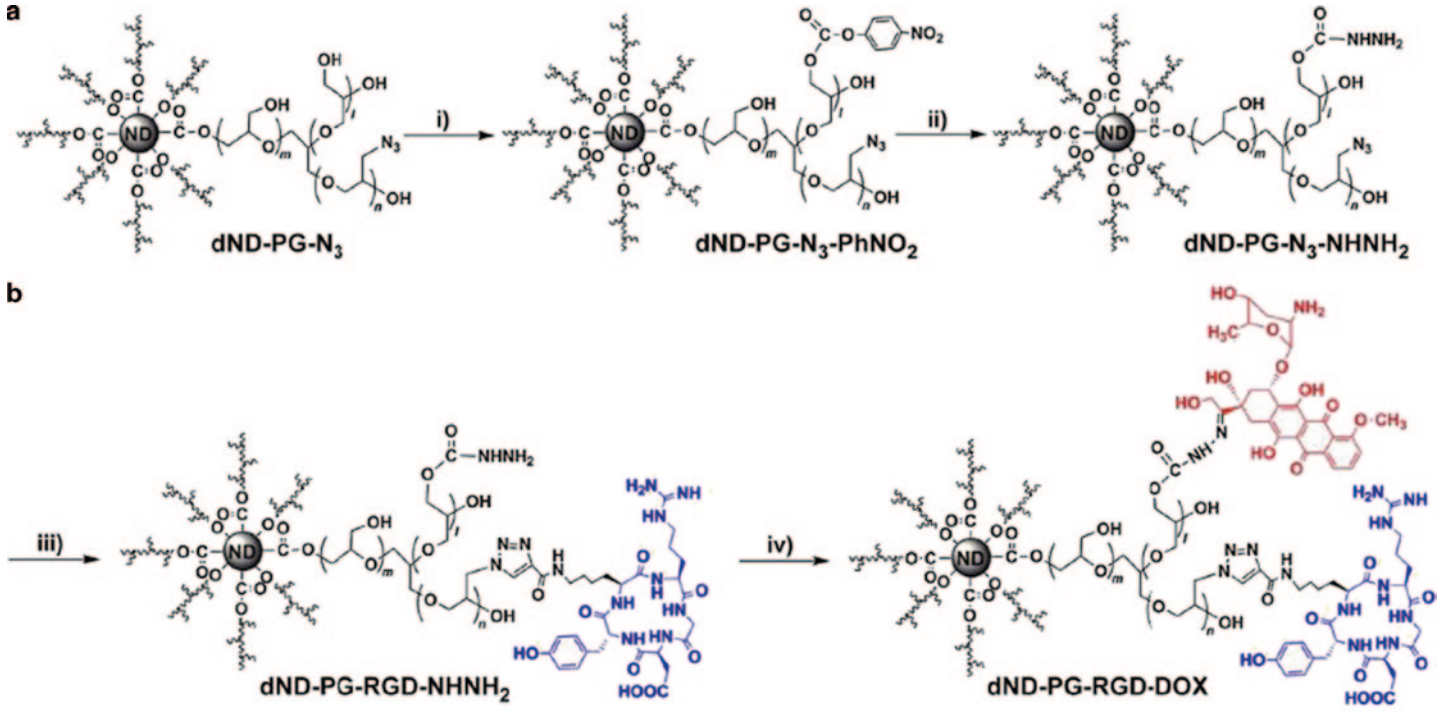

Fig. 2.25 Synthesis of DND–PG–RGD–DOX from DND–PG–N_3. (i) bis(4-nitrophenyl) carbonate, triethylamine, r. t., 24 h; (ii) hydrazine monohydrate, 90 °C, overnight; (iii) RGD propargyl amide, copper (II) sulfate pentahydrate, sodium ascorbate, r. t., 48 h; (iv) doxorubicin hydrochloride, pH 7, 50 °C, 24 h. *DND* detonation nanodiamond

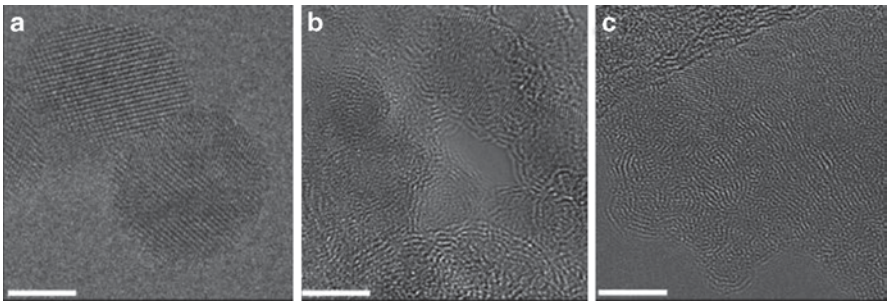

Fig. 2.26 HR-TEM images of oxidized (ND, **A)**, chemical reduced (ND R1, **B)**, and plasma reduced (ND R2, **C)** samples. The *white bars* indicate 5 nm

after incubation for 48 h. When the pH was decreased to 5.0 (phosphate–citrate solution), the released DOX by 48 h was calculated to be 63.3 %, due to the preferential cleavage of hydrazone linkage. From this point of view, DND–PG–DOX is expected to show enhanced drug release in the lysosomes of cells pH 5.0-5.5 but minimal premature drug release during circulation in bloodstream (pH 7.4). Two kinds of cancer cells, human leukemic monocyte lymphoma cells (U937) and lung adenocarcinoma epithelial cells (A549) were incubated with the DOX-loaded NDs. The inhabitation effects of DND–PG–DOX for different cancer cells were very close. Cellular DOX level resulted from DND–PG–DOX at each concentration was less than half of that caused by free DOX within the linear range for DOX. However, when the target molecule, RGD peptide was attached to the DND–PG–DOX, the resulting DND–PG–RGD–DOX exhibited much higher growth inhabitation for the cells expressing RGD peptide receptors. On the other hand, DND–PG–RGD–DOX at each concentration resulted in a markedly higher DOX level than DND–PG–DOX in A549 cells that express RGD peptide receptors. But in U937 macrophages devoid of RGD peptide receptors, this material at each concentration only caused a slightly higher DOX level than ND–PG–DOX, which was still pronouncedly lower than that caused by free DOX.

Besides the physical adsorption of various drugs, the NDs can be further modified by oxidation (ND), reduction (ND R1), and plasma methods (ND R2), as shown in Fig. 2.26 [83]. Multifuctional groups such as carboxylate and hydroxyl groups were decorated on the nanocores. They can enhance the drug loading to NDs by physical force or chemical covalents. The plant secondary metabolites, ciproten, and quercetin can be adsorbed to the ND, ND R1, and ND R2. The ciproten loaded to ND R2 was exceptionally higher, while the ciproten or quercetin loaded to the other two samples, on the average, was about 0.5 mmol. Cell treatment with 200 mg/mL of drug-functionalized NDs was corresponding to treating cells directly with a 100 mM solution of the pure drug. ND ciproten, ND R2 ciproten, ciproten, ND quercetin, ND R1 quercetin, ND R2 quercetin and quercetin treatments reduced cell growth of 65.3, 57.4, 23 , 25 , 41.4, 54.2 and 54.6 %, respectively, after 48 h of treatment. On the other hand, in the same condition, ND R1 ciproten sample only increased cell amount of 3.5 %. After 72 h, all specimens showed antiproliferative

properties of 60.2, 11.4, 55, 40, 29.3, 74.5, 67.7, and 72.9%, with respect to the control, in that order ND ciproten, ND R1 ciproten, ND R2 ciproten, ciproten, ND quercetin, ND R1 quercetin, ND R2 quercetin, and quercetin. In all cases, the exposure with pure NDs did not influence cell proliferation high sensibility that HeLa cells showed to the exposure with pure plant compounds. However, for the B16F10 murine melanoma cells, ND ciproten, ND R2 ciproten, ND R1 quercetin, and ND R2 quercetin caused the reduction of cell proliferation better than the treatment with their respective pure ciproten and quercetin. B16F10 cell growth inhibition after treatment with C and Q alone was highly lower with respect to the effects that pure plant compounds induced on HeLa cells. B16F10 murine melanoma cells is well-known high aggressive and drug-resistant phenotype. The effects of this investigation on various tumor cell lines can be different. Chemical and structural modifications of ND surfaces could influence biological effects of transported molecules, in particular, plasma reduced NDs enhanced ciproten and quercetin bioactivity while chemical reduced and oxidized NDs just intensified, respectively in that order, quercetin and ciproten.

Dipeptide (phe–lys) is cathepsin B sensitive peptide. Cathepsin B is localized in lysosomes and overexpressed in various malignant tumors [84]. Conjugating the dipeptide to DOX, followed by loading on the NDs, would produce higher tumor cellular uptake. The adsorption capacity was found to be 190 mg/g at pH 7.0 while it decreased to 170 and 130 mg/g at pH 5.0 and 3.0, respectively. Higher the concentration of NaCl is, the lower the adsorption capacity of NDs exhibits.

Cancer therapies can fail due to increases in activity of cellular efflux mechanisms. Higher levels of chemotherapeutic efflux lead to reductions in intracellular drug concentration and subsequent progression of drug insensitivity. Multidrug resistance (MDR) is a type of resistance to a wide spectrum of cancer therapeutics that develops after exposure to only a single drug. Overexpression of these transporters has also been correlated with more aggressive phenotypes of cancer and malignant progression, such as cell migration and invasion. Overcoming MDR is a serious problem that confronts many cancer therapies. Methods that utilize nanoparticles such as NDs as drug delivery vehicles may be useful toward developing a nonspecific strategy to bypass efflux mechanisms in MDR. Nanoparticles are able to shuttle their cargo into cells through different pathways, primarily endocytosis, which can bypass transport proteins and significantly improve drug efficacy by increasing intracellular drug concentration. Resistant K562 cells were able to overcome treatment from daunorubicin (DNR) alone as compared with non-resistant K562 cells, NDs were able to improve DNR delivery into resistant K562 cells [85]. NDs/DNR conjugates resulted in significantly better performance over DNR in killing resistant K562 cells. The IC_{50} of K562/DNR dropped three fold with treatment from NDs/DNR.

The targeting RGD peptide and Pt-based drug were immobilized on the PG functionalized ND, producing the novel DDS (ND–PG–RGD–Pt). In contrast, they synthesized ND–PG–RGD, ND–PG–Pt. The ND was covalently functionalized by ring-opening polymerization of glycidol. The ND–PG showed very good solubility ($\geq$20 mg/mL) and stability in water. The resulting ND–PG–RGD–Pt was produced

through click chemistry and ligand exchange under a slightly basic condition [86]. The fND, fND–PG, and fND–PG–RGD all showed good biocompatibility in the U87MG and HeLa cells even at 400 μg/mL for 24 h. The uptake of fND in U87MG and HeLa was concentration dependent. The fND–PG did not show significant uptake even at the highest concentration of 200 μg/mL for 24 h. The fND–PG–RGD uptake was dose-dependent in U87MG, but was not observed in HeLa even at the maximal concentration. They found that fND–PG–RGD localized in the lysosomes by fluorescence microscopy. The Pt release from the ND–PG–Pt was acid responsive and release rate was 57 and 30 μg/h in first stage (0–12 h) at the pH of 5.0 and 7.4, respectively. The Pt release rates followed the first-order kinetics and the rate constants were 2.9×10^{-3} and 1.7×10^{-3} h^{-1} in second stage (12–98 h) at the pH of 5.0 and 7.4, respectively. Compared with ND–PG–Pt showing 95% cell viability in both cells, the cell viability treated with ND–PG–RGD–Pt was 35 and 95% in U87MG and in HeLa, respectively, suggesting the targeting effect of RGD as well as the stealth effect of PG.

The stable ND-drug complex based on epirubicin adsorbed in basic solution was designed to kill chemoresistant hepatic cancer stem cells [87]. The ATP binding cassette (ABC) transporter proteins can recognize and efflux drug molecules and resulted in chemoresistance of cancer stem cells. Nanomedical approaches can overcome this mechanism of chemoresistance. The epirubicin can be reversibly bound onto the NDs by physical adsorption. The 19.66 ± 0.2% loading efficiency was achieved. The epirubicin release from epirubicin–ND drug complex (EPND) was pH dependent in aqueous solution. The cumulative release of epirubicin was > 80% within 9 h at pH 2, while was lowered to 10% at pH 10 and pH 12. In addition, the epirubicin release was also protein concentration dependent. High concentration of fetal bovine serum could facilitate the release of epirubicin. The mechanism of EPND uptake is macropinocytosis as confirmed by treating cells with 5-(*N*-ethyl-*N*-isopropyl) amiloride, the inhibitor of macropinocytosis using LT2-MYC, a cell line derived from liver tumors of Teto-MYC/LAP-tTA (LT2-MYC) mice. Compared with free epirubicin, EPND showed high amount of intracellular epirubicin in period of efflux of 12 h. The half maximal inhibitory concentration (IC_{50}) values of epirubicin and EPND was16 nM and 450 nM, respectively, suggesting the slow and sustained release of epirubicin from EPND. The tumor-bearing mice were treated with either epirubicin (5 mg/kg) or EPND (5 mg/kg epirubicin equivalent) or controls over a 12-day period and showed that decrease in the side population percentage compared to the increase in the percentage of side population cell treated with free epirubicin. The dosages of epirubicin caused obviouse decrease in bodyweight and acute death, while equivalent concentration of EPND resulted in no difference compared to PBS control.

The DDS based on NDs (ND)-mediated drug retention in chemoresistant breast cancer cells was developed [88]. The mitoxantrone can be reversibly bond and released from NDs surface. The loading capacity of mitoxantrone on NDs was 87.2 ± 8.51% as confirmed by UV–visible spectroscopy. The average size of agglomerates was 23.3 ± 0.09 and 54.6 ± 0.29 nm of NDs and ND-mitoxantrone, respectively. The 7.3 ± 3.2 and 2.5 ± 2.4% cumulative release of mitoxantrone from the ND-mitoxantrone conjugate was achieved at pH 10 and pH 12 in 6 h,

respectively compared with 19 ± 3.8 % cumulative release at pH 7 and 37.5 ± 4.1 % cumulative release at pH 4 within 6 h. The 54.8 ± 4.3 % of mitoxantrone was released in 6 h in acidic conditions of pH 2. The 80.3 ± 0.33 % (80 μg of mitoxantrone) and 62.0 ± 1.30 % (62 μg of mitoxantrone) cumulative release of mitoxantrone was obtained in 1:1 and 1:10 of Dulbecco's modified Eagle medium (DMEM; 50 % FBS)/PBS media over 3 weeks, respectively. The breast cancer cell MDA-MB-231-ABCG2 cells (mitoxantrone IC_{50}, 38 nM) showed almost twofold more resistant to mitoxantrone compared to normal MDA-MB-231 cells (mitoxantrone IC_{50}, 20.1 nM), due to increase of ABCG2 expression, while ND-mitoxantrone showed a 6.4-fold decrease in IC_{50} in MDA-MB-231-ABCG2 cells (ND-mitoxantrone IC_{50}, 78.2 nM) compared with ND-mitoxantrone treated with normal MDA-MB-231 cells (ND-mitoxantrone IC_{50}, 503 nM). It was found that ND as drug vehicles significantly improved mitoxantrone retention. The ND-mitoxantrone exhibited higher drug retention efficiency (35 ± 9.6 %) than mitoxantrone (14 ± 4.8 %) in 6 h. The ND-mitoxantrone and mitoxantrone showed 39 ± 5.4 and 6 ± 1.9 % retention efficiency after 24 h, respectively.

Wei et al. [89] reported the polyPEGylated functionalized ND (ND–polyPEGMA) prepared by surface-initiated ATRP using ND–Br as the initiator, $PEGMA_{475}$ as monomer and Cu(Br)/*N, N,N″,N″,N″*-pentamethyl diethylenetriamine (PMDETA) as the catalyst/ligand. It was found that the molecular weight of ND–polyPEGMA related to the polymerization time. The ND–polyPEGMA showed improved dispersion compared with unmodified ND in PBS, and no obviously difference was observed in H_2O. The cells incubated with 20 μg mL^{-1} ND–polyPEGMA for 24 h showed no significant cell morphology change, and the cells morphology is still normal even concentration of ND at 80 μg mL^{-1}. The cell viability of A549 cells incubated with pristine ND and ND–polyPEGMA still over 90 % even at the concentrations of 160 μg mL^{-1} in 24 h. The DOX-loading efficiency is 65 % (W/W). The 60 % cumulative release of DOX from the ND–polyPEGMA was achieved in first 20 h. The cell viability against polyPEG–ND–DOX is dosage dependent.

Dean Ho et al. designed multimodal ND (ND)-based DDS for selective targeting, imaging and enhanced therapy [90]. The epidermal growth factor receptor (EGFR) was overexpressed in over one third of all solid tumors, including breast, lung, colorectal, and brain cancers. The NDs functionalized with anti-EGFR mAbs was designed as increase internalization and delivery of anticancer agents into EGFR overexpressing cells. The multimodal ND conjugate was prepared by three steps: (i) ND surface was functionalized with the hetero-bifunctional cross-linker sulfosuccinimidyl 6-(3′ -[2-pyridyldithio]propionamido)hexanoate (sulfo-LC-SPDP); (ii) the PTX–DNA was synthesized by amine coupling chemistry between the PTX and the oligonucleotide strand; (iii) the resulting PTX–DNA/mAb@NDs was obtained by simultaneous linking thiolated PTX–DNA and mAbs with SPDP functionalized NDs.

Compared with 2.2 ± 0.4 nmol of PTX and 53.5 ± 2.1 μg of mAb per mg of PTX–DNA/mAb@ND, the loading capacity of PTX was 3.1 ± 0.7 nmol per mg of PTX–DNA@ND. The basal EGFR expressing MCF7 and EGFR overexpressing MDA-MB-231 cells were used as contrast. The similar fluorescence intensity was observed by MCF7 cells treated with PTX–DNA@ND and PTX–DNA/mAb@ND, respectively, even in the presence of competitive agent EGF, indicating the

nearly equivalent internalization. The MDA-MB-231 cells treated with PTX–DNA/mAb@ND showed significantly higher fluorescence than that of PTX–DNA@ND, meanwhile the free EGF inhibited internalization of PTX–DNA/mAb@ND, suggesting receptor-mediated endocytosis. It was found that the ND conjugates mainly localized into lysosomes using confocal microscopy. The cell viability incubated with PTX–DNA@NDs and PTX–DNA/mAb@NDs was dosage dependent in MCF7 and MDA-MB-231 cells, respectively. The IC_{50} of PTX–DNA@NDs and PTX–DNA/mAb@NDs was 24.1 nM and 17.7 nM in MCF7 cells, respectively. As sharp contrast, PTX–DNA/mAb@NDs(IC_{50}, 43.8 nM) showed almost two fold efficacy compared with PTX–DNA@NDs (IC_{50}, 83.3 nM) in MDA-MB-231 cells.

The NDs surface coated DOX was achieved by immersing the NDs in a DOX aqueous solution, and the 95.7% loading efficiency and 23.9 wt% loading capacity were obtained [91] The release of DOX from the ND-DOX is pH-triggered. Compared with 1.6% (pH 8), 77% of the cumulative release of DOX was achieved at pH 4 after 4 h, while the 81% (pH 4) and 2.7% (pH 8) of cumulative release of DOX was showed in 72 h. The cell viability of PC3 (human bone metastatic hormone-refractory prostate cancer) treated with 100 μg mL^{-1} ND in cell culture media with and without serum was 95 and 6% in 24 h, respectively, indicated that ND exhibited good biocompatibility in media containing serum. It observed that ND–DOX with 2.4 μg mL^{-1} DOX incubation with PC3 cells showed significantly cytotoxicity than free DOX at same dose in 24 and 48 h, respectively. The ND-DOX with 1.2 μg mL^{-1} DOX showed 42% cell death was comparable to that of cells treated with 2.4 μg mL^{-1} free DOX (40% cell death). The superior efficacy of ND–DOX compared to free DOX was further confirmed by fluorescence microscopy, as shown in Fig. 2.27.

2.6 Conclusion

In this chapter, we summarized recent development of functionalized carbon-based nanomaterials (including of GO, CNTs, CNHs, and NDs) as intelligent drug carriers for the delivery of anticancer drugs and non anticancer drugs in vitro and in vivo.

The carbon-based nanomaterials attracted the interesting of scientific workers due to the EPR effect. We systematically reviewed biocompatibility, drug-loading capacity and loading efficiency of modified GO, CNTs, CNHs, and NDs in aqueous solution by covalent and noncovalent manners, and drug release amounts of functionalized carbon-based nanomaterials in different pH (from the acidic to basic solution) value was also evaluated. The drug efficacy of complex and free drugs was detailed studied in vitro and in vivo. This chapter concerns of different cell lines including of human breast cancer cells, human melanoma cells, murine breast cancer cells, gastric cancer stem cells, cervical cancer cells, human hepatic cancer cells, glioma cancer cells, prostate cancer, and so on. The functionalized carbon-based nanomaterials loaded with anticancer drugs showed super cytotoxicity than free drugs at same dose incubation with cancer cells, but good biocompatibility for

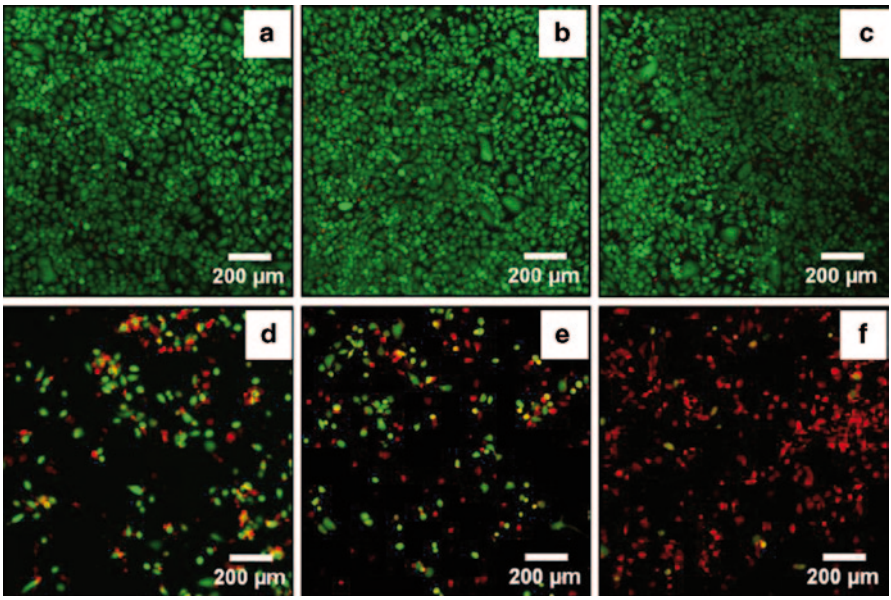

Fig. 2.27 Live/dead assay of PC3 cell viability after 48 h exposure to **a** no treatment, **b** 5 μg mL^{-1} ND, **c** 10 μg mL^{-1} ND, **d** ND-DOX with 1.2 μg mL^{-1} DOX **e** 2.4 μg mL^{-1} free DOX, and **f** ND-DOX with 2.4 μg mL^{-1} DOX. ND-DOX with 1.2 μg mL^{-1} DOX displayed decreased cell viability comparable to that of cells treated with 2.4 μg mL^{-1} free DOX. Live cells are represented in *green,* and dead cells are presented in *red*. Images are 10 × magnification

the normal cells. Thus, carbon-based nanomaterials have great potential as DDS for the scientific research and clinic applications.

Acknowledgments The authors thank Dr Shengju Ou for useful discussions and peer workers for their contributions to the work cited. We are also grateful for financial support from the Chinese National Nature Science Foundation (21405115, 51202167), and Wenzhou Bureau of Science and Technology (Y20120218) are acknowledged.

References

1. D. Lison, J. Muller, Lung and systemic responses to carbon nanotubes (CNT) in mice. Toxicol. Sci. **101**, 179–180 (2008)
2. M.L. Schipper, N. Nakayama-Ratchford, C.R. Davis, N.W. Kam, P. Chu, Z. Liu, X. Sun, H. Dai, S.S. Gambhir, A pilot toxicology study of single-walled carbon nanotubes in a small sample of mice. Nat. Nanotechnol. **3**, 216–221 (2008)
3. K.T. Nguyena, Y. Zhao, Integrated graphene/nanoparticle hybrids for biological and electronic applications. Nanoscale **6**, 6245–6266 (2014)
4. K. Hola, Y. Zhang, Y. Wang, E.P. Giannelis, R. Zboril, A.L. Rogach, Carbon dots——emerging light emitters for bioimaging, cancer therapy and optoelectronics. Nano Today **9**, 590–603 (2014)

5. Y. Chen, H. Chen, J. Shi, Inorganic nanoparticle-based drug codelivery nanosystems to overcome the multidrug resistance of cancer cells. Mol. Pharm. **11**, 2495–2510 (2014)
6. L. Lacerda, J. Russier, G. Pastorin, M.A. Herrero, E. Venturelli, H. Dumortier, K.T. Al-Jamal, M. Prato, K. Kostarelos, A. Bianco, Translocation mechanisms of chemically functionalised carbon nanotubes across plasma membranes. Biomaterials **33**, 3334–3343 (2012)
7. A.K. Iyer, G. Khaled, J. Fang, H. Maeda, Exploiting the enhanced permeability and retention effect for tumor targeting. Drug Discov. Today **11**, 812–818 (2006)
8. B.S. Wong, S.L. Yoong, A. Jagusiak, T. Panczyk, H.K. Ho, W.H. Ang, G. Pastorin, Carbon nanotubes for delivery of small molecule drugs. Adv. Drug Deliv. Rev. **65**, 1964–2015 (2013)
9. W.S. Hummers Jr., R.E. Offeman, Preparation of graphitic oxide. J. Am. Chem. Soc. **80**, 1339–1339 (1958)
10. X. Yang, X. Zhang, Z. Liu, Y. Ma, Y. Huang, Y. Chen, High-efficiency loading and controlled release of doxorubicin hydrochloride on graphene oxide. J. Phys. Chem. C **112**, 17554–17558 (2008)
11. X. Yang, X. Zhang, Y. Ma, Y. Huang, Y. Wang, Y. Chen, Superparamagnetic graphene oxide–Fe_3O_4 nanoparticles hybrid for controlled targeted drug carriers. J. Mater. Chem. **19**, 2710–2714 (2009)
12. W. Sun, N. Zhang, A. Li, W. Zou, W. Xu, Preparation and evaluation of N-3-O-toluyl-fluorouracil-loaded liposomes. Int. J. Pharm. **353**, 243–250 (2008)
13. X. Yang, Y. Wang, X. Huang, Y. Ma, Y. Huang, R. Yang, H. Duan, Y. Chen, Multi-functionalized graphene oxide based anticancer drug-carrier with dual-targeting function and pH-sensitivity. J. Mater. Chem. **21**, 3448–3454 (2011)
14. Y. Gao, X. Zou, J.X. Zhao, Y. Li, X. Su, Graphene oxide-based magnetic fluorescent hybrids for drug delivery and cellular imaging. Colloids Surf. B Biointerfaces 112,128–133 (2013)
15. G. Wang, C. Wang, W. Dou, Q. Ma, P. Yuan, X. Su, The synthesis of magnetic and fluorescent bi-functional silica composite nanoparticles via reverse microemulsion method. J. Fluoresc. **19**, 939–946 (2009)
16. Y. Sun, L. You, Y. Cao, J. Ma, Y. Guan, Y. Du, G. Lu, One-pot synthesis and gas sensitivies of SnO_2 hollow microspheres. Sens. Lett. **9**, 856–860 (2011)
17. C. Wang, J. Li, C. Amatore, Y. Chen, H. Jiang, X. Wang, Gold nanoclusters and graphene nanocomposites for drug delivery and imaging of cancer cells. Angew. Chem. Int. Ed. Engl. **50**, 11644–11648 (2011)
18. M. Sano, J. Okamura, S. Shinkai, Colloidal nature of single-walled carbon nanotubes in electrolyte solution: The schulze-hardy rule. Langmuir **17**, 7172–7173 (2001)
19. X. Sun, Z. Liu, K. Welsher, J.T. Robinson, A. Goodwin, S. Zaric, H. Dai, Nano-graphene oxide for cellular imaging and drug delivery. Nano Res. **1**, 203–212 (2008)
20. Z. Liu, J.T. Robinson, X. Sun, H. Dai, PEGylated nanographene oxide for delivery of water-insoluble cancer drugs. J. Am. Chem. Soc. **130**, 10876–10877 (2008)
21. W. Miao, G. Shim, S. Lee, S. Lee, Y.S. Choe, Y.K. Oh, Safety and tumor tissue accumulation of pegylated graphene oxide nanosheets for co-delivery of anticancer drug and photosensitizer. Biomaterials **34**, 3402–3410 (2013)
22. H. Kim, D. Lee, J. Kim, T. Kim, W.J. Kim, Photothermally triggered cytosolic drug delivery via endosome disruption using a functionalized reduced graphene oxide. ACS Nano **7**, 6735–6746 (2013)
23. H. Wen, C. Dong, H. Dong, A. Shen, W. Xia, X. Cai, Y. Song, X. Li, Y. Li, D. Shi, Engineered redox-responsive PEG detachment mechanism in PEGylated nano-graphene oxide for intracellular drug delivery. Small **8**, 760–769 (2012)
24. F. Meng, W.E. Hennink, Z. Zhong, Reduction-sensitive polymers and bioconjugates for biomedical applications. Biomaterials **30**, 2180–2198 (2009)
25. G. Liu, H. Shen, J. Mao, L. Zhang, Z. Jiang, T. Sun, Q. Lan, Z. Zhang, Transferrin modified graphene oxide for glioma-targeted drug delivery: in vitro and in vivo evaluations. ACS Appl. Mater. Interfaces **5**, 6909–6914 (2013)
26. H. Bao, Y. Pan, Y. Ping, N.G. Sahoo, T. Wu, L. Li, J. Li, L.H. Gan, Chitosan-functionalized graphene oxide as a nanocarrier for drug and gene delivery. Small **7**, 1569–1578 (2011)

27. D. Depan, J. Shah, R.D.K. Misra, Controlled release of drug from folate-decorated and graphene mediated drug delivery system: synthesis, loading efficiency, and drug release response. Mater. Sci. Eng. C **31**, 1305–1312 (2011)
28. R. Cheng, R. Zou, S. Ou, R. Guo, R. Yan, H. Shi, S. Yu, X. Li, Y. Bu, M. Lin, Y. Liu, L. Dai, Graphene oxide complex as a pH-sensitive antitumor drug. Polym. Chem. **6**, 2401–2406 (2015)
29. Y. Pan, H. Bao, N.G. Sahoo, T. Wu, L. Li, Water-soluble poly(*N* -isopropylacrylamide)–graphene sheets synthesized via click chemistry for drug delivery. Adv. Funct. Mater. **21**, 2754–2763 (2011)
30. T. Kavitha, I.K. Kang, S.Y. Park, Poly(N-vinyl caprolactam) grown on nanographene oxide as an effective nanocargo for drug delivery. Colloids Surf. B Biointerfaces **115,** 37–45 (2014)
31. P. Chen, X. Wang, G. Wang, Y. Duo, X. Zhang, X. Hu, X. Zhang, Double network self-healing graphene hydrogel by two step method for anticancer drug delivery. Mater. Technol.: Adv. Perform. Mater. **29,** 210–213 (2014)
32. Y. Yang, Y. Zhang, Y. Chen, D. Zhao, J. Chen, Y. Liu, Construction of a graphene oxide based noncovalent multiple nanosupramolecular assembly as a scaffold for drug delivery. Chem.-Eur. J. **18**, 4208–4215 (2012)
33. J. An, Y. Gou, C. Yang, F. Hu, C. Wang, Synthesis of a biocompatible gelatin functionalized graphene nanosheets and its application for drug delivery. Mater. Sci. Eng. C **33**, 2827–2837 (2013)
34. K. Liu, J. Zhang, F. Cheng, T. Zheng, C. Wang, J. Zhu, Green and facile synthesis of highly biocompatible graphene nanosheets and its application for cellular imaging and drug delivery. J. Mater. Chem. **21**, 12034–12040 (2011)
35. H. Hu, J. Yu, Y. Li, J. Zhao, H. Dong, Engineering of a novel pluronic F127/graphene nanohybrid for pH responsive drug delivery. J. Biomed. Mater. Res. A **100A**, 141–148 (2012)
36. G. Wei, M. Yan, R. Dong, D. Wang, X. Zhou, J. Chen, J. Hao, Covalent modification of reduced graphene oxide by means of diazonium chemistry and use as a drug-delivery system. Chem.-Eur. J. **18**, 14708–14716 (2012)
37. S. Dhar, Z. Liu, J. Thomale, H. Dai, S.J. Lippard, Targeted single-wall carbon nanotube-mediated Pt(IV) prodrug delivery using folate as a homing device. J. Am. Chem. Soc. **130**, 11467–11476 (2008)
38. A.A. Bhirde, V. Patel, J. Gavard, G. Zhang, A.A. Sousa, A. Masedunskas, R.D. Leapman, R. Weigert, J.S. Gutkind, J.F. Rusling, Targeted killing of cancer cells in vivo and in vitro with EGFdirected carbon nanotube-based drug delivery. ACS Nano **3**, 307–316 (2009)
39. Y. Gu, J. Cheng, J. Jin, S. Cheng, W.T. Wong, Development and evaluation of pH-responsive single-walled carbon nanotube-doxorubicin complexes in cancer cells. Int. J. Nanomedicine **6**, 2889–2898 (2011)
40. X. Zhang, L. Meng, Q. Lu, Z. Fei, P.J. Dyson, Targeted delivery and controlled release of doxorubicin to cancer cells using modified single wall carbon nanotubes. Biomaterials **30**, 6041–6047 (2009)
41. W. Shao, A. Paul, B. Zhao, C. Lee, L. Rodes, S. Prakash, Carbon nanotube lipid drug approach for targeted delivery of a chemotherapy drug in a human breast cancer xenograft animal model. Biomaterials **34**, 10109–10119 (2013)
42. Y. Guo, D. Shi, H. Cho, Z. Dong, A. Kulkarni, G.M. Pauletti, W. Wang, J. Lian, W. Liu, L. Ren, Q. Zhang, G. Liu, C. Huth, L. Wang, R.C. Ewing, In vivo imaging and drug storage by quantum-dot-conjugated carbon nanotubes. Adv. Funct. Mater. **18**, 2489–2497 (2008)
43. T.L. Moore, J.E. Pitzer, R. Podila, X. Wang, R.L. Lewis, S.W. Grimes, J.R. Wilson, E. Skjervold, J.M. Brown, A. Rao, F. Alexis, Multifunctional polymer-coated carbon nanotubes for safe drug delivery. Part. Part. Syst. Char. **30**, 365–373 (2013)
44. W. Wu, R. Li, X. Bian, Z. Zhu, D. Ding, X. Li, Z. Jia, X. Jiang, Y. Hu, Covalently combining carbon nanotubes with anticancer agent: Preparation reparation and antitumor activity. ACS Nano **3**, 2740–2750 (2009)
45. N.M. Dinan, F. Atyabi, M.R. Rouini, M. Amini, A.A. Golabchifar, R. Dinarvand, Doxorubicin loaded folate-targeted carbon nanotubes: Preparation, cellular internalization, in vitro

cytotoxicity and disposition kinetic study in the isolated perfused rat liver. Mater. Sci. Eng. C **39**, 47–55 (2014)
46. H. Wu, H. Shi, H. Zhang, X. Wang, Y. Yang, C. Yu, C. Hao, J. Du, H. Hu, S. Yang, Prostate stem cell antigen antibody-conjugated multiwalled carbon nanotubes for targeted ultrasound imaging and drug delivery. Biomaterials **35**, 5369–5380 (2014)
47. H. Yao, Y. Zhang, L. Sun, Y. Liu, The effect of hyaluronic acid functionalized carbon nanotubes loaded with salinomycin on gastric cancer stem cells. Biomaterials **35**, 9208–9223 (2014)
48. O. Vittorio, M. Brandl, G. Cirillo, U.G. Spizzirri, N. Picci, M. Kavallaris, F. Iemma, S. Hampel, Novel functional cisplatin carrier based on carbon nanotubes–quercetin nanohybrid induces synergistic anticancer activity against neuroblastoma in vitro. RSC Adv. **4**, 31378–31384 (2014)
49. N.K. Mehra, N.K. Jain, One platform comparison of estrone and folic acid anchored surface engineered MWCNTs for doxorubicin delivery. Mol. Pharm. **12**, 630–643 (2015)
50. J. Liu, C. Wang, X. Wang, X. Wang, L. Cheng, Y. Li, Z. Liu, Mesoporous silica coated single-walled carbon nanotubes as a multifunctional light-responsive platform for cancer combination therapy. Adv. Funct. Mater. **25**, 384–392 (2015)
51. A.A. Faraj, A.P. Shaik, A.S. Shaik, Magnetic single-walled carbon nanotubes as efficient drug delivery nanocarriers in breast cancer murine model: noninvasive monitoring using diffusion-weighted magnetic resonance imaging as sensitive imaging biomarker. Int. J. Nanomedicine **10**, 157–168 (2015)
52. S. Brahmachari, M. Ghosh, S. Dutta, P.K. Das, Biotinylated amphiphile-single walled carbon nanotube conjugate for target-specific delivery to cancer cells. J. Mater. Chem. B **2**, 1160–1173 (2014)
53. J.M. Tan, G. Karthivashan, P. Arulselvan, S. Fakurazi, M.Z. Hussein, Characterization and in vitro studies of the anticancer effect of oxidized carbon nanotubes functionalized with betulinic acid. Drug Des. Devel. Ther. **8**, 2333–2343 (2014)
54. S. Liu, A.C.T. Ko, W. Li, W. Zhong, M. Xing, NIR initiated and pH sensitive single-wall carbon nanotubes for doxorubicin intracellular delivery. J. Mater. Chem. B **2**, 1125–1135 (2014)
55. H.R. Darabi, A. Roozkhosh, M.J. Tehrani, K. Aghapoor, H. Sayahi, Y. Balavar, F. Mohsenzadeh, Characterization of ester-or thioamide-functionalized single walled carbon nanotube-azithromycin conjugates. Appl. Surf. Sci. **288**, 122–129 (2014)
56. G.D. Vuković, S.Z. Tomić, A.D. Marinković, V. Radmilović, P.S. Uskoković, M.Č. olić, The response of peritoneal macrophages to dapsone covalently attached on the surface of carbon nanotubes. Carbon **48**, 3066–3078 (2010)
57. V.K. Prajapati, K. Awasthi, S. Gautam, T.P. Yadav, M. Rai, O.N. Srivastava, S. Sundar, Targeted killing of leishmania donovani in vivo and in vitrowith amphotericin B attached to functionalized carbon nanotubes. J. Antimicrob. Chemother. **66**, 874–879 (2011)
58. M. Benincasa, S. Pacor, W. Wu, M. Prato, A. Bianco, R. Gennaro, Antifungal activity of amphotericin B conjugated to carbon nanotubes. ACS Nano **5**, 199–208 (2011)
59. W. Wu, S. Wieckowski, G. Pastorin, M. Benincasa, C. Klumpp, J.P. Briand, R. Gennaro, M. Prato, A. Bianco, Targeted delivery of amphotericin B to cells by using functionalized carbon nanotubes. Angew. Chem. Int. Ed. Engl. **44**, 6358–6362 (2005)
60. P. Saudagar, V.K. Dubey, Carbon nanotube based betulin formulation shows better efficacy against Leishmania parasite. Parasitol. Int. **63**, 772–776 (2014)
61. D. Iannazzo, A. Mazzaglia, A. Scalab, A. Pistonea, S. Galvagno, M. Lanza, C. Riccucci, G.M. Ingo, I. Colao, M.T. Sciortino, F. Valle, A. Piperno, G. Grassi, β-Cyclodextrin-grafted on multiwalled carbon nanotubes as versatile nanoplatform for entrapment of guanine-based drugs. Colloids Surf. B Biointerfaces **123**, 264–270 (2014)
62. X. Luo, C. Matranga, S. Tan, N. Alba, X.T. Cui, Carbon nanotube nanoreservior for controlled release of anti-inflammatory dexamethasone. Biomaterials **32**, 6316–6323 (2011)
63. U.G. Spizzirri, S. Hampel, G. Cirillo, M.V. Mauro, O. Vittorio, P. Cavalcanti, C. Giraldi, M. Curcio, N. Picci, F. Iemma, Functional gelatin-carbon nanotubes nanohybrids with enhanced antibacterial activity. Int. J. Polym. Mater. Polym. Biomater. **64**, 439–447 (2015)

64. J. Xu, M. Zhang, M. Nakamura, S. Iijima, M. Yudasaka, Double oxidation with oxygen and hydrogen peroxide for hole-forming in single wall carbon nanohorns. Appl. Phys. A: Mater. Sci. Process. **100**, 379–383 (2010)
65. N. Li, Q. Zhao, C. Shu, X. Ma, R. Li, H. Shen, W. Zhong, Targeted killing of cancer cells in vivo and in vitro with IGF-IR antibody-directed carbon nanohorns based drug delivery. Int. J. Pharm. **478**, 644–654 (2015)
66. D. Chen, C. Wang, F. Jiang, Z. Liu, C. Shu, L. Wan, In vitro and in vivo photothermally enhanced chemotherapy by single-walled carbon nanohorns as a drug delivery system. J. Mater. Chem. B **2**, 4726–4732 (2014)
67. M. Zhang, X. Zhou, S. Iijima, M. Yudasaka, Small-sized carbon nanohorns enabling cellular uptake control. Small **8**, 2524–2531 (2012)
68. K. Ajima, T. Murakami, Y. Mizoguchi, K. Tsuchida, T. Ichihashi, S. Iijima, M. Yudasaka, Enhancement of in vivo anticancer effects of cisplatin by incorporation inside single-wall carbon nanohorns. ACS Nano **2**, 2057–2064 (2008)
69. T. Murakami, K. Ajima, J. Miyawaki, M. Yudasaka, S. Iijima, K. Shiba, Drug-loaded carbon nanohorns: adsorption and release of dexamethasone in vitro. Mol. Pharm. **1**, 399–405 (2004)
70. T. Murakami, J. Fan, M. Yudasaka, S. Iijima, K. Shiba, Solubilization of single-wall carbon nanohorns using a PEG–Doxorubicin conjugates. Mol. Pharm. **3**, 407–414 (2006)
71. L.A. De Souza, C.A.S. Nogueira, J.F. Lopes, H.F. Dos Santos, W.B. De Almeida, DFT study of cisplatin@carbon nanohorns complexes. J. Inorg. Biochem. **129**, 71–83 (2013)
72. J. Xu, M. Yudasaka, S. Kouraba, M. Sekido, Y. Yamamoto, S. Iijima, Single wall carbon nanohorn as a drug carrier for controlled release. Chem. Phys. Lett. **461**, 189–192 (2008)
73. M. Nakamura, Y. Tahara, Y. Ikehara, T. Murakami, K. Tsuchida, S. Iijima, I. Waga, M. Yudasaka, Single-walled carbon nanohorns as drug carriers: adsorption of prednisolone and anti-inflammatory effects on arthritis. Nanotechnology **22**, 465102 (2011)
74. S. Matsumura, K. Ajima, M. Yudasaka, S. Iijima, K. Shiba, Dispersion of cisplatin-loaded carbon nanohorns with a conjugate comprised of an artificial peptide aptamer and polyethylene glycol. Mol. Pharm. **4**, 723–729 (2007)
75. S. Matsumura, S. Sato, M. Yudasaka, A. Tomida, T. Tsuruo, S. Iijima, K. Shiba, Prevention of carbon nanohorn agglomeration using a conjugate composed of comb-shaped polyethylene glycol and a peptide aptamer. Mol. Pharm. **6**, 441–447 (2009)
76. X. Ma, C. Shu, J. Guo, L. Pang, L. Su, D. Fu, W. Zhong, Targeted cancer therapy based on single-wall carbon nanohorns with doxorubicin in vitro and in vivo. J. Nanopar. Res. **16**, 2497 (2014)
77. K.K. Liu, C.L. Cheng, C.C. Chang, J.I. Chao, Biocompatible and detectable carboxylated nanodiamond on human cell. Nanotechnology **18**, 325102–325112 (2007)
78. H. Huang, E. Pierstorff, E. Osawa, D. Ho, Protein-mediated assembly of nanodiamond hydrogels into a biocompatible and biofunctional multilayer nanofilm. ACS Nano **2**, 203–212 (2008)
79. F. Fan, J. Liu, H. Li, Combining nanodiamond and all trans retinoic acid to increase the apoptosis of HL-60 cell. Mater. Lett. **133**, 262–265 (2014)
80. J. Li, Y. Zhu, W. Li, X. Zhang, Y. Peng, Q. Huang, Nanodiamonds as intracellular transporters of chemotherapeutic drug. Biomaterials **31**, 8410–8418 (2010)
81. J. Xiao, X. Duan, Q. Yin, Z. Zhang, H. Yu, Y. Li, Nanodiamonds-mediated doxorubicin nuclear delivery to inhibit lung metastasis of breast cancer. Biomaterials **34**, 9648–9656 (2013)
82. L. Zhao, Y. Xu, T. Akasaka, S. Abe, N. Komatsu, F. Watari, X. Chen, Polyglycerol-coated nanodiamond as a macrophage-evading platform for selective drug delivery in cancer cells. Biomaterials **35**, 5393–5406 (2014)
83. A. Gismondi, G. Reina, S. Orlanducci, F. Mizzoni, S. Gay, M.L. Terranova, A. Canini, Nanodiamonds coupled with plant bioactive metabolites: a nanotech approach for cancer therapy. Biomaterials **38**, 22–35 (2015)
84. S. Huang, J. Shao, L. Gao, Y. Qi, L. Ye, Adsorption of cathepsin B-sensitive peptide conjugated DOX on nanodiamonds. Appl. Surf. Sci. **257**, 8617–8622 (2011)

85. H.B. Man, H. Kim, H.J. Kim, E. Robinson, W.K. Liu, E.K. Chow, D. Ho, Synthesis of nanodiamond-daunorubicin conjugates to overcome multidrug chemoresistance in leukemia. Nanomed-Nanotechnol. **10**, 359–369 (2014)
86. L. Zhao, Y. Xu, H. Qin, S. Abe, T. Akasaka, T. Chano, F. Watari, T. Kimura, N. Komatsu, X. Chen, Platinum on nanodiamond: A promising prodrug conjugated with stealth polyglycerol, targeting peptide and acid-responsive antitumor drug. Adv. Funct. Mater. **24**, 5348–5357 (2014)
87. X. Wang, X.C. Low, W. Hou, L.N. Abdullah, T.B. Toh, M.M.A. Rashid, D. Ho, E.K.H. Chow, Epirubicin-adsorbed nanodiamonds kill chemoresistant hepatic cancer stem cells. ACS Nano **8**, 12151–12166 (2014)
88. T.B. Toh, D.K. Lee, W. Hou, L.N. Abdullah, J. Nguyen, D. Ho, E.K.H. Chow, Nanodiamond–mitoxantrone complexes enhance drug retention in chemoresistant breast cancer cells. Mol. Pharm. **11**, 2683–2691 (2014)
89. X. Zhang, S. Wang, C. Fu, L. Feng, Y. Ji, L. Tao, S. Li, Y. Wei, PolyPEGylated nanodiamond for intracellular delivery of a chemotherapeutic drug. Polym. Chem. **3**, 2716–2719 (2012)
90. X. Zhang, R. Lam, X. Xu, E.K. Chow, H.J. Kim, D. Ho, Multimodal nanodiamond drug delivery carriers for selective targeting, imaging, and enhanced chemotherapeutic efficacy. Adv. Mater. **23**, 4770–4775 (2011)
91. A.D. Salaam, P.T.J. Hwang, A. Poonawalla, H.N. Green, H.W. Jun, D. Dean, Nanodiamonds enhance therapeutic efficacy of doxorubicin in treating metastatic hormone-refractory prostate cancer. Nanotechnology **25**, 425103 (2014)

Chapter 3
Cytotoxicity, Drug Delivery, and Photothermal Therapy of Functionalized Carbon Nanomaterials

Ye Wang, Jingquan Liu, Liang Cui and Dusan Losic

3.1 Introduction

The majority of pharmaceutical development and medical research in the past 50 years has been focused on the development of new drugs, which are applied by systemic drug delivery (DD) administration (oral and intravenous). However, the systemic DD has many disadvantages such as limited drug solubility, degradation, poor biodistribution, lack of selectivity, unfavorable pharmacokinetics, toxicity, and unwanted side effects [1, 2]. To address these problems, considerable research has been directed towards the development of new and more efficient DD systems (DDSs) [3]. A new discipline called nanomedicine based on biomedical research and nanotechnology has emerged that is expected to revolutionize medical treatment using new nanomaterials and advanced DDSs [4, 5].

The concept of nanomedicine is to utilise nano-sized drug carrier, so-called nanoparticles (NPs) to load drug molecules and selectively release drug into diseased tissues. These synthetic NPs with the size-range from 1 to 100nm can deliver therapeutic molecules much more efficiently than passively diffused chemical molecules [6, 7]. The most attractive feature of these nano-based drug carriers is their reduced off-target toxicity and enhanced DD owing to the enhanced permeability and retention (EPR) effect. Other advantages include improved drug-targeting capabilities, drug circulation times, controlled drug release kinetics, and superior dose scheduling for improved patient compliance which highlight their great potential for their clinical applications [8]. So far, more than 40 nanomaterial-based products have been approved by the Food and Drug Administration for clinical use, and the number of clinical trails and patents of nanomedicine increased dramatically recent years [9].

D. Losic (✉) · Y. Wang
School of Chemical Engineering, The University of Adelaide, Adelaide, SA 5005, Australia
e-mail: dusan.losic@adelaide.edu.au

J. Liu · L. Cui
College of Chemistry, Chemical and Environmental Engineering, Laboratory of Fiber Materials and Modern Textile, the Growing Base for State Key Laboratory, Qingdao University, 266071 Qingdao, China

M. Zhang et al. (eds.), *Carbon Nanomaterials for Biomedical Applications,*
Springer Series in Biomaterials Science and Engineering 5,
DOI 10.1007/978-3-319-22861-7_3

Thus far, numerous nanomaterial-based drug delivery systems have been developed, including liposomes, polymers, metal / metal oxide and carbon nanomaterials. Carbon nanomaterials (CNMs) are formed by allotropes of carbon at nanoscale which mainly composed of carbon and oxygen atoms. CNMs have generated great research interest on drug delivery due to their unique physiochemical properties. They have emerged as the most extensively explored nanomaterials, providing many advantages compared to polymer and inorganic NPs and exciting opportunities for their biomedical applications including DD [10]. To this end, the following CNMs have been explored so far: carbon nanotubes (CNTs), graphene, graphene oxide (GO) fullerenes, carbon nanohorns, and nano-diamonds. The scheme of these structures is presented in Fig. 3.1.

Graphene is a single layer of sp^2 carbon atoms densely packed into a benzene ring structure. Graphene can be described as the fundamental building block of all these graphitic forms and geometries, which can be wrapped into spherical structures (0D fullerenes), rolled into 1D structure (CNTs), or stacked into 3D layered structure (graphite) [11, 12]. Due to its unique structure and geometry, graphene possesses remarkable physical–chemical properties including high Young's modulus, excellent electrical and thermal conductivity, and ultra-large specific surface area, and biocompatibility [13, 14]. These properties enable graphene to be considered as an ideal material for very broad applications [11, 14, 16, 129, 130, 134].

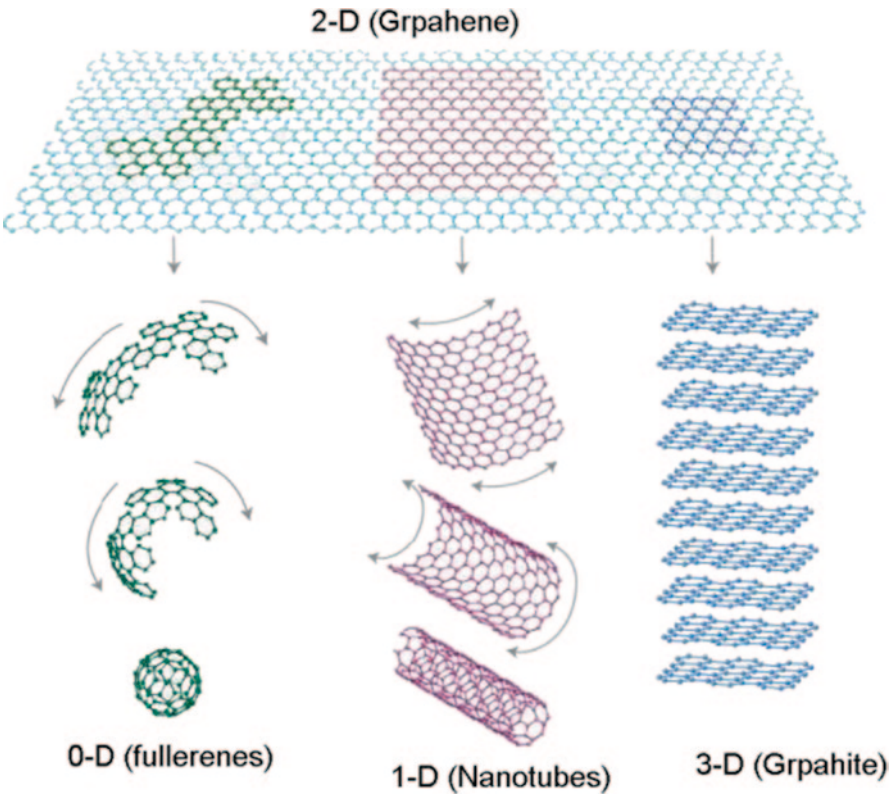

Fig. 3.1 Mother of all graphitic forms. Graphene is a 2D building material for carbon materials with other dimensions including 0D (fullerenes), 1D (carbon nanotubes), and 3D (graphite) [12]

CNTs are formed by the rolling up of graphene sheets (GSs) [17, 18], while the tips of CNTs are reminiscent of the structure of a fullerene hemisphere [19]. CNTs can be classified into single-walled CNT (SWCNT) and multiwall CNT (MWCNT). The diameter of SWCNTs is typically in the range of 0.4–2.0 nm in diameter, while for MWCNT the diameter is larger and can reach to more than 100 nm. The length of CNTs can also variously range from nanometers to centimeters [18].

Many synthetic approaches were developed for synthesis of CNTs where the chemical vapor deposition (CVD) is the dominant method because this method is easy to scale up and can provide controllable conditions for nanotube synthesis [18, 20]. Since the beginning of widespread CNTs research in the early 1990s, CNT-related commercial activity has grown substantially during the past decades [21]. From 2004, graphene, a new star was born that surged fresh and enormous research interests on CNMs for biomedical applications. Several methods for graphene synthesis have been introduced, mainly based on mechanical/chemical exfoliation from graphite which could produce scalable amount of GO [22].

The CNMs have attracted enormous attention as nanocarriers for DD applications and the development of new and promising DD concepts. However, the applications of CNMs for DD are still under development and depend on conclusive proof of their safe use and biocompatibility. The CNTs with their thin and elongated shape, remain fibrous-like toxic particles similar to asbestos particles, and their latent toxicity raised many concerns and conflicting debates [23]. Although graphene and GO have different (planar) morphology, they were found to be thrombogenic in mouse and evoked strong aggregatory response in human platelets, which questioned their biocompatibility [24]. However, an increasing number of studies have shown that the cell toxicity of CNMs is strongly related to their size (length and diameter) surface charge, surface chemistry, agglomeration, and purity [80]. Thus, there is a strong indication that their biocompatibility can be greatly improved by controlling these parameters, and that chemically modified CNMs can be considered as safe, nontoxic, and biocompatible materials [25–27].

In this chapter, we presented recent advances and developments of CNMs as nanocarriers for DD and photo-thermal therapy. First, we compiled the recent research progress on surface modifications and toxicological properties of CNMs. Second, we showed important concepts and examples of CNMs-based DD applications such as delivering different therapeutics (e.g. chemotherapeutic drugs, genes, proteins etc.) and photo-thermal therapy. Finally, we conclude this chapter with a summary of challenges and prospective over the future regarding to the CNMs-based DD research.

3.2 Carbon Nanomaterials as Nanocarriers for Drug Delivery: Concepts and Challenges

Compared to other drug nanocarriers, both CNTs and graphene possess several unique properties relevant to their DD and biological applications which include hollow and planar structure with ultrahigh surface area of $> 1000\ m^2/g$ and $2600\ m^2/g$, respectively. This enormous surface area provides the space for loading very large

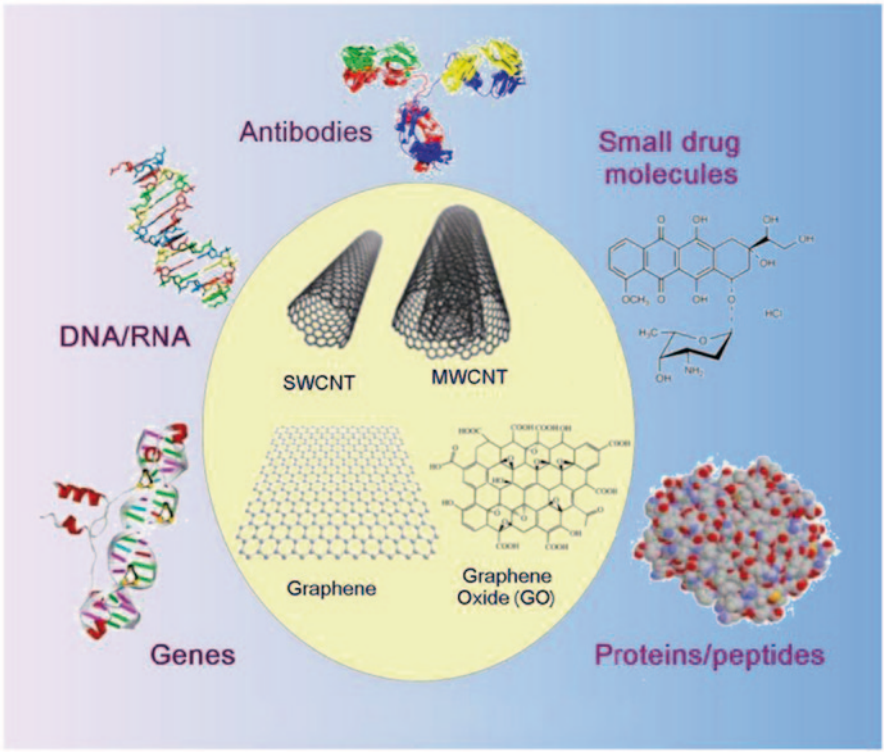

Fig. 3.2 Scheme of carbon nanomaterials (CNMs) including carbon nanotubes (CNTs), graphene, and graphene oxide *(GO)* for drug delivery of various therapeutics. *SWCNT* single-wall carbon nanotube, *MWCNT* multiwall carbon nanotube

amount of drug molecules that is not possible to achieve by other nanocarriers. This feature provides a great potential for CNMs to be applied for systemic targeting and local DD systems for many medical therapies, including chemotherapy. The scheme of CNTs, GO, and graphene as nanotherapeutic DD platform to carry different therapeutics from small drug molecules, antibodies, DNA, proteins, and genes is presented Fig. 3.2.

One of the key advantages of CNTs and graphene as drug nanocarriers, especially for cancer therapy, is their capability to evade the endosomal compartment and translocate directly into the cytoplasm of different types of cancer cells. Compared to other nanomaterials, they can provide considerable higher drug loading for a number of therapeutic molecules and deliver them directly into the cells. Both the CNTs and graphene have intrinsic physical properties which permit efficient electromagnetic stimulation including near-infra red (NIR) fluorescence, Raman, and photoacoustic scattering that could facilitate their tracing using various imaging strategies and used for photothermal therapy [28]. Recent in vitro and in vivo studies have highlighted their outstanding potential for cancer therapy demonstrating that CNMs were able to more successfully halt tumor growth in comparison to various therapeutic modalities including chemotherapy, hypothermia, and gene

silencing macromolecular and biomarker, thus providing a versatile platform to tailor the material for specific DD applications, including targeting DD [25, 26]. When combined with other materials such as polymers, quantum dots, gold, and magnetic NPs, CNM composites become a multifunctional platform for cancer diagnosis and on-demand DD [29]. These multifunctional DD systems generally consist of several parts including functionalized CNMs, tumor-targeting ligands, anticancer drugs, and bioimaging probe [30]. The concept has been further supported using different anticancer drugs (i.e., doxorubicin—DOX, paclitaxel, Pt complex immune therapeutics, and RNA).

The method of targeted delivery therapeutics to specific tissues using CNMs has a significant advantage compared to traditional administration, since it proves a viable approach to reduce side effects and improve efficacy [31]. The early works in this area, such as Doxil®, utilize the method of passive targeting approach, or the so-called EPR effect. This report on the EPR effect showed that the accumulation of anti-cancer protein at a tumor site is caused by the enhanced permeability in tumors due to the abnormal blood vessels and lymphatic drainage. [32]. Such angiogenic blood vessel gaps, as large as 600 nm between adjacent endothelial cells, allow nanoparticles to preferentially accumulate in tumors rather than spread into healthy tissues. In addition, it was found by other groups that blood vessels gaps, as large as 600–800 nm abnormal blood vascular can increase both the geometric resistance and viscous resistance of blood flow, which significantly lower the average velocity of red blood cell in tumor than that in normal cells [8]. The EPR effect provides several benefits when compared to free diffusion of drug molecules into tumor tissues. However, as a passive targeting method, it also faces some challenges: the EPR effect is highly dependent on tumor type and age, which means EPR is limited to specific stages and type of tumor [31]. Besides, the longer circulation times of drug-loaded particles, for example, PEGylated liposomal DOX, are associated with several adverse effects, such as stomatitis and palmar–plantar erythrodysesthesia [8]. Therefore, the heterogeneous properties of tumor and EPR effect require us to develop an alternative DD system to enhance the efficiency of targeting drugs by nanocarriers.

Another milestone in cancer therapy is the founding of cellular pH gradient in tumor versus normal tissue [33]. Tumor cells use glycolysis to obtain extra energy, which result in a relative acidic environment compared with normal cells. This characteristic of tumor cells provides a strong rationale for designing efficient drugs as a function of their pK and the cellular pH gradient. Based on this mechanism, several new concepts using CNTs and graphene loaded with anticancer drugs were developed showing drug release automatically at the tumor site where the pH is lower than normal cells.

A more promising way to provide specific DD in cancer therapy is to use an active drug targeting. The concept of this system is that drug vehicles containing specific ligands and monoclonal antibody can transport drugs to the cancer location or cross the biological barrier by a specific molecular recognition process (Fig. 3.3). The internalization of the CNM conjugates usually occurs via receptor-mediated endocytosis. The following step is the formation of endosome by invaginating plasma membrane to envelope the complex of the receptors and CNTs. Subsequently,

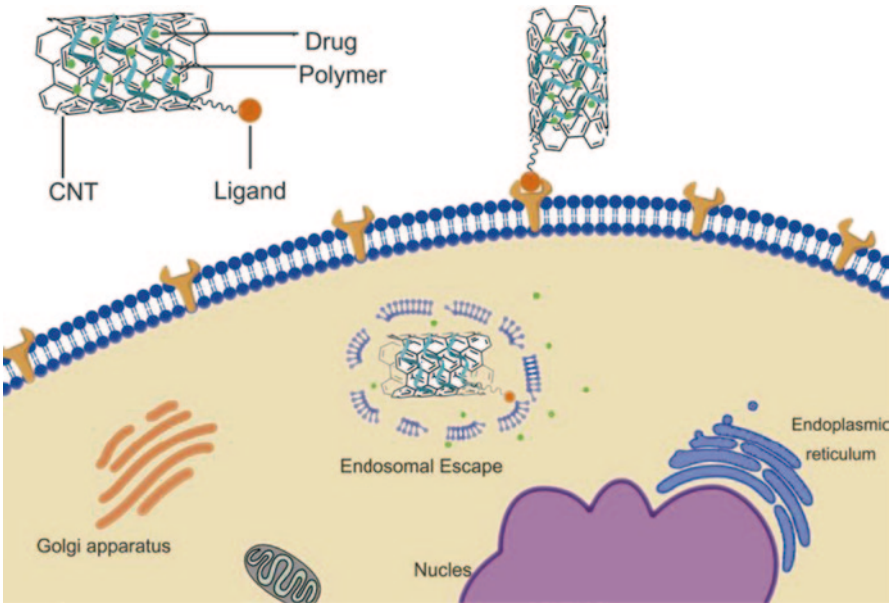

Fig. 3.3 CNT-based tumor-targeted drug delivery system: CNTs, drug, and tumor-targeting ligand. CNT carbon nanotube

newly formed endosomes are transferred to target organelles, and the drug molecules are released by increasing pH or the so-called proton sponge hypothesis [135]. Released drugs are then trafficked by their target organelle. Meanwhile, the receptor released from the conjugate returns to the cell membrane to start a second round of transport [5].

To increase the specificity, the corresponding antigen or receptor should be expressed exclusively on all tumor cells while not appearing on normal tissues. For example, the folate receptor is overexpressed on a tumor cell to increase the nutritional uptake, and thus folate is widely used as the homing molecule. But folate is also supplied by food, which might compete with ligand on nanocarriers [5]. To date, tumor-associated biomarkers, such as transferring receptors, growth factors, and other overexpressed characteristic protein, have already been used for developing DDSs [34]. For example, the arginine–glycine–aspartic acid (RGD) peptide-conjugated magnetic NP as well as CNT composites (have been designed for targeting integrin αvβ3-positive U87MG cells [35, 36].

Due to the molecular complexity and defense mechanism of a disease, the use single therapeutic agent capable of only hitting a single target is not adequate. The concept called “combination therapy” described as the simultaneous administration of two or more pharmacologically active agents with different mechanism of reactions is recently recognized as a more efficient approach for disease treatment. CNTs, graphene, and GO owing to intrinsic physical properties and high surface offer many advantages to use this strategy to load several different drugs and receptors and therefore used for the development of multifunctional DD platform for combined therapy including bioimaging [30]. The new concept of multifunctional

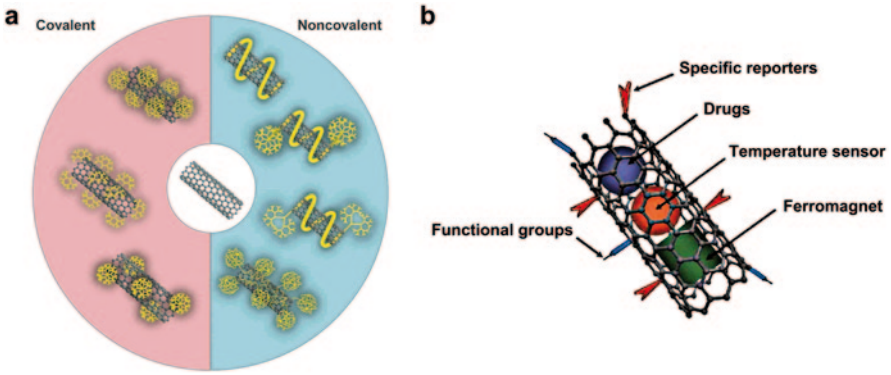

Fig. 3.4 Functionalization of CNTs with drug targeting and bioimaging molecules by combined covalent and non-covalent functionalization towards designing advanced and multifunctional CNM drug delivery systems. **a** The immobilization of drug molecules on the external surface of the CNT and **b** the loading of drug molecules, bioprobes, and releasing of magnetic NPs inside nanotubes [30]

CNM drug nanocarriers is schematically presented in Fig. 3.4 where CNTs are used as a model, but the concept can be applied for both graphene and GO. The multifunctional DDS can be composed of several drugs to provide different therapies, including antibodies for specific cell targeting and fluoroprobe (i.e., quantum dots) for tracking the nanocarrier inside the cell or body. The CNM drug carrier with and without fluoroprobe can also be used as a potential cancer biomarker sensing combined with biomedical imaging in addition to cancer-selective DD. The combined therapy concept is particularly promising in cancer treatment where different therapeutic approaches are important to improve efficacy with reduced dosage and side effects.

In summary, the designing of CNT, graphene, and GO for DD applications requires addressing many of the previously discussed issues. The first is to make optimal structural and surface functionalization for building an efficient nanocarrier with desired drug-loading capacity and optimized biocompatibility. The second is to improve the biocompatibility of CNM, which is essential for the development of DDS for preclinical and clinical studies. The third is to design advanced DDS with targeting DD capability to release one or several drugs in a controllable way with optimized dosage at specific site required for successful therapy. A significant progress towards addressing these issues and the development of advanced DDSs, including in vitro and in vivo studies, have been witnessed in the past several years.

3.3 Functionalization of Carbon Nanomaterials

The main issue for the application of CNMs for DDS is their limited solubility and dispersion in aqueous solutions. This is particularly critical for CNTs and graphene which are highly hydrophobic and do not have oxygen-containing hydrophilic

Table 3.1 Examples of typical covalent and non-covalent functionalization of CNT, graphene, and GO used for their drug delivery applications

Methods	Methods or mechanisms	References
Covalent	Polyethylene glycol (PEG)	[36, 39, 40]
	Polyacrylic acid (PAA)	[41, 42]
	Poly-L-lysine (PLL)	[43]
	Poly (vinyl alcohol) (PVA)	[44]
	Polyethylenimine (PEI)	[45–47]
	Poly(*N*-isopropylacrylamide) (PNIPAM)	[48]
	Polysebacic anhydride (PSA)	[49]
	Chitosan	[50–52]
	Gelatin	[53]
	Fe_3O_4	[35]
	Folic acid (FA)	[54, 55]
Non-covalent	π–π stacking interaction	[56, 57]
	Van der Waals force	[58, 59]
	Electrostatic	[60, 61]
	Hydrogen bonding	[58, 62–64]
	Coordination bonding	[65]

groups important for dispersion in water solution. In addition to the solubility, it is well known that the surface chemistry of these nanomaterials is the key to build the drug carriers with improved biocompatibility, lower toxicity, and controlled behaviors in biological systems. Thus, the surface functionalization of CNMs is essential for their DD and biomedical applications. Two general methods for the functionalization of CNMs were developed including the non-covalent immobilizations with amphiphilic molecules and the covalent functionalization by grafting various chemical groups [18, 37, 38]. These approaches were initially developed and explored for surface modification of CNTs and then applied for the functionalization of graphene and GO since their discovery in 2004. Most important examples of functionalization of CNMs used for DD applications are summarized in the Table 3.1. These modifications were used not only to improve physical properties of CNTs and graphene such as solubility and enhanced transport in biological system but also improve their biocompatibility, bioavailability, drug loading, and drug-releasing performances.

3.3.1 Covalent Functionalization

Numerous methods for covalent functionalization of CNMs was explored and extensively reviewed in literature [19]. They can be classified into two main approaches based on the defect-group chemistry, which utilizes the existing or introduced reactive oxygen-containing group in the area having the defect, and direct functionalization based on highly reactive reagents for addition reaction.

The most popular, defect-group chemistry uses strong oxidizing agents, for example, concentrated nitric acid [66] and ozone oxidation [136], to introduce oxygen-containing groups on the sidewall, open ends, as well as the defected sites. Based on this method, long-chain alkylamines can be coupled to carboxyl groups activated with thionyl chloride ($SOCl_2$) [37]. This approach has been successfully used for the modification of GO sheets with covalent attachment alkylamines using the solvothermal process [67, 68]. Amine-containing polymer, such as polyethylene glycol (PEG), poly (vinyl alcohol) (PVA), Polyethylenimine (PEI), and Poly (N-isopropylacrylamide) (PNIPAM) have also been grafted onto GO sheets and oxidized CNT [38] through covalent methods to increase their biocompatibility. Similarly, grafting of small molecules, such as peptides onto CNTs and GO surface, has been achieved by using $SOCl_2$ through formation of a covalent (amide linkage) with amino functional groups [54, 55]. In addition, Zhang et al. functionalized GO sheets with sulfonic acid groups (SO_3H), followed by a covalent grafting of folic acid (FA) molecules [54]. The FA-conjugated GO (FA-GO) could be well dispersed and maintained stable for several months in D-Hanks buffer, a physiological solution.

The direct sidewall functionalization with organic groups is possible by reactive species such as nitrenes, carbenes, and radicals [37]. For example, the thermal reaction of azidoformates at 160 degree leads to nitrogen extrusion and subsequently forms alkoxycarbonylaziridino-modified CNTs. It was also shown that the diazonium salts of para-nitroaniline can be grafted into the graphene surface for preparing organosoluble graphene [69, 70]. Another method is based on 1,3-dipolar cycloaddition reaction, or the so-called Prato reaction, which can introduce methotrexate group on the aromatic sidewall instead of nanotube ends and defects [71]. By this protocol, Kostarelos et al. explored a number of cases to study the CNTs cell toxicity, cell uptake, as well as delivering plasmid DNA, antibody, peptide into the cells [72–74].

3.3.2 Noncovalent Functionalization

Noncovalent modifications have been extensively used for the modifications of all CNMs based on van der Waals force, electrostatic interaction, hydrogen bonding, coordination bonds, and π–π stacking interaction of binding molecules and graphitic surface [19]. Non-covalent functionalization can be achieved by polymer wrapping, adsorption of surfactants or small molecules, and interactions with porphyrins or biomolecules such as DNA and peptides. These methods were well explored for the surface modification of carbon sp^2 materials, initially on CNTs and later applied to graphene and GO.

In the case of CNTs, Dai et al. developed a method to use PEGylated phospholipids as coating material, enabling to make them highly soluble and stable in various biological solutions including serum [75, 76]. Biopolymers, such as nucleic acid and chitosan, were proved as flexible and simple approach for surface functionalization of CNTs. Ming et al. found that synthesized single-stranded DNA (ssDNA) can form

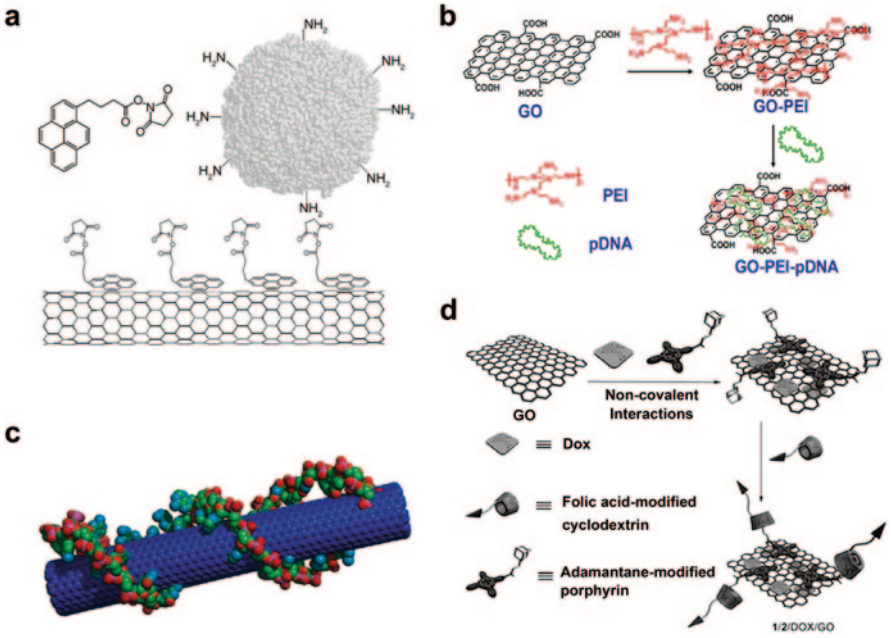

Fig. 3.5 Non-covalent modifications of CNTs, graphene, and GO using π–π stacking interaction for drug delivery applications. **a** proteins anchored on the SWCNT via pyrene π–π stacked on a nanotube surface [138]. **b** A SWCNT modified with single-stranded DNA by π–π stacking [78]. **c** the synthesis of GO–PEI–DNA complexes via a layer-by-layer (LBL) assembly process, which include the step of non-covalent functionalization by PEI polymers forming positively charged GO–PEI complexes followed by electrostatic assembly charged DNA molecules on the GO–PEI complexes. **d** Synthesis of 1/2/DOX/GO from graphene oxide, DOX, adamantine-modified porphyrin, and folic acid-modified cyclodextrin. *GO* graphene oxide, *PEI* polyethylenimine, *DOX* doxyrubicin, *pDNA* plasmid DNA [61].

π–π stacking interactions with the sidewall of CNTs. The DNA binding to CNTs is extremely effective and facile, because the surface chemistry of CNT can be easily controlled by modifying the sequence and length of DNA [133, 137] (Fig. 3.5).

In the case of GO and graphene, it was found that organic molecules and polymers with pyrene functional groups can easily make π–π stacking interaction with graphene. Stankovich et al. have reported the first example of non-covalent functionalization of graphitic nanoplatelets using poly (sodium 4-styrenesulphonate) or PSS [77]. Feng et al. functionalized GO with PEI polymers through non-covalent electrostatic interactions, yielding GO–PEI complex with strong positive charges, high stability in physiological solutions, and reduced cytotoxicity to cells [60]. The synthesis of GO–PEI–DNA hybrids via a layer-by-layer (LBL) assembly of DNA was also proved by this method [133, 137] (Fig. 3.5).

The large π-conjugated structure, abundant structural defects on CNMs, and presence of oxygen functional groups are also advantageous to perform attachments with NPs. NPs including Au, Ag, Pd, Pt, Ni, Cu, TiO_2, ZnO, MnO_2, Co_3O_4, and

Fe_3O_4 have been successfully incorporated with CNTs, graphene, and GO for their DD applications [58, 63, 64]. These CNM/NP composites have attracted substantial attention owing to their interesting magnetic and optical properties and capability to combine DD, with bioimaging, biosensing, and external stimulus DD approach (Fig. 3.4).

3.4 Cell Toxicity and Biocompatibility of CNMs

3.4.1 Cell Toxicity and Biocompatibility of Carbon Nanotubes

The distinctive properties of CNTs based on their extremely small size, large surface area, rigid structure, cylindrical rod-like shape, and chemical composition raised some concern about their biosafety due to their unique interactions with biological systems. The fundamentals of the toxicity of synthetic nanomaterials in general are still not well understood. However, it is widely accepted that the toxicity of these materials depend on many parameters including particle size and distribution, shape, impurities, degree of nanomaterial aggregation or agglomeration under the experimental conditions, surface chemistry, surface area, morphology, surface charge, reactivity, crystal structure, and persistence. The changing of these parameters can dramatically influence the toxicity of CNTs on the cells, so their toxicity cannot be generalized.

Considering the length and shape, the CNTs have a thin and long fiber-like shape, which has an aspect ratio (length/diameter) greater than three. Thus, the CNTs might be suitable to fit the "fiber toxicological paradigm" according to the World Health Organization (WHO) criteria used to describe the toxicity of asbestos fibers [23]. Early studies showed that the pharyngeal aspiration of micrometer-scale SWCNTs can induce a robust acute inflammatory reaction and the formation of granulomas in C57BL/6 mice, which is similar to a fibrogenic response [79]. Another pilot study demonstrates that carcinogenicity of CNTs and fiber amosite result from exposure to long (>20 μm), but not short (<5–10 μm) and low-aspect radio-tangled nanotube aggregates [80]. This suggests that the increased risk of cell toxicity, when exposed to CNTs and fibers for a longer time, is presumably because macrophages cannot completely overcome longer fibers. The scheme of this process is presented in Fig. 3.6. Their later study reports that the "frustrated phagocytosis" has a dramatic influence on the sustained generation of reactive oxygen species (ROS), which in turn contribute to the secretion of inflammatory mediators [139]. In contrast, the CNTs with short length can facilitate the cell uptake and thus cause stronger inflammatory response.

Impurity of CNT material, especially catalyst metal contaminants such as Fe, Ni, Mo, and Co, was found to be another important factor leading to their toxicity. The transition metals are widely used during CNT production by the CVD process

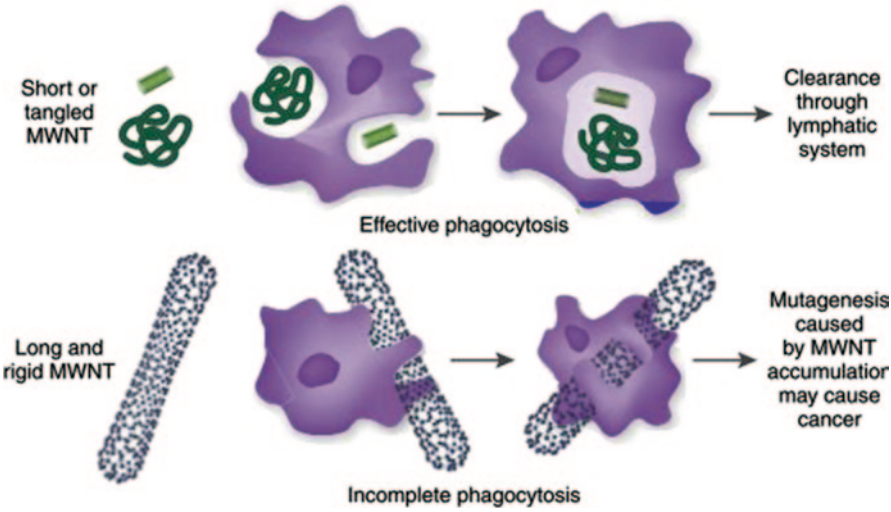

Fig. 3.6 The effect of CNT structure on phagocytosis by macrophages and clearing from tissues. Whereas macrophages can engulf MWNTs with a low-aspect ratio before their clearance by draining lymph vessels, MWNTs with a high-aspect ratio cannot be cleared and accumulate in tissues, where they promote carcinogenesis. *MWNT* multiwalled nanotube [80]

since they serve as the seeds for the growth of CNTs [18, 81]. Although the amount of catalyst can be largely reduced through a purification process, it is impossible to entirely remove these metal impurities, because some particles are enclosed by graphitic shells. The use of CNTs from different sources and impurities was the main reason to have many conflicting results in literature on their toxicity reported by different groups. These metal NP, when released to cell culture or human body, can induce oxidative stress by generating reactive oxygen species (ROS) into intracellular environment [82]. It has been found that the metal NP can cross cell membrane and therefore are able to catalyze one-electron reactions including some physiologically relevant reductants, such as ascorbate, thiol compounds, can reduce ferric iron to its ferrous form, which has the capacity to reduce oxygen to superoxide radical and further generate H_2O_2 and OH radicals [83]. These ROS, including free radicals, H_2O_2, and superoxide anions are known to enhance oxidative stress, induce inflammatory responses, and DNA damage [23, 132]. The scheme of the mechanism of how CNTs and their impurities (metal NPs) can induce cell damage is presented in Fig. 3.7.

Another important factor that influence the cytotoxicity of CNTs is their surface chemistry. The behaviors of CNTs in biological systems in vitro and in vivo are highly dependent on the surface chemistry. On one hand, the surface modification can significantly change the CNT solubility in water, organic solution, and biological environment. On the other hand, the cell uptake process of CNTs is influenced by the particle size and the surface chemistry. It has been reported that CNTs, functionalized by protein, polymer, oxidation, or wrapped by DNA, are able

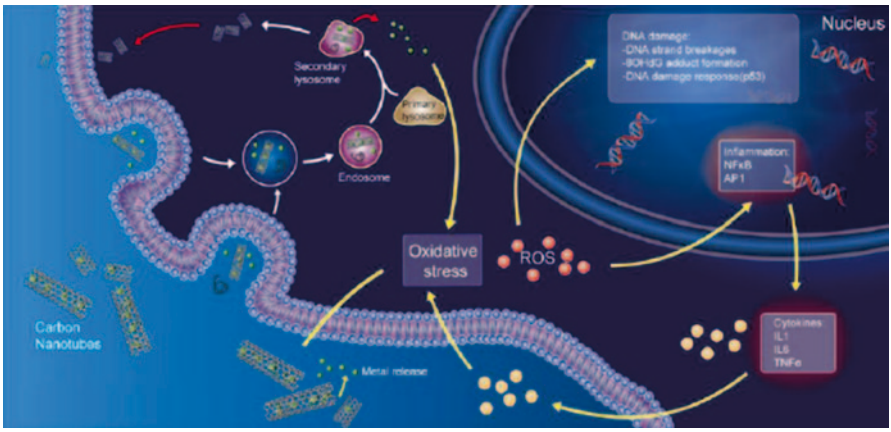

Fig. 3.7 The mechanisms by which CNTs induce cell damage and inflammation [23]. *ROS* reactive oxygen species, *IL* interleukin, *TNF-α* tumor necrosis factor, DNA deoxyribonucleic acid,

to be engulfed by cells via energy-dependent endocytosis pathways [84–87]. While another report shows a different result that CNTs functionalized by 1,3-dipolar cycloaddition can directly enter the cell similar to a "nanosyringe" [72]. Functionalized CNTs are found inside different types of cells even under endocytosis-inhibitor condition. Therefore, the cell uptake mechanism of CNTs is still unclear, but it is widely accepted that the CNT cell uptake is highly dependent on several factors, such as the size, the surface chemistry, and the type of cell.

3.4.2 Cell toxicity and Biocompatibility of Graphene and GO

The toxicity patterns of graphene and GO has dramatic difference as compare to CNTs because of their different synthesis route and structural morphology [88]. However, following the same principle generally accepted to all nanomaterials, the toxicity of graphene and GO is expected to be directed by the size, shape, surface chemistry, and charge of their planar structures. Many initial reports have indicated that these nanomaterials and their hybrid have a low cell toxicity, even though these reports are conflicting [89, 90].

The interaction between dispersed graphene or GO sheets and target cells has been studied in monolayer cultures of lung epithelial cells [58], fibroblasts [91], and neuronal cells [92]. Single-layer GO sheets were internalized and sequestered in cytoplasmic, membrane-bound vacuoles by human lung epithelial cells or fibroblasts and induced toxicity at doses above 20 μg/mL after 24 h. [91, 93]. Shen et al. using human lung epithelial cells found minimal toxicity at doses higher than 50 μg/mL and no cellular uptake [58]. Liao et al. explored the biocompatibility of graphene-related materials with controlled physical and chemical properties, and their results demonstrated that particle size, particulate state, and oxygen content/surface charge

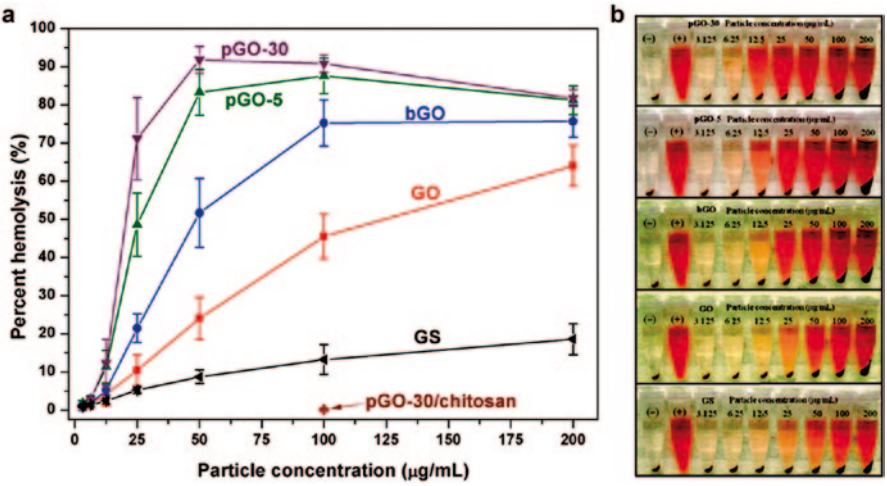

Fig. 3.8 **a** Percent hemolysis of red blood cells (RBCs) incubated with different concentrations (3.125–200 μg/mL) of GO *(red),* bGO *(blue),* pGO-5 *(green),* pGO-30 *(purple),* and GS *(black)* for 3 h at 37 °C with agitation. **b** Photographs of RBCs after a 3-h exposure to GO, bGO, pGO-5, pGO-30, and GS at different concentrations (3.125–200 μg/mL). The presence of red hemoglobin in the supernatant indicates RBCs with membrane damage. (+) and (−) symbols represent positive and negative control, respectively [94]. *GO* graphene oxide, GS graphene sheets, *pGO* polymer graphite oxide composite

of graphene have a strong impact on biological/toxicological responses to red blood cells (Fig. 3.8) [94].

To improve biocompatibility, Liu et al. developed a new modification approach for the preparation of gelatin functionalized graphene nanosheets (GNS) by using gelatin as a reducing reagent. The obtained biocompatible gelatin–GNS showed high aqueous solubility and stability in various physiological fluids and exhibited a high-drug-loading capacity. Another protocol combined GO with biocompatible polymer (PEG) and showed a minor in vitro toxicity to many cell lines, including Raji, HCT-116, OVCAR-3, U87MG, MDA-MB-435 and MCF-7, even at high concentrations of up to 100 mg/L [39, 40].

However, it was reported that GO was highly thrombogenic in mouse and evoked strong aggregatory response in human platelets [24]. As platelets play a central role in hemostasis and thrombus formation, thrombotoxicity of GO potentially limits its biomedical applications. It was found that amine-modified graphene had absolutely no stimulatory effect on human platelets, nor did it induce pulmonary thromboembolism in mice following intravenous administration, which contrasted strikingly the observations with unmodified GO. Another method reported recently is to use the biocompatible polymer, dextran, to covalently modify GO which shows improved stability in physiological solutions and remarkably reduces cell toxicity compared to plain non-functionalized GO [95].

All these studies clearly indicated that the toxicity of graphene and GO is closely associated with biocompatibility of their surface functionalization. The functionalized graphene, GO, and their derivatives are shown in most cases to be significantly

less toxic when compared with their non-functionalized counterparts. However, it is important to conduct long-term toxicity studies considering that animal experiments conducted on mouse models could have different results from humans. Hence, more preclinical toxicity studies are necessary before consideration to translate GO-based DDS into the clinic. Even though more continuous research is required to evaluate their long-term toxicology even from the current toxicity studies, their future biomedical applications look promising.

3.5 Drug Delivery Systems Based on Carbon Nanomaterials

3.5.1 Carbon Nanotube Drug Delivery Systems

The ultimate advantage of CNTs as a DD nanocarrier compared to other NPs is their distinct inner and outer surfaces, which are readily accessible by removal of the end caps, and an increased volume providing a high loading capacity for cargo molecules. Hence, they provide two options to load pharmaceutically functional molecules to the CNTs including exohedral and potential endohedral attachment. With exohedral binding, drug moieties are attached to the exterior of CNTs for their subsequent delivery into cells. The diverse functional groups can be introduced onto the surface and act as "linkers" to therapeutic moieties, for subsequent delivery into cells (Fig. 3.4a). With endohedral delivery, drug molecules or NPs are encapsulated and transported through the inner cavities of CNTs (Fig. 3.4b). Drug molecules can be bound onto the exterior CNT surface by either stable covalent bonds or supramolecular assemblies based on non-covalent electrostatic attractions (Table 3.1). Predominantly, reports showed the use of CNTs as drug carriers for loading large biomolecules on the external surface. The non-covalent binding of drug molecules on the sidewall is the simplest method for this purpose and a convenient pathway to load the drug on CNTs, which also protect the physical property of CNTs. Both SWCNTs and MWCNTs have been extensively explored as drug nanocarriers for loading a large number of therapeutics including small drug molecules, anticancer drugs, poorly soluble drugs, antibiotics, antibodies, enzymes, peptides, DNA, RNA, and genes [10, 14, 34].

Pioneering work by Prato and Dai's groups proves that the polycyclic aromatic structure of DOX, anticancer drug, can be loaded on the sidewall of CNT through π– π supramolecular stacking [36, 96] (Fig. 3.9). Based on the fluorescence property of DOX, the decrease of fluorescence intensity was observed with the increasing concentration of MWCNT in the solution, which indicates the static quenching of DOX molecules on CNTs' sidewall [96]. Almost during the same period, Dai's group proved that through non-covalent binding, DOX can be loaded on the surface of SWCNTs, which is first functionalized by PEG with either non-covalent or covalent treatment. The large surface area of SWCNTs will not be fully covered by PEG, thus enabling DOX to bind on the sidewall and form "forest–scrub"-like

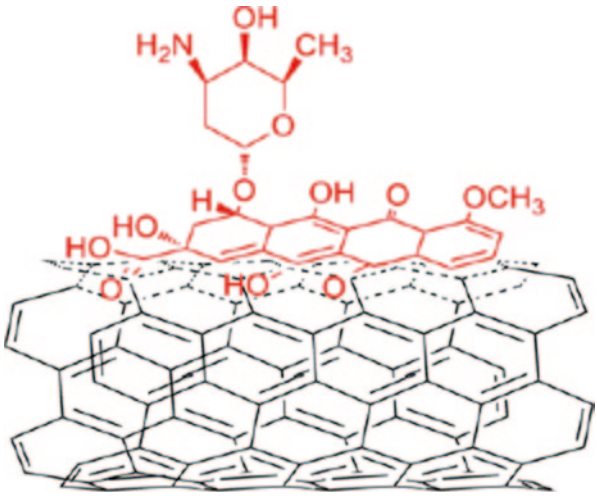

Fig. 3.9 The scheme of doxorubicin load *(red)* on the sidewall of CNT structure through π–π supramolecular stacking

assemblies. The ultra-large surface area of SWCNT provides large drug loading, which is almost 8–10 wt% higher than using conventional liposomes. It was also found that the binding of DOX molecules is diameter dependent and pH dependent. In their later in vivo study, it was shown that PEGylated DOX–SWCNTs significantly inhibit the growth of tumor than the free DOX at the equivalent dose (2.15 ± 0.16-fold tumor growth vs. 2.90 ± 0.19) [97]. Furthermore, the DOX–SWCNTs showed reduced toxicity to mice, since no weight and mortalities were found after the administration of DOX–SWCNT (5 mg/kg) within 2 weeks. The reduced toxicity of DOX -SWCNT proved that this novel drug formulation can achieve higher maximum tolerance dose, which is benefit for clinical chemotherapy.

Another promising concept is the modification of oxidized SWCNTs with natural polysaccharides based on non-covalent supramolecular interaction [85]. Two kinds of widely used biopolymer, sodium alginate (ALG) and chitosan (CHI), were used for the modification of SWCNTs followed by loading anticancer drug (DOX). The concept is shown in Fig. 3.10. The CHI, natural biodegradable copolymer, is soluble in acidic aqueous solutions but flocculates at pH > 6 due to the deprotonation of its amine groups. The amine group of CHI is flexible to link with other functional group, but the poor solubility of CHI limits its application in DD [98]. Compared with CHI, ALG is more suitable for loading DOX because ALG has a lower zeta potential, but it is not easy to react with other ligand. Therefore, the combination of CHI and ALG is an ideal design for both drug loading and drug targeting. In this experiment, folate is efficiently reacted with CHI for recognizing overexpressed folate receptor on the surface of the cancer cell. In the cellular uptake experiment with HeLa cells, the DOX–FA–CHI/ALG–SWCNTs was found to penetrate the cell membrane; while when the FA receptor is blocked by pretreatment, the much weaker accumulation of SWCNT was found inside the cell, thus demonstrating the role of FA in receptor-mediated endocytosis.

The covalent functionalization as another method was also used for loading drugs, where several key concepts were introduced. For example, based on

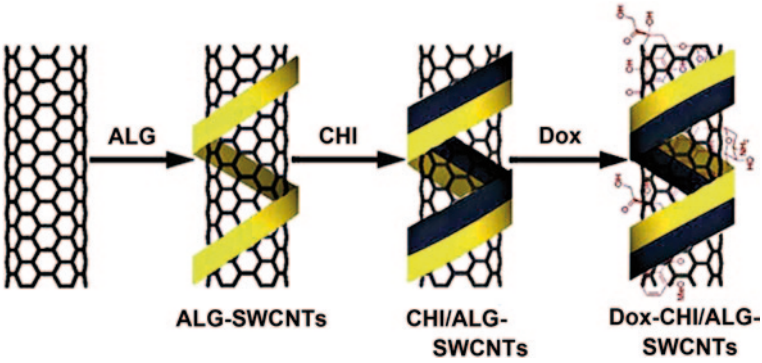

Fig. 3.10 Preparation of SWNTs–DOX after inclusion of biopolymers to enhance nanotubes dispersability in aqueous phase. [85] *ALG* sodium alginate *CHI* chitosan *DOX* doxyrubicin, SWCNTs single-walled carbon nanotubes

1,3-dipolar cycloaddition reaction of azomethine ylides, Pastorin et al. attached both methotrexate and fluorescein isothiocyanate (FITC) onto the sidewall of multiwalled nanotubes (MWNTs) and found that the functionalized MWNTs could be internalized by Human Jurkat T lymphocytes with a dose and time-dependent manner [99]. NPs, including CNTs, are generally susceptible to the opsonization-induced reticulo-endothelial system (RES) uptake, which can significantly lower their retention time in the blood stream and eventual bioavailability of the carried drug. Carefully modifying the suitable surface chemistry is an effective method to reduce RES uptake. Based on this concept, Wu et al. reported a MWNT-based DD system, in which the antitumor agent 10-hydroxycamptothecin (HCPT) is covalently linked with the MWNT by a hydrophilic spacer of diaminotriethylene glycol through biocleavable ester linkage [100]. The in vitro experiment shows the rapid drug release in fetal bovine serum due to the enzyme activity, while a relative slow release is found under phosphate-buffered saline (PBS) solution. The biodistribution assay shows the high uptake of MWNTs in the liver, spleen, lung, kidney, stomach (emptied), femur, and tumor, but the MWCNT still exhibits long blood circulation time, in which the half-life of MWNTs in the blood circulation is calculated to be 3.6 h. Finally, the in vivo tumor inhibition experiments confirmed the enhanced antitumor effect of the conjugates in comparison to its native formulation due to the long circulation time, increased drug loading (16%), and high cell uptake.

A novel DDS which conjugates SWCNT, cisplatin, quantum dots (Qdots), and epidermal growth factor (EGF) has been recently tested on head and neck squamous cell carcinoma cell culture (HNSCC; Fig. 3.11). The EGF is functionalized on SWCNT surface in order to enhance targeting to cancer cells by recognizing the overexpressed EGF receptor on tumor cell surface; while Qdots make the SWCNT conjugates visible by confocal microscopy. In their experiment, they first proved that the SWCNT bioconjugates are selectively taken up by tumor cell though video imaging. The image and video shows more than 75% HNSCC cells containing SWCNT–Qdot–EGF. But when EGF receptor silencing gene is introduced into the cancer cell, the cell uptake rate reduces to only 25%, which indicates the

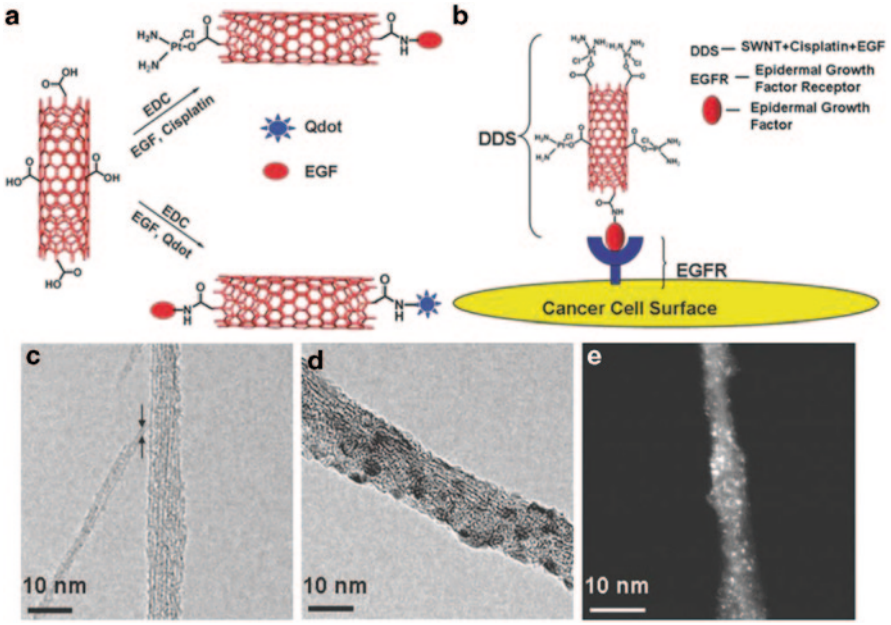

Fig. 3.11 **a** Illustration of chemical reactions used to attach *EGF, cisplatin,* and *Qdots* onto carboxylated SWNTs *(*in *red)* using *EDC* as the coupling agent. **b** Schematic showing *SWNT* bundles bioconjugated with *EGF* and cisplatin targeting the cell surface receptor *EGFR* on a single HNSCC cell. Transmission electron micrographs of **c** oxidized SWNT bundles with *arrows* showing a single *SWNT*. **d** SWNT–Qdot–EGF bioconjugate bundle. **e** STEM image of *SWNT* bundle showing cisplatin as the *bright spot* [101]. *EGF* epidermal growth factor, *DDS* drug delivery system, *EDC* epidermal differentiation complex, *Qdot* quantum dot

receptor-mediated endocytosis process during SWCNT bioconjugate cell uptakes. The video images also support the accumulation of SWCNT–Qdots–EGF in tumor tissue, while control group (SWCNT–Qdots) are rapidly cleared in blood vessels. The in vivo study showed that the SWCNT–cisplatin–EGF group inhibits tumor growth significantly in 10 days, while the SWCNT–cisplatin group did not show tumor regression effect [101].

In cancer chemotherapy, multidrug resistance (MDR) is a huge obstacle for the effective cancer therapy because the P-glycoprotein (P-gp), a broad-specificity transmembrane efflux pump, can recognize and pump the drug out of the cell once they are internalized. To overcoming MDR effect caused by the overexpression of P-gp, Ruibin Li et al. functionalized SWCNT with the antibody of P-gp and then loaded with DOX [102]. The drug loading is found to be the monomolecular adsorption based on Langmuir isotherm adsorption, and the drug release is significantly enhanced by NIR radiation. After that, DOX-loaded Ap–SWCNTs showed the high-binding affinity to human leukemia cells of K562 in vitro according to the confocal microscopy, and the cytotoxicity of DOX–Ap–SWCNTs is nearly 242 % higher than free DOX. The energy-dependent endocytosis process is also confirmed by incubating the cell in uptake inhibitor condition.

3.5.2 Graphene and Graphene Oxide Drug Delivery Systems

Inspired by the success of CNTs, the graphene and GO have been extensively explored in the past several years as a novel drug nanocarrier for a variety of therapeutics including anticancer drugs, poorly soluble drugs, antibiotics, antibodies, peptides, DNA, RNA, and genes [27, 107]. The most outstanding examples form this research are presented to show their applications for targeting, controlled, and stimulated DD including some specific applications for anticancer and gene therapies.

The simplest concept to use graphene and GO for DD applications is to directly immobilize drug molecules on the surface of graphitic sheets. The anthracycline DOX was the most explored drug model for anticancer, which is able to make a strong bond on GO surface through π–π interactions, in which hydrophobic part of DOX and hydrogen bond reaction between carboxyl groups or GO and amino groups of DOX contribute to the interactions [103]. This loading of DOX on GO is achieved by a simple mixing in an aqueous solution with the aid of sonication showing very high loading of 235 mg/mg. The release of loaded DOX molecules from GO nanocarrier was observed to be more extensive in acidic and basic conditions showing characteristic pH dependence [52]. This behavior is important in anticancer therapy because pH around cancer cells is slightly acidic and therefore promotes extensive drug release of DOX. To increase loading of DOX on GO, polymeric micelles, such as Pluronic-F127, were used showing very high loading efficiency of 289 % (w/w) on GO with low DOX concentration of 0.9 mg/ml [104, 105].

To increase the cancer targeting efficiency, conjugating cancer targeting lignads such as FA, peptides and antibodies have been widely used to design GO-based DDs. The first system was demonstrated by Zhang et al. who functionalized the GO with sulfonic acid groups, followed by covalent binding of FA molecules which allows specific target of MCF-7 cells, human breast cancer cells with FA receptors [54]. Two cancer drugs DOX and camptothecin (CPT) were loaded onto the FA-conjugated GO (FA–GO) via π–π stacking and hydrophobic interactions and their results showed remarkably high cytotoxicity of MCF-7 cells compared to GO loaded with either DOX or CPT only. Similarly, Huang et al. designed a FA-conjugated GO with good solubility and low cytotoxicity for targeting photodynamic therapy [106]. The GO nanocarriers are shown to significantly increase the accumulation of Ce6 in tumor cells and lead to a remarkable photodynamic efficacy on MGC803 cells upon irradiation (Fig. 3.12a) [106].

Preparing GO-based composite nanomaterials is another versatile strategy to enhance the drug delivery efficiency. by combining GO with gold NPs (AuNP) [25, 26]. It was found that DOX loaded on AuNP–GO inhibit HepG2 cell growth more strongly than DOX or/and AuNP–GO alone, suggesting more efficient transport into the cell by AuNP–GO compared with free DOX. This approach is successfully applied by Yang et al. through covalent attachment of magnetic NPs (MNP), on amino-modified GO followed by DOX loading (Fig. 3.12b) [55]. A multifunctional GO nanocarrier with dual-targeted delivery was designed, based on the force of a

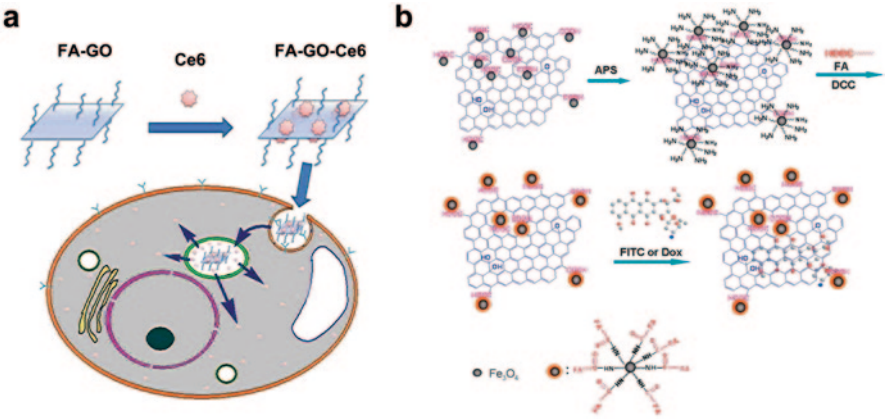

Fig. 3.12 **a** Scheme of FA–GO–Ce6 endocytosed by MGC803 cells, endosome-containing FA–GO–Ce6 complexes were located around the nucleus, Ce6 escaped from the endosome into the cytoplasm. **b** The preparation of the multifunctionalized GO-based anticancer drug carrier with dual-targeting function and pH sensitivity [55, 106]. *FA* folic acid, *GO* graphene oxide, *DOX* doxyrubicin, *FITC* fluorescein isothiocyanate, *APS* 3-aminopropyl-trimethoxysilane

magnetic field and the specific interaction between FA on the drug carriers and the overexpressed folate receptor on the surface of tumor cells, by conjugating GO–Fe3O4 nanohybrid with FA (Fig. 3.12b). The in-vitro studies showed that DOX–MNP–GO drug carriers exhibit much higher cytotoxicity to SK3 human breast cancer cells compared with free DOX [107].

Gene therapy is a promising approach to treat diseases caused by genetic disorders such as cancer. Transport gene into the nucleus of cells is challenging due to the existed biological barriers and nuclease degradation. Therefore, gene therapy requires to use a suitable gene vector to transport gene to the targets. While the virus-based gene vector have been widely studied, GO-based gene vector have been proved to be a suitable candidate for gene delivery. Previous studies also showed that ssDNA and RNA can be immobilized onto graphene and GO by non-covalent adsorption through stacking, electrostatic, and other molecular interactions which suggest the potential for application of graphene and GO as gene carriers [60]. Graphene was found to be able to protect oligonucleotides from enzymatic cleavage and was able to deliver ssDNA into cells [131]. Chen et al. designed a novel gene delivery system based on the GO chemically functionalized with branched PEI showing significantly lower cytotoxicity and substantially higher transfection efficacy of small interfering RNA (siRNA), at optimal N to P ratio. The PEI, a cationic polymer, has been used showing a strong binding to nucleic acids, efficient uptake by cells, and excellent proton sponge effect that triggers the endosomal release of DNA or RNA. Their results demonstrated that sequential delivery of siRNA and DOX by the PEI–GO nanocarrier leads to significantly enhanced anticancer efficacy. This concept was further successfully applied for GO-based gene delivery carrier through the installation of PEI which revealed that a hybrid gene carrier

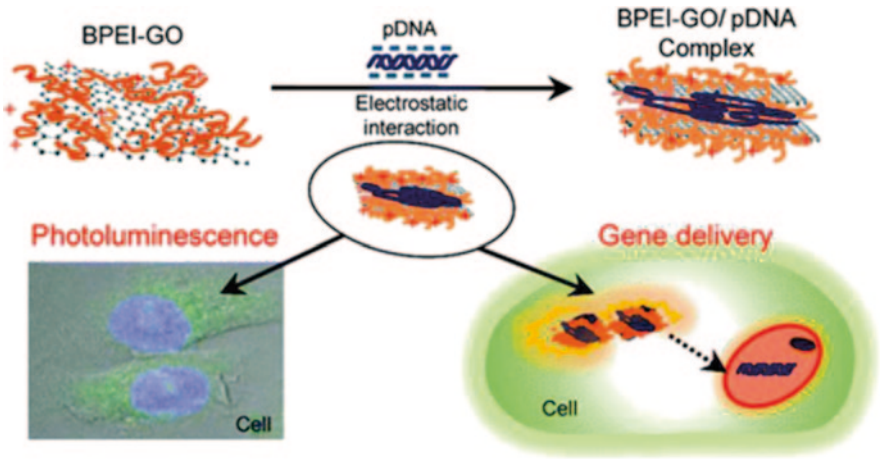

Fig. 3.13 Schematic representation of the delivery of pDNA into cells using branched polyethylenimine (BPEI)-modified GO (PEI–GO) [108]. *pDNA* plasmid DNA, *GO* graphene oxide

fabricated by conjugation of low-molecular-weight branched PEI (BPEI) to GO improved DNA binding, condensation, and transfection efficiency (Fig. 3.13) [108].

3.5.3 Carbon Nanomaterials- Based Photothermal Therapy System

Both CNTs and graphene are able to absorb NIR light in the wavelength range of 800–1600 nm [109]. It is known that biological systems are transparent to 700- to 1100-nm NIR light, while the strong absorbance of CNTs can convert NIR radiation into heat, thus killing cancer cells through so-called photothermal ablation. The application of CNTs in photothermal therapy was initiated in 2005 when Dai and coworker first reported the use of NIR-medicated cancer therapy by SWCNTs. After the internalization of DNA–SWCNTs, they found that six 10-s on-and-off pulses of 1.4 W/cm^2 laser radiations could offer the effective DNA releasing and nuclear translocation. They also proved that 2-min 808-nm NIR treatment at the power of 1.4 W/cm^2 causes cell death with the cell uptake of phospholipids PEG–FA–SWCNT [78]. In the following study, Chakravarty et al. used antibody (anti-CD22)-functionalized SWCNTs for thermal ablation of human Burkitt's lymphoma cells in vitro showing specific target ability to destroy various cancer cells [110].

Selective engineered defects introduced on the sidewall were shown to enhance the thermal property of MWCNTs, because such defects or dopants (N) will cause scattering in the travelling currents and also increase the heating of the nanotube [111]. These MWCNTs are expected to be more effective in adsorbing NIR radiation compared with materials such as SWCNTs, because MWCNTs have more available electrons for absorption. The MWCNTs contain more metallic tubes than

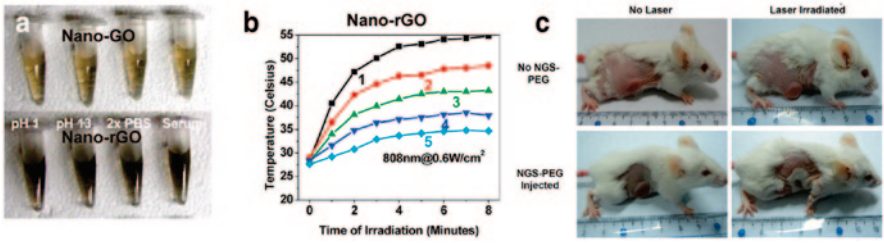

Fig. 3.14 **a** Photographs of vials contained 1 mL of covalently PEGylated nano-GO *(top photo)* or non-covalently PEGylated nano-RGO *(lower photo)* with the same GO mass concentration in the various solutions indicated. **b** Photothermal heating curves of **c** nano-RGO and **d** nano-GO solutions. *Black curve (1)* is 100 μL of solution with 20 mg/L concentration of nano-RGO or -GO, red curve *(2)* is 10 mg/L, *green curve (3)* is 5 mg/L, *dark blue curve (4)* is 2.5 mg/L, and *light blue curve (5)* is water. **c** Photos of tumor in mice after various treatment showed that laser-irritated tumor on GO sheets-injected mouse was completely destroyed [113, 114]. *PEG* polyethylene glycol, *NGO* nano-graphene oxide

SWCNTs, given that two thirds of SWCNTs are semiconducting [112]. Nitrogen-doped CNx–MWNTs are not inherently cytotoxic, and the length of nanotubes is proved to be a major determinant of their ability to transfer heat and kill the tumor. It was shown that CNx–MWCNTs with lengths between 700 and 1100 nm are most desirable to kill the tumor [111]. Another study using NIR radiation on MWCNTs showed the complete ablation of tumors and a >3.5-month durable remission in 80% of mice treated with 100 μg of MWCNT [112].

In the case of graphene and GO, it was shown that the PEGylated GNS themselves also exhibited ultrahigh in vivo tumor uptake and efficient photothermal therapy properties in mice under low-power NIR laser irradiation (2 W/cm^2; Fig. 3.14) [97]. They found how sizes and surface chemistry affect the in vivo behaviors of graphene and remarkably improve the performance of graphene-based in vivo photothermal cancer treatment by using ultrasmall reduced GO (RGO) with non-covalent PEG coating [108]. The PEG-coated RGO showed enhanced NIR absorbance and highly efficient tumor passive targeting leading to excellent behaviors during in vivo treatment efficacy with 100% of tumor elimination. The power density (0.15 W/cm^2, 5 min) was found in an order of magnitude lower than that usually applied for in vivo tumor ablation using many other nanomaterials.

Subsequently, Markovic et al. compared the photothermal anticancer activity of NIR-excited graphene NP and CNTs [115]. They found that suspension of polyvinylpyrrolidone-coated GSs exposed to NIR radiation (808 nm, 2W/cm^2) generated more heat than DNA or sodium dodecylbenzenesulfonate-solubilized SWCNT under the same conditions despite its lower NIR-absorbing capacity. It has also been found that GO exhibits a size-dependent visible and NIR fluorescence, although the mechanism is not yet fully understood [40, 95, 116]. Accordingly, GO can be utilized in biomedical imaging and photothermal therapy and has been considered as potential cancer biomarker sensors and nanoplatforms for cancer-selective DD. Robison et al. established nano-RGO as a novel photothermal agent by attaching a targeting peptide bearing the Arg–Gly–Asp (RGD) motif to PEG-functionalized nano-RGO,

which afforded selective cellular uptake in U87MG cancer cells and highly effective photoablation of cells in vitro [114]. Photothermal therapy is often used with other therapies. Zhang et al. studied the synergistic effect of chemo-photothermal therapy using PEGylated GO loaded with DOX both in vivo and in vitro [117]. Their results showed that the combined DOX and NGO–PEG photothermal treatment resulted in complete destruction of the tumors without weight loss or recurrence of tumors, while DOX chemotherapy alone or NGO–PEG photothermal treatment without DOX did not which is confirmed by another study [118]. Pan et al. used functionalized GS with PNIPAM via click chemistry. The PNIPAM-GS possessed a superior capability of binding CPTs with a high loading ratio of 18.5 wt%, and 16.9% and 19.4% CPT were released after 72 h at 37 °C in water and PBS, respectively [48].

3.5.4 Drug Delivery Applications of Other Carbon Nanomaterials

In addition to graphene and CNTs, other carbon nanomaterials such as fullerene (C60), carbon nanodots, and diamond were also explored for biomaterial applications including DD [119].

Fullerenes and their derivatives were used as DD vehicles, and, in certain circumstances, as nano-drugs by themselves as fullerenes have also shown drug-targeting capability [120, 121] (Chen et al. 2005). Tissue-selective targeting and intracellular targeting of mitochondria have been achieved using fullerene structures [122, 123]. Furthermore, fullerenes have also exhibited antioxidant and antimicrobial behavior. Ashcroft et al. created a new class of anticancer compound that contains both tumor-targeting antibodies and NPs using fullerenes (C60). This delivery system can be loaded with several different anticancer drugs. It is possible to load as many as 40 fullerenes onto a single skin cancer antibody called ZME-108, which can be used to deliver drugs directly into melanomas [124]. PEI-functionalized fullerenes were also conjugated with docetaxel (DTX) to fabricate a DD system. Compared with free DTX, the tumor-targeting DD could efficiently cross cell membranes, lead to more apoptosis, and afford higher antitumor efficacy in a cultured PC3 cells in vitro [125]. Recently, the first in vivo gene delivery experiment with fullerene derivatives was reported (Fig. 3.15). The cationic tetraamino fullerene, with a high water solubility, was used to complex pDNA, and its efficiency and toxicity were compared to Lipofectin [140].

Carbon nanodots (C-dots) can be produced inexpensively on a large scale by many approaches, ranging from simple candle burning to in situ dehydration reactions to laser ablation methods (Krüger et al. 2006). In striking contrast to semiconductor quantum dots, C-dots are superior fluorescent nanomaterials with low toxicity, high chemical stability, and low environmental hazard [126] Sun and coworkers reported the first study on C-dots for their bioimaging capabilities [127] Qu et al. report an example of aptamer C-dot-based sandwich for fluorescent detection of protein which shows high sensitivity and selectivity [128]. The diamond NPs were also modified with amino acid for the synthesis of surface-bound peptides and

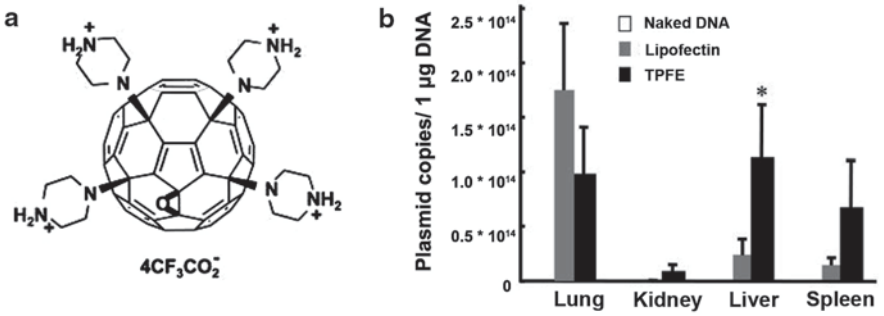

Fig. 3.15 **a** Molecular structure of the tetra(piperazino)fullerene epoxide (TPFE) used for in vivo gene delivery. **b** Distribution of injected plasmid DNA expression in each organ. After a 24-h injection, plasmid DNA was detected at several organs in the TPFE and the Lipofectin group. [140]

the attachment of biologically active building blocks, which potentially could be used in DD and fluorescence marker applications (Krüger et al. 2006).

3.6 Summary and Perspective

The research of CNMs-based drug delivery and photo-thermal therapy has increased dramatically in the last decade. Compared with other nanomaterials, CNMs have many unique properties because of their the remarkable carbon structures. The 1D and 2D CNMs provided large surface area for optimum drug loading, which is critical for increasing the maximum doses of therapeutics. In addition, CNMs can be feasibly modified by chemical functionalization due to their excellent stability under harsh reaction environment. Both covalent and non-covalent surface modification methods have been developed to improve the functions of CNMs such as collodial stability, biocompatibility, cancer targeting and on-demand drug release. Recently, the combination of imaging and drug delivery, which is so-called theranostic, have been achieved on CNMs-based DDs by taking advantage of their unique optical properties. The concept of CNM-based theranostic is expected to bring new opportunities to develop multifunctional DDs by expanding the photonic proprieties of CNMs.

The potential toxicity of CNMs have raised great concern. So far, toxicological studies have clarified the toxic paradigms of CNMs, making it possible to design non-toxic carbon-based nanocarriers for drug delivery. Surface treatment (e.g. PEGlytion and polymer coating) have been a golden rule of designing biocompatible CNM-based DDs without long term toxicity in small rodents. However, toxicity studies in larger animals should be assessed systematically to determine the bio-safety of CNMs. It should be note that the clinical-standard CNMs should be rapid cleared from body after administration , because the accumulation of non-degradable CNMs have been considered unfavourable. Therefore, preparing highly

reproducible CNMs with improved size control should be the focus for achieving future clinical transition.

Acknowledgment JL acknowledges the Natural Science Foundation of China (NSFC) (51173087), National Science Foundation (NSF) of Shandong (ZR2011EMM001), NSF of Qingdao (12-1-4-2-2-jc), and the Taishan Scholar fund from Shandong Province for financial support. DL acknowledges the support for Australian Future Fellowship (FT 110100711) from the Australian Research Council (ARC) and ARC Discovery grant (DP 120101680).

References

1. R. Langer, Drugs on target. Science **293**, 58–59 (2001)
2. P. Van Hoogevest, X. LIU, A. Fahr, Drug delivery strategies for poorly water-soluble drugs: the industrial perspective. Exp. Opin. Drug Deliv. **8**, 1481–1500 (2011)
3. R.M. Mainarades, L.P. Silva, Drug delivery systems: past, present, and future. Curr. Drug Targets. **5**, 449–455 (2004)
4. DA Lavan, T. McGuire, R. Langer, Small-scale systems for in vivo drug delivery. Nat. biotechnol. **21**, 1184–1191 (2003)
5. R. Misra, S. Acharya, S.K. Sahoo, Cancer nanotechnology: application of nanotechnology in cancer therapy. Drug Discov. Today **15**, 842–850 (2010)
6. A. Santos, Aw. Sinn, M. Bariana, M. Kumeria, T. Wang, Y. Losic D., Drug-releasing implants: current progress, challenges and perspectives. J. Mater. Chem. B **2** (37), 6157–6182 (2014)
7. J.L. Perry, C.R. Martin, J.D. Stewart, Drug-delivery strategies by using template-synthesized nanotubes. Chem. Eur. J. **17**, 6296–6302 (2011)
8. R.K. Jain, T. Stylianopoulos, Delivering nanomedicine to solid tumors. Nat. Rev. Clin. Oncol. **7**, 653–664 (2010)
9. Y. Wang, A. Santos, A. Evdokiou, et al., An overview of nanotoxicity and nanomedicine research: principles, progress and implications for cancer therapy. J. Mater. Chem. B, DOI: 10.1039/C5TB00956A (2015)
10. A. Bianco, K. Kostarelos, M. Prato, Application carbon nanotubes for drug delivery. Curr. Opin. Chem. Biol. **9**, 674–679 (2005)
11. K.S. Novoselov, A.K. Geim, S.V. Morozov, et.al. Electric field effect in atomically thin carbon films. Science **306**, 666–669 (2004)
12. A.K. Geim, K.S. Novoselov, The rise of graphene. Nat Mater. **6**, 183–191 (2007)
13. A.K. Geim, Graphene: status and prospects. Science **324**, 1530–1534 (2009)
14. M. Kakran, L. LI, Carbon nanomaterials for drug delivery. Key Eng. Mater. **508**, 76–80 (2012)
15. K.S. Kim, Y. Zhao, H. Jang, et al., Large-scale pattern growth of graphene films for stretchable transparent electrodes. Nature **457**, 706–710 (2009)
16. S. Stankovich, D.A. Dikin, R.D. Piner, R.S. Ruoff, et al., Synthesis of graphene-based nanosheets via chemical reduction of exfoliated graphite oxide. Carbon **45**, 1558–1565 (2007)
17. S. Iijima, Helical microtubules of graphitic carbon. Nature **354**, 56–58 (1991)
18. H. Dai, Carbon nanotubes: synthesis, integration, and properties. Acc. Chem. Res. **35**, 1035–1044 (2002)
19. M. Prato, K. Kostarelos, A. Bianco, Functionalized carbon nanotubes in drug design and discovery. Acc. Chem. Res. **41**, 60–68 (2007)
20. A. Bianco, K. Kostarelos, M. Prato, Opportunities and challenges of carbon-based nanomaterials for cancer therapy. Exp. Opin. Drug Deliv. **5**, 331–342 (2008)

21. M.F.L. De Volder, S.H. Tawfick, R.H. Baughman, A.J. Hart, Carbon nanotubes: present and future commercial applications. Science **339**, 535–539 (2013)
22. L.M. Viculis, J.J. Mack, R.B. Kaner, A chemical route to carbon nanoscrolls. Science **299**, 1361 (2003)
23. Y. Liu, Y. Zhao, B. Sun, C. Chen, Understanding the toxicity of carbon nanotubes. Acc. Chem. Res. **46**, 702–713 (2012b)
24. S.K. Singh, M.K. Singh, P.P. Kulkarni, et.al., Amine-modified graphene. Thrombo-protective safer alternative to graphene oxide for biomedical applications. Acs Nano **6**, 2731–2740 (2012)
25. Y. Wang, Z. Li, J. Wang, J. LI, Y. Lin, Graphene and graphene oxide: biofunctionalization and applications in biotechnology. Trends Biotechnol. **29**, 205–212 (2011)
26. C. Wang, J. Li, C. Amatore, Y. Chen, H. Jiang, X.M. Wang, Gold nanoclusters and graphene nanocomposites for drug delivery and imaging of cancer cells. Angew. Chem. Int. Ed. Engl. **50**, 11644–11648 (2011)
27. L. Feng, L. Wu, X. Qu, New horizons for diagnostics and therapeutic applications of graphene and graphene oxide. Adv. Mater. **25**, 168–86 (2013)
28. Z. Liu, S. Tabakman, K. Welsher, H. Dai, Carbon nanotubes in biology and medicine: in vitro and in vivo detection, imaging and drug delivery. Nano Res. **2**, 85–120 (2009b)
29. Z. Spitalsky, D. Tasis, K. Papagelis, C. Galiotis, Carbon nanotube–polymer composites: chemistry, processing, mechanical and electrical properties. Prog. Polym. Sci. **35**, 357–401 (2010)
30. R.G. Mendes, A. Bachmatiuk, B. Buchner, et al., Carbon nanostructures as multi-functional drug delivery platforms, J. Mater. Chem. B. **1**, 401–428 (2013)
31. Y. Yan, G.K. Such, F. Caruso, et al., Engineering particles for therapeutic delivery: prospects and challenges. ACS Nano. **6**, 3663–3669 (2012)
32. Y. Matsumura, H. Maeda, A new concept for macromolecular therapeutics in cancer chemotherapy: mechanism of tumoritropic accumulation of proteins and the antitumor agent smancs. Cancer Res. **46**, 6387–6392 (1986)
33. L.E. Gerweck, K. Seetharaman, Cellular pH gradient in tumor versus normal tissue: potential exploitation for the treatment of cancer. Cancer Res. **56**, 1194–1198 (1996)
34. S.-R. Ji, C. Liu, B. Zhang, et al., Carbon nanotubes in cancer diagnosis and therapy. Biochim. Biophys. Acta Rev. Cancer **1806**, 29–35 (2012)
35. J. Xie, K. Chen, H.-Y. Lee, C. Xu, et al., Ultrasmall c(RGDyK)-coated Fe3O4 nanoparticles and their specific targeting to integrin αvβ3-rich tumor cells. J. Am. Chem. Soc. **130**, 7542–7543 (2008)
36. Z. Liu, X. Sun, N. Nakayama-Ratchford, H. Dai, Supramolecular chemistry on water-soluble carbon nanotubes for drug loading and delivery. ACS Nano **1**, 50–56 (2007b)
37. A. Hirsch, Functionalization of single-walled carbon nanotubes. Angew. Chem. Int. Ed. Engl. **41**, 1853–1859 (2002)
38. V. Georgakilas, K. Kordatos, M. Prato, et al., Organic functionalization of carbon nanotubes. J. Am. Chem. Soc. **124**, 760–761 (2002a)
39. Z. Liu, J.T. Robinson, X.M. Sun, H.J. Dai, PEGylated nanographene oxide for delivery of water-insoluble cancer drugs. J. Am. Chem. Soc. **130**, 10876–10877 (2008)
40. X.M. Sun, Z. Liu, K. Welsher, J.T. Robinson, A. Goodwin, S. Zaric, H.J. Dai, Nano-graphene oxide for cellular imaging and drug delivery. Nano Res. **1**, 203–212 (2008)
41. G. Gollavelli, Y.C. Ling, Multi-functional graphene as an *in vitro* and *in vivo* imaging probe. Biomaterials **33**, 2532–2545 (2012)
42. Y.J. Lu, H.W. Yang, S.C. Hung, et al., Improving thermal stability and efficacy of BCNU in treating glioma cells using PAA-functionalized graphene oxide. Int. J. Nanomed. **7**, 1737–1747 (2012)
43. C. Shan, H. Yang, D. Han, Q. Zhang, A. Ivaska, L. Niu, Water-soluble graphene covalently functionalized by biocompatible poly-L-lysine. Langmuir **25**, 12030–12033 (2009)
44. N.G. Sahoo, H.Q. Bao, et al., Functionalized carbon nanomaterials as nanocarriers for loading and delivery of a poorly water-soluble anticancer drug: a comparative study. Chem. Commun. **47**, 5235–5237 (2011)

45. L.M. Zhang, Z.X. Lu, Q.H. Zhao, J. Huang, H. Shen, Z.J. Zhang, Enhanced chemotherapy efficacy by sequential delivery of siRNA and anticancer drugs using PEI-grafted graphene oxide. Small **7**, 460–464 (2011a)
46. B.A. Chen, M. Liu, L.M. Zhang, J. Huang, J.L. Yao, Z.J. Zhang, Polyethylenimine-functionalized graphene oxide as an efficient gene delivery vector. J. Mater. Chem. **21**, 7736–7741 (2011)
47. Y. Liu, D.-C. Wu, W.-D. Zhang, et al., Polyethylenimine-grafted multiwalled carbon nanotubes for secure noncovalent immobilization and efficient delivery of DNA. Angew. Chem. **117**, 4860–4863 (2005)
48. Y.Z. Pan, H.Q. Bao, N.G. Sahoo, T.F. Wu, L. Li, Water-soluble poly (N-isopropylacrylamide)-graphene sheets synthesized via click chemistry for drug delivery. Adv. Funct. Mater. **21**, 2754–2763 (2011)
49. J. Gao, F. Bao, L.L. Feng, K.Y. Shen, et al., Functionalized graphene oxide modified polysebacic anhydride as drug carrier for levofloxacin controlled release. Rsc. Adv. **1**, 1737–1744 (2011)
50. V.K. Rana, M.C. Choi, J.Y. Kong, et al., Synthesis and drug-delivery behavior of chitosan-functionalized graphene oxide hybrid nanosheets. Macromol. Mater. Eng. **296**, 131–140 (2011)
51. H.Q. Bao, Y.Z. Pan, Y. Ping, N.G. Sahoo, T.F. Wu, L. Li, J. Li, L.H. Gan, Chitosan-functionalized graphene oxide as a nanocarrier for drug and gene delivery. Small **7**, 1569–1578 (2011)
52. D. Depan, J. Shah, R.D.K. Misra, Controlled release of drug from folate-decorated and graphene mediated drug delivery system: synthesis, loading efficiency, and drug release response. Mater. Sci. Eng. C-Mater. Biol. Appl. **31**, 1305–1312 (2011)
53. K.P. Liu, J.J. Zhang, F.F. Cheng, T.T. Zheng, C.M. Wang, J.J. Zhu, Green and facile synthesis of highly biocompatible graphene nanosheets and its application for cellular imaging and drug delivery. J. Mater. Chem. **21**, 12034–12040 (2011)
54. L.M. Zhang, J.G. Xia, Q.H. Zhao, L.W. Liu, Z.J. Zhang, Functional graphene oxide as a nanocarrier for controlled loading and targeted delivery of mixed anticancer drugs. Small **6**, 537–544 (2010)
55. X.Y. Yang, Y.S. Wang, X. Huang, et al., Multi-functionalized graphene oxide based anticancer drug-carrier with dual-targeting function and pH-sensitivity. J. Mater. Chem. **21**, 3448–3454 (2010b)
56. J. Liu, L. Tao, W. Yang, D. Li, et al., Synthesis, characterization, and multilayer assembly of pH sensitive graphene-polymer nanocomposites. Langmuir **26**, 10068–10075 (2010a)
57. J. Liu, W. Yang, L. Tao, D. Li, C. Boyer, T.P. Davis, Thermosensitive graphene nanocomposites formed using pyrene-terminal polymers made by RAFT polymerization. J. Polym. Sci. A. Polym. Chem. **48**, 425–433 (2010b)
58. J. Shen, M. Shi, N. Li, B. Yan, et al., Facile synthesis and application of Ag-chemically converted graphene nanocomposite. Nano. Res. **3**, 339–349 (2010)
59. M.C. Duch, G.R.S. Budinger, Y.T. Liang, et al., Minimizing oxidation and stable nanoscale dispersion improves the biocompatibility of graphene in the lung. Nano Lett. **11**, 5201–5207 (2011)
60. L. Feng, S. Zhang, Z. Liu, Graphene based gene transfection. Nanoscale **3**, 1252–1257 (2011)
61. W. Hu, C. Peng, M. Lv, X. Li, et al., Protein corona-mediated mitigation of cytotoxicity of graphene oxide. Acs. Nano. **5**, 3693–3700 (2011)
62. X.T. Zheng, C.M. Li, Restoring basal planes of graphene oxides for highly efficient loading and delivery of beta-lapachone. Mol. Pharmac. **9**, 615–621 (2012)
63. X. Huang, X. Qi, F. Boey, H. Zhang, Graphene-based composites. Chem. Soc. Rev. **41**, 666–686 (2012)
64. W. Chen, P. Yi, Y. Zhang, L. Zhang, Z. Deng, Z. Zhang, Composites of aminodextran-coated Fe3O4 nanoparticles and graphene oxide for cellular magnetic resonance imaging. ACS. Appl. Mater. Interf. **3**, 4085–4091 (2011)

65. X.Y. Yang, X.Y. Zhang, Y.F. Ma, Y. Huang, Y.S. Wang, Y. S. Chen, Superparamagnetic graphene oxide-Fe3O4 nanoparticles hybrid for controlled targeted drug carriers. J. Mater. Chem. **19**, 2710–2714 (2009)
66. J. Liu, A.G. Rinzler, H. Dai, R.E. Smalley, et al., Fullerene pipes. Science **280**, 1253–1256 (1998)
67. A.B. Bourlinos, D. Gournis, D. Petridis, T. Szabó, A. Szeri, I. Dékány, Graphite oxide: chemical reduction to graphite and surface modification with primary aliphatic amines and amino acids. Langmuir **19**, 6050–6055 (2003)
68. G. Wang, B. Wang, J. Park, J. Yang, X. Shen, J. Yao, Synthesis of enhanced hydrophilic and hydrophobic graphene oxide nanosheets by a solvothermal method. Carbon **47**, 68–72 (2009)
69. G. Wei, M. Yan, R. Dong, D. Wang, X. Zhou, J. Chen, J. Hao, Covalent modification of reduced graphene oxide by means of diazonium chemistry and use as a drug-delivery system. Chem. Eur. J. **18**, 14708–16 (2012)
70. E. Bekyarova, M.E. Itkis, R.C. Haddon, et al., Chemical modification of epitaxial graphene: spontaneous grafting of Aryl Groups. J. Am. Chem. Soc. **131**, 1336–1337 (2009)
71. V. Georgakilas, N. Tagmatarchis, D. Pantarotto, A. Bianco, J.-P. Briand, M. Prato, Amino acid functionalisation of water soluble carbon nanotubes. Chem. Commun. **24**, 3050–3051 (2002b)
72. K. Kostarelos, L. Lacerda, G. Pastorin, W. Wu, et al., Cellular uptake of functionalized carbon nanotubes is independent of functional group and cell type. Nat. Nano. **2**, 108–113 (2007)
73. K. Kostarelos, A. Bianco, M. Prato, Promises, facts and challenges for carbon nanotubes in imaging and therapeutics. Nat. Nano. **4**, 627–633 (2009)
74. D. Pantarotto, C.D. Partidos, A. Bianco, et al., Synthesis, structural characterization, and immunological properties of carbon nanotubes functionalized with peptides. J. Am. Chem. Soc. **125**, 6160–6164 (2003)
75. Z. Liu, W. Cai, L. He, N. Nakayama, K. Chen, X. Sun, X. Chen, H. Dai, In vivo biodistribution and highly efficient tumour targeting of carbon nanotubes in mice. Nat. Nano. **2**, 47–52 (2007a)
76. Z. Liu, S.M. Tabakman, Z. Chen, H. Dai, Preparation of carbon nanotube bioconjugates for biomedical applications. Nat. Proto. **4**, 1372–1381 (2009c)
77. S. Stankovich, R.D. Piner, X. Chen, N. Wu, S.T. Nguyen, R.S. Ruoff, Stable aqueous dispersions of graphitic nanoplatelets via the reduction of exfoliated graphite oxide in the presence of poly (sodium 4-styrenesulfonate). J. Mater. Chem. **16**, 155–158 (2006)
78. N.W.S. Kam, M. O'Connell, J.A. Wisdom, H. Dai, Carbon nanotubes as multifunctional biological transporters and near-infrared agents for selective cancer cell destruction. Proc. Natl. Acad. Sci. U. S. A. **102**, 11600–11605 (2005)
79. A.A. Shvedova, E.R. Kisin, R. Mercer, et al., Unusual inflammatory and fibrogenic pulmonary responses to single-walled carbon nanotubes in mice. Am. J. Physiol Lung. Cell. Mol. Physiol. **289**, L698–L708 (2005)
80. K. Kostarelos, The long and short of carbon nanotube toxicity. Nat. Biotech. **26**, 774–776 (2008)
81. N.M. Rodriguez, A review of catalytically grown carbon nanofibers. J. Mater. Res. **8**, 3233–3250 (1993)
82. C. Bussy, M. Pinault, J. Cambedouzou, et al., Critical role of surface chemical modifications induced by length shortening on multi-walled carbon nanotubes-induced toxicity. Part. Fibre Toxicol. **9**, 1–15 (2012)
83. A.A. Shvedova, V. Castranova, E.R. Kisin, et al., Exposure to carbon nanotube material: assessment of nanotube cytotoxicity using human keratinocyte cells. J. Toxicol. Environ. Health-Part A. **66**, 1909–1926 (2003)
84. N.W. Shi Kam, T.C. Jessop, P.A. Wender, H. Dai, Nanotube molecular transporters: internalization of carbon nanotube–protein conjugates into mammalian cells. J. Am. Chem. Soc. **126**, 6850–6851 (2004)
85. X. Zhang, L. Meng, Q. Lu, Z. Fei, P.J. Dyson, Targeted delivery and controlled release of doxorubicin to cancer cells using modified single wall carbon nanotubes. Biomaterials. **30**, 6041–6047 (2009)

86. N.W.S. Kam, H. Dai, Carbon nanotubes as intracellular protein transporters: generality and biological functionality. J. Am. Chem. Soc. **127**, 6021–6026 (2005)
87. N.W.S. Kam, Z. Liu, H. Dai, Carbon nanotubes as intracellular transporters for proteins and DNA: an investigation of the uptake mechanism and pathway. Angew. Chem. Int. Ed. Engl. **45**, 577–581 (2006)
88. V.C. Sanchez, A. Jachak, R.H. Hurt, A.B. Kane, Biological interactions of graphene-family nanomaterials: an interdisciplinary review. Chem. Res. Toxicol. **25**, 15–34 (2011)
89. Y.L. Chang, S.T. Yang, J.H. Liu, et al., In vitro toxicity evaluation of graphene oxide on A549 cells. Toxicol. Lett. **200**, 201–210 (2011)
90. S.R. Ryoo, Y.K. Kim, M.H. Kim, D.H. Min, Behaviors of NIH-3T3 fibroblasts on graphene/carbon nanotubes: proliferation, focal adhesion, and gene transfection studies. Acs. Nano. **4**, 6587–6598 (2010)
91. X.Y. Li, X.L. Huang, D.P. Liu, et al., Synthesis of 3D hierarchical Fe3O4/graphene composites with high lithium storage capacity and for controlled drug delivery. J. Phys. Chem. C. **115**, 21567–21573 (2011)
92. H.W. Liu, S.H. Hu, Y.W. Chen, S.Y. Chen, Characterization and drug release behavior of highly responsive chip-like electrically modulated reduced graphene oxide-poly (vinyl alcohol) membranes. J. Mater. Chem. **22**, 17311–17320 (2012a)
93. S.K. Misra, P. Kondaiah, S. Bhattacharya, C.N.R. Rao, Graphene as a nanocarrier for Tamoxifen induces apoptosis in transformed cancer cell lines of different origins. Small. **8**, 131–143 (2012)
94. K.-H. Liao, Y.-S. Lin, C.W. Macosko, C.L. Haynes, Cytotoxicity of graphene oxide and graphene in human erythrocytes and skin fibroblasts. ACS. Appl. Mater. Interfaces, **3**, 2607–2615 (2011)
95. S.A. Zhang, K. Yang, L.Z. Feng, Z. Liu, In vitro and in vivo behaviors of dextran functionalized graphene. Carbon. **49**, 4040–4049 (2011b)
96. H. Ali-Boucetta, K.T. Al-Jamal, D. McCarthy, M. Prato, A. Bianco, K. Kostarelos, Multiwalled carbon nanotube-doxorubicin supramolecular complexes for cancer therapeutics. Chem. Commun. **4**, 459–461 (2008)
97. Z. Liu, A.C. Fan, K. Rakhra, H. Dai, et al., Supramolecular stacking of doxorubicin on carbon nanotubes for in vivo cancer therapy. Angew. Chem. Int. Ed. Engl. **48**, 7668–7672 (2009a)
98. H. Huang, Q. Yuan, J.S. Shah, R.D.K. Misra, A new family of folate-decorated and carbon nanotube-mediated drug delivery system: synthesis and drug delivery response. Adv. Drug Deliv. Rev. **63**, 1332–1339 (2011a)
99. G. Pastorin, W. Wu, S. Wieckowski, J.-P. Briand, K. Kostarelos, M. Prato, A. Bianco, Double functionalisation of carbon nanotubes for multimodal drug delivery. Chem. Commun. **11**, 1182–1184 (2006)
100. W. Wu, R. Li, X. Bian, Z. Zhu, D. Ding, X. Li, Z. Jia, X. Jiang, Y. Hu, Covalently combining carbon nanotubes with anticancer agent: preparation and antitumor activity. ACS. Nano. **3**, 2740–2750 (2009)
101. A.A. Bhirde, V. Patel, J. Gavard, et al., Targeted killing of cancer cells in vivo and in vitro with EGF-directed carbon nanotube-based drug delivery. ACS. Nano. **3**, 307–116 (2009)
102. R. Li, R.A. Wu, L. Zhao, M. Wu, L. Yang, H. Zou, P-Glycoprotein antibody functionalized carbon nanotube overcomes the multidrug resistance of human leukemia cells. ACS. Nano. **4**, 1399–1408 (2010)
103. X.Y. Yang, X.Y. Zhang, Z.F. Liu, Y.F. Ma, Y. Huang, Y. Chen, High-efficiency loading and controlled release of doxorubicin hydrochloride on graphene oxide. J. Phys. Chem. C. **112**, 17554–17558 (2008b)
104. S. Pei, H.-M. Cheng, The reduction of graphene oxide. Carbon. **50**, 3210–3228 (2012)
105. H.Q. Hu, J.H. Yu, Y.Y. Li, J. Zhao, H.Q. Dong, Engineering of a novel pluronic F127/graphene nanohybrid for pH responsive drug delivery. J. Biomed. Mater. Res. Part. A. **100A**, 141–148 (2012)
106. P. Huang, C. Xu, J. Lin, C. Wang, et al., Folic acid-conjugated graphene oxide loaded with photosensitizers for targeting photodynamic therapy. Theranostics. **1**, 240–250 (2011b)

107. Y. Pan, N.G. Sahoo, L. Li, The application of graphene oxide in drug delivery. Exp. Opin. Drug Deliv. **9**(11), 1365–1376 (2012)
108. K. Yang, J.M. Wan, S. Zhang, et al., The influence of surface chemistry and size of nanoscale graphene oxide on photothermal therapy of cancer using ultra-low laser power. Biomaterials. **33**, 2206–2214 (2012)
109. M.J. O'Connell, S.M. Bachilo, et al., Band gap fluorescence from individual single-walled carbon nanotubes. Science. **297**, 593–596 (2002)
110. P. Chakravarty, R. Marches, N.S. Zimmerman, et al., Thermal ablation of tumor cells with antibody-functionalized single-walled carbon nanotubes. Proc. Natl. Acad. Sci. U. S. A. **105**, 8697–8702 (2008)
111. S.V. Torti, F. Byrne, O. Whelan, P.M. Ajayan, et al., Thermal ablation therapeutics based on CNx multi-walled nanotubes. Int. J. Nanomed. **2**, 707 (2007)
112. A. Burke, X. Ding, R. Singh, et al., Long-term survival following a single treatment of kidney tumors with multiwalled carbon nanotubes and near-infrared radiation. Proc. Natl. Acad. Sci. U. S. A. **106**, 12897–12902 (2009)
113. K. Yang, S.A. Zhang, G.X. Zhang, X.M. Sun, S.T. Lee, Z.A. Liu, Graphene in mice: ultrahigh in vivo tumor uptake and efficient photothermal therapy. Nano. Lett. **10**, 3318–3323 (2010a)
114. J.T. Robinson, S.M. Tabakman, Y. Liang, et al., Ultrasmall reduced graphene oxide with high near-infrared absorbance for photothermal therapy. J. Am. Chem. Soc. **133**, 6825–6831 (2011)
115. Z.M. Markovic, L.M. Harhaji-Trajkovic, et al., In vitro comparison of the photothermal anticancer activity of graphene nanoparticles and carbon nanotubes. Biomaterials. **32**, 1121–1129 (2011)
116. K.P. Loh, Q. Bao, G. Eda, M. Chhowalla, Graphene oxide as a chemically tunable platform for optical applications. Nat. Chem. **2**, 1015–1024 (2010)
117. W. Zhang, Z.Y. Guo, D.Q. Huang, et al., Synergistic effect of chemo-photothermal therapy using PEGylated graphene oxide. Biomaterials. **32**, 8555–8561 (2011c)
118. B. Tian, C. Wang, S. Zhang, L.Z. Feng, Z. Liu, Photothermally enhanced photodynamic therapy delivered by nano-graphene oxide. ACS. Nano. **5**, 7000–7009 (2011)
119. A. Montellano, T. Da Ros, A. Bianco, M. Prato, Fullerene C60 as a multifunctional system for drug and gene delivery. Nanoscale. **3**, 4035–4041 (2011)
120. X.-J. Liang, H. Meng, Y. Wang, et al., Metallofullerene nanoparticles circumvent tumor resistance to cisplatin by reactivating endocytosis. Proc. Natl. Acad. Sci. U. S. A. **107**, 7449–7454 (2010)
121. T.Y. Zakharian, A. Seryshev, B. Sitharaman, et al., A fullerene-paclitaxel chemotherapeutic: synthesis, characterization, and study of biological activity in tissue culture. J. Am. Chem. Soc. **127**, 12508–12509 (2005)
122. K.A. Gonzalez, L.J. Wilson, W. Wu, G.H. Nancollas, Synthesis and In vitro characterization of a tissue-Selective fullerene: vectoring $C_{60(OH)16}$ AMBP to mineralized bone. Bioorg. Med. Chem. **10**, 1991–1997 (2002)
123. S. Foley, C. Crowley, M. Smaihi, et al., Cellular localisation of a water-soluble fullerene derivative. Biochem. Biophys. Res. Commun. **294**, 116–119 (2002)
124. J. Ashcroft, D. Tsyboulski, Fullerene (C60) immunoconjugates: interaction of water-soluble C60 derivatives with the murine anti-gp240 melanoma antibody. Chem. Commun. **28,** 3004–3006 (2006)
125. J. Shi, H. Zhang, L. Wang, L. Li, et al., PEI-derivatized fullerene drug delivery using folate as a homing device targeting to tumor. Biomaterials. **34**(1), 251–261 (2013)
126. S. Ray, A. Saha, N.R. Jana, R. Sarkar, Fluorescent carbon nanoparticles: synthesis, characterization, and bioimaging application. J. Phys. Chem. C. **113**, 18546–18551 (2009)
127. L. Cao, X. Wang, M.J. Meziani, F. LU, et al., Carbon dots for multiphoton bioimaging. Angew. Chem. Int. Ed. Engl. **129**, 11318–11319 (2007)
128. S.N. Baker, G.A. Baker, Luminescent carbon nanodots: emergent nanolights. Angew. Chem. Int. Ed. Engl. **49**, 6726–6744 (2012)

129. W. Choi, I. Lahiri, R. Seelaboyina, Y.S. Kang, Synthesis of graphene and its applications. Crit. Rev. Solid State Mater. Sci. **35**, 52–71 (2010)
130. C.H. Lu, H.H. Yang, C.L. Zhu, X. Chen, G.N. Chen, A graphene platform for sensing biomolecules. Angew. Chem. **121**, 4879–4881 (2009)
131. C.H. Lu, C.L. Zhu, J. Li, J.J. Liu, X. Chen, H.H. Yang, Using graphene to protect DNA from cleavage during cellular delivery. Chem. Commun. **46**, 3116–3118 (2010)
132. S.-T. Yang, X. Wang, G. Jia, Y. Gu, et al., Long-term accumulation and low toxicity of single-walled carbon nanotubes in intravenously exposed mice. Toxicol. Lett. **181**, 182–189 (2008a)
133. M. Zheng, A. Jagota, E.D. Semke, et al., Nat. Mater. **2**, 338–342 (2003)
134. J. Liu, L. Cui, D. Losic, Graphene and graphene oxide as new nanocarriers for drug delivery applications. Acta Biomater. **9**(12), 9243–9257 (2013)
135. W. Liang, J. K. W. Lam, Endosomal escape pathways for non-viral nucleic acid delivery systems. INTECH Open Access Publisher, 421–467 (2012)
136. D. B. Mawhinney, V. Naumenko, V. Kuznetsova, et al., Infrared spectral evidence for the etching of carbon nanotubes: ozone oxidation at 298 K. J. Am. Chem. Soc. **122**(10), 2383–2384 (2000)
137. M. Zheng, A. Jagota, E. D. Semke, et al., DNA-assisted dispersion and separation of carbon nanotubes. Nat Mater **2**(5), 338–342 (2003)
138. R. J. Chen, Y. Zhang, D. Wang, et al., Noncovalent sidewall functionalization of single-walled carbon nanotubes for protein immobilization. J. Am. Chem. Soc. **123**(16), 3838–3839 (2001)
139. A. Schinwald, K. Donaldson, Use of back-scatter electron signals to visualise cell/nanowires interactions in vitro and in vivo; frustrated phagocytosis of long fibres in macrophages and compartmentalisation in mesothelial cells in vivo. Part. Fibre Toxicol. **9**, (2012)
140. R. Maeda-Mamiya, E. Noiri, H. Isobe, W. Nakanishi, K. Okamoto, K. Doi, T. Sugaya, T. Izumi, T. Homma, E. Nakamura, In vivo gene delivery by cationic tetraamino fullerene. Proc. Natl. Acad. Sci. **107**, 5339–5344 (2010)

Chapter 4
Carbon Nanotubes with Special Architectures for Biomedical Applications

Jun Li, Foram Ranjeet Madiyar and LuxiZhang Swisher

4.1 Introduction

In this chapter, we focus on the special architectures of carbon nanotubes (CNTs) for biomedical applications including biosensors, gene delivery, cell/tissue culture, and neural stimulation/recording. Besides the unique long fiber-like structure with ultrasmall diameter and high-aspect ratio, the biomedical applications also rely on the physical properties of CNTs, including high electrical conductivity, chirality-dependent electronic structure, characteristic optical properties, and high mechanical strength. The optimum performance depends on both the intrinsic CNT microstructures and the architectures into which the CNTs are organized. We illustrate the potential of these applications with an emphasis on the utilization of various CNT architectures based on their electrical properties.

4.1.1 Various CNT Structures and Properties

CNTs consist of a family of tube-like fiber materials made of atomic layers of sp^2-bonded carbon atoms [1, 2]. As shown in Fig. 4.1, a single-walled CNT (SWNT) can be viewed as a single graphene layer rolling into a seamless tube, while a multiwalled CNT (MWNT) consists of multiple SWNTs packed in a tight concentric structure. All carbon atoms in CNTs share the similar physicochemical properties as those in graphene, that is, presenting in sp^2 form in an atomic layer with a hexagonal lattice, except a small number of sp^3 atoms at the edges or defects. Each atomic layer is a large conjugate system with delocalized π-electrons shared among the carbon

J. Li (✉) · F. R. Madiyar · L. Z. Swisher
Department of Chemistry, Kansas State University, Manhattan, KS 66506, USA
e-mail: junli@ksu.edu

F. R. Madiyar
Embry–Riddle Aeronautical University, Daytona Beach, FL 32114, USA

M. Zhang et al. (eds.), *Carbon Nanomaterials for Biomedical Applications,*
Springer Series in Biomaterials Science and Engineering 5,
DOI 10.1007/978-3-319-22861-7_4

atoms. The unique graphitic structure of the sp^2 atomic layers determines a strong interaction between atoms in the layer but little interaction between adjacent layers, leading to drastically different properties in and out of the graphitic plane. This is reflected in the highly anisotropic properties of macroscopic graphite, which can be viewed as a stack of atomic graphitic sheets. The electrical, thermal, mechanical, and electrochemical properties of graphite vary by orders of magnitude between in-plane and cross-plane measurements [3, 4]. The properties of all traditional carbon materials can be correlated with the variation in dimension and organization of the anisotropic graphitic domains in their internal structures [3, 4]. Such highly anisotropic properties also apply to CNTs. Many reported extraordinary electrical, thermal, and mechanical properties are the ideal properties along the axial direction inside a single CNT. Those obtained from macroscopic CNT ensembles are significantly inferior and vary in a wide range. Thus, it is critical to organize CNTs into proper configurations or architectures to achieve the optimum performance.

The internal graphitic microstructure of CNTs is equally important in determining their physical properties. A good example is carbon nanofibers (CNFs), a special type of CNT that consists of conically stacked graphene (or graphitic) cups [5] (as shown in Fig. 4.1d). This type of structure commonly presents in vertically aligned CNFs (VACNFs) grown on the surface of solid substrates by plasma-enhanced chemical vapor deposition (PECVD) [6–9] or powders of bulk-produced materials by catalytic chemical vapor deposition (CVD) using floating reactors [5]. A large body of literature simply called the conically stacked CNFs as MWNTs or bamboo-like MWNTs [6, 7], but later studies discovered that the unique structure of CNFs made them fundamentally different from normal MWNTs in many applications [9–15], as discussed in later sections.

All CNTs have high-aspect-ratio fiber-like structures. SWNTs present the smallest diameter (0.8–5 nm) and a variable length from tens of nanometers to millimeters, while MWNTs have a larger diameter (~3 to >100 nm) and similar lengths.

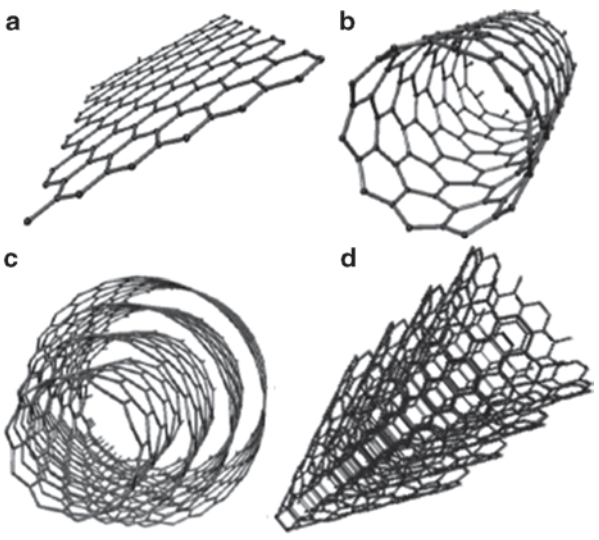

Fig. 4.1 The atomistic structure of **a** a layer of graphene, **b** a single-walled carbon nanotube, **c** a multiwalled carbon nanotube, and **d** a carbon nanofiber grown by DC-biased plasma-enhanced chemical vapor deposition showing the stacking of conical graphitic structures along the fiber axis

CNFs typically have an outer diameter of ~10 to ~300 nm, a length up to ~200 μm, and a characteristic mostly hollow core taking ~ one third to two third of the CNF's diameter. Fully dispersed short SWNTs have all atoms exposed at the surface, giving a specific surface area (SSA) up to 1600 m^2/g [16]. But the SSA of SWNT bundles, MWNTs, and CNFs is much lower. The sidewall of SWNTs and MWNTs is hydrophobic and chemically inert similar to graphite basal plane. Chemical functionalization relies on weak interactions such as surfactant encapsulation and π-π stacking of conjugate molecules. Strongly oxidized CNTs may present defects at the sidewall for covalent functionalization, but it tends to degrade other properties. In contrast, the sidewall of the hollow CNF consists of abundant broken graphitic edges, yielding a much more active surface for chemical functionalization [14] and interfacing with other electrochemically active materials [15, 17–19].

The electronic properties of an isolated defect-free SWNT depend on its helicity (or chirality). Statistically about two third of SWNTs are semiconducting (referred to as s-SWNTs) and one third of them are metallic (referred to as m-SWNTs) [20, 21]. The bandgap of an s-SWNT is inversely proportional to its diameter yielding optical absorption in visible to near infrared (IR) ranges [22]. Each individual tube in a small-diameter MWNT behaves similar to an SWNT, with little interaction between adjacent shells [23]. But MWNTs larger than 10 nm in diameter are essentially metallic conductors at room temperature. So are CNFs. The strong sp^2 bonding between the carbon atoms in CNTs yields remarkable mechanical strength represented by a large Young's modulus of ~1 TPa and a tensile strength of ~150 GPa [24–26], comparable to the in-plane properties of graphene. The strong C-C bond makes CNT one of the most resilient materials [27].The experimentally measured Young's modulus value of CNFs varied from 5–60 GPa [28] to 0.9–1.2 TPa [29]. As is discussed later, the strong mechanical properties are critical in maintaining the integrity of the architectures in complex wet biological environments.

4.1.2 General Architectures

Figure 4.2 summarizes four types of CNT architectures based on different mechanisms using specific properties of CNTs. In Fig. 4.2, a single s-SWNT, multiple parallel s-SWNTs, or a controlled SWNT network are used as the conduction channel in a field-effect transistor whose conductivity is modulated by the change in the surface charge density induced by biomolecular binding or biochemical reactions. These biosensors require extensive efforts to eliminate the metallic conduction pathway which may cause a short circuit between the source and drain electrodes. Alternatively, a resistive biosensor based on a randomly stacked CNT film between two electrodes may be used to measure the adsorption of biomolecules or accumulation of bioreaction products. While the fabrication is much easier, the sensitivity significantly decreased. A film of randomly stacked CNTs (including CNFs) may be deposited on an inert electrode and used as a porous electrode for electrochemical detection of biomolecules. In general, electron transport through the randomly stacked CNT films involves hopping between individual CNTs and is significantly

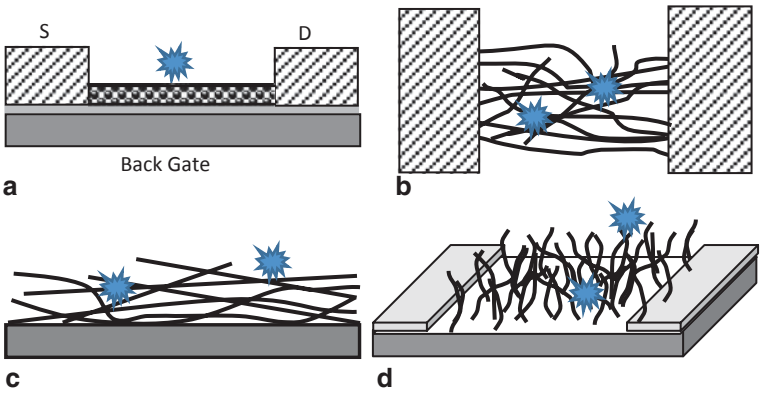

Fig. 4.2 Four representative CNT architectures in biomedical applications **a** a field-effect transistor biosensor based on a single s-SWNT, multiple parallel s-SWNT, or a controlled SWNT network as the conduction channel, **b** a resistive biosensor based on a randomly stacked CNT film between two electrodes, **c** an electrode based on a randomly stacked CNT or CNF film, and **d** an electrode based on vertically aligned CNTs or CNFs

slowed down due to the high contact resistance. To achieve better performance, vertically aligned CNTs, and particularly CNFs, have been grown from the conductive surface, in which all CNTs or CNFs are directly connected to the substrate, yielding much better electrical contact. Furthermore, the vertical structure can be fabricated into various micro-/nanopatterns with lithography [30, 31] and further encapsulated or modified with other processes [31–36]. We focus on illustrating various studies on vertically aligned architectures, particularly those based on the unique conical structure of CNFs.

4.2 Forest-Like Vertically Aligned Carbon Nanotubes

The as-prepared vertically aligned CNTs can serve as a forest-like 3D matrix with high surface area and nanostructured topography. With proper functionalization, they can be used as the electrical transducer in biosensors to wire active biomolecules with the macroscopic electrodes or as biocompatible electrodes for the development of implantable neural-electrical interfaces.

4.2.1 Electrochemical Biosensors

The common commercial SWNTs have the diameter of only ~2 nm and the length over tens of microns. To increase the solubility and make them more uniformly dispersed in solution in the form of isolated SWNTs, the long SWNTs are normally shortened to a length of tens to hundreds of nanometers by extensive acid oxidation.

Such shortened SWNTs still possess a relatively high aspect ratio. More importantly, the ends are open and dominated by –COOH groups which can be used for selectively attaching biomolecules through covalent bonds, while the sidewall remains rather inert to reduce electron backflow to solutions. These properties have inspired the study using them as conductive wires to make electrical connection between the electrode and the active center of redox proteins, particularly glycoproteins such as glucose oxidase whose active center is embedded deep inside the protein and difficult to reach by conventional electrodes [37–39]. One end of the SWNTs was attached through an amide bond to a gold electrode covered with a self-assembled monolayer containing cysteamine. The distal end of the SWNTs was functionalized with the flavin adenine dinucleotide (FAD) cofactor, also through an amide bond. After reconstitution of the apo-flavoenzyme glucose oxidase (GOx) with FAD, the SWNT was able to plug into the enzyme's redox center and effectively wire it to the electrode surface [38, 39]. About sixfold higher electron turnover rate from the GOx ($\sim$4100 s^{-1}) was obtained compared to its natural O_2 reaction acceptor (700 s^{-1}) [39]. The enhanced turnover rate was found to clearly depend on the SWNT length which can extend to 150 nm [39].

Though the above study provided useful insights into the fundamental properties of redox enzymes for bioelectronics, it cannot exclusively conclude that the SWNTs are present in truly vertically aligned forest-like structures. Stacked SWNT clusters may produce similar results. Ideally, vertically aligned SWNT arrays directly grown on the electrode surface may serve as a more convincing model to validate these studies. Liming Dai et al. demonstrated that vertically aligned CNTs can be fabricated on Au electrode surface and functionalized with single-stranded DNA chains [40]. The hybridization of ferrocene (Fc)-attached target DNA with the complementary sequence was electrochemically detected at high sensitivity (down to $\sim$10 ng/mL concentration) [40]. However, the plasma treatment activated both the end and the sidewall of CNTs, which generated a large background current and may have limited the detection limit. Due to the high aspect ratio, CNTs likely collapsed into microbundles due to the capillary force exerted by the solution during drying process after they were taken out from the solution. The nature of the CNTs (SWNTs or MWNTs) and the details of the vertical architecture at each step remain to be examined.

4.2.2 Neural-Electrical Interface

In recent years, electrical stimulation of neural tissues with implantable devices has been proved as an effective approach to restoring impaired neural functions and treating neurodegenerative diseases. A reliable neural–electrical interface (NEI) is critical for such devices. Current neuroprosthetic implants are typically constructed from metal electrodes that are at least tens of microns in diameter. The impedance of the NEI between the flat electrode surface and the surrounding tissue is rather high, thus requiring a large voltage amplitude to generate sufficient stimulation current. Consequently, it causes direct electrical damage to the neural tissue or triggers

water electrolysis to produce H^+ and OH^- ions which are toxic to cells. The rigid mechanical property and flat surface of metal electrodes are also incompatible with soft 3D tissues and thus limit the stability of the NEI [41]. Vertically aligned CNTs have attracted extensive attention as a biocompatible cell/tissue scaffold due to the 3D topography and highly permeable porous structure [42]. Particularly, the VACNFs grown by PECVD process on conductive substrates have demonstrated many advantages over seamless CNTs in NEI applications [33, 34, 43].

As shown in Fig. 4.3, VACNFs consist of freestanding CNFs of high aspect ratio (with a diameter of 50–200 nm and length of 3–10 μm for NEI applications) [33, 34, 43]. They are directly grown on the surface of a conductive substrate with a random lateral arrangement and can be fabricated into specific micro-/nanopatterns using lithography [31, 43]. Compared to the similar structure of vertically aligned CNTs (mostly MWNTs), VACNFs are fully separated from the neighbors with an average spacing of ~300–400 nm, forming a brush-like structure. The average diameter of CNFs is larger than normal CNTs, making them more conductive and mechanically more robust. The internal CNF structure consists of a stack of conical graphitic cups leaving abundant graphitic edges at the sidewall to form a good electrochemical interface and serve as active sites for covalent functionalization [9–15]. Each CNF in the VACNF array behaves as a soft lever, which can be elastically bent by a small lateral force when in contact with cells or tissue.

VACNFs have attracted interest as a promising material for neuroprosthetic devices due to following inherent properties [41, 42, 44, 45]: (1) the 3D topography

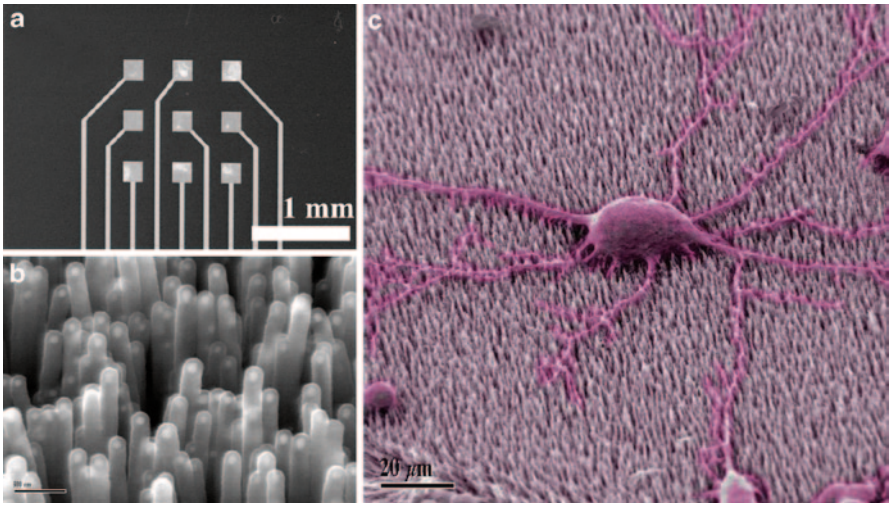

Fig. 4.3 VACNFs for 3D nanostructured neural–electrical interface. **a** A 3 × 3 microelectrode array patterned with UV lithography. **b** VACNFs grown on each microelectrode pad and then encapsulated with a thin layer of polypyrrole by electrodeposition. ([33]. With permission). **c** Neuron-like PC12 cells grown on the polypyrrole-coated VACNFs which is further coated with an ultrathin collagen IV for cell adhesion. Long neurites are formed after adding nerve growth factor in the culture media. The scale bars are 1 mm, 500 nm, and 20 μm, respectively. *PC* pheochromocytoma cell

that is compatible with the complex extracellular environment in a natural tissue, (2) reduced electrode impedance by the high surface area of nanostructure, and (3) soft mechanical contact with neural cells by the elasticity of freestanding CNFs. To improve the biocompatibility and ability for neural stimulation and recording, VACNFs have been further coated with polypyrrole (PPy), an electrically conductive polymer (ECP). As shown in Fig. 4.3b, the polymer sheath effectively reduces the VACNF from collapsing into microbundles due to the capillary force as the electrode is taken in and out of solutions and thus maintains their original vertical alignment [33]. This is essential in reducing the mechanical stress on neural cells at the local contact points. In addition, PPy is a redox-active material which enhances the capacitance of the electrodes by two orders of magnitude [33] and thus can provide the desired stimulation current without electrolyzing water. After modifying the outer PPy surface with an ultrathin collagen coating, neuron-like PC12 cells were found to effectively adhere to the surface and proliferate to form a monolayer [34]. With the stimulation of nerve growth factor, the cells produce long neurites extending over 100 μm on the surface (Fig. 4.3c) [34]. It is highly possible that they may form functional neuronal network under such conditions. The microelectrode arrays modified with PPy-coated VACNFs have been further demonstrated in effective electrical stimulation of rat hippocampal brain slices. The stimulation voltage can be lowered to below 1 V to eliminate water electrolysis. [43] With further development, VACNFs coated with a proper ECP, such as PPy, could serve as a novel electrode for future neuroprosthetic devices. The merits of 3D topography, soft mechanical properties, good biocompatibility with ECP modification, high electrical conductivity, low impedance, and miniaturization capability may significantly enhance the stability of NEI.

4.3 Nanoelectrode Arrays Based on Embedded Vertically Aligned Carbon Nanofibers

4.3.1 Fabrication and Electrochemical Properties

The high surface area of the exposed sidewall of forest-like vertically aligned CNTs or VACNFs in the previous section generates large capacitive background currents due to charging–discharging the electrical double layer. This may mask the weak signal in the form of faradaic current in electrochemical detection of small amounts of redox molecules. To solve this problem, Li et al. developed a method to encapsulate the VACNFs with SiO_2 by tetraethoxysilane (TEOS) CVD and then remove it from the top by mechanical polishing and/or plasma etching until the tip is exposed to a desired length, forming a nanoelectrode array (NEA) [31, 32]. As shown in Fig. 4.4a, b, such NEA can be fabricated as precisely defined regular pattern on predefined microscale contact pads. Low-cost random NEA can be fabricated using the same method but skipping the lithography steps [32]. As long as the average spacing between the exposed VACNF tips is larger than six times of the tip diameter

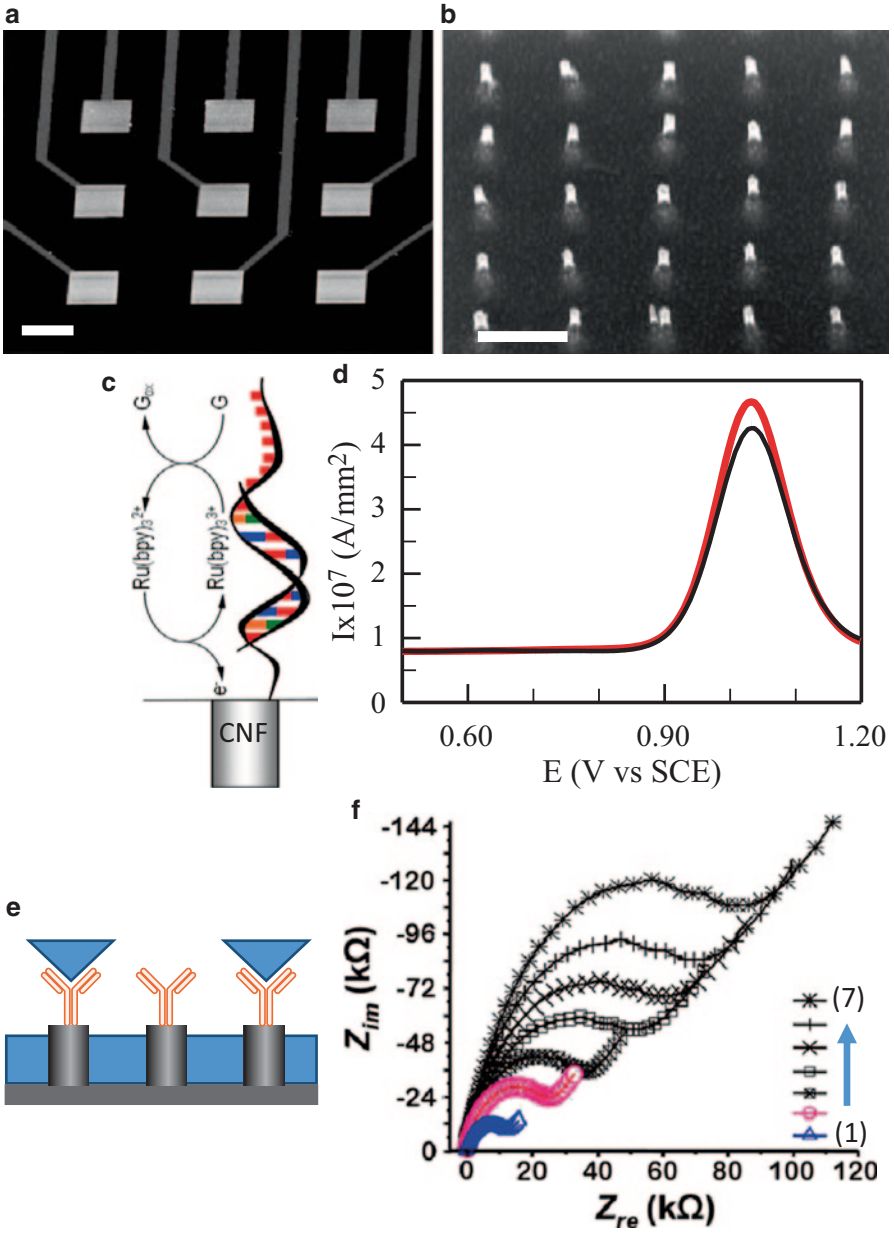

Fig. 4.4 VACNFs embedded in a dielectric insulator with only the tips exposed to form nanoelectrode arrays for biosensors. **a** A representative independently addressed 3 × 3 microelectrode array (scale bar: 200 μm). **b** An e-beam-patterned nanoelectrode array consisting of exposed tips of a regular VACNF array embedded in SiO_2 after mechanical polishing and plasma etching (scale bar: 1 μm). **c** Electrochemical detection of DNA hybridization on probe-functionalized VACNF nanoelectrode array based on a redox-mediated guanine oxidation mechanism. **d** The three consecutive AC voltammograms showing the guanine oxidation current from the hybridized target DNA. An enhanced peak current present in the first curve compared to later curves due to the irreversible oxidation of guanine bases. ([31]. With permission). **e** Schematic of protein

(~100 nm), the random NEAs show similar behavior as the e-beam-patterned regular arrays. Tu et al. [46] demonstrated a slightly different process for encapsulating VACNFs using spin-coated epoxy, rather than TEOS CVD, which also showed the characteristic nanoelectrode behavior.

It is known that the performance of an electrode with respect to temporal and spatial resolution and sensitivity scales inversely with the electrode radius. In the embedded VACNF NEA, the electrode diameter is much smaller than that of the diffusion layer thickness, thus the electrochemical properties become fundamentally different from a conventional macroelectrode. Cyclic voltammetry (CV) measurements of redox solutions typically show a sigmoidal shape with a steady-state limiting current defined by the nonlinear radial diffusion rather than time-dependent linear diffusion at the surface of macroscopic electrode [47]. The CV measurements in 1 mM $K_4Fe(CN)_6$ and 1.0 M KCl with a low-density embedded VACNF NEA of $\sim 7 \times 10^7$ electrodes/cm^2 indeed confirmed these features [31, 48]. The high temporal resolution of such NEA has been demonstrated by Koehne et al. in detecting dopamine, an important neural transmitter, using fast-scan cyclic voltammetry. The NEA on a 200×200 μm^2 micropad (similar to Fig. 4.4b) has shown the capability to detect submicromolar dopamine at 300 V/s scan rate, comparable to a 5-μm diameter conventional carbon fiber microelectrode with ~50 μm exposed length [49]. With the diameter approaching the size of biomolecules, nanoelectrodes can be efficiently used for biosensors. The exposed tip with broken graphitic structure facilitates selective covalent attachment of biomolecules. Lin et al. [50]. demonstrated that covalently attached GOx to the exposed VACNF tip in an embedded NEA can efficiently catalyze the glucose oxidation. A linear amperometric response can be obtained with such electrodes in glucose solution in a range from 0.08 mM to 30 mM. Both the linear range and detection limit surpass other electrochemical glucose sensors.

4.3.2 Affinity Biosensors

Besides being used as an electrode to detect the redox biomolecules in bulk solution, the embedded VACNF NEA can also be functionalized with biorecognition probes for the development of specific affinity biosensors. In such applications, the VACNFs are used as an electrochemical transducer whose signal changes upon the target molecules bind onto the surface through highly specific interaction with the probe. The most useful examples are the detection of DNA hybridization and immunochemical binding.

binding on an antibody-functionalized VACNF nanoelectrode array. **f** The electrochemical impedance spectroscopy of 5 mM $Fe(CN)_6^{3-/4-}$ mediator measured with *(1)* bare electrode; *(2)* anti-cTnI antibody-immobilized electrode; and *(3)–(7)* the anti-cTnI antibody-immobilized electrode incubated in 0.25, 0.5, 1.0, 5.0, and 10.0 ng/mL human cTnI antigen, respectively. The magnitude of the charge-transfer resistance (represented by the magnitude of the semicircle) represents the amount of human cTnI antigen binding to anti-cTnI antibody. *cTnI* cardiac troponin-1, *SCE* short-channel effect, *CNF* carbon nanofiber. ([54]. With permission)

Figure 4.4c, d shows one example for the ultrasensitive detection of DNA hybridization using embedded VACNF NEAs [31]. An oligonucleotide probe with 18 bases is covalently attached to the exposed CNF tip through amide bonds facilitated with carbodiimide reagents. This DNA sequence is a segment of the wild-type allele (Arg1443stop) of cancer-related *BRCA1* gene. It is estimated that there are about 100 probe molecules functionalized to a single CNF of ~100 nm in diameter. Incubation in a solution of target DNA with an 18-base complementary sequence and a 10-base polyG tag at the end generates duplex DNAs at the nanoelectrode surface. $Ru(bpy)_3^{2+}$ mediators are introduced to facilitate an amplified guanine oxidation, which efficiently transfer electrons from the guanine bases to the electrode even when they are not in direct contact. This mechanism can utilize all the inherent guanine bases within the hemispherical diffusion layer of $Ru(bpy)_3^{2+}$ mediators, generating a well-defined oxidation peak around 1.04 V in alternating current (AC) voltammogram as shown in Fig. 4.4d. Interestingly, guanine oxidation is irreversible. As a result, the first scan (red line) is clearly higher than the second (blue dotted line) and the third (black line) scans, while the latter two are nearly superimposed on each other. The guanine oxidation only occurs in the first scan. Subtracting the second scan from the first one gives a clear peak at 1.04 V with the peak amplitude representing the amount of guanine brought to the electrode surface through specific hybridization, while subtracting the third from the second curve gives a nearly flat background with only small active guanine residues. This method was further demonstrated in specific detection of the hybridization with 300-base long polymerase chain reaction (PCR) amplicons containing the sequence complementary to the probe [51]. Statistically, each target provides 75 guanine bases as the inherent components in the target, significantly amplifying the electrochemical signal without further labeling. More importantly, this technique can be potentially developed into a compact multiplex chip operated with a simple handheld system for rapid label-free DNA analyses [52].

Immunochemical biosensors represent another type of important affinity biosensor, which rely on the specific binding of antibody probes (or equivalent such as aptamers) with target proteins for analyses. The embedded VACNF NEA has been demonstrated as a label-free electronic technique in detecting ricin (a toxic glycoprotein) [53] and cardiac troponin-I (cTnI, a principal biomarker for myocardiac infarction) [54]. As illustrated in Fig. 4.4e, antibody or aptamer probes are functionalized at the exposed CNF tips in an embedded VACNF NEA. Incubating this electrode in the target solution induces protein binding on the surface in correlation with the protein concentration. The bound protein partially blocks the CNF surface and causes an increase in the charge transfer resistance of redox mediators at the electrode surface, which can be monitored with electrochemical impedance spectroscopy (EIS). Figure 4.4f shows the EIS at different stages of the electrode preparation and treatments. The charge-transfer resistance (represented by the amplitude of the dominant semicircle) clearly increases as the cTnI concentration is increased from 0.25 to 10.0 ng/mL [54]. It was concluded that detection limit by this method can reach ~0.2 ng/mL human cTnI, about 25 times lower than conventional methods [54].

4.3.3 Enzymatic Activity Analyses

4.3.3.1 Platform and Algorithm

The embedded VACNF NEAs can also be used to detect the activities of various enzymes such as proteases, kinases, and phosphatases, which are critical biomarkers involved in biological processes leading to diseases. Specific peptide substrates are functionalized at the exposed CNF tips in the NEAs, which are subjected to proteolysis or phosphorylation (or dephosphorylation). The reaction kinetics can be monitored with different electrochemical methods to provide the actual activity of these enzymes, rather than the concentrations measured with other techniques. The electrochemical detection of enzyme activities is attractive as portable systems for point-of-care diagnosis, therapeutic treatment monitoring, and drug screening for diseases such as cancers.

Besides presenting a characteristic steady-state limiting current in CV due to the nonlinear radial diffusion of redox species to the electrode surface [55], NEAs also afford to maintain the linear current–voltage relationship at much higher AC voltage in EIS measurements than macro- and microelectrodes [56]. Due to the small electrode size, the measured impedance of an NEA is very sensitive to the nature of the biomolecules bound at the electrode surface. In addition, the much smaller electrochemical cell time constant of NEA allows the electrochemical measurement to be carried out at a much higher speed. These properties make NEAs attractive for monitoring enzymatic reactions using peptide substrates attached to the CNF tip. The small radius of CNF tip protruding over the flat SiO_2 matrix surface also allows enzymes to access to the peptide substrates without suffering the steric hindrance effects encountered on macroscopic surfaces.

Phosphorylation of the peptides by kinase introduces phosphate groups and negative charges to the electrode surface. On the other hand, dephosphorylation of the phosphorylated substrates by phosphatase removes the negatively charged phosphate groups from the peptides. Phosphorylation and dephosphorylation are reversible dynamic processes, which are important regulatory mechanisms in both prokaryotic and eukaryotic organisms [57]. The changes in charge density and/or conformation of the peptides accompanying these reactions may induce changes in electrochemical impedance $|Z|$ [58]. Label-free real-time electrochemical impedance spectroscopy (REIS) method is employed which directly measures the impedance change at the electrode surface during enzymatic phosphorylation/dephosphorylation as shown in Fig. 4.5a. A long peptide substrate (biotin–AEEEIYGEFEAKKKKC) which is specific to c-Src kinase [59] is attached to the exposed CNF tip. When a solution containing c-Src kinase and adenosine-5′-triphosphate (ATP) is added to the solution, a phosphate group in ATP is transferred to the tyrosine residue (Tyr or Y) in the peptide, referred as phosphorylation. During this process, a negative charge is added to the peptide, which may be accompanied by a conformational change in the peptide. These effects are expected to affect the packing of peptides on the electrode surface and cause impedance change. On the other hand, the reverse

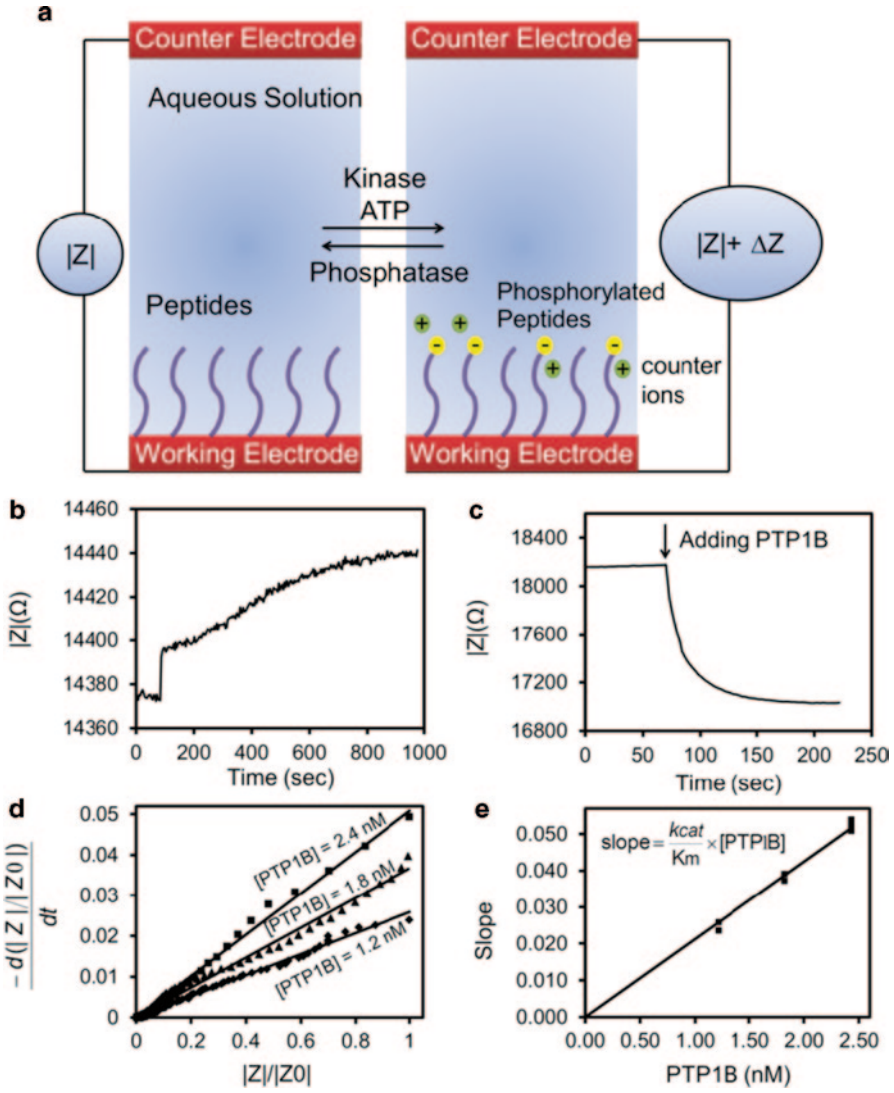

Fig. 4.5 **a** The reversible phosphorylation and dephosphorylation of peptide substrates attached to an embedded VACNF NEA catalyzed by *kinase* and *phosphatase,* respectively. **b** The real-time measurement showing that the impedance $|Z|$ increases slowly upon the addition of 5.9 nM c-Src and 0.30 mM *ATP* at 100 s into the kinase buffer. **c** The real-time measurement showing that the impedance $|Z|$ decreases rapidly upon the addition of 2.4 nM *PTP1B* at 73 s into the phosphatase buffer. **d** The plot of $-d(|Z|/|Z_0|)/dt$ versus $|Z|/|Z_0|$ and the fitting with straight lines for the kinetic data with 2.4 nM (■), 1.8 nM (▲), and 1.2 nM (♦) *PTP1B,* respectively. **e** The slopes in (**d**) at three *PTP1B* concentrations showing a linear relationship between the slope and the *PTP1B* concentration. *ATP* adenosine triphosphate, *PTP1B* protein tyrosine phosphatase 1B ([58]. With permission)

reaction to remove the phosphate group, that is, dephosphorylation, could happen after replacing the kinase solution with that of protein tyrosine phosphatase 1B (PTP1B). The impedance may change toward the opposite direction. This method is particularly suitable for fast reaction such as dephosphorylation.

For slower reactions such as proteolysis induced by proteases, the kinetics can be measured with a special AC voltammetry (ACV) technique. Compared to commonly used CV techniques based on direct current (DC) ramping, ACV measurements on VACNF NEAs show an anomalously high electron transfer rate with redox-active Fc molecules attached to the exposed CNF tips [10]. This is likely attributed to the unique conically stacked graphitic structure of the CNFs in the NEA. As a result, ACV on CNF NEAs can be carried out at much higher AC frequency (> 1 kHz) than that on macroscopic glassy carbon electrodes (GCEs) which is limited to ~ 75 Hz. Since the signal in ACV is nearly proportional to the AC frequency below certain limits, the detection sensitivity can be greatly enhanced with VACNF NEAs. The detection of the enzymatic activity of cancer-related proteases has been demonstrated by monitoring the decrease in the ACV signal of Fc attached to the CNF tip through a specific peptide linker.

The kinetics of the above two heterogeneous enzymatic reactions may be generally explained with a modified Michaelis–Menten model as shown in the following equation: [60]

$$\mathrm{E} + \mathrm{S_s} \underset{k_{-1}}{\overset{k_1}{\longleftrightarrow}} \mathrm{ES_s} \xrightarrow{k_{\mathrm{cat}}} \mathrm{E} + \mathrm{P_s} + \mathrm{P}, \tag{4.1}$$

where E, S_s, ES_s, P_s, and P represent the enzyme, the surface-bound peptide substrate, the enzyme-substrate complex on the electrode surface, the surface-attached product, and the product released to the solution, respectively. The reaction rate can be defined as

$$\upsilon = -\frac{d\Gamma_{Ss}}{dt} = \frac{d\Gamma_{Ps}}{dt} = \frac{k_{\mathrm{cat}}[E_0]\times\Gamma_{Ss}}{K_{\mathrm{M}} + [E_0]}, \tag{4.2}$$

where k_{cat} is the dissociation rate constant, $K_M = (k_{cat} + k_{-1})/k_1$ is the Michaelis–Menten constant, and Γ_{Ss} and Γ_{Ps} represent the surface densities of original and reacted peptide substrates, respectively. At low enzyme concentrations where $[E_0] << K_M$, an approximate relationship can be obtained as

$$\upsilon = -\frac{d\Gamma_{Ss}}{dt} = \frac{d\Gamma_{Ps}}{dt} = \frac{k_{\mathrm{cat}}}{K_{\mathrm{M}}}[E_0]\times\Gamma_{Ss}. \tag{4.3}$$

The reaction rate v (or $-d\Gamma_{Ss}/dt$) is a time-dependent quantity proportional to the change in electrochemical signals (dE/dt), where E is the kinetic electrochemical signal corresponding to the "extracted proteolytic signal" S in ACV measurements for protease, and the normalized impedance $|Z|/|Z_0|$ in REIS measurements for kinase/phosphatase, respectively. As a result, the slope of (dE/dt) versus the time-dependent E will be equal to $(k_{cat}/K_M)[E_0]$, namely,

$$-\frac{d\Gamma_{Ss}/dt}{\Gamma_{Ss}} = -\frac{dE/dt}{E} = \frac{k_{cat}}{K_M}[E_0]\cdot \tag{4.4}$$

Thus, by rearranging the kinetic electrochemical data, we can derive the value of "specificity constant" k_{cat}/K_M which is commonly used to represent the catalytic efficiency of enzymes. In another view, the kinetic electrochemical signal is essentially an exponential function

$$E = E_0 \exp(-t/\tau), \tag{4.5}$$

where the exponential time constant τ is related to the enzymatic activity by $1/\tau = (k_{cat}/K_M)[E_0]$.

4.3.3.2 Kinase/Phosphatase Detection

Figure 4.5b, c shows the REIS upon adding c-Src kinase or PTP1B phosphatase into corresponding buffer solutions. Only a small change (<0.5%) in the total impedance value $|Z|$ was observed after adding 5.9 nM of c-Src kinase (Fig. 4.5b) [61]. The change was slow, unreliable, and superimposed on a step function due to disturbance to the solution. The peptide at the VACNF NEA was fully phosphorylated with 1-h further incubation in c-Src kinase solution. The dephosphorylation reaction was much faster, showing a decrease in $|Z|$ by ~1150 Ω (~6.3%) over the ~100-s period after adding 2.4 nM PTP1B. These results indicated that the peptide attached to the VACNF NEA can be reversibly phosphorylated and dephosphorylated by switching the enzymes and corresponding buffers. The impedance change corresponding to the dephosphorylation by PTP1B was considerably larger than that of phosphorylation by c-Src kinase. This is correlated with the fact that the "specificity constant" k_{cat}/K_M is 1.1×10^6 M^{-1} s^{-1} for human PTP1B and 2.9×10^7 M^{-1} s^{-1} for rat PTP1 phosphatases [62, 63], much higher than that for c-Src kinase ranging from 2.4×10^3 to 2.5×10^4 M^{-1} s^{-1} [59, 64–66].

For quantitative analysis of the enzyme activity, the background-subtracted data $|Z|/|Z_0|$ in Fig. 4.5c was fit with an exponential decay

$$|Z|/|Z_0| = 0.944 \exp(-t/19.1)\cdot \tag{4.6}$$

The value $-\mathrm{d}(|Z|/|Z_0|)/\mathrm{d}t$ represents the reaction rate, which can be calculated from the exponential fitting function using Eq. (4.6) and then plotted versus $|Z|/|Z_0|$, as shown in Fig. 4.5d. The slope of the straight line gives $1/\tau = 0.0522 s^{-1} = (k_{cat}/K_M)[E_0]$. Since it is known $[E_0] = 2.4$ nM, the value of k_{cat}/K_m can then be derived as 2.2×10^7 M^{-1} s^{-1}, right in the range reported in the literature [62, 63]. As the PTP1B concentration is lowered to 1.8 and 1.2 nM, respectively, the slope decreases proportionally as shown in Fig. 4.5d. But the derived specificity constant k_{cat}/K_M remains the same as expected, giving an average value of 2.1×10^7 M^{-1} s^{-1}.

4.3.3.3 Protease Detection

ACV uses a sinusoidal AC voltage superimposed on a DC potential ramp for voltammetric measurements. It has advantages over commonly used DC-based CV, particularly for biosensors, due to the ability to amplify the electrochemical signal of small quantity of redox tags by shuffling the electron between the redox tag and the electrode many times. In general, the signal increases with AC frequency at low frequencies but is saturated and then decreases at higher frequencies. Using VACNF NEAs, the optimum frequency for Fc through a short NH_2CH_2- linker was found to be 40 times higher than macroscopic GCE [10]. Similar phenomena were also observed with Fc attached to the electrode surface through a tetrapeptide and linker groups, that is, $H_2N–(CH_2)_4–CO–Ala–Ala–Asn–Leu–NHCH_2–Fc$ which showed a peak current at ~0.2 V versus Ag/AgCl (3 M KCl) [12]. As shown in Fig. 4.6, the peak current density (i_p) in the ACVs with macro-GCE is maximum at 40 Hz but then drop to zero at 1500 Hz. In contrast, the ACV of the VACNF NEA gives a maximum i_p at 1500 Hz [11, 12]. Obviously, VACNF NEAs allows the Fc signal to be detected at much higher frequency. This provides a unique method for protease detection.

Figure 4.7 a shows the scheme of monitoring protease-induced proteolytic cleavage of the peptide substrates attached to the embedded VACNF NEA. Upon being supplied with the specific protease, the peptide is cleaved at the particular site and releases the Fc moiety from the electrode surface, causing the redox signal to decrease, which is monitored by continuously repeated ACV measurements. As shown in Fig. 4.7b, adding cathepsin B (at 15.5, 30.7, and 62.1 nM) into the electrochemical cell clearly cleaves the tetrapeptide $H_2N–(CH_2)_4–CO–Leu–Arg–Phe–Gly–NH–CH_2–Fc$ immobilized on VACNF NEA and causes the normalized ACV peak current S to decay exponentially [11, 12]. The decay time constant can be fitted with

$$S = [i_t - (bt + c)]/i_0 = \exp(-t/\tau)\cdot \tag{4.7}$$

The higher cathepsin B concentration apparently causes a faster decay, giving smaller decay time constant τ and higher protease activity, with $1/\tau = (k_{cat}/K_M)\cdot[E_0]$. The quantity of $(k_{cat}/K_M)\cdot[E_0]$ can be alternatively represented by the slope in Fig. 4.7c. The statistical values of $(k_{cat}/K_M)\cdot[E_0]$ from nine experiments at three enzyme concentrations are shown in Fig. 4.7d, which is linearly proportional to the enzyme concentration $[E_0]$, giving the average "specificity constant" $k_{cat}/K_M = (3.68 \pm 0.50) \times 10^4\ M^{-1}\ s^{-1}$ [67].

A major goal of today's research is to develop methods that can quantitatively detect protease in complex samples and correlate the results with cancer formation. The capability of VACNF NEA in detecting cathepsin B activity has been recently demonstrated with lysates of human epithelial mammary cell (HMEC), non-tumorigenic breast cell MCF-10 A, breast cancer cell T47D, and metastatic breast cell MDA-MB-231 [68]. As shown in Fig. 4.8, the decay time clearly varied among these different cell lysates, giving τ=497, 311, 248, and 215 s for 7.28 μg mL^{-1} of HMEC, MCF-10 A, T47D, and MDA-MB-231, respectively. The derived values of

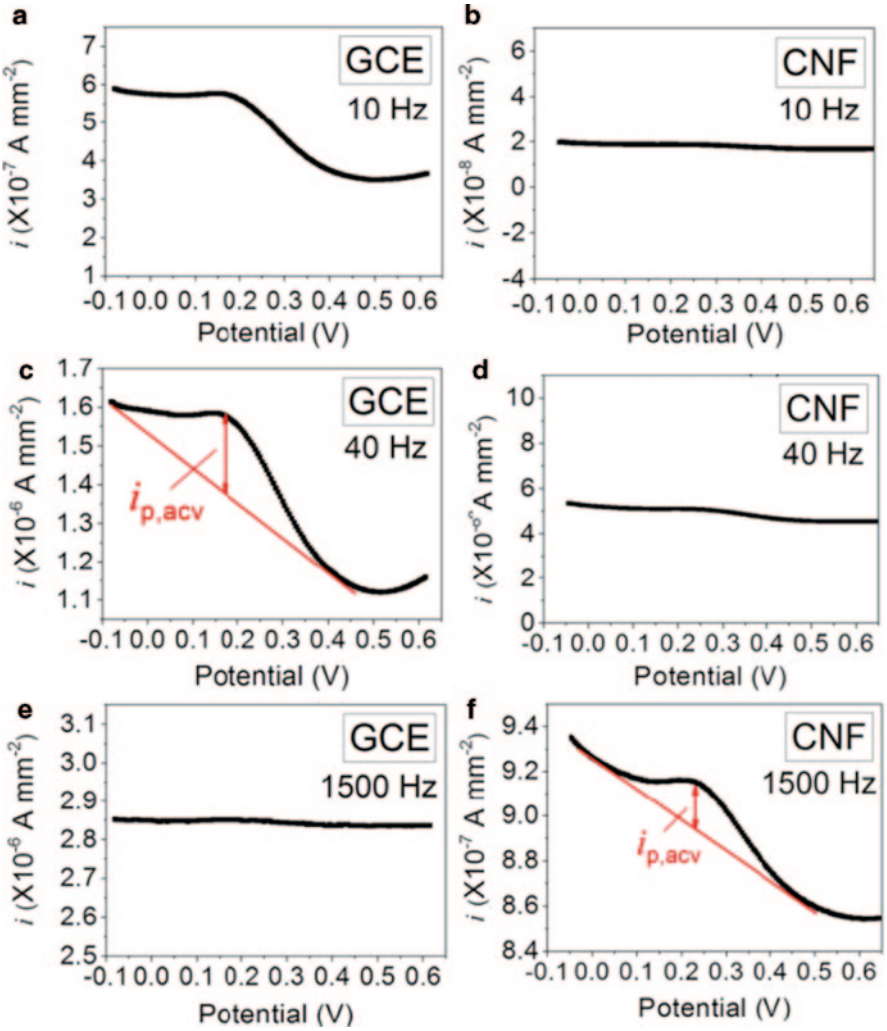

Fig. 4.6 Comparison of AC voltammograms *(ACVs)* measured at 10, 40, and 1500 Hz of H_2N–$(CH_2)_4$–CO–Ala–Ala–Asn–Leu–$NHCH_2$–Fc immobilized on a macro-*GCE* (**a**–**c**) and on a VACNF NEA (**d**–**f**). All measurements were done in 500 μL of 50 mM MES (pH 5.0) and 250 mM NaCl. Sinusoidal waves with the fixed amplitude of 25 mV were superimposed on a DC staircase ramp from −0.05 to +0.65 V at a scan rate of 10 mV·s^{-1}. The AC current density was calculated by normalization to the 7.1 mm^2 geometric surface area inside the 3-mm i.d. O-ring. The actual *CNF* surface area is ~100 times less. *CNF* carbon nanofiber, *GCE* glassy carbon electrode. ([12]. With permission)

$(k_{cat}/K_M)\cdot[E_0]$ are 2.00×10^{-3}, 3.20×10^{-3}, 4.02×10^{-3}, and 4.60×10^{-3} s^{-1}, showing a good correlation with the cancer formation. With further development, such electrochemical enzymatic biosensors based on VACNF NEAs may be potentially applied as portable multiplex electronic devices for rapid cancer diagnosis, treatment monitoring, and inhibitor screening.

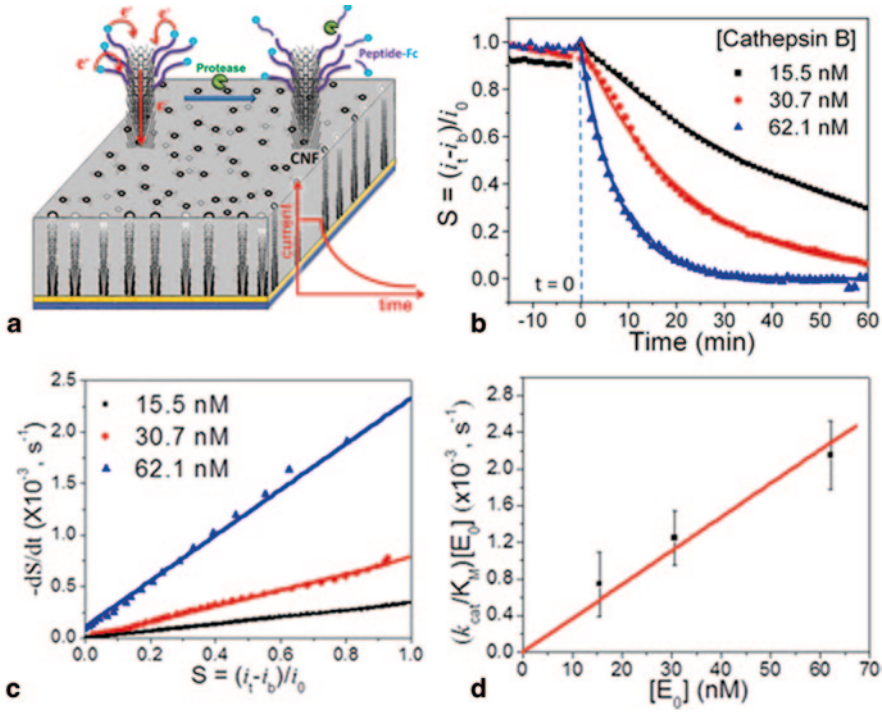

Fig. 4.7 **a** Schematic of protease-induced proteolytic cleavage of the peptide substrate. ([12]. With permission.) **b** The proteolysis kinetics represented by the extracted proteolysis signal $S=(i_t-i_b)/i_0$ versus the reaction time after adding purified *cathepsin B* into the electrochemical cell. The final concentrations of *cathepsin B* are 15.5, 30.7, and 62.1 nM, respectively. Each set of data is fitted with a simple exponential decay. **c** Plot of the reaction rate $-dS/dt$ versus extracted proteolysis signal $S=(i_t-i_b)/i_0$ at different *cathepsin B* concentrations. **d** Plot of $(k_{cat}/K_M)\cdot[E_0]$ with respect to *cathepsin B* concentration $[E_0]$ in the proteolytic reactions. The error bars are the standard deviation of the results from at least triplicated experiments. ([11]. With permission)

4.4 Integration of Nanoelectrode Arrays with Microfluidics

The embedded VACNF NEAs are mechanically robust, thermally and chemically stable, and able to sustain the traditional microfabrication process. Hence, they have been successfully integrated as active components in microfluidic chips for manipulating and detecting small redox chemicals, large biomolecules, microbial particles, and cells.

4.4.1 Redox Generator-Collector Pair in a Microfluidic Channel

The first study on the integration of VACNF nanoelectrodes in a microfluidic channel was reported by McKnight et al. [69]. To avoid detrimental arcing and sparking

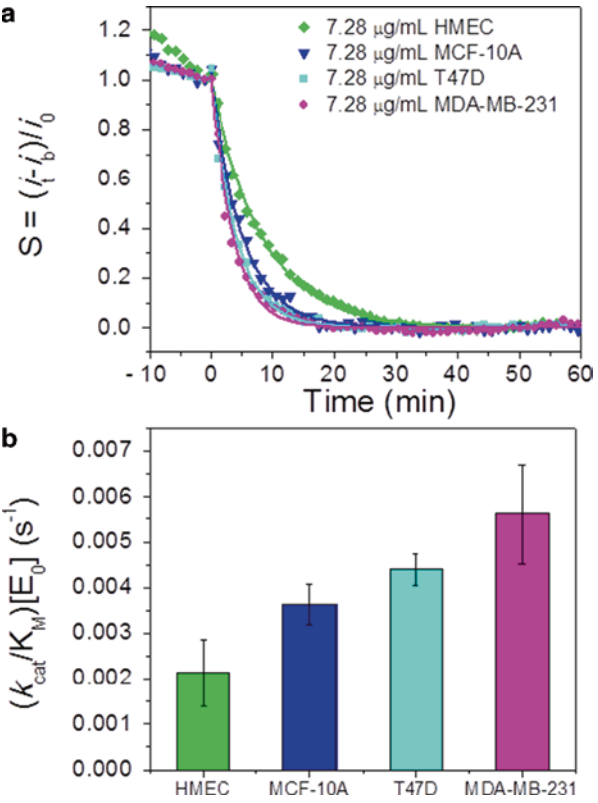

Fig. 4.8 **a** The normalized proteolysis curves measured in 7.28 μg mL^{-1} lysates of HMEC *(green diamond)*, MCF-10 A *(blue inverted triangle)*, T47D *(cyan square)* and MDA-MB-231 *(pink diamond)* cells, respectively. **b** Comparison of the $(k_{cat}/K_M)\cdot[E_0]$ values derived from 7.28 μg mL^{-1} of HMEC, MCF-10 A, T47D, and MDA-MB-231 cell lysates reacting with tetrapeptide $H_2N–(CH_2)_4–CO–Leu–Arg–Phe–Gly–NH–CH_2–Fc$ on VACNF NEAs. The error bars represent the standard deviations derived from three measurements. *HMEC* human epithelial mammary cell, *MCF* Michigan Cancer Foundation

during DC-biased PECVD process to the growth of VACNFs, the 4″ SiO_2-covered Si wafer was first deposited with a thin film consisting of the following material stacks Si/Ti/W/Ti. A UV lithography procedure was then employed to define Ni catalyst (40-nm thick Ni in 500-nm-diameter circular spots) using a liftoff process. The 10-nm thick Si top layer served as a critical interfacial layer to facilitate nucleation of singular Ni particles in the pregrowth process. With this unique approach, single CNFs can be grown from over 500-nm-diameter Ni spots which can be patterned easily with readily available wafer-scale reduction stepper photolithography instead of the slow and expensive e-beam lithography. The resulting VACNFs are spear shaped with ~500–700 nm in diameter at the base and 60–400 nm in diameter at the tip, with the length of ~5 μm. A recent study indicates that the spear shape could be attributed to the deposition of silicon nitride during PECVD growth of VACNFs due to the sputtering of the Si layer by NH_3 [70]. Nevertheless, the bigger base is useful in increasing the mechanical stability of the VACNFs. After VACNF growth, UV lithography was applied to define the metal contact pattern and the stacked film Si/Ti/W/Ti on rest of the surface area was removed by reactive ion etching (RIE). A layer of SiO_2 (~100 nm) was then conformally deposited by PECVD to encapsulate all surfaces. A 2-μm SU-8 layer was spun onto the wafer to further passivate the VACNF and define the area for exposing the metal contact by RIE. A second SU-8 layer (15–20 μm) was applied at the last to define the microfluidic channel.

Figure 4.9 shows the schematic view and a photograph of a completed single die consisting of up to 40 individually addressable VACNF nanoelectrodes [69]. Each VACNF is encapsulated with multiple layers of insulating materials leaving only the extreme tip exposed. CV characterization indicated that such nanoelectrodes have a wide potential window, over −1 to +1 V versus Ag/AgCl (3 M KCl) in various supporting electrolytes. In the solution containing redox molecules such as $Ru(NH_3)_6^{3+}$ and $Fe(CN)_6^{4-}$, well-defined sigmoidal shape was observed in CV curves. The steady-state current clearly depended on the exposed CNF length which can be controlled by hydrofluoric acid (HF) etching. The communication between two nanoelectrodes was studied using two fully exposed VACNFs separated by 10 μm as a generator–collector pair [69]. One VACNF was set at −0.5 V versus Ag/AgCl (3 M KCl) as the generator to reduce $Ru(NH_3)_6^{3+}$ to $Ru(NH_3)_6^{2+}$, while the other one was set at 0 V versus Ag/AgCl (3 M KCl) as the collector to oxidize $Ru(NH_3)_6^{2+}$ back into $Ru(NH_3)_6^{3+}$. At the steady state in 10 mM $Ru(NH_3)_6^{3+}$ solution, the concentration of the reduced specie $Ru(NH_3)_6^{2+}$ arriving at the collector at 10 μm distance was found to be as high as 0.8 mM, that is, ~8 %. Such design could be optimized in developing a novel amplification technology to detect very small amount of redox analytes by confining them in a small volume and recycling them between the generator and collector.

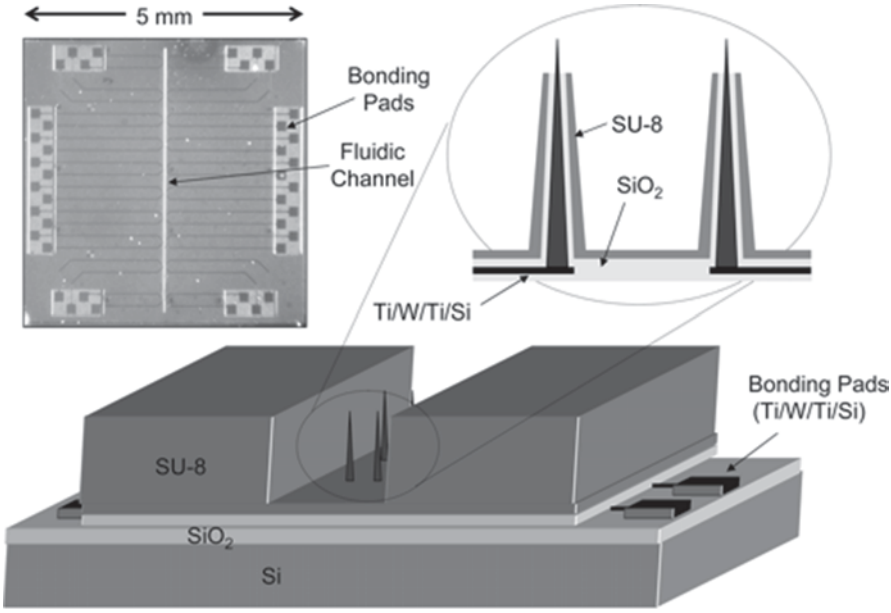

Fig. 4.9 Schematic view of a VACNF nanoelectrode array (not to scale) and photograph of a completed single die consisting of up to 40 individually addressed VACNFs (only four shown in the bottom schematic view) within an open microfluidic channel. The VACNFs are encapsulated with multiple layers of insulating materials leaving only the extreme tip exposed. ([69]. With permission)

4.4.2 VACNF NEA DNA Sensors Integrated in a Packed Microfluidic Chip

The DNA hybridization sensor based on embedded VACNF NEAs discussed earlier in Sect. 4.3.2 can be developed into a simple multiplex electronic DNA microarray technology for rapid DNA analyses [30, 31, 51, 52]. To fully realize their advantages, such DNA sensor chips need to be integrated with a microfluidic system for sample handling. Kim et al. demonstrated a fully packed microfluidic system toward this direction [71]. A chip consisting of nine independently addressed e-beam patterned regular NEA (similar to that in Fig. 4.4b) in a 3×3 microarray format was functionalized with single-stranded DNA (ss-DNA) probes and used as the working electrode. A glass slide deposited with a common Ag quasi-reference electrode and a common Pt counter electrode was bound with the NEA chip through a polydimethylsiloxane (PDMS) tape precut with the fluidic channels (width: 300 μm and height: 100 μm) and a circular chamber. All processes were under 65°C so that the prefunctionalized DNA probes were retained intact. The ability of such integrated chip was demonstrated with differential pulse voltammetry (DPV) measurements of ruthenium(II)-amplified oxidation of guanine bases brought to the electrode surface through the specific hybridization (as described in Sect. 4.3.2). The peak height difference between the first and second DPV scans, that is, the signal correlated to the hybridized DNA, clearly increased as the target DNA concentration was raised. In addition, a PDMS-based microspotter has been demonstrated to quickly spot each micropad in the 3×3 chip with a different ss-DNA probe [71]. This can potentially be developed to a complete system to fabricate integrated multiplex DNA chips for rapid DNA analyses in field applications.

4.4.3 VACNF NEA Nano-DEP in a Fluidic Chip for Pathogen Detection

The embedded VACNF NEA has also been integrated into a microfluidic system for dielectrophoretic capture and detection of small pathogenic particles such as bacteria and viruses [72–74]. Dielectrophoresis (DEP) is an attractive technique for on-chip capture, sorting, and concentration of small polarizable particles using programmable electric fields [75, 76]. The small size of pathogens, such as the viral particles (~100 nm) and bacterial particles (~2 μm), makes it difficult to manipulate them in a fluidic flow. Recently, we have developed a simple nanoscale DEP device based on an embedded VACNF NEA versus a macroscopic indium tin oxide counter electrode, which can effectively capture both bacterial cells and viral particles from high-velocity fluidic flows. The highly focused electric field at the CNF tip produces a large DEP force to pull bacterial cells and viral particles toward the CNF tip and concentrate them at the electrode surface. The DEP device can be further integrated with a Raman probe for rapid detection of pathogens by monitoring surface-enhanced Raman spectroscopy (SERS) tag specifically bound to the bacteria cells [77].

4.4.3.1 Principles, Device Design, and Fabrication of the Nano-DEP Chip

DEP is the process defining the motion of particles when they are exposed to a spatially nonuniform electric field [76]. It fundamentally differs from electrophoresis because the particle is not required to carry a net electric charge for motion to be induced, and both AC and DC voltages can be employed to impose the electric field [78]. The time-averaged DEP force $\langle F_{DEP} \rangle$ exerted on a spherical particle by an AC voltage is given by: [76]

$$\left\langle \boldsymbol{F}_{DEP} \right\rangle = 2\pi r^3 \varepsilon_m \,\mathrm{Re}[CM(\omega)]\nabla \boldsymbol{E}^2, \tag{4.8}$$

where r is the radius of the particle, ε_m is the permittivity of the suspending medium, ∇E^2 is the gradient of the square of the applied electric field strength, and Re[CM(ω)] is the real component of the complex Clausius–Mossotti (CM) factor given by:

$$CM(\omega) = \frac{\varepsilon_p^* - \varepsilon_m^*}{\varepsilon_p^* + 2\varepsilon_m^*}, \text{ where } \varepsilon^* = \varepsilon - j\frac{\sigma}{\omega} \tag{4.9}$$

where ε_p^* represents the complex permittivity of the particle and ε_m^* is complex permittivity of the medium. Parameter σ is the conductivity of the medium, ω is the angular frequency ($\omega = 2\pi f$) of the applied electric field, and $j = \sqrt{-1}$. Here, we focus on positive DEP (pDEP) where the proper medium is chosen to give Re[CM(ω)] > 0 so that the particles experience a DEP force directing toward higher electric field strength [76]. Due to the small size, the magnitude of ∇E^2 at the CNF tip can be enhanced by orders of magnitude so that even small viral particles can be captured effectively [79].

Figure 4.10a illustrates the design of the DEP device in a "points-and-lid" configuration [75], with an embedded VACNF NEA in the exposed 200 × 200 μm^2 region as the "points" electrode and a macroscopic transparent indium tin oxide (ITO) slide as the "lid" electrode. The two pieces are permanently bonded together through the SU–8 photoresist layers. The stretched lines in Fig. 4.10b represent the movement of individual bioparticles carried by the hydrodynamic flow. Figure 4.10d shows the forces acting on the particles, where F_{DEP} force acts in downward direction leading to captures of particle on the VACNF tip in the NEA, and F_{Drag} is the hydrodynamic drag force which carries the particle to flow in the channel [72, 74].

4.4.3.2 DEP Capture of Bacteria and Virus in a Microfluidic Flow

DEP capture was demonstrated with fluorescent-labeled *Escherichia coli* DHα5 bacterial cells [72, 73] and Bacteriophage T4r viral particles [74]. In viral experiments, 280 mM mannitol was added to the suspension medium to ensure a positive CM factor for pDEP [79, 80]. The DEP device was placed under an upright fluorescence optical microscope. The NEA employed in this study had an exposed CNF

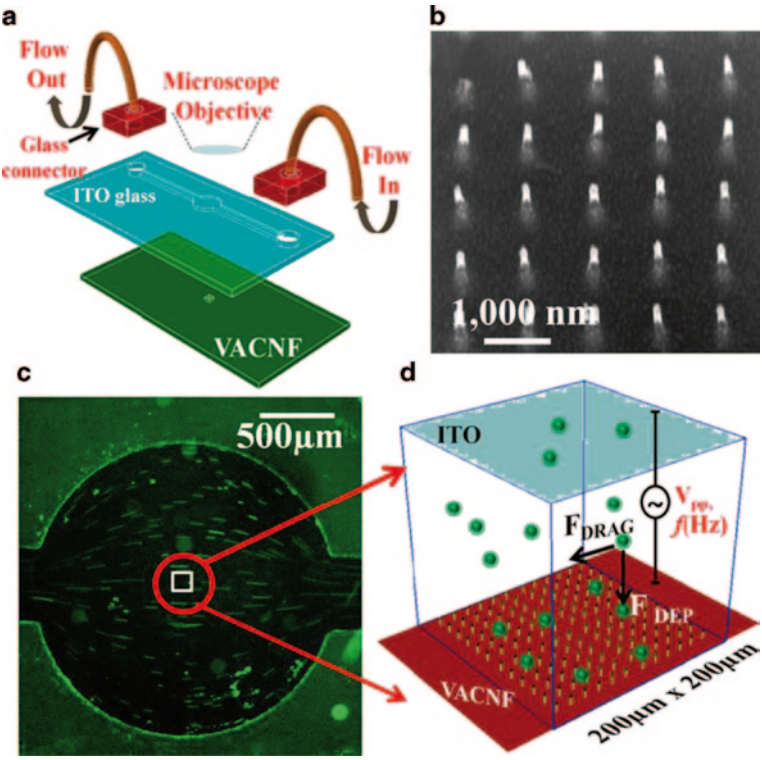

Fig. 4.10 Schematic of the microfluidic chip containing a *VACNF* NEA based nano-DEP device. **a** The main components of the device, including a top-lid electrode made of indium tin oxide *(ITO)*-coated glass and an 18-µm SU-8 photoresist layer containing a recessed microfluidic channel, a bottom NEA chip covered with 2 µm SU-8 photoresist with a 200×200 µm^2 open area. **b** SEM image of an NEA made of e-beam-patterned regular VACNFs. **c** 4X magnification optical microscope image showing the flow profile of fluorescent-labeled bacteriophage solution passing through the bonded device. **d** Schematic diagram of forces on the microbial particles in the active nano-DEP area. *VACNF* vertically aligned CNFs ([90]. With permission)

density of $\sim 2 \times 10^7$ CNFs/cm^2, with an average spacing of ~2.0 µm. Figure 4.11a shows the typical voltage waveform applied in a DEP experiment. Fluorescence video was recorded spanning over that period while the solution was forced to flow through the microfluidic channel. Figure 4.11b shows the integrated fluorescence intensity over the VACNF NEA area during the DEP capture of bacteriophage T4r with 10 V_{pp} AC voltage at 10 and 100 kHz frequency, respectively [74]. Clearly, the viral particles were captured immediately after the AC voltage was turned on and reached the saturation level within 10 s. The captured particles were reversibly released and washed away as soon as the voltage was turned off.

The captured bacterial cells present as isolated bright spots fixed on the surface as shown in the snapshot image in Fig. 4.11c [72]. The number of captured bacterial cells monotonically decreases as the flow velocity is increased, reflecting the larger drag force incurred by the flow. But for viral particles, the captured par-

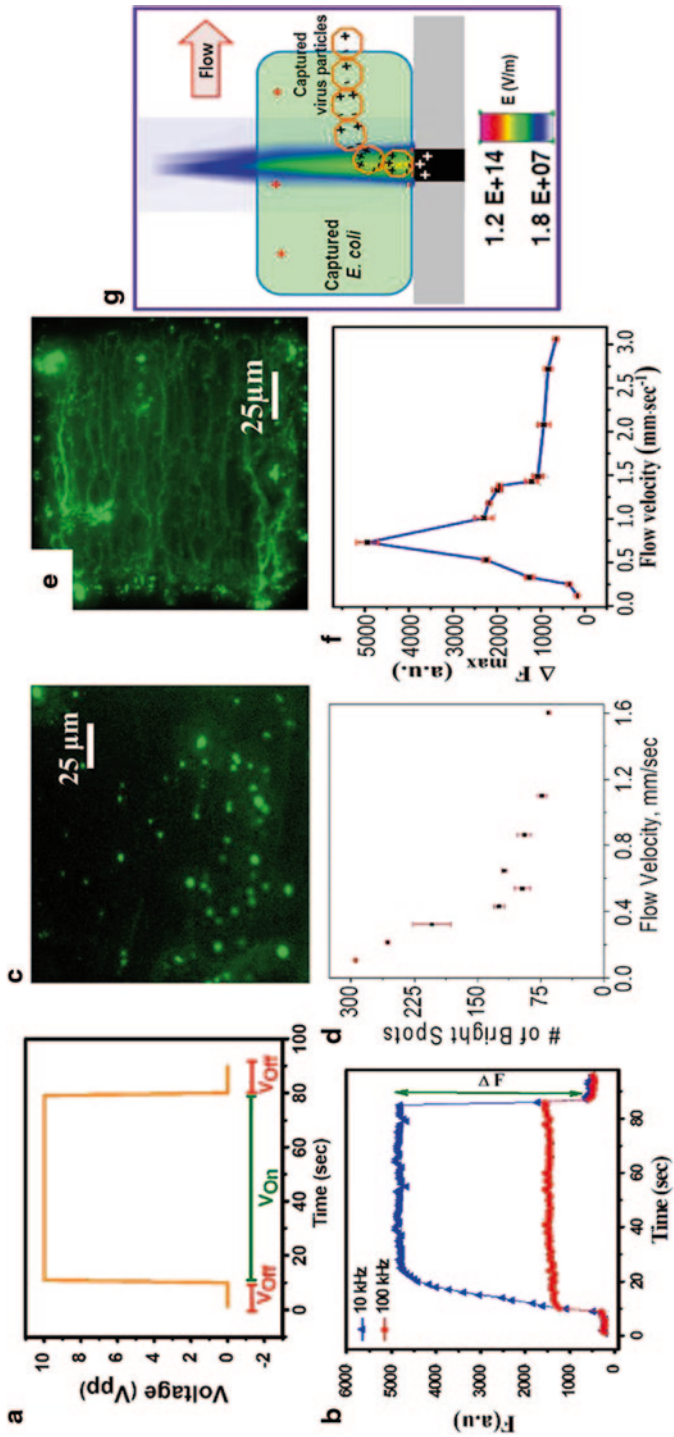

Fig. 4.11 Capture of bacteria and virus on VACNF NEA-based nano-DEP devices. **a** Typical voltage waveform in the DEP experiments: a 10 V_{pp} AC bias turned on at ~10 s for 70 s and then turned off at 80 s. **b** The corresponding kinetic curves of the integrated fluorescence intensity over the 200 μm × 200 μm NEA area as the AC voltage is turned on and off. ([74]. With permission.) **c** Snapshot of the *E. coli* cells captured on the NEA at flow velocity of 1.6 mm/s, frequency of 100 kHz, and AC voltage of 10 V_{pp}. **d** The correlation of the number of bright spots (representing captured individual *E. coli* cells) and the flow velocity. ([72]. With permission.) **e** A snapshot image of the *bacteriophage* T4r cells captured on the NEA at flow velocity 2.4 mm/s, with 10 kHz frequency and 10 V_{pp} AC bias. **f** The quantitative analysis of DEP capture, represented by the maximum increase of the integrated fluorescence intensity (ΔF max) in correlation with flow velocity which is peaked at flow velocity 0.73 mm/s. ([74]. With permission.) **g** The schematic representation of the relative polarization effects on viral particles (~150 nm) and an *E. coli* cell (~1–2 μm) based on the electric field profile by finite element simulation at the tip of a nanoelectrode (200 nm in diameter) embedded in the SiO_2 matrix. *E. coli Escherichia coli* ([90]. With permission)

ticles only present as isolated spots at flow velocity below 0.73 mm/s [74]. Above that, the snapshot shows fractal-like lightening patterns (see Fig. 4.11e) which are commonly generated under conditions where a high electric field is produced at a sharp electrode surrounded by charged or polarizable materials as is the case here (schematically shown in Fig. 4.11g) [74]. The generation of such patterns requires a relatively high concentration of polarizable particles at the electrode tip. Thus, it was seen only when the particle flux was sufficiently high to bring a large number of particles near the electrode and, at the meantime, the capture efficiency was sufficiently high to capture and keep them in place. Accordingly, as shown in Fig. 4.11f, the maximum DEP capture was obtained at the flow velocity of 0.73 mm/s, at the transition point from isolated spots to lightening patterns. For bacterial cells, the high electrical field at the VACNF was blocked once a single cell was captured, preventing it from capturing the second bacterial cell at this site.

Depending on the size, shape, and physicochemical properties, different microbes present very different CM factor over the frequency spectrum, and thus it is possible to selectively sort out a specific microbe from a mixture by DEP at the proper frequency. It has been demonstrated that optimum DEP capture condition for *E. coli* cells is at 100 kHz [72] and for *bacteriophage* T4r at 10 kHz [74]. Considering that mannitol had to be added to adjust the permittivity and conductivity of the media (i.e., water), it is clear that the small virus particles (*bacteriophage* T4r, 80–200 nm in size) have very different CM factor compared to larger bacterial cells (*E. coli,* ~1–2 μm in size). As expected, higher V_{pp} gives stronger DEP force in all cases. Normally, reliable results are only obtained with ≥ 6 V_{pp}.

4.4.3.3 Integrated SERS–DEP Chip for Specific Pathogen Detection

Despite DEP can, to a certain degree, selectively capture one type of microbe from others, it does not differentiate different strains or microbes with similar sizes and shapes. This problem can be solved by using DEP as a generic sample concentrating method which is coupled with other specific detection techniques based on bio-recognition labeling. Recently, we have demonstrated the integration of the nano-DEP device with surface-enhanced Raman spectroscopy (SERS) probe toward the development of a portable pathogen detection system for rapid field applications [77]. Bacterial cells were bounded with SERS nanotag through antibodies and then captured on VACNF tips in a microfluidic DEP chip, and the captured cells were then detected with SERS using a portable Raman system with a 100 μm diameter probe that was aligned to the active DEP site. The SERS nanotag is a complex structure consisting of a nano-oval-shaped plasmonic metallic substrate attached to a Raman marker molecule (QSY21 dye [81]) with a strong and unique Raman fingerprint [82, 83] co-functionalized with bio-recognition molecules such as antibodies, aptamers, etc. This structure ensures that the Raman is in close contact with the metal surface. As a result, when attached to a specific pathogen, a strong SERS signal can be obtained from the particular pathogenic species and not from other microorganisms. The SERS intensity of the captured nanotag-labeled *E. coli*

using a portable Raman setup was measured over the concentration range from ~10 to 1×10^9 cfu/mL and was found to be a linear function of the logarithm of bacteria concentration when the concentration is above ~100 cfu/mL. The concentration detection limit was determined to be ~210 cfu/mL, corresponding to one captured bacterial cell [84]. With further optimization, this integrated SERS–DEP chip may detect down to tens of cfu/mL from a sub-milliliter sample.

4.5 Low-Density VACNF Arrays for Gene Delivery, and Neural Stimulation

The high aspect ratio and strong mechanical properties make VACNFs attractive as sharp needles to penetrate the cell membrane and deliver DNA or drugs into the cell. McKnight et al. have demonstrated that an array of VACNFs can achieve this on a massively parallel basis [85, 86]. Regular spear-like VACNFs of ~100 nm in tip diameter, ~300–400 nm in base diameter, and a few microns in length were grown on Si surface with DC-biased PECVD similar to those discussed in Sect. 4.4.1. This can be fabricated in a regular array with a square lattice using routine UV lithography with the patterned Ni catalyst dots of 400 nm in diameter. The pitch size was designed as 5 μm which is comparable to the diameter of a typical unattached mammalian cell. As a result, it is expected that there is only one VACNF impaling into a single cell. The yellow fluorescent protein (YFP)-encoded DNA molecules, human cytomegalovirus immediate-early promoter (CMV_{IE}) reporter plasmid (pd2EYFP-N1), were covalently attached to the VACNFs through the amide bond. Chinese hamster ovary cells (CHO K_1BH_4) were dispensed on the VACNF chip and gently pressed by a sterilized PDMS slab to allow cell impalefection. The chip was then placed in growth media to allow cell recovery and proliferation. Ten days after impalefection, YFP expression was clearly observed, indicating that the genes tethered on the VACNFs retained the ability of transcription [86]. In contrast, physisorbed DNA molecules did not retain on the VACNF and were not able to show transfection to the cells. The small tip radius was believed critical in minimizing the mechanical damage to the cell and retaining its normal biological functions.

Yu et al. further demonstrated that the VACNFs can be grown deterministically at the desired spots that were electrically connected to the underlying metal lines and used for recording neuro-electrophysiological activity [87, 88]. Figure 4.12 shows a representative linear array consisting of 40 individually addressed VACNF electrodes spaced apart by 15 μm along a total length of 600 μm. Each electrode consists of about five to ten 10-μm long VACNFs grown from 2-μm diameter Ni catalyst spots but collapsed into a tapered microbundle with a tip size of ~100 nm in diameter [87]. Such a shape increased the mechanical robustness so that the electrode could sustain the harsh processes including wet and dry treatments and tissue penetration. Such VACNF array serves as 3D microneedle electrodes which can penetrate about 10 μm into the tissue. It is known that the surface of acutely sectioned tissue slices consist of injured or dead cells, and the surface

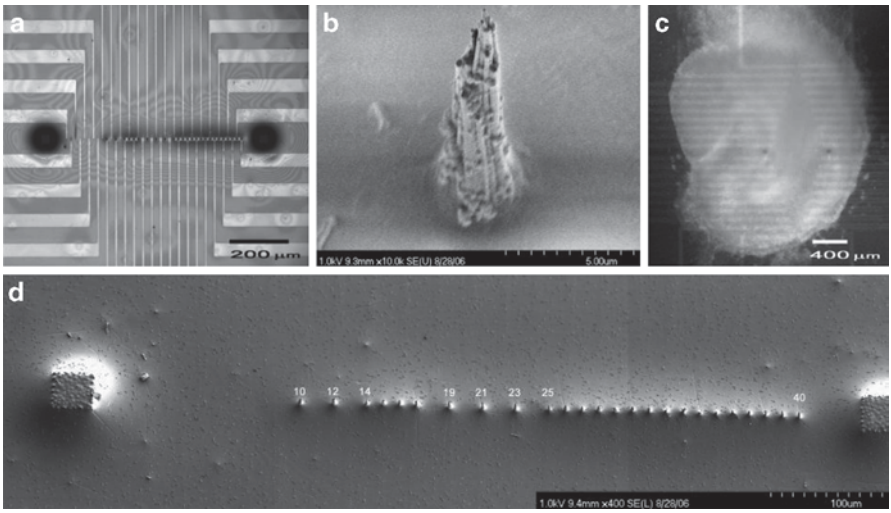

Fig. 4.12 A linear array of 40 individually addressed VACNF electrodes for recording neuroelectrophysiological activity of organotypic hippocampal slice cultures. **a** An optical image of the "as-fabricated" VACNF array. Electrodes *1–9, 11, 13, 18, 20, 22,* and *24* are missing in this sample. **b** SEM image of the entire VACNF array in (**a**). **c** An enlarged SEM image of a single VACNF electrode. **d** An optical image of a hippocampal slice (22 DIV) transferred to a pre-coated VACNF array chip. The scale bars are 200, 5, 400, and 100 µm, respectively. ([87]. With permission)

of slice cultures may consist of a reactive glia layer; both reduce signal propagation from the active cells to the electrodes [87]. Thus, the high-aspect ratio feature makes the VACNF microbundle electrode reach the active cells deeper in the tissue slices and provide better electrical–neural interface than traditional planar microelectrode arrays. While other state-of-the-art microneedle electrodes may be able to penetrate the tissue as well, their tip sizes are normally larger than 2 µm in diameter. The ability to reach down to 100 nm in diameter provides much higher spatial resolution.

Electrical stimulation and extracellular recording of the spontaneous and evoked neuroelectrical activity in organotypic hippocampal slices were demonstrated with the VACNF ultramicroelectrode [87]. The hippocampus slice of 400 µm in thickness was obtained from a postnatal day 8–11 rat pup. Slices were prepared 2–3 weeks before use. Prior to recording, VACNF chips were cleaned by air plasma treatment and then coated with a mixture of poly-L-lysine and laminin for improving the biocompatibility and cell adhesion. The array chip was then submerged in artificial cerebrospinal fluid with the organotypic hippocampal slice cultures laid on the VACNFs with electrode 1 located in CA3 pyramidal cell layer and electrode 40 in the dentate gyrus granule cell layer. Spontaneous complex spikes of ~50 μV_{pp} was readily detected with electrode 38 in the granule cell layer, above the background noise of ~25 μV_{pp}. By adding 1 mM tetrodotoxin, a voltage-sensitive sodium channel blocker, the spontaneous activity was blocked with the firing rate dropping from ~8 Hz to 0 Hz within 3 min after introduction. Furthermore, in-

troducing a gamma-aminobutyric acid A (GABAA) receptor blocker, bicuculline methiodide (BIC), demonstrated that the restriction of the spontaneous activity by GABAA receptor could be lifted. Epileptiform activity propagated throughout the hippocampal slice was recorded at the different electrode sites. The BIC-induced epileptiform activity consisted of large oscillations with amplitudes ten times greater than spontaneous complex spikes, up to 600 μV_{pp} [87]. Because the electrodes are carbon based, these arrays have potential advantages over metal electrodes and could enable a variety of future applications as precise, informative, and biocompatible neural interfaces.

4.6 Summary and Outlook

In summary, CNTs are a family of intrigue nanomaterials. Their properties not only strongly depend on the internal graphitic structure of the specific CNTs such as the seamless tube-like SWNTs or MWNTs and conically stacked CNFs but also the architectures into which they are organized into. In this chapter, we focused on the VACNFs with an emphasis on their unique electrochemical properties. The metallic nature, high electrical conductivity, great mechanical strength, and the presence of abundant active graphitic edges enable VACNFs as unique nanoelectrodes, which can be used in forest-like structure or embedded arrays. The biocompatibility and ease in functionalization with biomolecules make them attractive for biosensors and other biomedical applications. CNTs in organized architectures have provided an opportunity to expand the capability of traditional carbon electrodes into nanometer scale, reaching subcellular components and individual biomolecules. With the ability of micro- and nano- patterning and integration with microfluidic techniques for sample handling, it can be foreseen that extremely powerful systems for biomedical applications based on VACNFs will be developed in the near future [89].

References

1. S. Iijima, Helical microtubules of graphitic carbon. Nature **354**, 56–58 (1991)
2. T.W. Ebbesen, *Carbon nanotubes: preparation and properties*. (CRC Press, Boca Raton, 1997)
3. R.L. McCreery, Carbon electrodes: structural effects on electron transfer kinetics, in *Electroanalytical chemistry*, ed. by A.J. Bard (Marcel Dekker, New York, 1991), pp. 221–374
4. R.L. McCreery, Advanced carbon electrode materials for molecular electrochemistry. Chem. Rev. **108**, 2646–2687 (2008)
5. M. Endo, Y.A. Kim, T. Hayashi, Y. Fukai, K. Oshida, M. Terrones et al., Structural characterization of cup-stacked-type nanofibers with an entirely hollow core. Appl. Phys. Lett. **80**, 1267–1269 (2002)
6. Z.F. Ren, Z.P. Huang, D.Z. Wang, J.G. Wen, J.W. Xu, J.H. Wang et al., Growth of freestanding multiwall carbon nanotube on each each nanonickel dot. Appl. Phys. Lett. **75**, 1086–1088 (1999)
7. Z.F. Ren, Z.P. Huang, J.W. Xu, J.H. Wang, P. Bush, M.P. Siegal et al., Synthesis of large arrays of well-aligned carbon nanotubes on glass. Science **282**, 1105–1107 (1998)

8. B. Cruden, M. Meyyappan, Characterization of a radio frequency carbon nanotube growth plasma by ultraviolet absorption and optical emission spectroscopy. J. Appl. Phys. **97**, 084311 (2005)
9. A.V. Melechko, V.I. Merkulov, T.E. McKnight, M.A. Guillorn, K.L. Klein, D.H. Lowndes et al., Vertically aligned carbon nanofibers and related structures: controlled synthesis and directed assembly. J. Appl. Phys. **97**, 41301-1-39 (2005)
10. L.U. Syed, J. Liu, A.M. Prior, D.H. Hua, J. Li, Enhanced electron transfer rates by AC voltammetry for ferrocenes attached to the end of embedded carbon nanofiber nanoelectrode arrays. Electroanalysis **23**, 1709–1717 (2011)
11. L.Z. Swisher, A.M. Prior, S. Shishido, T.A. Nguyen, D.H. Hua, J. Li, Quantitative electrochemical detection of cathepsin B activity in complex tissue lysates using enhanced AC voltammetry at carbon nanofiber nanoelectrode arrays. Biosens. Bioelectron. **56**, 129–136 (2014)
12. L.Z. Swisher, L.U. Syed, A.M. Prior, F.R. Madiyar, K.R. Carlson, T.A. Nguyen et al., Electrochemical protease biosensor based on enhanced AC voltammetry using carbon nanofiber nanoelectrode arrays. J. Phys. Chem. C **117**, 4268–4277 (2013)
13. Q. Ngo, T. Yamada, M. Suzuki, Y. Ominami, A.M. Cassell, J. Li et al., Structural and electrical characterization of carbon nanofibers for interconnect via applications. IEEE Trans. Nanotechnol. **6**, 688–695 (2007)
14. E.C. Landis, R.J. Hamers, Covalent grafting of ferrocene to vertically aligned carbon nanofibers: electron-transfer processes at nanostructured electrodes. J. Phys. Chem. C **112**, 16910–16918 (2008)
15. S.A. Klankowski, R.A. Rojeski, B.A. Cruden, J. Liu, J. Wu, J. Li, A high-performance lithium-ion battery anode based on the core-shell heterostructure of silicon-coated vertically aligned carbon nanofibers. J. Mater. Chem. A **1**, 1055–1064 (2013)
16. M. Cinke, J. Li, B. Chen, A. Cassell, L. Delzeit, J. Han et al., Pore structure of raw and purified HiPco single-walled carbon nanotubes. Chem. Phys. Lett. **365**, 69–74 (2002)
17. J. Liu, J. Essner, J. Li, Hybrid supercapacitor based on coaxially coated manganese oxide on vertically aligned carbon nanofiber arrays. Chem. Mater. **22**, 5022–5030 (2010)
18. J. Liu, Y.-T. Kuo, K.J. Klabunde, C. Rochford, J. Wu, J. Li, Novel dye-sensitized solar cell architecture using TiO2-coated vertically aligned carbon nanofiber arrays. ACS Appl. Mater. Interfaces. **1**, 1645–1649 (2009)
19. J. Liu, J. Li, A. Sedhain, J. Lin, H. Jiang, Structure and photoluminescence study of TiO_2 nanoneedle texture along vertically aligned carbon nanofiber arrays. J. Phys. Chem. C **112**, 17127–17132 (2008)
20. T.W. Odom, J.L. Huang, P. Kim, C.M. Lieber, Structure and electronic properties of carbon nanotubes. J. Phys. Chem. B **104**, 2794–2809 (2000)
21. M. Anantram, F. Leonard, Physics of carbon nanotube electronic devices. Rep. Prog. Phys. **69**, 507–561 (2006)
22. J. Han, Structures and properties of carbon nanotubes, in *Carbon nanotubes science and applications*, ed. by M. Meyyappan (CRC Press, Boca Raton, 2005), pp. 1–24
23. P.C. Collins, M.S. Arnold, P. Avouris, Engineering carbon nanotubes and nanotube circuits using electrical breakdown. Science **292**, 706–709 (2001)
24. J.-P. Salvetat-Delmotte, A. Rubio, Mechanical properties of carbon nanotubes: a fiber digest for beginners. Carbon **40**, 1729–1734 (2002)
25. R.S. Ruoff, D. Qian, W.K. Liu, Mechanical properties of carbon nanotubes: theoretical predictions and experimental measurements. C.R. Phys. **4**, 993–1008 (2003)
26. D. Srivastava, Computational nanotechnology of carbon nanotubes, in *Carbon nanotubes: science and applications*, ed. by M. Meyyappan (CRC Press, Boca Raton, 2005), pp. 25–63
27. D. Srivastava, M. Menon, K.J. Cho, Nanoplasticity of single-wall carbon nanotubes under uniaxial compression. Phys. Rev. Lett. **83**, 2973–2976 (1999)
28. B.A. Cruden, A.M. Cassell, Vertically oriented carbon nanofiber based nanoelectromechanical switch. IEEE Trans. Nanotechnol. **5**, 350–355 (2006)

29. H.J. Qi, K.B.K. Teo, K.K.S. Lau, M.C. Boyce, W.I. Milne, J. Robertson et al., Determination of mechanical properties of carbon nanotubes and vertically aligned carbon nanotube forests using nanoindentation. J. Mech. Phys. Solids **51**, 2213–2237 (2003)
30. P.U. Arumugam, H. Chen, S. Siddiqui, J.A.P. Weinrich, A. Jejelowo, J. Li et al., Wafer-scale fabrication of patterned carbon nanofiber nanoelectrode arrays: a route for development of multiplexed, ultrasensitive disposable biosensors. Biosens. Bioelectron. **24**, 2818–2824 (2009)
31. J. Li, H.T. Ng, A. Cassell, W. Fan, H. Chen, Q. Ye et al., Carbon nanotube nanoelectrode array for ultrasensitive DNA detection. Nano Lett. **3**, 597–602 (2003)
32. J. Li, J.E. Koehne, A.M. Cassell, H. Chen, H.T. Ng, Q. Ye et al., Inlaid multi-walled carbon nanotube nanoelectrode arrays for electroanalysis. Electroanalysis **17**, 15–27 (2005)
33. T.B. Nguyen-Vu, H. Chen, A. Cassell, R. Andrews, M. Meyyappan, J. Li, Vertically aligned carbon nanofiber arrays: an advance toward electrical-neural interfaces. Small **2**, 89–94 (2006)
34. T.D.B. Nguyen-Vu, H. Chen, A.M. Cassell, R.J. Andrews, M. Meyyappan, J. Li, Vertically aligned carbon nanofiber architecture as a multifunctional 3-D neural electrical interface. IEEE Trans. Biomed. Eng. **54**, 1121–1128 (2007)
35. M. Gao, L.M. Dai, G.G. Wallace, Biosensors based on aligned carbon nanotubes coated with inherently conducting polymers. Electroanalysis **15**, 1089–1094 (2003)
36. M. Gao, S.M. Huang, L.M. Dai, G. Wallace, R.P. Gao, Z.L. Wang, Aligned coaxial nanowires of carbon nanotubes sheathed with conducting polymers. Angew. Chem.-Int. Ed. **39**, 3664–3667 (2000)
37. J.J. Gooding, R. Wibowo, J.Q. Liu, W.R. Yang, D. Losic, S. Orbons et al., Protein electrochemistry using aligned carbon nanotube arrays. J. Am. Chem. Soc. **125**, 9006–9007 (2003)
38. J. Liu, A. Chou, W. Rahmat, M.N. Paddon-Row, J.J. Gooding, Achieving direct electrical connection to glucose oxidase using aligned single walled carbon nanotube arrays. Electroanalysis **17**, 38 (2005)
39. F. Patolsky, Y. Weizmann, I. Willner, Long-range electrical contacting of redox enzymes by SWCNT connectors. Angew. Chem.-Int. Ed. **43**, 2113–2117 (2004)
40. P.G. He, L.M. Dai. Aligned carbon nanotube-DNA electrochemical sensors. Chem. Commun. (Camb) **7**(3), 348–9 (2004)
41. J.J. Pancrazio, Neural interfaces at the nanoscale. Nanomedicine **3**, 823–830 (2008)
42. S.K. Seidlits, J.Y. Lee, C.E. Schmidt, Nanostructured scaffolds for neural applications. Nanomedicine **3**, 183–199 (2008)
43. E.D. de Asis Jr., T.D.B. Nguyen-Vu, P.U. Arumugam, H. Chen, A. Cassell, R. Andrews et al., High efficient electrical stimulation of hippocampal slices with vertically aligned carbon nanofiber microbrush array. Biomed. Microdevices **11**, 801–808 (2009)
44. W. Zhu, C. O'Brien, J.R. O'Brien, L.G. Zhang, 3D nano/microfabrication techniques and nanobiomaterials for neural tissue regeneration. Nanomedicine **9**, 859–875 (2014)
45. T.J. Webster, M.C. Waid, J.L. McKenzie, R.L. Price, J.U. Ejiofor, Nano-biotechnology: carbon nanofibres as improved neural and orthopaedic implants. Nanotechnology **15**, 48–54 (2004)
46. Y. Tu, Y.H. Lin, Z.F. Ren, Nanoelectrode arrays based on low site density aligned carbon nanotubes. Nano. Lett. **3**, 107–109 (2003)
47. A.J. Bard, L.R. Faulkner, *Electrochemical methods: fundamental and applications*, 2nd edn. (Wiley, New York, 2001)
48. J. Koehne, J. Li, A.M. Cassell, H. Chen, Q. Ye, H.T. Ng et al., The fabrication and electrochemical characterization of carbon nanotube nanoelectrode arrays. J. Mater. Chem. **14**, 676–684 (2004)
49. J.E. Koehne, M. Marsh, A. Boakye, B. Douglas, I.Y. Kim, S.-Y. Chang et al., Carbon nanofiber electrode array for electrochemical detection of dopamine using fast scan cyclic voltammetry. Analyst **136**, 1802–1805 (2010)
50. Y.H. Lin, F. Lu, Y. Tu, Z.F. Ren, Glucose biosensors based on carbon nanotube nanoelectrode ensembles. Nano. Lett. **4**, 191–195 (2004)

51. J. Koehne, H. Chen, J. Li, A.M. Cassell, Q. Ye, H.T. Ng et al., Ultrasensitive label-free DNA analysis using an electronic chip based on carbon nanotube nanoelectrode arrays. Nanotechnology **14**, 1239–1245 (2003)
52. J.E. Koehne, H. Chen, A.M. Cassell, Q. Yi, J. Han, M. Meyyappan et al., Miniaturized multiplex label-free electronic chip for rapid nucleic acid analysis based on carbon nanotube nanoelectrode arrays. Clinic. Chem. **50**, 1886–1893 (2004)
53. A. Periyakaruppan, P.U. Arumugam, M. Meyyappan, J.E. Koehne, Detection of ricin using a carbon nanofiber based biosensor. Biosens. Bioelectron. **28**, 428–433 (2011)
54. A. Periyakaruppan, R.P. Gandhiraman, M. Meyyappan, J.E. Koehne, Label-free detection of cardiac troponin-I using carbon nanofiber based nanoelectrode arrays. Anal. Chem. **85**, 3858–3863 (2013)
55. C.E. Banks, T.J. Davies, G.G. Wildgoose, R.G. Compton, Electrocatalysis at graphite and carbon nanotube modified electrodes: edge-plane sites and tube ends are the reactive sites. Chem. Commun. (Camb) **2005**, 829–841 (2005)
56. S. Siddiqui, P.U. Arumugam, H. Chen, J. Li, M. Meyyappan, Characterization of carbon nanofiber electrode arrays using electrochemical impedance spectroscopy: effect of scaling down electrode size. ACS Nano. **4**, 955–961 (2010)
57. B.T. Houseman, J.H. Huh, S.J. Kron, M. Mrksich, Peptide chips for the quantitative evaluation of protein kinase activity. Nat. Biotechnol. **20**, 270–274 (2002)
58. Y. Li, L. Syed, J. Liu, D.H. Hua, J. Li, Lable-free electrochemical impedance detection of kinase and phosphatase activities using carbon nanofiber nanoelectrode arrays. Anal. Chim. Acta **744**, 45–53 (2012)
59. T.M. Johnson, J.W. Perich, J.D. Bjorge, D.J. Fujita, H.-C. Cheng, Common and differential recognition of structural features in synthetic peptides by the catalytic domain and the Src-Homology 2 (SH2) domain of pp60c-src. J.Peptide Res. **50**, 365–371 (1997)
60. O.A. Gutiérrez, M. Chavez, E. Lissi, A theoretical approach to some analytical properties of heterogeneous enzymatic assays. Anal. Chem. **76**, 2664–2668 (2004)
61. Y.-F. Li, L.U. Syed, J.-W. Liu, D.H. Hua, J. Li, Label-free electrochemical impedance detection of kinase and phosphatase activities using carbon nanofiber nanoelectrode arrays. Anal. Chim. Acta **744**, 45–53 (2012)
62. A. Salmeen, J.N. Andersen, M.P. Myers, N.K. Tonks, D. Barford, Molecular basis for the dephosphorylation of the activation segment of the insulin receptor by protein tyrosine phosphatase 1B. Mol. Cell. **6**, 1401–1412 (2000)
63. Z.Y. Zhang, D. Maclean, D.J. McNamara, T.K. Sawyer, J.E. Dixon, Protein tyrosine phosphatase substrate specificity: size and phosphotyrosine positioning requirements in peptide substrates. Biochemistry **33**, 2285–2290 (1994)
64. P.A. Cole, P. Burn, B. Takacs, C.T. Walsh, Evaluation of the catalytic mechanism of recombinant human CSK (C-terminal Src Kinase) using nucleotide analogs and viscosity effects. J. Biol. Chem. **269**, 30880–30887 (1994)
65. Y. Liu, K. Shah, F. Yang, L. Witucki, K.M. Shokat, Engineering Src family protein kinases with unnatural nucleotide specificity. Chem. Biol. **5**, 91–101 (1998)
66. J. Shaffer, G.Q. Sun, J.A. Adams, Nucleotide release and associated conformational changes regulate function in the COOH-terminal Src kinase, Csk. Biochemistry **40**, 11149–11155 (2001)
67. S.L. Z., P.A. M., S. Shishido, T.A. Nguyen, D.H. Hua, J. Li, Quantitative electrochemical detection of cathepsin B activity in complex tissue lysates using enhanced AC voltammetry at carbon nanofiber nanoelectrode arrays. Biosens. Bioelectron. **56**, 129–136 (2014)
68. L.Z. Swisher, A.M. Prior, M.J. Gunaratna, S. Shishido, F. Madiyar, T.A. Nguyen et al., Quantitative electrochemical detection of Cathepsin B activity in breast cancer cell lysates using carbon nanofiber nanoelectrode arrays toward identification of cancer formation. In press
69. T.E. McKnight, A.V. Melechko, D.W. Austin, T. Sims, M.A. Guillorn, M.L. Simpson, Microarrays of vertically-aligned carbon nanofiber electrodes in an open fluidic channel. J. Phys. Chem. B **108**, 7115–7125 (2004)

70. R.C. Pearce, J.G. Railsback, B.D. Anderson, M.F. Sarac, T.E. McKnight, J.B. Tracy et al., Transfer of vertically aligned carbon nanofibers to polydimethylsiloxane (PDMS) while maintaining their alignment and impalefection functionality. ACS Appl. Mater. Interfaces **5**, 878–882 (2013)
71. J. Kim, J. Elsnab, C. Gehrke, J. Li, B.K. Gale, Microfluidic integrated multi-walled carbon nanotube (MWCNT) sensor for electrochemical nucleic acid concentration measurement. Sens. Actuators B **185**, 370–376 (2013)
72. L.U. Syed, J. Liu, A.K. Price, Yi-f. Li, C.T. Culbertson, J. Li, Dielectrophoretic capture of E. coli cells at micropatterned nanoelectrode arrays. Electrophoresis **32**, 2358–2365 (2011)
73. P.U. Arumugam, H. Chen, A.M. Cassell, J. Li, Dielectrophoretic trapping of single bacteria at carbon nanofiber nanoelectrode arrays. J. Phys. Chem. A **111**, 12772–12777 (2007)
74. F.R. Madiyar, L.U. Syed, C.T. Culbertson, J. Li, Manipulation of bacteriophages with dielectrophoresis on carbon nanofiber nanoelectrode arrays. Electrophoresis **34**, 1123–1130 (2013)
75. J. Voldman, Electrical forces for microscale cell manipulation. Annu. Rev. Biomed. Eng. **8**, 425–454 (2006)
76. H.A. Pohl. Dielectrophoresis: the behavior of neutral matter in nonuniform electric fields. (Cambridge University Press, Cambridge, 1978)
77. F.R. Madiyar, S. Bhana, L. Swisher, C. Culbertson, X. Huang, J. Li Integration of nanostructured dielectrophoretic device and surface-enhanced raman probe for highly sensitive rapid bacteria detection. Nanoscale. **7**, 3726–3736 (2015)
78. H.A. Pohl, Nonuniform field effects in poorly conducting media. J. Electrochem. Soc. **107**, 386–390 (1960)
79. M.P. Hughes, H. Morgan, F.J. Rixon, J.P.H. Burt, R. Pethig Manipulation of herpes simplex virus type 1 by dielectrophoresis. Biochim. Biophys. Acta **1425**, 119–26 (1998)
80. M.P. Hughes, H. Morgan, F.J. Rixon, Dielectrophoretic manipulation and characterization of herpes simplex virus-1 capsids. Eur. Biophys. J. **30**, 268–272 (2001)
81. E.C. Dreaden, A.M. Alkilany, X. Huang, C.J. Murphy, M.A. El-Sayed, The golden age: gold nanoparticles for biomedicine. Chem. Soc. Rev. **41**, 2740–2779 (2012)
82. J. Kneipp, H. Kneipp, A. Rajadurai, R.W. Redmond, K. Kneipp, Optical probing and imaging of live cells using SERS labels. J. Raman Spectrosc. **40**, 1–5 (2009)
83. M.D. Porter, R.J. Lipert, L.M. Siperko, G. Wang, R. Narayanan, SERS as a bioassay platform: fundamentals, design, and applications. Chem. Soc. Rev. **37**, 1001–1011 (2008)
84. F.R. Madiyar, S. Bhana, L.Z. Swisher, X. Huang, C.T. Culbertson, J. Li, Integration of nanostructured dielectrophoretic device and surface-enhanced Raman Probe for highly sensitive rapid bacteria detection, Chapter 5, Nanoelectrode based devices for rapid pathogen detection and identification, Foram Madilar Ph.D. Thesis, Kansas State University, page 175 (2015).
85. T.E. McKnight, A.V. Melechko, G.D. Griffin, M.A. Guillorn, V.I. Merkulov, F. Serna et al., Intracellular integration of synthetic nanostructures with viable cells for controlled biochemical manipulation. Nanotechnology **14**, 551–556 (2003)
86. T.E. McKnight, A.V. Melechko, D.K. Hensley, D.G.J. Mann, G.D. Griffin, M.L. Simpson, Tracking gene expression after DNA delivery using spatially indexed nanofiber arrays. Nano. Lett. **4**, 1213–1219 (2004)
87. Z. Yu, T.E. McKnight, M.N. Ericson, A.V. Melechko, M.L. Simpson, B. Morrison, Vertically aligned carbon nanofiber arrays record electrophysiological signals from hippocampal slices. Nano. Lett. **7**, 2188–2195 (2007)
88. Z. Yu, T.E. McKnight, M.N. Ericson, A.V. Melechko, M.L. Simpson, B. Morrison Iii, Vertically aligned carbon nanofiber as nano-neuron interface for monitoring neural function. Nanomed. Nanotechnol. Biol. Med. **8**, 419–423 (2012)
89. J. Li, N.Q. Wu, Biosensors based on nanomaterials and nanodevices, in *Nanomaterials and their applications*, ed. by M. Meyyppan (CRC Press, Boca Raton, 2014), p. 517
90. F.R. Madiyar, et.al. Adv. Appl. Nanotechnol. Agric., Am. Chem. Soc. **1143**, 109–124 (2013)

Chapter 5
Photodynamic Therapy with Water-Soluble Cationic Fullerene Derivatives

Min Wang, Yingying Huang, Felipe F. Sperandio, Liyi Huang, Sulbha K. Sharma, Pawel Mroz, Michael R. Hamblin and Long Y. Chiang

5.1 Introduction

Photodynamic therapy (PDT) is a rapidly advancing treatment for multiple diseases. It is becoming more widely recognized as a valuable treatment option for localized cancers and precancers of the skin, mouth, larynx (voice box), and other places. Potential PDT treatments also involve other skin problems including psoriasis, atopic dermatitis, seborrheic dermatitis and keratosis, eczema, alopecia areata (scalp hair loss), and chronic cutaneous graft-versus-host disease. In general, there are a number of advantages for PDT over chemotherapy and radiotherapy showing no long-term side effects when proper PS is applied, noninvasive care with little or no scarring after the site heals as compared to surgery, highly targeted precision at the disease site, repeatable treatments at the same site if needed, less cost than other cancer treatments, and taking only a short period of time for each treatment to be

L. Y. Chiang (✉) · M. Wang
Department of Chemistry, Institute of Nanoscience Engineering Technology, University of Massachusetts Lowell, Lowell, MA 01854, USA
e-mail: Long_Chiang@uml.edu

Y. Huang · F. F. Sperandio · L. Huang · S. K. Sharma · P. Mroz · M. R. Hamblin
Wellman Center for Photomedicine, Massachusetts General Hospital, Boston, MA 02114, USA

Y. Huang · P. Mroz · M. R. Hamblin
Department of Dermatology, Harvard Medical School, Boston, MA 02115, USA

F. F. Sperandio
Instituto de Ciencias Biomedicas, Universidade Federal de Alfenas, Alfenas, MG, Brazil 37130-000

L. Huang
Department of Infectious Diseases, Guangxi Medical University, First Affiliated College & Hospital, Nanning 530021, China

M. R. Hamblin
Harvard-MIT Division of Health Sciences and Technology, Cambridge, MA 02139, USA

M. Zhang et al. (eds.), *Carbon Nanomaterials for Biomedical Applications,*
Springer Series in Biomaterials Science and Engineering 5,
DOI 10.1007/978-3-319-22861-7_5

practiced as an outpatient. The main limitation of PDT exists as its effectiveness shown only at treatment areas where light can reach. This implies that the major PDT medication should be performed in the lining of organs or just under the skin that can be reached by the light source.

The method of PDT is based on the administration of a nontoxic light-absorptive chromophore-dye drug, known as a photosensitizer (PS), systemically, locally, or topically to a patient bearing a tumor lesion or cancer [1], followed by illumination on the lesion with visible light. In the procedure, applied photoenergy activates the PS and, in the presence of molecular oxygen, leads to the generation of cytotoxic reactive oxygen species (ROS) that consequently results in the cell death and tissue destruction [2–6]. A semi-purified preparation of hematoporphyrin derivative (HPD) known as Photofrin® (PF, Axcan Pharma, Canada) was the first PS to gain regulatory approval for treatment of various cancers in a number of countries, including the USA [7, 8]. Other porphyrinoid and chlorin derivatives that have received approval from the US FDA and regulatory authorities in other countries include benzoporphyrin derivative monoacid ring A (BPD-MA, verteporfin or Visudyne for the treatment in combination therapies of ophthalmologic choroidal neovascularization, such as age-related macular degeneration (AMD), QLT Phototherapeutics, Canada), meta-tetra(hydroxyphenyl)chlorin (m-THPC or Foscan for the treatment of neck and scalp cancer, Biolitec, Germany), *N*-aspartyl chlorin-e6 (NPe6 for the treatment of lung cancer, Nippon Chemical, Japan), and precursors to endogenous protoporphyrin IX (PpIX): 1,5-aminolevulinic acid (ALA or Levulan® for treatments of actinic keratosis and esophageal dysplasia, DUSA, USA), methyl aminolevulinate (MAL, methyl ester of ALA, Metvixia® cream for treatment of some types of actinic keratoses of the face and scalp), and hexaminolevulinate (HAL). Additional texaphyrins (Lutrin) and sulfonated aluminum phthalocyanines (AlPcSn) analogs are under consideration for PDT drug applications and being evaluated currently at the stage of both preclinical and clinical trials [9].

The treatment of tumors using HPD–PDT was realized with several disadvantages, including prolonged skin sensitivity necessitating avoidance of sunlight for many weeks [10], suboptimal tumor selectivity [11], poor light penetration into the tumor due to the relatively short wavelength used (630 nm) [12], and the fact that it was a complex mixture of uncertain structure [13]. Therefore, much research effort has been made on developing new PSs [14, 15] for PDT in the literature. The vast majority of these compounds are based on the chemical structures with a tetrapyrrole aromatic nucleus backbone [16] found in many naturally occurring pigments such as heme, chlorophyll, and bacteriochlorophyll. Tetrapyrroles usually have a relatively large absorption band in the region of 400 nm known as the Soret band, and they have a set of progressively smaller absorption bands as the spectrum moves into the red wavelengths known as the Q bands. Another broad class of potential PS includes completely synthetic, non-naturally occurring, conjugated pyrrolic ring systems. These comprise structures such as texaphyrins [9], porphycenes [17], and phthalocyanines [18].

Some of the characteristics that the ideal PS should possess are (1) absorption bands at long wavelengths in the so-called optical window (600–900 nm where

the tissue is much more transparent) for sufficiently deeper tissue penetration of light to allow the treatment of larger tumors, (2) high absorption extinction coefficient (>20,000–30,000 $M^{-1}cm^{-1}$) of the band to minimize the dose of PS needed to achieve the desired PDT effect, (2) preferential uptake in target tissue, (3) high triplet and singlet oxygen quantum yields, (4) low photobleaching and high chemical and photostability, (5) intrinsic fluorescence to permit their detection by optical dosimetry (microscopy) techniques, and (6) low levels of dark toxicity to prevent harmful side effect to the surrounding normal tissue. The usefulness of various PSs proposed for antimicrobial PDT has to be judged on different criteria. One of the requirements is that an antimicrobial PS should be able to kill multiple classes of microbes at relatively low concentrations and low fluences of light. PS should be reasonably nontoxic in the dark and should show selectivity for microbial cells over mammalian cells. Up to the present date, there is no perfect PS that meets all the characteristics of an ideal PS. The reason why fullerenes are seen as potential PDT agents is that they possess some of the characteristics which render them well suited as a photosensitizing drug as detailed below.

Fullerene derivatives with condensed aromatic rings and an extended π-conjugated system of molecular orbitals are molecules of great potential for a variety of photonic applications that has drawn attention of physicists, chemists, and engineers. Although pristine C_{60} can form nanocrystalline preparations that have been reported to have biological activity [19–22], most researchers have studied chemically modified or functionalized fullerenes that acquire solubility in water or biologically compatible solvents and thereby have increased versatility [23–26]. Accordingly, these functionalized nanostructures (and others in the nanotechnology revolution) have been studied recently for their biological activities with a view to using them in medicine [27–29]. We are particularly interested in the biomedical PDT applications of fullerene derivatives [30] as a nonsurgical, minimally invasive approach that has been used in the treatment of solid tumors and many nonmalignant diseases [31]. PDT is a nonthermal photochemical reaction, which requires the simultaneous presence of a photosensitizing drug (PS), molecular oxygen, and visible light. It is a two-step procedure that involves the administration of a PS, followed by activation of the drug with the appropriate wavelength of light [1, 8, 32]. The photoactivation of the drug generates singlet oxygen and other ROS, which cause a lethal oxidative stress and membrane damage in the treated cells and in the case of tumors, leads to cell death by direct cytotoxicity and a dramatic antivascular action that impairs blood supply to the area of light exposure [3]. It is known that depending on the parameters involved, in vitro PDT can kill cancer cells via apoptosis, necrosis, or autophagy. The direct killing effect of PDT on malignant cancer cells that has been studied in detail in vitro, also clearly applies in vivo, but, in addition, two separate in vivo mechanisms leading to PDT-mediated tumor destruction have been described. They are the vascular shutdown effect mentioned above [33] and the PDT-induced activation of the host immune system [34]. In case of antimicrobial PDT, the gram-positive bacteria are found to be more susceptible as compared to the gram-negative bacteria. This observation is explained by the difference in the structure of their cell walls [35].

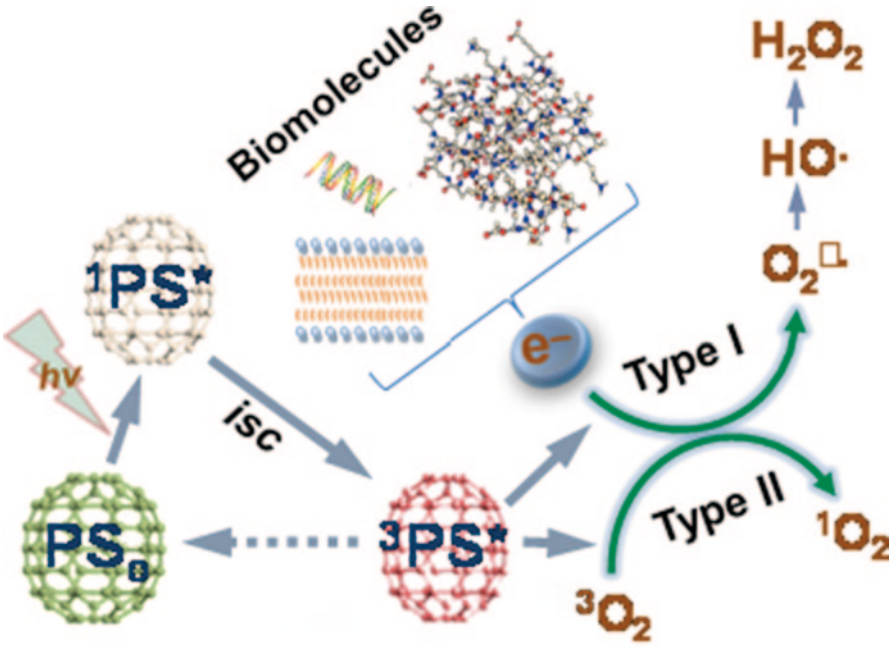

Fig. 5.1 A schematic outline of Type I and Type II photochemistry of fullerenes in producing ROS

In this chapter review, we cover the existing literature on fullerenes for PDT, summarize results from our laboratory, and outline future possibilities concerning applications of fullerenes as PS for PDT. Figure 5.1 gives a schematic outline of the PDT applications that have been reported for fullerenes either pristine or functionalized with various solubilizing groups.

5.2 Type I and Type II Photochemistry of Fullerene Derivatives

In the photophysical chemistry of PDT, the light is absorbed by the PS molecule and an electron is excited to the first excited singlet state. In addition to losing energy by fluorescence or internal conversion, the excited singlet can undergo the process known as intersystem crossing *(isc)* to the long-lived triplet state [3] $(PS)^*$. The excited triplet can then interact with ground state molecular oxygen ($^3O_2$) to form ROS. This process may occur either by the energy transfer from the excited triplet to $^3O_2$ to produce singlet oxygen ($^1O_2$) or by the electron transfer from the e^- donor to $^3(PS)^*$ to form superoxide anion ($O_2^{-\cdot}$) in the presence of $^3O_2$ [4], as shown in Fig. 5.1. Reaction of singlet oxygen with biological molecules, such as proteins, unsaturated lipids, and nucleic acids causing oxidative damage, is thought to be re-

sponsible for the cell death, frequently occurring via the apoptosis pathway initiated by mitochondrial damage [36].

In the case of fullerene derivatives, it is being increasingly realized that as compared with the standard Type II ROS (singlet oxygen), the ROS produced during PDT with fullerene derivatives are inclined towards Type I photochemical products (superoxide, hydroxyl radical, lipid hydroperoxides, and hydrogen peroxide). These two pathways ($^1O_2$ and $O_2^{-}\cdot$) are analogous to the Type II and Type I photochemical mechanisms frequently discussed in PDT with tetrapyrroles [37, 38]. It is known that both pristine and functionalized [60] fullerenes are able to catalyze the formation of ROS after illumination [39] in a similar fashion to the tetrapyrrole PS used for PDT. However, fullerenes dissolved in nonpolar organic solvents in the presence of oxygen seem to preferentially produce reactive singlet oxygen (Eq. 5.1) [40]. It is reasoned by the fact that the $C_{60}>$ cage of the derivative is excited from the S_0 ground state to a short-lived (~1.3 ns) S_1^* excited state upon photoexcitation with visible light. The S_1^* state rapidly decays to a lower lying triplet state T_1^* with a relatively long lifetime of 50–100 μs (Eq. 5.1). The $S_1^* \rightarrow T_1^*$ decay is formally a spin-forbidden *isc,* but is driven by an efficient spin–orbit coupling. In the presence of dissolved molecular oxygen ($^3O_2$), which exists as a triplet in its ground state, the fullerenyl T_1^* state is quenched (as a consequence of the quenching, its lifetime is reduced to ~330 ns) to generate singlet oxygen ($^1O_2^*$) by energy transfer at a rate of $2 \times 10^9\,M^{-1}s^{-1}$. The singlet oxygen quantum yield (φ_Δ) for this process (at 532 nm excitation) has been reported to be near theoretical maximum of 1.0 [40]. Example of $^1O_2$-production was demonstrated by highly water-soluble hexa(sulfobutyl)fullerenes (FC_4S) synthesized by the treatment of C_{60} in dimethoxyethane with sodium naphthalide (6.0 equiv.) followed by reacting the resulting hexaanionic fullerene intermediates with an excess of 1,4-butanesulfone [41]. Direct detection of $^1O_2$ production after irradiation at 500–600 nm of FC_4S self-assembled nanovesicles was obtained by the measurement of its near-infrared (NIR) luminescence at 1270 nm. Despite having a relatively low optical absorption of FC_4S at 600 nm, appreciable $^1O_2$ signal was detected comparable to that of Photofrin® at the same molar concentration, but less than sulfonated aluminum phthalocyanine (AlS_4Pc). The quantum yield of FC_4S for the generation of $^1O_2$ in H_2O was roughly estimated to be 0.36 using the relative correlation to that of C_{60} encapsulated in γ-cyclodextrin. These results demonstrated efficient energy transfer from [3] $(FC_4S)^*$ triplet state to molecular oxygen in the nanovesicle structure:

$$^1(C_{60}>) + h\nu \rightarrow {}^1(C_{60}>)^* \rightarrow {}^3(C_{60}>)^* + {}^3O_2 \rightarrow {}^1(C_{60}>) + {}^1O_2^*, \quad (5.1)$$

$$2[{}^1(C_{60}>)^* \text{ or } {}^3(C_{60}>)^*] + NADH \rightarrow 2[(C_{60}>)^-\cdot] + NAD^+ + H^+, \quad (5.2)$$

$$(C_{60}>)^-\cdot + O_2 \rightarrow C_{60}> + O_2^-\cdot, \quad (5.3)$$

$$2(O_2^-\cdot) + 2H^+ \rightarrow O_2 + H_2O_2, \quad (5.4)$$

$$H_2O_2 + Fe^{2+} \rightarrow OH\cdot + OH^- + Fe^{3+}, \quad (5.5)$$

$$Fe^{3+} + O_2^- \cdot \rightarrow Fe^{2+} + O_2 \cdot \quad (5.6)$$

In the presence of electron donors in polar solvents, especially those containing reducing agents such as nicotinamide adenine dinucleotide (NADH) at concentrations found in cells (Eq. 5.2), illumination of various fullerene derivatives will generate more Type I ROS, such as superoxide anions and hydroxyl radicals, than $^1O_2$ (Type II ROS) [42, 43]. The phenomena were correlated to C_{60}'s triply degenerate low-lying lowest unoccupied molecular orbital (LUMO) making it an excellent electron acceptor capable of accepting as many as six electrons, as demonstrated in cyclic voltammetry measurements [44]. There is some evidence that fullerenyl excited states (in particular the triplet) are even better electron acceptors than the corresponding ground state, forming the anionic C_{60} radical ($C_{60}^{-\cdot}$) [45]. Subsequent intermolecular electron transfer from the reduced fullerene triplet or radical anion to molecular oxygen forms superoxide anion radical ($O_2^{-\cdot}$, Eq. 5.3). It has been shown that this photophysical process is highly solvent dependent, whereas $^1O_2$ was generated effectively by photoexcited C_{60} in nonpolar solvents, such as benzene and toluene, while $O_2^{-\cdot}$ and $OH\cdot$ were produced in polar solvents such as benzonitrile and water [46]. The other evidence was shown by Miyata et al. using solubilized fullerenes in water with polyvinylpyrrolidone (PVP) as a detergent [47]. Visible light irradiation of PVP-solubilized C_{60} in water in the presence of NADH, as a reductant, and molecular oxygen resulted in the formation of $O_2^{-\cdot}$, which was detected by the electron paramagnetic resonance (EPR) spin-trapping method. Formation of $O_2^{-\cdot}$ was also evidenced by the direct observation of a characteristic signal of $O_2^{-\cdot}$ by the use of a low-temperature EPR technique at 77 K. On the other hand, no formation of $^1O_2$ was observed by the use of tetramethylpiperidine oxide (TEMP) as a $^1O_2$ trapping agent. No NIR luminescence of $^1O_2$ was also observed in the aqueous C_{60}/PVP/O_2 system. These results suggest that photoinduced bioactivities of the PVP-solubilized fullerene are caused not by $^1O_2$ but by reduced oxygen species such as $O_2^{-\cdot}$, which are generated by the electron transfer reaction of $C_{60}^{-\cdot}$ with molecular oxygen. Furthermore, in the biological system, hydrogen peroxide is formed by dismutation of superoxide anion (Eq. 5.4). Fenton chemistry (using small amounts of ferrous iron found in cells) is able to produce hydroxyl radicals from hydrogen peroxide (Eq. 5.5), while the Haber–Weiss reaction is able to reduce ferric iron back to ferrous iron in order to continue the cycle by regenerating the active divalent ferrous iron (Eq. 5.6). In two recent reports [48, 49], we studied the PS properties of two series of three functionalized fullerene compounds, one series with polar diserinol groups (BF1–BF3) and a second series of three compounds with quarternary pyrrolidinium groups (BF4–BF6; Fig. 5.2). We asked the question whether the photodynamic effects displayed by these compounds operated primarily by Type I mechanisms (superoxide) or Type II mechanisms (singlet oxygen) or a mixture of both and whether there was any difference between a fullerene (BF4) that was highly effective in killing cancer cells and a fullerene (BF6) that was highly effective in killing pathogenic microorganisms (see later).

The photochemical mechanism studies confirmed that depending on the precise conditions of the experiment, illuminated fullerenes can produce both superoxide

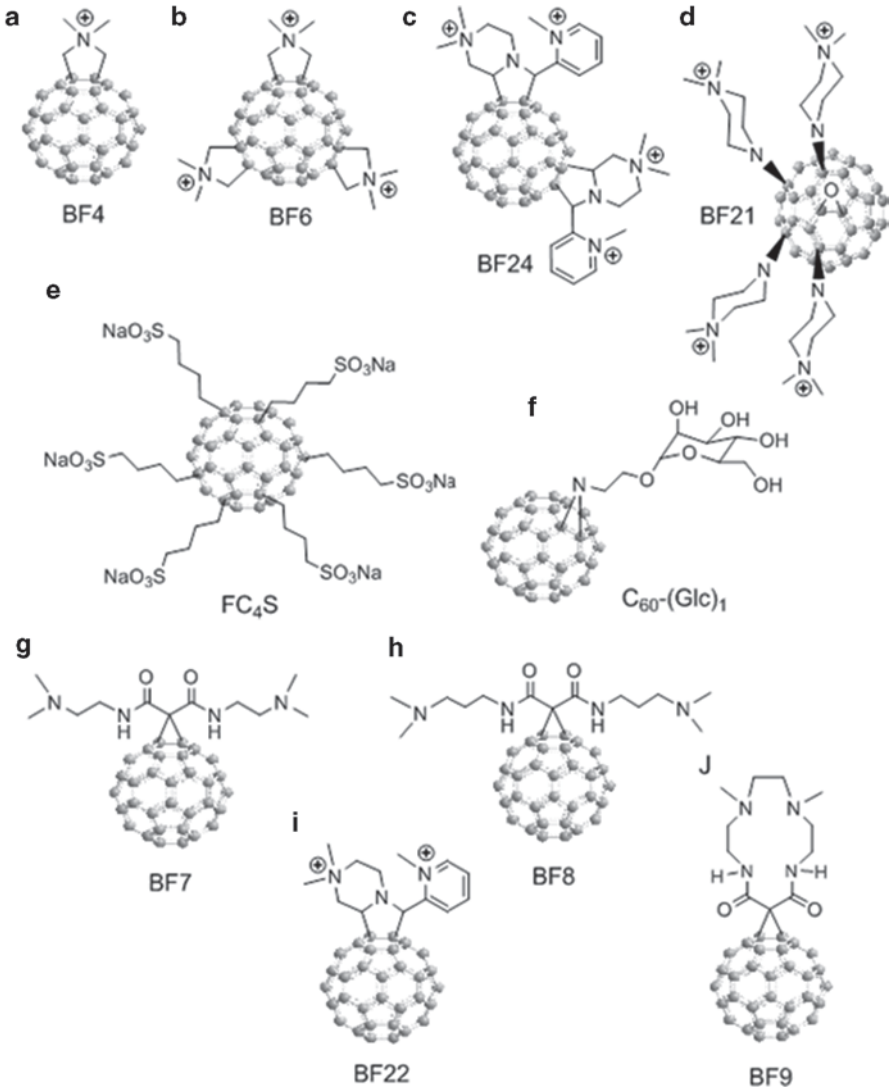

Fig. 5.2 Chemical structures of ten functionalized fullerenes used for PDT. **a** mono-pyrrolidinium fullerene, BF4, **b** tris-pyrrolidinium fullerene BF6, **c** tetracationic fullerene BF24, **d** tetracationic fullerene BF21, **e** hexaanionic fullerene FC_4S, and **f** mono-glycosylated fullerene C_{60}–$(Glc)_1$

and singlet oxygens. The singlet oxygen production of the more hydrophobic BF4 dropped to almost zero when the solvent was changed from organic to aqueous. This is consistent with the aggregation of the compound in aqueous media, while the more polar BF6 remained completely in solution. The production of superoxide as measured by specific EPR spin trapping was as expected much higher in the presence of a reducing agent (NADH) than in the presence of a singlet oxygen trap

(histidine). In both cases, BF6 gave more superoxide than BF4, and the difference was significant in the presence of NADH. The fact that the reduction of oxygen consumption by both BF4 and BF6 was almost completely inhibited by azide in the presence of histidine confirmed that in the absence of an electron donor and in the presence of a singlet oxygen substrate, the mechanism is almost all Type II for both fullerenes. However, in the presence of NADH, the relative reduction of oxygen consumption by azide was much less and proportionately lower for BF6 than for BF4 suggesting that about 40 % of the oxygen was transformed into superoxide, and the overall production was higher for BF6 than for BF4.

One apparent contradiction that arises in this area is the observation that most of fullerene derivatives are able to act as effective antioxidants or scavengers of ROS. These antioxidant effects of C_{60} derivatives have generally been studied in the absence of light [21, 50–58]. How then can we reconcile the established ability of fullerene derivatives to scavenge ROS acting as antioxidants and at the same time demonstrate the ability to operate as efficient producers of ROS under illumination with the correct light parameters? It was assumed that the double (sp^2) bonds of the fullerene cage reacted with ROS forming covalent sp^3 bonds thereby reducing the quantity of ROS to react with sensitive biomolecules similar to those damaged during PDT. If this hypothesis were true, it would be difficult to explain how fullerenes could act as efficient generators of ROS during PDT. A hypothesis that may explain this seeming contradiction was reported in 2009 by Andrievsky et al. [59]. The report showed that the main mechanism by which hydrated C_{60} can inactivate the highly reactive ROS, hydroxyl radical, is not by covalently scavenging the radicals, but rather by action of the coat of "ordered water" that was associated with the fullerene nanoparticle [60]. Andrievsky et al. claimed that the ordered water coat could slow down or trap the hydroxyl radicals for sufficient time for two of the hydroxyl radicals to react with each other thus producing the less reactive ROS, hydrogen peroxide. The alternative argument includes the competitive diffusion rate of ROS away from the fullerene cage region and the reaction kinetic rate between ROS and fullerene cage. The ROS production efficiency of fullerenes decreases as the degree of functionalization increases, including the attack of ROS. To fully eliminate the ROS production capability of fullerenes, the number of addends on each C_{60} cage may have to reach an estimated figure of >16–18 that allows the monoadducts and bisadducts to uphold a sufficiently long ROS production period before being converted to polyhydroxylated derivatives.

5.3 Fullerene Derivatives as Candidates of PSs for PDT

Rapidly growing interest in the medical application of fullerenes in the area of nanotechnology and nanomedicines [61] led to considerable gain and attention for the use of these nanostructures [62] as possible PS for mediating PDT of various diseases. Pristine C_{60} is highly insoluble in water and biological media and forms nanoaggregates that prevent its efficient photoactivity [63]. However, when fullerenes are derivatized by attaching hydrophilic functional groups to the carbon cage

making them soluble in water and biological solvents, their biological usefulness is markedly improved [64]. Different hydrophilic or amphiphilic side chains or fused ring structures have been covalently bound to the spherical C_{60} core. This functionalization imparts a higher ability to produce singlet oxygen, hydroxyl radicals, and superoxide anion upon illumination due to the interruption of forbidden highest occupied molecular orbital (HOMO)–LUMO transition of C_{60} that increases the visible absorption of derivatives at long wavelengths. Accordingly, these reactive species produced by functionalized C_{60} have been proposed as effective PDT mediators in several applications. Some of the advantages that fullerene derivatives possess over the traditional PS used for PDT are:

1) Fullerenes are comparatively more photostable and demonstrate less photobleaching compared to tetrapyrroles and synthetic dyes.
2) Fullerenes show both kinds of photochemistry comprising Type I (free radicals) and Type II (singlet oxygen) while tetrapyrroles demonstrate largely Type II photochemistry.
3) Fullerenes can be chemically modified for tuning the drug's partition coefficient (Log P or partition coefficient for [drug in *n*-octanol]/[drug in H_2O]) and pK_a values for the variation of in vivo lipophilicity and the prediction of their distribution in biological systems.
4) Fullerenes can be chemically attached by light-harvesting chromophore antennae to extend their absorption spectrum further into the red wavelengths and, thus, enhance the overall quantum yield and the ROS production
5) Fullerene cages are prone to undergo molecular self-assembly into vesicles that allows the formation of self-assembled nanoparticles, as so-called fullerosomes or buckysomes, for improved drug delivery.The resulting fullerosomes may have different tissue-targeting properties.

Besides these advantages, fullerenes show some disadvantages though they can be overcome by applying special strategies. One of the concerns for the use of fullerenes is questions concerning biodegradibility as nanostructures with conceivable possibility of accumulation in the environment during blood circulation [65]. However, studies have concluded that C_{60} itself is remarkably nontoxic [21]. Another concern was their extreme cage hydrophobicity and innate tendency to aggregate, which renders them less promising for application as drugs in biomedicine. For the remedy, some strategies have been illustrated or applied to either solubilize or modify fullerenes for improving the drug delivery of fullerenes, for example, liposomes [66–68], micelles [69, 70], dendrimers [71, 72], polyethylene glycol (PEG) ylation [73–76], cyclodextrin encapsulation [77, 78], and self-nanoemulsifying systems (SNES) [79–82] to overcome this shortcoming of fullerenes. Other than these disadvantages, the main optical absorption band of fullerenes is in the blue and green regions, whereas the absorption spectra of tetrapyrrole PS, except porphyrins, such as chlorins, bacteriochlorins, and phthalocyanines, have been designed to exhibit substantial absorption peaks in the red or far-red regions of the spectrum. For PS to be useful in vivo, it is considered that the light used to excite them should be in the red/NIR spectral region where scattering and absorption of light by tissue is minimized. This unfavorable absorption spectrum of fullerenes can be overcome by

various strategies such as covalent attachment of light-harvesting antennae to fullerenes [83–89] by using optical clearing agents [90–94] or by applying two-photon excitation where two NIR photons are simultaneously delivered to be equivalent to one photon of twice the energy (and half the wavelength, so that two 800-nm photons are equivalent to one 400-nm photon) [89, 95–99].

5.4 Synthesis of Fullerenyl PSs

5.4.1 Example 1: Synthesis of Monocationic and Polycationic Fullerene Derivatives

Cationic functional groups are generally considered as the addend of choice for attachment on the fullerene cage due to their potential surface-binding contact with anionic residues of the bacteria cell wall via static charge interactions. A systematic trend to increase the number of positive charges per fullerene cage was observed in the recent report [49, 100, 101] to maximize such interactions and use them as the approach for targeting bacteria having a significant density of anionic residues at the cell wall surface. A number of chemical functionalization methods of fullerenes have been reviewed [23, 102–104]. Among them, common convenient methods for the preparation of cationic fullerene derivatives include cyclopropanation [105] and pyrrolidination [106] reactions due to their high consistency in the product reproducibility. Examples of the latter were given in the preparation of quaternized dimethylpyrrolidinium [60] fullerenyl monoadduct (BF4) and trisadduct (BF6) [107, 108]. In a typical reaction condition, C_{60} was treated with 1.0 or 3.0 equivalent of *N*-methylglycine (sarcosine) and paraformalaldehyde in toluene at the reflexing temperature to afford either mono-*N*-methylpyrrolidino[60] fullerene or a large number of regioisomers of tris(*N*-methylpyrrolidino)[60] fullerene derivatives, as shown in Fig. 5.3. Upon quaternization of these intermediates using methyl iodide as the methylation agent, corresponding monocationic and tricationic products as BF4 and BF6 were obtained, respectively. Similarly, the reaction of C_{60} in toluene with either 1.0 or 2.0 equivalent of azomethine ylide produced by piperazine-2-carboxylic acid dihydrochloride dissolved in methanol and triethylamine in the presence of 4-pyridinecarboxaldehyde at the refluxing temperature gave the corresponding mono-piperazinopyrrolidino[60] fullerene or a number of regioisomers of bis(piperazinopyrrolidino)[60] fullerene derivatives. Quaternization of both intermediates with methyl iodide led to the corresponding monocationic and dicationic products as BF22 and BF24, respectively.

In the case of cyclopropanation reaction of C_{60} as the functionalization method, it was applied recently for the attachment of a highly complex decacationic moiety to the fullerene cage leading to the formation of $C_{60}[>M(C_3N_6{}^+C_3)_2]\text{-}(I^-)_{10}$ (LC14) [109, 110] and $C_{70}[>M(C_3N_6{}^+C_3)_2]\text{-}(I^-)_{10}$ (LC17) [101], as shown in Fig. 5.4. The decacationic functional moieties of C_{60}, C_{70}, and $C_{84}O_2$ fullerenes were designed to both increase the water solubility and provide surface-binding interactions with *–D-*

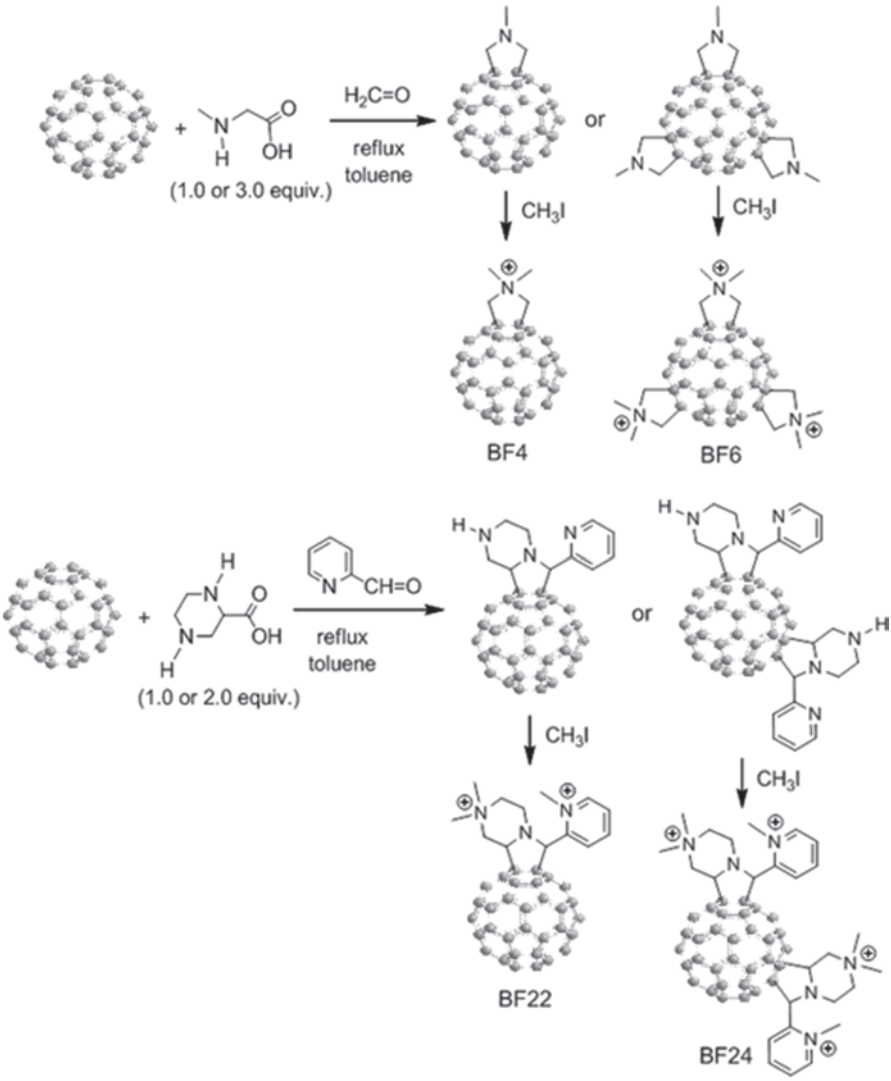

Fig. 5.3 Synthesis of monocationic (BF4) and tricationic dimethylpyrrolidinium[60] fullerenes (BF6) and mono- (BF22) and bis(piperazinopyrrolidinium)[60] fullerenes (BF24)

Ala-*D*-Ala residues of the bacteria cell wall by incorporating multiple H bondings and positive quaternary ammonium charges. It included two esters and two amide moieties to give a sufficient number of carbonyl and –NH groups in a short length of ~20 Å to provide effective multi-binding sites with the use of a well-defined water-soluble pentacationic moiety $C_3N_6{}^+C_3$-OH at each side of the arm. In the synthetic reaction, a malonate precursor arm $N_6{}^+C_3$ was reported to be a common synthon for the structural modification of PDT nanomedicines. It was derived from the quaternization of *N,N′,N,N,N,N*-hexapropyl-hexa(aminoethyl)amine precursor N_6C_3. The

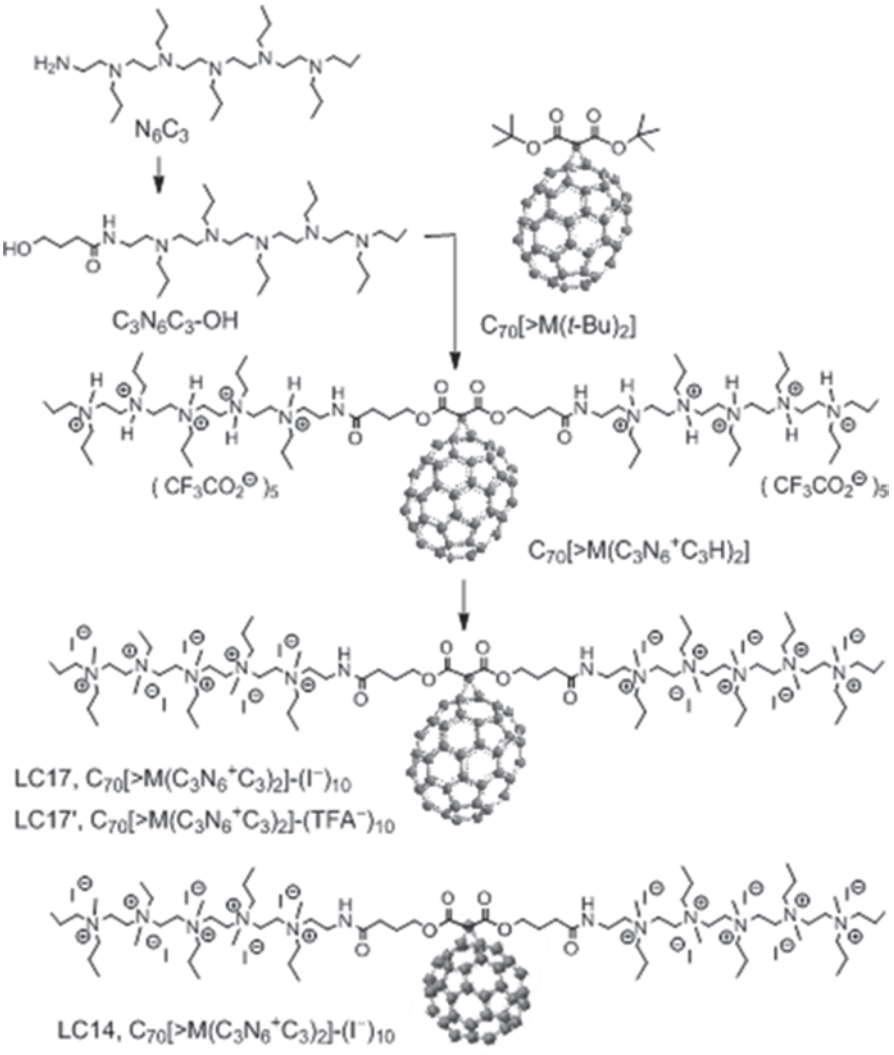

Fig. 5.4 Synthesis of $C_{60}[>M(C_3N_6^+C_3)_2]$-$(I^-)_{10}$ (LC14) and $C_{70}[>M(C_3N_{6+}C_3)_2]$-$(I^-)_{10}$ (LC17)

best method for the preparation of $C_{60}[>M(C_3N_6^+C_3)_2]$ and $C_{70}[>M(C_3N_6^+C_3)_2]$ was depicted in Fig. 5.4 to begin with a well-defined fullerene monoadduct derivatives, such as di(*tert*-butyl)fullerenyl malonates $C_{60}[>M(t\text{-}Bu)_2]$ and $C_{70}[>M(t\text{-}Bu)_2]$, respectively, followed by facile trans-esterification reaction with the well-characterized tertiary-amine precursor arm moiety, 4-hydroxy-[*N,N′,N,N,N,N*-hexapropyl-hexa(aminoethyl)butanamide ($C_3N_6C_3$-OH) using trifluoroacetic acid as the catalytic reagent to afford protonated quaternary ammonium trifluoroacetate salt $C_{70}[>M(C_3N_6^+C_3H)_2]$. Conversion of this salt to $C_{70}[>M(C_3N_6^+C_3)_2]$ was accompanied by neutralization of trifluoroacetic acid by sodium carbonate and subsequent quaternization by methyl iodide to give decacationic quaternary

ammonium iodide salts. A similar conversion procedure was applied for the case of $C_{60}[>M(C_3N_6{}^+C_3)_2]$. This synthesis represented the first examples of decacationic fullerene monoadducts to incorporate a well-defined high number of cation without the use of multiple addend attachments to preserve the intrinsic photophysical properties of fullerene cages.

Similar reaction sequence with a malonate precursor arm $M(C_3N_6C_3)_2$ was also applied for the preparation of $C_{84}O_2[>M(C_3N_6{}^+C_3)_2]$-$(I^-)_{10}$(LC19) [111], as shown in Fig. 5.5. The decacationic arm was prepared by first the treatment of *N,N′,N,N,N,N*-hexapropyl-hexa(aminoethyl)amine N_5C_3–NH_2 with γ-butyrolactone (1.15 equiv.) in CH_2Cl_2 in the presence of $BF_3{\cdot}Et_2O$−Et_3N at room temperature for overnight to give the product of 4-hydroxy-*N*-(3,6,9,12,15-pentapropyl-3,6,9,12,15-pentaazaoctadecyl)-butanamide, $C_3N_6C_3$–OH, as viscous light yellow liquid in 60% yield. Incorporation of $C_3N_6C_3$–OH on the malonate moiety was carried out by an esterification reaction with malonyl chloride in anhydrous dichloromethane at 0 °C to room temperature in the presence of pyridine to afford bis-[*N,N′,N,N,N,N*-hexapropylhexa(aminoethyl)amino]carbonyl-propanoxymalonate, $M(C_3N_6C_3)_2$, in a yield of 78%. Quaternization of $M(C_3N_6C_3)_2$ to the corresponding quaternary methyl ammonium iodide salt, $M(C_3N_6{}^+C_3)_2$, was performed in anhydrous dimethylformamide (DMF) with an excess of iodomethane added in portions at 45 °C for a period of 3.0 days. Its reaction with $C_{84}O_2$ was carried out by the cyclopropanation reaction in a solvent mixture of toluene−DMF in the presence of 1.8-diazabicyclo[5.4.0]-undec-7-ene (DBU) using iodine as the halogenation agent. To ensure the formation of a monoadduct only and minimize the possibility of multi-adducts as by-products, an excess quantity of fullerenes was applied. The resulting product bis(20-oxo-4,7,10,13,16-pentapropyl-4,7,10,13,16,19-hexaaza-tricosan-23-yl)-diepoxy [83] fullerenyl malonate quaternary methylammonium triiodide salt, $C_{84}O_2[>M(C_3N_6{}^+C_3)_2]$ (LC19-I_3^-), were obtained in a yield of 60% as brown solids. Subsequent attachment of the second bis-hexa(aminoethyl)amidated malonate $M(C_3N_6C_3)_2$ to LC19 was carried out by nearly identical cyclopropanation reaction conditions as those for the preparation of LC17 and LC19. Brown solids of decacationic bis[bis(20-oxo-4,7,10,13,16-pentapropyl-4,7,10,13,16,19-hexaaza-tricosan-23-yl)malonato]-diepoxy-[83] fullerene quaternary methylammonium iodide salt, $C_{84}O_2[>M(C_3N_6{}^+C_3)_2][>M(C_3N_6C_3)_2]$(LC20) 112, were isolated in a yield of 85% after the removal of iodine in complexation with iodide for the procedure. Similarly, decacationic bis-[bis(20-oxo-4, 7, 10, 13, 16-pentapropyl-4, 7, 10, 13, 16, 19-hexaaza-tricosan-23-yl)malonato][70]fullerenene quaternary methylammonium iodide salt, $C_{70}[>M(C_3N_6{}^+C_3)_2][>M(C_3N_6C_3)_2]$(LC18) was synthesized in a yield of 65%.

5.4.2 *Example 2: Synthesis of Hexaanionic Fullerene Derivatives*

Fullerene molecules are highly hydrophobic. It can be dispersed into aqueous medium in a micelle form with the application of surfactants. However, the micelle

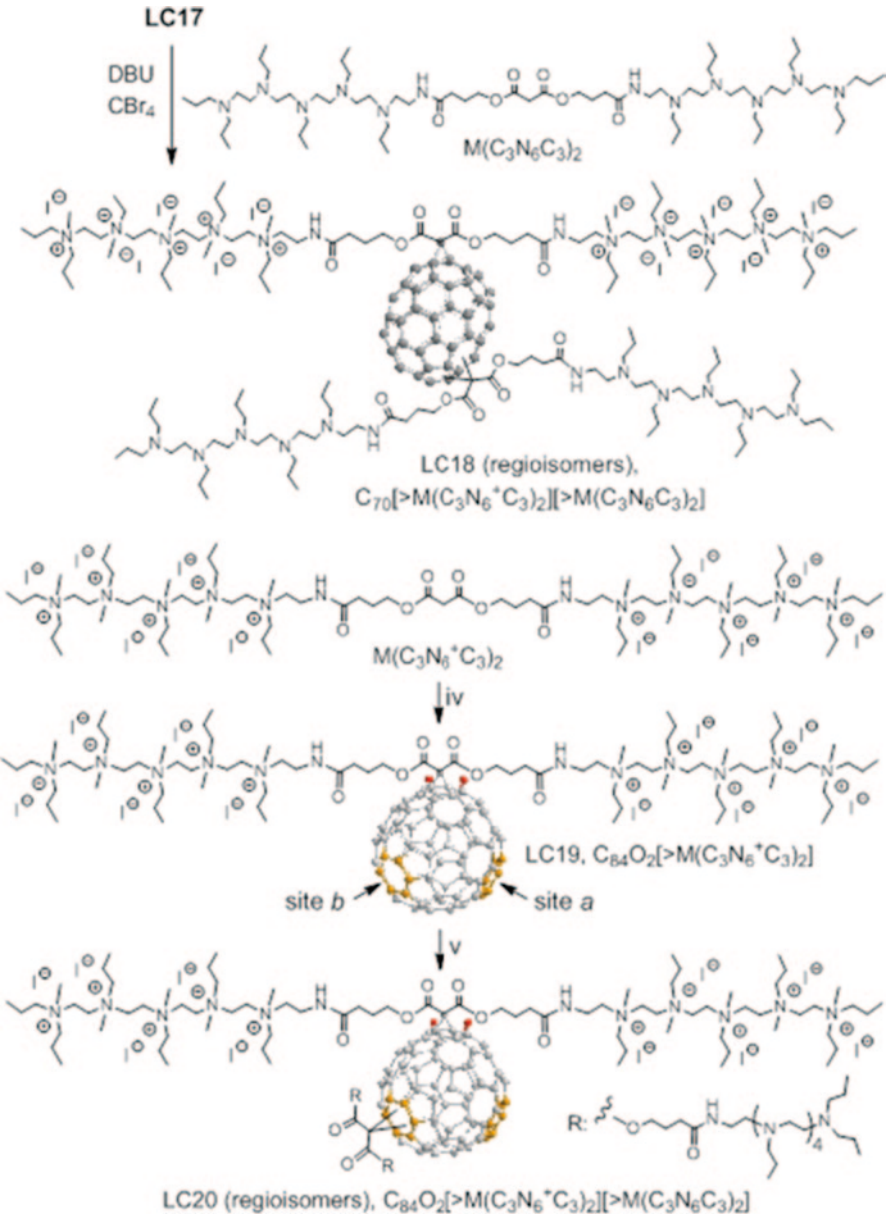

Fig. 5.5 Structures of $C_{70}[>M(C_3N_{6+}C_3)_2]$ $[>M(C_3N_6C_3)_2]$ (LC18) and $C_{84}O_2$ analogs LC19 and LC20

structure may not be stable enough in biological environment. In a recent report, a strategy of creating a covalently bonded surfactants directly on the fullerene cage was made in the synthesis of hexa(sulfo-*n*-butyl)-C_{60} (FC_4S) leading to structurally stable *molecular micelle* in H_2O [53]. The synthesis involves the use of hexaanionic

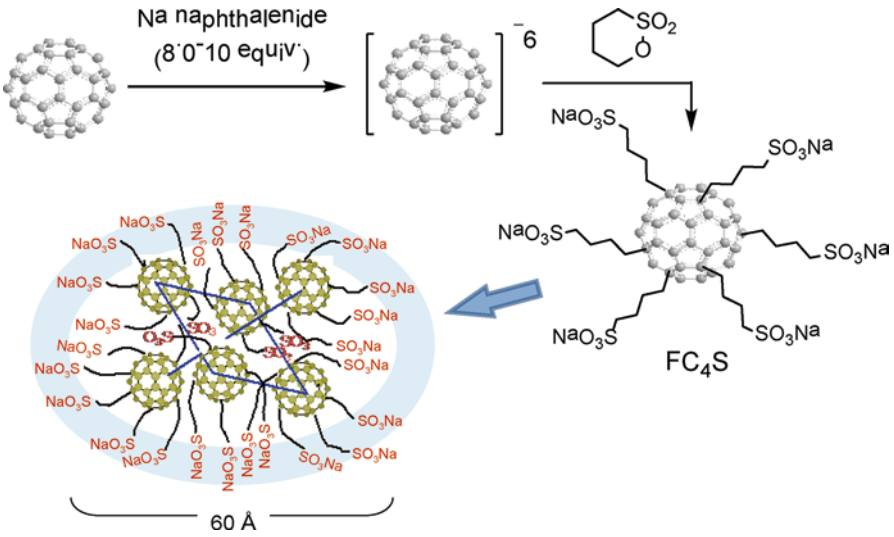

Fig. 5.6 Synthesis and nanovesicle of hexaanionic hexa(sulfo-*n*-butyl)-C_{60} (FC_4S)

C_{60} (C_{60}^{-6}) chemistry for attaching six sulfo-*n*-butyl arms on C_{60} in one-pot reaction, as shown in Fig. 5.6.

5.4.3 Synthesis of Light-Harvesting Chromophore Antenna-Linked Fullerene Derivatives

Fullerenes are nanocarbon cages with all sp^2 carbons interlinked in a structure of hollow sphere. Highly strained curving regions of the cage surface consist of chemically reactive six fulvalenyl bridging olefins that can be utilized for making nucleophilic addition reactions. Chemical modification of C_{60} on only a limited number of functionalization sites may not lead to much alternation of the cage's photophysical properties. Conversely, nucleophilic addition of one or two light-harvesting antenna chromophores will largely enhance the cage's ability to respond and perform various photoinduced electronic and energy-related events by acting as an electron acceptor [42, 45]. The most abundant [60]fullerene is more readily available commercially in up to kilogram quantities than a number of higher fullerenes. However, its visible absorption extinction coefficient is rather low. To circumvent this shortcoming, several reported approaches were described to use the highly fluorescent donor chromophore antenna attachment as light-harvesting antenna units, such as porphyrin [112, 113] or dialkyldiphenylaminofluorene (DPAF-C_n), to enhance visible absorption of the resulting conjugates and, in the latter cases, also two-photon absorption (2PA) cross-sections in the NIR wavelengths [114–116]. The absorbed photoenergy by the donor antenna was able to undergo efficient intramolecular transfer to the fullerene acceptor moiety, leading to the generation of excited triplet

cage state $^3(C_{60}>)^*$ after the *isc* from its excited singlet state $^1(C_{60}>)^*$. Triplet energy transfer from $^3(C_{60}>)^*$ to molecular oxygen produces singlet oxygen ($^1O_2$) that gives the cytotoxic effect to the cells in the Type II photochemistry [117, 118]. Attachment of donor antenna DPAF-C_n was designed to occur at a very close vicinity of C_{60} cage via a periconjugation linkage, within a contact distance of 2.6–3.5 Å, to facilitate ultrafast intramolecular energy transfer and electron transfer from the donor antenna to C_{60} for enhancing PDT efficacy. This specific donor antenna was first introduced to give an increased optical absorption at 400 nm that led to the realization of ultrafast intramolecular energy transfer and/or electron transfer from photoexcited antenna moiety to C_{60} in <130–150 fs [116] that made this type of C_{60}–antenna conjugates, $C_{60}(>\text{DPAF-C}_n)_x$, capable of exhibiting photoresponse in a nearly instantaneous time scale to protect against high-intensity radiation. By increasing the number of attached antennae to four per C_{60} cage giving starburst pentad nanostructures, highly enhanced fs 2PA cross-section values were observed in a concentration-dependent manner [119]. Upon the chemical alteration of the keto group of $C_{60}(>\text{DPAF-C}_n)$ bridging between C_{60} and the antenna moiety to a highly electron-withdrawing 1,1-dicyanoethylenyl (DCE) group, it was possible to extend the π-conjugation in the resulting dark burgundy-red C_{60}(>cyanophenylaminofluorene (CPAF)-C_n) analogous chromophore molecules to a close contact with the cage current. This led to a large bathochromic shift of the linear optical absorption of $C_{60}(>\text{CPAF-C}_2)$ moving from 410 nm (λ_{max}) of the parent keto-compound to 503 nm with the shoulder band being extended beyond 550 nm in the UV-visible spectrum. The shift considerably increased its light-harvesting ability in visible wavelengths and caused a nearly sixfold higher production of quantum yield of singlet oxygen ($^1O_2$) from $C_{60}(>\text{CPAF-C}_{2M})$ as compared with that of $C_{60}(>\text{DPAF-C}_{2M})$. The mechanism of $^1O_2$ production was originated from the intermolecular triplet energy transfer from the $^3(C_{60}>)^*$ cage moiety to $^3O_2$. A large increase in the production of ROS by excited $C_{60}(>\text{CPAF-C}_{2M})$ explained its effective photokilling of HeLa cells in vitro, via 1γ-PDT [120]. The observation demonstrated the intramolecular and intramolecular interaction between the excited CPAF-C_n donor antenna moiety and the acceptor C_{60} cage that was also confirmed by transient absorption spectroscopic measurements using nanosecond (ns) laser pulses at 480–500 nm [121]. The behavior resembles that of DPAF-C_n antenna with transient photoexcitation at 380–410 nm reported previously [122].

Preparation of $C_{60}(>\text{CPAF-C}_{2M})$, as an example, was made by Friedel–Craft acylation of 9,9-dimethoxyethyl-2-diphenylaminofluorene with bromoacetyl bromide in the presence of $AlCl_3$ to yield 7-bromoactyl-9,9-dimethoxyethyl-2-diphenylamino-fluorene, followed by cyclopropanation reaction with C_{60}, as shown in Fig. 5.7. The resulting product $C_{60}(>\text{DPAF-C}_{2M})$ was then further treated with malanonitrile and pyridine in the presence of titanium tetrachloride in dry toluene to yield $C_{60}(>\text{CPAF-C}_{2M})$ after chromatographic purification. Similarly, selective attachment of two antenna moiety types DPAF-C_n and CPAF-C_n in combination as hybrid chromophore addends to a single C_{60} cage was made to result in the formation of new methano[60]fullerene triads, $C_{60}(>\text{DPAF-C}_{18})(>\text{CPAF-C}_{2M})$, and tetrads, $C_{60}(>\text{DPAF-C}_{18})(>\text{CPAF-C}_{2M})_2$ (Fig. 5.7). The core chromophore moiety of triads and tetrads will be capable of performing dual-band 2γ-PDT-based

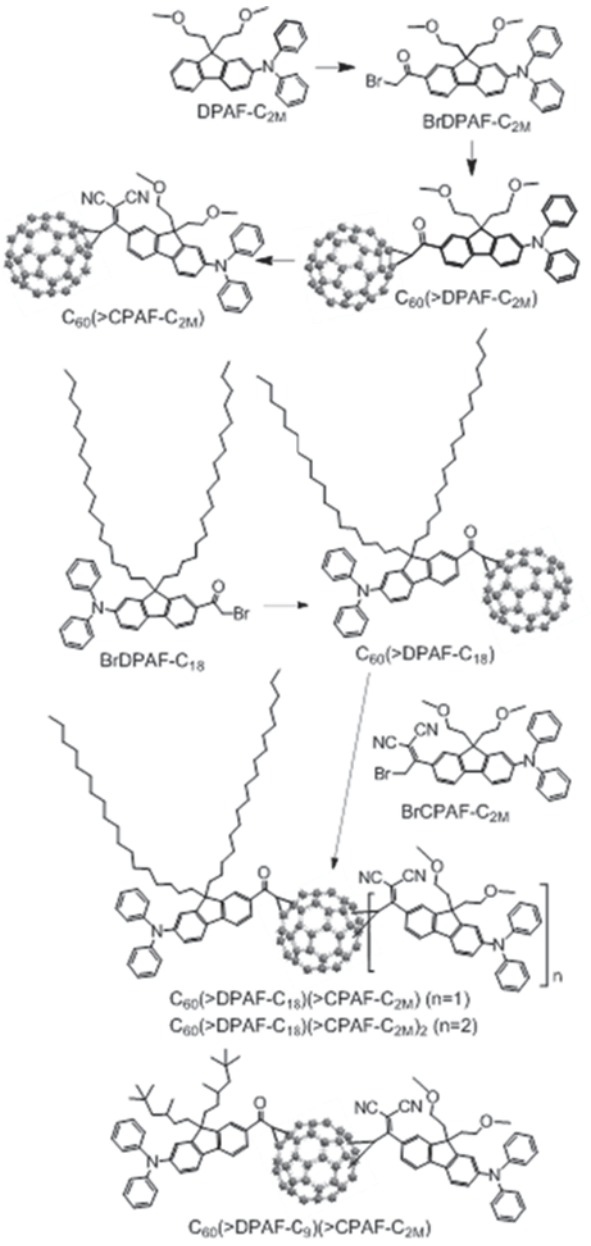

Fig. 5.7 Synthetic method of C_{60}(> CPAF-C_{2M}), triads C_{60}(> DPAF-C_{18}) (> CPAF-C_{2M}), and tetrads C_{60}(> DPAF-C_{18}) (> CPAF-C_{2M})$_2$. DPAF dialkyldiphenylaminofluorene

photoinduced biocidal effects with enhanced penetration depth at 800–1100 nm. Synthetically, preparation of triads and tetrads was accomplished by the synthesis of a structurally well-defined monoadduct C_{60}(> DPAF-C_{18}) followed by the attachment of one or two CPAF-C_{2M} antenna in sequence. A key intermediate precursor, 7-α-bromoacetyl-9,9-dioctadecyl-2-diphenylaminofluorene, BrDPAF-C_{18}, was

prepared by a three-step reaction involving first palladium-catalyzed diphenylamination of commercially available 2-bromofluorene at the C2 position of the fluorene ring to afford DPAF. It was followed by dialkylation at the C9 carbon position of DPAF using 1-bromooctadecane as the reagent in the presence of potassium *t*-butoxide, as a base, in tetrahydrofuran (THF) to give the corresponding 9,9-dioctadecyl-2-diphenylaminofluorene (DPAF-C_{18}) in 97% yield. Friedel–Crafts acylation of DPAF-C_{18} with α-bromoacetyl bromide and $AlCl_3$ afforded the compound BrDPAF-C_{18} in a yield of 96%. Its addition reaction to C_{60} was carried out in the presence of 1,8-diazabicyclo[5.4.0]undec-7-ene (DBU, 1.0 eq.) to result in C_{60}(>DPAF-C_{18}) in 65% yield after column chromatographic purification.

A similar reaction sequence was applied for the synthesis of the compound C_{60}(>CPAF-C_{2M}) by replacing two octadecyl groups with 2-methoxyethyl groups. Thus, conversion of the keto group of BrDPAF-C_{2M} to the corresponding DCE group was carried out by the reaction using malononitrile as a reagent, pyridine as a base, and titanium tetrachloride as a deoxygenation agent in dry chloroform. The reaction resulted in the corresponding diphenylaminofluorene BrCPAF-C_{2M} in a yield of 89% after chromatographic purification. Attachment of a CPAF-C_{2M} antenna arm to a C_{60} cage was carried out with DBU (1.0 eq.) to afford 7-(1,2-dihydro-1,2-methanofullerene[60]-61-{1,1-dicyanoethyl-ene})-9,9-di(methoxyethyl)-2-diphenylaminofluorene, C_{60}(>CPAF-C_{2M}), as orange red solids in 53% yield. The bulkiness of DPAF-C_{18} and CPAF-C_{2M} in size can prevent these two types of antenna moieties form locating in close vicinity to each other at the cage surface. By considering the regio-location of reactive bicyclopentadienyl olefin bonds on the fullerene surface, when the first antenna is bound at the north-pole location, the second antenna arm is most likely to be pushed away to the equator area of the C_{60} sphere. Therefore, only a very limited number of multiadduct regioisomers per C_{60} are likely to form. Indeed, by controlling the reaction kinetic rate with two molar equivalents of CPAF-C_{2M} applied in the reaction with C_{60}(>DPAF-C_{18}) in the presence of DBU (2.0 eq.), only two clear preparative thin-layer chromatography (PTLC) bands in the product mixtures were observed in addition to the starting C_{60}(>DPAF-C_{18}) (~15%). The first less polar product band at $R_f = 0.5$ was found to be the bisadduct C_{60}(>DPAF-C_{18})(>CPAF-C_{2M}) isolated as orange-brown solids in 28% yield. The second more polar product band at $R_f = 0.4$ was determined to be the trisadduct C_{60}(>DPAF-C_{18})(>CPAF-C_{2M})$_2$ isolated as red-brown solids in 40% yield.

5.5 Molecular Self-Assembly of Chromophore–Fullerene Conjugates

It was found that molecular self-assemblies of FC_4S resulted in the formation of nearly monodisperse spheroidal nanospheres with the sphere radius of gyration $R_g \approx 19$ Å, where the major axe ≈ 29 Å and the minor axe ≈ 21 Å for the ellipsoid-like aggregates, or an estimated long sphere diameter of 60 Å [the radius = $(5/3)^{1/2}R_g$] for the aggregates, as determined by small-angle neutron scattering (SANS) in D_2O

and small-angle X-ray scattering (SAXS) in H_2O [123]. This radius of gyration was found to remain relatively constant over a concentration range from 0.35 to 26 mM in H_2O, revealed strong hydrophobic interaction between core fullerene cages overcoming loose charge repulsion at the surface of the molecular micelle. It allowed the nanosphere formation at a low concentration despite of steric hindrance and high hydrophilicity arising from 6 sulfo-*n*-butyl arms surrounding C_{60}. Based on the SANS data, the mean number of FC_4S molecules for the nanosphere was determined to be 6.5 ± 0.7 that led to the elucidation of its nanocluster structure with each FC_4S molecule located at the vertex of an octahedron-shaped nanosphere shown in Fig. 5.6 [41].

Strong hydrophobic interactions and association among fullerene cages serve as the major attractive driving force for amphiphilic fullerene derivatives, such as C_{60}-methanocarbonyl-9, 9-dipolyethyleneglycol-2-diphenylamino-fluorene, $C_{60}(>\text{DPAF-EG}_{12}\text{C}_1)$ (Fig. 5.8), to organize into an ordered shape and form in aqueous solution that resulted in efficient molecular assembly. In close resemblance to small amphiphilic surfactant molecules in forming micelle structures in water, [60] fullerenyl amphiphilics exhibit high tendency in forming a hydrophobic bilayer shell that consists of an array of C_{60} cages in a submicrospheric membrane, below the critical aggregation concentration, known as buckysome or fullerosome vesicles [124–127]. Above the critical aggregation concentration, formation of multi-bilayered vesicles is also possible. In the molecular structure of $C_{60}(>\text{DPAF-EG}_{12}\text{C}_1)$, the moiety of $C_{60}>$ and DPAF can be regarded as water-insoluble chromophore units that give irregular packing in the solid particle due to dismatched moiety shapes. Competitive intermolecular interaction force among like-moieties C_{60}–C_{60} and DPAF−DPAF will govern the molecular self-assembly character of $C_{60}(>\text{DPAF-EG}_{12}\text{C}_1)$. Therefore, to maximize the packing order among $C_{60}>$ moieties, the compound was dissolved in a minimum amount of water-miscible organic solvent, such as THF−dimethyl sulfoxide (DMSO; 1:1, v/v), to dissociate each C_{60}-DPAF chromophore unit from each other under the ultrasonication condition prior to its addition into water. Initiation of molecular self-assembly was assisted by continuing ultrasonication for few minutes in aqueous solution. Carbon-copper film grids in a 200-mesh size were used for the topography investigation of molecularly assembled structures, derived from $C_{60}(>\text{DPAF-EG}_{12}\text{C}_1)$, by transmission electron microscopy (TEM) images. Samples were prepared by coating the grid with a solution at 1.0×10^{-6} M, followed by the freeze-dry technique under vacuum to retain to the vesicle shape on the grid. Consistent TEM microimages of nanovesicles were reported to be obtained and revealed by many regular bilayer spheres in a size ranging from 20 to 70 nm in diameter, as shown in Fig. 5.8b. Majority of the spheres were larger than the typical micelle size of 20−30 nm in diameter derived from lipid molecules. Interestingly, no obvious large solid particles were detected even though this sample solution was not filtered through a filter membrane of 0.45 μm in pore size that we normally followed as a procedure. Morphology of the vesicle shell membrane was revealed by a dark ring area with a roughly even wall width and a smooth shape around the ring image. Measurement of the vesicle wall thickness marked by the cross-ended lines gave a wall width of roughly 9.0−10 nm. This length fits

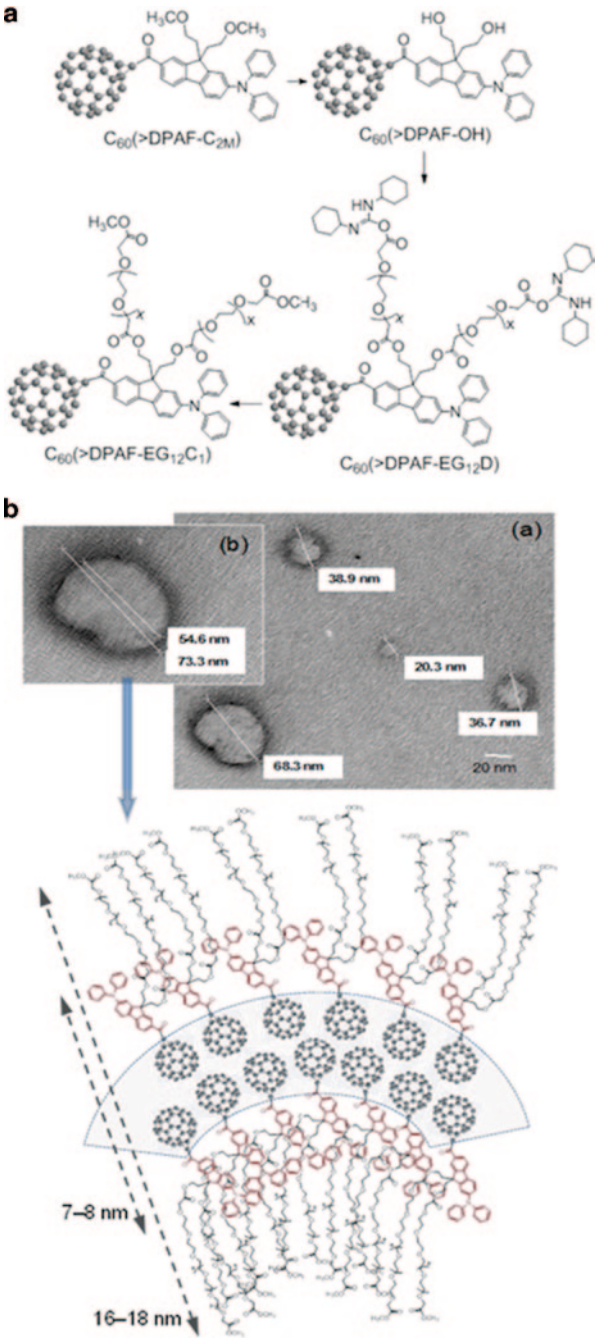

Fig. 5.8 Synthesis and nanovesicles of C_{60}(> $DPAFEG_{12}C_1$). *DPAF* dialkyldiphenylaminofluorene

approximately with the linear bilayer molecular dimension of C_{60}(>DPAF-$EG_{12}C_1$) in 16−18 and 7.0−8.0 nm, estimated by the three-dimensional (3D) molecular structural modeling with a fully stretched oligo(ethylene glycol) chain and chromophore core width. This implied a shell-like bilayer consisting of a head-to-head packing of C_{60}(>DPAF) chromophore moieties in the nanovesicle membrane region. It is also consistent with the X-ray single crystal structure of the related analogs C_{60}(>CPAF-C_2) showing a highly ordered array of C_{60}> cages in the unit cell packing in the presence of similar planar diphenylaminofluorene chromophores [120].

5.6 Delivery Systems of Fullerene Derivatives for PDT

Several fullerene derivatives have also been tested for their photodynamic efficacy by employing some of the delivery vehicles. Ikeda and coworkers used a series of liposomal preparations of C_{60} containing cationic or anionic lipids together. Illumination with 136 J/cm^2 light at 350–500 nm gave 85 % cell killing in the case of cationic liposomes, and apoptosis was demonstrated [128]. Akiyama et al. solubilized unmodified C_{60} with high stability using various types of PEG-based block copolymer micelles which showed cytotoxicity under photoirradiation in HeLa cells [70]. In another study, direct and short-time uptake within 10 min of fullerene into the cell membrane using an exchange reaction from a fullerene-γ-cyclodextrin complex and the resulting PDT activity against cancer cells was demonstrated [129]. Doi et al. compared [68] the PDT activity of C_{60} and C_{70} encapsulated in dimyristoylphosphatidylcholine liposomes against HeLa cells and found C_{70} was five times more active than C_{60} attributing the difference to an improved absorption spectrum in the latter case. In another publication [130], this group compared delivery of C_{70} encapsulated in surface cross-linked lipid vesicles called cerasomes with the above-mentioned liposomes. They found additional stability of cerasomes coupled with equivalent PDT activity against HeLa cells suggesting the fullerene could mediate cell killing without being released from its delivery vehicle.

5.7 Photophysical Properties of Chromophore–Fullerene Conjugates

Photoexcitation of C_{60} and fullerene derivatives induces a singlet fullerenyl excited state that is transformed to the corresponding triplet excited state, via intersystem energy crossing, with nearly quantitative efficiency [45]. Subsequent energy transfer from the triplet fullerene derivatives to molecular oxygen produces singlet molecular oxygen in aerobic media. This photocatalytic effect becomes one of key mechanisms in photodynamic treatments using fullerene derivatives as PSs. However, a high degree of functionalization on C_{60} for the enhancement of solubility and compatibility in biomedia resulted in a progressive decrease of the singlet oxygen

production quantum yield [$\Phi(^1O_2)$]. Examples were given by Bingel-type malonic acid, $C_{60}[C(COOH)_2]_n$, and malonic ester, $C_{60}[C(COOEt)_2]_n$, [60]fullerene adducts [131], showing a decreasing trend of $\Phi(^1O_2)$ as the number of addends *(n)* increases. When the number *n* reached 6 for a hexaadduct, its $\Phi(^1O_2)$ value declined to only 13 % or less of that for C_{60} [132]. However, it was not the case for molecular micellar FC_4S [41], a relatively high singlet oxygen production quantum yield for FC_4S may indicate its unique electronic features in difference with Bingel-type malonic hexaadducts of C_{60}. The efficiency was substantiated by direct detection of $^1O_2$ emission at 1270 nm upon photoirradiation of self-assembled FC_4S nanospheres at 500–600 nm.

In the cases of light-harvesting electron-donor chromophore-assisted fullerene conjugate systems, such as C_{60}(>CPAF-C_n) derivatives, their photophysical properties involve the primary photoexcitation events of either the fullerene moiety at UV wavelengths or the DPAF-C_n moiety at both UV and visible wavelengths up to 600 nm [120]. Much higher optical absorption capability of DPAF-C_n than the C_{60}> cage in visible wavelengths enables the former moiety to serve as a light-harvesting antenna. Accordingly, formation of the photoexcited ^{1}(DPAF)*-C_n moiety should be considered as the early event in the photophysical process. Alteration of the keto group of C_{60}(>DPAF-C_n) to the DCE group of C_{60}(>CPAF-C_n) effectively extended its photoresponsive region to longer red wavelengths. Photoexcitation processes of C_{60}(>DPAF-C_n) and C_{60}(>CPAF-C_n) pump an electron from their HOMO to the LUMO. By the molecular orbital calculation and energy minimization, the majority of the HOMO electron density was reported to be delocalized over the DPAF-C_n moiety, whereas the LUMO electron density was located on the C_{60} spheroid, and therefore C_{60}^{-}·(>CPAF^{+}·-C_n) was suggested as the most stable charge-separated (CS) state in polar solvents, including H_2O [121]. These CS states may be generated by photoinduced intramolecular electron transfer between the diphenylaminofluorene donor and C_{60}> acceptor moieties. The process effectively quenches fluorenyl fluorescence that can be observed in the most of C_{60}(>DPAF-C_n) and C_{60}(>CPAF-C_n) monoadducts. Even during energy transfer events of C_{60}(>CPAF-C_n), normally favorable in nonpolar solvents, observed short fluorescence lifetime of the model compound ^{1}CPAF*-C_9 (241 ps) as compared with that of the keto analogs Br-^{1}DPAF*-C_9 (2125 ps) may be indicative of a facile photoinduced intramolecular charge polarization process forming the corresponding [C=C(CN)$_2$]$^{-}$·–DPAF^{+}·-C_9 CS state that will facilitate the formation of C_{60}^{-}·(>CPAF^{+}·-C_n) in the subsequent electron transfer event.

Intramolecular formation of transient CS states in chromophore–fullerene conjugates is crucial for the generation of radical ROS, initially with O_2^{-}·and subsequently HO·, in PDT treatments. Therefore, direct detection of a transient absorption band of (C_{60}>)$^{-}$· radical–ion pairs centered at 1020 nm during nanosecond laser flash photolysis of C_{60}(>CPAF-C_n) in polar solvents provided clear confirmation of the formation of photoinduced CS transient state C_{60}^{-}·(>CPAF^{+}·-C_n) [121]. Interestingly, it was also reported [121] that by time-resolved fluorescence emission measurement of $^1O_2$ at 1270 nm upon photoexcitation of C_{60}(>DPAF-C_n) and C_{60}(>CPAF-C_n) for comparison using a laser light source at 523 nm (λ_{ex}) in

the presence of O_2 in toluene,the $^1O_2$ production yield of the latter compound was found to be nearly sixfold higher than that of the former analogs indicating an enhanced light-harvesting capability of the CPAF-C_n moiety in visible range and subsequent efficient triplet state generation of the C_{60}>cage moiety. The fluorescence intensity of $^1C_{60}{}^*$(>DPAF-C_n) and $^1C_{60}{}^*$(>CPAF-C_n) was significantly quenched by increasing the solvent polarity from toluene to benzonitrile and DMF that led to a near disappearance of $^1O_2$ luminescence in DMF implying the domination of $C_{60}{}^{-}\cdot$(>DPAF$^{+}\cdot$-C_n) and $C_{60}{}^{-}\cdot$(>CPAF$^{+}\cdot$-C_n) CS state in polar solvents.

5.8 Microscopic Technique for Detecting Localization of Fullerene Derivatives

Though fullerenes have been widely used for PDT not much attention has been given to studying their interaction with different intracellular organelles and determining the cellular site of their potential action. The main reason for this lack of attention is that in contrast to the vast majority of other PS that are highly fluorescent, fullerenes are nonfluorescent; thus, it is not feasible to use the common technique of fluorescence (confocal) microscopy to examine the intracellular uptake and subcellular localization of fullerenes. Overcoming this limitation, Scrivens et al. [133] were the first to demonstrate its uptake by human keratinocytes in tissue culture by preparing a radiolabeled fullerene. In serum-free medium, they found a time (up to 6.0 h) and concentration-dependent uptake so that 50% of added fullerene was taken up. One group used indirect immunofluorescence staining with antibodies that recognize fullerenes and other organelle probes to explain that a dicarboxylic acid derivative localized in mitochondria and other intracellular membranes [134]. A recent paper described the use of the related techniques of energy-filtered transmission electron microscopy and electron tomography to visualize the cellular uptake of pristine C_{60} nanoparticulate clusters. When human monocyte-derived macrophages were examined, C_{60} was found in the plasma membrane, in lysosomes, and in the nucleus [135]. In another study, a pristine C_{60} preparation was obtained by sonication in methanol (different from the more commonly used toluene) giving uniformly sized particles with photoluminescence detection at 750 nm after excitation at 488 nm. This emission was used to demonstrate cell uptake in normal and malignant breast cells after culturing them on fullerene-coated dishes [19].

5.9 ROS Production by Fullerene Derivatives

Illumination of C_{60} or C_{70} monoadduct derivatives with visible or UVA light promotes its transition to a long-lived triplet excited state (Fig. 5.1), via *isc* processes, and subsequent intermolecular energy transfer to the molecular oxygen yielding a highly reactive singlet oxygen ($^1O_2$) in Type II reactions [45]. In the presence

of physiological concentration of reductants, such as NADH, more reactive ROS species, such as superoxide anion ($O_2^{-\cdot}$) and hydroxyl radical ($HO\cdot$), may be produced in polar solvent and water [44]. In our study, a comparative singlet oxygen production efficiency study of two decacationic $C_{60}[>M(C_3N_6{}^+C_3)_2]$-$(I^-)_{10}$(LC14) [109, 110] and $C_{70}[>M(C_3N_6{}^+C_3)_2]$-$(I^-)_{10}$(LC17) [101] in DMSO−$H_2O$ (1:520, 1.0×10^{-6} M) was carried out by many increamental exposures of the sample to a UVB-enhanced visible lamp (200 W, 250−600 nm with several λ_{max} at 315, 370, 430, 550, and 570 nm) in an exposure interval period of 5.0 s (the light dose measured to be ~5.0 mJ/cm^2 per period) followed by the flourescence emission measurement of the probe. For highly efficient in situ selective trapping of singlet oxygen, highly water-soluble 9,10-anthracenediyl-bis(methylene)dimalonic acid (ABMA, 8.0×10^{-6} M) was applied as a fluorescent probe which exhibits the emission maximum at 429 nm. The corresponding most effective excitation wavelengths were found to be 379 and 400 nm with the later one closer to the visible range used. At this wavelength, the optical absorption extinction coefficient value of LC17 is slightly higher than that of LC14. The chemical trapping of $^1O_2$ by highly fluorescent ABMA leads to the formation of non-fluorescent 9,10-endoperoxide product (Fig. 5.9a). The conversion allows us to follow the loss of fluorescence emission intensity at 429 nm for its correlation to the proportional quantity of $^1O_2$ produced due to the high kinetic rate constant of the trapping reaction in aqueous media [136]. As a result, a slightly higher $^1O_2$ production rate of $C_{60}[>M(C_3N_6{}^+C_3)_2]$ was observed even though the difference is not statistically significant, as shown in Fig. 5.9d. The use of a lower irradiation dose for the similar measurement directly in the UV-vis-NIR spectrometer, operated at λ_{ex} 400 nm (single wavelength excitation) with the monochromator, gave a much slower production rate of $^1O_2$ for both cases that displayed a clearly higher rate for $C_{60}[>M(C_3N_6{}^+C_3)_2]$ at this excitation wavelength.

A similar trend was also confirmed by using $^1O_2$ probe singlet oxygen sensor green (SOG) reagent. Upon the tapping of $^1O_2$ by the anthracene moiety of SOG, the resulting 9,10-endoperoxide-linked fluorescein product SOG-EP is highly green fluorescent (excitation/emission maxima ~504/525 nm) that can be used for the correlation of relative $^1O_2$ quantity produced. It is worthwhile to mention that the SOG probe chemistry is potentially more complicated than the statement above due to the fact that both SOG and SOG-EP are capable of sensitizing $^1O_2$ production and undergoing photobleaching processes themselves, resembling those of fluorescein derivatives [137]. This complication can be lessened by using blue light for fullerene excitation that is not absorbed by the probe. However, if we assume the amount of the additional $^1O_2$ molecules derived from SOG and SOG-EP and the photobleaching rate being nearly identical among experiments under the same conditions, the fluorescence emission intensity of SOG-EP detected will still be valuable for the relative comparison purpose. Accordingly, Fig. 5.10a showed the results from the SOG-based fluorescence probe assay experiments of LC14 and LC17 in 96-well black-sided plates under incremental irradiation with a blue light-emitting diode (LED) light source (415 ± 15 nm) under the total fluence intensity range of 0−6.0 J/cm^2. It is evident that $C_{60}[>M(C_3N_6{}^+C_3)_2]$-$(I^-)_{10}$ (LC14) gave a significantly higher rate of $^1O_2$ detected than that of $C_{70}[>M(C_3N_6{}^+C_3)_2]$-$(I^-)_{10}$ (LC17).

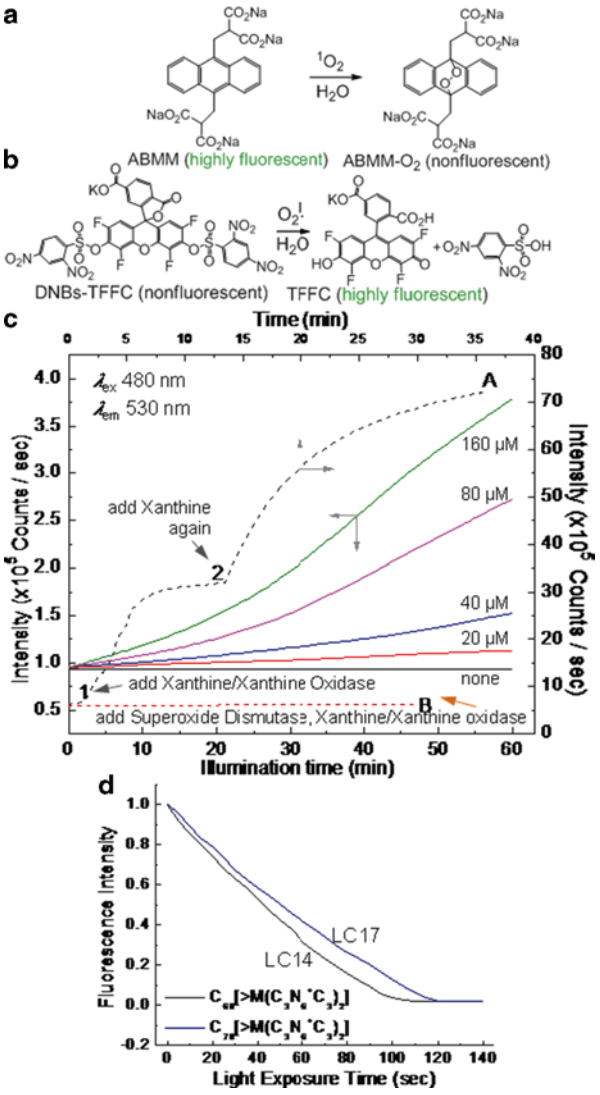

Fig. 5.9 Illumination time-dependent fluorescent **a** and **b** ROS-trapping mechanism of two types of fluorescent probes ABMM and TFFC **c** intensity increase of fluorescein probe tetrafluorofluorescein carboxylic acid (TFFC) (λ_{ex} 480 nm/λ_{em} 530 nm) in PBS media (pH 7.4) with LC14 using a LED (365 nm) light source for detecting $O_{2-\cdot}$ production and **d** intensity decrease of ABMM probe (λ_{ex} 350 nm/λ_{em} 428 nm). *ABMM* anthracenediyl-bis(methylene)dimalonic acid, *PBS* PBS

Indeed, under the similar experimental procedures relevant to PDT as those used for the data collection of Fig. 5.10a, but with the application of the fluorescent probe of 3′-*p*-(hydroxyphenyl)-fluorescein [138] (HPF) instead, a reverse relationship was observed with higher fluorescence emission intensity of fluorescein for $C_{70}[>M(C_3N_6{}^+C_3)_2]$-$(I^-)_{10}$ than that for $C_{60}[>M(C_3N_6{}^+C_3)_2]$-$(I^-)_{10}$ under the total fluence intensity range of 0−5.0 J/cm^2, as shown in Fig. 5.10b. Since the HPF probe is an essential tool for the selective detection of HO· and peroxynitrite, via quinone formation detached from the fluorescein moiety (excitation/emission maxima ~490/515 nm), with the detection sensitivity reported to be roughly 145-fold and

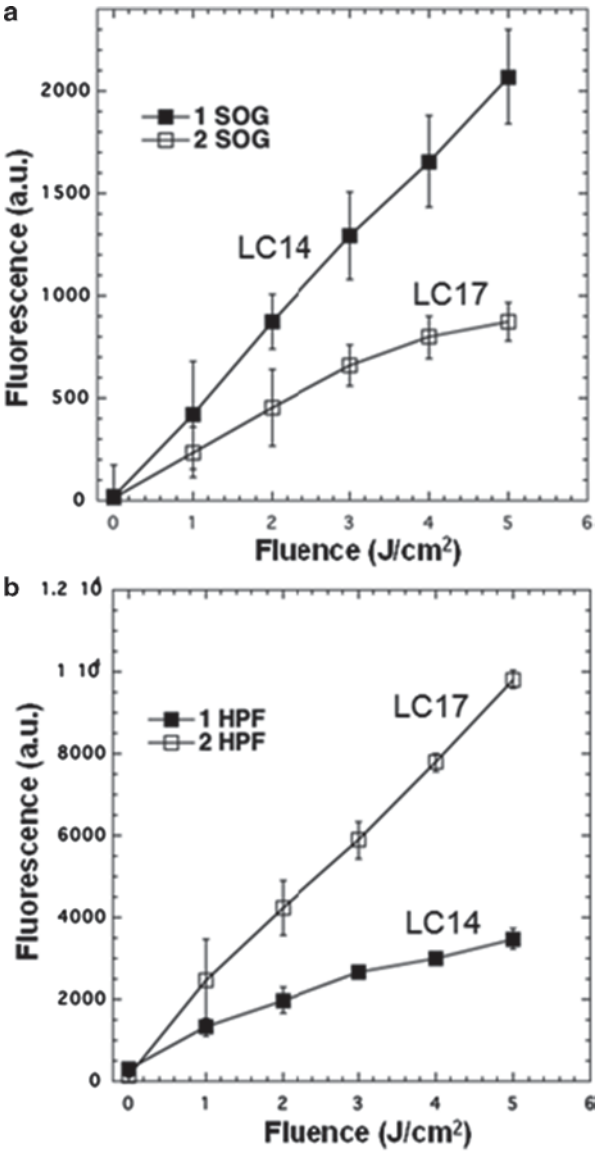

Fig. 5.10 Illumination time-dependent fluorescent intensity increase of **a** fluorescein probe SOG-EP (λ_{ex} 504 nm/λ_{em} 525 nm) for detecting 1O2 produced and **b** fluorescein probe HPF (λ_{ex} 490 nm/λ_{em} 515 nm) for detecting O_{2-}· produced in the presence of LC14 and LC17 using a blue LED (415 nm) light. *SOG* singlet oxygen sensor green, *HPF* 3′-*p*-(hydroxyphenyl)-fluorescein

90-fold higher for HO· than $^1O_2$ and O_2^{-}·, respectively [139], the measured fluorescence intensity can be correlated roughly to the yield of hydroxyl radicals produced. Besides, O_2^{-}· is the precusor species to the formation of HO·, directly monitoring the presence of HO· will also serve the confirmation purpose of superoxide radical formation, that is, higher yield for $C_{70}[>M(C_3N_6{}^+C_3)_2]$ than $C_{60}[>M(C_3N_6{}^+C_3)_2]$.

It is well recognized that $^1O_2$ can give rise to several other types of ROS, including O_2^{-}·, H_2O_2, and HO·, in a sequential reaction with iodide anion (I^-) [140]. In

this case, the yield of $O_2^{-\cdot}$ or HO· should be proportional to the quantity of $^1O_2$. Therefore, our observation of a higher $^1O_2$ production yield of $C_{60}[>M(C_3N_6^+C_3)_2]$ in phosphate-buffered saline (PBS) solution (Fig. 5.10a) giving a lower production yield of radical species (Fig. 5.10b) revealed no direct correlation of $^1O_2$ to $O_2^{-\cdot}$ or HO· yields, or the latter species may not derive directly from the former one in these experiments. Contrarily, they may be in a competitive production process to each other in either the triplet energy transfer (Type II) or electron transfer (Type I) mechanism involving the electron-donating iodide anion (I^-) and the electron-accepting fullerene cage. This mechanistic path can be realized by the facile photo-excitation of C_{60}/C_{70} cages to their singlet excited state followed by the quantitative *isc* to their corresponding excited triplet transient states, $^3C_{60}{}^*[>M(C_3N_6^+C_3)_2]$ and $^3C_{70}{}^*[>M(C_3N_6^+C_3)_2]$. Apparently, the latter molecule exhibited a higher electron-accepting capability to allow electron transfer from the iodide anion leading to the formation of $C_{70}^{-\cdot}[>M(C_3N_6^+C_3)_2]$ prior to the further transfer this electron to O_2 that gave a higher yield of $O_2^{-\cdot}$ and, thus, HO·. These results were summarized in Fig. 5.11 to emphasize the significant importance of decacationic structural design of fullerene derivatives aiming at shifting their Type II to Type I photochemistry for the more reactive radical ROS in photokilling of pathogens. Accordingly,

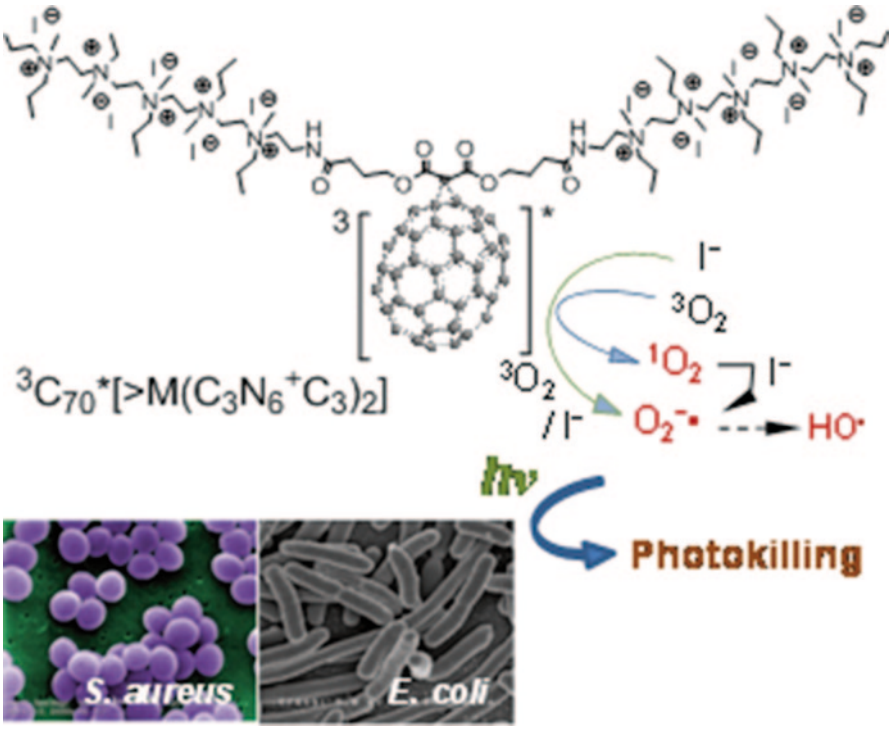

Fig. 5.11 A schematic presentation of enhanced Type I photochemistry of LC17 in producing radical ROS

in the presence of a high number of electron-donating iodide anions as parts of quaternary ammonium salts in the arm region, we found that $C_{70}[>M(C_3N_6{}^+C_3)_2]$-$(I^-)_{10}$ produced more HO· than $C_{60}[>M(C_3N_6{}^+C_3)_2]$-$(I^-)_{10}$, in addition to $^1O_2$. The observed production of HO· may arise partially from the photoinduced electron transfer (Type I) mechanism involving the electron-donating iodide anions (I^-) and the fullerene cages at their excited triplet transient states, $^3C_{60}{}^*[>M(C_3N_6{}^+C_3)_2]$ and $^3C_{70}{}^*[>M(C_3N_6{}^+C_3)_2]$ having different electron-accepting strength. The presence of electrolyte salts makes the ion exchange and I^--dissociation possible and increases the efficiency of electron transport that forms the corresponding $C_{60}{}^{-}\cdot[>M(C_3N_6{}^+C_3)_2]$ and $C_{70}{}^{-}\cdot[>M(C_3N_6{}^+C_3)_2]$, respectively, as the source for the $O_2{}^{-}\cdot$ and the derived ROS radicals generation.

5.10 In Vitro Photoinactivation of Microbials and Viruses by Mono- to Decacationic Fullerene Derivatives

The effectiveness of various PS proposed for antimicrobial PDT can be judged on several criteria. These PS should be able to kill multiple classes of microbes at relatively low concentrations and low fluences of light. PS should be reasonably nontoxic in the dark and should demonstrate selectivity for microbial cells over mammalian cells. PS should ideally have large extinction coefficients in the red part of the spectrum and demonstrate high triplet and singlet oxygen quantum yields. We have shown in a series of reported experiments that cationic fullerenes fulfill many, but not all of the aforementioned criteria. Our laboratory was the first to demonstrate that the soluble functionalized fullerenes described above, especially the cationic compounds BF4–BF6, were efficient antimicrobial PS and could mediate photodynamic inactivation (PDI) of various classes of microbial cells [49]. We used a broadband-pass filter giving an output of the entire visible spectrum (400–700 nm) to excite the fullerenes that maximized the absorption.

Our initial screening experiment carried out against *Staphylococcus aureus* at 100 μM concentrations showed that the C_{60} substituted with pyrrolidinium groups behaved very differently than the series substituted with di-serinol groups. The cationic fullerenes gave high levels of dark toxicity (except for BF4) while the di-serinol-functionalized C_{60} had no dark toxicity, but showed a typical light dose-dependent loss of colony-forming ability. However, it needed concentrations as high as 100 μM and white-light fluences as high as 120 J/cm^2 to achieve significant killing (2.0–3.0 logs or up to 99.9%) of the gram-positive *S. aureus*. Even with these relatively high doses of both PS and light, the gram-negative *Escherichia coli* was only slightly killed (less than 1.0 log or 90%). In sharp contrast, the cationic fullerenes were highly effective PS at much lower concentrations and much lower light doses. BF4–BF6 were all surprisingly effective in causing light-mediated killing of *S. aureus*. BF5 and BF6 needed only 1 μM concentration and 1.0 or 2.0 J/cm^2 of white light to kill 4–5 logs. BF4–6 were tested against *E. coli* at 10 μM, and BF5 and BF6 showed similar high levels of activity (up to 6.0 logs). These findings

agree with numerous reports in the literature that demonstrate that PS with one (or preferably more cationic groups) are efficient antimicrobial PS [141–145]. Quaternary nitrogen-based groups are superior to primary, secondary, or tertiary amino groups as the positive charge is less dependent on the pH of the surrounding media, or the pK_a of the molecules that the PS is interacting with. Microbial cells possess overall negative charges, and it is thought that cationic PS bind to these groups on the outer layers of the cell surface. Gram-positive cells have relatively permeable outer layers of peptidoglycan and lipoteichoic acid or β-glucan, respectively. This allows cationic and to a lesser extent non-cationic PS to diffuse inwards to the plasma membrane where the generation of ROS under illumination can damage the membrane structure allowing leakage of essential components and cause cell death. Cationic compounds are able to displace divalent cations (Ca^{2+} and Mg^{2+}) that play a role in the attachment of lipopolysaccharide to the outer membrane [146]. This displacement weakens the structure of the outer permeability allowing the PS to penetrate further in a process that has been termed "self-promoted uptake" [35]. The fact that this mechanism requires cationic compounds explains why BF1–BF3 were relatively noneffective against the gram-negative *E. coli* and such findings have been reported with numerous other non-cationic PS [143].

A recent study by Spesia et al. reported [147] that a novel *N,N*-dimethyl-2-(4′-*N,N,N*-trimethylaminophenyl)fulleropyrrolidinium iodide (DTC_{60}^{2+}) was synthesized by 1,3-dipolar cycloaddition using 4-(*N,N*-dimethylamino) benzaldehyde, *N*-methylglycine, and C_{60} and quaternization with methyl iodide. Photodynamic properties of DTC_{60}^{2+}were compared with a non-charged *N*-methyl-2-(4′-acetamidophenyl)fulleropyrrolidine (MAC_{60}) and a monocationic *N,N*-dimethyl-2-(4′-acetamidophenyl)fulleropyrrolidinium iodide (DAC_{60}^{+}). The photodynamic effect was strongly dependent on the medium, and diminished when the sensitizer aggregated and increased in an appropriately surrounded microenvironment. The PDI produced by these fullerene derivatives was investigated in vitro on *E. coli*. Photosensitized inactivation of *E. coli* cellular suspensions by DTC_{60}^{2+} exhibited an approximately 3.5 log decrease of cell survival when the cultures are treated with 1.0 μM of sensitizer and irradiated for 30 min. This photosensitized inactivation remains high even after one washing step. Also, the photodynamic activity was confirmed by growth delay of *E. coli* cultures. The growth was arrested when *E. coli* was exposed to 2.0 μM of cationic fullerene and irradiated, whereas a negligible effect was found for the non-charged MAC_{60}. In our laboratory, we have tested a group of six functionalized fullerenes which were prepared in two groups of three compounds [48]. We demonstrated that the C_{60} molecule monosubstituted with a single pyrrolidinium group (BF4) was a very efficient PS which efficiently killed a panel of mouse cancer cells at the low concentration of 2.0 μM on exposure to white light. We have shown, in a series of reported experiments that cationic fullerenes fulfill many of the desirable characteristics for efficient photoinactivation of bacteria and other pathogens. Our laboratory was the first to demonstrate that the soluble functionalized fullerenes, especially the tricationic compound BF6, were efficient and selective broad spectrum antimicrobial PS and could mediate PDI of various classes of microbial cells [49]. In a study by Spesia et al. [147], it was reported that

a novel fulleropyrrolidinium iodide (DTC_{60}^{2+}) produced PDI in vitro of *E. coli.* Lee et al. showed that C_{60} derivatives were efficient in inactivating *E. coli* and MS-2 bacteriophage [148]. Recently we have demonstrated the use of innovative cationic fullerenes as broad-spectrum light-activated antimicrobials and carried out quantitative structure–function relationships to determine the optimal chemical structure of the fullerene derivatization [100]. The most effective compound overall against the various classes of microbial cells had the tetracationic structure illustrated as BF24 in Fig. 5.3. Another recent paper from our laboratory [108] looked at a further series of functionalized cationic fullerenes as antimicrobial PS and found a highly effective structure was the previously reported [149] tetracationic compound BF21 (Fig. 5.2).

Antimicrobial effect of two highly water-soluble decacationic fullerenes LC14 [109, 110] and LC17 [101] (Fig. 5.4) were applied for comparison in the PDT killing of the gram-positive *S. aureus*. In general, it is known that gram-positive bacteria are more sensitive and susceptible to PDT destruction than gram-negative bacteria. This allowed us to use a lower concentration (up to 10 μM) of fullerene derivatives for *S. aureus* killing than that (up to 100 μM) needed for effective *E. coli* killing. Our previous PDT experiments have indicated a fast-binding process of PS to microbial cells [150]. Thus, a short incubation time of 30 min was applied for both species. As a result shown in Fig. 5.12, neither decacationic fullerene derivative LC14 and LC17 gave any detectable toxicity to both bacteria in the dark in a concentration up to 10 μM. A pronounced PDT effect was observed after illumination on the LC14/LC17-incubated cells using a broad-band white light source with total fluence intensity of 100 J/cm^2 with a sharp cytotoxicity trend even at low fullerene concentration of 1.0 μM, giving 3-log killing for $C_{60}[>M(C_3N_6^+C_3)_2]$ and 2-log killing for $C_{70}[>M(C_3N_6^+C_3)_2]$. As the administered dose increased to a concentration of 3.0 μM, a 5-log killing effectiveness was observed for the compound LC14 and a corresponding 3-log for the compound LC17. Interestingly, $C_{60}[>M(C_3N_6^+C_3)_2]$ was able to eradicate the cells at higher concentrations than 3.0 μM. In the case of $C_{70}[>M(C_3N_6^+C_3)_2]$, a 5-log effective killing was achieved at a concentration of 10 μM. Two killing curves of LC14 and LC17 were significantly different from each other ($p < 0.01$). In the PDT experiments against *E. coli,* the need to use eight-times higher concentrations of fullerene drugs led to the observation of some dark toxicity (1.0−2.0 logs) at the higher concentrations of 60 and 80 μM. Surprisingly, the order of PDT effectiveness of these two fullerene drugs was opposite to that seen with *S. aureus.* In this case, $C_{70}[>M(C_3N_6^+C_3)_2]$ was most effective for *E. coli* killing with 3.0 logs at 40 μM, 5.0 logs at 60 μM, and eradicating the cells at 80 μM, as shown in Fig. 5.12b. On the other hand, $C_{60}[>M(C_3N_6^+C_3)_2]$ only killed 1.0 log at 40 μM, 2.0 logs at 60 μM, and 3.0 logs at 80 μM. These two curves were significantly different ($p < 0.01$).

The data showed interesting differences between the photoactivity of decacationic fullerene compounds that differ only in the number of carbon atoms in the fullerene cage. The decacationic arms attached to these fullerenes served to give the molecules rapid binding to the anionic residues displayed on the outer parts of bacterial cell walls. The large number of ionic groups attached to the fullerene also

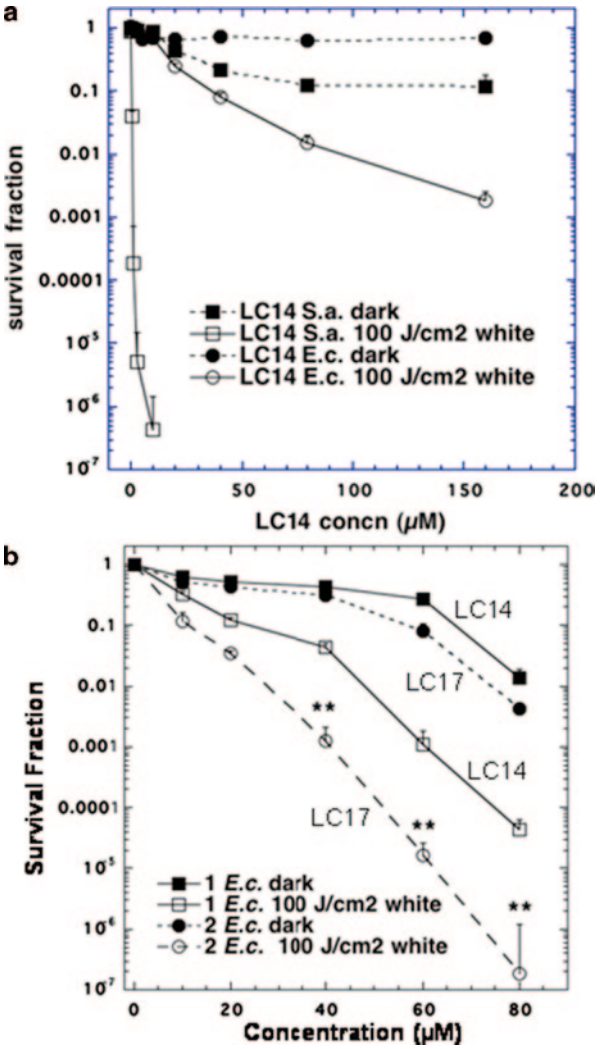

Fig. 5.12 PDT killing of **a** LC14 with or without light and **b** gram-negative bacteria, *E. coli*. Bacteria [10(8) cells/mL] were incubated with LC14 or LC17 (for comparison) for 30 min followed by delivery or not of 100 J/cm^2 of white light. $^{**}p<0.01$

provided enhanced water solubility, which is a necessary requirement for biological activity. Even though these fullerenes displayed a rapid ability to photoinactivate bacteria, they were also efficient in mediating the PDT killing of cancer cells although a longer incubation time was needed. A large molecular weight of these fullerenes (around 3300) means that they are too large to diffuse through the plasma membrane of mammalian cells, which is a rapid process, and are therefore taken up by the slower process of adsorptive endocytosis. The differences in effectiveness we found between C_{60} and C_{70} was interesting. For gram-positive bacteria, $C_{60}[>M(C_3N_6{}^+C_3)_2]$ was better at photokilling than $C_{70}[>M(C_3N_6{}^+C_3)_2]$, while for gram-negative bacteria and for cancer cells the opposite was the case, in that $C_{70}[>M(C_3N_6{}^+C_3)_2]$ was better at photokilling than $C_{60}[>M(C_3N_6{}^+C_3)_2]$. We have

previously reported [151] that Type II ROS, that is, singlet oxygen, $^1O_2$, are better at killing gram-positive bacteria than Type I ROS, that is, hydroxyl radicals, HO·, while the reverse is true for gram-negative bacteria (HO· is better at killing than $^1O_2$). Therefore, we decided to test the type of ROS (HO· or $^1O_2$) produced when LC14 and LC17 were illuminated in simple PBS solution. To do this, it was necessary to employ blue light to excite the fullerene, because if white light was used, the light alone would activate the probe to some extent through the green absorption peak. The results demonstrated that $C_{60}[>M(C_3N_6{}^+C_3)_2]$ produced more $^1O_2$ while $C_{70}[>M(C_3N_6{}^+C_3)_2]$ produced more HO·. This finding offers an explanation of the preferential killing of gram-positive bacteria by LC14 and the preferential killing of gram-negative bacteria by LC17. The hypothesis is that $^1O_2$ can diffuse more easily into porous cell walls of gram-positive bacteria to reach sensitive sites, while the less permeable gram-negative bacterial cell wall needs the more reactive HO· to cause real damage [152, 153]. It has not been reported whether HO· or $^1O_2$ is more efficient in killing cancer cells, but our data would suggest that HO· may be more effective in this case as well.

Photodynamic reactions induced by photoactivated fullerenes have been shown to inactivate enveloped viruses [154]. Buffered solutions containing pristine C_{60} and Semliki Forest virus *(Togaviridae)* or vesicular stomatitis virus (VSV; *Rhabdoviridae*), when illuminated with visible light for up to 5.0 h, resulted in up to seven logs of loss of infectivity. Viral inactivation was oxygen dependent and equally efficient in solutions containing protein [155]. Hirayama et al. [156] used a methoxy–PEG conjugated fullerene at 400 μM in combination with 120 J/cm^2 white light to destroy more than five logs of plaque forming units of VSV. VSV inactivation was inhibited by oxygen removal or by the addition of sodium azide, a known singlet oxygen quencher. The substitution of H_2O by D_2O, which is known to prolong the lifetime of singlet oxygen, promoted the virucidal activity. These results indicate that singlet oxygen may play a major role in VSV photoinactivation by the water-soluble fullerene derivative. The concentration needed for virus inactivation was higher than that of other sensitizers such as methylene blue. Lin and coworkers [157] compared light-dependent and light-independent inactivation of dengue-2 and other enveloped viruses by the two regio-isomers of carboxyfullerene and found that asymmetric isomer had greater dark activity (albeit at much higher concentrations than needed for its PDT effect) due to its interaction with the lipid envelope of the virus. Photodynamic reactions induced by photoactivated fullerenes have also been shown by many workers to inactivate enveloped viruses [154–157].

5.11 PDT Enhancement Using Light-Harvesting Antenna Attachments on Fullerene Derivatives

We reported [121] the synthesis of a new class of photoresponsive C_{60}–*DCE*–diphenylaminofluorene nanostructures and their intramolecular photoinduced energy and electron transfer phenomena. Structural modification was made by chemical

conversion of the keto group in C_{60}(>DPAF-C_n) to a stronger electron-withdrawing DCE unit leading to C_{60}(>CPAF-C_n) with an increased electronic polarization of the molecule, as discussed the Sect. 5.4.3. The modification also led to a large bathochromic shift of the major band in visible spectrum giving measureable absorption up to 600 nm and extended the photoresponsive capability of C_{60}–*DCE*–DPAF nanostructures to longer red wavelengths than C_{60}(>DPAF-C_n). Production efficiency of singlet oxygen by C_{60}(>DPAF-C_{2M}), as the structure shown in Fig. 5.7, was found to be comparable with that of tetraphenylporphyrin PS. Remarkably, the $^1O_2$ quantum yield of C_{60}(>CPAF-C_{2M}; Fig. 5.7) was found to be nearly sixfold higher than that of C_{60}(>DPAF-C_{2M}), [120] demonstrating the large light-harvesting enhancement of CPAF-C_{2M} moiety and leading to more efficient triplet state generation of the C_{60}> cage moiety.

We tested C_{60}(>DPAF-C_{2M}) and C_{60}(>CPAF-C_{2M}) as PSs to kill cancer cells after illumination. We used the human cervical cancer cell line, HeLa and incubated the cells for 3.0 h with increasing concentrations of fullerenes dissolved in 9,10-dimethylanthracene (DMA). Broad-band white light irradiation (200 J/cm^2) was delivered and the cells were returned to the incubator overnight. A 4-h 3-(4,5-dimethylthiazol-2-yl)-2,5-diphenyltetrazolium bromide (MTT) assay was then carried out for mitochondrial reductase activity as a surrogate measure of the cell viability. As a result, a significant, dose-dependent loss of viability in the presence of light was observed using C_{60}(>CPAF-C_{2M}) as the PS. The phenomena were not seen either in the dark or with C_{60}(>DPAF-C_{2M}) in either light or dark conditions. These data clearly show the markedly enhanced photocatalytic activity of C_{60}(>CPAF-C_{2M}) compared to that of C_{60}(>DPAF-C_{2M}), due to higher absorption intensity in visible wavelengths and an increased singlet oxygen quantum yield of the former compound. We interpret the phenomena in terms of the contributions by the extended π-conjugation and stronger electron-withdrawing capability associated with DCE group compared to that of the keto group. Accordingly, C_{60}(>CPAF-C_n) may allow 2γ-PDT using a light wavelength of 1000–1200 nm for enhanced tissue penetration depth.

5.12 In Vitro PDT Study of Cationic Fullerene Derivatives on Cancer Cells: DNA Cleavage and Membrane Damage

Phototoxicity using fullerenes combined with illumination to kill various cells in vitro has been demonstrated in many studies. It is thought that one requirement for any PS to produce cell killing after illumination is that the PS should actually be taken up inside the cell, and that the generation of ROS outside the cell (unless in very large quantities) will not be sufficient to produce efficient cell death. Because fullerenes (in contrast to the vast majority of PS) are non-fluorescent, it is impossible to use the common technique of fluorescence microscopy to examine the intracellular uptake and subcellular localization of fullerenes. Taking these considerations into account, Scrivens et al. [133] were the first to prepare a radiolabeled

fullerene and demonstrate its uptake by human keratinocytes in tissue culture. In serum-free medium they found a time- (up to 6.0 h) and concentration-dependent uptake so that 50 % of added fullerene was taken up. Foley et al. [134] used indirect immunofluorescence staining with antibodies that recognize fullerenes and other organelle probes to show that a dicarboxylic acid derivative localized in mitochondria and other intracellular membranes. The first demonstration of phototoxicity in cancer cells mediated by fullerenes was in 1993 when Tokuyama et al. [158] used carboxylic acid functionalized fullerenes at 6.0 μM and white light to produce growth inhibition in human HeLa cancer cells. However, these same authors later reported that other carboxylic acid derivatives of C_{60} and C_{70} were completely without any photoactivity as PDT agents at 50 μM [159]. Burlaka et al. [160] used pristine C_{60} at 10 μM with visible light from a mercury lamp to produce some phototoxicity in Ehrlich carcinoma cells or rat thymocytes and used EPR spin-trapping techniques to demonstrate the formation of ROS. The cytotoxic and photocytotoxic effects of two water-soluble fullerene derivatives, a dendritic C_{60} mono-adduct and the malonic acid C_{60} trisadduct were tested on Jurkat cells when irradiated with UVA or UVB light [161]. The cell death was mainly caused by membrane damage and it was UV dose dependent. Tris-malonic acid fullerene was found to be more phototoxic than the dendritic derivative. This result is in contrast to the singlet oxygen quantum yields determined for the two compounds. Three C_{60} derivatives with two to four malonic acid groups (dimalonic acid C_{60}, $DMAC_{60}$; trimalonic acid, $TMAC_{60}$; and tetra-malonic acid C_{60}, $QMAC_{60}$) were prepared and the phototoxicity of these compounds against HeLa cells was determined by MTT assay and cell cycle analysis [162]. The relative phototoxicity of these compounds was $DMAC_{60} > TMAC_{60} > QMAC_{60}$. Hydroxyl radical quencher mannitol (10 mM) was not able to prevent cells from the damage induced by irradiated $DMAC_{60}$. $DMAC_{60}$, together with irradiation, was found to decrease the number of G1 cells from 63 to 42 % and increase G2/M cells from 6.0 to 26 %.

Rancan et al. [163] used the following approach to overcome the necessity to use UV or short-wavelength visible light to photoactivate fullerenes. They synthesized two new fullerene-bis-pyropheophorbide-a derivatives: a mono-(FP1) and a hexaadduct (FHP1). The photophysical characterization of the compounds revealed significantly different parameters related to the number of addends at the fullerene core. In this study, the derivatives were tested with regard to their intracellular uptake and photosensitizing activity towards Jurkat cells in comparison with the free sensitizer, pyropheophorbide-a. The C_{60} hexaadduct FHP1 had a significant phototoxic activity (58 % cell death, after a dose of 400 mJ/cm^2 of 688 nm light) but the monoadduct FP1 had a very low phototoxicity and only at higher light doses. Nevertheless, the activity of both adducts was less than that of pure pyropheophorbide-a, probably due to the lower cellular uptake of the adducts. A group from Argentina has also studied the phototoxicity produced by tetrapyrrole–fullerene conjugates. Milanesio et al. [164] compared PDT with a porphyrin-C_{60} dyad (P-C_{60}) and its metal complex with Zn(II) (ZnP-C_{60}) were compared with 5-(4-acetamidophenyl)-10,15,20-tris(4-methoxyphenyl)porphyrin (P), in both homogeneous medium containing photooxidizable substrates and in vitro on the Hep-2 human larynx carcinoma cell line. $^1O_2$

yields (Φ_Δ) were determined using DMA. The values of Φ_Δ were strongly dependent on the solvent polarity. Comparable Φ_Δ values were found for dyads and P in toluene, while $^1O_2$ production was significantly diminished for the dyads in DMF. In more polar solvent, the stabilization of charge-transfer state takes place, decreasing the efficiency of porphyrin triplet-state formation. Also, both dyads photosensitize the decomposition of *L*-tryptophan in DMF. In biological medium, no dark cytotoxicity was observed using sensitizer concentrations < or = 1.0 μM and 24 h of incubation. The uptake of sensitizers into Hep-2 was studied using 1.0 μM of sensitizer and different times of incubation. Under these conditions, a value of approximately 1.5 nmol/10^6 cells was found between 4 and 24 h of incubation. The cell survival after irradiation of the cells with visible light was dependent upon light-exposure level. A higher phototoxic effect was observed for P-C_{60}, which inactivates 80 % of cells after 15 min of irradiation. Moreover, both dyads keep a high photoactivity even under argon atmosphere. In a subsequent paper [165], they showed the cells died by apoptosis by analysis using Hoechst-33258, toluidine blue staining, terminal deoxynucleotidyl transferase mediated dUTP nick end labeling (TUNEL) and DNA fragmentation. Changes in cell morphology were analyzed using fluorescence microscopy with Hoechst-33258 under low oxygen concentration. Under this anaerobic condition, necrotic cellular death predominated over the apoptotic pathway. It was found that P-C_{60} induced apoptosis by a caspase-3-dependent pathway. Ikeda and coworkers [128] used a series of liposomal preparations containing cationic or anionic lipids together with dimyristoylphosphatidylcholine and introduced C_{60} into the lipid bilayer by exchange from cyclodextrin. By adding a phosopholipid with an additional fluorochrome, they were able to use fluorescence microscopy to demonstrate uptake of the liposomes by HeLa cells after 24 h incubation. Illumination with 136 J/cm^2 350–500 nm light gave 85 % cell killing in the case of cationic liposomes and apoptosis was demonstrated.

In our laboratory, we have tested the hypothesis that fullerenes would be able to kill cancer cells by PDT in vitro. We studied the same group of fullerene derivatives described above BF1–BF3 and BF4–BF6 [48]. We showed that the C_{60} molecule monosubstituted with a single pyrrolidinium group (BF4) is a remarkably efficient PS and can mediate killing of a panel of mouse cancer cells at the low concentration of 2.0 μM with very modest (5.0 J/cm^2) exposure to white light. The cells were all cancer cells; lung (LLC) and colon (CT26) adenocarcinoma and reticulum cell sarcoma (J774) and the latter showed much higher susceptibility perhaps due to having an increased uptake of fullerene because J774 cells behave like macrophages [166]. Besides the exceptionally active BF4, the next group of compounds has only moderate activity (BF2, BF5, and BF6) against J774 cells showing some killing at high fluences. The last two compounds (BF1 and BF3) had no detectable PDT killing up to 80 J/cm^2. For the first time we indirectly demonstrated that photoactive fullerenes are taken up into cells by measuring the increase in fluorescence of an intracellular probe (H_2DCFDA) that is specific for the formation of ROS (in particular hydrogen peroxide). We believe that the superoxide produced from the illuminated fullerene undergoes dismutation either catalyzed by superoxide dismutase or spontaneously, to produce H_2O_2 resulting in the increased and diffused fluorescence of the probe.

We also demonstrated the induction of apoptosis by PDT mediated by BF4 and BF6 in CT26 cells at 4–6 h after illumination. The relatively rapid induction of apoptosis after illumination might suggest the fullerenes are localized in subcellular organelles such as mitochondria, as has been previously shown for PS such as benzoporphyrin derivative [167–169]. PS that localize in lysosomes tend to produce apoptosis more slowly after illumination than mitochondrial PS, due to the release of lysosomal enzymes that subsequently activate cytoplasmic caspases [170].

The mono-pyrrolidinium substituted fullerene was the most effective PS by a considerable margin. The explanation for this observation is probably linked to its relative hydrophobicity as demonstrated by its logP value of over 2.0. The single cationic charge possessed by BF4 is also likely to play an important role in determining its relative phototoxicity. Many lipophilic monocations have been shown to localize fairly specifically in mitochondria [171–173] and this property has been proposed as a strategy to target drugs to mitochondria [174]. We have also performed preliminary experiments comparing effectiveness of BF4 to Photofrin®, one of the clinically approved PSs for cancer therapy [175]. We found that BF4 was far superior at PDT-mediated killing of human ovarian cancer cells in vitro than Photofrin. Both compounds, BF4 and Photofrin show very little dark toxicity as evidenced by the survival fraction at zero fluence, which was after 24 h incubation of the cells with each PS. Also, both show a light-dose-dependent response. However, the response of BF4 at the light fluence used was much more pronounced than that of Photofrin, demonstrating that BF4 is a significantly better PS than Photofrin against ovarian cancer cells in vitro.

We also devised a study to test whether the high degree of light-mediated antimicrobial activity of fullerenes in vitro could produce to an in vivo therapeutic effect in a mouse model of bacterial infection [107]. We used stable bioluminescent bacteria and a low light imaging system to follow the progress of the infection noninvasively in real time in two potentially lethal mouse models of infected wounds. An excisional wound on the mouse back was contaminated with one of two bioluminescent gram-negative species, *Proteus mirabilis* (2.5×10^7 cells) or *Pseudomonas aeruginosa* (5×10^6 cells). A solution of tricationic BF6 was placed into the wound followed by delivery of up to 180 J/cm^2 of broadband white light (400–700 nm). Our results showed that in both cases there was a light-dose-dependent reduction of bioluminescence from the wound not observed in control groups (light alone or BF6 alone). Fullerene-mediated PDT of mice infected with *P. mirabilis* led to 82% survival compared with 8% survival without treatment ($p < 0.001$). PDT of mice infected with highly virulent *P. aeruginosa* did not lead to survival, but when PDT was combined with a suboptimal dose of the antibiotic tobramycin (6.0 mg/kg for 1.0 day) there was a synergistic therapeutic effect with a survival of 60% compared with a survival of 20% with tobramycin alone ($p < 0.01$). In conclusion, these data suggest that cationic fullerenes have clinical potential as an antimicrobial PS for superficial infections where red light is not needed to penetrate tissue.

In the case of anti-cancer effect of LC14 and LC17-mediated PDT [101], a longer incubation period of 24 h was applied for the experiments with cancer cells owing to their relatively slow process to uptake fullerene derivatives. Furthermore, as it appears that cancer cells are more sensitive to the dark toxicity effects

of both fullerene derivatives and DMA organic solvent, we kept the concentration to a single low value of 2.0 μM. The irradiation was made by a white light source (400−700 nm) delivered at the intensity of 100 mW/cm^2 with a variable fluence dose of 0, 10, 20, 40, and 80 J/cm^2 for giving the demonstration of a light-dose dependence of cell killing. As depicted in Fig. 5.13a, $C_{70}[>M(C_3N_6{}^+C_3)_2]$ was apparently more effective at cancer cell killing than $C_{60}[>M(C_3N_6{}^+C_3)_2]$, with 1.0 log of cells

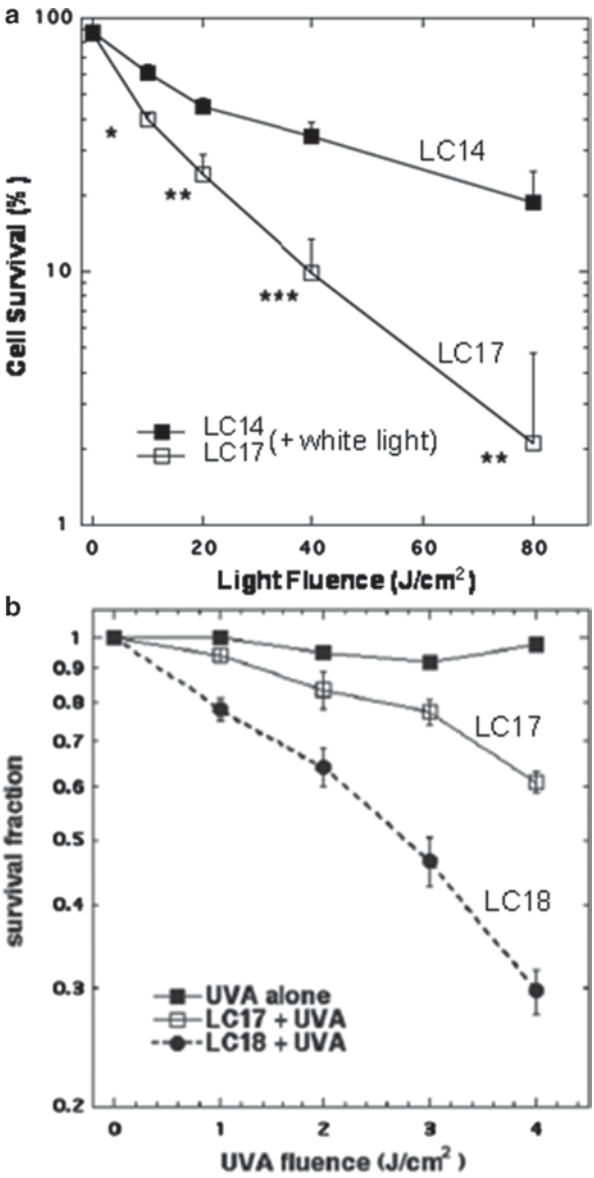

Fig. 5.13 Fluence-dependent PDT killing of human cancerous HeLa cells incubated with **a** 2.0 μM of LC14 or LC17 for 24 h and subsequent white light illumination and **b** 4.0 μM of LC17 or LC18 for 24 h and subsequent UVA light illumination. $^{**}p < 0.01$

killing at 40 J/cm^2 and 2.0 logs at 80 J/cm^2. Since the MTT assay cannot reliably measure more than 2.0 logs of killing, the latter light-dose effectiveness is equivalent to eradication. In contrast, the fullerene drug LC14 killed less than 1.0 log at all fluences up to 80 J/cm^2. Comparing LC17 with LC18 [111], $C_{70}[>M(C_3N_6{}^+C_3)_2][>M(C_3N_6C_3)_2]$-$(I^-)_{10}$, on HeLa cell PDT killing using UVA light, LC18 that possessed the additional deca-tertiary ethyleneamine chain gave significantly more cell killing than that found with LC17 that lacked the decatertiary amine chain (Fig. 5.13b). When red light was used, the situation was reversed and the decacationic LC17 gave significantly more killing than that found with LC18 with both chains. This interesting and unexpected finding prompted us to repeat the HeLa cell killing studies with the novel PDT compounds $C_{84}O_2[>M(C_3N_6{}^+C_3)_2]^-(I_3{}^-)_{10}$ (LC19-$I_3{}^-$) and $C_{84}O_2[>M(C_3N_6{}^+C_3)_2][>M(C_3N_6C_3)_2]$-$(I^-)_{10}$ (LC20) using a wider range of different wavelengths of light (Fig. 5.14, showing only either UVA or red) [111]. There was more killing with LC20 than with LC19-$I_3{}^-$ when UVA was used (Fig. 5.4a) and when blue light was used. These differences are presumably due to the greater likelihood of electron transfer processes taking place with shorter wavelengths and the presence of electron-donating tertiary-ethyleneamine chain. When white light was used, the difference between LC20 and LC19-$I_3{}^-$ was smaller but LC20 still gave more killing, while green light gave equal killing for the two fullerenes. Interestingly, when red light was used (Fig. 5.14b), the situation was reversed and LC19-$I_3{}^-$ gave significantly more killing than LC20. All the utilized compounds induced a very low dark toxicity at these concentrations.

One of the first biological applications of photoactivated fullerenes was to produce cleavage of DNA strands after illumination. Cleavage of supercoiled pBR322 DNA was observed after incubation with a fullerene carboxylic acid under visible light irradiation but not in the dark [158]. Both nicked circular and linear duplex form DNA were observed and there was considerable selectivity for cleavage at guanine bases. The photoinduced action was more pronounced in D_2O in which singlet oxygen has a longer lifetime. An and coworkers prepared [176] a covalent conjugate between an oligodeoxynucleotide and either a fullerene or eosin. Cleavage of target complementary 285-base single-stranded DNA was observed at guanosine residues in both cases upon illumination. However, the fullerene conjugate was more efficient in cleavage than the eosin conjugate. Moreover, the cleavage was not quenched by azide or increased by deuterium oxide as was found for the eosin conjugate, suggesting the mechanism followed a Type I pathway. Boutorine et al. [177] described a fullerene-oligonucleotide that can bind single- or double-stranded DNA, and which also cleaves the strand(s) proximal to the fullerene moiety upon exposure to light. Nakanishi et al. [178] also observed DNA cleavage by functionalized C_{60}. Yamakoshi et al. studied biological activities of fullerenes under illumination including DNA cleavage, hemolysis, mutagenicity, and cell toxicity [179]. They prepared a conjugate between a fullerene and an acridine molecule as a DNA intercalating agent and compared its DNA photocleavage capacity on pBR322 supercoiled plasmid with pristine fullerene both solubilized in PVP. This compound showed much more effective DNA-cleaving activity in the presence of NADH than pure C_{60} [180]. Liu and coworkers [181] used a water-soluble conjugate between anthryl-cyclodextrin and C_{60} to carry out photocleavage of pGEX5X2 DNA. Ikeda

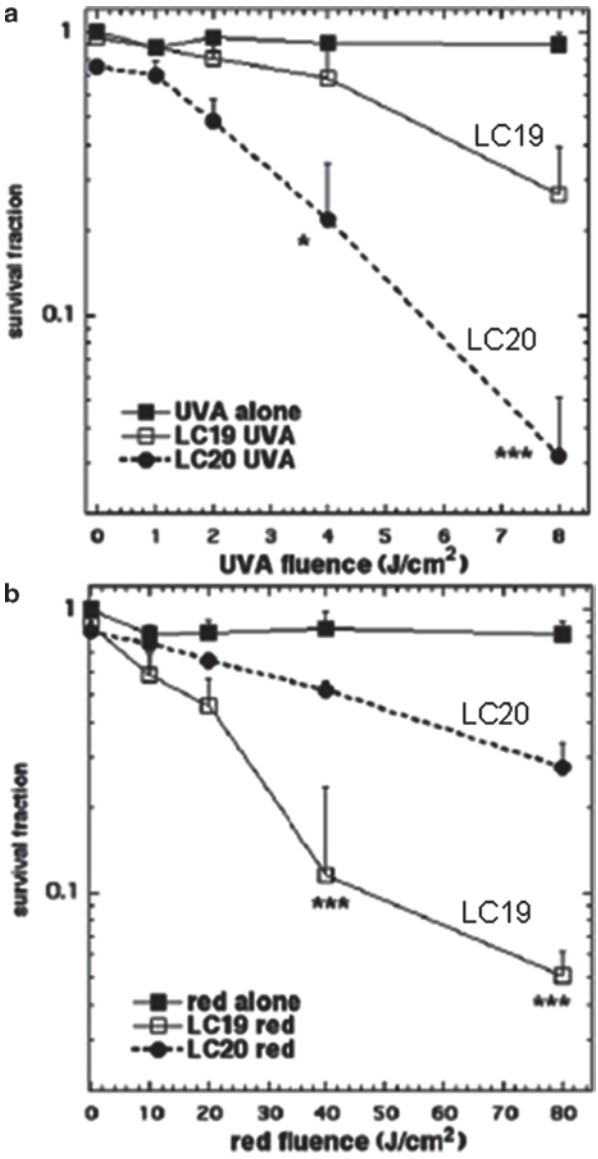

Fig. 5.14 Fluence-dependent PDT killing of human cancerous HeLa cells incubated with 4.0 μM of LC19 or LC20 for 24 h and subsequent **a** UVA light and **b** red light illumination. *$p < 0.05$, ***$p < 0.01$

et al. [182] used functionalized liposomes encorporating both C_{60} and C_{70} fullerenes into the lipid bilayer to carry out photocleavage of ColE1 supercoiled plasmid DNA using $\lambda > 350$ nm light. Interestingly, C_{70} was significantly better (3.5 times) than C_{60} in photocleaving DNA.

It has also been shown that fullerene-mediated PDT may lead to mutagenic effects. PVP-solubilized fullerene was found to be mutagenic for *Salmonella* strains TA102, TA104, and YG3003 in the presence of rat liver microsomes when it was irradiated by visible light [183]. The mutagenicity was elevated in strain YG3003,

a repair enzyme-deficient mutant of TA102. The mutation was reduced in the presence of *β*-carotene and parabromophenacyl bromide, a scavenger and an inhibitor, respectively, of phospholipase. The results suggested that singlet oxygen was generated by irradiating the C_{60} by visible light and that the mutagenicity was due to oxidized phospholipids in rat liver microsomes. The linoleate fraction isolated by high-performance liquid chromatography was a major component, and it played an important role in mutagenicity. The results of electron spin resonance (ESR) spectrum analysis suggested generation of radicals at the guanine base but not thymine, cytosine, and adenine bases and formation of 8-hydroxydeoxyguanosine (8-OH-dG). The mechanism was proposed to involve indirect action of singlet oxygen due to lipid peroxidation of linoleate that causes oxidative DNA damage.

A group from India has studied the ability of fullerenes to produce oxidative damage to lipids in microsomal preparations. Cyclodextrin encapsulated C_{60} added to rat liver microsomes followed by exposure to UV or visible light produced lipid peroxidation as assayed by thiobarbituric acid reactive substances, lipid hydroperoxides, damage to proteins as assessed by protein carbonyls and loss of the membrane-bound enzymes [184]. Quenchers of singlet oxygen (β-carotene and sodium azide) inhibited peroxidation, and deuteration of the buffer enhanced peroxidation, indicating that the photochemical mechanism is predominantly due to Type II ($^1O_2$). In a subsequent study [185], they compared pristine C_{60} with a polyhydroxylated derivative $C_{60}(OH)_{18}$ and found that the latter produced more pronounced peroxidative damage and the mechanism was different and was mediated primarily by radical species. Lipid peroxidation was also shown in sarcoma 180 ascites microsomes. Yang et al. [186] used human erythrocyte membranes (EMs) as a model system to examine photoinduced lipid peroxidation by a bis(methanophosphonate)fullerene (BMPF) and four other fullerene derivatives including a mono-methanophosphonic acid fullerene (MMPF), a $DMAC_{60}$, a $TMAC_{60}$, and a polyhydroxylated fullerene (fullerenol). Lipid peroxidation was assessed as the malondialdehyde (MDA) level measured by the thiobarbituric acid assay. It was observed that BMPF increased the MDA level of EMs after irradiation in both time- and dose-dependent manners. The photoinduced activity became very significant ($p < 0.01$) under the conditions of either the concentration of 10 μM and irradiation time of 30 min or the concentration of 5.0 μM and irradiation time of 60 min. Involvement of ROS in the activity was also examined by specific inhibitors of singlet oxygen, superoxide anions, and hydroxyl radicals, respectively. While all three kinds were found responsible for the activity, the former two might play more important roles than the last one.

5.13 In Vivo PDT of Tumors and Third-Degree Burn Infections

Fullerenes should have a photodynamic effect on tumors, if (a) the compound is accumulated in the tumor tissue, (b) a reasonably efficient way to administer the compound to tumor-bearing animals is found, and (c) enough excitation light can

be delivered to the photosensitized tumors. The first report of fullerenes being used to carry out PDT of actual tumors was by Tabata [76] in 1997. They chemically modified the water-insoluble C_{60} with PEG, not only to make it soluble in water but also to enlarge its molecular size. When injected intravenously into mice carrying a subcutaneous tumor on the back, the C_{60}–PEG conjugate exhibited higher accumulation and more prolonged retention in the tumor tissue than in normal tissue. The conjugate was excreted without being accumulated in any specific organ. Following intravenous injection of C_{60}–PEG conjugate or Photofrin (a recognized PS) to tumor-bearing mice, coupled with exposure of the tumor site to visible light, the volume increase of the tumor mass was suppressed and the C_{60} conjugate exhibited a stronger suppressive effect than Photofrin. Histological examination revealed that conjugate injection plus light irradiation strongly induced tumor necrosis without any damage to the overlying normal skin. The antitumor effect of the conjugate increased with increasing fluence delivered and C_{60} dose, and cures were achieved by treatment with a low dose of 424 μg/kg at a (very high) fluence of 10^7 J/cm^2. Liu and others [75] conjugated PEG to C_{60} (C_{60}–PEG), and diethylenetriaminepentaacetic acid (DTPA) was subsequently introduced to the terminal group of PEG to prepare C_{60}–PEG–DTPA that was mixed with gadolinium acetate solution to obtain Gd^{3+}-chelated C_{60}–PEG–DTPA–Gd. Following intravenous injection of C_{60}–PEG–DTPA–Gd into tumor-bearing mice, the PDT antitumor effect and MRI tumor imaging were evaluated. Similar generation of superoxide upon illumination was observed with or without Gd^{3+} chelation. Intravenous injection of C_{60}–PEG–DTPA–Gd into tumor-bearing mice plus light (400–500 nm, 53.5 J/cm^2) showed significant antitumor PDT effect and the effect depended on the timing of light irradiation that correlated with tumor accumulation as detected by the enhanced intensity of MRI signal.

A preliminary in vivo study PDT using hydrophilic nanovesicles formed from hexa(sulfo-*n*-butyl)-C_{60} (FC_4S, Fig. 5.6) was performed by Chiang and his coworkers [41, 187]. The median lethal dose (LD50) of FC_4S was defined as approximately 600 mg/kg in acute toxicity studies. No adverse effects were noted in the animals when the FC_4S was administered orally [188]. This study was performed in imprinting control region (ICR) mice bearing sarcoma 180 subcutaneous tumors. They were given either intraperitoneal or intravenous injection of water-soluble FC_4S in PBS (5.0 mg/kg body weight). The tumor site was subsequently irradiated with an argon ion laser beam at a wavelength of 515 or an argon-pumped dye laser at 633 nm with the beam focused to a diameter of 7–8 mm with the total light dose adjusted to a level of 100 J/cm^2 in each experiment. Consistently, inhibition of tumor growth was found more effective using the low wavelength, that is, in case of better-absorbed 515-nm laser than the 633-nm laser. Administration of FC_4S to mice by the IP method had slightly better inhibition effectiveness than the IV method. These data summarized above not only suggest that PDT with fullerenes is possible in animal tumor models but also demonstrate the potential use of these compounds as PS for PDT of cancer.

Because cancer cells endocytose glucose more effectively than normal cells due to upregulation of glucose receptors, Otake and colleagues prepared a set of C_{60}–

glucose conjugates that also served the purpose of solubilizing the fullerene [189]. The glycoconjugated C_{60} compounds produced selective phototoxicity (after irradiation with UVA1) towards cancer cells compared to normal fibroblasts showing the importance of targeting glucose receptors. Inhibition by sodium azide showed the involvement of singlet oxygen in the cell killing. In order to investigate the effect of PDT in vivo, human-melanoma (COLO679)-xenograft-bearing mice were injected intratumorally with C_{60}– $(Glc)_1$ (0.1 or 0.2 mg/tumor) and irradiated with 10 J/cm^2 UVA1 after a 4-h drug-light interval. PDT with C_{60}– $(Glc)_1$ was reported to suppress the tumor growth with the higher dose performing better than the lower dose. We have recently shown [190] that intraperitoneal PDT with a fullerene and white light was able to demonstrate significant therapeutic effects in a challenging mouse model of disseminated abdominal cancer. In humans, this form of cancer is characterized as a thin covering of tumor nodules on intestines, and other abdominal organs and responds poorly to standard treatment such as surgery or chemotherapy. In this study, we formulated the monocationic BF4 in micelles composed of Cremophor EL to treat intraperitoneally disseminated colorectal cancer in a mouse model. We used a colon adenocarcinoma cell line (CT26) expressing firefly luciferase to allow monitoring of IP tumor burden by noninvasive optical imaging. IP injection of a preparation of BF4 formulated in micelles (5.0 mg/kg), followed by white light illumination (100 J/cm^2) delivered through the peritoneal wall produced a statistically significant reduction in bioluminescence and a survival advantage in mice. White light was more effective than green light, while red light produced unacceptable toxicity to the mice due to excessive tissue penetration of the light into abdominal organs. A drug-light interval of 24 h was more effective than a 3-h drug-light interval showing the importance of allowing enough time for the fullerene to be taken up into the cancer cells. The IP tumors were destroyed by the process of necrosis rather than the more usual apoptosis.

In the case of third-degree burns, they are particularly susceptible to bacterial infection as the barrier function of the skin is destroyed, the dead tissue is devoid of host-defense elements, and a systemic immune suppression is a worrying consequence of serious burns [191]. Furthermore, the lack of perfusion of the burned tissue means that systemic antibiotics are generally ineffective [192]. Although excision and skin grafting is now standard treatment for third-degree burns [193], superimposed infection is still a major problem. Patients with gram-negative burn infections have a higher likelihood of developing sepsis than gram-positive infections [194]. Topical antimicrobials are the mainstay of therapy for burn infections and PDT may have a major role to play in the management of this disease [195].

We tested the in vivo PDT activity of some fullerenes in a mouse model of a third-degree burn infected with gram-negative bioluminescent bacterial species. We initially used the pathogenic variant of *E. coli* (enteropathogenic *E. coli*, EPEC) and inoculated the burns with $1.5 \times 10(8)$ colony-forming unit (CFU). UVA light appeared to be the most effective in killing all the tested species. After considerable experimentation we settled on an 80-μM solution of fullerenes in PBS containing 8% v/v DMA. The DMA solvent is important in keeping the fullerene in solution and encouraging penetration of the PS into the infected tissue of the burn. The

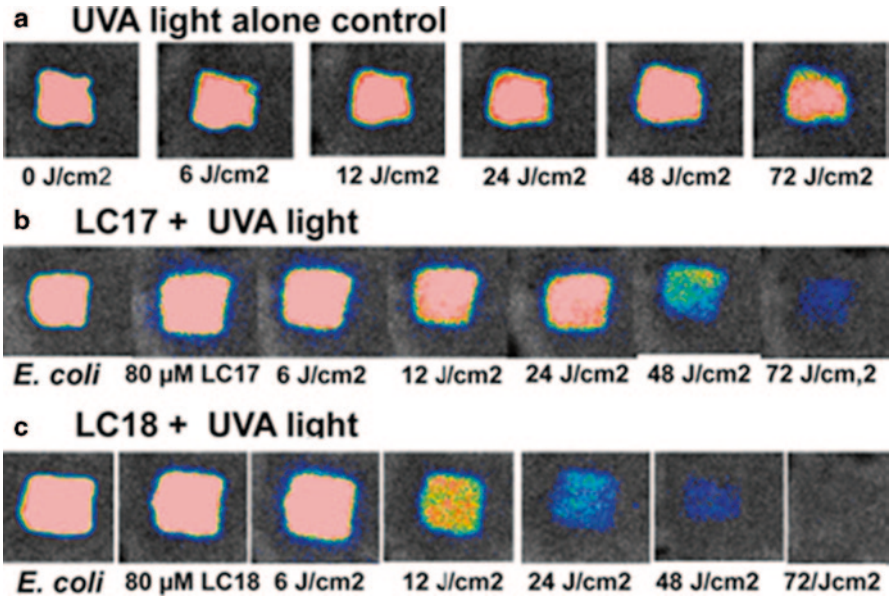

Fig. 5.15 Representative bioluminescence images from mice with *E. coli* burn infections and treated with successive fluences of PDT or UVA light alone. **a** UVA control. **b** LC17+UVA light. **c** LC18+UVA light

light-dose-dependent reduction of bioluminescent signal is shown in Fig. 5.15 [196]. As shown in Fig. 5.15a that UVA plus PBS containing 8% DMA (no fullerene) as a light alone control gave only a slight reduction in bioluminescent signal even after 72 J/cm^2 of light had been delivered. When LC17 was used (Fig. 5.15b) there was a significant reduction in bioluminescence signal apparent at 48 J/cm^2 and only a trace remaining after 72 J/cm^2. When LC18 was used (Fig. 5.15c) it can be seen there was a noticeable drop in signal after only 12 J/cm^2 had been delivered, and by the time 72 J/cm^2 had been delivered the signal had been effectively eliminated. Both PDT groups were significantly lower than the UVA control at all fluences, and LC18 was significantly lower than LC17 at 12, 24, and 48 J/cm^2. Because we observed recurrence of the *E. coli* in the mouse burn in the days following the PDT treatment, we asked whether a therapeutically useful single PDT treatment could be demonstrated. We formed the hypothesis that the recurrence observed with PDT of *E. coli* was due to a combination of factors. Firstly, that a few remaining viable bacteria were left in the burn even after disappearance of the luminescence signal. Secondly, that the virulence of the bacteria was an important factor. To overcome these adverse factors we changed several parameters in the experiment. Firstly, we changed to *Acinetobacter baumannii,* which although is clinically problematic due to high antibiotic resistance, appears to be less virulent in this mouse model, and we used a lower inoculum [5 × 10(7) compared to 1.5 × 10(8)]. Secondly, we raised the concentration of fullerene from 80 to 300 μM. Thirdly, we raised the concentration of DMA from 8 to 15%. Figure 5.16 shows the bioluminescence signals of

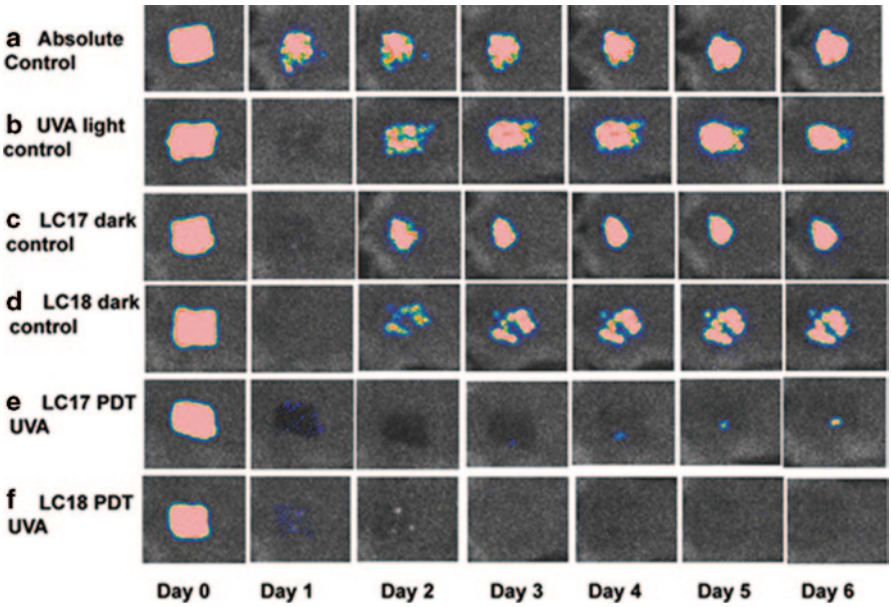

Fig. 5.16 Representative bioluminescence images from mice with *A. baumannii* burn infections and treated with PDT, UVA light alone, or absolute control, captured day 0 (before PDT) and then daily for six days. **a** Absolute control. **b** UVA control + 15% DMA. **c** LC17 + 15% DMA. **d** LC18 + 15% DMA. **e** LC17 + 15% DMA + UVA light. **f** LC18 + 15% DMA + UVA light

representative mice captured daily from days 0 (before PDT) to day 6 post PDT. It can be seen that the absolute control (Fig. 5.16a, no light, no fullerene, no DMA) showed a continuing infection in the burn that lasted for 6 days. All other groups (B–F) showed a loss of bioluminescence signal on day 1 (the day after PDT). However, in the three control groups, UVA alone (Fig. 5.16b), LC17 in dark (Fig. 5.16c), and LC18 alone (Fig. 5.16d) there were significant recurrence of bioluminescence on day 2 that lasted until day 6. In the LC17 PDT group (Fig. 5.16e), there was only a tiny recurrence visible at day 4 that remained tiny on days 5 and 6. In the LC18 PDT group, there was no recurrence of bioluminescence visible on any day of follow-up. Accordingly, we obtained good light-dose-dependent loss of bioluminescence signal in the mouse model of *E. coli* burn infection, and LC18 was more effective than LC17 in mediating PDT under UVA illumination, consistent with the in vitro results. However, despite this success, recurrence of bioluminescence was observed in the succeeding days. While it is entirely possible that the PDT treatment could be repeated each day until the infection was defeated, we considered that it would be preferable if a single PDT treatment could be shown to be effective in eliminating the bacteria from the burn. This goal was achieved with an *A. baumannii* model, which is of high clinical relevance as this species has been found to be the most prevalent in a military burns hospital [197] and is notorious for its antibiotic resistance [198]. Again LC18 was found to be superior to LC17 in this application

of PDT for burn infection. Lu et al. [107] reported an in vivo study where a tricationic C_{60} fullerene excited by white light was used to treat a mouse model of excisional wound infection by the gram-negative *P. aeruginosa* or *P. mirabilis*. This is a highly invasive infection model and fullerene mediated PDT was able to save the lives of mice infected with *P. mirabilis,* and, in the case of *P. aeruginosa,* when used in combination with subtherapeutic doses of antibiotics (tobramycin).

Furthermore, due to the aforementioned limitation of being nonfluorescent, not much has been studied about the in vivo pharmacokinetic characteristics of fullerenes such as the biodistribution and the organ/target specific binding. It is considerably challenging to get good biodistribution data of fullerenes. The approaches that can be applied for studying the biodistribution would be by radiolabeling fullerene by I^{125} or by C^{14}. In one of the study fullerenes were labeled with I^{125} and biodistribution studies were carried out. It was shown that after injection in the tumor-bearing mice C_{60}–PEG conjugate disappeared gradually from the blood circulation and 78% was excreted from the body within 24 h. This conjugate did not show any marked accumulate in any of the organ though the accumulation in the liver increased up to 24 h but decreased with time and was undetectable at 144 h after injection. The fullerene accumulated in the carcass and the gastrointestinal tract in the early period but was eliminated thereafter in the same manner as liver. This fullerene accumulated in the tumor tissue to a significantly higher extent than in the skin and the muscles, and it was also retained in the tumor tissue for a longer period than the normal tissue [76]. Liu and others conjugated PEG to C_{60} (C_{60}–PEG), and DTPA was subsequently introduced to the terminal group of PEG to prepare C_{60}–PEG–DTPA that was mixed with gadolinium acetate solution to obtain Gd^{3+}-chelated C_{60}–PEG–DTPA–Gd. Following intravenous injection of C_{60}–PEG–DTPA–Gd into tumor-bearing mice, they observed tumor accumulation by enhanced intensity of MRI signal [75].

5.14 Conclusions

At the end of this chapter, we must ask ourselves whether in all reality it is likely that fullerenes will ever be accepted as viable PS for PDT of any disease. As discussed previously, these compounds have certain unique features that could make them favorable candidates and, at the same time, other unique features that would argue against them as PS for PDT. The most important favorable property is their rather unusual photochemical mechanism. As shown by us and by others, in aqueous solutions and particularly in the presence of reducing agents, these compounds produce a substantial amount of superoxide anion in a Type I photochemical process involving electron transfer from the excited triplet to molecular oxygen. Although many workers in the PDT field think that the product of the Type II photochemical process, singlet oxygen, is the major cytotoxic species operating in PDT-induced cell killing, there have been reports that Type I mechanisms may be equally effective

or even more effective than Type II. This is because hydroxyl radicals are the most reactive and potentially the most cytotoxic of all ROS. It is assumed that hydroxyl radicals are formed from hydrogen peroxide by Fenton chemistry reactions catalyzed by Fe^{2+} or Cu^{+} ions, and that the hydrogen peroxide is produced by dismutation of superoxide anion either by enzyme catalysis or naturally. Another possible mechanism of cytotoxicity is the diffusion-controlled reaction between superoxide and nitric oxide to form the highly toxic species, peroxynitrite. Elevated levels of nitric oxide are present in both cancers and infections thus giving the possibility of additional levels of selectivity for target-specific damage.

The chief disadvantage of fullerenes is likely to be their optical absorption properties. The absorption spectrum of fullerenes is highest in the UVA and blue regions of the spectrum where the tissue penetration depth of illumination is shortest due to a combination of light absorption by cellular chromophores and light scattering by cellular structures. However, the molar absorption coefficients of fullerenes are relatively high and the tail of absorption does stretch out into the red regions of the visible spectrum. Fullerenes are not the most amenable molecules for drug delivery, and choosing appropriate formulations may be difficult. Nevertheless, the polycationic modifications described in this chapter demonstrate that with the correct functionalities present on the fullerene cage, these difficulties may be overcome.

5.15 Future Perspectives

Fullerenes have been widely studied in recent years as potential PS that could mediate PDT of diverse diseases. Most of these reports have been confined to in vitro studies where viruses, bacteria, fungi, or cancer cells have been incubated with a diverse array of functionalized or solubilized fullerene compounds followed by illumination with light that is usually UVA, blue, green, or white because the absorption spectrum of fullerenes is biased towards lower wavelengths. Since in vivo PDT usually uses red light for its improved tissue-penetrating properties, it was unclear whether fullerenes would mediate effective PDT in vivo. This question can now be answered in the affirmative. In fact, the report in which mice suffered toxicity after fullerene PDT with red light but exhibited a beneficial therapeutic effect after white light illumination suggests that this supposed drawback may actually be an advantage instead. Future studies will include synthesis of new fullerene derivatives particularly those with light-harvesting antennae to broaden the range of activating light that can be used, hence increasing the light penetration depth into tissue. More experiments should be designed to increase the understanding of the mechanisms that govern the balance between Type I and Type II ROS. These studies will establish whether fullerenes can compete with more traditional PS in clinical applications of PDT.

Acknowledgments We thank the financial support of National Institute of Health (NIH) under the grant numbers R01CA137108 and R01AI058075.

References

1. D.E. Dolmans, D. Fukumura, R.K. Jain, Photodynamic therapy for cancer. Nat. Rev. Cancer **3**, 380–387 (2003)
2. B.C. Wilson, Photodynamic therapy for cancer: principles. Can. J. Gastroenterol. **16**(6), 393–396 (2002)
3. B.W. Henderson, T.J. Dougherty, How does photodynamic therapy work? Photochem. Photobiol. **55**(1), 145–157 (1929)
4. A.P. Castano, T.N. Demidova, M.R. Hamblin, Mechanisms in photodynamic therapy: part one–photosensitizers, photochemistry and cellular localization. Photodiag. Photodyn. Ther. **1**, 279–293 (2004)
5. A.P. Castano, T.N. Demidova, M.R. Hamblin, Mechanisms in photodynamic therapy: part two–cellular signalling, cell metabolism and modes of cell death. Photodiag. Photody. Ther. **2**, 1–23 (2005)
6. A.P. Castano, T.N. Demidova, M.R. Hamblin, Mechanisms in photodynamic therapy: part three–photosensitizer pharmacokinetics, biodistribution, tumor localization and modes of tumor destruction. Photodiagn. Photodyn. Ther. **2**, 91–106 (2005)
7. T.J. Dougherty, A brief history of clinical photodynamic therapy development at Roswell Park Cancer Institute. J. Clin. Laser Med. Surg. **14**, 219–221 (1996)
8. T.J. Dougherty, C.J. Gomer, B.W. Henderson, G. Jori, D. Kessel, M. Korbelik, J. Moan, Q. Peng, Photodynamic therapy. J. Natl. Cancer Inst. **90**, 889–905 (1998)
9. M.R. Detty, S.L. Gibson, S.J. Wagner, Current clinical and preclinical photosensitizers for use in photodynamic therapy. J. Med. Chem. **47**, 3897–3915 (2004)
10. P. Baas, I. van Mansom, H. van Tinteren, F.A. Stewart, N. van Zandwijk, Effect of N-acetylcysteine on Photofrin-induced skin photosensitivity in patients. Lasers Surg. Med. **16**, 359–367 (1995)
11. A. Orenstein, G. Kostenich, L. Roitman, Y. Shechtman, Y. Kopolovic, B. Ehrenberg, Z. Malik, A comparative study of tissue distribution and photodynamic therapy selectivity of chlorin e6, Photofrin II and ALA-induced protoporphyrin IX in a colon carcinoma model. Br. J. Cancer **73**, 937–944 (1996)
12. J.D. Spikes, Chlorins as photosensitizers in biology and medicine. J. Photochem. Photobiol. B. **6**, 259–274 (1990)
13. D. Kessel, P. Thompson, Purification and analysis of hematoporphyrin and hematoporphyrin derivative by gel exclusion and reverse-phase chromatography. Photochem. Photobiol. **46**, 1023–1025 (1987)
14. R.W. Boyle, D. Dolphin, Structure and biodistribution relationships of photodynamic sensitizers. Photochem. Photobiol. **64**, 469–485 (1996)
15. C.J. Gomer, Preclinical examination of first and second generation photosensitizers used in photodynamic therapy. Photochem. Photobiol. **54**, 1093–1107 (1991)
16. E.S. Nyman, P.H. Hynninen, Research advances in the use of tetrapyrrolic photosensitizers for photodynamic therapy. J. Photochem. Photobiol. B. **73**, 1–28 (2004)
17. R.M. Szeimies, S. Karrer, C. Abels, P. Steinbach, S. Fickweiler, H. Messmann, W. Bäumler M. Landthaler, 9-Acetoxy-2,7,12,17-tetrakis-(beta-methoxyethyl)-porphycene (ATMPn), a novel photosensitizer for photodynamic therapy: uptake kinetics and intracellular localization. J. Photochem. Photobiol. B. **34**(1), 67–72 (1996)
18. I. Rosenthal, Phthalocyanines as photodynamic sensitizers. Photochem. Photobiol. **53**(6), 859–870 (1991)
19. N. Levi, R.R. Hantgan, M.O. Lively, D.L. Carroll, G.L. Prasad, C_{60}-fullerenes: detection of intracellular photoluminescence and lack of cytotoxic effects. J. Nanobiotechnol. **4**, 14–25 (2006)
20. B. Belgorodsky, L. Fadeev, J. Kolsenik, M. Gozin, Formation of a soluble stable complex between pristine C_{60}-fullerene and a native blood protein. Chembiochem. **7**, 1783–1789 (2006)

21. N. Gharbi, M. Pressac, M. Hadchouel, H. Szwarc, S.R. Wilson, F. Moussa, [60]fullerene is a powerful antioxidant in vivo with no acute or subacute toxicity. Nano Lett. **5**, 2578–2585 (2005)
22. C.M. Sayes, A.M. Gobin, K.D. Ausman, J. Mendez, J.L. West, V.L. Colvin, Nano-C_{60} cytotoxicity is due to lipid peroxidation. Biomaterials. **26**, 7587–7595 (2005)
23. E. Nakamura, H. Isobe, Functionalized fullerenes in water. The first 10 years of their chemistry, biology, and nanoscience. Acc. Chem. Res. **36**, 807–815 (2003)
24. D. Pantarotto, N. Tagmatarchis, A. Bianco, M. Prato, Synthesis and biological properties of fullerene-containing amino acids and peptides. Mini Rev. Med. Chem. **4**, 805–814 (2004)
25. A. Bagno, S. Claeson, M. Maggini, M.L. Martini, M. Prato, G. Scorrano, [60]Fullerene as a substituent. Chemistry **8**, 1015–1023 (2002)
26. B.H. Chen, J.P. Huang, L.Y. Wang, J. Shiea, T.L. Chen, L.Y. Chiang, Synthesis of octadecahydroxylated C_{70}. Synth. Commun. **28**, 3515–3525 (1998)
27. S. Bosi, T. Da Ros, G. Spalluto, M. Prato, Fullerene derivatives: an attractive tool for biological applications. Eur. J. Med.Chem. **38**, 913–923 (2003)
28. A.W. Jensen, S.R. Wilson, D.I. Schuster, Biological applications of fullerenes. Bioorg.Med. Chem. **4**, 767–779 (1996)
29. N. Tagmatarchis, H. Shinohara, Fullerenes in medicinal chemistry and their biological applications. Mini Rev. Med. Chem. **1**, 339–348 (2001)
30. P. Mroz, G.P. Tegos, H. Gali, T. Wharton, T. Sarna, M.R. Hamblin, Photodynamic therapy with fullerenes. Photochem. Photobiol. Sci. **6**(11), 1139–1149 (2007)
31. M.R. Hamblin, P. Mroz, *Advances in Photodynamic Therapy: Basic, Translational and Clinical*. (Artech House, Norwood, 2008)
32. P. Agostinis, K. Berg, K.A. Cengel et al., Photodynamic therapy of cancer: an update. CA Cancer J. Clin. **61**, 250–281 (2011)
33. C. Abels, Targeting of the vascular system of solid tumours by photodynamic therapy (PDT). Photochem. Photobiol. Sci. **3**(8), 765–771 (2004)
34. A.P. Castano, P. Mroz, M.R. Hamblin, Photodynamic therapy and anti-tumour immunity. Nat. Rev. Cancer **6**(7), 535–545 (2006)
35. R.E. Hancock, A. Bell, Antibiotic uptake into gram-negative bacteria. Eur. J. Clin. Microbiol. Infect. Dis. **7**(6), 713–720 (1988)
36. P. Agostinis, E. Buytaert, H. Breyssens, N. Hendrickx, Regulatory pathways in photodynamic therapy induced apoptosis. Photochem. Photobiol. Sci. **3**, 721–729 (2004)
37. C.S. Foote, Definition of Type-I and Type-II photosensitized oxidation. Photochem. Photobiol. **54**, 659–659 (1991)
38. M. Ochsner, Photophysical and photobiological processes in the photodynamic therapy of tumours. J. Photochem. Photobiol. B. **39**, 1–18 (1997)
39. C.S. Foote, Photophysical and photochemical properties of fullerenes. Top Curr. Chem. **169**, 347–363 (1994)
40. J.W. Arbogast, A.P. Darmanyan, C.S. Foote et al., Photophysical properties of C_{60}. J. Phys. Chem. (A Mol Spectrosc Kinet Environ Gen Theory) **95**(1), 11–12 (1991)
41. C. Yu, T. Canteenwala, M.E. El-Khouly, Y. Araki, L.Y. Chiang, B.C. Wilson, O. Ito, K. Pritzker, Efficiency of singlet oxygen production from nanospheres of molecular micelle-like photodynamic sensitizers hexa(sulfo-*n*-butyl)[60]fullerenes (FC_4S). J. Mater. Chem. **15**,1857–1864 (2005)
42. M. Fujitsuka, O. Ito, in *Encyclopedia of Nanoscience and Nanotechnology*, ed. by H.S. Nalwa (American Scientific Publishers, Stevenson Ranch 2004), pp. 593–615
43. Y. Yamakoshi, N. Umezawa, A. Ryu, K. Arakane, N. Miyata, Y. Goda, T. Masumizu, T. Nagano, Active oxygen species generated from photoexcited fullerene (C_{60}) as potential medicines: O_2^{-}* versus $^1O_2$. J. Am. Chem. Soc. **125**(42), 12803–12809 (2003)
44. Q. Xie, E. Perez-Cordero, L. Echegoyen, Electrochemical detection of C_{60}^{6-} and C_{70}^{6-}: enhanced stability of fullerides in solution. J. Am. Chem. Soc. **114**, 3978–3980 (1992)
45. D.M. Guldi, M. Prato, Excited-state properties of C_{60} fullerene derivatives. Acc. Chem. Res. **33**(10), 695–703 (2000)

46. T. Nojiri, A. Watanabe, O. Ito, Photoinduced electron transfer between C_{60}/C_{70} and zinc tetraphenylporphyrin in polar solvents. J. Phys. Chem. A. **102**, 5215–5219 (1998)
47. N. Miyata, Y. Yamakoshi, I. Nakanishi, Reactive species responsible for biological actions of photoexcited fullerenes. Yakugaku zasshi: Jpn. J. Pharmaceut. Soc. **120**, 1007–1016 (2000)
48. P. Mroz, A. Pawlak, M. Satti, H. Lee, T. Wharton, H. Gali, T. Sarna, M.R. Hamblin, Functionalized fullerenes mediate photodynamic killing of cancer cells: Type I versus Type II photochemical mechanism. Free Radic. Biol. Med. **43**, 711–719 (2007)
49. G.P. Tegos, T.N. Demidova, D. Arcila-Lopez, H. Lee, T. Wharton, H. Gali, M.R. Hamblin, Cationic fullerenes are effective and selective antimicrobial photosensitizers. Chem. Biol. **12**, 1127–1135 (2005)
50. L.Y. Chiang, F.J. Lu, J.T. Lin, Free-radical scavenging activity of water-soluble fullerenols. J. Chem. Soc., Chem. Commun. 1283–1284 (1995)
51. M.C. Tsai, Y.H. Chen, L.Y. Chiang, Polyhydroxylated C_{60} fullerenol 1, a novel free radical trapper, prevented the hydrogen peroxide and cumene hydroperoxide elicited changes in rat hippocampus in vitro. J. Pharm. Pharmacol. **49**, 438–445 (1997)
52. Y.L. Lai, L.Y. Chiang, Water-soluble fullerene derivatives attenuate exsanguination-induced bronchoconstriction of guinea pigs. J. Auton. Pharmacol. **17**, 229–235 (1997)
53. J.B. Bhonsle, Y. Chi, J.P. Huang, J. Shiea, B.J. Chen, L.Y. Chiang, Novel water-soluble hexa(sulfobutyl)fullerenes as potent free radical scavengers. Chem. Lett. **5**, 465–466 (1998)
54. Y.L. Lai, W.Y. Chiou, F.J. Lu, L.Y. Chiang, Roles of oxygen radicals and elastase in citric acid-induced airway constriction of guinea pigs. Brit. J. Pharmacol. **126**, 778–784 (1999)
55. M. Lens, L. Medenica, U. Citernesi, Antioxidative capacity of C_{60} (buckminsterfullerene) and newly synthesized fulleropyrrolidine derivatives encapsulated in liposomes. Biotechnol. Appl. Biochem. **51**(Pt 3), 135–140 (2008)
56. P. Spohn, C. Hirsch, F. Hasler, A. Bruinink, H.F. Krug, P. Wick, C_{60} fullerene: a powerful antioxidant or a damaging agent? The importance of an in-depth material characterization prior to toxicity assays. Environ. Pollut. **157**(4), 1134–1139 (2009)
57. X. Cai, H. Jia, Z. Liu et al., Polyhydroxylated fullerene derivative $C_{60}(OH)_{24}$ prevents mitochondrial dysfunction and oxidative damage in an MPP(+)-induced cellular model of Parkinson's disease. J. Neurosci. Res. **86**(16), 3622–3634 (2008)
58. L.L. Dugan, J.K. Gabrielsen, S.P. Yu, T.S. Lin, D.W. Choi, Buckminsterfullerenol free radical scavengers reduce excitotoxic and apoptotic death of cultured cortical neurons. Neurobiol. Dis. **3**(2), 129–135 (1996)
59. G.V. Andrievsky, V.I. Bruskov, A.A. Tykhomyrov, S.V. Gudkov, Peculiarities of the antioxidant and radioprotective effects of hydrated C_{60} fullerene nanostuctures in vitro and in vivo. Free Radic. Biol. Med. **47**(6), 786–793 (2009)
60. D.R. Weiss, T.M. Raschke, M. Levitt, How hydrophobic buckminsterfullerene affects surrounding water structure. J. Phys. Chem. B. **112**(10), 2981–2990 (2008)
61. F. Cataldo, T. Da Ros, *Medicinal Chemistry and Pharmacological Potential of Fullerenes and Carbon Nanotubes*, vol. 1 (Springer, New York, 2008)
62. L.K. Duncan, J.R. Jinschek, P.J. Vikesland, C_{60} colloid formation in aqueous systems: effects of preparation method on size, structure, and surface charge. Environ. Sci. Technol. **42**(1), 173–178 (2008)
63. E.M. Hotze, J. Labille, P. Alvarez, M.R. Wiesner, Mechanisms of photochemistry and reactive oxygen production by fullerene suspensions in water. Environ. Sci. Technol. **42**(11), 4175–4180 (2008)
64. L. Culotta, D.E. Koshland Jr.. Buckyballs: wide open playing field for chemists. Science **254**(5039), 1706–1709 (1991)
65. G. Oberdorster, Safety assessment for nanotechnology and nanomedicine: concepts of nanotoxicology. J. Intern. Med. **267**(1), 89–105 (2010)
66. S. Kato, aH. Aoshim, Y. Saitoh, N. Miwa, Biological safety of liposome-fullerene consisting of hydrogenated lecithin, glycine soja sterols, and fullerene-C_{60} upon photocytotoxicity and bacterial reverse mutagenicity. Toxicol. Ind. Health **25**(3), 197–203 (2009)

67. S. Kato, H. Aoshima, Y. Saitoh, N. Miwa, Fullerene-C_{60}/liposome complex: defensive effects against UVA-induced damages in skin structure, nucleus and collagen type I/IV fibrils, and the permeability into human skin tissue. J. Photochem. Photobiol. B. **98**, 99–105 (2010)
68. Y. Doi, A. Ikeda, M. Akiyama, M. Nagano, T. Shigematsu, T. Ogawa, T. Takeya, T. Nagasaki, Intracellular uptake and photodynamic activity of water-soluble [60]- and [70]fullerenes incorporated in liposomes. Chemistry **14**(29), 8892–8897 (2008)
69. A. Yan, A. Von Dem Bussche, A.B. Kane, R.H. Hurt, Tocopheryl polyethylene glycol succinate as a safe, antioxidant surfactant for processing carbon nanotubes and fullerenes. Carbon **45**(13), 2463–2470 (2007)
70. M. Akiyama, A. Ikeda, T. Shintani, Y. Doi, J. Kikuchi, T. Ogawa, K. Yogo, T. Takeya, N. Yamamoto, Solubilisation of [60]fullerenes using block copolymers and evaluation of their photodynamic activities. Org. Biomol. Chem. **6**(6), 1015–1019 (2008)
71. C. Kojima, Y. Toi, A. Harada, K. Kono, Aqueous solubilization of fullerenes using poly(amidoamine) dendrimers bearing cyclodextrin and poly(ethylene glycol). Bioconjug. Chem. **19**(11), 2280–2284 (2008)
72. B. Pan, D. Cui, P. Xu, C. Ozkan, G. Feng, M. Ozkan, T. Huang, B. Chu, Q. Li, R. He, G. Hu, Synthesis and characterization of polyamidoamine dendrimer-coated multi-walled carbon nanotubes and their application in gene delivery systems. Nanotechnology **20**(12), 125101 (2009)
73. J.B. Hooper, D. Bedrov, G.D. Smith, Supramolecular self-organization in PEO-modified C_{60} fullerene/water solutions: influence of polymer molecular weight and nanoparticle concentration. Langmuir **24**(9), 4550–4557 (2008)
74. N. Nitta, A. Seko, A. Sonoda, S. Ohta, T. Tanaka, M. Takahashi, K. Murata, S. Takemura, T. Sakamoto, Y. Tabata, Is the use of fullerene in photodynamic therapy effective for atherosclerosis? Cardiovasc. Intervent. Radiol. **31**(2), 359–366 (2008)
75. J. Liu, S. Ohta, A. Sonoda, M. Yamada, M. Yamamoto, N. Nitta, K. Murata, Y. Tabata, Preparation of PEG-conjugated fullerene containing Gd^{3+} ions for photodynamic therapy. J. Control. Release **117**(1), 104–110 (2007)
76. Y. Tabata, Y. Murakami, Y. Ikada, Photodynamic effect of polyethylene glycol-modified fullerene on tumor. Jpn. J. Cancer Res. **88**(11), 1108–1116 (1997)
77. S. Filippone, F. Heimann, A. Rassat, A highly water-soluble 2:1 beta-cyclodextrin-fullerene conjugate. Chem. Commun. 1508–1509 (2002)
78. B. Zhao, Y.Y. He, P.J. Bilski, C.F. Chignell, Pristine (C_{60}) and hydroxylated [$C_{60}(OH)_{24}$] fullerene phototoxicity towards HaCaT keratinocytes: type I vs type II mechanisms. Chem. Res. Toxicol. **21**(5), 1056–1063 (2008)
79. T. Bansal, G. Mustafa, Z.I. Khan, F.J. Ahmad, R.K. Khar, S. Talegaonkar, Solid self-nanoemulsifying delivery systems as a platform technology for formulation of poorly soluble drugs. Crit. Rev. Ther. Drug Carrier Syst. **25**(1), 63–116 (2008)
80. F. Shakeel, M.S. Faisal, Nanoemulsion: a promising tool for solubility and dissolution enhancement of celecoxib. Pharm. Dev. Technol. **15**, 53–56 (2009)
81. V. Bali, M. Ali, J. Ali, Novel nanoemulsion for minimizing variations in bioavailability of ezetimibe. J. Drug Target **18**(7), 506–519 (2010)
82. A. Amani, P. York, H. Chrystyn, B.J. Clark, Factors affecting the stability of nanoemulsions-use of artificial neural networks. Pharm. Res. **27**(1), 37–45 (2010)
83. P.D. Boyd, C.A. Reed, Fullerene-porphyrin constructs. Acc. Chem. Res. **38**(4), 235–242 (2005)
84. M.E. El-Khouly, Y. Araki, O. Ito, S. Gadde, A.L. McCarty, P.A. Karr, M.E. Zandler, F. D'Souza, Spectral, electrochemical, and photophysical studies of a magnesium porphyrin-fullerene dyad. Phys. Chem. Chem. Phys. **7**(17), 3163–3171 (2005)
85. H. Imahori, Porphyrin-fullerene linked systems as artificial photosynthetic mimics. Org. Biomol. Chem. **2**(10), 1425–1433 (2004)
86. D.I. Schuster, P. Cheng, P.D. Jarowski, D.M. Guldi, C. Luo, L. Echegoyen, S. Pyo, A.R. Holzwarth, S.E. Braslavsky, R.M. Williams, G. Klihm, Design, synthesis, and photophysical studies of a porphyrin-fullerene dyad with parachute topology; charge recombination in the marcus inverted region. J. Am. Chem. Soc. **126**(23), 7257–7270 (2004)

87. S.A. Vail, D.I. Schuster, D.M. Guldi, M. Isosomppi, H. Lemmetyinen, A. Palkar, L. Echegoyen, X. Chen, J.Z.H. Zhang, Energy and electron transfer in beta-alkynyl-linked porphyrin-[60]fullerene dyads. J. Phys. Chem. B. **110**(29), 14155–14166 (2006)
88. M.E. El-Khouly, R. Anandakathir, O. Ito, L.Y. Chiang, Prolonged photoinduced charge-separated states in starburst tetra(diphenylaminofluoreno) [60]fullerene adducts. J. Phys. Chem. A. **111**, 6938–6944 (2007)
89. H.I. Elim, S.-H. Jeon, S. Verma, W. Ji, L.-S. Tan, A. Urbas, L.Y. Chiang, Nonlinear optical transmission properties of C_{60} dyads consisting of a light-harvesting diphenylaminofluorene antenna. J. Phys. Chem. B. **112**, 9561–9564 (2008)
90. S.C. Gebhart, W.C. Lin, A. Mahadevan-Jansen, In vitro determination of normal and neoplastic human brain tissue optical properties using inverse adding-doubling. Phys. Med. Biol. **51**(8), 2011–2027 (2006)
91. V.V. Tuchin, R.K. Wang, A.T. Yeh, Optical clearing of tissues and cells. J. Biomed. Opt. *13*(2), 021101 (2008)
92. J. Hirshburg, B. Choi, J.S. Nelson, A.T. Yeh, Correlation between collagen solubility and skin optical clearing using sugars. Lasers Surg. Med. **39**(2), 140–144 (2007)
93. J. Jiang, M. Boese, P. Turner, R.K. Wang, Penetration kinetics of dimethyl sulphoxide and glycerol in dynamic optical clearing of porcine skin tissue in vitro studied by Fourier transform infrared spectroscopic imaging. J. Biomed. Opt. **13**(2), 021105 (2008)
94. A. Kogan, N. Garti, Microemulsions as transdermal drug delivery vehicles. Adv. Colloid. Interface Sci. **123–126**, 369–385 (2006)
95. M. Goeppert-Mayer, Über Elementarakte mit zwei Quantensprüngen. Ann. Phys. **9**, 273–295 (1931)
96. J.D. Bhawalkar, N.D. Kumar, C.F. Zhao, P.N. Prasad, Two-photon photodynamic therapy. J. Clin. Laser Med. Surg. **15**(5), 201–204 (1997)
97. A. Karotki, M. Khurana, J.R. Lepock, B.C. Wilson, Simultaneous two-photon excitation of photofrin in relation to photodynamic therapy. Photochem. Photobiol. **82**(2), 443–452 (2006)
98. K.S. Samkoe, A.A. Clancy, A. Karotki, B.C. Wilson, D.T. Cramb, Complete blood vessel occlusion in the chick chorioallantoic membrane using two-photon excitation photodynamic therapy: implications for treatment of wet age-related macular degeneration. J. Biomed. Opt. **12**(3), 034025 (2007)
99. K.S. Samkoe, D.T. Cramb, Application of an ex ovo chicken chorioallantoic membrane model for two-photon excitation photodynamic therapy of age-related macular degeneration. J. Biomed. Opt. **8**(3), 410–417 (2003)
100. L. Huang, M. Terakawa, T. Zhiyentayev, Y.Y. Huang, Y. Sawayama, A. Jahnke, G.P. Tegos, T. Wharton, M.R. Hamblin, Innovative cationic fullerenes as broad-spectrum light-activated antimicrobials. Nanomedicine **6**(3), 442–452 (2010)
101. M. Wang, L. Huang, S.K. Sharma, S. Jeon, S. Thota, F.F. Sperandio, S. Nayka, J. Chang, Mi.R. Hamblin, L.Y. Chiang, Synthesis and photodynamic effect of new highly photostable decacationically armed [60]- and [70]fullerene decaiodide monoadducts to target pathogenic bacteria and cancer cells. J. Med. Chem. **55**, 4274–4285 (2012)
102. K.M. Kadish, R.S. Ruoff (eds.), *Fullerenes: Chemistry, Physics and Technology* (John Wiley & Sons Inc., New York, 2000)
103. F. Diederich, M. Gómez-López, Supramolecular fullerene chemistry. Chem. Soc. Rev. **28**, 263–277 (1999)
104. M.A. Yuroskaya, I.V. Trushkov, Cycloaddition to buckminsterfullerene C_{60}: advancements and future prospects. Russ. Chem. Bull., Int. Ed. **51**, 367–443 (2002)
105. C. Bingel, Cyclopropylation of fullerenes. Chem. Ber. **126**, 1957–1959 (1993)
106. M. Maggini, G. Scorrano, M. Prato, Addition of azomethine ylides to C_{60}–synthesis, characterization, and functionalization of fullerenes pyrrolidines. J. Am. Chem. Soc. **115**, 9798–9799 (1993)
107. Z. Lu, T. Dai, L. Huang, D.B. Kurup, G.P. Tegos, A. Jahnke, T. Wharton, M.R. Hamblin, Photodynamic therapy with a cationic functionalized fullerene rescues mice from fatal wound infections. Nanomedicine (Lond) **5**(10), 1525–1533 (2010)

108. K. Mizuno, T. Zhiyentayev, L. Huang, S. Khalil, F. Nasim, G.P. Tegos, H. Gali, A. Jahnke, T. Wharton, M.R. Hamblin, Antimicrobial photodynamic therapy with functionalized fullerenes: quantitative structure-activity relationships. J. Nanomed. Nanotechnol. **2**(2), 100109–100117 (2011)
109. M. Wang, S. Maragani, L. Huang, S. Jeon, T. Canteenwala, M.R. Hamblin, L.Y. Chiang, Synthesis of decacationic [60]fullerene decaiodides giving photoinduced production of superoxide radicals and effective PDT-mediation on antimicrobial photoinactvation. Eur. J. Med. Chem. **63**, 170–184 (2013)
110. S. Thota, M. Wang, S. Jeon, S. Maragani, M.R. Hamblin, L.Y. Chiang, Synthesis and characterization of positively charged pentacationic [60]fullerene monoadducts for antimicrobial photodynamic inactivation. Molecules **17**, 5225–5243 (2012)
111. F.F. Sperandio, S.K. Sharma, M. Wang, S. Jeon, Y.-Y. Huang, T. Dai, S. Nayka, S.C.O.M. de Sousa, L.Y. Chiang, M.R. Hamblin, Photoinduced electron-transfer mechanisms for radical-enhanced photodynamic therapy mediated by water-soluble decacationic C_{70} and $C_{84}O_2$ fullerene derivatives. Nanomedicine: Nanotech. Biol. Med. **9**(4), 570–579 (2013)
112. S. MacMahon, R. Fong II, P.S. Baran, I. Safonov, S.R. Wilson, D.I. Schuster, Synthetic approaches to a variety of covalently linked porphyrin-fullerene hybrids. J. Org. Chem. **66**, 5449–5455 (2001)
113. K. Li, D.I. Schuster, D.M. Guldi, M.A. Herranz, L. Echegoyen, Convergent synthesis and photophysics of [60]fullerene/porphyrin-based rotaxanes. J. Am. Chem. Soc. **126**, 3388–3389 (2004)
114. L.Y. Chiang, P.A. Padmawar, T. Canteewala, L.-S. Tan, G.S. He, R. Kanna, R. Vaia, T.-C. Lin, Q. Zheng, P.N. Prasad, Synthesis of C60-diphenylaminofluorene dyad with large 2PA cross-sections and efficient intramolecular two-photon energy transfer. Chem. Commun. 1854–1855 (2002)
115. P.A. Padmawar, T. Canteenwala, L.-S. Tan, L.Y. Chiang, Synthesis and characaterization of two-photon absorbing diphenylaminofluorenocarbonyl-methano[60]fullerenes. J. Mater. Chem. **16**, 1366–1378 (2006)
116. P.A. Padmawar, J.O. Rogers, G.S. He, L.Y. Chiang, T. Canteenwala, L.-S. Tan, Q. Zheng, C. Lu, J.E. Slagle, E. Danilov, D.G. McLean, P.A. Fleitz, P.N. Prasad, Large cross-section enhancement and intramolecular energy transfer upon multiphoton absorption of hindered diphenylaminofluorene-C_{60} dyads and triads. Chem. Mater. **18**, 4065–4074 (2006)
117. Y.Y. Huang, S.K. Sharma, T. Dai, H. Chung, A. Yaroslavsky, M. Garcia-Diaz, J. Chang, L.Y. Chiang, M.R. Hamblin, Can nanotechnology potentiate photodynamic therapy? Nanotechnol. Rev. **1**, 111–146 (2012)
118. F.F. Sperandio, A. Gupta, M. Wang, R. Chandran, M. Sadasivam, Y.-Y. Huang, L.Y. Chiang, M.R. Hamblin, *Photodynamic Therapy Mediated by Fullerenes and Their Derivatives*. Biomed. Nanomed. Technol.(B & NT): Concise Monographs Series, (ASME Press, New York 2013), pp. 1–51. ISBN: 9780791860083
119. H.I. Elim, R. Anandakathir, R. Jakubiak, L.Y. Chiang, W. Ji, L.S. Tan, Large concentration-dependent nonlinear optical responses of starburst diphenylaminofluorenocarbonyl methano[60]fullerene pentaads. J. Mater. Chem. **17**, 1826–1838 (2007)
120. L.Y. Chiang, P.A. Padmawar, J.E. Rogers–Haley, G. So, T. Canteenwala, S. Thota, L.-S. Tan, K. Pritzker, Y.-Y. Huang, S.K. Sharma, D.B. Kurup, M.R. Hamblin, B. Wilson, A. Urbas, Synthesis and characterization of highly photoresponsive fullerenyl dyads with a close chromophore antenna–C_{60} contact and effective photodynamic potential. J. Mater. Chem. **20**, 5280–5293 (2010)
121. M.E. El-Khouly, P. Padmawar, Y. Araki, S. Verma, L.Y. Chiang, O. Ito, Photoinduced processes in a tricomponent molecule consisting of diphenylaminofluorene-dicyanoethylene-methano[60]fullerene. J. Phys. Chem. A. **110**, 884–891 (2006)
122. H. Luo, M. Fujitsuka, Y. Araki, O. Ito, P. Padmawar, L.Y. Chiang, Inter- and intramolecular photoinduced electron-transfer processes between C_{60} and diphenylaminofluorene in solutions. J. Phys. Chem. B. **107**, 9312–9318 (2003)

123. U.S. Jeng, T.L. Lin, C.S. Tsao, C.H. Lee, T. Canteenwala, L.Y. Wang, L.Y. Chiang, C.C. Han, Study of aggregates of fullerene-based ionomers in aqueous solutions using small angle neutron and x-ray scattering. J. Phys. Chem. B. **103**, 1059–1063 (1999)
124. M. Sawamura, N. Nagahama, M. Toganoh, U.E. Hackler, H. Isobe, E. Nakamura, S. Zhou, B. Chu, Pentaorgano[60]fullerene $R_5C_{60}^-$: a water soluble hydrocarbon anion. Chem. Lett. 1098–1099 (2000)
125. M. Brettreich, S. Burghardi, C. Bottcher, T. Bayerl, S. Bayerl, A. Hirsch, Globular amphiphiles: membrane-forming hexaadducts of C_{60}. Angew. Chem. Int. Ed. **39**, 1845–1848 (2000)
126. S. Zhou, C. Burger, B. Chu, M. Sawamura, N. Nagahama, M. Toganoh, U.E. Hackler, H. Isobe, E. Nakamura, Spherical bilayer vesicles of fullerene-based surfactants in water: a laser light scattering study. Science **291**, 1944–1947 (2001)
127. A.M. Cassell, C.L. Asplund, J.M. Tour, Self-assembling supramolecular nanostructures from a C_{60} derivative: nanorods and vesicles. Angew. Chem. Int. Ed. **38**, 2403–2405 (1999)
128. A. Ikeda, Y. Doi, K. Nishiguchi, K. Kitamura, M. Hashizume, J.-I. Kikuchi, K. Yogo, T. Ogawa, T. Takeya, Induction of cell death by photodynamic therapy with water-soluble lipid-membrane-incorporated [60]fullerene. Org. Biomol. Chem. **5**(8), 1158–1160 (2007)
129. A. Ikeda, M. Matsumoto, M. Akiyama, J. Kikuchi, T. Ogawa, T. Takeya, Direct and short-time uptake of [70]fullerene into the cell membrane using an exchange reaction from a [70] fullerene-gamma-cyclodextrin complex and the resulting photodynamic activity. Chem. Commun. 1547–1549 (2009)
130. A. Ikeda, M. Nagano, M. Akiyama, M. Matsumoto, S. Ito, M. Mukai, M. Hashizume, J. Kikuchi, K. Katagiri, T. Ogawa, T. Takeya, Photodynamic activity of C70 caged within surface-cross-linked liposomes. Asian J. Chem. **4**(1), 199–205 (2009)
131. D.M. Guldi, K.D. Asmus, Photophysical properties of mono- and multiply-functionalized fullerene derivatives. J. Phys. Chem. **101**, 1472–1481 (1997)
132. R.V. Bensasson, M.N. Berberan-Santos, M. Bretreich, J. Frederiksen, H. Göttinger, A. Hirsch, E.J. Land, S. Leach, D.J. McGarvey, H. Schönberger, C. Schröder, Triplet state properties of malonic acid C_{60} derivatives $C_{60}[C(COOR)_2]_n$; R = H, Et; n = 1–6. Phys. Chem. Chem. Phys. **3**, 4679–4683 (2001)
133. W.A. Scrivens, J.M. Tour, K.E. Creek, L. Pirisi, Synthesis of C-14-labeled C_{60}, its suspension in water, and its uptake by human keratinocytes. J. Am. Chem. Soc. **116**, 4517–4518 (1994)
134. S. Foley, C. Crowley, M. Smaihi, C. Bonfils, B.F. Erlanger, P. Seta, C. Larroque, Cellular localisation of a water-soluble fullerene derivative. Biochem. Biophys. Res. Commun. **294**(1), 116–119 (2002)
135. A.E. Porter, M. Gass, K. Muller, J.N. Skepper, P. Midgley, M. Welland, Visualizing the uptake of C_{60} to the cytoplasm and nucleus of human monocyte-derived macrophage cells using energy-filtered transmission electron microscopy and electron tomography. Environ. Sci. Technol. **41**(8), 3012–3017 (2007)
136. N.A. Kuznetsova, N.S. Gretsova, O.A. Yuzhakova, V.M. Negrimovskii, O.L. Kaliya, E.A. Luk'yanets, New reagents for determination of quantum efficiency of singlet oxygen generation in aquesou media. Russ. J. Gen. Chem. **71**, 36–41 (2001)
137. X. Ragas, A. Jimenez-Banzo, D. Sanchez-Garcia, X. Batllori, S. Nonell, Singlet oxygen photosensitisation by the fluorescent probe Singlet Oxygen Sensor Greens. Chem. Commun. 2920–2922 (2009)
138. K.-I. Setsukinai, Y. Urano, K. Kakinuma, H.J. Majima, T. Nagano, Development of novel fluorescence probes that can reliably detect reactive oxygen species and distinguish specific species. J. Biol. Chem. **278**, 3170–3175 (2003)
139. K.-I. Setsukinai, Y. Urano, K. Kakinuma, H.J. Majima, T. Nagano, Development of novel fluorescence probes that can reliably detect reactive oxygen species and distinguish specific species. J. Biol. Chem. **278**, 3170–3175 (2003)
140. A.K. Gupta, K.K. Rohatgi-Mukherjee, Solvent effect on photosensitized oxidation of iodide ion by anthracene sulphonates. Photochem. Photobiol. **27**, 539–543 (1978)

141. A. Minnock, D.I. Vernon, J. Schofield, J. Griffiths, J.H. Parish, S.B. Brown, Photoinactivation of bacteria. Use of a cationic water-soluble zinc phthalocyanine to photoinactivate both gram-negative and gram-positive bacteria. J. Photochem. Photobiol. B. **32**, 159–164 (1996)
142. M. Merchat, G. Bertolini, P. Giacomini, A. Villanueva, G. Jori, Meso-substituted cationic porphyrins as efficient photosensitizers of gram-positive and gram-negative bacteria. J. Photochem. Photobiol. B. **32**, 153–157 (1996)
143. M.R. Hamblin, T. Hasan, Photodynamic therapy: a new antimicrobial approach to infectious disease? Photochem. Photobiol. Sci. **3**, 436–450 (2004)
144. T.N. Demidova, M.R. Hamblin, Photodynamic therapy targeted to pathogens. Int. J. Immunopathol. Pharmacol. **17**, 245–254 (2004)
145. T.N. Demidova, M.R. Hamblin, Effect of cell-photosensitizer binding and cell density on microbial photoinactivation. Antimicrob. Agents Chemother. **49**, 2329–2335 (2005)
146. S.A. Lambrechts, M.C. Aalders, D.H. Langeveld-Klerks, Y. Khayali, J.W. Lagerberg, Effect of monovalent and divalent cations on the photoinactivation of bacteria with meso-substituted cationic porphyrins. Photochem. Photobiol. **79**, 297–302 (2004)
147. M.B. Spesia, M.E. Milanesio, E.N. Durantini, Synthesis, properties and photodynamic inactivation of Escherichia coli by novel cationic fullerene C_{60} derivatives. Eur. J. Med. Chem. **43**(4), 853–861 (2008)
148. I. Lee, Y. Mackeyev, M. Cho, L.I. Dong, J.-H. Kim, L.J. Wilson, P.J.J. Alvarez, Photochemical and antimicrobial properties of novel C_{60} derivatives in aqueous systems. Environ. Sci. Technol. **43**(17), 6604–6610 (2009)
149. H. Isobe, N. Tomita, E. Nakamura, One-step multiple addition of amine to [60]fullerene. synthesis of tetra(amino)fullerene epoxide under photochemical aerobic conditions. Org. Lett. **2**(23), 3663–3665 (2000)
150. L. Huang, T. Dai, M.R. Hamblin, Antimicrobial photodynamic inactivation and photodynamic therapy for infections. Methods Mol. Biol. **635**, 155–173 (2010)
151. L. Huang, Y. Xuan, Y. Koide, T. Zhiyentayev, M. Tanaka, M.R. Hamblin, Type I and Type II mechanisms of antimicrobial photodynamic therapy: an in vitro study on gram-negative and gram-positive bacteria. Laser Surg. Med. **44**(6), 490–499 (2012)
152. G. Valduga, G. Bertoloni, E. Reddi, G. Jori, Effect of extracellularly generated singlet oxygen on gram-positive and gram-negative bacteria. J. Photochem. Photobiol. B. **21**, 81–86 (1993)
153. T.A. Dahl, W.R. Midden, P.E. Hartman, Comparison of killing of gram-negative and gram-positive bacteria by pure singlet oxygen. J. Bacteriol. **171**, 2188–2194 (1989)
154. F. Kasermann, C. Kempf, Photodynamic inactivation of enveloped viruses by buckminsterfullerene. Antiviral Res. **34**, 65–70 (1997)
155. F. Kasermann, C. Kempf, Buckminsterfullerene and photodynamic inactivation of viruses. Rev. Med. Virol **8**, 143–151 (1998)
156. J. Hirayama, H. Abe, N. Kamo, T. Shinbo, Y. Ohnishi-Yamada, S. Kurosawa, K. Ikebuchi, S. Sekiguchi, Photoinactivation of vesicular stomatitis virus with fullerene conjugated with methoxy polyethylene glycol amine. Biol. Pharm. Bull. **22**, 1106–1109 (1999)
157. Y.L. Lin, H.Y. Lei, Y.Y. Wen, T.Y. Luh, C.K. Chou, H.S. Liu, Light-independent inactivation of dengue-2 virus by carboxyfullerene C3 isomer. Virology **275**, 258–262 (2000)
158. H. Tokuyama, S. Yamago, E. Nakamura, Photoinduced biochemical activity of fullerene carboxylic acid. J. Am. Chem. Soc. **115**, 7918–7919 (1993)
159. K. Irie, Y. Nakamura, H. Ohigashi, H. Tokuyama, S. Yamago, E. Nakamura, Photocytotoxicity of water-soluble fullerene derivatives. Biosci. Biotechnol. Biochem. **60**, 1359–1361 (1996)
160. A.P. Burlaka, Y.P. Sidorik, S.V. Prylutska, O.P. Matyshevska, O.A. Golub, Y.I. Prylutskyy, P. Scharff, Catalytic system of the reactive oxygen species on the C_{60} fullerene basis. Exp. Oncol. **26**, 326–327 (2004)
161. F. Rancan, S. Rosan, F. Boehm, A. Cantrell, M. Brellreich, H. Schoenberger, A. Hirsch, F. Moussa, Cytotoxicity and photocytotoxicity of a dendritic C_{60} mono-adduct and a malonic acid C_{60} tris-adduct on Jurkat cells. J. Photochem. Photobiol. B. Biol. **67**, 157–162 (2002)

162. X.L. Yang, C.H. Fan, H.S. Zhu, Photo-induced cytotoxicity of malonic acid [C_{60}]fullerene derivatives and its mechanism. Toxicol. in Vitro **16**, 41–46 (2002)
163. F. Rancan, M. Helmreich, A. Molich, N. Jux, A. Hirsch, B. Roder, C. Witt, F. Bohm, Fullerene-pyropheophorbide a complexes as sensitizer for photodynamic therapy: uptake and photo-induced cytotoxicity on Jurkat cells. J. Photochem. Photobiol. B. **80**, 1–7 (2005)
164. M.E. Milanesio, M.G. Alvarez, V. Rivarola, J.J. Silber, E.N. Durantini, Porphyrin-fullerene C_{60} dyads with high ability to form photoinduced charge-separated state as novel sensitizers for photodynamic therapy. Photochem. Photobiol. **81**, 891–897 (2005)
165. M.G. Alvarez, C. Prucca, M.E. Milanesio, E.N. Durantini, V. Rivarola, Photodynamic activity of a new sensitizer derived from porphyrin-C_{60} dyad and its biological consequences in a human carcinoma cell line. Int. J. Biochem. Cell Biol. **38**,2092–2101 (2006)
166. C.J. Liang-Takasaki, P.H. Makela, L. Leive, Phagocytosis of bacteria by macrophages: changing the carbohydrate of lipopolysaccharide alters interaction with complement and macrophages. J. Immunol. **128**, 1229–1235 (1982)
167. R. Li, D.J. Bounds, D. Granville, S.H. Ip, H. Jiang, P. Margaron, D.W. Hunt, Rapid induction of apoptosis in human keratinocytes with the photosensitizer QLT0074 via a direct mitochondrial action. Apoptosis **8**, 269–275 (2003)
168. D.J. Granville, C.M. Carthy, H. Jiang, G.C. Shore, B.M. McManus, D.W. Hunt, Rapid cytochrome c release, activation of caspases 3, 6, 7 and 8 followed by Bap31 cleavage in HeLa cells treated with photodynamic therapy. FEBS Lett. **437**, 5–10 (1998)
169. S. Gupta, N. Ahmad, H. Mukhtar, Involvement of nitric oxide during phthalocyanine (Pc4) photodynamic therapy-mediated apoptosis. Cancer Res. **58**,1785–1788 (1998)
170. D. Kessel, Y. Luo, P. Mathieu, J.J. Reiners Jr., Determinants of the apoptotic response to lysosomal photodamage. Photochem. Photobiol. **71**, 196–200 (2000)
171. M.G. Alvarez, F. Principe, M.E. Milanesio, E.N. Durantini, V. Rivarola, Photodynamic damages induced by a monocationic porphyrin derivative in a human carcinoma cell line. Int. J. Biochem. Cell Biol. **37**, 2504–2512 (2005)
172. M.F. Ross, T. Da Ros, F.H. Blaikie, T.A. Prime, C.M. Porteous, I.I. Severina, V.P. Skulachev, H.G. Kjaergaard, R.A. Smith, M.P. Murphy, Accumulation of lipophilic dications by mitochondria and cells. J. Biochem. **400**, 199–208 (2006)
173. H. Rottenberg, Membrane potential and surface potential in mitochondria: uptake and binding of lipophilic cations. J. Membr. Biol. **81**, 127–138 (1984)
174. M.P. Murphy, R.A. Smith, Targeting antioxidants to mitochondria by conjugation to lipophilic cations. Annu. Rev. Pharmacol. Toxicol. **47**, 629–656 (2007)
175. S.M. Hahn, M.E. Putt, J. Metz, D.B. Shin, E. Rickter, C. Menon, D. Smith, E. Glatstein, D.L. Fraker, T.M. Busch, Photofrin uptake in the tumor and normal tissues of patients receiving intraperitoneal photodynamic therapy. Clin. Cancer Res. **12**, 5464–5470 (2006)
176. Y.Z. An, C.B. Chen, J.L. Anderson, D.S. Sigman, C.S. Foote, Y. Rubin, Sequence-specific modification of guanosine in DNA by a C_{60}-linked deoxyoligonucleotide: evidence for a non-singlet oxygen mechanism. Tetrahedron **52**, 5179–5189 (1996)
177. A.S. Boutorine, M. Takasugi, C. Helene, H. Tokuyama, H. Isobe, E. Nakamura, Fullerene-oligonucleotide conjugates: photoinduced sequence-specific DNA cleavage. Angew. Chem. Int. Ed. **33**, 2462–2465 (1995)
178. I. Nakanishi, S. Fukuzumi, T. Konishi, K. Ohkubo, M. Fujitsuka, O. Ito, N. Miyata, in *DNA cleavage via electron transfer from NADH to molecular oxygen photosensitized by g-cyclodextrin-bicapped C_{60}*, ed. by P.V. Kamat, D.M. Guldi, D.M. Kadish. Fullerenes for the New Millennium, vol. 11 (The Electrochemical Society, Pennington, 2001) pp. 138–151
179. Y. Yamakoshi, S. Sueyoshi, N. Miyata, Biological activity of photoexcited fullerene. Kokuritsu Iyakuhin Shokuhin Eisei Kenkyujo Hokoku, Bull. NIH Sci. **117**, 50–60 (1999)
180. Y.N. Yamakoshi, T. Yagami, S. Sueyoshi, N. Miyata, Acridine adduct of [60]fullerene with enhanced DNA-cleaving activity. J. Org. Chem. **61**, 7236–7237 (1996)
181. Y. Liu, Y.L. Zhao, Y. Chen, P. Liang, L. Li, A water-soluble beta cyclodextrin derivative possessing a fullerene tether as an efficient photodriven DNA-cleavage reagent. Tetrahedron Lett. **46**, 2507–2511 (2005)

182. A. Ikeda, Y. Doi, M. Hashizume, J. Kikuchi, T. Konishi, An extremely effective DNA photocleavage utilizing functionalized liposomes with a fullerene-enriched lipid bilayer. J. Am. Chem. Soc. **129**, 4140–4141 (2007)
183. N. Sera, H. Tokiwa, N. Miyata, Mutagenicity of the fullerene C_{60}-generated singlet oxygen dependent formation of lipid peroxides. Carcinogen **17**, 2163–2169 (1996)
184. J.P. Kamat, T.P. Devasagayam, K.I. Priyadarsini, H. Mohan, J.P. Mittal, Oxidative damage induced by the fullerene C_{60} on photosensitization in rat liver microsomes. Chemico-Biol. Interact. **114**, 145–159 (1998)
185. J.P. Kamat, T.P. Devasagayam, K.I. Priyadarsini, H. Mohan, Reactive oxygen species mediated membrane damage induced by fullerene derivatives and its possible biological implications. Toxicol. **155**, 55–61 (2000)
186. X.L. Yang, C. Huang, X.G. Qiao, L. Yao, D.X. Zhao, X. Tan, Photo-induced lipid peroxidation of erythrocyte membranes by a bis-methanophosphonate fullerene. Toxicol. In Vitro **21**(8), 1493–1498 (2007)
187. Y. Chi, T. Canteenwala, H.C. Chen, B.J. Chen, M. Canteenwala, L.Y. Chiang, Hexa(sulfobutyl)fullerene-induced photodynamic effect on tumors in vivo and toxicity study in rats. Proc. Electrochem. Soc. **99**, 234–249 (1999)
188. H.H. Chen, C. Yu, T.H. Ueng, S. Chen, B.J. Chen, K.J. Huang, L.Y. Chiang, Acute and subacute toxicity study of water-soluble polyalkylsulfonated C_{60} in rats. Toxicol. Pathol. **26**(1), 143–151 (1998)
189. E. Otake, S. Sakuma, K. Torii, A. Maeda, H. Ohi, S. Yano, A. Morita, Effect and mechanism of a new photodynamic therapy with glycoconjugated fullerene. Photochem. Photobiol. **86**(6), 1356–1363 (2010)
190. P. Mroz, Y. Xia, D. Asanuma, A. Konopko, T. Zhiyentayev, Y.Y. Huang, S.K. Sharma, T. Dai, U.J. Khan, T. Wharton, M.R. Hamblin, Intraperitoneal photodynamic therapy mediated by a fullerene in a mouse model of abdominal dissemination of colon adenocarcinoma. Nanomedicine **7**(6), 965–974 (2011)
191. B.R. Sharma, Infection in patients with severe burns: causes and prevention thereof. Infect. Dis. Clin. North Am. **21**, 745–759 (2007)
192. R.N. Ollstein, C. McDonald, Topical and systemic antimicrobial agents in burns. Ann. Plast. Surg. **5**, 386–392 (1980)
193. J.R. Saffle, Closure of the excised burn wound: temporary skin substitutes. Clin. Plast. Surg. **36**, 627–641 (2009)
194. C.I. Kang, S.H. Kim, W.B. Park, K.D. Lee, H.B. Kim, E.C. Kim, M.-D. Oh, K.-W. Choe, Bloodstream infections caused by antibiotic-resistant gram-negative bacilli: risk factors for mortality and impact of inappropriate initial antimicrobial therapy on outcome. Antimicrob. Agents Chemother. **49**, 760–766 (2005)
195. T. Dai, Y.Y. Huang, S.K. Sharma, J.T. Hashmi, D.B. Kurup, M.R. Hamblin, Topical antimicrobials for burn wound infections. Recent Pat. Antiinfect. Drug Discov. **5**(2), 124–151 (2010)
196. L. Huang, M. Wang, T. Dai, F.F. Sperandio, Y.-Y. Huang, Y. Xuan, L.Y. Chiang, M.R. Hamblin, Antimicrobial photodynamic therapy with decacationic monoadduct and bisadducts of [70]fullerene: in vitro and in vivo studies. Nanomedicine (Lond). **9**(2), 253–266 (2013). doi:10.2217/NNM.13.22
197. E.F. Keen 3rd, B.J. Robinson, D.R. Hospenthal, W.K. Aldous, S.E. Wolf, K.K. Chung, C.K. Murray, Incidence and bacteriology of burn infections at a military burn center. Burns **36**, 461–468 (2010)
198. P. Asadollahi, M. Akbari, S. Soroush, M. Taherikalani, K. Asadollahi, K. Sayehmiri, A. Maleki, M.H. Maleki, P. Karimi, M. Emaneini, Antimicrobial resistance patterns and their encoding genes among Acinetobacter baumannii strains isolated from burned patients. Burns **38**(8), 1198–1203 (2012)

Chapter 6
Carbon Nanotube Field-Emission X-Ray-Based Micro-computed Tomography for Biomedical Imaging

Laurel M. Burk, Yueh Z. Lee, Jianping Lu and Otto Zhou

6.1 Biomedical X-Ray Imaging

X-rays are used today for a variety of applications, but their most widely recognized application is in transmission contrast imaging. When an object is placed between an X-ray source and a photo plate or detector, photon–matter interactions such as Compton and Raleigh scattering and the photoelectric effect cause absorption or deflection of some photons from their direct path, creating a shadow cast on the detector. This shadow offers information about the internal structures of the object under investigation. For some applications, a simple 2-D planar image generated by X-ray provides sufficient detail, but the overlapping of out-of-plane structures can obscure features of interest. In these cases, systematically acquiring many X-ray projections over multiple viewing angles, through computed tomography (CT), results in full spatial information about the interiors of objects.

Both 2-D and 3-D X-ray imaging modalities are commonly used in industrial applications and for security screening at checkpoints and in airports, but the most familiar application of X-ray is medical imaging. In addition to the simple 2-D radiograph, X-rays are used for fluoroscopy, angiography, breast cancer screening (mammography and digital breast tomosynthesis), and CT.

O. Zhou (✉)
Physics and Astronomy, Lineberger Comprehensive Cancer Center, The University of North Carolina at Chapel Hill, 120 East Cameron Street, Chapel Hill, NC 27599-3255, USA
e-mail: zhou@email.unc.edu

L. M. Burk · J. Lu
Department of Physics and Astronomy, The University of North Carolina at Chapel Hill, 120 East Cameron Street, Chapel Hill, NC 27599-3255, USA

Y. Z. Lee
Department of Radiology, The University of North Carolina at Chapel Hill, 120 East Cameron Street, Chapel Hill, NC 27599-3255, USA

M. Zhang et al. (eds.), *Carbon Nanomaterials for Biomedical Applications,*
Springer Series in Biomaterials Science and Engineering 5,
DOI 10.1007/978-3-319-22861-7_6

6.2 Conventional X-Ray Source Design

The fundamental design of the X-ray source has changed very little since the developments made by William Coolidge a century ago. In a conventional X-ray tube, the source of electrons is a cathode filament of tungsten wire or a similar material which is heated via electrical resistance so that electrons are released through thermionic emission. The anode within the X-ray tube is set at a high positive voltage with respect to the other tube components so that the electron beam is strongly accelerated, gaining kinetic energy which will be imparted to the X-ray beam. When the target is bombarded by electrons, X-rays are generated through Bremsstrahlung and characteristic radiation. The spatial resolution of an X-ray source is determined by the size of this focal spot on the anode, and the intensity of X-rays generated is proportional to the current of electrons generated by the cathode and by the square of the acceleration voltage applied to the anode. However, since a large amount of heat is generated within the anode along with X-ray production, heat dissipation constraints are the primary limitation of the total intensity of X-rays able to be generated from the source. Thus, increasing the transmission of heat away from the anode is a major design concern. Most commercial X-ray sources require a complex rotating anode rather than the simple stationary option in order to spread the heat load over a much larger volume of material in order to address this limitation.

Because of these heat dissipation concerns, it becomes impractical to pack conventional X-ray sources closely together, so that X-ray devices are largely restricted to a single-pixel design. Therefore, for applications such as CT where X-ray acquisitions are required over many angles, physical rotation of the imaging object or the source and detector are required, which can increase acquisition time and introduce motion blur.

Thermionic electron emission also creates practical limitations to the temporal resolution of a system, since thermionic electron emission cannot be switched rapidly with a filament cathode. Instead, external mechanical shuttering must be used to create temporally narrow pulses. In general, this leads to a poor response time and difficultly in generating uniform and nonperiodic pulses, both of which are necessary for gated imaging to reduce the blur in moving objects.

Moreover, physical shuttering is inefficient from an anode heat load perspective, because bombardment of the target by electrons occurs at all times and not just when X-ray pulses are required. This further limits the overall tube flux. Finally, thermionic electron emission is spatially isotropic, so a negatively biased focusing cup is necessary to bend the electron trajectory into a more focused beam, and the emitted electrons have a very wide energy distribution.

6.3 Carbon Nanotube Field-Emission X-Ray Source

To avoid the drawbacks of thermionic emission, an alternative mechanism for the generation of electrons for X-ray production is the well-understood process of quantum tunneling. In field emission, the effective work function of a material is

lowered through the application of a high electric field over its surface so that electrons nearest the Fermi level are able to tunnel through to the vacuum level [1]. Field emission has clear benefits for electron emission when compared with thermionic emission: The only heat generated is that created through anode bombardment for X-ray generation, and the switching speed of the source is limited only by the simple modulation of an electric field over the cathode surface. Electron flow is shut off at moments when there is no X-ray flux, reducing the anode heat load when the source is operated at duty cycles less than 100%.

The current generated from a material by field emission is expressed with the Fowler–Nordheim equation, $I = aV_2 \exp(-b\ 3/2/\beta V)$, where I, V, ϕ, and β are the emission current, the applied voltage, the emitter material's work function, and a geometric field enhancement factor, respectively [1]. Choice of a low-work function emitter material is necessary, but even metals with typical work functions on the order of 100 V/μm require impractically high voltages to achieve enough field emission for significant X-ray generation. Another crucial consideration is optimization of the field enhancement factor β, which is maximized by creating an emitter surface with an extremely sharp tip or profusion [2]. An optimal geometry maximizes the electric field at the emitter tip for easier electron tunneling without the application of high voltages.

Some of the first explored field-emission electron sources for X-ray generation used sharp metal tips as cathodes [3, 4]. Later efforts involved other materials as field emitters, such as Spindt tips and diamond [5, 6], but these X-ray sources could only achieve currents on the order of a microampere [6]. Because of their extremely high aspect ratios (~10^3), strength, high electrical and thermal conductivity, and resistance to oxidation, carbon nanotubes are an excellent choice of field emitter material for electron emission and have been considered for this application as early as 1995 [7]. In the two decades that have followed, this carbon nanotube (CNT) field emission has been used for many different applications including X-ray sources [8–12], field-emission display [13], and liquid crystal backlight display [14].

6.3.1 Benefits of Field Emission for X-ray

Compared with conventional thermionic X-ray sources, a CNT field-emission X-ray tube is preferable for many reasons. Because field emission is controlled through the application of an electric field, the source has an inherently fast response time and is easily operated electronically. Due to the elimination of heat and focusing concerns at the cathode, emitter arrays can be built compactly with individually controllable pixels that each creates its own focal spot on the anode, generating an array of X-ray sources. Such X-ray sources allow rapid tomographic imaging without introducing motion blur, by switching sources in series rather than rotating or translating a single source [15]. In addition to reducing scan times, source arrays allow the possibility of multiplexing [16].

6.3.2 CNT Field-Emission X-ray Source

While field emission from a single nanotube is theoretically straightforward, and currents of up to 1 μA may be obtained from an individual CNT [17], the current obtained from a macroscopic cathode of numerous emitters does not scale up linearly. Limits in emission current and functional lifetime arise from the electrical screening effect and nonuniformity in dimensions of individual emitters within the cathode. Adhesion of nanotubes to the substrate is another important factor, as poorly adhered CNTs may become dislodged under high voltages, causing arcing and accelerated degradation of the X-ray source. Thus, optimization of fabrication techniques is essential for the fabrication of high-quality field-emission cathodes.

Many methods have been proposed for fabrication of field emission cathodes, including surface chemical vapor deposition and screen printing. Our chosen process is liquid-phase room-temperature electrophoretic deposition (EPD) combined with photolithography [18], which we describe in greater detail in the next section.

6.3.2.1 CNT Cathode Fabrication

Multiwalled CNTs with small diameters created through thermal CVD were purified and then dispersed in alcohol with an $MgCl_2$ charger. Glass frits were added to the EPD ink as well to improve adhesion to the selected glass substrates with Ag contact lines [19]. Under a direct current (DC) electrical field, charged CNTs and binders are driven and deposited onto the substrate surface in a film. The density of CNT emitters is controlled by adjusting the initial concentration of CNTs in the EPD ink, and the film thickness is controlled by the applied voltage and the deposition time. The bond between CNTs and substrate was strong enough to withstand photoresist liftoff, with one end of each randomly oriented CNT embedded into the matrix.

6.3.2.2 Cathode Performance and Lifetime

Through careful optimization of the growth process, improved adhesion, density, and emitter orientation have led to high stability at voltages necessary for X-ray generation over a long operating lifetime. Due to these advancements in cathode manufacture, film thicknesses are uniform with only 10% variation, and current densities of over 1500 mA/cm^2 are obtained [19, 20].

The results of a study investigating current strength from different dimensions of elliptical CNT cathodes are displayed in Fig. 6.1a, and lifetime performance of a 2 × 15-mm CNT cathode is shown in Fig. 6.1b (data courtesy of Xintek, Inc.). The cathodes were operated in 10-ms pulses at a rate of 1 Hz with an anode–cathode gap of 150 μm. One-hundred hours of operation were recorded for the 2 × 15-mm cathode, over which a stable emission current of 1 A was achieved [20]. The 1-A

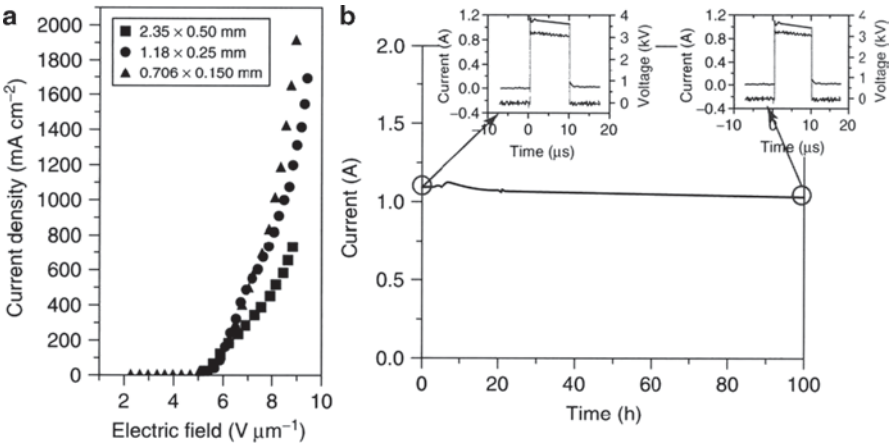

Fig. 6.1 **a** The field-emission current density versus applied electrical field from different size cathodes. The voltage was applied to the anode in 10-ms pulses at a 1-Hz rate. **b** A pulsed emission current of 1 A (10 ms pulse width) at 0.1 % duty cycle from a 2 × 15-mm CNT cathode measured in the diode mode with a fixed extraction voltage. (Figure reproduced from Zhou and Calderon 2010)

value is significant for the clinical future of CNT X-ray imaging devices, as this is the output power of commercial CT scanners.

6.3.2.3 X-Ray Source Design

In our current generation of X-ray tube based on field emission, a CNT cathode and a stationary metal anode are contained inside of a vacuum enclosure along with a 2-D grid gate electrode and electrostatic focusing structures. A bias voltage is applied to the gate electrode to extract electrons from the tips of the CNT emitters in the cathode, the stationary anode both accelerates the electron beam and acts as a target, and the static Einzel-type focusing electrodes are held at appropriate voltages to minimize the focal spot size on the anode while maintaining high transmission rates. Figure 6.2 shows the interior design of a compact, CNT-based microfocus X-ray source developed at the University of North Carolina, including the cathode, gate mesh, focusing, and stationary anode [21]. The simulated electron beam paths are indicated through multicolored vectors, demonstrating the effectiveness of the static focusing at maintaining a small focal spot on the anode.

6.3.3 Applications of CNT X-Ray Sources

Since our laboratory first introduced its CNT cathode field-emission X-ray setup capable of biological imaging in 2002, this technology has been implemented in stationary source tomography devices [22], radiation therapy applications [23], and

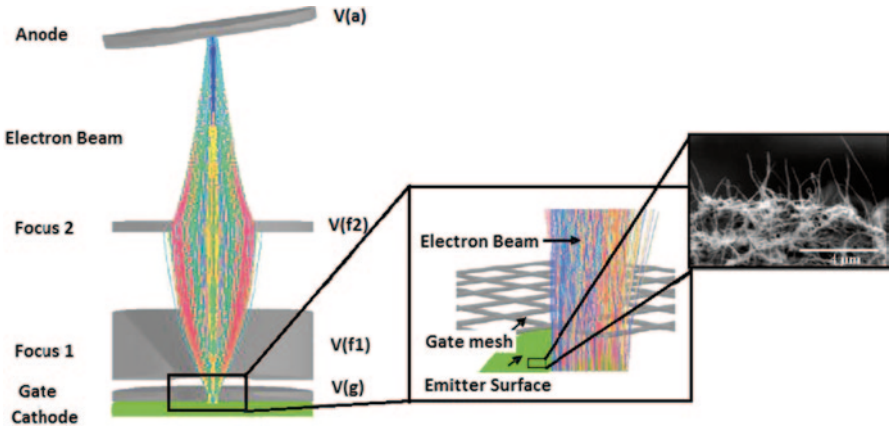

Fig. 6.2 Schematic of a CNT-based field-emission X-ray source. The first *inset* highlights in the extraction of electrons via application of a bias voltage on the gate mesh. Second *inset* provides a close-up view of the CNT cathode surface. (Reproduced from Shabana et al SPIE Medical Imaging 7622 76225G)

small-animal micro-CT imaging. X-ray sources based on field emission can be built compactly because of the lack of heat considerations from the cathode, and the CNT cathodes have been built into arrays so that emitted beams can be conformed into various shapes [23]. For micro-CT applications, a particularly crucial advantage of field-emission X-ray technology is the rapid source modulation enabled by electric field switching at the cathode surface, rather than physical shuttering of a thermionic filament.

In this chapter, we focus specifically on the application of CNT field-emission X-ray sources for live small-animal imaging, pictured in Figs. 6.3 and 6.4. A description of the specific challenges of in vivo small-animal imaging follows, along with a detailed description of a micro-CT device capable of such imaging, and finally an overview of several biomedical research applications of this device.

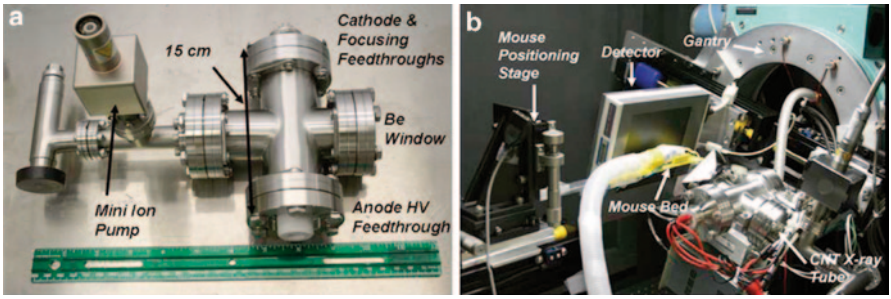

Fig. 6.3 **a** The CNT microfocus tube and **b** the main hardware components of the CNT micro-CT scanner. *CNT* carbon nanotube, *HV* high voltage. (Reproduced from Cao et al. Med Phys)

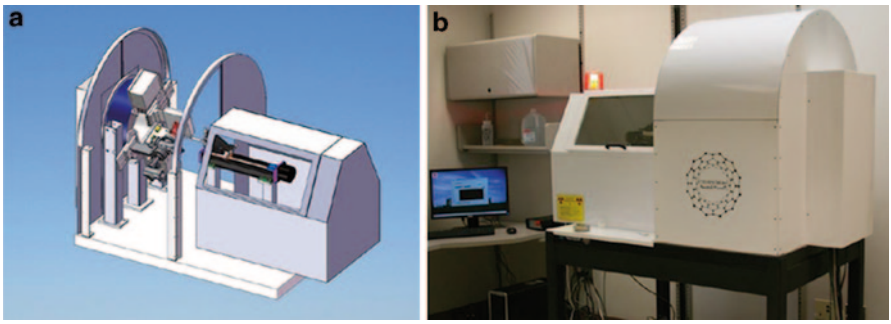

Fig. 6.4 **a** CNT micro-CT scanner as a CAD drawing and **b** the finished construction, housed inside the fitted lead shielding. End-user devices are in operation at the biomedical research imaging center at the University of North Carolina and at the University of Iowa

6.4 Pre-clinical High-Resolution CT (Micro-CT)

Due to the success and ubiquity of CT in human-scale and clinical imaging, CT has also been extended to nonclinical imaging applications such as tissue samples, biopsies, and living small animals. Micro-computed tomography (micro-CT or μ-CT) is the small-scale high-resolution counterpart to the CT scanners used in hospitals. In particular, use of in vivo small-animal imaging has recently increased to meet the demands of researchers studying models of human disease in genetically engineered mouse models (GEMMs) or other small animals and rodents such as rats and rabbits. Mice in particular are highly desired as subjects for biomedical studies of disease because of a widely known murine genome, fast reproduction, and inexpensive housing requirements. Researchers studying disease in mice require the same tools of diagnosis and disease monitoring as are available in the clinic, including optical and fluorescence imaging, ultrasound, magnetic resonance, and of course CT.

6.5 In Vivo Micro-CT

Live small-animal micro-CT is in many ways analogous to clinical CT for human patients. High spatial resolution is necessary, but compromise is also required because radiation dose and scanning time must be minimized. Especially in longitudinal imaging studies, radiation dose must be kept well below the maximum tolerable dose to avoid negative health consequences. At the same time, imaging duration is a crucial consideration, both because physiological processes of interest may evolve over the span of seconds or minutes, and also because rapid respiration and cardiac rates of mice (~120 and ~500 bpm, respectively) can introduce significant motion blur in images if not accounted for.

6.5.1 Respiratory-Gated In Vivo Micro-CT

The use of in vivo micro-CT has been recently demonstrated for a variety of preclinical murine abdominal, cardiac, and pulmonary imaging applications [24, 25]. The high contrast between air and soft tissue makes micro-CT particularly useful for studies of diseases such as lung carcinoma and emphysema [26], while iodine-based blood pool contrast agents provide enhanced contrast against soft tissue to permit studies of the heart [27–30] and vascular systems. However, as a consequence of an animal's rapid respiration rates, clinical breath-hold imaging techniques, where entire scans occur within a single phase of respiration, are not feasible. Some method of respiratory and/or cardiac gating must be employed to reduce motion blur of the thorax when performing in vivo imaging of the heart and lungs. In a method known as physiological gating, projection X-ray images to be used in reconstruction are matched to a particular phase of the respiratory or cardiac cycles (or both), depending upon the imaging application.

When using retrospective respiratory gating, X-ray projection images are acquired and each projection is sorted into a bin corresponding to a different phase of the respiratory cycle. Then during reconstruction, only projections corresponding to a single phase of respiration are used to generate the 3-D CT image. To guarantee full angular coverage in the phase of interest, multiple rotations of the gantry are necessary [31, 32]. Retrospective gating techniques have the benefit of easy implementation and fast scan times, but they result in an increased radiation dose to the subject due to the necessary oversampling. The increased radiation dose can be especially significant in small animals where the imaging dose is a large fraction of the 50% lethal dose [33].

Another technique, prospective respiratory gating, circumvents this problem by synchronizing X-ray exposure with the physiological phase of interest. One possible method of prospective gating involves intubating subjects and directly manipulating airway pressure through a ventilator, controlling the amplitude and periodicity of the respiratory motion so that it matches X-ray exposure windows [34–36]. This protocol eliminates the wasted radiation dose of retrospective gating, but it requires advanced animal handling techniques to prevent damage to the trachea and vocal chords. In addition, the process of mechanical ventilation has been shown to induce lung injury in otherwise previously healthy specimens [37–40]. Due to these risks, forced breathing and breath-hold gating methods are not ideal for longitudinal studies, particularly for sensitive disease models. Also, external manipulation of lung pressure and volume can result in measures of tidal lung volumes and related values which are not accurate or physiologically relevant to the study.

Prospective gating can be performed less invasively if the mice can be permitted to breathe freely, instead tracking the natural abdominal motion through either a pressure sensor or charged-coupled device (CCD) camera and synchronizing X-ray pulses with a desired phase in the respiration cycle [41]. Although breathing is not directly controlled, a healthy adult mouse under anesthesia and temperature control generally exhibits a stable, reproducible, quasi-periodic respiratory motion allowing blur-free abdominal imaging to be performed easily [41]. Free-breathing

prospective gating leads to an increase in scan time but a reduction in delivered radiation dose, avoiding the risks of intubation. To achieve the best results, a rapid-response X-ray source with good temporal resolution (100 ms or less) to achieve blur-free respiration images [42] is needed.

6.5.2 Cardiac-Gated In Vivo Micro-CT

CT imaging of murine cardiac disease presents a set of unique challenges [43]. For human cardiac imaging, acquisition times of 75.5 ms or less per slice are required to eliminate in-plane arterial motion blur in a typical patient [44]. Replicating the clinical imaging technique with a murine subject requires imaging in less than 10–15 ms. Thus, a cardiac imaging protocol requires that a single X-ray exposure must last no more than 15 ms in order to capture the diastolic phase without blur. Given flux and gantry speed limitations of commercial micro-CT systems, a full CT scan cannot be acquired in less than 15 ms, and so either prospective or retrospective gating techniques must be applied. The general concept and implications are the same as for respiratory-gated imaging. One additional concern is that respiratory blur will obscure the heart unless it is controlled for as well, so cardiac-gated imaging is by definition the gating of both lungs and heart simultaneously.

For successful prospective physiologically gated in vivo small-animal micro-CT imaging, the scanner's X-ray source must have a small focal spot size, be capable of high flux for short pulse generation, yet also be capable of generating these pulses nonperiodically with almost instantaneous response time. Fortunately, these very high demands are met by an X-ray source based on carbon nanotube field-emission technology.

6.6 CNT Micro-CT System Components and Characteristics

The CNT micro-CT is a tabletop device consisting of a compact, high-flux X-ray source (Fig. 6.3a), a flat panel detector, and power supplies and other electrical components which are mounted on a rotating gantry [45]. The system design was chosen to mimic clinical scanners, allowing the imaging subject to be naturally oriented horizontally along the axis of rotation. An image of the system and all of its major components is shown in Fig. 6.2b.

The X-ray source used in the CNT micro-CT system is the tube described in Sect. 4.2. The interior components were shown in Fig. 6.2. The CNT cathode is shaped into a 2.35×0.5-mm ellipse, corresponding to an optimal focal spot size for micro-CT. Optimal voltages were experimentally determined for the static focusing structure to optimize the focal spot size, which for the selected parameters resulted in a 117×117-μm focal spot [45]. The exit window of the X-ray chamber consists of 200 μm of beryllium, and an additional 0.5 mm of aluminum in filter material

is placed over the X-ray exit window in order to reduce low-energy photons and beam-hardening effects. X-ray pulses as short as 15 ms can be generated with this X-ray source while still providing sufficient flux for a high contrast-to-noise ratio in the images [45, 46].

The flat panel detector used to capture X-ray projections is a high-speed model with a CsI scintillator deposited on an array of photodiodes (C7940DK-02, Hamamatsu). The active area contains 2400 × 2400 pixels, with each pixel measuring 50 × 50 μm (total active area of 12 cm x 12 cm), but only the central one fourth of its area is used. Both this detector and the compact CNT X-ray source are mounted on a small-bore goniometer (Huber 430, Germany) on opposite sides of the rotating gantry [46]. A small plastic animal bed is positioned horizontally along the gantry's axis of rotation, allowing the mouse to lie comfortably in the prone position during image acquisition. An automated control program was written in LabVIEW (National Instruments, Austin, TX, USA) to rotate the goniometer in a step-and-shoot mode during image acquisition.

Scanner geometry is optimized for maximum tube flux by reducing the object-to-detector distance as much as possible while still keeping the bore diameter sufficiently wide for subject clearance. The source-to-object distance was set for the best compromise between large magnification and low overall distance for maximum flux full coverage of the detector active area by the cone beam angle (20°) without photon drop-off from anode heel effect. The final geometric configuration included a source-to-object distance of 120 mm and an object-to-detector distance of 40 mm (minimum for subject clearance). This results in a magnification factor of 1.3 at the detector [45]. The overall effective field of view of the scanner is 46 × 46 mm. System modulation transfer function (MTF) has been measured at 6.2 lp/mm for 10% MTF and 7.3 lp/mm for 5% MTF (corresponding to resolutions of 81 and 68 μm, respectively) [45].

The angular range was chosen to span 180° plus the cone beam angle opening of 20°. The detector frame rate is fixed at 1 Hz, but total scan times for a prospectively gated protocol ranged from 5 to 20 min depending upon the rate of physiological motion and the type of gating chosen for a particular application [45, 46].

Because of the fast response time and uniform output of the CNT X-ray source, dynamic prospective respiratory gating is possible with this micro-CT scanner. With the period of respiration for a sedated mouse in the range of 80–150 bpm, the system temporal resolution of 10 ms allows the acquisition of blur-free images during the low-motion portions of both the peak inhalation and full exhalation phases of respiration, as well as the diastolic and systolic phases of the cardiac cycle.

6.6.1 Animal Handling Protocol

All of the animal studies described in this chapter were performed under the direction of the Institutional Animal Care and Use Committee at the University of North Carolina in approved protocols. During live small-animal imaging, subjects were anesthetized with approximately 1.5% vaporized isoflurane anesthesia in medical

grade oxygen at a flow rate of 1.5–2 L per minute, which is delivered through a nose cone attached to the animal bed. Precise isoflurane dosage is adjusted as necessary throughout the study to maintain steady respiration rates between 80 and 120 bpm. Subjects are placed in prone position on the imaging bed with their abdomens resting atop a pneumatic pillow pressure sensor which records abdominal respiratory motion. The sensor is attached to a pressure transducer, and the signal is monitored using a commercial physiological monitoring system (BioVet, m2m Imaging Corp, Cleveland, OH, USA). A small piece of stretchable medical bandage (Coban, 3 M Medical, St. Paul, MN) is used to lightly restrain subjects around the abdomen. Animals are not intubated; instead, they freely breathe the anesthesia/oxygen mixture throughout imaging. During cardiac imaging protocols, an ECG signal is obtained by affixing three neonatal electrodes to both of the mouse's forepaws and one hind paw. The signals from these electrodes are also read into the BioVet software for monitoring and gating.

For cardiac imaging and other applications where the blood pool and vessels must be distinguished from the surrounding soft tissue, an iodinated contrast agent is necessary. For most such applications, a blood-pool contrast agent (Fenestra VC, 50 mg I/mL, Advanced Research Technologies, Inc., Montreal, Canada) is administered immediately before imaging in a single bolus via tail-vein injection at the manufacturer-recommended dosage of 0.02 mL per gram animal body weight. This contrast agent has a demonstrated retention time in the blood pool of up to 2 h [47], providing contrast enhancement with respect to the surrounding soft tissue.

6.6.2 Physiological Gating Protocol

The timing circuit for prospective respiratory micro-CT imaging in step-and-shoot mode can be seen in Fig. 6.5 [45]. The camera readout time is 470 ms, and the acceptable exposure window for X-ray synchronization is defined as the time window between the end of the previous frame's readout and the beginning of the next frame readout, minus the temporal width of the X-ray pulse (Fig. 6.5a). This is defined such that X-ray pulses could only fire during the camera exposure window (preventing misfires and wasted dose). X-ray exposures are synchronized with the physiological trigger signal from Biovet. Dynamic physiological gating resulted from the logic AND operation between the detector exposure window and the physiological trigger from Biovet.

The physiological trigger generated by Biovet can be set to output for either pure respiratory gating or simultaneous cardiac and respiratory gating. For respiratory gating protocols, a TTL high signal was produced from the Biovet program when the signal from the respiratory pressure sensor coincided with the preset level corresponding to the desired phase of the respiratory cycle. For cardiac/respiratory gating, also referred to simply as cardiac gating, the physiological trigger was generated when the preselected levels in the cardiac and respiration signals were achieved within the same acquisition window (Fig. 6.5b).

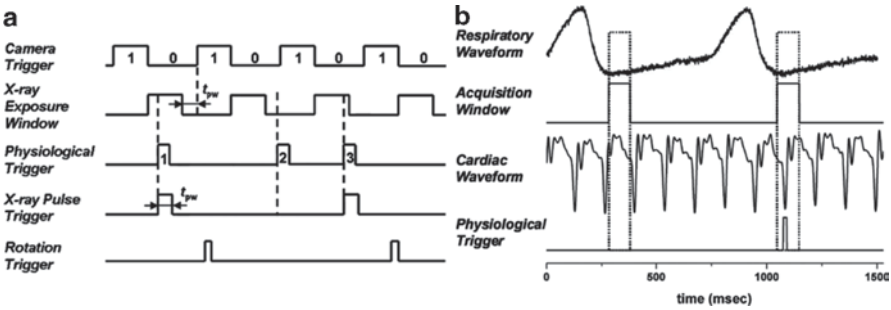

Fig. 6.5 **a** The timing schematic for X-ray acquisition, incorporating synchronization of the camera exposure, physiological trigger, and X-ray pulse generation. **b** In a simultaneous cardiac- and respiratory-gated protocol, the physiological trigger is generated when the selected respiration and cardiac phases occur within the same acquisition window. (Reproduced from Cao et al Medical Physics)

For the respiratory signal, a threshold level is manually selected in to correspond with the point of maximum inhalation. When the end-exhalation phase is preferred, a user-defined delay ranging from 150 to 200 ms elapses before the trigger signal occurs [46]. Similarly, for the cardiac ECG signal, the threshold level is manually set on the *R* wave for diastole, and a delay of 55 ms was inserted before the trigger output for systole [45].

In order to evaluate lung function as quantified by tidal lung volume, two sets of CT images are acquired for each animal in lung imaging protocols: one during peak inspiration and one during full exhalation. For assessment of cardiac function via ejection fraction, two sets of cardiac-gated CT images are generally acquired per subject: one during diastole and one during systole.

6.6.3 Image Acquisition

For respiratory-gated micro-CT, the CNT X-ray source was operated with 50 kV anode voltage, 1.66 mA anode current, and 30 ms X-ray pulse widths [46]. For cardiac imaging, a 2-mA anode current was used with 15-ms X-ray pulse widths [45]. In addition to projection acquisition, averaged bright and dark images were collected for detector calibration. A total of 400 projections were acquired over 200° total gantry rotation in step-and-shoot mode, with each step covering 0.5°. After processing with a custom MATLAB program to correct for raw air values and remove dark pixels and lines, CT volumes were reconstructed with a voxel size of 76 μm using a commercial Feldkamp-based software package (Cobra, Exxim Computing Corp, Livermore, CA, USA). The total reconstructed volume array is 512^3 voxels [46].

6.6.4 *Respiratory-Gated and Cardiac-Gated Imaging of Wild-Type Mice*

The results of respiratory- and cardiac-gated in vivo micro-CT imaging of wild-type mice are shown in Figs. 6.6 and 6.7 and in Fig. 6.8, respectively.

Respiratory gating eliminates motion blur, which is visualized in coronal views (Fig. 6.6c and d) as a sharp transition from the lungs to the diaphragm and in axial views (6.6a and b) with the distinction of fine vessels within the lungs. Changes in lung volume between inhalation and exhalation are seen in coronal views (Fig. 6.6c and d), but exact volume measurements are instead derived from 3D volume segmentations of the lungs and airways as displayed in Fig. 6.7. CT-derived lung volume measurements from the full inhalation and end-exhalation respiratory phases allow the calculation of tidal lung volume, a quantitative measure of pulmonary function.

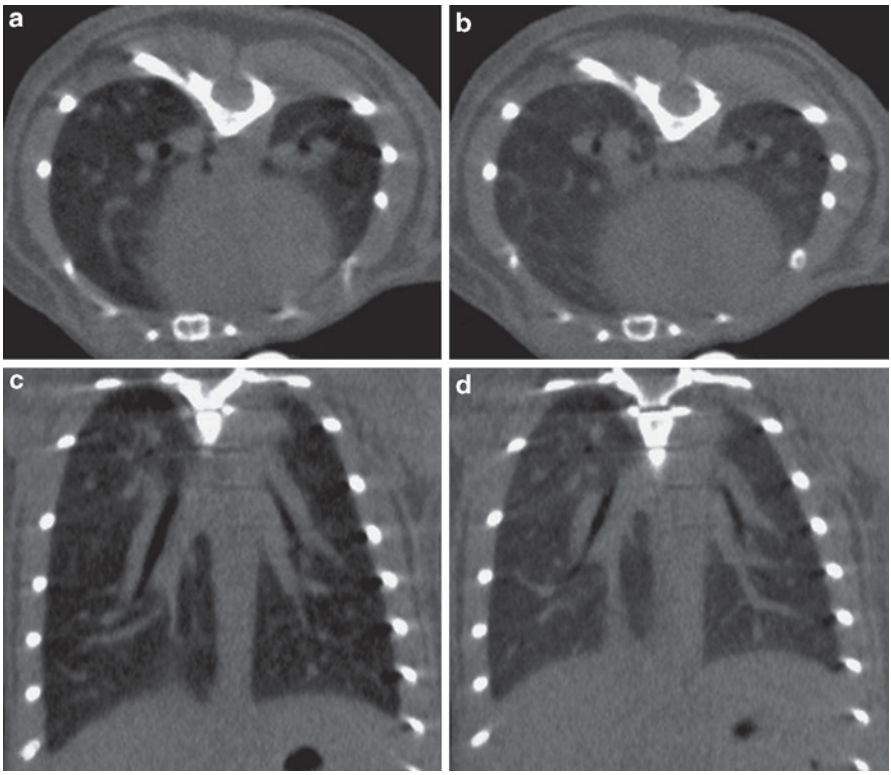

Fig. 6.6 Micro-CT of healthy mouse lungs during full inhalation (**a** and **c**) and end exhalation (**b** and **d**). Successful gating has reduced motion blur, allowing visualization of fine structures in the axial (**a** and **b**) slice views. Differences in lung volume between inhalation and exhalation are best visualized in the coronal slice views (**c** and **d**). (Reproduced from Lee et al. Academic Radiology)

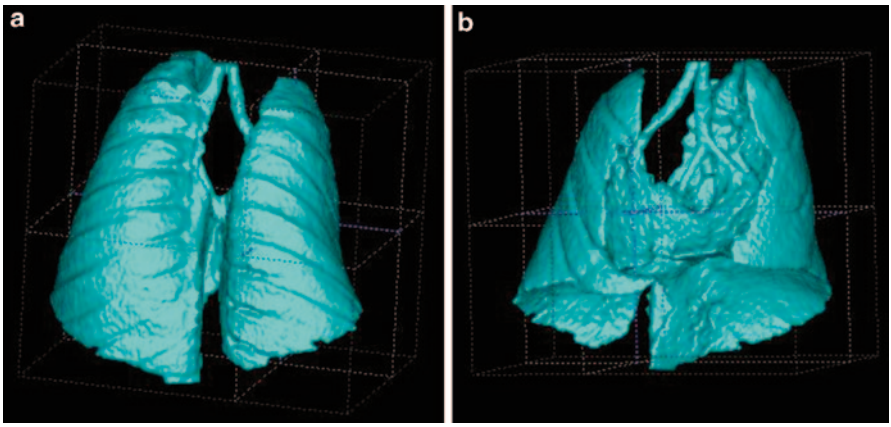

Fig. 6.7 **a** Front and **b** rear views of a volume rendering of healthy murine lungs generated from a respiratory-gated in vivo micro-CT image. Accurate lung volume measurements can be derived from micro-CT, providing data on pulmonary function

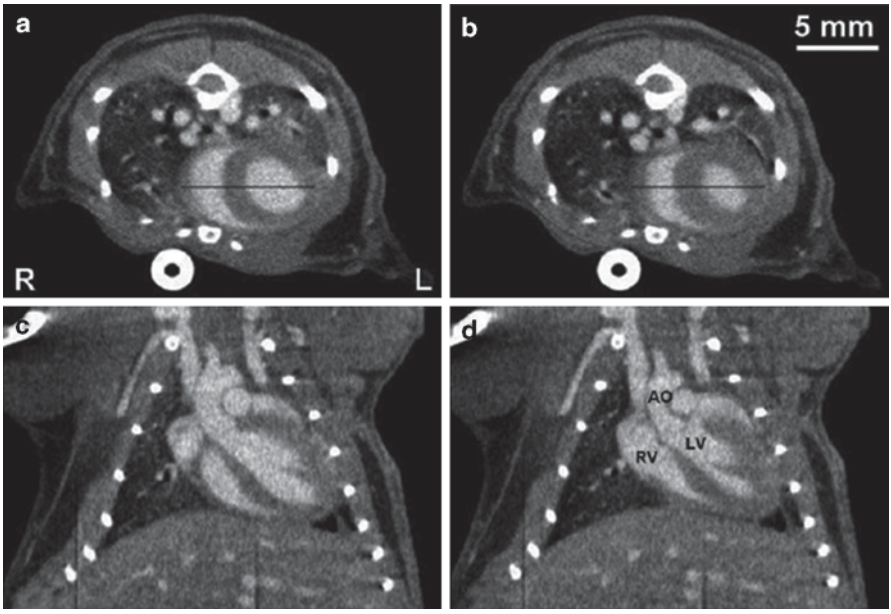

Fig. 6.8 Cardiac-gated in vivo micro-CT images of a wild-type mouse, acquired during the diastolic (**a** and **c**) and systolic (**b** and **d**) phases. Iodine contrast agent enhances blood-pool contrast, and the gated protocol removes motion blur because the ventricles and aorta are clearly distinguished from the myocardium. *AO* aorta, *RV* right ventricle, *LV* left ventricle. (Reproduced from Cao et al Medical Physics)

Though diaphragmatic blur is eliminated with respiratory gating, significant blur is still present surrounding the heart in the axial CT slices (6.6a and 6.6b). The addition of cardiac gating to the imaging protocol eliminates this motion from the axial views in Fig. 6.6. With the addition of iodine contrast agent into the blood pool, the ventricles and aorta are clearly distinguishable from myocardium. By 3-D volume segmentation of the ventricles within the heart from images of diastole and systole, cardiac output can be calculated via the ejection fraction [46].

6.7 Examples of Imaging Applications for CNT Micro-CT

Having proven the utility of the CNT micro-CT for wild-type healthy animals, we now move to several disease applications, including mouse models for pulmonary, abdominal, and cardiac disease. These imaging applications are much more challenging than healthy small-animal imaging, pushing the envelope of what can be achieved through small-animal in vivo micro-CT.

6.7.1 Lung Tumor Imaging

Lung cancer is one of the leading causes of death in the USA with 222,520 new cases reported in 2010 and 157,300 deaths [48]. New innovations for diagnosis and treatment are dependent upon preclinical research of murine models for lung carcinoma. The noninvasive nature of respiratory-gated CNT micro-CT makes this technology ideal for longitudinal studies of mouse models for lung cancer.

Adult mice with multifocal, LSL-induced lung tumors (LSL-Kras) were imaged with prospective respiratory-gated micro-CT imaging in a longitudinal study to track disease development [48]. Tumor growth was appreciable over a period of several weeks, so imaging was performed at two time points over a month. Despite appreciable progression of disease over the course of the study, all animals survived through the final micro-CT imaging. Successfully respiratory-gated micro-CT images and optical signals were obtained for all animals. The tumors were readily identified on the CT images in all lobes for the Kras + mice; the smallest, readily identifiable tumor measured approximately 300 μm in diameter.

In Fig. 6.9, side-by-side axial CT slices acquired over a period of 3 weeks show the growth of two large masses [49]. Three-dimensional renderings of respiratory-gated lung imaging highlight the increase in lesion size and number over the course of 3 weeks (Fig. 6.10). Though masses are inherently difficult to distinguish from other soft tissues, they stand in stark contrast from the airways of the lungs, and their presence is seen in the negative space of the 3-D images.

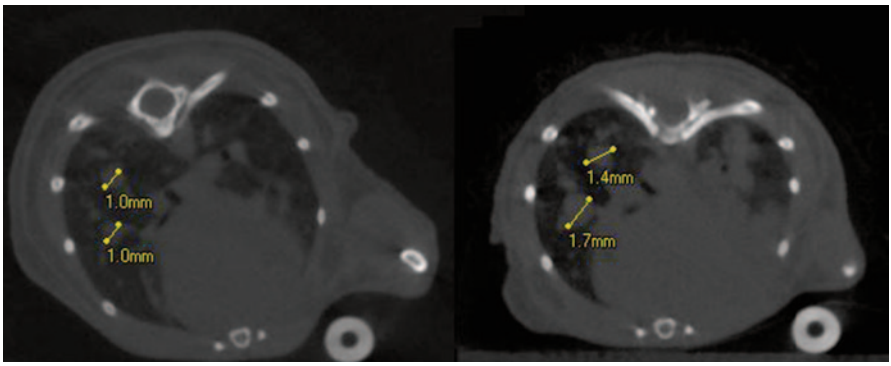

Fig. 6.9 Matching reconstructed axial CT slices of a male lung tumor model mouse acquired at 3-week intervals. Diameters of the two largest masses are labeled. (Reproduced from Burk et al. 2011, Proc. of SPIE Vol. 7965 79651L)

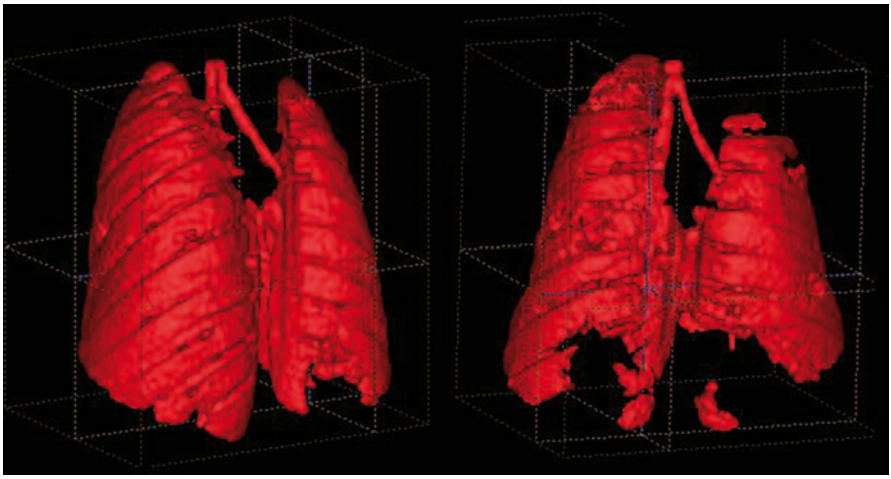

Fig. 6.10 Volume rendering of tumor-burdened mouse lungs during full inhalation (shown from front and back), showing progression over a 3-week time period. Negative space in the volumes represents the location of masses within the lungs. Tidal lung volume measurements derived from micro-CT images quantify changes in lung function as the result of disease progression

6.7.2 Congenital Diaphragmatic Hernia

Congenital diaphragmatic hernia is a birth defect characterized by deformation of the diaphragm in infants. This deformation allows the lower organs to breach the diaphragm wall and displace the lungs, causing pulmonary hypoplasia and pulmonary hypertension [50]. Studying a model for this disease in mice is difficult using standard respiratory-gated techniques because the characteristic diaphragmatic weakness of this disease does not permit pressure to be applied at the abdomen.

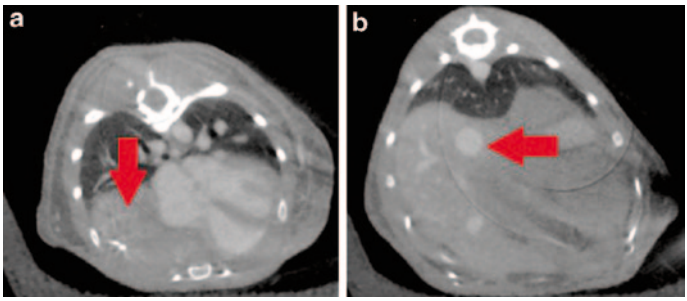

Fig. 6.11 **a** Mid-lung and **b** mid-liver axial slices from respiration-gated micro-CT of the knock-out hernia model. (Figure reproduced from Burk et al Phys. Med. Biol. 2012)

Fortunately, recent development of a contactless displacement respiration sensor [51] has allowed in vivo micro-CT to be performed without any physical manipulation of the study subjects. Using this new device to provide the respiratory signal for physiological gating, adult mouse models for congenital diaphragmatic hernia [52] and age-matched controls were imaged using the standard gated abdominal imaging protocol.

CTs of wild-type animals display healthy heart and lungs (Fig. 6.11a) and vasculature of the liver (Fig. 6.11b) [51]. However, in the case of the diaphragmatic hernia model, a large volume of the right lung is displaced by the liver and other organs penetrating the diaphragm, and the heart is compressed and distorted in shape (left). In the lower axial slice, where one would expect only the base of the lungs and the liver, lower organs are visible. Because the respiration monitoring apparatus did not involve applied pressure or any direct contact with the subject, the abnormal physiology can be attributed solely to disease progression.

6.7.3 Osteoclastogenesis and Rib Fractures

Our collaborators in the laboratory of Arjun Deb, Department of Medicine at the University of North Carolina at Chapel Hill, have studied site-specific β-catenin-regulated osteoclastogenesis and the effect of corticosteroids in reversing this rapid bone loss in adult mice [53]. Due to the extreme delicacy of the ribs of animals experiencing rapid osteoclastogenesis, micro-CT images of disease progression could not be obtained through conventional methods, and our system was again paired with the contactless respiration sensor to obtain a respiration signal for gating.

To create the model, *Cre* transgenic mice (C57Bl/6) were crossed for two generations with mice with both their β-catenin alleles floxed (β-catenin fl/fl), then injected intraperitoneally for 11 days with tamoxifen dissolved in corn oil. Three populations were studied: the previously described genetic mouse model, control C57Bl/6 mice injected with tamoxifen, and controls injected with oil representatives of each of the three populations were imaged on day 0 (1 day before injections commenced) and day 10 using a CNT field-emission micro-CT.

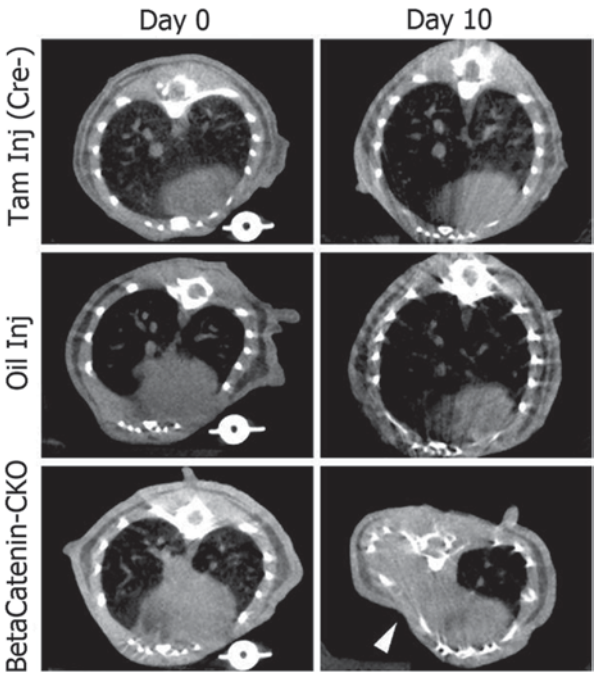

Fig. 6.12 Reconstructed axial slices of respiratory-gated micro-CT images acquired on day 0 (before injection) and day 10 of three mice representing three populations. (Figure reproduced from Burk et al Phys. Med. Biol. 2012)

Figure 6.12 shows representative reconstructed axial micro-CT slices of mice from the three populations during day 0 and day 10 [53]. Dramatic lung and rib deformation is seen in the day-10 images of the β-catenin–CK mice after tamoxifen injection, and complete atelectasis of one of the lungs has occurred spontaneously. Even in the presence of such severe disease, respiratory abdominal motion was able to be measured with the contactless fiber-optic sensor. Successful in vivo imaging of this model was possible only with the use of the CNT micro-CT and contactless respiratory gating.

6.7.4 Mouse Pups

Noninvasive imaging of mouse pups is desirable for the study of diseases which affect children and infants. One prime example is cystic fibrosis, which is a pathology present from birth in humans, and also in murine models for the disease [54]. It has been seen in this mouse model that tracheal mucus obstruction can lead to neonatal mortality in some subjects, while others survive to maturity [55]; study of this phenomenon requires the ability to perform in vivo imaging on young animals of less than 2 weeks of age. Due to the difficulties of working with such young animals, physiologically gated high-resolution micro-CT imaging had previously not been achieved for mouse pups younger than 2 weeks of age. As a demonstration of our capability for imaging young subjects with noncontact CT techniques,

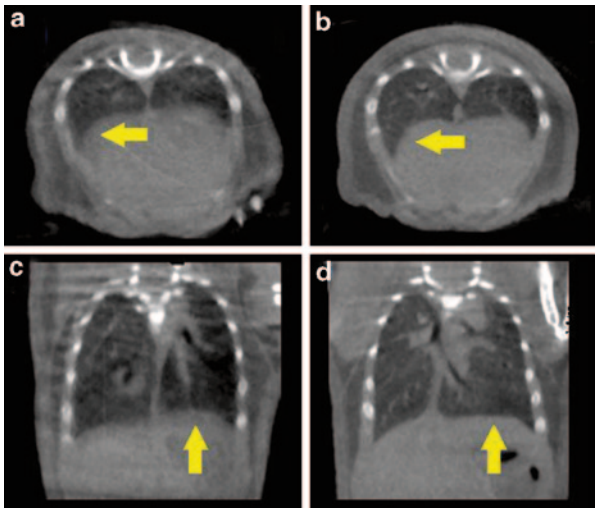

Fig. 6.13 Nongated (**a** and **c**) and respiratory-gated (**b** and **d**) CT images of an 11-day-old mouse pup. *Arrows* indicate regions of diaphragmatic blurring in ungated images and corresponding regions of sharp delineation on respiratory-gated images. (Figure reproduced from Burk et al. Phys. Med. Biol. 2012)

we performed respiration-gated micro-CT on four 11-day-old wild-type animals (9 C57BL/6 N), with average masses of 4.4 +/− 0.3 g [51].

CTs acquired both with and without prospective respiration gating are displayed in Fig. 6.13. Fine pulmonary structures are more clearly visible with gated imaging than in images without gating, and sharper contrast across the diaphragm, an indication of low respiratory motion blur, is seen in the gated images.

6.7.5 Cardiovascular Diseases

Cardiovascular disease is currently the leading cause of mortality worldwide [56]. This provides significant motivation for research and advancements in cardiac animal modeling, diagnostic testing and imaging, as well as new treatment and disease management. To this aim, researchers have created murine models of many cardiac diseases [57–59], but all studies are limited by the imaging options for the evaluation of murine cardiac structure and function. With the CNT field-emission-based micro-CT device and a cardiac-gated imaging protocol, we have participated in studies of many types of cardiac disease, including aortic calcification, left ventricular hypertrophy, and myocardial infarction.

6.7.5.1 Aortic Calcification

The presence of calcifications within the aortic arch correlates with an increase in risk of cardiovascular diseases, independent of other risk factors [60]. While obtaining high contrast between calcified plaques and the surrounding tissue and blood of the aortic arch is not difficult to achieve in CT, high spatial resolution and

elimination of cardiac motion blur in images is necessary to visualize and quantify such plaques for small animals in vivo. Using the standard cardiac-gated imaging protocol, CNT micro-CT has proven superior to conventional micro-CT in accurate visualization and distinction of calcification in the aortic arch. This superiority is quantified by a twofold increase in edge sharpness when compared with a commercial micro-CT imaging system [61]. This work demonstrates that cardiac-gated CNT micro-CT is a sacrifice-free alternative to histology for the assessment of the distribution and severity of aortic calcifications in mouse research models.

6.7.5.2 Left Ventricular Hypertrophy

The utility of the CNT-based imaging system for quantitative cardiac evaluation of normal mice has been demonstrated using respiratory and cardiac-gated CNT micro-CT imaging techniques and a blood pool contrast-protocol. From the resulting micro-CT images, quantitative measurements of ejection fraction and myocardial wall thicknesses can be made to assess both cardiac function and morphology. The use of this device has been demonstrated for pathology by investigating a murine model of left ventricular hypertrophy [62]. Transverse aortic constriction (TAC), an effective technique for inducing left ventricular hypertrophy (LVH) in mice, was the model investigated for this work [63]. Studying the murine LVH model offered a quantitative evaluation of the adaptive cardiac response to increased hemodynamic load, which is often a symptom of cardiomyopathies, aortic stenosis, aortic insufficiency, and hypertension [64].

In our investigation, LVH was induced in wild-type male mice. In vivo images of the subjects were acquired prior to the TAC procedure and at 2 and 4 weeks following the procedure. By obtaining cardiac-gated micro-CT images of LVH mice during the diastolic and systolic phases, for multiple time points following the induction of LVH, we were able to track changes in cardiac output as quantified by ejection fraction. Concurrently, high-resolution images allowed accurate measurements of myocardial wall thicknesses over time, so that the relationship between wall thickness and ejection fraction could be studied in detail. This was made possible because of the noninvasive nature of prospective cardiac gating and the high spatial and temporal resolution offered by CNT micro-CT.

6.7.5.3 Myocardial Infarction

During myocardial infarction, more commonly known as heart attack, blood flow to portions of the heart is blocked causing ischemic damage. To determine a treatment plan, the severity of the damage must be assessed through standard clinical imaging techniques. Though the current standard for in vivo murine cardiac imaging is echocardiography, this modality cannot easily distinguish between nonfunctional infarct, ischemic, stunned, hibernating, and healthy myocardium. However, the clinical technique of delayed contrast enhancement, considered the gold standard

for imaging of infarcted tissue using MRI [65], can be applied to small-animal micro-CT to successfully highlight regions of infarcted tissue. This imaging technique is possible because the small particles of blood contrast agents distribute themselves in the extracellular spaces of healthy myocardium soon after intravenous administration, while these agents are too large to be admitted into the normal myocardial cells. However, the cellular changes resulting from ischemia affect arterial flow rate and the permeability of the capillaries. Necrotic and acute infarcted regions of the myocardium suffer a loss of membrane integrity, allowing contrast agent molecules to leak into these regions over time; furthermore, the contrast is retained in these tissues past the typical washout time in healthy extracellular spaces. The result is a characteristic delayed enhancement in necrotic regions of the myocardium captured in the CT or MR images acquired during an appropriate time window during which iohexol has diffused into infarcted tissue but has not yet washed out again [66].

We evaluated a murine model for acute myocardial infarction using the CNT micro-CT and a delayed contrast enhancement technique using iohexol administered in a bolus [67]. The surgical model for ischemia and reperfusion was produced by surgical occlusion of the left anterior descending artery (LAD) with a suture for 30 min followed by 24 h of reperfusion prior to imaging. Iohexol 300 mg/mL (Omnipaque 300, Novation, Irving TX) was administered to the subjects via tail-vein catheter. In CT images acquired over multiple time points following IV contrast administration, necrosis of the myocardium resulting from LAD obstruction was observed. After imaging, subjects were sacrificed and their hearts were cut into 1-mm slices and stained with triphenyl tetrazolium chloride (TTC) to visualize healthy and necrotic tissues.

Images acquired an average of 13 min after administration of iohexol contrast agent showing hyper-enhancement within the myocardial wall (Fig. 6.14) corresponding with the region most at risk of ischemia during LAD obstruction. Matching TTC-stained axial heart slices clearly exhibit regions lacking protein uptake in the same regions of the myocardial wall, and they are equivalent in size and shape to regions displaying delayed contrast enhancement in micro-CT [67].

6.8 Summary and Outlook

In the decade since carbon nanotube X-ray emission was first achieved at the University of North Carolina, the technology has progressed dramatically into applications for security, small-animal radiation therapy and imaging, and clinical breast cancer screening. Using CNT field emission, high-flux, fast-response, compact X-ray sources can be built in novel geometry source arrays. Within the field of small-animal in vivo imaging, the unique capabilities of the CNT micro-CT have expanded the number of animal disease models which can be studied noninvasively and without sacrifice, providing another tool with which researchers can work to find treatments and cures for cancers and cardiovascular diseases. Despite this progress, we believe that the full potential of CNT field-emission X-ray imaging for biomedical application is still yet to come.

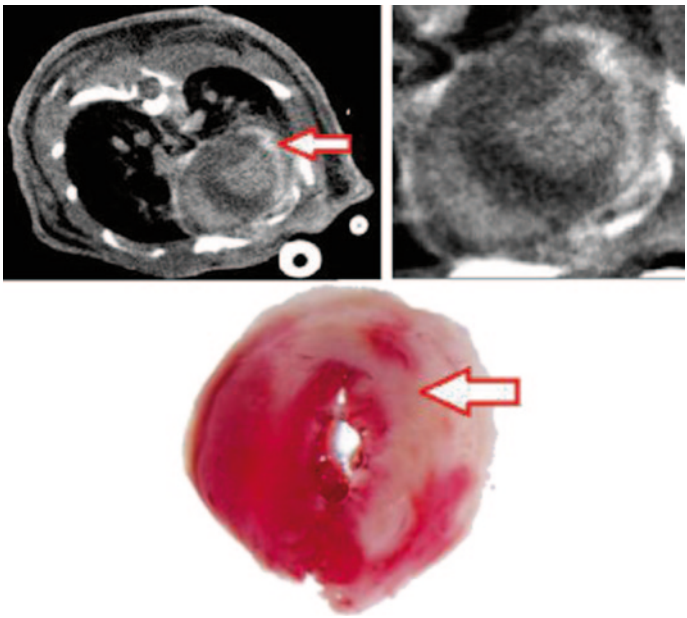

Fig. 6.14 An average of 15 min after administration of iohexol contrast agent, a delayed enhancement is seen within a region of the *left* ventricle myocardial wall (indicated with an *arrow*). This enhanced contrast region correlates in size and shape with the region of necrosis indicated in histological gross slices by a lack of TTC uptake. (Reproduced from Burk et al. 2011, Proc. of SPIE Vol. 7965 79651 N)

Acknowledgments This chapter summarizes research which was performed at the University of North Carolina (UNC) at Chapel Hill under the guidance of principal investigators Otto Zhou, Jianping Lu, and Yueh Lee. This interdisciplinary work was performed by current and former PhD students and postdoctoral researchers affiliated with UNC with backgrounds in physics, materials science, biomedical engineering, and chemistry. The authors wish to especially thank our current and former colleagues for their contributions, including Christy Inscoe, Mike Hadsell, Andrew Tucker, Emily Gidcumb, Lei Zhang, Jing Shan, Pavel Chtcheprov, Marci Potuzco, Jabari Calliste, Guohua Cao, Jerry Zhang, Xin Qian, Shabana Sultana, Xiomara Calderon-Colon, David Bordelon, Ramya Rajaram, Sigen Wang, Tuyen Phan, Ko-Han Wang, and Matt Wait. We gratefully acknowledge support for this research through grants from the National Institute of Biomedical Imaging and BioEngineering, the National Cancer Institute, and the University Cancer Research Fund at the UNC.

References

1. R. Gomer, *Field Emission and Field Ionization*. (Harvard University Press, Cambridge, 1961)
2. Y. Cheng, O. Zhou, Electron field emission from carbon nanotubes. C. R. Phys. **4**, 1021–1033 (2003)
3. F.M. Charbonnier, J.P. Barbour, W.P. Dyke, Resolution of field emission x-ray sources. Radiology **117**, 165 (1974)

4. G.S. Hallenbeck, Clinical evaluation of the 250-KV chest radiography system. Radiology **117**, 1–4 (1974)
5. R. Baptist, X-ray tube comprising an electron source with microtips and magnetic guiding means. US Pat. **6**(259), 765 (2001)
6. P. Rangstein et al., Field-emitting structures intended for a miniature X-ray source. Sens. Actuators **82**, 24–29 (2000)
7. W.A.D. Heer, A. Chatlelain, D. Ugarte, A carbon nanotube field-emission electron source. Science **270**, 1179–1180 (1995)
8. O. Zhou, J.P. Lu, New X-ray generating mechanism using electron field emission cathode. US Patent **6**(553), 096 (2003)
9. H. Sugie et al., Carbon nanotubes as electron source in an X-ray tube. Appl. Phys. Lett. **78**, 2578 (2001)
10. G.Z. Yue et al., Generation of continuous and pulsed diagnostic imaging X-ray radiation using a carbon-nanotube-based field-emission cathode. Appl. Phys. Lett. **81**(2), 355 (2002)
11. J. Zhang et al., A stationary scanning X-ray source based on carbon nanotube field emitters. Appl. Phys. Lett. **86**, 184104 (2005)
12. O. Zhou, J.P. Lu, X-ray generating mechanism using electron field emission cathode. US Patent **6**(850), 595 (2006)
13. W.B. Choi et al., Fully sealed, high-brightness carbon-nanotube field-emission display. Appl. Phys. Lett. **75**, 3129–3131 (1999)
14. Y. Ye et al., Fabrication of carbon nanotubes field emission backlight unit applied to LCD. Photonics and Optoelectronics, (2009) pp. 1–3
15. J. Zhang et al., A multi-beam X-ray imaging system based on carbon nanotube field emitters. *Proceedings of SPIE*, Vol. 6142 (eds J.M. Flynn and H. Jiang), Medical Imaging, (2006) p. 614204
16. G. Cao, J. Zhang, O. Zhou, J. Lu, Temporal multiplexing radiography for dynamic x-ray imaging. Rev. Sci. Instrum. **80**, 093902 (2009) PMCID: 2766412
17. Z.L. Wang et al., In-situ imaging of field emission from individual carbon nanotubes and their structural damage. Appl. Phys. Lett. **80**(5), 856–858 (2002)
18. S.J. Oh et al., Liquid-phase fabrication of patterned carbon nanotube field emission cathodes. Appl. Phys. Lett. **87**(19), 3738 (2004)
19. O. Zhou, X. Calderon-Colon, in *Carbon Nanotube and Related Field Emitters: Fundamentals and Applications*, ed. by Y. Saito. Carbon Nanotube-Based Field Emission X-Ray Technology (Wiley-VCH Verlag GmbH & Co, Weinheim, 2010)
20. X. Calderon-Colon, H. Geng, B. Gao, L. An G. Cao O. Zhou, A carbon nanotube field emission cathode with high current density and long-term stability. Nanotechnology **20**(2009) 325707 (5 pp)
21. S. Sultana et al., Design and characterization of a carbon nanotube based micro-focus X-ray tube for small animal imaging. *Medical Imaging 2010: Physics of Medical Imaging. Proceedings of SPIE*, 7622 (2010) p. 76225G
22. X. Qian et al., High resolution stationary digital breast tomosynthesis using distributed carbon nanotube X-ray source array. Med. Phys. **39**, 2090 (2012)
23. S. Wang et al., A carbon nanotube field emission multipixel X-ray array source for microradiotherapy application. Appl. Phys. Lett. **98**(21), 213701 (2011)
24. E.L. Ritman, Current status of developments and applications of micro-CT. Annu. Rev. Biomed. Eng. **13**, 531–552 (2011)
25. S.J. Schambach et al., Application of micro-CT in small animal imaging. Methods **50**, 2–13 (2010)
26. N.L. Ford et al., In vivo characterization of lung morphology and function in anesthetized free-breathing mice using micro-computed tomography. J. Appl. Physiol. **102**(5), 2046–2055 (2007)
27. S. Mukundan, Jr. et al., A liposomal nanoscale contrast agent for preclinical CT in mice. AJR Am. J. Roentgenol. **186**(2), 300–307 (2006)

28. C.T. Badea et al., Cardiac micro-computed tomography for morphological and functional phenotyping of muscle LIM protein null mice. Mol. Imaging. **6**, 261–268 (2007)
29. M. Drangova et al., Fast retrospectively gated quantitative four-dimensional (4D) cardiac micro computed tomography imaging of free-breathing mice. Invest Radiol. **42**, 85–94 (2007)
30. S.A. Detombe et al., Longitudinal follow-up of cardiac structure and functional changes in an infarct mouse model using retrospectively gated micro-computed tomography. Invest. Radiol. **43**, 520–529 (2008)
31. S.H. Bartling et al., Retrospective motion gating in small animal CT of mice and rats. Invest. Radiol. **42**(10), 704–714 (2007)
32. S.H. Bartling et al., Intrinsic respiratory gating in small-animal CT. Eur. Radiol. **18**, 1375–1385 (2008)
33. J.G. Fox et al., (eds.), *The Mouse in Biomedical Research*, vol. 3 (ACLAM Series). (Academic, New York, 2007), pp. 453–454.
34. D. Cavanaugh et al., In vivo respiratory-gated micro-CT imaging in small-animal oncology models. Mol Imaging **3**(1), 55–62 (2004)
35. E.B. Walters et al., Improved Method of in vivo respiratory-gated micro-CT imaging. Phys. Med. Biol. **49**, 4163–4172 (2004)
36. E. Namati et al., In vivo micro-CT lung imaging via a computer-controlled intermittent isopressure breath hold (IIBH) technique. Phys Med Biol. **51**(23), 6061–6075 (2006)
37. G.F. Curley, L.G. Kevin, J.G. Laffey, Mechanical ventilation: Taking its toll on the lung. Anesthesiology **111**(4), 701–703 (2009)
38. L.W. Hedlund, G.A. Johnson, Mechanical ventilation for imaging the small animal lung. ILAR J. **43**(3), 159–174 (2002)
39. M. Vaneker et al., Mechanical ventilation induces a toll/interleukin-1 receptor domain-containing adapter-inducing interferon beta-dependent inflammatory response in healthy mice. Anesthesiology **111**(4), 836–843 (2009)
40. E.K. Wolthuis et al., Mechanical ventilation using non-injurious ventilation settings causes lung injury in the absence of pre-existing lung injury in healthy mice. Crit Care **13**(1), R1 (2009)
41. N.L. Ford et al., Prospective respiratory-gated micro-CT of free breathing rodents. Med. Phys. **32**(9), 2888–2898 (2005)
42. W. Maï et al., Effects of breathing and cardiac motion on spatial resolution in the microscopic imaging of rodents. Magn. Reson. Med. **53**, 858–865 (2005)
43. S.J. Schambach et al., Vascular imaging in small rodents using micro-CT. Methods **50**, 26–35 (2010)
44. B. Lu et al., Coronary artery motion during the cardiac cycle and optimal ECG triggering for coronary artery imaging. Invest. Radiol. **36**, 250–256 (2001)
45. G. Cao, L.M. Burk, Y.Z. Lee, X. Calderon-Colon, S. Sultana, J.P. Lu, O. Zhou, Prospective-gated cardiac micro-CT imaging of free-breathing mice using carbon nanotube field emission x-ray. Med. Phys. **37**, 5306 (2010)
46. Y.Z. Lee, L.M. Burk, K. Wang, G. Cao, J. Volmer, J. Lu, O. Zhou, Prospective respiratory gated carbon nanotube micro-computed tomography. Acad. Radiol. **18**(5), 588–593 (2011)
47. D. Balkan et al., Polyiodinated triglyceride lipid emulsions for use as hepatoselective contrast agents in CT—Effects of physicochemical properties on biodistribution and imaging profiles. Invest. Radiol. **35**, 158–169 (2000)
48. www.cancer.gov/cancertopics/types/lung.
49. L.M. Burk, Y.Z. Lee, S. Heathcote, K.-h. Wang, W.Y. Kim, J. Lu, O. Zhou, Carbon nanotube based respiratory gated micro-CT imaging of a murine model of lung tumors with optical imaging correlation. *Proceedings SPIE 7965, Medical Imaging 2011: Biomedical Applications in Molecular, Structural, and Functional Imaging, 79651 L (March 08, 2011); doi:10.1117/12.877465*
50. A. Gaxiola, J. Varon, G. Valladolid, Congenital diaphragmatic hernia: An overview of the etiology and current management. Acta. Paediatr. **98**(4), 621–627 (2009)

51. L.M. Burk, J.M. Wait, Y.Z. Lee, J.P. Lu, O.Z. Zhou, Non-contact respiration monitoring for in-vivo murine micro computed tomography: Characterization and imaging applications. Phys. Med. Biol. **57**, 5749–5763 (2012)
52. W. Yuan et al., A genetic model for a central (septum transversum) congenital diaphragmatic hernia in mice lacking Slit3. Proc. Nati. Acad. Sci. **100**(9), 5217–5222 (2003)
53. J. Duan, Y. Lee, C. Jania, J. Gong, M. Rojas, L. Burk, M. Willis, J. Homeister, S. Tilley, J. Rubin, A. Deb, Rib fractures and death from deletion of osteoblast catenin in adult mice is rescued by corticosteroids, PLoS One. 8(2), e55757 (2013). doi:10.1371/journal.pone.0055757
54. M. Mall, B.R. Grubb, J.R. Harkema, W.K. O'Neal, R.C. Boucher, Increased airway epithelial Na + absorption produces cystic fibrosis-like lung disease in mice. Nat. Med. **10**, 487–493 (2004)
55. A. Livraghi, B.R. Grubb, E.J. Hudson, K.J. Wilkinson, J.K. Sheehan, M.A. Mall, W.K. O'Neal, R.C. Boucher, S.H. Randell, Airway and lung pathology due to mucosal surface dehydration in b-epithelial Na + channel-overexpressing mice: Role of TNF-a and IL-4Ra signaling, influence of neonatal development, and limited efficacy of glucocorticoid treatment. J. Immunol. **182**, 4357–4367 (2009)
56. The International Journal of Public Health, media centre of cardiovascular diseases, the world health report 2012. http://www.who.int/mediacentre/factsheets/fs317/en/index.html. Accessed 1 April 2013
57. A.M. Abarbanell et al., Animal models of myocardial and vascular injury. J. Surg. Res. **162**, 239–249 (2010)
58. C. Zaragoza et al., Animal models of cardiovascular diseases. J Biomed. Biotechnol. 2011, 497841 (2011)
59. G. Christensen, Y. Wang, K.R. Chien, Physiological assessment of complex cardiac phenotypes in genetically engineered mice. Heart and circulatory physiology. Am. J. Physiol. **272**, H2513–H2524 (1997)
60. C. Iribarren et al., Calcification of the aortic arch: Risk factors and association with coronary heart disease, stroke, and peripheral vascular disease. J. Am. Med. Assoc. **283**, 2810–2815 (2000)
61. J.M.S. Wait, H. Tomita, L. Burk, J.P. Lu, O. Zhou, N. Maeda, Y.Z. Lee, Detection of aortic arch calcification in apolipoprotein E-null mice using carbon nanotube based micro-CT system. J. Am. Heart Assoc. **2**(1) (2013)
62. M.F. Meijs, M.L. Bots, E.J. Vonken et al., Rationale and design of the SMART heart study: A prediction model for left ventricular hypertrophy in hypertension. Neth. Heart J. **15**(9), 295–298 (2007)
63. W.E. Stansfield et al., Characterization of a model to independently study regression of ventricular hypertrophy. J. Surg. Res. **142**, 387–393 (2007)
64. G. Schillaci et al., Continuous relation between left ventricular mass and cardiovascular risk in essential hypertension. Hypertension **35**, 580–586 (2000)
65. K.G. Ordovas, C.B. Higgins, Delayed contrast enhancement on mr images of myocardium: Past, present, future. Radiology **261**(2), 358–374 (2011)
66. A.H. Mahnken et al., Assessment of myocardial edema by computed tomography in myocardial infarction. JACC Cardiovasc. Imaging **2**(10), 1167–1174 (2009)
67. L.M. Burk, K. Wang, E. Kang, M. Rojas, M. Willis, Y.Z. Lee, J. Lu O. Zhou, Imaging of myocardial infarction using carbon nanotube micro-computed tomography and delayed contrast enhancement. *Proceedings SPIE 7965, Medical Imaging 2011: Biomedical Applications in Molecular, Structural, and Functional Imaging, 79651 N*, 08 March 2011

Chapter 7
Nanotubes/Polymethyl Methacrylate Composite Resins as Denture Base Materials

Russell Wang, Ramazan Kayacan and Cenker Küçükeşmen

7.1 Introduction

Denture base acrylics resins are subjected to many different types of stresses. Intraorally, repeated masticatory forces lead to fatigue phenomena. Several studies have investigated the incidence and types of fracture of dentures [1–3]. Darbar et al. [4] reported that 33 % of the repairs carried out were caused by debonded/detached teeth and 29 % were repairs to midline fractures more commonly seen in upper complete dentures. The midline fracture in a denture is often a result of flexural fatigue. Impact failures usually occur due to sudden blow to the denture by accidental dropping.

The fracture resistance of denture base polymers has been investigated [5–9]. Reinforcement of denture base material has been a subject of interest to the dental material community. Polymethyl methacrylate (PMMA) resin is the principal material of dental prosthesis. To improve the properties of PMMA, many have incorporated an ample variety of additive materials into the polymer, including glass fibers, long carbon fibers, and metal wires [10–13], although success has been limited [14, 15]. Flexural strength of PMMA resin such as Lucitone-199 (Dentsply Trubyte, New York, PA, USA), which is a high-impact resin with butadiene and styrene additives, has been evaluated by several investigators, showing conflicting values but generally without significant material strengthening [1, 8, 16, 17].

R. Wang (✉)
Department of Comprehensive Care, Case Western Reserve University, School of Dental Medicine, 10900 Euclid Ave. Cleveland, OH 44106-4905, USA
e-mail: rxw26@case.edu

R. Kayacan
Department of Mechanical Engineering, Süleyman Demirel University, Isparta, Turkey

C. Küçükeşmen
Department of Prosthodontics, Süleyman Demirel University School of Dentistry, Isparta, Turkey

M. Zhang et al. (eds.), *Carbon Nanomaterials for Biomedical Applications,*
Springer Series in Biomaterials Science and Engineering 5,
DOI 10.1007/978-3-319-22861-7_7

Carbon nanotubes (CNTs) have shown extremely high mechanical properties with reported strengths 10–100 times higher than the strongest steel at a fraction of the weight [18, 19]. They have light weight. There are two main types of CNTs that can have high structural perfection: single-walled nanotubes (SWCNTs) consisting of a single graphite sheet seamlessly wrapped into a cylindrical tube, and multi-walled carbon nanotubes (MWCNTs) composed of an array of such nanotubes concentrically nested like rings of a tree trunk. In addition to the exceptional mechanical properties associated with CNTs (elastic modulus of 1 TPa. diamond: 1.2 TPa), they also possess superior thermal and electric properties [20, 21].

The incorporation of carbon fibers into a matrix not only confers strength and elasticity to the material but also greatly enhances toughness [22]. Research on nanotube composites has concentrated on polymer–CNT-based materials, wherein they exhibit mechanical properties that are superior to conventional polymer-based composites due to their considerably higher intrinsic strengths and moduli, and the fact that the stress transfer efficiency can be ten times higher than that of traditional additives [23]. It is generally believed that most MWCNTs have a "Russian doll" structure in which each constituent tubule is only bonded to its neighbors by weak van der Waals forces. This immediately raises a problem when one is considering incorporating CNTs into matrices [24].

The second concern is the even dispersion of CNTs into a polymer matrix. Methods of using sonic dismembrators, such as chemical modification, have been proposed by Fiedler et al. [20, 25, 26]. Sui and Wagner [27] observed unusually large deformation in PMMA electrospun fibers under tension when MWCNTs or SWCNTs were included as a second phase in the fibers. The addition of CNTs caused a striking, visible transformation in the deformation mode of PMMA fibers. In pure PMMA fibers, sparse and unstable polymer necking occurs under increasing tension, leading to failure at relatively small strains. However, the presence of either SWCNTs or MWCNTs causes the failure strain to reach comparatively enormous values. According to Marrs, MWCNTs are believed to effectively bridge cracks and reduce the extent of plastic deformation experienced by a PMMA matrix. MWCNTs can successfully reinforce the craze by strengthening the fibrils and bridging the recesses or submicron voids to prevent their coalescence, thus enhancing the fatigue performance of the material.

The effects of CNTs reinforcement on mechanical properties of denture base materials have not been explored. The purpose of this study was to evaluate the effect of CNT reinforcement on mechanical properties of a commonly used PMMA denture base material. The null hypothesis is that the addition of CNTs to a PMMA polymer matrix will improve its mechanical properties.

7.2 Materials and Methods

The specimens were fabricated using the denture base resin, Lucitone-199® original shade (Dentsply International Inc., New York, PA, USA). The MWCNTs, as received from the manufacturer (Designed Nanotubes, LLC., Austin, TX, USA),

were added to the measured acrylic monomer at 0.50, 1, and 2 wt% of total weight in a glass beaker. The liquid monomer was then under ultrasonic mixing for 20 min (Model UP400S, Hielscher Ultrasonics GmbH, Teltow, Germany). Following the manufacturer's instructions, the powder to liquid ratio of 21 g (32 cc)/10 ml and a mixing time of 20 s were used. Liquid monomer with and without MWCNTs was added to the powder and mixed for 20 s to assure wetting of all powder particles. The mixture was covered for 9 min at room temperature and allowed to reach packing consistency. The mixture was packed using conventional denture flasks (Hanau Type, Whip-Mix Corporation, Louisville, KY, USA). Samples were molded as rectangular beams prepared in standard denture flasks, using a template measuring $70 \times 40 \times 3$ mm. The flasks were tightened by spring clamp and samples were cured in a water bath for a period of 9 h at 160 °F, followed by a cooling time of 30 min in water at 60–80 °F. The flasks were bench-cooled for 30 min and submerged in cool water for 15 min before deflasking. The specimens were removed from the flasks and cleaned from stone particles. After deflasking, each mold was prepared to the size of $70 \times 10 \times 3$ mm for a three-point flexural test. The specimens were sequentially polished with SiC papers (600, 800, and 1000 grit) to achieve smooth surfaces.

Mechanical Tests

The flexural strength and flexural modulus were determined by using the three-point bending test as specified by the ISO specification 20795-1:2008. Four groups were prepared at 0.0, 0.5, 1, and 2 wt% of MWCNTs with seven samples per group. The specimens were tested without thermocycles using a universal testing machine (Sintech Renew 1121, Instron Engineering Corp., Canton, MA, USA). Before each test, the specimen thickness and width were measured with a digital micrometer and recorded. A standard three-point bending jig was attached to the machine controlled by a computer. The testing parameters were set at the rate of 0.5 mm/min and load was recorded by a 1000-lb load cell. The same flexural test was performed for another set of four groups of same MWNCT fractions, which underwent 5000 thermocycles from 20 to 80 °C at 1-min intervals using a thermocycle machine (Model Haake EK30, thermo Electron Corporation, Feldkirchen, Germany).

The flexural strength S was calculated using the following formula:

$$S = 3FL / 2bd^2$$

where S is the flexural strength in MPa, F is the failure load, L is the span of specimen between supports (50 mm), b is the width of each specimen, and d is the thickness of each specimen.

Based on the load–displacement (F–Δ) curves of a three-point bending test, mechanical properties were determined. Stiffness was calculated as the slope of the load–displacement curve obtained by linear regression. The yield point was calculated as the intersection of the load–displacement curve with a line having a slope that was 95 % that of the stiffness (Fig. 7.1). The load and displacement at the yield point were taken as the yield load (F_Y) and the yield displacement (Δ_Y). The elastic work was calculated as the area under the load–displacement curve within the elastic range using the trapezoidal rule.

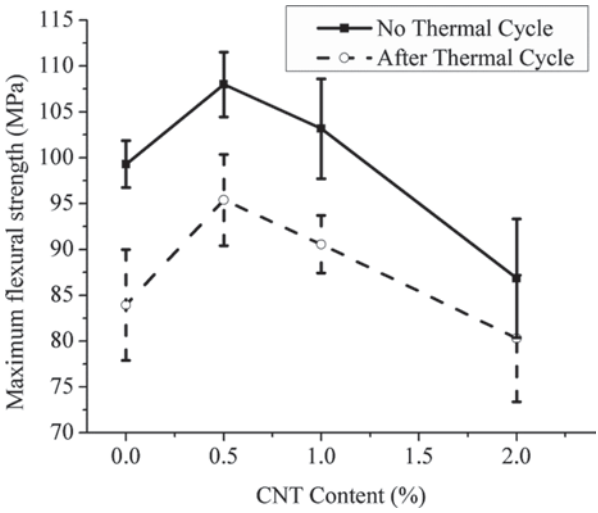

Fig. 7.1 *Maximum flexural strength* versus *CNT content* (0, 0.5, 1.0, 2.0 wt% of MWCNTs). *CNT* carbon nanotubes

The moment of inertia about the bending axis (I) and the thickness (t) of each specimen was used to calculate yield stress, yield strain, resilience, maximum flexural strength, and flexural modulus according to Akkus et al. [28]:

$$\text{Yield stress} = (F_Y L t)/(8I)$$

$$\text{Yield strain} = (12\Delta_Y t)/(2L^2)$$

$$\text{Resilience} = 0.5\ (\text{Yield stress} \times \text{Yield strain})$$

$$\text{Maximum flexural strength} = (F_U L t)/(8I)$$

$$\text{Flexural modulus} = \text{Stiffness}\ L^3/(48I)$$

$$\text{Flexural regidity} = \text{Flexural modulus} \times I$$

where Lt is the span length between the two outer support points and F_U is the ultimate load.

Microhardness Test

The hardness test was performed for each sample in the dry condition. Fractured specimens from the flexural strength test were used for the Knoop hardness test. Each sample was tested six times with a Knoop hardness tester (Lecco® Corp. M-400 St. Joseph, MI, USA) using a 200 g load and 20 s dwell time. Microhardness number for each specimen was based on the average of six repeat measurements from the same sample. The Knoop hardness number (KHN) is the ratio of the load applied to the area of the indentation calculated from the following formula: $\text{KHN} = L/2 \times \lfloor C_p$. In this equation, L is the load applied in kilogram force, $\lfloor$ is the

length of the long diagonal of the indentation in millimeters, and C_p is a constant relating ⌊ to the projected area of the indentation.

Statistical Method
After data collection, mean values of the surface microhardness, maximum flexural strength, resilience, bending modulus, yield stress, and yield strain for each group were analyzed with two-way analysis of variance (ANOVA) to determine the main significant effects of CNT percentage, thermocycle process, and their interactions. Furthermore, the Tukey's honest significant difference (HSD) post hoc (multiple comparisons) analysis was applied to determine the significant effects. All statistical analysis was performed with statistical software (IBM SPSS Statistics 19, Statistical Package for Social Science; SPSS Inc, Chicago, IL, USA).

7.3 Results

Figures 7.1, 7.2, 7.3, 7.4, 7.5 summarize the mechanical behaviors of MWCNT/PMMA composites of maximal flexural strength, resilience, bending modulus, yield stress, and yield strain with and without thermocycling (TC). Tables 7.1, 7.2, 7.3, 7.4, 7.5, 7.6 are the summary of means and overall means of the results of each mechanical property and microhardness evaluated in this study.

Maximum Flexural Strength
When all the tested groups were compared, there was no significant interaction between CNT level and TC process on the PMMA's maximum flexural strength ($P=0.22$). However, the fraction of MWCNT significantly affected the PMMA's maximum flexural strength ($P<0.0001$). When 0.5 wt% of MWCNT was used, a clear significant improvement of maximum flexural strength (101.8 MPa vs.

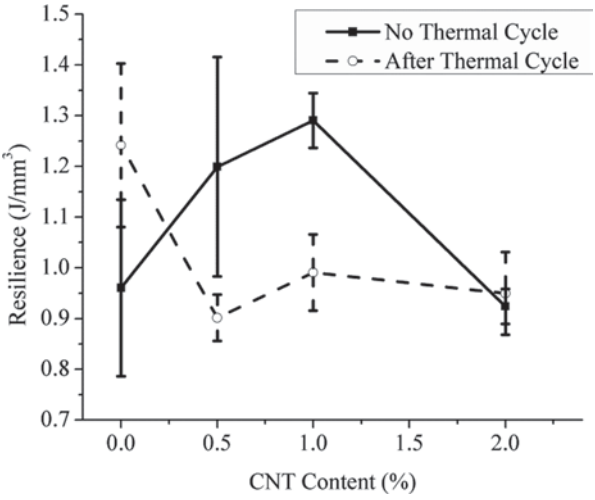

Fig. 7.2 *Resilience* versus *CNT content* (0, 0.5, 1.0, 2.0 wt% MWCNTs). *CNT* carbon nanotubes

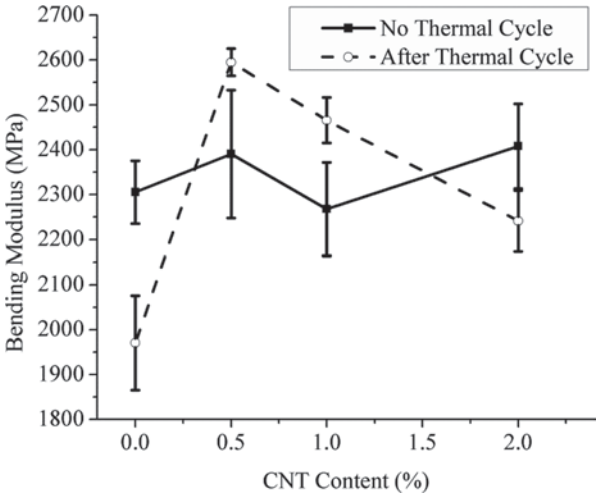

Fig. 7.3 *Bending modulus* versus *CNT content* (0, 0.5, 1.0, 2.0 wt% MWCNTs). *CNT* carbon nanotubes

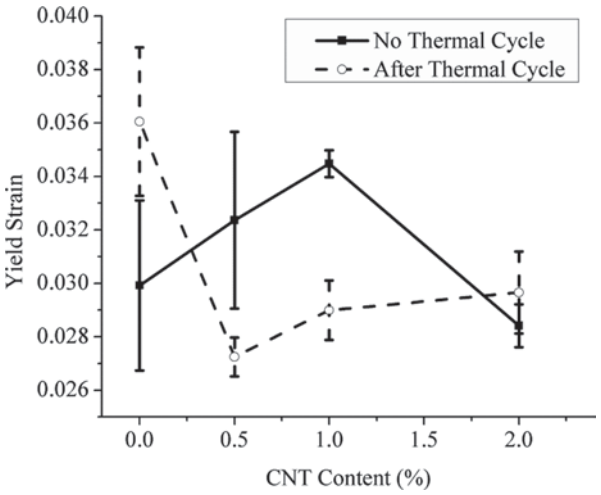

Fig. 7.4 *Yield strain* versus *CNT content* (0, 0.5, 1.0, 2.0 wt% of MWCNTs). *CNT* carbon nanotubes

91.5 MPa, $P<0.0001$) was found in comparison with that of the control group (a 9.3% increase). Contrarily, the increase in the percentage of CNT to 2.0% actually weakened the maximum flexural strength (84.1 MPa vs. 91.5 MPa, $P=0.002$). The TC process also significantly decreased the PMMA's maximum flexural strength ($P<0.0001$). In general, 10–13% of flexural strength was lost among the groups after 5000 thermocycles.

Resilience

There was significant interaction between CNT level and thermocycle process on the PMMA's resilience ($P=4.2e-06$). Without the thermocycle, there was an improvement of resilience when MWCNTs were added to PMMA at 0.5 and 1 wt% level ($P=0.017$). There was a reduction in resilience when CNT levels increased

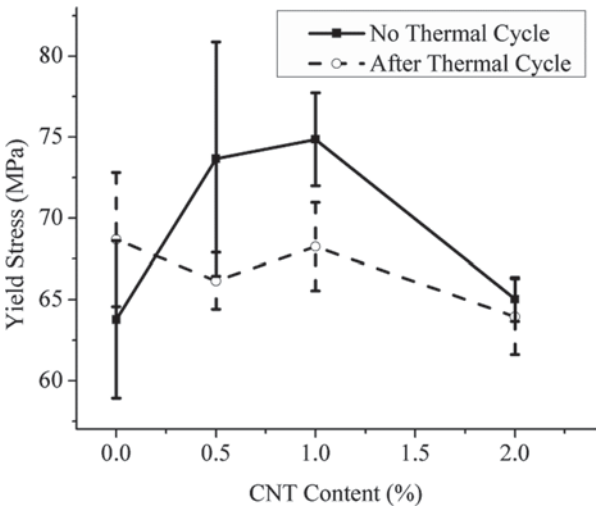

Fig. 7.5 *Yield stress* versus *CNT content* (0, 0.5, 1.0, 2.0 wt% of MWCNTs). *CNT* carbon nanotubes

Table 7.1 Summary of means and overall means of maximum flexural strength (MPa)

Flexural strength	Thermocycle (no)	Thermocycle (yes)	Mean (overall)
MWCNT = 0%	99.29857	83.62571	91.46214
MWCNT = 0.5%	108.18571	95.39	101.787855
MWCNT = 1.0%	103.16857	90.44429	96.80643
MWCNT = 2.0%	87.97143	80.29429	84.13286
Mean (overall)	99.65607	87.4385725	–

MWCNT multi-walled carbon nanotubes

Table 7.2 Summary of means and overall means of resilience ($10^{-3}/mm^2$)

Resilience	Thermocycle (no)	Thermocycle (yes)	Mean (overall)
CNT = 0%	1.003	1.2525714	1.1277857
CNT = 0.5%	1.1548571	0.9012857	1.0280714
CNT = 1.0%	1.2905714	0.9811429	1.13585715
CNT = 2.0%	0.9717143	0.9495714	0.96064285
Mean (overall)	1.1050357	1.02114285	–

CNT carbon nanotubes

Table 7.3 Summary of means and overall means of bending modulus (MPa)

Bending modulus	Thermocycle (no)	Thermocycle (yes)	Mean (overall)
CNT = 0%	2291.714	1950.571	2121.1425
CNT = 0.5%	2379.571	2595	2487.2855
CNT = 1.0%	2267.429	2487.429	2377.429
CNT = 2.0%	2379.286	2241.286	2310.286
Mean (overall)	2329.5	2318.5715	–

CNT carbon nanotubes

Table 7.4 Summary of means and overall means of yield stress (MPa)

Yield stress	Thermocycle (no)	Thermocycle (yes)	Mean (overall)
CNT = 0%	64.98714	68.66429	66.825715
CNT = 0.5%	72.05	66.15	69.1
CNT = 1.0%	74.86571	68.15429	71.51
CNT = 2.0%	66.06143	63.94714	65.004285
Mean (overall)	69.49107	66.72893	–

CNT carbon nanotubes

Table 7.5 Summary of means and overall means of yield strain (mm/mm)

Yield strain	Thermocycle (no)	Thermocycle (yes)	Mean (overall)
CNT = 0%	0.03061429	0.0364	0.033507145
CNT = 0.5%	0.03181429	0.02724286	0.029528575
CNT = 1.0%	0.03447143	0.02877143	0.03162143
CNT = 2.0%	0.02932857	0.02964286	0.029485715
Mean (overall)	0.031557145	0.030514288	–

CNT carbon nanotubes

Table 7.6 Summary of means and overall means of microhardness (kg/mm^2)

Microhardness	Thermocycle (no)	Thermocycle (yes)	Mean (overall)
CNT = 0%	16.56667	16.07381	16.32024
CNT = 0.5%	15.89524	15.27619	15.585715
CNT = 1.0%	15.36667	14.50238	14.934525
CNT = 2.0%	11.35238	11.33333	11.342855
Mean (overall)	14.79524	14.2964275	–

CNT carbon nanotubes

from 1.0 to 2.0% ($P = 0.008$). The thermocycle also significantly reduced the resilience; a further study is needed to improve the dispersion of MWCNTs into the commercial denture base system at 0.5 and 1 wt% groups ($P = 1.5e\text{-}06$).

Bending Modulus

There was significant interaction between CNT level and thermocycle process on the PMMA's bending modulus ($P < 0.0001$). In the absence of TC, there was no overall significant effect of CNT levels on the PMMA's bending modulus ($P = 0.14$). However, with the thermocycle process there is an overall significant effect of CNT levels on the PMMA's bending modulus ($P < 0.0001$). When CNT level of 0.5% was used, a clear significant improvement of bending modulus (2595 MPa vs. 1950.6 MPa, $P < 0.0001$) was found in comparison with the strength of the control samples (0% CNT). Contrarily, the increase in the percentage of CNT to 2.0% actually weakened the bending modulus in comparison with the CNT percentage of 0.5%. On the other hand, at the same CNT levels, the TC process led to an improvement of bending modulus with the existence of CNT (0.5–1.0%), but a weakening of bending modulus in the control samples (0% CNT) and in the sample with the 2.0% CNT level.

Yield Stress

There was significant interaction between CNT level and thermocycle process on the PMMA's yield stress ($P=0.007$). Where without the thermocycle process there was an improvement of yield stress when CNT levels going from 0 to 1.0% (74.9 MPa vs. 64.9 MPa, $P=0.008$), and there was a weakening of yield stress when CNT levels going from 1.0 to 2.0% (74.8 MPa vs. 66.1 MPa, $P=0.021$). With the thermocycle process, there was an overall weakening effect of CNT levels ($P=0.013$) on yield stress. The smallest yield stress (63.9 MPa) was found in the samples with 2.0% CNT.

Yield Strain

There was significant interaction between CNT level and thermocycle process on the PMMA's yield strain ($P<0.0001$). Without the thermocycle process there was an overall significant effect of CNT levels ($P=0.012$) on yield strain, and there was a weakening of yield strain when CNT levels going from 1.0 to 2.0% (0.34 mm/mm vs. 0.29 mm/mm, $P=0.009$). With the thermocycle process, there was an overall weakening effect of CNT levels ($P<0.0001$) on yield strain, the smallest yield strain (0.027 mm/mm) was found in the samples with 0.5% CNT.

Surface Microhardness

There was no significant interaction between CNT level and thermocycle process on the PMMA's surface microhardness ($P=0.42$). Increasing CNT level significantly decreased the PMMA's surface microhardness ($P<0.0001$). The mean surface microhardness of the control samples (0% MWCNT) was found stronger (16.32), whereas the mean surface microhardness of samples with 2.0% CNT was found actually weaker (11.34). The thermocycle process also significantly decreased the PMMA's surface microhardness ($P=0.0086$) (Fig. 7.6).

Figure 7.7 is the micrograph of a fracture surface of a 0.5 wt% MWNCT/PMMA sample. Even dispersion of MWCNTs on the fractured surface is evident. The rods with bright appearance range from 25 to 35 nm in diameter. The figure also shows

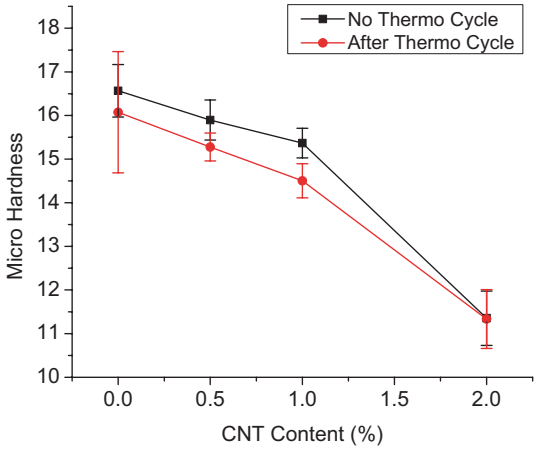

Fig. 7.6 Microhardness (Knoop hardness number) versus CNT content (0, 0.5, 1.0, 2.0 wt% of MWCNTs). *CNT* carbon nanotubes

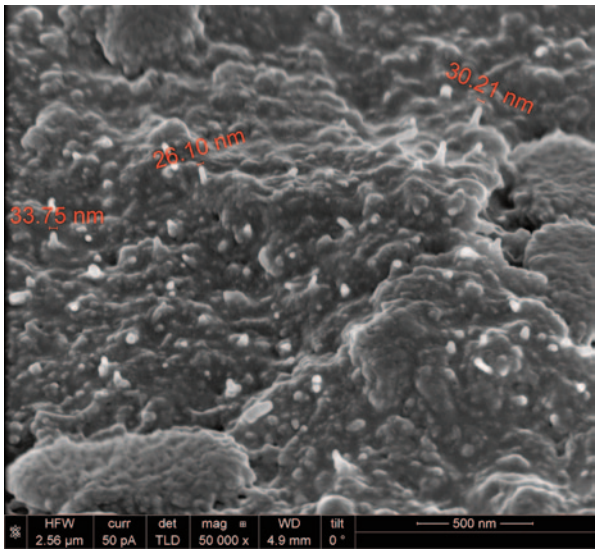

Fig. 7.7 Micrograph (50,000×) of fractured surface of 0.5 % CNT/PMMA. *Bright rods* are CNTs with 25–35 nm diameter

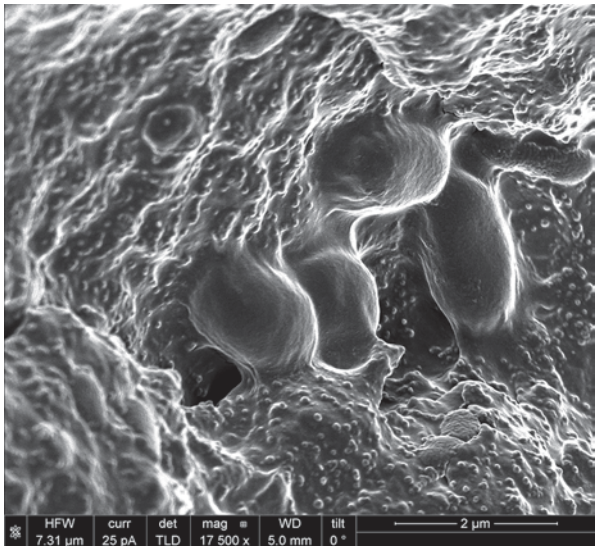

Fig. 7.8 Micrograph (17,500×) of fractured surface of 1 % CNT/PMMA. *Bright dots* are CNTs and *dark voids* are porosities

that the bright and protruded MWCNTs are perpendicular to the surface with clean cleavage fracture, which is indicative of the lack of adhesion of MWCNTs to the PMMA matrix..

Figure 7.8 presents voids at fracture surface. The amount of voids likely was introduced into the samples during powder/liquid mixing and packing the material into a denture flask. The amount of voids might affect the mechanical strength of a sample.

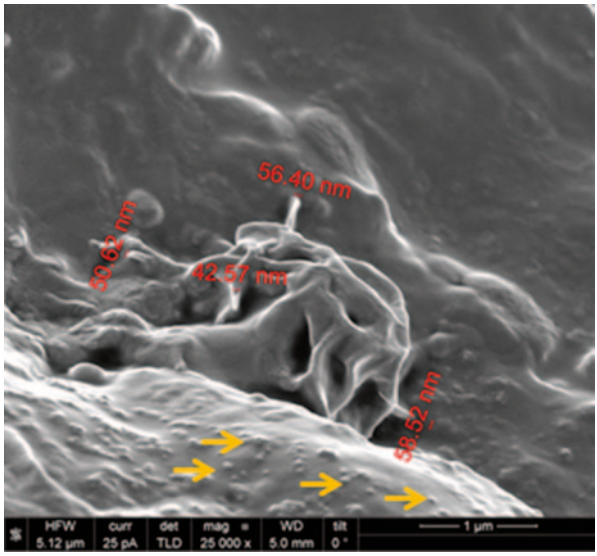

Fig. 7.9 Micrograph (25,000×) of fractured surface of a 2 wt% MWCNT/PMMA sample. Center of the image shows an agglomeration MWCNTs and *arrows* are single fibrils MWCNTs

Figure 7.9 is the representation of fractured surface of a 2 wt% MWCNT/PMMA sample. The center of the figure shows an agglomeration of MWCNTs with polymerized monomer. This characteristic is noticed on the other fractured surface of 2 wt% MWCNT/PMMA samples. The arrows are the small single MWCNTs embedded in PMMA matrix.

7.4 Discussion

The introduction of MWCNT–polymer composites has been advocated to usher in fresh opportunities for engineering new materials with high-performance capabilities. Some researchers believe that the nanoscale dimensions and extraordinary properties of MWCNTs directly address the submicron damage mechanisms (such as crazing) that culminate during the fatigue failure of most polymers. The large traditional glass or graphite fibers commonly used in composite materials do little to address these microscopic mechanisms of cyclic deformation; thus, MWCNTs may potentially offer a new promise for improving the performance of polymer systems, such as PMMA, where the previous successes of traditional fibers were limited. To test this theory, we added small amounts (0–2 wt%) of MWCNTs to Luciton-199, a PMMA denture base polymer, to examine any effect on mechanical properties of MWNCT/PMMA composites. We also tested the effect of thermocycles on those properties of the composite.

We demonstrate that while MWCNT reinforcement improves the mechanical properties of the composite structure mainly by elevating the yield point without affecting the modulus or fracture strength, yield point is the region where the elastic

deformation ends and plastic/damage-related mechanisms initiate. Elevation of this point indicates that MWCNTs would delay the damage initiation and may improve the longevity of the denture base material under impact forces or static loadings.

Without thermocycles, the values of our control groups, such as flexural strength, flexural modulus, and microhardness number of Lucitone-199®, are in the same range of the ones reported in the literature [6, 14, 16]. Our results showed that adding 0.5–1 wt% of MWCNTs to Luciton-199® enhanced the flexural strength (4–11 %), resilience (15–30 %), and bending modulus (27–33 %) performance of PMMA. However, the addition of 2 wt% of MWCNTs to PMMA had no effect or even decreased the performance of PMMA. This unfavorable result for 2 wt% group may attribute to some improper dispersion of MWCNTs into PMMA monomer. For example, more agglomerations were found on the fracture surfaces in 2 wt% group. Agglomerations of MWCNTs could nucleate pores and other nonhomogeneous regions in the resulting nanocomposite. While individual nanotubes and perhaps even clumps of nanotubes can reinforce polymer matrices, clumps of such nanotubes also could have a detrimental role. An elevated number of MWCNT agglomerations likely contributed to the premature failure of the 2 wt% MWCNT specimens.

The mode of thermocycles in this work may differ from other studies; the results show a general trend that TC decreases in mechanical properties of the MWCNT/PMMA composites. The microhardness values have an inverse relationship to the increase of MWCNTs in PMMA. Large standard deviations in some test groups are believed to related to the amount of voids (Fig. 7.9) in the samples resulting from polymer and monomer mixing during denture base packing.

Clean adhesive fracture rather than cohesive fracture exists at the interface of MWCNTs and PMMA matrices on all samples. This indicates that there is no chemical bonding between MWCNTs and PMMA. Future improvement by adding functional groups on MWCNTs may be desirable to enhance chemical bonding between Luciton-199® and MWCNTs.

7.5 Conclusions

The addition of MWCNTs at 0.5 and 1 wt% level to PMMA improves the mechanical properties of Luciton-199®. Furthermore, the effectiveness of MWCNT reinforcement is dependent on the concentration of MWCNTs and the dispersion of the MWCNTs into PMMA matrix. Subsequent efforts need to be focused on dispersing MWCNTs into the commercial denture base system (both liquid and powder phases), and thereby allow testing of the effect of MWCNTs on denture base materials as it is prepared in clinics or dental laboratories. Additionally, surface treating or functionalizing the surface of the MWCNTs could improve dispersion and bonding within the denture base materials, which should lead to material performance enhancements that exceed those presented here. The results of this study show that further efforts to develop a clinically relevant material formulation with appropriate mixing techniques are justified given the benefits of nanotube reinforcement of the

present polymer matrix. Furthermore, the results obtained in this study have broader implications for other applications in dentistry and the medical industry.

References

1. J. Chai, Y. Takahashi, M. Kawaguchi, The flexural strengths of denture base acrylic resins after relining with a visible-light activated material. Int. J. Prosthodont. **91**, 121–124 (1998)
2. D.C. Jagger, A. Harrison, K.D. Jandt, The reinforcement of dentures. J. Oral. Rehabil. **26**, 185–194 (1999)
3. O. Karacaer, T.N. Polat, A. Tezvergil, L.V. Lassila, P.K. Vallittu, The effect of length and concentration of glass fibers on the mechanical properties of an injection- and a compression-molded denture base polymer. J. Prosthet. Dent. **90**, 385–393 (2003)
4. U.R. Darbar, R. Huggett, A. Harrison, Denture fracture—a survey. Br. Dent. J. **176**, 342–345 (1994)
5. A.M. Vuorine, S.R. Dyer, L.V. Lassila, P.K. Vallittu, Effect of rigid rod polymer filler on mechanical properties of poly-methyl methacrylate denture base material. Dent. Mater. **24**, 708–713 (2008)
6. C. Machado, E. Sanchez, S.S. Azer, J.M. Uribe, Comparative study of the transverse strength of three denture base materials. J. Dent. **35**, 930–933.(2007)
7. S.H. Kim, D.C. Watts, The effect of reinforcement with woven E-glass fibers on the impact strength of complete dentures fabricated with high-impact acrylic resin. J. Prosthet. Dent. **91**, 274–280 (2004)
8. D.C. Jagger, R.G. Jagge, S.M. Allen, A. Harrison, An investigation into the transverse and impact strength of 'high strength' denture base resins. J. Oral Rehab. **29**, 263–267 (2002)
9. L.T. Smith, J.M. Powers, D. Ladd, Mechanical properties of new denture resins polymerized by visible light, heat, and microwave energy. Int. J. Prosthodont. **5**, 315–320 (1992)
10. P. Franklin, D.J. Wood, N.L. Bubb, Reinforcement of poly(methyl methacrylate) denture base with glass flake. Dent. Mater. **24**, 365–370 (2005)
11. T. Kanie, K. Fujii, H. Arikawa, K. Inoue, Flexural properties and impact strength of denture base polymer reinforced with woven glass fibers. Dent. Mater. **16**, 150–158 (2000)
12. H.D. Stipho, Effect of glass fiber reinforcement on some mechanical properties of autopolymerizing polymethyl methacrylate. J Prosthet. Dent. **79**, 580–584 (1998)
13. A.J. Bowman, T.R. Manley, The elimination of breakages in upper dentures by reinforcement with carbon fibre. Br. Dent. J. **156**, 87–89 (1984)
14. G. Zappini, A. Kammann, W. Wachter, Comparison of fracture tests of denture base materials. J. Prosthet. Dent. **90**, 578–585 (2003)
15. K.K. Narva, L.V. Lassila, P.K. Vallittu, The static strength and modulus of fiber reinforced denture base polymer. Dent. Mater. **21**, 421–428 (2005)
16. D.L. Dixon, L.C. Breeding, The transverse strengths of three denture base resins reinforced with polyethylene fibers. J. Prosthet. Dent. **67**, 417–419 (1992)
17. Z. Khan, J.A. von Fraunhofer, R. Razavi, The staining characteristics, transverse strength, and microhardness of a visible light-cured denture base material. J. Prosthet. Dent. **57**, 384–386 (1988)
18. E.R. Thostenson, T. Chou, Advances in the science and technology of carbon nanotubesand their composites: a review. Comp. Sci. Technol. **61**, 1899–9112 (2001)
19. M.J. Treacy, T.M. Gibson, Exceptionally high Young's modulus observed for individual carbon nanotubes. Nature **381**, 680–687 (1996)
20. B. Fiedler, F. Gojny, M.H. Wichmann, M.C. Nolte, K. Schulte, Fundamental aspects of nano-reinforced composites. Comp. Sci. Technol. **16**, 3115–3125 (2006)

21. M. Cadek, N.J. Coleman, J. Barron, K. Hedicke, W.J. Blau, Morphological and mechanical properties of carbon-nanotube-reinforced semicrystalline and amorphous polymer composites. Appl. Phys. Lett. **81**, 5123–5128 (2002)
22. P. Harris, *Carbon nanotubes and related structures*, (Cambridge University Press, New York, 2002)
23. S. Iijima, Helical microtubules of graphitic carbon. Nature **354**, 56–58 (1991)
24. R.H. Baughman, A.A. Zakhidov, W.A. de Heer, Carbon nanotubes—the route toward applications. Science **297**, 787–792 (2002)
25. B. Safadi, E.A. Grulke, Multiwalled carbon nanotube polymer composites: synthesis and characterization of thin films. J. Appl. Polym. Sci. **84**, 2260–2269 (2002)
26. B. Marrs, R. Andrews, T. Rantell, D. Pienkowski, Augmentation of acrylic bone cement with multiwall carbon nanotubes. J. Biomed. Mater. Res. A. **77**, 269–276 (2006)
27. X. Sui, H.D. Wagner, Tough nanocomposites: the role of carbon nanotube type. Nano Lett. **9**, 1423–1436 (2009)
28. O. Akkus, F. Adar, M.B. Schaffler, Age-related changes in physicochemical properties of mineral crystals are related to impaired mechanical function of cortical bone. Bone **34**, 443–453 (2004)

Chapter 8
Graphene for Biomedical Applications

Yufei Ma, Jie Huang, He Shen, Mengxin Zhang, Saijie Song and Zhijun Zhang

Graphene is a one-atom-thick sheet of sp^2 carbon atoms with hexagonal lattice. The unique two-dimensional (2D) structure of graphene and its distinctive electrical features owing to numerous free electrons have been attracting increasing interests in the field of electronics [1], sensors [2], energy [3], etc., since its discovery in 2004 [4]. In addition, due to its ultralarge surface area and unique optical properties, graphene and its derivatives triggered massive explorations in environmental [5] and biomedical applications [6, 7]. In this chapter, we survey the emerging applications of graphene and its related derivatives in the field of biology and medicine, including drug delivery, therapeutics, imaging and sensing, as well as cell culture substrates and antibacterial performance.

8.1 Preparation and Modification

Most of the biological incidents occur in physiological conditions which normally require good aqueous stability in terms of graphene's biomedical applications. In order to obtain excellent physiological stability, graphene oxide (GO), a very important derivative of graphene, is usually used. To date, various oxidative protocols for gram-scaled GO preparation from graphite have been developed [8], including Brodie's method (formic HNO_3 and $KClO_3$), Hummer's method ($KMnO_4$ and H_2SO_4), and Marcano's method (H_2SO_4 and H_3PO_4). Although nice control over the quality and reproducibility has always been a challenge, GO samples with various lateral size, oxygen content, functional groups, and thus biocompatibility can be synthesized by tuning the synthetic routes. Among them, a modified Hummer's method is widely used for further biomedical applications of GO, due to its mild reaction condition and relatively facile preparation. A typical synthetic procedure consists of pre-oxidation of graphite with concentrated H_2SO_4, $K_2S_2O_8$, and P_2O_5, subsequent oxidation with H_2SO_4 and $KMnO_4$, followed by mediation with H_2O_2

Z. Zhang (✉) · Y. Ma · J. Huang · H. Shen · M. Zhang · S. Song
CAS Key Laboratory of Nano-Bio Interface, Suzhou Key Laboratory for Nanotheranostics, Division of Nanobiomedicine, Suzhou Institute of Nano-Tech and Nano-Bionics, Chinese Academy of Sciences, Suzhou 215123, China
e-mail: zjzhang2007@sinano.ac.cn

M. Zhang et al. (eds.), *Carbon Nanomaterials for Biomedical Applications,*
Springer Series in Biomaterials Science and Engineering 5,
DOI 10.1007/978-3-319-22861-7_8

and elimination of metal ions with dilute HCl, ultrasonic exfoliation, and final purification through dialysis [9].

The physiological stability of bare GO rarely meets the needs of biomedical study, since it still possesses a large surface area and a strong π–π interaction for self-aggregation. Therefore, GO preparations for biological studies involve further steps, such as surface passivation (such as polymer modification and phospholipids coating) and size reduction (resulting deficient attraction against Brownian motion). For example, functionalization of GO by polyethylene glycol (PEG), polyethylenimine (PEI), dextran, and hyaluronic acid (HA) can significantly improve the biocompatibility of GO; ultrasmall GO (usGO < 10 nm), also named with graphene quantum dots (GQD) due to its inherent fluorescence, displays no obvious in vitro and in vivo toxicity [10]; moreover, a branched polymer (six-armed PEG) coating facilitates the size reduction of GO under ultrasonic condition, resulting in a GO with small size (10–30 nm) [11].

In some cases, GO can be reduced using $NaBH_4$, N_2H_4, or $NH_3 \cdot H_2O$, generating reduced GO (rGO). The reduction greatly decreases oxygen-containing functional groups on GO surface, enabling rGO with enhanced adsorbing ability, increased near-infrared (NIR) absorbance, and improved charge mobility. With no doubt, rGO needs further modification with hydrophilic polymers to be used in biomedical fields, such as drug delivery and photothermal or photodynamic therapies.

8.2 Graphene-based Therapeutics

As unique two-dimensional (2D) nanomaterials, graphene and its derivatives (especially GO) benefit from their large surface area, and thus have been extensively explored as a versatile platform for the deliberate delivery of drugs, proteins, and genes. Moreover, GO displays strong absorption in the NIR region, attracting much attention for its potentials in photothermal and photodynamic therapies, as well as photoacoustic imaging.

8.2.1 GO for Drug Delivery

GO, as a representative member among the family of graphene-based nanomaterials, has abundant functional groups (such as hydroxyl, carboxyl, carbonyl, and epoxy groups) for flexible modification, as well as high specific surface area for excellent loading capacity. Therefore, GO and rGO show potential application in drug delivery as long as their physiological stability is improved through conjugation with hydrophilic molecules.

Dai et al. first reported the use of GO as a drug delivery system in 2008, opening up the application of GO in biomedical field. Their pioneering study demonstrated the feasibility of nanoscale GO (NGO) as a novel nanocarrier for efficient loading and delivery of hydrophobic aromatic anticancer drugs into cells. NGO was first

modified with an amine-terminated six-armed PEG molecule, and then loaded with SN38, a hydrophobic camptothecin (CPT) analogue, via non-covalent π–π stacking interaction. The NGO/SN38 complex showed excellent aqueous solubility and high cytotoxicity for HCT-116 cells. Moreover, the same group anchored rituxan (CD 20^+ antibody) for targeted delivery of doxorubicin (DOX) into cells, and showed a pH-dependent drug release due to π–π stacking interaction between DOX and NGO [11]. Similarly, Zhang group also demonstrated that the release of DOX from GO surface was pH-responded, through tracking the surface-enhanced Raman spectroscopy (SERS) signal of DOX loaded on Ag–GO. As the results suggested, Ag–GO/DOX was taken up by cells through endocytosis and then captured into the lysosomes, followed by DOX detaching from GO and escaping from the lysosomes into the cytoplasm in an acidic environment [12].

To efficiently deliver drug molecules to a specific tumor site and reduce the toxicity to normal cells, Yang et al. grafted adamantane-modified porphyrin on GO via π–π stacking between porphyrin and GO, and then folic acid (FA)-modified β-cyclodextrin (β-CD) through the hydrophobic interaction between CD cavity and adamantane. DOX was loaded on the composites, which could specifically target to the tumor cells and exhibited significant antitumor effect to HeLa cells. Meanwhile, DOX loaded on this nanocarrier showed much lower toxicity to normal cells (cell viability 97%, 24 h) than that of free DOX (cell viability 57%, 24 h), indicating this GO nanocomposites to be promising in the clinical cancer therapy with fine biosafety [13].

Controlled loading and targeted delivery of multiple drugs is widely accepted by clinical practice in cancer therapy, in order to weaken the drug resistance of cancer cells and finally enhance the antitumor effect [14]. In order to achieve an enhanced efficacy, Zhang et al. explored the feasibility of GO as a nanocarrier for delivery of multiple anticancer drugs (Fig. 8.1) [9, 15]. In their study, NGO was functionalized with sulfonic acid groups to improve the physiological stability and with FA molecule to allow targeted delivery of anticancer drugs into human breast cancer cells (MCF-7 cells, with FA receptors). Then two common anticancer drugs, DOX and CPT, were loaded onto this FA-conjugated NGO via π–π interaction. NGO could load DOX as much as fourfold of its own weight, while the loading payload of CPT was only 4.5%. Different loading ability of GO for these two drugs was ascribed to the difference in chemical structures of the two drugs and thus in the interactions between GO and drug molecules. In addition, the loading ratio of GO was linearly correlated to the concentration of DOX, indicating possibility of controlled loading and targeted delivery simultaneously. Compared with single drug loaded onto NGO, co-delivery of DOX and CPT with NGO induced much higher cytotoxicity to cancer cells [9].

8.2.2 GO for Gene Delivery

Gene therapy is a promising approach to treat multifarious diseases caused by gene damage, for example, cancer. Compared to current antitumor therapies, gene ther-

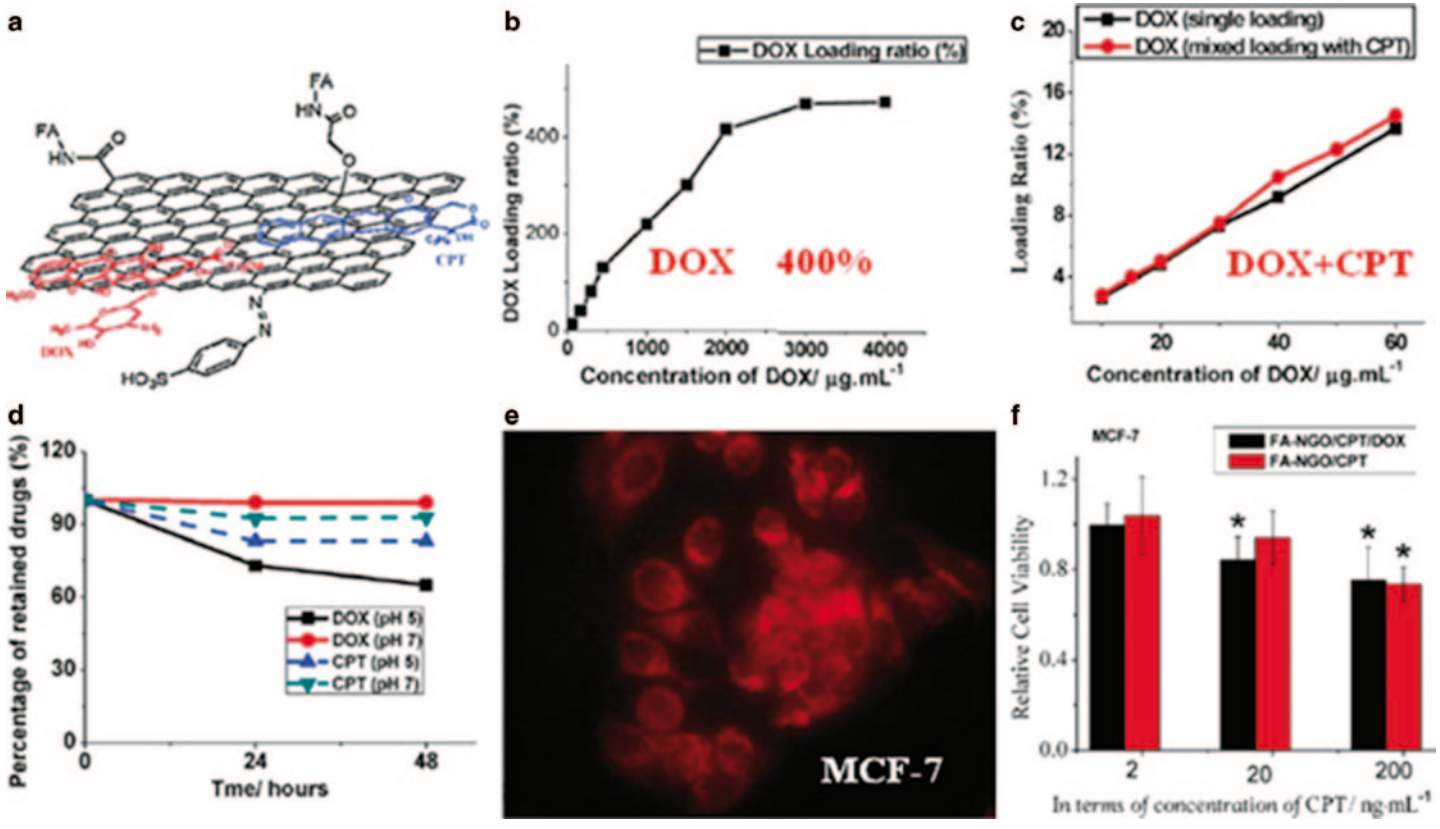

Fig. 8.1 **a** DOX and CPT loaded onto FA–NGO. **b** The loading ratio of DOX to FA–NGO versus the concentration of DOX. **c** The loading ratio of DOX to FA–NGO versus concentration of DOX in a mixture of DOX and CPT (concentration of CPT 100 μgmL^{-1}). **d** The release of DOX and CPT from FA–NGO at pH 5 and 7, respectively. **e** Image of MCF-7 cells incubated with FA–NGO/Rho B for 2 h. **f** Relative cell viability of MCF-7 treated with FA–NGO/CPT and FA–NGO/DOX/CPT. *DOX* doxorubicin, CPT camptothecin, *FA–NGO* folic acid–nanoscale graphene oxide. (Adapted with permission from Ref. [9]. Copyright 2010 Wiley-VCH Verlag GmbH & Co. KGaA, Weinheim)

apy can avoid severe side effects of chemical drugs to normal cells and tissues due to its targeting effect to specific cancer cells [16]. In order to help a piece of DNA to successfully reach specific cancer cells, suitable gene vectors with low toxicity, cell or tissue specificity, and good transfection efficiency are highly demanded [17].

Zhang group and Liu group, respectively, investigated gene delivery by GO modified with PEI to supply positive charges and to allow the condensation of the negatively charged plasmid DNA (pDNA) onto GO surface by electrostatic interaction [18, 19]. Zhang group conjugated GO with PEI via amide bond, and utilized this GO–PEI to deliver pDNA. According to the authors, PEI not only improved GO's physiological stability but also facilitated the condensation of pDNA and GO (ratio of PEI–GO to pDNA > 1:1). As the in vitro study suggested, high DNA transfection efficiency with GO–PEI in HeLa cells was achieved even in the presence of 10% phosphate-buffered saline (PBS), which largely improved the degradation of PEI's transfection efficiency when grafted to other systems [18]. Liu and colleagues further demonstrated that GO could significantly improve the transfection efficiency of PEI with low molecular weight (1.2 K) and decrease the cytotoxicity of large PEI (10 K) [19]. In addition, Kim et al. grafted a low-molecular weight branched PEI (BPEI) onto GO and applied this system to deliver genes into HeLa and PC-3 cells. BPEI–GO exhibited high cell viability and improved gene transfection efficiency, owing to the multivalent effect of BPEI conjugated to GO and the formation of stable polyelectrolyte complexes of BPEI–GO and pDNA [20].

In order to overcome multiple drug resistance (MDR) of cancer cells, Zhang et al. employed PEI-grafted GO nanocarrier for sequential delivery of Bcl-2-targeted small interfering ribonucleic acid (siRNA) and DOX. Because Bcl-2 protein is one of the main antiapoptotic defense proteins, Bcl-2-targeted siRNA was utilized to reduce the Bcl-2 protein expression level in cancer cells and thus to overcome the MDR of cancer cells [21]. The sequential delivery of siRNA and DOX with PEI–GO showed remarkedly enhanced chemotherapy efficacy due to strong synergistic effect of DOX and Bcl-2-targeted siRNA, which significantly inhibited Bcl-2 expression [14]. Similarly, Bao et al. developed positively charged chitosan (CS)-modified GO (CS-GO) for the co-delivery of (pRL-CMV) genes and anticancer drug CPT into HeLa cells [22].

The photothermal property of GO has been integrated to gene delivery, in addition to drug delivery. Feng et al. fabricated NGO with both PEG and PEI (NGO–PEG–PEI) and demonstrated its gene delivery application with excellent physiological stability, superior gene transfection efficiency, and low cytotoxicity [23]. In addition, they found that photothermally induced local heating accelerated intracellular trafficking of nano-vectors, resulting in remarkably enhanced plasmid DNA transfection efficiency under NIR laser irradiation at a low power density.

8.2.3 GO for Protein Delivery

Proteins play important roles in physiological activities of cells and functions of living organisms by regulating the expression of gene and cellular signaling pathways.

Protein-based biotherapy has significant advantages over traditional chemotherapy, such as high specificity to cell functions, and very low side effects and immune responses [24]. However, proteins have difficulties to penetrate the cell membrane, requiring suitable delivery vehicles to facilitate their entry into cells [6].

Shen et al. delivered proteins into cells with PEG–GO [24]. In their study, proteins were loaded onto GO–PEG via non-covalent interaction and then efficiently delivered into cytoplasm with the protection of GO–PEG. More importantly, this work demonstrated that after delivered into cells by GO, the proteins retained their functions to determine cell fate. The ribonuclease A (RNase A) delivered by GO–PEG led to cell death while protein kinase A (PKA)-induced cell growth.

8.2.4 GO for Photothermal Therapy

Photothermal therapy (PTT), as a minimally invasive treatment, employs hyperthermia to kill cancer cells. In this treatment, NIR-absorbing photothermal agents are first delivered to tumor site and then irradiated with an NIR laser. The NIR light can safely penetrate tissues as deep as several millimeters and was converted to heat by PTT agents to generate localized hyperthermia and destroy nearby cells [25].

GO itself is very suitable for PTT because of its strong NIR absorption, excellent photo-stability, and high photothermal conversion efficiency. Liu group [25] demonstrated GO's potential for efficient in vivo PTT without obvious side effects. In this work, GO was modified with amine-terminated six-arm-branched PEG to increase its biocompatibility. They have demonstrated that the branched PEG facilitated the exfoliation of GO sheets while broke the sheets into smaller ones (< 50 nm), and thus enhanced its stability and biocompatibility [11]. The PEGylated GO exhibits highly efficient tumor passive targeting and relatively low retention in reticuloendothelial systems (RES) due to its unique 2D structure, small size, and biocompatible PEG coating. Then, an NIR laser of 808 nm was utilized to irradiate GO (intravenous administration) for in vivo photothermal therapy, leading to ultraefficient tumor ablation, even with low-power NIR laser irradiation suitable for clinical use (Fig. 8.2). Dai group [26] developed nano-sized, reduced GO (nano-rGO) sheets and stabilized this GO with PEGylated lipids though non-covalent adsorption. Interestingly, they found that the nano-rGO shown sixfold higher NIR absorption than the nonreduced, covalently PEGylated nano-GO due to the stronger absorption of rGO in the visible and NIR region. In addition, the tumor treated with nano-rGO still showed 100 % tumor elimination efficacy [27], even under low power density laser irradiation (0.15 W/cm^2, 808 nm, 5 min), which is an order of magnitude lower than that usually applied for many other nanomaterials in vivo tumor ablation. This work also discussed how surface chemistry and size of GO affect the in vivo performance of graphene. As the results showed, GO with smaller size and more PEG coating appears to be a more effective agent for in vivo PTT ablation of cancers.

GO acts as a carrier for drug delivery and can also serve as a platform to combine other therapeutic modalities for improved PTT anticancer efficacy. For example,

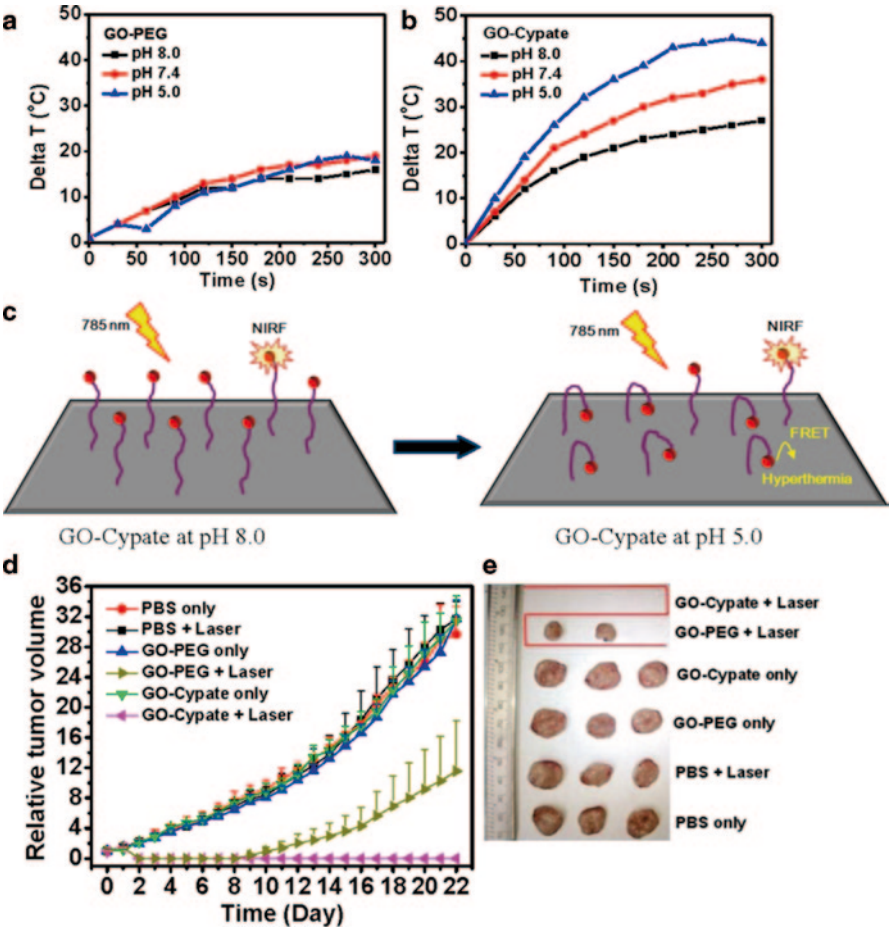

Fig. 8.2 Photothermal effects of GO–PEG (**a**) and GO–Cypate (**b**) in the buffers at various pH within 5 min of photoirradiation, respectively. **c** Conformation illustration of GO–Cypate at different pH and thereof FRET between GO and Cypate. **d** Tumor growth inhibition profiles of the mice bearing 4T1 tumor injected with GO–Cypate and GO–PEG at the same concentration of GO, respectively, followed by 785 nm PTT treatments (5 min, 1.0 W/cm^2) at 24 h post injection. **e** Photos of the tumors extracted from the mice at the end of the PTT therapy (day 22). *GO* graphene oxide, *PEG* polyethylene glycol, *PBS* phosphate-buffered saline, *FRET* fluorescence resonance energy transfer. (Adapted with permission from Ref. [28] Copyright 2014 Wiley-VCH Verlag GmbH & Co. KGaA, Weinheim)

photosensitizers, CuS nanoparticles, and gold nanostructures have been conjugated with GO for the PTT therapy, leading to superior therapeutic efficacy compared to bare GO-induced PTT treatment. Guo et al. [28] covalently conjugated GO with Cypate, an NIR fluorescence imaging agent approved for clinical use by Federal Drug Administration. They demonstrated that GO could increase the dispersibility, half-life in circulation and the targeting ability of Cypate. Upon the irradiation of NIR light at 785 nm (1.5 W/cm^2), a rapid increase of temperature in a GO–Cypate

solution was observed, and GO was also proved to prevent the light-induced decomposition of Cypate (Fig. 8.2). In addition, GO–Cypate at pH 5.0 exhibited much higher temperature increase under photo-irradiation than that at pH 7.4 and 8.0. This phenomenon was attributed to more efficient fluorescence resonance energy transfer (FRET) from Cypate to GO, based on the facts of weakened fluorescence intensity and enhanced PTT ability, because Cypate molecules might form severe aggregation on GO surface in acidic environment. GO was also conjugated with metal nanoparticles to obtain a synergistically improved photothermal effect. El-Shall et al. [29] conjugated laser-reduced GO with Au nanomaterials of different size and shape, and successfully adjusted the photothermal effects by controlling the shape and size of the gold nanomaterials. As the authors illustrated, decrease in size of the gold nanostructures led to a prominent increase in the heating effciency, and composites of ultrasmall gold nanoparticles of 2–4 nm anchoring onto graphene surface generated a highly efficient photothermal effects. Liu group [30] decorated GO with both iron oxide nanoparticles (IONPs) and gold nanoparticles to construct GO–IONP–Au nanocomposites. Compared to PEGylated GO used in their earlier studies, GO–IONP–Au nanocomposites significantly enhanced optical absorbance in the NIR region, and remarkably enhanced photothermal cancer ablation effect in the in vitro and in vivo experiments.

8.2.5 GO for Photodynamic Therapy

Photodynamic therapy (PDT) has emerged as a promising cancer treatment since it can selectively destroy the diseased tissues after the uptake of photo sensitizers (PSs) by cancer cells followed by irradiation [31]. PDT involves the systemic, local, or topical administration of photosensitizers, then light irradiation with appropriate wavelength and dosage, and subsequent production of reactive singlet oxygen ($^1O_2$) species inducing cytotoxic effect [32].

GO offers great promise in PDT applications. In 2011, Cui group first studied the graphene-based carriers on the controlled loading and targeted delivery of chlorine-6 (Ce6), a promising photosensitizer with a high sensitizing efficacy [33]. In this experiment, FA molecules were covalently conjugated with GO for specific targeting to the cells with folate receptors, and Ce6 was loaded onto GO via π–π staking. As the results indicated, GO efficiently transported Ce6 to tumor cells, resulting in significant increase of the Ce6 accumulation in tumor cells, and thus remarkable photodynamic efficacy on MGC803 cells upon irradiation. Chen group [34] demonstrated tumor ablation by PDT modality with novel nanocomposites of GO–PEG–HPPH, in which graphene serves as the carrier and 2-(1-hexyloxyethyl)-2-devinyl pyropheophorbide-alpha (HPPH) as the photosensitizer to treat xenograft tumors with PDT. GO–PEG–HPPH revealed higher tumor uptake than free HPPH after intravenous administration, resulting in significant tumor destruction upon the irradiation of 671 nm laser with low power (75 mW/cm^2). These results demonstrated that graphene can improve PDT efficacy as a carrier of PDT agents and significantly increase long-term survival of tumor-bearing mice following the treatment.

In addition, usGO, or GQD, has been illustrated as a photodynamic agent. Markovic et al. showed that electrochemically produced GQD generated reactive oxygen species, including singlet oxygen when irradiated with blue light (470 nm, 1 W), and then killed U251 human glioma cells by causing oxidative stress [35]. Similarly, Ge et al. reported a new PDT agent based on GQDs derived from hydrothermal treatment of polythiophene [36]. This GQD sample displayed an extremely high quantum yield of ~1.3 for $^1O_2$ generating, via a multistate sensitization process of energy transfer from the excited triplet state (T_1) and the excited singlet state (S_1) to the ground-state oxygen ($^3O_2$). Also, the in vitro and in vivo imaging of GQD was demonstrated in this study.

8.2.6 GO for Multimodal Therapy

While conventional cancer therapy techniques often fail to completely eradicate the tumor, there is a trend of combinational therapy with several therapeutic agents or multimodal therapy leading to synergistic effect. Owing to its high surface area and easy surface functionalization, GO is often used as a multitasking nanocarrier for multiple anticancer drugs and NIR dyes to achieve photothermal–photodunamic, chemo-photodynamic, or chemo-photothermal synergistic therapies.

Tae group [37] integrated PTT and PDT agents into a GO system for advanced in vivo cancer therapy by loading hydrophilic photosensitizer (methylene blue, MB) on NGO. The NGO efficiently localized in cancer cells with photosensitizer and caused complete ablation of tumor under exposure to NIR light, due to the combination of PDT induced by MB and subsequent photothermal therapy from NGO. This PDT–PTT combined therapy utilized smaller GO dose (10 mg/kg) and short irradiation time (3 min) compared to PTT alone (20 mg/kg, 5 min) [25], indicating synergistic effect of dual phototherapy. In another work from Liu group [38], Ce6 was loaded on GO–PEG via π–π stacking (GO–PEG–Ce6) showed a remarkably improved cancer cell photodynamic destruction effect. Interestingly, the photothermal effect of GO can further enhance the PDT effcacy against cancer cells, because NIR light-induced local heating increased the cellular uptake of GO–PEG–Ce6 although GO slightly inhibit the singlet oxygen generation of Ce6. In this way, complete tumor elimination with mild local heating at a low power density (0.3 W/cm^2) of the NIR laser was achieved.

Similarly, the photothermal effect of GO has been demonstrated to improve the chemotherapy of tumor. Wang and colleagues [39] prepared a novel nanostructure NGO–AuNRs with gold nanorods (AuNRs) encapsulated in NGO shells through electrostatic self-assembly between the negatively charged NGO and the positively charged AuNRs. Adipic acid dihydrazide (ADH)-modified HA (HA-ADH) was conjugated onto the surface of NGO–AuNRs to increase the targeting to hepatoma Huh-7 cells. DOX was then loaded on NGO–AuNRs composites by π–π stacking as a model anticancer drug. Compared to bare AuNRs and NGO, the HA-conjugated NGO-enwrapped AuNR nanocomposites (NGOHA–AuNRs) yielded higher photothermal effciency. Due to the superior photothermal promotion of NGOHA–

AuNRs to the release of DOX, NGOHA–AuNRs–DOX performed 1.5-fold and 4-fold higher targeted cell death rates than single chemotherapy and photothermal therapy, respectively.

The Kim group combined gene therapy and photothermal therapy together with the help of GO [40]. They developed nano-sized, PEG–BPEI–rGO nanocomposite as a potential PTT agent, which combined rGO sheets with BPEI and PEG through covalent conjugation. The transfection efficiency of PEG–BPEI–rGO with laser irradiation was increased approximately two- to threefold than the transfection without irradiation. As the authors demonstrated, endosomal membrane was ruptured due to the local increase in temperature caused by NIR irradiation, and then the PEG–BPEI–rGO complex escaped from endosomal, which induced high gene transfection.

Zhang et al. explored GO as an adjuvant for immune therapy [41], by using a usGO–Au composite through in situ growth of gold nanoparticles on usGO sheets. Excellent adsorbing capacity of GO could improve the binding capacity of usGO-supported AuNPs to ovalbumin (OVA) proteins. In vivo study revealed that usGO–Au@OVA could promote robust OVA-specific antibody response, $CD4^+$ and $CD8^+$ T cells proliferation, and the secretion of tumor necrosis factor (TNF)-α and interferon (IFN)-γ.

8.3 Bioimagimg

Over the past several years, graphene and its derivatives, especially GO, have displayed appealing prospects in bioimaging field. Owing to their versatile surface modification, graphene and GO have been explored with various molecular imaging techniques, including magnetic resonance imaging (MRI), positron emission tomography (PET) imaging, photoacoustic, and fluorescence imaging. Besides, due to their high drug-loading capability and photothermal effects, integration of diagnostics and therapies into one graphene platform, namely theranostics, has recently drawn increasing attention in the treatment of diseases.

The imaging ability of GO is mostly achieved by conjugation to one or multiple imaging components. Therefore, a linkage molecule with additional chemical reaction sites is required for further functional modifications, and the linkers are normally among macromolecules, such as PEG [42], and poly(amido amine) (PAMAM) [43]. Moreover, these macromolecules can also enhance the biocompatibility and stability of GO in physiological solutions. Figure 8.3 shows the common structure of GO composites for imaging or/and therapy.

8.3.1 Optical Imaging

The technique of fluorescence imaging has been widely studied in tracking and monitoring live cells with graphene and its derivatives, through decorating GO or

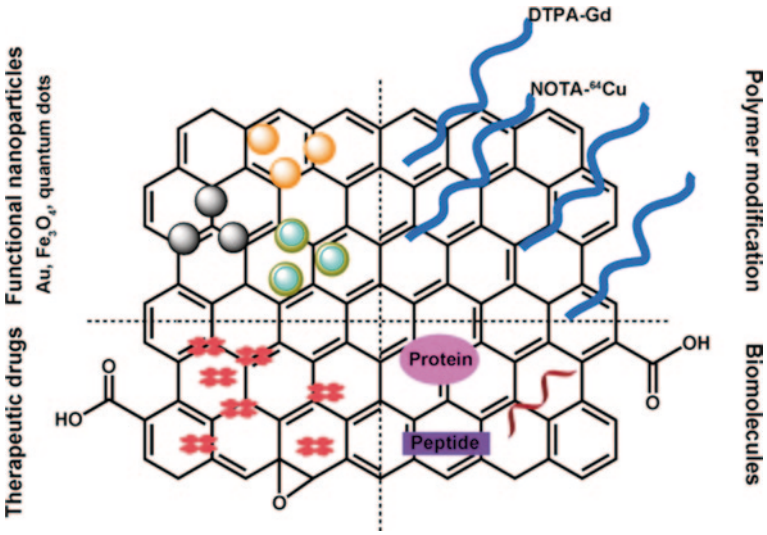

Fig. 8.3 Surface modification of graphene and graphene oxide for bioimaging and therapy. Different functional moieties (*polymers, nanoparticles, anticancer drugs, biomolecules*) could be anchored for specific purposes. *NOTA* 1,4,7-triazcyclonoane-1,4,7-triacetic acid, *DTPA* diethylene triamine pentaacetic acid

rGO with highly fluorescent inorganic fluorophores or organic dyes [43, 44]. To avoid the fluorescence quenching by GO, it is necessary to shield GO from fluorescent component with long molecular linkers, such as PEG [45], BSA [46], or an SiO_2 shell [47]. In addition, passivating the surface reactive sites of GO by using alkylamines [48] or branched PEI [20] has also been attempted.

Peng et al. linked fluorescein with PEGylated GO and used this fluorescent GO as an intracellular fluorescence imaging probe [45]. Fluorescein-modified GO exhibited excellent green fluorescence when incubated with HeLa cells for 6 h, while GO as the control group showed no fluorescence. Similarly, Hu et al. decorated quantum dots (CdSe/ZnS) with polypeptide-modified rGO through physical adsorption. The surface of quantum dots was covered with tri-*n*-octylphosphine oxdie (TOPO) and 11-mercaptoundecanoic acid (MUA), which served as a spacer to prevent fluorescence quenching. In this preliminary experiment, significant fluorescence can be monitored when two kinds of QDs–rGO with different color were subcutaneously injected into nude mice. Moreover, owing to the strong NIR absorbance of rGO, a QDs–rGO system can kill cancer cells through photothermal effect at the same time [49]. According to the authors, the fluorescence of QDs provided indicative information for the heat dosage and the treatment process, leading to subsequent cancer ablation with minimized damages to healthy organs and tissues. In addition, precise monitoring of the tumor change can be obtained during photothermal therapy.

Wang et al. covalently grafted upconversion nanoparticles ($Tm^{3+}/Er^{3+}/Yb^{3+}$ co-doped $NaYF_4$) onto PEGylated GO and then loaded a photosensitizer (phthalocyanine) to build a multifunctional theranostic platform for in vivo imaging and combination of PDT/PTT [50]. In this study, strong upconversion luminescence imaging

of a white Kunming mouse was monitored and further applied to demonstrate the enhanced efficacy of combinational therapy of PDT/PTT compared to PDT or PTT alone. The synergistic effect probably was ascribed to the photothermal property of GO, which not only heated the cancer cells but also enhanced the delivery of PDT agents to the cancer cells.

As a representative fluorescence probe in the family of graphene, GQD are small graphene fragments with size range below 10 nm. Owing to its good biocompatibility and excellent optical properties, GQD has been explored widely for bioimaging applications based on its size-related fluorescence [51]. Zhang et al. employed a yellow-light-emitted GQD to simultaneously monitor three kinds of stem cells, neurospheres cells (NSCs), pancreas progenitor cells (PPCs), and cardiac progenitor cells (CPCs). According to their study, GQD mainly retained in cytoplasmic area and did not affect the viability, proliferation, or differentiation of the stem cells [52]. Nurunnabi et al. prepared a series of GQD samples with different colors by regulating the reaction temperature during oxidative cutting of carbon fibers. These GQDs possessed varied emission ranging from 460 to 805 nm in wavelength, due to various oxygen contents defining the band gaps. In addition, GQDs were intravenously injected into nude mice to illustrate their attractiveness as new noninvasive imaging agents [53].

8.3.2 MR Imaging

MRI is a powerful noninvasive imaging technique in clinical diagnosis. Among various MRI contrast agents which provide more precise information in pathological tissues, superparamagnetic Fe_3O_4 nanoparticles are most commonly used in T_2-weighted MRI. Chen et al. conjugated Fe_3O_4 nanoparticles onto GO and demonstrated that the Fe_3O_4–GO composites significantly improved T_2 relaxivity and thus enhanced the cellular MRI effect, owing to the formation of aggregates of the Fe_3O_4 nanoparticles on the GO sheets. In another study, Yang et al. in situ synthesized Fe_3O_4–rGO nanocomposites through hydrothermal reaction and expanded the application of GO/Fe_3O_4 nanocomposites not only for imaging but also for cancer therapy. Due to the strong NIR optical absorbance and T_2 MRI of the nanocomposites, rGO–IONP–PEG exhibited remarkable photoacoustic imaging and MRI effect and photothermal therapy efficacy [54].

To obtain T_1-enhanced MRI signal, Zhang et al. conjugated Gd–diethylene triamine pentaacetic acid (DTPA) to PEGylated GO and demonstrated the significant improvement of T_1 MRI relaxivity for GO–DTPA–Gd and cellular MRI with effective internalization of the composites into cells [55]. In a recent report, Yang et al. prepared Gd–DTPA grafted NGO (Gd–NGO) and then loaded with Let-7 g miRNA and anticancer drug epirubicin (EPI). This system (Gd–NGO) showed combined chemo- and gene therapy effect to malignant glioblastoma cells. Moreover, Gd–NGO was utilized to monitor the location and extent of blood–brain barrier (BBB) opening, which was induced by focused ultrasound (FUS) in the presence of circulating microbubbles. The in vivo experiment demonstrated that more intensive signals in the region of interest can be detected by using Gd–NGO [56].

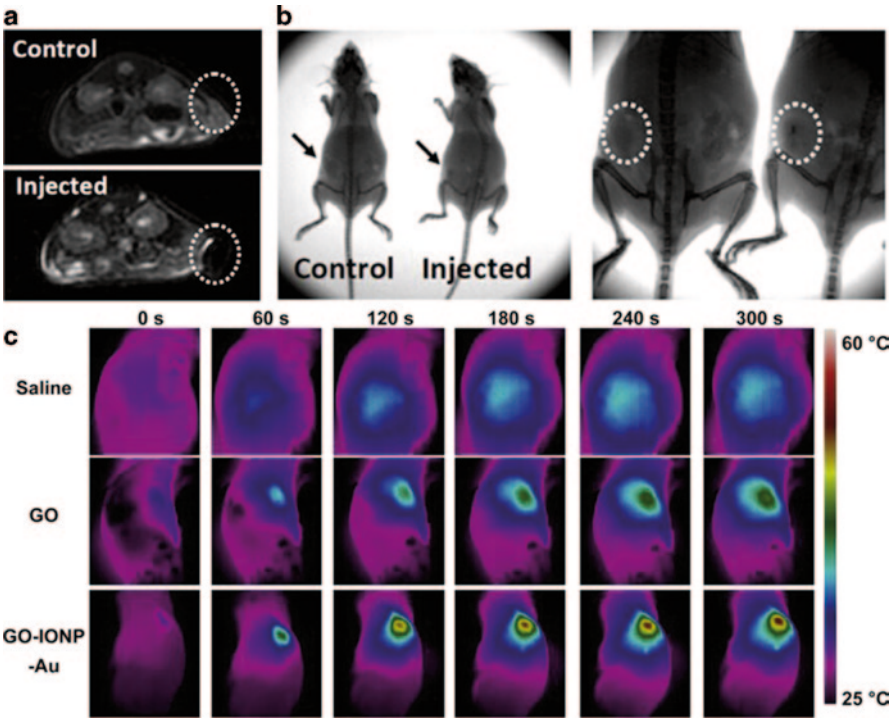

Fig. 8.4 In vivo dual-modal MRI/X-ray imaging and PTT. **a** T_2-weighted MR images of 4T1 tumor-bearing mice before (*top*) and after (*bottom*) intratumoral injection of GO–IONP–Au. **b** X-ray images of tumor-bearing mice before (*left*) and after (*right*) intratumoral injection of GO–IONP–Au. Tumors are highlighted by *black arrows* or *white circles*. **c** IR thermal images of tumor-bearing mice injected with *saline*, GO or GO–IONP–Au under laser irradiation (808 nm, 0.75 W/cm^2). *GO–IONP* graphene oxide–iron oxide nanoparticle. (Adapted with permission from Ref. [30]. Copyright 2013 Elsevier B.V.)

Since each molecular imaging tool has its own merits and limitations, the integration of multiple techniques into a single platform can provide distinct and synergistic advantages. Particularly, GO is a suitable candidate for such a platform due to its unique physicochemical properties, such as large surface area and versatile functionalization. Shi et al. decorated GO with iron oxide and gold nanoparticles and demonstrated synergistic imaging through in vivo experiment (Fig. 8.4). In addition to enhanced photothermal cancer ablation, this system was used for enhanced MRI and X-ray dual-modal imaging by taking the advantage of iron oxide and gold nanoparticles [30].

8.3.3 Photoacoustic Imaging

As a newly emerged imaging technique, photoacoustic imaging has attracted ever increasing interest in recent years because it offers significant increase in imaging

depth in diagnosis. Sheng et al. developed a simple method to fabricate rGO by using bovine serum albumin (BSA) as a reductant and a stabilizer. Due to the strong NIR absorbance of BSA-functionalized nano-rGO, it was used for in vivo photoacoustic imaging as well as photothermal therapy, which are both triggered by the transformation between light and heat [57].

8.3.4 PET Imaging

Initially developed in the mid-1970s, PET imaging is another noninvasive imaging technique that provides a three-dimensional (3D) image in the body. It is capable of quantitatively measuring the radioisotope concentrations in vivo with excellent tissue penetration [58]. Shi et al. designed a PET imaging agent based on rGO conjugated with 1,4,7-triazcyclonoane-1,4,7-triacetic acid (NOTA), which was used as an effective chelator to ^{64}Cu for radiolabeled PET imaging. Particularly, TRC105, a human/murine chimeric immunoglobulin G (IgG)1 monoclonal antibody, was conjugated to rGO as a tumor vasculature-targeting ligand to CD105, which serves as an ideal vascular target expressed on proliferating tumor endothelial cells. Tumor vasculature targeting is important since it is more instantly accessible upon intravenous injection. Moreover, new blood vessel formation is a critical process in tumor growth and metastasis. Through the noninvasive PET imaging technique, the specific targeting of ^{64}Cu–NOTA–rGO–TRC105 to CD105 in 4T1 murine breast tumors model was demonstrated, suggesting rGO conjugates as promising candidates for in vivo tumor vasculature targeting [59].

8.3.5 Raman Imaging

Raman spectroscopy is another powerful technique for biological imaging, as it provides a high signal-to-noise ratio and can distinguish different fingerprints of the Raman probes in a nondestructive way. It is well known that metal nanoparticles, especially Au and Ag nanoparticles, can significantly improve the Raman signal of probe molecules [60–62], that is, surface-enhanced Raman scattering (SERS) effect. Based on the distinctive Raman spectra of GO, researchers have decorated Au or Ag nanoparticles onto GO for detection or cellular imaging by using this SERS technique. Au/GO hybrids was employed as a Raman probe to investigate the internalization mechanism of GO, which was found to be a clathrin-mediated, energy-dependent endocytosis [15].

In another study, Wang et al. built a nanocomposite by anchoring gold nanoclusters (GNCs) on rGO, and further utilized it as a Raman spectroscopy probe to investigate the interactions between the GNC–rGO nanocomposites and proteins and DNA. Their study suggested that the presence of GNC–rGO induced DNA chain disorder and affected the protein α helices without disturbing β folding [63].

8.4 Graphene for Biological Sensors

8.4.1 Graphene-based Electrochemical Sensors

Graphene has been extensively studied to fabricate electrodes for electrochemical sensors, due to its excellent absorbing ability, efficient charge transfer, large electrochemical potential window, and tunable chemical and electrical properties. In order to gain facile fabrication, rGO, rather than pristine graphene or GO, was generally applied due to its abundant functional groups and high electrochemical activity [2].

Interestingly, benefited from its high potential (~2.5 V), rGO shows significant catalytic activity toward some small enzymatic products such as H_2O_2 and nicotinamide adenine dinucleotide (NADH). In addition, the large surface area of GO facilitates target loading, making it attractive for enzyme-based sensors. For example, hemoglobin embedded in an rGO-CS film can facilitate a H_2O_2 sensor with a limit of detection (LOD) of 0.51 uM [64]. Furthermore, with the help of horseradish peroxidase (HRP) to hydrolyze H_2O_2, and sodium dodecyl benzene sulfonate to improve the enzyme loading because of intercalation, a lower LOD of 0.1 uM was achieved by Zeng and coworkers [65].

Glucose oxidase (GOD) can specifically recognize glucose which is a significant element for the diagnosis of diabetes, so it can be incorporated into graphene-based electrodes for the electrochemical detection of glucose. Kang et al. showed a GOD–rGO–CS electrode with high sensitivity (0.02 mM of LOD) [66]; while Alwarappan et al. constructed a conducting porous matrix with GOD, rGO, and polypyrrole (ppy), and improved the LOD to 3 uM [67]. In addition, decoration of in situ-grown metal nanoparticles on rGO can further lower the LOD to 0.6 uM [68], of which the high performance was attributed to the facts that the highly conductive nature of the metal nanoparticles facilitates rapid charge transfer on rGO sheets.

Thanks to the strong π–π stacking and electrostatic attraction between GO and nucleobases, development of DNA sensors based on rGO are also realized. Huang et al. applied GO with abundant carboxylic groups for highly sensitive detection of guanine (50 nM) and adenine (25 nM) [69]. Du et al. decorated an rGO electrode with AuNPs through potentiostatic electrodeposition for the detection of single-stranded DNA (ssDNA) [70]. Furthermore, they demonstrated that the oxidation signal of thymine can be distinguished from that of adenine, making the detection of single-base mutation possible without any labeling or probe DNA. In a work of Lim et al., double-stranded DNA (dsDNA) could be differentiated from ssDNA with a graphene-based SiC electrode, which is impossible for conventional electrodes because of their limited electrochmemical potential window [71]. In addition, GO-modified electrode was introduced to detect DNA hybridization, through the guanine oxidation signal from the target ssDNA molecules without guanine base [72].

Graphene-based electrochemical sensors have been used to detect various protein markers, when an antibody was applied. Su et al. used the interaction between alpha fetoprotein (AFP) and anti-AFP antibody to partially block HRP reducing H_2O_2, with an LOD of 0.7 ng/mL [73]. The authors applied HRP and electropolymerized

thionine (TH) films, which was constructed with GO-CS through layer-by-layer assembly, to mediate the electron transfer from H_2O_2 to the electrode. On the other hand, Wei et al. directly embedded TH in rGO film through π–π stacking and then covalently cross-linked AFP antibody with TH. With intimate interaction of rGO and TH for efficient electron transfer, as well as high loading of TH and AFP antibody molecules on the rGO film, they achieved a much lower LOD of 5.77 pg/mL, and successfully applied this sensor to AFP detection in serum [74].

A highly sensitive and selective dopamine sensor (0.01 uM) was demonstrated by Hou et al. [75]. In this report, ethylenediamine triacetic acid (EDTA)-modified graphene (EDTA-GO) was chosen to fabricate a glass carbon electrode for several reasons. (1) EDTA-GO greatly enhanced the electrochemical activity in physiological solutions and effectively increased the surface area on electrode, (2) EDTA groups could concentrate DA from the solution, (3) EDTA groups linked to GO surface promoted the electron transfer, and (4) carboxylic groups of EDTA could block the diffusion of ascorbic acid and thus avoid its interference. Furthermore, Tan et al. [76] illustrated that β-cyclodextrin could greatly enhance the electron transfer for the rGO electrode, obtaining a lower LOD of 5 nM for the detection of dopamine.

8.4.2 Graphene-based Electronic Sensors

Graphene-based electronic sensors, normally considered as field effect transistors (FETs), are expected to display a high signal-to-noise ratio for several reasons. First, graphene and GO show high carrier mobility and carrier density, as well as low intrinsic noises; second, graphene's planar structure enables its extreme exposure to the environmental variation and thus highly sensitive conductance of graphene; and third, the gate voltage of graphene can be manipulated with various doping for different charge transfer. In addition, graphene provides a large detection area for cell detection and allows simultaneous optical observation during electrical measurement. Therefore, graphene and its derivatives have been applied to various electronic sensors, providing vast new possibilities.

A graphene-based electronic sensor for the detection of glucose and glutamate was illustrated by Chen et al., with an LOD of 0.1 mM and 5 μM [77]. The detection through increased conductance of graphene film was mediated by H_2O_2 (p-dopant), which was generated by specific enzymes, GOD, and glutamate dehydrogenase, respectively. Similarly, proteins bearing charges or dipoles can bind onto the surface of graphene via π–π interaction, and thus can be detected through the doping effect. Ohno et al. developed a pristine graphene device for the detection of BSA with an LOD of 0.3 nM, based on the nonspecific adsorption of graphene to BSA molecules, which is negatively charged under physiological condition [78]. However, the adsorption lacks recognition to targets, missing specificity in detection.

In order to offer an electronic immunoglobulin E (IgE) sensor with specificity, Ohno et al. modified the graphene surface of the sensor with IgE-specific aptamers, observing dramatic decrease in the conductance of p-type graphene due to field

effect when positively charged substances interacted with graphene [79]. In another work, Mao et al. assembled AuNPs and anti-IgG antibody on an rGO film, and they employed a blocking buffer to minimize nonspecific binding, obtaining an LOD of 13 pM. Similarly, BSA was used to improve the specificity of a graphene immunosensor for the detection of prostate-specific antigen (PSA) using rGO sheets, leading to an immunoglobulin G electronic sensor with wide detection range (0.1–100 ng/mL) [80].

Mohanty et al. reported a DNA sensor made of GO sheets, which was modified with probe ssDNA via simple π–π stacking. When hybridization of the target DNA occurred, the conductance of GO sheets increased owing to p-doping effect, as the author determined. Since the measurement of conductance was performed under dry condition, field effect did not fit the situation because DNA molecules contained no charges [81]. On the contrast, Dong et al. developed an electronic DNA sensor with chemical vapor deposited (CVD)-grown graphene and suggested that the detection of hybridization of DAN in solution was based on n-doping effect [82]. In addition, this sensor could detect single-base mismatch of the target ssDNA with an LOD of 10 fM.

Cells can intimately interact with graphene film, without damage to the local curvature. Therefore, graphene-based electronic sensors have been applied to the detection of cells due to the tight and homogeneous interaction between cells and graphene, as well as sensitive electronic properties of graphene. Cohen-Karni et al. demonstrated a graphene FET for the detection of cardiomyocyte cell bioactivity (Fig. 8.5) [83]. It was the field effect that triggered the device response, because electrical potential changed at the nano-interface between the cell and the FET due to the ionic current flows through the membrane ion channels. Compared to conventional metallic microelectrodes and a silicon nanowire FET, the graphene FET showed comparable sensitivity and signal-to-noise ratio. He et al. fabricated a centimeter-long and a micrometer-wide ultrathin rGO film through microfluidic patterning and coupled the rGO film with neuroendocrine PC-12 cells (Fig. 8.5) [84]. This rGO FET could detect rapid vesicular secretion of hormone catecholamine of PC-12 cells due to membrane depolarization, because catecholamine molecules released from the cells interacted with rGO sheets through p–p interaction, and increased p-type rGO conductance via p-doping. In addition, the authors claimed that microfluidic patterning technique enabled flexible sensors for curved targets, for example, organs. In addition, Kempaiah et al. [85] coupled rGO coating on a yeast cell, and monitored in real time the dynamic mechanical response of a yeast cell to osmotic stresses or heat shock based on the change in the electrical conductance of the rGO layer.

8.4.3 Optical Sensors

Graphene and its derivatives possess strong absorption over a wide range from ultraviolet to IR region, showing highly efficient quenching effect to fluorescence. In

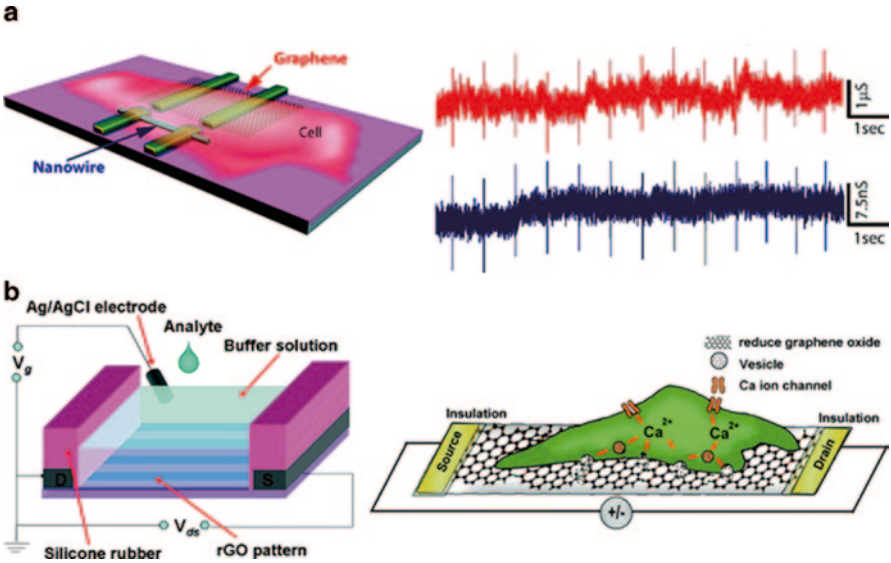

Fig. 8.5 **a** Graphene and nanowire transistors for cellular interfaces and electrical recording chip, from which the signals from cardiomyocytes was recorded at different applied water gate potentials. (Adapted with permission from Ref. [83]. Copyright 2010 American Chemical Society). **b** The interface between a PC-12 cell and rGO FET. *rGO* reduced grphene oxide. (Adapted with permission from Ref. [84]. Copyright 2010 American Chemical Society)

addition, the defects, mostly oxygen-containing functional groups, on graphene and GO surface restrict free π electrons, and thus create a wide range of local energy gaps due to various sizes of sp^2 domain. Therefore, GO was extensively explored as optical sensors based on FRET. Generally, a GO-based FRET sensor contains three components, including GO flakes as quencher, a reporter as fluorescence donor, and a recognition probe linked to the reporter. The detection of target molecules relies on that the probe molecules associate with the targets and then induces turn-on fluorescence due to the release of fluorescent reporter from the GO surface.

Graphene can selectively adsorb ssDNA over dsDNA, due to strong π–π interaction between nucleosides and graphene. Taking advantage of protection of ssDNA from enzymatic cleavage by GO, Tang et al. designed a DNA optical sensor based on a ssDNA and DNAse I, obtaining an LOD of nanometer range [86]. Furthermore, the authors showed that ssDNA was intact to DNAase when adsrobed on the GO surface. This design strategy of selectively interacting with ssDNA has also been applied to build other DNA sensors [87, 88]. In addition, Huang et al. developed a graphene-based DNA sensor for simultaneous detection of multiple ssDNAs, through distinctly colored probes linked with different DNA targets. As the study revealed, the interference between different targets was negligible, and the detection limit reached as low as 100 pM [89].

Using highly specific binding of aptamers, protein sensors have also been developed based on similar designs. Lu et al. demonstrated graphene-derived sensors

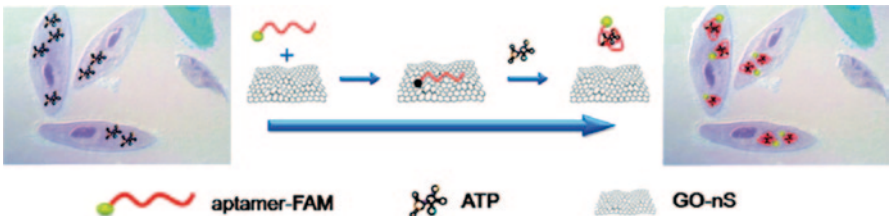

Fig. 8.6 Illustration of in situ molecular probing in living cells by using an aptamer-carboxyfluorescein (FAM)/graphene oxide nanosheet (GO-nS) nanocomplex. *ATP* adenosine triphosphate. (Adapted with permission from Ref. [93]. Copyright 2010 American Chemical Society)

with nanometer detection of proteins, including human serum albumin (HSA), BSA, human IgG, and bovine thrombin [90]. Chang et al. reported a graphene FRET aptasensor for thrombin with a detection limit of 31.3 pM [91]. Wang et al. developed an ultrasensitive (LOD of 0.5 nM) and selective assay for the detection of cyclin A_2, a prognostic indicator in early-stage cancer, using fluorescent-labeled $p^{21(WAF-1)}$ derived from cyclin A_2 binding sequence [92]. Furthermore, similar construction of an aptamer/GO sensor has been demonstrated for in situ adenosine triphosphate (ATP) probing in living cells, with the capability of cellular delivery of DNA (Fig. 8.6) [93].

8.5 Biological Applications of Graphene-based Substrates

8.5.1 Scaffolds for Cell Culture and Differentiation

Graphene-based substrates have been developed for potential applications in tissue engineering. Min's group first utilized GO film as a scaffold for mammalian cell culture [94]. NIH-3T3 mouse fibroblasts seeded on GO film did not display obvious change of cell shape, inhibition of cell adhesion and growth, and abnormal expression of cytoskeletal genes. This work indicated that mammalian cells could attach and proliferate on GO substrate with high gene transfection efficiency, and thereby providing a new insight into development of graphene-based materials for implantable applications.

Based on the above study, graphene-based materials were further explored as promising substrates for multipotent progenitor cells culture and tissue engineering due to the unique physicochemical properties of graphene. Recently, researchers developed graphene-based substrates for mesenchymal stem cells (MSC) [95], neural stem cells (NCS; enhanced differentiation of human neural stem cells into neurons on graphene), and induced pluripotent stem cells (iPSCs) [96] growth and controllable differentiation. By tuning the superficial oxygen content, the mechanics and topography of graphene-based scaffolds and the differentiation of these multipotent progenitor cells could be regulated.

Several groups have explored graphene-based scaffolds for musculoskeletal tissue engineering, as graphene-based substrates could direct MSC differentiation into osteoblast and myoblast. For example, graphene-based materials can pre-concentrate growth agents (serum) and differential inducers (such as β-glycerolphosphate and dexamethasone) through π–π stacking interactions between aromatic rings of these molecules and graphene platform [97]. Graphene and GO substrates could act as pre-concentration platforms for enriching agents in culture medium, and therefore efficiently enhanced MSC attachment, growth, and osteogenic differentiation. MSCs possess the capacity to osteogenic differentiation under favorable mechanical stimuli from the surrounding microenvironments [98, 99]. Nayak et al. [100] also reported promotion of osteogenic differentiation of MSCs induced by graphene substrate. However, they found that this phenomenon was not only because of the collection of another osteogenic inducers (bone morphogenetic protein) but also the stiffness and strain properties of graphene films. They found that differentiation level of MSCs grown on graphene substrates (on Si/SiO_2) were much higher than that of MSCs grown on graphene substrates (on polydimethylsiloxane (PDMS), polyethylene terephthalate (PET), and glass slide). It has been suggested that graphene on softer substrates such as PET and PDMS would impact MSCs differentiation, since the lateral stress of graphene scaffolds could provide appropriate cytoskeletal tension for accelerated osteogenic differentiation. Additionally, GO would induce mouse MSCs myoblast differentiation [101]. A study by Ku et al. indicated that graphene-based platforms could significantly accelerate myogenic differentiation from myogenic protein expression analyses, multinucleate myotube formation, and expression of differentiation-specific genes (MyoD, myogenin, troponin T, and MHC). It has also been found that GO would significantly enhance the myogenic differentiation, which was attributed to the serum protein adsorption and stiffness of graphene.

Graphene substrates can promote NSC adhesion and its differentiation toward neurons, rather than glial cells. Since graphene has a good electrical conductivity, the neural activity of the differentiated cells could be evaluated by electrical stimulation using the graphene electrode [102]. Cheng's group reported that CVD-grown graphene substrate accelerated growth-associated protein-43 (GAP-43) expression, and promoted neurite sprouting and outgrowth of neurons extracted from mouse hippocampal [103]. As the formation of neural network and performance in the assembled neural network is one of the key issues for neural tissue engineering, Cheng et al. further studied its impact on the unique electrical and mechanical properties of graphene. As they demonstrated, the graphene film could support the growth of functional neural circuits and improve the neural performance and electrical signaling in neural network (Fig. 8.7) [104]. Inspired by these investigations, they reported a 3D porous structure based on graphene foam (GF), which could support NSCs growth and keep them at an active proliferation state with an upregulation of Ki67 expression. More importantly, 3D-GFs accelerated NSCs differentiation toward astrocytes and especially neurons [105]. Additionally, they found 3D graphene substrate could remarkably rescue lipopolysaccharide-induced neuro-inflammation, while 2D graphene could not [106].

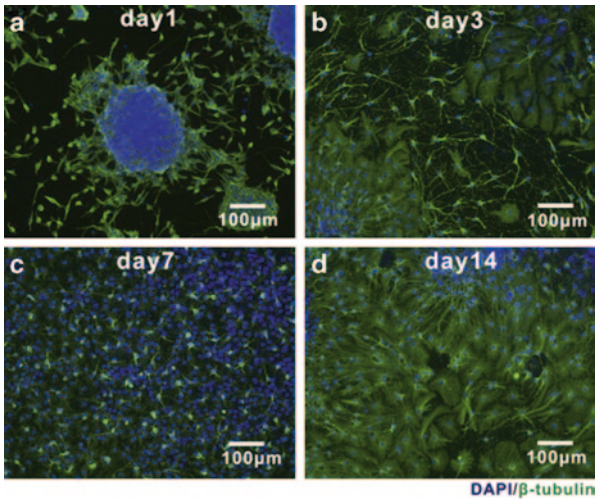

Fig. 8.7 The development of neural networks by NSC differentiation on graphene substrates. (**a–d**) Representative images immunostained by DAPI (nucleus) and antibody against β-tubulin (neurons) at different culturing times (day 1 to day 14). (Adapted with permission from Ref. [104]. Copyright 2013 Elsevier B.V.)

Moreover, graphene (CVD grown) and GO (films made) substrates could support the mouse iPSCs adherence and proliferation [96]. Chen et al. revealed graphene and GO substrates could induce iPSCs spontaneous differentiation into ectodermal and mesodermal lineages; however, they led to distinct differentiation characteristics due to the different surface chemical properties. Graphene suppressed the iPSCs differentiation toward the endodermal lineage, while GO enhanced the endodermal differentiation. All these investigations suggested that graphene-based platforms might find promising applications for stem cell research and tissue engineering with excellent biocompatibility and incredible capability of enhanced differentiation. Although much progress has been made on biomedical applications of graphene-based substrates in tissue regeneration, more efforts should be made on the interactions of biosystems and graphene, such as the long-term in vivo toxicity and immunity after implantation, and efficiency of in vivo tissue repair.

8.5.2 Substrates for Antibacterial Effects

Nowadays, antibacterial nanomaterials, such as silver nanoparticles [107], titanium oxide nanoparticles [108], and carbon nanotubes (CNTs) [109], are widely used in daily life, since they show less drug resistance than the traditional antibiotics. The potential use of graphene-based nanomaterials for antibacterial applications also attracts increasing interests. Fan and Huang's groups explored the antibacterial properties of GO and rGO, which was obtained through modified Hummers' method (Fig. 8.8) [110]. They found that both GO and rGO at low concentration (85 ug/mL) could effectively inhibit the growth of gram-negative bacteria, *Escherichia coli*. The mechanism of antibacterial property is that GO induced cell membrane

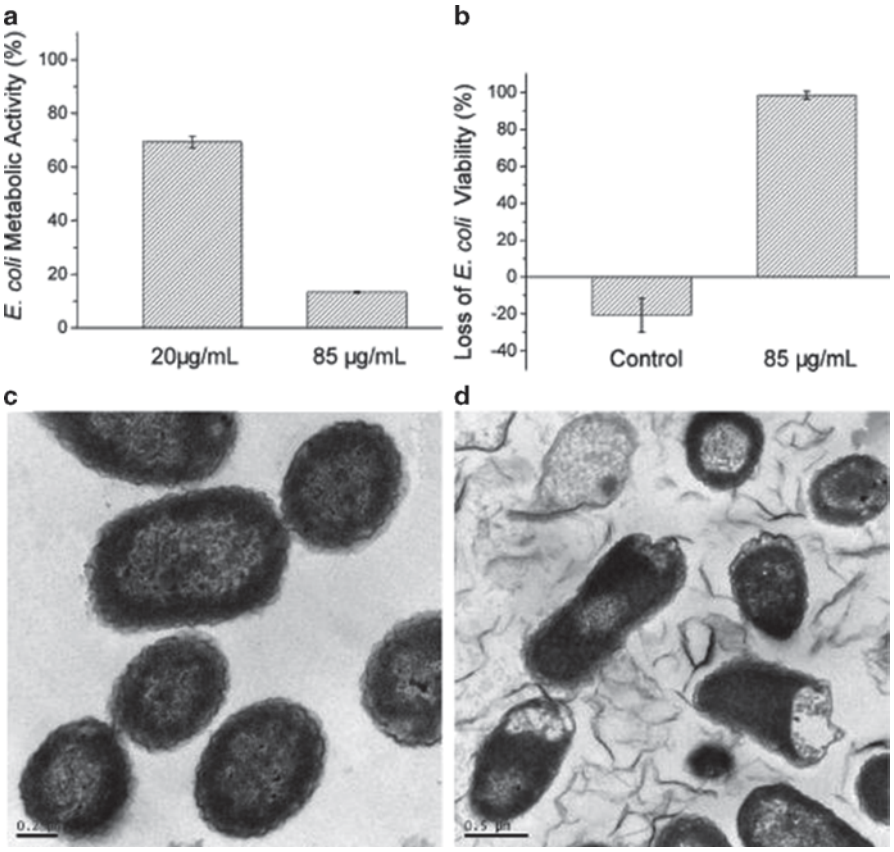

Fig. 8.8 Antibacterial activity of GO nanosheets. Metabolic activity of *E. coli* incubation with GO (**a**), antibacterial activity of GO nanosheets against *E. coli* (**b**), TEM images of *E. coli* (**c**), and *E. coli* exposed to GO nanosheets (**d**). (Adapted with permission from Ref. [110]. Copyright 2010 American Chemical Society)

damage and consequently led to cytoplasm leakage. Moreover, GO and rGO suspensions were conveniently fabricated into macroscopic antibacterial papers via vacuum filtration. Therefore, mass production of antibacterial paper with low cost can be expected with graphene-based materials. Moreover, GO and rGO nanowells showed remarkable destruction of gram-positive bacteria, such as *Staphylococcus aureus*, compared to gram-negative bacteria *E. coli* [111]. Sharp edges of GO or rGO nanowells directly interacted with *S. aureus*, which lacks an outer membrane, and then restrained the activity of microorganism. Besides bacteria, the mycelial growth could be inhibited by rGO nanosheets. Sawangphruk et al. has applied three fungi models, including *Aspergillus niger, Aspergillus oryzae*, and *Fusarium oxysporum* in their study. The IC_{50} values of rGO against three types of fungi were 50, 100, and 100 μg/mL, respectively [112].

The mechanism of antibacterial and antifungal activity of graphene-based materials was suggested mainly in two possible ways [110–113]: (1) GO or rGO damages membrane of microorganisms by theirs sharpened edges, leading to the leakage of cytoplasm. (2) Graphene-based nanomaterials cause the membrane and oxidative stress to induce bacterial toxicity.

On the other hand, there were some controversial reports regarding antimicrobial performance of the graphene-based materials. Das et al. found that GO was not harmful to bacteria, such as *E. coli* and *Pseudomonas aeruginosa* [114]. Similarly, Sun and coworkers demonstrated that GO could enhance the microbial attachment and growth rather than inhibition. However, they did observe that graphene-modified nanoparticles showed an enhanced bacterial toxicity. For instance, *E. coli* adsorbed on the surface of rGO/TiO_2 composite thin film is more sensitive to photoinactivation [115], and GO/Ag complexes showed an enhanced antibacterial activity [116]. Based on the investigation of highly enhanced antibacterial property of GO/Ag complex, Gao et al. have further studied its stability and long-term antibacterial properties. They found that GO/Ag@Fe_2O_3 complexes showed significantly enhanced stability by decreasing the release rate of Ag^+ iron compared to Ag@Fe_2O_3. The presence of GO obviously slowed down the oxidation process of the Ag nanoparticles and enabled Ag^+ ions recrystallization on GO surface, therefore exhibiting long-term antibacterial property against bacteria (both gram negative and gram positive) [117]. This work revealed the origin of enhanced antibacterial effect of nanoparticles combined with GO. Shen's group has coordinated lanthanum (III) on GO sheets (GO–La complexes) for inhibition of *E. coli* growth [118].

8.6 Outlook

Graphene and its derivatives have been extensively studied for their biological applications since 2008. As the encouraging yet preliminary studies show, the large surface area ensures graphene-based nanomaterials as efficient vehicle to transport therapeutics or imaging agents into cells. In addition to active or passive targeting, strong NIR absorbance of graphene facilitates the enhanced cargo accumulation in the tumor sites through light-induced local temperature increase. Graphene's excellent electronic properties make it popular in biological sensing; besides, unique planar structure and physicochemical properties of graphene and GO attract much attention with regard to their use as cell culture scaffolds and anti-bacterial substrates. Clearly, the positive feedbacks of graphene-based biomedical investigations so far will accelerate the research in the related fields, and inspire more explorations of these nanomateirals in biomedical applications. Here, we list several possible directions of biological and medical research on graphene in the future:

1. Development of graphene-based multifunctional delivery systems. There has been a trend of development of nanotheranostic platform based on GO. Future research interests with graphene, especially GO, will be focused on the

applications of GO for co-delivery of multiple therapeutics and/or imaging agents, integration of multiple modalities of clinical purpose, including diagnosis, controlled loading and release of cargoes, targeting, in situ tracking inside cells or tumor sites, and multimodal therapy, for better clinical outcome. In addition, oral transmucosal delivery of non-cancer therapeutics may deserve special attention in the future research.

2. Size-, morphology-, and property-controllable, and scalable production of graphene. Although many synthetic routes of graphene and its derivatives have been developed, a protocol of biocompatible graphene with controlled size, size distribution, and surface nature, as well as scale-up production and fine reproducibility, are urgently demanded. Moreover, inside look into the mechanism of graphene oxidation is currently a priority to rationally optimize the preparation of GO.
3. Biological effects and safety issues of graphene and its derivatives. There are increasing concerns regarding the in vitro and in vivo toxicity of graphene-based nanomaterials, and significant progress has been made to develop biocompatible graphene derivatives through appropriate surface coating and functionalization. However, different and even contrary results reported so far complicate the situation, making it difficult to draw a clear conclusion regarding the toxicity of graphene at in vitro and in vivo levels, because it is defined by purity, size, oxygen content, and surface chemistry of graphene. Therefore, a profound understanding of the interactions between graphene and biosystems, especially the toxicity of graphene nanomaterials, both in vitro and in vivo, is highly desired before their clinical applications.

After all, graphene and its derivatives have shown promising future in the field of biology and medicine, based on numerous efforts and rapidly increasing attention from researcher and the society. Despite facing many problems and challenges at current stage, we have strong faith that the exploration of the biomedical applications of graphene, GO, and its other related derivatives will move forward, and finally reach clinical stages, with strong, continuous, and joint efforts from researchers with backgrounds spanning from materials chemistry, nanotechology, biology, to medicine.

References

1. T. Palacios, Nat. Nanotechnol. **6**, 464 (2011)
2. Y. Liu, X. Dong, P. Chen, Chem. Soc. Rev. **41**, 2283 (2012)
3. D.A. Brownson, D.K. Kampouris, C.E. Banks, J. Power Sources **196**, 4873 (2011)
4. K.S. Novoselov, A.K. Geim, S. Morozov, D. Jiang, Y. Zhang, S. Dubonos, I. Grigorieva, A. Firsov, Science **306**, 666 (2004)
5. D. Cohen-Tanugi, J.C. Grossman, Nano Lett. **12**, 3602 (2012)
6. Z. Liu, J.T. Robinson, S.M. Tabakman, K. Yang, H. Dai, Mater. Today **14**, 316 (2011)
7. H. Shen, L. Zhang, M. Liu, Z. Zhang, Theranostics **2**, 283 (2012)
8. D.R. Dreyer, S. Park, C.W. Bielawski, R.S. Ruoff, Chem. Soc. Rev. **39**, 228 (2010)

9. L. Zhang, J. Xia, Q. Zhao, L. Liu, Z. Zhang, Small **6**, 537 (2010)
10. Y. Chong, Y. Ma, H. Shen, X. Tu, X. Zhou, J. Xu, J. Dai, S. Fan, Z. Zhang, Biomaterials **35**, 5041 (2014)
11. Z. Liu, J.T. Robinson, X. Sun, H. Dai, J. Am. Chem. Soc. **130**, 10876 (2008)
12. J. Huang, C. Zong, H. Shen, Y. Cao, B. Ren, Z. Zhang, Nanoscale **5**, 10591 (2013)
13. Y. Yang, Y.M. Zhang, Y. Chen, D. Zhao, J.T. Chen, Y. Liu, Chem. A. Eur. J. **18**, 4208 (2012)
14. L. Zhang, Z. Lu, Q. Zhao, J. Huang, H. Shen, Z. Zhang, Small **7**, 460 (2011)
15. J. Huang, C. Zong, H. Shen, M. Liu, B. Chen, B. Ren, Z. Zhang, Small **8**, 2577 (2012)
16. C.F. Rochlitz, Swiss Med. Weekly **131**, 4 (2001)
17. L. Naldini, U. Blömer, P. Gallay, D. Ory, R. Mulligan, F.H. Gage, I.M. Verma, D. Trono, Science **272**, 263 (1996)
18 B. Chen, M. Liu, L. Zhang, J. Huang, J. Yao, Z. Zhang, J. Mater. Chem **21**, 7736 (2011)
19. L. Feng, S. Zhang, Z. Liu, Nanoscale **3**, 1252 (2011)
20. H. Kim, R. Namgung, K. Singha, I.-K. Oh, W.J. Kim, Bioconjug. Chem. **22**, 2558 (2011)
21. C.W. Beh, W.Y. Seow, Y. Wang, Y. Zhang, Z.Y. Ong, P.L.R. Ee, Y.-Y. Yang, Biomacromolecules **10**, 41 (2008)
22. H. Bao, Y. Pan, Y. Ping, N.G. Sahoo, T. Wu, L. Li, J. Li, L.H. Gan, Small **7**, 1569 (2011)
23. L. Feng, X. Yang, X. Shi, X. Tan, R. Peng, J. Wang, Z. Liu Small **9**, 1989 (2013)
24. H. Shen, M. Liu, Y. Chong, J. Huang, Z. Zhang, Toxicol. Res. **2**, 379 (2013)
25. K. Yang, S. Zhang, G. Zhang, X. Sun, S.-T. Lee, Z. Liu, Nano Lett. **10**, 3318 (2010)
26. J.T. Robinson, S.M. Tabakman, Y. Liang, H. Wang, H. Sanchez Casalongue, D. Vinh, H. Dai, J. Am. Chem. Soc. **133**, 6825 (2011)
27. K. Yang, J. Wan, S. Zhang, B. Tian, Y. Zhang, Z. Liu, Biomaterials **33**, 2206 (2012)
28. M. Guo, J. Huang, H. Shen, M. zhang, A. Zhu, Y. Li, Y. Deng, H. He, Y. Wang, X. Yang, Z. Zhang, H. Chen, Adv. Func. Mater. **25**, 59 (2015)
29. A.F. Zedan, S. Moussa, J. Terner, G. Atkinson, M.S. El-Shall, ACS nano **7**, 627 (2012)
30. X. Shi, H. Gong, Y. Li, C. Wang, L. Cheng, Z. Liu, Biomaterials **34**, 4786 (2013)
31. Z. Huang, H. Xu, A.D. Meyers, A.I. Musani, L. Wang, R. Tagg, A.B. Barqawi, Y.K. Chen, Technol. Cancer Res. Treat **7**, 309 (2008)
32. C.M. Allen, W.M. Sharman, J.E. Van Lier, J. Porphyrins Phthalocyanines **5**, 161 (2001)
33. P. Huang, C. Xu, J. Lin, C. Wang, X. Wang, C. Zhang, X. Zhou, S. Guo, D. Cui, Theranostics **1**, 240 (2011)
34. P. Rong, K. Yang, A. Srivastan, D.O. Kiesewetter, X. Yue, F. Wang, L. Nie, A. Bhirde, Z. Wang, Z. Liu, Theranostics **4**, 229 (2014)
35. Z.M. Markovic, B.Z. Ristic, K.M. Arsikin, D.G. Klisic, L.M. Harhaji-Trajkovic, B.M. Todorovic-Markovic, D.P. Kepic, T.K. Kravic-Stevovic, S.P. Jovanovic, M.M. Milenkovic, Biomaterials **33**, 7084 (2012)
36. J. Ge, M. Lan, B. Zhou, W. Liu, L. Guo, H. Wang, Q. Jia, G. Niu, X. Huang, H. Zhou, Nat. Commun. **5**, (2014)
37. A. Sahu, W.I. Choi, J.H. Lee, G. Tae, Biomaterials **34**, 6239 (2013)
38. B. Tian, C. Wang, S. Zhang, L. Feng, Z. Liu, ACS Nano **5**, 7000 (2011)
39. C. Xu, D. Yang, L. Mei, Q. Li, H. Zhu, T. Wang, ACS Appl.Mater. Interfaces **5**, 12911 (2013)
40. H. Kim, W.J. Kim, Small **10**, 117 (2014)
41. Y.H. Cao, Y.F. Ma, H.M. Wang, M.X. Zhang, X.L. Tu, H. Shen, J.W. Dai, H.C. Guo, Z.J. Zhang, Adv. Funct. Mater. **24**, 6963 (2014)
42. X. Sun, Z. Liu, K. Welsher, J.T. Robinson, A. Goodwin, S. Zaric, H. Dai, Nano Res. **1**, 203 (2008)
43. P.S. Wate, S.S. Banerjee, A. Jalota-Badhwar, R.R. Mascarenhas, K.R. Zope, J. Khandare, R.D.K. Misra, Nanotechnology **23**, 415101 (2012)
44. Y. Wang, H.-B. Yao, X.-H. Wang, S.-H. Yu, J. Mater. Chem. **21**, 562 (2011)
45. C. Peng, W. Hu, Y. Zhou, C. Fan, Q. Huang, Small **6**, 1686 (2010)
46. M.-L. Chen, J.-W. Liu, B. Hu, M.-L. Chen, J.-H. Wang, Analyst **136**, 4277 (2011)
47. M.-L. Chen, Y.-J. He, X.-W. Chen, J.-H. Wang, Bioconjug. Chem. **24**, 387 (2013)
48. Q. Mei, K. Zhang, G. Guan, B. Liu, S. Wang, Z. Zhang, Chem. Commun. **46**, 7319 (2010)

49. S.H. Hu, Y.W. Chen, W.T. Hung, I.W. Chen, S.Y. Chen Adv. Mater. **24**, 1748 (2012)
50. Y. Wang, H. Wang, D. Liu, S. Song, X. Wang, H. Zhang, Biomaterials **34**, 7715 (2013)
51. L. Zhang, Y. Xing, N. He, Y. Zhang, Z. Lu, J. Zhang, Z. Zhang, J. Nanosci. Nanotechnol. **12**, 2924 (2012)
52. M. Zhang, L. Bai, W. Shang, W. Xie, H. Ma, Y. Fu, D. Fang, H. Sun, L. Fan, M. Han, J. Mater. Chem. **22**, 7461 (2012)
53. M. Nurunnabi, Z. Khatun, G.R. Reeck, D.Y. Lee, Y. Lee, Chem. Commun. (Camb) **49**, 5079 (2013)
54. K. Yang, L. Hu, X. Ma, S. Ye, L. Cheng, X. Shi, C. Li, Y. Li, Z. Liu Adv. Mater. **24**, 1868 (2012)
55. M. Zhang, Y. Cao, Y. Chong, Y. Ma, H. Zhang, Z. Deng, C. Hu, Z. Zhang, ACS Appl. Mater. Interfaces **5**, 13325 (2013)
56. H.-W. Yang, C.-Y. Huang, C.-W. Lin, H.-L. Liu, C.-W. Huang, S.-S. Liao, P.-Y. Chen, Y.-J. Lu, K.-C. Wei, C.-C.M. Ma, Biomaterials **35**, 6534 (2014)
57. Z. Sheng, L. Song, J. Zheng, D. Hu, M. He, M. Zheng, G. Gao, P. Gong, P. Zhang, Y. Ma, Biomaterials **34**, 5236 (2013)
58. Y. Zhang, T.R. Nayak, H. Hong, W. Cai, Nanoscale **4**, 3833 (2012)
59. S. Shi, K. Yang, H. Hong, H.F. Valdovinos, T.R. Nayak, Y. Zhang, C.P. Theuer, T.E. Barnhart, Z. Liu, W. Cai, Biomaterials **34**, 3002 (2013)
60. J. Huang, L. Zhang, B. Chen, N. Ji, F. Chen, Y. Zhang, Z. Zhang, Nanoscale **2**, 2733 (2010)
61. Z. Liu, Z. Guo, H. Zhong, X. Qin, M. Wan, B. Yang, Phys. Chem. Chem. Phys. **15**, 2961 (2013)
62. X. Ma, Q. Qu, Y. Zhao, Z. Luo, Y. Zhao, K.W. Ng, Y. Zhao, J. Mater. Chem. B **1**, 6495 (2013)
63. C. Wang, J. Li, C. Amatore, Y. Chen, H. Jiang, X.M. Wang, Angew. Chem. Int. Ed. **50**, 11644 (2011)
64. H. Xu, H. Dai, G. Chen, Talanta **81**, 334 (2010)
65. Q. Zeng, J. Cheng, L. Tang, X. Liu, Y. Liu, J. Li, J. Jiang, Adv. Funct. Mater. **20**, 3366 (2010)
66. X. Kang, J. Wang, H. Wu, I.A. Aksay, J. Liu, Y. Lin, Biosens. Bioelectron. **25**, 901 (2009)
67. S. Alwarappan, C. Liu, A. Kumar, C.-Z. Li, J. Phys. Chem. C **114**, 12920 (2010)
68. H. Wu, J. Wang, X. Kang, C. Wang, D. Wang, J. Liu, I.A. Aksay, Y. Lin, Talanta **80**, 403 (2009)
69. K.-J. Huang, D.-J. Niu, J.-Y. Sun, C.-H. Han, Z.-W. Wu, Y.-L. Li, X.-Q. Xiong, Colloids Surf. B **82**, 543 (2011)
70. M. Du, T. Yang, K. Jiao, J. Mater. Chem. **20**, 9253 (2010)
71. C.X. Lim, H.Y. Hoh, P.K. Ang, K.P. Loh, Anal. Chem. **82**, 7387 (2010)
72. M. Muti, S. Sharma, A. Erdem, P. Papakonstantinou, Electroanalysis **23**, 272 (2011)
73. B. Su, J. Tang, J. Huang, H. Yang, B. Qiu, G. Chen, D. Tang, Electroanalysis **22**, 2720 (2010)
74. Q. Wei, K. Mao, D. Wu, Y. Dai, J. Yang, B. Du, M. Yang, H. Li, Sens. Actuators B **149**, 314 (2010)
75. S. Hou, M.L. Kasner, S. Su, K. Patel, R. Cuellari, J. Phys. Chem. C **114**, 14915 (2010)
76. L. Tan, K.-G. Zhou, Y.-H. Zhang, H.-X. Wang, X.-D. Wang, Y.-F. Guo, H.-L. Zhang, Electrochem. Commun. **12**, 557 (2010)
77. C. MingáLi, Nanoscale **2**, 1485 (2010)
78. Y. Ohno, K. Maehashi, Y. Yamashiro, K. Matsumoto, Nano Lett. **9**, 3318 (2009)
79. O. Yasuhide, M. Kenzo, I. Koichi, M. Kazuhiko, Japanese J. Appl. Phys **50**, 070120 (2011)
80. M. Yang, S. Gong, Chem. Commun **46**, 5796 (2010)
81. G.-B.S.-B.R. Biodevice, D. Transistor, Nano Lett. **8**, 4469 (2008)
82. X. Dong, Y. Shi, W. Huang, P. Chen, L.J. Li, Adv. Mater. **22**, 1649 (2010)
83. T. Cohen-Karni, Q. Qing, Q. Li, Y. Fang, C.M. Lieber, Nano Lett. **10**, 1098 (2010)
84. Q. He, H.G. Sudibya, Z. Yin, S. Wu, H. Li, F. Boey, W. Huang, P. Chen, H. Zhang, ACS Nano **4**, 3201 (2010)
85. R. Kempaiah, A. Chung, V. Maheshwari, ACS Nano **5**, 6025 (2011)
86. Z. Tang, H. Wu, J.R. Cort, G.W. Buchko, Y. Zhang, Y. Shao, I.A. Aksay, J. Liu, Y. Lin, Small **6**, 1205 (2010)

87. C.H. Lu, J. Li, J.J. Liu, H.H. Yang, X. Chen, G.N. Chen, Chem. A. Eur. J. **16**, 4889 (2010)
88. J.W. Yi, J. Park, N.J. Singh, I.J. Lee, K.S. Kim, B.H. Kim, Bioorg. Med. Chem. Lett. **21**, 704 (2011)
89. S. He, B. Song, D. Li, C. Zhu, W. Qi, Y. Wen, L. Wang, S. Song, H. Fang, C. Fan, Adv. Funct. Mater. **20**, 453 (2010)
90. M.J. Aldegunde, L. Castedo, J.R. Granja, Chem. A. Eur. J. **15**, 4785 (2009)
91. H. Chang, L. Tang, Y. Wang, J. Jiang, J. Li, Anal. Chem. **82**, 2341 (2010)
92. X. Wang, C. Wang, K. Qu, Y. Song, J. Ren, D. Miyoshi, N. Sugimoto, X. Qu, Adv. Funct. Mater. **20**, 3967 (2010)
93. Y. Wang, Z. Li, D. Hu, C.-T. Lin, J. Li, Y. Lin, J. Am. Chem. Soc. **132**, 9274 (2010)
94. S.-R. Ryoo, Y.-K. Kim, M.-H. Kim, D.-H. Min, ACS Nano **4**, 6587 (2010)
95. H. Fan, L. Wang, K. Zhao, N. Li, Z. Shi, Z. Ge, Z. Jin, Biomacromolecules **11**, 2345 (2010)
96. G.-Y. Chen, D.-P. Pang, S.-M. Hwang, H.-Y. Tuan, Y.-C. Hu, Biomaterials **33**, 418 (2012)
97. W.C. Lee, C.H.Y. Lim, H. Shi, L.A. Tang, Y. Wang, C.T. Lim, K.P. Loh, ACS Nano **5**, 7334 (2011)
98. A.J. Engler, S. Sen, H.L. Sweeney, D.E. Discher, Cell **126**, 677 (2006)
99. M.F. Pittenger, A.M. Mackay, S.C. Beck, R.K. Jaiswal, R. Douglas, J.D. Mosca, M.A. Moorman, D.W. Simonetti, S. Craig, D.R. Marshak, Science **284**, 143 (1999)
100. T.R. Nayak, H. Andersen, V.S. Makam, C. Khaw, S. Bae, X. Xu, P.-L.R. Ee, J.-H. Ahn, B.H. Hong, G. Pastorin, ACS Nano **5**, 4670 (2011)
101. S.H. Ku, C.B. Park Biomaterials **34**, 2017 (2013)
102. S.Y. Park, J. Park, S.H. Sim, M.G. Sung, K.S. Kim, B.H. Hong, S. Hong, Adv. Mater. **23**, H263 (2011)
103. N. Li, X. Zhang, Q. Song, R. Su, Q. Zhang, T. Kong, L. Liu, G. Jin, M. Tang, G. Cheng, Biomaterials **32**, 9374 (2011)
104. M. Tang, Q. Song, N. Li, Z. Jiang, R. Huang, G. Cheng, Biomaterials **34**, 6402 (2013)
105. N. Li, Q. Zhang, S. Gao, Q. Song, R. Huang, L. Wang, L. Liu, J. Dai, M. Tang, G. Cheng Sci. Rep. **3**, 1604 (2013)
106. Q. Song, Z. Jiang, N. Li, P. Liu, L. Liu, M. Tang, G. Cheng Biomaterials 2014
107. J.S. Kim, E. Kuk, K.N. Yu, J.-H. Kim, S.J. Park, H.J. Lee, S.H. Kim, Y.K. Park, Y.H. Park, C.-Y. Hwang, Nanomed. Nanotechnol. Biol. Med. **3**, 95 (2007)
108. C. Wei, W.Y. Lin, Z. Zainal, N.E. Williams, K. Zhu, A.P. Kruzic, R.L. Smith, K. Rajeshwar, Environ. Sci. Technol. **28**, 934 (1994)
109. S. Kang, M. Herzberg, D.F. Rodrigues, M. Elimelech, Langmuir **24**, 6409 (2008)
110. W. Hu, C. Peng, W. Luo, M. Lv, X. Li, D. Li, Q. Huang, C. Fan, ACS Nano **4**, 4317 (2010)
111. O. Akhavan, E. Ghaderi, ACS Nano **4**, 5731 (2010)
112. M. Sawangphruk, P. Srimuk, P. Chiochan, T. Sangsri, P. Siwayaprahm, Carbon **50**, 5156 (2012)
113. S. Liu, T.H. Zeng, M. Hofmann, E. Burcombe, J. Wei, R. Jiang, J. Kong, Y. Chen, ACS Nano **5**, 6971 (2011)
114. M.R. Das, R.K. Sarma, R. Saikia, V.S. Kale, M.V. Shelke, P. Sengupta, Colloids Surf., B **83**, 16 (2011)
115. O. Akhavan, E. Ghaderi J. Phys. Chem. C, **113**, 20214 (2009)
116. W.-P. Xu, L.-C. Zhang, J.-P. Li, Y. Lu, H.-H. Li, Y.-N. Ma, W.-D. Wang, S.-H. Yu, J. Mater. Chem. **21**, 4593 (2011)
117. N. Gao, Y. Chen, J. Jiang, ACS Appl. Mater Interfaces **5**, 11307 (2013)
118. X. Wang, N. Zhou, J. Yuan, W. Wang, Y. Tang, C. Lu, J. Zhang, J. Shen, J. Mater. Chem. **22**, 1673 (2012)

Chapter 9
Bionic Graphene Nanosensors

Yong Lin Kong, Manu S. Mannoor and Michael C. McAlpine

9.1 Bionic Nanosensors

9.1.1 Introduction

Bionics is defined by Dictionary.com as "the utilization of electronic devices and mechanical parts to assist humans in performing difficult, dangerous, or intricate tasks, by supplementing or duplicating parts of the body" [1]. It is believed that the term bionics was coined in 1958 by Dr. Jack E. Steele, M.D. The etymology of the word is a portmanteau of *bio* (as in life) + *onics* (as in electronics) [2]. Thus, "bionics" represents the functionalities of classes of systems that are formed by merging biological systems with engineered functional electronic and/or mechanical systems [3]. In modern medicine, prosthetic implants such as pacemakers, retinal, and cochlear implants are manifestations of advanced bionic devices that aim to restore lost or impaired biological functionalities [4, 5]. For example, a cochlear implant consists of an external digital audio device that links with internal components to stimulate the auditory nerve fibers with transmitted audio signals, enabling some degree of speech recognition for otherwise completely deaf patients [6]. Likewise, retinal prosthetics such as the Argus II System involve surgical implantation of electrode arrays to stimulate optical nerve cells and offer some degree of visual perception to retinitis pigmentosa patients [7].

Applications of bionic sensing devices extend beyond prosthetic devices, and are expected to proliferate in use over the coming decades. For instance, wearable electronic systems are rapidly emerging with the expectation of radical advancements in personalized medicine and continuous healthcare monitoring. Electronic sensors can be used to measure physiological conditions such as blood pulsation [8], saliva

M. C. McAlpine (✉) · Y. L. Kong · M. S. Mannoor
Department of Mechanical and Aerospace Engineering, Princeton University,
Engineering Quad, Olden Street, Princeton, NJ 08544, USA
e-mail: mcm@princeton.edu

M. Zhang et al. (eds.), *Carbon Nanomaterials for Biomedical Applications,*
Springer Series in Biomaterials Science and Engineering 5,
DOI 10.1007/978-3-319-22861-7_9

[9], and sweat chemical content [10], and provide portable electrocardiography [11], ballistocardiograms [12], and electromyography [13]. Data acquired from these wearable systems can also improve our understanding of diseases [14] such as epilepsy [15] and heart arrhythmias [16].

Conventional wearable devices consist of electronics that can be "strapped" onto the body in the form of common objects such as clothing [17], watches [18], patches [12], and bandages [13]. Yet, effective implementation of wearable systems can be constrained by patient compliance as well as mechanical incompatibilities at the interface of the electronic systems and the biological tissue [19]. Prolonged usage of conventional wearable devices can cause discomfort and irritation, limiting their application and effectiveness [16]. Indeed, biological tissue is soft, stretchable, flexible, heat sensitive, and three dimensional (3D), while high-performance inorganic electronic materials are rigid, brittle, and two-dimensional (2D) materials which require high temperatures for crystallization. For instance, the Young's modulus of skin is on the order of 10^5–10^6 Pa [20]; in contrast, the moduli of bulk electronic materials such as gold and silicon are on the order of 10^9–10^{11} Pa [21]. Human skin can exceed strains up to 30 % [22], while inorganic electronic materials typically fracture at strains of ca. 1 % [19]. These dichotomies prevent seamless interfacing of electronics with biology [14].

Conformal integration of wearable devices with biological systems lies in enabling close, intimate contact and attachment between the two [23]. Nanotechnology involves the creation of reduced dimensionality nanomaterials, such as quantum dots (0D) [24, 25], nanotubes/nanowires (1D) [26], and graphene (2D) [27–30], that exhibit an assortment of unique, size-dependent properties. Interestingly, despite the disparities between biology and electronic materials in their bulk forms, these two systems can become more compatible at the nanoscale [31, 32]. In the case of mechanical properties, a simple equation which helps to elucidate this is $x = 2SL^2/3t$ [33]. This describes the deflection x at the end of a cantilever beam (clamped at the other end) of length L and thickness t, with a maximum permissible material surface strain given by S. Thus, even brittle crystals possessing intrinsically small values of S (ca. 0.1 %) may overcome these mechanical constraints, provided they are geometrically designed to small thicknesses and large lengths. In particular, developing structures with nanoscale thicknesses is critical for achieving macroscale deflections [34]. Examples include one-dimensional (1D) and 2D nanostructures, for example, nanowires [35–37], nanotubes [38–41], nanoribbons [42, 43], nanomembranes (thin films), and graphene [44]. In addition to these mechanical advantages, size-scaling of materials can reveal new fundamental electrical and mechanoelectric insights [45]. Further, increases in surface-to-volume ratios can lead to improved capabilities, such as highly sensitive biochemical sensing [46, 47] and larger interfacial adhesion [48]. Indeed, both protein molecules and nanowire cross-sections are on the order of 10 nm, while the influence of van der Waals forces increases significantly as the size scale of the structure decreases [49]. A number of promising strategies have been enabled by the interfacing of nanoscale electronic materials onto organs such as the epidermis [10, 50, 51], the lung [52], and the brain [53].

9.1.2 Graphene as Sensing Nanomaterial

Electronic sensors based on nanoscale materials such as nanowires [54], carbon nanotubes (CNTs) [55], and graphene [56] have been shown to boast parts-per-billion (ppb) sensitivities, a consequence of the high surface areas of these materials [50]. CNT-based composite materials with passive circuits have enabled wireless chemical and gas sensors [41]. Single-atom-thick sp^2 graphene is a particularly interesting material due to its remarkable electrical [57], mechanical [58], and sensing [59, 60] properties. As shown in Fig. 9.1a, graphene is a foundational fullerene that can be wrapped up into C_{60} buckyballs (0D), rolled up into CNTs (1D) [61, 62], or stacked to form graphite [63, 64]. The growth of graphene films on supporting metallic films (Ni or Cu) using chemical vapor deposition (CVD) methods [65], combined with post-etching of the underlying metal, offers the ability to efficiently transfer graphene films to other substrates over large areas [66] for biocompatible sensing and flexible electronics applications [67, 68]. These properties render graphene an ideal active material for direct interfacing onto smooth and rugged surfaces. Despite its atomically thin structure, graphene is thermodynamically stable due to 3D warping, which increases elastic energy and suppresses thermal vibrations, minimizing the total free energy above a certain temperature range [69].

Graphene exhibits remarkable mechanical properties, including an ultimate tensile strength of 130 GPa, an intrinsic strength of 42 N/m, and a Young's modulus of ~1 TPa [27]. Van der Waals forces clamp graphene onto substrates [70], and monolayer graphene exhibits a high interfacial adhesion energy of 0.45 J/m^2 on silicon dioxide, as determined by pressure blister tests (Fig. 9.1b) [48]. This high adhesion energy is due to conformal lamination of the highly flexible thin graphene layer on substrates [71], and enables the intimate and robust transfer of graphene onto alternative surfaces, such as biomaterials.

Most excitingly, graphene exhibits extraordinary electronic properties, which manifest in high sensitivity of graphene nanosensors. The charge carriers of ambipolar graphene can be continuously tuned between holes and electrons, and graphene exhibits very high mobilities even under ambient condition, up to 15,000 $cm^2 V^{-1} s^{-1}$ (Fig. 9.1c) [64]. Significantly, graphene sensors have been shown capable of sensitivities even down to the ultimate detection limit of individual gas molecules (Fig. 9.1d) [56, 64, 72]. This sensitivity is explained by several contributing factors. First, the effect of adsorbate molecules is maximized on the 2D material, as every atom is a surface atom and thus the entire volume of graphene is exposed. Second, graphene has low level of excess $1/f$ noise caused by thermal switching due to its few crystal defects. Finally, graphene exhibits high metallic conductivity, which translates into low Johnson noise operation and provides a large relative change of carrier concentration when exposed to low concentrations of analyte molecules [56].

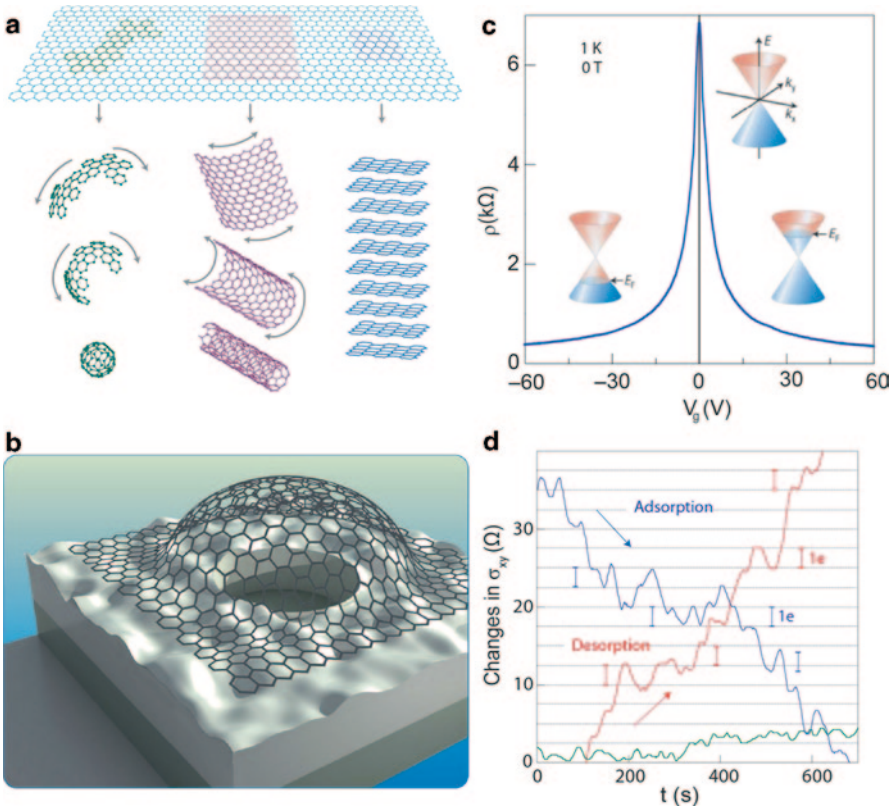

Fig. 9.1 **a** Graphene is a building block for fullerenes of all other dimensionalities [64]. **b** Blister test of a graphene membrane on a SiO_2 substrate, used to determine the mechanical properties and adhesion energy of graphene [48]. A graphene membrane seals gas molecule inside microcavities and bulges due to excess pressure within the micro-cavity. Copyright Victor Tzen and Rex Tzen (2011). **c** Graphene displays ambipolar characteristics. The steep slope of the curve indicates a *very high* mobility ($\mu \approx 5000\ cm^2\ V^{-1}\ s^{-1}$). *Insets* show the change in position of the Fermi energy E_F with changing gate voltage [64]. **d** Single-molecule detection with a graphene sensor. The *blue* and *red curves* show Hall resistivity changes during adsorption and desorption of NO_2, respectively. The *green curve* shows the response to helium as a reference. The *grid line* corresponds to changes caused by the addition of 1 electron charge [56]. Figures 9.1a and c are reprinted with permission from Macmillan Publisher Ltd.: Nature Materials [64], Copyright 2007. Figure 9.1b is reprinted with permission from Macmillan Publisher Ltd.: Nature Nanotechnology [70], Copyright 2011. Figure 9.1d is reprinted with permission from Macmillan Publisher Ltd.: Nature Materials [56], Copyright 2007

9.1.3 Bionic Integration and Biomimicry

Progress in the development of selective sensors has recently accelerated due to increased concerns about chemical and biological threats [26, 36, 38, 56, 60, 73–79]. While DNA and protein biomolecular sensors can exploit well-established

"lock-and-key" interactions to achieve selectivity, obtaining high selectivity in electronic sensing devices while maintaining robustness is a significant challenge. The association constant (K_a) for a low-affinity antibody–antigen complex is ca. 10^4–10^5 L/mol, while the K_a value for high-affinity complexes can be as high as 10^{11} L/mol [80]. Arrays of sensors ("electronic noses") offer an alternative approach, in which the unique "fingerprint" response patterns acquired from semi-selective arrays can be correlated to particular analytes. For the case of traditional e-noses, selectivity is increased by employing larger sensor libraries. An alternative approach is to exploit naturally derived compounds and couple them to sensors in order to increase the degree of selectivity [81]. Accurate recognition requires sensors to detect a unique molecular feature of the analyte. For example, antibodies and peptide aptamers [82–85] are biorecognition molecules that can bind targets with varying degrees of selectivity.

Molecular biomimetics is an emerging field in which the tools of molecular biology and nanotechnology are synergized [86]. Biomimicry [55, 86–88] enables the functionalization and modification of electronic sensing materials to impart biorecognition selectivity to an otherwise promiscuous platform. Further, self-assembly [89, 90] can be employed as a facile method for binding, patterning, and depositing biomolecules onto nanomaterials in a programmable manner. The end result is the creation of nano–bio interfaces which synergistically combine the ultrasensitive response of the nanoscale sensor with the selectivity afforded by the biological recognition component.

9.2 Biointerfaced Graphene Nanosensors

9.2.1 Introduction

Direct interfacing of graphene sensors onto the human body could revolutionize health quality monitoring and adaptive threat detection [4]. Interfacing electronic devices and sensors with biomaterials has been of interest for decades, for on-body physiological and analytical measurements [91–93]. Traditionally, device designs for such applications involved either implantation of device electrodes into tissue [94] or mechanical mounting of components on the body using braces, clamps, or adhesive tapes. Such systems encased rigid and bulky onboard power sources, associated circuitry, and direct physical connections between the sensing probes and data processing electronics [95, 96]. Further, the large form factors and rigid substrates prohibited intimate integration onto the soft and curvilinear surfaces of biological tissue, causing discomfort during continuous use. Device designs and platforms that minimize the mechanical discrepancy between such abiotic/biotic interfaces are thus highly desired for conformal biointegrated electronics and sensors. Here, we explore the use of a novel method for interfacing ultrasensitive graphene sensors onto biological materials via a silk substrate intermediary.

9.2.2 *Biotransfer of Graphene Sensors Using Silk as a Transfer Medium*

Silk, a textile industry staple for thousands of years, has recently sparked increased interest within the materials science community due to its impressive mechanical properties including high elastic modulus, tensile strength, ductility, and toughness [53, 97]. Silk has also been shown to be an efficient "middleman" medium for transferring materials such as passive metallic electrodes onto tissues via intimate contact and dissolution—a consequence of the elasticity and biodegradability imparted by the unique molecular structure of silk. When crystallized in air, the silk fibroin secondary structure kinetically favors a disordered collection of α-helices and random coils which results in aqueous solubility. Hence, silk possesses programmable solubility rates that are dependent on β-sheet content and fibroin concentration. Silk films have been patterned with metal electrodes and intimately "bioresorbed" onto the brain and skin for electro-mapping experiments [51, 53]. Recent work has demonstrated the ability to fabricate active electronic components such as transistors [98] and metamaterials [99, 100] on films of regenerated silk.

The fundamental operation and key functionalities of the sensor design are schematically illustrated in Fig. 9.2. First, CVD-grown graphene is transferred to a polydimethylsiloxane (PDMS) stamp via removal of the underlying Ni layer with $FeCl_3$. Graphene was then transfer printed onto silk films (50 μm) by moistening the silk surface with a wet cotton swab. Next, a graphene-based sensing element with a wireless readout coil was generated on silk fibroin (Fig. 9.2a). A customized gold electrode (150–200 nm) was then fabricated via shadow mask-assisted deposition on silk fibroin.

The ultrathin nanosensors can be intimately biotransferred from the silk platform onto biomaterials, such as tooth enamel, via dissolution of the supporting silk film (Fig. 9.2b). The extremely large surface area of the graphene and electrodes ensures high adhesive conformability to the rugged surfaces of biomaterials. Specificity

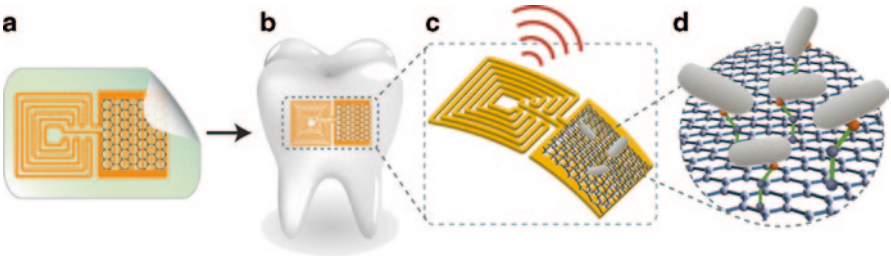

Fig. 9.2 Biotransferable graphene wireless nanosensor. **a** Graphene is printed onto bioresorbable silk and contacts are formed containing a wireless coil. **b** Biotransfer of the nanosensing architecture onto the surface of a tooth. **c** Magnified schematic of the sensing element, illustrating wireless readout. **d** Binding of pathogenic bacteria by peptides self-assembled onto the graphene nanotransducer. The graphene images were reproduced with permission from James Hedberg (www.jameshedberg.com). The tooth image was reproduced courtesy of Georgianax/Vecteezy.com

in biological recognition is achieved by self-assembling biorecognition molecules such as peptides or antibodies onto the graphene monolayer (Fig. 9.2c). Further, Fig. 9.2c illustrates the two other major functionalities of the hybrid biosensor unit: battery-free operation and remote wireless sensing capability. Upon recognition and binding of specific targets (Fig. 9.2d), the electrical conductivity of the graphene film is modulated and wirelessly monitored using an inductively coupled radio frequency (RF) reader device. The key functionalities of the graphene/silk hybrid sensing elements are thus derived from a synergistic integration of the individual materials properties and components.

Figure 9.3a shows large area graphene integrated with water-soluble silk fibroin films following the transfer printing process. Figure 9.3b shows the fully formed biosensing device after electrode deposition. Specifically, the architecture consists of a parallel inductance, resistance, and capacitance (LRC) resonant circuit with a gold inductive coil for wireless transmission, and interdigitated capacitive electrodes contacting graphene resistive sensors. The resulting device is a passive

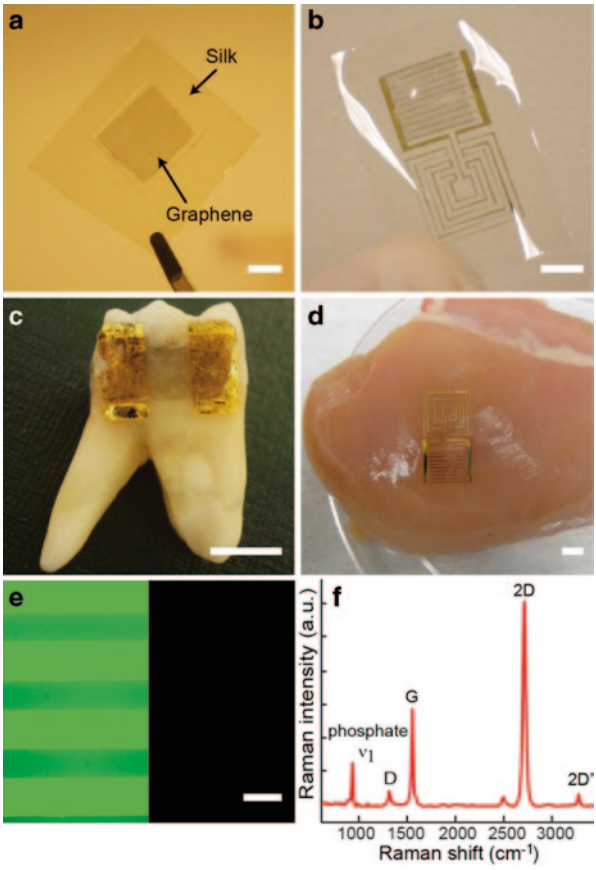

Fig. 9.3 Graphene biotransfer and characterization. **a** Graphene printed onto a bioresorbable silk film. **b** Passive wireless telemetry system consisting of a planar meander line inductor and interdigitated capacitive electrodes integrated onto the graphene/silk film. Graphene sensor biotransferred onto the surface of a human molar (**c**) and onto muscle tissue (**d**). Scale bars are 5 mm. **e** Fluorescent image of sensor fabricated on a fluorescent silk film and laminated onto the surface of a tooth, before *(left)* and after *(right)* dissolution of silk. The absence of a fluorescence signal confirmed complete removal of the silk matrix. Scale bar is 250 μm. **f** Raman spectrum following interfacing of graphene onto the tooth surface

wireless telemetry system, obviating the need for onboard power sources and external connections.

The thin film sensing elements thus fabricated on silk are then biotransferred and intimately integrated onto a variety of substrates. Complete dissolution of the silk matrix template in water led to strong attachment of the graphene–Au electrode structure within a time period of 15–20 min. Significantly, Fig. 9.3c shows a photograph of the graphene nanomaterial with patterned gold electrodes integrated onto the surface of a human molar, and Fig. 9.3d shows a photograph of the graphene sensor biotransferred directly on muscle tissue. To ensure complete dissolution of the silk substrate, sensor biotransfer experiments were performed using fluorescent silk films, before and after the dissolution of the silk (Fig. 9.3e, left). Complete quenching of fluorescence was verified after immersion in water for 20 min (Fig. 9.3e, right). Electronic and structural properties of the graphene were interrogated using Raman spectroscopy [101]: Figure 9.3f shows the Raman spectrum of a monolayer region of the graphene following biotransfer onto a tooth surface. The spectrum is in good agreement with other graphene monolayer spectra [101], and the phosphate ν_1 peak from the tooth enamel substrate is evident [102].

9.2.3 Graphene Functionalization for Bacteria Detection

Pathogenic contamination and resistant "superbug" infections remain critical concerns in both developed and developing nations, due to extremely low minimum infective doses (MID) for many bacteria and the lack of inexpensive and portable methods to detect at these limits [103]. Currently available methods for the detection of microbiological threats utilize specific enrichment media to separate, identify, and count bacterial cells [104]. Alternatively, polymerase chain reaction (PCR) [105] and DNA-based nanobarcode [106] detection strategies have proven to be fast and highly sensitive, but such methods require pretreatment and cell lysis to extract DNA. An alternative strategy is the development of methods that allow for direct and sensitive detection of whole microbial cells or endotoxins. Particularly interesting are sensors that can be directly interfaced with contamination sources, including the body, food, and hospital equipment.

Aptamer-functionalized nanotube electrodes have been shown to detect single bacterial cells in real time [104]. Further, we have recently shown that phage display can be utilized to determine peptide sequences which selectively bind to CNTs and graphene [55, 107–109]. This has enabled the generation of bifunctional peptides containing a carbon nanomaterial recognition moiety combined with an analyte binder to noncovalently self-assemble and impart selectivity on graphene sensor arrays. Another study has demonstrated the ability of naturally occurring antimicrobial peptides (AMPs) to serve as robust biorecogniton moieties with broad-spectrum activity in electronic biosensing platforms [110]. Unlike antibodies, AMPs are more stable and exhibit broadband selectivity toward a range of pathogenic bacteria [81, 111, 112].

Here, graphene nanosensors were functionalized with a chemically synthesized bifunctional peptide, consisting of (1) a dodecapeptide graphene-binding peptide (GBP), (2) a triglycine linker, and (3) the AMP odorranin-HP (OHP), which shows activity toward both the gram-negative bacteria *Escherichia coli* and *Helicobacter pylori* and the gram-positive bacteria *Saphylococcus aureus* [113]. Figure 9.4a shows a molecular drawing of the resulting 38 amino acid sequence, HSSYWYAF-NNKT–GGG–GLLRASSVWGRKYYVDLAGCAKA (GBP–OHP). Raman spectroscopic analysis of the peptide functionalized graphene surface indicated slight doping of graphene (Fig. 9.4b), consistent with our previous electronic measurements [114].

The activity of the immobilized GBP–OHP toward *S. aureus* and *H. pylori* cells were compared via fluorescent assays with activity toward erythrocytes (Fig. 9.4c, 9.4d, and 9.4e, respectively). The concentration of the bacterial cells used for the assays was 10^6 CFU/mL and the concentration for erythrocytes was 40% hematocrit. The assays clearly show higher binding to bacterial cells, evident by the higher fluorescent density. The specificity of the interaction of *S. aureus* cells with GBP–OHP peptides was further analyzed via flow-through electrical measurements of the graphene sensors (Fig. 9.4f). Following elution with deionized (DI) water, the response of GBP–OHP toward *S. aureus* is fourfold larger than the response toward both a GBP-functionalized sensor and a GBP–OHP sensor exposed to erythrocytes.

9.2.4 Wireless Detection and Monitoring

Wireless detection, readout, and power are critical to bionic applications, which provide the bionic sensing devices with a minimal footprint by eliminating power sources, wire ports, and connections. A wireless sensor consists of the sensor and the reader. A single-layer inductive–capacitive (LC) resonant circuit, integrated in parallel with the resistive (R) graphene monolayer, formed the basis of the wireless sensor unit here. The reader device consisted of a two-turn coil antenna connected to a frequency response analyzer (Hewlett Packard 4191A RF impedance analyzer). The wireless reader transmits power as well as receives data from the remote passive sensor via inductive coupling. The reader continuously monitors the complex impedance spectrum of the reader–sensor system. The impedance analyzer passes an alternating current (AC) signal through the antenna and generates a magnetic field and induction current in the coil of the sensing element that results in a potential drop which is dependent on the resistance of the graphene sensor. Biological or chemical changes at the surface of graphene will induce resistance changes via charge transfer and/or the field effect, which are reflected as changes in the frequency characteristics (bandwidth) around the resonance point. The characteristic frequencies and bandwidth are quantities that are primarily determined by the resonant circuit; hence, the readout is relatively insensitive to the coupling coefficient between the sensor and reader coil.

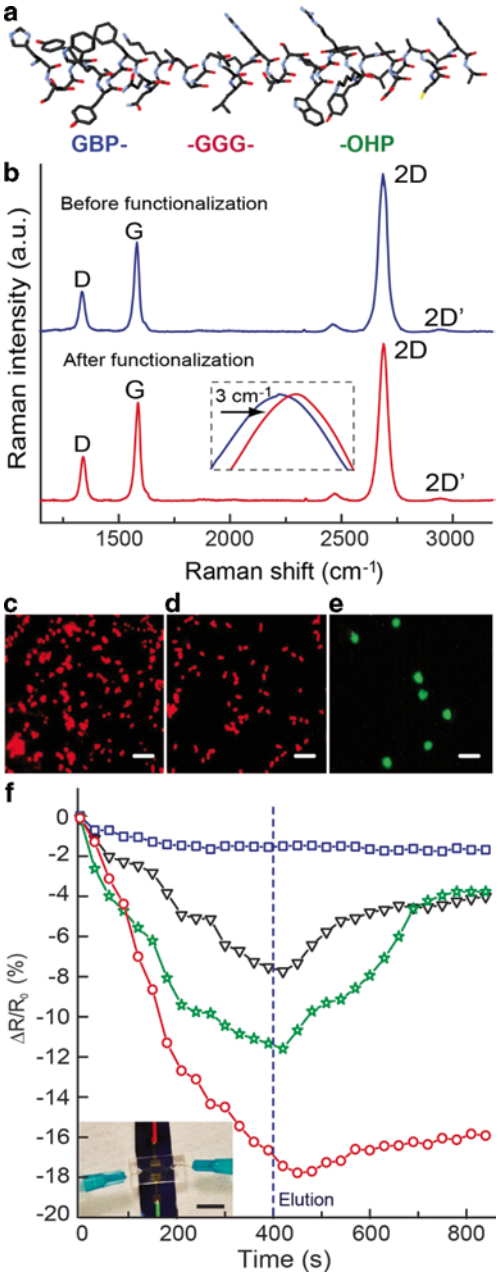

Fig. 9.4 Graphene functionalization with antimicrobial peptides (AMPs). **a** Molecular model of a bifunctional peptide consisting of a graphene-binding peptide (GBP) coupled to an AMP odorranin-HP (OHP) via a triglycine linker (–GGG–). **b** Raman spectra before *(blue line)* and after *(red line)* immobilization of bifunctional peptides on the graphene surface. The *inset* shows a shift in the 2D band of graphene due to molecular doping. Fluorescent images of the binding of *Staphylococcus aureus* (**c**), *Helicobacter pylori* (**d**), and erythrocytes (**e**) to GBP–OHP-functionalized graphene. Scale bars are 10 μm. **f** Selectivity of GBP–OHP functionalized graphene sensor. (□)

A major functionality of the sensor construction is wireless remote query capability. Certain strains of *S. aureus* are notoriously antibiotic resistant and responsible for over 500,000 post-surgical wound infections in the USA each year [115, 116]. *S. aureus* has been reported to survive up to 9 weeks on standard plastic and similar dry hospital environments [116]. To simulate the use of graphene wireless sensors in hospital sanitation and biohazard monitoring, we interfaced the nanosensors with an intravenous (IV) bag (Fig. 9.5a). Next, solutions containing various concentrations (10^3–10^8 CFU/mL) of bacterial cells were allowed to dry on the sensor surface for 30 min. The change in graphene resistance upon bacterial binding was wirelessly monitored as a bandwidth change in the sensor resonance curve [41]. Different concentrations of *S. aureus* cells were incubated on the sensor surface. The percentage change in graphene resistance is depicted in Fig. 9.5b; significantly, wireless detection limits of one bacterium per microliter were achievable in wireless operation mode.

To investigate the performance of the sensor when directly integrated with biological tissue, the sensor was biotransferred onto the surface of a bovine tooth (Fig. 9.6a). Teeth are in continuous contact with breath and saliva, which represent rich biologic media that can be probed for the presence of disease, infectious agents, or metabolic changes [117–119]. Monitoring dynamic characteristics of respiration,

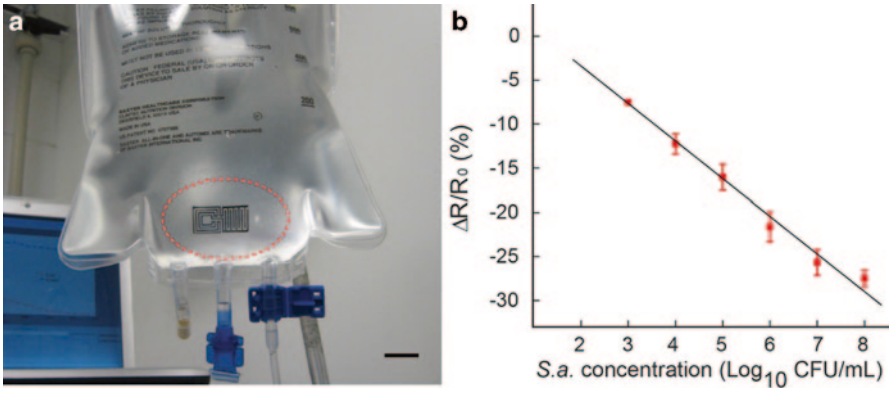

Fig. 9.5 Wireless monitoring of *S. aureus*. **a** Optical image of the graphene wireless sensor integrated onto the surface of an intravenous (IV) bag. Scale bar is 1 cm. **b** Percentage change in graphene resistance versus concentration of *S. aureus* cells, which were incubated on the sensor surface and dried. Error bars show standard deviation ($N = 3$)

Indicates resistance of graphene sensor functionalized with GBP–OHP upon exposure to deionized *(*DI) water. (▽) Indicates resistance of graphene sensor functionalized with only GBP upon exposure to *S. aureus*. (☆) Indicates resistance of graphene sensor functionalized with GBP–OHP upon exposure to erythrocytes. (○) Indicates resistance of graphene sensor functionalized with GBP–OHP upon exposure to *S. aureus*. The *dotted line* indicates elution with DI water. The *inset* shows image of the flow-through measurement system. Scale bar is 1 cm. Concentrations of the bacterial cells used for the assays is 10^6 CFU/mL, and the concentration of erythrocytes is 40 % hematocrit

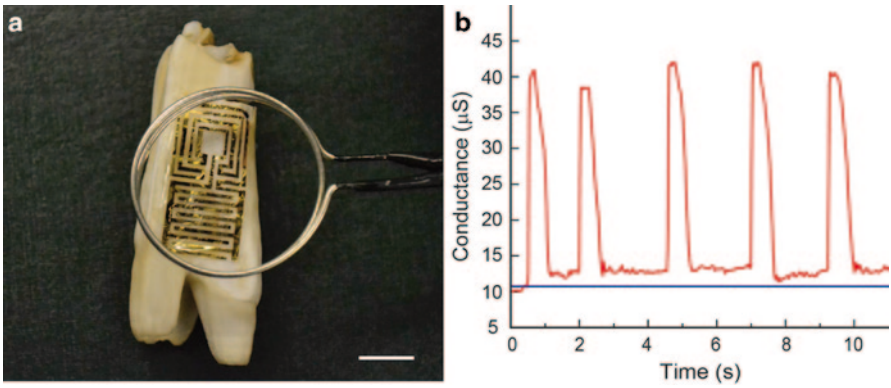

Fig. 9.6 Tooth sensor for wireless monitoring of breath. **a** Optical image of the graphene wireless sensor biotransferred onto the surface of a tooth. Scale bar is 1 cm. **b** Electrical conductance versus time upon exposure of the sensor to pulses of exhaled breath *(red line)*. Baseline conductance is shown as the *blue line*

including the presence of biomarkers and volatile organic compounds (VOCs) in exhaled breath, is of growing interest in noninvasive disease diagnosis [78, 118, 119]. Significantly, integration of the tooth sensor enabled remote monitoring of breath when exhaling on the tooth. Figure 9.6b depicts the real-time change in graphene conductance on exposure to breath. Importantly, the sensor shows rapid response to breath, and the signal was observed to restore back to the baseline after the breath pulse.

9.3 Graphene Nanosensors for Disease Analyte Detection

9.3.1 Introduction

Reports of asthma, a fatal and chronic inflammatory lung disease, have increased by 21 % in the previous decade in the USA. Improving asthma patient outcomes requires early diagnosis; yet, children often find it difficult to perform traditional airway function assessments such as sputum induction and bronchoalveolar lavage. The development of a highly sensitive, selective, and portable or even biointerfaced molecular sensor could provide for more effective, noninvasive diagnosis and promote advanced mediation of asthma via early onset detection. However, conventional methods for detecting these biomarkers, such as enzyme-linked immunosorbent assay (ELISA), require several rounds of washing and incubation, and cannot be biointerfaced. Label-free nanoelectronic sensors such as the graphene sensors described above suggest an alternative approach, while still achieving high sensitivity, ability to be biointerfaced, and compatibility with conventional microfabrication approaches if large-scale arrays are desired for multi-analyte detection.

Here we describe an approach involving patterning and functionalizing graphene surfaces with selective antibodies, in order to develop arrays of ultrasensitive graphene nanosensors tuned to targets of interest to asthma detection from exhaled breath condensate (EBC). Specifically, by functionalizing these sensors with antibody agents for key asthma-related target analyte cytokines, including tumor necrosis factor (TNF)-α, interleukin (IL)-4, and IL-5, detection limits down to femtogram per milliliter levels were achieved. By sensing these key cytokines of asthma from human EBC, this graphene nanosensor platform could eventually promote accurate and noninvasive diagnosis of asthma, as well as provide warning of an impending asthma attack.

9.3.2 Pathology of Asthma

Asthma is a chronic obstructive lung disorder and inflammatory disease which affects approximately 300 million worldwide [120, 121]. Patients with asthma have swollen, inflamed, and sensitive airways. This causes recurring coughing, chest tightness, and wheezing. When agitated by inhaled substances, the muscles can swell and tighten, and excessive mucus is released, leading to a tightening and constriction of the airway. Asthma attacks cause an estimated 250,000 deaths annually [122]. Asthma has no cure, and despite an increasingly better understanding of how the body reacts during an asthma attack, the exact causes of asthma remain poorly understood [123]. As a result, worldwide prevalence of asthma has increased dramatically, and in the USA, asthma rates among children under 18 increased from 3.6% in 1980 to 9% in 2001 [124]. This is especially true for children in lower-income and urban areas, and thus it is generally believed that levels of car exhaust, ozone, VOCs, and other pollutants are significant environmental factors in the development of asthma [125].

Equally discouraging are the limited methods for diagnosing asthma. The diagnostic criteria set forth by the British Thoracic Society are based on variations in peak flow rate in response to various triggers and treatments [126, 127]. Yet, these tests can take weeks to perform and require a comprehensive medical history evaluation, but asthma patients can have a relatively long symptom-free period before an unexpected asthma attack [128]. Other diagnosis methods, such as the bronchial challenge test, are physically demanding, prone to false positives/negatives, and children often find it difficult to perform airway function measurements. These points are critical, because currently the most effective treatments for asthma are (1) identification and minimization of environmental triggers, and (2) early diagnosis, since timely intervention can prevent harmful effects later in life [129].

A key challenge in accurately diagnosing asthma is the difficulty in distinguishing asthma from other lung diseases that exhibit similar symptoms, such as chronic obstructive pulmonary disease (COPD) [130]. For instance, inflammation induced by COPD and asthma could cause similar symptoms despite the fact that the underlying pathways and mechanisms are different (Table 9.1) [131]. Inflammation of

Table 9.1 Comparison of symptoms and underlying mechanisms of asthma versus COPD

	Asthma	COPD
Inflammation	Significant	Significant
Eosinophil	Significantly higher	Normal
Neutrophil	Normal	Significantly higher
Lymphocytes	T_H2 type	T_H1 and T_C1 type

COPD chronic obstructive pulmonary disease

asthma is largely due to eosinophilic inflammation, while COPD is due to neutrophilic inflammation [131]. Thus, accurate diagnosis of the disease is critical, since these distinct lung diseases could have a very different treatment strategies despite the similar symptoms [132].

One promising method for accurate asthma diagnosis is via the direct measurement of cytokine levels [133, 134]. Cytokines are regulatory proteins important in intercellular communication, which are secreted by numerous cells in response to stimuli [80]. Asthma, which is primarily caused by eosinophilic inflammation, has been linked with an increased number of type 2 T helper cells, and the concentrations of secreted cytokines [133] such as IL-4 [135–137], IL-13[135], TNF-α [135, 136], and IL-5 [135, 138–141] have been found to be correlated with asthma. Yet, direct sampling of cytokines from the lung, using methods such as bronchoalveolar lavage, is invasive. The insertion and removal of the fiber-optic bronchoscope might also preferentially select or activate some cells, changing the epithelial lining fluid composition. Children, who are particularly vulnerable to asthma [124], often are physically incapable of performing these invasive sampling and diagnosis tests.

EBC is a noninvasive collection method that samples the airway lining fluid [142]. Compared to traditional methods, the relatively noninvasive nature of EBC collection allows for more frequent collection, with minimal alteration of the airway environment [143], which is important to accurately represent the cytokine levels that correlate to asthma diagnosis. However, the concentrations of cytokine collected using this method are miniscule, in the range of femtogram per milliliter to picograms per millileter, and thus their quantification requires a reliable and robust ultrasensitive measurement tool. In addition, due to the overlapping roles that cytokines play in biological responses and the complexity of the asthma disease itself, there is no single signature biomarker that can be used to distinguish asthma from other diseases. Hence, the diagnosis of asthma requires the multiplexed determination of concentrations from a panel of biomarkers in order to fingerprint asthma from other pulmonary infections or diseases.

Current measurement methods, such as ELISA, require several rounds of washing and incubation and expensive optical equipment, and thus cannot be biointerfaced for the purpose of rapid, real-time, continuous multi-array diagnoses [144–146]. In addition, EBC collection traps both water-soluble volatile gases and aerosolized particles, so it contains a vast number of nontarget molecules and proteins [143, 147]. This renders the detection of small cytokine concentrations in a complex solution particularly challenging and prone to false positive results. Likewise,

preserving the stability of cytokines in EBC is difficult. The actual concentrations of cytokines in EBC are susceptible to variations in the protocols of collection and preservation times [148]. In other words, without a direct, real-time measurement of the collected samples, the cytokine measured with conventional laboratory instruments might not be representative of the actual concentration levels in the patient, increasing the likelihood of misdiagnosis.

Our approach represents a paradigm shift from these methods, by enabling rapid, highly sensitive, and specific antibody monitoring of asthmatic breath indicators. A direct, real-time measurement of cytokine levels immediately following collection of EBC, or perhaps even from a device immobilized on teeth that continuously samples the breath itself, could enable unique and effective measurement methods for the purpose of noninvasive diagnosis. Indeed, highly sensitive and selective sensors which can be generically tailored to serve both as "molecular shields" for environmental triggers, and to noninvasively detect asthma *before* the appearance of symptoms, would be tremendously useful. A number of challenges exist to the implementation of such devices. Here, we provide a progress report of our results to date.

9.3.3 Device Design and Fabrication

As discussed previously, nanoelectronic sensors can provide exceptionally low detection limits [50, 56, 64]. Graphene is a particularly interesting candidate, due to its high chemical stability and mechanical strength, which enables the efficient transfer of graphene films to other substrates for biointerfaced sensing. Further, the large-scale synthesis of 2D graphene lends itself to compatibility with conventional microfabrication techniques, in order to create arrays of devices for multiplexed target analyte detection. Here we describe a wafer-scale graphene sensor fabrication process for creating graphene sensor device arrays.

First, CVD was used to nucleate and grow a monolayer of graphene from a copper metal substrate [28]. Poly(methyl methacrylate) (PMMA) polymer was then spin-coated on top of the graphene, and the copper layer was etched away chemically using ferric(III) chloride. The stack of PMMA and graphene was then transferred as a monolayer to a Si wafer containing a surface silicon dioxide (SiO_2). The PMMA polymer was dissolved in chloroform and subsequently annealed to remove any PMMA residue. Figure 9.7a shows the successful transfer of a large area, 2″ × 2″ monolayer of graphene onto SiO_2, wherein the monolayer graphene is visible via a purple color [149]. The graphene was then patterned using photolithography and defined via oxygen plasma reactive-ion etch (RIE), as shown in the dashed box in Fig. 9.7b. A total of 100/10 nm Au/Ti were then deposited using electron beam deposition in a patterned region to form the source and drain electrodes of the defined graphene area, as shown in Fig. 9.7c. To minimize electrical noise during the solution measurement, a 2-μm-thick layer of insulating SU-8 was patterned on top of

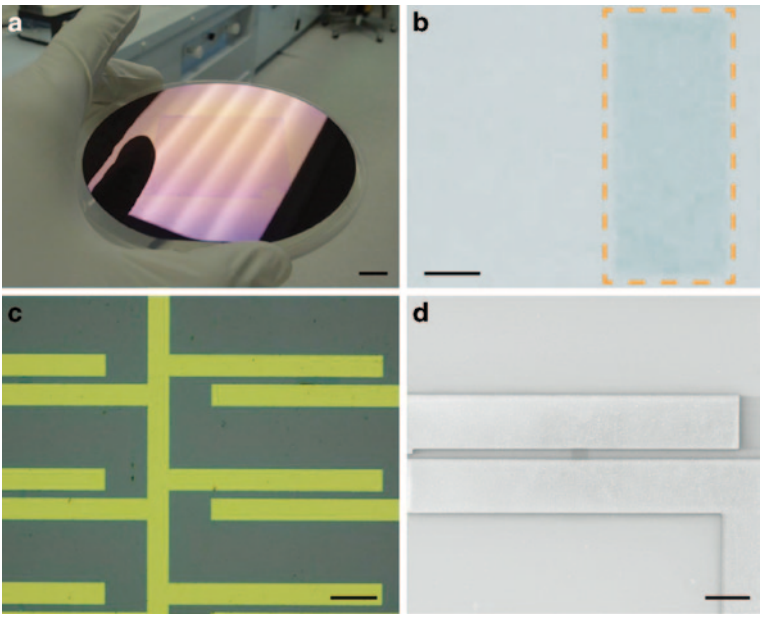

Fig. 9.7 Fabrication of graphene nanosensor arrays. **a** CVD grown graphene, transferred to a Si wafer via PMMA. Scale bar is 1 cm. **b** A plasma-defined graphene area is shown inside the *orange dashed box*. Scale bar is 10 µm. **c** Electrode arrays containing graphene sensing elements patterned via photolithography. Scale bar is 100 µm. **d** Electron microscopy image showing a graphene sensor with passivated gold electrodes. Scale bar is 100 µm

the electrodes to provide passivation. Figure 9.7d is a scanning electron microscopy (SEM) image that shows the electrodes topped with SU-8, exposing a 10-µm × 20-µm region of the graphene for analyte sensing.

Finally, the wafer was diced into 6 mm × 6 mm square pieces of graphene device arrays using a wafer dicing saw. As shown in Fig. 9.8a, the fabrication process yielded a total of 81 graphene sensing chips, for a total of 810 graphene sensors from a 2″ × 2″ monolayer graphene. A plastic tube made from a treated hydrophobic pipette was then attached to the graphene chip for solution measurements, as shown in Fig. 9.8b. Figure 9.8c shows a top view of the sensor chips, each of which contains 10 sensors. Device characterization prior to the functionalization process at this stage is crucial, as consistent electronic performance of graphene sensors is a prerequisite to accurate measurements of ultralow cytokine concentrations. Figure 9.8d shows the change in the drain current when a solution gate (Ag/AgCl electrode) [150] is varied from -0.5 to 0.5 V. Ambipolar field-effect characteristic curves were observed using both a solution gate and a back gate measurement. The graphene device exhibits p-type behavior, as the Dirac point is located at +0.12 V, which could be due to doping from adsorbed molecules such as water [151]. The measured mobility of the graphene device was determined to be 1700 $cm^2 V^{-1} s^{-1}$, which is of comparable order as other graphene devices that have been produced by

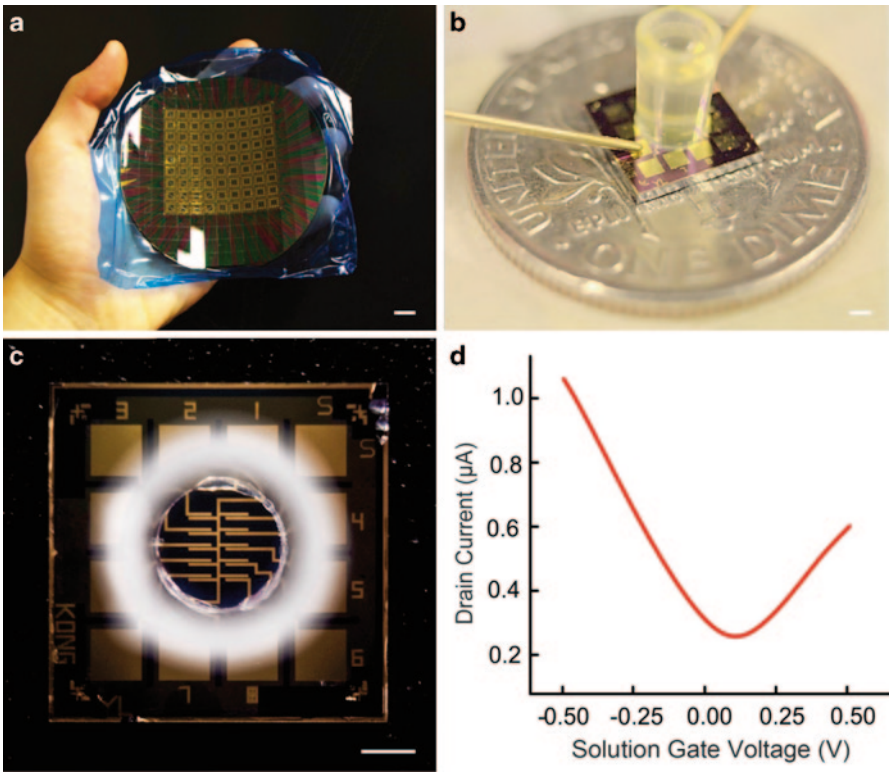

Fig. 9.8 **a** Large area fabrication of graphene sensors. Scale bar is 10 mm. **b** Solution gating of graphene sensors, and relative size of the chip to a dime. Scale bar is 1 mm. **c** Each chip contains 10 graphene sensors, and room temperature vulcanized (RTV) silicone is used to seal the tube (attached ring) to the chip for the solution measurement. Scale bar is 1 mm. **d** Gate response of the graphene sensor, where the voltage is applied through the Ag/AgCl solution gate

the PMMA transfer method [152]. The lower value of this mobility in comparison to the theoretical value of pristine graphene could be due to the effect of chemical residues on the CVD grown graphene following the transfer process [153].

9.3.4 Graphene Surface Functionalization

Graphene is inherently ultrasensitive, but not selective. Yet, EBC contains a rich variety of molecules with a wide range of concentrations [142, 143, 147, 154, 155]. Thus, it is crucial that selectivity be imparted to the graphene sensors by modifying graphene with biorecognition molecules that can target the cytokines of interest. The strong binding between antibodies and their corresponding antigens, with association constants (K_a) of 10^4–10^{11} L/mol, could enable highly selective detection of

cytokines [80]. The idea is to capture the target molecule within the Debye screening length [156], so that only molecules of interest modulate the charge density of graphene via a gate effect. The screening effect is the result of the electrostatic potential from charges on cytokines and other proteins decaying exponentially toward zero with distance from the graphene surface [157]. The Debye screening length can be adjusted by tuning the ionic concentration, such that nontarget charged molecules that are located outside the Debye screening length will have minimal effects on the response of the graphene sensor [158].

The functionalization strategy should be non-covalent in nature, in order to preserve the intrinsic properties of graphene, as covalent bond breaking may introduce scattering centers in the graphene [159, 160]. Figure 9.9a shows a schematic of the functionalization process, by binding immunoglobulin G (IgG) antibody non-covalently with poly-l-lysine (PLL) coated on the graphene. Afterward, a buffer blocking solution (bovine serum albumin, BSA) is added to shield the remainder of

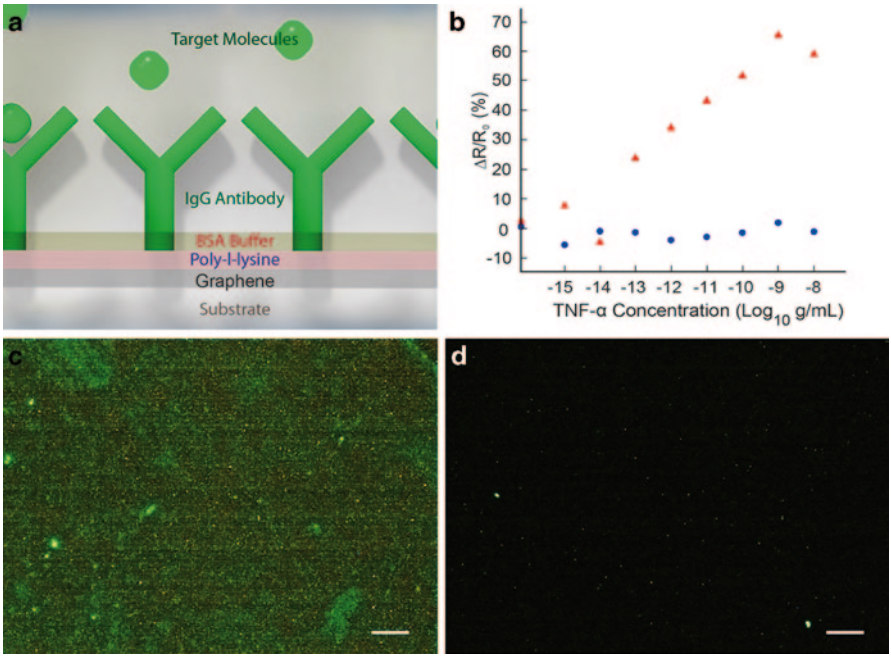

Fig. 9.9 Functionalization of graphene with antibodies. **a** Schematic of the non-covalent functionalization method used to impart selectivity to graphene nanosensor. Poly-l-lysine acts as a linker that couples the IgG antibody to the graphene surface, and BSA buffer serves as a blocking agent to cover the unbound sites to reduce nonspecific binding to the graphene surface. **b** Response curve of TNF-α on an anti-TNF-α functionalized device *(red triangles)* and a graphene device without anti-TNF-α antibody *(blue dots)*. Effectiveness of binding of fluorescently tagged antibodies to different binding molecules, in which a stronger brightness represents a higher concentration of antibody attachment to **(c)** poly-l-lysine, and **(d)** 1-pyrenebutanoic acid, succinimidyl ester (PBSE). Scale bars are 20 μm. *BSA* bovine serum albumin, *IgG* immunoglobulin G, *TNF* tumor necrosis factor

the exposed area of graphene from exposure to nontarget molecules in subsequent experiments. The effectiveness of the immobilization techniques was then assessed via control experiments. For example, Fig. 9.9b shows the strong response of a sensor toward TNF-α that has been immobilized with anti-TNF-α, in comparison to a negligible response of a sensor that was not immobilized with anti-TNF-α.

Different methods for non-covalent functionalization of antibodies have been explored. We investigated the use of (a) PLL, and (b) 1-pyrenebutanoic acid, succinimidyl ester (PBSE), as immobilization reagents. PLL is a positively charged molecule which attaches to the graphene surface, and subsequently, the negative surface charges of the antibody electrostatically attach to the PLL. PBSE is a bifunctional molecule with a pyrenyl group at one end and a succinimidyl ester at the other end [159]. The pyrenyl group will attach to the surface of graphene via π-stacking, while the succinimidyl ester groups can form amide bonds with secondary amines that exist in abundance on the surface of proteins [159]. Figures 9.9c and d show the distributions of the fluorescently tagged antibody on graphene surfaces that have been immobilized with PLL and PBSE, respectively. Comparing the two methods reveals that PLL yields a stronger fluorescence signal, suggesting that it is more effective than PBSE in the non-covalent functionalization of antibodies. Improving the surface density of the antibody on the sensor also improves the dynamic response of the sensor, since the maximum number molecules that can be attached to the surface is significantly increased.

9.3.5 Sensing Response and Calibration Curve

A platform consisting of a multiplexed array of graphene sensors can be fabricated to distinguish and sense a wide variety of target cytokines for disease diagnosis (Fig. 9.10a). Importantly, the graphene sensing platform shows promising results for the detection of dilute concentrations of three key cytokines that are relevant to the pathology of asthma. Due to the inherently high sensitivity of the graphene transducer [56], the detection limits for the sensing platform are extremely low, on the order of femtogram per milliliter. Further, the detection range toward the target molecules is over six orders of magnitude. The response exhibits a logarithmic dependence on target molecule concentration, due to nonlinear screening by the electrolyte of the system, which is expected in nanosensors [161]. This is particularly important in sensing cytokines from EBC, as concentration variations between different individuals is expected to be significant [134, 135, 142, 143]. These results are promising as they can be used to generate calibration curves that relate clinical responses back to quantitative cytokine concentration levels.

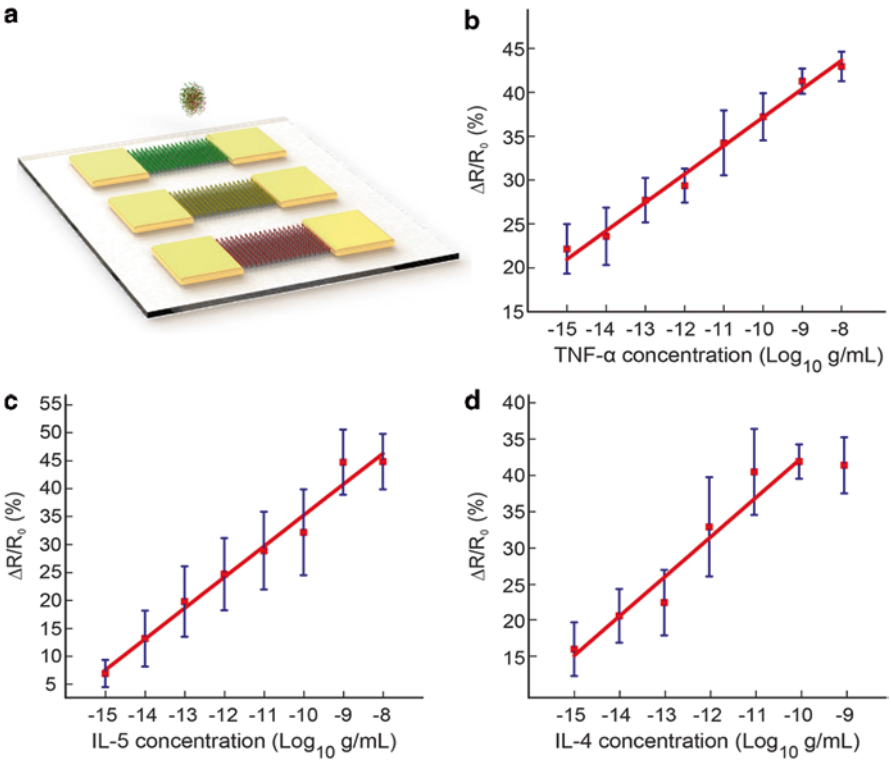

Fig. 9.10 **a** Schematic of functionalized sensor arrays. Percentage change in resistance of graphene sensors that have been functionalized with (**b**) TNF-α antibody, (**c**) IL-5 antibody, and (**d**) IL-4 antibody toward a wide range of concentrations of TNF- α, IL-4, and IL-5, respectively. *TNF* tumor necrosis factor, *IL* interleukin

9.3.6 Outlook: Noninvasive Diagnosis of Complex Diseases

We have demonstrated a fabrication strategy for generating a multiplexed platform of highly sensitive and specific antibody-based graphene sensor arrays. For future directions, EBC samples can be collected from patients, deposited on the graphene sensors, and the concentrations of key biomarkers can be measured by correlating the electrical readout to the calibration curves. Employing this multiplexed sensor array, in tandem with a large population cohort, could enable the collection of rich, multidimensional data from different groups (control vs. asthmatic vs. COPD, etc.) within a rapid period of time. Collection of data from a large population is critical to account for individual variations as well as other factors such as the overlapping roles of the biomarkers in complex diseases. The acquired data can then be analyzed using statistical tools such as principal component analysis (PCA) to identify those key biomarkers and their concentration levels to distinguish diseases with overlapping symptoms. This analysis will eventually enable graphene nanosensors

to fingerprint different diseases. With this ever-expanding library of statistical data, the graphene sensing platform will become a more accurate and powerful tool in disease diagnosis.

More excitingly, by coupling the capability of direct sensing with on-body attachment of the graphene sensor with wireless readout, the concentration profile of an array of target biomarkers could be monitored continuously and in real time. For this purpose, more robust biorecognition compounds, such as peptides, might be useful. Phage display can be used to determine new peptide sequences that target specific molecules [55, 107–109], and we have shown the ability to rapidly generate peptide sequences toward the key asthma biomarkers, TNF-α, IL-5, and IL-4 using a multiplexed microfluidic device [162]. Machine learning approaches can be used to interpret the continuously acquired multivariate data [163]. Real-time, on-body monitoring of an asthmatic patient would enable early onset warnings of an asthma attack, and predictive care and treatment can be then applied to minimize the probability of fatalities.

9.4 Summary

In conclusion, we have demonstrated a novel bionic graphene sensing platform demonstrating the following key capabilities: (1) ability to be biointerfaced onto a variety of different platforms, (2) ultra-high sensitivities, down to femtogram per milliliter levels for cytokine detection, (3) wireless power and remote readout capabilities, (4) ease of multiplexing using standard microfabrication techniques, and (5) decoration of these devices with biorecognition molecules that provide selectivity to the arrays. Given these unique advantages, we envision that these platforms can potentially enable noninvasive, on-body, real-time detection and diagnosis of diseases. Future studies will thus involve transitioning this paradigm-shifting new platform to clinical settings.

Acknowledgments We acknowledge support of this work by the Air Force Office of Scientific Research (#FA9550-09-1-0096 and #FA9550-12-1-0368), by the American Asthma Foundation (#09–0038), and by the Grand Challenges Program at Princeton University.

References

1. In *Dictionary.com Unabridged*. (Random House, Inc)
2. In *Online Etymology Dictionary*. (Douglas Harper, Historian.)
3. W. Craelius, The bionic man: restoring mobility. Science **295**, 1018–1019 + 1021 (2002)
4. R.F. Service, Bioelectronics. The cyborg era begins. Science **340**, 1162–1165 (2013)
5. M.S. Mannoor, Z. Jiang, T. James, Y.L. Kong, K.A. Malatesta, W.O. Soboyejo, N. Verma, D.H. Gracias, M.C. McAlpine, 3D printed bionic ears. Nano Lett. **13**, 2634–2639 (2013)
6. B.S. Wilson, C.C. Finley, D.T. Lawson, R.D. Wolford, D.K. Eddington, W.M. Rabinowitz, Better speech recognition with cochlear implants. Nature **352**, 236–238 (1991)

7. L. da Cruz, B.F. Coley, J. Dorn, F. Merlini, E. Filley, P. Christopher, F.K. Chen, V. Wuyyuru, J. Sahel, P. Stanga, M. Humayun, R.J. Greenberg, G. Dagnelie, The Argus II epiretinal prosthesis system allows letter and word reading and long-term function in patients with profound vision loss. Br. J. Ophthalmol. **97**, 632–636 (2013)
8. S. Gong, W. Schwalb, Y. Wang, Y. Chen, Y. Tang, J. Si, B. Shirinzadeh, W. Cheng, A wearable and highly sensitive pressure sensor with ultrathin gold nanowires. Nat. Commun. **5**, 3132 (2014)
9. J. Kim, G. Valdes-Ramirez, A.J. Bandodkar, W. Jia, A.G. Martinez, J. Ramirez, P. Mercier, J. Wang, Non-invasive mouthguard biosensor for continuous salivary monitoring of metabolites. Analyst **139**, 1632–1636 (2014)
10. A.J. Bandodkar, D. Molinnus, O. Mirza, T. Guinovart, J.R. Windmiller, G. Valdes-Ramirez, F.J. Andrade, M.J. Schoning, J. Wang, Epidermal tattoo potentiometric sodium sensors with wireless signal transduction for continuous non-invasive sweat monitoring. Biosens. Bioelectron. **54**, 603–609 (2014)
11. P. Chulsung, P.H. Chou, B. Ying, R. Matthews, A. Hibbs, in IEEE Biomed. Circuits Syst Conf. 2006. 241–244, doi:10.1109/BIOCAS.2006.4600353
12. H. Eunjeh, N. Seungwoo, Y. Chiyul, K. Hee Chan, in IEEE Sens. Appl. Symp. (SAS). 2014. 94–96, doi:10.1109/SAS.2014.6798924
13. W. Honda, S. Harada, T. Arie, S. Akita, K. Takei, Wearable, human-interactive, health-monitoring, wireless devices fabricated by macroscale printing techniques. Adv. Funct. Mater. **24**, 3299–3304 (2014)
14. D. Son, J. Lee, S. Qiao, R. Ghaffari, J. Kim, J.E. Lee, C. Song, S.J. Kim, D.J. Lee, S.W. Jun, S. Yang, M. Park, J. Shin, K. Do, M. Lee, K. Kang, C.S. Hwang, N. Lu, T. Hyeon, D.H. Kim, Multifunctional wearable devices for diagnosis and therapy of movement disorders. Nat. Nanotech. **9**, 397–404 (2014)
15. W.C. Stacey, B. Litt, Technology insight: neuroengineering and epilepsy–designing devices for seizure control. Nat. Clin. Pract. Neuro. **4**, 190–201 (2008)
16. S.S. Lobodzinski, M.M. Laks, New devices for very long-term ECG monitoring. Cardiol. J. **19**, 210–214 (2012)
17. A.G. Avila, J.P. Hinestroza, Smart textiles: tough cotton. Nat. Nanotech. **3**, 458–459 (2008)
18. E. Dolgin, Technology: dressed to detect. Nature **511**, 16–17 (2014)
19. J.A. Rogers, T. Someya, Y. Huang, Materials and mechanics for stretchable electronics. Science **327**, 1603–1607 (2010)
20. P.G. Agache, C. Monneur, J.L. Leveque, J. De Rigal, Mechanical properties and Young's modulus of human skin in vivo. Arch. Dermatol. Res. **269**, 221–232 (1980)
21. M.F. Ashby, *Materials Selection in Mechanical Design*, 1st edn. (Pergamon Press, Oxford, 1992)
22. M.A. Nicolelis, D. Dimitrov, J.M. Carmena, R. Crist, G. Lehew, J.D. Kralik, S.P. Wise, Chronic, multisite, multielectrode recordings in macaque monkeys. Proc. Natl. Acad. Sci. USA. **100**, 11041–11046 (2003)
23. S. Giselbrecht, B.E. Rapp, C.M. Niemeyer, The chemistry of cyborgs—interfacing technical devices with organisms. Angew. Chem., Int. Ed. Engl. **52**, 13942–13957 (2013)
24. Y. Shirasaki, G.J. Supran, M.G. Bawendi, V. Bulovic, Emergence of colloidal quantum-dot light-emitting technologies. Nat. Photonics. **7**, 13–23 (2013)
25. S.W. Lee, C. Mao, C.E. Flynn, A.M. Belcher, Ordering of quantum dots, using genetically engineered viruses. Science **296**, 892–895 (2002)
26. M.C. McAlpine, H. Ahmad, D. Wang, J.R. Heath, Highly ordered nanowire arrays on plastic substrates for ultrasensitive flexible chemical sensors. Nat. Mater. **6**, 379–384 (2007)
27. C. Lee, X. Wei, J.W. Kysar, J. Hone, Measurement of the elastic properties and intrinsic strength of monolayer graphene. Science **321**, 385–388 (2008)
28. X. Li, W. Cai, J. An, S. Kim, J. Nah, D. Yang, R. Piner, A. Velamakanni, I. Jung, E. Tutuc, S.K. Banerjee, L. Colombo, R.S. Ruoff, Large-area synthesis of high-quality and uniform graphene films on copper foils. Science **324**, 1312–1314 (2009)

29. Y.M. Lin, A. Valdes-Garcia, S.J. Han, D.B. Farmer, I. Meric, Y. Sun, Y. Wu, C. Dimitrakopoulos, A. Grill, P. Avouris, K.A. Jenkins, Wafer-scale graphene integrated circuit. Science **332**, 1294–1297 (2011)
30. K.S. Novoselov, A.K. Geim, S.V. Morozov, D. Jiang, Y. Zhang, S.V. Dubonos, I.V. Grigorieva, A.A. Firsov, Electric field effect in atomically thin carbon films. Science **306**, 666–669 (2004)
31. T. Cohen-Karni, C.M. Lieber, Nanowire nanoelectronics: Building interfaces with tissue and cells at the natural scale of biology. Pure Appl. Chem. **85**, 883–901 (2013)
32. T. Dvir, B.P. Timko, M.D. Brigham, S.R. Naik, S.S. Karajanagi, O. Levy, H. Jin, K.K. Parker, R. Langer, D.S. Kohane, Nanowired three-dimensional cardiac patches. Nat. Nanotech. **6**, 720–725 (2011)
33. M.J. Troughton, *Handbook of Plastics Joining: A Practical Guide*, 2nd edn. 191 (William Andrew Inc., USA, 2008)
34. T. Starner, Human-powered wearable computing. IBM Syst. J. **35**, 618–629 (1996)
35. Y. Xia, P. Yang, Y. Sun, Y. Wu, B. Mayers, B. Gates, Y. Yin, F. Kim, H. Yan, One-dimensional nanostructures: synthesis, characterization, and applications. Adv. Mater. **15**, 353–389 (2003)
36. Y. Cui, Q. Wei, H. Park, C.M. Lieber, Nanowire nanosensors for highly sensitive and selective detection of biological and chemical species. Science **293**, 1289–1292 (2001)
37. P.A. Smith, C.D. Nordquist, T.N. Jackson, T.S. Mayer, B.R. Martin, J. Mbindyo, T.E. Mallouk, Electric-field assisted assembly and alignment of metallic nanowires. Appl. Phys. Lett. **77**, 1399 (2000)
38. J. Kong, N.R. Franklin, C. Zhou, M.G. Chapline, S. Peng, K. Cho, H. Dai, Nanotube molecular wires as chemical sensors. Science **287**, 622–625 (2000)
39. P. Kim, L. Shi, A. Majumdar, P.L. McEuen, Thermal transport measurements of individual multiwalled nanotubes. Phys. Rev. Lett. **87**, 215502 (2001)
40. P.G. Collins, K. Bradley, M. Ishigami, A. Zettl, Extreme oxygen sensitivity of electronic properties of carbon nanotubes. Science **287**, 1801–1804 (2000)
41. K.J. Loh, J.P. Lynch, N.A. Kotov, Passive wireless sensing using SWNT-based multifunctional thin film patches. Int. J. Appl. Electrom. **28**, 87–94 (2008)
42. L. Jiao, L. Zhang, X. Wang, G. Diankov, H. Dai, Narrow graphene nanoribbons from carbon nanotubes. Nature **458**, 877–880 (2009)
43. D.Y. Khang, H. Jiang, Y. Huang, J.A. Rogers, A stretchable form of single-crystal silicon for high-performance electronics on rubber substrates. Science **311**, 208–212 (2006)
44. J.A. Rogers, M.G. Lagally, R.G. Nuzzo, Synthesis, assembly and applications of semiconductor nanomembranes. Nature **477**, 45–53 (2011)
45. E. Roduner, Size matters: why nanomaterials are different. Chem. Soc. Rev. **35**, 583–592 (2006)
46. J.L. West, N.J. Halas, Engineered nanomaterials for biophotonics applications: improving sensing, imaging, and therapeutics. Annu. Rev. Biomed. Eng. **5**, 285–292 (2003)
47. E. Stern, J.F. Klemic, D.A. Routenberg, P.N. Wyrembak, D.B. Turner-Evans, A.D. Hamilton, D.A. LaVan, T.M. Fahmy, M.A. Reed, Label-free immunodetection with CMOS-compatible semiconducting nanowires. Nature **445**, 519–522 (2007)
48. S.P. Koenig, N.G. Boddeti, M.L. Dunn, J.S. Bunch, Ultrastrong adhesion of graphene membranes. Nat. Nanotech. **6**, 543–546 (2011)
49. G.A. Rance, D.H. Marsh, S.J. Bourne, T.J. Reade, A.N. Khlobystov, van der Waals interactions between nanotubes and nanoparticles for controlled assembly of composite nanostructures. ACS Nano. **4**, 4920–4928 (2010)
50. M.S. Mannoor, H. Tao, J.D. Clayton, A. Sengupta, D.L. Kaplan, R.R. Naik, N. Verma, F.G. Omenetto, M.C. McAlpine, Graphene-based wireless bacteria detection on tooth enamel. Nat. Commun. **3**, 763 (2012)
51. D.H. Kim, N. Lu, R. Ma, Y.S. Kim, R.H. Kim, S. Wang, J. Wu, S.M. Won, H. Tao, A. Islam, K.J. Yu, T.I. Kim, R. Chowdhury, M. Ying, L. Xu, M. Li, H.J. Chung, H. Keum, M. McCormick, P. Liu, Y.W. Zhang, F.G. Omenetto, Y. Huang, T. Coleman, J.A. Rogers, Epidermal electronics. Science **333**, 838–843 (2011)

52. T.D. Nguyen, N. Deshmukh, J.M. Nagarah, T. Kramer, P.K. Purohit, M.J. Berry, M.C. McAlpine, Piezoelectric nanoribbons for monitoring cellular deformations. Nat. Nanotech. **7**, 587–593 (2012)
53. D.H. Kim, J. Viventi, J.J. Amsden, J. Xiao, L. Vigeland, Y.S. Kim, J.A. Blanco, B. Panilaitis, E.S. Frechette, D. Contreras, D.L. Kaplan, F.G. Omenetto, Y. Huang, K.C. Hwang, M.R. Zakin, B. Litt, J.A. Rogers, Dissolvable films of silk fibroin for ultrathin conformal bio-integrated electronics. Nat. Mater. **9**, 511–517 (2010)
54. G. Zheng, F. Patolsky, Y. Cui, W.U. Wang, C.M. Lieber, Multiplexed electrical detection of cancer markers with nanowire sensor arrays. Nat. Biotechnol. **23**, 1294–1301 (2005)
55. Z. Kuang, S.N. Kim, W.J. Crookes-Goodson, B.L. Farmer, R.R. Naik, Biomimetic chemosensor: designing peptide recognition elements for surface functionalization of carbon nanotube field effect transistors. ACS Nano. **4**, 452–458 (2010)
56. F. Schedin, A.K. Geim, S.V. Morozov, E.W. Hill, P. Blake, M.I. Katsnelson, K.S. Novoselov, Detection of individual gas molecules adsorbed on graphene. Nat. Mater. **6**, 652–655 (2007)
57. L. Liao, Y.C. Lin, M. Bao, R. Cheng, J. Bai, Y. Liu, Y. Qu, K.L. Wang, Y. Huang, X. Duan, High-speed graphene transistors with a self-aligned nanowire gate. Nature **467**, 305–308 (2010)
58. C. Chen, S. Rosenblatt, K.I. Bolotin, W. Kalb, P. Kim, I. Kymissis, H.L. Stormer, T.F. Heinz, J. Hone, Performance of monolayer graphene nanomechanical resonators with electrical readout. Nat. Nanotech. **4**, 861–867 (2009)
59. Y. Liu, D. Yu, C. Zeng, Z. Miao, L. Dai, Biocompatible graphene oxide-based glucose biosensors. Langmuir **26**, 6158–6160 (2010)
60. C. Staii, A.T. Johnson Jr., M. Chen, A. Gelperin, DNA-decorated carbon nanotubes for chemical sensing. Nano Lett. **5**, 1774–1778 (2005)
61. G. Peng, E. Trock, H. Haick, Detecting simulated patterns of lung cancer biomarkers by random network of single-walled carbon nanotubes coated with nonpolymeric organic materials. Nano Lett. **8**, 3631–3635 (2008)
62. J.H. Ahn, H.S. Kim, K.J. Lee, S. Jeon, S.J. Kang, Y. Sun, R.G. Nuzzo, J.A. Rogers, Heterogeneous three-dimensional electronics by use of printed semiconductor nanomaterials. Science **314**, 1754–1757 (2006)
63. A.H. Castro Neto, F. Guinea, N.M.R. Peres, K.S. Novoselov, A.K. Geim, The electronic properties of graphene. Rev. Mod. Phys. **81**, 109–162 (2009)
64. A.K. Geim, K.S. Novoselov, The rise of graphene. Nat. Mater. **6**, 183–191 (2007)
65. W. Choi, I. Lahiri, R. Seelaboyina, Y.S. Kang, Synthesis of graphene and its applications: a review. Crit. Rev. Solid State Mater. Sci. **35**, 52–71 (2010)
66. W. Yang, K.R. Ratinac, S.R. Ringer, P. Thordarson, J.J. Gooding, F. Braet, Carbon nanomaterials in biosensors: should you use nanotubes or graphene? Angew. Chem. **49**, 2114–2138 (2010)
67. X. Dong, Y. Shi, W. Huang, P. Chen, L.J. Li, Electrical detection of DNA hybridization with single-base specificity using transistors based on CVD-grown graphene sheets. Adv. Mater. **22**, 1649–1653 (2010)
68. N. Mohanty, V. Berry, Graphene-based single-bacterium resolution biodevice and DNA transistor: interfacing graphene derivatives with nanoscale and microscale biocomponents. Nano Lett. **8**, 4469–4476 (2008)
69. J.C. Meyer, A.K. Geim, M.I. Katsnelson, K.S. Novoselov, T.J. Booth, S. Roth, The structure of suspended graphene sheets. Nature **446**, 60–63 (2007)
70. R. Huang, Graphene: show of adhesive strength. Nat. Nanotech. **6**, 537–538 (2011)
71. M. Ishigami, J.H. Chen, W.G. Cullen, M.S. Fuhrer, E.D. Williams, Atomic structure of graphene on SiO_2. Nano Lett. **7**, 1643–1648 (2007)
72. A.K. Geim, Graphene: status and prospects. Science **324**, 1530–1534 (2009)
73. W. Yang, O. Auciello, J.E. Butler, W. Cai, J.A. Carlisle, J.E. Gerbi, D.M. Gruen, T. Knickerbocker, T.L. Lasseter, J.N. Russell, L.M. Smith, R.J. Hamers DNA-modified nanocrystalline diamond thin-films as stable, biologically active substrates. Nat. Mater. **1**, 253–257 (2002)

74. Z. Bao, M.R. Weatherspoon, S. Shian, Y. Cai, P.D. Graham, S.M. Allan, G. Ahmad, M.B. Dickerson, B.C. Church, Z. Kang, H.W. Abernathy III, C.J. Summers, M. Liu, K.H. Sandhage, Chemical reduction of three-dimensional silica micro-assemblies into microporous silicon replicas. Nature **446**, 172–175 (2007)
75. A. Ponzoni, E. Comini, G. Sberveglieri, J. Zhou, S.Z. Deng, N.S. Xu, Y. Ding, Z.L. Wang, Ultrasensitive and highly selective gas sensors using three-dimensional tungsten oxide nanowire networks. Appl. Phys. Lett. **88**, 203101–203103 (2006)
76. D. Zhang, Z. Liu, C. Li, T. Tang, X. Liu, S. Han, B. Lei, C. Zhou, Detection of NO_2 down to ppb levels using individual and multiple In_2O_3 nanowire devices. Nano Lett. **4**, 1919–1924 (2004)
77. Y.L. Bunimovich, Y.S. Shin, W.S. Yeo, M. Amori, G. Kwong, J.R. Heath, Quantitative real-time measurements of DNA hybridization with alkylated nonoxidized silicon nanowires in electrolyte solution. J. Am. Chem. Soc. **128**, 16323–16331 (2006)
78. O. Kuzmych, B.L. Allen, A. Star, Carbon nanotube sensors for exhaled breath components. Nanotechnology **18**, 375502 (2007)
79. M.J. Thorpe, K.D. Moll, R.J. Jones, B. Safdi, J. Ye, Broadband cavity ringdown spectroscopy for sensitive and rapid molecular detection. Science **311**, 1595–1599 (2006)
80. R.A. Goldsby, *Immunology*, 5th edn. (W.H. Freeman, USA 2003)
81. J.R. Uzarski, C.M. Mello, Detection and classification of related lipopolysaccharides via a small array of immobilized antimicrobial peptides. Anal. Chem. **84**, 7359–7366 (2012)
82. T.Z. Wu, Y.R. Lo, E.C. Chan, Exploring the recognized bio-mimicry materials for gas sensing. Biosens. Bioelectron. **16**, 945–953 (2001)
83. M. Mascini, A. Macagnano, D. Monti, M. Del Carlo, R. Paolesse, B. Chen, P. Warner, A. D'Amico, C. Di Natale, D. Compagnone, Piezoelectric sensors for dioxins: a biomimetic approach. Biosens. Bioelectron. **20**, 1203–1210 (2004)
84. C. Buerger, K. Nagel-Wolfrum, C. Kunz, I. Wittig, K. Butz, F. Hoppe-Seyler, B. Groner, Sequence-specific peptide aptamers, interacting with the intracellular domain of the epidermal growth factor receptor, interfere with Stat3 activation and inhibit the growth of tumor cells. J. Biol. Chem. **278**, 37610–37621 (2003)
85. P. Colas, B. Cohen, T. Jessen, I. Grishina, J. McCoy, R. Brent, Genetic selection of peptide aptamers that recognize and inhibit cyclin-dependent kinase 2. Nature **380**, 548–550 (1996)
86. Y. Cui, S.N. Kim, R.R. Naik, M.C. McAlpine, Biomimetic peptide nanosensors. Acc. Chem. Res. **45**, 696–704 (2012)
87. M. Sarikaya, C. Tamerler, A.K. Jen, K. Schulten, F. Baneyx, Molecular biomimetics: nanotechnology through biology. Nat. Mater. **2**, 577–585 (2003)
88. R.R. Naik, S.J. Stringer, G. Agarwal, S.E. Jones, M.O. Stone, Biomimetic synthesis and patterning of silver nanoparticles. Nat. Mater. **1**, 169–172 (2002)
89. N. Bowden, A. Terfort, J. Carbeck, G.M. Whitesides, Self-assembly of mesoscale objects into ordered two-dimensional arrays. Science **276**, 233–235 (1997)
90. D. Kisailus, Q. Truong, Y. Amemiya, J.C. Weaver, D.E. Morse, Self-assembled bifunctional surface mimics an enzymatic and templating protein for the synthesis of a metal oxide semiconductor. Proc. Natl. Acad. Sci. USA. **103**, 5652–5657 (2006)
91. R.F Service. Can sensors make a home in the body? Science 297, 962–963 (2002)
92. H. Yao, A.J. Shum, M. Cowan, I. Lahdesmaki, B.A. Parviz, A contact lens with embedded sensor for monitoring tear glucose level. Biosens. Bioelectron. **26**, 3290–3296 (2011)
93. A.C.R. Grayson, R.S. Shawgo, A.M. Johnson, N.T. Flynn, Y. Li, M.J. Cima, R. Langer, A bioMEMS review: MEMS technology for physiologically integrated devices. Proc. IEEE. **92**, 6–21 (2004)
94. M.L. Neat, R. Peacock, R.T. Brittain, Implantation of electrodes in the dentine of an upper canine tooth in the dog. Br. J. Pharmacol. **43**, 476P–477P (1971)
95. C.M. Li, H. Dong, X. Cao, J.H. Luong, X. Zhang, Implantable electrochemical sensors for biomedical and clinical applications: progress, problems, and future possibilities. Curr. Med. Chem. **14**, 937–951 (2007)

96. M.O. Schurr, S. Schostek, C.N. Ho, F. Rieber, A. Menciassi, Microtechnologies in medicine: an overview. Minim. Invasiv. Ther. **16**, 76–86 (2007)
97. C. Vepari, D.L. Kaplan, Silk as a Biomaterial. Prog. Polym. Sci. **32**, 991–1007 (2007)
98. D.H. Kim, Y.S. Kim, J. Amsden, B. Panilaitis, D.L. Kaplan, F.G. Omenetto, M.R. Zakin, J.A. Rogers, Silicon electronics on silk as a path to bioresorbable, implantable devices. Appl. Phys. Lett. **95**, 133701 (2009)
99. K.G. Ong, C.A. Grimes, C.L. Robbins, R.S. Singh, Design and application of a wireless, passive, resonant-circuit environmental monitoring sensor. Sens. Actuators, A **93**, 33–43 (2001)
100. K.G. Ong, J. Wang, R.S. Singh, L.G. Bachas, C.A. Grimes, Monitoring of bacteria growth using a wireless, remote query resonant-circuit sensor: application to environmental sensing. Biosens. Bioelectron. **16**, 305–312 (2001)
101. A.C. Ferrari, J.C. Meyer, V. Scardaci, C. Casiraghi, M. Lazzeri, F. Mauri, S. Piscanec, D. Jiang, K.S. Novoselov, S. Roth, A.K. Geim, Raman spectrum of graphene and graphene layers. Phys. Rev. Lett. **97**, 187401 (2006)
102. J.A. Timlin, A. Carden, M.D. Morris, R.M. Rajachar, D.H. Kohn, Raman spectroscopic imaging markers for fatigue-related microdamage in bovine bone. Anal. Chem. **72**, 2229–2236 (2000)
103. U.B. Schaad, Which number of infecting bacteria is of clinical relevance? Infection **11**(Suppl 2), S87–89 (1983)
104. G.A. Zelada-Guillen, J. Riu, A. Duzgun, F.X. Rius, Immediate detection of living bacteria at ultralow concentrations using a carbon nanotube based potentiometrie aptasensor. Angew. Chem. Int. Ed. Engl. **48**, 7334–7337 (2009)
105. P. Belgrader, W. Benett, D. Hadley, J. Richards, P. Stratton, R. Mariella Jr., F. Milanovich, PCR detection of bacteria in seven minutes. Science **284**, 449–450 (1999)
106. Y. Li, Y.T. Cu, D. Luo, Multiplexed detection of pathogen DNA with DNA-based fluorescence nanobarcodes. Nat. Biotechnol. **23**, 885–889 (2005)
107. Y. Cui, S.N. Kim, S.E. Jones, L.L. Wissler, R.R. Naik, M.C. McAlpine, Chemical functionalization of graphene enabled by phage displayed peptides. Nano Lett. **10**, 4559–4565 (2010)
108. M.J. Pender, L.A. Sowards, J.D. Hartgerink, M.O. Stone, R.R. Naik, Peptide-mediated formation of single-wall carbon nanotube composites. Nano Lett. **6**, 40–44 (2006)
109. M. Zelzer, R.V. Ulijn, Next-generation peptide nanomaterials: molecular networks, interfaces and supramolecular functionality. Chem. Soc. Rev. **39**, 3351–3357 (2010)
110. M.S. Mannoor, S. Zhang, A.J. Link, M.C. McAlpine, Electrical detection of pathogenic bacteria via immobilized antimicrobial peptides. Proc. Natl. Acad. Sci. USA. **107**, 19207–19212 (2010)
111. N.V. Kulagina, K.M. Shaffer, G.P. Anderson, F.S. Ligler, C.R. Taitt, Antimicrobial peptide-based array for *Escherichia coli* and *Salmonella* screening. Anal. Chim. Acta. **575**, 9–15 (2006)
112. M. Zasloff, Antimicrobial peptides of multicellular organisms. Nature **415**, 389–395 (2002)
113. L. Chen, Y. Li, J. Li, X. Xu, R. Lai, Q. Zou, An antimicrobial peptide with antimicrobial activity against *Helicobacter pylori*. Peptides **28**, 1527–1531 (2007)
114. S.N. Kim, Z. Kuang, J.M. Slocik, S.E. Jones, Y. Cui, B.L. Farmer, M.C. McAlpine, R.R. Naik, Preferential binding of peptides to graphene edges and planes. J. Am. Chem. Soc. **133**, 14480–14483 (2011)
115. M.A. Beard-Pegler, E. Stubbs, A.M. Vickery, Observations on the resistance to drying of staphylococcal strains. J. Med. Microbiol. **26**, 251–255 (1988)
116. M.A. Beard-Pegler, A.M. Vickery, Lysogenicity of methicillin-resistant strains of *Staphylococcus aureus*. J. Med. Microbiol. **20**, 147–155 (1985)
117. R.A. Potyrailo, W.G. Morris, Multianalyte chemical identification and quantitation using a single radio frequency identification sensor. Anal. Chem. **79**, 45–51 (2007)
118. N. Strand, A. Bhushan, M. Schivo, N.J. Kenyon, C.E. Davis, Chemically polymerized polypyrrole for on-chip concentration of volatile breath metabolites. Sens. Actuators B **143**, 516–523 (2010)

119. M. Phillips, Method for the collection and assay of volatile organic compounds in breath. Anal. Biochem. **247**, 272–278 (1997)
120. S. Webb, Attacks on asthma. Nat. Biotechnol. **29**, 860–863 (2011)
121. R. Beasley, J. Crane, C.K. Lai, N. Pearce, Prevalence and etiology of asthma. J. Allergy Clin. Immunol. **105**, 466–472 (2000)
122. World Health Organization, *W. H. O. Global surveillance, prevention and control of chronic respiratory diseases: a comprehensive approach*. (World Health Organization, Switzerland, 2007)
123. S. Kazani, E. Israel, Update in Asthma. Am. J. Respir. Crit. Care Med. **184**, 291–296 (2011)
124. L.J. Akinbami, K.C. Schoendorf, Trends in childhood asthma: prevalence, health care utilization, and mortality. Pediatrics **110**, 315–322 (2002)
125. P.A. Eggleston, Environmental causes of asthma in inner city children. The national cooperative inner city asthma study. Clin. Rev. Allergy Immunol. **18**, 311–324 (2000)
126. H. Pinnock, R. Shah, Asthma. BMJ **334**, 847–850 (2007)
127. American Thoracic Society/European Respiratory Society (ATS/ERS) recommendations for standardized procedures for the online and offline measurement of exhaled lower respiratory nitric oxide and nasal nitric oxide, 2005. Am. J. Respir. Crit. Care Med. **171**, 912–930 (2005)
128. R.F. Lemanske, W.W. Busse, Asthma: clinical expression and molecular mechanisms. J. Allergy Clin. Immunol. **125**, 95–102 (2010)
129. F.D. Martinez, Development of wheezing disorders and asthma in preschool children. Pediatrics **109**, 362–367 (2002)
130. A.L. Lefkovitz, B.J. Zarowitz, Is that case of asthma really COPD, and does the diagnosis matter? Geriatr. Nur. (Lond.). **30**, 409–413 (2009)
131. P.J. Barnes, Immunology of asthma and chronic obstructive pulmonary disease. Nat. Rev. Immunol. **8**, 183–192 (2008)
132. S.T. Holgate, R. Polosa, Treatment strategies for allergy and asthma. Nat. Rev. Immunol. **8**, 218–230 (2008)
133. J.C. Renauld, New insights into the role of cytokines in asthma. J. Clin. Pathol. **54**, 577–589 (2001)
134. C.M. Robroeks, Q. Jobsis, J.G. Damoiseaux, P.H. Heijmans, P.P. Rosias, H.J. Hendriks, E. Dompeling, Cytokines in exhaled breath condensate of children with asthma and cystic fibrosis. Ann. Allergy Asthma. Immunol. **96**, 349–355 (2006)
135. C.M. Robroeks, G.T. Rijkers, Q. Jobsis, H.J. Hendriks, J.G. Damoiseaux, L.J. Zimmermann, O.P. van Schayck, E. Dompeling, Increased cytokines, chemokines and soluble adhesion molecules in exhaled breath condensate of asthmatic children. Clin. Exp. Allergy. **40**, 77–84 (2010)
136. T. Ichinose, K. Sadakane, H. Takano, R. Yanagisawa, M. Nishikawa, I. Mori, H. Kawazato, A. Yasuda, K. Hiyoshi, T. Shibamoto, Enhancement of mite allergen-induced eosinophil infiltration in the murine airway and local cytokine/chemokine expression by Asian sand dust. J. Toxicol. Environ. Health A **69**, 1571–1585 (2006)
137. S.K. Shahid, S.A. Kharitonov, N.M. Wilson, A. Bush, P.J. Barnes, Increased interleukin-4 and decreased interferon-gamma in exhaled breath condensate of children with asthma. Am. J. Respir. Crit. Care Med. **165**, 1290–1293 (2002)
138. W. Chen, Z. Lu, C.M. Li, Sensitive human interleukin 5 impedimetric sensor based on polypyrrole-pyrrolepropylic acid-gold nanocomposite. Anal. Chem. **80**, 8485–8492 (2008)
139. H.H.H. Shen, S.I. Ochkur, M.P. McGarry, J.R. Crosby, E.M. Hines, M.T. Borchers, H.Y. Wang, T.L. Biechelle, K.R. O'Neill, T.L. Ansay, D.C. Colbert, S.A. Cormier, J.P. Justice, N.A. Lee, J.J. Lee, A causative relationship exists between eosinophils and the development of allergic pulmonary pathologies in the mouse. J. Immunol. **170**, 3296–3305 (2003)
140. C.J. Sanderson, Interleukin-5, eosinophils, and disease. Blood **79**, 3101–3109 (1992)
141. K. Takatsu, A. Tominaga, N. Harada, S. Mita, M. Matsumoto, T. Takahashi, Y. Kikuchi, N. Yamaguchi, T cell-replacing factor (TRF)/interleukin 5 (IL-5): molecular and functional properties. Immunol. Rev. **102**, 107–135 (1988)

142. J. Hunt, Exhaled breath condensate: an evolving tool for noninvasive evaluation of lung disease. J. Allergy Clin. Immunol. **110**, 28–34 (2002)
143. G.M. Mutlu, K.W. Garey, R.A. Robbins, L.H. Danziger, I. Rubinstein, Collection and analysis of exhaled breath condensate in humans. Am. J. Respir. Crit. Care Med. **164**, 731–737 (2001)
144. A. Koch, J. Knobloch, C. Dammhayn, M. Raidl, A. Ruppert, H. Hag, D. Rottlaender, K. Muller, E. Erdmann, Effect of bacterial endotoxin LPS on expression of INF-gamma and IL-5 in T-lymphocytes from asthmatics. Clin. Immunol. **125**, 194–204 (2007)
145. L. Borg, J. Kristiansen, J.M. Christensen, K.F. Jepsen, L.K. Poulsen, Evaluation of accuracy and uncertainty of ELISA assays for the determination of interleukin-4, interleukin-5, interferon-gamma and tumor necrosis factor-alpha. Clin. Chem. Lab. Med. **40**, 509–519 (2002)
146. M. Tary-Lehmann, D.E. Hricik, A.C. Justice, N.S. Potter, P.S. Heeger, Enzyme-linked immunosorbent assay spot detection of interferon-gamma and interleukin 5-producing cells as a predictive marker for renal allograft failure. Transplantation **66**, 219–224 (1998)
147. R.M. Effros, R. Casaburi, J. Su, M. Dunning, J. Torday, J. Biller, R. Shaker, The effects of volatile salivary acids and bases on exhaled breath condensate pH. Am. J. Respir. Crit. Care Med. **173**, 386–392 (2006)
148. I. Horvath, J. Hunt, P.J. Barnes, K. Alving, A. Antczak, E. Baraldi, G. Becher, W.J. van Beurden, M. Corradi, R. Dekhuijzen, R.A. Dweik, T. Dwyer, R. Effros, S. Erzurum, B. Gaston, C. Gessner, A. Greening, L.P. Ho, J. Hohlfeld, Q. Jobsis, D. Laskowski, S. Loukides, D. Marlin, P. Montuschi, A.C. Olin, A.E. Redington, P. Reinhold, E.L. van Rensen, I. Rubinstein, P. Silkoff, K. Toren, G. Vass, C. Vogelberg, H. Wirtz, Exhaled breath condensate: methodological recommendations and unresolved questions. Eur. Respir. J. **26**, 523–548 (2005)
149. K.S. Novoselov, D. Jiang, F. Schedin, T.J. Booth, V.V. Khotkevich, S.V. Morozov, A.K. Geim, Two-dimensional atomic crystals. Proc. Natl. Acad. Sci. USA. **102**, 10451–10453 (2005)
150. E.D. Minot, A.M. Janssens, I. Heller, H.A. Heering, C. Dekker, S.G. Lemay, Carbon nanotube biosensors: the critical role of the reference electrode. Appl. Phys. Lett. **91**, 093507 (2007)
151. T. Lohmann, K. von Klitzing, J.H. Smet, Four-terminal magneto-transport in graphene p-n junctions created by spatially selective doping. Nano Lett. **9**, 1973–1979 (2009)
152. F. Schwierz, Graphene transistors. Nat. Nanotech. **5**, 487–496 (2010)
153. A. Pirkle, J. Chan, A. Venugopal, D. Hinojos, C.W. Magnuson, S. McDonnell, L. Colombo, E.M. Vogel, R.S. Ruoff, R.M. Wallace, The effect of chemical residues on the physical and electrical properties of chemical vapor deposited graphene transferred to SiO_2. Appl. Phys. Lett. **99**, 122108 (2011)
154. M.Y. Yeh, E.L. Burnham, M. Moss, L.A. Brown, Non-invasive evaluation of pulmonary glutathione in the exhaled breath condensate of otherwise healthy alcoholics. Respir. Med. **102**, 248–255 (2008)
155. T. Ueno, M. Kataoka, A. Hirano, K. Iio, Y. Tanimoto, A. Kanehiro, C. Okada, R. Soda, K. Takahashi, M. Tanimoto, Inflammatory markers in exhaled breath condensate from patients with asthma. Respirology **13**, 654–663 (2008)
156. J.N. Israelachvili, *Intermolecular and Surface Forces*, 3rd edn. (Academic, USA 2011)
157. E. Stern, R. Wagner, F.J. Sigworth, R. Breaker, T.M. Fahmy, M.A. Reed, Importance of the Debye screening length on nanowire field effect transistor sensors. Nano Lett. **7**, 3405–3409 (2007)
158. S. Sorgenfrei, C.Y. Chiu, M. Johnston, C. Nuckolls, K.L. Shepard, Debye screening in single-molecule carbon nanotube field-effect sensors. Nano Lett. **11**, 3739–3743 (2011)
159. R.J. Chen, Y. Zhang, D. Wang, H. Dai, Noncovalent sidewall functionalization of single-walled carbon nanotubes for protein immobilization. J. Am. Chem. Soc. **123**, 3838–3839 (2001)

160. D.W. Boukhvalov, M.I. Katsnelson, Chemical functionalization of graphene with defects. Nano Lett. **8**, 4373–4379 (2008)
161. P.R. Nair, M.A. Alam, Screening-limited response of nanobiosensors. Nano Lett. **8**, 1281–1285 (2008)
162. K. Cung, R.L. Slater, Y. Cui, S.E. Jones, H. Ahmad, R.R. Naik, M.C. McAlpine, Rapid, multiplexed microfluidic phage display. Lab Chip. **12**, 562–565 (2012)
163. L. Clifton, D.A. Clifton, M.A.F. Pimentel, P.J. Watkinson, L. Tarassenko, Predictive monitoring of mobile patients by combining clinical observations with data from wearable sensors. IEEE J. Biomed. Health. **18**, 722–730 (2014)

Chapter 10
Functionalized Carbon Nanodots for Biomedical Applications

Yun Kyung Jung, Yuri Choi and Byeong-Su Kim

10.1 Introduction

The use of biological labels has greatly assisted the study of complex biochemical interactions and the monitoring of their localization during disease diagnosis and therapy. Fluorescent labeling using organic fluorophores, genetically encoded fluorescent proteins, and semiconducting quantum dots (QDs) has been demonstrated as an indispensable tool for both in vivo and in vitro cellular imaging [1–5]. In contrast to the conventional organic dyes and the fluorescent proteins showing several deficiencies like broad-spectrum profiles, very short excited-state lifetimes, and their sensitivity to photobleaching, QDs have been intensively studied as a promising luminescent probe due to high resistance to photobleaching, large stokes shift, narrow size-dependent emission spectra, broad excitation spectra, and long fluorescence lifetime [1–5]. In addition, they have been engineered to carry therapeutic agents for simultaneous diagnosis and therapy (theranostics). Despite these notable advantages, the implementation of QDs to a broader clinical setting is still limited because of their intrinsic toxicity and the potential environmental concerns associated with the heavy metals present in the QDs.

In an attempt to develop benign alternatives, new kinds of nanoparticles with combined properties of carbon-based materials and QDs, such as graphene QDs (GQDs)[6–12] and carbon nanodots (also known as C-dots, carbon dots (CDs)) [12–25], have emerged. The GQDs, which are small graphene fragments with diameters below 30 nm, are fabricated by fragmentation or cutting from graphene oxide, and they have been used to deliver drugs to cells. However, because their fluorescence intensity is weak, and their emission wavelength often overlaps with cellular autofluorescence [8], the GQDs have limited application for biolabels.

Another carbon nanoparticle, the CD has emerged as a promising class of biolabels by virtue of their biocompatibility, low toxicity, tunable photoluminescence,

B.-S. Kim (✉) · Y. K. Jung
Department of Chemistry, School of Natural Science, Ulsan, Republic of Korea
e-mail: bskim19@unist.ac.kr

Y. Choi · B.-S. Kim
Department of Energy Engineering, School of Energy and Chemical Engineering, UNIST, Ulsan 689-798, Republic of Korea

M. Zhang et al. (eds.), *Carbon Nanomaterials for Biomedical Applications,*
Springer Series in Biomaterials Science and Engineering 5,
DOI 10.1007/978-3-319-22861-7_10

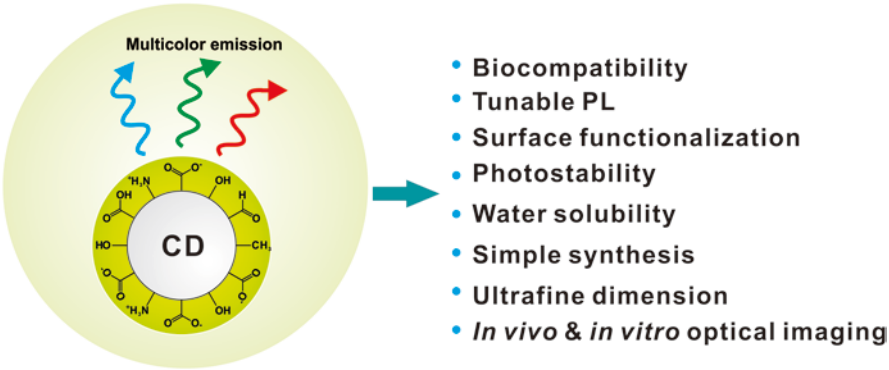

Fig. 10.1 Advantages of carbon dots (CDs) for optical imaging and drug delivery

high chemical/photostability, and mass production by a simple preparation method, while retaining the advantageous photophysical features of QDs (Fig. 10.1) [12–16]. The fluorescence emission spectra of CDs exhibited an excitation-dependent feature, which is quite different from that of QDs and organic dyes, enabling multicolor fluorescence detection for in vitro optical imaging [17–19]. Furthermore, the CDs are generally composed of a mixed phase of sp^2- and sp^3-hybridized carbon nanostructures in the form of conjugated carbon clusters functionalized with oxygen-bearing functional groups [17]. Aside the strong fluorescence of CDs, their unique chemical structure allows the integration of active therapeutic molecules into the sp^2 carbon frame via strong π–π interactions, and their surface functional groups enable further conjugation with other molecules such as biological affinity ligands. These unique characteristics make CDs ideal drug carriers, which lead to advances in personalized medicine [20–25]. Therefore, in this chapter, the application of the CDs for photodynamic therapy (PDT) and chemotherapy is discussed, and enhanced therapeutic efficacy of drugs by CD-aided delivery is evaluated in vitro and in vivo.

10.2 CD-Based Photodynamic Therapy for Cancer In Vitro and In Vivo

Due to high fluorescence and photostability, CDs have gained attention as biolabeling materials [16]. Also, with sp^2 carbon structure and the abundant functional groups, CDs can be easily functionalized with biological affinity ligands and act as drug carriers in aqueous solution [17].

Recently, as photosensitizer (PS) carrier for PDT, highly biocompatible and fluorescent CDs were developed (Fig. 10.2) [21]. With oxygen functional groups, the

surface of the CD was subsequently passivated with poly(ethylene glycol) diamine (PEG) and folic acid (FA) to enhance its fluorescence as well as increase the affinity for cancerous cells [21, 26]. As a second-generation PS, zinc phthalocyanine (ZnPc) possesses good cytotoxic efficiency. This carbon nanomaterial (CD–PEG–FA) has dual ability, which is simultaneous biological imaging and targeted PDT in vitro and in vivo.

In fluorescence spectrum, the fluorescence emission maxima of CD–PEG–FA were located at 450 nm and excited at 360 nm (Fig. 10.3a). Also, 10.9 % of quantum yield and 5.52 ns of the exciton lifetime were calculated. The broad UV/vis absorption represented the successful functionalization of FA onto the CD surface from the peak at 283 nm, and CD–PEG–FA displayed bright blue emission under UV irradiation (Fig. 10.3b). Furthermore, Fourier-transform infrared (FT-IR) spectroscopy revealed changes in the chemical functional groups on the CDs upon surface passivation. After passivation with PEG and FA, CD–PEG–FA exhibited characteristic peaks at the peak 1102 cm^{-1} from C–O groups of PEG and 1481, 1605, and 1697 cm^{-1} which corresponded to FA (Fig. 10.3c) [27]. The transmission electron microscopy (TEM) images showed a spherical morphology of the CDs with an average diameter of 4.5 ± 0.2 nm for CD–PEG–FA (Fig. 10.3d). The interlayer spacing of 0.34 nm, observed using high-resolution TEM, corresponded to that of graphitic carbon, representing the graphitic nature of the CDs. For photodynamic therapy, CD–PEG–FA/ZnPc composite was synthesized via π-π stacking interaction, which had 60 μg of ZnPc per milligram of CD–PEG–FA (Fig. 10.3e).

To confirm the efficacy of CD–PEG–FA and CD–PEG–FA/ZnPc in targeted bioimaging, the targeting of CDs was evaluated after incubation with the HeLa cells for 12 h, by monitoring the blue and red fluorescence of CD ($\lambda_{ex}/\lambda_{em}$ = 358/461 nm) and ZnPc ($\lambda_{ex}/\lambda_{em}$ = 647/665 nm), respectively (Fig. 10.4). As a result, the cells incubated with CD–PEG–FA displayed intense CD fluorescence in the cytoplasm, and CD–PEG–FA/ZnPc showed prominent fluorescence signals of both the blue (CD) and red (ZnPc) channels, indicating the successful intracellular delivery of ZnPc by the CD carrier. To clarify the targeting role of FA, a competition assay was performed with free FA, which resulted to no cellular internalization. This result indicated that CD–PEG–FA successfully targeted to cancer cell.

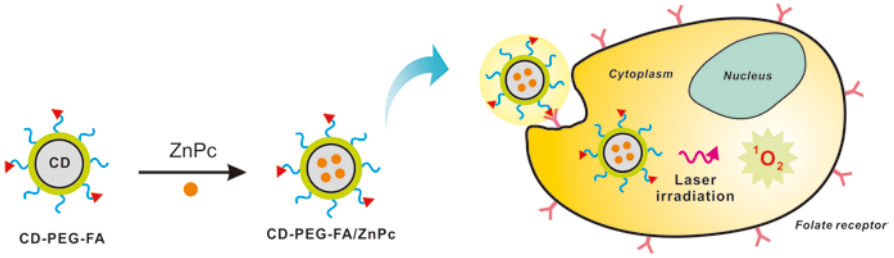

Fig. 10.2 Schematic illustration of targeted PDT with folic-acid-functionalized carbon nanodots loaded with zinc phthalocyanine (CD–PEG–FA/ZnPc)

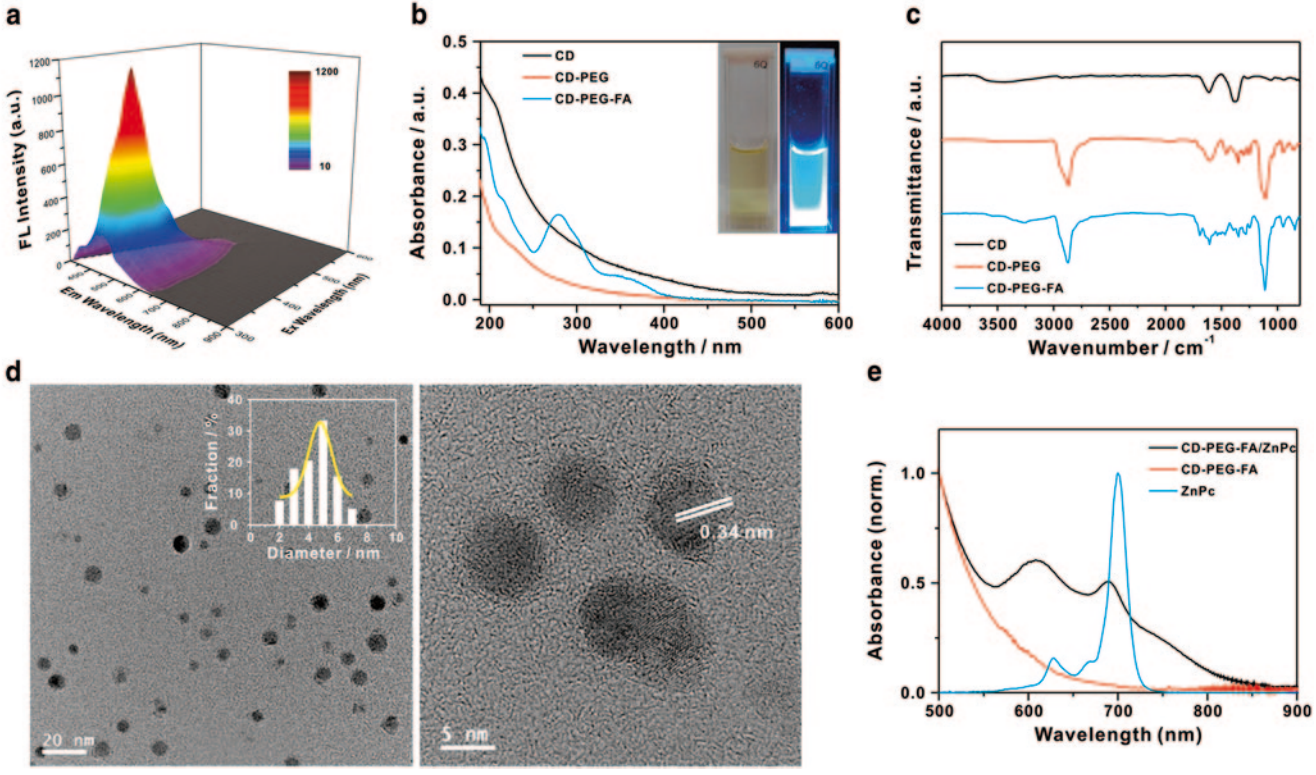

Fig. 10.3 **a** Three-dimensional fluorescence spectra of CD–PEG–FA under varying excitation wavelengths from 300 to 600 nm with 10-nm increments. **b** UV–vis absorbance spectra of CD, CD–PEG, and CD–PEG–FA. **c** FT-IR spectra of CD, CD–PEG, and CD–PEG–FA. **d** TEM images of CD–PEG–FA with a corresponding size distribution histogram. Inset shows the CD–PEG–FA suspension *(left)* under room light and *(right)* UV illumination at 365 nm. **e** UV–vis absorbance spectra of *(red)* CD–PEG–FA, *(black)* CD–PEG–FA/ZnPc, and *(blue)* free ZnPc.

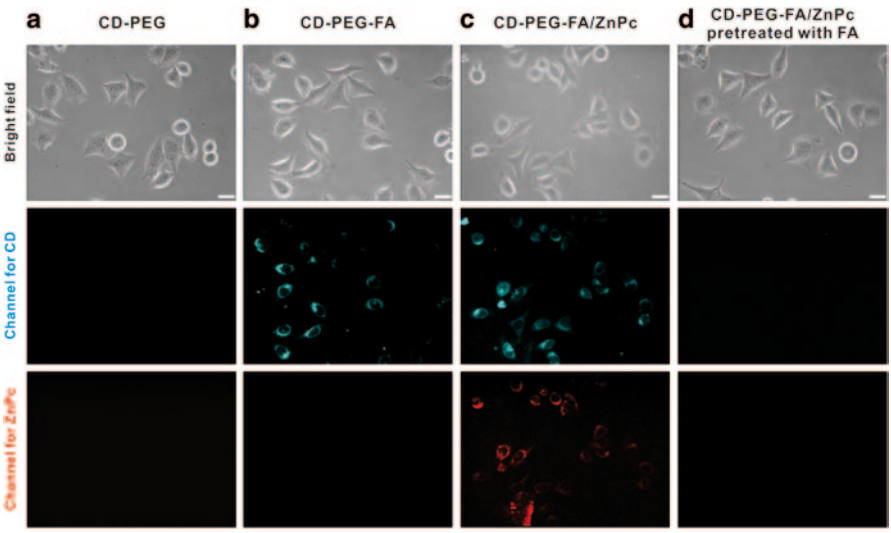

Fig. 10.4 (**a**–**d**) Bright-field and fluorescence images of HeLa cells treated with CD derivatives (50 μg/ml) for 12 h. **a** CD–PEG, **b** CD–PEG–FA, **c** CD–PEG–FA/ZnPc, and **d** CD–PEG–FA/ZnPc pretreated with FA. Fluorescence signals of *(blue)* CDs and *(red)* ZnPc were observed at 461 (λ_{ex} = 358 nm) and 665 nm (λ_{ex} = 647 nm), respectively. Scale bar is 20 μm

PDT was performed on the HeLa cells with the CD derivatives. CD–PEG–FA/ZnPc exhibited excellent PDT efficiency with significant cell death, whereas other samples treated with CD–PEG, CD–PEG–FA and FA-pretreated CD–PEG–FA/ZnPc did not exhibit measurable photodynamic activity (Fig. 10.5a–d).

In addition, the generation of the active singlet oxygen species via photoinduced energy transfer from ZnPc was quantified by using the singlet oxygen sensor green (SOSG) reagent, which reacts with singlet oxygen generated from the PS [28, 29]. Figure 10.6a showed the fluorescence intensity as a function of irradiation time; the intensity gradually increased upon irradiation with a light-emitting diode (LED; 30 mW/cm^2). While the control ZnPc without SOSG did not exhibit any fluorescence changes, ZnPc and CD–PEG–FA/ZnPc mixed with SOSG showed an increase in the fluorescence intensity upon irradiation. Because of intermolecular energy transfer between ZnPc and CD, the CD–PEG–FA/ZnPc did not effectively generate singlet oxygen relative to free ZnPc with SOSG. However, singlet oxygen generation was considerably accelerated upon the addition of cell lysate (Fig. 10.6a, t = 25 min), indicating the release of ZnPc from CD via the competitive displacement of ZnPc by interaction with the biomolecules in cell lysate, thus enhancing the therapeutic efficiency of PDT (Fig. 10.6b).

Encouraged by the high PDT efficacy in vitro, the PDT efficacy of the CD-mediated PS delivery system in animal models was investigated. As shown in Fig. 10.7a, b, the mice treated with CD–PEG–FA/ZnPc showed strong fluorescence signals

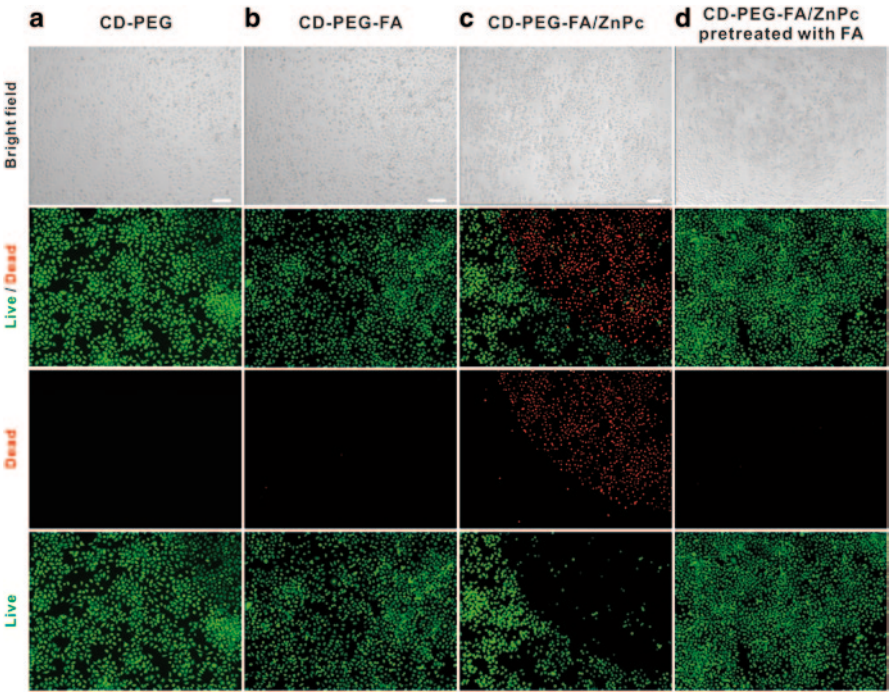

Fig. 10.5 (**a**–**d**; *top* panel) Bright-field and fluorescence images of HeLa cells treated with CD derivatives (50 μg/ml) for 12 h, followed by irradiation for 10 min with a 660-nm laser (30 mW/cm^2), and (*bottom* panels) live and dead cells colored *green* and *red,* respectively, by live/dead assay. **a** CD–PEG, **b** CD–PEG–FA, **c** CD–PEG–FA/ZnPc, and **d** CD–PEG–FA/ZnPc with pretreatment of excess free FA. Scale bar is 100 μm

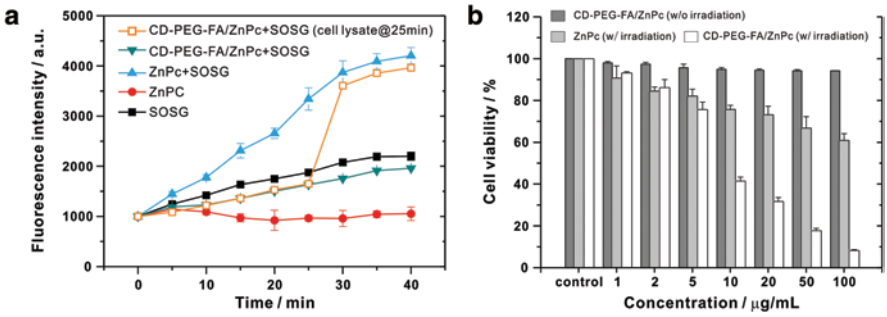

Fig. 10.6 Quantitative evaluation of photodynamic effect. **a** Singlet oxygen detection test using an SOSG reagent. Time-dependent fluorescent intensity ($\lambda_{ex}/\lambda_{em}$ = 504/530 nm) with irradiation by using a 660-nm laser (30 mW/cm^2). **b** Cell viability assay depending on the concentration of ZnPc-loaded CD–PEG–FA and ZnPc with and without irradiation for 10 min

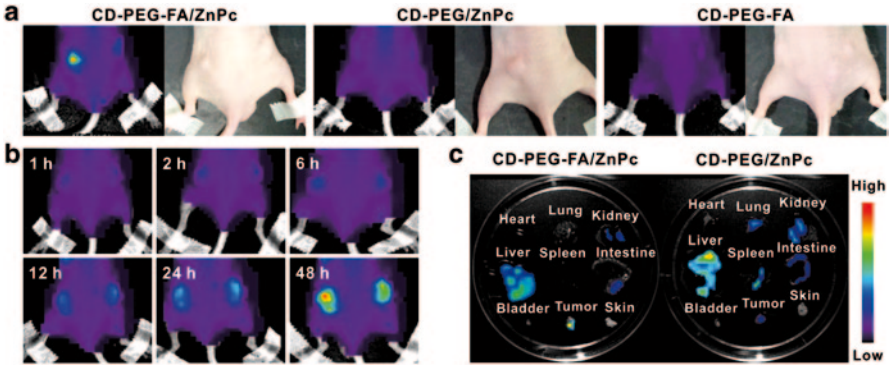

Fig. 10.7 **a** Fluorescence of ZnPc (excited at 660 nm) in tumor was imaged after a 12-h injection of CD–PEG–FA/ZnPc, CD–PEG/ZnPc, and CD–PEG–FA (0.5 mg of ZnPc/kg mouse). **b** CD–PEG–FA/ZnPc suspensions were injected into tail veins of tumor-bearing mice, and the fluorescent signals were obtained at various time points (1, 2, 6, 12, 24, and 48 h). **c** Ex vivo fluorescence images of major organs of mice. The fluorescent signals corresponding to ZnPc (excited at 660 nm) from major organs, tumor, and skin were obtained after 12 h of IV injection of CD–PEG–FA/ZnPc and CD–PEG/ZnPc into tumor-bearing mice. FA-conjugated CD delivered and released ZnPc to tumor effectively, in contrast with the CD lacking FA

corresponding to ZnPc in tumors, with gradual increase in the fluorescence intensity over time, in contrast to the mice treated with CD–PEG/ZnPc or CD–PEG–FA. Fluorescence images of the major organs in Fig. 10.7c showed that the fluorescence corresponding ZnPc were intense in liver and spleen rather than tumor in case of the mouse injected with CD–PEG/ZnPc, suggesting that most of the CDs omitting targeting ligand FA leaked out by circulation and prominently accumulated in reticuloendothelial system of the liver and spleen [30, 31]. These results showed that conjugation of FA to CD played an important role in greatly improving the active tumor-targeting capability of the ZnPc delivery vehicle to folate receptor-overexpressing tumors.

Finally, to investigate the therapeutic efficacy in vivo, changes in tumor volumes were monitored for 10 days after CD–PEG–FA, CD–PEG/ZnPc, and CD–PEG–FA/ZnPc (0.5 mg of ZnPc/kg of mouse) were intravenously injected to mice whose tumor volumes were ~70 mm^3 (Fig. 10.8). After irradiation with a 660-nm laser (0.3 W/cm^2, 20 min), the mice treated with CD–PEG–FA/ZnPc showed remarkable suppression of tumor growth as compared to the control mice for 8 days. However, the mice treated with CD–PEG/ZnPc and CD–PEG–FA, with or without laser irradiation, showed no notable difference in tumor size compared to the controls. Collectively, the in vivo study suggested that the present tumor-targeted CD-based PDT therapeutic agent delivery system can effectively induce the accumulation of the PS-loaded CDs in tumors, thus leading to enhanced therapeutic efficacy with a relatively small quantity of ZnPc.

In conclusion, CD–PEG–FA successfully demonstrated the targeted delivery of a PS via FA-mediated endocytosis of biocompatible CD–PEG–FA/ZnPc and

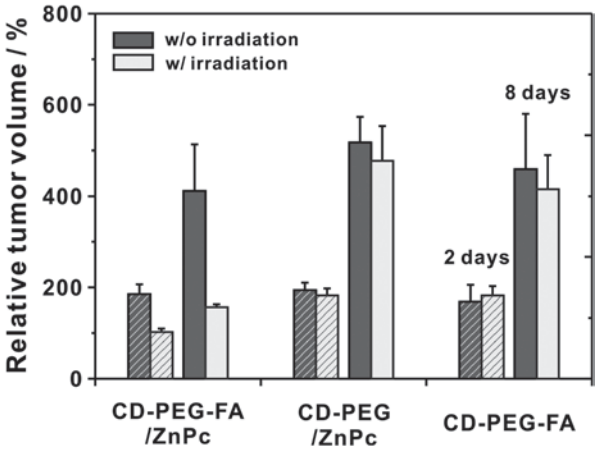

Fig. 10.8 Relative tumor volumes measured over time after the tumor-bearing mice were treated with various CD derivatives

therapeutic photodynamic efficacy by singlet oxygen generation from the internalized ZnPc upon light irradiation in vitro and in vivo. We anticipate that the present CD-based targeted delivery of the PS would offer a convenient and effective platform for enhanced PDT to treat cancers in the near future because of its excellent biocompatibility, bioimaging and targeting capability, and therapeutic efficacy.

10.3 Zwitterionic CD-Based Drug Delivery for Chemotherapy In Vitro and In Vivo

Nuclear-targeting drug-delivery systems (DDSs) have attracted significant attention in the biomedical applications, because they substantially increase the healing efficiency especially for tumor therapy [32–34]. Since many anticancer drugs are required to enter the cell nucleus where the drugs damage the genes to stop proliferation of the cancer cell, the construction of the nuclear-targeting DDSs is crucial to treat the tumors. Typically, for nuclear targeting, carriers need to be functionalized with the proper ligands such as nuclear localization signaling (NLS) peptides (nuclear membrane-penetrating peptides) on the surface [32–34]. Moreover, since the carriers cannot be acted as a fluorescent imaging probe, it should be conjugated with an organic fluorescent dye for tracking the individual drug-delivery event.

The highly luminescent CDs have emerged as a prospective class of biolabels by virtue of their tunable photoluminescence, biocompatibility, low toxicity, and mass production by a simple preparation method [12–25]. Furthermore, the CDs contain an sp^2- and sp^3-hybridized carbon structure that can load aromatic drugs via strong π–π interactions, making them a promising drug carrier for disease treatment. However, most CDs reported to date are localized to the cell cytoplasm, including the lysosomes, mitochondria, Golgi apparatus, and endoplasmic reticulum [12–25]. Therefore, it is evident that the next step in the evolution of CD is enabling it to reach the cell nucleus without being trapped in the cell cytoplasm.

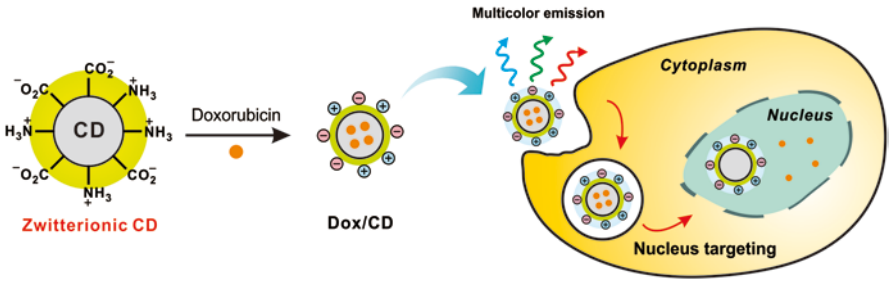

Fig. 10.9 Schematic illustration of the fabrication of doxorubicin-loaded carbon dot (*Dox/CD*), and simultaneous cell imaging and efficient Dox delivery to the nucleus by the zwitterionic *CD* vehicle

Cytoplasmic and nuclear uptake of nanoparticle cargo in live cells can be determined by the size [35] and surface charge [36–39]. In addition, positively charged nanoparticles are preferentially internalized by cells and negatively charged ones interact with nuclei whose pH is consistently 0.3–0.5 units above that of the cytosol [36–39]. Based on this observation, it is expected that the preparation of zwitterionic CDs, with both positively and negatively charged functional groups, can facilitate cytoplasmic uptake and subsequent nuclear translocation of theranostic drug–vehicle conjugates [40–45].

Multifunctional zwitterionic CDs have been fabricated via a simple one-pot synthesis using citric acid (CA) as a carbon source and an amino acid derivative, β-alanine (β-Ala), as a zwitterionic passivating agent, thus avoiding complexity and safety concerns. In vitro study has shown that the synthesized CDs were delivered into cell nuclei by their multicolor fluorescence. Furthermore, the CD-based DDS constructed by the non-covalent grafting of anticancer drug doxorubicin (Dox) not only efficiently accelerated nuclear and tumor accumulation of Dox but also markedly enhanced the cytotoxicity in cancer both in vitro and in vivo, which is superior to many other nanoparticle-based Dox delivery systems (Fig. 10.9).

Zwitterionic CDs with 21.9% of quantum yield showed two characteristic absorption peaks at 248 and 335 nm, which is suggestive of an sp^2 carbon network[19, 21] and the n–π* transition of the carbonyl group [19, 24], respectively (Fig. 10.10a). A bright blue fluorescence under UV light with a maximum emission wavelength at 418 nm was observed upon excitation at 335 nm. Bulk production by a simple manufacturing process is another advantage of CDs over other QDs and GQDs, yielding over a gram-scale powder in a highly efficient manner (average isolated yield over 30%, inset in Fig. 10.10a). The CDs exhibited superior stability in aqueous solution, with a nearly neutral ς-potential (−5.09 ± 6.47 mV) at pH 7, due to the presence of the zwitterionic β-Ala, which has both negatively charged carboxylic acid and positively charged amine moieties. The surface charge of the CDs gradually increased from −44.1 ± 1.63 to 7.73 ± 1.43 mV with a decrease in pH from 11 to 3 (Fig. 10.10b).

FT-IR spectroscopy exhibited that the as-prepared CDs showed peaks at 1174 (C–O stretching), 1772 (C = O stretching), 2947 (C–H stretching), 1708, and

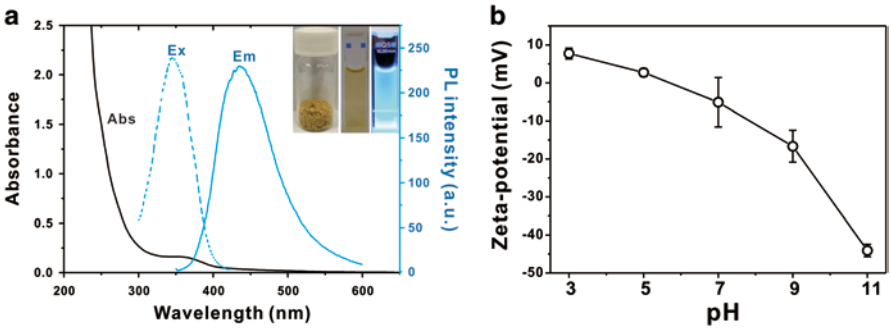

Fig. 10.10 **a** UV–vis absorbance, fluorescence excitation (λ_{em} = 435 nm) and emission (λ_{ex} = 340 nm) spectra of the CDs. Inset shows photographs of the CD powder (*left*), suspension under white light (*middle*), and suspension under UV light at 365 nm (*right*). **b** ς-potential of CDs with respect to pH

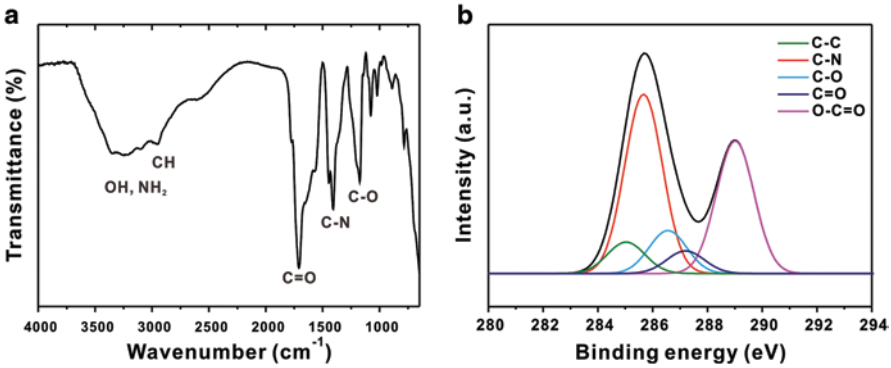

Fig. 10.11 **a** FT-IR spectrum and **b** deconvoluted high-resolution XPS C1s spectra of CD

1616 (the asymmetric and symmetric stretching vibrations of the carboxylate groups (COO^-)), and a broad peak around 3317 cm^{-1} (O–H and N–H stretching; Fig. 10.11a). The successful passivation of β-Ala was confirmed by the presence of amide bond bands at 3095 (N–H stretching) and 1409 cm^{-1} (C–N stretching). High-resolution X-ray photoelectron spectroscopy (XPS) spectra of the CDs further confirmed the successful surface passivation which indicates C–C (285.0 eV), C–N (285.7 eV), C–O (286.6 eV), C = O (287.2 eV), and O–C = O (289.0 eV) groups within CDs (Fig. 10.11b).

Figure 10.12a shows a high-resolution TEM (HRTEM) image of the CDs, revealing that the CDs had spherical shape with an average diameter of 3.09 ± 0.51 nm. In addition, aberration-corrected HRTEM allows to observe the hexagonal unit cells and a crystalline structure with an interlayer spacing of 0.24 nm (Fig. 10.12b), which corresponds to (111) lattice spacing of the graphite hexagons as confirmed by the fast Fourier transform (FFT) profile of a single CD (inset of Fig. 10.12b) [6, 10, 11].

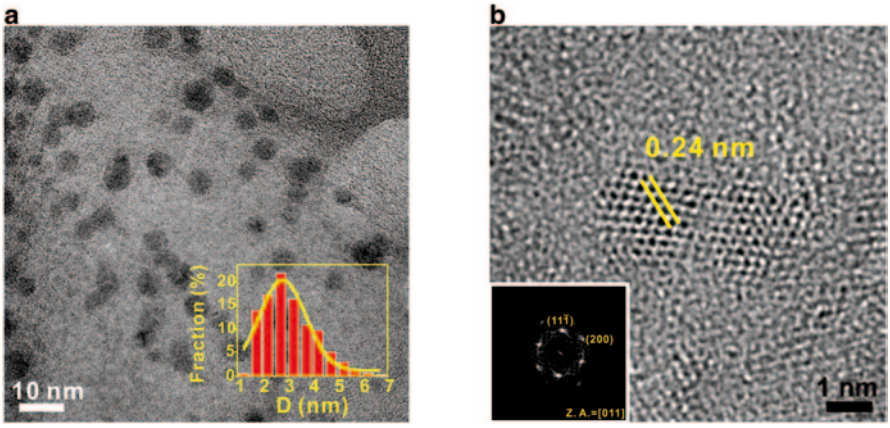

Fig. 10.12 **a**. TEM image of CDs with a corresponding size distribution histogram. **b** High-resolution TEM image showing the arrangement of carbon atoms in CDs with a lattice spacing of 0.24 nm. Inset is the corresponding *FFT* profile of a CD

The fluorescence emission spectra of CDs exhibited an excitation-dependent feature, which is quite different from that of QDs and organic dyes, enabling multicolor fluorescence detection. To evaluate the intracellular uptake and nuclear transport of the CD vehicles, the time-dependent localization of the CDs was studied after incubation with the human cervical cancer cell line, HeLa, for varying lengths of time by monitoring the blue, green, and red multicolor fluorescence signals of CD itself as well as by quantitatively measuring the fluorescence intensity within the cells (Fig. 10.13). The fluorescence of CDs began to appear in the cytoplasm after a 2-h treatment, suggesting that the CDs permeated the cell membrane. After a 6-h incubation, the CDs proceeded to move into the nucleus, a partially delocalized fluorescent signal was observed at the perinuclear region, and similar levels of fluorescence were monitored on both sides. Noticeably, significantly strong fluorescence of the cells after longer incubation periods (24 and 48 h) originates mainly from the nuclei.

The Bio-TEM images further demonstrated the clear nuclear localization of the CDs, in agreement with the strong fluorescence signals appeared in the nucleus after a 24-h incubation (Fig. 10.14). It should be noted that, although the CDs were not modified with any nuclear-targeted signals or chemicals, the CDs were successfully internalized into the cells as well as the nucleus which is attributed to the zwitterionic surface state and small size of CDs.

To use the CDs as a potential drug-delivery vehicle, the cytotoxicity of the CDs was evaluated in normal human WI-38 cells and cancer HeLa cells by 3-(4,5-dimethylthiazol-2-yl)-2,5-diphenyltetrazolium bromide (MTT) assay. The CDs were incubated for 24 h in a dose-dependent manner (10–1000 μg/mL) in triplicate. The CDs displayed remarkably low cytotoxicity (Fig. 10.15), with greater than 95 % cell viability at concentrations up to 500 μg/mL in both cell lines. These results indicate that the CDs are safe as a potential carrier for drug delivery.

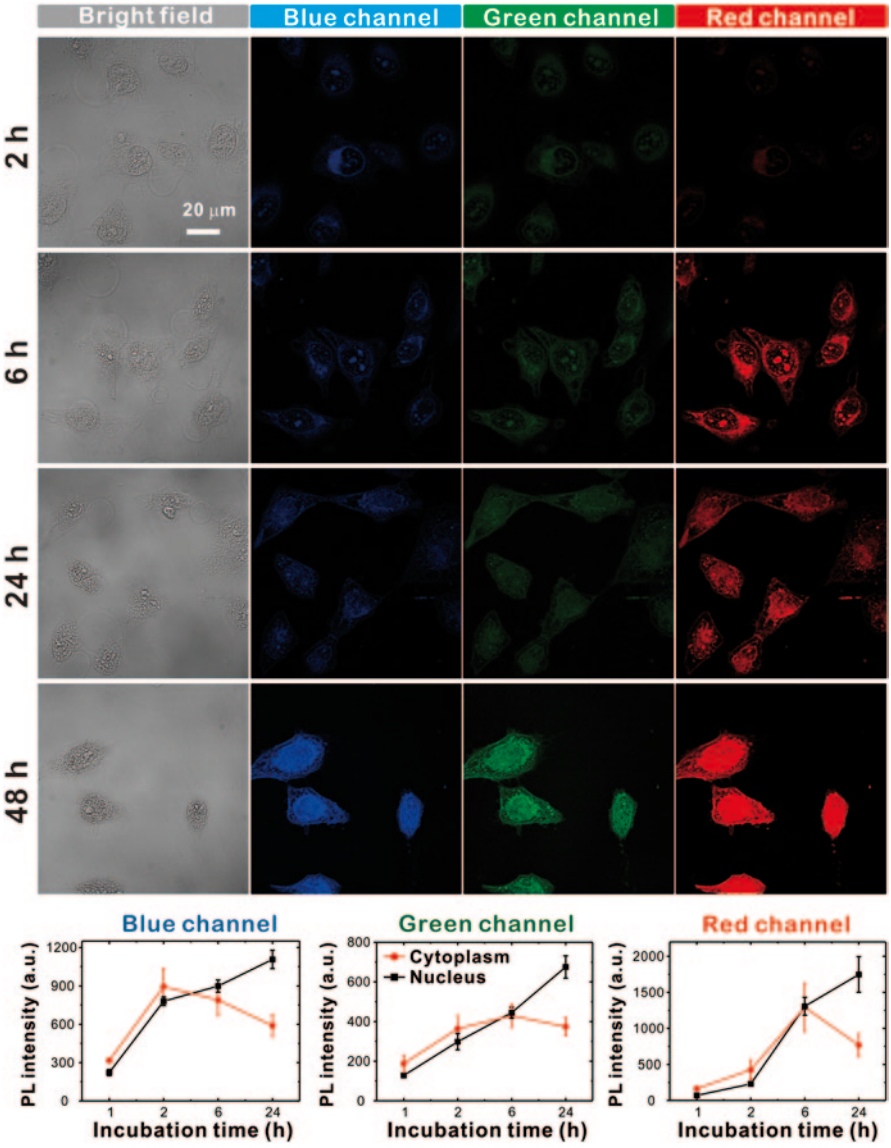

Fig. 10.13 Confocal fluorescence microscopy images showing the cytoplasmic and nuclear transport of CDs in HeLa cells. After treatment with 500 μg/mL CDs for varying amount of time, the *blue, green,* and *red* fluorescence signals of the CDs were observed under ultraviolet (405 nm), *blue* (473 nm), and *green* (559 nm) laser excitations, respectively. The fluorescence intensity in the nucleus and cytoplasm is measured separately and plotted in a time-dependent manner for each channel

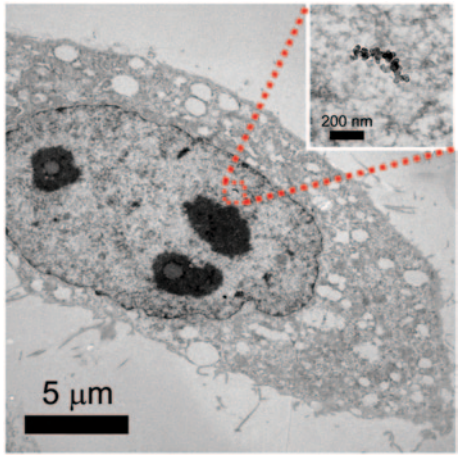

Fig. 10.14 Bio-TEM image of HeLa cells shows nuclear localization of CD. Inset is a zoom-in image of the *red* box in the main image

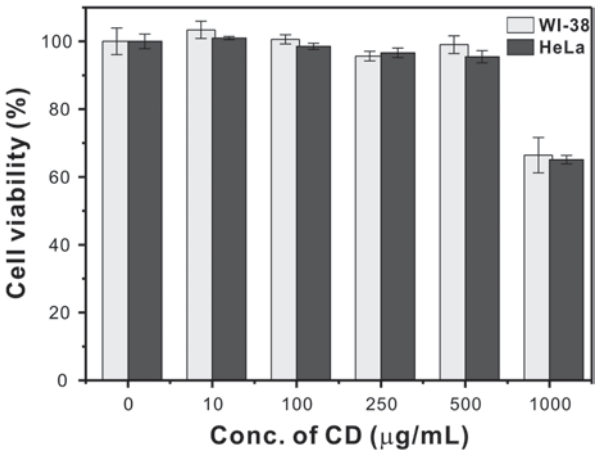

Fig. 10.15 Cell viability of WI-38 and HeLa cells treated with various CD concentrations for 24 h

The well-known anticancer chemotherapeutic drug Doxorubicin (Dox) has been widely used to treat a range of cancers, including cervical, gastric, and lung cancer, because it can directly intercalate with DNA to kill cancer cells [46]. However, when Dox is administered directly without a carrier, it displays low antitumor activity, due to lack of efficiency in reaching the nucleus. The CD-based drug-delivery vehicle was constructed by the non-covalent grafting of the anticancer drug Dox via strong π–π staking interactions between the sp^2-carbon network of CDs and the aromatic structure of Dox [12, 22–24]. The successful loading of Dox onto the CD was evident from the peaks at 339 and 474 nm, arising from respective CD and Dox, resulting in a loading of 14 wt% Dox in the CDs (Fig. 10.16a). Importantly, the ς-potential of the Dox/CD complex remained around zero (−5.92 ± 1.20 mV) at pH 7.0, indicating that the zwitterionic properties were preserved. The anticancer efficacy of Dox was evaluated by treating the HeLa cells with varying Dox or Dox/CD concentrations for 24 h. The HeLa cell viability clearly demonstrated that Dox/CD

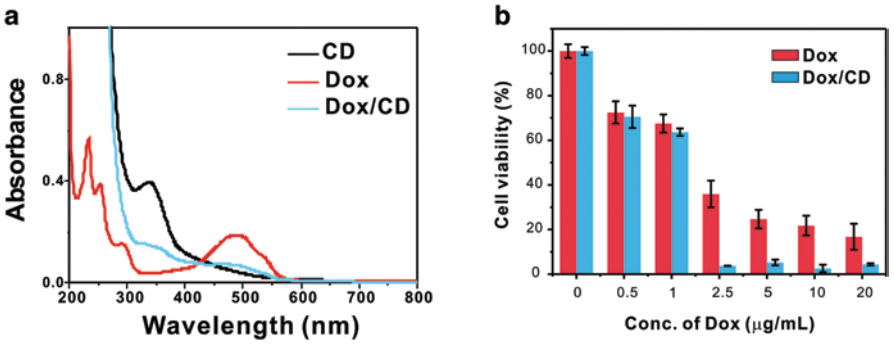

Fig. 10.16 **a** UV–vis absorbance spectra of CDs, Dox, and Dox-loaded CDs (Dox/CD). **b** Cell viability of the HeLa cancer cells exposed to different concentrations of Dox alone and Dox/CD (μg/mL) for 24 h

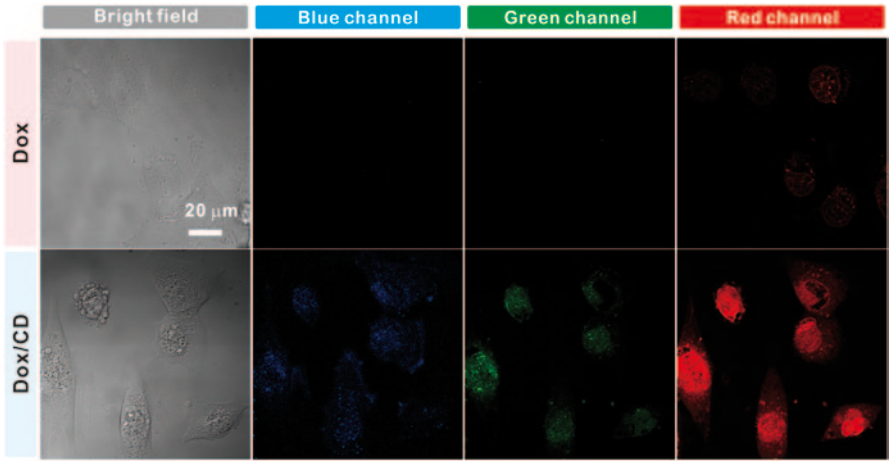

Fig. 10.17 Bright-field and confocal fluorescence images of HeLa cells treated with Dox and Dox/CD (2 μg/mL) for 24 h. Dox/CD delivers Dox to the nucleus more efficiently than Dox alone

considerably improved the therapeutic efficacy through CD-aided delivery, as compared to free Dox (Fig. 10.16b).

Enhanced Dox uptake by the CD carrier was confirmed by monitoring prominent red Dox fluorescence in the nucleus ($\lambda_{ex/em}$ = 480/520–640 nm) under a fluorescence microscope (Fig. 10.17). However, the cells treated with Dox alone showed weak fluorescence in the red channel. Therefore, the Dox/CD complex delivered Dox to the nucleus more efficiently than Dox alone, thereby suppressing cancer cell proliferation and acting as a fluorescent label for intracellular monitoring.

The nanoparticles with zwitterionic surfaces have shown higher colloidal stability over a wide pH range and reduced nonspecific interactions with serum components, thereby prolonging blood circulation for enhanced tumor accumulation

through the enhanced permeability and retention (EPR) effect [40–45]. We evaluated the accumulation of Dox/CD complexes in tumor tissue after intravenous administration into nude mice bearing 4T1-luc2 breast cancer xenografts (Fig. 10.18). 4T1-luc2 cells injected into nude mice were used for tumor induction, as well as monitoring of tumor growth by luminescence of cell itself [47]. To monitor the inhibition of tumor growth by Dox and Dox/CD, each suspension was injected into the tail vein five times at designated time points, and luminescence images of the whole body were collected. Figure 10.18a showed that the mouse with no treatment had fast-growing luminescence signals corresponding to rapid increase in tumor size over time. In contrast, the mice treated with Dox or Dox/CD exhibited moderate or slow increases in luminescence signals. This discrepancy was confirmed by changes in tumor volume (Fig. 10.18b). The tumor inhibition effect of Dox/CD and free Dox treatment was quantitatively analyzed by comparing with tumor volume of no treatment (control) object, displaying 48 and 35 % inhibition of tumor growth, respectively, after 22 days. Based on the results of the in vivo test, inhibition of cancer cell growth was improved with the Dox/CD complex compared to free Dox.

In a separate study, tumor-bearing mice without D-luciferin treatment were intravenously injected with Dox or Dox/CD suspensions after 22 days of post-xenograft implantation (Fig. 10.19). Dox-treated mouse did not show any signal; however, Dox/CD-injected mouse displayed its luminescent signal on the tumor. These re-

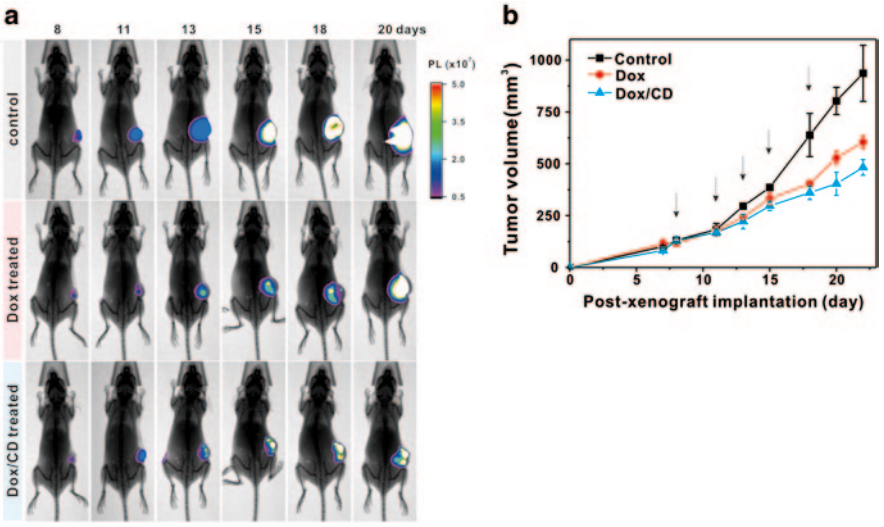

Fig. 10.18 Tumor growth inhibition by Dox/CD in nude mice bearing 4T1-luc2 murine breast cancer xenografts after tail-vein injection of Dox and Dox/CD ($n = 5$, dose: 0.05 mg Dox/kg mouse body weight). **a** Luminescence of 4T1-luc2 cells in tumors was imaged after a 20-min incubation with D-luciferin. Dox and Dox/CD suspensions were injected into the tail veins of tumor-bearing mice after 8, 11, 13, 15, and 18 days of post-xenograft implantation. **b** Volume inhibition (mm^2) of cancer cell following no treatment (control), free Dox, and Dox/CD treatments

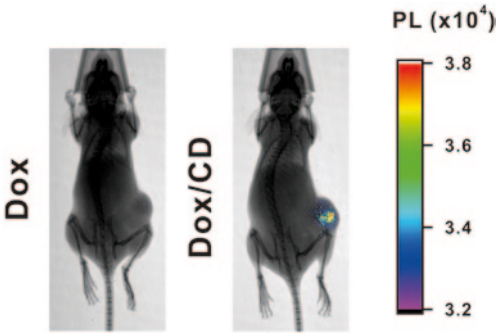

Fig. 10.19 Luminescence images of tumor-bearing mice after intravenous injection of Dox or Dox/CD. Dox/CD-treated mouse shows luminescent signals on tumors

sults indicate that our CDs can emit their photoluminescent signals even in vivo. Thus, the Dox-loaded CD delivery vehicle can effectively enhance the accumulation of Dox in tumors via its zwitterionic properties, consequently leading to an enhanced anticancer effect.

In conclusion, zwitterionic CDs function as an optical probe as well as drug carrier to the cell nucleus and tumors. Therefore, the zwitterionic CDs with good biocompatibility, low cytotoxicity, excellent solubility, and stable photoluminescence are a promising multifunctional platform capable of expediting and sensing the delivery of drugs in a simple and efficient manner.

10.4 Conclusion

CDs have emerged as a new class of promising luminescent nanomaterials as well as attractive vehicles for drug delivery. Their tunable photoluminescence, simple and scalable synthesis, surface engineering, low cost, biocompatibility/nontoxicity, and nonblinking properties make the CDs be used in optical imaging. Furthermore, the ability to easily introduce versatile functionality at the CD surface by rational conjugation chemistry or non-covalent grafting enables them to be a drug/gene-delivery carrier for specific targeting in biomedical applications. Once the CDs with various colors, sizes, and shapes are synthesized and their fundamental properties are understood, the extensive research continues to develop advanced CD-based systems for cancer and PDT.

References

1. F. Wang, W.B. Tan, Y. Zhang, X. Fan, M. Wang, Luminescent nanomaterials for biological labelling. Nanotechnology **17**, R1–R13 (2006)
2. U. Resch-Genger, M. Grabolle, S. Cavaliere-Jaricot, R. Nitschke, T. Nann, Quantum dots versus organic dyes as fluorescent labels. Nat. Method **5**, 763–775 (2008)

3. I.L. Medintz, H.T. Uyeda, E.R. Goldman, H. Mattoussi, Quantum dot bioconjugates for imaging, labelling and sensing. Nat. Mater. **4**, 435–446 (2005)
4. V. Bagalkot, L. Zhang, E. Levy-Nissenbaum, S. Jon, P.W. Kantoff, R. Langer, O.C. Farokhzad, Quantum dot-aptamer conjugates for synchronous cancer imaging, therapy, and sensing of drug delivery based on bi-fluorescence resonance energy transfer. Nano Lett. **7**, 3065–3070 (2007)
5. R. Savla, O. Taratula, O. Garbuzenko, T. Minko, Tumor targeted quantum dot-mucin 1 aptamer-doxorubicin conjugate for imaging and treatment of cancer. J. Control. Release **153**, 16–22 (2011)
6. S. Kim, S.W. Hwang, M.-K. Kim, D.Y. Shin, D.H. Shin, C.O. Kim, S.B. Yang, J.H. Park, E. Hwang, S.-H. Choi, G. Ko, S. Sim, C. Sone, H.J. Choi, S. Bae, B.H. Hong, Anomalous behaviors of visible luminescence from graphene quantum dots: interplay between size and shape. ACS Nano. **6**, 8203–8208 (2012)
7. H. Sun, L. Wu, W. Wei, X. Qu, Recent advances in graphene quantum dots for sensing. Mater. Today **16**, 433–442 (2013)
8. C. Wang, C. Wu, X. Zhou, T.H.X. Xin, J. Wu, J. Zhang, S. Guo, Enhancing cell nucleus accumulation and DNA cleavage activity of anti-cancer drug via graphene quantum dots. Sci. Rep. **3**, 2852 (2013)
9. Z. Wang, J. Xia, C. Zhou, B. Via, Y. Xia, F. Zhang, Y. Li, L. Xia, J. Tang, Synthesis of strongly green-photoluminescent graphene quantum dots for drug carrier. Colloid. Surf. B. **112**, 192–196 (2013)
10. H. Zhu, W. Zhang, S.F. Yu, Realization of lasing emission from graphene quantum dots using titanium dioxide nanoparticles as light scatterers. Nanoscale **5**, 1797–1802 (2013)**.**
11. D. Qu, M. Zheng, L. Zhang, H. Zhao, Z. Xie, X. Jing, R.E. Haddad, H. Fan, Z. Sun, Formation mechanism and optimization of highly luminescent N-doped graphene quantum dots. Sci. Rep. **4**, 5294 (2014)
12. X.T. Zheng, A. Ananthanarayanan, K.Q. Luo, P. Chen, Glowing graphene quantum dots and carbon dots: properties, syntheses, and biological applications. Small **11**, 1620–1636 (2015)
13. S.N. Baker, G.A. Baker, Luminescent carbon nanodots: emergent nanolights. Angew. Chem. Int. Ed. **49**, 6726–6744 (2010)
14. P.G. Luo, S. Sahu, S.-T. Yang, S.K. Sonkar, J. Wang, H. Wang, G.E. LeCroy, L. Cao, Y.-P. Sun, Carbon "quantum" dots for optical bioimaging. J. Mater. Chem. B. **1**, 2116–2127 (2013)
15. P.G. Luo, F. Yang, S.-T. Yang, S.K. Sonkar, L. Yang, J.J. Broglie, Y. Liu, Y.-P. Sun, Carbon-based quantum dots for fluorescence imaging of cells and tissues. RSC Adv. **4**, 10791–10807 (2014)
16. S.T. Yang, L. Cao, P.G.J. Luo, F.S. Lu, X. Wang, H.F. Wang, M.J. Meziani, Y.F. Liu, G. Qi, Y.P. Sun, Carbon dots for optical imaging in vivo. J. Am. Chem. Soc. **131**, 11308–11309 (2009)
17. S.C. Ray, A. Saha, N.R. Jana, R. Sarkar, Fluorescent carbon nanoparticles: synthesis, characterization, and bioimaging application. J. Phys. Chem. C**. 113**, 18546–18551 (2009)
18. Y.-P. Sun, B. Zhou, Y. Lin, W. Wang, K.A.S. Fernando, P. Pathak, M.J. Meziani, B.A. Harruff, X. Wang, H. Wang, P.G. Luo, H. Yang, M.E. Kose, B. Chen, L.M. Veca, S.-Y. Xie, Quantum-sized carbon dots for bright and colorful photoluminescence. J. Am. Chem. Soc. **128**, 7756–7757 (2006)
19. D. Kim, Y. Choi, E. Shin, Y.K. Jung, B.-S. Kim, Sweet nanodot for biomedical imaging: carbon dot derived from xylitol. RSC Adv. **4**, 23210–23213 (2014)
20. C. Liu, P. Zhang, X. Zhai, F. Tian, W. Li, J. Yang, Y. Liu, H. Wang, W. Wang, W. Liu, Nanocarrier for gene delivery and bioimaging based on carbon dots with PEI-passivation enhanced fluorescence. Biomaterials **33**, 3604–3613 (2012)
21. Y. Choi, S. Kim, M.-H. Choi, S.-R. Ryoo, J. Park, D.-H. Min, B.-S. Kim, Highly biocompatible carbon nanodots for simultaneous bioimaging and targeted photodynamic therapy in vitro and in vivo. Adv. Funct. Mater. **24**, 5781–5789 (2014)

22. H.U. Lee, S.Y. Park, E.S. Park, B. Son, S.C. Lee, J.W. Lee, Y.-C. Lee, K.S. Kang, M.I. Kim, H.G. Park, S. Choi, Y.S. Huh, S.-Y. Lee, K.-B. Lee, Y.-K. Oh, J. Lee, Photoluminescent carbon nanotags from harmful cyanobacteria for drug delivery and imaging in cancer cells. Sci. Rep. **4**, 4665 (2014)
23. C.-W. Lai, Y.-H. Hsiao, Y.-K. Peng, P.-T. Chou, Facile synthesis of highly emissive carbon dots from pyrolysis of glycerol; gram scale production of carbon dots/$mSiO_2$ for cell imaging and drug release. J. Mater. Chem. **22**, 14403–14409 (2012)
24. A. Mewada, S. Pandey, M. Thakur, D. Jadhav, M. Sharon, Swarming carbon dots for folic acid mediated delivery of doxorubicin and biological imaging. J. Mater. Chem. B. **2**, 698–705 (2014)
25. P. Pierrat, R. Wang, D. Kereselidze, M. Lux, P. Didier, A. Kichler, F. Pons, L. Lebeau, Efficient *in vitro* and *in vivo* pulmonary delivery of nucleic acid by carbon dot-based nanocarriers. Biomaterials **51**, 290–302 (2015)
26. C.P. Leamon, P.S. Low, Folate-mediated targeting: from diagnostics to drug and gene delivery. Drug. Disc. Today **6**, 44–51 (2001)
27. H. Huang, Q. Yuan, J.S. Shah, R.D.K. Misra, A new family of folate-decorated and carbon nanotube-mediated drug delivery system: synthesis and drug delivery response. Adv. Drug Deliv. Rev. **63**, 1332–1339 (2011)
28. R. Bonnett, Photosensitizers of the Porphyrin and Phthalocyanine series for Photodynamic therapy. Chem. Soc. Rev. **24**, 19–33 (1995)
29. C. Dohmen, T. Frohlich, U. Lachelt, I. Rohl, H.P. Vornlocher, P. Hadwiger, E. Wagner, Defined folate-PEG-siRNA conjugates for receptor-specific gene silencing. Mol. Ther. Nucleic Acid. **1**, e7 (2012)
30. T. Lammers, P. Peschke, R. Kuehnlein, V. Subr, K. Ulbrich, P. Huber, W. Hennink, G. Storm, Effect of Intratumoral Injection on the Biodistribution and the therapeutic potential of HPMA Copolymer-based drug delivery systems. Neoplasia **8**, 788–795 (2006)
31. H.K. Moon, S.H. Lee, H.C. Choi, *In vivo* near-infrared mediated tumor destruction by photothermal effect of carbon nanotubes. ACS Nano. **3**, 3707–3713 (2009)
32. A.K. Oyelere, P.C. Chen, X. Huang, I.H. El-Sayed, M.A. El-Sayed, Peptide-conjugated gold nanorods for nuclear targeting. Bioconjugate Chem. **18**, 1490–1497 (2007)
33. C.-W. Kuo, D.-Y. Chueh, N. Singh, F.-C. Chien, P. Chen, Targeted nuclear delivery using peptide-coated quantum dots. Bioconjugate Chem. **22**, 1073–1080 (2011)
34. A. Jana, B. Saha, D.R. Banerjee, S.K. Ghosh, K.T. Nguyen, X. Ma, Q. Qu, Y. Zhao, N.D.P. Singh, Photocontrolled nuclear-targeted drug delivery by single component photoresponsive fluorescent organic nanoparticles of acridin-9-methanol. Bioconjugate Chem. **24**, 1828–1839 (2013)
35. E.V.B. Gaal, R.S. Oosting, R. Eijk, M. Bakowska, D. Feyen, R.J. Kok, W.E. Hennink, D.J.A. Crommelin, E. Mastrobattista, DNA nuclear targeting sequences for non-viral gene delivery. Pharm. Res. **28**, 1707–1722 (2011)
36. R.R. Arvizo, O.R. Miranda, M.A. Thompson, C.M. Pabelick, R. Bhattacharya, J.D. Robertson, V.M. Rotello, Y.S. Prakash, P. Mukherjee, Effect of nanoparticle surface charge at the plasma membrane and beyond. Nano Lett. **10**, 2543–2548 (2010)
37. R. Lawaczeck, P.K. Nandi, C. Nicolau, Interaction of negatively charged liposomes with nuclear membranes: adsorption, lipid mixing and lysis of the vesicles. Biochim. Biophys. Acta, Biomembr. **903**, 123–131 (1987)
38. O. Seksek, J. Bolard, Nuclear pH gradient in mammalian cells revealed by laser microspectrofluorimetry. J. Cell Sci. **109**, 257–262 (1996)
39. M. Mehiri, B. Jing, D. Ringhoff, V. Janout, L. Cassimeris, S.L. Regen, Cellular entry and nuclear targeting by a highly anionic molecular umbrella. Bioconjugate Chem. **19**, 1510–1513 (2008)
40. V.V. Breus, C.D. Heyes, K. Tron, G.U. Nienhaus, Zwitterionic biocompatible quantum dots for wide pH stability and weak nonspecific binding to cells. ACS Nano. **3**, 2573–2580 (2009)

41. J. Park, J. Nam, N. Won, H. Jin, S. Jung, S. Jung, S.-H. Cho, S. Kim, Compact and stable quantum dots with positive, negative, or zwitterionic surface: specific cell interactions and non-specific adsorptions by the surface charges. Adv. Funct. Mater. **21**, 1558–1566 (2011)
42. M. Sun, L. Yang, P. Jose, L. Wang, J. Zweit, Functionalization of quantum dots with multidentate zwitterionic ligands: impact on cellular interactions and cytotoxicity. J. Mater. Chem. B. **1**, 6137–6146 (2013)
43. Y.-Y. Yuan, C.-Q. Mao, X.-J. Du, J.-Z. Du, F. Wang, J. Wang, Surface charge switchable nanoparticles based on zwitterionic polymer for enhanced drug delivery to tumor. Adv. Mater. **24**, 5476–5480 (2012)
44. N. Zhan, G. Palui, M. Safi, X. Ji, H. Mattoussi, Multidentate zwitterionic ligands provide compact and highly biocompatible quantum dots. J. Am. Chem. Soc. **135**, 13786–13795 (2013)
45. L. Cheng, Y. Li, X. Zhai, B. Xu, Z. Cao, W. Liu, Polycation-b-polyzwitterion copolymer grafted luminescent carbon dots as a multifunctional platform for serum-resistant gene delivery and bioimaging. ACS Appl. Mater. Interface **6**, 20487–20497 (2014)
46. L.H. Hurley, DNA and its associated processes as targets for cancer therapy. Nat. Rev. Cancer **2**, 188–200 (2002)
47. J.-B. Kim, K. Urban, E. Cochran, S. Lee, A. Ang, B. Rice, A. Bata, K. Campbell, R. Coffee, A. Gorodinsky, Z. Lu, H. Zhou, T.K. Kishimoto, P. Lassota, Non-invasive detection of a small number of bioluminescent cancer cells in vivo. PLoS ONE **5**, e9364 (2010)

Chapter 11
Nanodiamonds: Behavior in Biological Systems and Emerging Bioapplications

Ivan Řehoř, Jitka Šlegerová, Jan Havlík, Helena Raabová, Jakub Hývl, Eva Muchová and Petr Cígler

11.1 Introduction

Nanodiamond (ND) particles were first produced 50 years ago in the USSR by detonation of explosives [1]. Although diamond microcrystals have been used extensively in industry during the past half century, diamond nanoparticles have been largely overlooked. Interest in using NDs for biological and medicinal applications began only about one decade ago. Since then, we have witnessed a boom in ND basic research and development of ND-based applications in various fields.

The properties and applications [2\7], preparation [8], chemistry [9, 10], and photophysics of NDs [11–13] and their use in bioimaging [14–18], drug delivery [19], and nanoscale medicine [20–22] have been recently reviewed. Here, we present a comprehensive survey of current research related to the biological properties of NDs, and we critically assess the differences between individual types of NDs. In addition to this main focus, we also introduce the basics of ND structure, physicochemical properties, and available synthetic schemes for the attachment of various molecules to ND surfaces. Finally, we describe the emerging medical applications and bioapplications of these low-toxic, biocompatible carbon nanoparticles.

11.1.1 Nanodiamond Basics: Classification, Structure, and Preparation

Elemental carbon occurs in various forms with different crystal lattice arrangements. The most well-known carbon allotropes are graphite, which is planar, and diamond, which has cubic geometry. Other forms of carbon include hexagonal lonsdaleite [23] and a broad family of nanocarbons including fullerenes, tubes, on-

P. Cígler (✉) · I. Řehoř · J. Šlegerová · J. Havlík · H. Raabová · J. Hývl · E. Muchová
Laboratory of Synthetic Nanochemistry, Institute of Organic Chemistry and Biochemistry AS CR, v. v. i., Flemingovo nam. 2, 160 00 Prague 6, Czech Republic
e-mail: cigler@uochb.cas.cz

M. Zhang et al. (eds.), *Carbon Nanomaterials for Biomedical Applications,*
Springer Series in Biomaterials Science and Engineering 5,
DOI 10.1007/978-3-319-22861-7_11

ions, rods, platelets, and graphene [24, 25]. Graphite consists of planar sheets of sp^2-hybridized carbon atoms, which are weakly connected by delocalized electrons in p_z orbitals. Diamonds have tetrahedral symmetry and contain interconnected sp^3-hybridized carbon atoms. Thanks to the absence of free electron pairs and relatively high strength bonds, the diamond structure is considered extremely inert. However, the reactivity of NDs is affected by their large surface to volume ratio [10, 26].

Under ambient conditions, graphite is the most thermodynamically favorable carbon allotrope [2]. Although the diamond structure is thermodynamically favorable only at high temperature and pressure, in the case of NDs, the phase balance also depends on particle size. This effect is caused by surface energy, a part of Gibbs free energy that is inversely proportional to particle volume [27, 28]. For single-digit NDs (particles smaller than 10 nm), the preference for sp^3 or sp^2 carbon structure formation also depends on particle shape and functional group termination [29, 30].

NDs can be classified by size as nanocrystalline (< 100 nm) or ultrananocrystalline (< 10 nm) [31]. They can also be classified into three basic types based on their synthesis: detonation NDs (DNDs), high-pressure high-temperature (HPHT) NDs (see Fig. 11.1), and chemical vapor deposition (CVD) NDs. In addition, NDs can be synthesized by less common methods such as laser ablation [32], ion irradiation of graphite [33], or electron irradiation of carbon onions [34].

DNDs are synthesized by controlled detonation of explosives with negative oxygen balance, which prevents complete conversion of carbon to gaseous products [35]. The resulting detonation soot contains primary particles of 4–5 nm diameter in the form of clusters with a diameter range of 100–200 nm [36]. In addition to

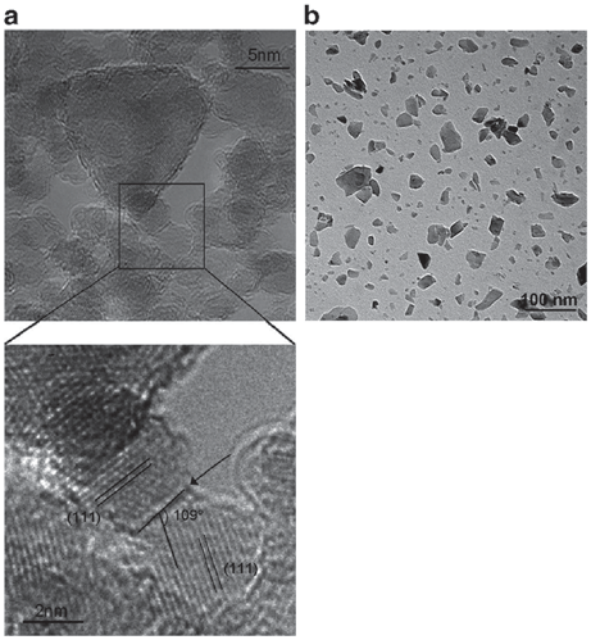

Fig. 11.1 Transmission electron microscopy (TEM) images of **a** DNDs adapted from [45] and **b** HPHT NDs

DNDs, detonation soot contains graphitic and incombustible impurities [37, 38]. Detonation soot can be purified by treatment with mixtures of oxidants such as HNO_3, H_2SO_4, $HClO_4$, H_2O_2, Na_2O_2, KNO_3, and CrO_3 [38–40]. Graphitic carbon can be alternatively oxidized by air or ozone at elevated temperatures [37, 41, 42]. DNDs are tightly connected together by van der Waals [43] or electrostatic [44, 45] interactions (it is not known which contribution is dominant) as well as covalent linkages of sp^2-hybridized carbons [36]. Conventional techniques of disintegration, such as milling, emulsification, and low-power sonication, have been ineffective in breaking down the tightly bound core aggregates of DNDs to less than 10 nm. Successful de-aggregation has been achieved by milling DND suspensions with ceramic microbeads and microbead-assisted ultrasonic disintegration [36, 46–48]. An alternative method, which does not result in insoluble by-products, involves dry milling of aggregated DNDs with sodium chloride and sucrose [49].

HPHT NDs are prepared from larger, micron-sized crystals grown from graphite at 5 GPa at >1400 °C. The processing of micron-sized particles to smaller fractions includes grinding, purification, and grating of the powder. Monocrystalline nanoparticles with primary particle sizes in the range of several tens of nanometers can be isolated this way. Synthetic HPHT type Ib monocrystalline NDs (typically with 100–300 ppm nitrogen atoms) are used for production of fluorescent NDs (FNDs) containing nitrogen vacancy (NV) color centers (see below) [6, 50].

Nanocrystalline and ultrananocrystalline films prepared by CVD are used to create biocompatible coatings with superior mechanical and wear-resistant properties. Depending on the deposition parameters, grain size can vary from 5 nm to several micrometers with various morphologies and crystallinity. Ultrananocrystalline films are generally grown in argon-rich, hydrogen-poor CVD environments, while nanocrystalline films are grown in hydrogen-rich, carbon-lean environments [51–53].

11.1.2 Colloidal Properties of Nanodiamonds

For NDs to be useful in bioapplications, they usually must be in the form of a stable colloidal dispersion. Agglomerates of NDs are useless for drug delivery, as fluorescent probes and in other applications. Colloidal properties are determined by ND size, origin, surface charge, and the chemical groups present on the nanoparticle surface.

Zeta potential, which is closely related to surface charge, provides information about the stability of a colloid (generally, a colloid is considered stable when the zeta potential is lower than −30 mV or higher than 30 mV). The zeta potential of DNDs is dependent on the preceding ND treatment. After bead-assisted milling or sonication, primary DND particles have highly positive zeta potential (~+40 mV), presumably due to dense hydroxylation of the surface [36, 46]. DND aggregates are usually treated with oxidizing agents, which are responsible for partial removal of sp^2 carbons and stabilization of colloids by creating various oxidic groups on the surface [6]. The zeta potentials of treated DNDs differ significantly according to the type of oxidative treatment. For example, DNDs treated with a H_2SO_4–CrO_3

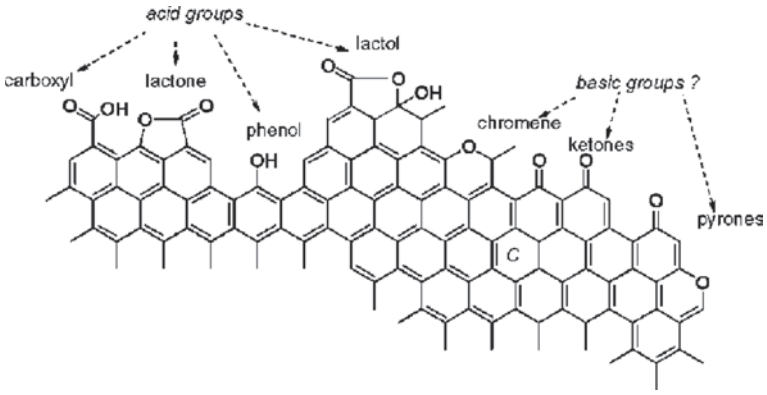

Fig. 11.2 Proposed acidic and basic oxygen functionalities on sp^2 carbon surface. (Figure adapted from [57])

mixture have a zeta potential of approximately +40 mV, while DNDs treated with H_2SO_4–$KMnO_4$ can exhibit −40 mV [54]. The phenomenon of positively charged oxidized diamond surfaces has been widely studied, and the creation of basic groups on sp^2 carbons has been accepted as a possible explanation [55–57] (Fig. 11.2).

Diamonds obtained by the HPHT process and subsequent milling form stable colloids when their surfaces are oxidized with a mixture of oxidizing mineral acids. The surface of an acid-treated HPHT diamond is highly acidic.

ND stability has been tested in aqueous and nonaqueous solvents. Generally, thermodynamically strong solvents like dimethyl sulfoxide (DMSO) [58] are good solvents for oxidized diamonds. Deagglomerated DNDs can also be well dispersed in alcohols or ethylene glycol [59]. Solubilization of NDs in nonpolar solvents requires chemical modification of the surface with aliphatic chains [60–63].

Stable ND–water colloids are a good starting material for general handling and processing of NDs. However, for bioapplications, NDs must be stable in solutions of electrolytes. The presence of an electrolyte contracts the stabilizing electric double layer, which leads to aggregation of ND colloids [64, 65]. For preparation of NDs that are stable in biological buffers, the particles must be further modified with charged groups that strengthen their electrostatic stabilization [66] or, preferably, with high-molecular-weight molecules that introduce steric stabilization of particles (e.g., polymers [67] or proteins [64]). These can be either covalently bound [65] or adsorbed [62, 68] on the ND surface.

11.1.3 Possibilities for Chemical and Macromolecular Modification: Creating Surfaces with Defined Reactivities

Chemical treatment of ND surfaces and subsequent introduction of various functionalities have a critical impact on the features and behavior of the resulting NDs. Chemical modification offers the possibility to effectively improve ND properties and has, therefore, been the subject of intensive research in recent years [2, 9].

The properties and reactivity of NDs vary significantly based on the method of their synthesis (DND, HPHT, or CVD NDs) due in part to the different sizes, shapes, and chemical compositions of the particles [9, 17]. Most of the work reported to date focuses on surface modification of DNDs, the member of the ND family studied for the longest time. The toolbox of diverse and useful reactions developed for DNDs is, however, not always directly applicable to HPHT and CVD NDs. DNDs are generally considered to be the most reactive type of NDs. However, the differences in reactivity of the different types of NDs have not yet been evaluated in a comprehensive study.

The predominant functional groups present at the ND surface are carboxylic acids, ketones, hydroxyl groups, hydrogen atoms, and groups containing double bonds, varying from an isolated double bond to highly conjugated systems [69–71]. NDs with surfaces containing various groups are not suitable for selective or precise tailoring of subsequent functionality. Therefore, an initial chemical pretreatment step is performed to achieve homogenous surfaces containing one functional group. Carboxylic groups, hydroxyl groups, hydrogen atoms, halogen atoms, and sp^2 carbon atoms are common functionalities that can be enriched on ND surfaces (Fig. 11.3).

Various mixtures of mineral acids [37, 38, 71–73], hydrogen peroxide with sulfuric acid [74], hydrogen peroxide [73], and air oxidation [37, 75] are used to yield NDs with carboxylated surfaces. Subsequent treatment of carboxylated NDs with reagents such as borane [76, 77], $LiAlH_4$ [78, 79], or Fenton reagent [80, 81] lead

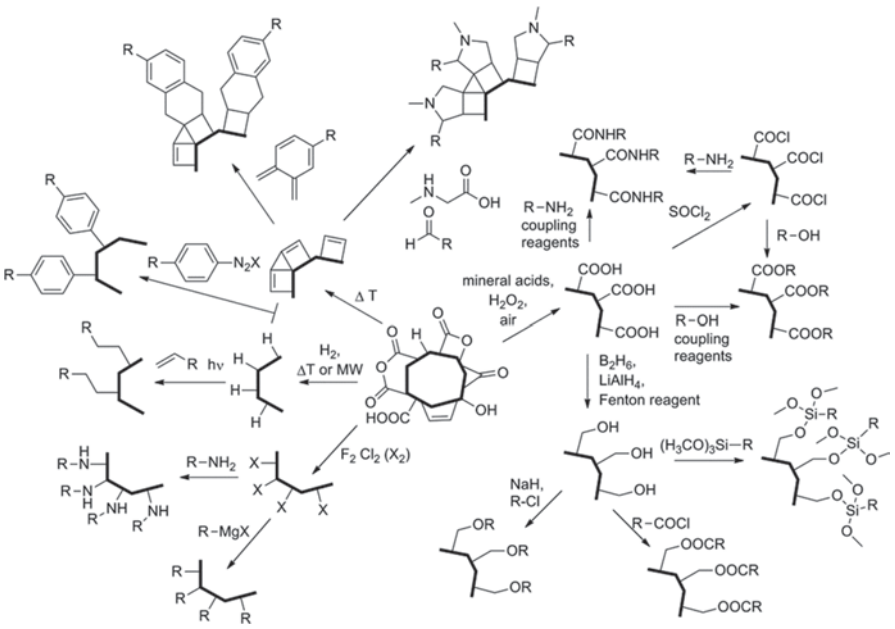

Fig. 11.3 Overview of frequently used chemical modifications of ND surfaces. Notably, the ND always bears a mixture of various moieties because the reactions never reach 100% completion

to the formation of hydroxylated NDs. Hydrogenated NDs can be produced by reaction with hydrogen at elevated temperatures [82, 83] or in a microwave plasma reactor [84]. The formation of NDs covered with sp^2 carbons is achieved by thermal processing [85–87]. Fluorinated [88, 89] or chlorinated [80, 90] NDs are obtained by reaction with elemental gas or halogenating reagents.

Known organic reactions are used for secondary surface modification of NDs with homogenous surfaces. One popular method for subsequent modification is nucleophilic substitution of halogenated NDs with amine and organometallic reagents [88, 90]. Although the mechanism remains elusive, the reaction works on chlorinated and even fluorinated NDs [91]. Carboxylated NDs can be easily converted to corresponding esters and amides through acyl chloride intermediates [63, 92] or directly with the use of a peptide-coupling reagent [93]. The modification of hydroxylated NDs is mainly based on the formation of ethers [78], esters [94], and silyl ethers [48, 76] through reaction with alkylchloride/NaH, acyl chloride, and trimethoxysilanes, respectively. Reaction of hydrogenated NDs can proceed on photochemically activated terminal alkenes [95, 96] and aromatic diazonium salts [84, 95], affording alkylated and arylated NDs, respectively. Similarly, NDs with carbon sp^2 surfaces undergo reaction with aromatic diazonium salts [87], dienes [97], and azomethine ylides [98] in a Prato reaction. Last but not least, click chemistry has been demonstrated to be a valuable tool for orthogonal molecule grafting to surface-modified NDs bearing alkyne or azide groups [93, 99, 100].

Grafting polymers to ND surfaces is another method used to improve and homogenize ND properties. Both “grafting-to” and “grafting-from” approaches have shown to be reliable methods for producing NDs with surface polymers. Several “grafting-to” approaches have been reported. For example, opening of the epoxy ring present in copolymers [72] or resins [101] allowed coupling with NDs with terminal carboxyl and amino groups, respectively. NDs with grafted poly(ethylene glycol or PEG were obtained through reaction of amine-terminated NDs with PEG-containing active ester [102] and esterification of PEG–alcohol with acyl chloride–ND derived from carboxylated ND [103]. The grafting of copolymers containing ferrocene moieties to NDs with sp^2 carbon surfaces was performed by ligand-exchange reactions [104]. However, more popular principle for covering ND surfaces with polymers remains the “grafting-from” approach. Atom transfer radical polymerization (ATRP) has been shown to be an efficient method for growing polymer brushes on ND surfaces terminated with an initiator [64, 103, 105]. The grafting can also be carried out with self-initiated photografting and photopolymerization under UV conditions [106, 107]. Additional protocols include free radical addition reaction [85], polyimide condensation [108], and ring-opening polymerization of glycidol [67]. Polymers can also be non-covalently grafted to ND surfaces. This approach is typical for grafting of biomolecules (as discussed later) [109, 110].

Recently, novel NDs with porous silica coatings were introduced. This modification opens new horizons for subsequent chemical treatment based on silica chemistry [111–113].

11.1.4 Conjugation of Biomolecules to Nanodiamond Surfaces

Connecting molecules to ND surfaces is desirable for a number of applications, including cellular targeting, internalization, and drug or gene delivery.

Different types of molecules have been conjugated to NDs. Various types of proteins (antibodies [114–116], toxins [117–119], enzymes [68, 120–125], and serum proteins such as transferrin [126–128] and bovine serum albumin (BSA) [64, 129–132]), vitamins [79, 133–135], enzyme cofactors [81], peptides [76, 136, 137], drugs (such as doxorubicin) [138], and nucleic acid fragments are among the most common biomolecules conjugated to NDs [139, 140].

Both non-covalent and covalent linkages are suitable for biomolecule attachment to ND surfaces. Covalent immobilization was shown to be twice as effective as non-covalent adsorption for attachment of cytochrome [141]. Non-covalent connections are mediated by adsorption that involves charge compensation of carboxylic groups at the ND surface, water displacement, screening of hydrophobic patches, and other mechanisms that lower the free energy of particle to the thermal energy of its environment [142]. Non-covalent connections can be easily created by incubating NDs in a solution containing the biomolecule. For example, lysozyme [68, 122–125], BSA [129, 131, 132], cytochrome [141], toxins [118, 119], and DNA [143] have been connected to ND surfaces by adsorption. DNA can also be bound on pretreated particles such as poly-L-lysine- [144] or thionine-coated [81] NDs. The major disadvantage of adsorption is the nonspecificity of the interaction, that is, NDs can bind almost every protein in solution. This quality can, however, be exploited for high-affinity nonspecific capture of proteins from solution [145]. Covalent grafting, on the other hand, creates a much more specific and strong connection between a molecule and the ND surface. However, the grafting procedure is exacting and time consuming [141]. Amide bonds are used most frequently to connect biomolecules to ND surfaces; either biomolecule amines are bound to carboxyls on the ND surface [64, 65, 115, 117, 121, 126–128, 130, 135, 144, 146] or vice versa [79]. Silane linkers are also often used to mediate connection of biomolecules and ND surfaces by forming a covalent amide bond [76, 133] or by reaction of isocyanate with an amino group to yield urea [81].

A few studies have compared the effectiveness of biomolecule binding to DND and HPHT ND surfaces [122, 141]. DNDs can adsorb biomolecules more effectively than HPHT NDs due to their higher surface to volume ratio and larger specific surface available for immobilizing biomolecules. Twofold and fourfold higher amounts of cytochrome [141] and lysozyme [122], respectively, were adsorbed on DNDs compared to HPHT NDs. Despite this nonuniformity, both types of NDs are stable and can be modified in similar ways. In this section, the type of NDs is not distinguished.

Maintaining the bioactivity of the conjugated molecules is crucial [14]. Various spacers may be inserted between a biomolecule and ND to reduce steric constraints and retain the function of the biomolecule. This is a particularly important consideration for enzymes with active sites that may be sterically hindered by attachment

to ND surfaces [147]. Spacers are also used for suppressing nonspecific interactions [148] and protein conformational changes caused by strong biomolecule–particle interactions [68, 149]. In addition, enzymatic activity sometimes decreases as surface coverage is lowered. To solve this issue, the surface can be blocked with supplementary proteins to create a more "crowded" environment. This strategy increased the activity of ND-bound lysozyme from 60 to 70 % [68].

11.1.5 Behavior and Impact of Nanodiamonds on Biological Systems

11.1.5.1 Biocompatibility of NDs

Biocompatibility is a frequently used measure of nanoparticle performance in a biological system. According to William's general definition, biocompatibility refers to the "ability of a material to perform with an appropriate host response in a specific situation" [150]. Biocompatibility is, however, contextual; it is related to a specific interaction and use of a biomaterial. The results and conclusions of many studies concerning the biocompatibility of NDs are not directly comparable, because they use different evaluation methods and criteria to judge the material's biocompatibility. Furthermore, the results depend primarily on the type of particle studied (i.e., DNDs or HPHT NDs), their concentrations, and surface modifications. Biocompatibility also depends on the types of cells used.

A parallel to another carbon nanomaterial, carbon nanotubes, should be mentioned here. A number of conflicting reports have been published: Some investigators have reported toxic effects following exposure of several cell types to nanotubes, while others demonstrate very low or insignificant cellular responses [151]. Currently, it is apparent that surface charge, shape, length, diameter, agglomeration, and purity, which are hard to keep consistent due to different nanotube preparation and purification procedures, influence their toxicity.

This section describes the importance of similar factors on the behavior of NDs in biological systems. We also focus on distinguishing the origin of NDs and separating the effects of individual ND types. Overall, after purification and post-synthetic modifications, NDs are often considered to be a most biocompatible carbon nanostructure and a low-toxicity material [138, 152–154].

In Vitro Biocompatibility of DNDs

Schrand et al. reported that DNDs are biocompatible in vitro in a variety of cell types [152]. Different measurements, such as 3-[4,5-dimethylthiazol-2-yl]− 2,5-diphenyltetrazolium bromide (MTT) assay, showed biocompatibility and low cytotoxicity of both modified (DND–COOH, DND–COONa, DND–SO_3Na) and non-modified (nonoxidized "raw" DNDs) DNDs. Eventual reduction of MTT corre-

sponds to lower cellular viability based on mitochondrial function. No disruption of mitochondrial membrane permeability, morphological alterations, or viability changes (using luminescence measurement of adenosine triphosphate; ATP production) were observed with 5–100 μg/ml DNDs. Furthermore, DNDs did not induce generation of reactive oxygen species (ROS) and did not cause oxidative stress leading to membrane dysfunction, protein degradation, and DNA damage [152]. In a subsequent study, the same biocompatibility measurements were performed with other carbon nanomaterials, including single- and multiwalled carbon nanotubes (SWNTs or MWNTs) [153]. The DNDs showed higher biocompatibility than carbon black, MWNTs, or SWNTs [153]. Huang et al. reported no change in expression of genes serving as indicators of inflammation and protection against apoptosis after incubation of macrophages or colorectal cancer cells with DNDs [138].

In general, nanoparticles are considered potentially toxic because of their small size and ability to enter cells and localize in critical organelles [6]. Recent studies have indicated that DNDs can be toxic under certain conditions [81, 129, 155–166]. The observed toxicities were concentration dependent, time dependent or both; notably, however, DNDs were described to have much lower toxicity than other carbon materials, such as MWNTs [153, 165–167].

Harmful effects of DNDs were first reported in 2004. Destruction of human red and white blood cells after incubation with raw DNDs was observed [160]. Influence of DNDs on gene expression in human neoplastic cells was also shown [155]. Karpukhin et al. observed concentration-dependent toxicities in neutrophils, such as ROS formation and phagocytosis of oxidized DNDs [157]. Data suggest that the DND surface charge is a crucial determinant of toxicity due to the affinity of cationic particles for the negatively charged cell membrane. The cytotoxicity of modified DNDs (at concentrations higher than 50 μg/ml) toward human embryonic kidney cells can be ranked as follows: $–NH_2$ >> –OH > –COOH (Fig. 11.4) [158]. The influence of surface charge, or more precisely zeta potential, and DND concentration on cell viability and growth was also reported by Horie et al. [156]. Toxicity studies on modified DNDs have been performed with polyaniline-modified DNDs in human embryonic kidney cells (where toxicity was observed in a concentration-dependent manner) [168]. In various studies, Fenton-treated DNDs showed different levels of toxicity, ranging from biocompatibility in HeLa cells [159] to stimulation of ROS production and other effects in human umbilical vein endothelial cell human umbilical vein endothelial cells (HUVEC) [161, 164].

Serum proteins can also influence the biological response to raw DNDs. Serum proteins adsorb on the surface of NDs and reduce their toxicity. One study showed that the toxicity of DNDs toward a variety of cell types depends on the presence of serum in the medium [129]. In contrast, other studies showed that DNDs are nontoxic in serum-free media [152, 153].

A DND genotoxicity study was performed on mouse embryonic stem cells, which are highly sensitive to DNA damage [165]. DNA damage caused by both unmodified and oxidized DNDs was assessed by observing the activation of DNA repair proteins such as p53. Oxidized DNDs caused more DNA damage and cell differentiation than raw DNDs. This effect is likely due to the formation of aggregates

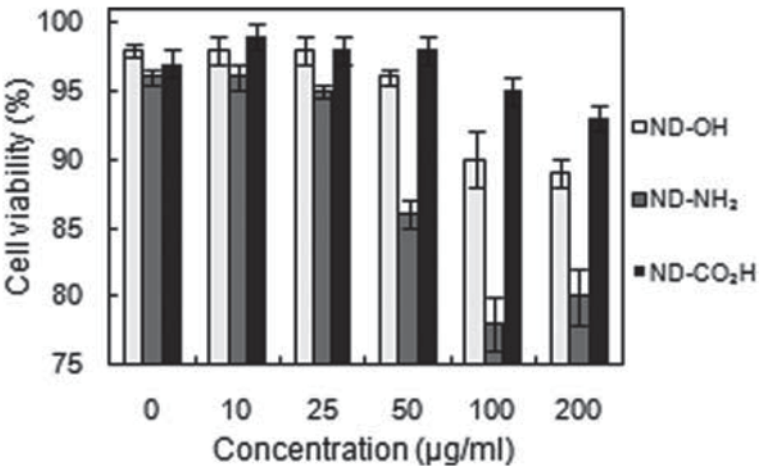

Fig. 11.4 Effect of DNDs with various surface functionalities on human embryonic kidney cell (HEK293) survival (based on trypan blue dye exclusion assays). Cells were treated with different concentrations (10–200 μg/ml) of functionalized NDs for 24 h. (Figure adapted from [158])

that inhibit the entry of DNDs into cells. Raw DNDs are more likely to aggregate, while oxidized DNDs create better colloids. However, both types of DNDs caused much less DNA damage than MWNTs [165].

In Vitro Biocompatibility of HPHT NDs

Biocompatibility of oxidized HPHT NDs was first examined in 2005 in human kidney cells by Chang et al. [169] and assessed in subsequent studies by the same lab and others [137, 144, 170–175]. Most studies assessed biocompatibility by MTT assay or measuring levels of enzymatic activity. These studies showed that surface modification, for example, with peptides [137], proteins, or polymers [172], does not alter the biocompatibility of HPHT NDs. Using HeLa cells, Faklaris et al. observed that biocompatibility of HPHT NDs is dose dependent; cell viability decreases at ND concentrations equal to or greater than 50 μg/ml [171]. Liu et al. [175] showed that HPHT NDs are noncytotoxic during cell division and differentiation of lung cancer cells and embryonic fibroblasts. NDs do not interfere with expression of genes or proteins that regulate cell-cycle progression, spindle formation, and chromosome segregation. NDs also do not alter long-term (10 days) cell growth [175]. Fang et al. also did not observe significant alteration in growth or proliferation of a variety of cell types incubated with NDs for 8 days [174]. On the other hand, Weng et al. observed an approximately twofold reduction in the proliferation rate of HeLa cells treated with 10 μg/ml NDs modified with amino groups or transferrin [128]. This demonstration of toxicity is rather exceptional, and it is analogous to the observation of Marcon et al. [158] with DNDs. This HPHT ND-mediated toxicity was, however, observed to be much lower than that of other carbon nanomaterials, such as MWNTs (Fig. 11.5) [167].

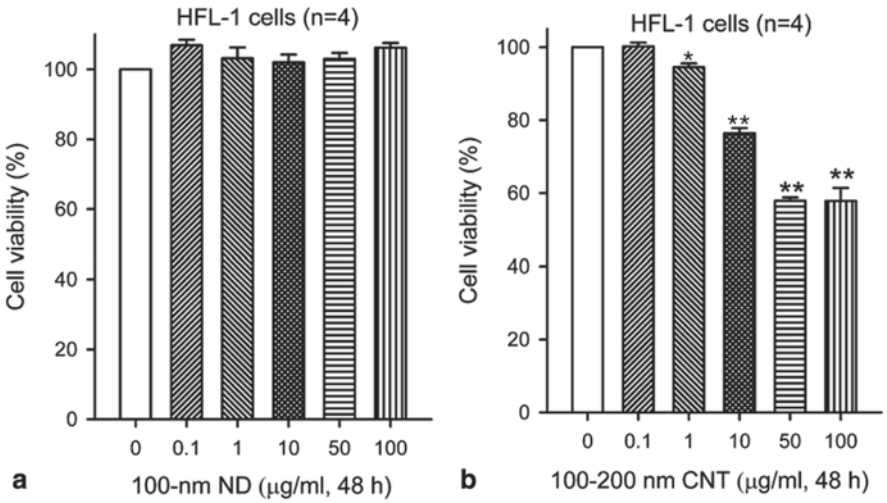

Fig. 11.5 Cytotoxic effects of HPHT NDs and multiwalled carbon nanotubes (MWNTs) on human lung fibroblast cells (HFL-1). Cells incubated alone or with 100-nm HPHT NDs **a** or 100–200 nm MWNTs **b** in concentrations ranging from 0.1 to 100 μg/ml for 48 h. Cell viability was measured by MTT assay. Figure adapted from [167])

Comparative In Vitro ND Biocompatibility Studies

The comparative toxicities of different ND types have also been studied [167, 176–179]. Smaller DNDs show higher toxicity than larger HPHT NDs, as evidenced by effects on cell viability, proliferation, apoptosis, and metabolic activity [167, 176–179]. This phenomenon can be explained not only by the different sizes (and surface area) of the particles but also by the presence of reactive disordered carbon structures on the surface of DNDs, which contrasts with the highly ordered (and oxidized) sp^3 carbons on HPHT ND surfaces [176, 177]. Similarly, DNDs were found to be more toxic than HPHT NDs toward microorganisms, presumably for the same reasons [177].

Origin-dependent toxicity was also evidenced by comparison of DNDs with CVD NDs. Compared to DNDs, large CVD ND particles showed lower cytotoxicity toward HUVEC cells, lower biological activity, and a lower level of apoptotic cells [162, 163]. These findings support the notion that origin and size could be the main determinants of ND cytotoxicity.

11.1.5.2 Cellular Internalization and Exocytosis of Nanodiamonds

Both DNDs [129, 152, 167, 176, 178] and HPHT NDs [134, 144, 167, 171, 176, 178] can spontaneously enter cultured cells. The half-life of the uptake depends on the surface charge and modifications [128, 158] and particle size [128, 170, 172, 180]. Uptake of DNDs was observed to be more efficient than for carbon materials such as MWNTs and graphene oxide [166].

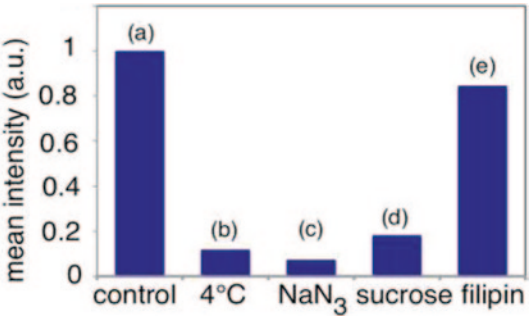

Fig. 11.6 HPHT NDs (20 μg/ml) were incubated with HeLa cells for 2 h and internalized by endocytosis. The mean photoluminescence intensity of NDs per cell is normalized to that of control cells: **a** at 37 °C (control), **b** at 4 °C, or at 37 °C after pretreatment with either **c** NaN_3 (10 mM), **d** sucrose (0.45 M), or **e** filipin (5 μg/ml). (Figure adapted from [181])

The clathrin-mediated pathway, in which ligand first binds to a cell surface receptor and is then internalized, is the most frequent process for internalization of different NDs. Receptor-mediated endocytosis is facilitated by serum proteins adsorbed onto the ND surface [181]. The mechanism of internalization has been studied primarily with HPHT NDs. To examine the cellular uptake of NDs, cells were incubated at low temperature in the presence of sodium azide or 2-deoxyglucose. The decrease in ND uptake under these conditions indicated that internalization depends on temperature and the energetic status of a cell (sodium azide and 2-deoxyglucose create an ATP-depleted environment) and implies active transport by endocytosis (Fig. 11.6) [170, 181]. Reduced uptake in the presence of sucrose or phenyl arsine oxide, which are known to disrupt the formation of clathrin-coated vesicles, implies that a clathrin-mediated pathway is employed [154, 170, 181]. The endocytosis mechanism has been confirmed by several groups [137, 169, 174]. Clathrin-mediated endocytosis of NDs modified with cationic polymers [180], poly-L-lysine [170], or transferrin [128] has been observed. Actin filaments and microtubules are also involved in this process [170].

Another common process of receptor-mediated endocytosis is the caveolae pathway. This pathway is not thought to be used for ND internalization, as the presence of the blocking compound filipin does not reduce ND uptake (Fig. 11.6) [170, 181]. However, a different uptake mechanism, macropinocytosis, has been observed. Macropinocytosis likely also plays an important role in the uptake of NDs, particularly if they are aggregated [128, 175, 180].

The short-term exocytosis of NDs from cells was low. The long-term exocytosis (after 6 days) in three different cell types was observed to be between 15 and 30 % [174].

11.1.5.3 Cellular Localization

Both DNDs and HPHT NDs localize inside the cell [134, 137, 138, 144, 167, 175, 178]. Some studies imply that a fraction of NDs is entrapped and localized in endo-

somes; vesicles involved in the transport of extracellular materials [154, 156, 180, 181]. During endocytosis, the extracellular material containing ND is engulfed by the cell membrane and trapped in a newly created endosome. Inside the cell, endosomes containing NDs can be transformed into lysosomes [154, 177, 180, 181]. NDs have not been observed in the nucleus [154, 169, 175, 180, 181], except in one study concerning DNDs modified with thionine [81].

The smallest particles can be observed in the cytoplasm [154, 171, 181]. It is not clear if these small NDs (approximately 5 nm) are directly internalized via passive transport across the cellular membrane or if they are released from endosomes [171]. The fact that NDs might not remain inside the endosomes offers promise for applications such as drug delivery.

11.1.5.4 In Vivo Toxicity and Biocompatibility Studies

Biodistribution and Clearance of DNDs

Biodistribution and clearance of DNDs have been studied using mouse and rat models. In mice, DNDs accumulate mostly in the lungs, spleen, kidneys, and liver. In some studies, the highest retention of DNDs was observed in the lungs following injection [182] or intratracheal instillation [183]. Other studies show that the mouse liver contains the highest concentration of DND particles following injection [184, 185]. High concentrations of DNDs in mouse blood and heart have been reported, and DNDs have not been found in the brain [183]. Redistribution of DNDs is possible; DNDs can easily pass through the alveolar wall of the capillary barrier, enter the bloodstream, and travel to other tissues [183, 185]. Smaller DNDs, which are not trapped in organs, are excreted through the urinary tract [182]. DNDs can be slowly eliminated from tissues over time [183, 185]. Whole-body clearance was observed in mice within 10 days [184].

The importance of the colloidal properties of NDs was established by filtration experiments. Removing larger DNDs caused a change in the particles' regular distribution: The small, filtered particles localized to the bladder and were excreted [182]. Co-injection of DNDs with increasing doses of MWNTs decreased the hepatic and splenic accumulation of DNDs and gradually increased lung retention [185]. The addition of surfactant agents did not lead to significant changes in distribution [182].

Biodistribution and Clearance of HPHT NDs

Similar to DNDs, HPHT NDs modified with BSA accumulated mostly in the mouse liver, lungs, and spleen; however, no time-dependent elimination of NDs from tissues was observed [186]. NDs were entrapped at a constant level over 28 days. After intratracheal instillation, HPHT NDs in addition to DNDs were present only in mouse lungs, not in the liver or spleen [187].

Comparative In Vivo Biocompatibility of Different ND Types

After DND injection, mice did not undergo a change in blood parameters such as interleukin-6, indicating a lack of systemic inflammation, or alanine transferase, indicating that DNDs did not influence liver function [184]. There were no indications of inflammatory processes 3 months after injection, suggesting the long-term biocompatibility of DNDs [188]. On the other hand, DNDs modified with carboxyl groups showed potential concentration-dependent embryotoxicity and teratogenicity. These DNDs particles caused malformations in *Xenopus laevis* embryos. Strikingly, the higher in vivo toxicity of ND–COOH over ND–NH_2 and ND–OH is the opposite of the in vitro toxicity of these types of surface modifications [158].

The lungs, liver, kidneys, and hematological system of mice were adversely influenced after intratracheal instillation of DNDs [183]. No difference in body weight and no abnormal pathology changes were observed. The lungs suffered the most severe toxicological effects, such as inflammation and tissue damage, due to the high uptake and long retention time of DNDs in lung tissue [183]. However, in contrast to these results, Yuan et al. did not observe pulmonary toxicity in mice after intratracheal instillation of both DNDs and HPHT NDs. However, Yuan et al. used an approximately 20-fold lower dose of NDs [187].

No in vivo toxicity and no apparent side effects, such as a stress response, were observed after HPHT NDs were microinjected into *Caenorhabditis elegans*. Moreover, development of HPHT ND-containing *C. elegans* embryos appeared to be normal [130]. HPHT NDs were also stable in rats over a 5-month period, with no significant differences observed between control and HPHT ND-treated organisms [189].

11.2 Nanodiamonds as Probes and Contrast Agents

11.2.1 Color Centers in Nanodiamonds

The unique optical and magnetic properties of NDs underlie their success in applications ranging from quantum computing to bioimaging [12, 16, 167, 190] and single-spin magnetometry [191–194]. NDs host more than 500 color centers [195], some of which have been identified as bright single-photon sources. NV centers have been particularly well studied because they function as a source of single photons. In addition, their spin can be manipulated at room temperature by a magnetic field, electric field, or a combination of both. The NV center is considered a basic unit of quantum computing and has many novel applications in spintronics and cryptography. Other important single-photon sources showing nonclassical emission include Si–V [196, 197] (738 nm), Ni–N complexes called NE8 centers [198, 199] (793–802 nm), chromium-based emitters [200, 201] (750–770 nm), and carbon-related TR12 centers [202] (470 nm).

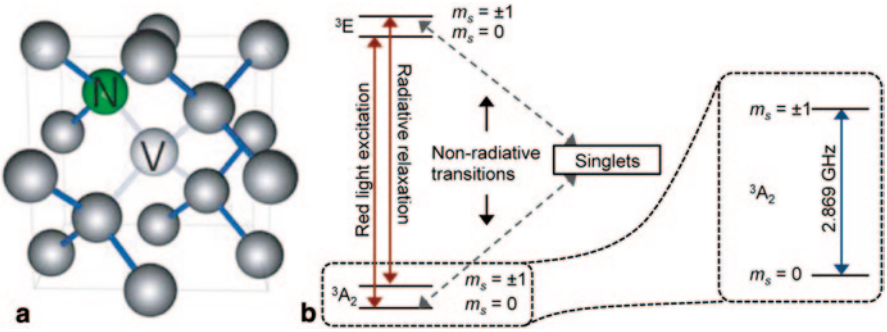

Fig. 11.7 **a** Schematic picture of an NV center. *N* is a substitutional nitrogen; *V* is a vacancy of a carbon atom. (Figure adapted from [213]). **b** Electronic level structure of NV depicting radiative and non-radiative transitions. Excitation from $^3A_2$ ($m_s = 0$) is followed by radiative decay back to ground state. Excitation from $^3A_2$ ($m_s = \pm 1$) is followed not only by radiative decay but also by non-radiative decay through a singlet state, decreasing the overall fluorescence intensity. The decay processes can be modulated by ESR: the frequency 2.869 GHz is needed for excitation from $^3A_2$ ($m_s = 0$) to $^3A_2$ ($m_s = \pm 1$). (Figure adapted from [214])

NV centers consist of a nearest-neighbor pair of a nitrogen atom, which is naturally present as a lattice defect, and a lattice vacancy (Fig. 11.7a). NV centers are typically created by irradiation of purified HPHT NDs with ionizing radiation followed by annealing in vacuo or under an inert atmosphere at 600–900 °C [74, 190, 203, 204]. Irradiation of NDs creates vacancies [205], which migrate during annealing and get trapped by nitrogen atoms. To improve fluorescence intensity and colloidal stability, FNDs are then air oxidized at 500 °C or treated with molten KNO_3 followed by HNO_3/H_2SO_4 wet oxidation [203].

Two charge states—negative NV^- and neutral NV^0—have been identified; each has different photoluminescence and spin properties. One NV center can exist in both states, depending on its surroundings [11, 206]. These centers are thermally stable up to 1000 °C and resistant to photobleaching and photoblinking [207, 208]. The neutral NV^0 is nonparamagnetic and has a zero-phonon line (ZPL) emission wavelength at 575 nm. NV^- is paramagnetic and has a ZPL at 637 nm, which is suitable for optical bioimaging (the cell autofluorescence signal is low in this region). Both ZPLs are followed by broad phonon side bands [209, 210] (Fig. 11.11).

NV centers are the predominant end product of irradiation followed by annealing [211]. NV contains a three-level emission system. This means that, in addition to the desired optical transition, the centers have a parallel decay channel through a metastable state. The metastable state has a long emission time, which reduces single-photon emission. The energy levels of an NV^- center labeled according to C_{3v} symmetry group is shown in Fig. 11.7b. Two of the six electrons of the center are unpaired, meaning that both the ground and the first excited state are triplets. The uniaxial crystal field and mutual magnetic interaction between electrons splits the electronic spin states to $^3A_2$ ($m_s = 0$) and doubly degenerate $^3A_2$ ($m_s = \pm 1$) sublevels. The energy gap between these two sublevels is 2.87 GHz. Optical excitation from

$^3A_2$ ($m_s=0$) to ^3E ($m_s=0$) is followed by a radiative decay. In contrast, excitation from spin sublevels having $m_s=\pm1$ results either in radiative decay to the ground state $^3A_2$ ($m_s=\pm1$) or in intersystem crossing through the intermediate singlet state $^1A_1$ preferentially to the ground state $^3A_2$ ($m_s=0$), which quenches the fluorescence. Upon optical cycling, the spin ends up in the $m_s=0$ sublevel, which has brighter fluorescence than $m_s=\pm1$ sublevels [212]. This optically pumped spin polarization can be destroyed by a resonant microwave field (at 2.87 GHz), which induces transition between $m_s=0$ and $m_s=\pm1$ spin sublevels. In this way, fluorescence intensity can be modulated or switched off, as transitions from $m_s=\pm1$ sublevels fluoresce less. This approach also enables optical detection of a single electron spin resonance (ESR) spectrum [213, 214].

In the presence of an external magnetic field, the $m_s=\pm1$ sublevels are no longer degenerate due to Zeeman splitting. This is evidenced by the appearance of two lines in the ESR spectrum (there is one line at zero magnetic field). Measuring the line positions in the ESR spectrum allows for calculation of the magnitude of the external field with high accuracy and sensitivity. This system can, therefore, be used as an atom-sized scanning probe vector magnetometer [194, 213, 215], detecting magnetic or electric fields produced by a single electron located tens of nanometers away from an NV^- center.

Intensity and positions of lines can be further modulated by an electric field or a combination of magnetic and electric fields. In addition to static perturbation, dynamic effects like spin echo or Rabi oscillations can be exploited.

Low brightness is a major drawback of NV centers that limits their wider applications. One approach to boost fluorescence is to couple the NV center to surface plasmons of a metallic nanostructure [216, 217]. The excitation of plasmon resonances leads to highly localized photon fields, and therefore to enhanced excitation of nearby emitters, resulting in higher fluorescence.

Another approach to boost ND fluorescence is to increase the number of NV centers during synthesis. Optimal thermal and kinetic conditions for NV production and oxidation have been described [203]. Particles prepared by this approach are about one order of magnitude brighter than particles prepared by commonly used procedures.

In addition to the red fluorescence of the NV center, NDs can also emit green fluorescence [218, 219]. This fluorescence arises from the excitation of N−V−N color centers, called H3 centers, which have ZPL at 503 nm. Similar to the NV center, H3 centers are thermally stable and do not photobleach or photoblink. For example, diamonds containing H3 color centers are used as a lasing medium for room-temperature color-center lasers.

11.2.2 Nanodiamonds as Optical Nanosensors

While in most cases NDs containing NV centers serve as fluorescent or magnetic labels, recent research has opened the possibility of using FNDs as optical sensing devices. The switch between the neutral (NV^0, ZPL emission wavelength at

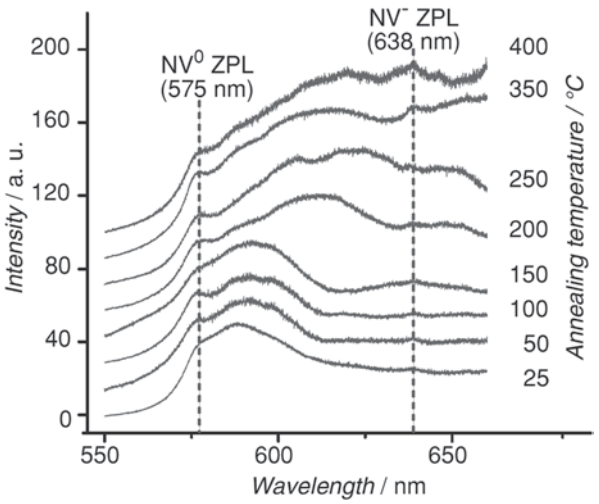

Fig. 11.8 Changes in fluorescence spectra of hydrogenated FNDs (40 nm) upon air annealing at different temperatures. Before measurement, samples were heated to the target temperature, kept at the set temperature for 30 min, and then cooled to room temperature. Upon consecutive oxidation caused by heating the hydrogenated surface in air, the fluorescence of NV^- (ZPL at 638 nm) gradually increases. (Figure adapted from [220])

575 nm) and negatively charged (NV^-, ZPL at 637 nm) states of the NV center can be used for ratiometric, double-color reading of electronic changes in the vicinity of the NV center. These surface-induced charge state conversions in NV^0/NV^- populations, which are sensitive to the chemical nature of various diamond surfaces, have been described for bulk diamond [192, 220–227, 228] as well as NDs [74, 75, 206, 220, 221, 229, 230] (for a recent review, see [11]).

The original NV center charge state is influenced by distance from the diamond surface (particle size), surface termination, and electron donor (i.e., nitrogen) content [220]. In bulk high-purity nitrogen-implanted diamond crystals, NV^- centers prevail. However, close to the diamond surface, these centers become unstable and switch to NV^0 [222]. This also occurs in diamond nanoparticles [74]. The charge state of NV centers near the surface can be converted from NV^0 to NV^- by various types of oxidation, which cause removal of sp^2-hybridized carbon surface layers or removal of CH bonds [74, 203, 220, 222, 223] (see Fig. 11.8). The most significant differences in fluorescence spectra have been observed not for bulk crystals but for HPHT NDs, because of their high surface-to-volume ratio [220].

The influence of various diamond surface terminations on NV luminescence has been explained using the band gap model [220, 221] and quantum chemical calculations [206, 226, 227, 230]. A similar procedure leads to boosting and prolongation of fluorescence (different from NV centers) of DNDs [75]. Certain changes in the fluorescence spectra dependent on the excitation wavelength have also been observed on carboxylated NDs after protein adsorption [231].

Ratiometric reading of NV^0/NV^- fluorescence is becoming a promising tool for optical monitoring of the chemical environment and biochemical interactions close to the ND surface [220].

11.2.3 Bioimaging Using Fluorescent Nanodiamonds

Visualization and tracking of subcellular structures, biomolecules, and their interactions in cells is a key biological technique. Nonfluorescent biomolecules can be modified with a fluorescent label to enable real-time imaging in living cells. The ideal fluorescent label should meet a certain set of requirements, including chemical stability and solubility, convenient size, minimal interference, low toxicity, and high brightness. Among the most frequently used labels are fluorescent proteins, organic dyes, and semiconductor nanocrystals (quantum dots) [232, 233]. Fluorescent NDs are an exciting alternative to these probes, because they provide unique properties. Notably, they do not contain toxic elements and are considered to be the most biocompatible of carbon nanoparticles. Fluorescent NDs containing NV centers have unlimited resistance to photobleaching, the time profile of their emission is very stable, and particles > 5 nm do not photoblink [234]. These properties make them well suited for cell imaging applications.

Imaging using fluorescence probes? in living organisms is a challenging task. The surrounding tissue can shield a probe's emission and is also a source of autofluorescence, which originates from photoexcitation of endogenous fluorophores such as collagens, retinols, retinoic acids, porphyrins, flavins, and nicotinamide adenine dinucleotides (NADHs). One major advantage of FND probes is their emission wavelength in the near-infrared region, where both autofluorescence and tissue absorption (Fig. 11.9) are low (so-called tissue imaging window) [235]. On the other hand, the fluorescence intensity of FNDs is much lower compared to the same mass concentration of molecular dyes. Very bright FNDs are essential for in vivo fluorescence imaging; therefore, exclusively HPHT NDs at sizes around 100–150 nm are used [130, 189, 214, 236, 237].

The following paragraphs briefly describe achievements in cellular and in vivo imaging of FNDs, primarily fluorescent HPHT NDs containing NV centers. The use of other types of ND fluorescence or DNDs in a few exceptional cases is highlighted.

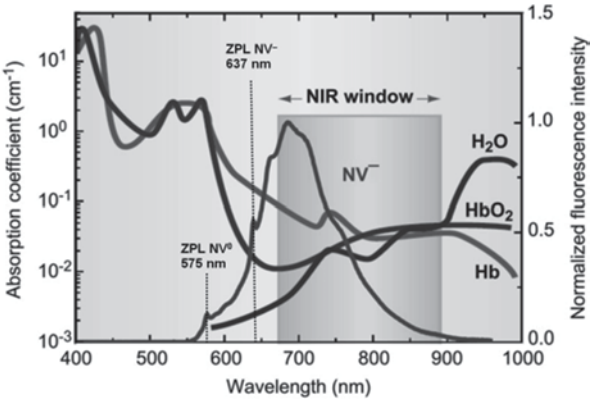

Fig. 11.9 Comparison of the fluorescence spectrum of NV centers in FNDs in the near-infrared imaging window of biological tissues. The *black, dark-gray*, and *light-gray* curves represent the absorption spectra of H_2O, oxygen-bound hemoglobin (HbO_2), and hemoglobin (Hb), respectively. *NIR* near-infra red. (The absorption spectra were adapted from [235])

11.2.3.1 Nanodiamonds as Fluorescent Probes for Intracellular Tracking

NDs were first described as suitable in vitro fluorescent labels by Chang et. al [169]. Confocal fluorescence images were used to show the cellular uptake of NDs. NDs emit in the deep red region (around 700 nm), which falls into the tissue imaging window. ND fluorescence is well separated from the spectral region where cellular endogenous fluorescence occurs [126, 127, 135, 144, 169, 190]. NDs can also be distinguished from background cellular autofluorescence by time-gated imaging, thanks to their long fluorescence lifetime (>10 ns for NV color centers) [127, 171]. Nowadays, fluorescent NDs are widely used as labels for in vitro tracking detected by confocal microscopy or flow cytometry [112, 115, 117, 118, 126–128, 134, 135, 144, 167, 169, 171, 174, 178, 181, 190, 219, 238–240].

Due to their stable fluorescence and resistance to photobleaching and photoblinking, NDs can be used for long-term tracking to follow fast and slow events in cells [115, 135, 144, 171, 174, 181, 190, 238]. Fang et al. used NDs detected by confocal microscopy for long-term labeling and tracking of stem cell division, proliferation, and differentiation [174]. Flow cytometry was used to study exocytosis of NDs from cancer and stem cells [174]. Due to its excellent photostability and high brightness, a single 35-nm ND was tracked inside a HeLa cell over a time span of more than 200 s, using a mean square displacement analysis of the three-dimensional (3D) trajectory (Fig. 11.10). The diffusion coefficient for internalized ND within an endosome was determined from this measurement [190]. Other groups have also determined the trajectory and diffusion motion of NDs in HeLa cells [134, 135, 144]. Long-term tracking offers promise for revealing details of intracellular activities such as drug delivery and viral infections.

Although observations have been made using fluorescent NDs and NDs have been shown to perform similarly as quantum dots and dyes [144, 238], some have pointed out the current limitations of FNDs. The largest concern is brightness (related to the weight of the material), which is relatively low compared to that of other fluorescent probes [203]. Smaller NDs (<50 nm) can be detected only by fluorescence that has a sufficiently high signal-to-background ratio and not by backscat-

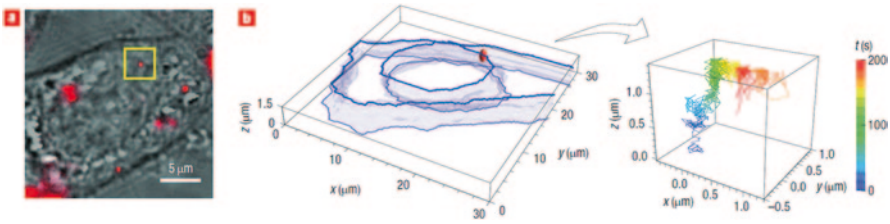

Fig. 11.10 Three-dimensional tracking of a single 35-nm HPHT ND in a live HeLa cell. **a** Bright-field and epifluorescence *(red pseudo-color)* images of the cell after ND uptake. **b** Three-dimensional reconstruction *(left panel)*, showing the boundaries of the nucleus and the cytoplasm of the cell. Three-dimensional trajectory (shown in pseudo-color, *right panel*) and displacements of a single FND (labeled with a *yellow box* in (**a**) inside the cell over a time span of 200 s). (Figure adapted from [190])

tered light from the excitation laser [181]. On the other hand, Neugart et al. were able to observe single diffusing NDs in living HeLa cells, although most particles only contained two defects [134]. The intrinsic fluorescence of non-treated NDs has been proposed to be strong enough for imaging both HPHT NDs and DNDs by confocal microscopy or flow cytometry. NDs are typically excited at 488 nm, and fluorescence is collected in the range from 510 to 530 nm [115, 118, 167, 178, 219, 239]. Natural defects and impurities and the large surface-to-volume ratio of nanoparticles are likely responsible for this green-light emission [167]. Similar to red fluorescent NDs, the concentration- and incubation-time-dependent uptake of 70-nm green fluorescent NDs in HeLa cells has been observed by both confocal microscopy and flow cytometry [240].

11.2.3.2 Cellular Targeting by Surface-Modified Nanodiamonds

The fluorescent properties of NDs are not altered by surface functionalization with certain biomolecules, which allows imaging of ND–biomolecule conjugates in cells. Biomolecules that bind to specific cell surface receptors have been used for cellular targeting of NDs (mostly to cancer cells). Conjugates with transferrin (ND-Tf) are a typical example [126–128]. In media supplemented with serum, negligible cellular internalization of carboxylated NDs and high uptake of ND-Tf conjugates were observed by flow cytometry and confocal microscopy. Transferrin receptors are overexpressed on the surfaces of HeLa cells, and ND-Tf is, therefore, highly effective at targeting cancer cells [128]. The assumption that ND-Tf conjugates specifically target transferrin receptors on cancer cells was confirmed by preincubation with free transferrin. An increase in free transferrin concentration causes a decrease of ND-Tf cellular uptake, as measured by flow cytometry [126]. The receptor-mediated uptake of ND-Tf was further confirmed using confocal fluorescence spectroscopy [128]. Fluorescence spectra and lifetimes of pristine and surface-modified NDs were very similar, confirming the negligible effects of chemical surface modifications [128].

NDs have also been conjugated with folic acid (ND–FA). Folic acid receptors are overexpressed on cancer cells, and the uptake of ND–FA is enhanced compared to pristine ND particles. The amount of ND–folic acid internalized was drastically reduced when the HeLa cells were pretreated with free FA (Fig. 11.11). These particles can be used for single-particle tracking in three dimensions and over a time span of more than 5 min during endocytosis. The uptake of ND–FA particles is concentration and incubation time dependent, as measured by flow cytometry [135].

ND and chlorotoxin conjugates (ND–Tx) specifically bind to glioma cell surfaces, as Fu et al. revealed. After NDs and ND–Tx were incubated with glioma cells in medium supplemented with serum, confocal microscopy showed that intracellular localization of ND–Tx was much higher than that of unmodified NDs [117]. DNDs with various bound antibodies were able to selectively target intracellular structures such as actin filaments, mitochondria, and membranes [115, 219].

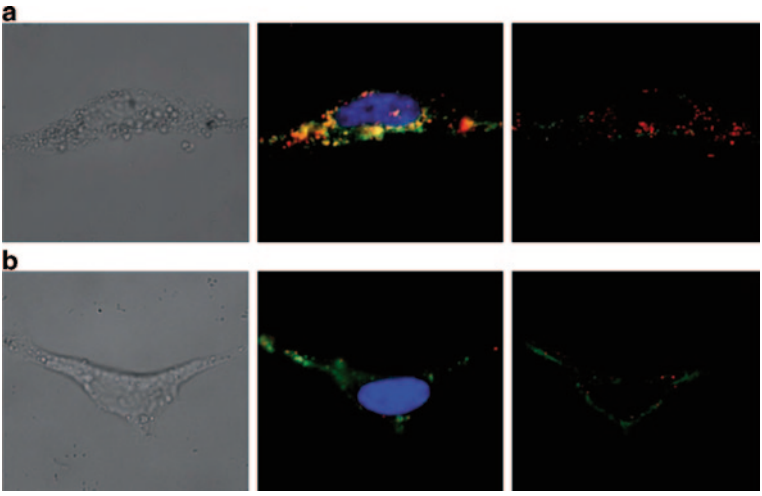

Fig. 11.11 Images of ND–FA internalized by HeLa cells with or without free FA in the media. **a** ND–FA, **b** ND–FA pretreated with free FA. The images displayed are differential interference contrast *(left)*, epifluorescence *(middle)*, and confocal fluorescence *(right)* images of the same cells with their membranes and endoplasmic reticulums stained in *green* with wheat germ agglutinin Alexa Fluor 488 conjugates and nuclei stained in *blue* with Hoechst 33258. All cells were incubated with NDs for 3 h at a particle concentration of 10 μg/ml. (Figure adapted from [135])

11.2.3.3 Fluorescence Imaging In Vivo

The first in vivo ND imaging was performed in 1 mm long transparent worms, *C. elegans*. The worms were fed with FNDs, which were subsequently visualized using a fluorescence microscope [130]. One worm contained an estimated 2 ng of 120-nm FNDs, corresponding to approximately 10^6 particles, which allowed easy imaging. Stable dispersions of dextran or serum albumin-coated FNDs were absorbed into intestinal cells after peroral administration, with very few remaining in the gut lumen [130]. Penetration of FNDs through the tissue of one *C. elegans* was documented by fluorescence microscopy. FNDs microinjected into the distal gonads of gravid hermaphrodites were incorporated into oocytes. Their fluorescence signals persisted throughout embryogenesis, suggesting that fluorescence ND labels can be used for long-term tracking in vivo [130]. Notably, no harmful effects were observed throughout the study.

Although the results from *C. elegans* were encouraging, observing FND fluorescence in mammals is much more challenging due to the large absorption and scattering of light in their bulky bodies and strong tissue autofluorescence. Recently, FNDs were visualized in mouse and rat with a fluorescence camera [189]. Autofluorescence excited at short wavelength (430 nm) was subtracted from the obtained data. FNDs administered to rats by subcutaneous (s.c.) and intraperitoneal (i.p.) injection were observed. For s.c. injection, FNDs could be visualized more than 1 month after administration, confirming their promise as long-term fluorescent

labels. Notably, imaging in rats is considerably more challenging than imaging in mice due to rats' greater skin thickness (ca. fivefold) and resulting higher absorption of light [189]. No optical degradation of FNDs or toxic effects on the animals were observed, even at huge doses of FNDs (5 mg/kg, repetitively, administered i.p.).

FNDs were successfully used for in vivo fluorescence imaging of a mouse lymph node [189]. Serum albumin-coated FNDs (100 nm) injected intradermally into the foot migrated into the axillary lymph node (Fig. 11.12). This observation was performed over several days, showing a gradual increase in fluorescence intensity in the node. Notably, a dose of only 40 μg of FNDs was administered, showing the high sensitivity of this experimental setup. This method represents a breakthrough in FND in vivo imaging because it can be used not only to visualize particles in the place of administration but also to track them throughout the body. These results can be applied to sentinel lymph node mapping, a technique widely used in cancer diagnosis and treatment [241]. The remarkable in vivo imaging results achieved by Chang et. al were mainly due to their ability to prepare extraordinarily bright FNDs [190] and to their carefully designed imaging protocols that included background autofluorescence subtraction during fluorescence scanning [189].

Two remarkable optical properties of NV centers have been applied to suppress background signals from surrounding tissue during in vivo fluorescence imaging—long fluorescence lifetimes and the unique electronic structure of NV centers. One approach [236] exploits the radiative lifetime of an excited NV center (>10 ns), which is quite long compared to that of sources of autofluorescence (1–4 ns). Fluorescence lifetime imaging microscopy (FLIM) measures fluorescence lifetimes and therefore allows filtering of short radiating signals that do not originate from NV centers. Standard fluorescence acquisition suffered from a strong background signal in *C. elegans* fed with 100 nm FNDs, while FLIM could distinguish between these two types of signals.

A second approach for background fluorescence suppression takes advantage of the fact that an NV center has a ground triplet state of $^3A_2$, which is due to

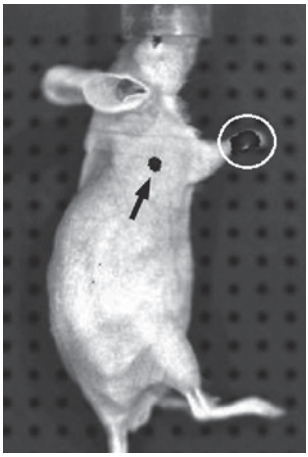

Fig. 11.12 In vivo imaging of FNDs, intradermally injected into mouse foot (marked with a *white circle*) and their accumulation in lymph node *(black arrow)* 8 days after injection. (Figure adapted from [189])

the crystal field and onsite magnetic interactions separated into two energy levels ($m_s = \pm 1$) [194, 237] (see Fig. 11.7). Fluorescence intensity is significantly stronger when excitation starts from $^3A_2$ ($m_s = 0$) than from $^3A_2$ ($m_s = \pm 1$). In the absence of an external magnetic field, these two energy levels are separated with an energy corresponding to 2.87 GHz resonant frequency. Irradiation of FNDs with this resonant frequency leads to a decrease in their fluorescence intensity, while all other fluorescence sources remain unchanged (for more details and other applications of this phenomenon, see [194, 213, 237, 242, 243]). This unique FND behavior allowed background-free imaging of FNDs in *C. elegans* (peroral administration) and mice (i.p. injection of 10 μg NDs) by fluorescence scanning with a 2.87 GHz field repetitively turned on and off [237]. If an external magnetic field is applied, the degenerate $^3A_2$ ($m_s = \pm 1$) states split, and the rising energy barrier between them rises linearly with the applied magnetic field [214]. This phenomenon was used by Hegyi and Yablonovitch, who, by application of gradient magnetic fields (in a somewhat similar manner as in MRI), achieved 3D imaging of FNDs in a chicken breast phantom [214]. Although this is not in vivo imaging, the elaborate technology and promising results are noteworthy.

In summary, in vivo imaging of FNDs still remains a challenging task, but the achievements made in recent years, such as FND tracking in mice, represent huge progress in the field.

11.3 Other Bioapplications of Nanodiamonds

11.3.1 Drug Delivery

Important parameters in the design of suitable drug carriers for intracellular delivery are sufficient loading capacity in proportion to the weight of the carrier, strong binding of active molecules to the carrier surface, and a mechanism of targeted release. Thanks to their enormous surface area, good biocompatibility, and easy functionalization with biomolecules, NDs comply with all these requirements. Current ND drug delivery research mainly focuses on design of carriers for delivery of small biomolecules, with an emphasis on chemotherapeutic agents. With a few exceptions, active substances are attached to the particle surface via non-covalent bond interactions, which allows easier carrier formation.

11.3.1.1 Small Molecules

The Ho laboratory made a pioneering step in the investigation of NDs as possible drug carriers by establishing non-covalent bonding of doxorubicin (DOX) hydrochloride to oxidized DND surfaces [138]. Negatively charged groups at the surface of DNDs form ionic interactions with the positively charged amino group of

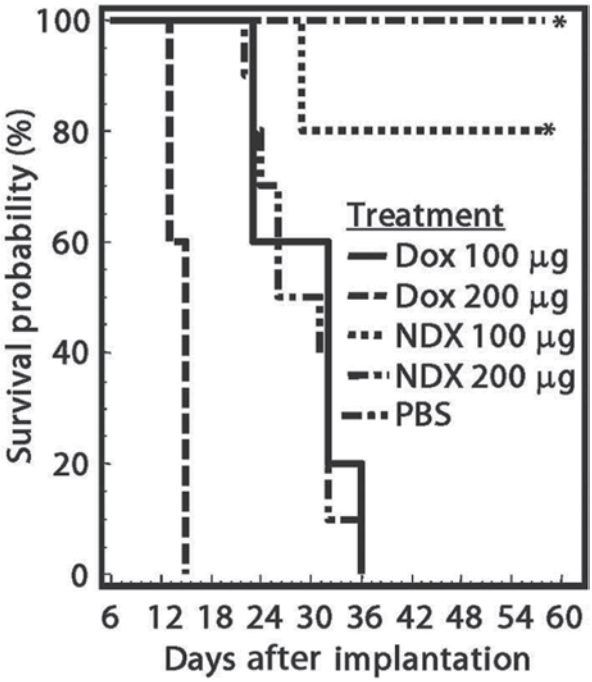

Fig. 11.13 ND delivery of doxorubicin (DOX) inhibits tumor growth in a murine mammary carcinoma model (4T1 cells). Survival plot for tumor-bearing mice treated with phosphate buffer saline (PBS) ($n=7$), DOX (100 mg) ($n=10$), DND–DOX conjugate (NDX; 100 mg DOX equivalent; $n=10$), DOX (200 mg; $n=5$), or NDX (200 mg DOX equivalent; $n=5$) by tail-vein injection every 6 days. *$P<0.003$. NDX nanodiamond–doxorubicin complex (Figure adapted from [184])

DOX. The resulting particles are in the form of clusters. The amount of bound DOX increases with the ionic strength and basicity of the environment [244, 245]. This effect allows in vivo release of DOX upon a change in environmental conditions and enables highly efficient tumor treatment in an animal model (Fig. 11.13) [184]. Similar particles including cisplatin and 10-hydroxycamptothecin (HCPT) have been developed [129, 246]. Intracellular delivery of DND-DOX particles can be enhanced by conjugation with the cell-penetrating protein TAT (trans-activator of transcription protein) [247]. Non-covalently bound DND-DOX particles, which allow long-term fluorescence localization of particles within the cell, have also been developed [248].

NDs can also be used to increase the solubility of hydrophobic drugs, such as purvalanol A and 4-hydroxytamoxifen [249]. Paclitaxel, a chemotherapy drug, has been covalently linked to the surface of NDs [239]. Hybrid carriers with both covalent and non-covalent bonds have also been developed. These particles are composed of NDs with non-covalently bound epirubicin, coated with a lipid double layer with a small amount of biotinylated lipids. These are connected to biotinylated targeting antibodies via a streptavidin anchor [250].

11.3.1.2 Biomolecules

The potential use of NDs as biomolecule carriers was illustrated by pH-controlled release of bovine insulin bound on ND surfaces [136]. Use of NDs for gene deliv-

ery is hindered by the negative charge and high molecular weight of bound nucleic acids.

One possible way to overcome these obstacles is modifying the particle architecture by covering NDs with positively charged polyethyleneimine-800 (PEI-800). PEI-800 forms electrostatic interactions with negatively charged plasmid DNA [140]. Use of PEI-800-coated NDs led to substantial improvement in the efficiency of transfection without an increase in cytotoxicity. Other work has shown the possibility of using DNDs or HPHT FNDs coated with non-covalently bound cationic polymers for intracellular transport of small interfering RNA (siRNA) [139, 180, 251]. For DNDs, different surface architectures that enable intracellular plasmid transfer include covalently bound triethylamine [81] and lysine [252] functional groups or the use of a cationic 2-(dimethylamino)ethyl methacrylate NDs-polymer brush [253].

11.3.2 Nanodiamonds as a Tool for Mass Spectrometry

In recent years, NDs have been recognized as a valuable tool for mass spectrometry (MS) of various biomolecules [254], due to their large surface area and high affinity to macromolecules. The use of NDs in MS studies is based on solid-phase extraction (SPE) of biopolymers (peptide, protein, or DNA) on the ND surface with subsequent separation of NDs by centrifugation [255] or filtration [256]. After washing, NDs with adsorbed analyte are suitable for immediate MS analysis. The preferred ionization methods are matrix-assisted laser desorption/ionization (MALDI) and electrospray ionization (ESI), which provide sufficiently soft conditions for biomolecular analysis.

Chemical modification of ND surfaces allows adjustment of ND affinity to different types of biomolecules. Carboxylated NDs have a remarkably high affinity to peptides [255, 257] and proteins [141, 145, 258]. The high affinity of peptides [68] and proteins [145] to negatively charged carboxylated NDs might be due to a combination of their ionic interactions, hydrogen bonding, hydrophobic, and van der Waals interactions. Covalent or non-covalent coating of NDs with basic polylysine [141, 256, 259] or polyarginine [260] leads to the formation of positively charged films on the surfaces of carboxylated NDs. Polylysine- and polyarginine-coated NDs show a strong affinity for negatively charged species such as DNA [261] and phosphoproteins [260]. Similarly, NDs functionalized with boronic acid exhibit affinity for glycopeptides [262]. Last but not least, a major advantage of NDs as selective extractors of biomolecules from solution is their inertness, which allows modifications of the adsorbed analytes in subsequent MS studies [255, 259].

11.3.3 Other Applications

In this section, we briefly discuss some interesting bio-related applications of NDs.

One of these bioapplications is enzyme immobilization. Several disadvantages of enzymes, such as short-term stability and difficulties in recovery and recycling,

can be eliminated and improved by non-covalent [68] or covalent [121] immobilization of enzymes on HPHT ND or DND surfaces. This immobilization increases stability, enables repeated use and easy separation from the reaction mixture, and can improve the catalytic properties of an enzyme [263]. One advantage of using NDs rather than other nanoparticles for this purpose is their biocompatibility. For example, the catalytic activity of immobilized trypsin on DND surfaces was not altered significantly [121]. Both the Michaelis constant and maximum effective velocity of ND-bound trypsin were within the same order of magnitude as for free trypsin. In fact, immobilized trypsin catalyzed protein cleavage with even higher efficiency than free trypsin. Unlike free trypsin, the immobilized enzyme did not undergo autolysis. The catalytic reaction with immobilized enzyme can, therefore, be performed more quickly and with higher enzyme concentrations than the reaction with free trypsin. Five minutes of BSA and myoglobin cleavage by immobilized trypsin was comparable to 12 h of cleavage by free trypsin, according to mass spectrometry [121].

HPHT NDs have been used as an adjuvant—an agent used to enhance immune responses [264]. Common adjuvants shield epitopes critical for evoking an immune response. Mussel adhesive protein bound to a conventional adjuvant evokes a weak immune response, while exposure to antigen immobilized on cellobiose-modified NDs evokes a strong response. Using this ND adjuvant, antibodies against mussel adhesive protein were prepared in rabbits [264].

NDs modified with lysozyme were able to bind *Escherichia coli* from solution. The ND–lysozyme complex interacted with *E. coli*, while non-modified NDs had no affinity for the bacteria. Lysozyme is an enzyme that lyses the bacterial cell wall. The ND–lysozyme complex showed high antibacterial activity in a bacteria survival test [124, 178]. NDs non-covalently modified with specific antibodies were able to interact with *Salmonella typhimurium* and *Staphylococcus aureus*. ND-antibody conjugates can serve as effective probes for the detection of bacteria or other pathogens in solution [114].

NDs can also be used for construction of powder electrodes either in the form of powder [265] or immobilized on metal electrode [266] to improve their electrochemical properties [267]. A wide potential window (~3,5 V), low capacitance, high electrochemical stability, and corrosion resistance are typical features of diamond electrodes. To induce conductivity, diamond electrodes are commonly boron doped [268]. In the case of NDs with a high surface to volume ratio (usually DNDs several nanometer in diameter), surface defects, and surface modifications can induce conductive behavior [265]. Zang et al. showed that the redox behavior of a DND powder electrode is similar to that of a diamond film [269]. Zhao et al. prepared an electrode for glucose biosensing based on carboxy-terminated NDs coated on a gold disc electrode. Glucose oxidase molecules were covalently bound to the carboxy groups. Anodic oxidation pretreatment led to increased oxygen reduction [266]. Highly sensitive electrochemical detection of the immunosuppressive drug azathioprine was achieved by glassy carbon electrodes modified with a film of ND–graphite/chitosan [270]. ND-based sponges with entrapped horseradish peroxidase

showed excellent biocatalytic properties toward reduction of hydrogen peroxide [271].

In addition to these examples, there are many other medical applications and bioapplications of NDs. For example, because of their high surface area, biocompatibility, and nontoxicity, DNDs can be used as novel carbon-based enterosorbents for a group of mycotoxins called aflatoxins [272].

An interesting potential application of NDs involves photothermal cancer therapy. Growth hormone-modified DNDs were adsorbed onto the surface of cancer cells. Laser irradiation at 532 nm was absorbed by DND nitroso groups (two-photon absorption), which causes local membrane damage followed by cell death [273]. This photothermal effect was also demonstrated with transferrin-modified HPHT FNDs internalized into HeLa cells. The mechanism of action is hyperthermia following laser irradiation, caused by intensive absorption of isolated nitrogen atoms in the FND lattice [128]. Hybrid FND particles connected to urchin-like gold nanoparticles were also developed. These nanoparticles allow a combination of fluorescence imaging using excitation at 488 nm and photothermal ablation at 800 nm [274].

DNDs containing composites are promising materials for bone tissue engineering. Octadecylamine–DNDs were dispersed in the biodegradable polymer poly(L-lactic acid) to form fluorescent composite bone scaffold material. DNDs significantly improved the mechanical properties of the poly(L-lactic) acid matrix [275]. Addition of DNDs to a simulated body fluid resulted in more effective hydroxyapatite growth, which was attributed to the character of –OH groups on the DND surface [276]. Designs of ND-based biochips have also been suggested [277, 278]. Mannose-modified NDs showed highly specific anti-adhesive behavior toward biotic and abiotic surfaces [279]. According to patent literature, DNDs are a promising ingredient in cosmetic and health-care products [280, 281]. Today, diamond powder is included in more than 70 cosmetic products such as nail polishes, shampoos, and sunscreens (www.cosmeticdatabase.com).

11.4 Conclusions and Outlook

Compared with other carbon nanomaterials, NDs became in a short time period an important and promising material for a wide range of potential applications. Their intriguing diversity in structure, size, surface chemistry, and photophysical properties has resulted in use of NDs in diverse fields, including in vivo imaging, super-resolution microscopy, drug delivery, mass spectrometry, and photothermal cancer therapy. Indeed, their use as selective cellular and intracellular probes currently remains under development (as for all nanoparticle probes), because they cannot be genetically encoded like fluorescent proteins. However, further studies on their structure, surface chemistry, and coatings; improved control of their colloidal properties; and development of functionalization and targeting methods promise to move this issue forward. In the near future, the unprecedented photophysical

and spin properties of NV centers embedded in properly modified ND crystals are expected to fulfill the demands required for construction of extremely stable and highly biocompatible optical and magnetic bionanosensors.

Acknowledgment This work was supported by the MZ-VES project no. 15-33094A.

References

1. V.V. Danilenko, On the history of the discovery of nanodiamond synthesis. Phys. Solid State **46**, 595–599 (2004)
2. V.N. Mochalin, O. Shenderova, D. Ho, Y. Gogotsi, The properties and applications of nanodiamonds. Nat. Nanotechnol. **7**, 11–23 (2011). doi:10.1038/nnano.2011.209
3. A. Krueger (2010) *Nanodiamond*. In: Carbon Materials and Nanotechnology. (Wiley-VCH Verlag GmbH & Co. KGaA, p 329–388)
4. K.B. Holt, Diamond at the nanoscale: applications of diamond nanoparticles from cellular biomarkers to quantum computing. Philos. Trans. A. Math. Phys. Eng. Sci. **365**, 2845–2861 (2007). doi:10.1098/rsta.2007.0005
5. A. Krueger, Beyond the shine: recent progress in applications of nanodiamond. J. Mater. Chem. **21**, 12571 (2011). doi:10.1039/c1jm11674f
6. A.M. Schrand, S.A.C. Hens, O.A. Shenderova, Nanodiamond particles: properties and perspectives for bioapplications. Crit. Rev. Solid State Mater. Sci. **34**, 18–74 (2009). doi:10.1080/10408430902831987
7. A. Krueger, New carbon materials: biological applications of functionalized nanodiamond materials. Chemistry **14**, 1382–1390 (2008). doi:10.1002/chem.200700987
8. B.I. Kharisov, O.V. Kharissova, L. Chávez-Guerrero, Synthesis techniques, properties, and applications of nanodiamonds. Synth. React. Inorg. Metal-Org. Nano-Metal Chem. **40**, 84–101 (2010)
9. A. Krueger, D. Lang, Functionality is key: recent progress in the surface modification of nanodiamond. Adv. Funct. Mater. **22**, 890–906 (2012). doi:10.1002/adfm.201102670
10. A. Krueger, The structure and reactivity of nanoscale diamond. J. Mater. Chem. **18**, 1485 (2008). doi:10.1039/b716673g
11. J. Wrachtrup, F. Jelezko, B. Grotz, L. McGuinness, Nitrogen-vacancy centers close to surfaces. MRS Bull. **38**, 149–154 (2013). doi:10.1557/mrs.2013.22
12. I. Aharonovich, A.D. Greentree, S. Prawer, Diamond photonics. Nat. Photonics **5**, 397–405 (2011). doi:10.1038/nphoton.2011.54
13. F. Jelezko, J. Wrachtrup, Single defect centres in diamond: a review. Phys. Status Solidi A **203**, 3207–3225 (2006). doi:10.1002/pssa.200671403
14. V. Vaijayanthimala, H.C. Chang, Functionalized fluorescent nanodiamonds for biomedical applications. Nanomedicine **4**, 47–55 (2009). doi:10.2217/17435889.4.1.47
15. J.H. Liu, S.T. Yang, X.X. Chen, H. Wang, Fluorescent carbon dots and nanodiamonds for biological imaging: preparation, application, pharmacokinetics and toxicity. Curr. Drug Metab. **13**, 1046–1056 (2012). doi:10.2174/138920012802850083
16. Y.Y. Hui, C.L. Cheng, H.C. Chang, Nanodiamonds for optical bioimaging. J. Phys. Appl. Phys. **43**, 374021 (2010)
17. A.S. Barnard, Diamond standard in diagnostics: nanodiamond biolabels make their mark. Analyst **134**, 1751 (2009). doi:10.1039/b908532g
18. A. Krueger, Diamond nanoparticles: jewels for chemistry and physics. Adv. Mater. **20**, 2445–2449 (2008). doi:10.1002/adma.200701856
19. Y. Zhu, The biocompatibility of nanodiamonds and their application in drug delivery systems. Theranostics **2**, 302–312 (2012). doi:10.7150/thno.3627

20. D. Ho, *Nanodiamonds: applications in biology and nanoscale medicine*. (Springerverlag, USA, 2010)
21. H.B. Man, D. Ho, Diamond as a nanomedical agent for versatile applications in drug delivery, imaging, and sensing. Phys. Status Solidi A **209**, 1609–1618 (2012). doi:10.1002/pssa.201200470
22. D. Ho, Beyond the sparkle: the impact of nanodiamonds as biolabeling and therapeutic agents. ACS. Nano. **3**, 3825–3829 (2009). doi:10.1021/nn9016247
23. C. Frondel, U.B. Marvin, Lonsdaleite, a hexagonal polymorph of diamond. Nature **214**, 587–589 (1967). doi:10.1038/214587a0
24. O.A. Shenderova, V.V. Zhirnov, D.W. Brenner, Carbon nanostructures. Crit. Rev. Solid State Mater. Sci. **27**, 227–356 (2002). doi:10.1080/10408430208500497
25. A.K. Geim, K.S. Novoselov, The rise of graphene. Nat. Mater. **6**, 183–191 (2007). doi:10.1038/nmat1849
26. O.A. Williams, J. Hees, C. Dieker, W. Jäger, L. Kirste, C.E. Nebel, Size-dependent reactivity of diamond nanoparticles. ACS. Nano. **46**, 595–599 (2004)
27. D.S. Zhao, M. Zhao, Q. Jiang, Size and temperature dependence of nanodiamond-nanographite transition related with surface stress. Diam. Relat. Mater. **11**, 234–236 (2002). doi:10.1016/S0925-9635(01)00694-X
28. Q. Jiang, Z.P. Chen, Thermodynamic phase stabilities of nanocarbon. Carbon **44**, 79–83 (2006). doi:10.1016/j.carbon.2005.07.014
29. J.Y. Raty, G. Galli, Ultradispersity of diamond at the nanoscale. Nat. Mater. **2**, 792–795 (2003). doi:10.1038/nmat1018
30. A.S. Barnard, M. Sternberg, Crystallinity and surface electrostatics of diamond nanocrystals. J. Mater. Chem. **17**, 4811–4819 (2007). doi:10.1039/B710189A
31. O.A. Williams, Nanocrystalline diamond. Diam. Relat. Mater. **20**, 621–640 (2011). doi:10.1016/j.diamond.2011.02.015
32. G.W. Yang, J.B. Wang, Q.X. Liu, Preparation of nano-crystalline diamonds using pulsed laser induced reactive quenching. J. Phys. Condens. Matter **10**, 7923 (1998)
33. T.L. Daulton, M.A. Kirk, R.S. Lewis, L.E. Rehn, Production of nanodiamonds by high-energy ion irradiation of graphite at room temperature. Nucl. Instrum. Methods Phys. Res. Sect. B. Beam Interact. Mater. Atoms **175–177**, 12–20 (2001). doi:10.1016/S0168-583 × (00)00603-0
34. F. Banhart, P.M. Ajayan, Carbon onions as nanoscopic pressure cells for diamond formation. Nature **382**, 433–435 (1996). doi:10.1038/382433a0
35. V.Y. Dolmatov, Detonation-synthesis nanodiamonds: synthesis, structure, properties and applications. Russ. Chem. Rev. **76**, 339–360 (2007). doi:10.1070/RC2007v076n04ABEH003643
36. A. Krueger, F. Kataoka, M. Ozawa, T. Fujino, Y. Suzuki, A.E. Aleksenskii, A.Y. Vul, E. Osawa, Unusually tight aggregation in detonation nanodiamond: identification and disintegration. Carbon **43**, 1722–1730 (2005). doi:10.1016/j.carbon.2005.02.020
37. S. Osswald, G. Yushin, V. Mochalin, S.O. Kucheyev, Y. Gogotsi, Control of sp2/sp3 carbon ratio and surface chemistry of nanodiamond powders by selective oxidation in air. J. Am. Chem. Soc. **128**, 11635–11642 (2006). doi:10.1021/ja063303n
38. V. Pichot, M. Comet, E. Fousson, C. Baras, A. Senger, L. Normand F, D. Spitzer, An efficient purification method for detonation nanodiamonds. Diam. Relat. Mater. **17**, 13–22 (2008). doi:10.1016/j.diamond.2007.09.011
39. V.G. Sushchev, V.Y. Dolmatov, V.A. Marchukov, M.V. Veretennikova, Fundamentals of chemical purification of detonation nanodiamond soot using nitric acid. J. Superhard Mater. **30**, 297–304 (2008). doi:10.3103/S1063457608050031
40. NATO Advanced Research Workshop on Synthesis, Properties and Applications of Ultrananocrystalline Diamond, *Synthesis, properties, and applications of ultrananocrystalline diamond*. (Springer, Dordrecht, 2005)

41. O. Shenderova, I. Petrov, J. Walsh, V. Grichko, V. Grishko, T. Tyler, G. Cunningham, Modification of detonation nanodiamonds by heat treatment in air. Diam. Relat. Mater. **15**, 1799–1803 (2006). doi:10.1016/j.diamond.2006.08.032
42. I. Petrov, O. Shenderova, V. Grishko, V. Grichko, T. Tyler, G. Cunningham, G. McGuire, Detonation nanodiamonds simultaneously purified and modified by gas treatment. Diam. Relat. Mater. **16**, 2098–2103 (2007). doi:10.1016/j.diamond.2007.05.013
43. Q. Xu, X. Zhao, Electrostatic interactions versus van der Waals interactions in the self-assembly of dispersed nanodiamonds. J. Mater. Chem. **22**, 16416 (2012). doi:10.1039/c2jm32918b
44. A.S. Barnard, Self-assembly in nanodiamond agglutinates. J. Mater. Chem. **18**, 4038 (2008). doi:10.1039/b809188a
45. L.Y. Chang, E. Ōsawa, A.S. Barnard, Confirmation of the electrostatic self-assembly of nanodiamonds. Nanoscale **3**, 958 (2011). doi:10.1039/c0nr00883d
46. M. Ozawa, M. Inaguma, M. Takahashi, F. Kataoka, A. Krueger, E. Ōsawa, Preparation and behavior of brownish, clear nanodiamond colloids. Adv. Mater. **19**, 1201–1206 (2007). doi:10.1002/adma.200601452
47. E.D. Eidelman, V.I. Siklitsky, L.V. Sharonova, M.A. Yagovkina, A.Y. Vul', M. Takahashi, M. Inakuma, M. Ozawa, E. Ōsawa, A stable suspension of single ultrananocrystalline diamond particles. Diam. Relat. Mater. **14**, 1765–1769 (2005). doi:10.1016/j.diamond.2005.08.057
48. Y. Liang, M. Ozawa, A. Krueger, A general procedure to functionalize agglomerating nanoparticles demonstrated on nanodiamond. ACS. Nano. **3**, 2288–2296 (2009). doi:10.1021/nn900339s
49. A. Pentecost, S. Gour, V. Mochalin, I. Knoke, Y. Gogotsi, Deaggregation of nanodiamond powders using salt- and sugar-assisted milling. ACS. Appl. Mater. Interfaces **2**, 3289–3294 (2010). doi:10.1021/am100720n
50. J.P. Boudou, P.A. Curmi, F. Jelezko, J. Wrachtrup, P. Aubert, M. Sennour, G. Balasubramanian, R. Reuter, A. Thorel, E. Gaffet, High yield fabrication of fluorescent nanodiamonds. Nanotechnology **20**, 235602 (2009). doi:10.1088/0957-4484/20/23/235602
51. J. Philip, P. Hess, T. Feygelson, J.E. Butler, S. Chattopadhyay, K.H. Chen, L.C. Chen, Elastic, mechanical, and thermal properties of nanocrystalline diamond films. J. Appl. Phys. **93**, 2164–2171 (2003). doi:10.1063/1.1537465
52. J.E. Butler, A.V. Sumant, The CVD of nanodiamond materials. Chem. Vap. Depos. **14**, 145–160 (2008). doi:10.1002/cvde.200700037
53. J.J. Gracio, Q.H. Fan, J.C. Madaleno, Diamond growth by chemical vapour deposition. J. Phys. Appl. Phys. **43**, 374017 (2010). doi:10.1088/0022-3727/43/37/374017
54. Z.H. Yongwei, X. Shen, Z. Feng, X. Xu, B. Wang, On the zeta-potential of nanodiamond in aqueous systems. J. Mater. Sci. Technol. **20**, 469 (2004)
55. H. Boehm, Surface oxides on carbon and their analysis: a critical assessment. Carbon **40**, 145–149 (2002). doi:10.1016/S0008-6223(01)00165-8
56. E. Fuente, J.A. Menéndez, D. Suárez, M.A. Montes-Morán, Basic surface oxides on carbon materials: a global view. Langmuir **19**, 3505–3511 (2003). doi:10.1021/la026778a
57. M.A. Montes-Morán, D. Suárez, J.A. Menéndez, E. Fuente, On the nature of basic sites on carbon surfaces: an overview. Carbon **42**, 1219–1225 (2004). doi:10.1016/j.carbon.2004.01.023
58. O. Shenderova, S. Hens, G. McGuire, Seeding slurries based on detonation nanodiamond in DMSO. Diam. Relat. Mater. **19**, 260–267 (2010)
59. M. Ozawa, M. Inaguma, M. Takahashi, F. Kataoka, A. Krueger, E. Osawa, Preparation and behavior of brownish, clear nanodiamond colloids. Adv. Mater. **19**, 1201–1206 (2007). doi:10.1002/adma.200601452
60. C.C. Li, C.L. Huang, Preparation of clear colloidal solutions of detonation nanodiamond in organic solvents. Colloids Surf. Physicochem. Eng. Asp. **353**, 52–56 (2010). doi:10.1016/j.colsurfa.2009.10.019
61. X. Xu, Z. Yu, Y. Zhu, B. Wang, Effect of sodium oleate adsorption on the colloidal stability and zeta potential of detonation synthesized diamond particles in aqueous solutions. Diam. Relat. Mater. **14**, 206–212 (2005)

62. U. Maitra, A. Gomathi, C.N.R. Rao, Covalent and noncovalent functionalisation and solubilisation of nanodiamond. J. Exp. Nanosci. **3**, 271–278 (2008). doi:10.1080/17458080802574155
63. V.N. Mochalin, Y. Gogotsi, Wet chemistry route to hydrophobic blue fluorescent nanodiamond. J. Am. Chem. Soc. **131**, 4594–4595 (2009). doi:10.1021/ja9004514
64. S.A. Dahoumane, M.N. Nguyen, A. Thorel, J.P. Boudou, M.M. Chehimi, C. Mangeney, Protein-functionalized hairy diamond nanoparticles. Langmuir **25**, 9633–9638 (2009). doi:10.1021/la9009509
65. V.K.A. Sreenivasan, E.A. Ivukina, W. Deng, T.A. Kelf, T.A. Zdobnova, S.V. Lukash, B.V. Veryugin, O.A. Stremovskiy, A.V. Zvyagin, S.M. Deyev, Barstar:barnase—a versatile platform for colloidal diamond bioconjugation. J. Mater. Chem. **21**, 65 (2011). doi:10.1039/c0jm02819c
66. Y. Liang, T. Meinhardt, G. Jarre, M. Ozawa, P. Vrdoljak, A. Schöll, F. Reinert, A. Krueger, Deagglomeration and surface modification of thermally annealed nanoscale diamond. J. Colloid. Interface Sci. **354**, 23–30 (2011). doi:10.1016/j.jcis.2010.10.044
67. L. Zhao, T. Takimoto, M. Ito, N. Kitagawa, T. Kimura, N. Komatsu, Chromatographic separation of highly soluble diamond nanoparticles prepared by polyglycerol grafting. Angew. Chem. Int. Ed. Engl. **50**, 1388–1392 (2011). doi:10.1002/anie.201006310
68. T. Nguyen, H.C. Chang, V.W.K. Wu, Adsorption and hydrolytic activity of lysozyme on diamond nanocrystallites. Diam. Relat. Mater. **16**, 872–876 (2007)
69. T. Jiang, K. Xu, FTIR study of ultradispersed diamond powder synthesized by explosive detonation. Carbon **33**, 1663–1671 (1995). doi:10.1016/0008-6223(95)00115-1
70. V. Mochalin, S. Osswald, Y. Gogotsi, Contribution of functional groups to the raman spectrum of nanodiamond powders. Chem. Mater. **21**, 273–279 (2009). doi:10.1021/cm802057q
71. J.S. Tu, E. Perevedentseva, P.H. Chung, C.L. Cheng, Size-dependent surface CO stretching frequency investigations on nanodiamond particles. J. Chem. Phys. **125**, 174713-174713-7 (2006). doi:10.1063/1.2370880
72. J. Cheng, J. He, C. Li, Y. Yang, Facile approach to functionalize nanodiamond particles with V-shaped polymer brushes. Chem. Mater. **20**, 4224–4230 (2008). doi:10.1021/cm800357g
73. D. Mitev, R. Dimitrova, M. Spassova, C. Minchev, S. Stavrev, Surface peculiarities of detonation nanodiamonds in dependence of fabrication and purification methods. Diam. Relat. Mater. **16**, 776–780 (2007). doi:10.1016/j.diamond.2007.01.005
74. L. Rondin, G. Dantelle, A. Slablab, F. Grosshans, F. Treussart, P. Bergonzo, S. Perruchas, T. Gacoin, M. Chaigneau, H.C. Chang, V. Jacques, J.F. Roch, Surface-induced charge state conversion of nitrogen-vacancy defects in nanodiamonds. Phys. Rev. B (2010). doi:10.1103/PhysRevB.82.115449
75. B.R. Smith, D. Gruber, T. Plakhotnik, The effects of surface oxidation on luminescence of nano diamonds. Diam. Relat. Mater. **19**, 314–318 (2010). doi:10.1016/j.diamond.2009.12.009
76. A. Krueger, Y. Liang, G. Jarre, J. Stegk, Surface functionalisation of detonation diamond suitable for biological applications. J. Mater. Chem. **16**, 2322–2328 (2006). doi:10.1039/B601325B
77. A. Krueger, M. Ozawa, G. Jarre, Y. Liang, J. Stegk, L. Lu, Deagglomeration and functionalisation of detonation diamond. Phys. Status Solidi A **204**, 2881–2887 (2007). doi:10.1002/pssa.200776330
78. W.W. Zheng, Y.H. Hsieh, Y.C. Chiu, S.J. Cai, C.L. Cheng, C. Chen, Organic functionalization of ultradispersed nanodiamond: synthesis and applications. J. Mater. Chem. **19**, 8432–8441 (2009). doi:10.1039/B904302K
79. S.C. Hens, G. Cunningham, T. Tyler, S. Moseenkov, V. Kuznetsov, O. Shenderova, Nanodiamond bioconjugate probes and their collection by electrophoresis. Diam. Relat. Mater. **17**, 1858–1866 (2008). doi:10.1016/j.diamond.2008.03.020
80. R. Martín, P.C. Heydorn, M. Alvaro, H. Garcia, General strategy for high-density covalent functionalization of diamond nanoparticles using Fenton chemistry. Chem. Mater. **21**, 4505–4514 (2009). doi:10.1021/cm9012602
81. R. Martín, M. Álvaro, J.R. Herance, H. García, Fenton-treated functionalized diamond nanoparticles as gene delivery system. ACS. Nano. **4**, 65–74 (2010). doi:10.1021/nn901616c

82. B.V. Spitsyn, S.A. Denisov, N.A. Skorik, A.G. Chopurova, S.A. Parkaeva, L.D. Belyakova, O.G. Larionov, The physical-chemical study of detonation nanodiamond application in adsorption and chromatography. Diam. Relat. Mater. **19**, 123–127 (2010). doi:10.1016/j.diamond.2009.10.020
83. S. Ida, T. Tsubota, O. Hirabayashi, M. Nagata, Y. Matsumoto, A. Fujishima, Chemical reaction of hydrogenated diamond surface with peroxide radical initiators. Diam. Relat. Mater. **12**, 601–605 (2003). doi:10.1016/S0925-9635(02)00334-5
84. H.A. Girard, J.C. Arnault, S. Perruchas, S. Saada, T. Gacoin, J.P. Boilot, P. Bergonzo, Hydrogenation of nanodiamonds using MPCVD: a new route toward organic functionalization. Diam. Relat. Mater. **19**, 1117–1123 (2010). doi:10.1016/j.diamond.2010.03.019
85. I.P. Chang, K.C. Hwang, J.A. Ho, C.C. Lin, R.J.R. Hwu, J.C. Horng, Facile surface functionalization of nanodiamonds. Langmuir **26**, 3685–3689 (2010). doi:10.1021/la903162v
86. V.L. Kuznetsov, A.L. Chuvilin, Y.V. Butenko, I.Y. Malkov, V.M. Titov, Onion-like carbon from ultra-disperse diamond. Chem. Phys. Lett. **222**, 343–348 (1994). doi:10.1016/0009-2614(94)87072-1
87. Y. Liang, T. Meinhardt, G. Jarre, M. Ozawa, P. Vrdoljak, A. Schöll, F. Reinert, A. Krueger, Deagglomeration and surface modification of thermally annealed nanoscale diamond. J. Colloid Interface Sci. **354**, 23–30 (2011). doi:10.1016/j.jcis.2010.10.044
88. Y. Liu, Z. Gu, J.L. Margrave, V.N. Khabashesku, Functionalization of nanoscale diamond powder: fluoro-, alkyl-, amino-, and amino acid-nanodiamond derivatives. Chem. Mater. **16**, 3924–3930 (2004). doi:10.1021/cm048875q
89. M.A. Ray, T. Tyler, B. Hook, A. Martin, G. Cunningham, O. Shenderova, J.L. Davidson, M. Howell, W.P. Kang, G. McGuire, Cool plasma functionalization of nano-crystalline diamond films. Diam. Relat. Mater. **16**, 2087–2089 (2007). doi:10.1016/j.diamond.2007.07.016
90. K.I. Sotowa, T. Amamoto, A. Sobana, K. Kusakabe, T. Imato, Effect of treatment temperature on the amination of chlorinated diamond. Diam. Relat. Mater. **13**, 145–150 (2004). doi:10.1016/j.diamond.2003.10.029
91. J.S. Hovis, S.K. Coulter, R.J. Hamers, M.P. D'Evelyn, J.N. Russell, J.E. Butler, Cycloaddition chemistry at surfaces: reaction of alkenes with the diamond(001)-2 × 1 surface. J. Am. Chem. Soc. **122**, 732–733 (2000). doi:10.1021/ja9929077
92. C.L. Park, A.Y. Jee, M. Lee, S. Lee Gelation, functionalization, and solution behaviors of nanodiamonds with ionic liquids. Chem. Commun. (Camb). **37**, 5576–5578. (2009). doi:10.1039/B910836J
93. A. Barras, S. Szunerits, L. Marcon, N. Monfilliette-Dupont, R. Boukherroub, Functionalization of diamond nanoparticles using "click". chemistry. Langmuir **26**, 13168–13172 (2010). doi:10.1021/la101709q
94. A. Krueger, T. Boedeker, Deagglomeration and functionalisation of detonation nanodiamond with long alkyl chains. Diam. Relat. Mater. **17**, 1367–1370 (2008). doi:10.1016/j.diamond.2008.01.033
95. H.A. Girard, T. Petit, S. Perruchas, T. Gacoin, C. Gesset, J.C. Arnault, P. Bergonzo, Surface properties of hydrogenated nanodiamonds: a chemical investigation. Phys. Chem. Chem. Phys. **13**, 11517–11523 (2011). doi:10.1039/C1CP20424F
96. T. Nakamura, T. Ohana, Y. Hagiwara, T. Tsubota, Chemical modification of diamond powder with optically active functionalities and its chiral recognition behavior. Appl. Surf. Sci. **257**, 1368–1370 (2010). doi:10.1016/j.apsusc.2010.08.051
97. G. Jarre, Y. Liang, P. Betz, D. Lang, A. Krueger, Playing the surface game-Diels-Alder reactions on diamond nanoparticles. Chem. Commun. (Camb). **47**, 544–546 (2010). doi:10.1039/C0CC02931A
98. D. Lang, A. Krueger, The Prato reaction on nanodiamond: surface functionalization by formation of pyrrolidine rings. Diam. Relat. Mater. **20**, 101–104 (2011). doi:10.1016/j.diamond.2010.09.001
99. L. Marcon, Z. Kherrouche, J. Lyskawa, D. Fournier, D. Tulasne, P. Woisel, R. Boukherroub, Preparation and characterization of Zonyl-coated nanodiamonds with antifouling properties. Chem. Commun. (Camb). **47**, 5178–5180 (2011). doi:10.1039/C1CC10338E

100. T. Meinhardt, D. Lang, H. Dill, A. Krueger, Pushing the functionality of diamond nanoparticles to new horizons: orthogonally functionalized nanodiamond using click chemistry. Adv. Funct. Mater. **21**, 494–500 (2011). doi:10.1002/adfm.201001219
101. V.N. Mochalin, I. Neitzel, B.J.M. Etzold, A. Peterson, G. Palmese, Y. Gogotsi, Covalent incorporation of aminated nanodiamond into an epoxy polymer network. ACS. Nano. **5**, 7494–7502 (2011). doi:10.1021/nn2024539
102. T. Takimoto, T. Chano, S. Shimizu, H. Okabe, M. Ito, M. Morita, T. Kimura, T. Inubushi, N. Komatsu, Preparation of fluorescent diamond nanoparticles stably dispersed under a physiological environment through multistep organic transformations. Chem. Mater. **22**, 3462–3471 (2010). doi:10.1021/cm100566v
103. X. Zhang, C. Fu, L. Feng, Y. Ji, L. Tao, Q. Huang, S. Li, Y. Wei, PEGylation and polyPEGylation of nanodiamond. Polymer **53**, 3178–3184 (2012). doi:10.1016/j.polymer.2012.05.029
104. I. Cha, K. Shirai, K. Fujiki, T. Yamauchi, N. Tsubokawa, Suface grafting of polymers onto nanodiamond by ligand-exchange reaction of ferrocene moieties of polymers with polycondensed aromatic rings of the surface. Diam. Relat. Mater. **20**, 439–444 (2011). doi:10.1016/j.diamond.2011.01.014
105. L. Li, J.L. Davidson, C.M. Lukehart, Surface functionalization of nanodiamond particles via atom transfer radical polymerization. Carbon **44**, 2308–2315 (2006). doi:10.1016/j.carbon.2006.02.023
106. N.A. Hutter, A. Reitinger, N. Zhang, M. Steenackers, O.A. Williams, J.A. Garrido, R. Jordan, Microstructured poly(2-oxazoline) bottle-brush brushes on nanocrystalline diamond. Phys. Chem. Chem. Phys. **12**, 4360 (2010). doi:10.1039/b923789p
107. M. Steenackers, S.Q. Lud, M. Niedermeier, P. Bruno, D.M. Gruen, P. Feulner, M. Stutzmann, J.A. Garrido, R. Jordan, Structured polymer grafts on diamond. J. Am. Chem. Soc. **129**, 15655–15661 (2007). doi:10.1021/ja075378c
108. Q. Zhang, K. Naito, Y. Tanaka, Y. Kagawa, Grafting polyimides from nanodiamonds. Macromolecules **41**, 536–538 (2008). doi:10.1021/ma702268x
109. S.H. Kim, D. Debnath, W.S. Lee, K.E. Geckeler, Poly (vinylpyrrolidone) as a tool: aqueous dispersion of nanodiamonds by wrapping in the solid state. Polym. Int. **61**, 1228–1233 (2012). doi:10.1002/pi.4269
110. H.B. Man, R. Lam, M. Chen, E. Osawa, D. Ho, Nanodiamond-therapeutic complexes embedded within poly(ethylene glycol) diacrylate hydrogels mediating sequential drug elution. Phys. Status Solidi A **209**, 1811–1818 (2012). doi:10.1002/pssa.201200073
111. E. von Haartman, H. Jiang, A.A. Khomich, J. Zhang, S.A. Burikov, T.A. Dolenko, J. Ruokolainen, H. Gu, O.A. Shenderova, I.I. Vlasov, J.M. Rosenholm, Core-shell designs of photoluminescent nanodiamonds with porous silica coatings for bioimaging and drug delivery I: fabrication. J. Mater. Chem. B **1**, 2358–2366 (2013). doi:10.1039/C3TB20308E
112. N. Prabhakar, T. Nareoja, E. von Haartman, D. Karaman, H. Jiang, S. Koho, T.A. Dolenko, P.E. Hanninen, D.I. Vlasov, V.G. Ralchenko, S. Hosomi, I.I. Vlasov, C. Sahlgren, J.M. Rosenholm, Core-shell designs of photoluminescent nanodiamonds with porous silica coatings for bioimaging and drug delivery II: application. Nanoscale **5**, 3713 (2013). doi:10.1039/c3nr33926b
113. A. Bumb, S.K. Sarkar, N. Billington, M.W. Brechbiel, K.C. Neuman, Silica encapsulation of fluorescent nanodiamonds for colloidal stability and facile surface functionalization. J. Am. Chem. Soc. **135**, 7815–7818 (2013). doi:10.1021/ja4016815
114. T.S. Huang, Y. Tzeng, Y.K. Liu, Y.C. Chen, K.R. Walker, R. Guntupalli, C. Liu, Immobilization of antibodies and bacterial binding on nanodiamond and carbon nanotubes for biosensor applications. Diam. Relat. Mater. **13**, 1098–1102 (2004). doi:10.1016/j.diamond.2003.11.047
115. M. Mkandawire, A. Pohl, T. Gubarevich, V. Lapina, D. Appelhans, G. Rödel, W. Pompe, J. Schreiber, J. Opitz, Selective targeting of green fluorescent nanodiamond conjugates to mitochondria in HeLa cells. J. Biophotonics. **2**, 596–606 (2009). doi:10.1002/jbio.200910002

116. K.V. Purtov, A.I. Petunin, A.E. Burov, A.P. Puzyr, V.S. Bondar, Nanodiamonds as carriers for address delivery of biologically active substances. Nanoscale Res. Lett. **5**, 631–636 (2010). doi:10.1007/s11671-010-9526-0
117. Y. Fu, N. An, S. Zheng, A. Liang, Y. Li, BmK CT-conjugated fluorescence nanodiamond as potential glioma-targeted imaging and drug. Diam. Relat. Mater. **21**, 73–76 (2012). doi:10.1016/j.diamond.2011.10.010
118. K.K. Liu, M.F. Chen, P.Y. Chen, T.J.F. Lee, C.L. Cheng, C.C. Chang, Y.P. Ho, J.I. Chao, Alpha-bungarotoxin binding to target cell in a developing visual system by carboxylated nanodiamond. Nanotechnology **19**, 205102 (2008). doi:10.1088/0957-4484/19/20/205102
119. A.P. Puzyr, K.V. Purtov, O.A. Shenderova, M. Luo, D.W. Brenner, V.S. Bondar, The adsorption of aflatoxin B1 by detonation-synthesis nanodiamonds. Biochem. Biophys. **417**, 299–301 (2007). doi:10.1134/S1607672907060026
120. E. Nicolau, J. Méndez, J.J. Fonseca, K. Griebenow, C.R. Cabrera, Bioelectrochemistry of non-covalent immobilized alcohol dehydrogenase on oxidized diamond nanoparticles. Bioelectrochemistry **85**, 1–6 (2012). doi:10.1016/j.bioelechem.2011.11.002
121. L. Wei, W. Zhang, H. Lu, P. Yang, Immobilization of enzyme on detonation nanodiamond for highly efficient proteolysis. Talanta **80**, 1298–1304 (2010)
122. P.H. Chung, E. Perevedentseva, J.S. Tu, C.C. Chang, C.L. Cheng, Spectroscopic study of bio-functionalized nanodiamonds. Diam. Relat. Mater. **15**, 622–625 (2006). doi:10.1016/j.diamond.2005.11.019
123. E. Perevedentseva, P.J. Cai, Y.C. Chiu, C.L. Cheng, Characterizing protein activities on the lysozyme and nanodiamond complex prepared for bio applications. Langmuir **27**, 1085–1091 (2011). doi:10.1021/la103155c
124. E. Perevedentseva, C.Y. Cheng, P.H. Chung, J.S. Tu, Y.H. Hsieh, C.L. Cheng, The interaction of the protein lysozyme with bacteria E. coli observed using nanodiamond labelling. Nanotechnology **18**, 315102 (2007). doi:10.1088/0957-4484/18/31/315102
125. V.W.K. Wu, Preparation for optimal conformation of lysozyme with nanodiamond and nanosilica as carriers. Chin. J. Chem. **28**, 2520–2526 (2010)
126. Y. Li, X. Zhou, Transferrin-coupled fluorescence nanodiamonds as targeting intracellular transporters: an investigation of the uptake mechanism. Diam. Relat. Mater. **19**, 1163–1167 (2010)
127. M.F. Weng, S.Y. Chiang, N.S. Wang, H. Niu, Fluorescent nanodiamonds for specifically targeted bioimaging: application to the interaction of transferrin with transferrin receptor. Diam. Relat. Mater. **18**, 587–591 (2009)
128. M.F. Weng, B.J. Chang, S.Y. Chiang, N.S. Wang, H. Niu, Cellular uptake and phototoxicity of surface-modified fluorescent nanodiamonds. Diam. Relat. Mater. **22**, 96–104 (2012). doi:10.1016/j.diamond.2011.12.035
129. J. Li, Y. Zhu, W. Li, X. Zhang, Y. Peng, Q. Huang, Nanodiamonds as intracellular transporters of chemotherapeutic drug. Biomaterials **31**, 8410–8418 (2010). doi:10.1016/j.biomaterials.2010.07.058
130. N. Mohan, C.S. Chen, H.H. Hsieh, Y.C. Wu, H.C. Chang, In vivo imaging and toxicity assessments of fluorescent nanodiamonds in *Caenorhabditis elegans*. Nano Lett. **10**, 3692–3699 (2010). doi:10.1021/nl1021909
131. Y.K. Tzeng, O. Faklaris, B.M. Chang, Y. Kuo, J.H. Hsu, H.C. Chang, Superresolution imaging of albumin-conjugated fluorescent nanodiamonds in cells by stimulated emission depletion. Angew. Chem. Int. Ed. Engl. **50**, 2262–2265 (2011). doi:10.1002/anie.201007215
132. H.D. Wang, C.H. Niu, Q. Yang, I. Badea, Study on protein conformation and adsorption behaviors in nanodiamond particle-protein complexes. Nanotechnology **22**, 145703 (2011). doi:10.1088/0957-4484/22/14/145703
133. A. Krueger, J. Stegk, Y. Liang, L. Lu, G. Jarre, Biotinylated nanodiamond: simple and efficient functionalization of detonation diamond. Langmuir **24**, 4200–4204 (2008). doi:10.1021/la703482v

134. F. Neugart, A. Zappe, F. Jelezko, C. Tietz, J.P. Boudou, A. Krueger, J. Wrachtrup, Dynamics of diamond nanoparticles in solution and cells. Nano Lett. **7**, 3588–3591 (2007). doi:10.1021/nl0716303
135. B. Zhang, Y. Li, C.Y. Fang, C.C. Chang, C.S. Chen, Y.Y. Chen, H.C. Chang, Receptor-mediated cellular uptake of folate-conjugated fluorescent nanodiamonds: a combined ensemble and single-particle study. Small **5**, 2716–2721 (2009). doi:10.1002/smll.200900725
136. R.A. Shimkunas, E. Robinson, R. Lam, S. Lu, X. Xu, X.Q. Zhang, H. Huang, E. Osawa, D. Ho, Nanodiamond-insulin complexes as pH-dependent protein delivery vehicles. Biomaterials **30**, 5720–5728 (2009). doi:10.1016/j.biomaterials.2009.07.004
137. S. Vial, C. Mansuy, S. Sagan, T. Irinopoulou, F. Burlina, J.P. Boudou, G. Chassaing, S. Lavielle, Peptide-grafted nanodiamonds: preparation, cytotoxicity and uptake in cells. Chembiochem. **9**, 2113–2119 (2008). doi:10.1002/cbic.200800247
138. H. Huang, E. Pierstorff, E. Osawa, D. Ho, Active nanodiamond hydrogels for chemotherapeutic delivery. Nano Lett. **7**, 3305–3314 (2007). doi:10.1021/nl071521o
139. A. Alhaddad, M.P. Adam, J. Botsoa, G. Dantelle, S. Perruchas, T. Gacoin, C. Mansuy, S. Lavielle, C. Malvy, F. Treussart, J.R. Bertrand, Nanodiamond as a vector for siRNA delivery to Ewing sarcoma cells. Small **7**, 3087–3095 (2011). doi:10.1002/smll.201101193
140. X.Q. Zhang, M. Chen, R. Lam, X. Xu, E. Osawa, D. Ho, Polymer-functionalized nanodiamond platforms as vehicles for gene delivery. ACS. Nano. **3**, 2609–2616 (2009). doi:10.1021/nn900865g
141. L.C.L. Huang, H.C. Chang, Adsorption and immobilization of cytochrome c on nanodiamonds. Langmuir **20**, 5879–5884 (2004). doi:10.1021/la0495736
142. E. Mahon, A. Salvati, F. Baldelli Bombelli, I. Lynch, K.A. Dawson, Designing the nanoparticle-biomolecule interface for "targeting and therapeutic delivery". J. Control Release 161, 164–174 (2012). doi:10.1016/j.jconrel.2012.04.009
143. K.V. Purtov, L.P. Burakova, A.P. Puzyr, V.S. Bondar, The interaction of linear and ring forms of DNA molecules with nanodiamonds synthesized by detonation. Nanotechnology **19**, 325101 (2008). doi:10.1088/0957-4484/19/32/325101
144. C.C. Fu, H.Y. Lee, K. Chen, T.S. Lim, H.Y. Wu, P.K. Lin, P.K. Wei, P.H. Tsao, H.C. Chang, W. Fann, Characterization and application of single fluorescent nanodiamonds as cellular biomarkers. Proc. Natl. Acad. Sci. U S A **104**, 727–732 (2007)
145. X.L. Kong, L.C.L. Huang, C.M. Hsu, W.H. Chen, C.C. Han, H.C. Chang, High-affinity capture of proteins by diamond nanoparticles for mass spectrometric analysis. Anal. Chem. **77**, 259–265 (2005). doi:10.1021/ac048971a
146. C.Y. Cheng, E. Perevedentseva, J.S. Tu, P.H. Chung, C.L. Cheng, K.K. Liu, J.I. Chao, P.H. Chen, C.C. Chang, Direct and in vitro observation of growth hormone receptor molecules in A549 human lung epithelial cells by nanodiamond labeling. Appl. Phys. Lett. **90**, 163903 (2007). doi:10.1063/1.2727557
147. L. Cao, Immobilised enzymes: science or art? Curr. Opin. Chem. Biol. **9**, 217–226 (2005). doi:10.1016/j.cbpa.2005.02.014
148. W.S. Yeap, Y.Y. Tan, K.P. Loh, Using detonation nanodiamond for the specific capture of glycoproteins. Anal. Chem. **80**, 4659–4665 (2008). doi:10.1021/ac800009v
149. A.A. Vertegel, R.W. Siegel, J.S. Dordick, Silica nanoparticle size influences the structure and enzymatic activity of adsorbed lysozyme. Langmuir **20**, 6800–6807 (2004). doi:10.1021/la0497200
150. D.F. Williams (ed.), Biomaterials ES for definitions in biomaterials, in *Proceedings of a Consensus Conference of the European Society for Biomaterials*, Chester, England, March 3–5, 1986 (Elsevier, 1987)
151. Y. Liu, Y. Zhao, B. Sun, C. Chen, Understanding the toxicity of carbon nanotubes. Acc. Chem. Res. **46**, 702–713 (2013). doi:10.1021/ar300028m
152. A.M. Schrand, H. Huang, C. Carlson, J.J. Schlager, E. Osawa, S.M. Hussain, L. Dai, Are diamond nanoparticles cytotoxic? J. Phys. Chem. B. **111**, 2–7 (2007)

153. A.M. Schrand, L. Dai, J.J. Schlager, S.M. Hussain, E. Osawa, Differential biocompatibility of carbon nanotubes and nanodiamonds. Diam. Relat. Mater. **16**, 2118–2123 (2007). doi:10.1016/j.diamond.2007.07.020
154. A.M. Schrand, J.B. Lin, S.C. Hens, S.M. Hussain, Temporal and mechanistic tracking of cellular uptake dynamics with novel surface fluorophore-bound nanodiamonds. Nanoscale **3**, 435 (2011). doi:10.1039/c0nr00408a
155. K. Bakowicz-Mitura, G. Bartosz, S. Mitura, Influence of diamond powder particles on human gene expression. Surf. Coat. Technol. **201**, 6131–6135 (2007). doi:10.1016/j.surfcoat.2006.08.142
156. M. Horie, L.K. Komaba, H. Kato, A. Nakamura, K. Yamamoto, S. Endoh, K. Fujita, S. Kinugasa, K. Mizuno, Y. Hagihara, Y. Yoshida, H. Iwahashi, Evaluation of cellular influences induced by stable nanodiamond dispersion; the cellular influences of nanodiamond are small. Diam. Relat. Mater. **24**, 15–24 (2012). doi:10.1016/j.diamond.2012.01.037
157. A.V. Karpukhin, N.V. Avkhacheva, R.Y. Yakovlev, I.I. Kulakova, V.A. Yashin, G.V. Lisichkin, V.G. Safronova, Effect of detonation nanodiamonds on phagocyte activity. Cell Biol. Int. **35**, 727–733 (2011). doi:10.1042/CBI20100548
158. L. Marcon, F. Riquet, D. Vicogne, S. Szunerits, J.F. Bodart, R. Boukherroub, Cellular and in vivo toxicity of functionalized nanodiamond in Xenopus embryos. J. Mater. Chem. **20**, 8064 (2010). doi:10.1039/c0jm01570a
159. R. Martín, C. Menchón, N. Apostolova, V.M. Victor, M. Álvaro, J.R. Herance, H. García, Nano-jewels in biology. Gold and platinum on diamond nanoparticles as antioxidant systems against cellular oxidative stress. ACS. Nano. **4**, 6957–6965 (2010). doi:10.1021/nn1019412
160. A.P. Puzyr, D.A. Neshumayev, S.V. Tarskikh, G.V. Makarskaya, V.Y. Dolmatov, V.S. Bondar, Destruction of human blood cells in interaction with detonation nanodiamonds in experiments in vitro. Diam. Relat. Mater. **13**, 2020–2023 (2004). doi:10.1016/j.diamond.2004.06.003
161. K. Solarska, A. Gajewska, J. Skolimowski, R. Woś, G. Bartosz, K. Mitura, Effect of nonmodified and modified nanodiamond particles by Fenton reaction on human endothelial cells. Manuf. Eng. **43**, 603–607 (2010)
162. K. Solarska, A. Gajewska, G. Bartosz, K. Mitura, Induction of apoptosis in human endothelial cells by nanodiamond particles. J. Nanosci. Nanotechnol. **12**, 5117–5121 (2012). doi:10.1166/jnn.2012.4952
163. K. Solarska, A. Gajewska, W. Kaczorowski, G. Bartosz, K. Mitura, Effect of nanodiamond powders on the viability and production of reactive oxygen and nitrogen species by human endothelial cells. Diam. Relat. Mater. **21**, 107–113 (2012). doi:10.1016/j.diamond.2011.10.020
164. K. Solarska-Ściuk, A. Gajewska, J. Skolimowski, K. Mitura, G. Bartosz, Stimulation of production of reactive oxygen and nitrogen species in endothelial cells by unmodified and Fenton-modified ultradisperse detonation diamond. Biotechnol. Appl. Biochem. **60**, 259–265 (2013). doi:10.1002/bab.1071
165. Y. Xing, W. Xiong, L. Zhu, E. Osawa, S. Hussin, L. Dai, DNA damage in embryonic stem cells caused by nanodiamonds. ACS. Nano. **5**, 2376 (2011)
166. X. Zhang, W. Hu, J. Li, L. Tao, Y. Wei, A comparative study of cellular uptake and cytotoxicity of multi-walled carbon nanotubes, graphene oxide, and nanodiamond. Toxicol. Res. **1**, 62 (2012). doi:10.1039/c2tx20006f
167. K.K. Liu, C.L. Cheng, C.C. Chang, J.I. Chao, Biocompatible and detectable carboxylated nanodiamond on human cell. Nanotechnology **18**, 325102 (2007)
168. P. Villalba, M.K. Ram, H. Gomez, V. Bhethanabotla, M.N. Helms, A. Kumar, A. Kumar, Cellular and in vitro toxicity of nanodiamond-polyaniline composites in mammalian and bacterial cell. Mater. Sci. Eng. C. **32**, 594–598 (2012). doi:10.1016/j.msec.2011.12.017
169. S.J. Yu, M.W. Kang, H.C. Chang, K.M. Chen, Y.C. Yu, Bright fluorescent nanodiamonds: no photobleaching and low cytotoxicity. J. Am. Chem. Soc. **127**, 17604–17605 (2005). doi:10.1021/ja0567081

170. V. Vaijayanthimala, Y.K. Tzeng, H.C. Chang, C.L. Li, The biocompatibility of fluorescent nanodiamonds and their mechanism of cellular uptake. Nanotechnology **20**, 425103 (2009). doi:10.1088/0957–4484/20/42/425103
171. O. Faklaris, D. Garrot, V. Joshi, F. Druon, J.P. Boudou, T. Sauvage, P. Georges, P.A. Curmi, F. Treussart, Detection of single photoluminescent diamond nanoparticles in cells and study of the internalization pathway. Small **4**, 2236–2239 (2008)
172. J.W. Lee, S. Lee, S. Jang, K.Y. Han, Y. Kim, J. Hyun, S.K. Kim, Y. Lee, Preparation of non-aggregated fluorescent nanodiamonds (FNDs) by non-covalent coating with a block copolymer and proteins for enhancement of intracellular uptake. Mol. Biosyst. **9**, 1004 (2013). doi:10.1039/c2mb25431j
173. S.P. Blaber, C.J. Hill, R.A. Webster, J.M. Say, L.J. Brown, S.C. Wang, G. Vesey, B.R. Herbert, Effect of labeling with iron oxide particles or nanodiamonds on the functionality of adipose-derived mesenchymal stem cells. PLoS ONE **8**, e52997 (2013). doi:10.1371/journal.pone.0052997
174. C.Y. Fang, V. Vaijayanthimala, C.A. Cheng, S.H. Yeh, C.F. Chang, C.L. Li, H.C. Chang, The exocytosis of fluorescent nanodiamond and its use as a long-term cell tracker. Small **7**, 3363–3370 (2011). doi:10.1002/smll.201101233
175. K.K. Liu, C.C. Wang, C.L. Cheng, J.I. Chao, Endocytic carboxylated nanodiamond for the labeling and tracking of cell division and differentiation in cancer and stem cells. Biomaterials **30**, 4249–4259 (2009). doi:10.1016/j.biomaterials.2009.04.056
176. V. Thomas, B.A. Halloran, N. Ambalavanan, S.A. Catledge, Y.K. Vohra, In vitro studies on the effect of particle size on macrophage responses to nanodiamond wear debris. Acta Biomater **8**, 1939–1947 (2012). doi:10.1016/j.actbio.2012.01.033
177. Y.C. Lin, E. Perevedentseva, L.W. Tsai, K.T. Wu, C.L. Cheng, Nanodiamond for intracellular imaging in the microorganisms in vivo. J. Biophotonics **5**, 838–847 (2012). doi:10.1002/jbio.201200088
178. J.I. Chao, E. Perevedentseva, P.H. Chung, K.K. Liu, C.Y. Cheng, C.C. Chang, C.L. Cheng, Nanometer-sized diamond particle as a probe for biolabeling. Biophys. J. **93**, 2199–2208 (2007)
179. T. Burleson, N. Yusuf, A. Stanishevsky, Surface modification of nanodiamonds for biomedical application and analysis by infrared spectroscopy. J. Achiev. Mat. Manuf. Eng. **37**, 258–263 (2009)
180. A. Alhaddad, C. Durieu, G. Dantelle, L. Cam E, C. Malvy, F. Treussart, J.R. Bertrand, Influence of the internalization pathway on the efficacy of siRNA delivery by cationic fluorescent nanodiamonds in the Ewing sarcoma cell model. PLoS. ONE **7**, e52207 (2012). doi:10.1371/journal.pone.0052207
181. O. Faklaris, V. Joshi, T. Irinopoulou, P. Tauc, M. Sennour, H. Girard, C. Gesset, J.C. Arnault, A. Thorel, J.P. Boudou, Photoluminescent diamond nanoparticles for cell labeling: study of the uptake mechanism in mammalian cells. ACS. Nano. **3**, 3955–3962 (2009)
182. S. Rojas, J.D. Gispert, R. Martín, S. Abad, C. Menchón, D. Pareto, V.M. Víctor, M. Álvaro, H. García, J.R. Herance, Biodistribution of amino-functionalized diamond nanoparticles. In vivo studies based on 18F radionuclide emission. ACS. Nano. **5**, 5552–5559 (2011). doi:10.1021/nn200986z
183. X. Zhang, J. Yin, C. Kang, J. Li, Y. Zhu, W. Li, Q. Huang, Z. Zhu, Biodistribution and toxicity of nanodiamonds in mice after intratracheal instillation. Toxicol. Lett. **198**, 237–243 (2010). doi:10.1016/j.toxlet.2010.07.001
184. E.K. Chow, X.Q. Zhang, M. Chen, R. Lam, E. Robinson, H. Huang, D. Schaffer, E. Osawa, A. Goga, D. Ho, Nanodiamond therapeutic delivery agents mediate enhanced chemoresistant tumor treatment. Sci. Transl. Med. **3**, 73ra21 (2011)
185. Q. Wei, L. Zhan, B. Juanjuan, W. Jing, W. Jianjun, S. Taoli, G. Yi'an, W. Wangsuo, Biodistribution of co-exposure to multi-walled carbon nanotubes and nanodiamonds in mice. Nanoscale Res. Lett. **7**, 1–9 (2012)
186. Y. Yuan, Y. Chen, J.H. Liu, H. Wang, Y. Liu, Biodistribution and fate of nanodiamonds in vivo. Diam. Relat. Mater. **18**, 95–100 (2009). doi:10.1016/j.diamond.2008.10.031

187. Y. Yuan, X. Wang, G. Jia, J.H. Liu, T. Wang, Y. Gu, S.T. Yang, S. Zhen, H. Wang, Y. Liu, Pulmonary toxicity and translocation of nanodiamonds in mice. Diam. Relat. Mater. **19**, 291–299 (2010). doi:10.1016/j.diamond.2009.11.022
188. A.P. Puzyr, A.V. Baron, K.V. Purtov, E.V. Bortnikov, N.N. Skobelev, O.A. Mogilnaya, V.S. Bondar, Nanodiamonds with novel properties: a biological study. Diam. Relat. Mater. **16**, 2124–2128 (2007). doi:10.1016/j.diamond.2007.07.025
189. V. Vaijayanthimala, P.Y. Cheng, S.H. Yeh, K.K. Liu, C.H. Hsiao, J.I. Chao, H.C. Chang, The long-term stability and biocompatibility of fluorescent nanodiamond as an in vivo contrast agent. Biomaterials **33**, 7794–7802 (2012). doi:10.1016/j.biomaterials.2012.06.084
190. Y.R. Chang, H.Y. Lee, K. Chen, C.C. Chang, D.S. Tsai, C.C. Fu, T.S. Lim, Y.K. Tzeng, C.Y. Fang, C.C. Han, H.C. Chang, W. Fann, Mass production and dynamic imaging of fluorescent nanodiamonds. Nat. Nanotechnol. **3**, 284–288 (2008). doi:10.1038/nnano.2008.99
191. A. Laraoui, J.S. Hodges, C.A. Meriles, Nitrogen-vacancy-assisted magnetometry of paramagnetic centers in an individual diamond nanocrystal. Nano. Lett. **12**, 3477–3482 (2012). doi:10.1021/nl300964g
192. F. Dolde, H. Fedder, M.W. Doherty, T. Nöbauer, F. Rempp, G. Balasubramanian, T. Wolf, F. Reinhard, L.C.L. Hollenberg, F. Jelezko, J. Wrachtrup, Electric-field sensing using single diamond spins. Nat. Phys. **7**, 459–463 (2011). doi:10.1038/nphys1969
193. H.J. Mamin, M. Kim, M.H. Sherwood, C.T. Rettner, K. Ohno, D.D. Awschalom, D. Rugar, Nanoscale nuclear magnetic resonance with a nitrogen-vacancy spin sensor. Science **339**, 557–560 (2013). doi:10.1126/science.1231540
194. J.R. Maze, P.L. Stanwix, J.S. Hodges, S. Hong, J.M. Taylor, P. Cappellaro, L. Jiang, M.V.G. Dutt, E. Togan, A.S. Zibrov, A. Yacoby, R.L. Walsworth, M.D. Lukin, Nanoscale magnetic sensing with an individual electronic spin in diamond. Nature **455**, 644–647 (2008). doi:10.1038/nature07279
195. A.M. Zaitsev, Vibronic spectra of impurity-related optical centers in diamond. Phys. Rev. B. **61**, 12909–12922 (2000). doi:10.1103/PhysRevB.61.12909
196. C.L. Wang, C. Kurtsiefer, H. Weinfurter, B. Burchard, Single photon emission from SiV centres in diamond produced by ion implantation. J. Phys. B-At. Mol. Opt. Phys. **39**, 37–41 (2006). doi:10.1088/0953-4075/39/1/005
197. E. Neu, D. Steinmetz, J. Riedrich-Moeller, S. Gsell, M. Fischer, M. Schreck, C. Becher, Single photon emission from silicon-vacancy colour centres in chemical vapour deposition nano-diamonds on iridium. New J. Phys. (2011). doi:10.1088/1367-2630/13/2/025012
198. E. Wu, J.R. Rabeau, G. Roger, F. Treussart, H. Zeng, P. Grangier, S. Prawer, J.-F. Roch, Room temperature triggered single-photon source in the near infrared. New J. Phys. (2007). doi:10.1088/1367-2630/9/12/434
199. J.R. Rabeau, Y.L. Chin, S. Prawer, F. Jelezko, T. Gaebel, J. Wrachtrup, Fabrication of single nickel-nitrogen defects in diamond by chemical vapor deposition. Appl. Phys. Lett. (2005). doi:10.1063/1.1896088
200. I. Aharonovich, S. Castelletto, B.C. Johnson, J.C. McCallum, D.A. Simpson, A.D. Greentree, S. Prawer, Chromium single-photon emitters in diamond fabricated by ion implantation. Phys. Rev. B (2010). doi:10.1103/PhysRevB.81.121201
201. I. Aharonovich, S. Castelletto, D.A. Simpson, A. Stacey, J. McCallum, A.D. Greentree, S. Prawer, Two-level ultrabright single photon emission from diamond nanocrystals. Nano Lett. **9**, 3191–3195 (2009). doi:10.1021/nl9014167
202. B. Naydenov, R. Kolesov, A. Batalov, J. Meijer, S. Pezzagna, D. Rogalla, F. Jelezko, J. Wrachtrup, Engineering single photon emitters by ion implantation in diamond. Appl. Phys. Lett. (2009). doi:10.1063/1.3257976
203. J. Havlik, V. Petrakova, I. Rehor, V. Petrak, M. Gulka, J. Stursa, J. Kucka, J. Ralis, T. Rendler, S.Y. Lee, R. Reuter, J. Wrachtrup, M. Ledvina, M. Nesladek, P. Cigler, Boosting nanodiamond fluorescence: towards development of brighter probes. Nanoscale **5**, 3208–3211 (2013). doi:10.1039/c2nr32778c
204. G. Dantelle, A. Slablab, L. Rondin, F. Lainé, F. Carrel, P. Bergonzo, S. Perruchas, T. Gacoin, F. Treussart, J.F. Roch, Efficient production of NV colour centres in nanodiamonds

using high-energy electron irradiation. J. Lumin. **130**, 1655–1658 (2010). doi:10.1016/j.jlumin.2009.12.003
205. B. Slepetz, I. Laszlo, Y. Gogotsi, D. Hyde-Volpe, M. Kertesz, Characterization of large vacancy clusters in diamond from a generational algorithm using tight binding density functional theory. Phys. Chem. Chem. Phys. **12**, 14017–14022 (2010). doi:10.1039/c0cp00523a
206. I. Kratochvilova, A. Kovalenko, A. Taylor, F. Fendrych, V. Rezacova, J. Vlcek, S. Zalis, J. Sebera, P. Cigler, M. Ledvina, M. Nesladek, The fluorescence of variously terminated nanodiamond particles: quantum chemical calculations. Phys. Status Solidi A **207**, 2045–2048 (2010). doi:10.1002/pssa.201000012
207. A. Gruber, A. Drabenstedt, C. Tietz, L. Fleury, J. Wrachtrup, C. von Borczyskowski, Scanning confocal optical microscopy and magnetic resonance on single defect centers. Science **276**, 2012–2014 (1997). doi:10.1126/science.276.5321.2012
208. J. Tisler, R. Reuter, A. Lammle, F. Jelezko, G. Balasubramanian, P.R. Hemmer, F. Reinhard, J. Wrachtrup, Highly efficient FRET from a single nitrogen-vacancy center in nanodiamonds to a single organic molecule. ACS. Nano. **5**, 7893–7898 (2011). doi:10.1021/nn2021259
209. K. Iakoubovskii, G.J. Adriaenssens, M. Nesladek, Photochromism of vacancy-related centres in diamond. J. Phys. Condens. Matter **12**, 189–199 (2000). doi:10.1088/0953-8984/12/2/308
210. T. Gaebel, M. Domhan, C. Wittmann, I. Popa, F. Jelezko, J. Rabeau, A. Greentree, S. Prawer, E. Trajkov, P.R. Hemmer, J. Wrachtrup, Photochromism in single nitrogen-vacancy defect in diamond. Appl. Phys. B. **82**, 243–246 (2006). doi:10.1007/s00340-005-2056-2
211. G. Davies, M. Hamer, Optical studies of 1.945 Ev vibronic band in diamond. Proc. R. Soc. Lond. Ser. –Math. Phys. Sci. **348**, 285–298 (1976). doi:10.1098/rspa.1976.0039
212. N.B. Manson, J.P. Harrison, M.J. Sellars, Nitrogen-vacancy center in diamond: model of the electronic structure and associated dynamics. Phys. Rev. B. (2006). doi:10.1103/PhysRevB.74.104303
213. G. Balasubramanian, I.Y. Chan, R. Kolesov, M. Al-Hmoud, J. Tisler, C. Shin, C. Kim, A. Wojcik, P.R. Hemmer, A. Krueger, T. Hanke, A. Leitenstorfer, R. Bratschitsch, F. Jelezko, J. Wrachtrup, Nanoscale imaging magnetometry with diamond spins under ambient conditions. Nature **455**, 648–651 (2008). doi:10.1038/nature07278
214. A. Hegyi, E. Yablonovitch, Molecular imaging by optically detected electron spin resonance of nitrogen-vacancies in nanodiamonds. Nano Lett. **13**, 1173–1178 (2013). doi:10.1021/nl304570b
215. N. Zhao, J. Honert, B. Schmid, M. Klas, J. Isoya, M. Markham, D. Twitchen, F. Jelezko, R.-B. Liu, H. Fedder, J. Wrachtrup, Sensing single remote nuclear spins. Nat. Nanotechnol. **7**, 657–662 (2012). doi:10.1038/NNANO.2012.152
216. Y. Chi, G. Chen, F. Jelezko, E. Wu, H. Zeng, Enhanced photoluminescence of single-photon emitters in nanodiamonds on a gold film. IEEE Photonics Technol. Lett. **23**, 374–376 (2011). doi:10.1109/LPT.2011.2106488
217. S. Schietinger, M. Barth, T. Aichele, O. Benson, Plasmon-enhanced single photon emission from a nanoassembled metal-diamond hybrid structure at room temperature. Nano Lett. **9**, 1694–1698 (2009). doi:10.1021/nl900384c
218. G. Davies, S.C. Lawson, A.T. Collins, A. Mainwood, S.J. Sharp, Vacancy-related centers in diamond. Phys. Rev. B. **46**, 13157 (1992). doi:10.1103/PhysRevB.46.13157
219. J. Opitz, M. Sorge, N. Rose, M. Rudolph, P. Krueger, I. Hannstein, J. Schreiber, M. Mkandawire, W. Pompe, G. Roedel, V.A. Lapina, D. Appelhans, Green fluorescent nanodiamond conjugates and their possible applications for biosensing in Mohseni H; Society of Photo-Optical Instrumentation Engineers -SPIE-, Bellingham/Wash.: Biosensing III, August 2010 (technical conference, San Diego, California, United States, 2010), pp. 775914–775918
220. V. Petrakova, A. Taylor, I. Kratochvilova, F. Fendrych, J. Vacik, J. Kucka, J. Stursa, P. Cigler, M. Ledvina, A. Fiserova, P. Kneppo, M. Nesladek, Luminescence of nanodiamond driven by atomic functionalization: towards novel detection principles. Adv. Funct. Mater. **22**, 812–819 (2012). doi:10.1002/adfm.201101936

221. V. Petrakova, M. Nesladek, A. Taylor, F. Fendrych, P. Cigler, M. Ledvina, J. Vacik, J. Stursa, J. Kucka, Luminescence properties of engineered nitrogen vacancy centers in a close surface proximity. Phys. Status Solidi A **208**, 2051–2056 (2011). doi:10.1002/pssa.201100035
222. K.M.C. Fu, C. Santori, P.E. Barclay, R.G. Beausoleil, Conversion of neutral nitrogen-vacancy centers to negatively charged nitrogen-vacancy centers through selective oxidation. Appl. Phys. Lett. **96**, 121907 (2010). doi:10.1063/1.3364135
223. M.V. Hauf, B. Grotz, B. Naydenov, M. Dankerl, S. Pezzagna, J. Meijer, F. Jelezko, J. Wrachtrup, M. Stutzmann, F. Reinhard, J.A. Garrido, Chemical control of the charge state of nitrogen-vacancy centers in diamond. Phys. Rev. B. (2011). doi:10.1103/PhysRevB.83.081304
224. B. Grotz, M.V. Hauf, M. Dankerl, B. Naydenov, S. Pezzagna, J. Meijer, F. Jelezko, J. Wrachtrup, M. Stutzmann, F. Reinhard, J.A. Garrido, Charge state manipulation of qubits in diamond. Nat. Commun. **3**, 729 (2012). doi:10.1038/ncomms1729
225. A. Stacey, T.J. Karle, L.P. McGuinness, B.C. Gibson, K. Ganesan, S. Tomljenovic-Hanic, A.D. Greentree, A. Hoffman, R.G. Beausoleil, S. Prawer, Depletion of nitrogen-vacancy color centers in diamond via hydrogen passivation. Appl. Phys. Lett. **100**, 071902–071902 (2012)
226. W. Hu, Z. Li, J. Yang, J. Hou, Nondecaying long range effect of surface decoration on the charge state of NV center in diamond. J. Chem. Phys. **138**, 034702 (2013). doi:10.1063/1.4775364
227. H. Pinto, R. Jones, D.W. Palmer, J.P. Goss, A.K. Tiwari, P.R. Briddon, N.G. Wright, A.B. Horsfall, M.J. Rayson, S. Öberg, First-principles studies of the effect of (001) surface terminations on the electronic properties of the negatively charged nitrogen-vacancy defect in diamond. Phys. Rev. B. (2012). doi:10.1103/PhysRevB.86.045313
228. J.J. Sakon, G.J. Ribeill, J.M. Garguilo, J. Perkins, K.R. Weninger, R.J. Nemanich, Fluorescence quenching effects of nanocrystalline diamond surfaces. Diam. Relat. Mater. **18**, 82–87 (2009). doi:10.1016/j.diamond.2008.10.028
229. C. Bradac, T. Gaebel, C.I. Pakes, J.M. Say, A.V. Zvyagin, J.R. Rabeau, Effect of the nanodiamond host on a nitrogen-vacancy color-centre emission state. Small **9**, 132–139 (2013). doi:10.1002/smll.201200574
230. H. Pinto, R. Jones, D.W. Palmer, J.P. Goss, P.R. Briddon, S. Öberg, Theory of the surface effects on the luminescence of the NV-defect in nanodiamond. Phys. Status Solidi A **208**, 2045–2050 (2011). doi:10.1002/pssa.201100013
231. E. Perevedentseva, N. Melnik, C.Y. Tsai, Y.C. Lin, M. Kazaryan, C.L. Cheng, Effect of surface adsorbed proteins on the photoluminescence of nanodiamond. J. Appl. Phys. **109**, 034704 (2011). doi:10.1063/1.3544312
232. U. Resch-Genger, M. Grabolle, S. Cavaliere-Jaricot, R. Nitschke, T. Nann, Quantum dots versus organic dyes as fluorescent labels. Nat. Methods **5**, 763–775 (2008). doi:10.1038/nmeth.1248
233. H. Sahoo, Fluorescent labeling techniques in biomolecules: a flashback. RSC. Adv. **2**, 7017–7029 (2012). doi:10.1039/C2RA20389H
234. C. Bradac, T. Gaebel, N. Naidoo, M.J. Sellars, J. Twamley, L.J. Brown, A.S. Barnard, T. Plakhotnik, A.V. Zvyagin, J.R. Rabeau, Observation and control of blinking nitrogen-vacancy centres in discrete nanodiamonds. Nat. Nanotechnol. **5**, 345–349 (2010). doi:10.1038/nnano.2010.56
235. R. Weissleder, V. Ntziachristos, Shedding light onto live molecular targets. Nat. Med. **9**, 123–128 (2003). doi:10.1038/nm0103-123
236. Y. Kuo, T.Y. Hsu, Y.C. Wu, J.H. Hsu, H.C. Chang, in *Fluorescence lifetime imaging microscopy of nanodiamonds in vivo*, ed. by Z.U. Hasan, P.R. Hemmer, H. Lee, C.M. Santori, 2013, p 863503–863503-7
237. R. Igarashi, Y. Yoshinari, H. Yokota, T. Sugi, F. Sugihara, K. Ikeda, H. Sumiya, S. Tsuji, I. Mori, H. Tochio, Y. Harada, M. Shirakawa, Real-time background-free selective imaging of fluorescent nanodiamonds in vivo. Nano Lett. **12**, 5726–5732 (2012). doi:10.1021/nl302979d

238. O. Faklaris, D. Garrot, F. Treussart, V. Joshi, P. Curmi, J.P. Boudou, T. Sauvage Comparison of the photoluminescence properties of semiconductor quantum dots and non-blinking diamond nanoparticles. Observation of the diffusion of diamond nanoparticles in living cells. ArXiv Prepr. ArXiv09042648 2009
239. K.K. Liu, W.W. Zheng, C.C. Wang, Y.C. Chiu, C.L. Cheng, Y.S. Lo, C. Chen, J.I. Chao, Covalent linkage of nanodiamond-paclitaxel for drug delivery and cancer therapy. Nanotechnology **21**, 315106 (2010). doi:10.1088/0957-4484/21/31/315106
240. T.L. Wee, Y.W. Mau, C.Y. Fang, H.L. Hsu, C.C. Han, H.C. Chang, Preparation and characterization of green fluorescent nanodiamonds for biological applications. Diam. Relat. Mater. **18**, 567–573 (2009). doi:10.1016/j.diamond.2008.08.012
241. J.W. Jakub, S. Pendas, D.S. Reintgen, Current status of sentinel lymph node mapping and biopsy: facts and controversies. Oncologist **8**, 59–68 (2003). doi:10.1634/theoncologist.8-1-59
242. L.T. Hall, G.C.G. Beart, E.A. Thomas, D.A. Simpson, L.P. McGuinness, J.H. Cole, J.H. Manton, R.E. Scholten, F. Jelezko, J. Wrachtrup, S. Petrou, L.C.L. Hollenberg High spatial and temporal resolution wide-field imaging of neuron activity using quantum NV-diamond. Sci. Rep. **2**, (2012). doi:10.1038/srep00401
243. L.P. McGuinness, Y. Yan, A. Stacey, D.A. Simpson, L.T. Hall, D. Maclaurin, S. Prawer, P. Mulvaney, J. Wrachtrup, F. Caruso, R.E. Scholten, L.C.L. Hollenberg, Quantum measurement and orientation tracking of fluorescent nanodiamonds inside living cells. Nat. Nanotechnol. **6**, 358–363 (2011). doi:10.1038/nnano.2011.64
244. A. Adnan, R. Lam, H. Chen, J. Lee, D.J. Schaffer, A.S. Barnard, G.C. Schatz, D. Ho, W.K. Liu, Atomistic simulation and measurement of pH dependent cancer therapeutic interactions with nanodiamond carrier. Mol. Pharm. **8**, 368–374 (2011). doi:10.1021/mp1002398
245. J. Yan, Y. Guo, A. Altawashi, B. Moosa, S. Lecommandoux, N.M. Khashab, Experimental and theoretical evaluation of nanodiamonds as pH triggered drug carriers. New J. Chem. **36**, 1479 (2012). doi:10.1039/c2nj40226b
246. B. Guan, F. Zou, J. Zhi, Nanodiamond as the pH-responsive vehicle for an anticancer drug. Small **6**, 1514–1519 (2010). doi:10.1002/smll.200902305
247. X. Li, J. Shao, Y. Qin, C. Shao, T. Zheng, L. Ye, TAT-conjugated nanodiamond for the enhanced delivery of doxorubicin. J. Mater. Chem. **21**, 7966 (2011). doi:10.1039/c1jm10653h
248. Y. Li, X. Zhou, D. Wang, B. Yang, P. Yang, Nanodiamond mediated delivery of chemotherapeutic drugs. J. Mater. Chem. **21**, 16406 (2011). doi:10.1039/c1jm10926j
249. M. Chen, E.D. Pierstorff, R. Lam, S.Y. Li, H. Huang, E. Osawa, D. Ho, Nanodiamond-mediated delivery of water-insoluble therapeutics. ACS. Nano. **3**, 2016–2022 (2009). doi:10.1021/nn900480m
250. L. Moore, E.K.H. Chow, E. Osawa, J.M. Bishop, D. Ho, Diamond-lipid hybrids enhance chemotherapeutic tolerance and mediate tumor regression. Adv. Mater. **25**, 3532–3541 (2013). doi:10.1002/adma.201300343
251. M. Chen, X.Q. Zhang, H.B. Man, R. Lam, E.K. Chow, D. Ho, Nanodiamond vectors functionalized with polyethylenimine for siRNA delivery. J. Phys. Chem. Lett. **1**, 3167–3171 (2010). doi:10.1021/jz1013278
252. I. Badea, R. Kaur, D. Michel, J.M. Chitanda, J. Maley, P. Yang, F. Borondics, R.E. Verrall, Lysine-functionalized nanodiamonds: synthesis, physiochemical characterization, and nucleic acid binding studies. Int. J. Nanomedicine 3851 (2012). doi:10.2147/IJN.S32877
253. P. Zhang, J. Yang, W. Li, W. Wang, C. Liu, M. Griffith, W. Liu, Cationic polymer brush grafted-nanodiamond via atom transfer radical polymerization for enhanced gene delivery and bioimaging. J. Mater. Chem. **21**, 7755 (2011). doi:10.1039/c1jm10813a
254. X. Kong, P. Cheng, Application of nanodiamonds in biomolecular mass spectrometry. Materials **3**, 1845–1862 (2010). doi:10.3390/ma3031845
255. W.H. Chen, S.C. Lee, S. Sabu, H.C. Fang, S.C. Chung, C.C. Han, H.C. Chang, Solid-phase extraction and elution on diamond (SPEED): a fast and general platform for proteome analysis with mass spectrometry. Anal. Chem. **78**, 4228–4234 (2006). doi:10.1021/ac052085y

256. X. Kong, S. Sahadevan, Rapid MALDI mass spectrometric analysis with prestructured membrane filters and functionalized diamond nanocrystals. Anal. Chim. Acta. **659**, 201–207 (2010). doi:10.1016/j.aca.2009.11.037
257. S. Sabu, F.C. Yang, Y.S. Wang, W.H. Chen, M.I. Chou, H.C. Chang, C.C. Han, Peptide analysis: solid phase extraction-elution on diamond combined with atmospheric pressure matrix-assisted laser desorption/ionization-Fourier transform ion cyclotron resonance mass spectrometry. Anal. Biochem. **367**, 190–200 (2007). doi:10.1016/j.ab.2007.04.033
258. L.M. Wei, Y. Xue, X.W. Zhou, H. Jin, Q. Shi, H.J. Lu, P.Y. Yang, Nanodiamond MALDI support for enhancing the credibility of identifying proteins. Talanta **74**, 1363–1370 (2008). doi:10.1016/j.talanta.2007.09.020
259. X.L. Kong, Nanodiamonds used as a platform for studying noncovalent interaction by MALDI-MS. Chin. J. Chem. **26**, 1811–1815 (2008). doi:10.1002/cjoc.200890326
260. C.K. Chang, C.C. Wu, Y.S. Wang, H.C. Chang, Selective extraction and enrichment of multiphosphorylated peptides using polyarginine-coated diamond nanoparticles. Anal. Chem. **80**, 3791–3797 (2008). doi:10.1021/ac702618h
261. X. Kong, L.C.L. Huang, S.C.V. Liau, C.C. Han, H.C. Chang, Polylysine-coated diamond nanocrystals for MALDI-TOF mass analysis of DNA oligonucleotides. Anal. Chem. **77**, 4273–4277 (2005). doi:10.1021/ac050213c
262. G. Xu, W. Zhang, L. Wei, H. Lu, P. Yang, Boronic acid-functionalized detonation nanodiamond for specific enrichment of glycopeptides in glycoproteome analysis. Analyst **138**, 1876–1885 (2013). doi:10.1039/C3AN36623E
263. U.T. Bornscheuer, Immobilizing enzymes: how to create more suitable biocatalysts. Angew. Chem. Int. Ed. Engl. **42**, 3336–3337 (2003)
264. N. Kossovsky, A. Gelman, H.J. Hnatyszyn, S. Rajguru, R.L. Garrell, S. Torbati, S.S. Freitas, G.M. Chow, Surface-modified diamond nanoparticles as antigen delivery vehicles. Bioconjug. Chem. **6**, 507–511 (1995)
265. J.B. Zang, Y.H. Wang, S.Z. Zhao, L.Y. Bian, J. Lu, Electrochemical properties of nanodiamond powder electrodes. Diam. Relat. Mater. **16**, 16–20 (2007). doi:10.1016/j.diamond.2006.03.010
266. W. Zhao, J.J. Xu, Q.Q. Qiu, H.Y. Chen, Nanocrystalline diamond modified gold electrode for glucose biosensing. Biosens. Bioelectron **22**, 649–655 (2006). doi:10.1016/j.bios.2006.01.026
267. K.B. Holt, C. Ziegler, D.J. Caruana, J. Zang, E.J. Millán-Barrios, J. Hu, J.S. Foord, Redox properties of undoped 5 nm diamond nanoparticles. Phys. Chem. Chem. Phys. **10**, 303 (2008). doi:10.1039/b711049a
268. A. Kraft, Doped diamond: a compact review on a new, versatile electrode material. Int. J. Electrochem. Sci. **2**, 355–385 (2007)
269. K.B. Holt, Undoped diamond nanoparticles: origins of surface redox chemistry. Phys. Chem. Chem. Phys. **12**, 2048 (2010). doi:10.1039/b920075d
270. S. Shahrokhian, M. Ghalkhani, Glassy carbon electrodes modified with a film of nanodiamond-graphite/chitosan: application to the highly sensitive electrochemical determination of azathioprine. Electrochim. Acta **55**, 3621–3627 (2010). doi:10.1016/j.electacta.2010.01.099
271. A.I. Gopalan, S. Komathi, G. Sai Anand, K.P. Lee, Nanodiamond based sponges with entrapped enzyme: a novel electrochemical probe for hydrogen peroxide. Biosens. Bioelectron **46**, 136–141 (2013). doi:10.1016/j.bios.2013.02.036
272. N. Gibson, O. Shenderova, T.J.M. Luo, S. Moseenkov, V. Bondar, A. Puzyr, K. Purtov, Z. Fitzgerald, D.W. Brenner, Colloidal stability of modified nanodiamond particles. Diam. Relat. Mater. **18**, 620–626 (2009). doi:10.1016/j.diamond.2008.10.049
273. C.C. Chang, P.H. Chen, H.L. Chu, T.C. Lee, C.C. Chou, J.I. Chao, C.Y. Su, J.S. Chen, J.S. Tsai, C.M. Tsai, Y.P. Ho, K.W. Sun, C.L. Cheng, F.R. Chen, Laser induced popcornlike conformational transition of nanodiamond as a nanoknife. Appl. Phys. Lett. **93**, 033905 (2008). doi:10.1063/1.2955840

274. L.C. Cheng, H.M. Chen, T.C. Lai, Y.C. Chan, R.S. Liu, J.C. Sung, M. Hsiao, C.H. Chen, L.J. Her, D.P. Tsai, Targeting polymeric fluorescent nanodiamond-gold/silver multi-functional nanoparticles as a light-transforming hyperthermia reagent for cancer cells. Nanoscale **5**, 3931–3940 (2013). doi:10.1039/C3NR34091K
275. Q. Zhang, V.N. Mochalin, I. Neitzel, I.Y. Knoke, J. Han, C.A. Klug, J.G. Zhou, P.I. Lelkes, Y. Gogotsi, Fluorescent PLLA-nanodiamond composites for bone tissue engineering. Biomaterials **32**, 87–94 (2011). doi:10.1016/j.biomaterials.2010.08.090
276. L. Pramatarova, R. Dimitrova, E. Pecheva, T. Spassov, M. Dimitrova, Peculiarities of hydroxyapatite/nanodiamond composites as novel implants. J. Phys. Conf. Ser. **93**, 012049 (2007). doi:10.1088/1742-6596/93/1/012049
277. I.O. Pozdnyakova, Design of a luminescent biochip with nanodiamonds and bacterial luciferase. Phys. Solid State **46**, 761–763 (2004)
278. Y.L. Liu, K.W. Sun, Protein functionalized nanodiamond arrays. Nanoscale Res. Lett. **5**, 1045–1050 (2010). doi:10.1007/s11671-010-9600-7
279. A. Barras, F.A. Martin, O. Bande, J.S. Baumann, J.M. Ghigo, R. Boukherroub, C. Beloin, A. Siriwardena, S. Szunerits, Glycan-functionalized diamond nanoparticles as potent *E. coli* anti-adhesives. Nanoscale **5**, 2307 (2013). doi:10.1039/c3nr33826f
280. Chien-Min Sung, Healthcare and cosmetic compositions containing nanodiamond (US patent Nr. 2007184121)
281. A.O. Schenderova, V.P. Grichko, Nanodiamond UV protectant formulations (Patent WO2007027656)

Part II
Nanotechnology for Biomedical Applications: From Carbon Nanomaterials to Biomimetic/Bioinspired Systems

Chapter 12
Bio-Inspired Engineering of 3D Carbon Nanostructures

Rajesh Kumar, Hyun-Jun Kim and Il-Kwon Oh

12.1 Introduction

Carbon is a unique and versatile element which is capable of forming different architectures at the nanoscale level. Control of carbon nanostructure on the nanometer scale relies on intermolecular interactions whose specificity and geometry can be treated on a predictive basis. The study of the synthesis, characterization, and mechanism of formation of carbon nanostructure materials has a long history and studies in particular on fullerene, carbon fibers (CNFs), and carbon nanotubes (CNTs) dates back over many decades [1]. In 2004, the new form of carbon known as graphene, a one-atom-thick planar sheet of sp^2-bonded carbon atoms densely packed in a honeycomb crystal lattice, has grabbed extraordinary appreciable attention to be used as a next-generation electronic material, due to its exceptional properties including high current density, ballistic transport, chemical inertness, high thermal conductivity, optical transmittance, and super hydrophobicity at nanometer scale [2]. Recent progress has shown that the graphene-based materials can have a profound impact on electronic and optoelectronic devices, chemical sensors, nanocomposites, and energy storage. The Nobel Prize in Physics 2010 was awarded to Andre Geim and Konstantin Novoselov "for ground breaking experiments regarding the two-dimensional material graphene," a layer of graphite in the pencil. Graphene, one of the allotropes (CNT, fullerene, diamond) of elemental carbon, is a planar monolayer of carbon atoms arranged into a 2D honeycomb lattice with a carbon–carbon bond length of 0.142 nm. It has a large theoretical specific surface area of 2.6×10^3 m^2 g^{-1} [3] and high thermal conductivity (3×10^3 W m^{-1} K^{-1}) and Young's modulus (1.06×10^3 GPa) [5]. The electrical transfer rate show 1.5×10^4 cm^2 V^{-1} s^{-1}

I.-K. Oh (✉) · R. Kumar · H.-J. Kim
Department of Mechanical Engineering, Korea Advanced Institute of Science and Technology (KAIST), Daehak-ro 291, Yuseong-gu, Daejeon 34141, Republic of Korea
e-mail: ikoh@kaist.ac.kr
Homepage: http://active.kaist.ac.kr

M. Zhang et al. (eds.), *Carbon Nanomaterials for Biomedical Applications,*
Springer Series in Biomaterials Science and Engineering 5,
DOI 10.1007/978-3-319-22861-7_12

at room temperature [6]. With respect to its unique physical, chemical, and mechanical properties, graphene has gained an explosion of interest and opened up a new research area for material science and nanotechnology. The first graphene was extracted from graphite using a technique called micromechanical cleavage [6]. This approach allowed easy and simple production of high-quality graphene nanosheets (GNSs) and further led to enormous experimental activities [7]. These well-studies properties have generated tremendous interest among material researchers and engineers. The recent applications in various fields such as in large-scale assembly, field effect devices, sensors, transparent electrodes, photo detectors, solar cells, energy storage devices, polymer composites, and nanocomposites are reviewed with a brief update on toxicology. The conclusion and outlook summarizes the research activities and presents the possible future research directions.

In current time, there are several synthesis methods and application of three-dimensional (3D) graphene–carbon nanostructures. These type of hybrid graphene–carbon nanostructure has opened up new challenges in energy application and storage field.

12.1.1 History of New Carbon Nanostructures

12.1.1.1 Carbon Nanotubes

In the early 1952, Radushkevich and Lukyanovich published a report on hollow CNFs. In 1953, Davis et al. [8] found a deposition of an unusual form of carbon from carbon monoxide at an optimized temperature of 450 °C on an iron oxide substrate. However, their transmission electron microscopic (TEM) work could not reveal the architectures of such an unusual form of carbon. In 1960, Bacon [8] found the growth of graphite whiskers in direct current (DC) arc under a pressure of 92 atm of argon at 3900 K. Formation of these graphite whiskers was believed to be through a scroll mechanism. After few years, carbon filaments with hollow tubes of diameter were reported to be in the range of 2–50 nm. In the early 1970s, notable work on the formation of filamentous carbon was carried out by Terry Baker's group [10–13]. Carbon filaments formation both from the disproportionation of carbon monoxide and from the decomposition of hydrocarbons was investigated. In the 1976, Oberlin [14] carried out a typical experiment, in which high-purity hydrogen would be passed through benzene, and the resulting mixture would then flow across a catalytically treated substrate held in a furnace at an initial temperature of approximately 1000 °C. This initially produced hollow nanofibres approximately 10 nm in diameter which is now called a single- or double-walled CNT. In 1984, Tibbetts [15] reported tubular carbon filaments or carbon whiskers which were formed from the decomposition of hydrocarbon at 900 °C with submicron catalytic particles.

In 1991, a breakthrough in the research on one-dimensional (1D) carbon nanostructures came when S. Iijima [16] reported the arc discharge synthesis and high-resolution electron microscopic characterization of such "helical microtubules."

These microtubules, later known as CNTs, are molecular-scale fibers with structures related to fullerenes. S. Iijima was looking for new carbon structures in the deposit formed on graphite cathode surfaces during the electric arc evaporation that is commonly employed to produce fullerene soot. CNTs also known as tubular fullerenes are cylindrical graphene sheets of sp^2-bonded carbon atoms. These nanotubes are concentric graphitic cylinders closed at either end due to the presence of five-membered rings.

12.1.1.2 Graphene

Graphene is the name given to a 2D one-atom-thick planar sheet of sp^2-bonded carbon atoms, which is considered as the fundamental foundation for all carbon nanostructure, for example, fullerenes, CNTs, and graphite, as shown in Fig. 12.1. Graphene can be stacked to form 3D graphite, rolled to form 1D CNTs, and wrapped to form zero-dimensional (0D) fullerenes.

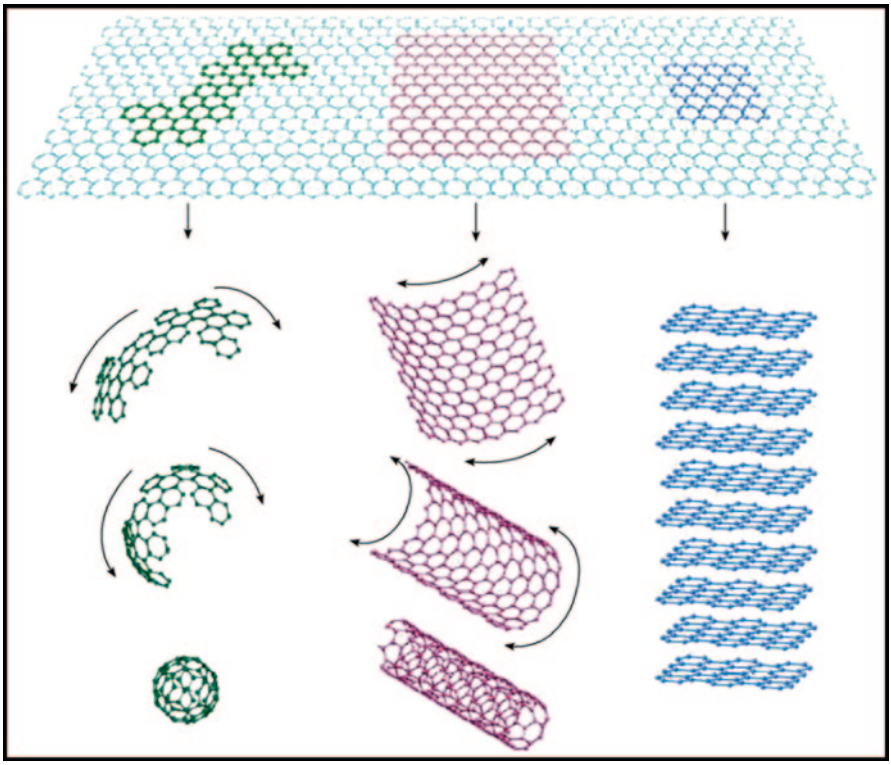

Fig. 12.1 Graphene, the building block of all graphitic forms, can be wrapped to form the 0D buckyballs, rolled to form the 1D nanotubes, and stacked to form the 3D graphite [17]

Discovery of Graphene Graphene is the basic fundamental structural unit of some carbon allotropes, including graphite, CNTs, and fullerenes. The rolling up of graphene along a given direction can produce a CNT. A 0D fullerene can also be obtained by wrapping up graphene. In 1947, Wallace et al. [18] established theoretically that graphene is the building block of graphite. While studies of graphite have included those utilizing fewer and fewer layers for some time [19], the field was delivered a jolt in 2004, when Geim and coworkers at Manchester University first isolated single-layer samples from graphite in a simple tabletop experiment. The Nobel Prize in Physics 2010 was awarded jointly to Andre Geim and Konstantin Novoselov "for groundbreaking experiments regarding the two-dimensional material graphene." The graphene is a 2D crystal which was previously considered to be thermodynamically unstable and could not exist under ambient conditions.

Synthesis of Graphene Despite intense interest and continuing experimental success by device physicists, widespread implementation of graphene has yet to occur. This is primarily due to the difficulty of reliably producing high-quality samples, especially in any scalable fashion [20]. The challenge is really twofold because performance depends on both the number of layers present and the overall quality of the crystal lattice [21–23]. So far, the original top-down approach of mechanical exfoliation has produced the highest-quality samples, but the method is neither high throughput nor high yield. In order to exfoliate a single sheet, van der Waals (VDW) attraction between exactly the first and second layers must be overcome without disturbing any subsequent sheets. Therefore, a number of alternative approaches to obtaining single layers have been explored, a few of which have led to promising proof-of-concept devices.

Alternatives to mechanical exfoliation include primarily three general approaches: chemical efforts to exfoliate and stabilize individual sheets in solution [24–27], bottom-up methods to grow graphene directly from organic precursors [28], and attempts to catalyze growth in situ on a substrate [29–31]. Each of these approaches has its drawbacks. For chemically derived graphene, complete exfoliation in solution so far requires extensive modification of the 2D crystal lattice, which degrades device performance [32]. Alternatively, bottom-up techniques has yet to produce large and uniform single layers. Total organic syntheses are size limited because macromolecules become insoluble and the occurrence of side reactions increases with molecular weight [28]. Substrate-based growth of single layers by chemical vapor deposition (CVD) or the reduction of silicon carbide relies on the ability to walk a narrow thermodynamic tightrope [33]. After nucleating a sheet, conditions must be carefully controlled to promote crystal growth without seeding additional second layers or forming grain boundaries.

12.1.2 Recent Progress on Graphene-Based 3D Nanostructures

The study of 3D graphene-based materials in recent years has been popular and extensive, particularly with respect to electrochemical applications. Underpinning

the significance of 3D graphene-based materials in electrochemistry are the very specific properties that although relevant to graphene are not typical of pristine graphene. These include its facile synthesis, high dispersibility in a range of solvents, capability of coupling electroactive species onto the surface, and unique optical properties. In addition, the use of 3D graphene-based materials also provides control over the local microenvironment. This is because in most cases 3D graphene-based materials can be deposited, with extremely well-defined surfaces, through solution processing. This can be highly advantageous when incorporating sensitive or electroactive species into an electrochemical system. Another important issue is consideration of the costs when manufacturing an electrode for use in any real system. In terms of the manufacture of 3D graphene-based materials devices, costs can be reduced compared with the costs for conventional electrodes. The excellent electrical, thermal, and mechanical properties, as well as the immunity to electro migration make graphene an ideal material candidate for high-performance interconnects. Monolayer graphene nanoribbon (GNR) is expected to outperform Cu at ultra-scaled width dimensions. Although the maximum current-carrying density up to 10^8 Acm^{-2} (~100 times of Cu) was reported, current density of monolayer graphene is limited by its 2D atomically thin geometry, sensitivity to ambient, poor noise tolerance, and conductance degradation due to edge-related effects. 3D nanocarbon, or vertically stacked multilayer graphene (s-MLG), can potentially be employed to address this challenge, yielding an ultra-conductive material system. Graphene multilayer has received significant amount of theoretical and experimental attentions in recent years. However, in the case of *Bernal stacking* (in which graphene layers have an *ABAB*-ordered lattice arrangement), the composing graphene monolayers are electronically coupled and form graphite which lacks the appealing electronic properties of individual 2D graphene sheets. It is therefore ideal to have electronically decoupled layers in 3D stacked multilayer system.

12.2 Synthesis of Graphene-Based 3D Nanostructures

Existing methods for producing the 3D graphene nanostructures include directed CVD [34–37], template-directing method [38–41], cross-linking method [42–46], and in situ reduction-assembly method [47–51]. The directed CVD method, 3D nickel foams are generally used as substrates, onto which graphene is deposited under high-temperature conditions. The template-directing method uses ice crystals, water droplets, or colloidal particles as the templates for the pore formation, and generally requires precise control over the amount of graphene used and subsequent template removal. The cross-linking method employs cross-linkers, such as sol–gel polymerization precursors, polymers, and ion linkages, whose presence has unfortunately been found to lead to a decrease or a complete loss of the electrically conducting properties of the thus-prepared 3D macrostructures.

The various structural interconnections of 3D carbon-based hybrid nanostructures possess a higher electrical conductivity as well as better structural mechani-

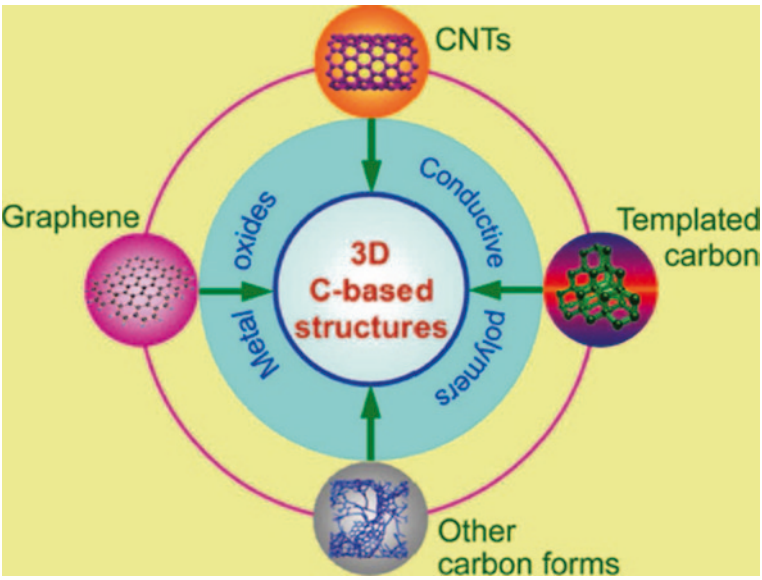

Fig. 12.2 3D carbon-based nanostructures [52]. *CNT* carbon nanotubes

cal stability. The fabrication and optimization of 3D carbon-based nanostructures are definitely important technique since each of the respective building block's properties can be dramatically enhanced. In this chapter, a brief summary of recent research progress on 3D carbon-based electrode materials is presented, mainly including CNTs-based networks, graphene-based nanostructures, graphene-based architectures, hierarchical porous carbon-based nanostructures, and even more complex carbon-based 3D configurations [52], as shown in Fig. 12.2.

12.2.1 Synthesis of Graphene–Graphene, Graphene–Fullerene, and Graphene–CNT Hybrids

Wang et al. [53] has demonstrated a novel 3D hierarchical few-layer graphene/multiwalled carbon nanotubes (MWNT) hybrid foam nanostructure by ambient pressure CVD method using a mixture of acetylene and hydrogen on 1.0 mm thick nickel foam, which is typically used as current collector in the battery industry. The growth of graphene/MWNT foam nanostructure is proposed and the scheme is illustrated in Fig. 12.3. The few-layer graphene/MWNT foam electrode shows a performance with a high-energy density of 39.72 Wh kg^{-1} at 3.74 kW kg^{-1} which gradually reduces to 25.78 Wh kg^{-1} at 154.67 kW kg^{-1}. This type of new nanocarbon architecture offers a facile, scalable, and low-cost approach for supercapacitor and battery applications. The low density (normally < 500 g m^{-2}), excellent ductility, high electrochemical stability (99.34 % capacitance retention over 85,000

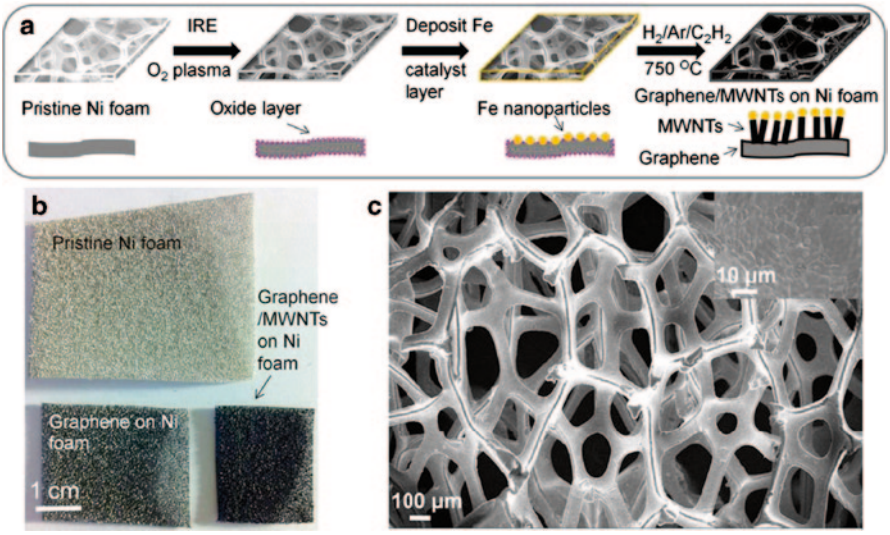

Fig. 12.3 Growth of graphene/MWNT hybrid foam nanostructure. **a** Schematic illustration of the synthesis process of the graphene/MWNT nanostructure foam. **b** Optical micrograph of inch-scale pristine nickel foam, graphene foam, graphene/MWNT foam. **c** SEM image of the pristine nickel foam structure. Inset shows the high magnification morphology of the nickel foam [53]. *MWNTs* multiwalled carbon nanotubes

cycles), and excellent capacitive performance (specific capacitance, 286 F g^{-1}; energy density, 39.72 Wh kg^{-1}; and power density, 154.67 kW kg^{-1}) indicate that this unique 3D structure is promising for future energy storage applications.

12.2.2 Synthesis of Graphene Aerogel

Aerogels are ultralight and highly porous nanomaterials with large pore volumes, high surface areas, and tunable porosity. These properties are derived from their microstructures, which are typically composed of 3D networks of interconnected nanoparticles (NPs). Graphene aerogels (GAs) have been focused recently due to novel properties of graphene (extremely low electrical and thermal resistivity, large carrier mobility, high surface area, and mechanical elasticity) and the low cost and easy preparation of graphene from graphite. Cong et al. reported graphene-based hydrogels and aerogels by metal ion-induced self-assembly process [50]. This shows a facile one-step approach for the synthesis of macroscopic 3D-graphene/iron oxide hydrogels interconnected networks under the synergistic effects of the self-assembly of graphene oxide (GO) sheets. Figure 12.4 shows the scanning electron microscopy (SEM) images with different magnifications of the graphene/FeOOH aerogels. In a typical synthesis, a certain amount of $FeSO_4$ was quickly added into 10 mL of a 2 mg mL^{-1} GO aqueous suspension stored in a 25-mL cylindrical sampler vial. The pH value of the GO suspension was adjusted with ammonia

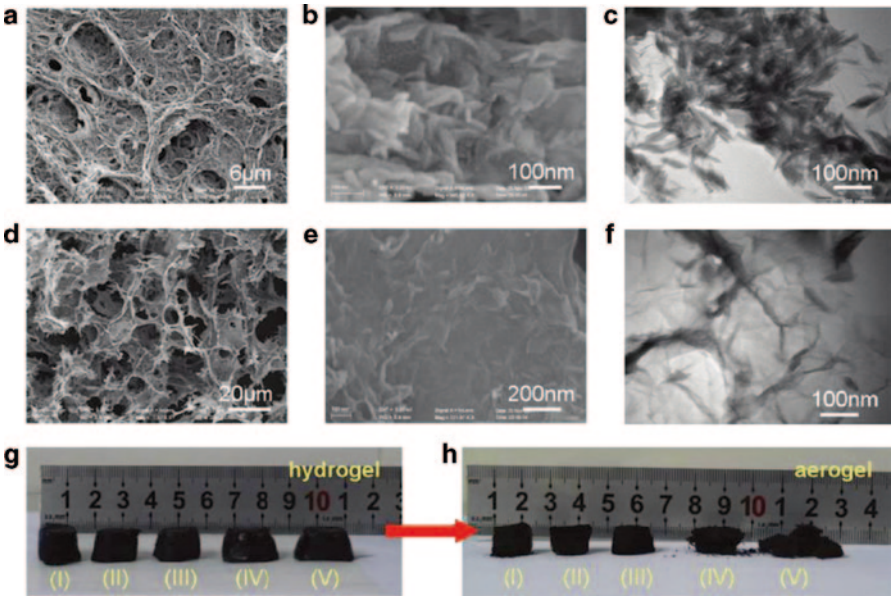

Fig. 12.4 SEM images with different magnifications of the graphene/FeOOH aerogels dried from the hydrogels prepared with 10 mL of a GO (2 mg mL^{-1}) suspension at pH 3, using different amounts of $FeSO_4$ [50]

from 3 to 11 to investigate the influences of the pH value on the synthesis of graphene/FeOOH and graphene/Fe_3O_4. Then, the reaction vessel was placed in an oil bath for 6 h at 90 °C without stirring. The multifunctional graphene-based hydrogels and aerogels are ideal candidates as adsorbents with high adsorption capacity for removal of heavy ions and oils in industrial water purification. The versatile synthesis method shows the extent to induce the assembly of graphene sheets and other functional metal oxides via one step into different macroscopic monoliths with multifunctionalities for different applications.

Chen et al. reported the preparation of magnetic NPs into 3D graphene networks under the assistance of reducing agent ($NaHSO_3$, Na_2S, vitamin C, HI, and hydroquinone) [48, 54] (Fig. 12.5). Magnetic 3D graphene/Fe_3O_4 architectures are prepared via an in situ self-assembly of graphene obtained by a mild chemical reduction of GO in water under atmospheric pressure in the presence of Fe_3O_4 NPs. It was found that the shape of the as-prepared graphene hydrogel is reactor dependent. The various shapes of graphene hydrogels such as taper like, cylindrical, pear shaped, and spherical can be prepared when the relative shape of reactor was utilized. This indicates that the shrinkage of the as-formed hydrogel during the self-assembly is isotropic, and it provides a chance to prepare shape-controlled graphene hydrogels as desired.

Zhang et al. [49] reported an easy synthesis approach for GAs from aqueous gel precursors processed by supercritical CO_2 drying or by freeze drying as shown in Fig. 12.6. The resulting aerogels with densities in the range 12–96 mg cm^{-3} show

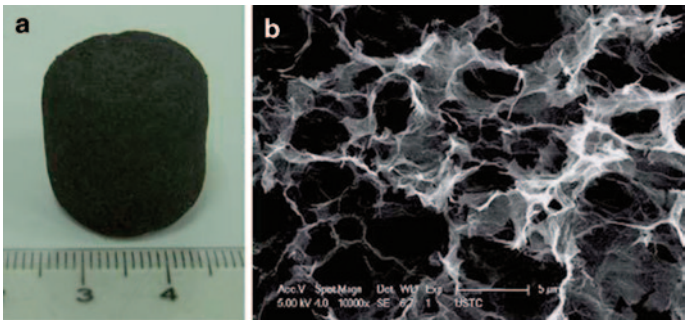

Fig. 12.5 A photograph of a GA (**a**), and its cross-section SEM image (**b**) [48]

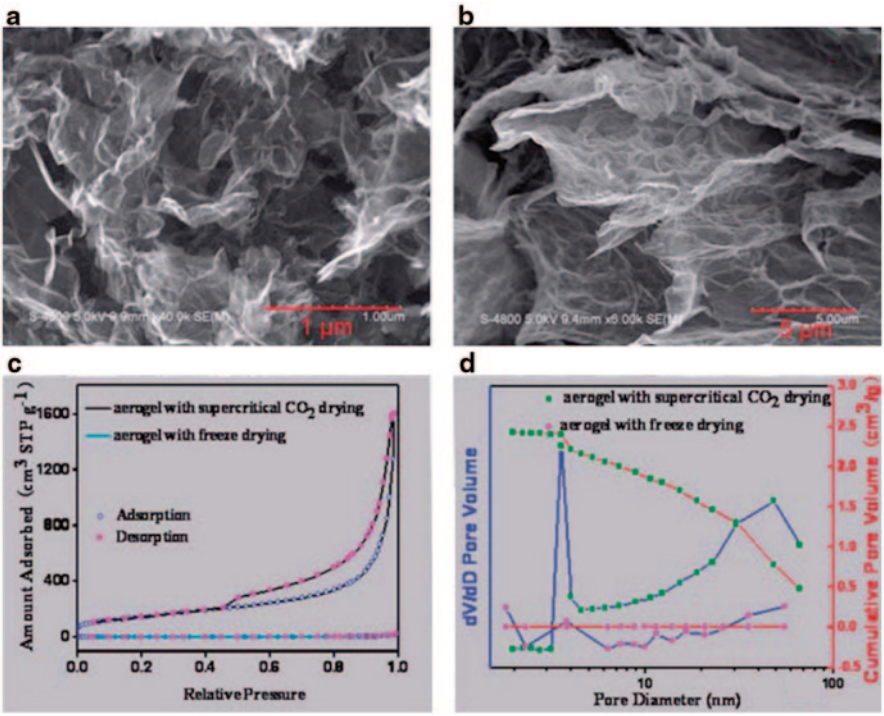

Fig. 12.6 SEM images of supercritical CO_2 dried (**a**) and freeze dried (**b**) GAs, and typical nitrogen sorption isotherms (**c**), BJH desorption pore size distribution (**d**) of these GAs [49]

large Brunauer–Emmett–Teller (BET) surface areas (512 $m^2\ g^{-1}$) and pore volumes (2.48 $cm^3\ g^{-1}$) with wide pore size distribution revealed by SEM and nitrogen adsorption investigation.

Nguyen et al. [55] synthesized aerogel using hydrothermal method. They have synthesized graphene aerosol with different GO concentrations and different hy-

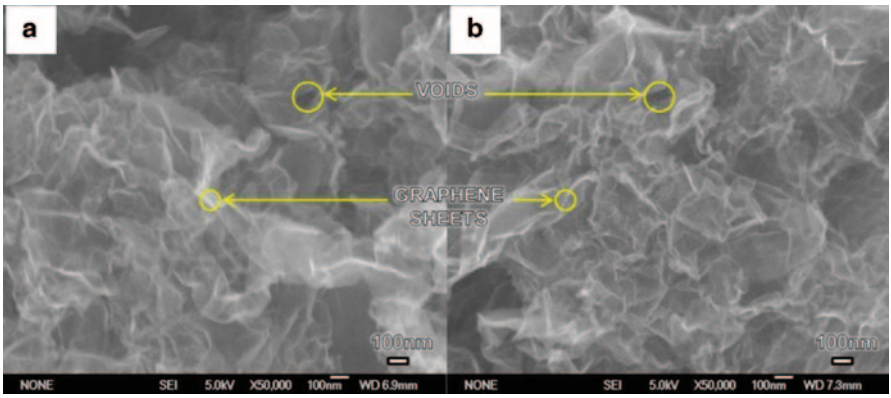

Fig. 12.7 FESEM images of GAs with **a** 2 and **b** 5 mg GO mL^{-1} [55]

drothermal treatment times as shown in Fig. 12.7. The hydrothermal treatment time has greater impact on the BET areas of graphene aerosol than GO concentration. Longer hydrothermal treatment time reduced their BET surface area, pore volume and increased the bulk density. This behavior confirms that the formation of hydrophobic sites and π–π interactions between graphene sheets under hydrothermal condition is the main factor deciding the porous structure of the graphene aerosol.

12.2.3 Metal Foam-Based 3D Graphene Nanostructures

Maiyalagan et al. [56] have shown platinum NPs deposited on 3D graphene and CNFs scaffold by the pulse electrodeposition method exhibit different catalytic activity toward methanol oxidation. The 3D graphene foams were synthesized by chemical vapor deposition using nickel foam as the template and ethanol as precursors as shown in Fig. 12.8. Typically, nickel foams (0.5 mm in thickness, 320 g m–^{2} in areal density) were cut into 2×2 cm^2 and placed in a quartz tube furnace with temperature gradually increased to 1000 °C under H_2 (25 sccm) and Ar (50 sccm) environment. After annealing for 10 min to clean the nickel surface, the ethanol vapor was introduced into the tube by H_2/Ar mixture gas at ambient pressure. After 20 min, the samples were rapidly cooled to room temperature at a rate of 100 °C min^{-1}. After the growth process, the nickel substrates were etched away with HCl (3 M) solution at 80 °C to obtain free-standing 3D graphene foams.

This difference in catalytic activity can be attributed to the geometry difference of these carbonaceous supports. The enhancement in the Pt/3D-graphene catalyst is attributed to the superior electrical conductivity, large surface area and efficient mass transport, and dense coating of small platinum NPs. Detailed electrochemical characterization shows the 3D graphene structure as a new kind of supporting material with higher catalytic activity and stability for methanol oxidation. The present approach can be readily extended by decorating free-standing 3D graphene with NPs of other noble.

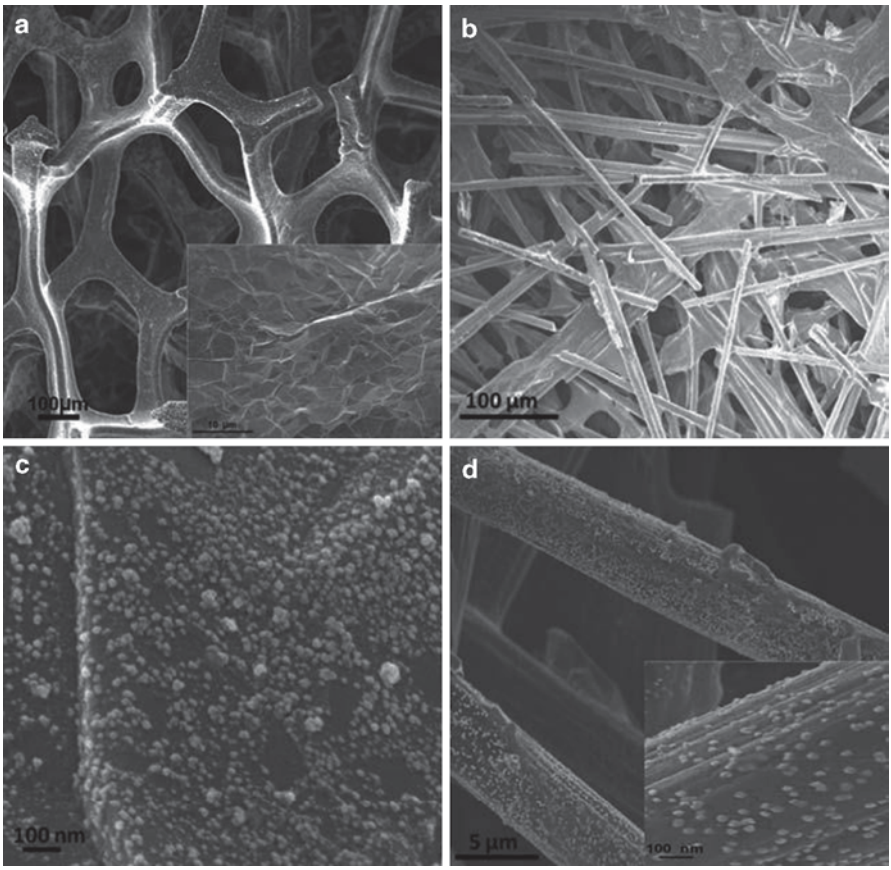

Fig. 12.8 SEM images of the **a** 3D graphene support, **b** carbon fiber support, **c** Pt/3 D-GN catalyst, and **d** Pt/CF catalyst. Insets in **a** and **d** are the enlarged pictures [56]

Chen et al. [34] have developed the template-directed CVD technique for the fabrication of macroscopic 3D graphene foam structures using nickel foams as templates. The graphene sheets in the graphene foam are seamlessly interconnected into a graphene foam flexible network. The high quality of the graphene sheets and their perfect connection in three dimensions give the material an outstanding electrical conductivity that is superior to that of macroscopic graphene structures from chemically derived graphene sheets as shown in Fig. 12.9. The unique network structure, high specific surface area, and outstanding electrical and mechanical properties of graphene foam and their composites should enable many applications including high-performance electrically conductive polymer composites, elastic and flexible conductors, electrode materials for lithium ion batteries and supercapacitors, thermal management, catalyst and biomedical supports, and so on.

Worsley et al. [42] have synthesized ultralow-density 3D graphene sheets that exhibit high electrical conductivities and large internal surface areas which is shown in Fig. 12.10. These GAs show $\sim 1 \times 10^2$ S m^{-1} high electrical conductivity. The GAs

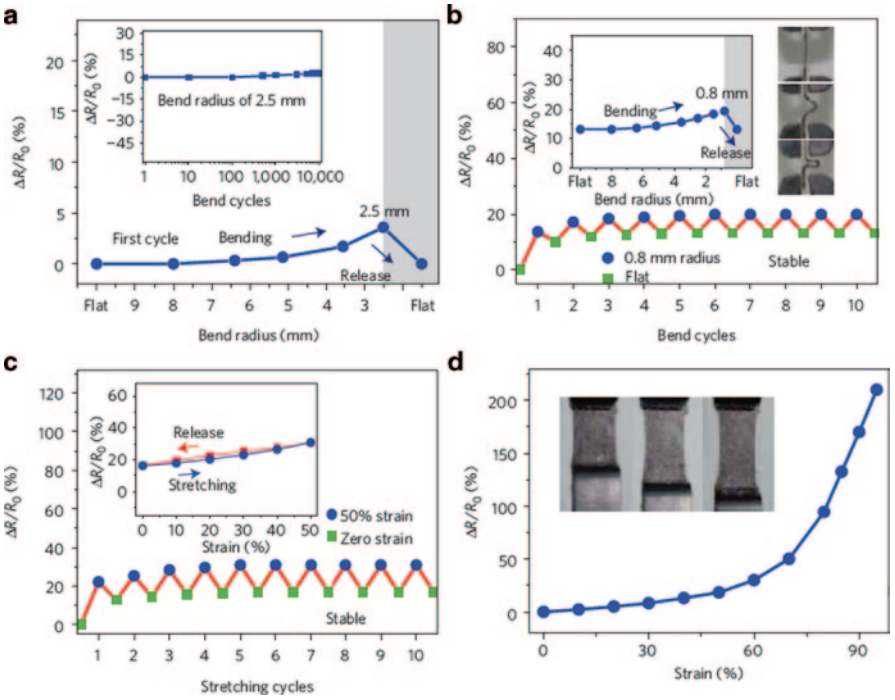

Fig. 12.9 Electrical resistance change of GF/PDMS composites under mechanical deformation [34]

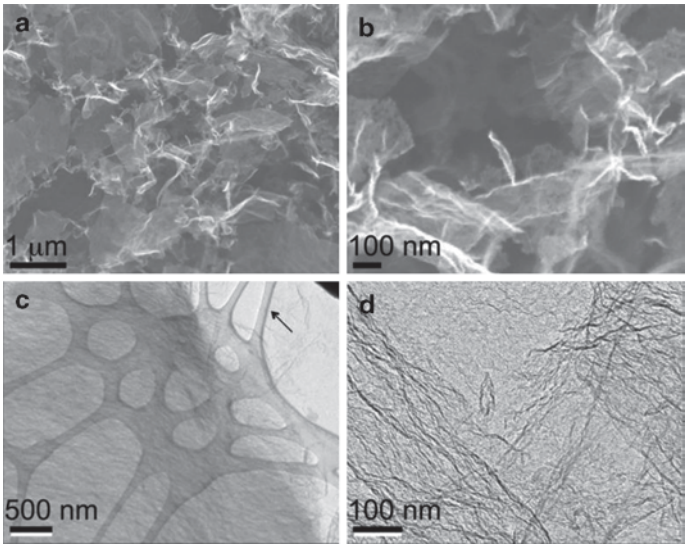

Fig. 12.10 FESEM of the GA at low (**a**) and high (**b**) magnification. TEM of the GA at low (**c**) and high (**d**) magnification. *Black arrow* denotes holey carbon on TEM grid [42]

also possess large surface areas (584 $m^2 g^{-1}$) and pore volumes (2.96 $cm^3 g^{-1}$). Due to the high surface area, mesoporosity, and conductivity of these 3D graphene assemblies, they have potential in a number of technologies for use as supercapacitors, batteries, catalysis, and sensors.

Recently, Zhang et al. [57] reported the GA by a novel chemical reduction-induced self-assembly method. In this work, the 3D assemblies of graphene were prepared by the in situ reduction-assembly method using a combination of oxalic acid and NaI as the reducing agents. Figure 12.11 represents the graphene hydrogels prepared from the GO suspension. The unique advantage of the current preparation method is that the volume of the thus-prepared GAs can be readily varied by varying the volume of the starting GO suspension with its concentration being constant. The as-obtained monolithic GA exhibits a good mechanical property. Due to their highly macroporous structures, the GAs exhibited very low densities. For instance, the GA prepared from a starting GO concentration of 4.5 mg mL^{-1} had a density of 14.2 mg cm^{-3}. As the GO starting concentrations decreased, the density of the resulted GAs decreased accordingly. Incidentally, the aerogels prepared from the starting GO concentrations ≤ 1.0 mg mL^{-1} showed deteriorated mechanical

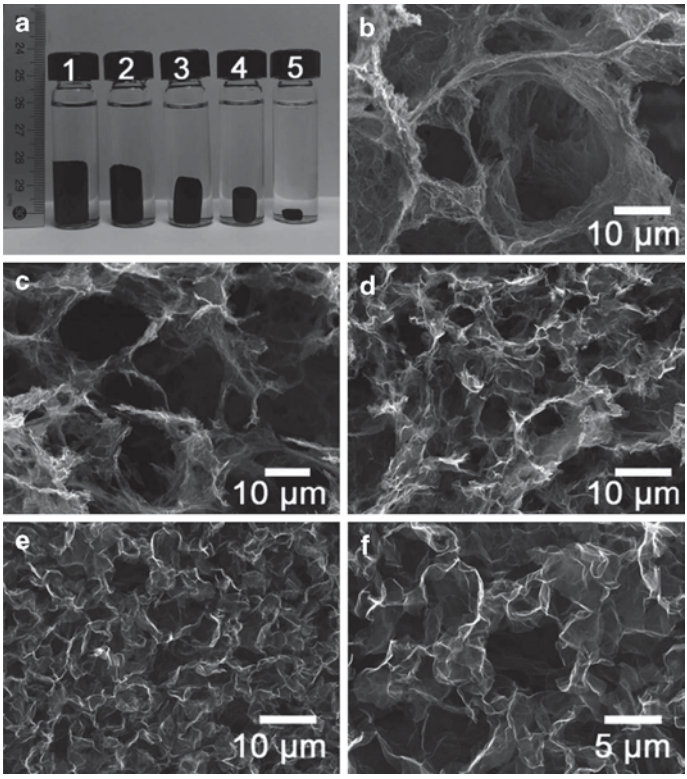

Fig. 12.11 Photograph showing the graphene hydrogels prepared from the GO suspension with concentrations [57]

strength, but as the GO concentration increased beyond 1.0 mg mL^{-1} (especially 2.5 and 4.5 mg mL^{-1}), stable GAs with high mechanical strength were obtained.

12.2.4 Synthesis of 3D Graphene–Polymer Nanocomposite

Both CNTs and G/GO are widely used to develop polymer composites with improved mechanical, thermal, and electrical performances. It is expected that the concurrent use of CNTs and G/GO would have synergistic effect. This has been demonstrated experimentally [58–60] and theoretically [61].

Wang et al. [60] have shown fibrous nanocomposites of CNTs and GO with synergetic mechanical and actuative performance. Mixing single-walled CNT (SWCNTs) and GO improves dispersion of both in the polymer matrix and leads to the synergetic enhancement of the strength of the fibers as shown in Fig. 12.12. The conductivity of the fibers was also increased by mixing SWCNTs and GO together at the ratio of 2:1. Adding concentrated HCl into the coagulation bath enhances the conductivity of the fibers significantly. SWCNT–GO (2:1) fibers coagulated from acid polyvinyl alcohol (PVA) solutions have both high strength and conductivity, and show excellent actuation performance. Contrary to GO fibers, graphene fibers exhibit high toughness upon the removal of carboxyl and hydroxyl groups. Fibers with tunable toughness were designed by mixing SWCNTs with graphene in different ratios. These tunable fibers have potential in a wide range of applications.

Wu et al. [62] presented a simple and effective route to fabricate the polymer composites with 3D interconnected graphene networks by using a self-assembly and hot press process. Figure 12.13 shows the SEM micrographs of 3D porous graphene network obtained by annealing the composite film shows better electrical conductivity as compared with the composite, possibly having potential applications including electrode materials for lithium ion batteries and supercapacitors. The self-assembly and hot press technique is a general strategy for fabrication of graphene-based composites with different polymer matrixes, including polystyrene matrixes. The as-prepared polystyrene composite with 4.8 vol% graphene shows a high electrical conductivity, which is superior to that of the graphene composite prepared by a solvent mixing method. This electrical property is closely related to the compact contact between graphene sheets in the 3D structures and the high reduction level of graphene sheets. The method to fabricate 3D graphene structures in polymer matrix is facile, green, low cost, and scalable, providing a universal route for the rational design and engineering of highly conductive polymer composites.

12.2.5 Growth of 3D Carbon Nanostructures by Thermal CVD

The thermal CVD method involves pyrolysis of gaseous, liquid, or solid hydrocarbons (acetylene, ethylene, propylene, methane, benzene, toluene, camphor, etc.) or other carbon feedstock source (polymers, carbon monoxide) diluted in the stream

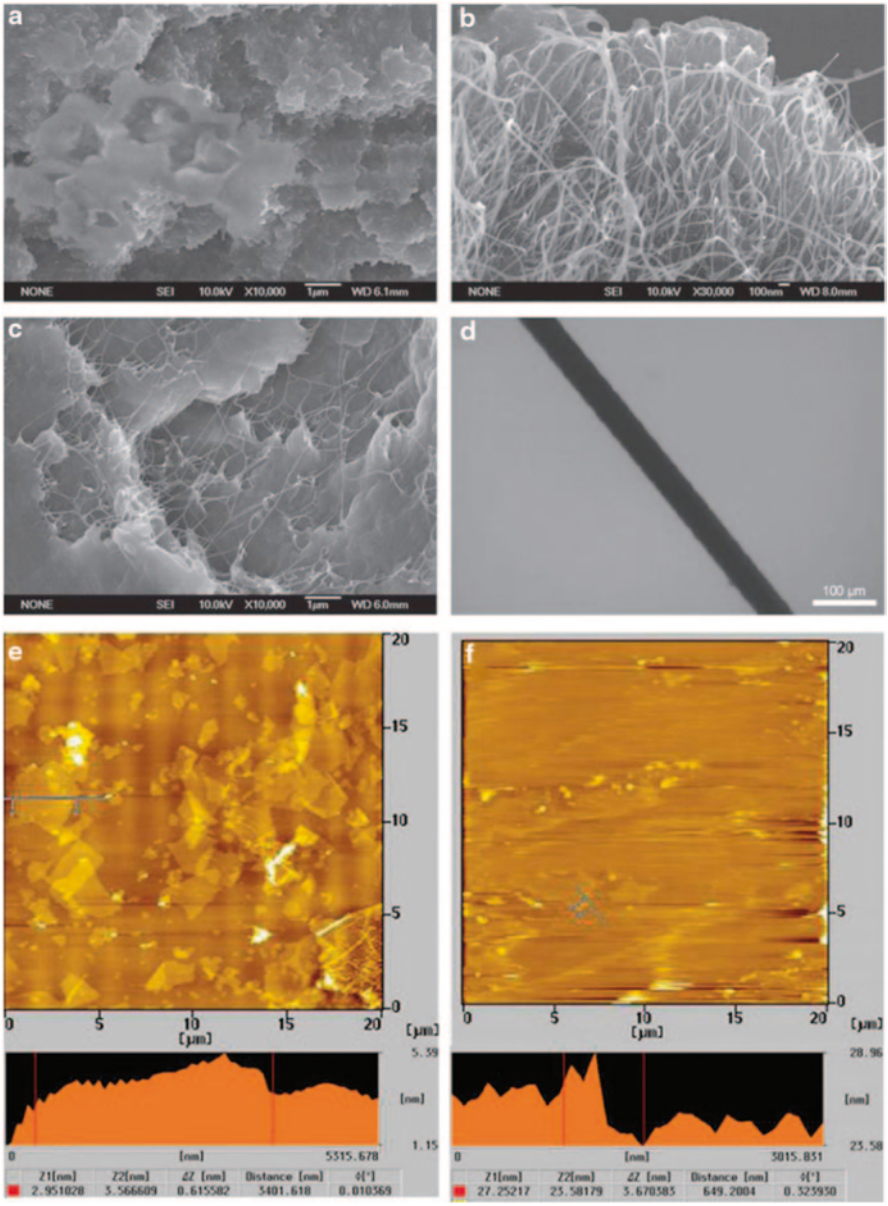

Fig. 12.12 SEM images of the cross-section of **a** GO fibers; **b** SWCNT fibers; **c** SWCNT–GO (2:1) composite fibers; **d** optical microscope image of the SWCNT–GO (2:1) composite fiber; **e** AFM image of GO sheets; **f** AFM image of graphene sheets which were reduced for 2 h [60]. *AFM* atomic force microscopy

of inert gas in the furnace system over the surface of metal catalysts. The catalyst material can be solid, liquid, or gas and can be placed inside the furnace or fed in continuously from outside. Decomposition of hydrocarbon species dissolves in the

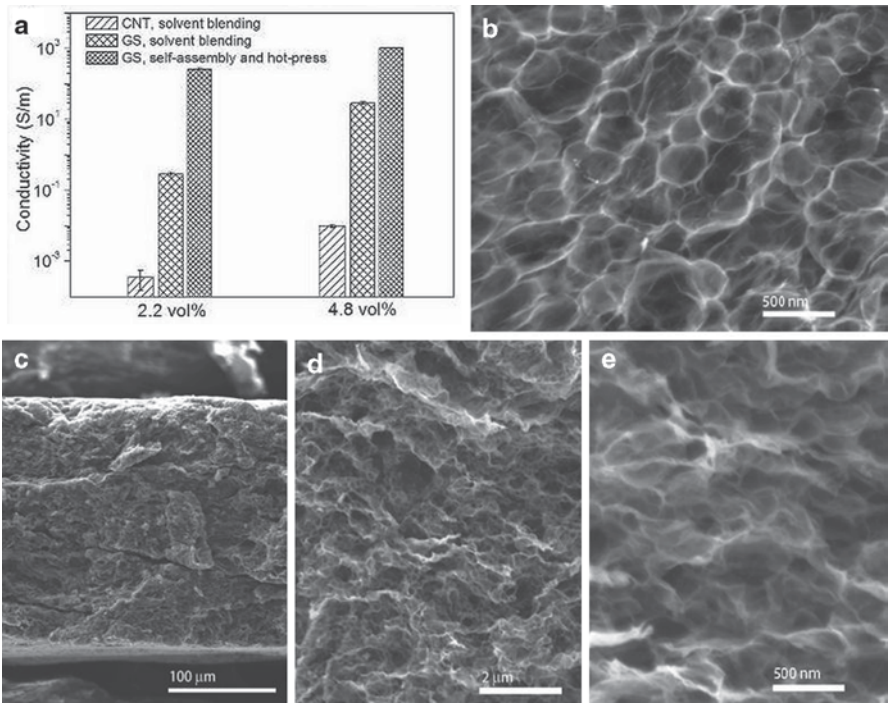

Fig. 12.13 **a** Electrical conductivity comparison of the graphene and carbon nanotube–polystyrene composites fabricated by the solution mixing and electrostatic self-assembly methods. **b** Top view and **c–e** cross-sectional SEM images of the remained graphene skeleton after annealing the testing samples at high temperature under nitrogen atmosphere [62]

metal NPs but, due to a finite solubility of carbon in the metallic particles, super saturation will be reached followed by carbon precipitation out in the form of carbon nanostructure. The more important aspect in CVD synthesis of graphene–inorganic composites is the vertical growth of CNTs on GNSs [63, 64].

Zhao et al. [63] prepared the GO/reduced GO (rGO) sheets pillared with CNTs using CVD method with acetonitrile as the carbon source and Ni NPs as the catalyst. The Ni NPs were deposited on GO/rGO platelets, and CNTs were then grown on them through a tip growth model with Ni catalysts residing at the top of them. Both the amount and length of CNTs could be adjusted by the amount of Ni catalyst and CVD times, respectively (Fig. 12.14).

With the same growth mechanism, Fan et al. [64] prepared an rGO–CNT composite with Co as a catalyst and CO as the carbon source (Fig. 12.15). They also employed Co NPs as a catalyst to deposit carbon nanofibers on the rGO sheets stemming from the pyrolysis of GO during the CVD process [65]. 3D CNT/graphene sandwich structures with CNT pillars grown in between the graphene layers are prepared by CVD. The unique structure endows the high-rate transportation of electrolyte ions and electrons throughout the electrode matrix and comprehensive utilization of pseudo and double-layer capacitance, resulting in excellent electrochemical

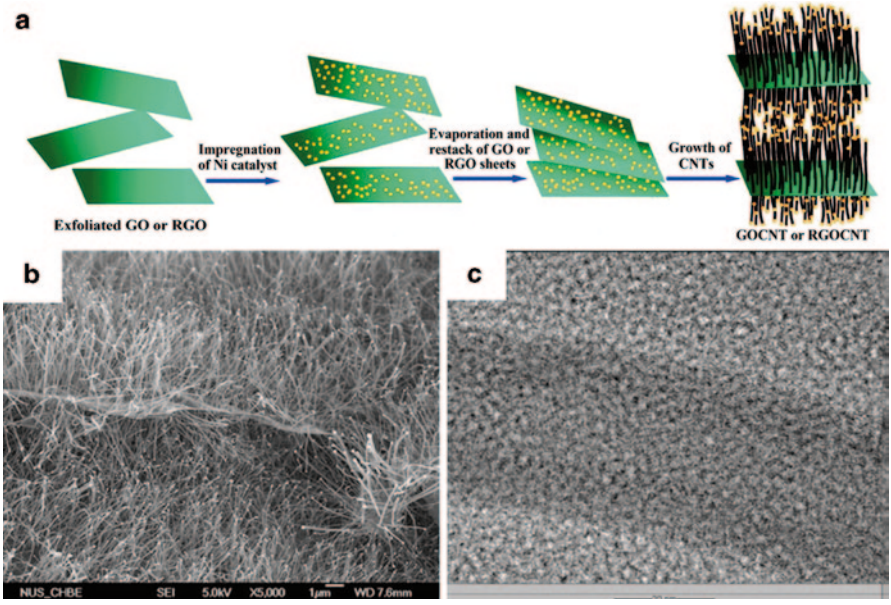

Fig. 12.14 **a** Scheme illustrating the experimental steps of pillaring GO/rGO platelets with CNTs **b** FESEM, and **c** TEM images of the CNT-pillared GO nanosheets [63]. *CNT* carbon nanotube, *GO* graphene oxide, *rGO* reduced graphene oxide

performances. The supercapacitor based on CGS exhibits a specific capacitance of 385 F g^{-1} at 10 mV s^{-1} in 6 M KOH solution. After 2000 cycles, a capacitance increase of ca. 20 % of the initial capacitance is observed, indicating excellent electrochemical stability of the electrode. This new carbon material is also expected to be useful as electrode material in Li-ion secondary batteries, as media for hydrogen storage, as catalysts for fuel cells, and as component for other clean energy devices.

Jousseaume et al. [66] investigated the growth of the composite material composed of vertically aligned CNTs capped by few graphene layers. Figure 12.16 shows that the CNTs grow epitaxially under the few layers of graphene. At the initial stage of CNT formation, graphene layers grow at the catalyst tip and catalyst atoms rapidly move toward the few layers of graphene-free region. This causes an elongation of the catalyst until the energy gained when binding graphene to the Ni surface no longer compensate the increase in the Ni surface energy.

Dong et al. [36] have synthesized cobalt oxide nanowires on 3D graphene foam grown by CVD as shown in Fig. 12.17. They have shown that Co_3O_4 nanowires with uniform diameter and high crystallinity form a dense nanomesh covering the 3D graphene skeleton. The superior mechanical strength of graphene, the 3D graphene/Co_3O_4 composite can work as a freestanding electrode despite its lightness. The monolithic 3D electrode demonstrates remarkable performance as a supercapacitor and for enzyme-free ultrasensitive detection of glucose. This is due to the synergistic integration of the two novel nanomaterials. The 3D nanostructure

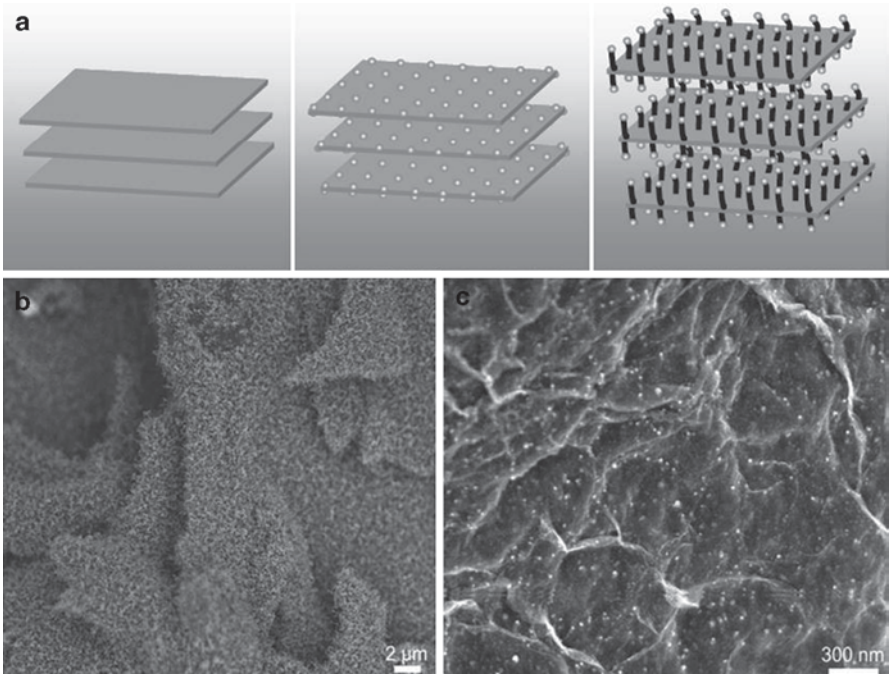

Fig. 12.15 **a** Illustration of the formation of hybrid materials with CNTs grown in between graphene nanosheets, **b**, **c** SEM images of the hybrid material with CNTs covering on the surfaces of graphene [64]

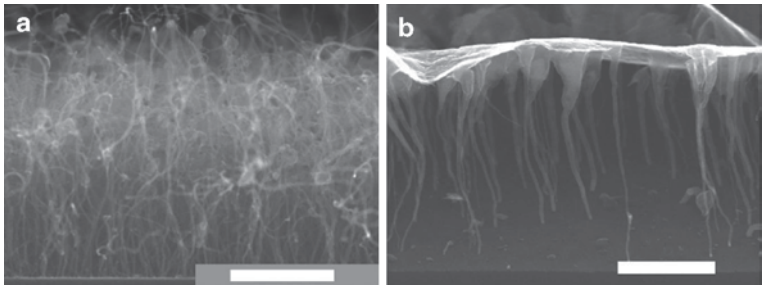

Fig. 12.16 **a**, **b** SEM images of 3D graphene–CNTs structure [66]

and highly conductive pathways provided by the defect-free graphene foam ensure rapid charge transfer and conduction. The Co_3O_4 nanowires exhibit exceptional electrochemical and electrocatalytic properties. This 3D graphene/Co_3O_4 electrode provides an enormous accessible active area. The bare graphene foam has a high specific surface area of ~850 m^2 g^{-1} and this is further increased greatly by the Co_3O_4 nanomesh surrounding the graphene scaffold. Open pore system of the composite is beneficial to ion diffusion and transport kinetics.

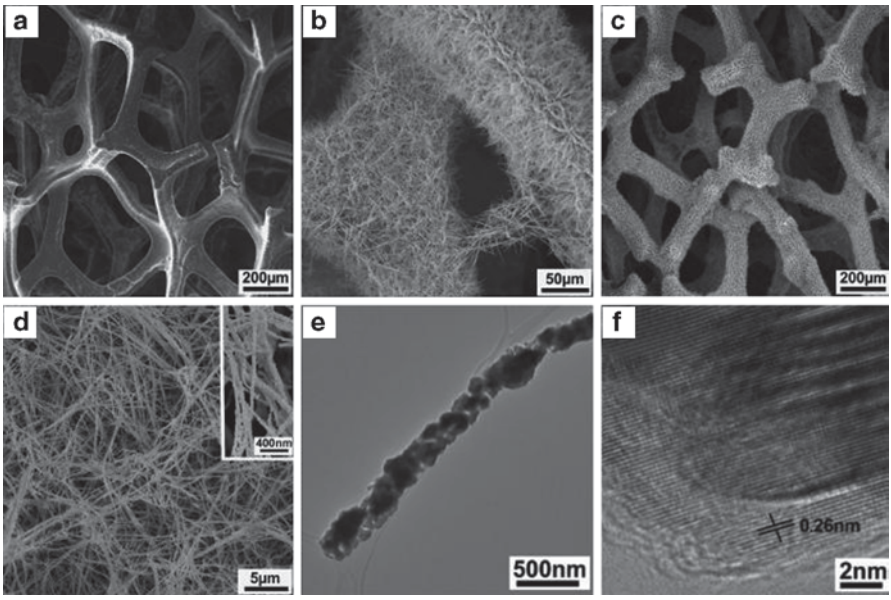

Fig. 12.17 SEM images of **a** 3D graphene foam, **b** 3D graphene/Co_3O_4 nanowire composite. **c**, **d** Low- and high-magnification SEM images of graphene/Co_3O_4 nanowire composite. Inset panel (**d**) shows an enlarged view. **e**, **f** Low- and high-resolution TEM images of Co_3O_4 nanowire grown on the surface of 3D graphene foam [36]

Zhou et al. [67] proposed a novel architecture of 3D graphene as shown in Fig. 12.18. The graphene films were first grown directly on anodic aluminum oxide (AAO) templates and porous Al_2O_3 ceramics by using a versatile ambient pressure CVD method. A versatile catalyst-free approach is proposed to directly grow large-area 3D graphene on AAO, micro-pore Al_2O_3 ceramic, and large-pore Al_2O_3 ceramic (PAO) by atmospheric pressure CVD method. The synthesis mechanism of graphene is based on the carbothermic reduction. This reduction at the Al_2O_3 surface and initiate the nucleation and growth of graphene. The graphene-coated AAO (G-AAO) containing 1D isolated graphene tubes is conductive along the tubes axis, which can act as a medium for directional thermal heat transport. The porous graphene/Al_2O_3 composite (G–Al_2O_3) indicates an interconnected macroporous framework of graphene sheets with an extremely low sheet electrical resistance down to 0.11 Ω sq^{-1} and thermal conductivity with 8.28 W m^{-1} K^{-1}. The G–Al_2O_3 provides enormous conductive pathways for electronic and thermal transport, suitable for heat sinks. Such a porous composite of G–Al_2O_3 is also attractive as a highly thermally conductive reservoir to hold phase change materials (stearic acid) for thermal energy storage, and the phase change material was assembled by stearic acid-filled PAO. These graphene-coated porous Al_2O_3 composites may play important role in thermal management applications. The formation of graphene is attributed to the carbothermic reduction occurring at the Al_2O_3 surface to initialize the nucleation and growth of graphene. The graphene films are coated on insulating

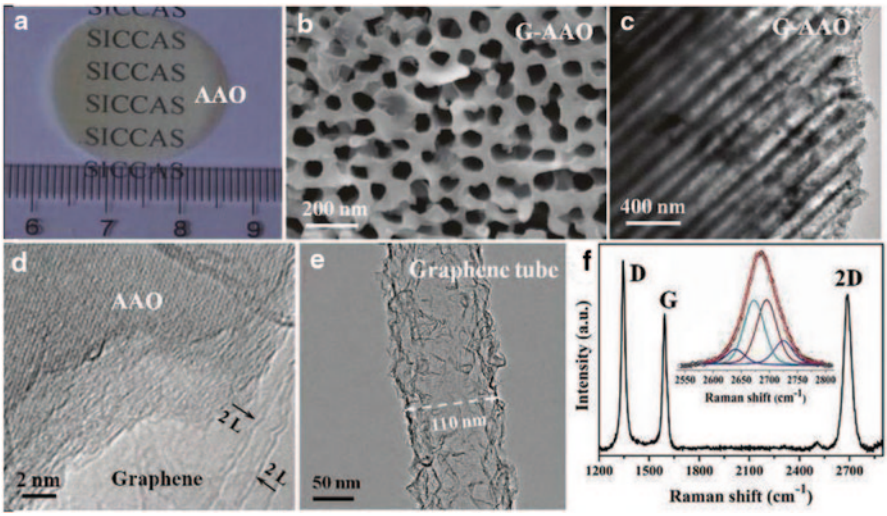

Fig. 12.18 **a** Photograph of anodic aluminum oxide *(AAO)*. **b** SEM, **c** TEM, and **d** HRTEM images of graphene-coated AAO (*G-AAO*) grown at 1200 °C for 30 min. **e** TEM image and **f** Raman spectrum of graphene tubes after etching of AAO template. The inset shows that the 2D peak can be deconvoluted into four components: $2D_{1B}$, $2D_{1A}$, $2D_{2A}$, and $2D_{2B}$ from the left to the right [67]

AAO templates and porous Al_2O_3 ceramic substrates. The graphene-coated AAO possesses 1D isolated graphene tubes, which can act as the media for directional thermal transport.

Chen et al. [68] synthesized Fe_2O_3–CNT–graphene hybrid materials with an open 3D nanostructure for a high-capacity lithium storage using CVD method. The as-prepared materials consist of Fe_2O_3 nanorings, bamboo-like CNTs and graphene nanosheets (GNS), which form an open 3D architecture. For the first time, we observed the growth of bamboo-like CNTs with open tips, which were catalyzed by iron nanorings. The synthesis process of Fe_2O_3–CNT–GNS hybrid materials is shown in Fig. 12.19.

The low- and high-magnification field-emission SEM (FESEM) images of Fe_2O_3–CNT–GNS-1 and Fe_2O_3–CNT–GNS-2 samples are shown in Fig. 12.20. The magnified views marked by white squares in (a) and (c) are shown in Fig. 12.20b and 12.20d, respectively. As shown in Fig. 12.20 (b) and (d), CNTs grew on both sides of GNS. The amount of CNTs in the Fe_2O_3–GNS-2 is almost double that of the Fe_2O_3–CNT–GNS-1 sample. The individual GNS shows a wavy and crumpled feature with an area of about 36 mm^2. In summary, Fe_2O_3–CNT–GNS hybrid materials consisting of bamboo-like CNTs and Fe_2O_3 nanorings were successfully prepared by a CVD synthesis method. Fe_2O_3 nanorings play critical roles informing bamboo-like CNTs. A modified "tip-growth" mechanism of CNTs and a unique lithiation process were proposed. When applied as anode materials in lithium ion batteries, the Fe_2O_3–CNT–GNS-2 hybrid materials exhibited a high specific capacity of 984 mAh g^{-1} with a superior cycling stability and high rate capacity. This

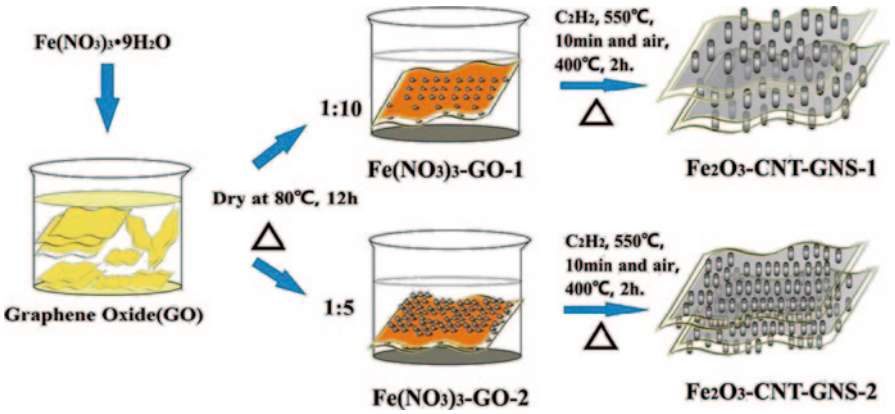

Fig. 12.19 A schematic diagram for the preparation of Fe_2O_3–CNT–GNS hybrid materials [68]

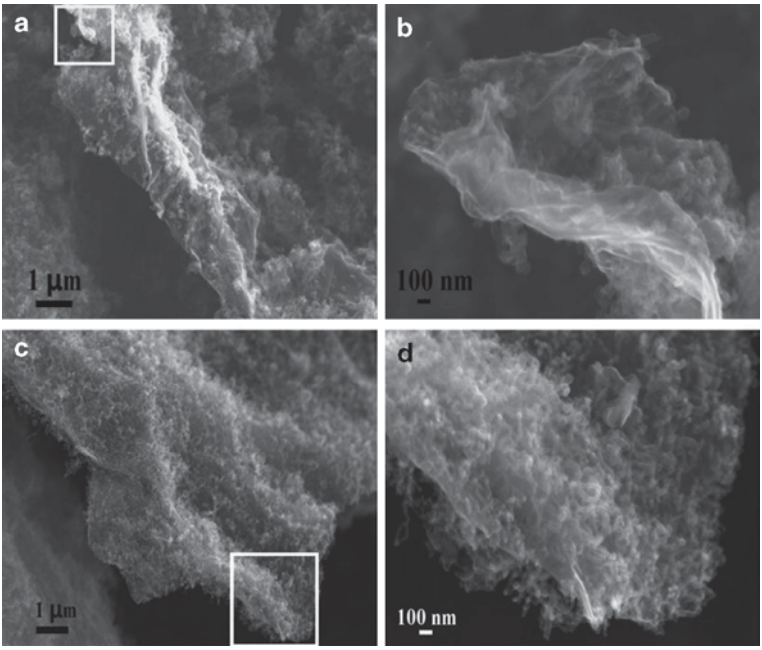

Fig. 12.20 Low and high magnification SEM images showing morphologies of Fe_2O_3–CNT–GNS-1 (**a** and **b**) and Fe_2O_3–CNT–GNS-2 (**c** and **d**). (**b**) and (**d**) are the magnified views, marked by a *white square* in (**a**) and (**c**), respectively [68]

could be credited to the facile Li^+ ions diffusion through the open tips of CNTs and cracks on the outside walls of CNTs, and extra lithium storage sites provided by arc-like graphene layers inside CNTs. Flexible and highly conductive GNS and open 3D architecture also contribute to the superior electrochemical performance.

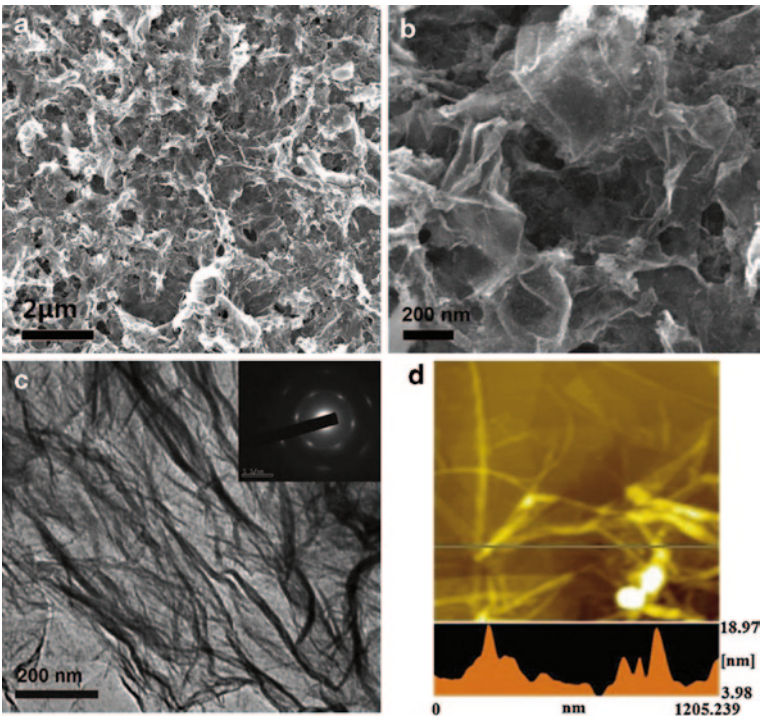

Fig. 12.21 SEM images (**a** and **b**), TEM image (**c**), the inset shows the SAED pattern of the 3D-CSGR mesostructures, and AFM image (**d**), of the 3D-CSGR mesostructures [69]. *AFM* atomic force microscopy, *SAED* selected area (electron) diffraction

The carbon-based hybrid materials with 3D structure could also be applied for lithium-air batteries, supercapacitors, and fuel cells. When applied as anode materials in lithium ion batteries, the Fe_2O_3–CNT–GNS hybrid materials exhibited a high specific capacity of 984 mAh g^{-1} with a superior cycling stability and high rate capability. This could be ascribed to short Li^+ diffusion path of bamboo-like CNTs, more active reactions sites provided by graphene layers inside CNTs, flexible and highly conductive GNSs, and an open 3D structure.

Cheng et al. [69] synthesized 3D chitosan (CS)–graphene mesostructures. They have shown a hydrophilic and biocompatible 3D CS–graphene mesostructures with large specific surface area. They have also developed a novel and simple thermal method to prepare 3D CS–graphene nanocomposites with large specific surface area (603.2 m^2 g^{-1}) and unique mesoporosity were prepared by simple thermal treatment of GO nanosheets and CS.

Figure 12.21 shows the 3D-chitosan-graphene mesostructures(CSGR) sample possessing mesoporous structures resulted from thermal exfoliation of materials. The magnified SEM image shown in Fig. 12.21b reveals that the 3D-CSGR composites have delaminated structures, in these layers of such delaminated 3D composites, one could even observe easily the paper-like wrinkled structures of

graphene, indicates that the 3D-CSGR product is made up of GNSs. Moreover, Fig. 12.21b demonstrates that the typical pore sizes are about 100 and 500 nm.

The use of 1D CNTs as spacers to separate 2D graphene-based sheets to preserve graphene's high surface area and exploit the high conductivity for CNTs to increase the conductivity of these carbon-based hybrids. However, since both the as-produced graphene and CNTs are generally in an agglomerated powder form, a suitable technique is needed to mix or disperse these two kinds of carbon-based nanomaterials in order to realize the chemical and physical synergies of their hybrids. Li et al. [70] developed a green and facile method to prepare water-soluble CS-grafted rGO (CS-rGO) sheets by functionalizing them with CS, which had a superior capability in dispersing and stabilizing MWNTs in acidic aqueous solutions via noncovalent interactions (Figs. 12.22 and 12.23). With incorporation of 1 wt% CS-GNS-MWCNTs, the tensile modulus, strength, and toughness of the nanocomposites could be increased by 49, 114, and 193 %, respectively. The load transfer was attributed to three kinds of interfacial interactions: interaction between graphene sheets and nanotubes, covalent bond between graphene sheets and grafted CS, and hydrogen bonds between grafted CS and the CS matrices.

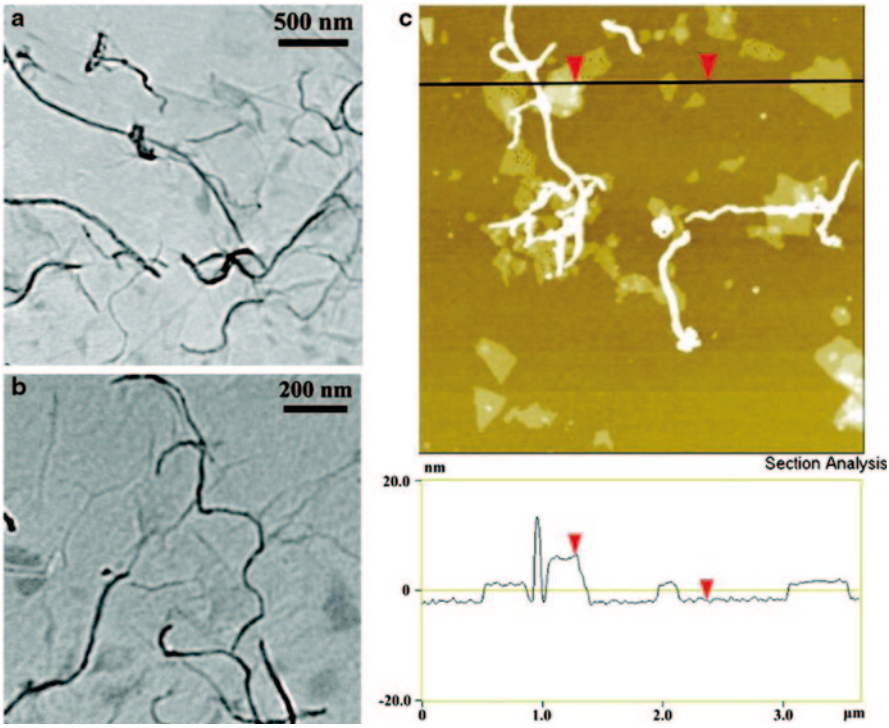

Fig. 12.22 **a**, **b** TEM images of CS-rGO/MWCNTs under different magnifications; **c** AFM image with corresponding surface profile of CS-rGO/MWCNTs [70]. *AFM* atomic force microscopy

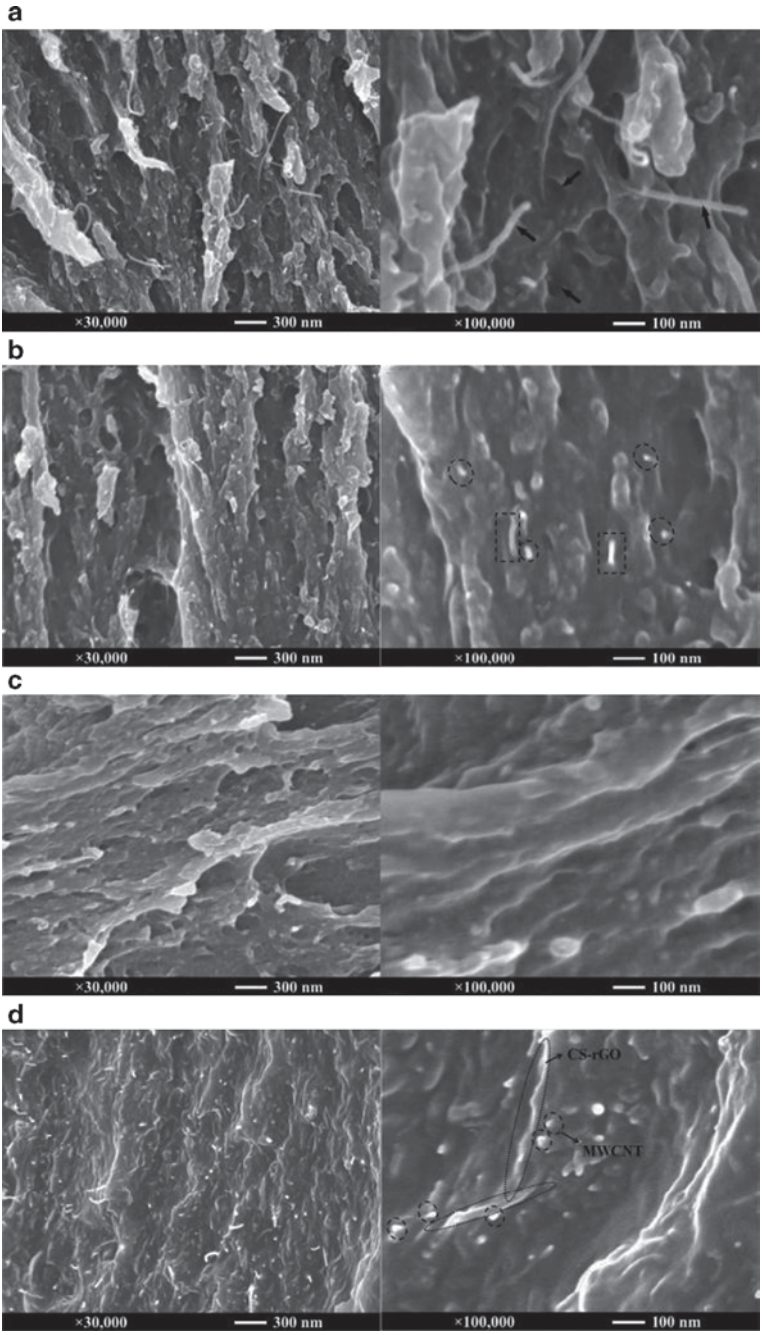

Fig. 12.23 FESEM images of cross-sectional facture surfaces of **a** 1 wt% MWCNT/CS, **b** CS-MWCNT/CS, **c** CS-rGO/CS, and **d** CS-rGO-MWCNT/CS nanocomposites [70]

Chen et al. [71] prepared stable small-walled nanotubes (SWNT) aqueous dispersion by using GO sheets as surfactant, and the SWNTs were completely wrapped by GO sheets to form a core-shell structure, as viewed in Fig. 12.24. To investigate the morphology and structure of SWCNT/GO hybrid, SEM and TEM characterizations were carried out. Heavily entangled SWCNT bundles with diameter about 20–30 nm are observed with SEM (Fig. 12.24a). Figure 12.24b is a SEM image of SWCNT/GO hybrids, which, as compared to SWCNTs, are disentangled and have a larger diameter (~50–80 nm). It is possible that GO nanosheets have wrapped onto the SWCNT bundle to form a core–shell structure through π–π stacking. To verify this, SWCNT/GO hybrids were observed under TEM. As seen from Fig. 12.24c, in addition to some flat GO nanosheets, the core–shell structures are evident. Furthermore, under high-resolution TEM (Fig. 12.24d), the lattice fringes of the graphitic structure of SWCNT bundle can be clearly resolved in the core of the hybrid.

Scrolled GOs (SGOs) with MWNT templates were prepared by Min et al. [72], and the synthesis strategies are shown in Fig. 12.25. GO sheets were successfully made to adopt a scroll conformation around the surface of aminated MWNT in solution by covalent bond formation, which would allow large-scale production of

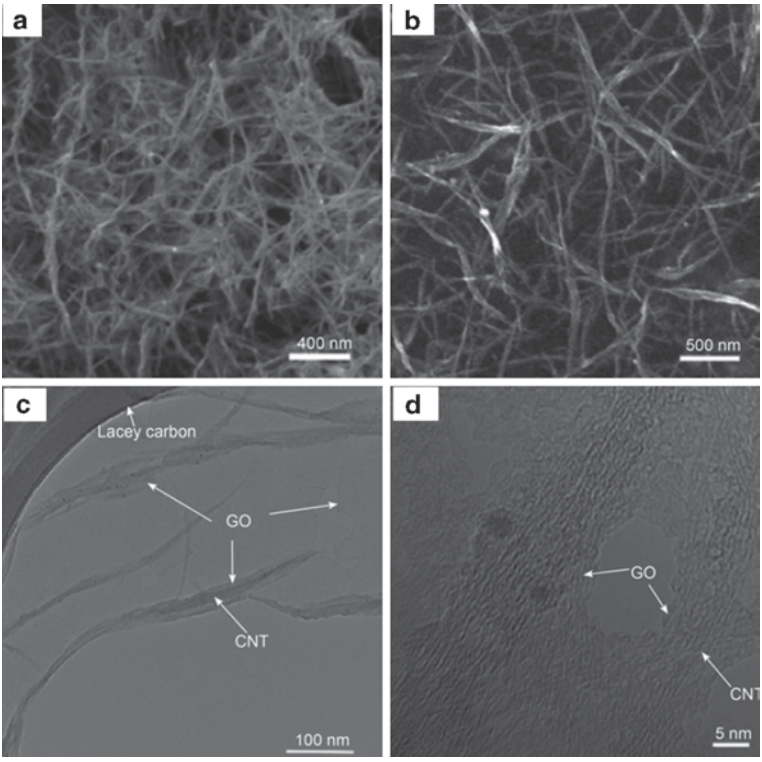

Fig. 12.24 **a** SEM image of SWNTs; **b** SEM image of SWNT/GO; **c** TEM image of SWNT/GO; **d** high-resolution TEM image of SWNT/GO [71]

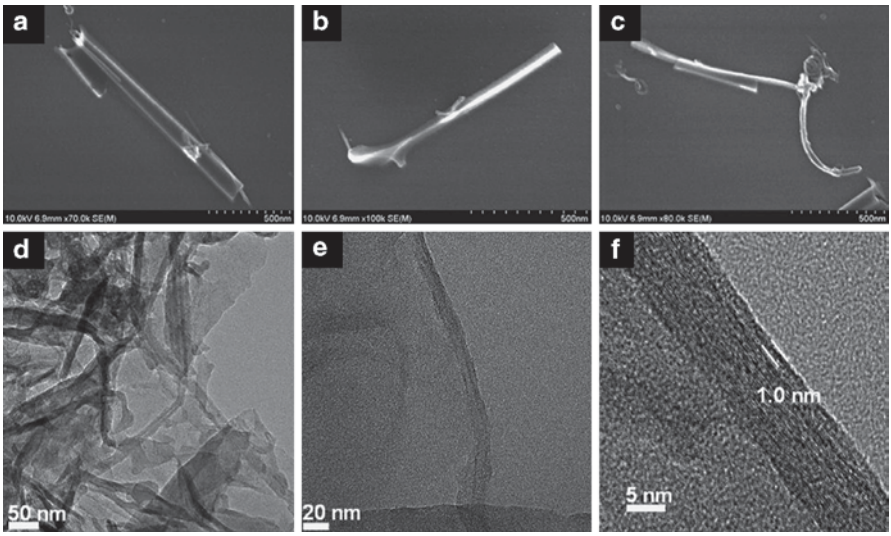

Fig. 12.25 FESEM (**a**–**c**), HRTEM (**d**–**f**) images of SGO with different magnifications show that tubular SGO structures formed on MWCNT surface. Interlayer space was observed with 1.0 nm distance between SGO and MWCNT template (**f**) [72]

SGO/MWNT hybrid materials as a good addition to existing MWNT- or GO-based hybrid materials. Besides the hybridization of GO and pristine CNTs, the reduction of GO to GNS would be of great importance and also extensively studied. The formation of 3D GNS–CNT hybrids by the immobilization of metal catalysts onto single-layered GNS followed by in situ CVD growth of CNTs has been reported. Zhao et al. [63] demonstrated the preparation of 3D CNT-pillared GO and GNS nanostructures with tunable length of the CNTs. Such nanostructures exhibited an excellent visible light photocatalytic performance in water.

Liu et al. [59] prepared 3D GNS–MWNT hybrids by direct reduction of GO sheets in the presence of acid-treated MWNTs (A-MWNTs) shown in Fig. 12.26. It is a simple and efficient method to fabricate novel water-dispersible GNS–MWNT hybrids due to π–π stacking interactions between GNS and A-MWNTs.

Direct evidence for the hybridization of the GNS with A-MWNTs can be obtained by TEM observation (Fig. 12.27). One can clearly see the rolled edge of the GNS which gives a folded appearance, and in some regions, the well-separated A-MWNTs were adsorbed on the GNS surface. Both the t-CNTs and rGO sheets dispersed uniformly at the nanoscale and no obvious aggregates were observed. From Fig. 12.27b, we can clearly see the rolled edge of the rGO sheets which gives a folded appearance, and in some regions the well-separated CNTs were adsorbed on the rGO surface. The high-performance PVA/(gelatin-multiwalled carbon nanotube, GCNT) ternary nanocomposites have been successfully prepared by a simple water casting method. Accompanied by t-CNTs assisted dispersion of rGO, the incorporation of rGO which acts as a CNT “carrier” plays an important role in immobilizing the t-CNTs on the rGO sheets, and thus uniform co-dispersion for both CNTs and

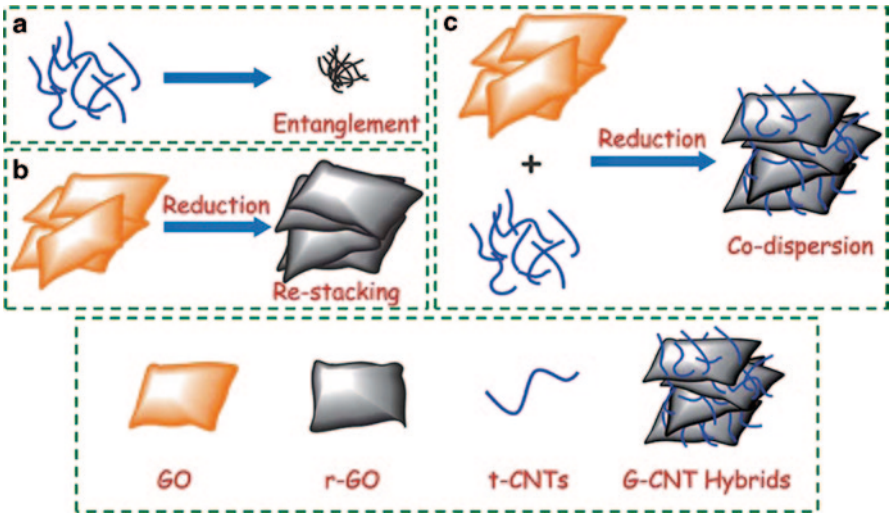

Fig. 12.26 Schematic illustration for the co-dispersion mechanism of rGO sheets with the aid of acid-treated multi-walled carbon nanotubes(t-CNTs) [59]

rGO in the PVA matrix is attained simultaneously. With the incorporation of only 0.6 wt% GCNT hybrids, the tensile strength and Young's modulus of the PVA are significantly improved by about 77 and 65 %, respectively; thus, a novel synergistic reinforcing effect between 2D rGO sheets and 1D t-CNTs in PVA nanocomposites has been observed. Besides, the addition of G-CNT hybrids into the PVA matrix slightly increases its thermal degradation temperature while significantly increasing the char residues formed during the pyrolysis of PVA, indicating a potential flame-retardant effect of the G-CNT hybrid composites.

In another work, Dai et al. [73] utilized an electrostatic self-assembly method to fabricate the graphene–CNT hybrid films. Stable aqueous dispersions of polymer-modified graphene sheets were first prepared via in situ reduction of GO nanosheets in the presence of cationic poly(ethyleneimine) (PEI), and then the resultant water-soluble PEI-modified graphene sheets were used for sequential self-assembly with acid-oxidized MWNTs to form hybrid carbon films (Fig. 12.28). These hybrid films possessed an interconnected network of carbon structures with well-defined

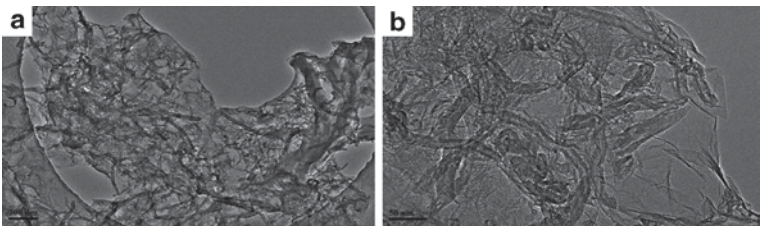

Fig. 12.27 TEM images of GNS/A-MWNT (1:1) hybrids at **a** low and **b** high magnifications [59]

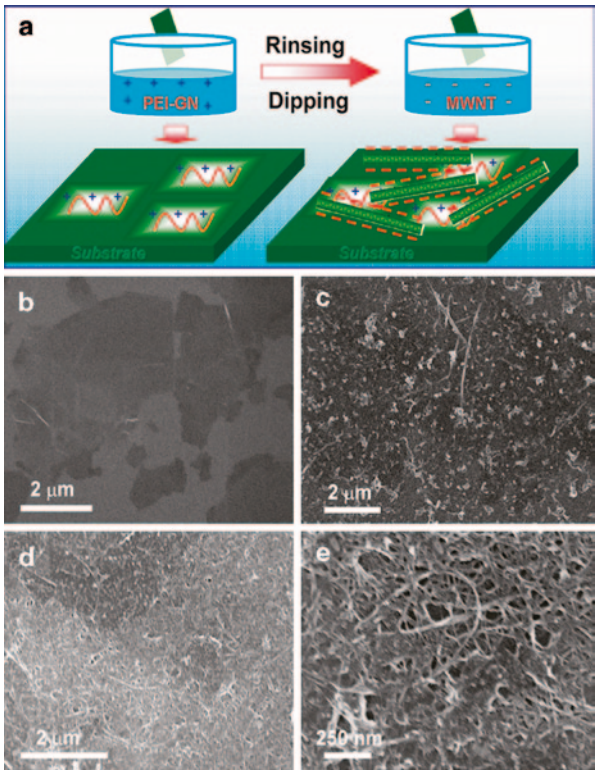

Fig. 12.28 **a** Illustration of positively charged PEI-GN and negatively charged MWNT film deposition process on an appropriate substrate (e.g., silicon wafer, ITO glass). SEM images of **b** the first layer PEI-GN and **c** the first bilayer (PEI-GN/MWNT-COOH) film deposited on a silicon substrate. **d**, **e** SEM images of the (PEI-GN/MWNT-COOH) film after the ninth deposition cycle under different magnifications [73]

nanopores for fast ion diffusion, which makes these hybrid films highly promising for supercapacitor electrodes. The shape of the cyclic voltammogram of this graphene–CNT hybrid electrode was quite rectangular, indicating potential for supercapacitor applications. Moreover, even at an exceedingly high scan rate of 1 V s^{-1}, an average specific capacitance of 120 F g^{-1} was still obtained for this graphene–CNT hybrid films.

Haddon et al. [58] reported that a synergistic effect in the thermal conductivity enhancement of epoxy composites was achieved by combining 1D SWNT and 2D GNP fillers. They considered that the synergism originates from the bridging of planar nanoplatelets by the flexible SWNTs which lead to a decreased thermal interface resistance along the (2D–1D) hybrid filler network due to the extended area of the SWNT–GNP junctions. The SEM and TEM images of epoxy composite with a hybrid filler loading of GNP: SWNT of 3:1 (7.5 wt% of GNPs and 2.5 wt% of SWNTs) are shown in Fig. 12.29. In comparison with individual SWNT or GNP fillers the 0D point contact geometry along the filler network is substituted by a 1D linear contact with significantly increased area of interface junctions within the hybrid filler network. This leads to a decreased thermal interface resistance and may be considered as the major reason for the observed synergistic effect of the 1D and 2D hybrid fillers. The images show a complex nanostructure with multiple SWNTs

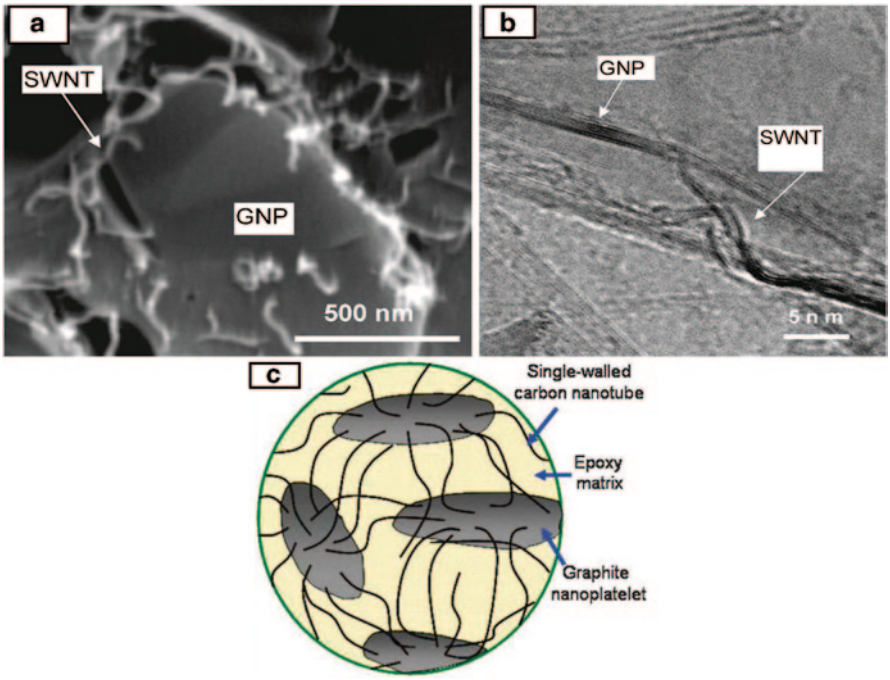

Fig. 12.29 **a** SEM and **b** TEM images of the cross-section of GNP–SWNT hybrid filler/epoxy composite. Note that SWNTs are bridging adjacent graphite nanoplatelets and SWNTs ends are extended along the nanoplatelet surfaces. **c** Schematic representation of GNP–SWNT network in polymer matrix [58]. *GNP* graphene nanoparticle, *SWNTs* single-walled nanotubes

bridging adjacent GNPs. The hybrid filler thus provides the highest efficiency in the thermal conductivity enhancement of composites and can be utilized at low filler loading which is important for decreasing the viscosity and improving the process ability of thermal interface materials.

One of the pioneering work Li et al. [74] explored GO as a dispersant to suspend the un-functionalized CNTs in aqueous solution and to develop a new solution processing strategy for making graphene–CNT hybrids for the supercapacitor applications (Fig. 12.30). The oxygen-containing groups rendered GO sheets hydrophilic and highly dispersible in water, whereas the aromatic regions offered active sites to make it possible to interact with the aromatic molecules of CNTs through π–π supramolecular interactions. Electrophoresis experiments were carried out to confirm that the CNTs were indeed strongly attached to the negatively charged GO nanosheets. Although the GO nanosheets are insulators, the electrical conductivity of the hybrid films can be increased after the electrochemical treatment. While the measured specific capacitance for the graphene-only electrode was about 140 F/g at a current density of 0.1 Ag^{-1}; it dropped to 30 F g^{-1} at a current density of 30 A g^{-1}. Significantly, supercapacitors based on the electrochemically rGO and CNTs (ER-GO/CNT) (1:1) exhibited a specific capacitance of over 90 F g^{-1} at a high current density of 100 A g^{-1}

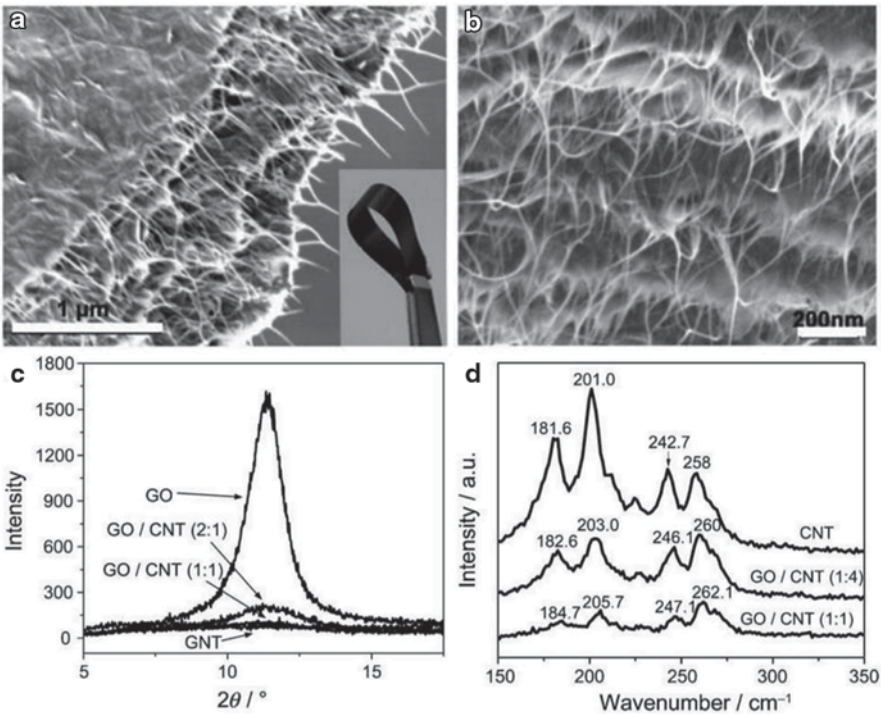

Fig. 12.30 Graphene–CNT hybrids for supercapacitor applications. **a**, **b** SEM images of the resulting GO/CNT hybrid film. The inset in (**a**) shows a *bent strip* of the resulting film. **c**, **d** XRD patterns and Raman spectra of the GO/CNT films with various weight ratios of GO and CNTs [74]. *GO* graphene oxide, *CNT* carbon nanotube

due to the effective synergies of the graphene-based materials and CNTs. The interaction between CNTs and GO makes the resulting hybrid paper very robust. The free-standing hybrid paper is shown in Fig. 12.30. Fig. 12.30a was found to have a Young's modulus of approximately 8.1 GPa. It is worth noting that in the preparation of CNT only bucky paper requires chemical functionalization of CNTs and the use of a significant amount of surfactants.

One of the pioneer works on CNTs–G hybrids was reported by Cai et al. [75]. They have shown the conducting nature of CNT/GO hybrid films. The as-prepared GO nanosheets by using the Hummers method. Both GO nanosheets and commercial MWCNTs with OH groups were dispersed in DMF by using ultrasonic treatment. The two dispersed solutions were mixed to form the precursor solutions. MWCNTs–GO thin films were prepared by casting the solutions on glass cover slips. The ratio of MWCNTs to GO was controlled by the ratio of their precursor solutions. The thickness of the final films was simply adjusted by the volumes of the solutions used for depositions. Representative SEM images of cross-section and natural surfaces of the MWCNTs–GO films are shown in Fig. 12.31. The films had multilayered microstructures and relatively homogeneous surface profiles. It was

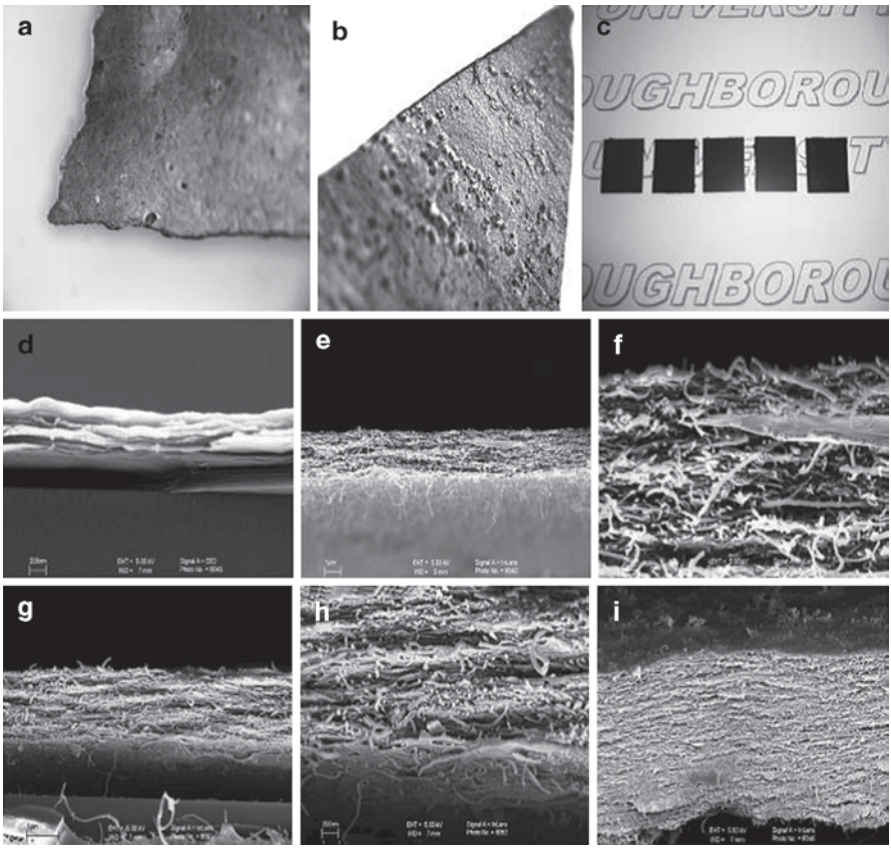

Fig. 12.31 Morphology of the GONP and GONP/MWCNT-OH films. **a** Optical microscopy image of the GONP film. **b** Optical microscopy image of the G(1)/M(0.5) film. **c** Digital camera picture of the hybrid films coated on the glass substrates (thickness: ca. 2 mm). **d** Cross-sectional SEM image of the GONP film. **e**, **f** Cross-sectional SEM images of the G(1)/M(0.5) film (thickness: ca. 2 mm). **g**, **h** Cross-sectional SEM images of the G(1)/M(0.5) film (thickness: ca. 3.5 mm). **i** Cross-sectional SEM images of the G(1)/M(0.5) film (thickness: ca. 8 mm) [75]

found that electrical conductivity of the films was increased with increasing content of CNTs because of the high conductivity of CNTs. Electrical conductivity was also increased with increasing thickness. However, the thin films were not optically transparent.

The α-Fe_2O_3 NPs anchored on graphene with 3D quasi-laminated architecture as reported by Chen et al. [76]. The fabrication process of the α-Fe_2O_3/graphene composite is schematically illustrated in Fig. 12.32. The α-Fe_2O_3 NPs anchored on graphene with a 3D quasi-laminated architecture have been synthesized by in situ wet chemistry method. The excellent electrochemical performance of α-Fe_2O_3/graphene composites can be attributed to the combined effects of the 3D quasi-laminated flexible architecture and high conductivity and structure stability of electrode by graphene. They have demonstrated a simple strategy to achieve optimum

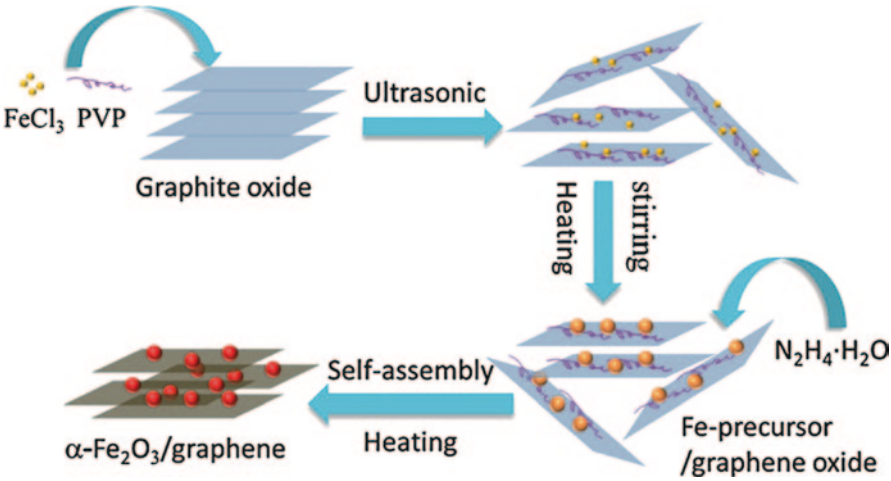

Fig. 12.32 Scheme of preparation of α-Fe_2O_3/graphene composite [76]

electrochemical properties by constructing a 3D quasi-laminated architecture from self-assembly of α-Fe_2O_3 and GNSs by the aid of surfactant under atmospheric pressure. The facile in situ wet chemistry approach is suitable for practical large-scale production of graphene-based metal oxide composites as advanced electrode materials for rechargeable lithium-ion batteries (LIBs).

The SEM images of the α-Fe_2O_3/graphene composite are shown in Fig. 12.33. The graphene-based 2D templates have provided a well-defined functionalized surface for good distribution of NPs, the graphene-based composites are randomly stacked to make electrodes, inevitably leading to the particle–particle aggregation. Because of the natural 2D sheet morphology, graphene decorated with NPs is prone to stack each other to construct 3D layer-by-layer architecture under control of a surfactant. As shown in Fig. 12.33a, it can be clearly observed that GNSs are hybridized with α-Fe_2O_3 particles to preserve a 3D quasi-laminated structure, and the nanosized α-Fe_2O_3 particles anchored on graphene uniformly (Fig. 12.33b).

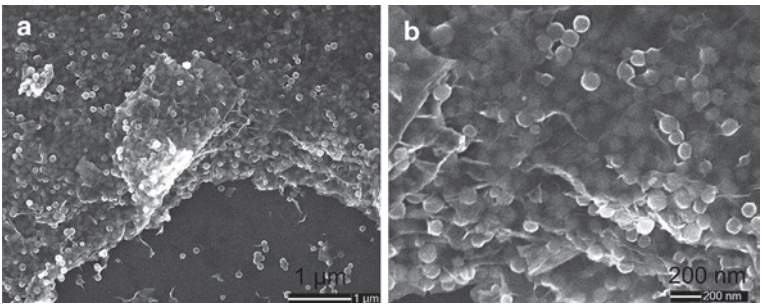

Fig. 12.33 FESEM images of α-Fe_2O_3/graphene composite with different magnifications. **a** Graphene nanosheets—α-Fe2O3 particles hybrids. **b** Graphene nanosheets—α-Fe2O3 particles anchoring [76]

Wang et al. [77] reported graphene-encapsulated Fe_3O_4 NPs with 3D-laminated structure. Fe_3O_4–graphene composites with 3D-laminated structures are synthesized by a simple in situ hydrothermal method. The Fe_3O_4 NPs, around 3–15 nm in size, are highly encapsulated in a GNS matrix. The as-synthesized Fe_3O_4–graphene nanocomposite electrodes show a significantly improved cycle life than that of the bare Fe_3O_4 electrode. The improvements can be attributed to the GNSs matrix in the composite, which serves several functions as enabling the GNSs in the composite materials to act as lithium storage active materials, maintaining the structural integrity of the composite electrodes by preventing large volume changes and particle agglomeration and increasing the electronic conductivity of the electrodes by forming an efficient electrically conductive network. The SEM morphology of the products, were collected for GNS, bare Fe_3O_4 and Fe_3O_4–GNS composite (38.0 wt%). Visualization of pristine GNS by FESEM (Fig. 12.34) shows well-packed layers of platelets composed of curved nanosheets. The image of the reference bare Fe_3O_4 NPs, developed by the same procedure as the one followed for the preparation of Fe_3O_4–GNS composite, but in the absence of GO and pyrenebutyric acid, reveals that the morphology of the Fe_3O_4 NPs is spherical, with diameters in the range of 40–60 nm (Fig. 12.34a). It can be clearly observed that the thin graphene layers are hybridized with nanosized Fe_3O_4 particles to preserve the 3D-laminated structure. The size of Fe_3O_4 particles in the composite is much smaller than that in the pure sample. Results of the SEM examination combined with energy-dispersive X-ray

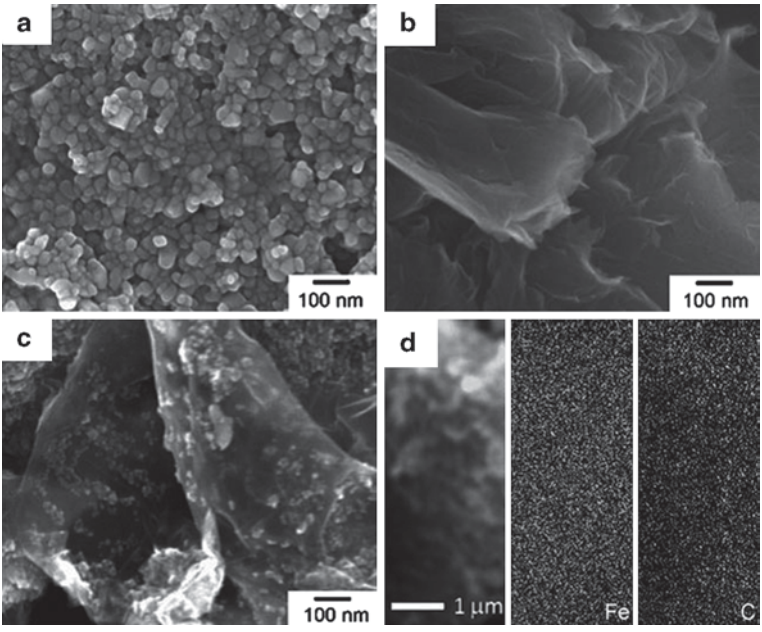

Fig. 12.34 FESEM images of **a** bare Fe_3O_4, **b** GNS, **c** Fe_3O_4–GNS composite and (38.0 wt%), and **d** SEM image obtained from Fe_3O_4–GNS composite (38.0 wt%) [77]

spectrometry (EDS) mapping for the elements Fe and C are shown in Fig. 12.34d. The bright regions correspond to the presence of the elements Fe and C, respectively, and indicate that Fe and C are distributed uniformly throughout the whole area.

12.3 Applications of Graphene-Based 3D Nanostructures

Hybrid carbon nanostructures such as graphene–metal oxide attract a deluge of interest of scholars nowadays due to their promising application several application and electronic devices. Nanomaterials prepared using carbon offer many advantages in energy conversion and storage applications. The carbon nanostructured materials are advantageous in offering huge surface to volume ratios, favorable transport properties, altered physical properties, and confinement effects resulting from the nanoscale dimensions, and have been extensively studied for energy-related applications such as solar cells, catalysts, thermoelectrics, lithium ion batteries, supercapacitors, and hydrogen storage systems [78, 79]. The enhancement in specific surface area and associated surface energy also renders some very important applications Thus, these 3D graphene-based architectures containing significant enhancement in the efficacy as compared to their 2D analogues or even opened the path to novel applications. The smaller dimensions of nanomaterials may also offer more favorable mass, heat, and charge transfer, as well as accommodate dimensional changes associated with some chemical reactions and phase transitions

12.3.1 Supercapacitors

Energy conversion and storage involve physical interaction and/or chemical reaction at the surface or interface, so the specific surface area, surface energy, and surface chemistry play a very important role. Supercapacitors are one of the crucial devices for energy storage applications as they can provide a higher power density than batteries and a higher energy density than conventional dielectric capacitors. Supercapacitors have attracted attention due to their great potential to meet the demand of both high energy density and power density in many advanced technologies. Various carbon-based nanocomposites are currently pursued as the supercapacitor electrodes because of the synergistic effect between carbon (high power density) and pseudo-capacitive nanomaterials (high energy density). This chapter aims to review most recent progress on 3D carbon-based nanostructures for advanced supercapacitor applications in view of their structural intertwinement which not only create the desired hierarchical porous channels but also possess higher electrical conductivity and better structural mechanical stability. The carbon nanostructures composed of CNTs-based networks, graphene-based architectures, hierarchical porous carbon-based nanostructures, and other even more complex carbon-based 3D configurations. Currently, 3D carbon-based nanostructures are a new hot topic for high-performance supercapacitors [34, 80–84]. Due to the struc-

tural interconnectivities, 3D carbon-based nanostructures not only create hierarchical porous channels but also possess a higher electrical conductivity and maintain better structural mechanical stability. Ruoff et al. [82] reported graphene-based ultracapacitors for high-performance, electrical energy storage devices. Ajayan et al. [83] demonstrated a simple approach for the fabrication of ultrathin planar graphene supercapacitors. Chen et al. [84] have shown the application of graphene-based materials in supercapacitors. There are also some others reports that depict the potential use of graphene for the application of supercapacitors. A wide range of metal compound are investigated for graphene-inorganic nanocomposite for supercapacitor electrode materials, Fe_3O_4 [85, 86], Co_3O_4 [87, 88], $Co(OH)_2$ [89], NiO [90, 91], $Ni(OH)_2$ [92, 93], $NiCo_2O_4$ [94], ZnO [95, 96], CeO_2 [97], Cu_2O [98], MnO_2 [99–104], Mn_3O_4 [105], Bi_2O_3 [106], SnO_2 [95, 107], and RuO_2 [108]. In all of these cases, the nanocomposites exhibited enhanced capacitive behaviors with better reversible charging/discharging ability and higher capacitance values, when compared with pure graphene and the bare compounds.

12.3.2 Batteries

The energy density and performance of LIBs largely depend on the physical and chemical properties of the cathode and anode materials. LIBs are a lithium ion-induced device for electricity supply, which is composed of an anode, electrolyte, and cathode. Graphite with a theoretical lithium storage capacity of 372 mAh g^{-1} is currently used as the anode material in commercial LIBs. Owing to its large surface-to-volume ratio and highly conductive nature, GN has a higher lithium storage capacity (theoretical lithium storage capacity of 744 mAh g^{-1} for single layer GN) [109]. However, GN nanosheets always naturally stack into multilayers and therefore lose their high surface area and intrinsic chemical and physical properties. A considerable enhancement can be expected from the incorporation of inorganic nanomaterials with high specific capacity into GN, which could not only limit the aggregation of GN but also boost the lithium storage capacity [110]. Honma et al. [111] demonstrated enhanced cyclic performance and lithium storage capacity of GN–SnO_2 nanoporous electrodes prepared with reassembly of GN in the presence of SnO_2 sol (Fig. 12.35a). It was demonstrated that the obtained GN–SnO_2 electrode exhibited an enhanced reversible capacity (810 mAh g^{-1}) as well as superior cycling performance (70% retention after 30 cycles) in comparison with that of the bare SnO_2 electrode (Fig. 12.35b, c). It is believed that the dimensional confinement of SnO_2 NPs by the surrounding GN limits the volume expansion upon lithium insertion, and the developed nanopores between SnO_2 and GN could be used as buffered spaces during charge–discharge, resulting in the superior cyclic performances (Fig. 12.35a).

On the basis of this concept, a wide range of nanomaterials of oxides and hydroxides, such as Fe_3O_4 [77, 86, 112–115], Fe_2O_3 [106–118], Co_3O_4 [119–122], CoO [118, 123] $Co(OH)_2$, [124], NiO [125], $Ni(OH)_2$ [126], SnO_2 [127–133], TiO_2 [134–138], Mn_3O_4 [139], CuO [140, 141], CeO_2 [142], MoS_2 [143, 144], and Li-

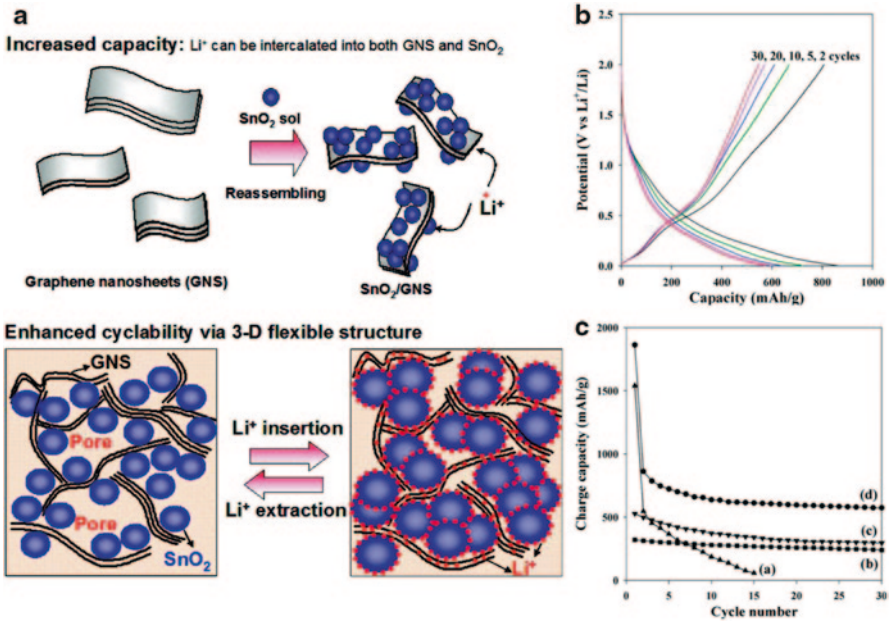

Fig. 12.35 **a** Schematic illustration for the synthesis and structure change of GN–SnO_2 nanocomposite during Li^+ insertion and extraction. **b** Charge–discharge profile for GN–SnO_2 nanocomposite. **c** Cyclic performances for (a) bare SnO_2 NPs, (b) graphite, (c) GN, and (d) GN–SnO_2 nanocomposite [111]

$_4Ti_5O_{12}$ [145, 146] have been anchored on GNSs for application as anode materials for LIBs. Graphene-supported Si [147–149], Sn-based NPs [150, 151], graphene–Sn multilayered nanostructure [152], and graphene-incorporated ceramic composite [153] have also been developed as anode materials for LIBs. All these composites showed large reversible capacities, excellent cycling performances, and high coulombic efficiencies. Fan et al. also reported an rGO–carbon nanofiber composite for high-performance anode materials for LIBs [154]. Honma and coworkers reported that the incorporation of CNT and C_{60} could further increase the specific capacity of graphene as anode materials [155]. The enhanced performance of the composites was attributed to the improvement of lithium accommodation in the increased layered spaces between graphene through intercalating CNT or C_{60}.

12.3.3 Hydrogen Storage

Hydrogen is a potential successor to gasoline due to its many advantages, including clean combustion and the highest energy content per weight unit of any known fuel. However, hydrogen is a gas with a very low density under ambient conditions.

Understanding the mechanisms of hydrogen adsorption on graphene under various environments would benefit various fields, including motor vehicles, fusion reactor design, and hydrogen storage [156]. Molecular dynamics (MD) simulations of the graphene hydrogen interface can be used to explore the nature of surface adsorption. Atomistic simulation avoids experimental noise and turbulence problems. It can be used to analyze molecular trajectories and thermodynamic properties. Many nano systems have been analyzed using MD, such as studies on nano wetting properties [157], nano imprinting [158], nano forming [159], and dip-pen nanolithography [160]. Herrero and Ramirez [161] studied the diffusion of hydrogen in graphite and found that hydrogen atoms jump from a C atom to a neighboring one with an activation energy of about 0.4 eV. Compared to atomic hydrogen, molecular hydrogen has a much smaller activation energy and faster diffusion speed. Lamari and Levesque [162] studied hydrogen adsorption on graphene and found that at a temperature of 77 K and a pressure of 1 MPa, the excess hydrogen physisorption is estimated to be equal to 7 wt%, and it decreases with increasing temperature. Du et al. [163] studied the separation of hydrogen and nitrogen gases by porous graphene membranes. They found that the separation mechanism is related to the VDW interactions of the gases with the graphene membrane. Recently, Zhang and coworkers synthesized graphene-supported RhNi catalyst by a facile co-reduction route, wherein the graphene plays a smart role as a dispersion agent and distinct support for the RhNi NPs [164].

12.3.4 Fuel Cell

Fuel cells are electrochemical energy devices containing electrocatalytic fuel oxidation at the anode and oxygen reduction at the cathode to produce electricity power. Before the discovery of graphene, CNTs have been investigated as catalyst-supporting materials in fuel cell applications, which have shown enhanced catalytic activities [149, 165]. However, many researchers have started to shift their research target toward graphene in the past few years after the existence of 2D honey comb structure of graphene was reported [167, 168]. Compared with CNTs, graphene have much higher surface area and conductivity for electrochemical applications. Graphene can be produced at a much lower cost as comparison to CNTs. Due to its outstanding properties as mentioned by the researchers, graphene has many potential applications. Graphene with inorganic nanocomposites exhibit excellent electrocatalytic performance, which show promising application in next-generation fuel cells, such as graphene–Pt nanocomposite in direct methanol fuel cells [169, 170], and proton-exchange membrane fuel cells (PEMFCs) [171, 172] as well as graphene–Pd nanocomposites in direct formic acid fuel cells [173, 174]. As an example, a PEMFC with rGO–Pt nanocomposites as the cathode and carbon black–Pt composites as the anode delivered a maximum power of 161 mW cm^{-2}, which is much higher than 96 mW cm^{-2} of the fuel cell with unsupported Pt as cathode [172]. Fuel cells undergo an ecofriendly process to produce electricity, water, and

heat only with no pollutant or toxic by-product, many researches are now focusing on cost-down and efficiency-up fuel cells. Fuel cells consist of three key parts: cathode, anode, and separation membrane. Among them, cathode materials are pivotal elements for the commercialization. Currently, expensive noble metals such as platinum (Pt), gold (Au), ruthenium (Ru), and their alloys are best known cathode materials for oxygen reduction reaction (ORR) [171, 175–177]. Among them, Pt is the most widely studied noble metal as electro catalyst. However, it is too expensive and limited reserve in earth. Thus, there must be at least one of three ways to solve the issues. One is to minimize the use of expensive catalysts by increasing surface area via NP approach [178, 179]. Another is to find alternative cheap but efficient metal catalysts to replace expensive noble metals [180, 181]. The last is to develop efficient metal-free catalysts. Although Pt-based catalysts have been widely studied and commercialized due to their high current density and low overpotential [182–184], there are still intensive efforts required for further maximizing the activity of Pt and minimize the use of Pt.

12.3.5 Solar Cell

Solar cells are devices which convert the energy of sunlight into electricity by photovoltaic effect. As the economies of scale cut down the production costs, rapid growth of the photovoltaic industry induces the depletion of the raw materials involved in the production of solar panels. Due to the high electron mobility and excellent optical transparency of GNSs, graphene–inorganic nanocomposites have emerged as one of the fascinating electrode materials for application in solar cells, mainly in the dye-sensitized solar cells and quantum dot (QD)-sensitized solar cells. Dye-sensitized solar cells have attracted much attention because of their moderate light to electricity conversion efficiency, easy fabrication, and low cost, which are mainly composed of a photo electrode (photo anode and photocathode), a dye, an electrolyte, and a counter electrode. The photo anodes of dye-sensitized solar cells are typically constructed using thick films of TiO_2 NPs, which provide a large surface area for anchoring enough dye molecules. However, the random transport of photo-generated electrons in disordered TiO_2 NPs increases the chance of charge recombination and thus decreases the efficiency of dye-sensitized solar cells [185].

Graphene–TiO_2 hybrid nanostructures [186, 187] and graphene–CNT with TiO_2 hybrid nanostructure [188] are employed as the photo anode for dye-sensitized solar cells, which enhance the conversion efficiency, in comparison with the TiO_2 photo anode. Kim et al. [189] reported graphene-TiO_2 nanocomposites as an interfacial layer between fluorine-doped tin oxide layer and TiO_2 film to reduce the back-transport reaction of electrons in dye-sensitized solar cells. Graphene–CNT composites with vertically aligned CNT also served as one of the promising candidates for counter electrodes to achieve high performance in dye-sensitized solar cells [190, 191]. Yang et al. [192] reported that graphene–NiO composite films were used to fabricate photocathode for dye-sensitized solar cells. The NiO–graphene composite

with an appropriate graphene amount offers faster hole transport and larger surface area than that of the plain NiO film, thus leading to significant improvement of charge transfer and increase of dye loading, in turn resulting in the increase in both short-circuit photocurrent and open-circuit photovoltage.

Graphene–inorganic hybrid nanostructures in solar cells are the development of QD-sensitized solar cells [193–195]. The QDs of CdSe and CdS with light absorption could harvest light energy and transfer excited electrons to the conduction band of TiO_2 or ZnO film. The capturing of photo-induced electrons as quickly as they are generated and efficiently transporting them in the metal oxide film is one of the most difficult challenges in QD-sensitized solar cells system. Pan et al. [193] reported CdS QD-sensitized solar cells, based on a GN incorporated TiO_2 film photo anode, which demonstrated a maximum power conversion efficiency of 1.44%, 56% higher than that without rGO. Deng et al. [195] demonstrated the use of a GN–ZnO nanorod (NR) composite as a photo anode, leading to 54.7% improvement of power conversion efficiency in CdSe QD-sensitized solar cells compared to a QD-sensitized ZnO NRs without the rGO layer.

12.3.6 Electronics

Graphene has recently attracted considerable attention owing to its remarkable electronic and structural properties and its possible applications in many emerging areas such as graphene-based electronic devices. The charge carriers in graphene behave like massless Dirac fermions, and graphene shows ballistic charge transport, turning it into an ideal material for circuit fabrication. However, graphene lacks a bandgap around the Fermi level, which is the defining concept for semiconductor materials and essential for controlling the conductivity by electronic means. Theory predicts that a tunable bandgap may be engineered by periodic modulations of the graphene lattice, but experimental evidence for this is so far lacking.

Graphene-based electronic devices have been designed to exhibit high carrier mobility, an ultrahigh speed, large-scale flexibility, and molecular-scale sensitivity; however, due to the absence of a bandgap, pristine graphene devices cannot be switched off, there by posing significant challenge to digital electronic device applications. To overcome this disadvantage, several approaches to enlarging the bandgap in graphene have been tested, including fabricating GNRs and implanting periodic hetero atoms on the graphene lattice [196–199]. Denis [196] reported the bandgap opening in monolayer and bilayer graphene by the doping of aluminum (Al), silicon (Si), phosphorus (P), and sulfur (S) for the application of electronics. Si-doped graphene has the lowest formation energy although it is semimetallic. P-doped graphene has a magnetic moment of 1 μ_B and for 3 at.% of doping the bandgap is 0.67 eV. Al-doped graphene is very unstable, but it is an attractive material because it is metallic. To reduce the formation energies of the substitutional defects we investigated the formation of interlayer bonds in bilayer graphene. Phosphorus forms the strongest bonds between layers giving particular stability to this material.

P-doped bilayer graphene has a gap of 0.43 eV but it is has no magnetic moment. Balog et al. [197] reported that bandgap opening in graphene induced by patterned hydrogen adsorption. They have demonstrated the existence of a bandgap opening in graphene, induced by the patterned adsorption of atomic hydrogen onto the Moiré superlattice positions of graphene grown on an Ir(111) substrate. Li et al. [198] have developed a chemical route to produce GNRs, as well as single ribbons with varying widths along their lengths or containing lattice-defined graphene junctions for potential molecular electronics.

On the other hand, bilayer graphene presents a unique alternative to bandgap engineering because a perpendicular electric field may be applied to break the inversion symmetry of graphene [200–203]. For instance, gate-controlled tunable bandgap bilayer graphene films are successfully demonstrated by fabricating field-effect transistors (FETs) with dual-gate structures. The resultant bandgap was nearly 250 meV, which corresponds to an on/off current ratio on the order of 10^2 [202]. Alternative purely chemical approaches for generating a built-in perpendicular electric field are also possible. Several researchers have reported that the presence of metal adatoms or molecular dopants with strong polarities can introduce an electric field onto the bilayer graphene and induce a bandgap, thereby producing an on/off current ratio similar to that of dual-gated transistors; however, because molecular dopants were applied only on one side of the bilayer graphene, the charge-carrier density varied along with the bandgap.

Using the density functional theory calculations, Bing [204] has shown systematical investigation of the electronic properties of armchair-edge GNRs doped with boron (B) and nitrogen (N) atoms. He has demonstrated the electronic structure and transport properties of boron and nitrogen-doped GNRs. *p*-type and *n*-type semiconducting behaviors are found in these nanoribbons after boron and nitrogen doping. This phenomenon can be used to design *p*-type and *n*-type transistors which are the key of realizing GNR-based electronic devices. As an example, *p*-type transistors have been studied by first-principles quantum transport calculations. The results show that the boron-doped GNR-FET can exhibit a high level of performance, with high on/off current ratio and subthreshold swing.

12.3.7 Graphene Sensors and Actuators

The rapid and cost-effective development of graphene-based 3D nanostructure provides new opportunities for the progress of analytical science and technology. In these days, graphene-based 3D nanostructure with large active area and high conductivity have been introduced into analytical chemistry and implanted novel functions into analytical sensing systems [205–208]. In this section, we present the application of GN-inorganic nanocomposites in constructing high-performance gas sensors and biosensors.

Crucial work has been carried out by different peoples on the effect of metal catalyst like, for example, Pd, Pt on gas sensing performance of graphene-based

sensors. For resistive gas sensors, the effect of catalytic metal contacts like Pt on H_2 sensing performance of graphene-like nanosheets deposited on SiC substrate has recently been investigated by Chu et al. [209] and Shafiei et al. [210]. Their sensors were operated at constant reverse bias (current) mode as the response was found to be more promising for reverse bias compared to its forward bias counterpart, and a voltage shift of 100 mV was recorded at 1 mA reverse bias current. Quite similar to the semiconducting oxide-based sensor, in this case also the role of Pt was to aid the H_2 dissociation leading to subsequent diffusion of H atom through the metal to graphene surface, which eventually resulted in higher response magnitude. In a similar study, Chu et al. [209] showed that epitaxial graphene deposited by CVD on SiC, when coated with Pt, acted as dopant and increased the conductance of graphene. Gas-testing results showed that the exposure to hydrogen decreased the resistance of the graphene/Pt, and depending on the temperature range three activation energies were observed.

CVD-grown monolayer graphene-based sensors on SiO_2/Si substrate was investigated by Gautam et al. for oxygen, NO_2, NH_3, and CH_4 [211–213] detection. In this study, the authors found that the electrical conductivity of graphene is sensitive to the reducing gases at elevated temperatures as well. The sensitivity of the device for the tested gases suggested that the device was most effective to operate in 150–200 °C ranges. Since the graphene films possess lower resistance (typically in few hundred ohms) compared with the metal oxide-based gas sensors (typically in few kilowatt up to few megawatt), graphene devices can be integrated with electronic circuits more suitably. In spite of somewhat lower response magnitude of graphene gas sensors compared to metal oxide-based gas sensors, fairly consistent response for different gases at low-temperature region explores the opening for practical commercial applications of graphene gas sensors.

Ko et al. [214] found the Pd/Au-decorated graphene for sensing NO_2 and it was found to be quite selective. The sensitivity was 9% with 100 ppm NO_2 gas for such MLG sensor with very good reproducibility. In another report, similar kind of selectivity improvement toward NO_2 was achieved using Pt/Ti contact by Nomani et al. [215]. Sensitivity down to parts-per-billion levels, with fast response, recovery and appreciable selectivity toward NO_2 in presence of commonly interfering gases like CO_2, H_2O (saturated vapor), NH_3 (550 ppm), and O_2 was reported. The root-mean-square (RMS) noise-limited sensitivity was calculated to be ~10 ppb, which is better than any commercial gas sensor available at present.

Cuong et al. reported a solution-processed gas sensor based on vertically aligned ZnO NRs on a chemically converted graphene film [216]. The prepared ZnO on a chemically converted graphene gas sensor device is able to detect 2 ppm of H_2S in oxygen at room temperature. Results from the study of Cuong et al. also suggested that the CCG film releases oxygen molecules during thermal reduction and evaporation of the byproduct process, which are adsorbed on the surface of ZnO NRs, thereby improving gas sensitivity. A high sensitivity of the gas sensor resulted from the growth of highly dense vertical ZnO NRs on the chemically converted graphene film with numerous tiny white dots on its surface, which may provide a sufficient number of sites for the nucleation and growth of the ZnO NRs. The adsorption of

oxygen on the surface of the ZnO NRs was found to be crucial for obtaining an excellent gas sensing performance of the ZnO NRs—chemically converted graphene sensor.

The enzyme electrodes based on graphene-based materials have attracted great interest for the detection of a wide range of analyses. An extremely important example is in the determination of glucose, which plays a crucial role in the diagnosis and therapy of diabetes. Recent studies have indicated that graphene-based materials are very capable of the sensitive and selective detection of glucose [217–225].

For example, Liu et al. [220] prepared a biocompatible graphene-based glucose biosensor using the covalent attachment between the carboxyl acid groups of the graphene sheets and the amines of glucose oxidase (GOx). They demonstrated that the resulting biosensors exhibited broad linearity, good sensitivity, excellent reproducibility, and storage stability. Lin et al. [218] studied the GOx/rGO/CS nanocomposite-modified electrode for direct electrochemistry and glucose sensing. It was found that the nanocomposite film can provide a favorable microenvironment for GOx to realize direct electron transfer at the modified electrode. The nanocomposite-based biosensor exhibited a wider linearity range from 0.08 to 12 mM glucose with a detection limit of 0.02 mM and much higher sensitivity (37.93 $\mu A\ mM^{-1}\ cm^{-2}$) compared with other nanostructured supports.

12.3.8 Catalysis

Catalysts to reduce the energy barrier for ORR are at the heart of these renewable energy devices. In recent years, the combination of TiO_2 and graphene had been proved to be an effective pathway to improve the photocatalytic activity of TiO_2 due to the excellent adsorbability and conductivity of graphene [226–229]. For example, Li et al. obtained a chemically bonded P25–graphene nanocomposite photocatalyst with a significant enhancement in photo degradation of methylene blue [227]. They attributed the high performance of P25–graphene to the enhanced adsorbability of dyes and efficient charge separation and transportation. Xiang et al. fabricated highly active graphene-modified TiO_2 nanosheets composite photocatalysts for H_2 production [228]. They for the first time demonstrated that inexpensive metal-free carbon material can be used as an effective co-catalyst for photocatalytic water splitting. Du et al. prepared hierarchical ordered macro-mesoporous TiO_2–graphene composite films with significant enhancement of photocatalytic activity for degrading the methyl blue [229]. However, the aforementioned studies mainly focused on the photocatalytic behavior of TiO_2–graphene composites for organic dyes or other liquid organic contaminants degradation. There is still scarce work on the usage of TiO_2–graphene composites for photodegradation of volatile organic compounds (VOCs). It is well-known that VOCs are triggering serious environmental problems such as stratospheric ozone depletion and tropospheric ozone increment. Among VOCs, acetone is one of the principle indoor air pollutants and long-term inhalation of it may cause serious heath disorders. Therefore, the degradation of gas-phased acetone is of particular importance.

Wang et al. [230] reported that as prepared TiO_2–graphene samples shows enhanced photocatalytic activity in photodegradation of acetone in air and graphene content exhibits a great influence on photocatalytic activity. At graphene content = 0.05 wt.%, the TiO_2–graphene composites exhibited the highest photocatalytic activity, which exceeds that of pure TiO_2 and P25 by a factor of 1.7 and 1.6, respectively. The enhanced photocatalytic activity is because graphene can act as an excellent electron acceptor and transporter, thus reducing the recombination of charge carriers and enhancing the photocatalytic activity. The transient photocurrent response experiment further confirmed the transfer of photogenerated electrons from conduction band of TiO_2 to graphene. The prepared hierarchical macro/mesoporous structured TiO_2–graphene composites should also find widely potential applications in photocatalysis, catalysis, solar-cell, separation, and purification processes.

Hu et al. [231] discussed the electrocatalytic activity toward the oxygen reduction and glucose oxidation of a graphene/Au composite that had a higher catalytic activity than Au NPs or graphene alone. Kim et al. [232] investigated the incorporation of Ag-doped graphene into polypyrrole (PPy) and the effect on its electrochemical properties. They found that the Ag NPs deposited onto the graphene improved the electrochemical performance of the catalyst by increasing of the charge transfer between graphene and PPy by the bridge effect. Liu et al. [233] reported that the expandable graphene nanocomposites containing platinum NPs that were synthesized via electrochemical reduction exhibited high catalytic activity and good stability for the oxidation of methanol, which was attributed to the improved electrical conductivity and the high specific surface area of the graphene catalyst support.

Fu et al. [234] fabricated graphene-based non-precious metal catalysts (NPMC) for ORR through pyrolysis of a mixture of Fe, Co salts, polyaniline, and rGO. They have demonstrated an effective approach for the large-scale fabrication of graphene-based NPMCs for the ORR through pyrolysis activation. Based on the experimental results, it is conclude that the Co–N_x moieties could facilitate the incorporation of Fe–N_x moieties during the pyrolysis process and the content of Fe–N_x active sites in rGO sheets plays a key role for ORR activity. In comparison to the commercial Pt/C catalyst, FeCo–N–rGO catalyst presented higher ORR onset potential and 46 mV more positive ORR half-wave potential in alkaline solution. Importantly, it also demonstrated good tolerance to methanol and better stability than Pt/C (loading: 52.6 μg Pt cm^{-2}) in the studied conditions. Though the FeCo–N_x embedded graphene material showed lower ORR performance compared to Pt/C in acidic solution at present, it certainly deserve to further study and may have the potential to replace the Pt/C catalyst in fuel cells.

Zhang et al. [235] found graphene sheets/cobalt nanocomposites as low-cost/high-performance catalysts for hydrogen generation. Graphene sheets/cobalt (GRs/Co) nanocomposites, which are highly efficient catalysts, have been prepared using a one-step solvothermal method in ethylene glycol. Co^{2+} salts were converted to Co NPs, which were simultaneously inserted into the graphene layers with the reduction of graphite oxide sheets to GRs. A number of Co NPs self-assemble on the surface of the GRs. The maximum saturation magnetization value of the composites

was 80.8 emu g^{-1}, which is enough to allow magnetic separation and control. The catalytic activity of the composite was also investigated. It is found that both of the highly conductive surface and increased surface area of the graphene support increases the hydrogen generation rate in the hydrolysis of $NaBH_4$ solutions. Moreover, it supplies a method for continuous gas generation using the catalyst dispersed on a filter for use in the production of clean fuels.

12.4 Conclusions, Challenges and Perspectives

In summary, we have reviewed the recent highlights of the development of novel 3D-GMO hierarchical nanostructure with various components including metal, nanocarbon, metal compounds and non-metals. Graphene could act as a substrate for the growth of nanostructure and supporting the metal NPs. We have also surveyed about 3D-graphene-metal oxide hierarchical nanostructure as the application for energy storage. GNS behaves like substrate for the supporting of the metal oxide NPs. Various approaches has been applied for the synthesis of 3D-GMO hybrid nanostructures such as template method, solution deposition method, hydrothermal techniques, solvothermal techniques, decomposition of hydrocarbon precursors, gas phase deposition, sol–gel technique, covalent grafting, and noncovalent interactions. The unusual layer-dependent energy-storage behavior was caused by different diffusion and charge transferring mechanisms due to the distinct interactions between metal NPs and graphene. Because of the 3D-GMO hierarchical nanostructure, efficient spacious utilization of multiple layered structures, these novel nanostructured materials may open numerous opportunities for producing exceptional ultra-capacitors and energy storage devices. These new 3D-GMO hybrid nanostructure materials have proven to demonstrate high potential for commercial applications in the field of energy storage and others synergetic fields. We hope that this chapter can help and provide valuable insights to researchers for gain further knowledge to speed up novel innovation in this area.

References

1. O.A. Shenderova, V.V. Zhirnov, D.W. Brenner, Carbon Nanostructures. Crit Rev Solid State Mater Sci. **27**, 227–356 (2002)
2. V. Singh, D. Joung, L. Zhai, S. Das, S. I. Khondaker,S. Seal, Graphene based materials: Past, present and future. Prog Mater Sci. **56**, 1178–1271 (2011)
3. M.D. Stoller, S. Park, Y. Zhu, J. An, R. S. Ruoff, Graphene-Based Ultracapacitors. Nano Lett. **8**, 3498–3502 (2008)
4. A. A. Balandin, S. Ghosh, W. Bao, I. Calizo, D. Teweldebrhan, F. Miao,C. N. Lau, Superior Thermal Conductivity of Single-Layer Graphene. Nano Lett. **8**, 902–907 (2008)
5. C. Lee, X. Wei, J. W. Kysar,J. Hone, Measurement of the Elastic Properties and Intrinsic Strength of Monolayer Graphene. Science **321**, 385–388 (2008)

6. K. S. Novoselov, A. K. Geim, S. V. Morozov, D. Jiang, Y. Zhang, S. V. Dubonos, I. V. Grigorieva,A. A. Firsov, Electric Field Effect in Atomically Thin Carbon Films. Science **306**, 666–669 (2004)
7. B. Sun, B. Wang, D. Su, L. Xiao, H. Ahn,G. Wang, Graphene nanosheets as cathode catalysts for lithium-air batteries with an enhanced electrochemical performance. Carbon **50**, 727–733 (2012)
8. W. R. Davis, R. J. Slawson,G. R. Rigby, An Unusual Form of Carbon. Nature **171**, 756–756 (1953)
9. R. Bacon, Growth, Structure, and Properties of Graphite Whiskers. J Appl Phys **31**, 283–290 (1960)
10. R. T. K. Baker,R. J. Waite, Formation of carbonaceous deposits from the platinum-iron catalyzed decomposition of acetylene. J Catal. **37**, 101–105 (1975)
11. R. T. K. Baker, M. A. Barber, P. S. Harris, F. S. Feates,R. J. Waite, Nucleation and growth of carbon deposits from the nickel catalyzed decomposition of acetylene. J Catal. **26**, 51–62 (1972)
12. R. T. K. Baker, G. R. Gadbsy,S. Terry, Formation of carbon filaments from catalysed decompasition of hydrocarbons. Carbon **13**, 245–246 (1975)
13. R. T. K. Baker, P. S. Harris, R. B. Thomas,R. J. Waite, Formation of filamentous carbon from iron, cobalt and chromium catalyzed decomposition of acetylene. J Catal. **30**, 86–95 (1973)
14. A. Oberlin, M. Endo,T. Koyama, Filamentous growth of carbon through benzene decomposition. J Cryst Growth **32**, 335-349 (1976)
15. G. G. Tibbetts, Lengths of carbon fibers grown from iron catalyst particles in natural gas. J Cryst Growth **73**, 431–438 (1985)
16. S. Iijima, Helical microtubules of graphitic carbon. Nature **354**, 56–58 (1991)
17. A.K. Geim, K.S. Novoselov, The rise of graphene. Nat. Mater. **6**, 183–191 (2007)
18. P.R. Wallace, The band theory of graphite. Phys. Rev. **71**, 622–634 (1947)
19. X. Lu, M. Yu, H. Huang, R.S. Ruoff, Tailoring graphite with the goal of achieving single sheets. Nanotechnology **10**, 269 (1999)
20. R. Ruoff, Graphene: calling all chemists. Nat. Nano. **3**, 10–11 (2008)
21. S.V. Morozov, K.S. Novoselov, M.I. Katsnelson, F. Schedin, D.C. Elias, J.A. Jaszczak, A.K. Geim, Giant intrinsic carrier mobilities in graphene and its bilayer. Phys. Rev. Lett. **100**, 016602 (2008)
22. E.V. Castro, K.S. Novoselov, S.V. Morozov, N.M.R. Peres, J.M.B.L. dos Santos, J. Nilsson, F. Guinea, A.K. Geim, A.H.C. Neto, Biased bilayer graphene: semiconductor with a gap tunable by the electric field effect. Phys. Rev. Lett. **99**, 216802 (2007)
23. J.C. Meyer, A.K. Geim, M.I. Katsnelson, K.S. Novoselov, T.J. Booth, S. Roth, The structure of suspended graphene sheets. Nature **446**, 60–63 (2007)
24. S. Stankovich, D.A. Dikin, R.D. Piner, K.A. Kohlhaas, A. Kleinhammes, Y. Jia, Y. Wu, S.T. Nguyen, R.S. Ruoff, Synthesis of graphene-based nanosheets via chemical reduction of exfoliated graphite oxide. Carbon **45**, 1558–1565 (2007)
25. Y. Hernandez, V. Nicolosi, M. Lotya, F.M. Blighe, Z. Sun, S. De, I.T. McGovern, B. Holland, M. Byrne, Y.K. Gun'Ko, J.J. Boland, P. Niraj, G. Duesberg, S. Krishnamurthy, R. Goodhue, J. Hutchison, V. Scardaci, A.C. Ferrari, J.N. Coleman, High-yield production of graphene by liquid-phase exfoliation of graphite. Nat. Nano. **3**, 563–568 (2008)
26. S. Gilje, S. Han, M. Wang, K.L. Wang, R.B. Kaner, A chemical route to graphene for device applications. Nano. Lett. **7**, 3394–3398 (2007)
27. D. Li, M.B. Muller, S. Gilje, R.B. Kaner, G.G. Wallace, Processable aqueous dispersions of graphene nanosheets. Nat. Nano. **3**, 101–105 (2008)
28. J. Wu, W. Pisula, K. Müllen, Graphenes as potential material for electronics. Chem. Rev. **107**, 718–747 (2007)
29. C. Berger, Z. Song, T. Li, X. Li, A.Y. Ogbazghi, R. Feng, Z. Dai, A.N. Marchenkov, E.H. Conrad, P.N. First, W.A. de Heer, Ultrathin epitaxial graphite: 2D electron gas properties and a route toward graphene-based nanoelectronics. J. Phys. Chem. B **108**, 19912–19916 (2004)

30. W.A. de Heer, C. Berger, X. Wu, P.N. First, E.H. Conrad, X. Li, T. Li, M. Sprinkle, J. Hass, M.L. Sadowski, M. Potemski, G. Martinez, Epitaxial graphene. Solid State Comm. **143**, 92–100 (2007)
31. M. Sveningsson, R.E. Morjan, O.A. Nerushev, Y. Sato, J. Bäckström, E.E.B. Campbell, F. Rohmund, Raman spectroscopy and field-emission properties of CVD-grown carbon-nanotube films. Appl. Phys. A **73**, 409–418 (2001)
32. A. Reina, X. Jia, J. Ho, D. Nezich, H. Son, V. Bulovic, M.S. Dresselhaus, J. Kong, Large area, few-layer graphene films on arbitrary substrates by chemical vapor deposition. Nano. Lett. **9**, 30–35 (2008)
33. J. Hass, W.A.d. Heer, E.H. Conrad, The growth and morphology of epitaxial multilayer graphene. J. Phys. Condens. Matter **20**, 323202 (2008)
34. Z. Chen, W. Ren, L. Gao, B. Liu, S. Pei, H.-M. Cheng, Three-dimensional flexible and conductive interconnected graphene networks grown by chemical vapour deposition. Nat. Mater. **10**, 424–428 (2011)
35. X. Dong, X. Wang, L. Wang, H. Song, H. Zhang, W. Huang, P. Chen, 3D graphene foam as a monolithic and macroporous carbon electrode for electrochemical sensing. ACS Appl. Mater. Interfaces **4**, 3129–3133 (2012)
36. X.-C. Dong, H. Xu, X.-W. Wang, Y.-X. Huang, M.B. Chan-Park, H. Zhang, L.-H. Wang, W. Huang, P. Chen, 3D graphene–cobalt oxide electrode for high-performance supercapacitor and enzymeless glucose detection. ACS Nano **6**, 3206–3213 (2012)
37. X. Cao, Y. Shi, W. Shi, G. Lu, X. Huang, Q. Yan, Q. Zhang, H. Zhang, Preparation of novel 3D graphene networks for supercapacitor applications. Small **7**, 3163–3168 (2011)
38. L. Estevez, A. Kelarakis, Q. Gong, E.H. Da'as, E.P. Giannelis, Multifunctional graphene/platinum/nafion hybrids via ice templating. J. Am. Chem. Soc. **133**, 6122–6125 (2011)
39. S.H. Lee, H.W. Kim, J.O. Hwang, W.J. Lee, J. Kwon, C.W. Bielawski, R.S. Ruoff, S.O. Kim, Three-dimensional self-assembly of graphene oxide platelets into mechanically flexible macroporous carbon films. Angew. Chem. Int. Ed. **49**, 10084–10088 (2010)
40. S. Yin, Y. Zhang, J. Kong, C. Zou, C.M. Li, X. Lu, J. Ma, F.Y.C. Boey, X. Chen, Assembly of graphene sheets into hierarchical structures for high-performance energy storage. ACS Nano **5**, 3831–3838 (2011)
41. J.L. Vickery, A.J. Patil, S. Mann, Fabrication of graphene–polymer nanocomposites with higher-order three-dimensional architectures. Adv. Mater. **21**, 2180–2184 (2009)
42. M.A. Worsley, P.J. Pauzauskie, T.Y. Olson, J. Biener, J.H. Satcher, T.F. Baumann, Synthesis of graphene aerogel with high electrical conductivity. J. Am. Chem. Soc. **132**, 14067–14069 (2010)
43. X. Jiang, Y. Ma, J. Li, Q. Fan, W. Huang, Self-assembly of reduced graphene oxide into three-dimensional architecture by divalent ion linkage. J. Phys. Chem. C **114**, 22462–22465 (2010)
44. S.-Z. Zu, B.-H. Han, Aqueous dispersion of graphene sheets stabilized by pluronic copolymers: formation of supramolecular hydrogel. J. Phys. Chem. C **113**, 13651–13657 (2009)
45. H. Bai, K. Sheng, P. Zhang, C. Li, G. Shi, Graphene oxide/conducting polymer composite hydrogels. J. Mater. Chem. **21**, 18653–18658 (2011)
46. Z. Tang, S. Shen, J. Zhuang, X. Wang, Noble-metal-promoted three-dimensional macroassembly of single-layered graphene oxide. Angew. Chem. Int. Ed. **49**, 4603–4607 (2010)
47. Z.-S. Wu, S. Yang, Y. Sun, K. Parvez, X. Feng, K. Müllen, 3D nitrogen-doped graphene aerogel-supported Fe_3O_4 nanoparticles as efficient electrocatalysts for the oxygen reduction reaction. J. Am. Chem. Soc. **134**, 9082–9085 (2012)
48. W. Chen, L. Yan, In situ self-assembly of mild chemical reduction graphene for three-dimensional architectures. Nanoscale, **3**, 3132–3137 (2011)
49. X. Zhang, Z. Sui, B. Xu, S. Yue, Y. Luo, W. Zhan, B. Liu, Mechanically strong and highly conductive graphene aerogel and its use as electrodes for electrochemical power sources. J. Mater. Chem. **21**, 6494–6497 (2011)
50. H.-P. Cong, X.-C. Ren, P. Wang, S.-H. Yu, Macroscopic multifunctional graphene-based hydrogels and aerogels by a metal ion induced self-assembly process. ACS Nano **6**, 2693–2703 (2012)

51. Y. Xu, K. Sheng, C. Li, G. Shi, Self-assembled graphene hydrogel via a one-step hydrothermal process. ACS Nano **4**, 4324–4330 (2010)
52. H. Jiang, P.S. Lee, C. Li, 3D carbon based nanostructures for advanced supercapacitors. Energy Environ. Sci. **6**, 41–53 (2013)
53. W. Wang, S. Guo, M. Penchev, I. Ruiz, K.N. Bozhilov, D. Yan, M. Ozkan, C.S. Ozkan, Three dimensional few-layer graphene–carbon nanotube foam architectures for high fidelity supercapacitors. Nano Energy **2**, 294–303 (2013)
54. W. Chen, S. Li, C. Chen, L. Yan, Self-assembly and embedding of nanoparticles by in Situ reduced graphene for preparation of a 3D graphene/nanoparticle aerogel. Adv. Mater. **23**, 5679–5683 (2011)
55. S.T. Nguyen, H.T. Nguyen, A. Rinaldi, N.P.V. Nguyen, Z. Fan, H.M. Duong, Morphology control and thermal stability of binderless-graphene aerogels from graphite for energy storage applications. Colloids Surf. A **414**, 352–358 (2012)
56. T. Maiyalagan, X. Dong, P. Chen, X. Wang, Electrodeposited Pt on three-dimensional interconnected graphene as a free-standing electrode for fuel cell application. J. Mater. Chem. **22**, 5286–5290 (2012)
57. L. Zhang, G. Chen, M.N. Hedhili, H. Zhang, P. Wang, Three-dimensional assemblies of graphene prepared by a novel chemical reduction-induced self-assembly method. Nanoscale **4**, 7038–7045 (2012)
58. A. Yu, P. Ramesh, X. Sun, E. Bekyarova, M.E. Itkis, R.C. Haddon, Enhanced thermal conductivity in a hybrid graphite nanoplatelet—carbon nanotube filler for epoxy composites. Adv. Mater. **20**, 4740–4744 (2008)
59. C. Zhang, S. Huang, W.W. Tjiu, W. Fan, T. Liu, Facile preparation of water-dispersible graphene sheets stabilized by acid-treated multi-walled carbon nanotubes and their poly(vinyl alcohol) composites. J. Mater. Chem. **22**, 2427–2434 (2012)
60. R. Wang, J. Sun, L. Gao, C. Xu, J. Zhang, Fibrous nanocomposites of carbon nanotubes and graphene-oxide with synergetic mechanical and actuative performance. Chem. Commun. **47**, 8650–8652 (2011)
61. L. Xu, N. Wei, Y. Zheng, Z. Fan, H.-Q. Wang, J.-C. Zheng, Graphene-nanotube 3D networks: intriguing thermal and mechanical properties. J. Mater. Chem. **22**, 1435–1444 (2012)
62. C. Wu, X. Huang, G. Wang, L. Lv, G. Chen, G. Li, P. Jiang, Highly conductive nanocomposites with three-dimensional, compactly interconnected graphene networks via a self-assembly process. Adv. Funct. Mater. **23**, 506–513 (2013)
63. L.L. Zhang, Z. Xiong, X.S. Zhao, Pillaring chemically exfoliated graphene oxide with carbon nanotubes for photocatalytic degradation of dyes under visible light irradiation. ACS Nano **4**, 7030–7036 (2010)
64. Z. Fan, J. Yan, L. Zhi, Q. Zhang, T. Wei, J. Feng, M. Zhang, W. Qian, F. Wei, A three-dimensional carbon nanotube/graphene sandwich and its application as electrode in supercapacitors. Adv. Mater. **22**, 3723–3728 (2010)
65. M.J. Allen, V.C. Tung, R.B. Kaner, Honeycomb carbon: a review of graphene. Chem. Rev. **110**, 132–145 (2009)
66. V. Jousseaume, J. Cuzzocrea, N. Bernier, V.T. Renard, Few graphene layers/carbon nanotube composites grown at complementary-metal-oxide-semiconductor compatible temperature. Appl. Phys. Lett. **98**, 123103–123103 (2011)
67. M. Zhou, T. Lin, F. Huang, Y. Zhong, Z. Wang, Y. Tang, H. Bi, D. Wan, J. Lin, Highly conductive porous graphene/ceramic composites for heat transfer and thermal energy storage. Adv. Functi. Mater. **23**, 2263–2269 (2013)
68. S. Chen, P. Bao, G. Wang Synthesis of Fe_2O_3–CNT–graphene hybrid materials with an open three-dimensional nanostructure for high capacity lithium storage. Nano Energy **2**, 425–434 (2013)
69. J.-S. Cheng, J. Du, W. Zhu, Facile synthesis of three-dimensional chitosan–graphene mesostructures for reactive black 5 removal. Carbohydr. Polym. **88**, 61–67 (2012)
70. Y. Pan, H. Bao, L. Li, Noncovalently functionalized multiwalled carbon nanotubes by chitosan-grafted reduced graphene oxide and their synergistic reinforcing effects in chitosan films. ACS Appl. Mater. Interfaces **3**, 4819–4830 (2011)

71. X. Dong, G. Xing, M.B. Chan-Park, W. Shi, N. Xiao, J. Wang, Q. Yan, T.C. Sum, W. Huang, P. Chen, The formation of a carbon nanotube–graphene oxide core–shell structure and its possible applications. Carbon **49**, 5071–5078 (2011)
72. Y.-K. Kim, D.-H. Min, Preparation of scrolled graphene oxides with multi-walled carbon nanotube templates. Carbon **48**, 4283–4288 (2010)
73. D. Yu, L. Dai, Self-assembled graphene/carbon nanotube hybrid films for supercapacitors. J. Phys. Chem. Lett. **1**, 467–470 (2009)
74. L. Qiu, X. Yang, X. Gou, W. Yang, Z.-F. Ma, G.G. Wallace, D. Li, Dispersing carbon nanotubes with graphene oxide in water and synergistic effects between graphene derivatives. Chem. Eur. J. **16**, 10653–10658 (2010)
75. D. Cai, M. Song, C. Xu, Highly conductive carbon-nanotube/graphite-oxide hybrid films. Adv. Mater. **20**, 1706–1709 (2008)
76. D. Chen, W. Wei, R. Wang, J. Zhu, L. Guo, α-Fe_2O_3 nanoparticles anchored on graphene with 3D quasi-laminated architecture: in situ wet chemistry synthesis and enhanced electrochemical performance for lithium ion batteries. New J. Chem. **36**, 1589–1595 (2012)
77. J.-Z. Wang, C. Zhong, D. Wexler, N.H. Idris, Z.-X. Wang, L.-Q. Chen, H.-K. Liu, Graphene-encapsulated Fe_3O_4 nanoparticles with 3D laminated structure as superior anode in lithium ion batteries. Chem. Eur. J. **17**, 661–667 (2011)
78. S. Bai, X. Shen, Graphene-inorganic nanocomposites. RSC Adv. **2**, 64–98 (2012)
79. H.-J. Choi, S.-M. Jung, J.-M. Seo, D.W. Chang, L. Dai, J.-B. Baek, Graphene for energy conversion and storage in fuel cells and supercapacitors. Nano Energy **1**, 534–551 (2012)
80. R.B. Rakhi, W. Chen, D. Cha, H.N. Alshareef, Nanostructured ternary electrodes for energy-storage applications. Adv. Energy Mater. **2**, 381–389 (2012)
81. Y. Zhai, Y. Dou, D. Zhao, P.F. Fulvio, R.T. Mayes, S. Dai, Carbon materials for chemical capacitive energy storage. Adv. Mater. **23**, 4828–4850 (2011)
82. M.D. Stoller, S. Park, Y. Zhu, J. An, R.S. Ruoff, Graphene-based ultracapacitors. Nano Lett. **8**, 3498–3502 (2008)
83. J.J. Yoo, K. Balakrishnan, J. Huang, V. Meunier, B.G. Sumpter, A. Srivastava, M. Conway, A.L. Mohana Reddy, J. Yu, R. Vajtai, P.M. Ajayan, Ultrathin planar graphene supercapacitors. Nano Lett. **11**, 1423–1427 (2011)
84. Y. Huang, J. Liang, Y. Chen, An overview of the applications of graphene-based materials in supercapacitors. Small **8**, 1805–1834 (2012)
85. W. Shi, J. Zhu, D.H. Sim, Y.Y. Tay, Z. Lu, X. Zhang, Y. Sharma, M. Srinivasan, H. Zhang, H.H. Hng, Q. Yan, Achieving high specific charge capacitances in Fe_3O_4/reduced graphene oxide nanocomposites. J. Mater. Chem. **21**, 3422–3427 (2011)
86. B. Li, H. Cao, J. Shao, M. Qu, J.H. Warner, Superparamagnetic Fe_3O_4 nanocrystals@graphene composites for energy storage devices. J. Mater. Chem. **21**, 5069–5075 (2011)
87. W. Zhou, J. Liu, T. Chen, K.S. Tan, X. Jia, Z. Luo, C. Cong, H. Yang, C.M. Li, T. Yu, Fabrication of Co_3O_4-reduced graphene oxide scrolls for high-performance supercapacitor electrodes. Phys. Chem. Chem. Phys. **13**, 14462–14465 (2011)
88. J. Yan, T. Wei, W. Qiao, B. Shao, Q. Zhao, L. Zhang, Z. Fan, Rapid microwave-assisted synthesis of graphene nanosheet/Co_3O_4 composite for supercapacitors. Electrochim. Acta **55**, 6973–6978 (2010)
89. S. Chen, J. Zhu, X. Wang, One-step synthesis of graphene–cobalt hydroxide nanocomposites and their electrochemical properties. J. Phys. Chem. C **114**, 11829–11834 (2010)
90. X. Xia, J. Tu, Y. Mai, R. Chen, X. Wang, C. Gu, X. Zhao, Graphene sheet/porous NiO hybrid film for supercapacitor applications. Chem. Eur. J. **17**, 10898–10905 (2011)
91. W. Lv, F. Sun, D.-M. Tang, H.-T. Fang, C. Liu, Q.-H. Yang, H.-M. Cheng, A sandwich structure of graphene and nickel oxide with excellent supercapacitive performance. J. Mater. Chem. **21**, 9014–9019 (2011)
92. J.W. Lee, T. Ahn, D. Soundararajan, J.M. Ko, J.-D. Kim, Non-aqueous approach to the preparation of reduced graphene oxide/α-$Ni(OH)_2$ hybrid composites and their high capacitance behavior. Chem. Commun. **47**, 6305–6307 (2011)

93. H. Wang, H.S. Casalongue, Y. Liang, H. Dai, $Ni(OH)_2$ nanoplates grown on graphene as advanced electrochemical pseudocapacitor materials. J. Am. Chem. Soc. **132**, 7472–7477 (2010)
94. H.-W. Wang, Z.-A. Hu, Y.-Q. Chang, Y.-L. Chen, H.-Y. Wu, Z.-Y. Zhang, Y.-Y. Yang, Design and synthesis of $NiCo_2O_4$-reduced graphene oxide composites for high performance supercapacitors. J. Mater. Chem. **21**, 10504–10511 (2011)
95. T. Lu, Y. Zhang, H. Li, L. Pan, Y. Li, Z. Sun, Electrochemical behaviors of graphene–ZnO and graphene–SnO_2 composite films for supercapacitors. Electrochim. Acta **55**, 4170–4173 (2010)
96. Y.-L. Chen, Z.-A. Hu, Y.-Q. Chang, H.-W. Wang, Z.-Y. Zhang, Y.-Y. Yang, H.-Y. Wu, Zinc oxide/reduced graphene oxide composites and electrochemical capacitance enhanced by homogeneous incorporation of reduced graphene oxide sheets in zinc oxide matrix. J. Phys. Chem. C **115**, 2563–2571 (2011)
97. Y. Wang, C.X. Guo, J. Liu, T. Chen, H. Yang, C.M. Li, CeO_2 nanoparticles/graphene nanocomposite-based high performance supercapacitor. Dalton Trans. **40**, 6388–6391 (2011)
98. B. Li, H. Cao, G. Yin, Y. Lu, J. Yin, Cu_2O@reduced graphene oxide composite for removal of contaminants from water and supercapacitors. J. Mater. Chem. **21**, 10645–10648 (2011)
99. Z. Li, J. Wang, X. Liu, S. Liu, J. Ou, S. Yang, Electrostatic layer-by-layer self-assembly multilayer films based on graphene and manganese dioxide sheets as novel electrode materials for supercapacitors. J. Mater. Chem. **21**, 3397–3403 (2011)
100. J. Zhang, J. Jiang, X.S. Zhao, Synthesis and capacitive properties of manganese oxide nanosheets dispersed on functionalized graphene sheets. J. Phys. Chem. C **115**, 6448–6454 (2011)
101. C. Zhu, S. Guo, Y. Fang, L. Han, E. Wang, S. Dong, One-step electrochemical approach to the synthesis of graphene/MnO_2 nanowall hybrids. Nano Res. **4**, 648–657 (2011)
102. Q. Cheng, J. Tang, J. Ma, H. Zhang, N. Shinya, L.-C. Qin, Graphene and nanostructured MnO_2 composite electrodes for supercapacitors. Carbon **49**, 2917–2925 (2011)
103. G. Yu, L. Hu, M. Vosgueritchian, H. Wang, X. Xie, J.R. McDonough, X. Cui, Y. Cui, Z. Bao, Solution-processed graphene/MnO_2 nanostructured textiles for high-performance electrochemical capacitors. Nano Lett. **11**, 2905–2911 (2011)
104. J. Yan, Z. Fan, T. Wei, W. Qian, M. Zhang, F. Wei, Fast and reversible surface redox reaction of graphene–MnO_2 composites as supercapacitor electrodes. Carbon **48**, 3825–3833 (2010)
105. B. Wang, J. Park, C. Wang, H. Ahn, G. Wang, Mn_3O_4 nanoparticles embedded into graphene nanosheets: preparation, characterization, and electrochemical properties for supercapacitors. Electrochim. Acta **55**, 6812–6817 (2010)
106. H.-W. Wang, Z.-A. Hu, Y.-Q. Chang, Y.-L. Chen, Z.-Q. Lei, Z.-Y. Zhang, Y.-Y. Yang, Facile solvothermal synthesis of a graphene nanosheet–bismuth oxide composite and its electrochemical characteristics. Electrochim. Acta **55**, 8974–8980 (2010)
107. F. Li, J. Song, H. Yang, S. Gan, Q. Zhang, D. Han, A. Ivaska, L. Niu, One-step synthesis of graphene/SnO_2 nanocomposites and its application in electrochemical supercapacitors. Nanotechnology **20**, 455602 (2009)
108. Z.-S. Wu, D.-W. Wang, W. Ren, J. Zhao, G. Zhou, F. Li, H.-M. Cheng, Anchoring hydrous RuO_2 on graphene sheets for high-performance electrochemical capacitors. Adv. Funct. Mater. **20**, 3595–3602 (2010)
109. G. Wang, X. Shen, J. Yao, J. Park, Graphene nanosheets for enhanced lithium storage in lithium ion batteries. Carbon **47**, 2049–2053 (2009)
110. M. Liang, L. Zhi, Graphene-based electrode materials for rechargeable lithium batteries. J. Mater. Chem. **19**, 5871–5878 (2009)
111. S.-M. Paek, E. Yoo, I. Honma, Enhanced cyclic performance and lithium storage capacity of SnO_2/graphene nanoporous electrodes with three-dimensionally delaminated flexible structure. Nano Lett. **9**, 72–75 (2008)
112. L. Ji, Z. Tan, T.R. Kuykendall, S. Aloni, S. Xun, E. Lin, V. Battaglia, Y. Zhang, Fe_3O_4 nanoparticle-integrated graphene sheets for high-performance half and full lithium ion cells. Phys. Chem. Chem. Phys. **13**, 7170–7177 (2011)

113. P. Lian, X. Zhu, H. Xiang, Z. Li, W. Yang, H. Wang, Enhanced cycling performance of Fe_3O_4–graphene nanocomposite as an anode material for lithium-ion batteries. Electrochim. Acta **56**, 834–840 (2010)
114. G. Zhou, D.-W. Wang, F. Li, L. Zhang, N. Li, Z.-S. Wu, L. Wen, G.Q. Lu, H.-M. Cheng, Graphene-wrapped Fe_3O_4 anode material with improved reversible capacity and cyclic stability for lithium ion batteries. Chem. Mater. **22**, 5306–5313 (2010)
115. M. Zhang, D. Lei, X. Yin, L. Chen, Q. Li, Y. Wang, T. Wang, Magnetite/graphene composites: microwave irradiation synthesis and enhanced cycling and rate performances for lithium ion batteries. J. Mater. Chem. **20**, 5538–5543 (2010)
116. G. Wang, T. Liu, Y. Luo, Y. Zhao, Z. Ren, J. Bai, H. Wang, Preparation of Fe_2O_3/graphene composite and its electrochemical performance as an anode material for lithium ion batteries. J. Alloys Compd. **509**, L216–L220 (2011)
117. X. Zhu, Y. Zhu, S. Murali, M.D. Stoller, R.S. Ruoff, Nanostructured reduced graphene oxide/Fe_2O_3 composite as a high-performance Anode Material for Lithium Ion Batteries. ACS Nano **6**, 183–191 (2011)
118. J. Zhu, T. Zhu, X. Zhou, Y. Zhang, X.W. Lou, X. Chen, H. Zhang, H.H. Hng, Q. Yan, Facile synthesis of metal oxide/reduced graphene oxide hybrids with high lithium storage capacity and stable cyclability. Nanoscale **3**, 1084–1089 (2011)
119. Z.-S. Wu, W. Ren, L. Wen, L. Gao, J. Zhao, Z. Chen, G. Zhou, F. Li, H.-M. Cheng, Graphene anchored with Co_3O_4 nanoparticles as anode of lithium ion batteries with enhanced reversible capacity and cyclic performance. ACS Nano **4**, 3187–3194 (2010)
120. S.Q. Chen, Y. Wang, Microwave-assisted synthesis of a Co_3O_4-graphene sheet-on-sheet nanocomposite as a superior anode material for Li-ion batteries. J. Mater. Chem. **20**, 9735–9739 (2010)
121. H. Kim, D.-H. Seo, S.-W. Kim, J. Kim, K. Kang, Highly reversible Co_3O_4/graphene hybrid anode for lithium rechargeable batteries. Carbon **49**, 326–332 (2011)
122. S. Yang, X. Feng, S. Ivanovici, K. Müllen, Fabrication of graphene-encapsulated oxide nanoparticles: towards high-performance anode materials for lithium storage. Angew. Chem. Int. Ed. **49**, 8408–8411 (2010)
123. J. Zhu, Y.K. Sharma, Z. Zeng, X. Zhang, M. Srinivasan, S. Mhaisalkar, H. Zhang, H.H. Hng, Q. Yan, Cobalt oxide nanowall arrays on reduced graphene oxide sheets with controlled phase, grain size, and porosity for Li-Ion battery electrodes. J. Phys. Chem. C **115**, 8400–8406 (2011)
124. Y.-S. He, D.-W. Bai, X. Yang, J. Chen, X.-Z. Liao, Z.-F. Ma, A $Co(OH)_2$–graphene nanosheets composite as a high performance anode material for rechargeable lithium batteries. Electrochem. Commun. **12**, 570–573 (2010)
125. Y. Zou, Y. Wang, NiO nanosheets grown on graphene nanosheets as superior anode materials for Li-ion batteries. Nanoscale **3**, 2615–2620 (2011)
126. B. Li, H. Cao, J. Shao, H. Zheng, Y. Lu, J. Yin, M. Qu, Improved performances of α-$Ni(OH)_2$@reduced-graphene-oxide in Ni-MH and Li-ion batteries. Chem Commun. **47**, 3159–3161 (2011)
127. X. Huang, X. Zhou, L. Zhou, K. Qian, Y. Wang, Z. Liu, C. Yu, A facile one-step solvothermal synthesis of SnO_2/graphene nanocomposite and its application as an anode material for lithium-ion batteries. Chem. Phys. Chem. **12**, 278–281 (2011)
128. X. Wang, X. Zhou, K. Yao, J. Zhang, Z. Liu, A SnO_2/graphene composite as a high stability electrode for lithium ion batteries. Carbon **49**, 133–139 (2011)
129. L.-S. Zhang, L.-Y. Jiang, H.-J. Yan, W.D. Wang, W. Wang, W.-G. Song, Y.-G. Guo, L.-J. Wan, Mono dispersed SnO_2 nanoparticles on both sides of single layer graphene sheets as anode materials in Li-ion batteries. J. Mater. Chem. **20**, 5462–5467 (2010)
130. Z. Wang, H. Zhang, N. Li, Z. Shi, Z. Gu, G. Cao, Laterally confined graphene nanosheets and graphene/SnO_2 composites as high-rate anode materials for lithium-ion batteries. Nano Res. **3**, 748–756 (2010)
131. J. Yao, X. Shen, B. Wang, H. Liu, G. Wang, In situ chemical synthesis of SnO_2–graphene nanocomposite as anode materials for lithium-ion batteries. Electrochem. Commun. **11**, 1849–1852 (2009)

132. S. Ding, D. Luan, F.Y.C. Boey, J.S. Chen, X.W. Lou, SnO_2 nanosheets grown on graphene sheets with enhanced lithium storage properties. Chem. Commun. **47**, 7155–7157 (2011)
133. Y. Li, X. Lv, J. Lu, J. Li, Preparation of SnO_2-nanocrystal/graphene-nanosheets composites and their lithium storage ability. J. Phys. Chem. C **114**, 21770–21774 (2010)
134. S. Ding, J.S. Chen, D. Luan, F.Y.C. Boey, S. Madhavi, X.W. Lou, Graphene-supported anatase TiO_2 nanosheets for fast lithium storage. Chem. Commun. **47**, 5780–5782 (2011)
135. N. Li, G. Liu, C. Zhen, F. Li, L. Zhang, H.-M. Cheng, Battery performance and photocatalytic activity of mesoporous anatase TiO_2 nanospheres/graphene composites by template-free self-assembly. Adv. Funct. Mater. **21**, 1717–1722 (2011)
136. D. Wang, D. Choi, J. Li, Z. Yang, Z. Nie, R. Kou, D. Hu, C. Wang, L.V. Saraf, J. Zhang, I.A. Aksay, J. Liu, Self-assembled TiO_2–graphene hybrid nanostructures for enhanced Li-ion insertion. ACS Nano **3**, 907–914 (2009)
137. Y. Qiu, K. Yan, S. Yang, L. Jin, H. Deng, W. Li, Synthesis of size-tunable anatase TiO_2 nanospindles and their assembly into Anatase@Titanium oxynitride/titanium nitride–graphene nanocomposites for rechargeable lithium ion batteries with high cycling performance. ACS Nano **4**, 6515–6526 (2010)
138. J.S. Chen, Z. Wang, X.C. Dong, P. Chen, X.W. Lou, Graphene-wrapped TiO_2 hollow structures with enhanced lithium storage capabilities. Nanoscale **3**, 2158–2161 (2011)
139. H. Wang, L.-F. Cui, Y. Yang, H. Sanchez Casalongue, J.T. Robinson, Y. Liang, Y. Cui, H. Dai, Mn_3O_4–graphene hybrid as a high-capacity anode material for lithium ion batteries. J. Am. Chem. Soc. **132**, 13978–13980 (2010)
140. Y.J. Mai, X.L. Wang, J.Y. Xiang, Y.Q. Qiao, D. Zhang, C.D. Gu, J.P. Tu, CuO/graphene composite as anode materials for lithium-ion batteries. Electrochim. Acta **56**, 2306–2311 (2011)
141. B. Wang, X.-L. Wu, C.-Y. Shu, Y.-G. Guo, C.-R. Wang, Synthesis of CuO/graphene nanocomposite as a high-performance anode material for lithium-ion batteries. J. Mater. Chem. **20**, 10661–10664 (2010)
142. G. Wang, J. Bai, Y. Wang, Z. Ren, J. Bai, Prepartion and electrochemical performance of a cerium oxide–graphene nanocomposite as the anode material of a lithium ion battery. Scripta Mater. **65**, 339–342 (2011)
143. K. Chang, W. Chen, In situ synthesis of MoS_2/graphene nanosheet composites with extraordinarily high electrochemical performance for lithium ion batteries. Chem. Commun. **47**, 4252–4254 (2011)
144. K. Chang, W. Chen, l-cysteine-assisted synthesis of layered MoS_2/graphene composites with excellent electrochemical performances for lithium ion batteries. ACS Nano **5**, 4720–4728 (2011)
145. H. Xiang, B. Tian, P. Lian, Z. Li, H. Wang, Sol–gel synthesis and electrochemical performance of Li4Ti5O12/graphene composite anode for lithium-ion batteries. J. Alloys Compd. **509**, 7205–7209 (2011)
146. L. Shen, C. Yuan, H. Luo, X. Zhang, S. Yang, X. Lu, In situ synthesis of high-loading $Li_4Ti_5O_{12}$-graphene hybrid nanostructures for high rate lithium ion batteries. Nanoscale **3**, 572–574 (2011)
147. J.K. Lee, K.B. Smith, C.M. Hayner, H.H. Kung, Silicon nanoparticles-graphene paper composites for Li ion battery anodes. Chem. Commun. **46**, 2025–2027 (2010)
148. J.-Z. Wang, C. Zhong, S.-L. Chou, H.-K. Liu, Flexible free-standing graphene-silicon composite film for lithium-ion batteries. Electrochem. Commun. **12**, 1467–1470 (2010)
149. S.-L. Chou, J.-Z. Wang, M. Choucair, H.-K. Liu, J.A. Stride, S.-X. Dou, Enhanced reversible lithium storage in a nanosize silicon/graphene composite. Electrochem. Commun. **12**, 303–306 (2010)
150. S. Chen, P. Chen, M. Wu, D. Pan, Y. Wang, Graphene supported Sn–Sb@carbon core-shell particles as a superior anode for lithium ion batteries. Electrochem. Commun. **12**, 1302–1306 (2010)
151. G. Wang, B. Wang, X. Wang, J. Park, S. Dou, H. Ahn, K. Kim, Sn/graphene nanocomposite with 3D architecture for enhanced reversible lithium storage in lithium ion batteries. J. Mater. Chem. **19**, 8378–8384 (2009)

152. L. Ji, Z. Tan, T. Kuykendall, E.J. An, Y. Fu, V. Battaglia, Y. Zhang, Multilayer nanoassembly of Sn-nanopillar arrays sandwiched between graphene layers for high-capacity lithium storage. Energy Environ. Sci. **4**, 3611–3616 (2011)
153. F. Ji, Y.-L. Li, J.-M. Feng, D. Su, Y.-Y. Wen, Y. Feng, F. Hou, Electrochemical performance of graphene nanosheets and ceramic composites as anodes for lithium batteries. J. Mater. Chem. **19**, 9063–9067 (2009)
154. Z.-J. Fan, J. Yan, T. Wei, G.-Q. Ning, L.-J. Zhi, J.-C. Liu, D.-X. Cao, G.-L. Wang, F. Wei, Nanographene-constructed carbon nanofibers grown on graphene sheets by chemical vapor deposition: high-performance anode materials for lithium ion batteries. ACS Nano **5**, 2787–2794 (2011)
155. E. Yoo, J. Kim, E. Hosono, H. Zhou, T. Kudo, I. Honma, Large reversible Li storage of graphene nanosheet families for use in rechargeable lithium ion batteries. Nano Lett. **8**, 2277–2282 (2008)
156. L. Schlapbach, A. Zuttel, Hydrogen-storage materials for mobile applications. Nature **414**, 353–358 (2001)
157. C.-D. Wu, L.-M. Kuo, S.-J. Lin, T.-H. Fang, S.-F. Hsieh, Effects of temperature, size of water droplets, and surface roughness on nanowetting properties investigated using molecular dynamics simulation. Comput. Mater. Sci. **53**, 25–30 (2012)
158. C.-D. Wu, T.-H. Fang, J.-F. Lin, An investigation of the effects of polymethylmethacrylate orientation and antistiction layer on the nanoimprint process using molecular dynamics. Adv. Sci. Lett. **4**, 36–43 (2011)
159. S.-J. Lin, C.-D. Wu, T.-H. Fang, L.-M. Kuo, Effects of forging temperature and velocity on nano-forming process using molecular dynamics simulation. Comput. Mater. Sci. **50**, 2918–2924 (2011)
160. C.-D. Wu, T.-H. Fang, J.-F. Lin, Formation mechanism and mechanics of dip-pen nanolithography using molecular dynamics. Langmuir **26**, 3237–3241 (2009)
161. C.P. Herrero, R. Ramírez, Diffusion of hydrogen in graphite: a molecular dynamics simulation. J. Phys. D: Appl. Phys. **43**, 255402 (2010)
162. F. Darkrim Lamari, D. Levesque, Hydrogen adsorption on functionalized graphene. Carbon **49**, 5196–5200 (2011)
163. H. Du, J. Li, J. Zhang, G. Su, X. Li, Y. Zhao, Separation of hydrogen and nitrogen gases with porous graphene membrane. J. Phys. Chem. C **115**, 23261–23266 (2011)
164. J. Wang, X.-B. Zhang, Z.-L. Wang, L.-M. Wang, Y. Zhang, Rhodium-nickel nanoparticles grown on graphene as highly efficient catalyst for complete decomposition of hydrous hydrazine at room temperature for chemical hydrogen storage. Energy Environ. Sci. **5**, 6885–6888 (2012)
165. W. Li, C. Liang, W. Zhou, J. Qiu, Zhou, G. Sun, Q. Xin, Preparation and characterization of multiwalled carbon nanotube-supported platinum for cathode catalysts of direct methanol fuel cells. J. Phys. Chem. B **107**, 6292–6299 (2003)
166. K. Gong, F. Du, Z. Xia, M. Durstock, L. Dai, Nitrogen-doped carbon nanotube arrays with high electrocatalytic activity for oxygen reduction. Science **323**, 760–764 (2009)
167. D.A. Dikin, S. Stankovich, E.J. Zimney, R.D. Piner, G.H.B. Dommett, G. Evmenenko, S.T. Nguyen, R.S. Ruoff, Preparation and characterization of graphene oxide paper. Nature **448**, 457–460 (2007)
168. K.S. Kim, Y. Zhao, H. Jang, S.Y. Lee, J.M. Kim, K.S. Kim, J.-H. Ahn, P. Kim, J.-Y. Choi, B.H. Hong, Large-scale pattern growth of graphene films for stretchable transparent electrodes. Nature **457**, 706–710 (2009)
169. M.H. Maneshian, F.-L. Kuo, K. Mahdak, J. Hwang, R. Banerjee, N.D. Shepherd, The influence of high dielectric constant aluminum oxide sputter deposition on the structure and properties of multilayer epitaxial graphene. Nanotechnology **22**, 205703 (2011)
170. Y.-G. Zhou, J.-J. Chen, F. Wang, Z.-H. Sheng, X.-H. Xia, A facile approach to the synthesis of highly electroactive Pt nanoparticles on graphene as an anode catalyst for direct methanol fuel cells. Chem. Commun. **46**, 5951–5953 (2010)

171. R. Kou, Y. Shao, D. Wang, M.H. Engelhard, J.H. Kwak, J. Wang, V.V. Viswanathan, C. Wang, Y. Lin, Y. Wang, I.A. Aksay, J. Liu, Enhanced activity and stability of Pt catalysts on functionalized graphene sheets for electrocatalytic oxygen reduction. Electrochem. Commun. **11**, 954–957 (2009)
172. B. Seger, P.V. Kamat, Electrocatalytically active graphene-platinum nanocomposites. Role of 2-D carbon support in PEM fuel cells. J. Phys. Chem. C **113**, 7990–7995 (2009)
173. H. Zhao, J. Yang, L. Wang, C. Tian, B. Jiang, H. Fu, Fabrication of a palladium nanoparticle/graphene nanosheet hybrid via sacrifice of a copper template and its application in catalytic oxidation of formic acid. Chem. Commun. **47**, 2014–2016 (2011)
174. D.H. Lee, J.E. Kim, T.H. Han, J.W. Hwang, S. Jeon, S.-Y. Choi, S.H. Hong, W.J. Lee, R.S. Ruoff, S.O. Kim, Versatile carbon hybrid films composed of vertical carbon nanotubes grown on mechanically compliant graphene films. Adv. Mater. **22**, 1247–1252 (2010)
175. L. Dong, R.R.S. Gari, Z. Li, M.M. Craig, S. Hou, Graphene-supported platinum and platinum–ruthenium nanoparticles with high electrocatalytic activity for methanol and ethanol oxidation. Carbon **48**, 781–787 (2010)
176. J. Hernández, J. Solla-Gullón, E. Herrero, Gold nanoparticles synthesized in a water-in-oil microemulsion: electrochemical characterization and effect of the surface structure on the oxygen reduction reaction. J. Electroanal. Chem. **574**, 185–196 (2004)
177. J. Luo, M.M. Maye, V. Petkov, N.N. Kariuki, L. Wang, P. Njoki, D. Mott, Y. Lin, C.-J. Zhong, Phase properties of carbon-supported gold–platinum nanoparticles with different bimetallic compositions. Chem. Mater. **17**, 3086–3091 (2005)
178. Y. Liang, Y. Li, H. Wang, J. Zhou, J. Wang, T. Regier, H. Dai, Co_3O_4 nanocrystals on graphene as a synergistic catalyst for oxygen reduction reaction. Nat. Mater. **10**, 780–786 (2011)
179. S. Guo, S. Dong, E. Wang, Three-dimensional Pt-on-Pd bimetallic nanodendrites supported on graphene nanosheet: facile synthesis and used as an advanced nanoelectrocatalyst for methanol oxidation. ACS Nano **4**, 547–555 (2009)
180. L. Qu, Y. Liu, J.-B. Baek, L. Dai, Nitrogen-doped graphene as efficient metal-free electrocatalyst for oxygen reduction in fuel cells. ACS Nano **4**, 1321–1326 (2010)
181. S. Yang, X. Feng, X. Wang, K. Müllen, Graphene-based carbon nitride nanosheets as efficient metal-free electrocatalysts for oxygen reduction reactions. Angew. Chem. Int. Ed. **50**, 5339–5343 (2011)
182. A.G. Pandolfo, A.F. Hollenkamp, Carbon properties and their role in supercapacitors. J. Power Sources **157**, 11–27 (2006)
183. S.M. Choi, M.H. Seo, H.J. Kim, W.B. Kim, Synthesis of surface-functionalized graphene nanosheets with high Pt-loadings and their applications to methanol electrooxidation. Carbon **49**, 904–909 (2011)
184. E. Yoo, T. Okata, T. Akita, M. Kohyama, J. Nakamura, I. Honma, Enhanced electrocatalytic activity of Pt subnanoclusters on graphene nanosheet surface. Nano Lett. **9**, 2255–2259 (2009)
185. Y.H. Hu, H. Wang, B. Hu, Thinnest two-dimensional nanomaterial—graphene for solar energy. ChemSusChem. **3**, 782–796 (2010)
186. C. Venkateswara Rao, A. Leela Mohana Reddy, Y. Ishikawa, P.M. Ajayan, $LiNi_{1/3}Co_{1/3}Mn_{1/3}O_2$–graphene composite as a promising cathode for lithium-ion batteries. ACS Appl. Mater. Interfaces **3**, 2966–2972 (2011)
187. N. Yang, J. Zhai, D. Wang, Y. Chen, L. Jiang, Two-dimensional graphene bridges enhanced photoinduced charge transport in dye-sensitized solar cells. ACS Nano **4**, 887–894 (2010)
188. M.-Y. Yen, M.-C. Hsiao, S.-H. Liao, P.-I. Liu, H.-M. Tsai, C.-C.M. Ma, N.-W. Pu, M.-D. Ger, Preparation of graphene/multi-walled carbon nanotube hybrid and its use as photoanodes of dye-sensitized solar cells. Carbon **49**, 3597–3606 (2011)
189. S.R. Kim, M.K. Parvez, M. Chhowalla, UV-reduction of graphene oxide and its application as an interfacial layer to reduce the back-transport reactions in dye-sensitized solar cells. Chem. Phys. Lett. **483**, 124–127 (2009)

190. S. Li, Y. Luo, W. Lv, W. Yu, S. Wu, P. Hou, Q. Yang, Q. Meng, C. Liu, H.-M. Cheng, Vertically aligned carbon nanotubes grown on graphene paper as electrodes in lithium-ion batteries and dye-sensitized solar cells. Adv. Energy Mater. **1**, 486–490 (2011)
191. H. Kim, H. Choi, S. Hwang, Y. Kim, M. Jeon, Fabrication and characterization of carbon-based counter electrodes prepared by electrophoretic deposition for dye-sensitized solar cells. Nanoscale Res. Lett. **7**, 53 (2012)
192. H. Yang, G.H. Guai, C. Guo, Q. Song, S.P. Jiang, Y. Wang, W. Zhang, C.M. Li, NiO/graphene composite for enhanced charge separation and collection in p-type dye sensitized solar cell. J. Phys. Chem. C **115**, 12209–12215 (2011)
193. G. Zhu, T. Xu, T. Lv, L. Pan, Q. Zhao, Z. Sun, Graphene-incorporated nanocrystalline TiO_2 films for CdS quantum dot-sensitized solar cells. J. Electroanal. Chem. **650**, 248–251 (2011)
194. S. Sun, L. Gao, Y. Liu, J. Sun, Assembly of CdSe nanoparticles on graphene for low-temperature fabrication of quantum dot sensitized solar cell. Appl. Phys. Lett. **98**, 093112–093113 (2011)
195. J. Chen, C. Li, G. Eda, Y. Zhang, W. Lei, M. Chhowalla, W.I. Milne, W.-Q. Deng, Incorporation of graphene in quantum dot sensitized solar cells based on ZnO nanorods. Chem. Commun. **47**, 6084–6086 (2011)
196. P.A. Denis, Band gap opening of monolayer and bilayer graphene doped with aluminium, silicon, phosphorus, and sulfur. Chem. Phys. Lett. **492**, 251–257 (2010)
197. R. Balog, B. Jorgensen, L. Nilsson, M. Andersen, E. Rienks, M. Bianchi, M. Fanetti, E. Laegsgaard, A. Baraldi, S. Lizzit, Z. Sljivancanin, F. Besenbacher, B. Hammer, T.G. Pedersen, P. Hofmann, L. Hornekaer, Bandgap opening in graphene induced by patterned hydrogen adsorption. Nat. Mater. **9**, 315–319 (2010)
198. X. Li, X. Wang, L. Zhang, S. Lee, H. Dai, Chemically derived, ultrasmooth graphene nanoribbon semiconductors. Science **319**, 1229–1232 (2008)
199. M.Y. Han, B. Özyilmaz, Y. Zhang, P. Kim, Energy band-gap engineering of graphene nanoribbons. Phys. Rev. Lett. **98**, 206805 (2007)
200. J.B. Oostinga, H.B. Heersche, X. Liu, A.F. Morpurgo, L.M.K. Vandersypen, Gate-induced insulating state in bilayer graphene devices. Nat. Mater. **7**, 151–157 (2008)
201. T. Taychatanapat, P. Jarillo-Herrero, Electronic transport in dual-gated bilayer graphene at large displacement fields. Phys. Rev. Lett. **105**, 166601 (2010)
202. Y. Zhang, T.-T. Tang, C. Girit, Z. Hao, M.C. Martin, A. Zettl, M.F. Crommie, Y.R. Shen, F. Wang, Direct observation of a widely tunable bandgap in bilayer graphene. Nature **459**, 820–823 (2009)
203. F. Xia, D.B. Farmer, Y. Lin, P. Avouris, Graphene field-effect transistors with high on/off current ratio and large transport band gap at room temperature. Nano Lett. **10**, 715–718 (2010)
204. B. Huang, Electronic properties of boron and nitrogen doped graphene nanoribbons and its application for graphene electronics. Phys. Lett. A **375**, 845–848 (2011)
205. M. Pumera, Graphene-based nanomaterials for energy storage. Energy Environ. Sci. **4**, 668–674 (2011)
206. D. Chen, L. Tang, J. Li, Graphene-based materials in electrochemistry. Chem. Soc. Rev. **39**, 3157–3180 (2010)
207. M. Pumera, A. Ambrosi, A. Bonanni, E.L.K. Chng, H.L. Poh, Graphene for electrochemical sensing and biosensing. TrAC Trends Anal. Chem. **29**, 954–965 (2010)
208. D. Chen, H. Feng, J. Li, Graphene oxide: preparation, functionalization, and electrochemical applications. Chem. Rev. **112**, 6027–6053 (2012)
209. B.H. Chu, C.F. Lo, J. Nicolosi, C.Y. Chang, V. Chen, W. Strupinski, S.J. Pearton, F. Ren, Hydrogen detection using platinum coated graphene grown on SiC. Sens. Actuators B **157**, 500–503 (2011)
210. M. Shafiei, R. Arsat, J. Yu, K. Kalantar-zadeh, W. Wlodarski, S. Dubin, R.B. Kaner, In Pt/graphene nano-sheet based hydrogen gas sensor. Sensors, 2009 IEEE, 25–28 Oct. 2009; 2009; pp 295–298

211. M. Gautam, A.H. Jayatissa, G.U. Sumanasekera, In Synthesis and characterization of transferable graphene by CVD method, Nanotechnology Materials and Devices Conference (NMDC), 2010 IEEE, 12–15 Oct. 2010; pp 1–5 (2010)
212. M. Qazi, G. Koley, NO2 detection using microcantilever based potentiometry. Sensors **8**, 7144–7156 (2008)
213. M. Gautam, A.H. Jayatissa, Gas sensing properties of graphene synthesized by chemical vapor deposition. Mater. Sci. Eng. C **31**, 1405–1411 (2011)
214. G. Ko, H.Y. Kim, J. Ahn, Y.M. Park, K.Y. Lee, J. Kim, Graphene-based nitrogen dioxide gas sensors. Curr. Appl. Phys. **10**, 1002–1004 (2010)
215. M.W.K. Nomani, R. Shishir, M. Qazi, D. Diwan, V.B. Shields, M.G. Spencer, G.S. Tompa, N.M. Sbrockey, G. Koley, Highly sensitive and selective detection of NO2 using epitaxial graphene on 6 H-SiC. Sens. Actuators B **150**, 301–307 (2010)
216. T.V. Cuong, V.H. Pham, J.S. Chung, E.W. Shin, D.H. Yoo, S.H. Hahn, J.S. Huh, G.H. Rue, E.J. Kim, S.H. Hur, P.A. Kohl, Solution-processed ZnO-chemically converted graphene gas sensor. Mater. Lett. **64**, 2479–2482 (2010)
217. Z. Wang, X. Zhou, J. Zhang, F. Boey, H. Zhang, Direct electrochemical reduction of single-layer graphene oxide and subsequent functionalization with glucose oxidase. J. Phys. Chem. C **113**, 14071–14075 (2009)
218. X. Kang, J. Wang, H. Wu, I.A. Aksay, J. Liu, Y. Lin, Glucose oxidase–graphene–chitosan modified electrode for direct electrochemistry and glucose sensing. Biosens. Bioelectron. **25**, 901–905 (2009)
219. T.T. Baby, S.S.J. Aravind, T. Arockiadoss, R.B. Rakhi, S. Ramaprabhu, Metal decorated graphene nanosheets as immobilization matrix for amperometric glucose biosensor. Sens. Actuators B **145**, 71–77 (2010)
220. Y. Liu, D. Yu, C. Zeng, Z. Miao, L. Dai, Biocompatible graphene oxide-based glucose biosensors. Langmuir **26**, 6158–6160 (2010)
221. Y. Zhang, S. Liu, L. Wang, X. Qin, J. Tian, W. Lu, G. Chang, X. Sun, One-pot green synthesis of Ag nanoparticles-graphene nanocomposites and their applications in SERS, H2O2, and glucose sensing. RSC Adv. **2**, 538–545 (2012)
222. J. Yang, S. Deng, J. Lei, H. Ju, S. Gunasekaran, Electrochemical synthesis of reduced graphene sheet–AuPd alloy nanoparticle composites for enzymatic biosensing. Biosens. Bioelectron. **29**, 159–166 (2011)
223. Y. Song, K. Qu, C. Zhao, J. Ren, X. Qu, Graphene oxide: intrinsic peroxidase catalytic activity and its application to glucose detection. Adv. Mater. **22**, 2206–2210 (2010)
224. C. Shan, H. Yang, D. Han, Q. Zhang, A. Ivaska, L. Niu, Graphene/AuNPs/chitosan nanocomposites film for glucose biosensing. Biosens. Bioelectron. **25**, 1070–1074 (2010)
225. J.-D. Qiu, J. Huang, R.-P. Liang, Nanocomposite film based on graphene oxide for high performance flexible glucose biosensor. Sens. Actuators B **160**, 287–294 (2011)
226. Y.H. Ng, A. Iwase, A. Kudo, R. Amal, Reducing graphene oxide on a visible-light $BiVO_4$ photocatalyst for an enhanced photoelectrochemical water splitting. J. Phys. Chem. Lett. **1**, 2607–2612 (2010)
227. H. Zhang, X. Lv, Y. Li, Y. Wang, J. Li, P25-Graphene composite as a high performance photocatalyst. ACS Nano **4**, 380–386 (2009)
228. Q. Xiang, J. Yu, M. Jaroniec, Enhanced photocatalytic H_2-production activity of graphene-modified titania nanosheets. Nanoscale **3**, 3670–3678 (2011)
229. J. Du, X. Lai, N. Yang, J. Zhai, D. Kisailus, F. Su, D. Wang, L. Jiang, Hierarchically ordered macro–mesoporous TiO_2–graphene composite films: improved mass transfer, reduced charge recombination, and their enhanced photocatalytic activities. ACS Nano **5**, 590–596 (2010)
230. W. Wang, J. Yu, Q. Xiang, B. Cheng, Enhanced photocatalytic activity of hierarchical macro/mesoporous TiO_2–graphene composites for photodegradation of acetone in air. Appl. Catal. B **119–120**, 109–116 (2012)

231. Y. Hu, J. Jin, P. Wu, H. Zhang, C. Cai, Graphene–gold nanostructure composites fabricated by electrodeposition and their electrocatalytic activity toward the oxygen reduction and glucose oxidation. Electrochim. Acta **56**, 491–500 (2010)
232. K.-S. Kim, I.-J. Kim, S.-J. Park, Influence of Ag doped graphene on electrochemical behaviors and specific capacitance of polypyrrole-based nanocomposites. Synth. Met. **160**, 2355–2360 (2010)
233. S. Liu, J. Wang, J. Zeng, J. Ou, Z. Li, X. Liu, S. Yang, "Green" electrochemical synthesis of Pt/graphene sheet nanocomposite film and its electrocatalytic property. J. Power Sources **195**, 4628–4633 (2010)
234. X. Fu, Y. Liu, X. Cao, J. Jin, Q. Liu, J. Zhang, FeCo–Nx embedded graphene as high performance catalysts for oxygen reduction reaction. Appl. Catal. B **130–131**, 143–151 (2013)
235. F. Zhang, C. Hou, Q. Zhang, H. Wang, Y. Li, Graphene sheets/cobalt nanocomposites as low-cost/high-performance catalysts for hydrogen generation. Mater. Chem. Phys. **135**, 826–831 (2012)

Chapter 13
Janus Nanostructures for Biomedical Applications: Dual-Surfaces of Single Particle for Multifunctionality

Donglu Shi, Feng Wang and Yilong Wang

13.1 Introduction

With the rapid development of nanotechnology, there has been an increasing need that nanomateirals can address the key clinical issues in drug delivery, hyperthermia, imaging, and cell targeting, preferably in a combined fashion, thus helping doctors with cancer diagnosis as well as treatment. There has been extensive study on establishing nano-carrier systems achieving isolated functionalities. However, driven by the clinical application, more research is being focused on developing an integrated nano-carrier system to achieve drug delivery, imaging, cell targeting, and hyperthermia simultaneously, which leads to the terminology of "multifunctionality."

Such nano-carrier system must have following features to achieve multifunctionality:

1. The surface of the nano-carrier system bears functional groups. This could allow further manipulation for attachment of biological moieties such as drugs and targeting ligands. The surface properties might be the most important to the nano-carrier because in most cases, bio-application is obtained through surface functionalization. Besides, surface properties determine the colloidal stability of the nano-carrier systems.
2. The nano-carrier needs to be ready for imaging. One way is to label the nano-carrier with fluorescent markers or the nano-carrier itself is fluorescent. The other

D. Shi (✉)
The Materials Science and Engineering Program, University of Cincinnati, Cincinnati, OH 45221, USA
e-mail: shid@ucmail.uc.edu

F. Wang
Department of Physics and TcSUH, University of Houston, Houston, TX 77057, USA

Y. Wang
The Institute for Biomedical Engineering and Nano Science, Tongji University School of Medicine, 200092 Shanghai, China

M. Zhang et al. (eds.), *Carbon Nanomaterials for Biomedical Applications,*
Springer Series in Biomaterials Science and Engineering 5,
DOI 10.1007/978-3-319-22861-7_13

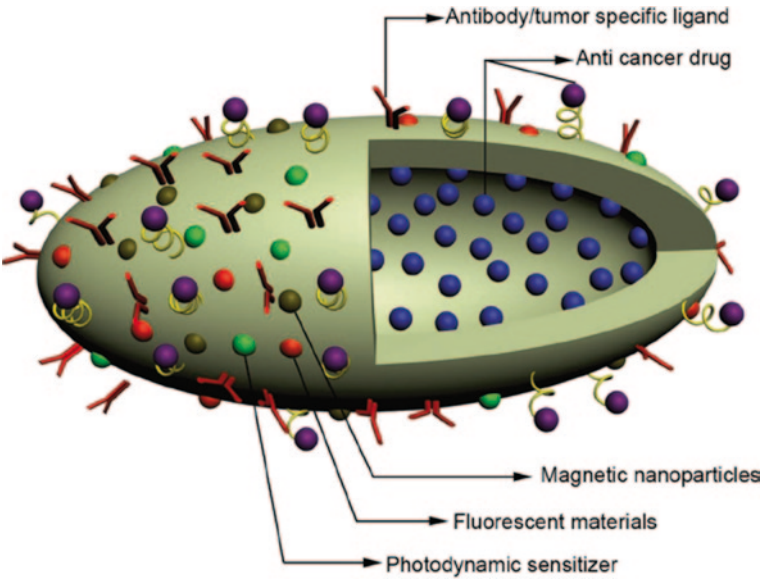

Fig. 13.1 Schematic illustration of an idealized nano-carrier for cancer treatment [1]

way is magnetic resonance imaging (MRI) if the nano-carrier has a magnetic component.

3. The nano-carrier has to be nontoxic, preferably biodegradable to be considered for clinical application.
4. Some nano-carriers are designed to be hollow structured for drug storage and appeared quite promising regarding the examples of mesoporous silica nanoparticles and polymer micelles.

An idealized multifunctional nano-carrier designed for diagnostic and therapeutic purpose is illustrated in Fig. 13.1.

13.1.1 Janus Particle Overview

Although many efforts were devoted to constructing nano-carrier systems that could potentially achieve multifunctionalities toward clinic [2], most of the approaches used currently have been surface functionalization of nanoparticles with different drugs [3], biological molecules, including DNA [4], RNA [5], peptide [6], antibodies [7], and imaging probes such as quantum dots (QDs) [8]. One of the major disadvantages in this approach is characteristically the single surface structure of the nanoparticles. A nanoparticle is normally assumed a symmetrical spherical or a tube geometry with limited surface available for multiple components. Furthermore, multifunctional conjugates on a single carrier often interact with each other, leading to adverse effects. The design and assembly of a single surface symmetrical

carrier is also complicated by difficulties in the structural and chemical arrangements of the functional components.

It is, therefore, critical to develop multi-surface nanostructures for the assembly of a variety of components on a clinically viable delivery system that can best utilize the intrinsic properties of nanomaterials. So far, scientists have well understood the fundamentals of isotropic nanoparticles. However, inspired by the new possibilities of desirable structures and behavior offered by anisotropic nanoparticles, researchers have begun to explore ways to fabricate asymmetric nanoparticles [9]. Attempts have been made to generate shape as well as functionality anisotropy on microparticles [10–12], but it has become challenging when it comes to the nanoscale. Janus nanoparticles, named after the Roman god who has two distinct faces, possess multiple surface structures that are anisotropic in shape, composition, and surface chemistry [13]. Their structural asymmetry is ideally suited for the assembly of multiple components on a single-particle system [14]. More importantly, the multiple surfaces with different functional groups can be used to selectively conjugate with targeting ligands, imaging probes, or drugs [15–17]. These characteristics of the Janus nanoparticles make them "truly multifunctional entities" [9].

13.1.2 Inorganic Janus Particles

Generally, inorganic Janus nanoparticles can be categorized into two types: [13]

1. The nanoparticle consists of two or more inorganic phase, each component expressing different optical, electrical, or magnetic properties.
2. The nanoparticle is composed of one material phase but possesses distinct chemical properties on both sides.

There has been a large amount of literature reporting the design and fabrication of inorganic Janus nanoparticles. One flexible method employed is masking, which involves partial coverage of the matrix materials and growth of other inorganic phases on the exposed matrix via chemical functionalization [18], electrostatic attraction [19], or metal evaporation [20]. For example, Bae et al. first crystallized silica nanoparticles on a silicon wafer several layers thick in a close-packed pattern. Then the surfaces of silica nanoparticles were coated with octadecyltrichlorosilane self-assembled monolayers (OTS-SAMs), the only areas left uncoated were those where the neighboring nanoparticles touched. After the top layers of silica nanoparticles were removed by tape, TiO_2 nanoparticles were deposited onto the uncoated areas of the silica nanoparticle surfaces [21]. In another example of masking, McConnell et al. produced multiregional Janus nanoparticles using a horizontal substrate to protect the bottom of the matrix materials [22]. They sank the amino group-functionalized silica nanoparticles into horizontal styrene–acrylic acid random copolymer films swollen by solvent. Then gold (Au) nanoparticles were deposited onto the exposed surfaces of silica nanoparticles by electrostatic interaction (Fig. 13.2).

Ligands can also be used to link the two distinct parts of a Janus nanoparticle. Zhang et al. employed hexadecyltrimethylammonium bromide (CTAB) as the link-

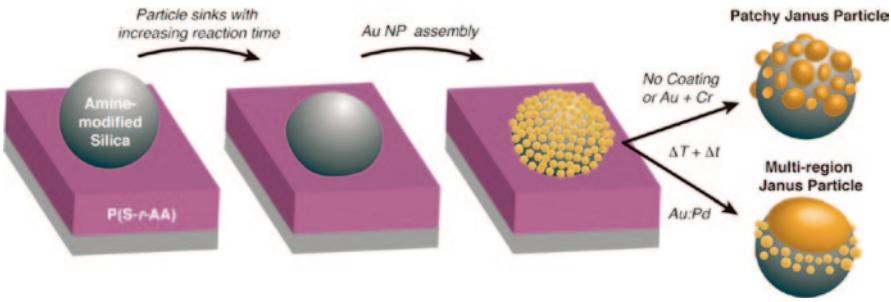

Fig. 13.2 Schematic illustration of the formation of multiregional Janus particles [22].

er as well as the template in aqueous solution to fabricate Janus nanoparticles with Fe_3O_4 heads and mesoporous silica tails. The length of silica tails could be manipulated by adjusting the amount of tetraethyl orthosilicate added [23].

To produce Janus nanoparticles with one single-material phase but two different surface properties, another method called Pickering emulsion was developed by Granick and coworkers [13, 24, 25]. In this model, nanoparticles are adsorbed onto the interface of an oil-in-water emulsion system. Then the oil phase is frozen and chemical modification is carried out on the particle surfaces exposed to water. Finally, the oil phase is removed to release nanoparticles with asymmetric surface functional groups. For example, Granick et al. dispersed fused silica particles in molten wax and mixed with water to form an emulsion. After wax cooled down to freezing point, the exposed surfaces of silica particles were functionalized with (aminopropyl) triethoxysilane to generate amino groups. The wax was later dissolved by chloroform, and silica particles were conjugated with OTS on the other side to make the silica particles amphiphilic [25]. This technique could also be considered in the category of masking method.

13.1.3 Polymeric Janus Particles

The most widely used method for producing polymeric Janus nanoparticles is phase separation which involves the interactions between polymers and monomers, among polymer chains, and between the nanoparticles and aqueous phase [26, 27]. One of the common approaches features using polymers as the seeds for the further growth of another polymer via emulsion polymerization. Another method is based on copolymer blocks ABC. The middle block B is cross-linked with the two ends A and C composing the two modules of the Janus particles. Although phase separation is an easy process, it is difficult to control the morphology of the Janus particles, and the production rate is often very low [13].

Very similar to inorganic Janus nanoparticle synthesis, the masking approach also finds its application in polymeric Janus particle fabrication. The mechanism is to functionalize partial surfaces of the pre-synthesized polymer particles, either by

masking the other part in a substrate or carrying out the modification at interfaces. So only the exposed surfaces would be subjected to subsequent growth of other polymers [28, 29]. For example, Bradley and Rowe attached positively charged poly(2-vinylpyridine) microgel particles to negatively charged poly(2-vinylpyridine-co-styrene) latex particles and grafted poly(N-isopropylacrylamide) to the exposed surfaces to produce asymmetric polymeric composites [30].

Microfluid can also be employed to prepare Janus particles. The dispersed phase containing monomers is injected perpendicular to the immiscible continuous phase to produce a stream of the droplets with monomers for polymerization [31]. Lone et al. took water as the dispersed phase and hexane as the continuous phase. The microfluidic device produced water droplets containing light-responsive polymers and cross-linkers. Under ultraviolet (UV) irradiation, Janus structures were formed in the droplets [31] (Fig. 13.3).

Compared to phase separation and masking, which are limited to production quantities, microfluid can be scaled-up for larger amounts [13]. However, the sizes from the microfluid approach are a lot bigger due to the droplet sizes formed during injecting.

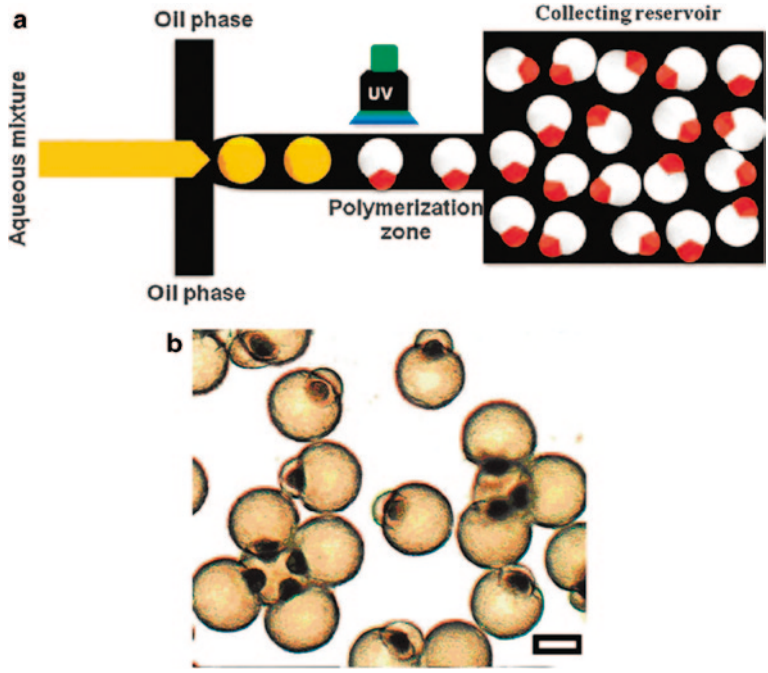

Fig. 13.3 **a** Route to fabricate Janus particles using microfluid. **b** Optical microscopic image of Janus particles [31]

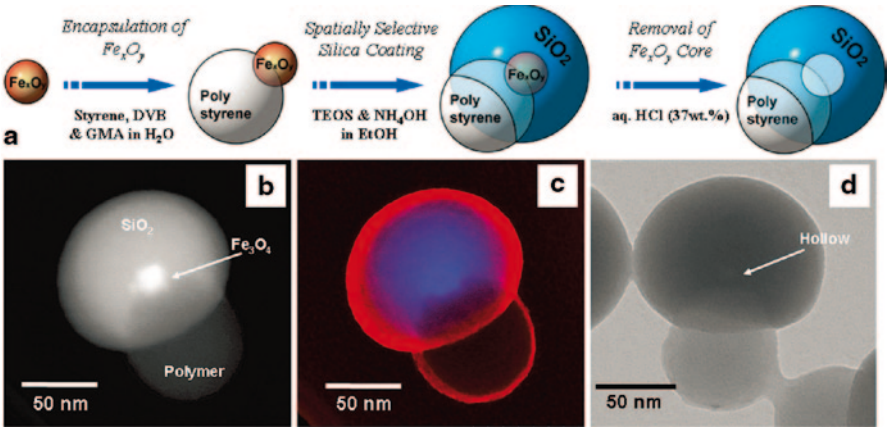

Fig. 13.4 **a** Process to produce mushroom Janus nanocomposites. **b** Dark-field STEM of PS/Fe_3O_4@SiO_2. **c** SEM and dark-field STEM overlapping image of PS/Fe_3O_4@SiO_2. **d** TEM image of PS/hollow SiO_2 after Fe_3O_4 is etched [32]. *GMA* glycidyl methacrylate, *DVB* divinylbenzene, STEM scanning transmission electron microscopy, *PS* polystyrene, *TEOS* tetraethoxysilane

13.1.4 Polymeric–Inorganic Janus Composites

Combining advantages from both organic and inorganic composition, the polymer–inorganic nanoparticles attracted extensive interest as they have potential application as catalysts, functional coatings, and biosensors [9]. Polystyrene (PS)/silica was investigated most among the model structures that have been developed, possibly because both have relatively simple and controllable fabrication process (Fig. 13.4).

Immobilization (selective coating) remains useful in fabrication of polymer–inorganic Janus nanocomposites. Feyen and coworkers managed to fabricate a mushroom ternary Janus structure of PS/iron oxides@Silica [32]. First, oxides were immobilized onto the PS nanoparticles through emulsion to serve as growth sites for silica. Then silica nanospheres were formed upon iron oxides via sol–gel reaction. The iron oxides could be etched away by hydrochloride to generate hollow silica nanoparticles. Gong et al. grew ZnO nanowires on part of the PS surfaces [33]. Carboxyl group-functionalized PS particles were sunk in a polymer film and incubated in the $ZnCl_2$ aqueous solution. As a result, Zn^{2+} ions deposited onto the exposed PS surfaces due to electrostatic attraction. Then ZnO nanowires could grow through an electrochemical process (Fig. 13.5).

Phase separation represents another important approach in generating polymer–inorganic composites. As PS can be synthesized easily through emulsion polymerization, phase separation often involves a miniemulsion process. Ge et al. made silica nanoparticles aggregate by introducing very small amount of water. Methacryloxypropyltrimethoxysilane (MPS) was attached to the exposed surfaces of silica as cross-linkers. Subsequent growth of PS occurred at the sites of MPS via miniemulsion and the morphology of Janus structures could be tuned by adjusting the amount of monomers [34]. Wang et al. used a similar method to fabricate PS/Silica asymmetric

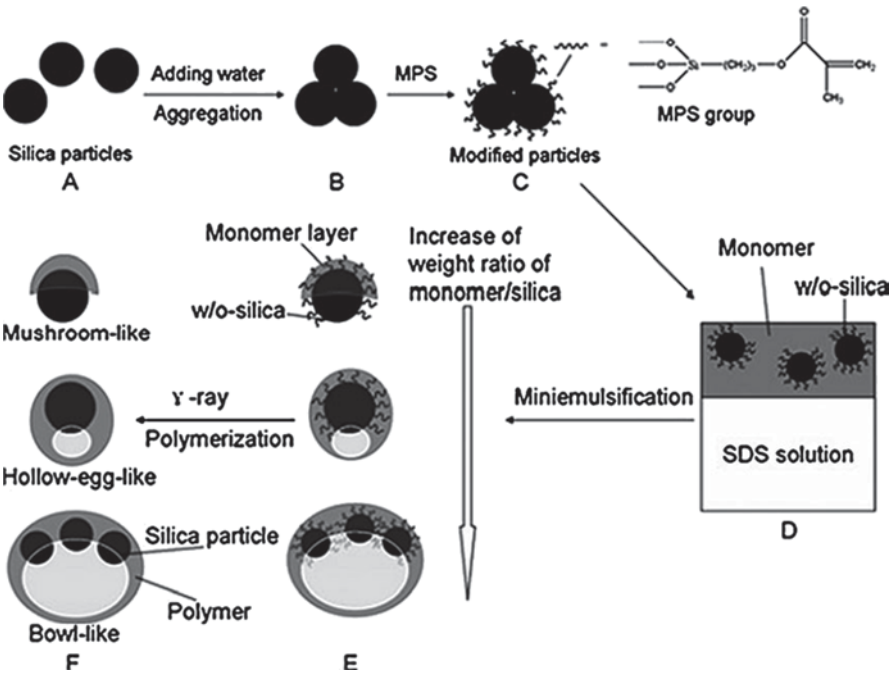

Fig. 13.5 Formation of asymmetric PS/SiO_2 composites by radiation-initiated miniemulsion polymerization [34]. *w/o* without, *SDS* sodium dodecyl sulfate, *MPS* methacryloxypropyltrimethoxysilane

nanocomposites. The surfaces of PS were functionalized by carboxyl groups by using the initiator 4,4′-azobis(4-cyanovaleric acid) (ACVA), and silica surfaces were modified with amino groups by coupling the silane 3-aminopropyl-triethoxysilane, thus making the nanocomposites dual functional [35]. They further extended this approach to synthesize ternary Janus structures [36]. Oleic acid-functionalized iron oxides were mixed with styrene and tetraethoxysilane (TEOS) and a miniemulsion system under sonication was formed. Emulsion polymerization began upon the addition of 2,2-azobis-(isobutyronitrile), and phase separation occurred due to the decrease of affinity between PS chains and hydrophobic components. Eventually, ternary PS/Fe_3O_4@SiO_2 Janus nanocomposites were produced. Interestingly, iron oxides were embedded in silica, which was different from Teo's report, [37], where iron oxides were found inside PS spheres.

13.1.5 Applications of Janus Particles

Due to the distinct surface properties, Janus nanoparticles can be modified to be amphiphilic, thus making them extremely suitable as surfactants to emulsify immiscible liquids [38]. For example, Kim and coworkers stabilized nonspherical emulsion drops with amphiphilic particles [39]. On the other hand, Janus nanoparticles that have magnetic components possess potential application in manipulation of devices

and imaging [13]. Kim et al. managed to control the movement direction of Janus particles in a microfluidic device by rotating the magnetic field [40]. With QDs embedded in the polymer matrix of the Fe_3O_4/polymer Janus particles, Yin et al. demonstrated interesting imaging capability of the Janus composites. Aligned in the external magnetic field, when the Fe_3O_4-doped side faced upward the particle displayed red-brown in daylight and black under UV. When the QD-embedded hemisphere faced upward, the particle showed white in daylight and blue under UV [41]. Xu et al. fabricated Au/Fe_3O_4 nanoparticles and conjugated Herceptin and Platin via stepwise functionalization to achieve targeted drug delivery. The conjugates released the drugs faster in mild acidic environment [17]. The Janus nanoparticles were also found capable of serving as catalyst. Seh et al. [42] tested the catalytic properties of TiO_2-coated Au nanoparticles in the reduction of 4-nitrophenol to 4-aminophenol and found that the Janus nanoparticles catalyzed the reaction as fast as the bare Au nanoparticles in the first cycle but could be reused for up to five cycles without much loss of activity. However, reports of delicate Janus nanoparticles for biomedical application via surface functionalization remain rather limited, mainly due to the complexity of chemistry involved. Shi's group has been working on Janus nanocomposites and developed a unique dual surface-functionalized Janus structure, successfully achieving cell targeting and drug delivery simultaneously [43].

13.2 Design and Development of Dual Surface-Functionalized SJNCs

13.2.1 Synthesis of SJNCs

Based on the previous work [35, 36], Wang et al. successfully fabricated a superparamagnetic Janus nanocomposites (SJNCs) of PS/Fe_3O_4@SiO_2 with both surfaces bearing functional groups. The nanocomposites are synthesized by a one-pot combination of miniemulsion followed by sol–gel reaction. In short, the oil phase (styrene monomers; TEOS; hexadecane; oleic acid capped iron oxides, OAIOs) is mixed with the aqueous phase to generate a miniemulsion system in the presence of sodium dodecyl sulfate as surfactant. One hour after styrene polymerization is triggered by 4,4′-ACVA) at 80 °C, NaOH is added to initiate silica formation via sol–gel reaction (Fig. 13.6).

The transmission electron microscopic (TEM) observation reveals that SJNCs are composed of a PS core covered by a half shell of silica embedded with Fe_3O_4 nanoparticles. From TEM image (Fig. 13.7), it can be derived that the SJNCs have diameters of around 300 nm, with the PS core of about 200 nm, and the Fe_3O_4@ Silica hybrid shell of around 100 nm thick. This is consistent with the dynamic light scattering (DLS) data (Fig. 13.9), displaying an average size of 313 nm with a polydispersity index (PDI) of 0.090. This indicates very narrow distribution of Janus nanocomposite diameters. As shown in the energy dispersive spectroscopy (EDS) spectra (Fig. 13.8b) accompanied with scanning transmission electron microscopic

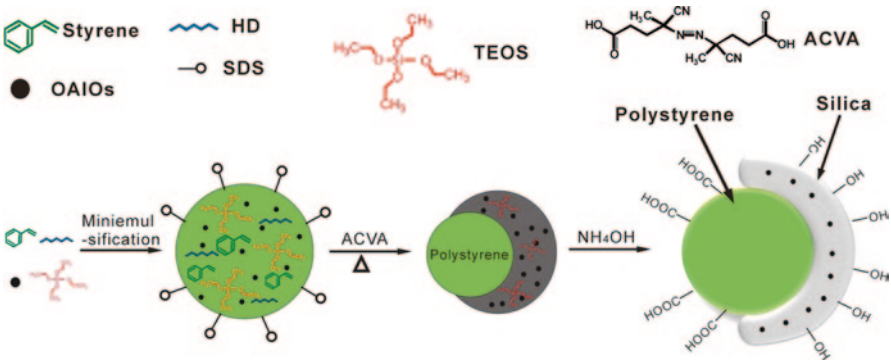

Fig. 13.6 Schematic illustration of the formation of polystyrene/Fe_3O_4@silica superparamagnetic Janus nanocomposites (SJNCs) [43]. *ACVA* 4-cyanovaleric acid, *TEOS* tetraethoxysilane, *SDS* sodium dodecyl sulfate, OAIOs oleic acid capped iron oxides, HD hexadecane

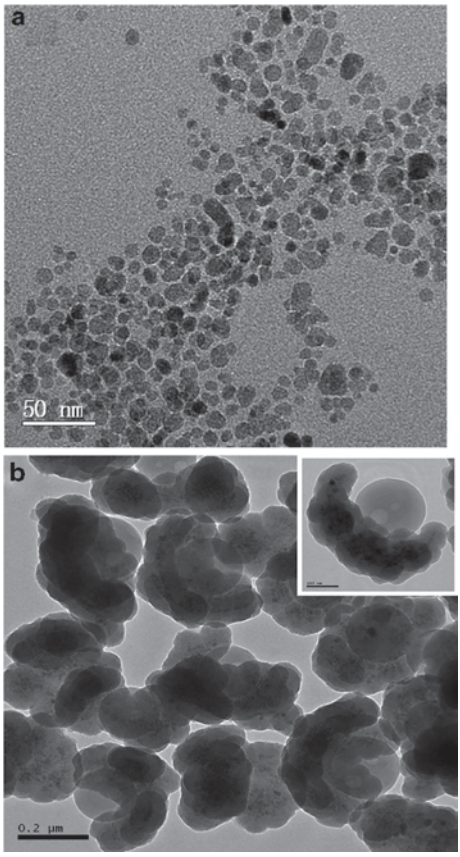

Fig. 13.7 TEM images of **a** oleic acid modified Fe_3O_4 nanoparticles (OAIOs; scale bar denotes 50 nm), and **b** the dual functionalized polystyrene/Fe_3O_4@silica Janus nanoparticles, the scale bar is 200 nm (*inset image* is the magnified image of one nanocomposite particle, scale bar is 100 nm) [43]

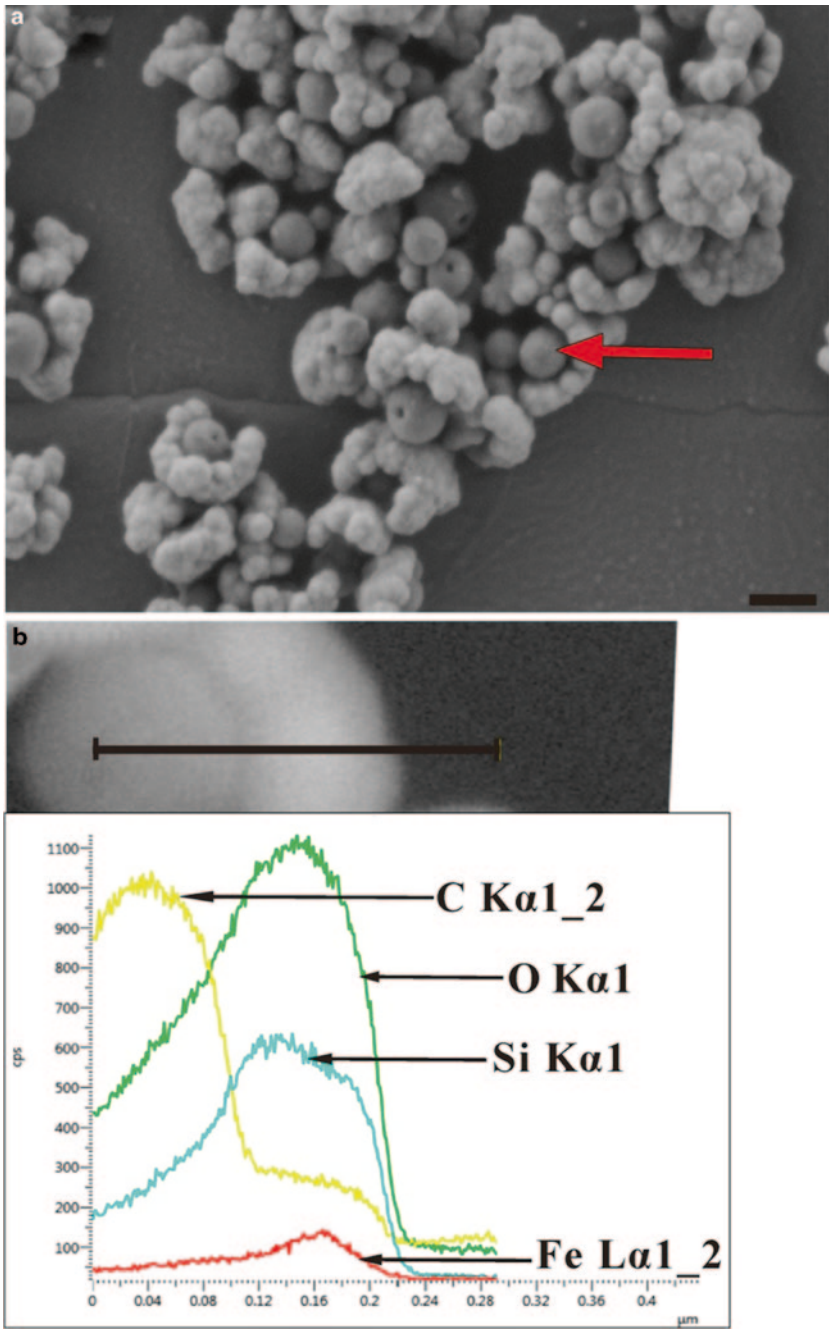

Fig. 13.8 **a** STEM image of the polystyrene/Fe_3O_4@silica Janus nanoparticles, scale bar denotes 200 nm. **b** Elemental mapping of one nanocomposite particle as pointed out by the *red arrow* in **(a)** [43]

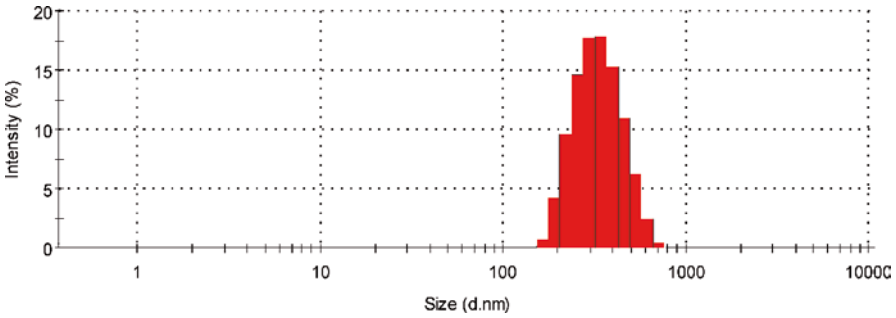

Fig. 13.9 DLS data of Janus nanocomposites suspended in deionized (DI) water [43].

(STEM) image, the core shows signal mainly from C and O with minor signals of Si and Fe coming from the hybrid shell at the back of the core. On the other hand, there are stronger signals from Si and Fe from the shell, compared to the core portion. These results indicate that the core of SJNCs is composed of pure polymer, which is PS in this case, while the shell is composed of iron oxide and silica. The observation that iron oxide nanoparticles are present in silica shell other than PS core is consistent with the results in the previous report [36]. But similarly, it is proposed that it is the phase separation between inorganic and organic components during polymerization followed by sol–gel reaction of TEOS that leads to the formation of SJNCs. When PS chains are formed during the miniemulsion polymerization, they tend to drive away the styrene monomers eccentrically, which also contain TEOS and OAIOs. The addition of NH_4OH initiate the sol–gel reaction of TEOS as well as the transformation of oleic acid to oleate. As a result, OAIOs have increased affinity to TEOS and are incorporated in the silica, rather than PS after condensation. It is possible under favorable thermodynamic condition (80 °C) that the silanol groups (–Si–OH) on the silica surface react with the carboxyl groups (–COOH) introduced by ACVA on the PS surface and form –Si–O–C– bonds. Therefore, once silica is formed from condensation, it grows along the curvature of PS particle surface to make a half shell to generate dual-functionalized SJNCs exhibiting anisotropy in both composition and surface properties.

Fourier transform infrared spectroscopy (FTIR) examination (Fig. 13.10a) shows that peaks from silica vibrations in the range of 800–1250 cm^{-1} are very strong, while the peaks at 2850 and 2920 cm^{-1} represent –CH stretching. The peak at 1712 cm^{-1} (Fig. b) can be assigned to carboxyl groups on the PS surface, with its weak intensity due to low quantities. Besides, the peaks at 1450 and 1500 cm^{-1} are attributed to the C═C frame stretching vibration in aromatic ring, while the peaks at 700 and 760 cm^{-1} are characteristic of single-replaced phenyl ring [44, 45]. The peak from –Si–O–C– bond is at around 1100 cm^{-1} but cannot be observed, possibly due to the overlapping with the strong signal from silica vibrations in the same range [43].

Due to the property of Fe_3O_4 nanoparticles, both OAIOs and SJNPs were superparamagnetic, exhibiting negligible magnetic remanence (Fig. 13.11), which endows SJNPs the ability to be redispersed after the external magnetic field is

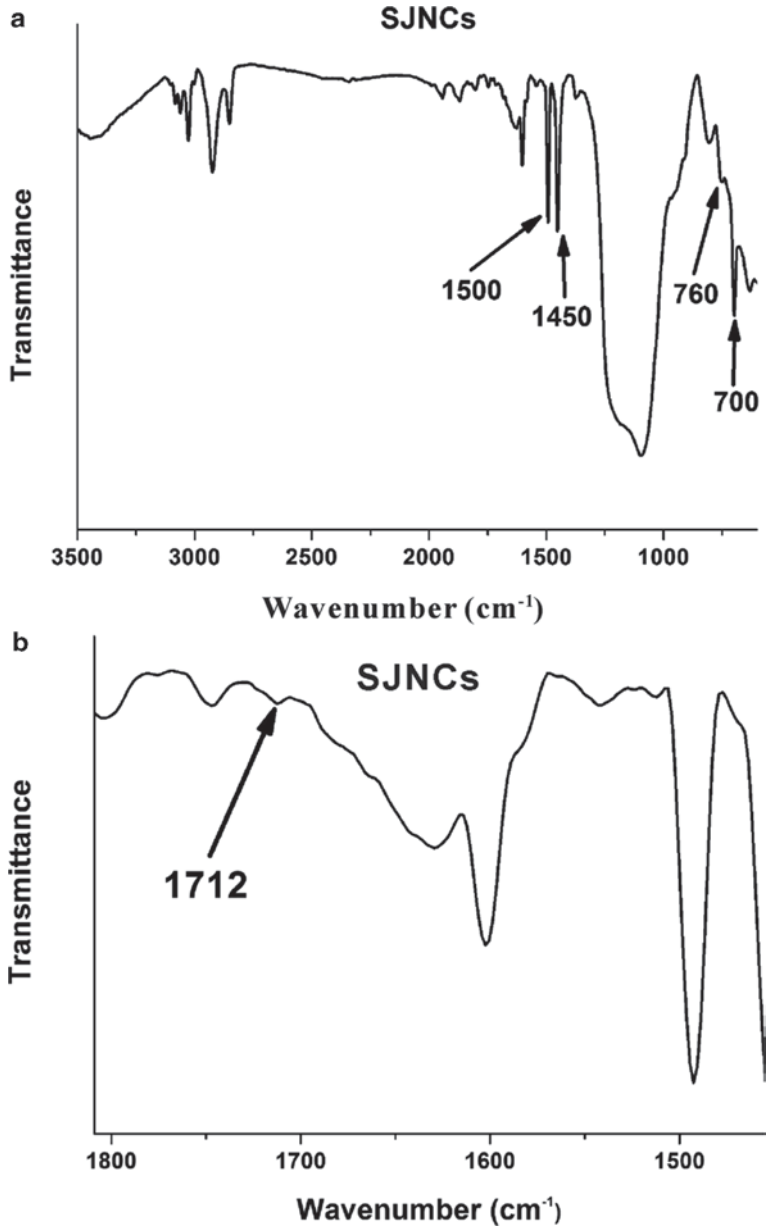

Fig. 13.10 **a** FTIR spectra of Polystyrene/Fe_3O_4@Silica Janus nanoparticles. **b** Magnified area (1450–1800 cm^{-1}) of spectra (**a**) [43]. *SJNCs* surface-functionalized superparamagnetic Janus nanocomposites

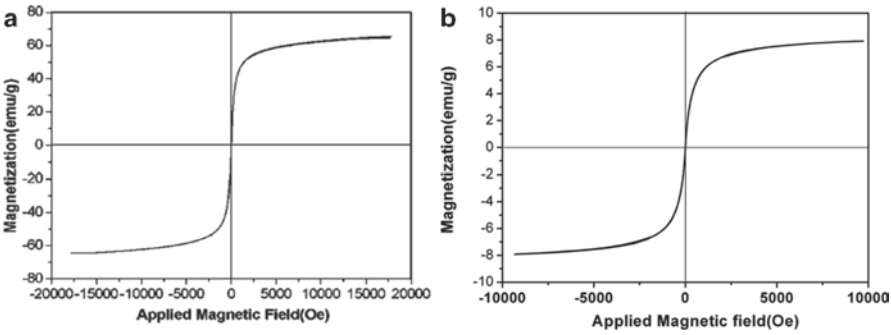

Fig. 13.11 Magnetization curves of **a** oleic acid-modified iron oxide nanoparticles. **b** superparamagnetic Janus nanoparticles at room temperature

removed. The superparamagnetism provided opportunities for applications in MRI, hyperthermia, and magnetic targeting.

13.3 Biomedical Application Evaluation

13.3.1 Surface Functionalization, Drug Loading and Release

Folic acid (FA) is a vitamin essential for cell proliferation. The cellular uptake of FA is mediated by the protein known as folate receptor [46]. Folate receptors can facilitate cellular internalization after binding to FA via receptor-mediated endocytosis [46–50]. Folate receptors are significantly overexpressed in malignant tissues [46, 51–54], which makes FA a widely used targeting ligand toward tumor cells [55–61]. Because the PS surfaces are also decorated with carboxyl groups, poly(ethylene glycol; PEG) bis-amine with (NH_2–PEG–NH_2) is taken as a linker. First, FA is linked to one amino ending group of NH_2–PEG–NH_2 and then the PEG–FA is functionalized to the PS surfaces via the other amino group (Fig. 13.12a).

Doxorubicin (DOX) is selected as the model drug to study the drug loading performance of SJNCs. DOX, with the trade name Adriamycin, is a cancer chemotherapeutic drug. It was discovered in the 1950s and has been widely studied by investigators throughout the world since then. DOX is often used in its hydrochloride salt form, interacting with DNA by intercalation and inhibition of macromolecular biosynthesis, thus preventing DNA chains from replication [62–65] _ENREF_1_ENREF_1_ENREF_1 _ENREF_3. However, DOX has many adverse effects, among which cardiotoxicity could cause death. It is proposed that DOX be conjugated to the hybrid shell surfaces via hydrazone bonds. A hydrazone bond is relatively stable at physiological condition (pH 7.2∼7.4) but could break at endocytic condition

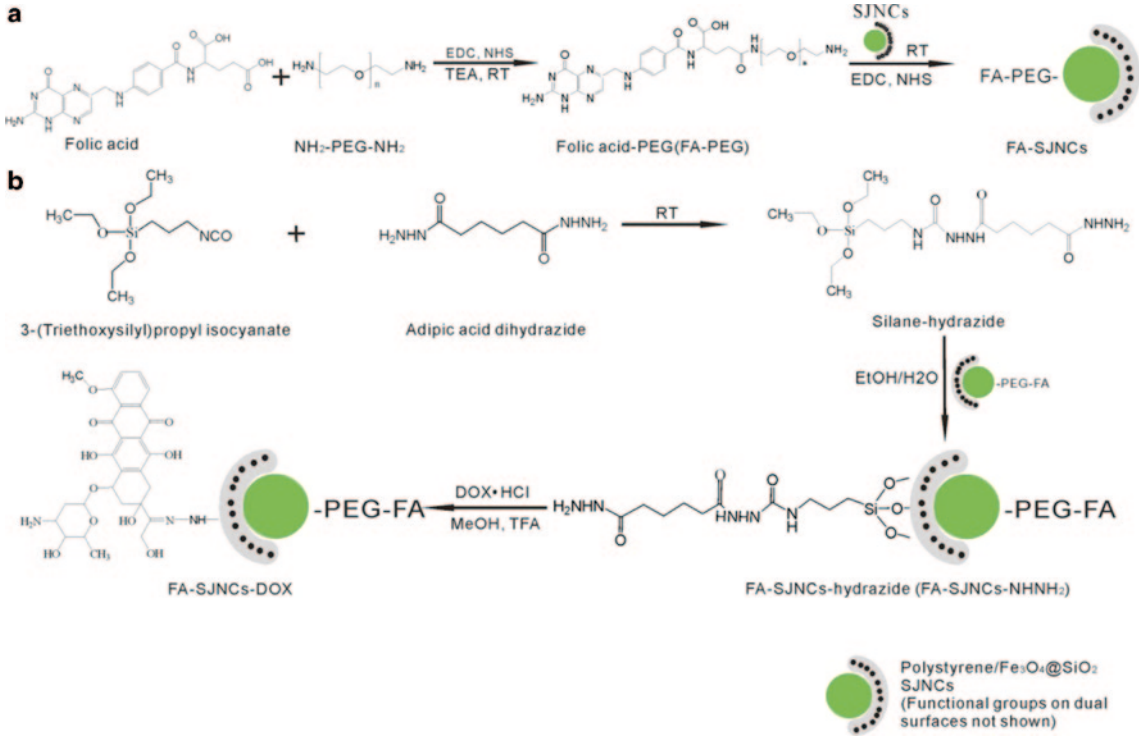

Fig. 13.12 Schematic drawing of **a** FA functionalization of polystyrene core surface and **b** DOX loading onto the Fe_3O_4@silica hybrid shell surface [43]. *FA* folic acid, *PEG* poly(ethylene glycol), *SJNC* superparamagnetic Janus nanocomposites

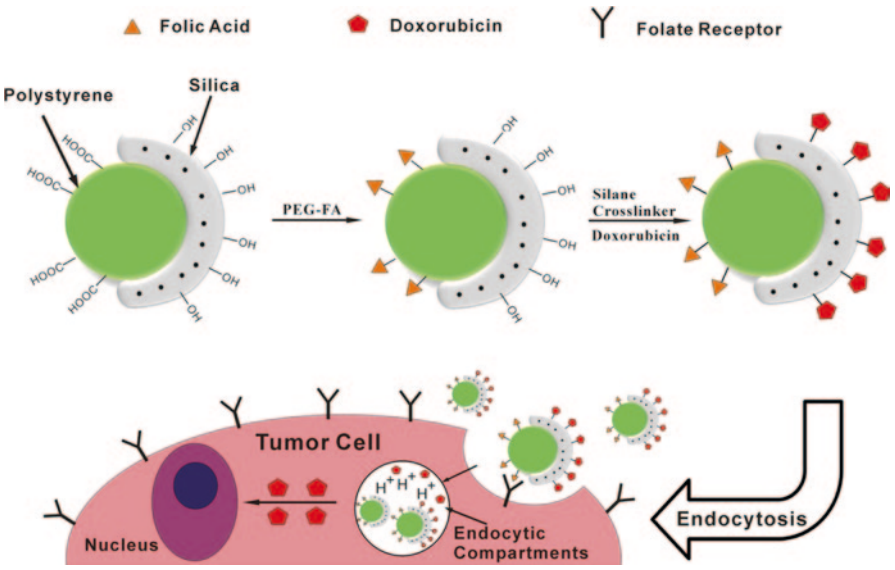

Fig. 13.13 Schematic illustration of FA conjugation and drug loading onto SJNCs and subsequent cell internalization through endocytosis [43]

(pH 4.5 ~ 6.5). This offers excellent opportunities for carrier systems because highly controlled release of DOX could significantly reduce the side effects [3, 66–70].

As shown in Fig. 13.12b, a silane-bearing hydrazide ending group is synthesized from 3-(triethoxysilyl)propyl isocyanat and adipic acid dihydrazide via carbodiimide-mediated coupling first. Then the Fe_3O_4/silica shell surfaces are modified with this silane–hydrazide cross-linker. Finally, DOX is conjugated to the hybrid shell surfaces via hydrazone bonds. It is hypothesized that the targeted SJNCs bearing anticancer drug could be internalized by tumor cells via folate receptor-mediated endocytosis and release DOX faster in endocytic compartments to achieve cytotoxicity (Fig. 13.13). In this way, less amount of drug was released during physiological conditions due to the relatively high stability of hydrazone bonds and side effects of DOX could be reduced.

Ultraviolet–visible (UV–Vis) spectroscopy confirms the conjugation of PEG–FA by exhibiting a broad shoulder centered at 363 nm (Fig. b), which is characteristic of FA [58, 71]. The low intensity is possibly due to the small amount of PEG–FA functionalized on the surfaces.

In the FTIR spectra (Fig. 13.14a), compared to FA–SJNCs, the hydrazide-modified FA–SJNCs (FA–SJNCs–$NHNH_2$) exhibit a small peak around at 1550 cm^{-1}, which is attributed to the ending amino groups of hydrazide. The relatively high and broad peak at 1670 cm^{-1} could be assigned to C═O bonds in the amide groups in silane–hydrazide. After DOX loading, the UV–Vis spectra of FA–SJNCs–DOX generates a broad shoulder with the peak at around 517 nm compared to the hydrazide-modified Janus nanocomposites (Fig. b). The deviation of this peak from the characteristic peak of pure DOX at around 480 nm is perhaps due to the covalent

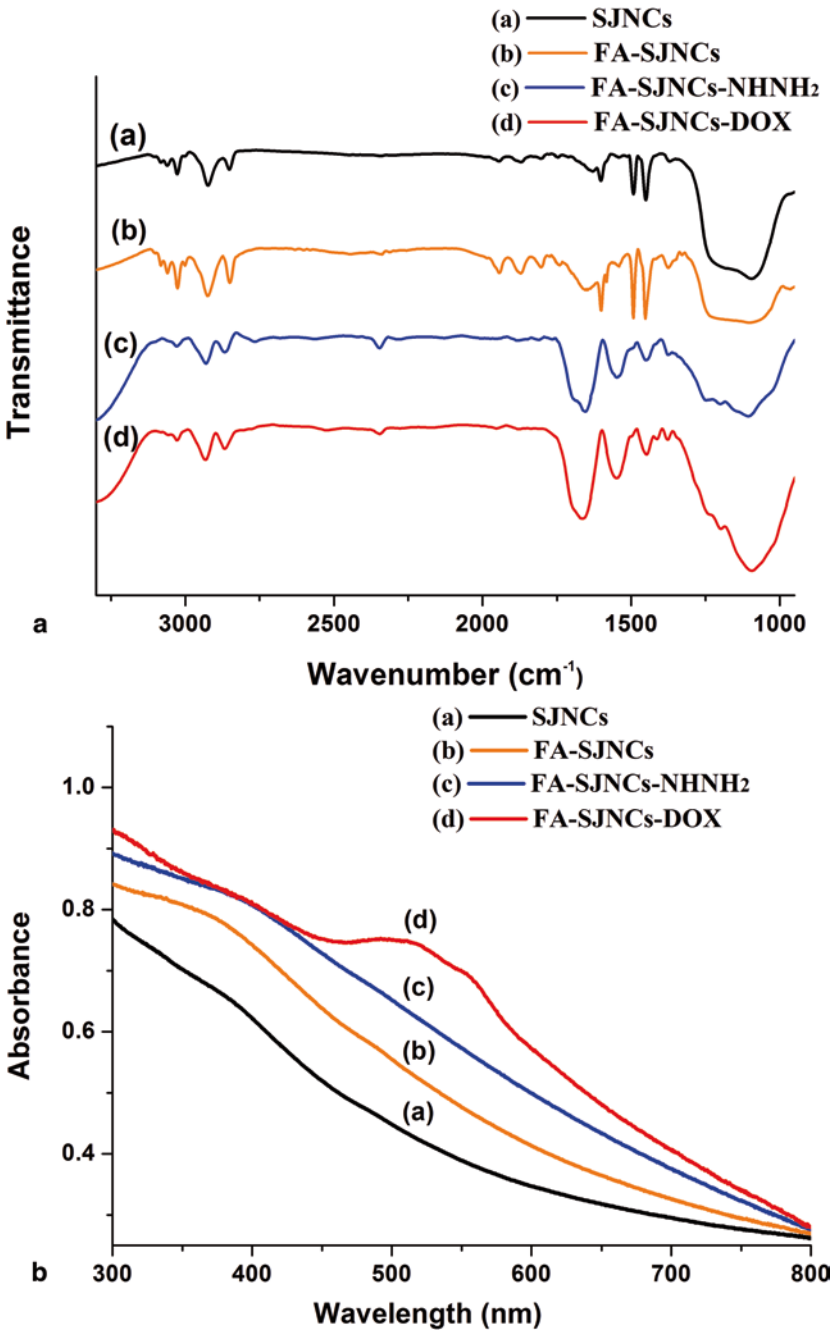

Fig. 13.14 FT-IR (**a**) and UV–V (**b**) is spectra of a SJNCs *(a),* FA–SJNCs *(b),* FA–SJNCs–NHNH2 *(c),* and FA–SJNCs–DOX *(d)* [43]. *FA* folic acid, *SJNC* superparamagnetic Janus nanocomposites, *DOX* doxyrubicin

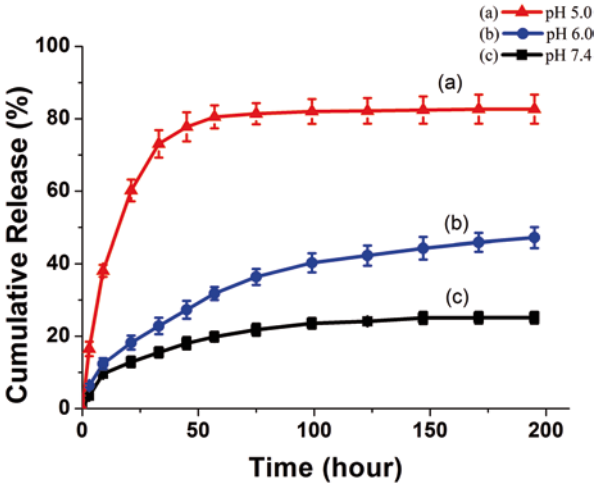

Fig. 13.15 DOX release profiles from DOX-conjugated SJNCs at **a** pH 5.0, **b** pH 6.0, and **c** pH 7.4

bonding formed between DOX and silica surfaces. Similar results were found by Q. Hu [72]. These results clearly confirmed the successful conjugation of DOX to the hybrid shell surface via hydrazone bonding. The DOX loading capacity is determined to be 2.08 ± 0.2 wt% using the subtraction method.

The pH dependence of DOX release behaviors are monitored in buffer solutions with different pH values. It can be seen in Fig. 13.15 that at pH 7.4, which simulated the physiological condition, accumulative DOX release after 195 h was about 25.1%. In contrast, at pH 5.0 and pH 6.0, which were similar to the environment in endocytic compartments and tumor sites, DOX releases were much faster and the accumulative releases reached 82.6 and 47.1% after 195 h, respectively. This observation is consistent with the acid-sensitive nature of hydrazone bonding. As the concentration of H^+ increases in the environment, the hydrolysis of hydrazone bond accelerates, thus releasing more DOX from the conjugates.

13.3.2 Cell Cytotoxicity Analysis

Targeting effect and pH-triggered DOX release are combined and evaluated against the human breast cell line MDA-MB-231 overexpressing folate receptors. SJNCs with or without drugs are incubated with cells for a period of 4 h. To avoid the potential aggregation issue from the electrostatic attraction between the nanocomposites and the protein in the cell culture media, Hank's balanced salts buffer solution (HBSS) is used to disperse nanocomposites. Then the cells are washed and incubated for another 48 h in fresh cell culture media before proceeding to cell viability evaluation (Fig. 13.16).

Two control experiments were designed to test the targeting effect of FA:

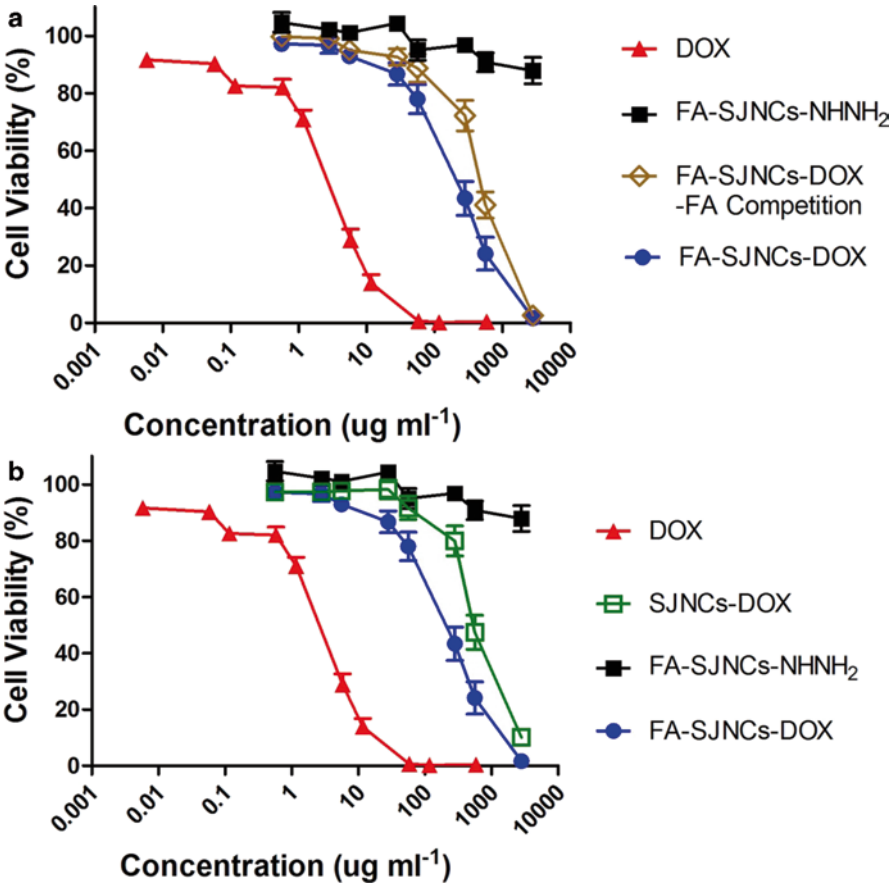

Fig. 13.16 Cytotoxicity assay curves of **a** targeted FA–SJNCs–DOX versus targeted FA–SJNCs–DOX in free FA competition. **b** Targeted FA–SJNCs–DOX versus non-targeted SJNCs–DOX against MDA-MB-231 cell line. Cytotoxicity assay curves for DOX and nanocomposites bearing FA but none drug (FA–SJNCs–NHNH2) are displayed as reference in both graphs [43]. *FA* folic acid, *SJNC* superparamagnetic Janus nanocomposites, *DOX* doxyrubicin

1. The drug bearing and FA-conjugated nanocomposites (FA–SJNCs–DOX) were subjected to a free FA competition experiment. Free FA is dissolved in the HBSS buffer to make a concentration of 1 mM. Then FA–SJNCs–DOX are dispersed in this buffer and incubated with cells.
2. The drug-bearing nanocomposites without FA (SJNCs–DOX) are dispersed in HBSS buffer and subjected to subsequent incubation with cells.

The curve of targeted FA–SJNCs–DOX lies to the right of the curve for DOX because the FA–SJNCs–DOX are much heavier than free DOX (Fig. 13.16). All curves show similar inhibitor response characteristic. However, compared with

Table 13.1 IC50 values of DOX, targeted FA–SJNCs–DOX, FA–SJNCs–DOX in free folic acid competition, and nontargeted SJNCs–DOX against MDA-MB-231 cells [43]

	DOX	FA–SJNCs–DOX	FA–SJNCs–DOX–FA competition	SJNCs–DOX
IC50 (μg ml^{-1})	3.3 ± 0.3	255.3 ± 55.1	781.2 ± 163.0	1030.2 ± 416.1

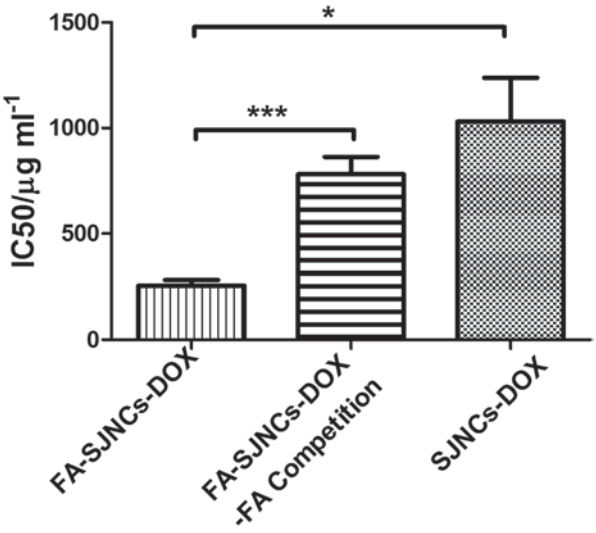

Fig. 13.17 Comparison of IC50 values from different experimental groups. $^{*}p<0.05$, $^{***}p<0.001$ [43]. *FA* folic acid, *SJNC* superparamagnetic Janus nanocomposites, *DOX* doxyrubicin

targeted FA–SJNCs–DOX, the cytotoxicity curve for the targeted FA–SJNCs–DOX in free FA competition experiment shows less cytotoxicity when treated with the same dosage. The same trend is observed when nontargeted SJNCs–DOX were incubated with cancer cells. The viability of the nontargeted group is much higher than the targeted group. To further analyze the cytotoxicity statistically, the IC50 values of three groups were calculated and displayed in Table 13.1. As shown in Fig. 13.17, the IC50 value of targeted FA–SJNCs–DOX conjugates is calculated at 255.3 ± 55.1 μg ml^{-1}. This value is significantly lower than that of the nontargeted group (IC50 = 781.2 ± 163.0 μg ml^{-1}, $p<0.001$) and the free FA competition group (IC50 = 1030.2 ± 416.1 μg ml^{-1}, $p<0.05$). These results clearly indicate the cell targeting effects of the dual-functionalized SJNCs.

Compared to the nontargeted and the free FA competition groups, much more targeted FA–SJNCs–DOX conjugates are internalized by tumor cells through the folate-receptor-mediated endocytosis. Once the FA–SJNCs–DOX conjugates are in the endocytic compartments, these are able to release DOX at a much faster rate, thus significantly enhancing the efficacy of DOX. The highly selective targeting of FA–SJNCs–DOX conjugates could also reduce cardiac side effects of DOX in cancer therapy.

13.4 Summary

Janus particles offer more opportunities with their novel configuration. As researchers understand the mechanism better, more structures with unique properties will appear. For biomedical applications that require increasingly higher integrity, Janus structures can serve as a versatile platform with great potential.

References

1. D.L. Shi, Integrated multifunctional nanosystems for medical diagnosis and treatment. Adv. Funct. Mater. **19**(21), 3356–3373 (2009)
2. M.E. Gindy, R.K. Prud'homme, Multifunctional nanoparticles for imaging, delivery and targeting in cancer therapy. Expert. Opin. Drug. Deliv. **6**(8), 865–878 (2009)
3. C.H. Lee, S.H. Cheng, I.P. Huang, J.S. Souris, C.S. Yang, C.Y. Mou, L.W. Lo, Intracellular pH-responsive mesoporous silica nanoparticles for the controlled release of anticancer chemotherapeutics. Angew. Chem. Int. Ed. Engl. **49**(44), 8214–8219 (2010)
4. F.M. Kievit, O. Veiseh, N. Bhattarai, C. Fang, J.W. Gunn, D. Lee, R.G. Ellenbogen, J.M. Olson, M.Q. Zhang, PEI-PEG-chitosan-copolymer-Coated iron oxide nanoparticles for safe gene delivery: synthesis, complexation, and transfection. Adv. Funct. Mater. **19**(14), 2244–2251 (2009)
5. G. Liu, J. Xie, F. Zhang, Z.Y. Wang, K. Luo, L. Zhu, Q.M. Quan, G. Niu, S. Lee, H. Ai, X.Y. Chen, N-Alkyl-PEI-functionalized iron oxide nanoclusters for efficient siRNA delivery. Small **7**(19), 2742–2749 (2011)
6. I. Ojea-Jimenez, L. Garcia-Fernandez, J. Lorenzo, V. F. Puntes, Facile preparation of cationic gold nanoparticle-bioconjugates for cell penetration and nuclear targeting. ACS. Nano. **6**(9), 7692–7702 (2012)
7. H.S. Cho, Z. Dong, G.M. Pauletti, J. Zhang, H. Xu, H. Gu, L. Wang, R.C. Ewing, C. Huth, F. Wang, D. Shi, Fluorescent, superparamagnetic nanospheres for drug storage, targeting, and imaging: a multifunctional nanocarrier system for cancer diagnosis and treatment. ACS. Nano. **4**(9), 5398–5404 (2010)
8. A.D. Quach, G. Crivat, M.A. Tarr, Z. Rosenzweig, Gold nanoparticle-quantum dot-polystyrene microspheres as fluorescence resonance energy transfer probes for bioassays. J. Am. Chem. Soc. **133**(7), 2028–2030 (2011)
9. M. Lattuada, T.A. Hatton, Synthesis, properties and applications of Janus nanoparticles. Nano. Today **6**(3), 286–308 (2011)
10. C.A. Serra, Z.Q. Chang, Microfluidic-assisted synthesis of polymer particles. Chem. Eng. Technol. **31**(8), 1099–1115 (2008)
11. D. Dendukuri, D.C. Pregibon, J. Collins, T.A. Hatton, P.S. Doyle, Continuous-flow lithography for high-throughput microparticle synthesis. Nat. Mater. **5**(5), 365–369 (2006)
12. D. Dendukuri, P.S. Doyle, The synthesis and assembly of polymeric microparticles using microfluidics. Adv. Mater. **21**(41), 4071–4086 (2009)
13. J. Hu, S.X. Zhou, Y.Y. Sun, X.S. Fang, L.M. Wu, Fabrication, properties and applications of Janus particles. Chem. Soc. Rev. **41**(11), 4356–4378 (2012)
14. S.H. Hu, X.H. Gao, Nanocomposites with spatially separated functionalities for combined imaging and magnetolytic therapy. J. Am. Chem. Soc. **132**(21), 7234–7237 (2010)
15. K.H. Roh, D.C. Martin, J. Lahann, Biphasic Janus particles with nanoscale anisotropy. Nat. Mater. **4**(10), 759–763 (2005)
16. K.H. Roh, M. Yoshida, J. Lahann, Compartmentalized, multiphasic nanocolloids with potential applications in drug delivery and biomedical imaging. Materialwiss. Werkst. **38**(12), 1008–1011 (2007)

17. C.J. Xu, B.D. Wang, S.H. Sun, Dumbbell-like Au-Fe_3O_4 nanoparticles for target-specific platin delivery. J. Am. Chem. Soc. **131**(12), 4216–4217 (2009)
18. A. Perro, S. Reculusa, F. Pereira, M.H. Delville, C. Mingotaud, E. Duguet, E. Bourgeat-Lami, S. Ravaine, Towards large amounts of Janus nanoparticles through a protection-deprotection route. Chem. Commun. **44**, 5542–5543 (2005)
19. L. Nagle, D. Ryan, S. Cobbe, D. Fitzmaurice, Templated nanoparticle assembly on the surface of a patterned nanosphere. Nano. Lett. **3**(1), 51–53 (2003)
20. M.A. Correa-Duarte, V. Salgueirino-Maceira, B. Rodriguez-Gonzalez, L.M. Liz-Marzan, A. Kosiorek, W. Kandulski, M. Giersig, Asymmetric functional colloids through selective hemisphere modification. Adv. Mater. **17**(16), 2014 (2005)
21. C. Bae, J. Moon, H. Shin, J. Kim, M.M. Sung. Fabrication of monodisperse asymmetric colloidal clusters by using contact area lithography (CAL). J. Am. Chem. Soc. **129**(46), 14232–14239 (2007)
22. M.D. McConnell, M.J. Kraeutler, S. Yang, R.J. Composto. Patchy and multiregion janus particles with tunable optical properties. Nano. Lett. **10**(2), 603–609 (2010)
23. L. Zhang, F. Zhang, W.F. Dong, J.F. Song, Q.S. Huo, H.B. Sun, Magnetic-mesoporous Janus nanoparticles. Chem. Commun. **47**(4), 1225–1227 (2011)
24. J. Zhang, J. Jin, H.Y. Zhao, Surface-initiated free radical polymerization at the liquid-liquid interface: a one-step approach for the synthesis of amphiphilic janus silica particles. Langmuir **25**(11), 6431–37 (2009)
25. L. Hong, S. Jiang, S. Granick, Simple method to produce Janus colloidal particles in large quantity. Langmuir **22**(23), 9495–9499 (2006)
26. K.M. Chen, Y. Zhu, Y.F. Zhang, L. Li, Y. Lu, X.H. Guo, Synthesis of magnetic spherical polyelectrolyte brushes. Macromolecules **44**(3), 632–639 (2011)
27. A. Misra, M.W. Urban, Acorn-shape polymeric nano-colloids: synthesis and self-assembled films. Macromol. Rapid. Commun. **31**(2), 119–127 (2010)
28. K. Nakahama, H. Kawaguchi, K. Fujimoto, A novel preparation of nonsymmetrical microspheres using the langmuir-blodgett technique. Langmuir **16**(21), 7882–7886 (2000)
29. S.Y. Zhang, Z. Li, S. Samarajeewa, G.R. Sun, C. Yang, K.L. Wooley, Orthogonally dual-clickable Janus nanoparticles via a cyclic templating strategy. J. Am. Chem. Soc. **133**(29), 11046–11049 (2011)
30. M. Bradley, J. Rowe, Cluster formation of Janus polymer microgels. Soft. Matter. **5**(16), 3114–3119 (2009)
31. S. Lone, S.H. Kim, S.W. Nam, S. Park, J. Joo, I.W. Cheong. Microfluidic synthesis of Janus particles by UV-directed phase separation. Chem. Commun. **47**(9), 2634–2636 (2011)
32. M. Feyen, C. Weidenthaler, F. Schuth, A.H. Lu, Regioselectively controlled synthesis of colloidal mushroom nanostructures and their hollow derivatives. J. Am. Chem. Soc. **132**(19), 6791–6799 (2010)
33. J.A. Gong, X.H. Zu, Y.H. Li, W. Mu, Y.L. Deng, Janus particles with tunable coverage of zinc oxide nanowires. J. Mater. Chem. **21**(7), 2067–2069 (2011)
34. X.P. Ge, M.Z. Wang, Q. Yuan, H. Wang, X.W. Ge, The morphological control of anisotropic polystyrene/silica hybrid particles prepared by radiation miniemulsion polymerization. Chem. Commun. **19**, 2765–2767 (2009)
35. Y. Wang, H. Xu, W. Qiang, H. Gu, D. Shi. Asymmetric composite nanoparticles with anisotropic surface functionalities. J. Nanomater. **2009**, 1–5 (2009)
36. Y.L. Wang, H. Xu, Y.S. Ma, F.F. Guo, F. Wang, D.L. Shi. Facile one-pot synthesis and morphological control of asymmetric superparamagnetic composite nanoparticles. Langmuir **27**(11), 7207–7212 (2011)
37. B.M. Teo, S.K. Suh, T.A. Hatton, M. Ashokkumar, F. Grieser, Sonochemical synthesis of magnetic Janus nanoparticles. Langmuir **27**(1), 30–33 (2011)
38. Q. Xu, X. Kang, R.A. Bogomolni, S. Chen, Controlled assembly of Janus nanoparticles. Langmuir **26**(18), 14923–14928 (2010)
39. J.W. Kim, D. Lee, H.C. Shum, D.A. Weitz, Colloid surfactants for emulsion stabilization. Adv. Mater. **20**(17), 3239–3243 (2008)

40. S.H. Kim, J.Y. Sim, J.M. Lim, S.M. Yang, Magnetoresponsive microparticles with nanoscopic surface structures for remote-controlled locomotion. Angew. Chem. Int. Ed. Engl. **49**(22), 3786–3790 (2010)
41. S.N. Yin, C.F. Wang, Z.Y. Yu, J. Wang, S.S. Liu, S. Chen, Versatile bifunctional magnetic-fluorescent responsive Janus supraballs towards the flexible bead display. Adv. Mater. **23**(26), 2915–2919 (2011)
42. Z.W. Seh, S.H. Liu, S.Y. Zhang, K.W. Shah, M.Y. Han, Synthesis and multiple reuse of eccentric Au@TiO_2 nanostructures as catalysts. Chem. Commun. **47**(23), 6689–6691 (2011)
43. F. Wang, G.M. Pauletti, J. Wang, J. Zhang, R.C. Ewing, Y. Wang, D. Shi, Dual surface-functionalized Janus nanocomposites of polystyrene/Fe(3)O(4)@SiO(2) for simultaneous tumor cell targeting and stimulus-induced drug release. Adv. Mater. **25**(25), 3485–3489 (2013)
44. L.B. Feng, H. Li, M.J. Yang, X.W. Wang, Synthesis of SiO_2/polystyrene hybrid particles via an esterification method. Colloid. Polym. Sci. **288**(6), 673–680 (2010)
45. K. Zhang, W. Wu, H. Meng, K. Guo, J.F. Chen, Pickering emulsion polymerization: preparation of polystyrene/nano-SiO_2 composite microspheres with core-shell structure. Powder Technol. **190**(3), 393–400 (2009)
46. R.J. Lee, P.S. Low, Folate as a targeting device for proteins utilizing folate receptor-mediated endocytosis. Methods Mol. Med. **25**, 69–76 (2000)
47. B. Stella, S. Arpicco, M.T. Peracchia, D. Desmaele, J. Hoebeke, M. Renoir, J. D'Angelo, L. Cattel, P. Couvreur, Design of folic acid-conjugated nanoparticles for drug targeting. J. Pharm. Sci. **89**(11), 1452–1464 (2000)
48. C.P. Leamon, P.S. Low, Delivery of macromolecules into living cells–a method that exploits folate receptor endocytosis. Proc. Natl. Acad. Sci. U S A. **88**(13), 5572–76 (1991)
49. A.C. Antony, The biological chemistry of folate receptors, Blood **79**(11), 2807–2820 (1992)
50. K.G. Rothberg, Y.S. Ying, J.F. Kolhouse, B.A. Kamen, R.G.W. Anderson, The glycophospholipid-linked folate receptor internalizes folate without entering the clathrin-coated pit endocytic pathway. J. Cell. Biol. **110**(3), 637–649 (1990)
51. M.R. Buist, C.F.M. Molthoff, P. Kenemans, C.J.L.M. Meijer, Distribution of Ov-Tl-3 and Mov18 in normal and malignant ovarian tissue. J. Clin. Pathol. **48**(7), 631–636 (1995)
52. J.F. Ross, P.K. Chaudhuri, M. Ratnam, Differential regulation of folate receptor isoforms in normal and malignant-tissues in-vivo and in established cell-lines–physiological and clinical implications. Cancer **73**(9), 2432–2443 (1994)
53. P. Garinchesa, I. Campbell, P.E. Saigo, J.L. Lewis, L.J. Old, W.J. Rettig, Trophoblast and ovarian-cancer antigen-Lk26–sensitivity and specificity in immunopathology and molecular-identification as a folate-binding protein. Am. J. Pathol. **142**(2), 557–567 (1993)
54. M.D. Salazar, M. Ratnam, The folate receptor: what does it promise in tissue-targeted therapeutics? Cancer. Metastasis. Rev. **26**(1), 141–152 (2007)
55. K. Kono, M.J. Liu, J.M.J. Frechet, Design of dendritic macromolecules containing folate or methotrexate residues. Bioconjug. Chem. **10**(6), 1115–1121 (1999)
56. X.N. Fei, Y. Liu, C. Li, Folate conjugated chitosan grafted thiazole orange derivative with high targeting for early breast cancer cells diagnosis. J. Fluoresc. **22**(6), 1555–1561 (2012)
57. A.J. Shen, D.L. Li, X.J. Cai, C.Y. Dong, H.Q. Dong, H.Y. Wen, G.H. Dai, P.J. Wang, Y.Y. Li. Multifunctional nanocomposite based on graphene oxide for in vitro hepatocarcinoma diagnosis and treatment. J. Biomed. Mater. Res. A **100A**(9), 2499–2506 (2012)
58. S. Mahajan, V. Koul, V. Choudhary, G. Shishodia, A.C. Bharti, Preparation and in vitro evaluation of folate-receptor-targeted SPION-polymer micelle hybrids for MRI contrast enhancement in cancer imaging. Nanotechnology **24**(1), 015603 (2013)
59. J. Hou, Q. Zhang, X. Li, Y. Tang, M.R. Cao, F. Bai, Q. Shi, C.H. Yang, D.L. Kong, G. Bai, Synthesis of novel folate conjugated fluorescent nanoparticles for tumor imaging. J. Biomed. Mater. Res. A **99A**(4), 684–689 (2011)
60. M. Barz, F. Canal, K. Koynov, R. Zentel, M.J. Vicent, Synthesis and in vitro evaluation of defined HPMA folate conjugates: influence of aggregation on folate receptor (FR) mediated cellular uptake. Biomacromolecules **11**(9), 2274–2282 (2010)

61. J.M. Saul, A. Annapragada, J.V. Natarajan, R.V. Bellamkonda, Controlled targeting of liposomal doxorubicin via the folate receptor in vitro. J. Control. Release **92**(1–2), 49–67 (2003)
62. W.J. Pigram, W. Fuller, L.D. Hamilton, Stereochemistry of intercalation–interaction of daunomycin with DNA. Nat. New Biol. **235**(53), 17–19(1972)
63. R.L. Momparler, M. Karon, S.E. Siegel, F. Avila, Effect of adriamycin on DNA, RNA, and protein-synthesis in cell-free systems and intact-cells. Cancer. Res. **36**(8), 2891–2895 (1976)
64. F.A. Fornari, J.K. Randolph, J.C. Yalowich, M.K. Ritke, D.A. Gewirtz, Interference by doxorubicin with DNA unwinding in Mcf-7 breast-tumor cells. Mol. Pharmacol. **45**(4), 649–656 (1994)
65. J.W. Lown, Anthracycline and anthraquinone anticancer agents: current status and recent developments. Pharmacol. Ther. **60**(2), 185–214 (1993)
66. J.E. Lee, D.J. Lee, N. Lee, B.H. Kim, S.H. Choi, T. Hyeon. Multifunctional mesoporous silica nanocomposite nanoparticles for pH controlled drug release and dual modal imaging. J. Mater. Chem. **21**(42), 16869–16872 (2011)
67. X.Q. Yang, J.J. Grailer, S. Pilla, D.A. Steeber, S.Q. Gong, Tumor-targeting, pH-responsive, and stable unimolecular micelles as drug nanocarriers for targeted cancer therapy. Bioconjugate Chem. **21**(3), 496–504 (2010)
68. D.X. Lu, X.T. Wen, J. Liang, Z.W. Gu, X.D. Zhang, Y.J. Fan, A pH-sensitive nano drug delivery system derived from pullulan/doxorubicin conjugate. J. Biomed. Mater. Res. B **89B**(1), 177–183 (2009)
69. S.C. Wuang, K.G. Neoh, E.T. Kang, D.E. Leckband, D.W. Pack, Acid-sensitive magnetic nanoparticles as potential drug depots. AIChE. J. **57**(6), 1638–1645 (2011)
70. Y.L. Chang, X.L. Meng, Y.L. Zhao, K. Li, B. Zhao, M. Zhu, Y.P. Li, X.S. Chen, J.Y. Wang, Novel water-soluble and pH-responsive anticancer drug nanocarriers: doxorubicin-PAMAM dendrimer conjugates attached to superparamagnetic iron oxide nanoparticles (IONPs). J. Colloid. Interf. Sci. **363**(1), 403–409 (2011)
71. D. Cheng, G.B. Hong, W.W. Wang, R.X. Yuan, H. Ai, J. Shen, B.L. Liang, J.M. Gao, X.T. Shuai, Nonclustered magnetite nanoparticle encapsulated biodegradable polymeric micelles with enhanced properties for in vivo tumor imaging. J. Mater. Chem. **21**(13), 4796–4804 (2011)
72. Q.D. Hu, H. Fan, Y. Ping, W.Q. Liang, G.P. Tang, J. Li, Cationic supramolecular nanoparticles for co-delivery of gene and anticancer drug. Chem. Commun. **47**(19), 5572–5574 (2011)

Chapter 14
Protein Nanopatterning

Christopher N. Lam, Dongsook Chang and Bradley D. Olsen

14.1 Introduction

Enzymes and globular proteins are highly optimized to perform reactions [1], transport charges [4], or convert energy [5] with efficiencies, rates, gentle operating conditions, and molecular-level specificity that often exceed synthetic materials. For example, compared to traditional synthetic catalysts, enzymes have much higher turnover frequencies k_{cat} ranging from 10^{-1} to 10^{7} s^{-1} [6, 7]. Large substrate binding affinities ($\sim 1/K_m$) and substrate specificities (k_{cat}/K_m) lead to minimal side reactions. In addition, transmembrane ion transporters such as the Na^+/Ca^{2+} exchanger have essential physiological functions related to their structure [8]. At the core of photosynthesis are pigment proteins—molecules that bind both chlorophylls and carotenoids that lead to a concerted series of reactions that absorb light for conversion into chemical energy [9]. Finally, antibodies are known to have specific interactions with antigens due to geometrical, physical, and chemical complementarity between the antibody and antigen surfaces [10]. Research in recent decades has focused on harnessing and enhancing the potential of all these categories of proteins to develop novel biodegradable and renewable biofunctional materials for a myriad of biotechnological applications.

Due to their substrate specificity and high catalytic activity, globular proteins and enzymes have garnered interest for addressing multiple industrial challenges. Enzymes can be used as molecular sensors—for example, glucose [11, 12] and neurotoxin sensors [13–15]—and as a critical component in the enzyme-linked immunosorbent assay (ELISA). Enzymes have also proven to be beneficial for synthesizing drug compounds in the pharmaceutical industry [16], and they have found utility in numerous industrial applications as biocatalysts for laundry and dishwasher detergents [17], industrial synthetic chemistry [18–20], and the food

B. D. Olsen (✉) · C. N. Lam · D. Chang
Department of Chemical Engineering, Massachusetts Institute of Technology,
77 Massachusetts Avenue, Cambridge, MA 02139, USA
e-mail: bdolsen@mit.edu

M. Zhang et al. (eds.), *Carbon Nanomaterials for Biomedical Applications,*
Springer Series in Biomaterials Science and Engineering 5,
DOI 10.1007/978-3-319-22861-7_14

industry[21]. Biocatalytic devices for carbon sequestration [22], carbon dioxide reduction [23–25], and hydrogen production [26–28] have also been proposed utilizing enzymes. Biofuel cells have attracted significant attention, offering the possibility of consuming biomass as fuel and eliminating the need for both transition metal catalysts and electrolyte membranes due to the high specificity of the enzymatic reactions on both electrodes [29, 30]. Beyond biocatalysis, reaction centers (RCs) [31], photosynthetic complexes, [32], and fluorescent proteins [33] can be incorporated into light-harvesting materials for bioelectronics and energy applications. Protein materials have also found utility in developing surfaces for studies of cell growth and cell–surface interactions and for biomedical applications including tissue engineering [34, 35].

The goal of protein nanopatterning is to improve the function of biosensors, biocatalysts, bioelectronics, and biomedical materials through control over the position, orientation, and density of proteins presented within a bioactive material. Because proteins are fairly large compared to transition metal catalysts, it is often desirable to achieve a high density of proteins localized within a small area, improving catalytic rate in biocatalysts or signal to noise in sensors. The orientation of the protein and transport through thin film or bulk materials must be carefully controlled to enable efficient transport of substrates, products, cofactors, or charges through the device. Furthermore, protein nanopatterning methods must not be deleterious to the native protein structure; ideally, the nanostructured material will provide an environment that enhances the stability and activity of the protein. Finally, practical applications require that the cost of patterning the material be commensurate with the value of the eventual application.

In order to prepare materials that meet as many of these engineering criteria as possible, three broad approaches to nanopatterning are typically employed (Fig. 14.1). First, a surface may be lithographically patterned, followed by adsorption or reaction of a protein with selective regions of a surface. Second, templates may be constructed into which protein is inserted or onto which protein is reacted/absorbed, where the structure of the template directs the location of the protein. Third, the protein itself or fusions or conjugates of protein with structure-directing elements may be prepared, enabling the direct self-assembly of proteins into nanomaterials. This chapter aims to provide a tutorial overview of the repertoire of protein-patterning techniques at a researcher's disposal, highlighting the merits of each approach to patterning proteins at the nanometer length scale and their corresponding applications and engineering trade-offs.

14.2 Lithography

Lithography enables top-down patterning of structures through the definition of a template, followed by the transfer of that template to produce a functional protein nanopattern. A wide variety of methods have been developed for fabricating such patterns, including photolithography, electron beam lithography (EBL), dip-pen nanolithography (DPN), nanografting, and nanocontact printing (nCP). Lithographic

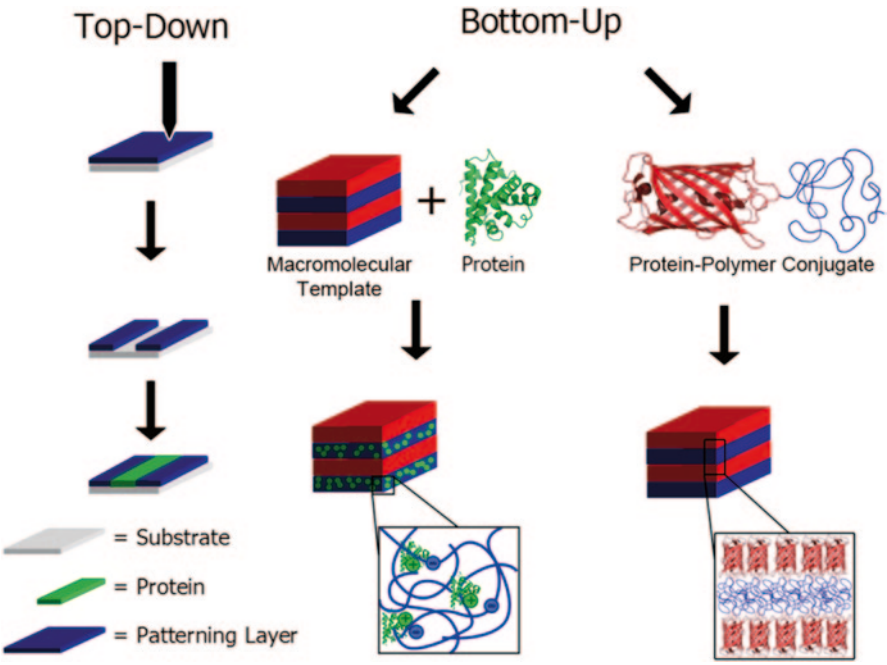

Fig. 14.1 Conceptual overview of the top-down and bottom-up approaches to protein nanopatterning. Top-down methods involve fabrication of patterns on substrates that direct protein immobilization. Bottom-up methods allow thermodynamic interactions to guide protein assembly through templated or direct self-assembly approaches

processes can form patterns of arbitrary shape (not necessarily periodic) with resolution that often approaches a single protein molecule. All of these patterning processes rely on forming areas that can selectively bind proteins using one of three approaches: physical adsorption, covalent immobilization, or bioaffinity interactions. Physical adsorption utilizes electrostatic, ionic, hydrophobic/hydrophilic, or hydrogen-bonding interactions to immobilize proteins to the substrate [36, 37] directly or indirectly. Chemisorption approaches to covalently attach proteins to functionalized patterned surfaces focus primarily on functional groups including amines, carboxyls, thiols, epoxies, and photoactive materials [38–41]. Amine and carboxyl chemistries are generally not site-specific, potentially leading to immobilization of proteins in a random orientation that may adversely impact protein function [42, 43]. Site-specific covalent immobilization reactions [42, 44–46] may enable control of protein orientation, and short linkers between the protein and patterned surface have been found to be beneficial for protein stability [40, 47–49]. Bioaffinity interactions—between enzyme and substrate, receptor protein and its recognition pair, or antigen–antibody pairs—such as that between biotin and avidin ($K_a \sim 10^{15}$ L mol^{-1}) [50], while not covalent, can provide very strong interactions for forming stable protein patterns [51–53]. Many of these chemistries have been extensively reviewed in a number of excellent recent articles [39, 54–59], and their integration into a variety of lithographic processes is described below.

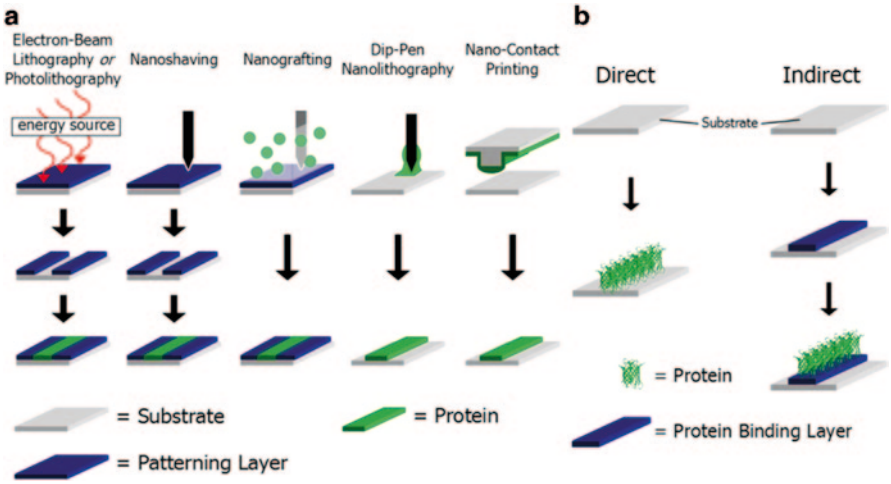

Fig. 14.2 **a** Schematic representation of top-down lithography methods for patterning proteins at the nanometer scale, including conventional photolithography and electron beam lithography, atomic force microscopy tip-based lithography, and stamping lithography. **b** Lithography can pattern proteins directly or create patterns that can pattern proteins indirectly through physisorption, chemisorption, or bioaffinity interactions

14.2.1 Photolithography

Conventional top-down photolithography is a well-developed technique for bulk processing and patterning of integrated circuits in the semiconductor industry, and it has been successfully adapted to patterning a wide variety of biomolecules, including proteins, into arrays for sensors [60, 61], or other bioanalytical applications [62]. A pattern defined by a photomask is transferred to an overlying layer of photoresist on a substrate. A variety of different techniques are then used to transform this pattern into a chemical pattern on the substrate surface to achieve a spatially defined arrangement of protein, with the resolution of the technique set by the resolution of the chosen photolithographic method (Fig. 14.2). Currently, a resolution of 500 nm has been achieved [63] for protein immobilization. Photolithography is a parallel technique with high throughput, but it is limited by high capital and operational costs. Harsh traditional processing conditions or chemical modification of proteins with photoreactive groups may also reduce protein activity [64, 65], making the technique most effective when protein is introduced after such processing steps are complete.

Protein patterning by photolithography can be accomplished by immobilizing the proteins onto the substrate by physical absorption, chemical reaction, or noncovalent binding interactions. Physical adsorption processes most commonly use photolithography to form patterned self-assembled monolayers (SAMs) or (3-aminopropyl)triethoxysilane (APTES) patterns to which proteins selectively adhere. For example, a photolithographically patterned SAM [66] can enable selective adsorption of proteins such as bovine serum albumin (BSA), which can then serve as

a chemical pattern for further functionalization. A methacrylate-based copolymer compatible with the photolithographic "liftoff" technique has also been demonstrated for patterning rabbit immunoglobulin G (IgG) and BSA down to a resolution of 3.75 μm through physisorption to an APTES surface [67]. Alternately, polystyrene (PS) nanoparticles have been used to fabricate macroporous poly(2-hydroethyl methacrylate or PHEMA) hydrogel micropatterns through a combination of colloidal crystal templating and photopatterning; the surface of the hydrogel was then modified with APTES for protein adsorption [68].

Photolithographic immobilization of proteins through chemisorption requires functionalization of the patterned surface with protein-reactive functional groups. A substrate functionalized with a photochemically labile species can be ultraviolet (UV) irradiated in a solution of protein which converts the photoreactive group to an active functionality that can bind the protein. One typical photoreactive group used is an arylazide: biotin-nitroarylazide can be immobilized onto an avidin-coated surface, and irradiation through a photomask produces a pattern of active nitrene for protein conjugation [69]. This technique was demonstrated in series using five different protein solutions to assemble antibodies into separate regions [70]. Using a substrate derivatized with a "caged" species, UV irradiation can also be used to remove the protecting group and leave a reactive functionality for protein patterning. For example, protected amine or carboxylic acid functionalities on a hydrophilic polymer surface can be photodeprotected to form a nanopattern for immobilization of multiple immunoglobulins down to 5-μm resolution [71]. Leggett and coworkers showed that an oligo(ethylene glycol) layer on glass is photodegradable upon UV light exposure, yielding aldehyde functional groups for covalent linkage to proteins using aldehyde–amine coupling [72]. Nanometer scale resolution was achieved using a Lloyd's mirror interferometer [72]. Deep UV irradiation of silane SAMs can deactivate derivatized surfaces, leaving the nonirradiated regions as a pattern for protein immobilization. This has been demonstrated to convert pendant thiol functionalities in a thiol-terminated silane film to nonreactive sulfonate groups, and the remaining pattern of thiols was used to covalently bind proteins [73].

Bioaffinity interactions such as biotin–streptavidin, the affinity of immunoglobulins toward protein A, [74, 75], and nitrilotriacetic acid (NTA) complexation with histidine (His)-tagged proteins [72] provide a third major route for photopatterning proteins. These interactions are often site specific and provide a means of controlling the protein orientation and potentially improving the protein stability and activity. The strong bioaffinity interaction between biotin and streptavidin has been combined with a photoresist processable under mild conditions to demonstrate patterning of multiple streptavidins in a serial patterning procedure [76]. An advantage of bioaffinity interactions is the strength and molecular-level specificity of these interactions, which has been used effectively to form a two-component pattern in a single step [77].

As conventional photoresists require processing conditions that may denature protein [62, 78, 79], maskless photolithographic approaches using a micromirror array (MMA) as a virtual photomask [80] or molecules that can be photopatterned directly have been explored. The design of an MMA for protein-patterning applications [81] eliminates the difficulties caused by photomasks and mask alignment,

and allows for patterned exposure of UV light onto a surface to create a pattern reactive toward proteins. This has been demonstrated on a glass surface functionalized with the photolabile protecting group nitroveratryloxycarbonyl (NVOC) which allowed for subsequent patterning of protein molecules [82]. In addition, photobiotin can be bound directly to an organic surface upon intense UV illumination, and this technique has been demonstrated to pattern horseradish peroxidase (HRP) [83]. Another alternative uses protein engineering to synthesize proteins containing the photoreactive noncanonical amino acid para-azidophenylalanine, which enables the protein to be patterned directly by photolithography on a poly(ethylene oxide) or PEO-coated glass surface [84]. Bailey and coworkers used UV light to generate a transient diradical from benzophenone as a universal method for patterning proteins and demonstrated the ability to pattern multicomponent surface patterns and gradients on the micron scale by controlling the amount of UV exposure [85]. They successfully applied this technique to conjugated benzophenone within collagen–glycosaminoglycan (CG) scaffolds to enable photocatalytic protein patterning within three-dimensional (3D) collagen biomaterials [86].

14.2.2 Electron Beam Lithography

Like photolithography, EBL has been conventionally used for semiconductor fabrication but has recently garnered interest for patterning of proteins and biomolecules. Patterning proteins by EBL requires fabricating a pattern using an electron beam (Fig. 14.2) to which proteins are immobilized through the same type of physical, chemical, or bioaffinity interactions used in other patterning processes. EBL is a maskless technique, and its primary advantage is its ability to create precise nanopatterns with the highest resolution of all lithographic techniques. Nanopatterns on the length scale of single proteins and other biomolecules are achievable, with features generated reproducibly with approximately 5 nm resolution. [87]. Although the electron beam can be focused down to approximately 0.5 nm in diameter, the resolution is governed by the size of resist molecules and secondary electron processes [88]. The limits of EBL are its high cost and the requirement of specialized equipment; furthermore, due to its serial processing, it is relatively slow compared to other printing and stamping techniques. Parallelization of EBL has focused on development of projection EBL [89, 90] and multibeam sources [91, 92], which have the potential to significantly increase processing speed.

EBL can directly pattern features onto different surfaces for adsorption of protein. The technique is effective at ablation of polymer monolayers for protein immobilization to the underlying substrate, such as ablation of poly(methyl methacrylate or PMMA to pattern gold nanoparticles coated with IgG onto the underlying silicon layer by adsorption [93]. While protein immobilization by adsorption can effectively control the positioning of the proteins with relatively high spatial resolution, it is unable to control their orientation, which may be beneficial for protein function and device application. The high-resolution capabilities of EBL have been demonstrated

to pattern proteins with control over their orientation by fabricating patterns with dimensions congruent with those of the protein crystal, promoting energetically favorable binding densities and alignments with the resulting nanopattern. Using EBL to fabricate 30–90 nm tracks of methyl-terminated alkylsilanes, 300 nm-long collagens could be selectively adsorbed and oriented on the hydrophobic alkylsilane regions [94]. This design concept has also been shown to control the orientation of the ellipsoidal globular antigen P.69 pertactin [95] with typical axis lengths of 10.6, 3.8, and 2.5 nm [96] through physisorption onto alkylsilane nanostripe patterns with widths less than 50 nm. Patterns may also be created by contamination writing, which has been demonstrated to pattern NeutrAvidin-coated fluorescent PS spheres [97]. Carbon-containing nanofeatures formed by electron beam writing on a polyethylene glycol (PEG)-coated glass substrate have been shown to selectively adsorb proteins with contrast factors greater than 1000; the protein density can be controlled over three orders of magnitude by modulating the electron beam dose [98]. EBL and reactive-ion etching were used to pattern SiO_2 on a layer of InSnO on a glass surface; binding dodecylphosphate (DDP) to the InSnO and passivation of the SiO_2 surface with poly-L-lysine-g-poly(ethylene glycol) led to indirect patterning of fluorescently labeled streptavidin through adsorption to DDP [99, 100]. Liftoff patterning of APTES has also been demonstrated as a method to electrostatically immobilize ferritin [101].

EBL is able to form features with reactive chemistries and specific bioaffinity interactions for patterning proteins. EBL can be used to selectively pattern a monolayer of mercaptohexadecanoic acid (MHDA) backfilled with cysteamine, allowing for the attachment of aldehyde-coated fluorescent PS beads. A cycling procedure was used to pattern both red and green fluorescent-coated PS beads on the same substrate [102]. Another example uses EBL to create a pattern in an inert SAM on silicon or gold substrates. Backfilling with APTES and subsequent reaction with an amine-reactive *N*-hydroxysuccinimide (NHS) ester linked to biotin was used to pattern anti-biotin antibodies [102]. EBL has also been demonstrated to pattern nanodots of a metal alloy which can be functionalized with a biotinylated thiol to pattern streptavidin [103]. PEG is well known to resist protein adsorption, and much work has explored the use of EBL to cross-link functionalized PEG chains to form patterned hydrogels containing alcohol, amine, aminooxy, alkyne, maleimide, biotin, nitriloacetic acid (NTA), and sodium styrene-4-sulfonate for subsequent immobilization of proteins over the length scales of nanometers to 1 mm (Fig. 14.3) [104, 105]. Fabrication of 3D nanopatterns by EBL has also been demonstrated by exposing porous silicon to an electron beam to generate protein-reactive silicon radicals [106].

14.2.3 Dip-Pen Nanolithography

DPN [107] has evolved since its invention [108] to become one of the most versatile techniques for nanopatterning biomolecules due to its ability to produce patterns

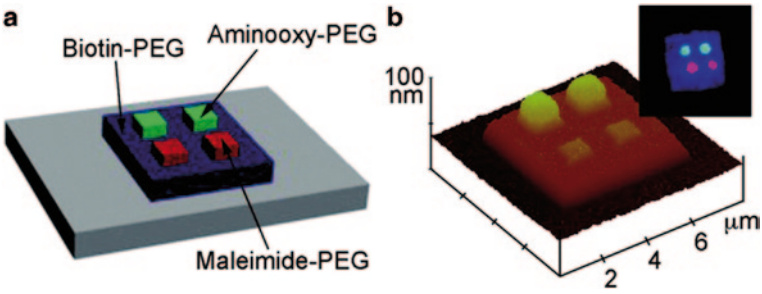

Fig. 14.3 Tricomponent structures prepared by electron beam lithography. **a** Schematic showing *biotin–PEG* is first cross-linked to the native oxide of an Si wafer, after which two *maleimide–PEG* and two *aminooxy–PEG* squares are then cross-linked on top of the original *biotin–PEG* pattern. **b** AFM height image of the aminooxy–maleimide–biotin pattern. *Inset*: overlay image of a blue fluorescent SAv on the biotin–PEG, a green fluorescent antibody-stained α-oxoamide myoglobin, and a red fluorescent BSA. *PEG* polyethylene glycol (Reproduced with permission [104]. Copyright 2009, American Chemical Society)

in conditions of ionic strength, pH, and hydration that are widely compatible with biological systems. Analogous to a quill pen in which a tip is dipped into an ink solution to write on a solid surface, DPN enables writing and patterning on the nanometer length scale using the infrastructure of atomic force microscopy (AFM, Fig. 14.2). Material transfer from the AFM tip to the substrate involves three primary steps: formation of the liquid bridge (water meniscus) due to capillary condensation [109–114], material transport [115–118], and surface diffusion of the material to form the final shape of the pattern [119–123]. DPN can pattern a diverse set of materials from long-chain alkanethiols to single cells with high precision and resolution from below 100 nm to a length scale of many micrometers, with the highest resolution of approximately 15 nm currently achieved for alkanethiol patterns fabricated on gold surfaces [124]. The technique is traditionally limited by its serial writing ability, but the recent development of passive probe arrays and active arrays with individually actuatable probes enables parallel writing by multiple arrays, allowing as many as 450 million sophisticated features to be written at the sub-100 nm scale within 30 min [125–129].

DPN can fabricate protein nanostructures by both direct and indirect writing methods. In direct-write DPN, the biomolecule is directly deposited onto a functional surface, and controlling the direct interaction between biomolecule and substrate surface through physisorption, chemisorption, or bioaffinity interactions is key to the lithography process. Direct-write DPN of functional IgG [130] and enhanced green fluorescent protein (EGFP) [131] has been demonstrated via electrostatic interactions. Covalent linkage of antibodies using aldehyde chemistry [130], binding of His-tagged ubiquitin and thioredoxin to a nickel oxide surface [132], and binding of His-tagged EGFP and DsRed to an Ni–NTA SAM-functionalized glass surface [131] have also been explored. The use of a larger linking functionality, such as the His tag, is thought to reduce the possibility for direct contact between the protein and the substrate that could lead to loss of activity. Because DPN pattern

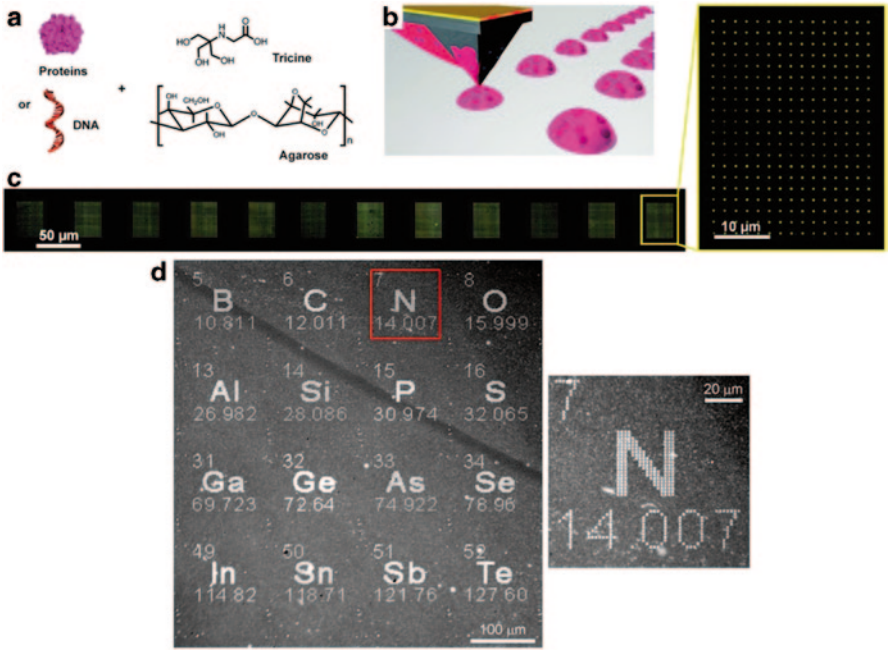

Fig. 14.4 **a** Schematic representation of *protein* or *DNA* that can serve as ink molecules and matrix components *agarose* and *tricine* as an accelerator molecule for **b** the process of agarose-assisted DPN. **c** Epiflourescent microscope image of a 15 × 20 array of 500-nm Cy_3-labeled oligonucleotide features generated in parallel from a 12-tip cantilever array. (Reproduced with permission [133]. Copyright 2009, American Chemical Society) **d** Optical micrograph of a portion of the periodic table of the elements patterned by a 4 × 4 active PPL pen array. The *inset* shows a magnified view of the "nitrogen" entry written by a single pen. (Reproduced with permission [152]; Copyright 2013, PNAS)

resolution depends upon a number of factors such as the formation of the water meniscus bridging the tip and substrate and allowing for molecular ink diffusion to the substrate, which depends upon the relative humidity, this creates challenges for patterning multiple proteins with different transport rates simultaneously. Mirkin and coworkers have demonstrated a direct-write approach for proteins within an agarose matrix as a universal biomolecule carrier with an accelerator molecule to pattern olignonucleotides and proteins (Fig. 14.4) [133]. Agarose is a thermoreversible hydrogel, and its higher viscosity and hydrophobicity compared to buffered solutions facilitate ink adsorption and provide a stabilizing environment for the protein. The agarose matrix-accelerator molecule contains a hydroxyl, amine, or carboxylic acid functional group that stabilizes the gel network through hydrogen bond interactions, and the combination of agarose and accelerator concentration provides an additional parameter for controlling patterned feature sizes by modulating the transfer of proteins with different diffusion properties from the tip to the substrate. The use of this fast technique with massively parallel two-dimensional tip arrays can potentially print nanoscale biomolecule dots at rates of 50 million features per minute with densities of 25 million spots per square centimeter [133].

In addition to patterning protein nanoarrays with relatively high throughput, DPN can also control the number of protein molecules immobilized. The number of protein molecules patterned within a given region has been shown to vary linearly with the protein ink solution concentration and to the third power of contact radius. Feature size can be controlled through the tip–substrate contact time [134], but the rates of transport by diffusion and adhesion to the substrate depend highly upon the protein composition. The deposition of ten, five, and even single ferritin particles on a dot with a diameter of 150 nm has been demonstrated by reducing the ferritin ink solution concentration [135].

In contrast to direct-write DPN, indirect patterning uses DPN to fabricate a pattern of physisorbing, chemisorbing, or bioadhesive molecules to which proteins are then bound. This approach has the potential advantage of utilizing gentler conditions for protein immobilization, since DPN performed on small molecules or binding moieties rather than fully folded proteins. Patterns are typically created on gold surfaces using 16-mercaptohexadecanoic acid (MHDA), and the nonpatterned areas are passivated with molecules such as 1-octadecanethiol (ODT), 11-mercaptoundecyl-tri(ethylene glycol) (EG_3–SH), or *n*-octadecyltrimethoxysilane (OTS) to resist nonspecific protein adsorption. The carboxylic acid functionality of MHA SAMs has been demonstrated to pattern lysozyme and IgG [136], and it can also be used for patterning amino-terminated biotin for subsequent immobilization of proteins using bioaffinity interactions [137]. Activation of carboxylic acid-terminated groups to form NHS esters followed by reaction with biotinyl-3,6,9-trioxaundecandediaimine (biotin–NH_2) was used to provide a platform for binding biotinylated proteins through biotin–streptavidin interactions [137]. Patterns using biotin–streptavidin interactions have also been reacted with tris–NTA biotin derivatives to allow reversible immobilization of proteins containing His tags by the addition of imidazole [138]. Thiol–maleimide coupling chemistry has been shown to effectively immobilize genetically engineered cysteine cowpea mosaic virus capsid particles to a maleimide functionalized surface [139]. Alkoxysilane patterns on glass substrates have been fabricated using 3′-mercaptopropyltrimethoxysilane (MPTMS) for reaction with biotin–maleimide to provide a platform for binding proteins through biotin–streptavidin system, and DPN has been shown to pattern nickel(II) ions onto an SAM NTA-functionalized glass surface, enabling immobilization of 6xHis-tagged proteins with orientation control into reversibly bound monolayers [140].

The design of new tip arrays and polymer pen lithography (PPL) has been explored to increase the patterning speed and throughput of DPN. The design of a tip array for parallel patterning originated from IBM, known as the “millipede” [141]. Methods for fabricating tip arrays to address and actuate individual cantilevers have been subsequently developed [142–144], and a combination of differently shaped and individually controlled tips has been incorporated into a complex micromachining process [145]. A recent extension to conventional DPN is PPL, where the tip is made of deformable elastomeric tips instead of hard, inorganic cantilevers typically used in scanning probe microscopy (SPM)-based lithographies. This technique provides the advantages of DPN with the large-area patterning capabilities of microcontact printing (μCP; discussed later) and offers a multitude of new

properties—many tips, addressable inking [146] and high ink capacity [147], pressure-dependent size pattern fabrication [148], and good alignment methods [149, 150]—that currently render it the fastest DPN technique available [151]. Active PPL in which each pen within the array is independently actuated has been demonstrated to print a 600×600 μm^2 image of part of the periodic table of elements that consisted of 5961 features where the average feature size was 1.28 ± 0.04 μm (Fig. 14.4).

14.2.4 Nanoshaving and Nanografting

Nanoshaving and nanografting are two SPM techniques in which a SAM resist is patterned using an AFM tip. The basic procedure (Fig. 14.2) for both techniques consists of three steps. First, the surface of a SAM is imaged by AFM operated at low force to select a region for patterning. Second, a raster scan of the tip at higher force is used to selectively remove regions of the SAM. Third, binding of "ink" molecules to holes in the SAM forms the pattern, which can then be imaged in situ [153]. Nanoshaving involves creating a negative pattern by selectively removing regions of a resist material, after which proteins may be immobilized. Nanografting is an extension of nanoshaving in which the new adsorbate or protein biomolecule adsorbs in tandem with removal of the resist material. Because this technique requires the mechanical removal of molecules on a substrate for pattern generation, sufficiently strong and local interactions between the AFM tip and substrate are important for pattern resolution [154]. Ideally, the fabrication force threshold is determined for each individual experiment, as the force is contingent upon the AFM tip, the SAM matrix, and other environmental factors [154].

Nanoshaving and nanografting are capable of achieving an edge resolution of 1 nm and line widths of 10 nm or less [153]. Proteins may be patterned directly upon removal of the matrix SAM, or proteins may be immobilized indirectly by creating nanopatterns using molecules with the appropriate chemical functionality. An advantage of nanografting is the ability to make modifications to existing patterns in situ without restarting the process or requiring a new mask [154]. For example, one of two parallel lines of octadecanethiol within a decanethiol matrix SAM was "erased" by nanografting in a solution of decanethiol, and then "rewritten" by nanografting in a solution of octadecanethiol, creating a new line shifted 65 nm from the original pattern [155]. SAMs, with a diverse set of functional groups including alkyl, alcohol, glycol, aldehyde, amine, carboxylate, and thiol, can be used to create a foundation upon which nanomaterials and biomolecules such as proteins may be patterned [156]. One final advantage is the ability to pattern under near-physiological conditions that promote protein stability.

The variety of functional SAMs can be exploited to control protein immobilization through electrostatic interactions, covalent chemistry, or specific bioaffinity interactions. Direct nanografting of proteins on a gold substrate can be accomplished by using a protein containing cysteine residues as the writing ink, which has

been demonstrated for three- and four-helix bundle metalloproteins [157, 158] and a dicysteine-terminated maltose-binding protein (MBP). Modifying existing patterns in situ allows patterns to be created serially with multiple functionalities for binding multiple proteins through indirect nanografting. For example, sequentially grafted regions of positive, neutral, and negative charge show that local charge effects contribute to selective binding of lysozyme, rabbit IgG, and bovine carbonic anhydrase at different pH [159]. Nanopatterns of a carboxylic acid functionality within an alkanethiol SAM matrix on a gold substrate have also been utilized to pattern both lysozyme and rabbit IgG through electrostatic interactions [160, 161] with the carboxylate anions at neutral pH. AFM characterization showed that lysozyme was patterned in multiple orientations, confirming the nonspecificity of electrostatic interactions. Examples of chemisorption include protein patterning through formation of amide [162] and imine bonds from reaction of lysines with carboxylic acid and aldehyde functional groups, respectively [160, 161, 163, 164]. In a recent study, nanografting was demonstrated to pattern a gold surface with thiolated single-stranded DNA (ssDNA) that successfully immobilized streptavidin tethered with a DNA oligomer through sequence-specific DNA hybridization [165]. Reversal nanografting [166] has also been demonstrated to fabricate high-resolution nanopatterns, in which a matrix SAM containing protein-binding termini is nanografted with inert molecules.

14.2.5 Nanocontact Printing

nCP [167, 168], a higher-resolution form of μCP [169, 170], has been demonstrated to pattern micrometer-scale regions rapidly and in parallel with small molecules [171, 172] and biomolecules [173–177]. μCP and nCP are soft lithographic techniques involving a structured elastomeric stamp prepared from a lithographically fabricated master that is coated with "ink" molecules that are stamped or printed through contact with a surface (Fig. 14.2). Molecules diffuse from the stamp to the substrate producing the nanopattern [169, 178]. Patterning large proteins and molecules reduces lateral diffusion and blurring of the pattern features relative to patterning small molecule alkanethiols. Furthermore, nCP is not diffraction limited, enabling higher resolution than conventional photolithographic processes. In principle, this method can pattern surfaces with molecular scale features, and features as small as 40 nm have been demonstrated [168]. Another significant advantage is the ability to print patterns rapidly over large areas. Protein patterning by μCP and nCP generally proceeds through physisorption of the proteins onto the patterned substrate; therefore, adsorption of the proteins onto the stamp and subsequent printing and transfer may induce conformational changes within the protein molecules, leading to decreased biofunctional activity. Patterning of multiprotein arrays is facile with μCP—both sequential inking and printing and parallel inking followed by a single stamping procedure have been demonstrated [174, 177].

Poly(dimethylsiloxane) or PDMS is most commonly used as the elastomeric stamping material, but the softness of PDMS has limited the resolution of nCP to

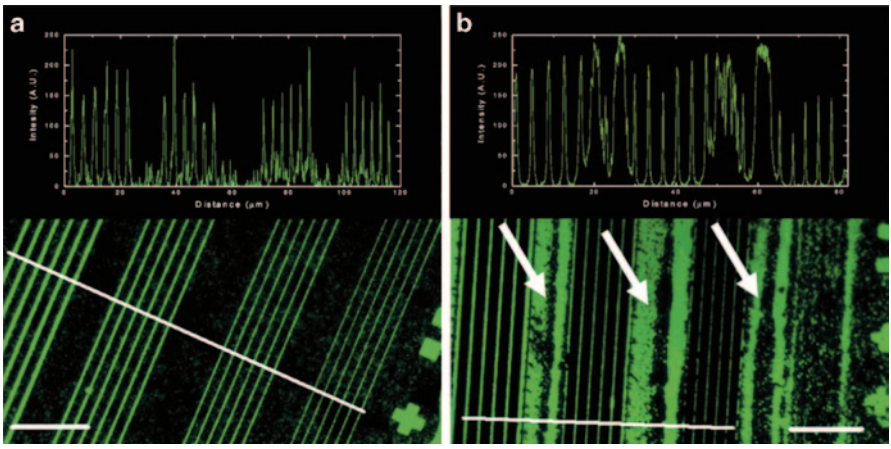

Fig. 14.5 Nanometer scale printing of Alexa488 Fibrinogen using **a** polyolefin plastomerVP8770 and **b** PDMS as stamp materials, as determined by fluorescence microscopy. The *lines* across the stripes indicate the positions at which cross sections shown in *insets* were measured. *Arrows* in **b** indicate regions where sagging of the stamp occurred. Scale bars are 20 μm. (Reproduced with permission [179]. Copyright 2003, American Chemical Society)

approximately 100 nm features. Sub-100 nm resolution has been achieved by using composite PDMS stamps, where a thick, flexible PDMS layer supports a thin layer of a polymeric composite with a high modulus of approximately 9 N/mm^2, referred to as *h*-PDMS ("hard" PDMS) [167]. A sharp, V-shaped composite stamp including *h*-PDMS has enabled protein patterning with a line-width resolution [168] as low as 68 nm. Spencer and coworkers introduced a new class of higher modulus polyolefin plastomers (POPs) [179] as stamping materials that improve the printing quality at submicrometer resolution (Fig. 14.5). By using high-resolution μCP to generate feature sizes below 100 nm and dilute protein "inking" solutions to decrease the density of pattern coverage, single antibodies and green fluorescent proteins were deposited and nanopatterned reproducibly [180]. Hydrogel stamps [181, 182] act as reservoirs for protein and biomolecular inks, providing a controlled aqueous environment to pattern proteins with higher retention of activity than hydrophobic stamps. However, the softer mechanical properties of hydrogels limits the maximum attainable spatial resolution. Covalent μCP has also been demonstrated where gold and silicon oxide substrates with amino-terminated SAMs were converted to aldehyde functional groups for patterning proteins through imine bond formation [175].

14.2.6 Other Lithographic Techniques

Other methods for lithographic patterning continue to expand the set of techniques available for controlling protein patterning. Nanoimprint lithography is another stamping technique where the stamp is lithographically prepared and used to imprint a pattern in a polymer film to be used for protein immobilization [183–185]. Focused

ion beams, similar in principle to electron beams, have been used to pattern 60 nm features for protein immobilization on gallium arsenide and silicon [186]. Nanopipettes or nanopens [187, 188], based upon scanning ion conductance microscopy, utilize pipettes with nanometer-scale inner diameters to pattern proteins onto a surface across a potential difference, and nanofountain atomic force microscopy probe (NFP) combines the high-resolution patterning capabilities of DPN with a continuous flow of biomolecules provided by a microfluidic system to a probe reservoir where an electric potential is used to deposit the biomolecules onto the substrate [189]. Using conductive AFM, applying a voltage to an AFM tip has been demonstrated to facilitate the transport of proteins from the tip to the substrate [190] and to create patterns for subsequent protein immobilization [191, 192]. A recent methodology using paramagnetic metal masks to define a magnetic field onto a substrate to assemble ferromagnetic nanoparticles has been demonstrated to create patterns for immobilizing proteins, and the use of a magnetic field does not limit the patterning technique to any specific surface topography or planarity, allowing it to pattern 3D and rough surfaces [193, 194].

14.3 Templating Using Macromolecular Assemblies

A second major approach for controlling the nanostructure of protein materials is to use a 3D template to guide protein structure. Templated assembly can be advantageous in three respects: nanostructured scaffolds can be prepared using well-known and widely investigated processing methods, templates enable protein nanostructure to be controlled in three dimensions, and a template can provide a local environment around the protein that can improve enzyme stability and activity. Templates may be divided into two categories. First, 3D structures that form interfaces such as silica sol–gel structures [195, 196] or nanoporous gold structures [197] may be prepared, and proteins can be bound to the surface of the structure of entrapped in the structure. Second, proteins may be co-assembled with polymers or lipids in order to produce self-assembled nanomaterials, where specific interactions between proteins and polymer or lipid are used to drive the protein into specific nanodomains of the self-assembled structure. Because of the exceptional degree of structural control that has been established with polymer and lipid self-assembly [198, 199], here we focus on the latter approach to incorporating proteins into these exquisitely nanostructured materials.

Templating proteins in self-assembled polymer or lipid structures relies on specific structure-directing interactions between proteins and polymers. For methods such as layer-by-layer (LbL) deposition and coacervate micelle formation, electrostatic interactions are primarily responsible for assembly of the structure. Because proteins have amino acid residues on the surface which can be ionized depending on the pH of solution, electrostatic interaction is convenient and broadly applicable for protein immobilization. In the case of selective protein adsorption to block copolymer (BCP)-patterned surfaces, hydrophobic interactions are thought to come into play. Conjugation of polymers to proteins may also be used in order to direct

proteins into chemically similar regions of a nanopattern [200]. Finally, hydrophobic/hydrophilic patterns may be used to direct the self-assembly of membrane proteins within lipid and polymer templates, providing a highly effective method to structure these molecules in a biomimetic environment [2, 201].

14.3.1 Deposition of Proteins Using Layer-by-Layer Assembly

LbL self-assembly of polymer thin films was first developed in the 1960s and popularized in the 1990s [202, 203], and it has been extensively studied due to its simple processing methods and versatility. In its original manifestation, LbL was based on sequential electrostatic adsorption of charged molecules (polyelectrolytes, proteins, etc.) to a charged substrate. It reliably produces thin films with well-controlled thicknesses on the nanometer length scale, and the physics of this process is covered in detail in a number of excellent reviews [204, 205]. Other types of interactions such as hydrogen bonding or strong and specific recognition between biotin and avidin have been also utilized to create LbL-type alternating layer architectures [53, 206, 207]. Because it may be used on a variety of surface geometries, LbL assembly has been widely applied to conventional flat substrates [208], micro- or nanoparticles [209, 210], or even substrates with complicated geometries such as implantable materials, enabling conformal coating [211].

Typical LbL film fabrication starts with dipping a charged substrate into an oppositely charged polyelectrolyte solution. As the polyelectrolyte molecules adsorb onto the substrate by electrostatic attraction, the charge of the substrate is reversed, and it eventually inhibits further adsorption of polyelectrolytes. The electrostatic interactions between polyions are driven in part by the entropy of releasing counterions into solution when the macroions form a charge complex [212, 213]. After the adhesion step, excess polyelectrolyte is rinsed off and the substrate is dipped into the second polyelectrolyte with opposite charge to create another half layer. By repeating these steps, a film with an alternating sequence of layers can be created.

Proteins are incorporated in the same way using a dilute protein solution instead of one of the polyelectrolyte solutions (Fig. 14.6). Most proteins have a net surface charge at physiological pH that can be controlled by varying pH, making proteins ideal candidates for LbL deposition. The interactions of proteins with polyelectrolytes are different than interactions between polyelectrolytes, about which much is known [214]. Proteins have a relatively low net charge compared to typical polyelectrolytes used in LbL but due to their anisotropically charged surfaces, they can absorb even when the net charge of the protein and polyelectrolyte at a given pH are the same. Also, because most functional enzymes have a globular shape that cannot adapt to form conformal coatings on surfaces, multilayer films require a flexible polyion to bridge between protein layers [215]. The flexible polyion chains penetrate to fill the space between globular proteins, forming an interconnected film. Various model proteins and functional enzymes including glucose oxidase (GOD) [216, 217], alkaline phosphatase (AP) [218], laccase [219], urease [220], myoglobin or hemoglobin [221–224], and insulin [225] have been successfully deposited using LbL.

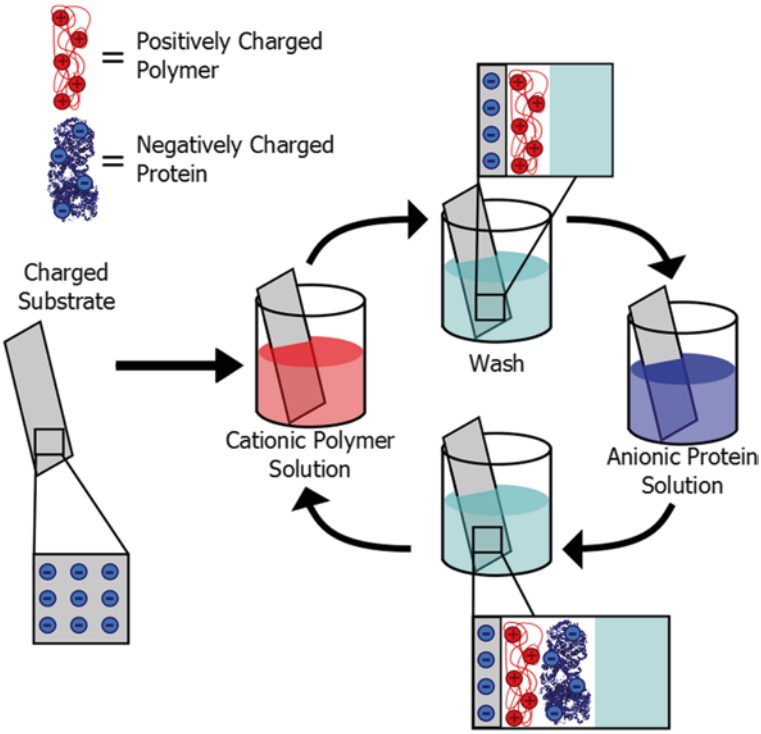

Fig. 14.6 Schematic illustrating layer-by-layer deposition process for a positively charged polyelectrolyte and negatively charged protein as an example. A *charged substrate* is immersed in polyelectrolyte and protein solution in alternating fashion, with intermediate washing steps to remove weakly bound polymers or proteins

While multilayer films created by LbL assembly can be viewed as one-dimensional (1D) patterns along the layer normal, X-ray and neutron reflectometry studies of internal LbL film structure show that the layers in the film are highly interpenetrated [226]. It was shown that the average concentration of one electrolyte in a multilayer film along the layer normal is nearly constant, although each layer can be distinguished when isotopically labeled. The charge density of the polyelectrolytes, controlled by the pH and ionic strength of the solution, affects the physical properties of the resulting multilayer films. Polyelectrolytes with lower charge density are shown to produce thicker and more permeable films with greater surface roughness [227, 228]. The permeability of the films in turn affects protein adsorption and penetration depth during each adsorption step. When myoglobin was adsorbed on the terminal layer of LbL films, loading was much higher at pH 5 than at pH 9 due to the more swollen and permeable nature of the multilayer film at pH 5 [229].

To determine a suitable pH for patterning LbL protein films, the pH range in which proteins maintain their stability needs to be considered. Then the pH of the dipping solution is chosen so that protein and polyelectrolyte have net opposite charges based on the pK_a of the polymer and the pI of the protein [217], although

proteins act as a dipole and can still adsorb to a polyelectrolyte layer with the same charge as mentioned above [214]. A variety of synthetic or natural polyelectrolytes with various pK_as, typically called strong or weak polyelectrolytes depending on their pK_a values, are available. Poly(styrene sulfonate) [216] and poly(acrylic acid) are widely used negatively charged polyelectrolytes, and poly(allylamine hydrochloride), poly(diallyldimethylammoniumchloride), and poly(ethyleneimine) are common choices for positively charged polyelectrolytes. Biocompatible polymers are often chosen for biomedical applications, including polypeptides such as poly(lysine) [230], poly(glutamic acid) [231, 232], or protamine [233], and polysaccharides such as alginate [224], hyaluronic acid [234], chitosan [235], chondroitin sulfate [236], or dextran sulfate [223].

LbL is promising for protein immobilization because the fabrication process utilizes mild aqueous conditions, and polyelectrolytes protect immobilized enzymes after fabrication. A linear increase in total enzyme activity, which is proportional to the mass of immobilized enzyme, is observed as the number of protein layers increases [218, 219]. However, the activity is limited by substrate diffusion within the film as film thickness increases. The proteins deposited in LbL films are shown to maintain their secondary structure and preserve enzyme activity after deposition, and enzymes loaded into LbL films are reported to have increased thermal stability and retain activity after several weeks of storage at 4 °C [219, 237, 238].

14.3.2 Coacervate Micelles and Thin Films

The same attractive interactions used to incorporate proteins into LbL assemblies can be used to drive protein segregation into charged block copolymers, forming coacervate core micelles that can be used to produce patterned films. In bulk solutions, mixtures of two oppositely charged polyelectrolytes spontaneously phase separate to form coacervate or precipitate phases when the mixture is close to its isoelectric condition [239]. The driving force for complexation is mainly electrostatic interactions, including both Coulombic attraction and entropy gain due to counterion release [240]. If one of the polyelectrolytes is a copolymer comprising one charged block and one neutral hydrophilic block, phase separation is dimensionally restricted by the formation of a layer of hydrophilic block around the coacervate complex, resulting in a coacervate micellar core surrounded by a neutral hydrophilic shell [240]. While this principle is also widely applied to fabricate gene delivery nanoparticles, where negatively charged DNA molecules are complexed with a block copolymer containing a positively charged block [241], proteins can be used as one of the polyelectrolytes to create micelles that have a biofunctional core (Fig. 14.7) [242]. Also, the micelles may be deposited onto a substrate to create a nanopatterned surface. Due to the lower charge density of proteins as compared to polyelectrolytes, electrostatic interactions are somewhat weaker, and protein coacervate micelles can disintegrate at much lower ionic strength [243]. Comprehensive review articles on coacervate core micelles are available [239, 244]. Coacervate core micelles are advantageous over micelles or vesicles made of amphiphilic molecules in protein patterning because of

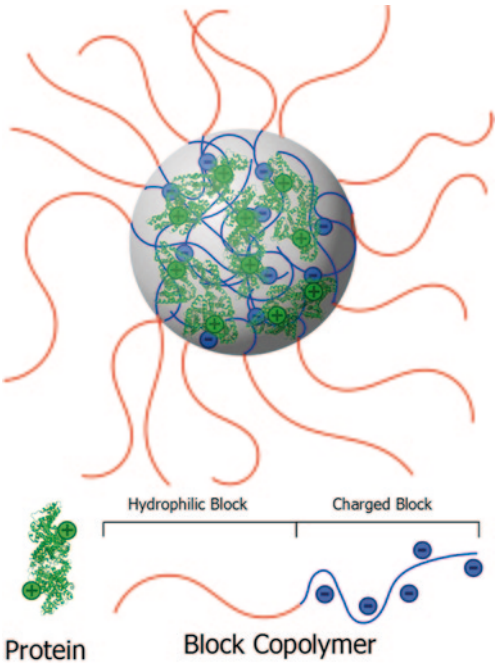

Fig. 14.7 Schematic representation showing coacervate core micelles formed by proteins and polyelectrolytes. The coacervate core is formed by electrostatic interaction between the protein and charged block of block copolymer, and the micelle is stabilized by a neutral hydrophilic block forming the corona

their ability to directly incorporate proteins into the hydrophilic core as opposed to incorporation into the hydrophobic core or indirect encapsulation, and because they eliminate the need for organic solvent during processing [244].

Micelles can be cast into thin films to create nanopatterned materials in a similar manner to block copolymer micelle nanolithography [245] or particle lithography [246, 247]. This was demonstrated using a globular red fluorescent protein, mCherry, as a model protein and poly(*N*-isopropylacrylamide-*b*-2-(dimethylamino)-ethyl acrylate) or PNIPAM-*b*-PDMAEA as a pH-responsive charged block copolymer [248]. Within a pH range above the pI of mCherry (6.0) and below the pK_a of the side-chain tertiary amine groups of the PDMAEA block ($pK_a = 8.5$), complex coacervate micelle formation via electrostatic interaction was observed. When cast as a thin film at pH 6.4, a nanopattern of disordered micelles with a domain spacing comparable to the diameter of micelles in solution, approximately 40 nm, was observed. Spectroscopic analysis showed no change in mCherry structure, and this film can be triggered to release protein at higher pH than the pK_a of PDMAEA. The film remains stable in aqueous environment due to the thermal transition of the PNIPAM block.

14.3.3 Selective Adsorption on Block Copolymer Nanopatterns

Microphase-separated block copolymer thin films can also serve as a guide for selective protein adsorption. Microphase separation of block copolymers in thin films

has been extensively studied, providing a variety of different strategies for structural control [249, 250]. Block copolymers composed of two chemically distinct polymers undergo microphase separation as a result of the thermodynamic balance between chemical incompatibility and chain stretching entropy [251]. Self-assembly of block copolymers in thin films is additionally governed by the interplay between surface energetics and spatial confinement effects [249]. A substrate with preferential interactions with one block promotes selective segregation of the block, while a neutral substrate promotes perpendicular orientation of nanodomains. Incommensurability between film thickness and block copolymer domain spacing results in rich morphological behaviors including island or hole structures [252]. The morphology and orientation of the nanodomains are further controlled by substrate surface modification, annealing, shear, or application of external fields [253]. The physics of these self-assembly processes are covered by a number of thorough reviews [249, 250, 253]. When proteins adsorb preferentially to one of the polymer domains, the block copolymer-patterned surface can be used to create protein nanopatterns. The domain size of block copolymer films is usually 5–50 nm, creating a pattern with a resolution on the order of tens of nanometers, often smaller than the length scales achievable with conventional photolithography [252]. The domain spacing can be precisely controlled by varying the block copolymer molecular weight. This technique is advantageous in that it can rapidly pattern very large areas with a high protein density.

Most studies on patterning proteins with block copolymer films [3, 254–259] have been performed using Poly(styrene-*b*-methyl methacrylate) (PS-*b*-PMMA), a well-characterized block copolymer exploited for block copolymer nanolithography [260, 261]. A pioneering study has shown that a variety of proteins can be selectively adsorbed to PS domains in PS-*b*-PMMA thin films [254]. The PS-rich block copolymer forms PMMA cylinders aligned parallel to the surface embedded in a continuous PS domain (Fig. 14.8) [254]. Since both domains have comparable surface energy at their air/polymer interface, both the PS matrix and PMMA cylindrical domains are exposed to the free surface, creating an alternating stripe pattern of PS and PMMA domains. The repeat spacing of the PS-*b*-PMMA—the average sum of the PS and PMMA domain widths—is comparable to the dimension of a few protein molecules. A wide variety of proteins [3] have been incubated in buffer with a PS-*b*-PMMA-patterned film, causing selective adsorption to the PS domain as confirmed by AFM imaging. Enzymes were shown to remain immobilized on the film even after the film was immersed in solution for 4 days.

As the PS domain is more hydrophobic than PMMA, it is thought the major mechanism that drives selective adsorption of proteins is hydrophobic interaction between PS and proteins. Although hydrophobic interaction can lead to denaturation or misorientation of enzymes, it was shown that horseradish peroxidase (HRP) maintains 85% of its free-solution-state activity after adsorption [262]. Protein–protein interaction sites were also proven to be maintained by sequential binding of IgG and FITC–anti IgG to the protein G immobilized surface, and FITC–anti IgG to an IgG immobilized surface [3]. Protein molecules prefer PS regions that are near PS–*b*–PMMA interfaces, and protein surface density within PS domain decreases as the distance from the PS–*b*–PMMA interface increases [256]. Correspondingly,

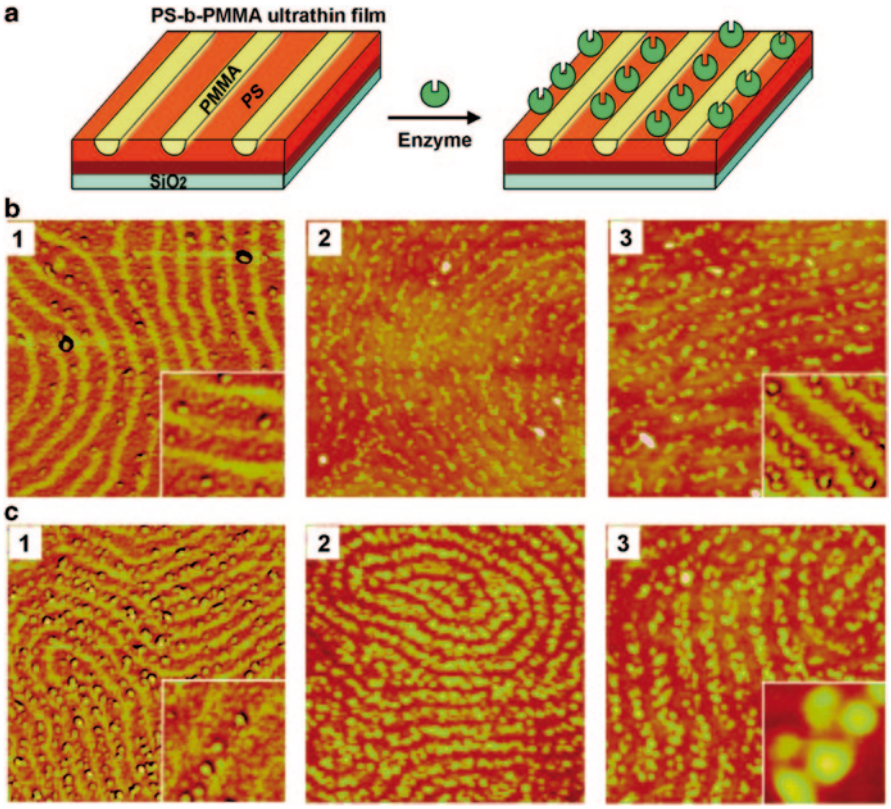

Fig. 14.8 **a** Schematic showing selective enzyme adsorption on phase-separated thin film of PS-*b*-PMMA block copolymer [3]. AFM images of **b** HRP molecules, and **c** mushroom tyrosinase molecules selectively adsorbed to PS domains. (*b1:* 500 × 500 nm^2 phase AFM image after deposition of 4 μg/ml, *b2:* 750 × 750 nm^2 topography AFM image after deposition of 10 μg/ml, *b3:* 500 × 500 nm^2 topography also 10 μg/ml. *c1:* 750 × 750 nm^2 phase AFM image 4 μg/m, *c2:* 750 × 750 nm^2 topography 10 μg/ml, *c3:* 500 × 500 nm^2 topography 10 μg/ml). (Reproduced with permission [3]. Copyright 2007, American Chemical Society)

protein loading on a PS-*b*-PMMA film is three- to fourfold greater than that on a PS homopolymer film. Electrostatic interactions, interfacial energy gradients, and topological differences are hypothesized to play roles in this distribution.

Subsequent work nanopatterned IgG and BSA on highly oriented hexagonal PS domains [257, 258], various serum, antithrombogenic, and cell adhesive proteins on lamellar-oriented PS-*b*-PMMA [259], and anti-IgG on micellar nanotemplates of PS-*b*-P4VP (poly(4-vinylpyridine)) [263]. These studies show the selective adsorption technique can create highly oriented protein nanopatterns. Considering the many complex nanopatterns developed in block copolymer lithography, including wagon-wheel structures and sinusoidally shaped lines [264], this technique has potential for broader application to create more complex nanopatterned protein surfaces.

14.3.4 Co-assembly of Protein and Polymer or Surfactant

Highly ordered protein nanostructures can be created by simultaneously self-assembling proteins with block copolymers or surfactants to take advantage of highly ordered structures and well-understood self-assembly physics of the copolymer and surfactant systems. Co-assembly is an attractive strategy, as the proteins are incorporated as an integral component instead of as an appended layer, and co-assembly enables the fabrication of 3D structures to form thick bioactive layers in nanostructured hybrid materials. Co-assembly with block copolymers poses challenges to find conditions under which both components are processable. Proteins are most often soluble in aqueous buffers, while most block copolymers have one or no hydrophilic blocks. Organic solvents traditionally used for processing of block copolymer thin films can irreversibly denature proteins, induce aggregation, or inhibit activity. One approach to this challenge is to use PEGylation of proteins to direct their self-assembly into PS-*b*-PEG diblock copolymers, where attractive interactions between PEG chains are responsible for segregating protein into the PEG domains [200]. PEGylation successfully improves the solubility of protein in organic solvents, and a large retention of activity was demonstrated with the model enzyme myoglobin. However, processing of materials in organic solvent was still required, and this technique may not generalize to a wide family of proteins.

Co-assembly of proteins and surfactants has also proven useful for controlling the nanostructured assembly of membrane proteins to create systems such as artificial photosynthetic devices. Membrane proteins are unstable in aqueous solution due to their hydrophobic domains designed for insertion into lipid bilayer membranes. Many artificial membrane systems have been developed including freestanding planar lipid membranes [265], liposomes [266], freestanding triblock copolymer membranes [267], and polymeric vesicles [268] for membrane protein insertion. For example, bacterial photosynthetic reaction centers (RCs), membrane protein complexes that are responsible for the initial steps of photosynthesis [269], must be stabilized by amphiphilic molecules that can interact with the hydrophobic domains. These membrane proteins have been assembled in mixed lipid phases, integrating into bilayer architectures which resemble their natural state in the membrane (Fig. 14.9) [2]. The mixed lipid phase is a ternary system made of phospholipid, lipopolymer (PEGylated phospholipid), and cosurfactant, and it self-assembles to form a lamellar structure above a thermal transition temperature. The lipid bilayer structure is maintained after introduction of RCs with only a small change in domain spacing. At lower temperature, the mixed lipid phase forms hexagonal structures (Fig. 14.9a) and transitions to a 3D cubic phase upon incorporation of RCs (Fig. 14.9c). The natural function of RCs in bilayer and cubic structures was preserved as confirmed by monitoring initial electron-transfer events.

Purely polymeric amphiphilic scaffolds are also used to co-assemble with light harvesting proteins. Poly(ethylene oxide)-*b*-poly(propylene oxide)-*b*-poly(ethylene oxide) or PEO–PPO–PEO block copolymer was used to immobilize a plant light-harvesting complex II (LHCII) protein [201]. In its natural state, this protein is known to interact with non-bilayer lipids (which in purified form assume non-

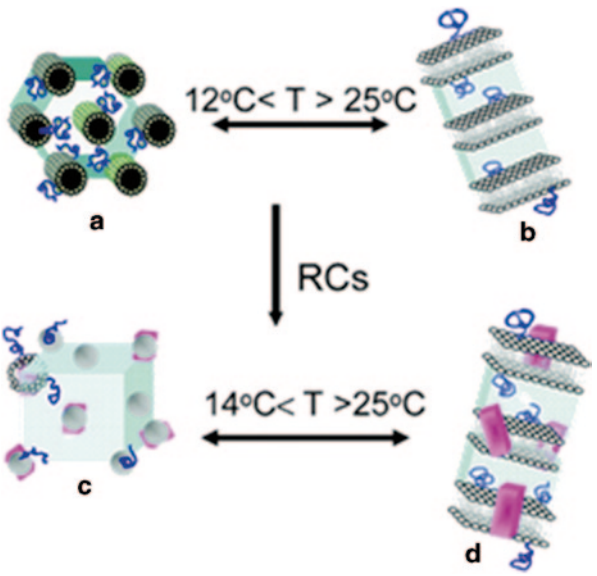

Fig. 14.9 Schematic representation of bacterial photosynthetic reaction centers (RCs) co-assembled with mixed lipid phases containing phospholipid, lipopolymer, and cosurfactant. **a** Normal hexagonal phase at low temperature, and **b** lamellar phase formed at high temperature by the mixed lipid phases. **c** Cubic micellar phase, and **d** lamellar phase when the mixed lipid phases are co-assembled with RCs. *T* temperature, *RCs* reaction centers (Reproduced with permission [2]. Copyright 2005, American Chemical Society)

lamellar structures) and plays a critical role in converting the membrane lipids to bilayer structures. In the study, the LHCII protein has the same effect on the triblock copolymer and induces a phase transition of the polymer from micelles to lamellar bilayers. The lamellar domain spacing is 7 nm, which is slightly larger than the natural thylakoid membrane thickness (5 nm). The proteins are shown to be highly oriented in the bilayer structure which is essential for light harvesting, and they were shown to catalyze a light-dependent hydrogen production reaction.

14.4 Direct Self-Assembly of Proteins

The direct self-assembly of proteins provides a final approach to nanostructure fabrication. However, most proteins do not themselves self-assemble; therefore, a structure-directing functionality must be conjugated to the protein. Typically, this is accomplished through two means: protein–polymer conjugation and engineering of fusion proteins. The advantage of both methods is that extremely high densities of proteins can be achieved within a 3D nanostructure because no templating material is required; however, these methods necessitate modifications to the protein itself. Self-assembly of protein–polymer bioconjugates provides a relatively simple bottom-up approach to templating proteins, exploiting a large body of literature on protein–polymer conjugates that provides a great deal of versatility in the approach taken to the synthesis of conjugates [270–274]. Given the large number of strategies, it has been possible to synthesize such conjugates for almost any protein of interest.

Improved synthesis methods over the past decades have enabled a multitude of routes toward synthesis of conjugated globular protein–polymer block copolymers

with site-specific control over conjugation of a single synthetic polymer [275–278]. Polymers are synthesized via living polymerizations—primarily atom transfer radical polymerization (ATRP) [279–283], reversible addition-fragmentation transfer (RAFT) [284–286], and nitroxide-mediated radical polymerization (NMRP) [287, 288]—to achieve controlled molecular weights and low dispersities. The protein and polymer are covalently linked through two main synthetic routes—*grafting to* in which the two blocks are reactively coupled and *grafting from* where a protein macroinitator is used to grow the polymer chain through a controlled free-radical polymerization. Mild reaction conditions are needed to maintain the protein's native conformation, and bioconjugate methods often require proteins with a single reactive functional group for site-specific conjugation, limiting the generalizability of this nanopatterning method. Often, genetic manipulation of the protein amino acid sequence is required to render them amenable for bioconjugation. Protein fusion systems using thermoresponsive elastin-like polypeptides (ELPs) as the coil-like domain are fully biosynthetic analogues to protein–polymer conjugates that can also be used to direct self-assembly. The relative ease of large-scale biosynthesis and purification, as well as the monodispersity and perfect control over the fusion block composition, makes fusion protein conjugates a potentially cost-effective alternative to protein–polymer conjugates. ELP fusions are solvated and unstructured at low temperatures, but they have an inverse thermal transition temperature (T_t) that can be rationally engineered by appropriate choice of the amino acid sequence [289]. The ELP sequence is typically designed such that T_t is around 20–30 °C for physiologically relevant applications.

14.4.1 Dilute Solution

Dilute solution nanostructures can be achieved from spontaneous or stimulus-triggered self-assembly. The type of nanostructure formed depends upon bioconjugate composition (polymer block length and protein sequence) and the specific processing used to induce nanostructure formation. Approximately two decades ago, Hoffman and coworkers studied protein–polymer bioconjugates consisting of a stimuli-responsive polymer component for affinity-based separations and control over protein–ligand recognition. Initial studies utilized succinimide esters to conjugate non-site specifically to proteins through lysine residues [290, 291], while subsequent studies used coupling reactions between thiol and maleimide or vinyl sulfone to achieve site-specific conjugations to polymers responsive to temperature, pH, and light, conferring the stimuli-responsive properties to their respective bioconjugates [292–303]. Above the thermoresponsive transition temperature of PNIPAM, mesoscale streptavidin–PNIPAM aggregates formed with hydrodynamic diameters between 250 and 900 nm [303]. Due to the biological compatibility and biomedical relevance of PNIPAM, a number of dilute solution characterizations of BSA–PNIPAM conjugates formed aggregates and micellar structures [304] that retained their activity and secondary structure [305, 306]. Protein–polymer conjugates using thermoresponsive polymer diblocks [307–309] have also been demonstrated to

form aggregated and micellar structures, and the effect of PNIPAM chain architecture on conjugate dilute solution behavior has been explored [310].

Super-amphiphiles are larger molecular weight analogues of surfactants comprising diblock copolymers with a hydrophilic and a hydrophobic block [311–314]. When the hydrophilic block of these molecules is protein, their surfactant-like self-assembly can be used to enable protein nanostructure formation in dilute solution. Monodisperse enzyme–polymer hybrids of *Candida antarctica* lipase B and PS, termed "giant amphiphiles," have been shown to self-assemble into micrometer-long fibers constructed from bundles of rods formed from self-assembled bioconjugates. Similar enzyme–polymer biohybrids of PS conjugated to BSA and apo-HRP self-assembled into micellar and vesicle nanostructures, respectively [315, 316]. Self-assembled nanostructures of biohybrid ABC triblock copolymers [317] consisting of PS-*b*-polyethylene glycol reconstituted to either the hemoprotein myoglobin (Mb) or HRP form a variety of structures, including Y-shapes, toroids, and figure-eight geometries. Because the PS blocks of the giant amphiphiles are highly hydrophobic and glassy at ambient temperatures, kinetic effects are certain to play a very large role in controlling the type of nanostructures formed by these systems.

Fusion protein polymers have also attracted interest as fully biosynthetic analogues to protein–polymer biohybrid molecules for nanostructuring proteins. The ability to design and synthesize such systems using protein engineering techniques alone eliminates concern over bioconjugation conversions and reaction conditions. Fusion constructs of proteins with thermoresponsive ELPs have been demonstrated by Chilkoti and coworkers to be highly expressible and able to form reversible aggregates while retaining biofunctionality of the folded protein block [318–323]. Potential applications include drug delivery and protein purification. In addition, a viral capsid protein and a thermally responsive ELP have been engineered into a single structural fusion protein by van Hest and coworkers that displays two unique self-assembly mechanisms owing to properties of each protein domain—pH-induced self-assembly from the viral capsid protein and temperature-induced self-assembly from the ELP—resulting in different solution nanostructures [324]. Bacterial cell-surface layer (S-layer) fusion protein assemblies [325, 326] have also been shown to pattern functional protein domains through the inherent ability of S-layer proteins to self-assemble into a protein lattice.

14.4.2 Concentrated Solution and Solid-State Self-Assembly

While protein–polymer conjugates in dilute solution have been shown to self-assemble into a multitude of solution nanostructures, globular protein–polymer diblock copolymers have only recently been demonstrated to self-assemble into canonical block copolymer nanostructures in both concentrated aqueous solution and the solid state (Fig. 14.10) [327–329]. This approach has the potential to extend the capability to produce biofunctional plastics and gels that combine dense 3D protein nanostructures, biphasic control over transport, and control over protein

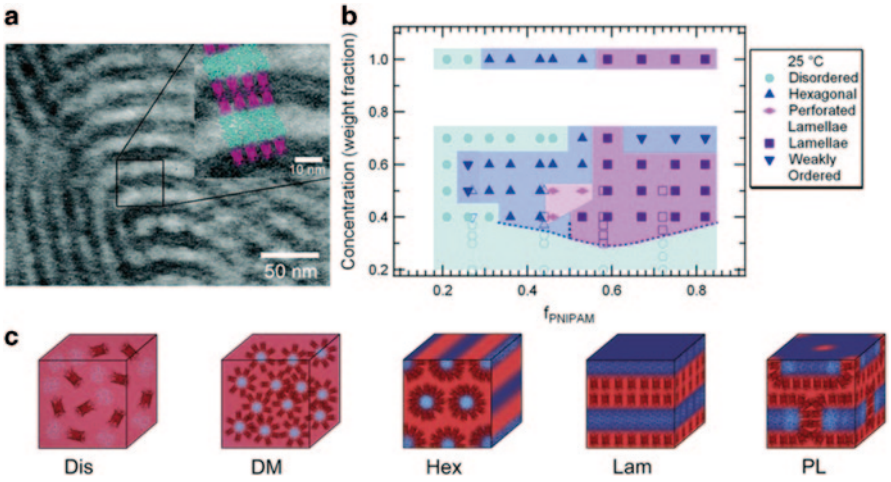

Fig. 14.10 **a** TEM showing bilayer lamellae formed by the globular protein–polymer block copolymer mCherry-*b*-PNIPAM in the solid-state, **b** phase diagrams for the self-assembly of mCherry-PNIPAM block copolymers as a function of polymer coil fraction and concentration at 25 °C, and **c** schematic of the various phases observed in concentrated solution and solid state, where the abbreviations represent disordered *(Dis),* disordered micellar *(DM),* hexagonally packed cylinders *(Hex),* lamellar *(Lam),* and perforated lamellar *(PL)*. (Adapted with permission [327, 329, 332]. Copyright 2014, Royal Society of Chemistry)

orientation. The highly specific protein shape [330, 331] and anisotropic hydrophobic, ionic, and hydrogen-bonding interactions between different protein molecules contribute complexity to the thermodynamics governing self-assembly of globular protein–polymer block copolymers, and the phase diagram has been shown to be significantly different than that of traditional coil–coil copolymers [332]. A number of studies and reviews of bioconjugate molecules incorporating structurally simple peptide motifs [330, 333–340] display peptide structure-dependent phase behavior, demonstrating the significant effects on block copolymer phase behavior from inter-peptide specific interactions. However, enzymes and other globular proteins demonstrate hierarchical structures and complex interactions beyond these simple peptide motifs, making their self-assembly a grand engineering challenge.

The red fluorescent protein mCherry conjugated to PNIPAM is an ideal model system for studying self-assembly of such molecules, with interactions tunable based on temperature and the fold of the protein easily assayed using UV–Vis spectroscopy. In concentrated solution, modulation of the aforementioned binary interactions as a function of concentration or temperature leads to an observed order–disorder transition concentration (C_{ODT}) and lyotropic and thermotropic order–order transitions (OOTs). mCherry–PNIPAM bioconjugate microphase separates into hexagonal, lamellar, and perforated lamellar morphologies between $\phi_{PNIPAM} = 0.25$ and $\phi_{PNIPAM} = 0.70$. Both mCherry and PNIPAM have positive second-virial coefficients [329, 341], suggesting that the protein–polymer interactions primarily govern the self-assembly behavior of these materials. Consistent with this hypothesis,

the C_{ODT} is observed to reach a minimum in mCherry–*b*–PNIPAM near symmetric coil fraction ϕ_{PNIPAM}, conditions where the binary protein–polymer interactions are maximized.

Removal of water under nonselective solvent conditions results in solid-state self-assembled morphologies resembling those formed by conventional coil–coil block copolymers [327, 328]. Circular dichroism (CD) confirmed preservation of the protein secondary structure after solid-state self-assembly, and UV–Vis determined that approximately 70% of the protein remained active. Extensive self-assembly studies of mCherry–PNIPAM as a function of coil fraction reveal a highly asymmetric phase diagram significantly different from that of traditional coil–coil block copolymers, including a reentrant order–disorder transition above approximately 70 wt.% in concentration (Fig. 14.10) [332].

Experiments comparing the effects of protein and polymer interactions on the self-assembly of protein–polymer conjugates suggest that coarse-grained protein properties and protein–polymer interactions dominate the thermodynamics of protein–polymer conjugate phase behavior. Conjugates of PNIPAM to mCherry and EGFP, two globular proteins with similar second-virial coefficients, size, and tertiary structure show similar phase behavior and point mutations to perturb the mCherry surface potential have little effect [342], confirming that coarse-grained models are more important than detailed protein interactions for formulating models of protein–polymer conjugates. Conversely, conjugating mCherry to the thermoresponsive polymers poly(hydroxypropylacrylate) and poly(oligoethylene glycol acrylate), which have different hydrogen-bonding interactions than PNIPAM, results in differences in protein–polymer interactions manifest by shifted phase transition lines and the appearance of a double gyroid phase. A high concentration reentrant order–disorder transition is observed for conjugates to all the different polymers, suggesting that this is a universal property of the shape of the molecules [343].

14.5 Summary and Outlook

Many protein-patterning technologies are relatively new, and a number of challenges and opportunities remain to advance the technology. The direct self-assembly of globular protein–polymer block copolymers is a recently explored area of research for controlling protein spatial position and orientation. The physical interactions at the molecular level between protein and polymer components are complicated by the anisotropic nature of the protein interactions, necessitating a deeper understanding of the physics behind self-assembly to enable design of different nanostructured morphologies. Protein engineering and bioconjugation chemistry provide access to a wide variety of block copolymer molecules, encouraging application of the technique to a myriad of biofunctional systems. Templating techniques using electrostatic or hydrophobic interactions between proteins and macromolecules to guide assembly also show great promise. Challenges include maximizing protein loading

within the template, understanding design rules that lead to optimal protein stability and activity within the material, and controlling transport through the templated nanostructure to reach all of the immobilized protein. In many cases, control over protein orientation represents an additional challenge. The scalability and relatively simple chemistry necessary for templated assembly motivate efforts to address these challenges, enabling templates to be applied in commercial settings.

Nonconventional lithography techniques are relatively young and are actively undergoing rapid developments and improvements. While lithographic patterning approaches such as EBL, DPN, and nanografting enable protein nanopatterning with high resolution at the single-molecule scale with high precision and reliability, the most significant barrier to these techniques is parallelization to increase throughput. Although the writing speeds of the tips in the AFM-based methods can be increased, the greatest improvement to increasing throughput will result from patterning using arrays of tips, and hardware and software issues are being addressed to provide control over individual tips within active arrays of multiple-tip platforms. In addition, a better understanding and improved methods of protein immobilization interactions and the transport processes of large biomolecules such as proteins from AFM tip or stamp material to the substrate that maximize the protein functionality is as equally important as addressing the fabrication challenges.

In summary, globular proteins and enzymes have the ability to specifically recognize a wide variety of molecules and catalyze a myriad of reactions under gentle conditions, making them invaluable for potential applications in proteomics and lab-on-a-chip devices, drug delivery and medicine, catalysis, sensing, decontamination, and energy conversion. Successful incorporation of globular proteins and enzymes for device and biofunctional nanomanufacturing requires removal from their native conditions, so the materials scientist and engineer must provide a way to control the nanostructure or nanopattern within an environment that fortifies their native conformation. Protein nanopatterning provides control over the spatial resolution and protein orientation of biomolecules for fabrication of biofunctional nanodevices in which both transport and reactivity properties can be optimized. Choosing among the many available nanopatterning techniques for a given application requires the material designer to weigh different criteria for material performance, identifying the patterning method with strengths that best match a given application. Patterning methods demonstrate differing abilities to control the spatial arrangements of protein, protein orientation, and the formation of 3D structures based on the specific chemistry and processing of each approach. It is imperative that the chemistry and processing used in patterning do not disrupt the native protein fold; however, there is no general strategy for preserving protein activity that can be readily exploited in all systems. Therefore, many of the techniques discussed in this review are complementary to one another, and ultimately the most optimal nanopatterning method depends upon the desired application and may involve a combination of techniques. With significant contributions from multiple scientific disciplines helping to overcome the challenges and limitations of current technologies, the future of enzyme and protein patterning is highly optimistic, and the set of top-down, bottom-up, and hybrid approaches will continue to improve and expand for exploring numerous applications in biotechnology, energy, and medicine.

Acknowledgments This work was supported by the Department of Energy Office of Basic Energy Sciences (award number DE-SC0007106), Air Force Office of Scientific Research (award number FA9550-12-0259), and National Science Foundation (DMR-1253306). The authors are very grateful to Carolyn E. Mills for the creation of artwork.

References

1. K.M. Koeller, C.-H. Wong, Nature **409**, 232 (2001)
2. P.D. Laible, R.F. Kelley, M.R. Wasielewski, M.A. Firestone, J. Phys. Chem. B **109**, 23679 (2005)
3. N. Kumar, O. Parajuli, A. Dorfman, D. Kipp, J.I. Hahm, Langmuir **23**, 7416 (2007)
4. A.L. Ghindilis, P. Atanasov, E. Wilkins, Electroanal **9**, 661 (1997)
5. J. Barber, Chem. Soc. Rev. **38**, 185 (2009)
6. T.D. Bugg, *Introduction to Enzyme and Coenzyme Chemistry* (Wiley, Chicheste, 2012)
7. S.G. Burton, D.A. Cowan, J.M. Woodley, Nat. Biotechnol. **20**, 37 (2002)
8. M.P. Blaustein, W.J. Lederer, Physiol. Rev. **79**, 763 (1999)
9. B. Green, D. Durnford, Annu. Rev. Plant Biol. **47**, 685 (1996)
10. E.A. Padlan, Mol. Immunol. **31**, 169 (1994)
11. A. Heller, J. Phys. Chem. **96**, 3579 (1992)
12. O. Yehezkeli, Y.-M. Yan, I. Baravik, R. Tel-Vered, I. Willner, Chem. Eur. J. **15**, 2674 (2009)
13. G.F. Drevon, A.J. Russell, Biomacromolecules **1**, 571 (2000)
14. A.J. Russell, J.A. Berberich, G.F. Drevon, R.R. Koepsel, Annu. Rev. Biomed. Eng. **5**, 1 (2003)
15. A.L. Simonian, J.K. Grimsley, A.W. Flounders, J.S. Schoeniger, T.-C. Cheng, J.J. DeFrank, J.R. Wild, Anal. Chim. Acta **442**, 15 (2001)
16. R.N. Patel, Coord. Chem. Rev. **252**, 659 (2008)
17. F. Hasan, A.A. Shah, A. Hameed, Enzyme Microb. Tech. **39**, 235 (2006)
18. A. Schmid, J. Dordick, B. Hauer, A. Kiener, M. Wubbolts, B. Witholt, Nature **409**, 258 (2001)
19. H.E. Schoemaker, D. Mink, M.G. Wubbolts, Science **299**, 1694 (2003)
20. A.J. Straathof, S. Panke, A. Schmid, Curr. Opin. Biotech. **13**, 548 (2002)
21. O. Kirk, T.V. Borchert, C.C. Fuglsang, Curr. Opin. Biotech. **13**, 345 (2002)
22. N. Favre, M.L. Christ, A.C. Pierre, J. Mol. Catal. B: Enzym. **60**, 163 (2009)
23. T. Reda, C.M. Plugge, N.J. Abram, J. Hirst, Proc. Natl. Acad. Sci. U S A **105**, 10654 (2008)
24. B.A. Parkinson, P.F. Weaver, Nature **309**, 148 (1984)
25. S. Kuwabata, R. Tsuda, H. Yoneyama, J. Am. Chem. Soc. **116**, 5437 (1994)
26. A.A. Karyakin, S.V. Morozov, E.E. Karyakina, S.D. Varfolomeyev, N.A. Zorin, S. Cosnier, Electrochem. Commun. **4**, 417 (2002)
27. M. Hambourger, M. Gervaldo, D. Svedruzic, P.W. King, D. Gust, M. Ghirardi, A.L. Moore, T.A. Moore, J. Am. Chem. Soc. **130**, 2015.(2008)
28. H. Krassen, A. Schwarze, B. Friedrich, K. Ataka, O. Lenz, J. Heberle, ACS Nano **3**, 4055 (2009)
29. S.D. Minteer, B.Y. Liaw, M.J. Cooney, Curr. Opin. Biotechnol. **18**, 228 (2007)
30. D. Leech, P. Kavanagh, W. Schuhmann, Electrochim. Acta **84**, 223 (2012)
31. R.J. Cogdell, A. Gall, J. Kohler, Q. Rev. Biophys. **39**, 227 (2006)
32. R. Das, P.J. Kiley, M. Segal, J. Norville, A.A. Yu, L. Wang, S.A. Trammell, L.E. Reddick, R. Kumar, F. Stellacci, N. Lebedev, J. Schnur, B.D. Bruce, S. Zhang, M. Baldo, Nano Lett. **4**, 1079 (2004)
33. J.W. Choi, M. Fujihira, Appl. Phys. Lett. **84**, 2187 (2004)
34. D. Falconnet, G. Csucs, H. Michelle Grandin, M. Textor, Biomaterials **27**, 3044 (2006)
35. J. Vörös, T. Blättler, M. Textor, MRS Bull. **30**, 202 (2005)
36. K. Nakanishi, T. Sakiyama, K. Imamura, J. Biosci. Bioeng. **91**, 233 (2001)

37. S. Hudson, E. Magner, J. Cooney, B.K. Hodnett, J. Phys. Chem. B **109**, 19496 (2005)
38. F. Rusmini, Z.Y. Zhong, J. Feijen, Biomacromolecules **8**, 1775 (2007)
39. W. Tischer, F. Wedekind, Immobilized enzymes: methods and applications. *Biocatalysis - From Discovery to Application* (Springer Berlin Heidelberg, 1999) pp 95–126, p. 95
40. I. Willner, E. Katz, Angew. Chem. Int. Ed. **39**, 1180 (2000)
41. L.S. Wong, F. Khan, J. Micklefield, Chem. Rev. **109**, 4025 (2009)
42. K. Hernandez, R. Fernandez-Lafuente, Enzym. Microb. Tech. **48**, 107 (2011)
43. M. Minier, M. Salmain, N. Yacoubi, L. Barbes, C. Methivier, S. Zanna, C.M. Pradier, Langmuir **21**, 5957 (2005)
44. M.T. Neves-Petersen, T. Snabe, S. Klitgaard, M. Duroux, S.B. Petersen, Protein Sci. **15**, 343 (2006)
45. M.S. Belluzo, M.E. Ribone, C. Camussone, I.S. Marcipar, C.M. Lagier, Anal. Biochem. **408**, 86 (2011)
46. C.A. Godoy, O. Romero, B. de la Rivas, C. Mateo, G. Fernandez-Lorente, J.M. Guisan, J.M. Palomo, J. Mol. Catal. B-Enzym. **87**, 121 (2013)
47. J.M. Bolivar, J. Rocha-Martin, C. Mateo, F. Cava, J. Berenguer, D. Vega, R. Fernandez-Lafuente, J.M. Guisan, J. Mol. Catal. B-Enzym. **58**, 158 (2009)
48. V. Grazu, F. Lopez-Gallego, T. Montes, O. Abian, R. Gonzalez, J.A. Hermoso, J.L. Garcia, C. Mateo, J.M. Guisan, Process Biochem. **45**, 390 (2010)
49. C. Mateo, O. Abian, G. Fernandez-Lorente, J. Pedroche, R. Fernandez-Lafuente, J.M. Guisan, Biotechnol. Progr. **18**, 629 (2002)
50. M. Gonzalez, L.A. Bagatolli, I. Echabe, J.L.R. Arrondo, C.E. Argarana, C.R. Cantor, G.D. Fidelio, J. Biol. Chem. **272**, 11288 (1997)
51. T. Hoshi, J. Anzai, T. Osa, Anal. Chem. **67**, 770 (1995)
52. P. Pantano, W.G. Kuhr, Anal. Chem. **65**, 623 (1993)
53. S.V. Rao, K.W. Anderson, L.G. Bachas, Biotechnol. Bioeng. **65**, 389 (1999)
54. J. Kim, J.W. Grate, P. Wang, Chem. Eng. Sci. **61**, 1017 (2006)
55. S.D. Minteer, *Methods and Protocols*, vol. 679. Series: Methods in Molecular Biology, (Springer, Heidelberg, 2010)
56. F. Rusmini, Z. Zhong, J. Feijen, Biomacromolecules **8**, 1775 (2007)
57. D. Brady, J. Jordaan, Biotechnol. Lett. **31**, 1639 (2009)
58. A. Sassolas, L.J. Blum, B.D. Leca-Bouvier, Biotechnol. Adv. **30**, 489 (2012)
59. U. Hanefeld, L. Gardossi, E. Magner, Chem. Soc. Rev. **38**, 453 (2009)
60. W. Lee, D. Choi, Y. Lee, D.-N. Kim, J. Park, W.-G. Koh, Sens. Actuators B **129**, 841 (2008)
61. H. Sorribas, C. Padeste, L. Tiefenauer, Biomaterials **23**, 893 (2002)
62. P.S. Petrou, M. Chatzichristidi, A.M. Douvas, P. Argitis, K. Misiakos, S.E. Kakabakos, Biosens. Bioelectron. **22**, 1994(2007)
63. K.L. Christman, V.D. Enriquez-Rios, H.D. Maynard, Soft Matter **2**, 928 (2006)
64. A.W. Flounders, D.L. Brandon, A.H. Bates, Biosens. Bioelectron. **12**, 447 (1997)
65. A.S. Blawas, W.M. Reichert, Biomaterials **19**, 595 (1998)
66. J.F. Mooney, A.J. Hunt, J.R. McIntosh, C.A. Liberko, D.M. Walba, C.T. Rogers, Proc. Natl. Acad. Sci. U S A **93**, 12287 (1996)
67. A. Douvas, P. Argitis, C.D. Diakoumakos, K. Misiakos, D. Dimotikali, S.E. Kakabakos, J. Vac. Sci. Technol. B **19**, 2820 (2001)
68. Y. Lee, S. Park, S.W. Han, T.G. Lim, W.G. Koh, Biosens. Bioelectron. **35**, 243 (2012)
69. D.J. Pritchard, H. Morgan, J.M. Cooper, Angew. Chem. Int. Ed. Engl. **34**, 91 (1995)
70. D.J. Pritchard, H. Morgan, J.M. Cooper, Anal. Chem. **67**, 3605 (1995)
71. P. Bhatnagar, G.G. Malliaras, I. Kim, C.A. Batt, Adv. Mater. **22**, 1242 (2010)
72. G. Tizazu, O. el Zubir, S. Patole, A. McLaren, C. Vasilev, D. Mothersole, A. Adawi, C.N. Hunter, D. Lidzey, G. Lopez, G. Leggett, Biointerphases **7**, 1 (2012)
73. S.K. Bhatia, L.C. Shriver-Lake, K.J. Prior, J.H. Georger, J.M. Calvert, R. Bredehorst, F.S. Ligler, Anal. Biochem. **178**, 408 (1989)
74. L.M. Lee, R.L. Heimark, R. Guzman, J.C. Baygents, Y. Zohar, Lab Chip **6**, 1080 (2006)

75. L.M. Lee, R.L. Heimark, J.C. Baygents, Y. Zohar, Nanotechnology **17**, S29 (2006)
76. M. Kim, J.-C. Choi, H.-R. Jung, J.S. Katz, M.-G. Kim, J. Doh, Langmuir **26**, 12112 (2010)
77. M. Dubey, K. Emoto, H. Takahashi, D.G. Castner, D.W. Grainger, Adv. Funct. Mater. **19**, 3046 (2009)
78. S. Lenci, L. Tedeschi, F. Pieri, C. Domenici, Appl. Surf. Sci. **257**, 8413 (2011)
79. R. Ganesan, K. Kratz, A. Lendlein, J. Mater. Chem. **20**, 7322 (2010)
80. D.-S. Shin, K.-N. Lee, K.-H. Jang, J.-K. Kim, W.-J. Chung, Y.-K. Kim, Y.-S. Lee, Biosens. Bioelectron. **19**, 485 (2003)
81. K.-N. Lee, Y.-K. Kim, J. Semicond. Technol. Sci. **1**, 132 (2001)
82. K.-N. Lee, D.-S. Shin, Y.-S. Lee, Y.-K. Kim, J. Micromech. Microeng. **13**, 18 (2003)
83. M. Hengsakul, A.E. Cass, Bioconjugate Chem. **7**, 249 (1996)
84. I.S. Carrico, S.A. Maskarinec, S.C. Heilshorn, M.L. Mock, J.C. Liu, P.J. Nowatzki, C. Franck, G. Ravichandran, D.A. Tirrell, J. Am. Chem. Soc. **129**, 4874 (2007)
85. C.R. Toh, T.A. Fraterman, D.A. Walker, R.C. Bailey, Langmuir **25**, 8894 (2009)
86. T.A. Martin, S.R. Caliari, P.D. Williford, B.A. Harley, R.C. Bailey, Biomaterials **32**, 3949 (2011)
87. M.J. Lercel, C.S. Whelan, H.G. Craighead, K. Seshadri, D.L. Allara, J. Vac. Sci. Technol. B: Microelectron. Nanometer Struct. **14**, 4085 (1996)
88. A.N. Broers, IBM J. Res. Dev. **32**, 502 (1988)
89. L.R. Harriott, J. Vac. Sci. Technol. B **15**, 2130 (1997)
90. N. Samoto, A. Yoshida, H. Takano, A. Endo, T. Fukui, J. Microlith. Microfab. **4**, 2005
91. J.P. Spallas, C.S. Silver, L.P. Muray, J. Vac. Sci. Technol. B **24**, 2892 (2006)
92. T. Haraguchi, T. Sakazaki, S. Hamaguchi, H. Yasuda, J. Vac. Sci. Technol. B **20**, 2726 (2002)
93. T. Powell, J.Y. Yoon, Biotechnol. Progr. **22**, 106 (2006)
94. F.A. Denis, A. Pallandre, B. Nysten, A.M. Jonas, C.C. Dupont-Gillain, Small **1**, 984 (2005)
95. A. Pallandre, B. De Meersman, F. Blondeau, B. Nysten, A.M. Jonas, J. Am. Chem. Soc. **127**, 4320 (2005)
96. P. Emsley, I.G. Charles, N.F. Fairweather, N.W. Isaacs, Nature **381**, 90–92 (1996)
97. J. Rundqvist, J.H. Hoh, D.B. Haviland, Langmuir **22**, 5100 (2006)
98. R. Schlapak, J. Danzberger, T. Haselgrubler, P. Hinterdorfer, F. Schaffler, S. Howorka, Nano Lett. **2012**, 12, (1983).
99. P.A. Kunzi, J. Lussi, L. Aeschimann, G. Danuser, M. Textor, N.F. de Rooij, U. Staufer, Microelectron. Eng. **78–79**, 582 (2005)
100. J.W. Lussi, C. Tang, P.A. Kuenzi, U. Staufer, G. Csucs, J. Voros, G. Danuser, J.A. Hubbell, M. Textor, Nanotechnology **16**, 1781 (2005)
101. S. Kumagai, S. Yoshii, K. Yamada, I. Fujiwara, N. Matsukawa, I. Yamashita, J. Photopolym. Sci. Technol. **18**, 495 (2005)
102. C.K. Harnett, K.M. Satyalakshmi, H.G. Craighead, Langmuir **17**, 178 (2000)
103. J. Abramson, M. Palma, S.J. Wind, J. Hone, Adv. Mater. **24**, 2207 (2012)
104. K.L. Christman, E. Schopf, R.M. Broyer, R.C. Li, Y. Chen, H.D. Maynard, J. Am. Chem. Soc. **131**, 521 (2009)
105. C.M. Kolodziej, H.D. Maynard, Chem. Mater. **24**, 774 (2012)
106. S. Borini, S. D'Auria, M. Rossi, A.M. Rossi, Lab Chip **5**, 1048 (2005)
107. D.S. Ginger, H. Zhang, C.A. Mirkin, Angew. Chem. Int. Ed. **43**, 30 (2004)
108. R.D. Piner, J. Zhu, F. Xu, S.H. Hong, C.A. Mirkin, Science **283**, 661 (1999)
109. J.Y. Jang, G.C. Schatz, M.A. Ratner, J. Chem. Phys. **116**, 3875 (2002)
110. J. Jang, G.C. Schatz, M.A. Ratner, Phys. Rev. Lett. **90**, 156104 (2003)
111. J.Y. Jang, G.C. Schatz, M.A. Ratner, Phys. Rev. Lett. **92**, 085504-1–085504-4 (2004)
112. B.L. Weeks, M.W. Vaughn, J.J. DeYoreo, Langmuir **21**, 8096 (2005)
113. B.L. Weeks, J.J. DeYoreo, J. Phys. Chem. B **110**, 10231 (2006)
114. M.G. Boyle, J. Mitra, P. Dawson, Nanotechnology **20**, 335202 (2009)
115. K. Salaita, A. Amarnath, T.B. Higgins, C.A. Mirkin, Scanning **32**, 9 (2010)
116. P.V. Schwartz, Langmuir **18**, 4041 (2002)
117. C.D. Wu, T.H. Fang, J.F. Lin, Langmuir **26**, 3237 (2010)

118. R.G. Sanedrin, N.A. Amro, J. Rendlen, M. Nelson, Nanotechnology **21**, 115302 (2010)
119. H. Kim, J. Jang, J. Phys. Chem. A **113**, 4313 (2009)
120. J.Y. Jang, S.H. Hong, G.C. Schatz, M.A. Ratner, J. Chem. Phys. **115**, 2721 (2001)
121. P. Manandhar, J. Jang, G.C. Schatz, M.A. Ratner, S. Hong, Phys. Rev. Lett. **90**, 115505-1–115505-4 (2003)
122. J.R. Hampton, A.A. Dameron, P.S. Weiss, J. Am. Chem. Soc. **128**, 1648 (2006)
123. H. Brunner, T. Vallant, U. Mayer, H. Hoffmann, B. Basnar, M. Vallant, G. Friedbacher, Langmuir **15**, 1899 (1999)
124. C.C. Wu, D.N. Reinhoudt, C. Otto, V. Subramaniam, A.H. Velders, Small **7**, 989 (2011)
125. K. Salaita, Y.H. Wang, C.A. Mirkin, Nat. Nanotechnol. **2**, 145 (2007)
126. K. Salaita, Y.H. Wang, J. Fragala, R.A. Vega, C. Liu, C.A. Mirkin, Angew. Chem. Int. Ed. **45**, 7220 (2006)
127. K. Salaita, S.W. Lee, X.F. Wang, L. Huang, T.M. Dellinger, C. Liu, C.A. Mirkin, Small **1**, 940 (2005)
128. J. Haaheim, O.A. Nafday, Scanning **30**, 137 (2008)
129. D. Bullen, S.-W. Chung, X. Wang, J. Zou, C.A. Mirkin, C. Liu, Appl. Phys. Lett. **84**, 789 (2004)
130. J.-H. Lim, D.S. Ginger, K.-B. Lee, J. Heo, J.-M. Nam, C.A. Mirkin, Angew. Chem. Int. Ed. **42**, 2309 (2003)
131. C.C. Wu, H.P. Xu, C. Otto, D.N. Reinhoudt, R.G.H. Lammertink, J. Huskens, V. Subramaniam, A.H. Velders, J. Am. Chem. Soc. **131**, 7526 (2009)
132. J.M. Nam, S.W. Han, K.B. Lee, X.G. Liu, M.A. Ratner, C.A. Mirkin, Angew. Chem. Int. Ed. **43**, 1246 (2004)
133. A.J. Senesi, D.I. Rozkiewicz, D.N. Reinhoudt, C.A. Mirkin, ACS Nano **3**, 2394 (2009)
134. K.-B. Lee, J.-H. Lim, C.A. Mirkin, J. Am. Chem. Soc. **125**, 5588 (2003)
135. E. Bellido, R. de Miguel, D. Ruiz-Molina, A. Lostao, D. Maspoch, Adv. Mater. **22**, 352 (2010)
136. K.B. Lee, S.J. Park, C.A. Mirkin, J.C. Smith, M. Mrksich, Science **295**, 1702 (2002)
137. J. Hyun, S.J. Ahn, W.K. Lee, A. Chilkoti, S. Zauscher, Nano Lett. **2**, 1203 (2002)
138. T. Rakickas, M. Gavutis, A. Reichel, J. Piehler, B. Liedberg, R. Valiokas, Nano Lett. **8**, 3369 (2008)
139. J.C. Smith, K.B. Lee, Q. Wang, M.G. Finn, J.E. Johnson, M. Mrksich, C.A. Mirkin, Nano Lett. **3**, 883 (2003)
140. C.C. Wu, D.N. Reinhoudt, C. Otto, A.H. Velders, V. Subramaniam, ACS Nano **4**, 1083 (2010)
141. P. Vettiger, G. Cross, M. Despont, U. Drechsler, U. Durig, B. Gotsmann, W. Haberle, M.A. Lantz, H.E. Rothuizen, R. Stutz, G.K. Binnig, IEEE Trans. Nanotechnol. **1**, 39 (2002)
142. J. Zou, D. Bullen, X.F. Wang, C. Liu, C.A. Mirkin, Appl. Phys. Lett. **83**, 581 (2003)
143. X.F. Wang, D.A. Bullen, J. Zou, C. Liu, C.A. Mirkin, J. Vac. Sc.i Technol. B **22**, 2563 (2004)
144. D. Bullen, C. Liu, Sens. Actuators A-Phys. **125**, 504 (2006)
145. X.F. Wang, C. Liu, Nano Lett. 5, 1867 (2005)
146. Z.J. Zheng, W.L. Daniel, L.R. Giam, F.W. Huo, A.J. Senesi, G.F. Zheng, C.A. Mirkin, Angew. Chem. Int. Ed. **48**, 7626 (2009)
147. H. Zhang, R. Elghanian, N.A. Amro, S. Disawal, R. Eby, Nano Lett. **4**, 1649 (2004)
148. X. Liao, A.B. Braunschweig, Z.J. Zheng, C.A. Mirkin, Small **6**, 1082 (2010)
149. F.W. Huo, Z.J. Zheng, G.F. Zheng, L.R. Giam, H. Zhang, C.A. Mirkin, Science **321**, 1658 (2008)
150. X. Liao, A.B. Braunschweig, C.A. Mirkin, Nano Lett. **10**, 1335 (2010)
151. A.B. Braunschweig, F.W. Huo, C.A. Mirkin, Nat. Chem. **1**, 353 (2009)
152. K.A. Brown, D.J. Eichelsdoerfer, W. Shim, B. Rasin, B. Radha, X. Liao, A.L. Schmucker, G. Liu, C.A. Mirkin, Proc Natl Acad. Sci. U S A **110**, 12921 (2013)
153. T. W. Kenny, Tip-Based Nanofabrication (TBN), BAA No. 07-59, US Defense Advanced Research Projects Agency, Arlington (2007)
154. G.-Y. Liu, S. Xu, Y. Qian, Acc. Chem. Res. **33**, 457 (2000)

155. S. Xu, S. Miller, P.E. Laibinis, G. Liu, Langmuir **15**, 7244 (1999)
156. T. Tian, Z. M. LeJeune, W. K. Serem, J.-J. Yu, J. C. Garno, in *Tip-Based Nanofabrication: Fundamentals and Applications*, ed. by A.A. Tseng (Springer, New York, 2011)
157. M.A. Case, G.L. McLendon, Y. Hu, T.K. Vanderlick, G. Scoles, Nano Lett. **3**, 425 (2002)
158. Y. Hu, A. Das, M.H. Hecht, G. Scoles, Langmuir **21**, 9103 (2005)
159. D. Zhou, X. Wang, L. Birch, T. Rayment, C. Abell, Langmuir **19**, 10557 (2003)
160. K. Wadu-Mesthrige, S. Xu, N.A. Amro, G. Liu, Langmuir **15**, 8580 (1999)
161. K. Wadu-Mesthrige, N.A. Amro, J.C. Garno, S. Xu, G. Liu, Biophys. J. **80**, 1891 (2001)
162. J.R. Kenseth, J.A. Harnisch, V.W. Jones, M.D. Porter, Langmuir **17**, 4105 (2001)
163. G.-Y. Liu, N.A. Amro, Proc. Natl. Acad. Sci. U S A **99**, 5165 (2002)
164. C.-H. Jang, B.D. Stevens, R. Phillips, M.A. Calter, W.A. Ducker, Nano Lett. **3**, 691 (2003)
165. F. Bano, L. Fruk, B. Sanavio, M. Glettenberg, L. Casalis, C.M. Niemeyer, G. Scoles, Nano Lett. **9**, 2614 (2009)
166. Y.H. Tan, M. Liu, B. Nolting, J.G. Go, J. Gervay-Hague, G. Liu, ACS Nano **2**, 2374 (2008)
167. T.W. Odom, J.C. Love, D.B. Wolfe, K.E. Paul, G.M. Whitesides, Langmuir **18**, 5314 (2002)
168. H.W. Li, B.V.O. Muir, G. Fichet, W.T.S. Huck, Langmuir **19**, 1963(2003)
169. A. Kumar, G.M. Whitesides, Appl. Phys. Lett. **63**, 2002(1993)
170. S.A. Ruiz, C.S. Chen, Soft Matter **3**, 168 (2007)
171. B.D. Gates, Q.B. Xu, J.C. Love, D.B. Wolfe, G.M. Whitesides, Annu. Rev. Mater. Res. **34**, 339 (2004)
172. B.D. Gates, Q.B. Xu, M. Stewart, D. Ryan, C.G. Willson, G.M. Whitesides, Chem. Rev. **105**, 1171 (2005)
173. A. Bernard, E. Delamarche, H. Schmid, B. Michel, H.R. Bosshard, H. Biebuyck, Langmuir **14**, 2225 (1998)
174. A. Bernard, J.P. Renault, B. Michel, H.R. Bosshard, E. Delamarche, Adv. Mater. **12**, 1067 (2000)
175. D.I. Rozkiewicz, Y. Kraan, M.W.T. Werten, F.A. de Wolf, V. Subramaniam, B.J. Ravoo, D.N. Reinhoudt, Chem. Eur. J. **12**, 6290 (2006)
176. J.D. Gerding, D.M. Willard, A. Van Orden, J. Am. Chem. Soc. **127**, 1106 (2005)
177. H.D. Inerowicz, S. Howell, F.E. Regnier, R. Reifenberger, Langmuir **18**, 5263 (2002)
178. Y.N. Xia, G.M. Whitesides, Angew. Chem. Int. Ed. **37**, 551 (1998)
179. G. Csucs, T. Künzler, K. Feldman, F. Robin, N.D. Spencer, Langmuir **19**, 6104 (2003)
180. J.P. Renault, A. Bernard, A. Bietsch, B. Michel, H.R. Bosshard, E. Delamarche, M. Kreiter, B. Hecht, U.P. Wild, J. Phys. Chem. B **107**, 703 (2003)
181. B.D. Martin, S.L. Brandow, W.J. Dressick, T.L. Schull, Langmuir **16**, 9944 (2000)
182. N. Coq, T. van Bommel, R.A. Hikmet, H.R. Stapert, W.U. Dittmer, Langmuir **23**, 5154 (2007)
183. D. Falconnet, D. Pasqui, S. Park, R. Eckert, H. Schift, J. Gobrecht, R. Barbucci, M. Textor, Nano Lett. **4**, 1909 (2004)
184. J.D. Hoff, L.J. Cheng, E. Meyhofer, L.J. Guo, A.J. Hunt, Nano Lett. **4**, 853 (2004)
185. V.N. Truskett, M.P.C. Watts, Trends Biotechnol. **24**, 312 (2006)
186. A.A. Bergman, J. Buijs, J. Herbig, D.T. Mathes, J.J. Demarest, C.D. Wilson, C.T. Reimann, R.A. Baragiola, R. Hull, S.O. Oscarsson, Langmuir **14**, 6785 (1998)
187. L. Ying, Biochem. Soc. Trans. **37**, 702 (2009)
188. H. Taha, R.S. Marks, L.A. Gheber, I. Rousso, J. Newman, C. Sukenik, A. Lewis, Appl. Phys. Lett. **83**, 1041 (2003)
189. O.Y. Loh, A.M. Ho, J.E. Rim, P. Kohli, N.A. Patankar, H.D. Espinosa, Proc. Natl. Acad. Sci. **105**, 16438 (2008)
190. G. Agarwal, R.R. Naik, M.O. Stone, J. Am. Chem. Soc. **125**, 7408 (2003)
191. T. Yoshinobu, J. Suzuki, H. Kurooka, W. Moon, H. Iwasaki, Electrochim. Acta **48**, 3131 (2003)
192. J. Gu, C.M. Yam, S. Li, C. Cai, J. Am. Chem. Soc. **126**, 8098 (2004)
193. A. Bardea, R. Naaman, Small **5**, 316 (2009)
194. A. Bardea, R. Naaman, Langmuir **25**, 5451 (2009)

195. R.B. Bhatia, C.J. Brinker, A.K. Gupta, A.K. Singh, Chem. Mater. **12**, 2434 (2000)
196. W. Jin, J.D. Brennan, Anal. Chim. Acta **461**, 1 (2002)
197. K. Stine, K. Jefferson, O. Shulga in *Enzyme Stabilization and Immobilization*, vol. 679, ed. by S.D. Minteer (Humana Press, New York, 2011), p. 67
198. H.A. Klok, S. Lecommandoux, Adv. Mater. **13**, 1217 (2001)
199. M. Antonietti, S. Förster, Adv. Mater. **15**, 1323 (2003)
200. A.D. Presley, J.J. Chang, T. Xu, Soft Matter **7**, 172 (2011)
201. M.B. Cardoso, D. Smolensky, W.T. Heller, K.L. Hong, H. O'Neill, Energ. Environ. Sci. **4**, 181 (2011)
202. G. Decher, J.D. Hong, Ber. Bunsen-Ges. Phys. Chem. **95**, 1430 (1991)
203. G. Decher, J.D. Hong, Makromol. Chem-M. Symp. **46**, 321 (1991)
204. G. Decher, Science **277**, 1232 (1997)
205. K. Ariga, J.P. Hill, Q.M. Ji, Phys. Chem. Chem. Phys. **9**, 2319 (2007)
206. J. Anzai, Y. Kobayashi, N. Nakamura, M. Nishimura, T. Hoshi, Langmuir **15**, 221 (1999)
207. W.B. Stockton, M.F. Rubner, Macromolecules **30**, 2717 (1997)
208. G. Decher, J.D. Hong, J. Schmitt, Thin Solid Films **210–211**, 831 (1992) (Part 2)
209. F. Caruso, H. Lichtenfeld, M. Giersig, H. Mohwald, J. Am. Chem. Soc. **120**, 8523 (1998)
210. G.B. Sukhorukov, E. Donath, H. Lichtenfeld, E. Knippel, M. Knippel, A. Budde, H. Mohwald, Colloid. Surf. A **137**, 253 (1998)
211. M.L. Macdonald, R.E. Samuel, N.J. Shah, R.F. Padera, Y.M. Beben, P.T. Hammond, Biomaterials **32**, 1446 (2011)
212. S. Bharadwaj, R. Montazeri, D.T. Haynie, Langmuir **22**, 6093 (2006)
213. C.B. Bucur, Z. Sui, J.B. Schlenoff, J. Am. Chem. Soc. **128**, 13690 (2006)
214. C.L. Cooper, P.L. Dubin, A.B. Kayitmazer, S. Turksen, Curr. Opini. Colloid Interface Sci. **10**, 52 (2005)
215. Y. Lvov, H. Möhwald, *Protein Architecture: Interfacing Molecular Assemblies and Immobilization Biotechnology* (CRC Press LLC, New York, 2000)
216. Y. Lvov, K. Ariga, I. Ichinose, T. Kunitake, J. Am. Chem. Soc. **117**, 6117 (1995)
217. J. Hodak, R. Etchenique, E.J. Calvo, K. Singhal, P.N. Bartlett, Langmuir **13**, 2708 (1997)
218. J.P. Santos, E.R. Welsh, B.P. Gaber, A. Singh, Langmuir **17**, 5361 (2001)
219. Q. Xing, S.R. Eadula, Y.M. Lvov, Biomacromolecules **8**, 1987(2007)
220. S. Disawal, H.H. Qiu, B.B. Elmore, Y.M. Lvov, Colloid Surf. B **32**, 145 (2003)
221. Y.M. Lvov, Z.Q. Lu, J.B. Schenkman, X.L. Zu, J.F. Rusling, J. Am. Chem. Soc. **120**, 4073 (1998)
222. Y.L. Zhou, Z. Li, N.F. Hu, Y.H. Zeng, J.F. Rusling, Langmuir **18**, 8573 (2002)
223. P.L. He, N.F. Hu, J. Phys. Chem. B **108**, 13144 (2004)
224. Y. Hu, N.F. Hu, J. Phys. Chem. B **112**, 9523 (2008)
225. K. Yoshida, K. Sato, J. Anzai, J. Mater. Chem. **20**, 1546 (2010)
226. J. Schmitt, T. Grunewald, G. Decher, P.S. Pershan, K. Kjaer, M. Losche, Macromolecules **26**, 7058 (1993)
227. L. Kolarik, D.N. Furlong, H. Joy, C. Struijk, R. Rowe, Langmuir **15**, 8265 (1999)
228. S.S. Shiratori, M.F. Rubner, Macromolecules **33**, 4213 (2000)
229. Y. Hu, N. Hu, J. Phys. Chem. B **112**, 9523 (2008)
230. T. Crouzier, K. Ren, C. Nicolas, C. Roy, C. Picart, Small **5**, 598 (2009)
231. Z.J. Song, J.B. Yin, K. Luo, Y.Z. Zheng, Y. Yang, Q. Li, S.F. Yan, X.S. Chen, Macromol. Biosci. **9**, 268 (2009)
232. L. Derbal, H. Lesot, J.C. Voegel, V. Ball, Biomacromolecules **4**, 1255 (2003)
233. O.P. Tiourina, G.B. Sukhorukov, Int. J. Pharmaceut. **242**, 155 (2002)
234. A. Khademhosseini, K.Y. Suh, J.M. Yang, G. Eng, J. Yeh, S. Levenberg, R. Langer, Biomaterials **25**, 3583 (2004)
235. K.Y. Cai, A. Rechtenbach, J.Y. Hao, J. Bossert, K.D. Jandt, Biomaterials **26**, 5960 (2005)
236. L. Ma, J. Zhou, C.Y. Gao, J.C. Shen, J. Biomed. Mater. Res B **83B**, 285 (2007)
237. V. Zucolotto, A.P.A. Pinto, T. Tumolo, M.L. Moraes, M.S. Baptista, A. Riul, A.P.U. Araujo, O.N. Oliveira, Biosens. Bioelectron. **21**, 1320 (2006)

238. M. Ferreira, P.A. Fiorito, O.N. Oliveira, S.I.C. de Torresi, Biosens. Bioelectron. **19**, 1611 (2004)
239. J. Van der Gucht, E. Spruijt, M. Lemmers, M.A. Cohen Stuart, J. Colloid Interface Sci. **361**, 407 (2011)
240. M.A.C. Stuart, N.A.M. Besseling, R.G. Fokkink, Langmuir **14**, 6846 (1998)
241. A.V. Kabanov, V.A. Kabanov, Adv. Drug Deliv. Rev. **30**, 49 (1998)
242. Y. Lee, S. Fukushima, Y. Bae, S. Hiki, T. Ishii, K. Kataoka, J. Am. Chem. Soc. **129**, 5362 (2007)
243. S. Lindhoud, R. de Vries, W. Norde, M.A. Cohen Stuart, Biomacromolecules **8**, 2219 (2007)
244. I.K. Voets, A. de Keizer, M.A.C. Stuart, Adv. Colloid Interfac. **147–148**, 300 (2009)
245. G. Roman, M. Martin, P.S. Joachim, Nanotechnology **14**, 1153 (2003)
246. Y.G. Cai, B.M. Ocko, Langmuir **21**, 9274 (2005)
247. D. Batra, S. Vogt, P.D. Laible, M.A. Firestone, Langmuir **21**, 10301 (2005)
248. B. Kim, C.N. Lam, B.D. Olsen, Macromolecules **45**, 4572 (2012)
249. M.J. Fasolka, A.M. Mayes, Ann. Rev. Mater. Res. **31**, 323 (2001)
250. R.A. Segalman, Mat. Sci. Eng. R **48**, 191 (2005)
251. F.S. Bates, G.H. Fredrickson, Phys. Today **52**, 32 (1999)
252. J.N.L. Albert, T.H. Epps, Mater. Today **13**, 24 (2010)
253. W. Gu, S.W. Hong, T.P. Russell, ACS Nano **6**, 10250 (2012)
254. N. Kumar, J.I. Hahm, Langmuir **21**, 6652 (2005)
255. N. Kumar, O. Parajuli, J.I. Hahm, J. Phys. Chem. B **111**, 4581 (2007)
256. N. Kumar, O. Parajuli, A. Gupta, J.I. Hahm, Langmuir **24**, 2688 (2008)
257. K.H.A. Lau, J. Bang, D.H. Kim, W. Knoll, Adv. Funct. Mater. **18**, 3148 (2008)
258. K.H.A. Lau, J. Bang, C.J. Hawker, D.H. Kim, W. Knoll, Biomacromolecules **10**, 1061 (2009)
259. M. Matsusaki, M. Omichi, K. Kadowaki, B.H. Kim, S.O. Kim, I. Maruyama, M. Akashi, Chem. Commun. **46** 1911 (2010)
260. D. Bucknall *Nanolithography and Patterning Techniques in Microelectronics* (Woodhead Publishing Limited, Abington; CRC Press, Boca Raton, 2005)
261. J. Bang, U. Jeong, D.Y. Ryu, T.P. Russell, C.J. Hawker, Adv. Mater. **21**, 4769 (2009)
262. O. Parajuli, A. Gupta, N. Kumar, J.I. Hahm, J. Phys. Chem. B **111**, 14022 (2007)
263. S. Sheng, M. Marissa, Z. Hebing, L. Thomas, H. Mark, H. Jong-in, Nanotechnology **24**, 095601 (2013)
264. H. Elbs, C. Drummer, V. Abetz, G. Krausch, Macromolecules **35**, 5570 (2002)
265. M. Winterhalter, Colloid. Surf. A **149**, 547 (1999)
266. M.T. Paternostre, M. Roux, J.L. Rigaud, BioChemistry **27**, 2668 (1988)
267. W. Meier, C. Nardin, M. Winterhalter, Angew. Chem. Int. Ed. **39**, 4599 (2000)
268. R. Stoenescu, W. Meier Chem. Commun. (Issue 24) 3016 (2002)
269. D.C. Rees, H. Komiya, T.O. Yeates, J.P. Allen, G. Feher, Annu. Rev. Biochem. **58**, 607 (1989)
270. M.A. Gauthier, H.-A. Klok, Polym. Chem-UK **1**, 1352 (2010)
271. J. Kalia, R.T. Raines, Curr. Org. Chem. **14**, 138 (2010)
272. J.C. van Hest, J. Macromol. Sci. Part C: Polym. Rev. **47**, 63 (2007)
273. C. Boyer, X. Huang, M.R. Whittaker, V. Bulmus, T.P. Davis, Soft Matter **7**, 1599 (2011)
274. K.L. Heredia, H.D. Maynard, Org. Biomol. Chem. **5**, 45 (2007)
275. J. Kalia, R.T. Raines, Curr. Org. Chem. **14**, 138 (2010)
276. A.J. de Graaf, M. Kooijman, W.E. Hennink, E. Mastrobattista, Bioconjugate Chem. **20**, 1281 (2009)
277. E.M. Sletten, C.R. Bertozzi, Angew. Chem. Int. Ed. **48**, 6974 (2009)
278. J.-F. Lutz, H.G. Börner, Prog. Polym. Sci. **33**, 1 (2008)
279. K. Matyjaszewski, J.H. Xia, Chem. Rev. **101**, 2921 (2001)
280. V. Coessens, T. Pintauer, K. Matyjaszewski, Prog. Polym. Sci. **26**, 337 (2001)
281. T.E. Patten, K. Matyjaszewski, Adv. Mater. **10**, 901 (1998)

282. K. Matyjaszewski, N.V. Tsarevsky, Nat. Chem. **1**, 276 (2009)
283. W.A. Braunecker, K. Matyjaszewski, Prog. Polym. Sci. **32**, 93 (2007)
284. G. Moad, E. Rizzardo, S.H. Thang, Aust. J. Chem. **58**, 379 (2005)
285. G. Moad, E. Rizzardo, S.H. Thang, Polymer **49**, 1079 (2008)
286. G. Moad, E. Rizzardo, S.H. Thang, Aust. J. Chem. **59**, 669 (2006)
287. R.B. Grubbs, Polym. Rev. **51**, 104 (2011)
288. C.J. Hawker, A.W. Bosman, E. Harth, Chem. Rev. **101**, 3661 (2001)
289. D.W. Urry, Prog. Biophys. Mol. Biol. **57**, 23 (1992)
290. J.P. Chen, H.J. Yang, A.S. Huffman, Biomaterials **11**, 625 (1990)
291. J.P. Chen, A.S. Huffman, Biomaterials **11**, 631 (1990)
292. A. Chilkoti, G. Chen, P.S. Stayton, A.S. Hoffman, Bioconjugate Chem. **5**, 504 (1994)
293. A.S. Hoffman, P.S. Stayton, T. Shimoboji, G. Chen, Z. Ding, A. Chilkoti, C. Long, M. Miura, J. Chen, T. Park, *Macromol Symp*, vol. 118 (Huthig & Wepf Verlag, Zug, 1997), p. 553
294. V. Bulmus, Z. Ding, C.J. Long, P.S. Stayton, A.S. Hoffman, Bioconjugate Chem. **11**, 78 (2000)
295. Z. Ding, C.J. Long, Y. Hayashi, E.V. Bulmus, A.S. Hoffman, P.S. Stayton, Bioconjugate Chem. **10**, 395 (1999)
296. A.S. Hoffman, Clin. Chem. **46**, 1478 (2000)
297. A.S. Hoffman, P.S. Stayton, V. Bulmus, G. Chen, J. Chen, C. Cheung, A. Chilkoti, Z. Ding, L. Dong, R. Fong, J. Biomed. Mater. Res. **52**, 577 (2000)
298. T. Shimoboji, Z. Ding, P.S. Stayton, A.S. Hoffman, Bioconjugate Chem. **12**, 314 (2001)
299. T. Shimoboji, Z.L. Ding, P.S. Stayton, A.S. Hoffman, Bioconjugate Chem. **13**, 915 (2002)
300. N. Malmstadt, D.E. Hyre, Z. Ding, A.S. Hoffman, P.S. Stayton, Bioconjugate Chem. **14**, 575 (2003)
301. T. Shimoboji, E. Larenas, T. Fowler, S. Kulkarni, A.S. Hoffman, P.S. Stayton, Proc. Natl. Acad. Sci. **99**, 16592 (2002)
302. T. Shimoboji, E. Larenas, T. Fowler, A.S. Hoffman, P.S. Stayton, Bioconjugate Chem. **14**, 517 (2003)
303. S. Kulkarni, C. Schilli, A.H. Müller, A.S. Hoffman, P.S. Stayton, Bioconjugate Chem. **15**, 747 (2004)
304. M. Li, P. De, S.R. Gondi, B.S. Sumerlin, Macromol. Rapid Comm. **29**, 1172 (2008)
305. P. De, M. Li, S.R. Gondi, B.S. Sumerlin, J. Am. Chem. Soc. **130**, 11288 (2008)
306. M. Li, P. De, H. Li, B.S. Sumerlin, Polym. Chem. **1**, 854 (2010)
307. H. Li, M. Li, X. Yu, A.P. Bapat, B.S. Sumerlin, Polym. Chem. **2**, 1531 (2011)
308. M. Li, H. Li, P. De, B.S. Sumerlin, Macromol. Rapid Comm. **32**, 354 (2011)
309. C. Lavigueur, J.G. Garcia, L. Hendriks, R. Hoogenboom, J.J.L.M. Cornelissen, R.J.M. Nolte, Polym. Chem. **2**, 333 (2011)
310. Y. Xia, S. Tang, B.D. Olsen, Chem. Commun. **49**, 2566 (2013)
311. I. Gitsov, K.L. Wooley, J.M.J. Frechet, Angew. Chem. Int. Ed. Engl. **31**, 1200 (1992)
312. J.C.M. Vanhest, D.A.P. Delnoye, M.W.P.L. Baars, M.H.P. Vangenderen, E.W. Meijer, Science **268**, 1592 (1995)
313. J.P. Spatz, S. Mossmer, M. Moller, Angew. Chem. Int. Ed Engl. **35**, 1510 (1996)
314. J.J.L.M. Cornelissen, M. Fischer, N.A.J.M. Sommerdijk, R.J.M. Nolte, Science **280**, 1427 (1998)
315. A.J. Dirks, S.S. van Berkel, N.S. Hatzakis, J.A. Opsteen, F.L. van Delft, J.J.L.M. Cornelissen, A.E. Rowan, J.C.M. van Hest, F.P.J.T. Rutjes, R.J.M. Nolte, Chem. Commun. (Issue 33) 4172 (2005)
316. M.J. Boerakker, J.M. Hannink, P.H.H. Bomans, P.M. Frederik, R.J.M. Nolte, E.M. Meijer, N. A. J. M. Sommerdijk, Angew. Chem. Int. Ed. **41**, 4239 (2002)
317. I.C. Reynhout, J.J.L.M. Cornelissen, R.J.M. Nolte, J. Am. Chem. Soc. **129**, 2327 (2007)
318. D.E. Meyer, K. Trabbic-Carlson, A. Chilkoti, Biotechnol. Progr. **17**, 720 (2001)
319. D.E. Meyer, A. Chilkoti, Nat. Biotechnol. **17**, 1112 (1999)
320. D.C. Chow, M.R. Dreher, K. Trabbic-Carlson, A. Chilkoti, Biotechnol. Progr. **22**, 638 (2006)

321. K. Trabbic-Carlson, D. Meyer, L. Liu, R. Piervincenzi, N. Nath, T. LaBean, A. Chilkoti, Protein Eng. Des. Sel. **17**, 57 (2004)
322. T. Christensen, M. Amiram, S. Dagher, K. Trabbic-Carlson, M.F. Shamji, L.A. Setton, A. Chilkoti, Protein Sci. **18**, 1377 (2009)
323. M.F. Shamji, H. Betre, V.B. Kraus, J. Chen, A. Chilkoti, R. Pichika, K. Masuda, L.A. Setton, Arthr. Rheum. **56**, 3650 (2007)
324. M.B. van Eldijk, J.C.-Y. Wang, I.J. Minten, C. Li, A. Zlotnick, R.J. Nolte, J.J. Cornelissen, J.C. van Hest, J. Am. Chem. Soc. **134**, 18506 (2012)
325. D. Moll, C. Huber, B. Schlegel, D. Pum, U.B. Sleytr, M. Sára, Proc. Natl. Acad. Sci. **99**, 14646 (2002)
326. N. Ilk, E.M. Egelseer, U.B. Sleytr, Curr. Opin. Biotech. **22**, 824 (2011)
327. C.S. Thomas, M.J. Glassman, B.D. Olsen, ACS Nano **5**, 5697 (2011)
328. C.S. Thomas, L. Xu, B.D. Olsen, Biomacromolecules **13**, 2781 (2012)
329. C.N. Lam, B.D. Olsen, Soft Matter **9**, 2393 (2013)
330. A. Carlsen, S. Lecommandoux, Curr. Opin. Colloid Interface Sci. **14**, 329 (2009)
331. O.S. Rabotyagova, P. Cebe, D.L. Kaplan, Biomacromolecules **12**, 269 (2011)
332. C.S. Thomas, B.D. Olsen Soft Matter **10**, 3093–3102 (2014)
333. J.P. Billot, A. Douy, B. Gallot Makromol. Chem. **177**, 1889 (1976)
334. B. Gallot, Prog Polym. Sci. **21**, 1035 (1996)
335. S. Tangbunsuk, G.R. Whittell, M.G. Ryadnov, G.W.M. Vandermeulen, D.N. Woolfson, I. Manners, Chemistry **18**, 2524 (2012) (A European Journal)
336. W.-W. Tsai, L. Li, H. Cui, H. Jiang, S.I. Stupp, Tetrahedron **64**, 8504 (2008)
337. M.G.J. ten Cate, N. Severin, H.G. Börner, Macromolecules **39**, 7831 (2006)
338. T. Xu, N. Zhao, F. Ren, R. Hourani, M.T. Lee, J.Y. Shu, S. Mao, B.A. Helms, ACS Nano **5**, 1376 (2011)
339. F. Versluis, H.R. Marsden, A. Kros, Chem. Soc. Rev. **39**, 3434 (2010)
340. H.G. Börner, Prog. Polym. Sci. **34**, 811 (2009)
341. K. Kubota, S. Fujishige, I. Ando, J. Phys. Chem. **94**, 5154 (1990)
342. C.N. Lam, M. Kim, C.S. Thomas, D. Chang, G.E. Sanoja, C.U. Okwara, B.D. Olsen Biomacromolecules **15**(4), 1248–1258 (2014)
343. D. Chang, C.N. Lam, S. Tang, B.D. Olsen Submitted **5**, 4884–4895 (2014)

Chapter 15
Biomimetic Approach to Designing Adhesive Hydrogels: From Chemistry to Application

Yuting Li and Bruce P. Lee

15.1 Introduction

Rapid and effective wound closure remains an important goal of virtually all modern endoscopic and conventional surgical procedures. Additionally, surgical reconnection of injured tissues is essential for restoration of their structure and function. While the discontinuity in soft tissues is traditionally secured with mechanical perforating devices (e.g., sutures, tacks, and staples), these devices are also a source of complications. The application of mechanical devices is inherently traumatic to the surrounding tissues, which can result in neural irritation and persistent pain [1–4]. They are also not suitable for complicated procedures, such as stopping leaks of bodily fluids and air in blood vessels and tissues with rather low cohesive properties such as lung, liver, spleen, and kidney. In tendon reconstruction, surgical repairs often fail as sutures pullout through the tendinous tissue with loading due to stress concentration at the suture sites [5, 6]. Similarly, early failure of a repaired rotator cuff often arises from rupture of the suture material, suture knot failure, the suture material pulling through and out of the tendon or bone, or suture anchors pulling out of the bone [7–10].

Tissue adhesives can potentially simplify complex procedures, reduce surgery time, and minimize trauma [11, 12]. Currently, there are several types of commercially available tissue adhesives, which can be classified into three categories: (1) biological, (2) synthetic, and (3) a hybrid adhesive that contains both natural and synthetic components. The biological tissue adhesives is exemplified by fibrin glues, which utilizes the final stages of the blood coagulation cascade to form a blood clot. Fibrin glue (e.g., Tisseel, Baxter, Inc.) is more widely used as a tissue sealant for hemostasis and its application is limited by weak materials properties, necessary for withstanding physiological loads [11, 13, 14]. Additionally, fibrin glue consists of human-derived components that are a potential source of viral transmission

B. P. Lee (✉) · Y. Li
Department of Biomedical Engineering, Michigan Technological University,
1400 Townsend Dr. Houghton, Houghton, MI 49931, USA
e-mail: bplee@mtu.edu

M. Zhang et al. (eds.), *Carbon Nanomaterials for Biomedical Applications,*
Springer Series in Biomaterials Science and Engineering 5,
DOI 10.1007/978-3-319-22861-7_15

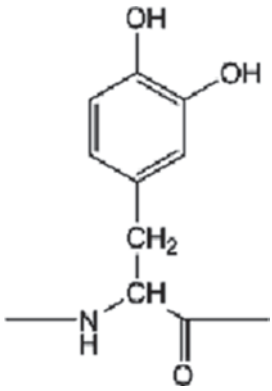

Fig. 15.1 Chemical structure of DOPA

(i.e., HIV, hepatitis) [15] and animal-derived components that have been found to lengthen curing time [16]. Synthetic cyanoacrylate-based adhesives (e.g., Dermabond, Ethicon, Inc.) have been shown to achieve high bond strengths and have been used in a wide range of applications including vascular repair [17–19], retinal repair [20, 21], hemostasis [22, 23], and tendon repair [24, 25]. The major concerns with cyanoacrylate-based adhesives are their cytotoxicity [26], propensity to cause acute and chronic inflammation [17, 27], toxic degradation product (formaldehyde) [11, 28], poor biomechanical compatibility with the repaired tissues [29], and excessively long degradation rate (>3 years). Similarly, hybrid adhesives such as gelatin–resorcinol–formaldehyde and BioGlue (contains bovine serum albumin and glutaraldehyde, CryoLife, Inc.) are hampered by similar biocompatibility issues and lengthy degradation rate despite having excellent bond strength [11, 30]. Although several other types of adhesives and sealants are currently under development, none of them have proven ideal. Thus, there is a continued need for the development of biocompatible and biodegradable tissue adhesives with superior adhesive strengths.

Marine mussels secrete a proteinaceous fluid that hardens to form an adhesive plaque and byssal thread complex that enables these organisms to anchor themselves to mineralized (e.g., shells, rocks) surfaces in wet, saline, and turbulent environments [31–33]. One unique structural component in these proteins is 3,4-dihydroxyphenylalanine (DOPA), a catecholic amino acid that is responsible for both the moisture-resistant adhesion and the energy dissipative properties of the byssal thread (Fig. 15.1). DOPA is a unique and versatile adhesive molecule capable of binding to both organic and inorganic surfaces through either covalent attachment or strong reversible bonds. This review introduces the unique interfacial binding and intermolecular cross-linking chemistries of DOPA and the use of DOPA and its derivatives in designing adhesive hydrogels with elevated adhesive strength and tunable physical and mechanical properties. The application of these bioadhesives as sealants and adhesives in wound healing, soft tissue reconstruction, immobilization of therapeutic cells, and drug delivery is described.

15.2 DOPA Chemistry

The catechol side chain of DOPA is capable of undergoing several types of catechol–catechol and catechol–surface interactions, leading to the curing of the catechol-containing adhesive and strong interfacial cross-linking (Fig. 15.2). Additionally, catechol is a unique molecule capable of forming strong bonds to both inorganic and organic substrates using either reversible physical or irreversible covalent cross-links.

15.2.1 Physical Bond Formation

Mussel byssus threads are known to accumulate metal ions at a concentration significantly higher than that of the surrounding sea water due to elevated DOPA content [34, 35]. Catechol is capable of forming strong complexes with various metal ions (Fe^{3+}, Ca^{2+}, Cu^{2+}, Ti^{3+}, Ti^{4+}, Mn^{2+}, Mn^{3+}, Zn^{2+}) with long stability? than 40 [32, 36–38]. DOPA-containing synthetic peptides have been shown to form mono-, bis-, and tris-catecholate complexes with metal ions depending on the molar ratio of DOPA to the metal ion, ion valency, and pH (Fig. 15.2a) [38–40]. Breaking and reformation of strong, reversible catechol–metal ion interaction contribute to the wear

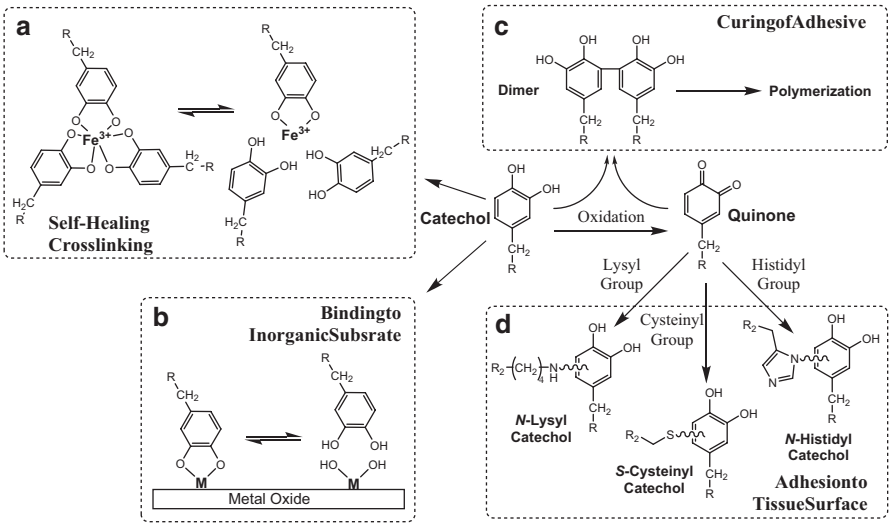

Fig. 15.2 Catechol side chain chemistry of DOPA. Catechol chelates transitional metal ions, which leads to self-healing cross-linking (**a**). Catechol forms strong reversible coordination bonds with metal oxide surfaces (**b**). Oxidation of catechol forms highly reactive quinone, which results in covalent cross-linking with other catechol moieties resulting in polymerization and curing of the adhesive (**c**). Quinone reacts with various functional groups (i.e., $–NH_2$, –SH) found on biological substrates resulting in interfacial covalent cross-linking (**d**)

resistance properties of the protective coatings on mussel byssus threads, which experience large cyclic strains in the turbulent intertidal zone [41, 42]. This interaction was incorporated into synthetic hydrogels to form self-healing networks with elastic moduli approaching those of covalently cross-linked hydrogels [43].

The affinity of catechols for metal ions is also extended to metal oxide surfaces (Fig. 15.2b) [44–47]. A single DOPA moiety demonstrated strong, reversible bond with titanium (Ti) surface with a bond strength averaging around 800 pN, reaching 40% that of a covalent bond (2000pN for carbon–silicon bond) [48]. Density functional theory analysis revealed that catechol readily displaces water molecules and adsorbs directly to the metal oxide surface with binding energy reaching 20–30 kcal/mol [49–51]. The ability to adsorb to various metal oxide surfaces makes DOPA a versatile anchoring group for surface modification of these substrates. DOPA has also been utilized as a robust surface anchor group for surface modification on various metal substrates (Au_2O_3, Al_2O_3, SiO_2, TiO_2, NiTi, and stainless steel) [52–54].

The catechol also forms hydrogen bonds, which allow it to compete with water for hydrogen bonding sites and absorb onto mucosal tissues [55–57] and hydroxyapatite [58]. Finally, catechol residues can interact with other aromatic rings through π-π electron interaction, which may contribute to adhesion to surfaces rich in aromatic compounds such as polystyrene [59] and gold substrates [60].

15.2.2 Covalent Bond Formation

Catechol can be easily oxidized by both enzymatic (e.g., tyrosinase, peroxidase) and chemical (e.g., periodate) oxidants to form highly reactive quinone, resulting in intermolecular covalent cross-links and rapid hardening of catechol-containing adhesives (Fig. 15.2c) [32, 61]. The cross-linking rate and degree of polymerization can be tailored by the oxidant type and concentration [62]. Additionally, quinone forms covalent cross-links with various functional groups (i.e., $–NH_2$, –SH, imidazole) found on biological substrates resulting in the formation of interfacial covalent cross-links (Fig. 15.2d) [63–65]. Catechols that contain a free amine group (i.e., dopamine) undergo intramolecular cyclization between the catechol side chain and the amine group to form a leukochrome that can undergo polymerization similar to melanin formation [62]. Recently, the use of polydopamine as an adhesive primer for further grafting of multifunctional polymers through a simple dip-coating process in an aqueous medium was reported [66].

15.3 Designing Synthetic Bioadhesive Hydrogels

An ideal tissue adhesive should have sufficient flow characteristics so that it can be applied to the tissue surface easily [67]. Additionally, the adhesive should transform quickly from liquid to solid status under physiological conditions. The ability to solidify in situ is advantageous, as liquid adhesive precursor can be potentially

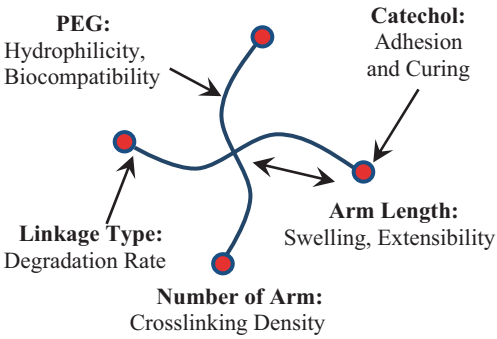

Fig. 15.3 Schematic representation of highly tunable PEG–catechol adhesives

delivered via minimally invasive means (e.g., arthroscopic surgery), while maximizing adhesive contact to the tissue surface. After solidification, the adhesive should maintain strong adhesion to the surrounding tissue substrate and have adequate bulk properties to withstand mechanical stresses present during functional use. Finally, the degradation products of the adhesives should be non-toxic and the degradation rate should match the rate of native tissue healing. Here, we summarize reports that incorporated the adhesive properties of catechol in designing highly tunable tissue adhesives.

15.3.1 Injectable PEG-Based Hydrogel Sealant

Poly(ethylene glycol) (PEG) is a water-soluble polymer widely used in the biomedical field due to its nontoxicity and nonimmunogenicity [68]. PEG end-functionalized with DOPA and its derivatives (e.g., dopamine, 3,4-dihydroxyhydrocinnamic acid) have been synthesized, where PEG served as a biocompatible polymeric support for designing injectable tissue adhesive and sealant (Fig. 15.3) [69–71]. These adhesives outperformed fibrin glue in various adhesion tests, including lap shear, burst strength, and peel adhesion tests. By controlling various variables such as PEG architecture (i.e., four- to eight-arm) and molecular weight (MW; 10,000–20,000 Da), number of terminal catechol residues (up to four), and linking group (i.e., ester, urethane, amide), adhesive with varying properties (i.e., rate of curing, extent of swelling, mechanical properties, and degradation rate) can be obtained. For example, varying PEG MW (length of each arm) while keeping the number of arm the same, modulated the extent of swelling in a straightforward fashion with longer-armed PEG resulting in a higher extent of swelling [71]. Longer-armed PEG also resulted in mechanically weaker hydrogels and lower adhesive performance as measure by the burst pressure. However, higher MW formulations cured at a faster rate as fewer cross-linking reactions need to occur to achieve solidification. The rate of degradation can be easily controlled via simple change to the linker hydrophobicity, with degradation rate ranging from 1 day to more than 3 months [71]. Modulating the degradation rate was performed without affecting the adhesive

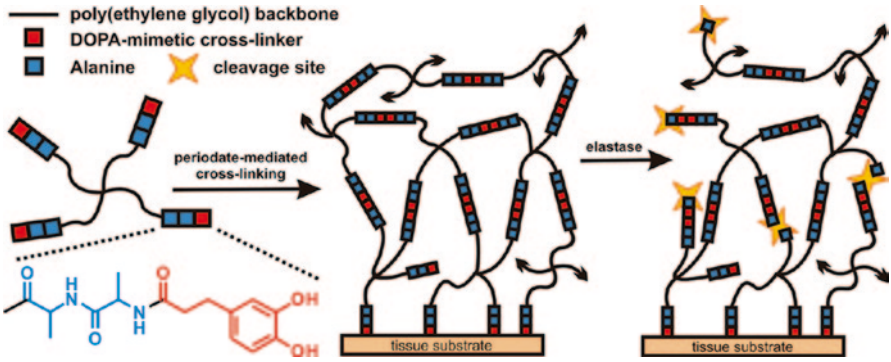

Fig. 15.4 Schematic representation of PEG–catechol with an esterase susceptible Ala–Ala linkage. Reprinted with permission from reference [77]. Copyright 2011 American Chemical Society

performance of these adhesives as measured by the burst testing (burst pressure of 130–170 mmHg/mm). In addition to PEG–catechol conjugates, sealants based on biologic polymers such as chitosan [72], hyaluronic acid [73], alginate [74], and gelatin [75, 76] have also been reported.

15.3.2 Enzymatically Degradable PEG-Based Adhesive

Unlike sutures and other commonly used wound closure materials, adhesives can act as a barrier for tissue growth and the union of the wound edges. Although it is possible to tailor the hydrolytic degradation rate of synthetic PEG-based adhesive through tuning its composition [70, 71], it is difficult to match the adhesive degradation rate with the rate of cell ingrowth for satisfactory wound healing. Brubaker and coworkers [77] inserted an alanine–alanine (Ala–Ala) dipeptide, an elastase substrate, between the PEG and DOPA mimetic catechol to develop an adhesive that is susceptible to cell-mediated degradation (Fig. 15.4). The Ala–Ala linker can be selectively cleaved by elastase secreted by activated neutrophils at the site of the wound or inflammation. This adhesive maintained the ability to cure rapidly (20–30 s) when mixed with oxidants, while exhibiting strong adhesive strength to porcine tissues. From subcutaneous implantation study in mice, immunohistochemical staining for elastase was found at the adhesive–tissue interface and the adhesive slowly degraded, while eliciting minimal inflammatory response.

15.3.3 PEG–DOPA-Based Hydrogel with Ideal Swelling Behavior

Chemically cross-linked hydrophilic polymer network can swell when submerged in an aqueous medium due to osmotic pressure. An opposite elasticity force balances

the stretching of the network and prevents its deformation against the osmotic force until an equilibrium is reached [78]. However, excessive swelling of medical adhesives and sealants *in vivo* can lead to severe medical complications, such as local nerve compression, and it reduces the bulk mechanical properties of the adhesive. Barret and coworkers [79] developed a zero- or negative-swelling adhesive composed of thermo-responsive Tetronic polymer functionalized with catechol. Tetronic is a four-armed, amphiphilic block copolymer consisting of a central hydrophobic polypropylene oxide (PPO) block and peripheral hydrophilic PEG blocks. At elevated temperature (37 °C), the PPO block in tetronic self-assembled to induce volume contraction and mechanical toughening of the cross-linked network. The tetronic–catechol adhesives demonstrated a three to five-fold increase in measured adhesive strength over those of PEG–catechol adhesive.

15.3.4 Nanocomposite Adhesive Hydrogel

Although catechol-modified PEG-based hydrogel presents effective adhesive and physical properties and can meet many specific demands, elevated water content makes them fragile and compromises their advantages in clinical applications. One approach to improve the fracture-resistant ability of hydrogel is incorporating inorganic nanoparticles into the hydrogel to form nanocomposite hydrogels [80, 81]. Polymer network and the encapsulated nanoparticles are binded by weak physical bonds, such as hydrogen bonding, electrostatic interaction. Therefore, the crosslinking density of the network is effectively increased [82–84]. When polyacrylamide-based hydrogels were functionalized with dopamine, the polymer-bound catechol demonstrated enhanced interfacial binding with encapsulated nanosilicate, Laponite, and greatly enhanced the materials properties of the nanocomposite hydrogel [85]. Strong physical bond formed between the catechol side chain of dopamine and Laponite likely dissipated fracture energy and improved fracture-resistant ability of the material for repeated loading. When Laponite was incorporated into an injectable branch of PEG–dopamine adhesive (Fig. 15.5), the work of adhesion increased by five fold over that of Laponite-free adhesive [86]. Additionally, Laponite did not interfere with the curing and degradation rates of PEG–dopamine adhesive. The enhanced adhesive properties can be attributed to the strong physical bonds formed between dopamine and Laponite.

15.3.5 Adhesive-Coated Biological Scaffolds

The use of surgical meshes or patches to reinforce suture closure is becoming popular in various surgical procedures such as hernia repair [87–89], tendon repair [90, 91], cardiovascular surgery [92], and dural repair [93]. Particularly, mesh materials derived from acellular tissues (dermal tissue, pericardium, etc.) provide a scaffold that promotes rapid tissue ingrowth, resulting in an organized collagenous

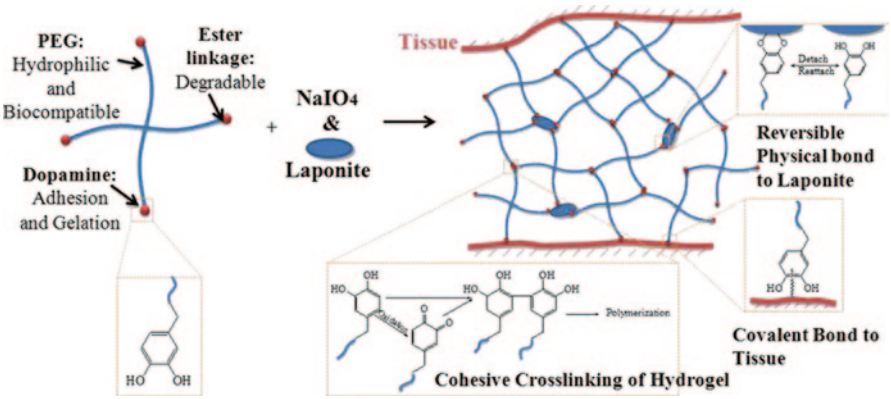

Fig. 15.5 Schematic representation of the formation of PEG–catechol nanocomposite hydrogel and its adhesion to biological tissue. Dopamine is capable of forming three types of cross-links in this system: reversible bonding between dopamine and Laponite (**a**), covalent cross-linking between dopamine molecules resulting in curing of the adhesive (**b**), and interfacial covalent cross-linking between dopamine and functional groups (e.g., $–NH_2$) found on tissue surface (**c**) [86]

tissue, while generating a reduced inflammatory response, fewer infections, and fewer postsurgical adhesions to surrounding tissues compared with their synthetic counterparts [94–97]. However, fixation of these prosthetic materials is typically achieved through the use of sutures, staples, or tacks, which can cause local impairment of circulation with compromised healing [98, 99]. To improve the efficacy of mesh use for soft tissue reconstruction, commercial biologic meshes were coated with a thin adhesive film (200–300 μm) containing biomimetic adhesive catechol [100, 101]. The films were composed of amphiphilic, multiblock copolymers of PEG and polycaprolactone (PCL). PEG allows the adhesive polymer to remain relatively hydrophilic to achieve good "wetting" or adhesive contact with the tissue substrate, while the hydrophobic PCL segments increase cohesive strength and provide ester linkage for hydrolysis. Adhesive-coated biologic mesh demonstrated adhesive strengths that were an order of magnitude higher than those of fibrin glue, while reaching 60% that of cyanoacrylate-based adhesive. The adhesive properties and rate of degradation, as well as the physical and mechanical properties of the adhesive films, can be tailored based on polymer composition, coating density, oxidant concentration, and additive content.

15.4 Applications of Biomimetic Tissue Adhesives

Unlike other biomimetic strategies where a peptide sequence is necessary to mimic the function of a naturally derived protein (e.g., arginine–glycine–aspartic acid for cellular adhesion), incorporation of a single DOPA amino acid or its derivatives can impart inert polymer systems with strong, water-resistant adhesive properties. The simplicity and the wide range of chemistry that catechol can participate in have

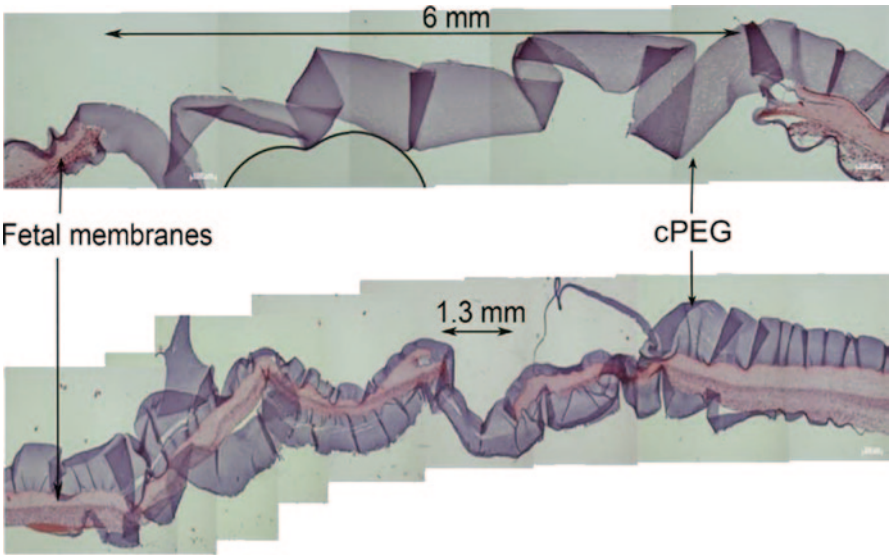

Fig. 15.6 Hematoxylin and eosin-stained cross section of a punctured fetal membranes sealed with PEG–catechol adhesive. The hydrogel appears as a ribbon-like structure that bridges the puncture edges. The *bottom* image shows a cross section of the same lesion at a narrow location. Reprinted from reference [103]

permitted scientists to design adhesives with tunable physical, adhesive, and degradation rate necessary to tailor the materials for a specific application. The use of catechol-containing bioadhesives functioning as fetal membrane sealant, sutureless wound closure, islet cell transplantation, drug delivery for diseased vasculature, and Achilles tendon repair is reviewed.

15.4.1 Sealing of Fetal Membrane

An intact fetal membrane is important to maintain amniotic fluid homeostasis and in the defense against ascending infection during pregnancy [102]. Invasive diagnostic and therapeutic fetal surgical procedures performed endoscopically require access using large-diameter fetoscopes and are frequently complicated by amniotic fluid leakage, separation of amnion and chorion, or iatrogenic preterm premature rupture of the fetal membranes (iPPROM). The morbidity and mortality associated with iPPROM may compromise the expected benefits of the medical intervention. PEG–catechol adhesive was evaluated as a candidate injectable surgical sealant for repair of gestational fetal membrane ruptures (Fig. 15.6) [103, 104]. When compared with commercial adhesives (e.g., cyanoacrylate-, fibrin-based adhesive, etc.), only PEG–catechol adhesive and Tissucol (a fibrin glue) successfully sealed human fetal membrane defects, while demonstrating non-cytotoxicity [103]. However, fibrin glue needed dry membrane surfaces for reliable sealing, whereas

PEG–catechol sealed a 3.7-mm fetal membrane defect up to 45 mmHg when applied under wet conditions [104].

15.4.2 Sutureless Wound Healing Hemostasis

Mehdizadeh *et al.* [105] explored the use of a PEG–citrate-based polymer modified with dopamine as a sutureless wound sealant. One-step polycondensation reaction was used to link citric acid, PEG, and dopamine to form degradable PEG–citrate–dopamine adhesives with adhesive strength that were 2.5–8.0-fold higher than those of fibrin glue. This adhesive also exhibited excellent biocompatibility, controllable degradation rate, and tissue-like elastomeric mechanical properties. Citric acid provides carboxyl groups, which will link to both PEG and dopamine and interact with blood protein to readily form insoluble interpolymeric complexes. This adhesive achieved hemostasis instantly without the need of sutures to close a 2-cm-long by 0.5-cm-deep wound created on the back of Sprague–Dawley rats. Fibrin glue, the current gold standard, was not able to close this wound due to weak adhesion strength. Additionally, PEG–catechol adhesive completely degraded within 28 days without eliciting significant inflammation. The mechanical properties of the adhesive-closed wound revealed better tensile strength when compared to that of suture-closed wounds. The sutureless wound closure may be particularly very useful for those wounds on which sutures are hard to be placed due to the lack of surrounding healthy collagenous structure and fascia supports.

15.4.3 Islet Cell Implantation

There are more than 26 million Americans with diabetes and the disease is the seventh leading cause of death in the USA [106]. Despite recent advances in insulin therapy, the need for strict patient adherence to frequent insulin administration regime has limited its therapeutic efficacy [107]. Transplantation of healthy islet cells to produce insulin and actively regulate blood glucose level was successfully established by the Edmonton protocol, which calls for intrahepatic islet delivery to the liver vasculature via portal vein cannulation [108]. However, long-term graft survival remains problematic due to instant blood-mediated inflammatory response, resulting in platelet and complement activation, neutrophil and monocyte infiltration, and decreased islet viability [109–111]. The performance of PEG–catechol adhesives in extrahepatic islet transplantation in a diabetic mice model was explored [112]. A rapid gelling and nondegradable PEG–catechol adhesive was used to immobilize islet cells onto adipose tissue surfaces, where the adhesive formed a thin, adherent hydrogel coating. From blood glucose level measurement, the period of time needed to reach normoglycemia posttransplantation for adhesive treatment was around 11 days, which was statistically the same as other transplantation methods (e.g., suture fixation and injected into liver vasculature following portal

vein exposure and cannulation). Normoglycemia was sustained for more than 112 days posttransplantation, at which point the islet grafts were removed. The mice survived the explant surgery and immediately became hyperglycemic, indicating the islet cells being responsible for blood sugar regulation. Histological analysis of the explant samples showed intact, rounded islet architecture, and direct islet contact with recipient tissue surfaces with the PEG–catechol adhesive maintained intimate fixation to islets and recipient tissues and induced minimal inflammatory response. The use of biomimetic tissue adhesive offers the potential advantages of convenient, rapid, and minimally invasive islet transplantation by direct apposition of the islet bolus onto tissue surfaces.

15.4.4 Adhesive Hydrogel for Drug Delivery

There are numerous diseases that are associated with the endothelium that line the interior surface of the blood vessels, including ischemia, inflammation, edema, oxidative stress, thrombosis and hemorrhage, and metabolic and oncological diseases [113]. However, therapeutic efficacy of drugs is limited due to the lack of affinity to the endothelium surface. Thus, bioadhesive drug carriers that demonstrate durable adherence capability to the endothelium are needed for the treatment of diseased vasculature. Kastrup *et al.* [74] explored the use of an alginate–catechol conjugate to formulate a drug-eluting adhesive hydrogel. Using a simplified vasculature model, the alginate–catechol gel demonstrated adhesive shear strength of 12 Pa, a shear stress that is several times higher than that generated by physiological blood flow. Different types of arteries were successfully coated with the adhesive, which included the common carotid, the bifurcation of the carotid, and the abdominal aorta. In a mouse model with atherosclerosis, inflamed plaques treated with steroid-eluting adhesive hydrogels demonstrated reduced macrophage content and developed protective fibrous caps covering the plaque core. The drug-eluting adhesive also lowered plasma cytokine levels and biomarkers of inflammation in the plaque.

15.4.5 Achilles Tendon Repair

The Achilles tendon is ruptured more frequently than any other tendon. It accounts for 40–60 % of all operative tendon repairs, with 75 % of these procedures stemming from sports-related activities [114–116]. The number of ruptures has increased over the past several decades, and the rate has doubled nearly every 10 years [117–119]. However, primary suture repair of ruptured Achilles tendons has resulted in partial or complete re-ruptures in more than 5 % of patients [115, 120, 121]. The suture–tendon junction is usually the weak link in primary tendon repairs as the strength between the tendon fibers is much less than that of the fibers themselves and sutures can tear through the tendon when force is applied [122]. Biologic meshes such as

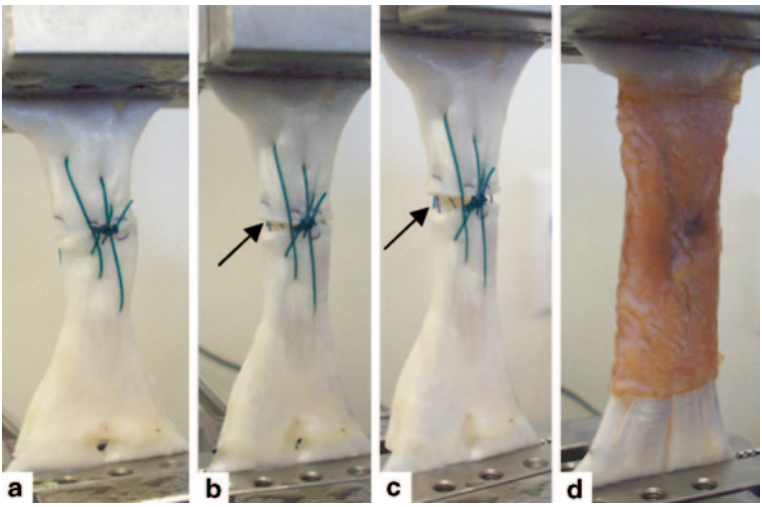

Fig. 15.7 Close-up images of the gap formation during tensile testing of sutured tendons loaded at 0 N (**a**), 50 N (**b**), and 100 N (**c**), and a sutured tendon augmented with adhesive-coated biologic mesh and loaded at 100 N (**d**). *Solid arrows* indicate gap formation for tendons repaired with suture alone. Reprinted from reference [123]. IOP Publishing

bovine pericardium or porcine dermal tissues coated with catechol-containing thin adhesive films were investigated for their potential in augmenting primary tendon repair [123]. These bioadhesive constructs were wrapped around transected cadaveric porcine Achilles tendons repaired with a combination of parallel and three-loop suture patterns. Tensile mechanical testing of the augmented repairs exhibited significantly higher stiffness (22–34 %), failure load (24–44 %), and energy to failure (27–63 %) when compared to control tendons with suture repair alone. Suture-only tendons readily formed a gap even at relatively low loads (Fig. 15.7), which potentially increases the risk of re-rupture in vivo [124]. Excessive elongation at the repair site has been associated with a poor functional outcome after tendon repair [124, 125]. Bioadhesive-coated meshes provided a stiffer repair, which may be strongly correlated with increased failure properties of repaired tendons during the early phase of healing [125]. This study demonstrated that the bioadhesive-coated biologic mesh can be utilized to reinforce the primary suture repair and may provide a new treatment option for Achilles tendon repair.

15.5 Conclusion and Future Trend of DOPA–PEG-Based Bioadhesive Hydrogels

Many different types of sealants or adhesives have been developed for clinical applications. However, due to inadequate adhesive properties and toxicity issues associated with existing adhesive products, their wide adoption in the clinical field

is limited. Inspired by the unique moisture-resistant properties of mussel adhesive proteins, researchers have developed a series of new biomimetic adhesive materials. These biomimetic adhesives have outperformed existing tissue adhesives in various side-by-side comparison studies in terms of adhesive performance and biocompatibility. While this chapter focused on the use of mussel-mimetic technology in designing tissue adhesives, similar analogues have been developed and applied as antifouling and antimicrobial coatings [126–130], drug delivery vehicles [131–133], and cell and tissue engineering applications [66, 134, 135] as well as development of self-healing [43, 136] and mechanically strong nanocomposite materials [85, 137]. Additionally, synthetic mimics of mussel adhesive proteins have found applications in various industries beyond biomedical fields (e.g., drinking water purification [138], controlled release of fertilizer [139], nanocomposite for tire rubbers [140], adhesive for battery [141] and plastics [142]).

Majority of the published works have largely focused on exploiting the chemistry of the DOPA side chain in designing functional materials. However, marine mussels rely on numerous ingenious designs found in both the adhesive plaque and byssus thread to resist repeated pounding by intertidal waves. Mussel byssus threads are composed of histidine-rich proteins [42]. The imidazole side chain of histidine forms reversible bonds with transitional metal ions (e.g., zinc and copper), which can break and reform, while minimizing permanent structural damage. This interaction was recently exploited to create a self-healing hydrogel [143]. The byssus thread also exhibits a stiffness gradient with a modulus of 900 MPa at the distal end and 20 MPa near the mussel tissue [144]. Similarly, the adhesive plaque exhibits a gradient in pore diameters, ranging from 200 nm near the substratum to nearly 3 μm, where the thread meets the plaque [145]. Gradation in the materials' properties may be nature's adaptation to prevent structural damage due to contact deformation between two dissimilar materials [146]. These structural designs provide new insights in developing novel adhesives with enhanced interfacial properties.

Acknowledgment The authors would like to acknowledge National Institutes of Health (GM104846) for financial support.

References

1. M. Hidalgo, M.J. Castillo, J.L. Eymar, A. Hidalgo, Lichtenstein inguinal hernioplasty: sutures versus glue. Hernia. **9**, 242–244 (2005)
2. J. Koniger, J. Redecke, M. Butters, Chronic pain after hernia repair: a randomized trial comparing Shouldice, Lichtenstein and TAPP. Langenbecks Arch. Surg. **389**, 361–365 (2004)
3. E. Stark, K. Oestreich, K. Wendl, B. Rumstadt, E. Hagmüller, Nerve irritation after laparoscopic hernia repair. Surg. Endosc. **13**, 878–881 (1999)
4. F.H. Berndsen, U. Petersson, D. Arvidsson, C.E. Leijonmarck, C. Rudberg, S. Smedberg, A. Montgomery, Discomfort five years after laparoscopic and Shouldice inguinal hernia repair: a randomised trial with 867 patients. Hernia. **12**, 445–446 (2008)
5. F.A. Barber, M.A. Herbert, M.H. Boothby, Ultimate tensile failure loads of a human dermal allograft rotator cuff augmentation. Arthroscopy. **24**, 20–24 (2008)

6. F.A. Barber, M.A. Herbert, D.A. Coons, Tendon augmentation grafts: biomechanical failure loads and failure patterns. Arthroscopy. **22**, 534–538 (2006)
7. M.J. Tingart, M. Apreleva, D. Zurakowski, J.J. Warner, Pullout strength of suture anchors used in rotator cuff repair. J. Bone Joint Surg. Am. **85-A**, 2190–2198 (2003)
8. G.L.J. Caldwell, J.J. Warner, M.D. Miller, D. Boardman, J. Towers, R. Debski, Strength of fixation with transosseous sutures in rotator cuff repair. J. Bone Joint Surg. Am. **79**, 1064–1068 (1997)
9. C. Gerber, A.G. Schneeberger, M. Beck, U. Schlegel, Mechanical strength of repairs of the rotator cuff. J. Bone Joint Surg. Am. **76-B**, 371–380 (1994)
10. M. Djurasovic, G. Marra, J.S. Arroyo, R.G. Pollock, E.L. Flatow, L.U. Bigliani, Revision rotator cuff repair: factors influencing results. J. Bone Joint Surg. Am. **83-A**, 1849–1855 (2001)
11. Y. Ikada, Tissue adhesives, in *Wound Closure Biomaterials and Devices*, ed. by C.C. Chu, J.A. von Fraunhofer, H.P. Greisler (CRC Press, Inc., Boca Raton, 1997), pp. 317–346
12. M. Mehdizadeh, H. Weng, D. Gyawali, L. Tang, J. Yang Injectable citrate-based mussel-inspired tissue bioadhesives with high wet strength for sutureless wound closure. Biomaterials. **33**(32), 7972–7983 2012
13. J.R. Eriksen, J.I. Bech, D. Linnemann, J. Rosenberg, Laparoscopic intraperitoneal mesh fixation with fibrin sealant (Tisseel) vs. titanium tacks: a randomised controlled experimental study in pigs. Hernia. **12**, 483–491 (2008)
14. E.J. Olivier ten Hallers, J.A. Jansen, H.A.M. Marres, G. Rakhorst, G.J. Verkerke Histological assessment of titanium and polypropylene fiber mesh implantation with and without fibrin tissue glue. J. Biomed Mater. Res. Part A. **80**, 372–380 (2006)
15. R. Saltz, D. Sierra, D. Feldman, M.B. Saltz, A. Dimick, L.O. Vasconez, Experimental and clinical applications of fibrin glue. Plast. Reconstr. Surg. **88**, 1005–1015 (1991) discussion 16–7
16. H. Banninger, T. Hardegger, A. Tobler, A. Barth, P. Schupbach, W. Reinhart, B. Lammle, M. Furlan, Fibrin glue in surgery: frequent development of inhibitors of bovine thrombin and human factor V. Br. J. Haematol. **85**, 528–532 (1993)
17. D.M. Toriumi, W.F. Raslan, M. Friedman, M.E. Tardy Jr., Variable histotoxicity of histoacryl when used in a subcutaneous site: an experimental study. Laryngoscope. **101**, 339–343 (1991)
18. M.F. Brothers, J.C. Kaufmann, A.J. Fox, J.P. Deveikis, n-Butyl 2-cyanoacrylate–substitute for IBCA in interventional neuroradiology: histopathologic and polymerization time studies. AJNR. Am. J. Neuroradiol. **10**, 777–786 (1989)
19. H. Celik, H. Caner, K. Tahta, O.E. Ozcan, A. Erbengi, B. Onol, Nonsuture closure of arterial defect by vein graft using isobutyl-2-cyanoacrylate as a tissue adhesive. J. Neurosurg. Sci. **35**, 83–87 (1991)
20. C.E. Gilbert, I. Grierson, D. McLeod, Retinal patching: a new approach to the management of selected retinal breaks. Eye. **3**, 19–26 (1989)
21. M.E. Hartnett, T. Hirose, Cyanoacrylate glue in the repair of retinal detachment associated with posterior retinal breaks in infants and children. Retina. **18**, 125–129 (1998)
22. A.R. Goldin, Control of duodenal haemorrhage with cyanoacrylate. Br. J. Radiol. **49**, 583–588 (1976)
23. T. Kakio, T. Ito, K. Sue, K. Sakaguchi, T. Shiota, T. Oka, H. Kobashi, N. Sakai, M. Omoto, M. Mikami, Hemostasis of gastric variceal hemorrhage by transileocoecal and transhepatic obliteration. Acta. Med. Okayama. **47**, 39–43 (1993)
24. P.M. Bonutti, G.G. Weiker, J.T. Andrish, Isobutyl cyanoacrylate as a soft tissue adhesive: an in vitro study in the rabbit achilles tendon. Clin. Orthop. Relat. Res. **229**, 241–248 (1988)
25. E.S. Powell, I.A. Trail, J. Noble, Non-suture repair of tendons. J. Biomed. Eng. **11**, 215–218 (1989)
26. C.E. Evans, G.C. Lees, I.A. Trail, Cytotoxicity of cyanoacrylate adhesives to cultured tendon cells. J. Hand. Surg. **24B**, 658–661 (1999)
27. Y.C. Tseng, Y. Tabata, S.H. Hyon, Y. Ikada, In vitro toxicity test of 2-cyanoacrylate polymers by cell culture method. J. Biomed. Mat. Res. **24**, 1355–1367 (1990)

28. M.F. Refojo, C.H. Dohlman, J. Koliopoulos, Adhesives in ophthalmology: a review. Surv. Ophthamol. **15**, 217–236 (1971)
29. R.H. Fortelny, A.H. Petter-Puchner, N. Walder, R. Mittermayr, W. Öhlinger, A. Heinze, H. Redl, Cyanoacrylate tissue sealant impairs tissue integration of macroporous mesh in experimental hernia repair. Surg. Endosc. **21**, 1781–1785 (2007)
30. S.K. Jain, A. Vindal, Gelatin–resorcin–formalin (GRF) tissue glue as a novel technique for fixing prosthetic mesh in open hernia repair. Hernia. **13**, 299–304 (2009)
31. B.P. Lee, P.B. Messersmith, J.N. Israelachvili, J.H. Waite, Mussel-inspired adhesives and coatings. Annu. Rev. Mater Res **41**, 99–132 (2011)
32. J.H. Waite, Nature's underwater adhesive specialist. Int. J. Adhes. Adhes. **7**, 9–14 (1987)
33. H. Yamamoto, Marine adhesive proteins and some biotechnological applications. Biotechnol. Genet. Eng. Rev. **13**, 133–165 (1996)
34. T.L. Coombs, P.J. Keller, Mytilus byssal threads as an environmental marker for metals. Aquat. Toxicol. **1**, 291–300 (1981)
35. P. Szefer, K. Ikuta, S. Kushiyama, K. Szefer, K. Frelek, J. Geldon, Distribution and association of trace metals in soft tissue and byssus of Mytilus edulis from the east coast of Kyushu Island, Japan. Arch. Environ. Contam. Toxicol. **32**, 184–190 (1997)
36. S. Martin, J. Kesselman, D. Park, N. Lewis, M. Hoffmann, Surface studies of 4-chlorocatechol adsorbed on titanium dioxide. Environ. Sci. Technol. **30**, 2535–2542 (1996)
37. M.J. Sever, J.J. Wilker. Visible absorption spectra of metal-catecholate and metal-tironate complexes. Dalton. Trans. **7**, 1061–1072 (2004)
38. S.W. Taylor, D.B. Chase, M.H. Emptage, M.J. Nelson, J.H. Waite, Ferric Ion complexes of a DOPA-containing adhesive protein from mytilus edulis. Inorg. Chem. **35**, 7572–7577 (1996)
39. S.W. Taylor, G.W. Luther III, J.H. Waite, Polarographic and spectrophotometric investigation of iron(III) complexation to 3,4-Dihydroxyphenylalanine-containing peptides and proteins from mytilus edulis. Inorg. Chem. **33**, 5819–5824 (1994)
40. M.J. Sever, J.J. Wilker, Absorption spectroscopy and binding constants for first-row transition metal complexes of a DOPA-containing peptide. Dalton Trans. **14**, 813–22 (2006)
41. M.J. Harrington, A. Masic, N. Holten-Andersen, J.H. Waite, P. Fratzl, Iron-clad fibers: a metal-based biological strategy for hard flexible coatings. Science. **328**, 216–220 (2010)
42. M.J. Harrington, H.S. Gupta, P. Fratzl, J.H. Waite, Collagen insulated from tensile damage by domains that unfold reversibly: In situ X-ray investigation of mechanical yield and damage repair in the mussel byssus. J. Struct. Biol. **167**, 47–54 (2009)
43. N. Holten-Andersen, M.J. Harrington, H. Birkedal, B.P. Lee, P.B. Messersmith, K.Y.C. Lee, J.H. Waite, pH-induced mussel metal-ligand crosslinks yield self-healing polymer networks with near-covalent elastic moduli. Proc. Natl. Acad. Sci. **15**, 2651–2655 (2011) (PMCID: PMC3041094)
44. R. Kummert, W. Stumm, The surface complexation of organic acids on hydrous g-alumina. J. Colloid Interface Sci. **75**, 373–385 (1980)
45. M.P. Soriaga, A.T. Hubbard, Determination of the orientation of aromatic molecules adsorbed on platinum electrodes. The effect of solute concentration. JACS. **104**, 3937–3945 (1982)
46. D.C. Hansen, S.C. Dexter, J.H. Waite, The inhibition of corrosion of S30403 stainless steel by a naturally occurring catecholic polymer. Corros. Sci. **37**, 1423–1441 (1995)
47. B.P. Lee, C.-Y. Chao, F.N. Nunalee, E. Motan, K.R. Shull, P.B. Messersmith, Rapid photocurable of amphiphilic block copolymers hydrogels with high DOPA contents. Maclomolecules. **39**, 1740–1748 (2006)
48. H. Lee, N.F. Scherer, P.B. Messersmith, Single-molecule mechanics of mussel adhesion. Proc. Natl. Acad. Sci. U S A. **103**, 12999–13003 (2006)
49. S.A. Mian, X. Gao, S. Nagase, J. Jang, Adsorption of catechol on a wet silica surface: density functional theory study. Theor. Chem. Acc. **130**, 333–339 (2011)
50. S.A. Mian, L.C. Saha, J. Jang, L. Wang, X. Gao, S. Nagase, Density functional theory study of catechol adhesion on silica surfaces. J. Phys. Chem. C. **114**, 20793–20800 (2010)

51. M. Vega-Arroyo, P.R. LeBreton, T. Rajh, P. Zapol, L.A. Curtiss, Density functional study of the TiO2–dopamine complex. Chem. Phys. Lett. **406**, 306–311 (2005)
52. J.L. Dalsin, B.-H. Hu, B.P. Lee, P.B. Messersmith, Mussel adhesive protein mimetic polymers for the preparation of nonfouling surfaces. JACS **125**, 4253–4258 (2003)
53. J.L. Dalsin, L. Lin, P.B. Messersmith, Antifouling performance of poly(ethylene glycol) anchored onto surfaces by mussel adhesive protein mimetic peptides. Polym. Mater. Sci. Eng. **90**, 247–248 (2004)
54. J.L. Dalsin, L. Lin, S. Tosatti, J. Voeroes, M. Textor, P.B. Messersmith, Protein resistance of titanium oxide surfaces modified by biologically inspired mPEG-DOPA. Langmuir. **21**, 640–646 (2005)
55. M.P. Deacon, S.S. Davis, J.H. Waite, S.E. Harding, Structure and mucoadhesion of mussel glue protein in dilute solution. Biochemical. **37**, 14108–14112 (1998)
56. K. Huang, B.P. Lee, D. Ingram, P.B. Messersmith, Synthesis and characterization of self-assembling block copolymers containing Bioadhesive end groups. Biomacromology. **3**, 397–406 (2002)
57. J. Schnurrer, C.-M. Lehr, Mucoadhesive properties of the mussel adhesive protein. Int. J. Pharm. **141**, 251–256 (1996)
58. W.M. Chirdon, W.J. O'Brien, R.E. Robertson, Adsorption of catechol and comparative solutes on hydroxyapatite. J. Biomed. Mat. Res. B. **66B**, 532–538 (2003)
59. A.M. Baty, P.K. Leavitt, C.A. Siedlecki, B.J. Tyler, P.A. Suci, R.E. Marchant, G.G. Geesey, Adsorption of adhesive proteins from the marine mussel, mytilus edulis, on polymer films in the hydrated state using angle dependent X-ray photoelectron spectroscopy and atomic force microscopy. Langmuir. **13**, 5702–5710 (1997)
60. B.R. Baker, A.N. Laiwalla, J.-Y. Yoon, J. Canavate, R.L. Garrell, Adhesion and cohesion of mussel adhesive protein on glass and gold through protein removal studies. Polym. Mater. Sci. Eng. **85**, 115–116 (2001)
61. L.M. McDowell, L.A. Burzio, J.H. Waite, J. Schaefer, Rotational echo double resonance detection of cross-links formed in mussel byssus under high-flow stress. J. Biol. Chem. **274**, 20293–20295 (1999)
62. B.P. Lee, J.L. Dalsin, P.B. Messersmith, Synthesis and gelation of DOPA-modified poly(ethylene glycol) hydrogels. Biomacromology. **3**, 1038–1047 (2002)
63. J.H. Waite, The phylogeny and chemical diversity of quinone-tanned glues and varnishes. Comp. Biochem. Physiol. B. **97**, 19–29 (1990)
64. M. Sugumaran, H. Dali, V. Semensi, Chemical- and cuticular phenoloxidase-mediated synthesis of cysteinyl-catechol adducts. Arch. Insect. Biochem. Physiol. **11**, 127–137 (1989)
65. H. Lee, N.F. Scherer, P.B. Messersmith, Single molecule mechanics of mussel adhesion. Proc. Natl. Acad. Sci. U S A **103**, 12999–13003 (2006)
66. H. Lee, S.M. Dellatore, W.M. Miller, P.B. Messersmith, Mussel-inspired surface chemistry for multifunctional coatings. Science. **318**, 426–430 (2007)
67. B.P. Lee, J.L. Dalsin, P.B. Messersmith. *Biomimetic adhesive polymers based on mussel adhesive proteins*. Biological Adhesives (Springer, Berlin, 2006), pp. 257–278
68. J.M. Harris, J.M. Dust, R.A. McGill, P.A. Harris, M.J. Edgell, R.M. Sedaghat-Herati, L.J. Karr, D.L. Donnelly. *New polyethylene glycols for biomedical applications*. Water-Soluble Polymer. ACS, DC Washington 418–29 (1991)
69. S.A. Burke, M. Ritter-Jones, B.P. Lee, P.B. Messersmith, Thermal gelation and tissue adhesion of biomimetic hydrogels. Biomed. Mater. **2**, 203–210 (2007)
70. P.B. Messersmith, B.P. Lee, J.L. Dalsin, S.A. Burke, inventors; DOPA-Functionized, Branched, Poly(Aklylene Oxide) Adhesives patent US Patent Application 20080247984 2008
71. J.L. Dalsin, B.P. Lee, L. Vollenweider, S. Silvary, J.L. Murphy, F. Xu, A. Spitz, A. Lyman, inventors; Multi-armed Catechol Compound Blends. US patent 8,119,742, 2012
72. J.H. Ryu, Y. Lee, W.H. Kong, T.G. Kim, T.G. Park, H. Lee, Catechol-functionalized chitosan/pluronic hydrogels for tissue adhesives and hemostatic materials. Biomacromology. **12**, 2653–2659 (2011)

73. Y. Lee, H.J. Chung, S. Yeo, C.-H. Ahn, H. Lee, P.B. Messersmith, T.G. Park, Thermo-sensitive, injectable, and tissue adhesive sol-gel transition hyaluronic acid/pluronic composite hydrogels prepared from bio-inspired catechol-thiol reaction. Soft. Matter. **6**, 977–983 (2010)
74. C.J. Kastrup, M. Nahrendorf, J.L. Figueiredo, H. Lee, S. Kambhampati, T. Lee, S.W. Cho, R. Gorbatov, Y. Iwamoto, T.T. Dang, P. Dutta, J.H. Yeon, H. Cheng, C.D. Pritchard, A.J. Vegas, C.D. Siegel, S. MacDougall, M. Okonkwo, A. Thai, J.R. Stone, A.J. Coury, R. Weissleder, R. Langer, D.G. Anderson, Painting blood vessels and atherosclerotic plaques with an adhesive drug depot. Proc. Natl. Acad. Sci. U S A. **109**, 21444–21449 (2012)
75. B.P. Lee, inventorB. Compounds, S.M. Therefor, US patent 7,622,533. 2009
76. B.P. Lee, inventorB. Compounds, S.M. Therefor, US patent 8,030,413. 2011
77. C.E. Brubaker, P.B. Messersmith, Enzymatically degradable mussel-inspired adhesive hydrogel. Biomacromolecules. **12**, 4326–4334 (2011)
78. F. Ganji, S. Vasheghani-Farahani, E. Vasheghani-Farahani, Theoretical description of hydrogel swelling: a review. Iran. Polym. J. **19**, 375–398 (2010)
79. D.G. Barrett, G.G. Bushnell, PB Messersmith, Mechanically robust, negative-swelling, mussel-inspired tissue adhesives. Adv. Healthc. Mater. **2**, 745–755 (2013)
80. K. Haraguchi, Synthesis and properties of soft nanocomposite materials with novel organic/inorganic network structures. Polym. J. **43**, 223–241 (2011)
81. S. Sarkar, E. Guibal, F. Quignard, A. SenGupta, Polymer-supported metals and metal oxide nanoparticles: synthesis, characterization, and applications. J. Nanopart. Res. **14**, 1–24 (2012)
82. A.K. Gaharwar, S.A. Dammu, J.M. Canter, C.J. Wu, G. Schmidt, Highly extensible, tough, and elastomeric nanocomposite hydrogels from poly(ethylene glycol) and hydroxyapatite nanoparticles. Biomacromology. **12**, 1641–1650 (2011)
83. K. Haraguchi, R. Farnworth, A. Ohbayashi, T. Takehisa, Compositional effects on mechanical properties of nanocomposite hydrogels composed of poly(N, N-dimethylacrylamide) and clay. Macromology. **36**, 5732–5741 (2003)
84. T. Wang, D. Liu, C. Lian, S. Zheng, X. Liu, Z. Tong, Large deformation behavior and effective network chain density of swollen poly(N-isopropylacrylamide)-Laponite nanocomposite hydrogels. Soft. Matter. **8**, 774–783 (2012)
85. S. Skelton, M. Bostwick, K. O'Connor, S. Konst, S. Casey, B.P. Lee, Biomimetic adhesive containing nanocomposite hydrogel with enhanced materials properties. Soft. Matter. **9**, 3825–3833 (2013)
86. Y. Liu, H. Zhan, S. Skelton, B.P. Lee, *Marine adhesive containing nanocomposite hydrogel with enhanced materials and bioadhesive properties*. MRS Proceedings. 2013;1569:mrss13-1569-LL05–09.
87. L. Ansaloni, F. Catena, S. Gagliardi, F. Gazzotti, L. D'Alessandro, A.D. Pinna, Hernia repair with porcine small-intestinal submucosa. Hernia. **11**, 321–326 (2007)
88. F. Catena, L. Ansaloni, F. Gazzotti, S. Gagliardi, S. Di Saverio, L. D'Alessandro, A.D. Pinna, Use of porcine dermal collagen graft (permacol) for hernia repair in contaminated fields. Hernia. **11**, 57–60 (2007)
89. M.E.J. Franklin, J.J. Gonzalez Jr., J.L. Glass, Use of porcine small intestinal submucosa as a prosthetic device for laparoscopic repair of hernias in contaminated fields: 2-year follow-up. Hernia. **8**, 186–189 (2004)
90. D.K. Lee, Achilles tendon repair with acellular tissue graft augmentation in neglected ruptures. J. Foot. Ankle. Surg. **46**, 451–455 (2007)
91. J.L. Bond, R.M. Dopirak, J. Higgins, J. Burns, S.J. Snyder, Arthroscopic replacement of massive, irreparable rotator cuff tears using a graftjacket allograft: technique and preliminary results. Arthroscopy. **24**, 403–409 (2008)
92. J.A. Santibáñez-Salgado, J.R. Olmos-Zúñiga, M. Pérez-López, C. Aboitiz-Rivera, M. Gaxiola-Gaxiola, R. Jasso-Victoria, A. Sotres-Vega, M. Baltazares-Lipp, J.V.-C. Pérez-Covarrubias D, Lyophilized glutaraldehyde-preserved bovine pericardium for experimental atrial septal defect closure. Eur. Cell. Mater. **19**, 158–165 (2010)

93. P.K. Narotam, K. Reddy, D. Fewer, F. Qiao, N. Nathoo, Collagen matrix duraplasty for cranial and spinal surgery: a clinical and imaging study. J. Neurosurg. **106**, 45–51 (2007)
94. T.P. Rauth, B.K. Poulose, L.B. Nanney, M.D. Holzman, A comparative analysis of expanded Polytetrafluoroethylene and small intestinal submucosa—implications for patch repair in ventral herniorrhaphy. J. Surg. Res. **143**, 43–49 (2007)
95. J.C.J. Lantis, E.K. Gallivan, R. Hekier, R. Connolly, S.D. Schwaitzberg, A comparison of collagen and PTFE patch repair in a rabbit model of congenital diaphragmatic hernia. J. Invest. Surg. **13**, 319–325 (2000)
96. M.L. Konstantinovic, P. Lagae, F. Zheng, E.K. Verbeken, D. De Ridder, J.A. Deprest, Comparison of host response to polypropylene and non-cross-linked porcine small intestine serosal-derived collagen implants in a rat model. J. Obstet. Gynecol. **112**, 1554–1560 BJOG: an International (2005)
97. W.B. Gaertner, M.E. Bonsack, J.P. Delaney, Experimental evaluation of four biologic prostheses for ventral hernia repair. J. Gastrointest Surg. **11**, 1275–1285 (2007)
98. B. Hohendorff, W. Siepen, L. Spiering, L. Staub, T. Schmuck, A. Boss, Long-term results after operatively treated Achilles tendon rupture: fibrin glue versus suture. J. Foot Ankle Surg. **47**, 392–399 (2008)
99. B. Hohendorff, W. Siepen, L. Staub, Treatment of acute Achilles tendon rupture: fibrin glue versus fibrin glue augmented with plantaris longus tendon. J. Foot Ankle Surg. **48**, 439–446 (2009)
100. J.L. Murphy, L. Vollenweider, F. Xu, B.P. Lee. Adhesive performance of biomimetic adhesive-coated biologic scaffolds. Biomacromol.**11**, 2976–2984 (2010) PMCID: PMC3027843
101. B.P. Lee, J.L. Dalsin, L. Vollenweider, J.L. Murphy, F. Xu, J. Virosco, W. Lew, J. White, inventors; Bioadhesive constructs. US patent 8,383,092. 2013
102. R. Devlieger, L.K. Millar, G. Bryant-Greenwood, L. Lewi, J. Deprest, Fetal membrane healing after spontaneous and iatrogenic membrane rupture: a review of current evidence. Am. J. Obstet. Gynecol. **195**, 1512–1520 (2006)
103. G. Bilic, C. Brubaker, P.B. Messersmith, A.S. Mallik, T.M. Quinn, C. Haller, E. Done, L. Gucciardo, S.M. Zeisberger, R. Zimmermann, J. Deprest, A.H. Zisch, Injectable candidate sealants for fetal membrane repair: bonding and toxicity in vitro. Am. J. Obstet. Gynecol.**202**(85), e1-9 (2010) PMCID: PMC2837921
104. C.M. Haller, W. Buerzle, A. Kivelio, M. Perrini, C.E. Brubaker, R.J. Gubeli, A.S. Mallik, W. Weber, P.B. Messersmith, E. Mazza, N. Ochsenbein-Koelble, R. Zimmermann, M. Ehrbar, Mussel-mimetic tissue adhesive for fetal membrane repair: an ex vivo evaluation. Acta. Biomater. **8**, 4365–4370 (2012)
105. M. Mehdizadeh, H. Weng, D. Gyawali, L. Tang, J. Yang, Injectable citrate-based mussel-inspired tissue bioadhesives with high wet strength for sutureless wound closure. Biomaterials. **33**, 7972–7983 (2012) PMCID: 3432175
106. The facts about diabetes: a leading cause of death in the U.S. [database on the Internet]. National Diabetes Education Program. 2011.http://ndep.nih.gov/media/fs_gensnapshot.pdf. Accessed July 2013.
107. M. Peyrot, A.H. Barnett, L.F. Meneghini, P.M. Schumm-Draeger, Insulin adherence behaviours and barriers in the multinational global attitudes of patients and physicians in insulin therapy study. Diabet. Med. **29**, 682–689 (2012)
108. A.M.J. Shapiro, J.R.T. Lakey, E.A. Ryan, G.S. Korbutt, E. Toth, G.L. Warnock, N.M. Kneteman, R.V. Rajotte, Islet transplantation in seven patients with type 1 diabetes mellitus using a glucocorticoid-free immunosuppressive regimen. N. Engl. J. Med. **343**, 230–238 (2000)
109. D.J. van der Windt, R. Bottino, A. Casu, N. Campanile, D.K.C. Cooper, Rapid loss of intraportally transplanted islets: an overview of pathophysiology and preventive strategies. Xenotransplantation. **14**, 288–297 (2007)
110. L. Moberg, O. Korsgren, B. Nilsson, Neutrophilic granulocytes are the predominant cell type infiltrating pancreatic islets in contact with ABO-compatible blood. Clin. Exp. Immunol. **142**, 125–131 (2005)

111. W. Bennet, C.G. Groth, R. Larsson, B. Nilsson, O. Korsgren, Isolated human islets trigger an instant blood mediated inflammatory reaction: Implications for intraportal islet transplantation as a treatment for patients with type 1 diabetes. Ups. J. Med. Sci. **105**, 125–133 (2000)
112. C.E. Brubaker, H. Kissler, L.-J. Wang, D.B. Kaufman, P.B. Messersmith, Biological performance of mussel-inspired adhesive in extrahepatic islet transplantation. Biomaterials. 31, 420–427 (2010) PMCID: PMC2783676
113. E. Simone, B.-S. Ding, V. Muzykantov, Targeted delivery of therapeutics to endothelium. Cell. Tissue. Res. **335**, 283–300 (2009)
114. J. Leppilahti, S. Orava, Total Achilles Tendon Rupture: A Review. Sports. Med. **25**, 79–100 (1998)
115. E.J. Strauss, C. Ishak, L. Jazrawi, O. Sherman, J. Rosen, Operative treatment of acute achilles tendon ruptures: an institutional review of clinical outcomes. Injury, Int. J. Care Inj. **38**, 832–838 (2007)
116. D.W. White, J.C. Wenke, D.S. Mosely, S.B. Mountcastle, C.J. Basamania, Incidence of major tendon ruptures and anterior cruciate ligament tears in US army soldiers. Am. J. Sports Med. **35**, 1308–1314 (2007)
117. N. Maffulli, Rupture of the achilles tendon. J. Bone Joint Surg. **81-A**, 1019–1036 (1999)
118. S. Houshian, T. Tscherning, P. Riegels-Nielsen, The epidemiology of Achilles tendon rupture in a Danish county. Injury. **29**, 651–654 (1998)
119. A. Pajala, J. Kangas, P. Ohtonen, J. Leppilahti, Rerupture and deep infection following treatment of total achilles tendon rupture. J. Bone Joint Surg. **84-A**, 2016–2021 (2002)
120. L. Nistor, Surgical and non-surgical treatment of achilles tendon rupture. J. Bone Joint Surg. **63-A**, 394–399 (1981)
121. E. Winter, K. Weise, S. Weller, T. Ambacher, Surgical repair of achilles tendon rupture: comparison of surgical with conservative treatment. Arch. Orthop. Trauma Surg. **117**, 364–367 (1998)
122. F.J. Kummer, K. Iesaka, The role of graft materials in suture augmentation for tendon repairs and reattachment. J. Biomed. Mater. Res. Part B: Appl. Biomater. 2005;74B:789–91.
123. M. Brodie, L. Vollenweider, J.L. Murphy, F. Xu, A. Lyman, W.D. Lew, B.P. Lee, Biomechanical properties of achilles tendon repair augmented with bioadhesive-coated scaffold. Biomed. Mater. **6**, 015014 (2011) PMCID: PMC3046464
124. R.H. Gelberman, M.I. Boyer, M.D. Brodt, S.C. Winters, M.J. Silva, The effect of gap formation at the repair site on the strength and excursion of intrasynovial flexor tendons: an experimental study on the early stages of tendon-healing in dogs. J. Bone Joint Surg. **81 A**, 975–982 (1999)
125. M.I. Boyer, R.H. Gelberman, M.E. Burns, H. Dinopoulos, R. Hofem, M.J. Silva, Intrasynovial flexor tendon repair an experimental study comparing low and high levels of in vivo force during rehabilitation in canines. J. Bone Joint Surg. **83**, 891–899 (2001)
126. N.D. Braulta, C. Gaoa, H. Xuea, M. Piliarik, J. Homolab, S. Jianga, Q. Yua, Ultra-low fouling and functionalizable zwitterionic coatings grafted onto SiO_2 via a biomimetic adhesive group for sensing and detection in complex media. Biosens. Bioelectron. **25**, 2276–2282 (2010)
127. A.R. Statz, R.J. Meagher, A.E. Barron, P.B. Messersmith, New peptidomimetic polymers for antifouling surfaces. JACS **127**, 7972–7973 (2005)
128. R. Ko, P.A. Cadieux, J.L. Dalsin, B.P. Lee, C.N. Elwood, H. Razvi, Novel uropathogen-resistant coatings inspired by marine mussels. J. Endourol. **22**, 1153–1160 (2008)
129. A. Pechey, C.N. Elwood, G.R. Wignall, J.L. Dalsin, B.P. Lee, M. Vanjecek, I. Welch, R. Ko, H. Razvi, P.A. Cadieux, Anti-adhesive coating and clearance of device associated uropathogenic escherichia coli cystitis. J. Urol. **182**, (2009) 1628–1636 PMCID: PMC2807180
130. T.S. Sileika, H.-D. Kim, P. Maniak, P.B. Messersmith, Antibacterial performance of polydopamine-modified polymer surfaces containing passive and active components. ACS Appl. Mater. Interfaces. **3**, 4602–4610 (2011)

131. J. Cui, Y. Wang, A. Postma, J. Hao, L. Hosta-Rigau, F. Caruso, Monodisperse polymer capsules: tailoring size, shell thickness, and hydrophobic cargo loading via emulsion templating. Adv. funct. mater. **20**, 1625–1631 (2010)
132. J. Su, F. Chen, V.L. Cryns, P.B. Messersmith, Catechol polymers for pH-responsive, targeted drug delivery to cancer cells. JACS. **133**, 11850–11853 (2011)
133. H.J. Lee, A.N. Koo, S.W. Lee, M.H. Lee, S.C. Lee, Catechol-functionalized adhesive polymer nanoparticles for controlled local release of bone morphogenetic protein-2 from titanium surface. J. Control. Release. **170**, 198–208 (2013)
134. R. Gunawan, J. King, B.P. Lee, P.B. Messersmith, W. Miller, Surface presentation of bioactive ligands in a non-adhesive background using DOPA-Tethered biotinylated poly(ethylene glycol). Langmuir. **23**, 10635–10643 (2007)
135. S.H. Ku, C.B. Park, Human endothelial cell growth on mussel-inspired nanofiber scaffold for vascular tissue engineering. Biomaterials. **31**, 9431–9437 (2010)
136. L. He, D.E. Fullenkamp, J.G. Rivera, P.B. Messersmith, pH responsive self-healing hydrogels formed by boronate–catechol complexation. Chem. Commun. **47**, 7497–7499 (2011)
137. P. Podsiadlo, Z. Liu, D. Paterson, P.B. Messersmith, N.A. Kotov, Fusion of seashell nacre and marine bioadhesive analogs: high strength nanocomposite by LBL of clay and DOPA-polymer. Adv. Mat. **19**, 949–955 (2007)
138. M. Lee, J. Rho, D.-E. Lee, S. Hong, S.-J. Choi, P.B. Messersmith, H. Lee, Water detoxification by a substrate-bound catecholamine adsorbent. ChemPlusChem. **77**, 987–990 (2012)
139. X. Jia, Z.Y. Ma, G.X. Zhang, J.M. Hu, Z.Y. Liu, H.Y. Wang, F. Zhou, Polydopamine film coated controlled-release multielement compound fertilizer based on mussel-inspired chemistry. J. Agric. Food Chem. **61**, 2919–2924 (2013)
140. X.-D. Pan, Z. Qina, Y.-Y. Yana, P. Sadhukhana, Elastomers with chain-end mussel-mimetic modification for nanocomposites: strong modifications to reinforcement and viscoelastic properties. Polymer. **51**, 3453–3461 (2010)
141. M.-H. Ryou, J. Kim, I. Lee, S. Kim, Y.K. Jeong, S. Hong, J.H. Ryu, T.-S. Kim, J.-K. Park, H. Lee, J.W. Choi, Lithium-Ion batteries: mussel-inspired adhesive binders for high-performance silicon nanoparticle anodes in lithium-ion batteries. Adv. Mat. **25**, 1571–1576 (2013)
142. G. Westwood, T.N. Horton, J.J. Wilker, Simplified polymer mimics of cross-linking adhesive proteins. Maclomolecules. **40**, 3960–3964 (2007)
143. D.E. Fullenkamp, L. He, D.G. Barrett, W.R. Burghardt, P.B. Messersmith, Mussel-inspired histidine-based transient network metal coordination hydrogels. Macromology. **46**, 1167–1174 (2013)
144. E. Bell, J. Gosline, Mechanical design of mussel byssus: material yield enhances attachment strength. J. Exp. Biol. **199**, 1005–1017 (1996)
145. A. Tamarin, P. Lewis, J. Askey, The structure and formation of the byssus attachment plaque in mytilus. J. Morphol. **149**, 199–221 (1976)
146. S. Suresh, Graded materials for resistance to contact deformation and damage. Science. **292**, 2447–2451 (2001)

Chapter 16
Measuring Lipid Bilayer Permeability with Biomimetic Membranes

Kristina Runas and Noah Malmstadt

16.1 The Biological Role of Plasma Membrane Permeability

While there are numerous active mechanisms controlling which molecules cross a cell's plasma membrane to enter the cytoplasm, these are not the only routes by which molecules can enter cells. In fact, transport by passive diffusion across the lipid bilayer of the plasma membrane represents a nearly universal mechanism of molecular entry. Passive transport represents a key route by which both drugs and environmental toxins can cross biological barriers. Understanding the barrier properties of the lipid bilayer and what molecular characteristics control its permeability is therefore of fundamental interest to toxicology and drug development. Methods of measuring and predicting this permeability have been the topics of research for decades. Today, sophisticated biomimetic cell membranes, coupled with advanced analytical tools and computer modeling, allow new insight into this important biological property.

16.1.1 Passive Transport of Drug Molecules

For an orally delivered drug to reach systemic circulation, it must first diffuse across the mucus gel layer, intestinal epithelial cells, the lamina propria, and finally, the capillary endothelium [1]. The route that orally administered drugs generally take from the gut into circulation involves passive diffusion through epithelial cell membranes, rather than interaction with proteins or other active modes of transport [2]. The observation is supported, for instance, by the work of Pade and Stavchansky in 1998, which demonstrated that measurements of passive transport in human intestinal epithelial (Caco-2) cell membranes were a good predictor of the oral adsorption

N. Malmstadt (✉) · K. Runas
Mork Family Department of Chemical Engineering and Materials Science,
University of Southern California, Los Angeles, USA
e-mail: malmstad@usc.edu

M. Zhang et al. (eds.), *Carbon Nanomaterials for Biomedical Applications,*
Springer Series in Biomaterials Science and Engineering 5,
DOI 10.1007/978-3-319-22861-7_16

of drug-like molecules [3]. There have been significant efforts to directly correlate observed oral bioavailability to the molecular characteristics of drugs. These are exemplified by the "Rule of Five" approach devised by Lipinski et al. in 1997 [4]. After evaluating chemical parameters for several thousand drugs, Lipinski et al. determined that molecules with low oral bioavailability tended to have molecular weights greater than 500, and octanol/water partition coefficient greater than five, more than five hydrogen bond donors, and more than five hydrogen bond acceptors [4]. This rule establishes a rough range of molecular weights and polarities that correlates with good oral bioavailability.

There have been studies correlating other molecular properties with oral bioavailability. Burton et al. determined that a decrease in hydrogen bond potential, rather than lipophilicity, is the primary indicator for increased permeability [5, 6]. In 1996, Navia and Chaturvedi argued that molecular flexibility increases drug absorption [7]. In 1997, Palm et al. demonstrated a correlation between bioavailability and dynamic polar molecular surface area [8], a relationship that was corroborated by Kelder et al. 2 years later [9]. Martin, in 2005, disputed the traditional mind-set that lipophilicity was the most important predictor, instead suggesting that permeability was more closely related to molecular charge at biological pH [10]. In 2009, Waring evaluated the relationship between octanol/water distribution coefficient and permeability [11]. He determined that there was a lower lipophilicity requirement, below which a molecule was no longer lipophilic enough to act as a viable drug candidate. Additionally, both the upper and lower lipophilicity values were dependent on molecular weight. Perola in 2010 established that viable drug candidates must have a strong binding efficiency, where binding efficiency is a measure of the binding energy per atom of a molecule relative to its binding partner [12]. Essentially, the binding efficiency is a correlation between permeability and molecular weight.

These bioavailability correlation studies give only limited insight into molecular mechanisms of passive transport, and the correlations themselves are imperfect. For instance, antibiotics, antifungals, vitamins, and cardiac glycosides are all orally delivered drug classes that are predicted to have low bioavailability by the Rule of Five [4, 13–15]. Ultimately, an understanding of molecular mechanisms of transmembrane passive diffusion will allow for more precise design of high-bioavailability drugs. One key route to obtaining this understanding is directly observing permeation of drug-like molecules through cell membranes. Given the critical importance of efficient absorption to the efficacy of oral drugs, this makes studying passive transport a priority for drug development.

16.1.2 Environmental Toxins and Passive Transport

Environmental toxins are also capable of permeating the cell membrane [16]. Some types of heavy metals have been shown to cross the cell membrane via passive transport [17]. Cyclic hydrocarbons are also assumed to passively transport through the plasma membrane [18]. Toxins can also interact directly with molecules in the membrane: Electrophile toxins, for example, tend to insert themselves into the cell

membrane via covalent bond formation [16]. Various classes of nanomaterials have also been observed to cross the cell membrane via a passive mechanism. These include polymer nanoparticles [19, 20], fullerenes [21], semiconductor quantum dots [22], and gold nanoparticles [23]. Understanding the characteristics and mechanisms by which toxins bypass the cell membrane can lead to a more complete understanding of environmental toxicity of chemicals and materials.

16.2 Advantages of Biomimetic Membranes for Measuring Passive Transport

Despite the multiple interfaces that drugs must cross during adsorption, a single layer of intestinal epithelium presents the most significant barrier to passive diffusion [24]. As such, one of the most common techniques for assaying the potential of a drug to be absorbed is by measuring its permeability through a monolayer of Caco-2 cells.

Caco-2 is a colorectal adenocarcinoma-derived cell line that can be cultured such that the cells differentiate to resemble the epithelium of the small intestine [25]. First, evaluated as a transport model system in 1989 by Hildalgo et al., the Caco-2 cells were shown to be stable in confluent monolayers up to at least 10 days after incubation [26]. In the Caco-2 permeability assay, a cell monolayer is cultured between a donor chamber and a receptor chamber, with the solute of interest (i.e., the drug candidate) added to the donor chamber [27]. Samples are removed from each chamber at regular intervals for analysis to develop a time course of permeation. The cells are typically cultured for periods of 2–3 weeks, until they achieve confluence and well-developed tight junctions [25, 28]. Transport experiments are performed on these confluent monolayers. The final step of the assay is measuring the solute concentration in the receptor chamber. Methods for measuring solute concentration include radiolabeling [28], ultraviolet (UV) spectrophotometry [3], and high-performance liquid chromatography (HPLC) [1, 29, 30]. Including cell monolayer growth, the transport experiment itself, and analysis, the total experimental duration of a Caco-2 assay can be upwards of 3 weeks.

Cell-based systems such as the Caco-2 assay have significant shortcomings as tools to understand mechanisms of transmembrane permeability. Caco-2 cell membranes are significantly less controlled than biomimetic membranes formed from artificial bilayers: Permeation pathways can include active and paracellular transport as well as passive transport [27]. This complexity makes it difficult to pinpoint the exact transport mechanism for a certain solute and limits the utility of the Caco-2 assay in understanding molecular mechanisms. The heterogeneity of Caco-2 cells leads to variation in cell shape, size, and multilayer formation [31]. Different culture ages can also lead to different assay results [32]. Caco-2 assays are also costly, that is, up to 15–20 times more expensive than cell-free assays [27]. For the purpose of rapid screening drug candidates, Caco-2 and other such cell assays are impractical, and as such, it is necessary to find a low-cost, high-throughput biomimetic cell membrane system to support rapid solute permeation analysis [27].

16.3 Theoretical Considerations in Passive Transport

Theoretical constructs describing passive transport are important both in analyzing data and in making the ultimate mechanistic connections between molecular structure and membrane permeability. Descriptive theories of passive transport include transport modeling of the permeation–diffusion process, simulations of molecular interactions between permeating molecules and the bilayer, and analytical treatments of the permeation mechanism.

16.3.1 Overton's Rule and the Solution–Diffusion Model

Early theoretical exploration of membrane permeation was driven by the widespread acceptance of Overton's rule, which indicates that the membrane permeability of a drug-like molecule scales with its lipophilicity [33–35]. The permeability coefficient (P) is a constant of proportionality between the flux of a molecular species through the membrane and the concentration gradient of that species across the membrane. The key consequence of Overton's rule is that more lipophilic molecules are better drug candidates, as they have increased oral bioavailability. One way of representing the lipophilicity of a molecule is through the oil/water partition coefficient (K). The partition coefficient of a solute is expressed as the ratio of its solubility in an oil to its solubility in water [35]. The most common oil used to estimate solubility in lipid systems is octanol, and as such, the octanol/water partition coefficient is often used as a predictor of permeability. Increased octanol solubility corresponds to increased partitioning into the lipid phase. Typically, Overton's rule is interpreted as a relationship between oil/water partition coefficient and permeability coefficient.

The simplest theoretical interpretation of the observations summarized by Overton's rule is the solution–diffusion model, which treats the membrane as a homogeneous hydrocarbon slab [36]. A model concentration profile across a membrane is shown in Fig. 16.1.

The solution–diffusion model assumes all transport to be diffusive, so the molar flux inside the membrane can be expressed using Fick's law [37]. Molar flux J through the membrane is then:

$$J = -D\frac{\Delta c}{\Delta x} = \frac{D}{l}(c_{\mathrm{Mo}} - c_{\mathrm{Mi}}), \tag{16.1}$$

where D is the diffusivity inside the membrane, c_{Mi} and c_{Mo} are the concentrations of the molecule inside the membrane at the interior and exterior boundaries, respectively, and l is the length through the membrane.

The values of c_{Mi} and c_{Mo} depend on the concentrations of the permeating species in solution immediately adjacent to the membrane (c'_{Mi} and c'_{Mo} in Fig. 16.1) and the equilibrium partitioning of the species between solution and the membrane. This

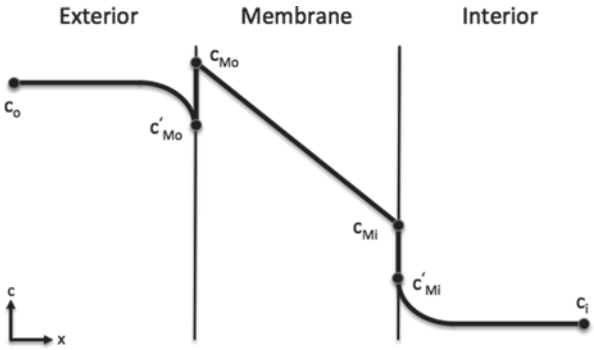

Fig. 16.1 Concentration profile across a membrane modeled as a homogeneous slab

equilibrium is described by the partition coefficient K, the equilibrium ratio of concentration dissolved in solution to concentration dissolved in the membrane. This value is simply a function of the thermodynamics of partitioning of the permeating species between the aqueous solution phase and the hydrocarbon membrane phase. Incorporating this relationship with Eq. 16.1, we have:

$$J = \frac{KD}{l}(c'_{\mathrm{Mo}} - c'_{\mathrm{Mi}}). \tag{16.2}$$

Finally, assuming a negligible concentration gradient in the fluid on either side of the membrane (an assumption that fails in many analytical cases, as described in Sect. 16.4.1), the flux can be expressed as:

$$J = P(c_{\mathrm{o}} - c_{\mathrm{i}}), \tag{16.3}$$

where the permeability P is defined as:

$$P = \frac{KD}{l}. \tag{16.4}$$

Since K tends to vary on a per-species basis much more than D, and l is roughly constant for all plasma membranes, the partition coefficient controls and can be used to predict membrane permeability [36, 38–41]. This is the crux of Overton's rule: Strong lipophilic partitioning leads to high permeability.

16.3.2 Molecular Dynamics Simulations: Complexity of Membrane Structure and Transport Pathways

Although Overton's rule may be capable of predicting permeability of many small molecules, the simplification of the cell membrane into a single solid slab does not accurately represent the membrane's complex structure and heterogeneity. In particular, treating the membrane as a uniform hydrocarbon ignores the charge state of

the lipid head groups, the presence of membrane proteins, lateral phase segregation in the membrane, and variations of membrane fluidity. For many molecules of varying charge state, size, or hydrogen bonding capacity, the solution–diffusion model may not be adequate to accurately estimate membrane permeability.

One technique for developing a more complex model of the cell membrane is through molecular dynamics simulations. The first molecular dynamics study to attempt to predict permeability was performed by Stouch et al. in 1993 [42]. In analyzing the permeation of benzene molecules through a single-component bilayer, the authors noticed there were two regions of transport in the bilayer. The first area was the head group region, characterized by tight packing and less available free space. The second region consisted of the tails towards the center of the bilayer, where there was a significant increase in free space, allowing the benzene to move more freely. This analysis inspired new approaches to modeling the bilayer: Instead of being approximated as a single uniform hydrocarbon slab, it can be divided into regions based on the type of transport within each region.

Building off of the work performed by Stouch et al., Marrink and Berendsen established in 1994 that even simple molecules such as water utilize transport pathways other than pure diffusion [43]. Their model, which accurately predicts the permeability of water as measured experimentally, relied on dividing the membrane into four separate regions. Each of the four regions is characterized by a different method of transport. As shown in Fig. 16.2, region 1 is defined as a free bulk region, where the water diffuses freely. Region 2 contains the lipid head groups; therefore, the transport is defined by bonding between the membrane and the water. The model indicates that these hydrogen and electrostatic bonds persist beyond the hydrophilic head groups, and into the hydrophobic areas. Region 3 is defined by tightly packed lipid tail groups with low water diffusivity. Finally, region 4 contains loosely spaced tail groups, allowing for decreased viscosity and increased water diffusivity.

Marrink and Berendsen's work was the first to explicitly define the regions based on transport mode, and it became a common structural model for lipid bilayers in considering transport processes. The four-region model devised by Marrink and Berendsen became a popular method for evaluating permeation through a lipid bilayer [45–50]. Other approaches increased the number of transport regions; for instance, Shinoda, Shinoda, and Mikami expanded the number of regions to 11 in 2008 [51].

One thing that these molecular dynamics models have in common is the introduction of transport pathways that describe the diffusion of solutes through an inhomogeneous medium. The idea of solute "hopping" from free volume pocket to free volume pocket was first introduced by Stouch and gained recognition as a likely possibility for transport not governed by uniform diffusion [42]. This transport pathway, sometimes called the "soft polymer" or the "mobile kink" hypothesis, particularly leads to deviations from Overton's rule predictions [39, 52, 53]. Recently, Zocher et al. published a molecular dynamics simulation which showed that for some classes of solutes, cholesterol concentration can have unanticipated effects on membrane permeability [54]. Simulation results in general have shown that the process of passive diffusion is more complex than what can be described by a simple partition/diffusion model.

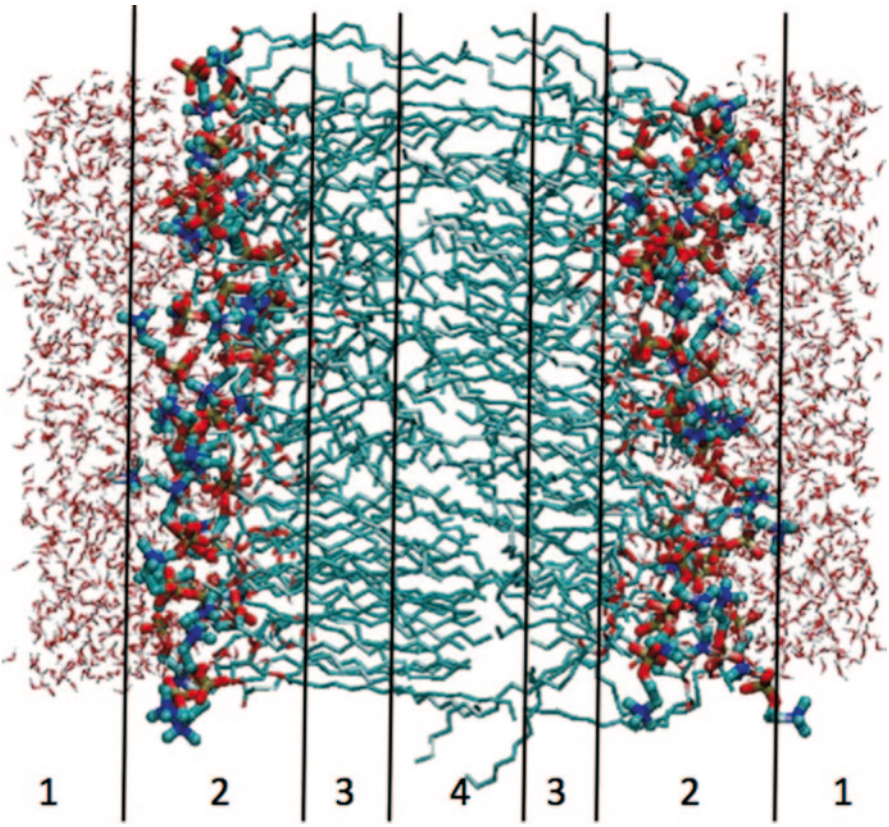

Fig. 16.2 A snapshot of a molecular dynamics simulation of a hydrated lipid bilayer. The atoms are colored by element: *cyan* = carbon, *blue* = nitrogen, *red* = oxygen, and *orange* = phosphorus. The four transport regions are labeled according to the Marrink and Berendsen model [43]. (The image was published by Bemporad et al. in 2005; [44])

16.3.3 Analytical Approaches and Empirical Correlations

Although molecular dynamics simulations can provide a wealth of information regarding the permeation of molecules across a bilayer, computational limitations restrict their size and complexity. In this respect, it is difficult to use a molecular dynamics simulation to draw general conclusions regarding solute properties and their relationship to permeability.

In 2008, Nagle et al. published a mathematical model of permeation through a bilayer [55]. In this approach, the bilayer was divided into three regions. The first layer was an inner hydrocarbon core, and the other two layers consisted of interfacial headgroups. The purpose of this model was to relate the permeability to bilayer properties such as area per lipid and bilayer thickness. The authors hoped to more accurately estimate permeability for a given bilayer composition by incorporating these parameters. Overton's rule was incorporated by relating permeability to the octanol/water partition coefficient.

Mitragotri et al. published a model in 1999 to relate the permeability to cross-sectional area, radius, and molecular volume of a solute [56]. Nitsche and Kasting expanded on this type of model in their 2013 publication [57]. Rather than focus entirely on relating permeability to solute size, they attempted to predict the permeability of neutral molecules by accounting for solute size, surface density variation, cholesterol fraction of the membrane, and temperature of the system. This complex relationship was unique in that it combined both solute and membrane properties to accurately determine the permeability of the system. This model was shown to be accurate except in the cases of halogenated compounds, although the authors believe this could be remedied with a more complex relationship for the lipophilicity of the solute.

Ultimately, validating any of these analytical or empirical approaches requires precise measurements of the rate of passive transport of small molecules across membranes. These measurements are facilitated by the techniques described in the next section.

16.4 Methods for Measuring Passive Transport

Isolating and understanding the molecular processes that underlie passive transport require well-controlled experimental systems. Precise control of lipid bilayer structure and composition, for instance, allows for the lipid-driven processes in passive transport to be isolated, something that is impossible in more complex systems such as the Caco-2 assay described in Sect. 16.2. Synthetic bilayer models such as liposomes and planar lipid bilayers were first introduced in the 1960s [58, 59]. There are numerous advantages to measuring transport in biomimetic lipid bilayer systems, such as the availability of a variety of methods for measuring the solute flux. The ideal experimental technique would allow for high-throughput data collection of highly controlled systems without artifacts.

16.4.1 The Unstirred Layer: Artifacts and Effects on Membrane Transport

Prior to discussing the various techniques for measuring membrane permeability, it is important to understand a major feature they have in common. These approaches all must cope with the existence of an unstirred layer (USL), or a region of static fluid close to the membrane in which the diffusion-driven transport of the permeant leads to a non-uniform concentration. The USL, indicated in gray in Fig. 16.3, is defined as the region in which the concentration of the solute cannot be assumed equal to the bulk concentration. While it is easy to measure the bulk concentrations on either side of the membrane (c_o and c_i in Fig. 16.3), it is the concentrations closest to the membrane (c'_{Mo} and c'_{Mi} in Fig. 16.3) that determine the driving force for membrane transport. Thus, it is necessary to be able to model the USL in order to accurately predict membrane permeability from

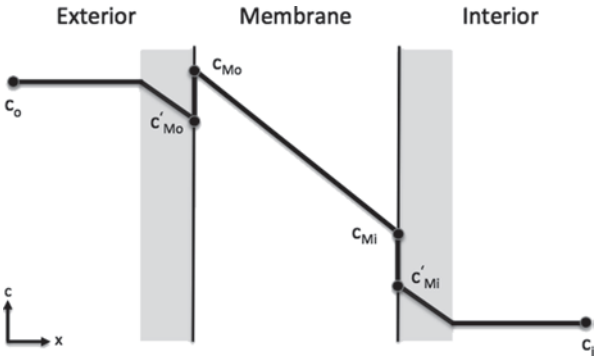

Fig. 16.3 Concentration profile across a membrane with the unstirred layer indicated in *gray*

bulk concentration measurements. In 1984, Barry and Diamond published an exhaustive description of the importance of the USL to membrane transport; this remains an excellent reference describing the fundamental issues involved [60].

The potential problems introduced by the USL can be understood by treating the entire system as a sum of resistances. If the USL is assumed to be symmetric on either side of the membrane, the measured permeability P_{meas} can be calculated based on the permeability of the solute through the USL, P_{USL}, and the permeability of the membrane, P. If permeability is taken as the reciprocal of resistance, the resistance through the total system can be defined as the sum of the resistances from the membrane and the USL [38]:

$$\frac{1}{P_{meas}} = \frac{1}{P} + \frac{1}{P_{USL}}. \tag{16.5}$$

If the permeability of the solute in the USL is estimated as D_{USL}, the diffusivity of the solute, divided by δ, the length of the USL, this relationship gives:

$$P_{meas} = \frac{1}{\frac{1}{P} + \frac{\delta}{D_{USL}}}. \tag{16.6}$$

As discussed by Barry and Diamond, determining P accurately becomes difficult if the USL is large [60]. In this case, the transport through the system is dominated by diffusion through the USL, rather than permeation across the membrane.

Characterizing the USL has been the focus of many research efforts. One method of determining USL size is by directly measuring solute depletion next to a membrane [61–63]. The most common technique for direct measurements in the USL is placement of microelectrodes adjacent to a planar membrane. Traditionally, it was assumed that the thickness of the USL was independent of the diffusivity of the solute [64–70]. However, extensive models of the USL have indicated that thickness should depend on the solute diffusivity [71, 72]. Microelectrode-based work by Pohl, Saparov, and Antonenko in 1998 confirmed that increasing solute diffusivity increased the thickness of the USL [73].

This is an important result because the thickness of the USL determines how much the USL alters measured permeability (see Eq. 16.6). Correcting for the presence of the USL depends on knowledge of the USL thickness, which in turn depends sensitively on the precise geometry and execution of the experimental method. The simplest example of this dependence is the effect of solution agitation on the size of the USL. Dainty and House quantified the stirring effect by measuring ion transport across a membrane of isolated frog skin cells [62]. Simply by increasing the stirring rate from 120 to 500 revolutions per minute, the USL thickness could be decreased by 230–100 μm. USL thickness also depends on aqueous phase viscosity [74–76]. Interestingly, the geometry of the membrane does not appear to have a significant impact on USL thickness. Poznansky et al. discussed the variations in USL size between planar and spherical geometries, and they found an insignificant difference [77].

Keeping in mind that all systems for measuring membrane permeability must take USL effects into account, we now survey some of the widely applied approaches.

16.4.2 Parallel Artificial Membrane Permeability Assay

The current dominant technique for high-throughput screening of drug permeability is the parallel artificial membrane permeability assay (PAMPA). PAMPA experiments use porous filter membranes impregnated with organic phospholipid solutions as mimics of the plasma membrane [78]. PAMPA has numerous advantages relative to Caco-2 assays, including lower cost, simpler implementation, and allowance for a larger pH range to better mimic the gastrointestinal tract [78, 79].

The PAMPA method was first described by Kansy et al. in 1998 [80]. The technique is based on multi-well microtiter plates with filter inserts (e.g., Corning Transwell® membrane filters). A schematic of the assay is shown in Fig. 16.4. The filters are impregnated with a lipid solution in an organic solvent; the lipid composition can be varied to simulate membranes of various tissues. The wells are filled with an aqueous buffer solution (the acceptor solution) and the filters are inserted. The solute of interest (in the donor solution) is added to the top chambers of the filter wells, and transport rates are determined by observing the change in concentration of the solute of interest in the acceptor solution [80]. PAMPA readout is by simultaneous UV measurements of the 96-well plate, allowing for high-throughput drug screening [80].

PAMPA is of comparable accuracy to Caco-2 assays, providing a much better assessment of drug viability than Overton's rule [79]. The two types of assays occasionally return contradictory results, however. For basic and cyclic peptide drugs, PAMPA consistently produces higher membrane permeability than Caco-2 [27]. Transport of these molecules is hindered by secretory mechanisms only present in Caco-2 cells [81]. Of course, PAMPA tends to produce lower than Caco-2 permeability for solutes that cross the plasma membrane through active transport channels [27]. This class of solutes includes zwitterionic peptides and peptide amides [81]. PAMPA also gives more accurate (in terms of fractional human absorption) results for situations of low/neutral pH [82].

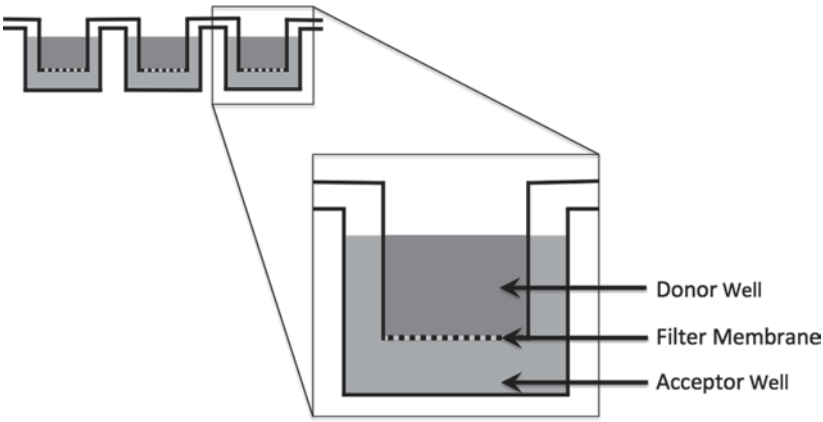

Fig. 16.4 A schematic of the PAMPA assay. Insert: a single well with the donor chamber, membrane, and acceptor chamber indicated. Lipid bilayers are formed by impregnating a porous filter with a lipid solution. Transport of a solute is measured across the membrane from the donor well to the acceptor well. Inset shows an expanded view of a single well, with the donor well, porous filter membrane, and acceptor well labeled

PAMPA studies have been broadly applied to understand fundamental mechanisms of passive transport in two categories: The first category involves establishing what types of solutes are more permeable than others based on properties such as size and structure, and the second category evaluates the permeability of different types of bilayers. In the first category, PAMPA was used to determine the permeability of cyclic peptides, showing that that ability for a peptide to form hydrogen bonds increases its permeability [81, 83]. Studies within the second category determined that highly permeable or non-neutral solutes are more sensitive to membrane fluidity and the ion pair effects caused by interaction with charged lipid head groups, while less permeable solutes were less sensitive to these membrane effects [84].

While the PAMPA assay is capable of producing high-throughput results [85], and while there is certainly a relationship between permeability in a PAMPA assay and cell membrane permeability, the filter system used in PAMPA is far from a perfect model of a plasma membrane lipid bilayer. For example, it is not clear that impregnation of filters with lipid solution leads to the reliable formation of bilayers in the filter pores. Although there is some evidence that bilayer formation occurs in similar systems [86], little characterization has been done to verify the presence, frequency, and stability of any pore-occupying bilayers in PAMPA systems. The formation of a bilayer in every pore in the filter membrane is not guaranteed; some might be empty and others might be clogged with lipid or solvent.

The necessary usage of solvent is another concern with the PAMPA technique. Large quantities of organic solvent present in the filter pores mean that in some cases, PAMPA results may depend on the interaction between the solute and this solvent. It has in fact been shown that the use of different solvents in PAMPA yields different permeability results for the same solute [82]. The combination of unknown

lipid structure and residual solvents can lead to false predictions of permeability values for common drugs using PAMPA techniques [87]. To accurately measure drug permeability through true lipid bilayers, it is necessary to use a biomimetic model system that can predictably, controllably, and reliably reproduce the bilayer structure.

16.4.3 Planar Lipid Membranes

Mueller et al. published the first technique for forming optically black lipid membranes in 1962 [58]. In this method, lipids dissolved in a hydrophobic solvent are brushed into an aperture positioned between two chambers. After the solvent has dried, the chambers are filled with an aqueous solution, and the aperture is painted with a lipid solution for a second time. This causes a bilayer to spontaneously form over the aperture. Walter and Gutknecht performed extensive experiments of transport across planar lipid bilayers in the 1980s [39]. Their experimental apparatus placed the bilayer between two chambers, a donor and a receptor chamber [88]. Both chambers were stirred magnetically to mix the solutions and minimize USL effects [88]. Their most comprehensive study was published in 1986, in which transport of 22 nonelectrolyte solutes was measured [39]. Most of the solutes were tagged with a radioactive tracer and assayed radiochemically with a liquid scintillation counter. For solutes that were not available in a radiolabeled form, transport was measured using various analytical chemical reactions. While the majority of the measured permeabilities agreed with the predictions based on Overton's rule, solutes with molecular weight less than 50 Da were measured as permeating 2–15 times faster than predicted.

To measure the permeation of species with a charged form (e.g., weak acids), microelectrodes can be used for detection. This method involves positioning microelectrodes at varying positions near the membrane to accurately measure the pH or ion concentration profile through the USL [89, 90]. First introduced by Ohki in 1980, the technique was originally used to measure the effect of membrane charge state on permeability [91]. Further work in the early 1980s involved characterizing the permeation of sodium ions via a carrier molecule across a planar membrane with either varying concentration or pH [92]. Walter and Gutknecht adapted their planar membrane technique to utilize microelectrodes to measure proton transport across membranes [88, 93–95]. Significant work was performed by Antonenko and Yaguzhinski in 1982 and 1984 to characterize the microelectrode method [96, 97], and this method was exploited extensively by Pohl and coworkers.

Initially, the Pohl group used this microelectrode procedure primarily to evaluate weak acid transport across lipid bilayers [68, 69, 98]. A diagram of a sample experimental setup is shown in Fig. 16.5a. After determining the effects of the buffers on the pH gradient, and subsequently acid transport rate across the membrane, the technique was then expanded to nonacid solute transport. Solutes such as water and ammonia were studied using the microelectrode method [70, 99]. Ammonia transport was measured using both ammonium ion-sensitive microelectrodes and pH-sensitive microelectrodes. The proton-sensitive microelectrodes demonstrated

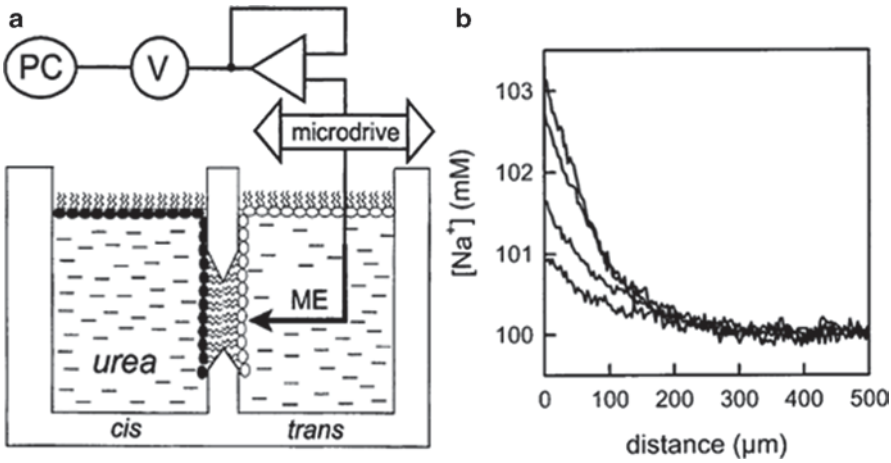

Fig. 16.5 Example of **a** a microelectrode experiment used to measure water transport across a bilayer and **b** resulting measurements of sodium ion concentration. **a** An osmotic gradient was induced across the bilayer by the addition of urea to the *cis* side. This gradient caused an increase of sodium ions within the *trans* compartment. As the ion concentration can be related to the transmembrane water flux, a sodium-sensitive microelectrode was used to determine the spatial concentration profile. The microelectrode is positioned at various distances from the membrane using the microdrive. Note that this diagram shows an asymmetric membrane, but the experiment apparatus is viable for symmetric bilayers as well. **b** Results from the apparatus shown for sodium ion concentration as a function of microelectrode position. This concentration was then used to determine water flux across the membrane due to the osmotic gradient. The four profiles represent four different gradient strengths, where an increase in osmotic gradient increases the sodium ion concentration gradient. This variation in concentration profile with respect to distance corresponds to the USL in the system. *ME* microelectrode. (Figure adapted from Krylov et al.; [99])

the importance of the USL—within it, there are proton transfer reactions between ammonia and ammonium ions. Variations in the proton concentration alter the ammonia permeation curve from the predictions made by Overton's rule [70]. Water transport has also been measured indirectly through solute concentration changes on either side of the membrane. Transmembrane water flux corresponds to changes in solute concentration on either side of the membrane [99]. A representative data set, where water permeability was measured through variations in sodium ion concentration on either side of the membrane, is shown in Fig. 16.5b [99].

Microelectrode-based approaches to membrane permeability measurements typically operate at steady state; in other words, the donor side of the membrane is treated as an infinite source of solute at fixed concentration and the receptor is treated as an infinite sink. Upon the establishment of constant-flux conditions, the system will take on a steady-state concentration profile that can be characterized by the microelectrode. Steady-state transport equations are then used to quantify the flux across and permeability of the membrane. A variation on this approach used a microelectrode to generate permeating protonated acid species and confocal microscopy to characterize the resulting pH gradient generated by these acids crossing the membrane [100]. It is not clear, however, that this system can achieve steady state in a reasonable experimental duration [101, 102].

Several recent approaches have focused on arraying planar bilayers. Patterned arrays of planar-supported lipid bilayers were originally developed by Boxer and coworkers in the late 1990s and early 2000s [103–105]. In 2010, Brozell et al. used supported lipid bilayers arrayed on colloidal crystals [106]. These crystals are formed spontaneously on substrates by evaporative self-assembly of colloids such as silica microspheres. A pH-sensitive dye was used to characterize proton transport across the crystal-supported bilayers. This technique allows for the collection of transient data on a large number of bilayers simultaneously.

Arrays of droplet bilayer membranes have also been used to build potentially high-throughput permeability measurement systems. Droplet bilayers are formed when two aqueous droplets submerged in an organic lipid solution are brought into contact. Lipid monolayers assemble on the droplet surfaces, and a bilayer forms when two monolayers touch [107]. Droplet bilayers can be formed by contacting droplets in microfluidic devices [108]. In 2013, Nisisako et al. utilized this method to perform a permeation study on a one-dimensional array of droplet interface bilayers [109]. For the purpose of this study, the donor droplet contained the molecule of interest, and the acceptor droplet contained only buffer. Transport was observed either by fluorescent microscopy or by UV microspectroscopy, allowing for measurements on unlabeled species (e.g., caffeine). Transient data were collected for permeation processes with halftimes as short as 5 min.

16.4.4 Vesicles

Vesicular bilayers represent another common biomimetic membrane system. Nanoscale liposomes in aqueous suspension serve as membrane-delineated compartments into or out of which a species of interest will passively diffuse [110]. Measuring permeation can be accomplished, for instance, by nuclear magnetic resonance (NMR) spectroscopy. Xiang and Anderson measured monocarboxylic acid transport by observing line broadening in NMR spectra [111]. An impermeable paramagnetic ion is added to the solution outside the vesicles to alter the spectral signal of the permeant species when it is on the outside of liposomes. NMR spectra in this system can be analyzed to derive the characteristic exchange time of a permeant species between vesicle interior and exterior [112]. This technique is limited to permeation processes in which the characteristic lifetime of a species inside the liposome is between 0.001 and 10 s [112]. NMR approaches operate at equilibrium, such that there should be no net concentration gradient of permeant and no USL. Data analysis is complex, however.

For relatively slow permeation processes, a permeant can be entrapped in liposomes and its changing concentration in the liposome exterior can be directly measured as a function of time. Xiang and Anderson accomplished this by preparing liposomes in the presence of permeant species and running them over a gel filtration column to obtain, in the void fraction, a sample consisting of permeant-containing liposomes with little or no permeant in the exterior [113, 114]. Permeation was

measured as a function of time by ultrafiltering samples to remove liposomes and measuring the increasing concentration of the permeant in the filter flow-through. This worked well for processes with halftimes on the order of tens of minutes to hours, for which the USL would be expected to be a relatively minor artifact.

An isotopic mass spectrometry approach has been used by Endeward and Gros to measure gas transport across red blood cell [115–117] and epithelial cell membranes [118]. Carbonic anhydrase is used to exchange ^{18}O between water and carbon dioxide on one side of the membrane. Gases evolved from the experimental apparatus are constantly sampled, and the ratio of ^{18}O-containing to ^{18}O-free carbon dioxide is continuously measured by mass spectrometry. The rate of change of this ratio is then connected to membrane permeability using a theoretical apparatus that takes into account membrane transport of biocarbonate ions, water, and carbon dioxide as well as the activity of carbonic anhydrase [115]. This system has recently been applied to measure carbon dioxide transport across fully synthetic liposome membranes [119].

Transient measurements in vesicles represent some of the key data describing transport of protons across lipid bilayers. In 1980, Deamer and Nichols developed an acid–base pulse titration method that could measure the kinetic process of proton transport across liposome membranes [120]. Drops of either acid or base were titrated into a stirred liposome suspension, and the pH change of the surrounding solution was measured with a standard pH electrode. After the initial pH spike, a transient decay in pH—corresponding to proton transport across the liposomal membrane—could be observed. A key aspect of this work was the characterization of the diffusion potential that retards proton transport at excessively high pH gradients [121]. This work eventually led to an expanded model of the proton transport mechanism across bilayers [122].

Stopped-flow techniques can also be used to measure solute transport into or out of liposomes. These techniques involve adding liquids to a mixing chamber via multiple injection syringes. The influx of liquid forces the old contents of the cell into a stop syringe. When the cell volume has been completely replaced with new reagents, the stop syringe will engage a trigger switch to stop the flow and begin acquisition. The time from initial insertion of liquid to stopping the flow is considered the “dead time” of the setup and is dependent on the design of the apparatus. This dead time represents the time the two inlet liquids have been in contact before observation [123].

Water transport across bilayers can be measured by stopped flow using an osmotic gradient across liposomes; as liposomes shrink or swell in response to osmotically driven transport of water, their scattering properties will change [123–125]. Ye and Verkman used stopped-flow experiments to measure the permeation of water into liposomes in 1989 [126]. Water permeation was again measured via stopped flow in 2000 by Dordas and Brown, and Mathai et al. in 2001 [127, 128]. USLs are a significant concern with stopped-flow techniques [129]. Some studies suggest that the USL in stopped-flow transport experiments can be up to 5.5 μm thick (many times larger than the liposomes themselves) [123].

Surface plasmon resonance (SPR) techniques have been used to measure the temporal variations in the refractive index inside a liposome during a permeation process [130]. In 2010, Brändén et al. used SPR to measure transport of alcohols through protein channels in liposomes [131]. For these experiments, liposomes suspended in and containing the molecule of interest were immobilized on the surface of an SPR sensor in a microfluidic channel. The exterior concentration was forced to zero using a rapid buffer exchange. The refractive index of the liposome interior was then measured with respect to time to analyze the concentration change. This is a promising label-free technique, but it cannot directly account for the USL.

Recent advances in imaging techniques allow for spatially resolved transient measurements of the transport process in through the membranes of giant unilamellar lipid vesicles (GUVs). In 2010, Li et al. published a method to measure the transport of fluorescently labeled short-chain poly(ethylene glycol) molecules into GUVs with spinning disc confocal microscopy [132]. Vesicles were dropped into a chamber containing a set concentration of the poly(ethylene glycol) species. Once the vesicles had settled to the bottom of the chamber, change in interior concentration could be tracked as a function of time using confocal fluorescence.

A similar imaging technique was employed by Heider et al. in 2011 to measure the transport of N-methylbutylamine (NMBA) into vesicles encapsulating a pH-sensitive dye (5,6-carboxy SNARF-1-dextran) [133]. Vesicles containing the dye were immobilized on a glass coverslip, and a buffer exchange was performed with a pipette to remove residual background fluorescence contributions from unencapsulated dye molecules. NMBA was then added to the chamber. A single vesicle was then imaged using epi-illumination spectral fluorescence microscopy for several minutes to visualize the transport process.

Other advanced microscopy techniques have been used to observe passive transmembrane transport. In 2011, Budzinski et al. used total internal reflection fluorescence (TIRF) microscopy to measure proton transport out of 30–160 nm diameter vesicles containing a pH-sensitive dye (SynaptopHluorin) [134]. Note that these vesicles are smaller than the optical diffraction limit: A low density of vesicles on the substrate combined with the low background fluorescence facilitated by TIRF allows for single-vesicle measurements to be made. One concern with this method as well as that presented by Heider et al. [133] is the issue of mixing time. Unlike the work performed by Li et al. [132], the background concentration within the microwell is not constant with respect to time. Thus, the calculation of permeability within this setup is a twofold process of mixing followed by permeation. To accurately measure the membrane permeability, it is necessary to measure a process with a time constant significantly larger than the mixing time.

Vesicle imaging can also be combined with rapid microfluidic buffer exchange, as demonstrated by Li et al. in 2011 [135]. To measure permeation of weak acid species, GUVs containing a pH-sensitive fluorophore were immobilized in a microfluidic channel. A buffer containing the solute of interest was then flowed past a single GUV, while the spatial distribution of fluorescence inside and surrounding the GUV was recorded. This technique allows for the direct observation of the

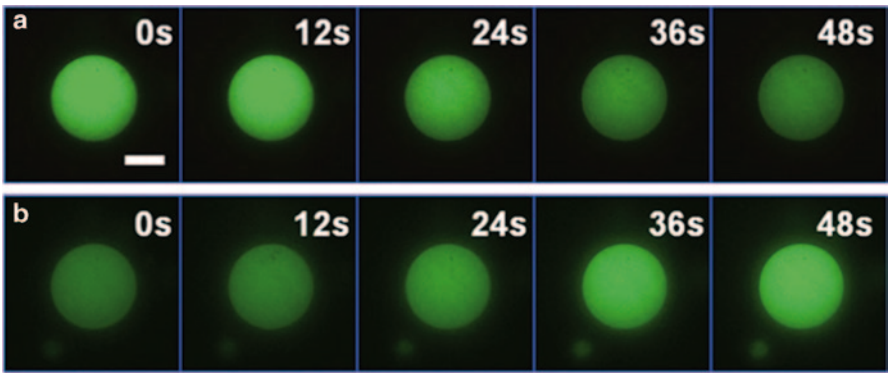

Fig. 16.6 A sample set of spinning disk confocal microscopy images. The encapsulated fluorescein dextran varies in intensity with the pH of the liquid and allows for a calculation of concentration of acid species with respect to time. The two times series show acetic acid transport **a** into and **b** out of the vesicle. (Figure reproduced from Li et al.; [135])

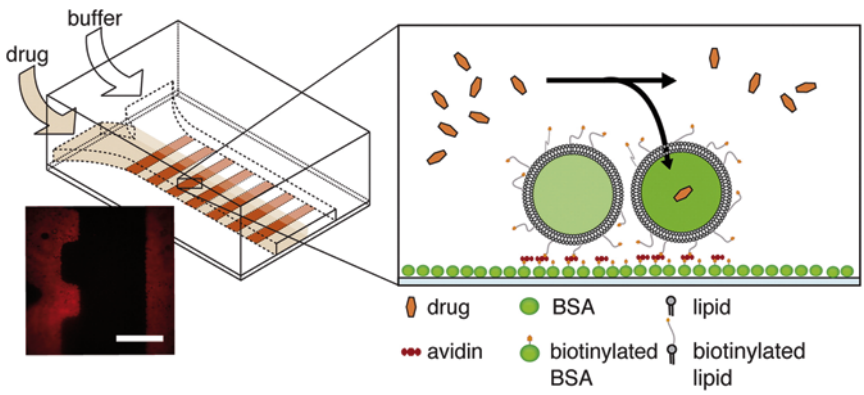

Fig. 16.7 The microfluidic device designed by Eyer et al. [137]. The channel has two inlets and a single outlet. Both the drug and the buffer streams were flowing simultaneously. Varying the individual flow rates, while maintaining a constant total flow rate, allowed for a fast buffer exchange. The bottom of the device was patterned in stripes of avidin, allowing vesicles to bond with only selective areas of the channel. The device pattern allows for the imaging of fluorescence changes in specific regions containing liposomes, and unspecific background regions. Figure reproduced from by Eyer et al. [137]

change in both vesicle interior and exterior concentrations as functions of time, allowing for transport from the bulk and into the vesicle interior to be directly modeled. Representative images of changing vesicle internal fluorescence in response to buffer exchange are shown in Fig. 16.6.

Microfluidic buffer exchange was also utilized by Kuhn et al. in 2011 to measure permeation through liposome membranes [136]. As shown in Fig. 16.7, liposomes were immobilized in a stripe pattern using the biotin–avidin interaction, and buffer exchange was performed to measure the transport of tetracyclines.

The purpose of the stripe pattern was to observe the fluorescence changes in two areas: the "specific" sites containing liposomes and the "nonspecific" background areas. By encapsulating europium inside the vesicles, it was possible to visualize the transport process. Once tetracycline permeated across the membrane, it bound to the europium inside of the liposomes forming a fluorescent complex. Transport was imaged with TIRF microscopy. In this apparatus, it took about 45 s for the buffer exchange to occur, limiting observable transport halflives to the range of minutes.

Continuing this microfluidic device work, Eyer et al. evaluated the permeation of several weak bases in 2013 [137]. Vesicles were immobilized in the same devices used by Kuhn et al. in 2011 [136]. This application reduced the buffer exchange time for the system to 800 ms.

Buffer exchange issues are minimized in device designs capable of rapid switching between buffers. Ohlsson et al. designed a microfluidic platform capable of trapping over a 100 liposomes and performing buffer exchange in less than 10 ms [138]. This rapid switching was performed by using a vacuum to rapidly move the laminar interface between two buffers. Liposomes encapsulating a pH-sensitive dye were immobilized in the channel. Transport of acetic acid was measured using epifluorescence and TIRF microscopy. A similar technique was used by Kuyper et al. in 2006 to measure proton permeation into single vesicles in a microfluidic platform, although the design of their device did not allow for such fast buffer exchange [139]. This technique utilized new advances in camera technology to visualize individual fluorescently labeled liposomes at a high frame rate. A significant advantage of this technique is the ability to measure multiple liposomes simultaneously.

One significant advantage of microfluidic approaches is that vesicles can be analyzed in an array, allowing for high-throughput permeability measurements. In 2013, Robinson et al. published a novel method for mechanically trapping vesicles in an array configuration [140]. GUVs were trapped using a series of posts, then individually isolated from the other compartments by lowering a circular valve around the vesicle. This technique was used to measure the transport of calcein through pores formed by the introduction of α-hemolysin. The interior fluorescence of the vesicles with respect to time was evaluated using confocal microscopy.

A majority of vesicle-based measurements are transient. While the collection of time data is advantageous, many of these techniques do not allow for the resolution of the USL. Steady-state measurements tend to be better at evaluating the USL, at the sacrifice of transient data. Ultimately, those techniques most capable of collecting transient data and minimizing artifacts such as the USL have typically been incapable of performing the high-throughput experimentation necessary for evaluating numerous compounds in a short period of time. Future efforts must be focused on obtaining spatially and temporally resolved data in a high-throughput, potentially array-based, format.

16.5 Advantages and Disadvantages of Various Transport Measurement Techniques

Selecting a method for measuring passive transport across a biomimetic bilayer is a matter of balancing the characteristics of the various techniques described above. While an approach that can directly resolve the USL is of obvious benefit; such approaches are generally limited in terms of the types of permeant species they can analyze (e.g., fluorophores or charged species). Methods that are amenable to general chemical species as permeants are inherently more prone to USL artifacts and thus are less accurate. Despite their biological relevance, fast permeating species are a difficult class of solutes, as many techniques are not capable of resolving relatively fast transport processes. High-throughput approaches, which are necessary for realistically scaled drug discovery efforts, generally suffer from both USL artifacts and a lack of a realistic biomimetic membrane.

16.5.1 Techniques Capable of Resolving the USL

As discussed in Sect. 16.4.1, the USL represents a fundamental challenge in obtaining accurate measurements of transport across a biomembrane. The size of the USL is linked to uncertainty in the measurement of membrane permeability [60]. As the size of the USL has been shown to vary with stirring [29, 30, 62], application of ultrasound [68], and solute diffusivity [73], direct measurement of the USL size is important for understanding the spatial changes during the transport process.

The key technology that has allowed for direct measurement of concentration gradients in the USL is microelectrode detection in a planar membrane chamber. Of course, microelectrode-based techniques are limited to detecting species with an electronic signature. These include acids and bases, which can cross bilayers in their uncharged state [68]. Similarly, proton transport can be simply observed [88], as can transport of ions through ion channels [92]. Ammonium-sensitive electrodes have been used to quantify ammonia transport [69], and water transport has been analyzed via a solute dilution effect [98]. In addition to requiring a permeant species that can be detected by electrodes, these approaches also generally operate in a steady state which, while simplifying data analysis, does require a number of assumptions [101].

Recent developments in imaging techniques have lead to the publication of methods capable of microscopy-based resolution of the USL [100, 132, 135]. These have been developed to operate in both steady-state [100] and transient modes [132, 135]. These techniques have so far been confined to fluorescence microscopy however, and they are limited to either fluorescent analytes or analytes that alter the fluorescence of a reporter molecule.

16.5.2 Techniques for Measuring Transport of Uncharged, Nonfluorescent Species

For species that are not detectable via microelectrodes or fluorescence microscopy, there are a large number of options available for measuring transport properties. While these approaches cannot directly resolve the USL, knowledge about the nature of the USL obtained from other systems can be used to predict transport behavior and correct for expected artifacts. In general, a method that relies on standard analytical chemistry techniques to detect the concentration of a general permeant species as it crosses the bilayer will be slow; such approaches are therefore often incapable of capturing fast transport processes.

An exception to this general rule is the stopped-flow approach, which relies on an optical signal coupled to transport across the bilayer. It has been used most often to detect water transport as a result of applied osmotic pressure. In this case, transport can be observed as liposomes grow or shrink and their scattering characteristics change. The stopped-flow approach is limited to species whose transport can be linked to an optical signal, and it makes no attempt to explicitly characterize the USL [129]. Similarly, recent work has been done to analyze permeability using SPR [131]. This technique measures the variations of refractive index of liposome contents with respect to time and does not require a fluorescent molecule to do so.

The most generalizable approaches involve transport across a planar lipid bilayer with sampling to determine concentration change with time. Radiolabels or arbitrary analytical chemistry approaches can be used to quantify concentration [39]. Stirring can be used to minimize (though never to eliminate) USL effects, which will begin to dominate as the speed of the transport process increases. Increasing permeability (i.e., faster transport across the membrane) will also place limits on the ability to accurately collect samples. A similar approach can be applied to vesicular systems, in which the solution exterior to the vesicles can be independently sampled by filtering the vesicles out [141]. Again, the accuracy of this technique is limited by sampling frequency, and it is best applied to relatively slow transport processes.

16.5.3 Considerations when Measuring Diffusion-Limited Transport

The definition of a “fast transport process” is complicated, as it cannot always be separated from the measurement technique or the bilayer classification. The fundamental limits of a fast transport process can be categorized as either (1) a process that violates an assumption of steady state, (2) a process in which transport is dominated by the USL, or (3) a process in which permeation is faster than the instrumentation can accurately resolve. For a transient experiment, this limitation

can be caused by four categories of issues: limitations due to sampling, limitations due to monitoring resolution, limitations due to reservoir size, and limitations due to mixing times.

First, fast transport process can violate the assumption of steady state. This tends to happen in situations where permeation is significantly faster than diffusion. This ratio leads to a large USL on either side of the membrane. As discussed by Missner et al. and reproduced in Eq. 16.7, the time to steady state is related to the size of the USL [101]:

$$\frac{t_1}{2} = 0.38\frac{\partial_{\text{USL}}^2}{D}. \tag{16.7}$$

As the size of the USL increases with fast transport, the time to reach steady state becomes larger as well, making experiments impractical. Fast flux across the membrane also makes it impossible to treat the reservoirs on either side as a perfect source/sink pair, violating steady-state assumptions.

A dominant USL is also a problem for transient techniques. As described in detail in Sect. 16.4.1, the larger the USL, the larger the experimental artifacts. Figure 16.8 shows how the character and size of the USL change with rate of permeation. In the fast permeating regime (Fig. 16.8b), the USL cannot be neglected.

Of the four types of experimental concerns regarding a transient data set, the first is sampling rate. Many techniques require removal of discrete quantities of solution for analysis during the permeation process. This sample removal rate must be significantly faster than permeation.

One example of a transient technique limited by sampling is PAMPA. The collection of data with this assay is limited by the frequency of samples collected, usually using automated robotic sample handling for UV analysis [80]. Measurements can typically only be collected on the order of minutes. This sampling rate means that PAMPA is better suited to compounds that permeate on the order of hours. Xiang and Anderson had a similar concern with sampling rate when they examined permeation out of liposomes purified by gel filtration and ultracentrifugation [113, 114]. The process of extracting samples using ultrafiltration was time-consuming enough that the measured processes must have halftimes of tens of minutes to hours.

For many transient techniques, it is in principle possible to continuously evaluate the concentration profile, but there are limitations on the time resolution of monitoring. Some examples of techniques in this group include either fluorescent microscopy-based analysis or stopped-flow techniques. Microscopy-based analysis techniques are limited by the frame rate of the camera [100, 132, 135]. Images collected with spinning disk confocal microscopy are restricted by the speed of pinhole rotation, and images captured by laser scanning confocal microscopy are limited by scan rate [142]. Stopped-flow experiments are restricted by the sampling rate of the spectrophotometer used to examine the scattering properties during transport [123]. If transport is too fast, the monitoring resolution will be insufficient to collect enough data for analysis.

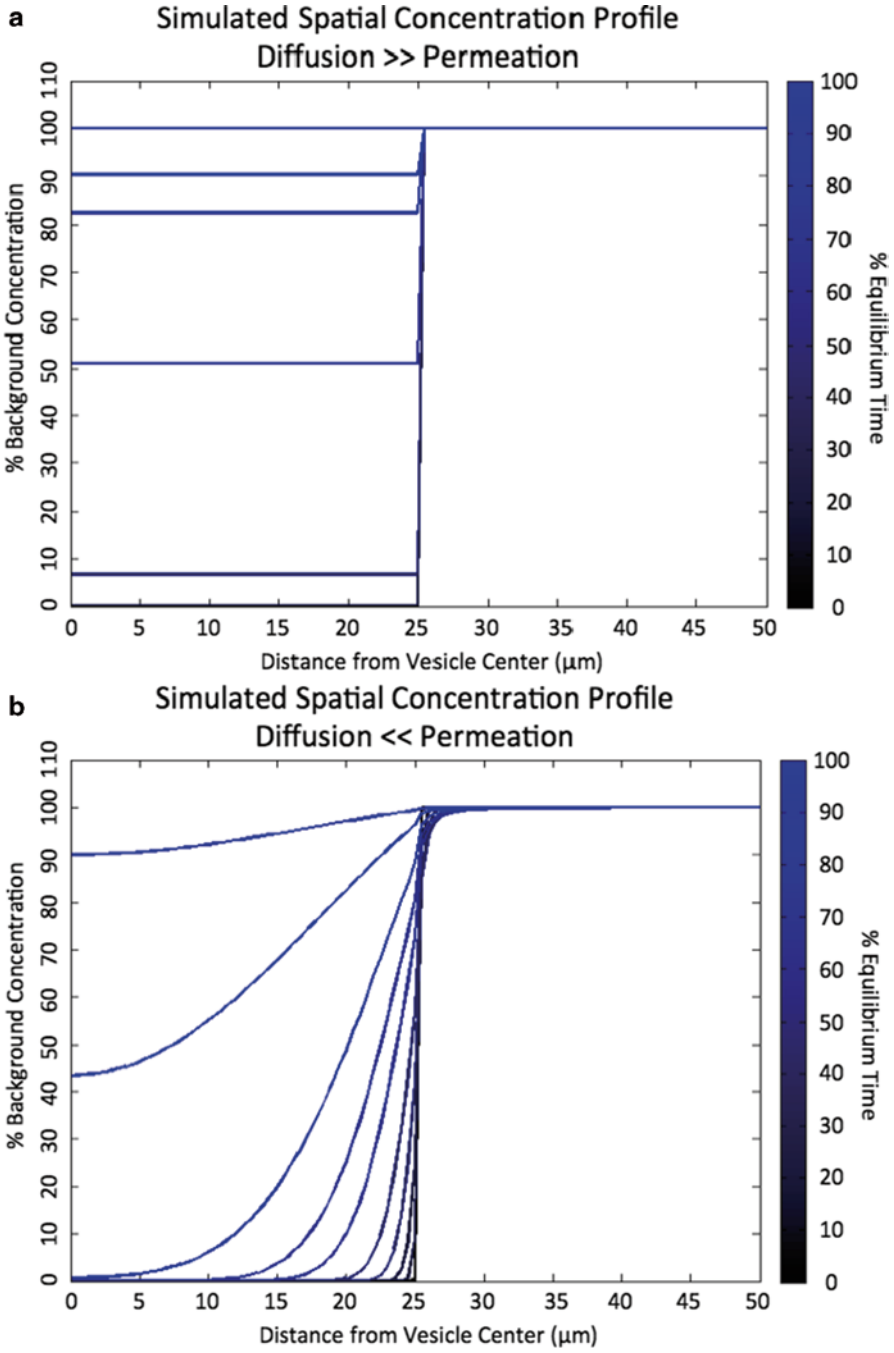

Fig. 16.8 A diffusion/permeation-based finite difference simulation of a spatial concentration profile for **a** a case where diffusivity is much larger than permeability and **b** a case where diffusivity is much smaller than permeability. Each *line* represents a single time step towards equilibrium. The zero point of the *x*-axis is the center of a vesicle, with the membrane positioned at 25 µm. The *right-hand side* of the *x*-axis represents bulk fluid

Some transient experiments are limited by reservoir size. The simplest example of this concerns permeation-limited transport into a vesicle. If we are assuming constant outside concentration c_o with time-varying but space-invariant concentration c_i inside, we can show that:

$$c_i = c_o\left(1 - e^{\frac{-6P}{d}t}\right), \tag{16.8}$$

where d is the vesicle diameter. The transport rate constant, therefore, increases with decreasing vesicle diameter. For faster permeating species, it may be necessary to measure permeation into larger reservoirs to allow for slower time to equilibrium. One application of this concept was demonstrated by Nisisako et al. [109]. As described above, this technique involves measuring the permeability of droplet interface bilayers formed in a microfluidic device. By varying the buffer flow rates, it is possible to change the droplet size. A smaller acceptor droplet allows the concentration to change more rapidly and decrease the transport time. Conversely, for a fast transport process, the size of the acceptor droplet can be increased to lengthen the measurement time.

The final issue with some transient experiments is instrument dead time, mixing time, or buffer exchange time. This generic "dead time" can be defined as a period during which data either cannot be accurately collected, or cannot be collected at all.

Stopped-flow techniques suffer from a dead time, while the liquid is being pumped into the mixing chamber, during which data are not collected. The dead time is usually estimated to be on the order of 1–10 ms, although this varies based on the device [123, 143]. As such, the permeation process must have a halftime at least double the dead time to accurately measure the permeability. Similarly, microfluidic devices, which have been gaining momentum over the past decade, are restricted by the dead time due to buffer exchange. The possibilities for buffer exchange times are restricted by the geometry of the device and the buffer flow rates.

16.5.4 Techniques Capable of High-Throughput Analysis

All of the techniques described above can be performed using synthetic bilayers with well-controlled structure and composition. Techniques for fabricating membranes with largely arbitrary composition are well developed in both planar bilayer and vesicular geometries. For transport experiments, planar bilayers have been demonstrated with single-component [39] and multicomponent lipid systems [69]. Planar bilayers can also be fabricated as compositionally asymmetric membranes to better match the configuration of the eukaryotic plasma membrane [99]. Vesicle fabrication techniques are similarly flexible. While asymmetry is more of a challenge in vesicles, recent work in generating asymmetric GUVs is promising [144, 145]. GUVs are also promising membrane formats for incorporating cytoskeletal structure and membrane proteins [146, 147].

This advantage—being able to construct a biomimetic membrane with true bilayer structure and controlled composition—is the major disadvantage presented by the one true high-throughput approach for permeation studies: the PAMPA assay.

Of all the experimental methods discussed in this review, only PAMPA has the high-throughput capabilities necessary for mass screening of drug candidates. For another experimental method to replace this assay for drug development, it is necessary that it be capable of such high-throughput analysis.

Some microfluidic platforms have the potential of becoming high-throughput techniques in the future by facilitating experiments on arrays of vesicles. Ohlsson et al. measured transport into a 100 liposomes simultaneously using a microfluidic chip [138], and Robinson et al. designed a device to capture and isolate 60 GUVs in an array configuration [140]. Patterns of binding surfaces on a coverslip can immobilize multiple vesicles for simultaneous measurement [135–137]. Although it has been suggested that droplet interface bilayers can be formed and analyzed in parallel microfluidic devices, this has yet to be accomplished [109].

16.5.5 The Future of Permeation Studies

The ideal transport measurement technique would be capable of forming consistent bilayers of both symmetric and asymmetric compositions and analyzing high-throughput data without suffering from USL artifacts.

Mimicking the lipid composition of biological plasma membranes requires recapitulating the compositional asymmetry of these membranes. Eukaryotic plasma membranes are concentrated in cholesterol and sphingolipids in the outer leaflet and in negatively charged lipids in the inner leaflet. Microelectrode systems have been used to measure transport across asymmetric planar bilayers [99]. The asymmetric bilayer measurement was then compared to two symmetric bilayers: one for the inner and another for the outer leaflet of the asymmetric system. Results indicate that the asymmetric system is two times more permeable than the outer leaflet alone and ten times less permeable than the inner leaflet alone. Much like Eq. 16.6, where measured permeability is calculated as the sum of resistances from the two USL and the membrane, this work demonstrated that an asymmetric bilayer permeability can be estimated as the sum of resistances from the two leaflets. Recent innovations in lipid bilayer fabrication have facilitated asymmetric bilayers in droplet interface [107] and GUV [144, 145, 148] formats. These innovations create opportunities for transport studies on asymmetric bilayers using a wide range of the technologies described above.

Given the increased use of light microscopy in transport studies, innovations in imaging technology will also have an impact on the field. Confocal microscopy has already been used to observe concentration gradients at scales capable of resolving the USL [100, 132, 135]. Improved resolution in all dimensions facilitated by techniques such as multiphoton [149], structured illumination [150], or super resolution [151] microscopy will make this possible in a wide range of experimental

formats. Emerging techniques in optical microspectroscopy have the potential to make imaging-based transport experiments possible for species without fluorescent labels. In addition to UV microspectroscopy [109], confocal Raman microscopy is a potentially powerful technique that eliminates any reliance on fluorescent labels [133, 152]. New camera technology is also improving microscopy techniques. The frame rate of some scientific complementary metal–oxide–semiconductor (CMOS) cameras is fast enough to measure with 100 frames per second, facilitating the observation of fast transport events.

Other label-free detection technologies can also play a role in measuring molecular transport across lipid bilayers. SPR of lipid vesicles has already been demonstrated in such an application [130, 131]. Other emerging label-free molecular detection technologies, such as optical microresonators [153] and surface-sensitive nanotube-based field-effect transistors [154, 155], have the potential to play a role in transport measurements that do not rely on fluorescent labels and are therefore directly applicable to drug candidates.

Given the current drug discovery pipeline, high-throughput capabilities are desirable in any transport measurement technology. As currently implemented, microelectrode studies are ill-suited for high-throughput assays. Recent efforts in electrode microfabrication applied to arrays of bilayers are promising, however, and could be modified for studies of transport of general charged species across bilayers [156–158]. Microfluidic approaches for forming bilayers and immobilizing arrays of lipid vesicles are promising platforms for adapting microscopy-based techniques to high-throughput formats [136, 137, 140]. Similarly, other microfluidic platforms allow for simultaneous measurement of multiple liposomes [138, 139]. These approaches increase the productivity of a single experiment, while simultaneously maintaining a high level of control over the bilayer structure and composition.

References

1. P. Artursson, J. Karlsson, Correlation between oral drug absorption in humans and apparent drug permeability coefficients in human intestinal epithelial (Caco-2) cells. Biochem. Biophys. Res. Commun. **175**(3), 880–885 (1991)
2. D.F. Veber, S.R. Johnson, H.-Y. Cheng et al., Molecular properties that influence the oral bioavailability of drug candidates. J. Med. Chem. **45**(12), 2615–2623 (2002)
3. V. Pade, S. Stavchansky, Link between drug absorption solubility and permeability measurements in Caco - 2 cells. J. Pharm. Sci. **87**(12), 1604–1607 (1998)
4. C.A. Lipinski, F. Lombardo, B.W. Dominy et al., Experimental and computational approaches to estimate solubility and permeability in drug discovery and development settings. Adv. Drug Delivery Rev. **23**(1), 3–25 (1997)
5. R.A. Conradi, A.R. Hilgers, N.F. Ho et al., The influence of peptide structure on transport across Caco-2 cells. II. Peptide bond modification which results in improved permeability. Pharm. Res. **9**(3), 435–439 (1992)
6. P.S. Burton, R.A. Conradi, N.F. Ho et al., How structural features influence the biomembrane permeability of peptides. J. Pharm. Sci. **85**(12), 1336–1340 (1996)
7. M.A. Navia, P.R. Chaturvedi, Design principles for orally bioavailable drugs. Drug Discov. Today **1**(5), 179–189 (1996)

8. K. Palm, P. Stenberg, K. Luthman et al., Polar molecular surface properties predict the intestinal absorption of drugs in humans. Pharm. Res. **14**(5), 568–571 (1997)
9. J. Kelder, P.D. Grootenhuis, D.M. Bayada et al., Polar molecular surface as a dominating determinant for oral absorption and brain penetration of drugs. Pharm. Res. **16**(10), 1514–1519 (1999)
10. Y.C. Martin, A bioavailability score. J. Med. Chem. **48**(9), 3164–3170 (2005)
11. M.J. Waring, Defining optimum lipophilicity and molecular weight ranges for drug candidates—Molecular weight dependent lower log D limits based on permeability. Bioorg. Med. Chem. Lett. **19**(10), 2844–2851 (2009)
12. E. Perola, An analysis of the binding efficiencies of drugs and their leads in successful drug discovery programs. J. Med. Chem. **53**(7), 2986–2997 (2010)
13. R. O'Shea, H.E. Moser, Physicochemical properties of antibacterial compounds: Implications for drug discovery. J. Med. Chem. **51**(10), 2871–2878 (2008)
14. M.-Q. Zhang, B. Wilkinson, Drug discovery beyond the 'rule-of-five'. Curr. Opin. Biotechnol. **18**(6), 478–488 (2007)
15. G.W. Burton, M.G. Traber, Vitamin E, antioxidant activity, biokinetics, and bioavailability. Annu. Rev. Nutr. **10**(1), 357–382 (1990)
16. R.L. Lipnick, Base-line toxicity predicted by quantitative structure-activity relationships as a probe for molecular mechanism of toxicity. Probi. Bioact. Mech. **413,** 366–389 (1989)
17. E. Foulkes, Transport of toxic heavy metals across cell membranes. Proc. Soc. Exp. Biol. Med. **223**(3), 234–240 (2000)
18. J. Sikkema, J. De Bont, B. Poolman, Mechanisms of membrane toxicity of hydrocarbons. Microbiol. Rev. **59**(2), 201–222 (1995)
19. S. Li, N. Malmstadt, Deformation and poration of lipid bilayer membranes by cationic nanoparticles. Soft Matter **9**(20), 4969–4976 (2013)
20. N.R. Yacobi, N. Malmstadt, F. Fazolallahi et al., Mechanisms of alveolar epithelial translocation of a defined population of nanoparticles. Am. J. Respir. Cell Mol. Biol. **42**(5), 604–614 (2010)
21. D. Bedrov, G.D. Smith, H. Davande et al., Passive transport of C-60 fullerenes through a lipid membrane: A molecular dynamics simulation study. J. Phys. Chem. B. **112**(7), 2078–2084 (2008)
22. T. Wang, J. Bai, X. Jiang et al., Cellular uptake of nanoparticles by membrane penetration: A study combining confocal microscopy with FTIR spectroelectrochemistry. ACS Nano **6**(2), 1251–1259 (2012)
23. A. Verma, O. Uzun, Y.H. Hu et al., Surface-structure-regulated cell-membrane penetration by monolayer-protected nanoparticles. Nat. Mater. **7**(7), 588–595 (2008)
24. M. Jackson, Drug transport across gastrointestinal epithelia. Physiol. Gastrointest. Tract. **2,** 1597 (1987)
25. S. Yee, In vitro permeability across Caco-2 cells (colonic) can predict in vivo (small intestinal) absorption in man—Fact or myth. Pharm. Res. **14**(6), 763–766 (1997)
26. I.J. Hidalgo, T.J. Raub, R.T. Borchardt, Characterization of the human colon carcinoma cell line (Caco-2) as a model system for intestinal epithelial permeability. Gastroenterology **96**(3), 736–749 (1989)
27. E.H. Kerns, L. Di, S. Petusky et al., Combined application of parallel artificial membrane permeability assay and Caco-2 permeability assays in drug discovery. J. Pharm. Sci. **93**(6), 1440–1453 (2004)
28. G. Wilson, I. Hassan, C. Dix et al., Transport and permeability properties of human Caco-2 cells: An in vitro model of the intestinal epithelial cell barrier. J. Control. Release **11**(1), 25–40 (1990)
29. J. Karlsson, P. Artursson, A method for the determination of cellular permeability coefficients and aqueous boundary layer thickness in monolayers of intestinal epithelial (Caco-2) cells grown in permeable filter chambers. Int. J. Pharm. **71,** 55–64 (1991)
30. J. Karlsson, P. Artursson, A new diffusion chamber system for the determination of drug permeability coefficients across the human intestinal epithelium that are independent of the unstirred water layer. Biochim. Biophys. Acta. **1111,** 204–210 (1992)

31. I. Behrens, W. Kamm, A.H. Dantzig et al., Variation of peptide transporter (PepT1 and HPT1) expression in Caco-2 cells as a function of cell origin. J. Pharm. Sci. **93**(7), 1743–1754 (2004)
32. D.A. Volpe, Variability in Caco-2 and MDCK cell-based intestinal permeability assays. J. Pharm. Sci. **97**(2), 712–725 (2008)
33. A. Kleinzeller, Ernest Overton's contribution to the cell membrane concept: A centennial appreciation. Physiology **12**(4), 49–52 (1997)
34. A. Missner, P. Pohl, 110 years of the Meyer-Overton rule: Predicting membrane permeability of gases and other small compounds. Chemphyschem **10**(9–10), 1405–1414 (2009)
35. C.E. Overton, in *Studies of Narcosis*, ed. and trans. by R. L. Lipnick (Chapman and Hall Ltd. and The Wood Library-Museum of Anesthesiology, New York, 1991). (Original Published in 1901)
36. A. Finkelstein, Water and nonelectrolyte permeability of lipid bilayer membranes. J. Gen. Physiol. **68**(2), 127–135 (1976)
37. J.D. Seader, E.J. Henley, D.K. Roper, *Separation Process Principles*, 3rd edn. (Wiley, New Jersey, 2010)
38. J.M. Wolosin, H. Ginsburg, Permeation of organic-acids through lecithin bilayers resemblance to diffusion in polymers. Biochim. Biophys. Acta. **389**(1), 20–33 (1975)
39. A. Walter, J. Gutknecht, Permeability of small nonelectrolyes through lipid bilayer membranes. J. Membr. Biol. **90**, 207–217 (1986)
40. C.A. Lipinsky, F. Lobardo, B.W. Dominy et al., Experimental and computational approaches to estimate solubility and permeability in drug discovery and development settings. Adv. Drug Deliv. Rev. **46,** 3–26 (2001)
41. F. Wohnsland, B. Faller, High-throughput permeability pH profile and high-throughput alkane/water log P with artificial membranes. J. Med. Chem. **44,** 923–930 (2001)
42. D. Bassolino-Klimas, H.E. Alper, T.R. Stouch, Solute diffusion in lipid bilayer membranes: An atomic level study by molecular dynamics simulation. Biochemistry **32,** 12624–12637 (1993)
43. S.J. Marrink, H.J.C. Berendsen, Simulation of water transport through a lipid membrane. J. Phys. Chem. **98,** 4155–4186 (1994)
44. D. Bemporad, C. Luttmann, J. Essex, Behaviour of small solutes and large drugs in a lipid bilayer from computer simulations. Biochim. Biophys. Acta. **1718**(1), 1–21 (2005)
45. S.J. Marrink, H.J.C. Berendsen, Permeation process of small molecules across lipid membranes studied by molecular dyanmics simulations. J. Phy. Chem. **100,** 16729–16738 (1996)
46. D. Bemporad, C. Luttmann, J.W. Essex, Computer simulation of small molecule permeation across a lipid bilayer: Dependence on bilayer properties and solute volume, size, and cross-sectional area. Biophys. J. **87**(1), 1–13 (2004)
47. D. Bemporad, J.W. Essex, C. Luttmann, Permeation of small molecules through a lipid bilayer: A computer simulation study. J. Phy. Chem. B. **108,** 4975–4884 (2004)
48. M. Orsi, W.E. Sanderson, J.W. Essex, Permeability of small molecules through a lipid bilayer: A multiscale simulation study. J. Phy. Chem. B. **113,** 12019–12029 (2009)
49. M. Orsi, J.W. Essex, Permeability of drugs and hormones through a lipid bilayer: Insights from dual-resolution molecular dynamics. Soft Matter **6**(16), 3797 (2010)
50. R. Vacha, M.L. Berkowitz, P. Jungwirth, Molecular model of a cell plasma membrane with an asymmetric multicomponent composition: Water permeation and ion effects. Biophys. J. **96**(11), 4493–4501 (2009)
51. K. Shinoda, W. Shinoda, M. Mikami, Efficient free energy calculation of water across lipid membranes. J. Comput. Chem. **29**(12), 1912–1918 (2008)
52. H. Träuble, The movement of molecules across lipid membranes: A molecular theory. J. Membr. Biol. **4**(1), 193–208 (1971)
53. R. Kimmich, A. Peters, K. Spohn, Solubility of oxygen in lecithin bilayers and other hydrocarbon lamellae as a probe for free volume and transport properties. J. Membr. Sci. **9**(3), 313–336 (1981)
54. F. Zocher, D. van der Spoel, P. Pohl et al., Local partition coefficients govern solute permeability of cholesterol-containing membranes. Biophys. J. **105**(12), 2760–2770 (2013)

55. J.F. Nagle, J.C. Mathai, M.L. Zeidel et al., Theory of passive permeability through lipid bilayers. J. Gen. Physiol. **131**(1), 77–85 (2008)
56. S. Mitragotri, M.E. Johnson, D. Blankschtein et al., An analysis of size selectivity of solute partitioning, diffusion, and permeation across lipid bilayers. Biophys. J. **77,** 1268–1283 (1999)
57. J.M. Nitsche, G.B. Kasting, Permeability of fluid-phase phospholipid bilayers: Assessment and useful correlations for permeability screening and other applications. J. Pharm. Sci. **102**(6), 2005–2032 (2013)
58. P. Mueller, D.O. Rudin, H. Ti Tien et al., Reconstitution of cell membrane structure in vitro and its transformation into an excitable system. Nature **194,** 979–980 (1962)
59. A. Bangham, M. Standish, J. Watkins, Diffusion of univalent ions across the lamellae of swollen phospholipids. J. Mol. Biol. **13**(1), 238–252 (1965)
60. P.H. Barry, J.M. Diamond, Effects of unstirred layers on membrane phenomena. Am. Physiol. Soc. **64**(3), 763–872 (1984)
61. F. Burczynski, Z. Cai, J. Moran et al., Palmitate uptake by cultured hepatocytes: Albumin binding and stagnant layer phenomena. Am. J. Physiol. **257**(4), G584–G593 (1989)
62. J. Dainty, C. House, Unstirred layers in frog skin. J. Physiol. **182**(1), 66 (1966)
63. C.U. Cotton, L. Reuss, Measurement of the effective thickness of the mucosal unstirred layer in Necturus gallbladder epithelium. J. Gen. Physiol. **93**(4), 631–647 (1989)
64. T.-X. Xiang, B.D. Anderson, Diffusion of ionizable solutes across planar lipid bilayer membranes: Boundary-layer pH gradients and the effect of buffers. Pharm. Res. **10**(11), 1654–1661 (1993)
65. M. Levitt, T. Aufderheide, C. Fetzer et al., Use of carbon monoxide to measure luminal stirring in the rat gut. J. Clin. Invest. **74**(6), 2056 (1984)
66. L.J. Jensen, J.N. Sørensen, E.H. Larsen et al., Proton pump activity of mitochondria-rich cells: The interpretation of external proton-concentration gradients. J. Gen. Physiol. **109**(1), 73–91 (1997)
67. A. Strocchi, G. Corazza, J. Furne et al., Measurements of the jejunal unstirred layer in normal subjects and patients with celiac disease. Am. J. Physiol. **270**(3), G487–G491 (1996)
68. P. Pohl, E. Rosenfelt, R. Millner, Effects of ultrasound on the steady state transmembrane pH gradient and permeability of acetic acid through bilayer lipid membranes. Biochim. Biophysica. Acta. **1145,** 279–283 (1993)
69. Y.N. Antonenko, G.A. Denisov, P. Pohl, Weak acid transport across bilayer lipid membrane in the presence of buffers. Biophys. J. **64,** 1701–1710 (1993)
70. Y.N. Antonenko, P. Pohl, G.A. Denisov, Permeation of ammonia across bilayer lipid membranes studied by ammonium ion selective microelectrodes. Biophys. J. **72,** 2187–2195 (1997)
71. T. Pedley, The interaction between stirring and osmosis. Part 1. J. Fluid Mech. **101**(04), 843–861 (1980)
72. V.G. Levich, D.B. Spalding, *Physicochemical Hydrodynamics* (Prentice-Hall, Englewood Cliffs, 1962)
73. P. Pohl, S.M. Saparov, Y.N. Antonenko, The size of the unstirred layer as a function of the solute diffusion coefficient. Biophy. J. **75,** 1403–1409 (1998)
74. C.A. Berry, A. Verkman, Osmotic gradient dependence of osmotic water permeability in rabbit proximal convoluted tubule. J. Membrane Biol. **105**(1), 33–43 (1988)
75. B. Flourie, N. Vidon, C. Florent et al., Effect of pectin on jejunal glucose absorption and unstirred layer thickness in normal man. Gut **25**(9), 936–941 (1984)
76. E. Guyon, *Physical Hydrodynamics* (Oxford University Press, New York, 2001)
77. M. Poznansky, S. Tong, P.C. White et al., Nonelectrolyte diffusion across lipid bilayer systems. J. Gen. Physiol. **67**(1), 45–66 (1976)
78. L. Escuder-Gilabert, J.J. Martínez-Pla, S. Sagrado et al., Biopartitioning micellar separation methods: Modelling drug absorption. J. Chromatogr. B. Analyt. Technol. Biomed. Life Sci. **797**(1–2), 21–35 (2003)

79. C. Zhu, L. Jiang, T.-M. Chen et al., A comparative study of artificial membrane permeability assay for high throughput profiling of drug absorption potential. Eur. J. Med. Chem. **37**(5), 399–407 (2002)
80. M. Kansy, F. Senner, K. Gubernator, Physicochemical high throughput screening: Parallel artificial membrane permeation assay in the description of passive absorption processes. J. Med. Chem. **41**(7), 1007–1010 (1998)
81. R. Ano, Y. Kimura, M. Shima et al., Relationships between structure and high-throughput screening permeability of peptide derivatives and related compounds with artificial membranes: Application to prediction of Caco-2 cell permeability. Bioorg. Med. Chem. **12,** 257–264 (2004)
82. K. Sugano, H. Hamada, M. Machida et al., Optimized conditions of bio-mimetic artificial membrane permeation assay. Int. J. Pharm. **228,** 181–188 (2001)
83. T. Rezai, J.E. Bock, M.V. Zhou et al., Conformational flexibility, internal hydrogen bonding, and passive membrane permeability: Successful in silico prediction of the relative permeabilities of cyclic peptides. J. Am. Chem. Soc. **128,** 14073–14080 (2006)
84. P.R. Seo, Z.S. Teksin, J.P. Kao et al., Lipid composition effect on permeability across PAMPA. Eur. J. Pharm. Sci. **29**(3–4), 259–268 (2006)
85. S.S. Leung, J. Mijalkovic, K. Borrelli et al., Testing physical models of passive membrane permeation. J. Chem. Inf. Model. **52**(6), 1621–1636 (2012)
86. M. Thompson, R.B. Lennox, R. McClelland, Structure and electrochemical properties of microfiltration filter-lipid membrane systems. Anal. Chem. **54**(1), 76–81 (1982)
87. P.V. Balimane, E. Pace, S. Chong et al., A novel high-throughput automated chip-based nanoelectrospray tandem mass spectrometric method for PAMPA sample analysis. J. Pharm. Biomed. Anal. **39**(1), 8–16 (2005)
88. J. Gutknecht, A. Walter, Transport of protons and hydrochloric acid through lipid bilayer membranes. Biochim. Biophys. Acta. **641,** 183–188 (1981)
89. Y.N. Antonenko, A.A. Bulychev, Measurements of local pH changes near bilayer lipid membrane by means of a pH microelectrode and a protonophore-dependent membrane potential. Comparison of the methods. Biochim. Biophys. Acta. **1070**(1), 279–282 (1991)
90. S.M. Dzekunov, Y.N. Antonenko, Dynamics of formation and dissipation of local pH gradients in the unstirred layers near bilayer lipid membranes. Bioelectrochem. Bioenerg. **41,** 187–190 (1996)
91. S. Ohki, Membrane Potential and ion permeability of lipid bilayer membranes. Bioelectrochem. Bioenerg. **7,** 487–501 (1980)
92. R. Sandeaux, J. Sandeaux, C. Gavach et al., Transport of Na^+ by monensin across biomolecular lipid membranes. Biochim. Biophys. Acta. **684,** 127–132 (1982)
93. J. Gutknecht, A. Walter, Hydroxyl ion permeability of lipid bilayer membranes. Biochim. Biophys. Acta. **645,** 161–162 (1981)
94. J. Gutknecht, A. Walter, Hydrofluoric and nitric acid transport through lipid bilayer membranes. Biochim. Biophys. Acta. **644**(1), 153–156 (1981)
95. A. Walter, J. Gutknecht, Monocarboxylic acid permeation through lipid bilayer membranes. J. Membrane Biol. **77**(3), 255–264 (1984)
96. Y.N. Antonenko, L. Yaguzhinsky, Generation of potential in lipid bilayer membranes as a result of proton-transfer reactions in the unstirred layers. J. Bioenerg. Biomembr. **14**(5–6), 457–465 (1982)
97. Y.N. Antonenko, L.S. Yaguzhinsky, The role of pH gradient in the unstirred layers in the transport of weak acids and bases through bilayer lipid membranes. Bioelectrochem. Bioenerg. **13**(1), 85–91 (1984)
98. Y.N. Antonenko, P. Pohl, Steady-state nonmonotonic concentration profiles in the unstirred layers of bilayer lipid membranes. Biochim. Biophys. Acta. **1235**(1), 57–61 (1995)
99. A.V. Krylov, P. Pohl, M.L. Zeidel et al., Water permeability of asymmetric planar lipid bilayers: Leaflets of different composition offer independent and additive resistances to permeation. J. Gen. Physiol. **118,** 333–339 (2001)

100. J.M. Grime, M.A. Edwards, N.C. Rudd et al., Quantitative visualization of passive transport across bilayer lipid membranes. Proc. Natl. Acad. Sci. U S A **105**(38), 14277–14282 (2008)
101. A. Missner, P. Kügler, Y.N. Antonenko et al., Passive transport across bilayer lipid membranes: Overton continues to rule. Proc. Natl. Acad. Sci. U S A **105**(52), E123–E123 (2008)
102. J.M. Grime, M.A. Edwards, P.R. Unwin, Reply to Missner et al.: Timescale for passive diffusion across bilayer lipid membranes. Proc. Natl. Acad. Sci. U S A **105**(52), E124–E124 (2008)
103. J.T. Groves, N. Ulman, S.G. Boxer, Micropatterning fluid lipid bilayers on solid supports. Science **275**(5300), 651–653 (1997)
104. J.S. Hovis, S.G. Boxer, Patterning and composition arrays of supported lipid bilayers by microcontact printing. Langmuir **17**(11), 3400–3405 (2001)
105. J.T. Groves, S.G. Boxer, Micropattern formation in supported lipid membranes. Acc. Chem. Res. **35**(3), 149–157 (2002)
106. A.M. Brozell, S. Inaba, A.N. Parikh, Lipid bilayers on topochemically structured planar colloidal crystals: A versatile platform for optical recording of membrane-mediated ion transport. Soft Matter **6**(21), 5334–5341 (2010)
107. H. Bayley, B. Cronin, A. Heron et al., Droplet interface bilayers. Mol. BioSyst. **4**(12), 1191–1208 (2008)
108. N. Malmstadt, M.A. Nash, R.F. Purnell et al., Automated formation of lipid-bilayer membranes in a microfluidic device. Nano Lett. **6**(9), 1961–1965 (2006)
109. T. Nisisako, S. Portonovo, J. Schmidt, Microfluidic passive permeability assay using nanoliter droplet interface lipid bilayers. Analyst **138**(22), 6793–6800 (2013)
110. F. Szoka Jr., D. Papahadjopoulos, Comparative properties and methods of preparation of lipid vesicles (liposomes). Annu. Rev. Biophys. Bioeng. **9**(1), 467–508 (1980)
111. T.-X. Xiang, B.D. Anderson, Influence of chain ordering on the selectivity of dipalmitoylphosphatisylcholine bilayer membranes for permeant size and shape. Biophys. J. **75,** 13 (1998)
112. J. Alger, J. Prestegard, Nuclear magnetic resonance study of acetic acid permeation of large unilamellar vesicle membranes. Biophys. J. **28**(1), 1–13 (1979)
113. T.-X. Xiang, J. Chen, B.D., Anderson, A quantitative model for the dependence of solute permeability on peptide and cholesterol content in biomembranes. J. Membr. Biol. **177**(2), 137–148 (2000)
114. T.-X. Xiang, Y.H. Xu, B.D. Anderson, The barrier domain for solute permeation varies with lipid bilayer phase structure. J. Membr. Biol. **165,** 77–90 (1998)
115. M. Wunder, P. Bollert, G. Gros, Mathematical modelling of the role of intra-and extracellular activity of carbonic anhydrase and membrane permeabilities of $HCO3^-$, H_2O and CO_2 in 18O exchange. Isotopes Environ. Health Stud. **33**(1), 197–206 (1997)
116. M. Wunder, G. Gros, 18O exchange in suspensions of red blood cells: Determination of parameters of mass spectrometer inlet system. Isotopes Environ. Health Stud. **34**(3), 303–310 (1998)
117. V. Endeward, G. Gros, Extra-and intracellular unstirred layer effects in measurements of CO_2 diffusion across membranes–a novel approach applied to the mass spectrometric 18O technique for red blood cells. J. Physiol. **587**(6), 1153–1167 (2009)
118. V. Endeward, G. Gros, Low carbon dioxide permeability of the apical epithelial membrane of guinea-pig colon. J. Physiol. **567**(1), 253–265 (2005)
119. F. Itel, S. Al-Samir, F. Oberg et al., CO_2 permeability of cell membranes is regulated by membrane cholesterol and protein gas channels. Faseb J. **26**(12), 5182–5191 (2012)
120. J.W. Nichols, D.W. Deamer, Net proton-hydroxyl permeability of large unilamellar liposomes measured by an acid-base titration technique. Proc. Natl. Acad. Sci. U S A **77**(4), 2038–2042 (1980)
121. D.W. Deamer, J.W. Nichols, Proton-hydroxide permeability of liposomes. Proc. Natl. Acad. Sci. U S A **80**(1), 165–168 (1983)
122. D.W. Deamer, J.W. Nichols, Proton flux mechanisms in model and biological membranes. J. Membrane Biol. **107**(2), 91–103 (1989)

123. R. Sha'Afi, G. Rich, V.W. Sidel et al., The effect of the unstirred layer on human red cell water permeability. J. Gen. Physiol. **50**(5), 1377–1399 (1967)
124. R. Lawaczeck, Water permeability through biological membranes by isotopic effects of fluorescence and light scattering. Biophys. J. **45**(3), 491–494 (1984)
125. H.J. Mlekoday, R. Moore, D.G. Levitt, Osmotic water permeability of the human red cell. Dependence on direction of water flow and cell volume. J. Gen. Physiol. **81**(2), 213–220 (1983)
126. R. Ye, A.S. Verkman, Simultaneous optical measurement of osmotic and diffusional water permeability in cells and liposomes. BioChemistry **28**(2), 824–829 (1989)
127. C. Dordas, P.H. Brown, Permeability of boric acid across lipid bilayers and factors affecting it. J. Membr. Biol. **175,** 95–105 (2000)
128. J.C. Mathai, G.D. Sprott, M.L. Zeidel, Molecular mechanisms of water and solute transport across archaebacterial lipid membranes. J. Biol. Chem. **276**(29), 27266–27271 (2001)
129. R. Holland, H. Shibata, P. Scheid et al., Kinetics of O_2 uptake and release by red cells in stopped-flow apparatus: Effects of unstirred layer. Respir. physiol. **59**(1), 71–91 (1985)
130. M. Brändén, S. Dahlin, F. Höök, Label-free measurements of molecular transport across liposome membranes using evanescent-wave sensing. Chemphyschem **9**(17), 2480–2485 (2008)
131. M. Brändén, S.R. Tabaei, G. Fischer et al., Refractive-index-based screening of membrane-protein-mediated transfer across biological membranes. Biophys. J. **99**(1), 124–133 (2010)
132. S. Li, P. Hu, N. Malmstadt, Confocal imaging to quantify passive transport across biomimetic lipid membranes. Anal. Chem. **82**(18), 7766–7771 (2010)
133. E.C. Heider, G.A. Myers, J.M. Harris, Spectroscopic microscopy analysis of the interior pH of individual phospholipid vesicles. Anal. Chem. **83**(21), 8230–8238 (2011)
134. K.L. Budzinski, M. Zeigler, B.S. Fujimoto et al., Measurements of the acidification kinetics of single SynaptopHluorin vesicles. Biophys. J. **101**(7), 1580–1589 (2011)
135. S. Li, P.C. Hu, N. Malmstadt, Imaging molecular transport across lipid bilayers. Biophys. J. **101**(3), 700–708 (2011)
136. P. Kuhn, K. Eyer, S. Allner et al., A microfluidic vesicle screening platform: Monitoring the lipid membrane permeability of tetracyclines. Anal. Chem. **83**(23), 8877–8885 (2011)
137. K. Eyer, F. Paech, F. Schuler et al., A liposomal fluorescence assay to study permeation kinetics of drug-like weak bases across the lipid bilayer. J. Control. Release **173,** 102–109 (2013)
138. G. Ohlsson, S.R. Tabaei, J. Beech et al., Solute transport on the sub 100 ms scale across the lipid bilayer membrane of individual proteoliposomes. Lab Chip **12**(22), 4635–4643 (2012)
139. C.L. Kuyper, J.S. Kuo, S.A. Mutch et al., Proton permeation into single vesicles occurs via a sequential two-step mechanism and is heterogeneous. J. Am. Chem. Soc. **128**(10), 3233–3240 (2006)
140. T. Robinson, P. Kuhn, K. Eyer et al., Microfluidic trapping of giant unilamellar vesicles to study transport through a membrane pore. Biomicrofluidics **7**(4), 044105 (2013)
141. M. Hope, M. Bally, G. Webb et al., Production of large unilamellar vesicles by a rapid extrusion procedure. Characterization of size distribution, trapped volume and ability to maintain a membrane potential. Biochim. Biophys. Acta. **812**(1), 55–65 (1985)
142. D.J. Needleman, Y. Xu, T.J. Mitchison, Pin-hole array correlation imaging: Highly parallel fluorescence correlation spectroscopy. Biophys. J. **96**(12), 5050–5059 (2009)
143. P. Brissette, D.P. Ballou, V. Massey, Determination of the dead time of a stopped-flow fluorometer. Anal. Biochem. **181**(2), 234–238 (1989)
144. P.C. Hu, S. Li, N. Malmstadt, Microfluidic fabrication of asymmetric giant lipid vesicles. ACS Appl. Mater. Interfaces **3**(5), 1434–1440 (2011)
145. D.L. Richmond, E.M. Schmid, S. Martens et al., Forming giant vesicles with controlled membrane composition, asymmetry, and contents. Proc. Natl. Acad. Sci. U S A **108**(23), 9431–9436 (2011)
146. L.-L. Pontani, J. van der Gucht, G. Salbreux et al., Reconstitution of an actin cortex inside a liposome. Biophys. J. **96**(1), 192–198 (2009)

147. J.S. Hansen, J.R. Thompson, C. Helix-Nielsen et al., Lipid directed intrinsic membrane protein segregation. J. Am. Chem. Soc. **135**(46), 17294–17297 (2013)
148. T. Hamada, Y. Miura, Y. Komatsu et al., Construction of asymmetric cell-sized lipid vesicles from lipid-coated water-in-oil microdroplets. J. Phys. Chem. B. **112**(47), 14678–14681 (2008)
149. S. Hell, E.H. Stelzer, Fundamental improvement of resolution with a 4Pi-confocal fluorescence microscope using two-photon excitation. Opt. Commun. **93**(5), 277–282 (1992)
150. M.G. Gustafsson, Nonlinear structured-illumination microscopy: Wide-field fluorescence imaging with theoretically unlimited resolution. Proc. Natl. Acad. Sci. U S A **102**(37), 13081–13086 (2005)
151. S.W. Hell, J. Wichmann, Breaking the diffraction resolution limit by stimulated emission: Stimulated-emission-depletion fluorescence microscopy. Opt. Lett. **19**(11), 780–782 (1994)
152. G.A. Myers, J.M. Harris, Confocal raman microscopy of pH-gradient-based 10,000-fold preconcentration of compounds within individual, optically trapped phospholipid vesicles. Anal. Chem. **83**(15), 6098–6105 (2011)
153. L.M. Freeman, S. Li, Y. Dayani et al., Excitation of Cy5 in self-assembled lipid bilayers using optical microresonators. Appl. Phys. Lett. **98**(14), 143703 (2011)
154. F. Patolsky, G. Zheng, C.M. Lieber, Nanowire-based biosensors. Anal. Chem. **78**(13), 4260–4269 (2006)
155. M. Curreli, R. Zhang, F.N. Ishikawa et al., Real-time, label-free detection of biological entities using nanowire-based FETs. IEEE Trans. Nanotechnol. **7**(6), 651–667 (2008)
156. A.M. El-Arabi, C.S. Salazar, J.J. Schmidt, Ion channel drug potency assay with an artificial bilayer chip. Lab Chip **12**(13), 2409–2413 (2012)
157. B. Lu, G. Kocharyan, J.J. Schmidt, Lipid bilayer arrays: Cyclically formed and measured. Biotech. J. **9**(3), 446–451 (2013)
158. P. Kongsuphol, K.B. Fang, D.Z. Peng, Lipid bilayer technologies in ion channel recordings and their potential in drug screening assay. Sens. Actuators B Chem. **185,** 530–542 (2013)

Chapter 17
Fluorescent Nanosensor for Drug Discovery

Sha Jin, Huantong Yao and Erika Ellis

There is a pressing need for developing new anti-HIV agents due to the emergence of drug-resistant HIV mutants, side effects of existing drugs, and the mutation of the virus. High-throughput screening (HTS) has been proven as a powerful technique for discovery of new anti-HIV drugs. The utilization of high-content screening (HCS) requires development of nanosensor that is suitable for HCS. We developed fluorescence imaging-based nanosensor for screening of inhibitors against activity of HIV-1 protease. We explored using AcGFP1 (a fluorescent mutant of the wild-type green fluorescent protein) and mCherry (a mutant of red fluorescent protein), as two fluorophores for Förster resonance energy transfer (FRET) microscopy imaging measurement of HIV-1 protease activity within living cells. Both in vitro and in vivo studies revealed that the novel molecular probes exhibit significant enhancement of FRET signals. The probe developed in this study enables HCS of new anti-HIV agents.

17.1 Introduction

The scope of the rapid progress in bionanotechnology ranges from in vivo imaging and diagnosis to therapeutics such as drug delivery and gene therapy. One of the most attractive applications of bionanotechnology is its ability to significantly improve the sensitivity of biosensors. Nanoparticle-based assay is able to detect proteins in the attomolar concentration range, a magnitude of six orders lower than concentrations detected by enzyme-linked immunosorbent assay (ELISA) [1]. This improvement allows early detection of many diseases such as cancer and cardiovascular diseases, saving millions of lives through the prevention and early treatment

S. Jin (✉) · H. Yao · E. Ellis
Department of Biomedical Engineering, College of Engineering,
University of Arkansas, Fayetteville, AR 72701, USA
e-mail: sjin@binghamton.edu

M. Zhang et al. (eds.), *Carbon Nanomaterials for Biomedical Applications,*
Springer Series in Biomaterials Science and Engineering 5,
DOI 10.1007/978-3-319-22861-7_17

of these diseases [2]. Another promising technique developed based on nanotechnology is the nanosensor system capable of conveying information from nanoscale to the macroscopic world. Nanosensors are able to distinguish among living cells and recognize intracellular events at the molecular level.

The state of the art in nanotechnologies applied to nanosensor development warrants significant study into improving drug discovery techniques from HTS to HCS. Previously, HTS allowed researchers to search for new drugs by screening a large population of molecules or compounds in a short period of time. It does not rely too much on mechanism studies, yet it provides time-effective and cost-effective alternatives for drug discovery research. HTS has long relied upon chemical analyses and measurements. Recently, with the advent of automated fluorescence microscopy techniques [3, 4], HCS has become a more powerful tool in drug discovery. HCS allows the application of automated fluorescence microscopy to high-throughput drug discovery. With automated high-resolution microscopy and robotic handling of cells in microtiter plates, HCS can be used to acquire knowledge on multiple biochemical pathways at the single-cell level at the early stage of new drug development [5–8]. More importantly, HCS enables not only the spatial but also the temporal characterization of cellular processes through robust and quantitative microscopy imaging measurements, such as the ratiometric Förster resonance energy transfer (FRET) image microscopy measurement [9–11].

In particular, FRET has been extensively applied to protein–protein interactions and development of molecular probes that can track various molecular activities inside a living cell [12–14]. The FRET technology allows making nanosensors for diverse purposes, including creating nanosensor for HCS. In this field of application, a fluorescent-based probe can be used for HTS of inhibitors of protein kinases [15, 16], identification of novel compounds for anesthesia and pain management [17], identification of small inhibitors against human immunodeficiency virus (HIV) reverse transcriptase (RT) [18], finding inhibitors to block the HIV-1 entry process during infection [19], screening inhibitors against HIV protease [20, 21] as well as characterization of inhibitors for Alzheimer's disease treatment [22–24]. Thus, fluorescent-based nanosensor is well suited for assessment of the potency of new hits and optimization of lead compounds against virus infection and cancer in living cells, as cellular response to therapeutics is readily visualized using fluorescent imaging.

This chapter describes the development of advanced fluorescence nanosensor for drug discovery in living cells and highlights strategy in an attempt to amplify nanosensor signal by genetic manipulation of the fluorescent protein structure. Efficiency of a FRET-based nanosensor for in vivo microscopy imaging measurement depends heavily on the type of fluorophores selected for the FRET pair, as well as the structure of the fusion protein that constitutes the FRET probe. Cyan fluorescent protein (CFP) and yellow fluorescent protein (YFP) have been widely used as a FRET pair for the microscopy imaging of molecular events within living cells due to the spectral qualities of CFP and YFP. However, CFP/YFP pair has a large spectral overlap of CFP/YFP emission: the emission peaks of CFP (510 nm) and YFP (527 nm). The crosstalk of the CFP/YFP pair because the close emission wavelengths and photobleaching of CFP greatly hinder the accuracy and reliabil-

ity of CFP/YFP-based FRET probes in microscopy imaging measurement within living cells. Therefore, an alternative FRET has been recently investigated in our group and the others [25–28]. It has been verified that a mutated enhanced green fluorescent protein (EGFP)-mCherry (a mutant of red fluorescent protein) shows ideal properties for FRET measurement and yields high accuracy both in vitro and in vivo [26]. On the other hand, the sandwich-like structure of FRET probe proteins and the link between the donor and acceptor proteins play a critical role in the sensitivity of the FRET signal. The sensitivity of a FRET-based nanosensor can be greatly improved by combining linker sequence optimization with fluorophore insertion to decrease the degrees of freedom for fluorophore positioning [29]. In this study, to avoid crosstalk and instability of CFP/YFP-based FRET probe, we explored a new FRET pair in which AcGFP1 (a fluorescent mutant of the wild-type green fluorescent protein) served as a donor and mCherry acted as an acceptor for FRET microscopy imaging measurement of HIV-1 protease activity inhibitors within living cells [20]. We demonstrated that AcGFP1 is more tolerant of photobleaching, which makes quantitative analysis using AcGFP1 more reliable, and the molecular probe designated as GcC is suitable for HCS of anti-HIV drugs through an automated FRET microscopy imaging measurement.

Furthermore, the efficiency of the FRET between a donor and an acceptor depends heavily upon the distance between them, and the characteristic Förster radius (R_0) relies upon the alignment of both the donor and the acceptor's fluorescence dipoles, the overlap of donor emission spectrum and acceptor excitation spectrum, the donor quantum yield, and the acceptor absorption coefficient [30]. Thus, FRET efficiency can be enhanced by the alignment of AcGFP1 and mCherry fluorescence dipoles. We developed a genetically engineered nanosensor with a tandem acceptor protein structured and designated as GcCC. Both in vitro and in vivo studies demonstrated that the novel structure of the molecular probe exhibits a significant enhancement in FRET signals. The FRET efficiency of the probe developed herein increased greatly, as measured by fluorescence lifetime imaging microscopy (FLIM) measurement.

17.2 Design of Nanosensors for Screening of Inhibitor of HIV-1 Infection

We engineered novel probes enabling the visualization of HIV-1 protease inhibition so that HCS can be applied to drug screening. It has been well documented that HIV-1 protease specifically cleaves HIV viral polyproteins. Twelve cleavage motifs have been identified. The molecular probes have been constructed by introducing a FRET signal transduction function directly into an HIV-1 protease cleavage motif in a manner that the HIV-1 protease inhibition can be detected or visualized through FRET imaging microscopy measurement within living cells. As shown in Fig. 17.1a, the probes have been engineered by flanking a peptide linker that entails an HIV-1 protease cleavage site, such as p2/p7 having amino acid sequence of ATIMMQRG with a donor fluorescent protein AcGFP1 and an acceptor fluorescent

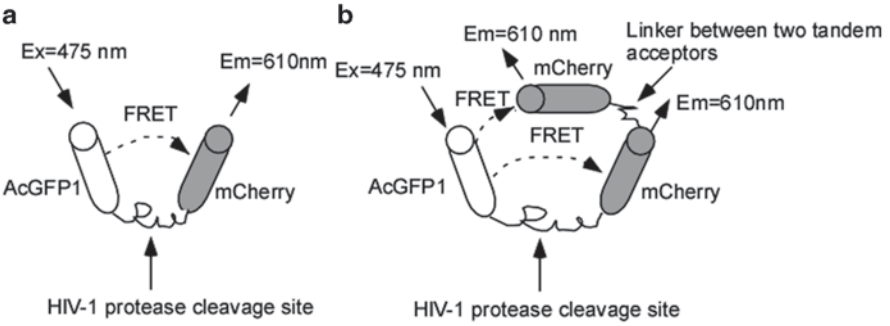

Fig. 17.1 Schematic diagram of FRET probes. **a** A donor fluorophore and an acceptor fluorophore are connected by an HIV-1 cleavable peptide stretch. **b** A donor fluorophore is linked with a tandem acceptor fluorophore through an HIV-1 protease cleavable peptide stretch

protein mCherry. To explore whether the reporting capability of a FRET nanosensor can be improved by optimizing its molecular structure, we also genetically engineered tandem acceptors as shown in Fig. 17.1b. It is predictable that the resonance energy can be transferred from the donor to the acceptor when they are linked by a peptide, generating a FRET signal. The cleavage of the peptide linker by the HIV-1 protease separates the acceptor from the donor, leading to the quenching of FRET, whereas the inhibition of the enzyme by an inhibitor prevents the separation of the acceptor from the donor, resulting in the retaining of FRET signals.

17.3 Characterization of the Nanosensors In Vitro

The probe proteins were produced using recombinant DNA cloning technique and purified as reported elsewhere [20, 21]. The ability of the probes for reporting HIV-1 protease inhibition in live cells was characterized in vitro. As revealed in Fig. 17.2,

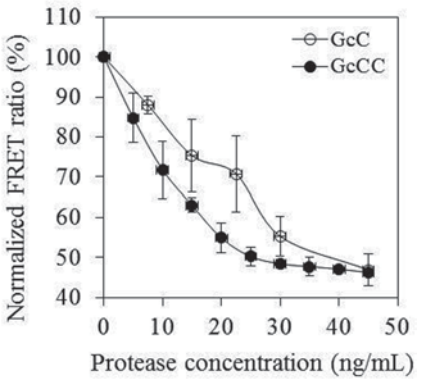

Fig. 17.2 Effect of HIV-1 protease concentration on the normalized FRET signal. A total of 50 μg/mL probe protein was incubated with 40 ng/mL of HIV-1 protease for 1 h. Experiments were performed in triplicates. Error bars show the standard deviations

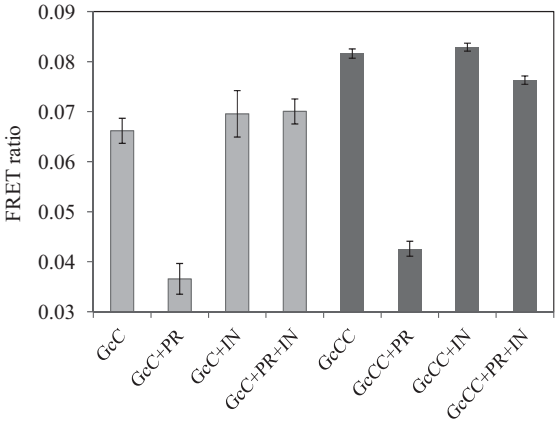

Fig. 17.3 Detection of HIV-1 protease's inhibition using the nanosensors. The reaction was conducted at 37 °C for 30 min and stopped by the addition of a stop buffer to the reaction buffer. All measurements were performed at room temperature. *PR* protease, *IN*, inhibitor. The experiments were performed in triplicate. Error bars show the standard deviations

the probes with a structure of AcGFP1-p2/p7-mCherry and AcGFP1-p2/p7-mCherry-mCherry were designated as GcC and GcCC, respectively. We observed that the FRET signal value decreased in response to the increase in protease concentration in the range of 0–45 ng/mL, indicating the cleavage of the probe protein by HIV-1 protease. The protease cleavage is concentration dependent. Interestingly, probe GcCC demonstrates a more sensitive property to the substrate concentration than that of probe GcC.

To confirm the probe's enzyme-specific decrease in FRET signal, the FRET signals were measured by adding the protease inhibitor ritonavir to the solution. As shown in Fig. 17.3, the GcCC probe is not cleavable by the protease in the presence of ritonavir, as FRET signal remains the same as that in GcCC alone. The probe signals did not change in the presence of the inhibitor in the solution. Taken together, the experimental results indicated that the incubation of the probe with the HIV-1 protease will not quench the probe's FRET, when the protease activity is inhibited by its inhibitor. Thus, the decrease of the probe GcCC's FRET signals in the presence of HIV protease is enzyme specific. Furthermore, the FRET signal obtained from probe GcCC has approximately 20 % magnification as compared with the signal from probe GcC. This result indicates an enhanced energy transfer by a tandem structure of the nanosensor.

17.4 Characterization of the Nanosensors in Living Cells

We next examined whether or not the probes can visualize HIV-1 protease inhibition within living cells. Human embryonic kidney (HEK) 293 T cells were used to examine the response of the nanosensors to HIV-1 protease inhibitors. The probe protein-encoding plasmid and HIV-1 protease expression plasmid were transiently transfected into the 293 T cells. Expression of the probe proteins were detected 50 h after transfection using an inverted fluorescence microscope from Olympus

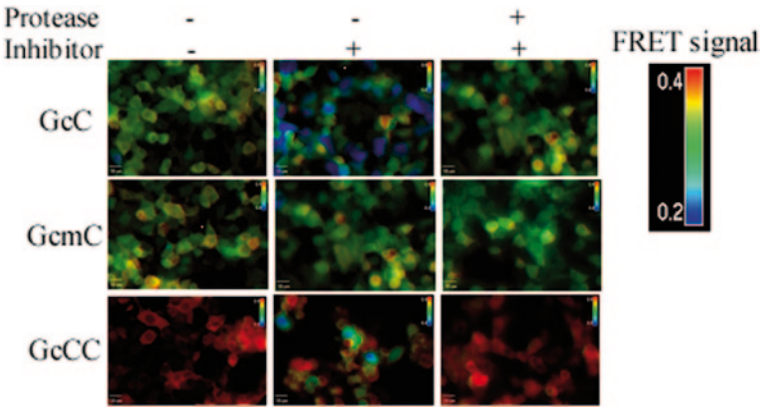

Fig. 17.4 Visualization of HIV-1 protease activity and inhibition in vivo. 293 T cells were either transfected with different structured probes alone or co-transfected with the probe and HIV-1 protease expression plasmids. FRET imaging microscopy measurement was performed at 50 h post transfection. Ritonavir, an HIV-1 protease inhibitor, was added to the cell culture medium to prevent the cleavage of the probe protein. The color bar indicates FRET ratio

and Slidebook software. Eight regions were randomly chosen to calculate the average value of the FRET signal. In addition, to ensure the specificity of the enzyme reaction, a mutated probe, GcmC, in which a mutated cleavage site was constructed to make the probe non-cleavable by HIV-1 protease, was also employed for validation. As displayed in Fig. 17.4, the probe GcCC and protease plasmid cotransduced cells in the absence of protease inhibitor displayed, overall, reduced FRET signals by showing a mixture of blue-, green-, yellow-, and red-colored cells (Fig. 17.4: GcCC protease+ and inhibitor−) as compared to the signals produced from cells in the presence of protease inhibitor (Fig. 17.4: GcCC protease+ and inhibitor+). However, all of the cells displayed a red color when protease activity was inhibited by its inhibitor, indicating a FRET ratio of 0.4 (GcCC protease+ inhibitor+). Cells co-transfected with GcCC and protease expression vectors emitted sensitized red fluorescence when an inhibitor, ritonavir, was added to the cell culture medium. The addition of the protease inhibitor to the cell culture medium prevented the cleavage of the peptide linker by the protease and thus retained the high FRET signal.

As a control, the mutated probe has no response to either the presence or absence of the protease, and neither does it respond to the protease inhibitor, suggesting that the molecular probe designed in this study is specific to HIV-1 protease activity and inhibition.

In the single donor–acceptor structure of the FRET probe GcC, FRET ratio changed from 0.20 to 0.32, as indicated by the blue to green colors in the absence or presence of protease inhibitor (Fig. 17.5a). By contrast, FRET ratio changed from 0.20 to 0.42 in single-donor–tandem-acceptor structure of FRET probe GcCC. Thus, an approximately 1.8-fold amplification of FRET signal can be obtained with the newly developed probe GcCC as compared to FRET-based probe GcC. To confirm the protease's cleavage of the probe, Western blot assay was carried out to

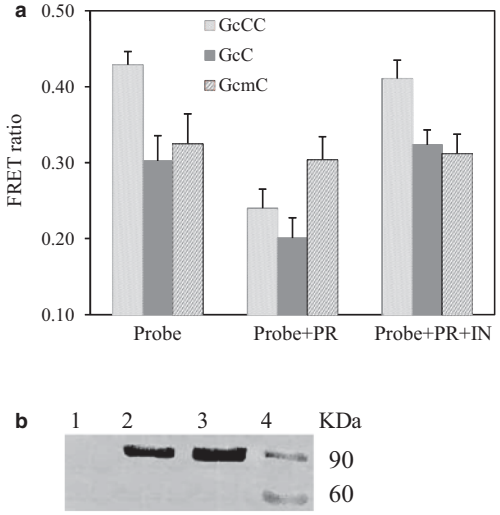

Fig. 17.5 Comparison of the signals of the FRET probes in vivo. **a** Detection of the FRET signal in the presence or absence of protease inhibitor. The average of the FRET ratios determined from eight random regions was used to represent the FRET signal of the probe from the living cells in each well. Error bars show the standard deviations. **b** Confirmation of the cleavage of the probe protein by Western blot assay. Cells were harvested at 50 h post transfection and lysed for Western blot. Lane 1: mock-transfected 293 T cells; Lane 2: probe plasmid transfected cells; Lane 3: probe and HIV-1 protease plasmid co-transfected cells in the presence of ritonavir; Lane 4: probe and HIV-1 protease plasmid co-transfected cells in the absence of ritonavir

characterize the size of the probe protein in the presence or absence of protease activity. As indicated in Lane 4 of Fig. 17.5b, two bands sized at 90 and 60 kDa were observed in GcCC and protease co-transfected cells, whereas 60 kDa band was not detected in the mock-transfected, GcCC alone transfected, and GcCC plus protease expressing vectors co-transfected cells in the presence of the inhibitor (Fig. 17.5b Lanes 1, 2, 3). Clearly, the presence of ritonavir in the cell culture medium prevented the cleavage of the probe (Fig. 17.5b, Lane 3), confirming the specific cleavage reaction for the probe detection system in vivo.

17.5 The Tandem Structure of the Nanosensor Improves FRET Efficiency

To quantify the FRET efficacy of the two nanosensors, the lifetime constants of the donor fluorophore under different structured FRET-based probes was quantified using FLIM. Before performing FLIM, the cell culture medium was replaced with a phosphate-buffered saline (PBS) buffer. The lifetime of the AcGFP1 expressing donor protein alone as well as the lifetime of the donor–acceptor protein probes

Table 17.1 Average fluorescence lifetime of AcGFP1 from 293 T cells expressing AcGFP1, GcC, and GcCC

	AcGFP1 alone	GcC	GcCC
Fluorescence lifetime (ns)	2.81 ± 0.26	1.99 ± 0.21	1.86 ± 0.29
FRET efficiency (E)		29.2%	33.9%

was acquired. Ten regions were randomly chosen to calculate the average value of the lifetime of each sample. FRET efficiency (E) was calculated by the following equation:

$$E = 1 - \frac{\tau_{DA}}{\tau_D}, \tag{17.1}$$

where τ_D is the lifetime constant of the donor protein in the absence of the acceptor protein, and τ_{DA} is the lifetime constant of the donor protein in the presence of the acceptor protein.

We found that the lifetime of AcGFP1 detected from AcGFP1 alone expressing cells was 2.81 ns, whereas the lifetime of AcGFP1 measured in GcC probe expressing cells was 1.99 ns (Table 17.1). The reduction of AcGFP1's lifetime suggests the occurrence of FRET between the AcGFP1 and mCherry pair within living cells. With the tandem mCherry as acceptors in the FRET probe, the lifetime of AcGFP1 measured in GcCC was 1.86 ns. The further reduction of the lifetime of AcGFP1 demonstrates more fluorescence energy transfer from the donor to the acceptors, indicating enhanced FRET efficiency. Calculation of the FRET efficiency using the above equation indicated a 4.7% increment in the FRET efficacy with nanosensor GcCC over an original value of 29.2% with nanosensor GcC, which is indeed a 16.1% improvement in FRET signaling. The comparison of FRET efficiency evidently demonstrates that the FRET signal can be enhanced using a tandem acceptor structure.

17.6 Conclusion

Fluorescent FRET-based nanosensors have been developed for HCS of anti-HIV drug in living cells. The nanosensors are very sensitive and specific to the HIV-1 protease activity and/or inhibition inside a living cell. Thus, they can be used to search for candidate compounds for inhibition of HIV-1 infection and replication. Furthermore, the reporting capability of the nanosensor can be improved by optimizing its molecular structure. In both in vitro and in vivo studies, the probe GcCC increases FRET signal by 1.8-fold, as compared to probe GcC. The modified FRET-based probe structure developed herein greatly improved FRET efficiency. Our experimental results suggest that the GcCC would be a better probe for drug discovery. It provides a useful and sensitive tool for visualizing protease inhibition within living cells and enables one to visualize HIV-1 targets within living

cells for HCS of anti-HIV-1 protease inhibitors. Taken together, our study results provide a strategy to promote signaling generated from a nanosensor that can be employed to a reliable and accurate HCS of anti-HIV-1 protease agents in living cells.

References

1. P. Fortina, L.J. Kricka, S. Surrey, P. Grodzinski, Nanobiotechnology: the promise and reality of new approaches to molecular recognition. Trends Biotechnol. **23**(4), 168–173 (2005)
2. S. Jin, K. Ye, Nanoparticle-mediated drug delivery and gene therapy. Biotechnol. Prog. **23**(1), 32–41 (2007)
3. M. Wolff, J. Wiedenmann, G.U. Nienhaus, M. Valler, R. Heilker, Novel fluorescent proteins for high-content screening. Drug Discov. Today. **11**(23–24), 1054–1060 (2006)
4. A.E. Carpenter, Image-based chemical screening. Nat. Chem. Biol. **3**(8), 461–465 (2007)
5. R.N. Ghosh, Y.T. Chen, R. DeBiasio, R.L. DeBiasio, B.R. Conway, L.K. Minor, K.T. Demarest, Cell-based, high-content screen for receptor internalization, recycling and intracellular trafficking. Biotechniques **29**(1), 170–175 (2000)
6. D.L. Taylor, E.S. Woo, K.A. Giuliano, Real-time molecular and cellular analysis: the new frontier of drug discovery. Curr. Opin. Biotechnol. **12**(1), 75–81 (2001)
7. Z. Li, Y. Yan, E.A. Powers, X. Ying, K. Janjua, T. Garyantes, B. Baron, Identification of gap junction blockers using automated fluorescence microscopy imaging. J. Biomol. Screen. **8**(5), 489–499 (2003)
8. D.L. Almholt, F. Loechel, S.J. Nielsen, C. Krog-Jensen, R. Terry, S.P. Bjorn, H.C. Pedersen, M. Praestegaard, S. Moller, M. Heide et al., Nuclear export inhibitors and kinase inhibitors identified using a MAPK-activated protein kinase 2 redistribution screen. Assay. Drug. Dev. Technol. **2**(1), 7–20 (2004)
9. B. Liu, S. Li, J. Hu, Technological advances in high-throughput screening. Am. J. Pharmacogenomics. **4**(4), 263–276 (2004)
10. M. Bickle, High-content screening: a new primary screening tool?. IDrugs **11**(11), 822–826 (2008)
11. E.H. Mouchet, P.B. Simpson, High-content assays in oncology drug discovery: opportunities and challenges. IDrugs **11**(6), 422–427 (2008)
12. T. Zal, Visualization of protein interactions in living cells. Adv. Exp. Med. Biol. **640,** 183–197 (2008)
13. P. Kalab, J. Soderholm, The design of Forster (fluorescence) resonance energy transfer (FRET)-based molecular sensors for Ran GTPase. Methods **51**(2), 220–232 (2010)
14. A. Masi, R. Cicchi, A. Carloni, F.S. Pavone, A. Arcangeli, Optical methods in the study of protein-protein interactions. Adv. Exp. Med. Biol. **674**, 33–42 (2010)
15. A. Uri, M. Lust, A. Vaasa, D. Lavogina, K. Viht, E. Enkvist, Bisubstrate fluorescent probes and biosensors in binding assays for HTS of protein kinase inhibitors. Biochim. Biophys. Acta. **1804**(3), 541–546 (2010)
16. M.C. Morris (2013) Fluorescent biosensors—probing protein kinase function in cancer and drug discovery. Biochim. Biophys. Acta. **1834,** 1387–1395
17. D.K. Saini, N. Gautam, Live cell imaging for studying g protein-coupled receptor activation in single cells. Methods Mol. Biol. **617,** 191–207 (2010)
18. M. Di Grandi, M. Olson, A.S. Prashad, G. Bebernitz, A. Luckay, S. Mullen, Y. Hu, G. Krishnamurthy, K. Pitts, J. O'Connell, Small molecule inhibitors of HIV RT Ribonuclease H. Bioorg. Med. Chem. Lett. **20**(1), 398–402 (2010)
19. G. Dams, K. Van Acker, E. Gustin, I. Vereycken, L. Bunkens, P. Holemans, L. Smeulders, R. Clayton, A. Ohagen, K. Hertogs, A time-resolved fluorescence assay to identify small-molecule inhibitors of HIV-1 fusion. J. Biomol. Screen. **12**(6), 865–874 (2007)

20. S. Jin, E. Ellis, J.V. Veetil, H. Yao, K. Ye Visualization of human immunodeficiency virus protease inhibition using a novel Forster resonance energy transfer molecular probe. Biotechnol. Prog. **27,** 1107–1114 (2011)
21. H. Yao, S. Jin, Enhancement of probe signal for screening of HIV-1 protease inhibitors in living cells. Sensors **12**(12), 16759–16770 (2012)
22. J. Lu, Z. Zhang, J. Yang, J. Chu, P. Li, S. Zeng, Q. Luo, Visualization of beta-secretase cleavage in living cells using a genetically encoded surface-displayed [corrected] FRET probe. Biochem. Biophys. Res. Commun. **362**(1), 25–30 (2007)
23. F. Jeppsson, S. Eketjall, J. Janson, S. Karlstrom, S. Gustavsson, L.L. Olsson, A.C. Radesater, B. Ploeger, G. Cebers, K. Kolmodin et al., Discovery of AZD3839, a potent and selective BACE1 inhibitor clinical candidate for the treatment of Alzheimer disease. J. Biol. Chem. **287**(49), 41245–41257 (2012)
24. Q. Lu, W.Y. Chen, Z.Y. Zhu, J. Chen, Y.C. Xu, M. Kaewpet, V. Rukachaisirikul, L.L. Chen, X. Shen, L655,240, acting as a competitive BACE1 inhibitor, efficiently decreases beta-amyloid peptide production in HEK293-APPswe cells. Acta. Pharmacol. Sinica. **33**(12), 1459–1468 (2012)
25. M. Tramier, M. Zahid, J.C. Mevel, M.J. Masse, M. Coppey-Moisan, Sensitivity of CFP/YFP and GFP/mCherry pairs to donor photobleaching on FRET determination by fluorescence lifetime imaging microscopy in living cells. Microsc. Res. Tech. **69**(11), 933–939 (2006)
26. L. Albertazzi, D. Arosio, L. Marchetti, F. Ricci, F. Beltram, Quantitative FRET analysis with the EGFP-mCherry fluorescent protein pair. Photochem. Photobiol. **85**(1), 287–297 (2009)
27. N. Akrap, T. Seidel, B.G. Barisas, Forster distances for fluorescence resonant energy transfer between mCherry and other visible fluorescent proteins. Anal. Biochem. **402**(1), 105–106 (2010)
28. J.V. Veetil, S. Jin, K. Ye, A glucose sensor protein for continuous glucose monitoring. Biosens. Bioelectron. **26**(4), 1650–1655 (2010)
29. H. Takanaga, B. Chaudhuri, W.B. Frommer, GLUT1 and GLUT9 as major contributors to glucose influx in HepG2 cells identified by a high sensitivity intramolecular FRET glucose sensor. Biochim. Biophys. Acta. **1778**(4), 1091–1099 (2008)
30. G.N. van der Krogt, J. Ogink, B. Ponsioen, K. Jalink, A comparison of donor-acceptor pairs for genetically encoded FRET sensors: application to the Epac cAMP sensor as an example. PloS One **3**(4), e1916 (2008)

Chapter 18
Biomimetic Surfaces for Cell Engineering

John H. Slater, Omar A. Banda, Keely A. Heintz and Hetty T. Nie

Cell behavior, in particular, migration, proliferation, differentiation, apoptosis, and activation, is mediated by a multitude of environmental factors: (i) extracellular matrix (ECM) properties including molecular composition, ligand density, ligand gradients, stiffness, topography, and degradability; (ii) soluble factors including type, concentration, and gradients; (iii) cell–cell interactions; and (iv) external forces such as shear stress, material strain, osmotic pressure, and temperature changes (Fig. 18.1). The coordinated influence of these environmental cues regulate embryonic development, tissue function, homeostasis, and wound healing as well as other crucial events in vivo [1–3]. From a fundamental biology perspective, it is of great interest to understand how these environmental factors regulate cell fate and ultimately cell and tissue function. From an engineering perspective, it is of interest to determine how to present these factors in a well-controlled manner to elicit a desired cell output for cell and tissue engineering applications. Both biophysical and biochemical factors mediate intracellular signaling cascades that influence gene expression and ultimately cell behavior [4–7], making it difficult to unravel the hierarchy of cell fate stimuli [8]. Accordingly, much effort has focused on the fabrication of biomimetic surfaces that recapitulate a single or many aspects of the in vivo microenvironment including topography [9–12], elasticity [5], and ligand presentation [13–17], and by structured materials that allow for control over cell shape [18–23], spreading [18, 23–25], and cytoskeletal tension [26–28]. Controlled presentation of these properties to develop a desired microenvironment can be harnessed to guide cell fate decisions toward chosen paths and has provided a wealth of knowledge concerning which cues regulate apoptosis [29–34], proliferation [35–39], migration, lineage-specific stem cell differentiation [7, 8, 15, 18, 23, 37, 40–44], and immune cell activation to name a few. This chapter focuses on the implementation of biomimetic surfaces that recapitulate and control one or more aspects of the cellular microenvironment to induce a desired cell response. More specifically, biomimetic

J. H. Slater (✉) · O. A. Banda · K. A. Heintz · H. T. Nie
Department of Biomedical Engineering, University of Delaware, Newark, DE 19716, USA
e-mail: jhslater@udel.edu

M. Zhang et al. (eds.), *Carbon Nanomaterials for Biomedical Applications,*
Springer Series in Biomaterials Science and Engineering 5,
DOI 10.1007/978-3-319-22861-7_18

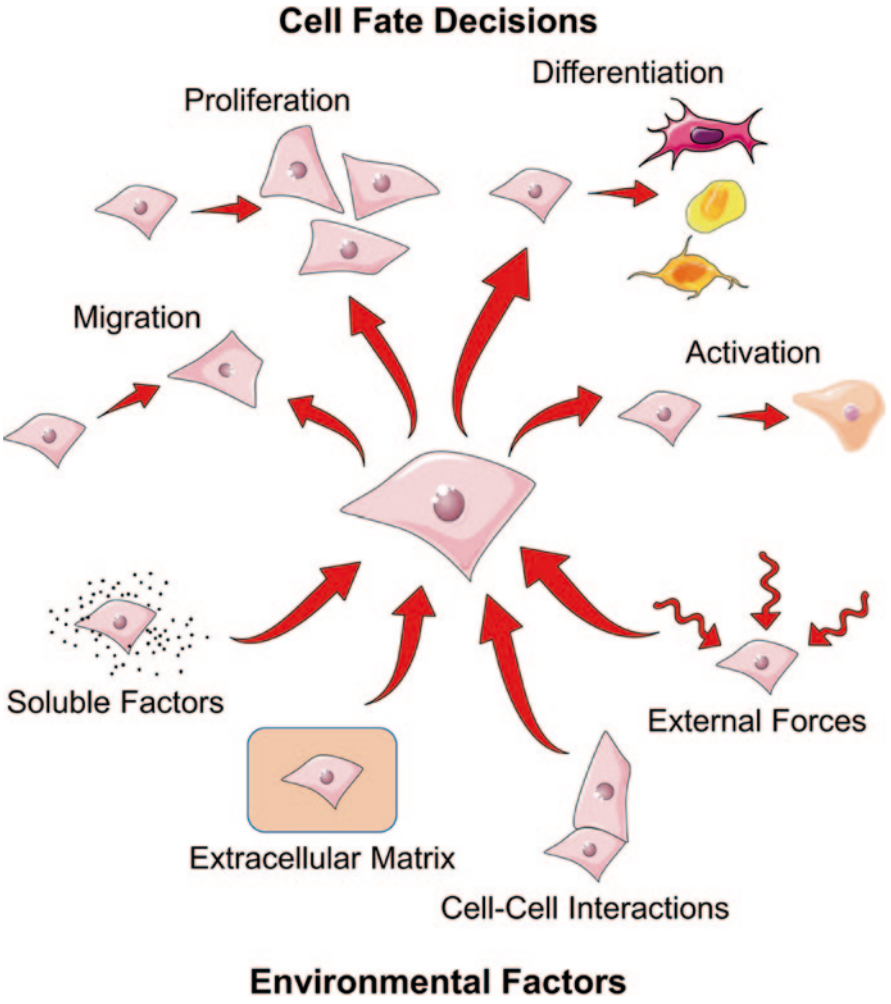

Fig. 18.1 Environmental stimuli regulate cell fate decisions. A multitude of environmental factors regulates cell fate decisions. Cells respond to both soluble and matrix-bound growth factors, extracellular matrix properties including composition, ligand density and spacing, stiffness, and topography, cell–cell interactions, and the application of external forces including shear stress, material strain, osmotic pressure, and temperature changes. The culmination of these environmental inputs regulates cell behavior with respect to migration, proliferation, differentiation, and activation to name a few. The major focus of much research involves the fabrication and implementation of biomimetic surfaces that allow for direct modulation over one or more of these environmental factors to elicit a desired cellular output.

surfaces that mimic in vivo ECM composition, density, gradients, stiffness, or topography; those that allow for control over cell shape, spreading, or cytoskeletal tension; and those that mimic cell surfaces are discussed.

18.1 Influence of ECM Properties on Cell Behavior

Many mammalian cells are adherent-dependent, meaning that they must adhere to ECM to maintain viability and to function properly. Accordingly, much research has focused on manipulating ECM properties to investigate its influence on cell fate. To understand how ECM properties influence cell behavior, it is important to understand how cells adhere and the process of adhesion maturation. Cell adhesion to the ECM is regulated by integrins; alpha/beta heterodimeric transmembrane glycoproteins that recognize short peptide sequences residing within ECM proteins [45]. Specific combinations of alpha/beta subunits recognize different ligands; some integrins recognize more than one ligand and some ligands ligate more than one integrin [46]. Upon activation, integrins interact with talin to form a small cluster that acts as an initiation site for adhesion formation [47]. Adhesions mature from small nascent adhesions, to focal complexes, to focal adhesions through force-mediated actomyosin contraction, and eventually fibrillar adhesions, if cultured on fibronectin [48]. This coordinated maturation process is regulated by both ECM composition and the transmission of force to adhesion plaques [49]. During the maturation process, the molecular composition, size, and location of adhesions change in addition to conformational changes in force- sensitive adhesion site proteins [47, 48, 50–53]. These molecular alterations induce changes in adhesion-mediated signaling events that regulate gene expression [49, 54, 55]. As anchoring units to the ECM, adhesions are also key mediators of migration. The coordinated formation of a lamellipodium and new adhesions at the leading edge, actomyosin contraction within the cell, and disassembly of mature adhesions at the trailing end are responsible for allowing cells to migrate on surfaces [56]. Migration is a critical function involved in wound healing, angiogenesis, immune responses, and embryonic development to name a few [57]. When integrin function is impaired or unregulated [58], adhesion properties can change drastically as observed in a number of disease states including cancer metastasis, arthritis, asthma, thrombosis [59], muscular dystrophy [60, 61], skin-blistering disease [62–64], and leukocyte adhesion deficiency [65]. A number of environmental cues influence these events including ECM composition, integrin/ligand affinity [66], presentation/orientation of integrin-ligating domains [44, 67–69], ligand gradients [70], and underlying material properties including wettability [71], stiffness [72, 73], topography [74], and degradability [75]. Cells also sense ligand and stiffness gradients that induce haptotaxis [76, 77] and durotaxis [78, 79], respectively.

Since adhesion formation and maturation play a large role in intracellular signaling of adherent-dependent cells, there has been much interest in fabricating engineered surfaces that control these processes. In many situations, it is advantageous to utilize ECM-derived peptides rather than full ECM proteins. In 1984, Pierschbacher and Ruoslahti discovered the $\alpha_v\beta_3$ ligating peptide RGD [80]. Since its discovery within fibronectin [80], additional proteins containing the RGD sequence have been identified including vitronectin [81], osteopontin [82], laminin [83], and collagen [84], although not all of these RGD sequences are readily accessible by cells [85].

In addition to RGD, a multitude of integrin-ligating peptide sequences have been discovered [85, 86] including IKVAV and YIGSR in laminin that ligate $\alpha_3\beta_1$, $\alpha_4\beta_1$, and $\alpha_6\beta_1$ integrins [87]; PHSRN [88] and REDV [89] in fibronectin that ligate $\alpha_5\beta_1$ and $\alpha_4\beta_1$, respectively, and GFOGER [88], a collagen-mimetic helical peptide [90], that ligates $\alpha_2\beta_1$ to name a few. As differential integrin ligation can significantly influence cell behavior [91], it is important to choose the proper ECM proteins or peptides for mimicking the tissue of interest. Generally, peptide sequences are not as efficacious as their native proteins, therefore cyclic peptides [92] and peptide fragments that span the entire binding domain have been developed [85]. Peptides have the advantage of being more stable and specific compared to the multiple ligation sites present in full proteins [93]. To demonstrate that a peptide behaves as expected, scrambled peptides are commonly used as nonadhesive controls [94, 95]. When using peptides, it is important to make them accessible for integrin ligation. By incorporating short spacers between the surface and conjugated peptide or protein, the biomolecule can become more accessible allowing efficient cell adhesion and spreading [95]. Interactions between poly(ethylene glycol) (PEG) spacers and peptides or proteins should be considered to prevent aggregation and maintain peptide and protein accessibility [67].

In addition to ECM proteins, various growth factors including epidermal growth factor (EGF) [96], basic fibroblast growth factor (bFGF) [97, 98], and vascular endothelial growth factor (VEGF) [99] have been studied as they can enhance proliferation, migration, and angiogenesis. In vivo, growth factors are continuously bound and released from the ECM [100]; therefore, the impacts of adsorption and tethering of these elements to surfaces to determine if efficacy and bioactivity can be retained have been investigated. Gradients of morphogenetic proteins are also involved in differential gene expression that determines cell fate [101]. The proteins tenascin, thrombospondin-1, and osteonectin/secreted protein acidic and rich in cysteine (SPARC) are of interest as they are known to control cell detachment from the ECM in wound healing and are also implicated in tumorigenesis [102–104]. Although not currently studied in conjunction with bioactive surfaces, these proteins could be useful in promoting and controlling cell migration and should be considered when creating biomimetic materials [86].

18.2 Surface Functionalization

As discussed in the previous section, many aspects of the ECM influence cell behavior. To create biomimetic surfaces, one must be able to functionalize surfaces with peptides and proteins of interest. There are countless methods and techniques used to link biomolecules including ECM-associated peptides, proteins, and growth factors to material surfaces [105, 106]. Even the simplest studies investigating the influence of ECM properties on cell behavior often involve advanced fabrication techniques. Biomimetic surfaces created using laser scanning lithography (LSL) [107–111], microcontact printing (μCP) [112], microfluidic devices [113, 114], and

block copolymer micelle nanolithography (BCMN) [115] as well as others have allowed researchers to study the influence of various surface-displayed biomolecules on cell behavior. Peptides are often covalently linked to surfaces via an amide bond between a carboxylic group on the substrate, and the N-terminus of the peptide [93], although many other bioconjugate methods applying various functional groups exist [116]. To investigate the spacing or size of ECM components on integrin spacing or adhesion site growth and maturation, it is crucial to possess subcellular control over how the ECM is displayed. Many techniques for high-resolution control of patterned ECM components have been developed and a few are discussed here. For sub-100-nm resolution patterning of proteins, dip-pen nanolithography allows alkanethiol self-assembled monolayers (SAMs) to be formed on a gold surface by direct writing with a SAM-coated atomic force microscope (AFM) tip. The self-assembled monomers are delivered to the surface via transport, the surrounding non-patterned areas functionalized with a nonadhesive SAM, typically a poly(ethylene oxide) (PEO)-terminated SAM, and protein is adsorbed to the patterned SAM providing a means to create high-resolution, subcellular-sized patterns of ECM components [117, 118]. Nanosphere lithography also allows for sub-100-nm to micrometer-sized patterning of ECM proteins and direct control over adhesion site growth, spacing between adhesions, and adhesion site density [119, 120]. BCMN is a method for patterning gold nanoparticles, which can be functionalized with single cyclic RGD peptides allowing for ligation of single integrins in desired locations. LSL can be applied to pattern a wide variety of proteins and peptides, works in 2D and 3D applications, and relies on laser-induced photocoupling of biomolecules to hydrogels or photothermal decoupling of SAMs on metallic surfaces [107–111]. Regardless of the method used when adsorbing or linking biomolecules to the surface of a material, it is important to note how these processes impact the structure and presentation of the proteins and ligands as these elements can further impact binding events [67, 68].

18.3 ECM Mimetic Surfaces

The physical spacing and clustering of ligands is of importance to cells. To vary the magnitude of cell adhesion, one can vary integrin expression level, integrin–ECM binding affinity, or ECM ligand surface density [66] and spacing. In vivo, different ligand densities and spacing can be optimal for different cellular processes, as integrin ligation controls intracellular signaling events [49, 54, 55]. Furthermore, if ligands are clustered at the appropriate spacing, integrins will cluster, thereby allowing stable adhesion formation and maturation [48]. Along with specific mechanical and chemical composition, it is important to note that the ECM can contain various structural features that correspond to the type of cells it is supporting [121]. The scale of these structural features varies from the nano- to microscale, with the arrangement and orientation of fibrillar fibronectin and collagen networks largely impacting how the ECM interacts with cells in tissues [122]. As an example of

how surface mimicry is important to cell migration, collagen-coated surfaces with and without D-periodicity were studied [123]. Collagen contains a banding pattern every 67 nm called the D-period; collagen prepared in the absence of potassium ions forms without banding. Cell orientation and direction of motion depend on the D-period where cells move parallel to the collagen fibers with the D-period, while cells cultured on collagen fibers without the D-period exhibit random motion. Thus, the D-period is an essential structural feature of the ECM for directional fibroblast migration [123]. To mimic these nanoscale structural elements in ECM proteins, several approaches have been developed for altering ligand density, cluster size, and integrin spacing including PEO bioconjugation [124, 125], BCMN [69, 92, 115], and nanopatterning [119, 120]. Using these structured materials, one can investigate the influence of integrin spacing or adhesion site growth on cell adhesion, migration, differentiation, and proliferation. To obtain surfaces with various spacing of RGD-modified PEO in a brush layer, the ratio of polystyrene-PEO-maleimide and polystyrene-PEO in a polystyrene homopolymer can be varied. The maleimide group can be reacted with cysteine-GRGDS or cysteine-GRGES peptides to vary the surface density of RGD to investigate the influence of RGD spacing on cell fate. Migration rates for human bone marrow mesenchymal stem cells (hMSCs) were fastest when the RGD peptides were spaced at 50 nm [125]. As lateral spacing of RGD was increased, cells displayed a more adipogenic morphology, while at smaller lateral spacing, the cells were more osteogenic [125]. These results indicate that simply altering integrin packing density can have a profound influence on cell fate. A similar bioconjugation technique varied the ratio of peptide-modified, YIGSR in this case, star-PEO molecules, to unmodified star-PEO molecules, and the number of peptides per star-PEO to obtain surfaces with varying ligand densities and spacing to control integrin clustering [124]. Using this approach, the impacts of peptide spacing and density can be decoupled. By increasing the cluster size of the adhesive ligand, similar cell migration rates can be obtained with a lower overall surface density. The ligand clusters created in this manner, however, are randomly spaced, and thus the surfaces can have areas with larger ligand clusters if two or more functionalized star-PEO molecules are in close proximity [124]. In a more controlled fashion, integrin spacing can be altered by depositing gold nanoparticles onto a surface using BCMN [115]. BCMN relies on the self-assembly of diblock copolymer micelles around small gold particles; these micelles are then dip-coated onto a substrate. After the micelle-coated substrate is subjected to plasma treatment, the gold particles remain on the surface [115]. After gold nanoparticle deposition, the open spaces on the surface are backfilled with PEG, and the particles functionalized with a cyclic RGD. The backfilling of PEG accounts for any topographical features on the surface, as the thickness of the PEG layer can be set to match the diameter of the nanoparticles to create a patterned surface free of topography [115]. Cells on these surfaces migrate along ligand gradients toward areas with denser ligand concentration [92]. This patterning approach was also implemented to determine the critical distance between individual RGD groups and subsequently integrin spacing for mesenchymal stem cell (MSC) adhesion. It was determined that a minimum integrin spacing of approximately 70 nm is needed for cell adhesion and spreading with

cells unable to effectively spread above that threshold [44]. The same integrin spacing was previously reported for both osteoblasts and fibroblasts indicating a universal distance needed for tight integrin packing to support adhesion formation [126]. It is suspected that this spacing reflects the distance between the integrin β-subunit binding domains of the talin1 protein [127]. BCMN can also be used to create disordered and ordered arrays of RGD functionalized gold nanoparticles against a non-adhesive background. Disordered arrays of cyclic RGD were able to support cell adhesion above the 70-nm interligand distance. When ligand spacing is ordered, and above 70 nm, minimal potential exists for integrin clustering; however, when ligand spacing is disordered, and above 70 nm, there is more potential for ligands to randomly be close enough for integrin clustering and stable adhesion formation [69]. Similarly, gold palladium nanodots can be deposited in defined clusters using nanoimprint lithography [128]. These cyclic RGD functionalized nanodots were utilized to investigate both the spacing between integrins and number of integrins per adhesion on cell migration. For 3T3 fibroblasts, it was determined that at least four nanodots per adhesion were required to achieve almost a threefold increase in the number of adherent cells compared to when only two or three nanodots existed per cluster. The optimal interdot spacing in a cluster was determined to be approximately 60 nm. The global density of nanodots did not impact cell spreading when the distance between nanodots in each cluster was held constant at 60 nm, indicating that the ability to cluster integrins is more important than the global ligand density in inducing stable adhesion and cell spreading [128]. Similar results were achieved using nanopatterned surfaces created with nanosphere lithography. It was demonstrated that local ligand density is more important than global ligand density in supporting cell adhesion and proliferation using nanopatterned surfaces displaying patterned fibronectin [120]. Interestingly, while nanopatterns ranging from ~ 100 to 1500 nm all supported adhesion and proliferation, cell migration was 4.8-fold faster on 100-nm-sized patterns [119]. Additionally, an exponential decay in cell migration with increased pattern size was observed indicating that stable adhesion formation retards migration [119]. All of these studies indicate that the formation of stable adhesions is crucial in cell attachment, spreading, and proliferation and that inducing unstable adhesion via increased integrin spacing or limiting adhesion site growth can induce highly migratory cell behavior. Findings from these high-resolution, nanopatterned biomimetic materials provide much insight into the influence of ECM nanoscale structure and organization on cell behavior and a means to locally control cell function via adhesion site manipulation. Using these highly structured surfaces, one may be able to spatially control cell migration, proliferation, and differentiation providing a single platform to investigate many aspects of cell fate as a function of ECM properties.

ECM composed of fibrillary proteins often contains well-organized topography that cells recognize and respond too. Various approaches to mimic these native protein structures exist. When grooves exist on the surface of a material, cell migration in the direction parallel to the grooves is often significantly higher than migration perpendicular to the grooves; cells migrating on grooved structures prefer to orient and migrate in the direction of the grooves; thus, grooves can be seen as guiding

cell motion [74, 129, 130]. Cells typically orient more with increasing groove depth and orient less with increasing groove width and pitch [131]. Using this knowledge, topographic features have been implemented to guide vascular organization of human endothelial colony forming cells (ECFCs) by creating fibronectin patterned polydimethylsiloxane (PDMS) micropillars. The micropillars induce the cells to align in a single-cell chain manner [132]. Different cell types are not equally sensitive to topographical features; endothelial cells (ECs), human fibroblasts cells (FCs), and smooth muscle cells (SMCs) all behave differently on identical grooved structures in PDMS. FCs show much higher alignment and directional migration than ECs and SMCs [133]. These results indicate that surface topography acts as another parameter that must be controlled or that can be utilized in inducing desired cell behavior.

While the influence of ECM proteins, ECM-derived peptides, or topography on cell behavior has been discussed, it has been shown that ECM-bound growth factors play a role in cell fate also. Methods to increase wound healing and endothelial tubule formation for tissue vascularization have been developed using combinations of ECM proteins and ECM-associated growth factors [99, 134]. ECs cultured on hydrogel surfaces co-patterned with RGDS and VEGF in 35–70-μm-wide strips undergo more tubulogenesis compared to hydrogels patterned with RGDS alone, indicating that matrix-bound VEGF plays a significant role in EC function [99]. The strips of ligand and protein are important for cells to align and form cords or prevascular structures [134]. To improve wound-healing capabilities, fibrin matrices have been engineered to contain a multifunctional recombinant fragment of fibronectin that has the ability to bind fibrin for incorporation into a fibrin matrix, interact with integrins for cell adhesion, and promiscuously bind growth factors [135]. Migration of SMCs, ECs, and MSCs were all enhanced when the growth-factor-binding component was incorporated [135], indicating that bound or conjugated growth factors can also be considered in cell engineering applications with biomimetic materials. These matrices were also tested for their wound-healing capabilities in skin and bone; cell staining showed rapid cell migration into the enhanced fibrin matrices and significant improvement in wound healing than when growth factors were delivered in a standard fibrin matrix [135]. A similar study using the growth-factor-binding component was completed using a composite PEG synthetic fibrin-mimetic matrix beneficial for its more likely straightforward path to clinical approval [136]. Due to the likely engineering benefits of incorporating matrix-bound growth factors, some growth factors have been genetically engineered to contain a domain of placenta growth factor-2 (PlGF-2) to increase affinity for ECM proteins [137]. The ability to incorporate surface-bound growth factors with desired ECM properties opens new avenues for cell engineering research.

Aside from substrate biochemical properties, the mechanical properties of a material have a profound influence on cell behavior [72, 73, 79, 138–145]. In vivo, cells experience regions of various stiffness corresponding to associated tissues [73]; muscle ranges from 3 to 6 kPa, and arteries range from 24 to 45 kPa [146], whereas brain tissue has stiffness values at several hundred pascals, and tendon and cartilage in the megapascal range [139]. Furthermore, stiffness gradients exist at the

interface between ligaments, articular cartilage, and bone; bone composition itself is also highly variant with sections ranging from compact to spongy [70]. In order to control cell behavior on biomimetic materials, it is important to consider mechanical properties as well as chemical properties. Investigating substrate stiffness on cell behavior, however, has found difficulty in decoupling stiffness from other material properties, as altering the substrate stiffness of a native ECM material can also influence ligand availability and pore size [8, 138]. Fortunately, the use of synthetic hydrogel matrices has allowed scientists to overcome some of these limitations; synthetic hydrogels allow for decoupling of matrix stiffness and ligand density but they cannot overcome variations of pore size and density associated with materials of variant stiffness [8, 138, 142]. It has been demonstrated that substrate stiffness can influence a number of cell fate decisions including migration and stem cell differentiation. For example, stiff substrates (>40 kPa) prove to induce osteogenesis, medium stiffness substrates (~10 kPa) induce myogenesis, and soft substrates induce adipogenesis and neurogenesis [27, 42]. However, surface porosity may alter and attenuate the effects of substrate stiffness. To modulate substrate elasticity of gels, the substrate cross-linking can be modified by adjustments in molecular weight or weight percent [147, 148]. On gel substrates, increased elastic modulus decreases the porosity, which may increase cell contact area [8, 149]. However, soft porous substrates have much larger pores than their stiff counterparts and therefore allow for less cell contact area [8]. Conversely, on nonporous substrates, the cell contact area is preserved and all samples tend to induce osteogenesis regardless of stiffness [8]. This indicates that cell contact area also influences stem cell differentiation and that materials used for such experiments must be well characterized to determine which parameters are influencing cell fate decisions. Although stiffness and porosity may conflict, cells patterned with high aspect ratios on soft substrates still tend toward osteogenesis [150]. Earlier methods approaching this problem involved the combination of synthetic and native substrates [151]. By using shaded patterns laser-printed on transparency slides [152] or a microfluidic gradient maker [153], polyacrylamide hydrogels were photopolymerized with graded stiffness. Using a layer of collagen covalently linked to the top of the gradient hydrogel, cells are exposed to a surface with uniform molecular composition, but they can sense the stiffness gradient of the underlying material. Thicknesses of various layers do have an influence; studies have been performed to determine how deeply cells can sense their substratum [154, 155]. Bovine vascular SMCs cultured on these combination surfaces migrate slightly faster on softer gels than on stiffer gels; however, cells migrate toward and accumulate in stiffer regions [151]. Normal rat kidney epithelial cells, NIH 3T3 fibroblasts, and bovine pulmonary arterial ECs also show increased motility on soft surfaces and accumulate in stiffer regions [72, 140, 156, 157]. Likewise, using combinations of soft and stiff materials, pieces of glass have been embedded in polyacrylamide hydrogels of varying thickness [146]. The thickness of the overlying hydrogel determines how stiff the material appears to cells, due to the close proximity of the underlying glass. When cells are cultured on thicker hydrogels, the cells lose the ability to sense the glass, and the material appears more compliant. One can also vary the substrate geometry to create gradients and

steps in stiffness. Using this approach, the overall pore size and material density remain constant while the apparent stiffness is altered. This assay could be applied to study cell migration due to substrate stiffness with a wide range of hydrogel materials and cell types [146]. Material stiffness can also be studied in how it relates to cancer cell migration. Explained by metastasis, mammary epithelial cells have been shown to be more ignorant of material stiffness as they transition from being non-transformed to fully transformed [158]. These results indicate that cells sense both biochemical and mechanical properties of ECM mimetic materials providing a large set of parameters researchers can utilize to develop engineered materials to guide cell fate decisions.

18.4 Utilizing Single-Cell Patterns to Regulate Spreading, Shape, and Cytoskeletal Tension

While the previous section discussed biomimetic materials that recapitulate in vivo ECM properties, this section discusses the implementation of patterned ECM for the creation of single-cell patterns that can be implemented to induce a desired cellular response. Culturing cells on engineered surfaces that present an array of a patterned ECM protein in a user-controlled, well-defined geometry against a biologically inert background has proven to be a viable method to create a more homogenous cell population during in vitro culture [159, 160]. These surfaces not only allow for the manipulation and investigation of individual cells but also, through arraying, allow for the generation of a large population of single cells to be investigated simultaneously [109, 159–161]. Culturing cells on ECM patterns of varying size or geometry allows for a high level of control over many cell properties including the extent of spreading [159, 162], shape [163, 164], and adhesion site arrangement with respect to size, spacing, and shape [120, 165–168]. Manipulation of these properties has been implemented to influence cell morphology [163, 164], cytoskeletal organization [169], the distribution of intracellular components (nucleus, centrosome, Golgi apparatus) [163], and cell polarity [163, 164], and to manipulate the extent of cytoskeletal tension generated in cells in order to modulate their behavior [159, 160, 162, 166]. For example, modulation of the extent of cell spreading was used to regulate hepatocyte function [162] and to direct lineage-specific MSC differentiation [159]. Similarly, regulation of cell shape, while maintaining a constant spread area, was implemented to guide lineage-specific MSC differentiation [160]. Variations of contact area and cell shape influence stem cell differentiation independently. Cells with large spread areas lead to greater osteogenesis [37] or myogenesis [18], while those with restricted cell spreading lead to greater adipogenesis [37] or chondrogenesis [18]. However, differences in lineage commitment are also seen in different shapes with the same spread area. Cells with high aspect ratios tended toward osteogenesis or neurogenesis, while those with the same spread area but an aspect ratio closer to one tended toward adipogenesis [37]. Additionally, cells of matching spread area with concave shapes and protruding

features also tend toward osteogenesis, while their rounded counterparts tended toward adipogenesis [23]. Protruding features create a cusp that allows for anchorage of many stress fibers, resulting in a potential increase in contractility and isometric cell tension than those with rounded features [170, 171]. Increased cellular tension alters cell signaling through force-mediated pathways [37] which act largely through myosin II isoforms [42]. Force-mediated differentiation is also the center of the "differential adhesion hypothesis" which suggests that different cell lineages have different numbers and compositions of adhesion proteins [172]. Cells cultured on substrates of matching elastic moduli and shape can differentiate into distinct mature lineages through use of different adhesive ligands [43]. Collagen induces greater neurogenesis, while laminin induces greater adipogenesis [173]. Surface chemistry alters cell fate as adhesive proteins ligate different integrins resulting in the activation of different signaling cascades [15, 43]. Cell shape, tension, substrate elasticity, and adhesive ligands are all able to dictate stem cell lineage commitment individually, under different conditions. However, these various factors may have some crosstalk. Therefore, biochemical and biophysical cues must work synergistically to create microenvironments to induce lineage-specific stem cell differentiation [174].

In addition to stem cell differentiation, patterned surfaces that regulate single-cell properties have been implemented to regulate cell proliferation. Cell–cell interactions were originally thought to arrest cell proliferation as cells plated at low density proliferated, while high-density populations arrested proliferation [37]. Although accurate, this observation overlooked the ability of low-density populations of cells to spread, while high-density populations cannot [37]. In cells with restricted spread area, having multiple cell–cell interactions arrested proliferation [36]. However, cells with restricted spread area but only one cell–cell interaction proliferated [39] revealing a regulatory role for cell–cell interactions in proliferation. Cell–cell interactions regulate proliferation first through rearrangement of cell cytoskeleton, as adherens junctions serve as cytoskeletal anchorage points for the similar to adhesion sites for cell–substrate interactions [175]. Likewise, these adherens junctions stimulate signaling cascades some of which, inclusive of RhoA [36], PI3K [38], and Rac1 [175], are known to induce proliferation. Wells that restrict cell spreading can be created by using capillary action to wick a polymer precursor solution between a PDMS master and a functionalized surface [36, 38, 39]. The precursors are thermally polymerized and the PDMS master removed to reveal wells. To alter the shape of the wells, new PDMS must be fabricated, either using replica molding or traditional photolithography [176]. Wells with simple geometries will collect one cell per well with passive seeding. For complex patterns where passively seeded cells will overpopulate the pattern, small electrodes can be included to act as electrical traps and ensure the collection of the desired number of cells [36]. Similar to observations of high and low plating density [37], cells cultured on adhesive surfaces tend to proliferate when spread, but arrest proliferation when cell spreading is restricted [25, 177]. Similar to cell spreading area, restricting adhesive area also arrests proliferation [24, 44]. Adhesion sites not only act as the interface between surfaces and cells but also aid in tension generation, and activate kinases [178], such as focal

adhesion kinase [25, 179, 180] and src [181] under high adhesive states and stimulate cell proliferation. The ability to modulate cell behavior through regulation of cell spreading or shape stems from differences in the amount of cytoskeletal tension generated in cells as dictated by the pattern size or geometry [159, 160]. While the specific force-sensitive proteins that regulate cytoskeletal tension-mediated control over intracellular signaling remain elusive, it is known that RhoA's influence over ROCK-mediated myosin contraction of actin stress fibers is the main regulator of tension generation [159], and cells with higher levels of intracellular tension display larger adhesion sites [159, 160, 182], more prominent actin stress fibers [159, 160, 182], increased JNK and ERK activation [160], and elevated Wnt signaling [160]. These results indicate the importance of cytoskeletal tension in determining cell behavior and that modulation of cellular tension can make cells more sensitive to [160] or override soluble signals [159]. Following this train of thought, a new biomimetic, cell-derived patterning technique was recently developed that allows for direct recapitulation of the morphology or adhesion site arrangement of user-chosen cells of interest [109]. Rather than implementing simple geometries, cell-derived patterning implements images of the cells of interest as templates for pattern formation resulting in direct recapitulation of the shape, adhesion site arrangement, and cytoskeletal architecture of user-chosen cells of interest [109]. As single-cell patterns become more sophisticated, tighter control over cell shape, adhesion, and cytoskeletal tension will allow for more thorough investigations of these properties on cell fate decisions and potentially lead to biomimetic surfaces that allow for direct control over cell phenotype.

18.5 Surfaces that Mimic Cell Surfaces

Another prevalent signaling source that regulates cell fate is communication between cells in close proximity: juxtacrine signaling. These signals are transmitted through interactions of transmembrane or membrane-bound proteins on adjacent cells. Tight junctions between adjacent epithelial cells serve as highly impermeable adhesions and help separate fluids on the apical side from the underlying basal membrane, thereby promoting cell polarization and control over soluble factor transport [183]. Cadherins, cell–cell adhesion proteins that are intracellularly linked to actin, are responsible for forming adherens junctions between adjacent cells that mediate cell–cell recognition, maintain structural integrity, and assist in some forms of cell migration [184]. More specialized juxtacrine signals include immunoglobulins and their ligands, such as major histocompatibility complex (MHC)/T cell receptor (TCR) complexes between T cells and their target antigen presenting cells (APCs) [185], and gap junction proteins, such as connexins used in synaptic communication between neurons [186]. Each of these communication modalities has been shown to initiate signaling cascades within cells leading to changes in cell morphology or differentiation states [187–191] and each bring their own set of challenges when attempting to model them in vitro. A major challenge in designing

a system that mimics the surface of a cell at a cell–cell junction is the presentation of the membrane proteins that regulate junction formation such that their function is preserved. This is due, in part, to the fact that many of these membrane proteins contain extracellular, transmembrane, and intracellular domains, and therefore may misfold and lose functionality when on a surface. To address this issue, a variety of conjugation methods have been developed to present truncated versions of these membrane proteins such that their activity is preserved and active domains remain accessible [192–195]. As an alternative, synthetic lipid-based membranes have also been developed to more closely mimic the presentation of these proteins in vivo [190, 196–198].

18.6 Biomimicry of Cell–Cell Contacts on Substrates

These methods involve passive adsorption or covalent linking of a protein or proteins of interest onto a substrate with controlled concentration and/or spatial presentation. One of the most straightforward methods to pattern protein is μCP [176]. An elastomer stamp, typically PDMS, is fabricated by curing against a photolithographically generated master. The surface of the stamp is inked with the desired protein solution, rinsed, dried, and brought into contact with the substrate, creating a pattern of protein matching the features on the stamp [176]. Successful patterning resolutions of several microns [199] up to several nanometers have been reported [200]. The nature of this method often promotes the use of truncated proteins containing only the extracellular domains of the original construct linked to an Fc region derived from an antibody; this minimizes the possibility of generating misfolded or inactivated ligands. The included Fc region allows for controlled and specific binding to the target surface as long as an Fc binding protein, such as Protein A or Protein G, is present. This methodology has been implemented to examine N-cadherin, E-cadherin, Neurexin, and many other extracellular domains of cell–cell contacts [194, 196, 201, 202]. In some cases, the spatial organization of multiple proteins in cell–cell junctions has been shown as a necessary precursor to some signaling cascades; therefore, it is often of interest to generate surfaces that allow for spatial patterning of multiple proteins in close proximity with each protein confined to its own pattern. Multiple rounds of μCP have been employed to spatially pattern multiple proteins to examine competitive effects or spatial display on cell–cell junction formation and cell activation [199]. For example, patterns of poly-L-lysine for neuron adhesion have been patterned along with the juxtacrine factors L1 or N-cadherin, which are essential for axon and neuron development, to compare the effects of both [203]. Additionally, laser-based methods have been implemented to pattern multiple proteins [107, 204, 205]. These approaches utilize digital masks to control laser position during patterning rather than the physical masters needed for μCP, allowing for quick changes to pattern design. Additionally, complex and image-derived patterns can be achieved [107, 204]. All of the aforementioned patterning methods are fundamentally limited for use in cell–cell contact studies since

the patterned proteins are not mobile as would occur in a cell membrane in their non-ligated states.

One major limitation of many patterning methods is the inability to mimic the more complex functionalities of membrane-associated proteins at cell–cell junctions. At these junctions, receptor–ligand pairs not only respond to each other but also often undergo conformational or spatiotemporal changes made possible by the fluidity and support of a lipid bilayer. Supported lipid bilayers (SLBs) are biologically inspired lipid-based surfaces that can mimic the fluidity of the cell membrane [206]. SLBs allow for the exploration of directed accumulation and dissipation of membrane-bound proteins involved in cellular processes, such as cadherin-dependent directed cell adhesion and migration [196], T cell activation [190, 199], and other membrane-dependent events. In the simplest lipid bilayer system, two separate chambers of an aqueous phase (most often a saline buffer solution) share an edge containing a small aperture (100 μm–1 mm) upon which the membrane will be deposited. The first synthetic lipid bilayers were created by "painting" a lipid solution (typically a suspension of phospholipids in some nonpolar organic solvent, such as decane) over the aperture [207]. This "painting" can be accomplished using a small painter's brush or by generating a lipid suspension over the entire aqueous phase and subsequently lowering and raising the aqueous phase about the aperture; each cycle performed in this way adds an additional monolayer to the membrane. Inclusion of electrodes within the saline chambers allows for the measure of changes in an electrical resistance of the membrane when a current passes through aperture. In this way, the lipid membrane—often referred to as black lipid membranes due to their appearance under the microscope—can be probed to investigate the adsorption of a variety water-soluble macromolecules. Although not all additions affect the resistance of the membrane, this is a common method to test for successful membrane modification, especially for ion-permeable additions such as channel proteins. The implementation of black lipid membranes is somewhat hindered due to their relative instability and to the limited scope of analytical tools available when compared to other methods utilizing synthetic membranes. SLBs address these shortcomings and often provide a much broader range of applications. SLBs are most commonly produced by the deposition and subsequent fusion of unilaminar or multilaminar lipid vesicles on the surface of a well. A variety of methods to generate SLBs exist as well as substrates on which to generate them [208–211], but they all share the same important features. To generate an SLB, the supporting surface must be smooth, clean, and hydrophilic. Contaminants or defects on the surface not only complicate characterization of the membranes but also compromise the integrity of the membranes themselves. As with the black lipid membranes, SLBs have a liquid phase on either side. Once the supported membrane has formed, a thin layer of water is suspended between the substrate and membrane. The depth of this layer typically falls between 20 and 40 Å [212]. As a result, the incorporation of transmembrane proteins with membrane protrusions larger than 20–40 Å may lead to contact between the protein and substrate, potentially resulting in misfolded intracellular or extracellular domains. To address this issue, SLBs have been generated on substrates functionalized with a polymer scaffold [213, 214]. The scaffold serves

as a cushion for the bilayer and provides a less rigid contact surface for proteins suspended within the membrane. Phospholipids chemically cross-linked to the polymer cushion can provide additional stability for supported bilayers. Much of the novelty of supported bilayer systems is generated from the plethora of compositions and chemistries available. Within the cell membrane, diversity is present not only in the associated proteins but also in lipid composition and organization. This diversity is necessary for cellular activity, and its organization plays roles in processes spanning from cell division to apoptosis. As a result, synthetic membranes must often involve the incorporation of lipids based on the process being studied. Lipids have been designed specifically for facilitated incorporation of truncated proteins. One example is biotin-conjugated lipids, commonly called "biotinylated" lipids. Biotin, also vitamin H or coenzyme R, is a cell-derived metabolic cofactor involved in several critical metabolic pathways. Its use in synthetic membranes, however, stems from a high non-covalent binding affinity to the protein avidin. Functionalizing a lipid with biotin and fusing the target protein with avidin facilitate the incorporation of select proteins to the cell membrane. The same outcome can be achieved through incorporation of metal-chelating lipids, such as nitrilotriacetic acid, which binds ionic nickel. A histidine-tagged protein can then form a non-covalent attachment to nickel allowing for tethering of the His-tagged protein to the membrane [215, 216].

18.7 T Cell Activation Using Biomimetic Surfaces for Cell–Cell Contacts

The activation of T cells using biomimetic surfaces that mimic APCs is of great interest in immunology. One of the goals of this research is developing a method to prime T cells in order to jump-start the immune system of patients who are unable to sufficiently mount the appropriate response to an infection [217, 218]. T cell activation itself occurs naturally when migrating T cells encounter an APC presenting antigen on extracellular MHC [219]. T cells bind MHC with TCR, and this binding triggers a T cell activation event leading to the release of various chemokines and growth factors, thereby initiating an immune response. Theoretically, new therapies could be developed for patients involving transplantation of activated T cells, assisting the patient's immune system and promoting natural defenses against a particular pathogen. Although many of the steps and components involved in this process have already been elucidated [220, 221], the exact mechanisms by which the process initiates and proceeds are not well understood. Immediately upon binding antigen presenting MHC, both the T cell and APC begin a process of actin-mediated accumulation of various membrane receptors to the binding site [221]. This site has been characterized into two distinct regions that form a bull's-eye-like pattern. The inner region, referred to as the central supramolecular activation complex (cSMAC), contains the TCR/MHC complex, as well as other associated proteins, and is surrounded by an outer region, the peripheral SMAC (pSMAC), which contains the ligand/integrin complex ICAM-1/LFA-1 (APC/T cell) used for T cell

adhesion to the APC [198, 220–222]. It has been shown that both regions play a role in T cell activation, and that certain components are relocated from the cSMAC to the pSMAC during the activation process. In recent years, several groups have used various methods to study various elements of the complex juxtacrine signaling that occurs during T cell activation. Using a μCP technique on a solid substrate, it was demonstrated that the organization of pSMAC components, the ligand–receptor pair CD80 (APC)/CD28 (T cell) had a major influence on the strength of a T cell response [199]. An Fc-coupled activating anti-CD28 was stamped onto the substrate in controlled patterns. The spacing of these patterned followed the scale of patterns typical of cSMAC and pSMAC spacing within the immunological synapse [199]. It was shown that when TCR and CD28 on the T cell were activated and IL-2 secretion was observed only when CD28 was deposited in regions analogous to a pSMAC, indicating spatial presentation of these ligand/receptor pairs plays a role in T cell activation. It was then shown that the stiffness of the substrate on which these ligand–receptor pairs were presented had a positive correlation with IL-2 secretion within the 10–200-kPa range [223]. Building on these findings, it was hypothesized that the mechanism dictating the spatial dependence of these ligands was the lateral mobility of proteins in the membrane involved in downstream signaling, such as Lck [224]. Using a BCMN method [225] to control presentation of an anti-CD3 activating antibody, it was shown that controlling the concentration of the ligands present during the immunological synapse formation also plays a role in the strength of an immune response, as seen by increasing expression of IL-2 and CD69 [226]. Later, another group designed an SLB system for high-throughput single T cell activation by creating a chip with an array of nanowells of approximately 30 μm [190]. Within these SLBs, they utilized biotin chemistry to incorporate anti-CD3 and MHC and incorporated ICAM-1 using a his-tag. T cells deposited in these nanowells formed T cell activation complexes, and the group was able to observe the process of this activation on an SLB. The ability to mimic cell surface fluidity and molecular composition adds another layer of control in generating biomimetic surfaces for cell engineering. These cell-surface mimetic materials will continue to increase our knowledge of how cell–cell interactions regulate cell fate, potentially impacting many areas of cell engineering.

18.8 Summary

The implementation of biomimetic surfaces to regulate cell function is still in its infancy. While a multitude of environmental factors that regulate cell function exist, it still remains a mystery as to which ones dominate basic cell function. From a fundamental biology perspective, biomimetic materials have shed light on which factors regulate cell fate decisions and will continue to provide insight into these relationships. From a cell engineering perspective, there are many environmental factors that can be recapitulated in in vitro environments, but knowing which ones to utilize for specific applications remains difficult. As biomimetic materials advance

further, new insights into both fundamental biology and cell engineering applications will be discovered leading to revolutionary new treatments and in vitro models for disease management.

References

1. H. Fujiwara, M. Ferreira, G. Donati, D.K. Marciano, J.M. Linton, Y. Sato, A. Hartner, K. Sekiguchi, L.F. Reichardt, F.M. Watt, The basement membrane of hair follicle stem cells is a muscle cell niche. Cell **144**, 577–589 (2011)
2. T. Sato, J.H. van Es, H.J. Snippert, D.E. Stange, R.G. Vries, M. van den Born, N. Barker, N.F. Shroyer, M. van de Wetering, H. Clevers, Paneth cells constitute the niche for Lgr5 stem cells in intestinal crypts. Nature **469**, 415–8 (2011)
3. A. Ashkenazi, V.M. Dixit, Death receptors: signaling and modulation. Science **281**, 1305–1308 (1998)
4. M.-H. Kim, M. Kino-oka, Switching between self-renewal and lineage commitment of human induced pluripotent stem cells via cell-substrate and cell-cell interactions on a dendrimer-immobilized surface. Biomaterials **35**, 5670–5678 (2014)
5. F. Chowdhury, Y. Li, Y.-C. Poh, T. Yokohama-Tamaki, N. Wang, T.S. Tanaka, Soft substrates promote homogeneous self-renewal of embryonic stem cells via downregulating cell-matrix tractions. PloS ONE **5**, e15655 (2010)
6. F. Guilak, D.M. Cohen, B.T. Estes, J.M. Gimble, W. Liedtke, C.S. Chen, Control of stem cell fate by physical interactions with the extracellular matrix. Cell Stem Cell **5**, 17–26 (2009)
7. J. Lee, A.A. Abdeen, K.A. Kilian, Rewiring mesenchymal stem cell lineage specification by switching the biophysical microenvironment. Sci. Rep. **4**, 5188 (2014)
8. B. Trappmann, J.E. Gautrot, J.T. Connelly, D.G.T. Strange, Y. Li, M.L. Oyen, M.a. Cohen Stuart, H. Boehm, B. Li, V. Vogel, J.P. Spatz, F.M. Watt, W.T.S. Huck, Extracellular-matrix tethering regulates stem-cell fate. Nat. Mater. **11**, 642–649 (2012)
9. I.D. de Souza, M.A.E. Cruz, A.N. de Faria, D.C. Zancanela, A.M.S. Simão, P. Ciancaglini, A.P. Ramos, Formation of carbonated hydroxyapatite films on metallic surfaces using dihexadecyl phosphate-lb film as template. Coll. Surf. B, Biointerfaces **118**, 31–40 (2014)
10. F. Benazzo, L. Botta, M.F. Scaffino, L. Caliogna, M. Marullo, S. Fusi, G. Gastaldi, Trabecular Titanium can induce in vitro osteogenic differentiation of human adipose derived stem cells without osteogenic factors. J. Biomed. Mater. Res. A. **102**, 2061–2071 (2014)
11. X. Deng, J. Lahann, Orthogonal surface functionalization through bioactive vapor-based polymer coatings. J. Appl. Polym. Sci. 131, 40315–40323 (2014)
12. S.J. Liliensiek, S. Campbell, P.F. Nealey, C.J. Murphy, The scale of substratum topographic features modulates proliferation of corneal epithelial cells and corneal fibroblasts. J. Biomed. Mater. Res. **79**, 185–192 (2006)
13. W.P. Daley, S.B. Peters, M. Larsen, Extracellular matrix dynamics in development and regenerative medicine. J. Cell Sci. **121**, 255–264 (2008)
14. C.M. Metallo, J.C. Mohr, C.J. Detzel, J.J. de Pablo, B.J. Van Wie, S.P. Palecek, Engineering the stem cell microenvironment. Biotechnol. Prog. **23**, 18–23 (2007)
15. K.Y. Tan, H. Lin, M. Ramstedt, F.M. Watt, W.T.S. Huck, J.E. Gautrot, Decoupling geometrical and chemical cues directing epidermal stem cell fate on polymer brush-based cell micropatterns. Integr. Biol. (Camb.). **5**, 899–910 (2013)
16. C. Mas-Moruno, R. Fraioli, F. Albericio, J.M. Manero, F.J. Gil, Novel peptide-based platform for the dual presentation of biologically active peptide motifs on biomaterials. Appl. Mater. Interfaces **6**, 6525–6536 (2014)
17. S.J. Ellis, G. Tanentzapf, Integrin-mediated adhesion and stem-cell-niche interactions. Cell Tissue Res. **339**, 121–130 (2010)

18. L. Gao, R. McBeath, C.S. Chen, Stem cell shape regulates a chondrogenic versus myogenic fate through Rac1 and N-Cadherin. Stem Cells **28**, 564–572 (2010)
19. S.R. Neves, P. Tsokas, A. Sarkar, E.A. Grace, P. Rangamani, S.M. Taubenfeld, C.M. Alberini, J.C. Schaff, R.D. Blitzer, I.I. Moraru, Iyengar, R. cell shape and negative links in regulatory motifs together control spatial information flow in signaling networks. Cell **133**, 666–680 (2008)
20. J. Meyers, J. Craig, D.J. Odde, Potential for control of signaling pathways via cell size and shape. Curr. Biol. **16**, 1685–1693 (2006)
21. S.A. Ruiz, C.S. Chen, Emergence of patterned stem cell differentiation within multicellular structures. Stem Cells **26**, 2921–2927 (2008)
22. J. Eyckmans, G.L. Lin, C.S. Chen, Adhesive and mechanical regulation of mesenchymal stem cell differentiation in human bone marrow and periosteum-derived progenitor cells. Biol. Open. **1**, 1058–1068 (2012)
23. K.A. Kilian, B. Bugarija, B.T. Lahn, M. Mrksich, Geometric cues for directing the differentiation of mesenchymal stem cells. Proc. Natl. Acad. Sci. U S A. **107**, 4872–4877 (2010)
24. Z.A. Cheng, O.F. Zouani, K. Glinel, A.M. Jonas, M.-C. Durrieu, Bioactive chemical nanopatterns impact human mesenchymal stem cell fate. Nano Lett. **13**, 3923–3929 (2013)
25. D.M. Pirone, W.F. Liu, S.A. Ruiz, L. Gao, S. Raghavan, C.A. Lemmon, L.H. Romer, C.S. Chen, An inhibitory role for FAK in regulating proliferation: a link between limited adhesion and rhoA-ROCK signaling. J. Cell Biol. **174**, 277–288 (2006)
26. J.H.C. Wang, B.P. Thampatty, Mechanobiology of adult and stem cells. Int. Rev. Cell Mol. Biol. **271**, 301–346 (2008)
27. D.E. Discher, P. Janmey, Y.-L. Wang, Tissue cells feel and respond to the stiffness of their substrate. Science **310**, 1139–1143 (2005)
28. S. Khetan, M. Guvendiren, W.R. Legant, D.M. Cohen, C.S. Chen, J.A. Burdick, Degradation-mediated cellular traction directs stem cell fate in covalently crosslinked three-dimensional hydrogels. Nat. Mater. **12**, 458–465 (2013)
29. H.B. Wang, M. Dembo, Y.L. Wang, Substrate flexibility regulates growth and apoptosis of normal but not transformed cells. Am. J. Physiol. Cell Physiol. **279**, C1345–1350 (2000)
30. K. Rana, J.L. Liesveld, M.R. King, Delivery of apoptotic signal to rolling cancer cells: a novel biomimetic technique using immobilized trail and e-selectin. Biotechnol. Bioeng. **102**, 1692–1702 (2009)
31. K. Rana, C.A. Reinhart-King, M.R. King, Inducing apoptosis in rolling cancer cells: a combined therapy with aspirin and immobilized trail and e-selectin. Mol. Pharm. **9**, 2219–2227 (2012)
32. S.M. Frisch, H. Francis, Disruption of epithelial cell-matrix interactions induces apoptosis. J. Cell Biol. **124**, 619–626 (1994)
33. A.J. Hale, C.A. Smith, L.C. Sutherland, V.E. Stoneman, V. Longthorne, A.C. Culhane, G.T. Williams, Apoptosis: molecular regulation of cell death. Eur. J. Biochem. **237**, 884 (1996)
34. J.L. Leight, M.A. Wozniak, S. Chen, M.L. Lynch, C.S. Chen, Y. Wang, Matrix rigidity regulates a switch between Tgf-B1—induced apoptosis and epithelial Â€″. Mesenchymal. Transit. **23, 781–791** (2012)
35. E. Hadjipanayi, V. Mudera, R.A. Brown, Close dependence of fibroblast proliferation on collagen scaffold matrix stiffness. J. Tissue Eng. Regen. Med. **3**, 77–84 (2009)
36. D.S. Gray, W.F. Liu, C.J. Shen, K. Bhadriraju, C.M. Nelson, C.S. Chen, Engineering amount of cell-cell contact demonstrates biphasic proliferative regulation through RhoA and the actin cytoskeleton. Exp. Cell Res. **314**, 2846–2854 (2008)
37. R. McBeath, D.M. Pirone, C.M. Nelson, K. Bhadriraju, C.S. Chen, Cell shape, cytoskeletal tension, and Rhoa regulate stem cell lineage commitment. Dev. Cell. **6**, 483–495 (2004)
38. C.M. Nelson, C.S. Chen, Cell-cell signaling by direct contact increases cell proliferation via a Pi3k-dependent signal. FEBS Lett. **514**, 238–242 (2002)
39. C.M. Nelson, C.S. Chen, VE-cadherin simultaneously stimulates and inhibits cell proliferation by altering cytoskeletal structure and tension. J. Cell Sci. **116**, 3571–3581 (2003)
40. Z.a. Cheng, O.F. Zouani, K. Glinel, A.M. Jonas, M.-C. Durrieu, Bioactive chemical nanopatterns impact human mesenchymal stem cell fate. Nano Lett. **13**, 3923–3929 (2013)

41. D.E. Discher, D.J. Mooney, P.W. Zandstra, Growth factors, matrices, and forces combine and control stem cells. Science **324**, 1673–1677 (2009)
42. A.J. Engler, S. Sen, H.L. Sweeney, D.E. Discher, Matrix elasticity directs stem cell lineage specification. Cell **126**, 677–689 (2006)
43. J. Lee, A.A. Abdeen, D. Zhang, K.A. Kilian, Directing stem cell fate on hydrogel substrates by controlling cell geometry, matrix mechanics and adhesion ligand composition. Biomaterials **34**, 8140–8148 (2013)
44. X. Wang, C. Yan, K. Ye, Y. He, Z. Li, J. Ding, Effect of RGD nanospacing on differentiation of stem cells. Biomaterials **34**, 2865–2874 (2013)
45. R.O. Hynes, Integrins: versatility, modulation, and signaling in cell adhesion. Cell **69**, 11–25 (1992)
46. A.S. Goldstein, In *Tissue Engineering,* ed. by J.P. Fisher, A.G. Mikos, J.D. Bronzino. Cell adhesion. (CRC Press, Boca Raton, 2007), pp. 5–1 to 5–17
47. R. Zaidel-Bar, C. Ballestrem, Z. Kam, B. Geiger, Early molecular events in the assembly of matrix adhesions at the leading edge of migrating cells. J. Cell Sci. **116**, 4605–4613 (2003)
48. R. Zaidel-Bar, M. Cohen, L. Addadi, B. Geiger, Hierarchical assembly of cell-matrix adhesion complexes. Biochem. Soc. Trans. **32**, 416–420 (2004)
49. B. Geiger, A. Bershadsky, R. Pankov, K.M. Yamada, Transmembrane crosstalk between the extracellular matrix and the cytoskeleton. Nat. Rev. Mol. Cell. Biol. **2**, 793–805 (2001)
50. B. Geiger, K.M. Yamada, Molecular architecture and function of matrix adhesions. Cold Spring Harb. Perspect. Biol. (2011). doi:10.1101/cshperspect.a005033
51. R. Zaidel-Bar, R. Milo, Z. Kam, B. Geiger, A paxillin tyrosine phosphorylation switch regulates the assembly and form of cell-matrix adhesions. J. Cell Sci. **120**, 137–148 (2007)
52. C. Ballestrem, N. Erez, J. Kirchner, Z. Kam, A. Bershadsky, B. Geiger, Molecular mapping of tyrosine-phosphorylated proteins in focal adhesions using fluorescence resonance energy transfer. J. Cell Sci. **119**, 866–875 (2006)
53. B. Zimerman, T. Volberg, B. Geiger, Early molecular events in the assembly of the focal adhesion-stress fiber complex during fibroblast spreading. Cell Motil. Cytoskeleton. **58**, 143–159 (2004)
54. C.M. Longhurst, L.K. Jennings, Integrin-mediated signal transduction. Cell. Mol. Life Sci. **54**, 514–526 (1998)
55. F.G. Giancotti, E. Ruoslahti, Integrin signaling. Science **285**, 1028–1033 (1999)
56. M.P. Sheetz, D. Felsenfeld, C.G. Galbraith, D. Choquet, Cell migration as a five-step cycle. Biochem. Soc. Symp. **65**, 233–243 (1999)
57. D.A. Lauffenburger, A.F. Horwitz, Cell migration: a physically integrated molecular process. Cell **84**, 359–369 (1996)
58. A. van der Flier, A. Sonnenberg, Function and interactions of integrins. Cell Tissue Res. **305**, 285–298 (2001)
59. S. Huveneers, H. Truong, E.H.J. Danen, Integrins: signaling, disease and therapy. Int. J. Radiat. Biol. **83**, 743–751 (2007)
60. U. Mayer, G. Saher, R. Faessler, A. Bornemann, F. Echtermeyer, H. von der Mark, N. Miosge, E. Poesch, K. von der Mark Absence of integrin alpha 7 causes a novel form of muscular dystrophy. Nat. Genet. **17**, 318–323 (1997)
61. Y.K. Hayashi, F.-L. Chou, E. Engvall, M. Ogawa, C. Matsuda, S. Hirabayashi, K. Yokochi, B.L. Ziober, R.H. Kramer, S.J. Kaufman, E. Ozawa, Y. Goto, I. Nonaka, T. Tsukahara, J. Wang, E.P. Hoffman, K. Arahata, Mutations in the integrin alpha 7 gene cause congenital myopathy. Nat. Genet. **19**, 94–97 (1998)
62. F. Vidal, D. Aberdam, C. Miquel, A.M. Christiano, L. Pulkkinen, J. Uitto, J.-P. Ortonne, G. Meneguzzi, Integrin Beta 4 mutations associated with junctional epidermolysis bullosa with pyloric atresia. Nat. Genet. **10**, 229–234 (1995)
63. C.M. Niessen, L.M.H. van der Raaij-Helmer, E.H.M. Hulsman, R. van der Neut, M.F. Jonkman, A. Sonnenberg, Deficiency of the integrin beta 4 subunit in junctional epidermolysis bullosa with pyloric atresia: consequences for hemidesmosome formation and adhesion properties. J. Cell Sci. **109**, 1695–1706 (1996)

64. L. Ruzzi, L. Gagnoux-Palacios, M. Pinola, S. Belli, G. Meneguzzi, M. D'Alessio, G. Zambruno, A homozygous mutation in the integrin alpha6 gene in junctional epidermolysis bullosa with pyloric atresia. J. Clin. Invest. **99**, 2826–2831 (1997)
65. N. Hogg, P.A. Bates, Genetic analysis of integrin function in man: lad-1 and other syndromes. Matrix Biol. **19**, 211–222 (2000)
66. S.P. Palecek, J.C. Loftus, M.H. Ginsberg, D.A. Lauffenburger, A.F. Horwitz, Integrin-ligand binding properties govern cell migration speed through cell-substratum adhesiveness. Nature **385**, 537–540 (1997)
67. Y. Xue, M.L. O'Mara, P.P.T. Surawski, M. Trau, A.E. Mark, Effect of poly(ethylene glycol) (peg) spacers on the conformational properties of small peptides: a molecular dynamics study. Langmuir **27**, 296–303 (2011)
68. S. Rao, K.W. Anderson, L.G. Bachas, Oriented immobilization of proteins. Mikrochimica Acta **128**, 127–143 (1998)
69. J. Huang, S.V. Graeter, F. Corbellini, S. Rinck, E. Bock, R. Kemkemer, H. Kessler, J. Ding, J.P. Spatz, Impact of order and disorder in RGD nanopatterns on cell adhesion. Nano Lett. **9**, 1111–1116 (2009)
70. S. Sant, M.J. Hancock, J.P. Donnelly, D. Iyer, A. Khademhosseini, Biomimetic gradient hydrogels for tissue engineering. Can. J. Chem. Eng. **88**, 899–911 (2010)
71. J.H. Lee, G. Khang, J.W. Lee, H.B. Lee, Interaction of different types of cells on polymer surfaces with wettability gradient. J. Coll. Interface Sci. **205**, 323–330 (1998)
72. R.J. Pelham, Y. Wang, Cell locomotion and focal adhesions are regulated by substrate flexibility. Proc. Natl. Acad. Sci. U. S. A. **94**, 13661–13665 (1997)
73. D.E. Discher, P. Janmey, Y. Wang, Tissue cells feel and respond to the stiffness of their substrate. Science **310**, 1139–1143 (2005)
74. J.-P. Kaiser, A. Reinmann, A. Bruinink, The effect of topographic characteristics on cell migration velocity. Biomaterials **27**, 5230–5241 (2006)
75. J.L. West, J.A. Hubbell, Polymeric biomaterials with degradation sites for proteases involved in cell migration. Macromolecules **32**, 241–244 (1999)
76. J.B. McCarthy, S.L. Palm, L.T. Furcht, Migration by haptotaxis of a schwann cell tumor line to the basement membrane glycoprotein laminin. J. Cell Biol. **97**, 772–777 (1983)
77. S.B. Carter, Haptotaxis and the mechanism of cell motility. Nature **213**, 256–260 (1967)
78. B. Harland, S. Walcott, S.X. Sun, Adhesion dynamics and durotaxis in migrating cells. Phys. Biol. **8**, 015011 (2011)
79. L.G. Vincent, Y.S. Choi, B. Alonso-Latorre, J.C. del Alamo, A.J. Engler, Mesenchymal stem cell durotaxis depends on substrate stiffness gradient strength. Biotechnol. J. **8**, 472–484 (2013)
80. M.D. Pierschbacher, E. Ruoslahti, Cell attachment activity of fibronectin can be duplicated by small synthetic fragments of the molecule. Nature **309**, 30–33 (1984)
81. I. Schvartz, D. Seger, S. Shaltiel, Vitronectin. Int. J. Biochem. Cell Biol. **31**, 539–544 (1999)
82. L. Liaw, V. Lindner, S.M. Schwartz, A.F. Chambers, C.M. Giachelli, osteopontin and beta 3 integrin are coordinately expressed in regenerating endothelium in vivo and stimulate Arg-Gly-Asp–dependent endothelial migration in vitro. Circ. Res. **77**, 665–672 (1995)
83. K.M. Malinda, H.K. Kleinman, The laminins. Int. J. Biochem. Cell. Biol. **28**, 957–959 (1996)
84. A.V. Taubenberger, M.A. Woodruff, H. Bai, D.J. Muller, D.W. Hutmacher, The effect of unlocking RGD-motifs in collagen I on Pre-osteoblast adhesion and differentiation. Biomaterials **31**, 2827–2835 (2010)
85. E. Ruoslahti, RGD and other recognition sequences for integrins. Annu. Rev. Cell. Dev. Biol. **12**, 697–715 (1996)
86. M.C. Farach-Carson, R.C. Wagner, K.L. Kiick, In *Tissue Engineering,* ed. by J.P. Fisher, A.G. Mikos, J.D. Bronzino, Extracellular matrix: structure, function, and applications to tissue engineering. (CRC Press, Boca Raton, 2007), pp. 3–1 to 3–22
87. J.E. Frith, R.J. Mills, J.E. Hudson, J.J. Cooper-White, Tailored integrin-extracellular matrix interactions to direct human mesenchymal stem cell differentiation. Stem Cells Dev. **21**, 2442–2456 (2012)

88. T.H. Barker, The role of ecm proteins and protein fragments in guiding cell behavior in regenerative medicine. Biomaterials **32**, 4211–4214 (2011)
89. S.P. Massia, J.A. Hubbell, Vascular endothelial cell adhesion and spreading promoted by the peptide redv of the iiics region of plasma fibronectin is mediated by integrin alpha 4 beta 1. J. Biol. Chem. **267**, 14019–14026 (1992)
90. A.M. Wojtowicz, A. Shekaran, M.E. Oest, K.M. Dupont, K.L. Templeman, D.W. Hutmacher, R.E. Guldberg, A.J. Garcia, Coating of biomaterial scaffolds with the collagen-mimetic peptide GFOGER for bone defect repair. Biomaterials **31**, 2574–2582 (2010)
91. Y.Q. Liu, D.R. Senger, Matrix-specific activation of src and rho initiates capillary morphogenesis of endothelial cells. Faseb. J. **18**, 457–468 (2004)
92. M. Arnold, V.C. Hirschfeld-Warneken, T. Lohmueller, P. Heil, J. Bluemmel, E.A. Cavalcanti-Adam, M. López-García, P. Walther, H. Kessler, B. Geiger, J.P. Spatz, Induction of cell polarization and migration by a gradient of nanoscale variations in adhesive ligand spacing. Nano Lett. **8**, 2063–2069 (2008)
93. U. Hersel, C. Dahmen, H. Kessler, RGD modified polymers: biomaterials for stimulated cell adhesion and beyond. Biomaterials **24**, 4385–4415 (2003)
94. G.A. Monteiro, A.V. Fernandes, H.G. Sundararaghavan, D.I. Shreiber, Positively and negatively modulating cell adhesion to type i collagen via peptide grafting. Tissue Eng. Part A. **17**, 1663–1673 (2009)
95. D.L. Hern, J.A. Hubbell, Incorporation of adhesion peptides into nonadhesive hydrogels useful for tissue resurfacing. J. Biomed. Mater. Res. **39**, 266–276 (1997)
96. A.S. Gobin, J.L. West, Effects of epidermal growth factor on fibroblast migration through biomimetic hydrogels. Biotechnol. Prog. **19**, 1781–1785 (2003)
97. C.L. Jackson, M.A. Reidy, Basic fibroblast growth factor: its role in the control of smooth muscle cell migration. Am. J. Pathol. **143**, 1024–1031 (1993)
98. S.A. DeLong, J.J. Moon, J.L. West, Covalently immobilized gradients of Bfgf on hydrogel scaffolds for directed cell migration. Biomaterials **26**, 3227–3234 (2005)
99. J.E. Leslie-Barbick, C. Shen, C. Chen, J.L. West, Micron-scale spatially patterned, covalently immobilized vascular endothelial growth factor on hydrogels accelerates endothelial tubulogenesis and increases cellular angiogenic responses. Tissue Eng. Part A. **17**, 221–229 (2011)
100. G.S. Schultz, A. Wysocki, Interactions between extracellular matrix and growth factors in wound healing. Wound Repair Regen. **17**, 153–162 (2009)
101. H.L. Ashe, J. Briscoe, The interpretation of morphogen gradients. Development **133**, 385–394 (2006)
102. K.S. Midwood, G. Orend, The role of tenascin-C in tissue injury and tumorigenesis. J. Cell. Commun. Signal. **3**, 287–310 (2009)
103. Z. Lopez-Dee, K. Pidcock, L.S. Gutierrez, Thrombospondin-1: multiple paths to inflammation. Mediat. Inflamm. **2011**, 1–10 (2011)
104. S.A. Arnold, R.A. Brekken, Sparc: a matricellular regulator of tumorigenesis. J. Cell. Commun. Signal. **3**, 255–273 (2009)
105. A.E. Rodda, L. Meagher, D.R. Nisbet, J.S. Forsythe, Specific control of cell-material interactions: targeting cell receptors using ligand-functionalized polymer substrates. Prog. Polym. Sci. **39**, 1312–1347 (2014)
106. R. Vasita, K. Shanmugam, D.S. Katti, Improved biomaterials for tissue engineering applications—surface modification of polymers. Curr. Top. Med. Chem. **8**, 341–353 (2008)
107. J.H. Slater, J.S. Miller, S.S. Yu, J.L. West, Fabrication of multifaceted micropatterned surfaces with laser scanning lithography. Adv. Funct. Mater. **21**, 2876–2888 (2011)
108. M.S. Hahn, J.S. Miller, J.L. West, Laser scanning lithography for surface micropatterning on hydrogels. Adv. Mater. **17**, 2939–2942 (2005)
109. J.H. Slater, J.C. Culver, B.L. Long, C.W. Hu, J. Hu, T.F. Birk, A.A. Qutub, M.E. Dickinson, J.L. West, Recapitulation and modulation of the cellular architecture of a user-chosen cell of interest using cell-derived, biomimetic patterning. ACS Nano **9**, 6128–6138 (2015)

110. J.H. Slater, J.L. West, Fabrication of multifaceted, micropatterned surfaces and image-guided patterning using laser scanning lithography. Methods. Cell. Biol. **119**, 193–217 (2014)
111. J.C. Culver, J.C. Hoffmann, R.A. Poché, J.H. Slater, J.L. West, M.E. Dickinson, Three-dimensional biomimetic patterning in hydrogels to guide cellular organization. Adv. Mater. **24**, 2344–2348 (2012)
112. S.R.K. Vedula, H. Hirata, M.H. Nai, A. Brugues, Y. Toyama, X. Trepat, C.T. Lim, B. Ladoux, Epithelial bridges maintain tissue integrity during collective cell migration. Nat. Mater. **13**, 87–96 (2013)
113. J. Goulpeau, B. Lonetti, D. Trouchet, A. Ajdari, P. Tabeling, Building up longitudinal concentration gradients in shallow microchannels. Lab. Chip. **7**, 1154–1161 (2007)
114. S. Allazetta, S. Cosson, M.P. Lutolf, Programmable microfluidic patterning of protein gradients on hydrogels. Chem. Commun. **47**, 191–193 (2011)
115. R. Glass, M. Moeller, J.P. Spatz, Block copolymer micelle nanolithography. Nanotechnology **14**, 1153–1160 (2003)
116. G.T. Hermanson, *Bioconjugate Techniques* (Academic Press, Waltham, 2008), p. 1323
117. K.-B. Lee, S.-J. Park, C.A. Mirkin, J.C. Smith, M. Mrksich, Protein nanoarrays generated by dip-pen nanolithography. Science **295**, 1702–1705 (2002)
118. D.S. Ginger, H. Zhang, C.A. Mirkin, The evolution of dip-pen nanolithography. Angew. Chem. Int. Ed. Eng. **43**, 30–45 (2004)
119. J.H. Slater, P.J. Boyce, M.P. Jancaitis, H.E. Gaubert, A.L. Chang, M.K. Markey, W. Frey, Modulation of endothelial cell migration via manipulation of adhesion site growth using nanopatterned surfaces. ACS. Appl. Mater. Interfaces. **7**, 4390–4400 (2015)
120. J.H. Slater, W. Frey, Nanopatterning of fibronectin and the influence of integrin clustering on endothelial cell spreading and proliferation. J. Biomed. Mater. Res. Part A. **87A**, 176–195 (2008)
121. V. Vogel, M. Sheetz,Local force and geometry sensing regulate cell functions. Nat. Rev. Mol. Cell. Biol. **7**, 265–275 (2006)
122. S.F. Badylak, D.O. Freytes, T.W. Gilbert, Extracellular matrix as a biological scaffold material: structure and function. Acta. Biomater. **5**, 1–13 (2009)
123. K. Poole, K. Khairy, J. Friedrichs, C. Franz, D.A. Cisneros, J. Howard, D. Mueller, Molecular-scale topographic cues induce the orientation and directional movement of fibroblasts on two-dimensional collagen surfaces. J. Mol. Biol. **349**, 380–386 (2005)
124. G. Maheshwari, G. Brown, D.A. Lauffenburger, A. Wells, L.G. Griffith Cell adhesion and motility depend on nanoscale RGD clustering. J. Cell. Sci. **113**, 1677–1686 (2000)
125. J.E. Frith, R.J. Mills, J.J. Cooper-White, Lateral spacing of adhesion peptides influences human mesenchymal stem cell behaviour. J. Cell. Sci. **125**, 317–327 (2012)
126. M. Arnold, E.A. Cavalcanti-Adam, R. Glass, J. Bluemmel, W. Eck, M. Kantlehner, H. Kessler, J.P. Spatz, Activation of integrin function by nanopatterned adhesive interfaces. ChemPhysChem **5**, 383–388 (2004)
127. D.R. Critchley, A.R. Gingras, Talin at a glance. J. Cell. Sci. **121**, 1345–1347 (2008)
128. M. Schvartzman, M. Palma, J. Sable, J. Abramson, X. Hu, M.P. Sheetz, S.J. Wind, Nanolithographic control of the spatial organization of cellular adhesion receptors at the single-molecule level. Nano Lett. **11**, 1306–1312 (2011)
129. K.A. Diehl, J.D. Foley, P.F. Nealey, C.J. Murphy, Nanoscale topography modulates corneal epithelial cell migration. J. Biomed. Mater. Res. A. **75A**, 603–611 (2005)
130. E. Lamers, J.T. Riet, M. Domanski, R. Luttge, C.G. Figdor, J.G.E. Gardeniers, X.F. Walboomers, J.A. Jansen, Dynamic cell adhesion and migration on nanoscale grooved substrates. Eur. Cell. Mater. **23**, 182–194 (2012)
131. J.Y. Lim, H.J. Donahue Cell sensing and response to micro- and nanostructured surfaces produced by chemical and topographic patterning. Tissue. Eng. **13**, 1879–1891 (2007)
132. L.E. Dickinson, D.R. Rand, J. Tsao, W. Eberle, S. Gerecht, Endothelial cell responses to micropillar substrates of varying dimensions and stiffness. J. Biomed. Mater. Res. A. **100A**, 1457–1466 (2012)

133. S.A. Biela, Y. Su, J.P. Spatz, R. Kemkemer, Different sensitivity of human endothelial cells, smooth muscle cells and fibroblasts to topography in the nano-micro range. Acta. Biomater. **5**, 2460–2466 (2009)
134. J.J. Moon, M.S. Hahn, I. Kim, B.A. Nsiah, J.L. West, Micropatterning of poly (ethylene glycol) diacrylate hydrogels with biomolecules to regulate and guide endothelial morphogenesis. Tissue. Eng. Part A. **15**, 579–585 (2008)
135. M.M. Martino, F. Tortelli, M. Mochizuki, S. Traub, D. Ben-David, G.A. Kuhn, R. Mueller, E. Livne, S.A. Eming, J.A. Hubbell, Engineering the growth factor microenvironment with fibronectin domains to promote wound and bone tissue healing. Sci. Transl. Med. **3**, 100ra89 (2011)
136. M.M. Martino, P.S. Briquez, A. Ranga, M.P. Lutolf, J.A. Hubbell, Heparin-binding domain of fibrin(ogen) binds growth factors and promotes tissue repair when incorporated within a synthetic matrix. Proc. Natl. Acad. Sci. U S A. **110**, 4563–4568 (2013)
137. M.M. Martino, P.S. Briquez, E. Guc, F. Tortelli, W.W. Kilarski, S. Metzger, J.J. Rice, G.A. Kuhn, R. Mueller, M.A. Swartz, J.A. Hubbell, Growth factors engineered for super-affinity to the extracellular matrix enhance tissue healing. Science **343**, 885–888 (2014)
138. B. Trappmann, C.S. Chen, How cells sense extracellular matrix stiffness: a material's perspective. Curr. Opin. Biotechnol. **24**, 948–953 (2013)
139. R.G. Wells, The role of matrix stiffness in regulating cell behavior. Hepatology **47**, 1394–1400 (2008)
140. C.-M. Lo, H.-B. Wang, M. Dembo, Y. Wang, Cell movement is guided by the rigidity of the substrate. Biophys. J. **79**, 144–152 (2000)
141. S.C. Wei, L. Fattet, J.H. Tsai, Y. Guo, V.H. Pai, H.E. Majeski, A.C. Chen, R.L. Sah, S.S. Taylor, A.J. Engler, J. Yang, Matrix stiffness drives epithelial-mesenchymal transition and tumour metastasis through a twist1-G3bp2 mechanotransduction pathway. Nat. Cell. Biol. **17**, 678–688 (2015)
142. J.H. Wen, L.G. Vincent, A. Fuhrmann, Y.S. Choi, K.C. Hribar, H. Taylor-Weiner, S. Chen, A.J. Engler, Interplay of matrix stiffness and protein tethering in stem cell differentiation. Nat. Mater. **13**, 979–987 (2014)
143. J.R. Tse, A.J. Engler, Stiffness gradients mimicking in vivo tissue variation regulate mesenchymal stem cell fate. PLoS ONE **6**, 9 (2011)
144. F. Rehfeldt, A.J. Engler, A. Eckhardt, F. Ahmed, D.E. Discher, Cell responses to the mechanochemical microenvironment–implications for regenerative medicine and drug delivery. Adv. Drug. Deliv. Rev. **59**, 1329–1339 (2007)
145. A.J. Engler, S. Sen, H.L. Sweeney, D.E. Discher, Matrix elasticity directs stem cell lineage specification. Cell **126**, 677–689 (2006)
146. C.-H.R. Kuo, J. Xian, J.D. Brenton, K. Franze, E. Sivaniah, Complex stiffness gradient substrates for studying mechanotactic cell migration. Adv. Mater. **24**, 6059–6064 (2012)
147. J.Hc Wang, B. Li, in *Microscopy: Science, Technology, Applications, and Education,* vol.1, ed. A. Mendez-Vilas, J.Diaz The principles and biological applications of cell traction force microscopy. (2010), 449–458
148. H. Zhang, L. Wang, L. Song, G. Niu, H. Cao, G. Wang, H. Yang, S. Zhu, Controllable properties and microstructure of hydrogels based on crosslinked poly (ethylene glycol) diacrylates with different molecular weights. J. Appl. Polym. Sci. **121**, 531–540 (2011)
149. J.H. Sung, M.-R. Hwang, J.O. Kim, J.H. Lee, Y.I. Kim, J.H. Kim, S.W. Chang, S.G. Jin, J.A. Kim, W.S. Lyoo, S.S. Han, S.K. Ku, C.S. Yong, H.-G. Choi, Gel characterisation and in vivo evaluation of minocycline-loaded wound dressing with enhanced wound healing using polyvinyl alcohol and chitosan. Int. J. Pharm. **392**, 232–240 (2010)
150. G.M. Harris, M.E. Piroli, E. Jabbarzadeh, Deconstructing the effects of matrix elasticity and geometry in mesenchymal stem cell lineage commitment. Adv. Funct. Mater. **24**, 2396–2403 (2014)
151. J.Y. Wong, A. Velasco, P. Rajagopalan, Q. Pham, Directed movement of vascular smooth muscle cells on gradient-compliant hydrogels. Langmuir **19**, 1908–1913 (2003)

152. S. Nemir, H.N. Hayenga, J.L. West, Pegda hydrogels with patterned elasticity: novel tools for the study of cell response to substrate rigidity. Biotechnol. Bioeng. **105**, 636–644 (2010)
153. N. Zaari, P. Rajagopalan, S.K. Kim, A.J. Engler, J.Y. Wong, Photopolymerization in microfluidic gradient generators: microscale control of substrate compliance to manipulate cell response. Adv. Mater. **16**, 2133–2137 (2004)
154. S. Sen, A.J. Engler, D.E. Discher, Matrix strains induced by cells: computing how far cells can feel. Cell. Mol. Bioeng. **2**, 39–48 (2009)
155. J. Maloney, E. Walton, C. Bruce, K. Van Vliet, Influence of finite thickness and stiffness on cellular adhesion-induced deformation of compliant substrata. Phys. Rev. E. **78**, 041923 (2008)
156. D.S. Gray, J. Tien, C.S. Chen, Repositioning of cells by mechanotaxis on surfaces with micropatterned Young's Modulus. J. Biomed. Mater. Res. A. **66**, 605–614 (2003)
157. S. Kidoaki, T. Matsuda, Microelastic gradient gelatinous gels to induce cellular mechanotaxis. J. Biotechnol. **133**, 225–230 (2008)
158. E.L. Baker, J. Srivastava, D. Yu, R.T. Bonnecaze, M.H. Zaman, Cancer cell migration: integrated roles of matrix mechanics and transforming potential. PLoS ONE **6**, 3700–3711 (2011)
159. R. McBeath, D.M. Pirone, C.M. Nelson, K. Bhadriraju, C.S. Chen, Cell shape, cytoskeletal tension, and rhoa regulate stem cell lineage commitment. Dev. Cell. **6**, 483–495 (2004)
160. K.A. Kilian, B. Bugarija, B.T. Lahn, M. Mrksich, Geometric cues for directing the differentiation of mesenchymal stem cells. Proc. Natl. Acad. Sci. U S A. **107**, 4872–4877 (2010)
161. M. Thery, Micropatterning as a tool to decipher cell morphogenesis and functions. J. Cell Sci. **123**, 4201–4213 (2010).
162. R. Singhvi, A. Kumar, G.P. Lopez, G.N. Stephanopoulos, D.I.C. Wang, G.M. Whitesides, D.E. Ingber, Engineering cell-shape and function. Science **264**, 696–698 (1994)
163. M. Thery, V. Racine, M. Piel, A. Pepin, A. Dimitrov, Y. Chen, J.B. Sibarita, M. Bornens, Anisotropy of cell adhesive microenvironment governs cell internal organization and orientation of polarity. Proc. Natl. Acad. Sci. U S A. **103**, 19771–19776 (2006)
164. J. James, E.D. Goluch, H. Hu, C. Liu, M. Mrksich, Subcellular curvature at the perimeter of micropatterned cells influences lamellipodial distribution and cell polarity. Cell. Motil. Cytoskeleton. **65**, 841–852 (2008)
165. N. Xia, C.K. Thodeti, T.P. Hunt, Q.B. Xu, M. Ho, G.M. Whitesides, R. Westervelt, D.E. Ingber, Directional control of cell motility through focal adhesion positioning and spatial control of rac activation. Faseb. J. **22**, 1649–1659 (2008)
166. J.M. Goffin, P. Pittet, G. Csucs, J.W. Lussi, J.J. Meister, B. Hinz, Focal adhesion size controls tension-dependent recruitment of alpha-smooth muscle actin to stress fibers. J. Cell Biol. **172**, 259–268 (2006)
167. D. Lehnert, B. Wehrle-Haller, C. David, U. Weiland, C. Ballestrem, B.A. Imhof, M. Bastmeyer, Cell behaviour on micropatterned substrata: limits of extracellular matrix geometry for spreading and adhesion. J. Cell Sci. **117**, 41–52 (2004)
168. J.A. Deeg, I. Louban, D. Aydin, C. Selhuber-Unkel, H. Kessler, J.P. Spatz, Impact of local versus global ligand density on cellular adhesion. Nano. Lett. **11**, 1469–1476 (2011)
169. M. Thery, A. Pepin, E. Dressaire, Y. Chen, M. Bornens, Cell distribution of stress fibres in response to the geometry of the adhesive environment. Cell. Motil. Cytoskeleton. **63**, 341–355 (2006)
170. W.F. Liu, C.S. Chen, Cellular and multicellular form and function. Adv Drug Deliv. Rev. **59**, 1319–1328 (2007)
171. S. Huang, D.E. Ingber, The structural and mechanical complexity of cell-growth control. Nat. Cell. Biol. **1**, E131–138 (1999)
172. R.A. Foty, M.S. Steinberg, The differential adhesion hypothesis: a direct evaluation. Dev. Biol. **278**, 255–263 (2005)
173. J. Lee, A.A. Abdeen, D. Zhang, K.A. Kilian, Directing stem cell fate on hydrogel substrates by controlling cell geometry, matrix mechanics and adhesion ligand composition. Biomaterials **34**, 8140–8148 (2013)

174. P.C.D.P. Dingal, D.E. Discher, Combining insoluble and soluble factors to steer stem cell fate. Nat. Mater. **13**, 532–537 (2014)
175. W.F. Liu, C.M. Nelson, D.M. Pirone, C.S. Chen, E-cadherin engagement stimulates proliferation via Rac1. J. Cell. Biol. **173**, 431–441 (2006)
176. Y. Xia, G.M. Whitesides, Soft lithography. Annu. Rev. Mater. Sci. **28**, 153–184 (1998)
177. C.J. Shen, S. Raghavan, Z. Xu, J.D. Baranski, X. Yu, M.a. Wozniak, J.S. Miller, M. Gupta, L. Buckbinder, C.S. Chen, Decreased cell adhesion promotes angiogenesis in a Pyk2-dependent manner. Exp. Cell. Res. **317**, 1860–1871 (2011)
178. N.Q. Balaban, U.S. Schwarz, D. Riveline, P. Goichberg, G. Tzur, I. Sabanay, D. Mahalu, S. Safran, A. Bershadsky, L. Addadi, B. Geiger, Force and focal adhesion assembly: a close relationship studied using elastic micropatterned substrates. Nat. Cell. Biol. **3**, 466–472 (2001)
179. S.M. Frisch, K. Vuori, E. Ruoslahti, P.Y. Chan-Hui, Control of adhesion-dependent cell survival by focal adhesion kinase. J. Cell. Biol. **134**, 793–799 (1996)
180. A. Hamadi, M. Bouali, M. Dontenwill, H. Stoeckel, K. Takeda, P. Rondé, Regulation of focal adhesion dynamics and disassembly by phosphorylation of fak at tyrosine 397. J. Cell. Sci. **118**, 4415–4425 (2005)
181. C. Lieu, S. Kpoetz, The Src family of protein tyrosine kinases: a new and promising traget for colorectal cancer therapy. Clin. Colorectal. Cancer. **9**, 89–94 (2010)
182. S.-Y. Tee, J. Fu, C.S. Chen, P.A. Janmey, Cell shape and substrate rigidity both regulate cell stiffness. Biophys. J. **100**, L25–27 (2011)
183. K. Shin, V.C. Fogg, B. Margolis, Tight junctions and cell polarity. Annu. Rev. Cell. Dev. Biol. **22**, 207–235 (2006)
184. B.M. Gumbiner, Regulation of cadherin-mediated adhesion in morphogenesis. Nat. Rev. Mol. Cell. Biol. **6**, 622–634 (2005)
185. I. Gutcher, B. Becher, Apc-derived cytokines and t cell polarization in autoimmune inflammation. J. Clin. Invest. **117**, 1119–1127 (2007)
186. J.I. Nagy, F.E. Dudek, J.E. Rash, Update on connexins and gap junctions in neurons and glia in the mammalian nervous system. Brain. Res. Brain. Res. Rev. **47**, 191–215 (2004)
187. K. Sugimoto, N. Ichikawa-Tomikawa, S. Satohisa, Y. Akashi, R. Kanai, T. Saito, N. Sawada, H. Chiba, The tight-junction protein claudin-6 induces epithelial differentiation from mouse F9 and embryonic stem cells. PloS ONE **8**, e75106 (2013)
188. N. Borghi, M. Lowndes, V. Maruthamuthu, M.L. Gardel, W.J. Nelson, Regulation of cell motile behavior by crosstalk between cadherin- and integrin-mediated adhesions. Proc. Natl. Acad. Sci. U S A. **107**, 13324–13329 (2010)
189. C. Rüffer, V. Gerke, The C-terminal cytoplasmic tail of claudins 1 and 5 but not its Pdz-binding motif is required for apical localization at epithelial and endothelial tight junctions. Eur. J. Cell. Biol. **83**, 135–144 (2004)
190. A.J. Torres, R.L. Contento, S. Gordo, K.W. Wucherpfennig, J.C. Love, Functional single-cell analysis of T-cell activation by supported lipid bilayer-tethered ligands on arrays of nanowells. Lab. Chip. **13**, 90–99 (2013)
191. L.K. Buehler, K.A. Stauffer, N.B. Gilula, N.M. Kumar, Single channel behavior of recombinant beta 2 gap junction connexons reconstituted into planar lipid bilayers. Biophy. J. **68**, 1767–1775 (1995)
192. R. Tsuruta, R.R. Cobb, M. Mastrangelo, E. Lazarides, P.M. Cardarelli, C. Ltc, Soluble vascular cell adhesion molecule (VCAM)-Fc fusion protein induces leukotriene C4 secretion in platelet-activating factor-stimulated eosinophils abstract: eosinophil adhesion to vascular cell adhesion molecule-1 (Vcam-1) is important for cell. J Leukoc Biol. **65**, 71–79 (1999)
193. J. Gavard, J.S. Gutkind, Vegf controls endothelial-cell permeability by promoting the beta-arrestin-dependent endocytosis of Ve-cadherin. Nat. Cell. Biol. **8**, 1223–1234 (2006)
194. F. Drees, A. Reilein, W.J. Nelson, Cell-adhesion assays: fabrication of an E-cadherin substratum and isolation of lateral and basal membrane patches. Methods. Mol. Biol. **294**, 303–320 (2005)

195. T. Ozawa, M. Horii, E. Kobayashi, A. Jin, H. Kishi, A. Muraguchi, The binding affinity of a soluble Tcr-Fc fusion protein is significantly improved by crosslinkage with an anti-Cb antibody. Biochem. Biophys. Res. Commun. **422**, 245–249 (2012)
196. T.D. Perez, W.J. Nelson, S.G. Boxer, L. Kam, E-cadherin tethered to micropatterned supported lipid bilayers as a model for cell adhesion. Langmuir **21**, 11963–11968 (2005)
197. C.-J. Huang, N.-J. Cho, C.-J. Hsu, P.-Y. Tseng, C.W. Frank, Y.-C. Chang, Type I collagen-functionalized supported lipid bilayer as a cell culture platform. Biomacromolecules **11**, 1231–1240 (2010)
198. J.T. Groves, M.L. Dustin, Supported planar bilayers in studies on immune cell adhesion and communication. J. Immunol. Methods. **278**, 19–32 (2003)
199. K. Shen, V.K. Thomas, M.L. Dustin, L.C. Kam, Micropatterning of costimulatory ligands enhances Cd4 + T cell functio*n.* Proc. Natl. Acad. Sci. U S A. **105**, 7791–7796 (2008)
200. L. Geppert, Semiconductor lithography for the next millennium. Spectrum, IEEE 33–38 (1996)
201. D. Fichtner, B. Lorenz, S. Engin, C. Deichmann, M. Oelkers, A. Janshoff, A. Menke, D. Wedlich, C.M. Franz, Covalent and density-controlled surface immobilization of e-cadherin for adhesion force spectroscopy. PloS One **9**, e93123 (2014)
202. K. Czöndör, M. Garcia, A. Argento, A. Constals, C. Breillat, B. Tessier, O. Thoumine, Micropatterned substrates coated with neuronal adhesion molecules for high-content study of synapse formation. Nat. Commun. **4**, 2252 (2013)
203. P. Shi, K. Shen, L.C. Kam, Local presentation of L1 and N-cadherin in multicomponent, microscale patterns differentially direct neuron function in vitro. Dev. Neurobiol. **67**, 1765–1776 (2007)
204. A.D. Doyle, F.W. Wang, K. Matsumoto, K.M. Yamada, One-dimensional three-dimensional underlies topography fibrillar cell migration. J. Cell. Biol. **184**, 481–490 (2014)
205. J.H. Slater, J.L. West, *Fabrication of Multifaceted, Micropatterned Surfaces and Image-Guided Patterning Using Laser Scanning Lithography*, 1st ed., vol. 119 (Elsevier Inc., Amsterdam, 2014), p 193–217
206. E.T. Castellana, P.S. Cremer, Solid supported lipid bilayers: from biophysical studies to sensor design. Surface. Sci. Rep. **61**, 429–444 (2006)
207. P. Mueller, D.O. Rudin, H.T. Tien, W.C. Wescott, Reconstitution of cell membrane structure in vitro and its transformation into an excitable system. Nature **194**, 979–980 (1962)
208. K.L. Weirich, J.N. Israelachvili, D.K. Fygenson, Bilayer edges catalyze supported lipid bilayer formation. Biophys. J. **98**, 85–92 (2010)
209. K. Funakoshi, H. Suzuki, S. Takeuchi, Lipid bilayer formation by contacting monolayers in a microfluidic device for membrane protein analysis. Anal. Chem. **78**, 8169–8174 (2006)
210. J.T. Groves, N. Ulman, S.G. Boxer, Micropatterning fluid lipid bilayers on solid supports. Science **275**, 651–653 (1997)
211. B.A. Suarez-isla, K. Wan, J. Lindstrom, M. Montal, Bio. Single-channel recordings from purified acetylcholine receptors. 10 634–636 22(1983)
212. S.J. Johnson, T.M. Bayerl, D.C. McDermott, G.W. Adam, A.R. Rennie, R.K. Thomas, E. Sackmann Structure of an adsorbed dimyristoylphosphatidylcholine bilayer measured with specular reflection of neutrons. Biophys. J. **59**, 289–294 (1991)
213. T. Wang, D. Li, X. Lu, A. Khmaladze, X. Han, S. Ye, P. Yang, G. Xue, N. He, Z. Chen, Single lipid bilayers constructed on polymer cushion studied by sum frequency generation vibrational spectroscopy. J. Phys. Chem. C Nanomater. Interfaces. **115**, 7613–7620 (2011)
214. E. Sackmann, M. Tanaka, Supported membranes on soft polymer cushions: fabrication, characterization and applications. Trends. Biotechnol. **18**, 58–64 (2000).
215. S. Chevalier, C. Cuestas-Ayllon, V. Grazu, M. Luna, H. Feracci, J.M. de la Fuente, Creating biomimetic surfaces through covalent and oriented binding of proteins. Langmuir **26**, 14707–14715 (2010)
216. S.F. Evans, D. Docheva, A. Bernecker, C. Colnot, R.P. Richter, M.L. Knothe, Biomaterials solid-supported lipid bilayers to drive stem cell fate and tissue architecture using periosteum derived progenitor cells. Biomaterials **34**, 1878–1887 (2013)

217. D.J. Powell, B.L. Levine, Adoptive T-cell therapy for malignant disorders. Haematologica **93**, 1452–1456 (2008).
218. C.H. June, Adoptive T cell therapy for cancer in the clinic. J. Clin. Invest. **117**, 1466–1476 (2007)
219. E.R. Unanue, Antigen-presenting function of the macrophage. Annu. Rev. Immunol. **2**, 395–428 (1984)
220. A. Grakoui, S.K. Bromley, C. Sumen, M.M. Davis, The immunological synapse: a molecular machine controlling T cell activation. Science **285**, 221–227 (1999)
221. M.M. Davis, M. Krogsgaard, J.B. Huppa, C. Sumen, M.a. Purbhoo, D.J. Irvine, L.C. Wu, L. Ehrlich, Dynamics of cell surface molecules during T cell recognition. Annu. Rev. Biochem. **72**, 717–742 (2003)
222. C.R.F. Monks, B.A. Freiberg, H. Kupfer, N. Sciaky, A. Kupfer, Three-dimensional segregation of supramolecular activation clusters in T cells. Nature **340**, 764–766 (1998)
223. E. Judokusumo, E. Tabdanov, S. Kumari, M.L. Dustin, L.C. Kam Mechanosensing in T lymphocyte activation. Biophys. J. **102**, L5–7 (2012)
224. K.T. Bashour, J. Tsai, K. Shen, J.-H. Lee, E. Sun, M.C. Milone, M.L. Dustin, L.C. Kam, Cross talk between Cd3 and Cd28 is spatially modulated by protein lateral mobility. Mol. Cell. Biol. **34**, 955–964 (2014)
225. R.G. Spatz, M. Martin, P. Joachim, Block copolymer micelle nanolithography. Nanotechnology **14**, 1153 (2003)
226. J. Matic, J. Deeg, A. Scheffold, I. Goldstein, J.P. Spatz, Fine tuning and efficient T cell activation with stimulatory Acd3 nanoarrays. Nano Lett. **13**, 5090–5097 (2013)

Index

M. Zhang et al. (eds.), *Carbon Nanomaterials for Biomedical Applications,*
Springer Series in Biomaterials Science and Engineering 5,
DOI 10.1007/978-3-319-22861-7